annual progress report

2008

VEHICLE TECHNOLOGIES PROGRAM

LIGHTWEIGHTING MATERIALS

U.S. Department of Energy
Energy Efficiency and Renewable Energy
Bringing you a prosperous future where energy is clean, abundant, reliable, and affordable

U.S. Department of Energy
Vehicle Technologies Program
1000 Independence Avenue S.W.
Washington, D.C. 20585-0121

FY 2008

Progress Report for Lightweighting Materials

Energy Efficiency and Renewable
Energy Office of Vehicle Technologies

Patrick Davis
Acting Program Manager, Vehicle Technologies Program

Carol Schutte
Team Leader, Advanced Materials Technology

Joseph Carpenter
Technology Area Development Manager

December 2009

CONTENTS

1. INTRODUCTION 1-1
2. AUTOMOTIVE METALS—WROUGHT 2-1
   - A. Thermomechanical Processing Design for Lightweight Materials 2-1
   - B. Development of High-Volume Warm Forming of Low-Cost Magnesium Sheet (AMD602) 2-26
   - C. Electromagnetic Forming of Aluminum Sheet 2-43
   - D. Pulse Pressure Forming of Lightweight Materials 2-48
   - E. Ultrafine Grained Foils and Sheets by Large Strain Machining Processes 2-51
   - F. Formability of Continuous Cast Magnesium Sheet 2-54
   - G. Development of High-Strength Superplastic Forming Aluminum Sheet for Automotive Applications 2-57
   - H. Aluminum Automotive Closure Panel Corrosion Test Program 2-61
3. AUTOMOTIVE METALS—CAST 3-1
   - A. Improved Automotive Suspension Components Cast with B206 Alloy 3-1
   - B. Magnesium Powertrain Cast Components (AMD304) 3-10
   - C. Ultra-Large Castings of Aluminum and Magnesium (AMD406) 3-18
   - D. High Integrity Magnesium Automotive Castings (AMD601) 3-27
   - E. Casting/Solidification of Magnesium Alloys 3-32
   - F. Multi-Material Metallurgical Bond Joining to Steel 3-42
4. AUTOMOTIVE METALS—TITANIUM 4-1
   - A. Low-Cost Titanium Powder for Feedstock 4-1
   - B. Production of Heavy Vehicle Components from Low-Cost Titanium Powder 4-7
   - C. Powder-Metal Performance Modeling of Automotive Components (AMD410) 4-14
   - D. Examining Fundamental Mechanisms of Tooling Wear for Powder Processing 4-25
5. AUTOMOTIVE METALS—STEEL 5-1
   - A. High-Strength Steel Joining Technologies 5-1
   - B. Hydroforming Materials and Lubricants 5-10
   - C. Sheet Steel Fatigue Characteristics (A/SP160) 5-16
   - D. Tribology (A/SP230) 5-24
   - E. Advanced High-Strength Steel Stamping (A/SP050) 5-27
   - F. Strain-Rate Characterization (A/SP190) 5-34
   - G. Future Generation Passenger Compartment—Validation (A/SP241) 5-39
   - H. Lightweight Rear Chassis Structure (A/SP601) 5-44
   - I. Characterization of Thermomechanical Behaviors of Advanced High-Strength Steels (AHSSs): Formability, Weldability, and Performance Evaluations of AHSS 5-50

J. Characterization of Thermomechanical Behavior of Advanced High-Strength Steels (AHSSs): Task 2—Weldability and Performance Evaluations of AHSS 5-61

K. Fundamental Study of the Relationship of Austenite-Ferrite Transformation to Austenite Retention in Carbon Steels 5-69

L. National Science Foundation Funding for the Development of Third Generation Advanced High-Strength Steels (A/SP280) 5-73

M. A Multiresolution Analysis of the Particle Size and Interface Effects on the Strength and Ductility of Advanced High-Strength Steels 5-76

N. Study of the Effects of Microstructure on the Mechanical Properties and Failure Mechanisms of Advanced High-Strength Steels 5-83

O. Development of Novel Finite-Element Simulation Tools that Implement Crystal-Plasticity Constitutive Theories Using an Efficient Spectral Framework 5-93

P. Advanced High-Strength Steel through Paraequilibrium Carbon Partitioning and Austenite Stabilization 5-99

Q. Development of a High-Strength, High-Toughness Bainitic Steel 5-106

R. Development of Nano-Acicular Duplex Steels 5-115

S. Sheet Formability and Springback of Advanced High-Strength Steels—CSM 5-124

T. Sheet Formabilty and Springback of Advanced High-Strength Steels—OSU 5-133

6. AUTOMOTIVE METALS—CROSSCUTTING 6-1

A. Magnesium Research and Technology Development 6-1

B. Magnesium Front-End Design and Development (AMD603) 6-5

C. Magnesium Front End Research and Development (AMD604) 6-13

D. Nanotechnology-Based Self-Healing Coating System to Enable Use of Magnesium Alloys in Automotives 6-24

E. High-Strain-Rate Characterization of Magnesium Alloys 6-29

F. High-Rate Damage and Fracture, Experimentation, Simulation, and Visualization 6-34

G. Integrated Computational Materials Engineering for Magnesium in Body Applications (Mg ICME) (AMD702 and 703) 6-40

H. Multiscale Microstructure-Property Plasticity Considering Uncertainty 6-54

I. Materials Design for Magnesium Alloys 6-69

J. High Throughput Isotopic Diffusion Databases for Integrated Computational Materials Engineering 6-81

K. Cyberinfrastructure 6-88

L. Simulation-Based Design Optimization 6-100

M. Fatigue of Lightweight Automotive Materials 6-116

7. LOW-COST CARBON FIBER 7-1

A. Low-Cost Carbon Fibers from Renewable Resources 7-1

B. Advanced Stabilization of Polyacrylonitrile Fiber Precursor 7-19

C. Advanced Oxidation of Polyacrylonitrile Fiber Precursor 7-25

D. Precursor and Fiber Evaluation 7-31

E. Commercialization of Textile and Lignin Precursors 7-34

8. POLYMER COMPOSITES RESEARCH AND DEVELOPMENT 8-1
A. Automotive Composites Consortium Focal Project 4 (ACC007) 8-1
B. Composite Underbody Attachment 8-16
C. Development of Next-Generation Programmable Preforming Process 8-23
D. Low-Cost Carbon-Fiber Composites for Lightweight Vehicle Parts 8-35
E. High Volume Processing of Composites (ACC115) 8-41
F. Natural Fiber Composite Retting, Preform, Manufacture, and Molding 8-49
G. Natural Fiber Composites for Structural Component Design 8-60
H. Evaluation of Composite Natural Fiber/Resin Compatibility 8-75
I. Composite Crash Energy Management (ACC100) 8-82
J. Engineering Property Prediction Tools for Tailored Polymer Composite Structures 8-93
K. Predictive Modeling of the Structure and Properties of Polymer-Matrix Composites: NSF/DOE Grant Projects 8-105
L. Hierarchical, Structure-Oriented Stochastic Approach to Model Liquid Molding Processes 8-108
M. Simulating Injection Molding of Thermoplastics Reinforced with Short and Long Fibers 8-120
N. Incorporating Higher-Order Tensors in the Computation of Polymer Composite Mechanical Properties 8-138
O. Linking Process-Induced Properties to Thermoplastic-Matrix Woven-Fabric Composites Performance 8-149
P. Structural Nanocomposite Design 8-169
9. JOINING 9-1
A. Forming Limits of Weld Metal in Aluminum Alloys and Advanced High-Strength Steels 9-1
B. Impact Modeling and Characterization of Spot Welds 9-8
C. Friction Stir Spot Welding of Advanced High-Strength Steel 9-15
D. Friction Stir and Ultrasonic Solid State Joining Magnesium to Steel 9-23
E. Friction Bit Joining—An Innovation in Dissimilar Metal Joining 9-28
F. Weld Element and Joining Process Technology Development 9-34
10. NONDESTRUCTIVE EVALUATION 10-1
A. Nondestructive Inspection of Adhesive Metal-Metal Bonds (NDE601) 10-1
B. Laser Ultrasonic Inspection of Adhesive Bonds Used in Automotive Body Assembly 10-10
C. Online Nondestructive Weld Quality Monitor and Control with Infrared Thermography 10-15
D. Enhanced Resonance Inspection for Light Metal Castings (NDE701) 10-23
E. Global Quality Assessment of Joining Technology for Automotive Body-in-White 10-31
11. RECYCLING 11-1
A. Recycling Assessments and Planning 11-1

B. Baseline Assessment of Recycling Systems and Technology 11-9
C. Development of Technology for Removal of PCBs and Other Substances of Concern from Shredder Residue 11-18
D. Post-Shred Materials Recovery Technology Development 11-27
E. Development of High Speed Multispectral Imaging for Sorting Automotive Plastics 11-39
12. MATERIALS CROSSCUTTING RESEARCH AND DEVELOPMENT 12-1
A. Technical Cost Modeling 12-1
B. Intermediate-Rate Crush Response of Crash-Energy Management Structures 12-7
C. Mission Eggcellence—K–12 Outreach Program 12-13
APPENDIX A. ACRONYMS AND ABBREVIATIONS A-1

1. INTRODUCTION

Lightweighting Materials Research and Development

As a major component of the U.S. Department of Energy's (DOE's) Vehicle Technologies Program (VTP), Lightweighting Materials (LM) focuses on the development and validation of advanced materials and manufacturing technologies to significantly reduce road transportation vehicle weight without compromising other attributes such as safety, performance, recyclability, and cost.

Increased fuel economy is the most obvious effect of lightweighting.* It has been estimated that with every 10% drop in weight, the fuel economy increases 6–8% (with mass compounding and everything else the same). Mass compounding means that in addition to the fuel-economy increase due to the direct loss of weight by the given component or structure, other mass may be shed in other vehicle components or structures such as the powertrain, the suspension, and the braking.

In addition, lightweighting offsets the increased weight of features (e.g., audio, video, and navigation systems), vehicle upsizing, and performance (e.g., acceleration, safety, and exhaust-gas pollution abatement) demanded by the customer or mandated by regulations. This has been the primary use of lightweighting in the recent past. In the future, more lightweighting may be needed to offset the added weight and cost per unit of power of hybrid, electric, and fuel-cell power trains and to extend the ranges of vehicles using them.

The current specific goals of LM are to develop material and manufacturing technologies by 2010 that, if implemented in high volume, could cost-effectively reduce the weight of passenger-vehicle body and chassis systems by 50% with safety, performance, and recyclability comparable to 2002 vehicles.

LM is pursuing five areas of research: cost reduction, manufacturability, design data and test methodologies, joining, and recycling and repair. The current long-range plan for activities in these areas is found at www.eere.energy.gov. Because the single greatest barrier to the use of lightweighting materials is cost, priority is given to activities aimed at reducing costs through development of new materials, forming technologies, and manufacturing processes. Priority lightweighting materials include advanced high-strength steels (AHSSs); aluminum (Al); magnesium (Mg); titanium (Ti); and glass-, natural-, and carbon-reinforced thermoset and thermoplastic polymeric-matrix composites.

Coordination, Cooperation, and Collaboration

LM coordinates, cooperates, and even collaborates to identify, select, and conduct its research and development (R&D) activities with others (Table 1). The primary interfaces have been and still are with entities of Chrysler, Ford, and General Motors (GM), namely, the FreedomCAR Materials Technical Team (MTT), the Automotive Composites Consortium (ACC), the United States Automotive Materials Partnership (USAMP), and the Vehicle Recycling Partnership (VRP). These are the main means for determining critical needs, identifying technical barriers, prioritizing, assessing, and selecting projects. Other important U.S. partners include the Auto/Steel Partnership (A/SP) of the American Iron and Steel Institute (AISI), the Plastics Division (formerly the American Plastics Council) of the American Chemistry Council (ACC-PD), the American Foundry Society, and the North American Die Casting Association. LM closely coordinates some of its R&D activities with those of Natural Resources Canada's CANMET Materials Technology Laboratory due to common interests in automotive lightweighting in North America. Contacts with similar efforts in other countries are maintained. A major thrust in Mg, initiated in fiscal year (FY) 2007,

*The term "lightweighting" is used here instead of "lightweight" so as not to imply just the use of lower-density materials. Steel, for instance, is not a low-density material, but by increasing its strength, less can be used for net weight reduction.

Table 1. Research areas and responsible organizations

Coordinated area	Organization
Fabrication of Mg	CANMET
Recycling and reuse of automotive parts and materials	VRP, ACC-PD
Fabrication of steel	A/SP
Fundamental materials and manufacturing research	NSF
Production and fabrication of composites	ACC-PD

is in collaboration with CANMET and the China Magnesium Center of the Chinese Ministry of Science and Technology (see reports 6.A–6.C). Fourteen projects at universities are jointly funded with the U.S. National Science Foundation (NSF) (see reports 5.L–5.T and 8.K–8.O). Other universities participate in several other projects (see especially reports 2.A, 4.C, 6.G, and 8.I). Projects 2.A, 3.E, 4.B and 4.D, 6.F, 6.H and 6.I, 6.K–6.M, 8.G and 8.P, 9.F, and 12.C at the Mississippi State University (MSST), funded under a congressional mandate, are coordinated with the mainstream LM activities. Three projects (6.D, 10.B, and 11.E) are funded under the DOE Small Business Innovation Research and Small Business Technology Transfer (SBIR-STTR) programs.

Projects Development and Selection

In cooperation with USAMP and MTT, a procedure has been established to help facilitate the development of projects. LM has only rarely done open solicitations of projects. Projects are typically developed through informal contacts with original equipment manufacturers (OEMs) and/or national laboratory researchers and are brought forth for consideration, assessed, and selected on the bases of recommendations from either USAMP or MTT. DOE, however, retains final say as to what is funded. This flexibility allows LM to select the most appropriate partners to perform critical tasks that have optimal chances of migrating to OEMs or suppliers as application-engineering projects and eventually being implemented in production vehicles.

Once selected, R&D projects are pursued through a variety of funding mechanisms, including cooperative research and development agreements (CRADAs), cooperative agreements (CAs), university grants, R&D subcontracts, and directed research. Those developed through a CA with USAMP are cost-shared equally (dollar-for-dollar) with the LM funds by USAMP or other non-federal sources, either in cash or (mostly) in-kind. Those projects developed through MTT are usually performed at national laboratories and universities and not cost-shared.

Laboratories currently involved include Argonne National Laboratory, Oak Ridge National Laboratory (ORNL), Pacific Northwest National Laboratory (PNNL), and Sandia National Laboratories. The National Energy Technology Laboratory provides external projects management including the CA with USAMP, the projects jointly funded with NSF, and half of the MSST projects; ORNL oversees the other MSST projects.

Research and development projects are assigned to one of three phases as depicted in Figure 1 and defined below: concept feasibility, technical feasibility, and demonstrated feasibility. Projects are guided to meet the requirements of each phase before they move on to the next phase. Not all projects must go through these phases under LM funding; some may enter the technical- or demonstrated-feasibility stages from efforts funded elsewhere.

Figure 1. Typical phases/stages of projects.

Concept Feasibility. Concept-feasibility projects focus on a specific idea to address a need or to create something new. Projects are usually exploratory and small in monetary requirements and time, typically less than $200,000 total over 1–2 years, to provide a yes/no answer to the value of the idea. All projects are required to have a detailed research plan, budget, and timing. They can be ended before proceeding to technical feasibility if there is a lack of technical progress or if the preliminary business case turns out to be unfavorable. The SBIR-STTR Phase I projects are of this nature.

Technical Feasibility. Technical-feasibility projects typically continue R&D for ideas with proven concept-feasibility merit or potential. These projects should identify the key barriers to implementing the technology and focus on overcoming them. Technical-feasibility projects should have well defined, industrial OEM and/or supplier participation and pull. They are usually larger and longer term than the concept feasibility projects with typical investment in the $1M to $2M (or more) range and lengths of 2–3 years (or more). Technical feasibility projects can be ended before proceeding to demonstrated feasibility if there is a failure to overcome the key barriers to implementation or if the cost or business case does not develop as favorably as initially assessed. SBIR-STTR Phase II projects fit this paradigm.

Demonstrated Feasibility. Technology projects that need larger scale validation may become demonstrated feasibility projects. Not all technical feasibility projects will need a demonstration or validation phase. These projects are few in number, are much larger in scale, and may involve component or system fabrication and tests. Support and leverage from the industrial OEMs and/or suppliers is a key requirement.

FY 2008 Accomplishments

The first design iteration of the Mg front end and technical cost modeling for the unibody steel front end (baseline) were completed by GM, Ford, Chrysler, Cosma, and Camanoe (see report 6.B). Gaps with respect to crash performance and meeting mass-reduction targets were identified. These are the first milestones in the joint effort between the United States, Canada, and China on developing and validating the front end, thereby demonstrating cost-effective weight reductions of 50% or more.

Selection of the material and process system and preliminary design for a structural-composite underbody were completed by the ACC, one of the formal consortia of the United States Council for Automotive Research (see report 8.A). This is an initial milestone in a roughly 5-year effort aimed at developing and validating technology for cost-effective weight reductions of 30% or more in a large, monolithic, safety-critical component.

ORNL established a partnership with FISIPE, S.A. in Lisbon, Portugal for producing commodity textile polyacrylonitrile (PAN) fiber precursor for lower-cost carbon fiber suitable for automotive body and chassis applications (see report 7.E). ORNL and FISIPE evaluated multiple PAN compositions and down-selected the most promising formulation. FISIPE selected a chemical pretreatment process for in-line modification of the precursor during the wet-spinning stage of processing, and ORNL established the stabilization, oxidation, and carbonization time-temperature-tension profiles for conversion of the precursor into carbon fiber. ORNL processed multiple 26,600 filament tows into carbon fiber using the ORNL carbon-fiber pilot line, exceeding program strength and modulus requirements. This is a step toward lower-cost carbon-fiber composites which are capable of effecting body and chassis weight reductions of 50% or more.

The A/SP fabricated and tested ten Phase-1 (materials substitutions) prototypes of a rear chassis structure using AHSSs and addressed the technology gaps related to fabricating AHSS structures (see report 5.H). They developed a methodology to determine the fatigue resistance of a chassis structure by virtual testing and prepared a Phase-2 design (complete redesign) which reduced the mass by 27% through use of AHSS, new architectures, and manufacturing innovations. Corrosion tests were passed successfully with coated substrates.

PNNL, ORNL, the University of Illinois at Urbana-Champaign, and Moldflow Corporation developed, validated, and implemented a new fiber-orientation model for long-fiber thermoplastic composites (see report 8.J). The model successfully predicted fiber-orientation tensor components for a glass-polypropylene ISO-plaque. This is part of a larger effort involving the above participants, the ACC-PD, and six other U.S. universities jointly funded by LM and NSF. This larger effort is aimed at improving the ability to predict the properties of fiber-reinforced composites.

A blue-ribbon panel of the National Materials Advisory Board of the National Research Council completed an 18-month study, partially supported by LM, of Integrated Computational Materials Engineering, the use of modern computational methods for the processing-structure-properties-relationships in materials. The work mentioned in the immediately preceding paragraph is an example. The study recognized that the materials field lags other engineering fields in the use of computerized modeling and made recommendations to overcome deficiencies. The study report is available at www.nap.edu.

Newly Started and Ended Projects

New starts in FY 2008 included Pulse Pressure Forming of Lightweight Materials (2.D), Formability of Continuous Cast Magnesium Sheet (2.F), Development of High-Strength Superplastic Aluminum Sheet (2.G), Multi-Material Metallurgical Bond Joining to Steel (3.F), Fundamental Study of the Relationship of Austenite-Ferrite Transformation (5.K), High-Strain-Rate Characterization of Magnesium Alloys (6.E), High Throughput Isotopic Diffusion Databases for Integrated Computational Materials Engineering (6.J), Precursor and Fiber Evaluation (7.D), Commercialization of Textile and Lignin Precursors (7.E), Composite Underbody Attachment (8.B), Evaluation of Composite Natural Fiber/Resin Compatibility (8.H), Friction Stir and Ultrasonic Joining of Magnesium to Steel (9.D), Friction Bit Joining (9.E), Online Nondestructive Weld Quality Monitor and Control with Infrared Thermography (10.C), Enhanced Resonance Inspection for Light Metal Castings (10.D), and Global Quality Assessment of Joining Technology for Automotive Body-in-White (10.E).

Uncharacteristically, no projects ended in FY 2008.

Future Directions

The current emphases on carbon-fiber-reinforced polymer-matrix composites and Mg will continue, as they have the greatest weight-reduction potential and costs. However, there will be some efforts on AHSSs, Al, and Ti because these materials will contribute in niche roles to the weight-reduction and cost-neutrality goals. Material-crosscutting work in general manufacturing will continue in joining, nondestructive evaluation, and recycling. Though technical feasibility (see above) projects will dominate as before, concept feasibility and demonstrated feasibility projects will also be pursued as will some university and national laboratory base-technology projects.

2. AUTOMOTIVE METALS—WROUGHT

A. Thermomechanical Processing Design for Lightweight Materials

Principal Investigator: Esteban B. Marin
Senior Structural Analyst
Center for Advanced Vehicular Systems
Mississippi State University
200 Research Blvd.
Mississippi State, MS 39762
(662) 325-6696; fax: (662) 325-5433; e-mail: ebmarin@cavs.msstate.edu

Co-Principal Investigators: Paul T. Wang
Manager, Computational Manufacturing and Design
Center for Advanced Vehicular Systems
Mississippi State University
P.O. Box 5405
Mississippi State, MS 39762-5405
(662) 325-2890; fax: (662) 325-5433; e-mail: pwang@cavs.msstate.edu

Wei Chen
Professor of Mechanical Engineering
Robert R. McCormick School of Engineering and Applied Science
Northwestern University
Department of Mechanical Engineering
2145 Sheridan Road
Evanston, Illinois 60208-3111
(847) 491-7019; fax: (847) 491-3915; e-mail: weichen@northwestern.edu

Jian Cao
Professor of Mechanical Engineering
Robert R. McCormick School of Engineering and Applied Science
Northwestern University
Department of Mechanical Engineering
2145 Sheridan Road
Evanston, Illinois 60208-3111
(847) 467-1032; fax: (847) 491-3915; e-mail: jcao@northwestern.edu

Participants:
Sebastien Groh
Center for Advanced Vehicular Systems
Mississippi State University
200 Research Blvd.
Mississippi State, MS 39762
(662) 325-5576; fax: (662) 325-5433; email: groh@cavs.msstate.edu

Stephen Horstemeyer
Center for Advanced Vehicular Systems
Mississippi State University
200 Research Blvd.
Mississippi State, MS 39762
(662) 325-3685; fax: (662) 325-5433; email: sjhorst@cavs.msstate.edu

Andrew Oppedal
Center for Advanced Vehicular Systems
Mississippi State University
200 Research Blvd.
Mississippi State, MS 39762
(662) 325-8502; fax: (662) 325-5433; email: aoppedal@cavs.msstate.edu

Balasubramaniam Radhakrishnan
Oak Ridge National Laboratory
P.O. Box 2008
Oak Ridge, TN 37831-6164
(865) 241-3861; fax: (865) 241-0381; e-mail: radhakrishnb@ornl.gov

Gorti Sarma
Oak Ridge National Laboratory
P.O. Box 2008
Oak Ridge, TN 37831-6164
(865) 574-5147; fax: (865) 241-0381; e-mail: sarmag@ornl.gov

Joe Horton
Oak Ridge National Laboratory
P.O. Box 2008
Oak Ridge, TN 37831-6487
(865) 574-5575; fax: (865) 574-7659; e-mail: hortonja@ornl.gov

Technology Area Development Manager: Joseph A. Carpenter
(202) 586-1022; fax: (202) 586-1600; e-mail: joseph.carpenter@ee.doe.gov

---

Contractor: Mississippi State University (MSST)
Contract No.: 4000054701

Objective

- Develop physics-based, experimentally-validated, thermomechanical processing (TMP) models and design methodologies for improving manufacturability and forming technology of lightweight materials such as wrought aluminum (Al) and magnesium (Mg) alloys.

Approach

- Build an experimental material database that captures the important features of microstructure evolution during hot/cold rolling and stamping, and extrusion processes of Al and Mg alloys.
- Develop a multiscale material model using an internal state variable (ISV) formalism that is able to predict microstructure evolution (hardening, recovery, recrystallization, and texture-induced anisotropy) of metals during TMP.

- Construct numerical models of metal forming (rolling, stamping, extrusion) for process design.
- Use optimization techniques with uncertainty to establish an integrated approach for material-process design using simulation-based techniques.
- Main activities (subtasks) planned to perform the proposed research areas are as follows.
  - — Develop plane-strain compression (rolling), biaxial stretching (stamping), and laboratory-scale extrusion techniques for Al/Mg alloys at room and elevated temperature.
  - — Build an experimental database capturing microstructure evolution of Al alloys.
  - — Perform pilot-scale rolling experiments and material characterization of Mg alloys.
  - — Extend experimental database with microstructure information for Mg alloys.
  - — Develop multiscale ISV model to predict microstructure evolution of Al and Mg alloys during TMP.
  - — Construct thermomechanical process models and develop manufacturability metrics for process design (rolling, stamping, and extrusion).
  - — Develop methodologies for uncertainty quantification and reliability based design optimization of metal-forming processes.

- Team members participating in this task are as follows.
  - — MSST: Paul Wang, Esteban Marin (macroscale ISV model development, extrusion modeling), Sebastien Groh (support ISV model development with microscale/discrete dislocation/crystal plasticity simulations), Stephen Horstemeyer (laboratory-scale extrusion experiments), and Andrew Opeddal (mechanical testing of magnesium).
  - — Oak Ridge National Laboratory (ORNL): Balasubramaniam Radhakrishnan and Gorti Sarma (support ISV model development with mesoscale/crystal plasticity simulations), and Joe Horton (pilot-scale rolling experiments and characterization of Mg alloys).
  - — Northwestern University (NWU): Jian Cao (biaxial stretching experiments and stamping simulations), and Wei Chen (design optimization under uncertainty).

Accomplishments

- Performed channel die compression (CDC) experiments at room temperature (RT) on Al 6022 with a new-designed fixture that improved the outcome of the plane-strain compression tests. Compressed specimens (reduction of 60%) were annealed at different temperatures and times, and then subjected to microindentation tests. Hardness measurements showed the sigmoidal shape typically depicted by plots of differential hardness versus annealed time. Electron backscatter diffraction (EBSD) studies have been initiated on the annealed specimens to quantify the fraction of recrystallized material and model the recrystallization kinetics of aluminum alloys.
- Completed mechanical testing and texture measurements of pure polycrystalline magnesium deformed under simple compression have been completed. In these experiments, samples extracted from extruded/rolled plates were compressed in the through thickness (TT) and in-plane transverse (IPT) directions. Results from these tests (stress-strain curves and texture) showed clearly the effect of twinning on the deformation behavior of the material. Additional experiments considering strain-path changes and temperature reloads are works in-progress.
- Rolled, tested, and analyzed 19 alloys from a set of 97 experimental alloy slabs cast by Magnesium Elektron North America Inc. (MENA). A recipe adapted to ORNL's mill size was developed to allow hot rolling of these slabs to a thickness of 1.5 mm. Several of the alloys have strengths and ductilities near those of AZ31. Recovery/recrystallization on one selected alloy (AZ31b-H24) showed that only 15 min at 200°C or 8 min at 250°C was required for recovery as contrasted with the standard *ASM Handbook* recommendations of 1 hour at 345°C.
- Performed preliminary extrusion tests on Mg AZ61 using a laboratory-scaled, indirect-extrusion fixture designed to learn about the process and generate experimental data for modeling purposes. Experiments were not fully successful but limited microstructure information (texture, grain maps and grain orientation spread) was obtained at specific points of the material as it was flowing through the die. A new design for the fixture is currently underway.

- Performed quasi-statics and dynamics calculations in Mg to establish a dislocation mobility rule for each slip system. Peierls stresses (minimum stress needed to move a dislocation at 0°K) were calculated for each slip system, and a good agreement with experimental data was obtained. At finite temperatures two types of anisotropy were identified, which were related to (1) the dislocation character and (2) the slip system. Independently of the slip systems, edge dislocations move faster than screw dislocations, and regardless of the dislocation character (edge or screw), dislocations moving in the basal plane travel faster than dislocations sliding in the prismatic plane. Viscous-drag coefficients were calculated for each character lying in each slip system.
- Implemented and tested kinematics, kinetics and hardening rules for twinning deformation in a crystal-plasticity code. Analyzed dislocation/twin activities in a Mg single crystal under different loading conditions and used that information to identify the parameters of slip-hardening rules. This multiscale material model of Mg alloys reproduced well the anisotropy reported in the literature.
- Developed a new recovery model for cube texture evolution in Al. The nucleation model was based on orientation dependent "excess dislocations" and was incorporated into Monte Carlo recrystallization simulations. The model successfully predicted strengthening of cube texture during recrystallization following plane-strain compression.
- Investigated kinematic-hardening behavior in sheet metals using a novel design of test apparatus and a new model. An attempt on simulating material behavior of Mg alloys was made using a phenomenological approach. A method was developed for establishing the multilength-scale statistical microstructure-constitutive property relations through the statistical volume element (SVE) method, statistical sensitivity analysis, and stochastic calibration. Efficient random field uncertainty propagation techniques were developed for robust and reliability-based design involving multiscale analysis. Generic computational methods were established for robust design considering uncertainty with arbitrary distributions.

Future Direction

- Finish EBSD analyses (i.e., local texture) on channel die compressed specimens. Extend the capabilities of the CDC setup to test materials at high temperatures. Initiate experimental recrystallization studies for Mg alloys.
- Finish experiments considering strain-path changes and temperature reloads of pure Mg. Characterize the microstructure of the deformed specimens: measure bulk texture via neutron diffraction and microtexture and evolution of twinning via EBSD. Develop a dislocation-based, strain-rate- and temperature-dependent constitutive model for Mg. Implement model in crystal-plasticity numerical codes and use it to predict the experimental results, in particular the evolution of deformation twinning.
- Perform laboratory-scale extrusion experiments to study the effect of processing parameters on the microstructure and material properties of extruded Mg alloys. Develop finite-element models of the extrusion process. Validate material and numerical models by comparing predictions with experimental data from the laboratory-scale experiments.
- Use molecular dynamics (MD) simulation to complete the calculation of dislocation velocities in pure Mg. Exercise the discrete dislocation simulation code to compute the interaction coefficient between different slip systems (basal, prismatic, and pyramidal) for use in the hardening law of crystal-plasticity models. Validate the multiscale methodology established previously for Al by predicting the mechanical response of Mg single crystals.
- Conduct experimental investigation of forming limits of Mg alloys and forming behavior in stamping, and correlate the results with numerical simulations. Demonstrate the use of robust and reliability-based design framework for optimizing the sheet-metal forming process for Mg alloys.
- No new activities are planned by the team members at ORNL due to the lack of funding.

Introduction

Thermomechanical processing is typically used to improve mechanical properties of a material by inducing changes in its microstructure (grain structure, texture, precipitates). Properties such as plasticity, strength, ductility, and formability can be tailored by a proper design of different steps in TMP (e.g., hot/cold rolling, extrusion, heat treatment, stamping) as well as the design of material microstructure. In this context, building robust design methodologies and multiscale material models under uncertainty for TMP can contribute to improve current manufacturing processes and/or fix many technical problems (e.g., formability) that at present hinder the production of selected lightweight materials such as Mg alloys.

The focus of this task is to build a comprehensive framework that facilitates the reliability based optimum design of TMP for lightweight materials. This framework includes building an extensive material database capturing the processing-structure-property relationship of Al and Mg alloys, developing a multiscale constitutive approach for the history-dependent response of the alloys, and establishing an integrated robust and reliability optimization method with uncertainty for TMP as applied to Al and Mg alloys.

Based on these three major activities, the presentation below has been divided in three sections; each of them describes the details of the work performed by team members during 2008.

Material Database for Al and Mg Alloys

Channel Die Compression and Annealing of Al 6022 (MSST)

A previously constructed CDC fixture was redesigned to better control the homogeneity of deformation during the RT plane-strain compression experiments (Figure 1). Using this new fixture, CDC tests were performed on samples of Al 6022 extracted from a 1/8 in. rolled plate.

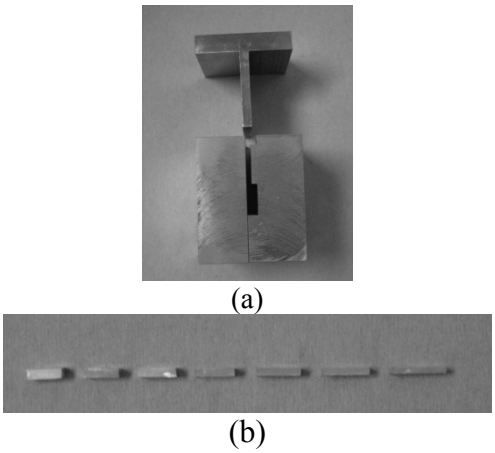

Figure 1. (a) Redesigned CDC fixture and (b) deformed specimen at different levels of strain (up to 50% strain). This new fixture promotes a more uniform deformation of the Al 6022 specimens.

Each CDC test used two specimens, with dimensions 5 mm × 10 mm, stacked and super-glued together to prevent the surfaces from sliding along one another. To reduce friction between the samples and the channel die, the samples were wrapped in Teflon tape and polytetraflouroethylene powder was applied to the surfaces. Using an Instron machine and the CDC fixture, the samples were then compressed up to a strain of 60% at a rate of 0.05 in./min.

The deformed samples were then annealed in a salt bath at temperatures of 375 and 400°C, with annealing times varying from 0 to 5,000 seconds (Figure 2). After the prescribed annealing time, each sample was removed from the furnace and immediately quenched in water.

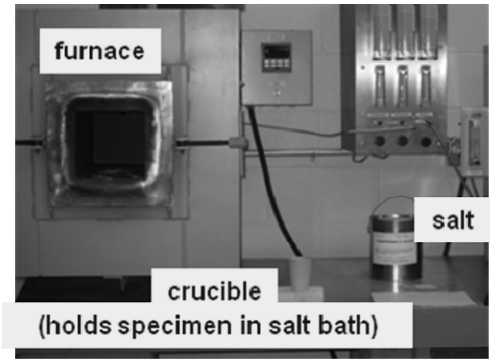

Figure 2. Annealing equipment for CDC samples of Al 6022.

The annealed samples were next prepared for hardness measurement using a microindenter. As expected, the hardness values decrease for longer annealing times and for higher temperatures [Figure 3(a)]. The plot of differential hardness versus annealing time [Figure 3(b)] shows a typical sigmoidal shape representative of recrystallization processes. Currently, the annealed samples are being prepared for EBSD studies to quantify the fraction of recrystallized grains, information needed to model the recrystallization kinetics in Al alloys.

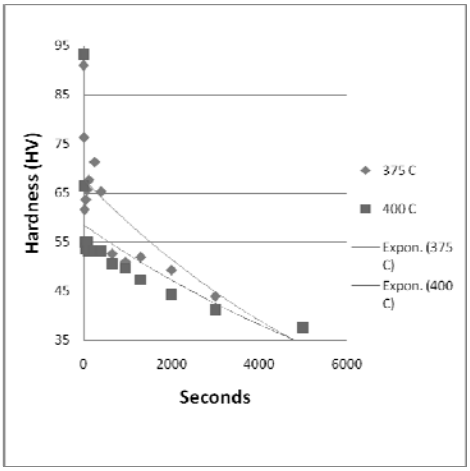

(a)

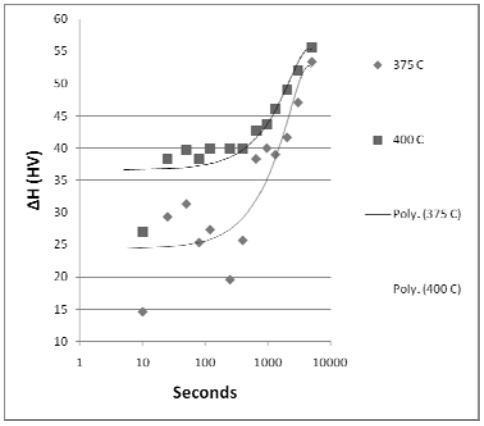

(b)

Figure 3. (a) Hardness vs time and (b) differential hardness vs time for the annealed Al 6022 specimens (HV denotes the Vickers Hardness).

Mechanical Testing and Texture Measurements on Pure Polycrystalline Magnesium (MSST)

Magnesium has attractive properties in applications that favor lower weight [1]. Its density (1.73 g/cm^3) is among the lowest of common structural metals, yet its hexagonal close-packed (hcp) structure demands additional consideration because of the limited ductility and mechanical anisotropy compared to face-centered cubic (fcc) and body-centered cubic (bcc) metals. Magnesium alloys such as AZ31, AM50, and AM60 and newer alloys recently developed such as AM30, AZ61, and AE44 will fill the market need as lighter-weight, more fuel-efficient vehicles become important. Because of this, understanding the structure-property relationships of Mg and its alloys, in particular the effect of deformation twinning on mechanical properties, will contribute to a better use of these materials in technological applications.

In this context, simple compression experiments have been conducted on polycrystalline pure Mg samples cut via electrical discharge machining from extruded and rolled plates. The samples were tested in the TT and IPT directions at RT and a strain rate of 10^{-3} s^{-1}. Figure 4 shows the

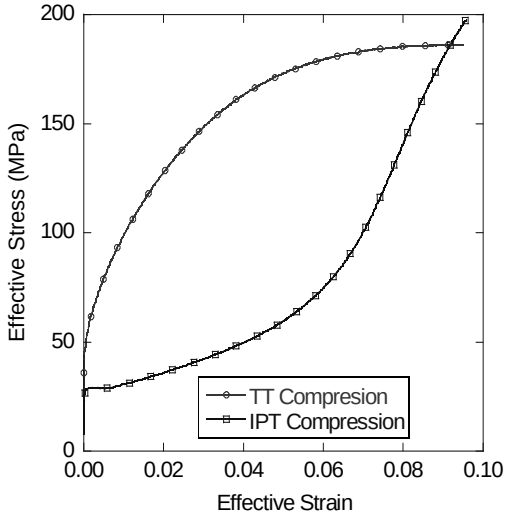

Figure 4. Simple compression of pure polycrystalline Mg showing anisotropy caused by basal texture and twinning. TT compression has the characteristic "parabolic" shape, while IPT compression has a characteristic "sigmoidal" shape caused by twinning activity.

mechanical behavior of the material while Figures 5, 6, and 7 show, respectively, the initial texture and resulting texture after mechanical testing. Note the effect of twinning on both the mechanical response and texture evolution. Texture was determined via neutron diffraction and represents the bulk texture of the material.

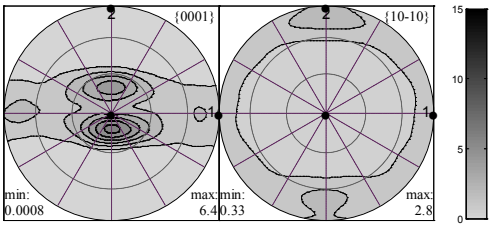

Figure 5. Initial texture of extruded/rolled material. The texture is dominated by the orientation of the basal poles.

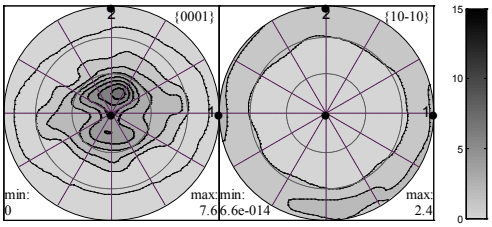

Figure 6. Texture after TT compression of 9.5%. Note the sharpening of the texture.

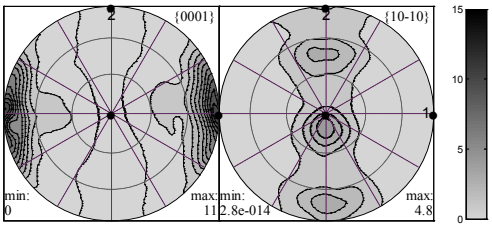

Figure 7. Texture after IPT compression of 9.6%. Note rotation of basal pole.

Additional experiments are being conducted to characterize the material under strain-path changes and temperature reloads. In the strain-path change experiment, an initial compression preload in the TT (IPT) direction is followed by a reload in the IPT (TT) direction. In the temperature-reload experiment, the material is preloaded in the TT (IPT) direction at liquid nitrogen temperature to create twinned structures, and subsequently reloaded in the TT (IPT) direction at RT. In all these experiments, the interplay between twin and slip will be examined and the results will be used for model development.

Rolling and Annealing Experiments on Magnesium Alloys (ORNL)

The goal of these experiments is to develop a wrought Mg alloy and/or processes for the cost-effective production of Mg sheet which is both economical and formable enough for practical application in vehicle structures. Current work is centered on an alloy development program to produce a lower-cost wrought alloy with properties close to those of AZ31. In this frame, activities during the last year were concentrated in two areas: (1) evaluating the feasibility of using innovative roll processing together with lower-cost alloyed ingots to reduce the total cost of sheet materials and (2) developing a basic understanding of the mechanisms of deformation and recrystallization in order to develop less-expensive processing methods.

Pilot-scale rolling experiments at ORNL were continued on 11 new alloy compositions provided by MENA. Eight other alloys failed to roll. The rolling schedule, developed for a laboratory-sized 6 in. mill, was similar to the one described in the previous annual report and essentially consisted of overnight annealing at 400°C, hot rolling at 400°C with different reductions and reheating steps and then cold rolling. Table 1 shows RT tensile properties at a strain rate of 10^{-3} for these laboratory-scale rolled alloys. As with the alloys reported previously, several of these new alloys have properties similar to those for AZ31.

Annealing experiments were also performed on specimens of as-received commercial AZ31b-H24. The annealing was carried out in air, for the times and temperatures indicated by the graph in Figure 8. This alloy in the as received condition cracked after 7% additional cold rolling, indicating that the cold work in the specimens was near a comfortable limit to simulate the required times and temperatures for intermediate anneals during multiple rolling operations. As evident from the graph, substantial recovery occurred in 15 min at 200°C or just 8 min at 250°C. Metallography for grain size and determination of when

Table 1. Tensile properties of successfully rolled experimental wrought magnesium alloys. (hr = hot rolling; cr = cold rolling

Alloy #	Processing	Yield (MPa)	Tensile (MPa)	Elong (%)
az31*	hr	145	263	14
	hr+10%cr	145	145	0
mel 102	hr	128	230	25
	hr+10%cr	246	257	5.2
	hr+20%cr	283	283	0.3
mel 105	hr	95	220	23
	hr+10%cr	242	254	2.8
	hr+20%cr	263	269	4.2
mel 108	hr	187	203	2.6
	hr+10%cr	23	238	0
mel 118	hr	142	236	21
	hr+10%cr	230	251	10
	hr+20%cr	274	281	2.3
mel 119	hr	165	239	14
	hr+10%cr	256	269	4
mel 120	hr	127	212	5.4
	hr+10%cr	220	237	0.6
mel 138	hr	111	238	24
	hr+10%cr	244	266	6
	hr+20%cr	287	294	3
mel 139	hr	114	225	13
	hr+10%cr	226	253	4.5
mel 140	hr	84	207	6.6
	hr+10%cr	216	216	0
mel 185	hr	123	179	19
	hr+10%cr	159	234	9
	hr+20%cr	211	231	9

*az31 cast into 1/2 slab at mel, hot rollec at ornl

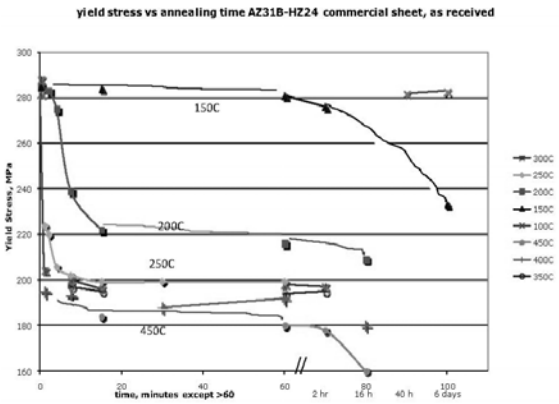

Figure 8. Recovery (tensile stress) of commercial AZ31b-H24 after the indicated times and temperatures for air anneals.

recrystallization occurred has not been performed yet.

In summary, a series of new compositions that were cast in laboratory-sized ingots by MENA were successfully hot rolled and tested at ORNL. Some of the compositions showed comparable results to AZ31, suggesting that this alloying approach may achieve the goal of a less-expensive alloy that is still comparable in properties. Recovery/recrystallization studies showed that 15 min at 200°C or 8 min at 250°C was sufficient for recovery, suggesting that a continuous rolling process should be possible.

Experimental and Numerical Investigation of Kinematic Hardening Behavior in Sheet Metals (NWU)

Northwestern University has been continuously working on the experimental apparatus for testing material's kinematic hardening behavior of thin sheets. A novel in-plane tension-compression device was introduced for sheet materials (Figure 9).

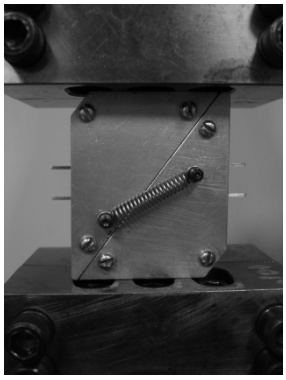

Figure 9. Front view of the test apparatus.

This double-wedge device is easy to fabricate and able to cover the specimen surface completely, preventing potential buckling of sheet. Using the developed device, the frictional force between the plate and specimen can be neglected for both tension and compression tests. The TT biaxial stress and plane-strain condition were also investigated by using the finite-element modeling (FEM) simulation for the compression test. Once the Teflon film was attached on the plate, the material status was not under the plane-strain condition, which is desired for the uniaxial tension-compression test. Also, the stress ratio between the equivalent stress and the compressive axial loading stress was less than 1.6%, so that the biaxial effect of the TT stress can be ignored in the

tension-compression test using the double-wedge device.

To measure the strain correctly, the transmission type laser extensometer was used and the double-side fins were considered in the specimen, as depicted in Figure 10. Through FEM simulations, it was found that the specimen with double-side fins resulted in a more uniform strain distribution than that from the specimen with single-side fins. Test results showed that the double-wedge device can perform stable tension-compression (15% prestrain) and compression-tension (9% prestrain) tests for a sheet thickness of 0.8 mm and a good repeatability for a couple of cyclic tests (Figure 11).

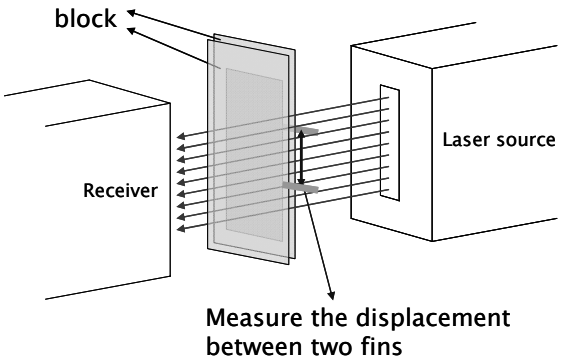

Figure 10. Strain measurement system used.

Laboratory-Scale Extrusion Experiments (MSST)

Extruded structural components of Mg alloys are increasingly being used in the automotive industry due to their good mechanical properties, including low density and high specific strength. However, the extrudability of these alloys is still limited because of their highly anisotropic mechanical behavior originating from their hcp structure. Because of this, understanding the microstructure-property relationship of these alloys as related to the extrusion process can help to improve their manufacturability.

In this subtask, we are developing a laboratory-scale indirect extrusion facility to determine the processing-structure-property relationship of extruded Mg AZ61 and AM30 alloys. Direct extrusion could be designed by this concept. The main goal is to understand the influence of process parameters (temperature, pressure, ram speed, extrusion ratio) on the microstructure and mechanical properties of extruded material and to generate experimental data for model validation.

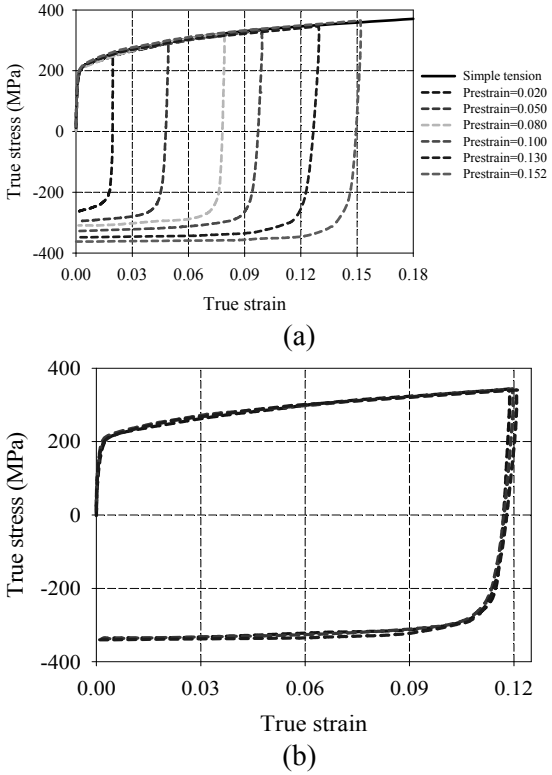

Figure 11. Test results of the 0.8 mm BH180 steel sheet: (a) tension-compression test; (b) repeatability (at 0.12 prestrain level).

A preliminary design of this device has been tested by extruding Mg AZ61 (Figure 12).

Although the test was not completely successful (extrudate came out in fractured parts) possibly due to unsuitable processing conditions (temperature and ram speed), some microstructure information was obtained through EBSD. Figures 13 and 14 show the device cut in half to exhibit the Mg alloy and the grain map, texture, and grain orientation spread (GOS) obtained at two points as the material was flowing though the die. This preliminary test gave some insights on how to modify the device to be reusable and hence able to test a batch of Mg alloy billets under new processing conditions. This new design is a work-in-progress.

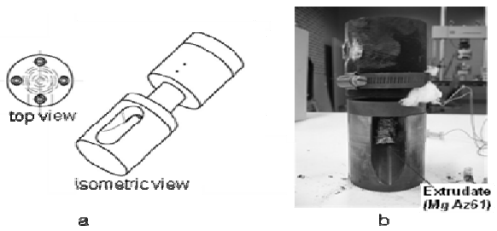

Figure 12. (a) Drawing of extrusion device; device is mounted in a servohydraulic loading frame with a capacity of 67,000 lb. (b) Device after preliminary testing; processing parameters used were temperature = 583°C, ram speed = 1.4 in./min, extrusion ratio = 22.

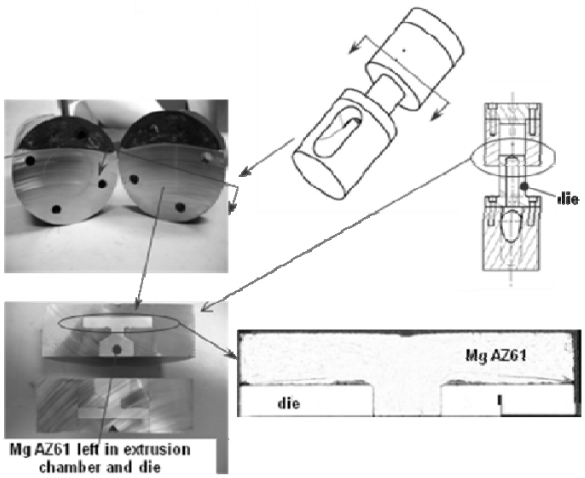

Figure 13. Details of extrusion chamber, die, and material (Mg AZ61) after preliminary test, the material welded to the walls of the chamber and die. Device had to be cut in half twice to exhibit the material flow during extrusion.

Constitutive Model Development/Implementation

Dislocation Motion in Magnesium by Molecular Static and Molecular Dynamics Simulations (MSST)

Metals with hcp crystal structure such as Mg have a wide variety of mechanical and physical properties, and understanding the links between atomic properties, microstructure, and mechanical properties can open the way for new applications. In this sense, atomistic simulations can provide a good deal of information to understand their deformation mechanisms and how these mechanisms affect the overall mechanical behavior of hcp materials.

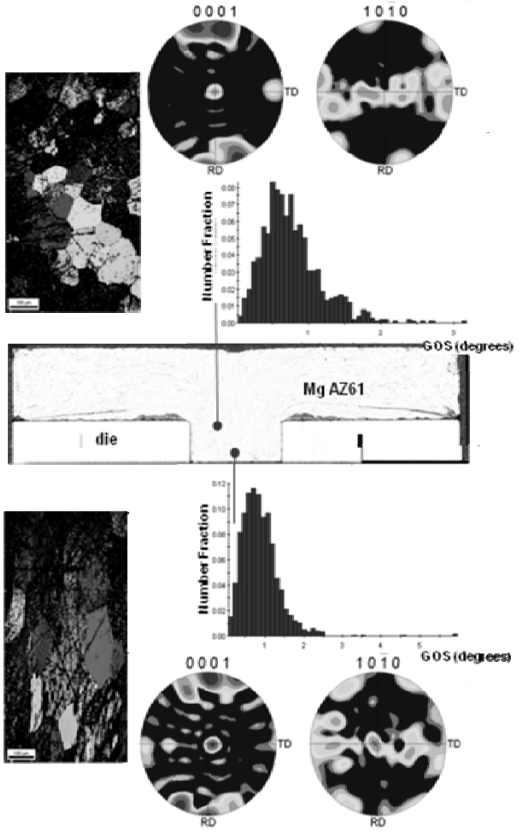

Figure 14. Microstructure information (texture, grain map, GOS) obtained from two points of the material as it was flowing through the extrusion die.

Figure 15 shows the possible dislocation slip systems able to accommodate plastic deformation in hcp crystals. From these, basal, prismatic, and <**c+a**>-pyramidal are the most active slip systems in Mg. basal and prismatic are perpendicular to the **c**-axis, and therefore, slip in <**a**> direction cannot produce strain parallel to the **c**-axis. Dislocations lying in the <**c+a**>-pyramidal slip plane can accommodate deformation along the **c**-axis, but such activity is mainly active at high temperatures. On the other hand, deformation twinning can contribute to the general deformation along the **c**-axis at low temperatures.

A multiscale modeling framework developed previously for fcc materials [2] has shown that the mechanical response of a material can be related to (1) the intersections and reactions between dislocations and (2) the average dislocation velocity. In an effort to extend such a framework to hcp materials, this work focused on studying the

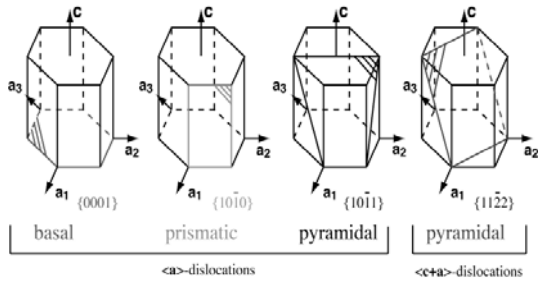

Figure 15. Slip system in hcp crystals.

motion of dislocations on basal, prismatic and <**a**>-pyramidal slip systems (Figure 15). In particular, the study investigates the mobility of edge/screw dislocations with a $1/3[11\bar{2}0]$ Burgers by both molecular statics (MS) and MD simulations. The goal is to derive a dislocation velocity rule usable for simulation at a higher length scale (i.e., discrete dislocations model). In what follows, we present a summary of the methodology, including the description of the dislocation core structures obtained to start the simulations, the quasi-static calculations performed to compute the Peierls stress and the dynamic calculations to determine the mobility of dislocations.

Simulation Setup

The evolution of the dislocation mobility as a function of dislocation character, temperature, and shear stress is studied using the MD code LAMMPS [3], where the simulations can be run under either static- or dynamic-loading conditions.

This section presents the main characteristics of the MS/MD simulation models that allow the analysis of edge/screw dislocations in an infinite periodic glide plane. The simulations employed the embedded-atom method (EAM) potential developed by [4]. For the edge dislocations, periodic boundary conditions were applied along the line and motion directions, while the top and bottom surfaces were fixed along their normal direction and constrained to two-dimensional dynamics. For the screw dislocations, periodicity along the line direction was insured by the invariance of the displacement field in this direction. Along the moving direction, periodic boundary conditions were applied with a shift of +b/2 (b is the Burgers vector) along the line direction for atoms leaving the cell from the left hand negative surface and the reentering the cell on the right hand positive surface. For atoms moving in the opposite direction, an opposite shift was applied.

For the static analysis, a rigid displacement was applied in the direction of the Burgers vector to model the motion of an edge dislocation. The critical stress value at which the dislocation moves defines the Peierls stress. The stress is calculated using the engineering definition (i.e., $\sigma_{dn} = F_{int}/A_{dL}$, where F_{int} is the applied force and A_{dL} is the area of the top surface).

In dynamic conditions and for temperatures greater than 0°K, the applied stress was implemented through a constant force to each atom on the top surface. Calculations were performed using the microcanonical ensemble (NVE) with a time step of 0.002 picoseconds (ps).

Structure of the Dislocation Core

Figure 16 shows the core structure of the basal, prismatic, and pyramidal-<a> edge dislocation, obtained after minimization of the potential energy. The core of the basal edge dislocation (c.f. Figure 16a) dissociated into two Shockley partials bounding an intrinsic fault I_2 according to the reaction

$$\frac{1}{3}[11\bar{2}0] \rightarrow \frac{1}{3}[10\bar{1}0] + \frac{1}{3}[01\bar{1}0],$$

and a distance close to 8b separated the two partials. The core structure of the prismatic edge dislocation (cf Figure 16b) was undissociated, but spreads in the plane $(10\bar{1}0)$, while the dislocation core structure of the edge dislocation lying in the pyramidal plane remained undissociated (c.f. Figure 16c), independently of the position of the origin chosen for the initial elastic solution. Note that the different core structures obtained will affect (1) the value of the Peierls stress and (2) the mechanism of motion.

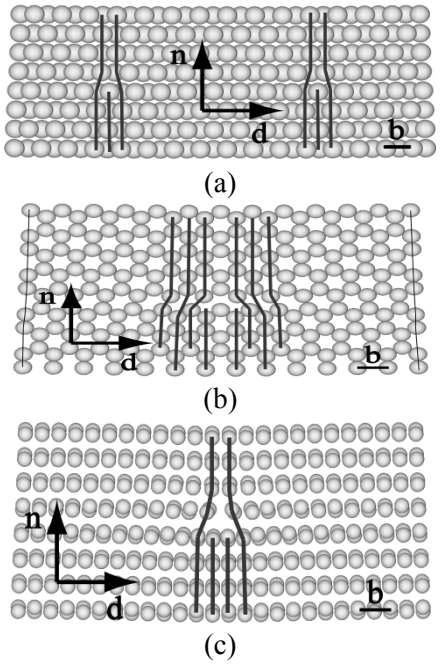

Figure 16. Core structure of <a> -edge dislocation in the (a) basal, (b) prismatic, and (c) pyramidal planes.

Estimation of the Peierls Stress by Molecular Statics

Molecular static calculations were performed to estimate the value of the Peierls stress for edge dislocations lying in the basal, prismatic, and pyramidal slip planes. As a reference, the size of the simulation cell was 100b × 100b along the displacement and normal directions. To capture the simple Peierls picture and not a more complicated mechanism of motion (simple kink or kink-pairs mechanisms), the dimension of the simulation cell along the dislocation line was restricted to one lattice period (i.e., 0.55 nm, 0.52 nm and 1.18 nm for basal, prismatic, and pyramidal crystallographic orientations, respectively). A strain increment $\Delta\varepsilon = 10^{-5}$ applied on the top surface followed by relaxation to the minimum potential energy was repeated until the total strain reached 0.2% for the basal and prismatic crystal orientations and 0.5% for the pyramidal orientation.

Figure 17 shows the strain-stress behaviors calculated for the basal, prismatic, and pyramidal edge dislocations. In the cases of prismatic and pyramidal edge dislocations, we observed that

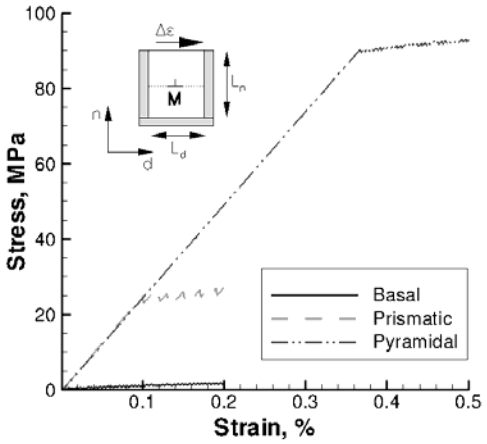

Figure 17. Strain-stress curves obtained by molecular static to model dislocation motion lying on the basal, prismatic, and pyramidal slip planes. ($\Delta\varepsilon = 10^{-5}$, L_n = 100b, and L_d = 100b).

before the dislocation moved, the stress increased linearly with the strain. The corresponding shear modulus was 12.6 GPa, which is in good agreement with the shear modulus reported by Sun et al. [4] (C_{44} = 12.8 GPa). The Peierls stress, which defines the minimum stress needed for moving a dislocation, was reached when the dislocation started to move without increasing the stress. A strong anisotropy between slip systems was observed (Table 2). The obtained Peierls stresses were in agreement with the nature of the dislocation core structures (i.e., a low Peierls stress for a dissociated core and a larger Peierls stress for an undissociated core) [5].

Table 2. Peierls stress (MPa) for basal, prismatic, and pyramidal slip systems in Magnesium calculated by molecular statics. (a: [6]; b: [7]; c: [8]; *numerical value.)

	Experimental data (MPa)	This study (MPa)	
		Liu et al. (1996)	Sun et al. (2006)
Basal 0.	52 (a)	14	0.35 ± 0.5
Prismatic 3	9.2 (b)	22	23.7 ± 0.5
Pyramidal 10	5* (c)	24	90–92

The Peierls stresses were not affected by a change of strain increment. Increasing the simulation cell size did not affect significantly the Peierls stress on the basal plane. On the other hand, increasing the cell size from 80b × 80b to 120b × 120b,

decreased the Peierls stress on the prismatic slip plane from 25.5 ± 1.5 MPa to 23.7 ± 0.5 MPa. The length of the edge dislocation lying in the prismatic plane (lengths ranging from one lattice period to thirty lattice periods were tested) did not affect its Peierls stress.

As reported in Table 2, the calculated Peierls stresses for each system are in a good agreement with experimental data. To determine the sensitivity of the Peierls stresses to the particular potential used, similar calculations were performed using the EAM potential proposed by Liu et al. [9]. Although the core structure for the edge dislocations was similar to the one reported above, the corresponding Peierls stresses (Table 2) were not in agreement with both the experimental data and the value calculated using the potential from [4].

Dislocation Mobility by Molecular Dynamics

MD simulations have been performed to determine the velocity of dislocations lying on the basal and prismatic slip planes. For comparison purposes, the velocities of edge/screw dislocations lying on these slip planes are plotted in Figure 18 as a function of the applied stress for a temperature of 100°K.

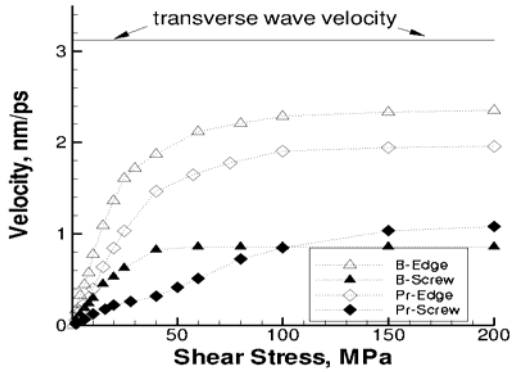

Figure 18. Dislocation velocity for edge and screw dislocations lying on the basal (B) and prismatic (Pr) slip planes.

Two types of anisotropy were observed: (1) anisotropy of the velocity related to the dislocation character and (2) anisotropy of the velocity related to the slip plane. Before the dislocation velocity saturates, the dislocation velocity increases linearly with the stress for a dislocation lying on either the basal or the prismatic slip planes. At 100°K, the drag coefficients are 4.7×10^{-6} Pa.s and 1.3×10^{-5} Pa.s for edge and screw dislocations on the basal slip plane, respectively, while 7.7×10^{-6} Pa.s and 3.7×10^{-5} Pa.s for edge and screw dislocations lying on the prismatic slip plane, respectively. In addition, as the Peierls barrier is higher in the prismatic than in the basal slip planes, the lower velocity for a dislocation lying in the prismatic plane compared to the velocity of a dislocation lying in the basal plane is the consequence of a stronger interaction between the dislocation and the Peierls barrier. For example, at 50 MPa, screw dislocations moved with a speed of 0.84 nm/ps and 0.41 nm/ps in the basal and prismatic slip planes, respectively, while edge dislocations moved with a speed of 2 nm/ps and 1.5 nm/ps in the basal and prismatic slip planes, respectively. Figure 19 shows two snapshots of the dislocation line under different conditions of loading. Figure 19a was obtained for an applied stress of 2 MPa at 100°K, while Figure 19b was obtained for an applied stress of 300 MPa at 500°K. Both configurations were extracted at the same time.

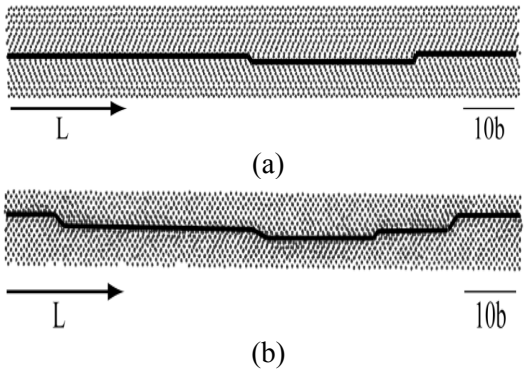

Figure 19. Projection on the (0001) plane of a screw dislocation lying on the basal plane after 1 ps. (a) 6 MPa, 100°K. (b) 300 MPa, 500°K.

Independent of the stress and temperature, the dislocation is moving by kink-pair mechanisms [5]. A portion of the line jumps to the next lattice position forming a pair of atomic-sized kinks. Driven by the stress, the kinks rapidly migrate along the dislocation line and recombine through the periodic boundary conditions. As a result, the entire dislocation translates to the next lattice

position. This mechanism explains generally the dislocation motion at low temperature when the applied stress is below the Peierls stress. However, although the Peierls stress in the basal plane is close to 0.3 MPa, the mechanism of motion by kink-pairs was still observed when the applied stress was above the Peierls stress.

Summary

In this work, we reported on the velocity of dislocation with <a> Burgers vector lying in either the basal, prismatic, or pyramidal slip plane, and calculated by either quasi-static calculations or MDs simulations. The effect of (1) the temperature and (2) the dislocation character on the dislocation mobility was investigated on each slip system. The Peierls stresses for edge and screw dislocations moving on either the basal, prismatic, or pyramidal slip plane were also determined, and a good agreement with experimental data from the literature was found.

From the dynamics calculations, we found a strong anisotropy of the dislocation velocity related to (1) the dislocation character and (2) the slip systems. In general, edge dislocations lying on the basal slip plane are moving two times faster than screw dislocations from the same slip system. On the other hand, edge dislocations lying on the prismatic slip plane are moving five times faster than screw dislocations gliding on the same slip plane. In addition, dislocations moving on the basal plane are two to three times faster (edge-screw) than dislocations from the prismatic slip system. The numerical dislocation velocities obtained during this study were correlated to a dislocation mobility rule following a viscous drag form, and the corresponding drag coefficients calculated at 100°K are reported in Table 3.

Table 3. Value of the drag coefficient (Pa.s) for edge/screw dislocations lying on the basal, prismatic, and pyramidal slip planes at 100°K

	Edge	Screw
Basal	4.7×10^{-6}	1.3×10^{-5}
Prismatic	7.7×10^{-6}	3.7×10^{-5}
Pyramidal	8.0×10^{-5}	Does not exist

Numerical Implementation of Deformation Twinning in a Crystal-Plasticity Model (MSST)

Mg single crystals and associated polycrystalline alloys are characterized by highly anisotropic mechanical behavior [10, 11, 12], with twinning being an important deformation mechanism at low temperatures. Hence, realistic modeling of Mg and its alloys requires accounting for deformation twinning in the constitutive equations. Over the last two decades, an extensive effort has been made to incorporate twinning deformation in polycrystalline modeling. The main assumption common to most models is to consider that a critical resolved shear stress exists to activate twinning, and therefore deformation twinning is considered as a polar pseudo-slip. Such an assumption is also considered in our development.

The aim of the work was to implement deformation twinning in an existing crystal plasticity framework. As a benchmark to validate the implementation, we applied the model to reproduce the anisotropic behavior of a Mg single crystal under plane-strain compression. The subsections below describe the implementation of deformation twinning in the crystal-plasticity framework and the numerical results obtained.

Modeling Framework

The crystal-plasticity framework developed in [13], where crystallographic slip is the only deformation mechanism, has been extended to account for deformation twinning. This development follows closely the work of [14]. This section presents solely the main aspects of the framework that need modifications to account for twinning.

The multiplicative decomposition of the local deformation gradient **F** can be written as the following (Figure 20):

$$\boldsymbol{F} = \boldsymbol{F}^e\boldsymbol{F}^p \text{ with } \boldsymbol{F}^e = \boldsymbol{V}^e\boldsymbol{R}^e \quad (1)$$

Here, $\boldsymbol{F}^e$ is the local elastic deformation gradient, decomposed in the elastic stretch, $\boldsymbol{V}^e$, and lattice rotation, $\boldsymbol{R}^e$, while $\boldsymbol{F}^p$ represents the local plastic deformation gradient due to both slip and deformation twinning.

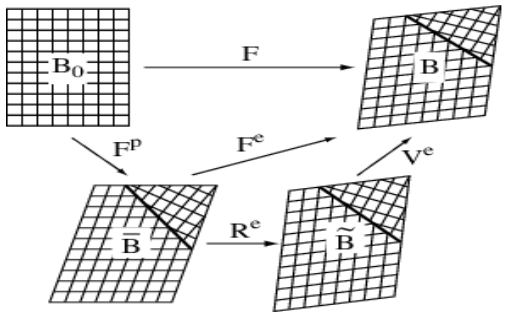

Figure 20. Kinematics of elastoplastic deformation of single crystals deforming by crystallographic slip and twinning.

In configuration $\bar{B}$, the plastic velocity gradient, $\bar{L}^{p}$, is written as the sum of the slip contribution in the nontwinned region and the twin contribution, and is given by

$$\bar{L}^{p} = \left(1 - \sum_{\beta}^{N^{tw}} f^{\beta}\right) \sum_{\alpha}^{N^{sl}} \dot{\gamma}^{\alpha} \bar{s}^{sl,\alpha} \otimes \bar{m}^{sl,\alpha} + \sum_{\alpha}^{N^{tw}} \delta \dot{f}^{\alpha} \gamma^{tw} \bar{s}^{tw,\alpha} \otimes \bar{m}^{tw,\alpha} \tag{2}$$

where $\dot{\gamma}^{\alpha}$ is the plastic shearing rate on the α-slip system which is defined by the unit vectors ($\bar{s}^{sl,\alpha}$, $\bar{m}^{sl,\alpha}$), $\dot{f}^{\alpha}$ is the rate of volume fraction of the α-twin system which is represented by the unit vectors ($\bar{s}^{tw,\alpha}$, $\bar{m}^{tw,\alpha}$), γ^{tw} is the constant shear strain associated with twinning, and δ is a material constant.

Note that Eq. (2) does not consider the slip system activity in the twinned region. This implies that the disorientation between the twin and the parent stays constant during the deformation. Also, this equation introduces the rate of the volume fraction on each α-twin system and the total volume fraction of twins in the formulation. The evolution equation of the twin volume fraction is represented by a power-law expression

$$\begin{cases} \dot{f}_v^{\alpha} = \dfrac{\dot{\gamma}_0}{\gamma^{tw}} \left(\dfrac{\tau^{\alpha}}{\kappa^{tw,\alpha}}\right)^{1/m} \text{ if } \left(\tau^{\alpha} > 0\right) \text{ and } \left(\sum_{\alpha} f_v^{\alpha} \le f_v^{sat}\right) \\ \dot{f}_v^{\alpha} = 0 \text{ if } \left(\tau^{\alpha} \le 0\right) \text{ or } \left(\sum_{\alpha} f_v^{\alpha} > f_v^{sat}\right) \end{cases} \tag{3}$$

where τ^{α} and $\kappa^{tw,\alpha}$ represent, respectively, the resolved shear stress on the α-twin system and the associated twin resistance. Note that the saturation of the twin volume fraction is controlled by the parameter f_v^{sat}. The hardening of the twin system is modeled by the expression

$$\kappa^{tw} = \kappa^{tw}{}_0 + h_{tw} \left(\sum_{i}^{N^{tw}} \frac{\dot{\gamma}^{i}}{\dot{\gamma}_{ref}}\right)^{d} \tag{4}$$

where $\kappa^{tw}{}_0$ is the twin critical resolve shear stress, $\dot{\gamma}_{ref}$ is a reference shear rate set up to 1 s^{-1}, and h_{tw} and d are material parameters.

Finally, slip-system hardening is modeled by an extended Palm-Voce rule [15] for each slip-system family: basal-<**a**>, prismatic-<**a**>, and pyramidal-<**c+a**>:

$$\dot{\kappa}_{sl}^{i} = h_{sl,s}^{i}(f) \left(\frac{\kappa_{sl,s}^{i}(f) - \kappa_{sl}^{i}}{\kappa_{sl,s}^{i}(f) - \kappa_{sl,0}^{i}}\right) \sum_{k}^{N^{sl,i}} |\dot{\gamma}^{k}| \tag{5}$$

$$\text{with} \quad \begin{cases} h_{sl,s}^{i}(f) = h_{sl,s0}^{i} \left(1 + C \sum_{\beta} f^{\beta}\right)^{b} \\ \kappa_{sl,s}^{i}(f) = \kappa_{sl,s0}^{i} + \kappa_{pr} \left(\sum_{\beta} f^{\beta}\right)^{0.5} \end{cases} \tag{5}$$

where $h_{sl,s0}^{i}$, $\kappa_{sl,0}^{i}$, $\kappa_{sl,s0}^{i}$ are material constants, and the parameters C, κ_{pr}, and b define the coupling between slip and twinning.

The developed framework has been implemented in both a material point simulator and an ABAQUS user material subroutine. These implementations have been used to determine the stress-strain behavior of Mg single crystals under plane- strain compression.

Numerical Results

Kelley and Hosford [12] have conducted deformation studies at RT on Mg single crystals. These crystals were oriented to suppress shear on the easily activated basal slip systems and were deformed by plane-strain compression. Table 4

Table 4. Direction of the compressive load and constraint for the plane-strain compression testing

Id	Compression	Constrain	Euler angle
A	< 0001 >	$< 10\bar{1}0 >$	(150, 0, 0)
B	< 0001 >	$< 1\bar{2}10 >$	(240, 0, 0)
C	$< 10\bar{1}0 >$	< 0001 >	(0, 90, 30)
D	$< 1\bar{2}10 >$	< 0001 >	(0, 90, –60)
E	$< 10\bar{1}0 >$	$< 1\bar{2}10 >$	(–90, 90, 30)
F	$< 1\bar{2}10 >$	$< 10\bar{1}0 >$	(90, 90, –60)

presents the six predefined orientations and the experimental results are given in Figure 21(a). Note that, for orientations E and F, twinning was observed at the beginning of the deformation to accommodate the compression perpendicular to the unconstrained **c**-axis. Once twinning was virtually completed, deformation continued by $\{10\bar{1}1\}$ banding.

Based on the analysis of the slip/twin activity for each orientation, the hardening parameters of the model were calibrated with the experimental data as follows.

- Orientation C gives the material parameters for the prismatic slip system.
- Orientation A gives the material parameters for the pyramidal slip system.
- Orientation E gives the materials parameters for the twinning activity.
- The coupling parameters between slip and twins, C, κ_{pr}, h_{tw}, b, and d were obtained using a parameter sensitivity study.

The computed stress-strain behaviors for the six orientations are given in Figure 21(b). Note that the trends observed in experiments are well predicted by the model.

Summary

In this work, an existent crystal-plasticity framework was extended to account for deformation twinning, where twins were considered as pseudo-dislocations. The framework was based on the multiplicative decomposition of the local deformation gradient. One of the main

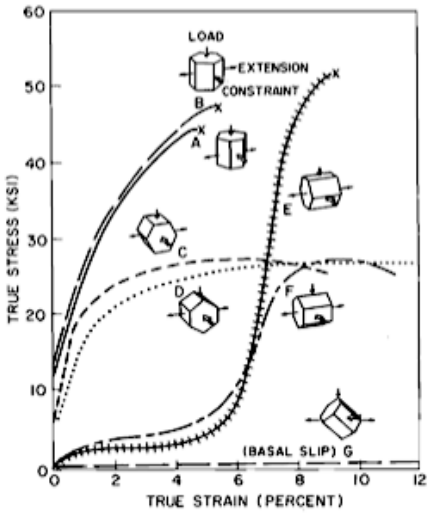

(a)

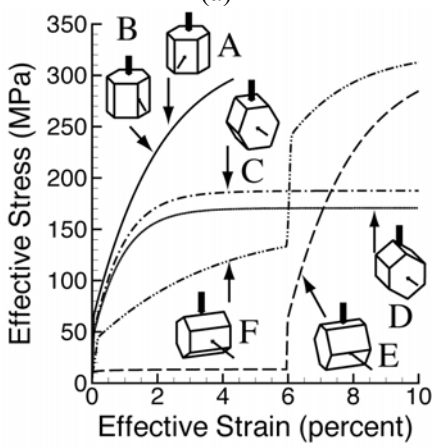

(b)

Figure 21. Stress vs strain in pure magnesium single crystal for the orientations given in Table 4: (a) experimental results [12] and (b) predictions from the model.

assumptions of this modeling approach is a constant orientation between the twinned region and the parent material. This assumption implies that no slip activity occurs in the twinned material. The model also assumes a power-law type for the evolution of the twin volume fractions and a constant hardening on both the slip and the twin systems.

The crystal-plasticity model was applied to predict stress-strain curves under plane-strain compression of Mg single crystals with six predefined orientations. Deformation twinning was only visible when the loading was applied perpendicularly to the unconstrained **c**-axis. The

predicted stress-strain curves agreed well with data from the open literature.

Recrystallization and Grain Growth Studies Using a Mesoscale Approach (ORNL)

The objective of these studies is to develop and validate mesoscale simulations of microstructure and texture evolution during TMP of Al- and Mg-alloy sheets, and to provide a comprehensive microstructure module that can be integrated with the ISV material model being developed by MSST for capturing the main features of microstructure evolution and corresponding history effects occurring during cold/hot working and heat treatment of Al and Mg alloys.

This work involves large-scale, crystal-plasticity modeling of microstructural deformation, extracting the deformation substructure, and evolving the substructure during annealing using a mesoscale technique that includes a nucleation model for recrystallization based on orientation-dependent recovery of subgrains.

Coupled Deformation-Recrystallization Simulations

TMP to produce optimum grain structure and texture is essential for the successful utilization of commercial Al and Mg alloys as sheet products. Several modeling techniques have been developed in the past with a reasonably good predictive capability for bulk deformation textures [16]. Significant progress has also been made in the last decade in the development of advanced measurement techniques for characterizing microtextures with high spatial resolution, both in two and three dimensions. However, prediction of microtexture evolution during deformation, and its subsequent evolution during recrystallization, remains very challenging because of uncertainties involved in predicting the mechanisms that lead to the formation of recrystallization nuclei with specific crystallographic orientations, and the uncertainties involved in predicting the grain/subgrain boundary properties that determine the growth kinetics of the nuclei. With the availability of large computers and advances in software, it is now possible to perform simulations of polycrystalline deformation with a high enough resolution to capture the formation of in-grain misorientations [17]. Mesoscale simulations of annealing have been combined with the output of deformation simulations to predict the evolution of recrystallization textures [18–21]. In these simulations, nucleation is modeled by heterogeneous subgrain growth, incorporating misorientation and structure-dependent boundary properties. A recent development in the modeling of nucleation is based on an assumption of orientation-dependent recovery of subgrains [22, 23]. Such an orientation-dependent recovery has been demonstrated in Al [24], copper [25] and steels [26, 27, 28]. It has also been shown that the cell morphology in the deformed structure is a function of the grain orientation. In the case of polycrystalline Al, it was shown that orientations in the vicinity of the cube had equiaxed cell structure while the other deformation orientations had a cell structure that had a linear morphology [29]. The orientation-dependent cell morphology was explained on the basis of the number of different noncoplanar active slip systems [29]. For example, a high number of noncoplanar active slip systems were correlated with more equiaxed cell morphology than when only a few coplanar slip systems are active during deformation. It has also been experimentally observed in Al polycrystals that orientations such as cube that have equiaxed cell structures also recover extremely fast compared to other deformation components.

Computational Approach

Microstructural Deformation: Mesoscale deformation simulations were performed using a polycrystal plasticity model incorporating neighboring grain interactions in which the applied deformation is distributed in a nonuniform fashion among the polycrystals [30]. Interactions with surrounding crystals are incorporated in the calculation of the deformation rate of each crystal through an appropriately defined local neighborhood. A compliance tensor is computed for each crystal based on a viscoplastic constitutive relation for deformation by crystallographic slip. The compliance of the crystal relative to that of its neighborhood provides a means for partitioning the macroscopic deformation rate among the crystals. The

deformation of fcc polycrystals under hot-rolling conditions was simulated using 18 slip systems, consisting of the 12 {111}<110> octahedral slip systems and the 6 {110}<110> nonoctahedral slip systems.

Recrystallization simulations were performed using a three-dimensional Monte Carlo approach on a cubic grid. For local-energy calculations, the energy of the site and a neighborhood consisting of the first, second, and third nearest neighbors was used. The input microstructure for the Monte Carlo simulations was obtained from the output of the crystal-plasticity simulations. The details of the Monte Carlo procedure are described elsewhere [18]. A combined simulation code that involves both deformation and recrystallization was developed for execution on parallel computers, in order to handle computational domains containing a large number of grains in the microstructure.

New Nucleation Model: A new model for the nucleation of recrystallized grains in fcc polycrystals was developed, based on the concept of "excess" hardening dislocations. The basic premise behind this approach is the existence of dislocations with mutually perpendicular Burgers vectors in fcc polycrystals. Interaction of these mutually perpendicular dislocations does not lead to hardening, since these dislocations remain mobile and do not form locks. The high mobility of the resulting special boundaries promotes rapid recovery of the dislocation substructure. Crystal orientations that have equal amounts of mutually perpendicular dislocations will recover very quickly to form recrystallized nuclei. While orientations with "excess" dislocations will form complex dislocation substructures that are slow to recover.

The nucleation step during recrystallization was modeled as follows. For each site in the simulation domain, the slip system deformation rate in the crystal coordinate system is calculated as

$$D_{ij}^{\alpha} = \dot{\gamma}_{\alpha} P_{ij}^{\alpha} \quad , \qquad (6)$$

where P_{ij}^{α} is the symmetric part of the Schmidt tensor and $\dot{\gamma}_{\alpha}$ is the shear rate on slip system α. Among the octahedral slip systems, those containing mutually- perpendicular Burgers vectors are identified, and "excess" dislocations are calculated by taking the absolute difference in slip system deformation rates on all such systems. A recovery factor is computed based on the sum of the "excess" dislocations over the entire deformation history, and a probability for nucleation is computed based on the recovery factor. An illustration of the distribution of slip system deformation rates in some of the commonly found orientations in rolled Al sheet is shown in Figures 22–24 for the D_{12}, D_{13} and D_{23} components, respectively. For cube orientation, the slip-system deformation rates are completely balanced, and can form high-mobility, low-energy boundaries contributing to quick recovery. On the other hand, for copper and S oriented grains, the slip-system deformation rates are not balanced, leading to "excess" dislocations that interact to form complex dislocation substructures and lead to slow recovery.

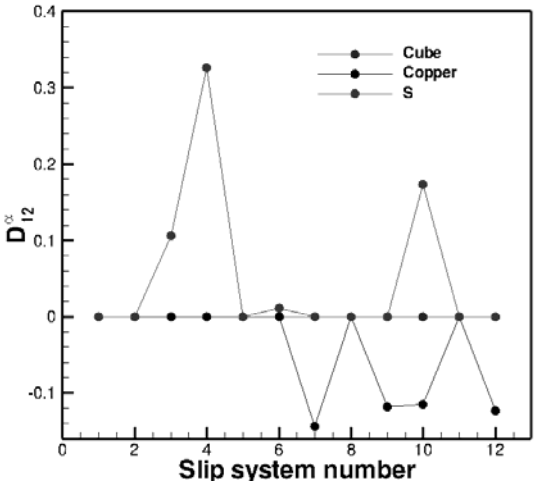

Figure 22. Distribution of deformation rate component D_{12} among various slip systems.

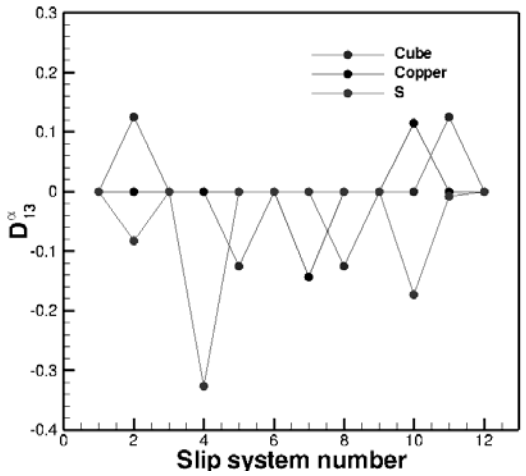

Figure 23. Distribution of deformation rate component D_{13} among various slip systems.

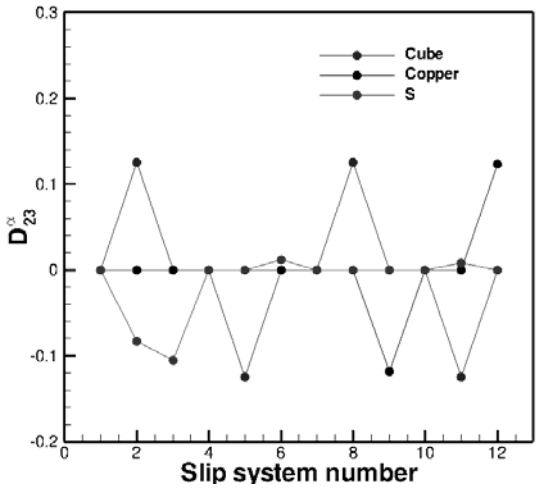

Figure 24. Distribution of deformation rate component D_{23} among various slip systems.

Results

The combined deformation and recrystallization model was used to simulate the deformation of an fcc polycrystal using a domain size of 180 × 180 × 180 sites. This problem was simulated on 216 processors. The input microstructure for the deformation model was obtained through grain growth, starting with a different orientation from a random distribution at each site. The grain-growth simulation was performed until the average grain size was about 8, which resulted in a microstructure with about 11,000 grains. The initial texture for this microstructure is shown in Figure 25 as a <111> pole figure.

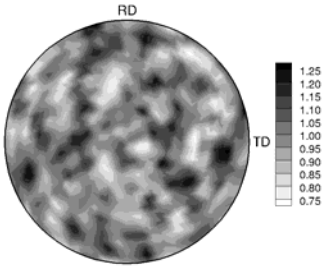

Figure 25. <111> pole figure showing the initial texture for the microstructure with about 11,000 grains.

The microstructure was deformed in plane-strain compression using the neighborhood compliance model described above under hot-rolling conditions to a compressive strain of –2.0 (about 86% reduction). The resulting deformation texture is shown as a <111> pole figure in Figure 26. The microstructure was then recrystallized, making use of the nucleation model discussed above. The result is a strong cube texture, as shown in Figure 27, even though Cube is not a major component in the deformed texture.

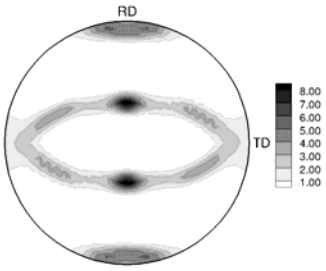

Figure 26. <111> pole figure showing the texture after deformation in plane-strain compression to 86% reduction.

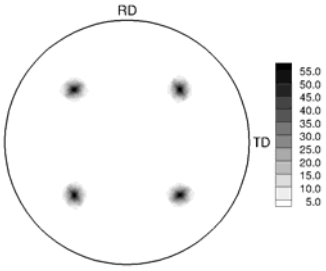

Figure 27. <111> pole figure showing the texture after recrystallization, indicating a strong cube component.

UMAT Subroutine for Magnesium Metals and Alloys (NWU)

Because of the light weight and ease of recycling, Mg alloys are of particular interest for automotive companies. However, due to the special material behaviors of these materials, few finite-element analysis implementations customized for magnesium constitutive law are available. Based on the existing theoretical work of orthotropic yield stress function by [31] and separate isotropic hardening law for tension and compression by [32], a numerical implementation procedure is proposed in this work. Our goal is to develop realistic finite-element simulations for modeling the behavior of magnesium alloys.

The proposed numerical implementation procedure consists of the following two phases: elastic and elastoplastic. In the elastic phase, a trial stress for a given discrete strain increment is evaluated assuming that the increment is elastic, while the equivalent plastic strain is kept as previous. If the effective stress given by the yield criterion is less than the yield stress calculated from the hardening law, the process is considered as elastic. Otherwise, the second phase is carried out. In the elastoplastic phase, a Newton-Raphson iteration method is used to solve the equivalent plastic strain increment, which allows effective stresses calculated separately from yield criterion and hardening law to be equal.

For verifying the numerical implementation procedure proposed above, a single shell element was created in the commercial FEM package ABAQUS and tested under uniaxial tension and compression in rolling and transverse directions using the developed user-defined material UMAT subroutine. As shown in Figure 28, the transverse direction exhibits higher yield strength than that in the rolling direction, which is consistent with the experimental data presented in [32]. Similar results are shown in Figure 29. If tension and compression results are compared, it can also be observed that the compression yield stress is less than the tension yield stress, which is a phenomenon observed from Mg alloys.

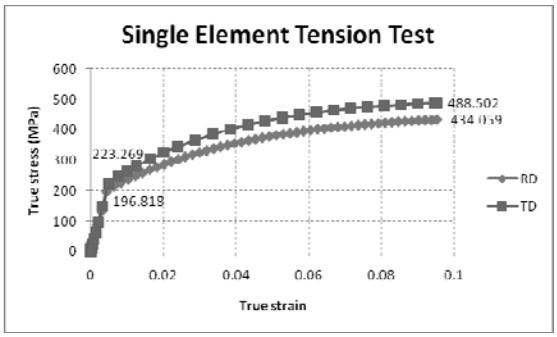

Figure 28. Stress-strain curve in uniaxial tension test.

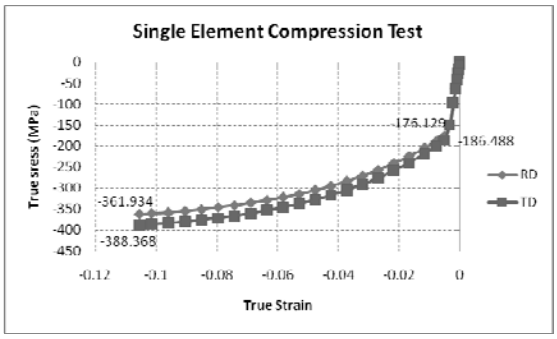

Figure 29. Stress-strain curve in uniaxial compression test.

Framework for Uncertainty Quantification and Reliability Based Design Optimization of Thermomechanical Processing

Statistical Volume Element Method for Predicting Microstructure-Constitutive Property Relations (NWU)

In materials design, there is an inevitable need to establish multilength scale statistical microstructure-constitutive property relations. In this research, we developed an SVE method to analyze, quantify, and calibrate such microstructure-constitutive property relations by statistical means. SVE simulations were adopted to predict material constitutive properties corresponding to various realizations of random microstructure configurations. As shown in Figure 30, a computing framework that links random configuration generators and finite-element analysis has been developed. A statistical cause-effect analysis approach was proposed to study the influence of random material microstructure on material constitutive properties.

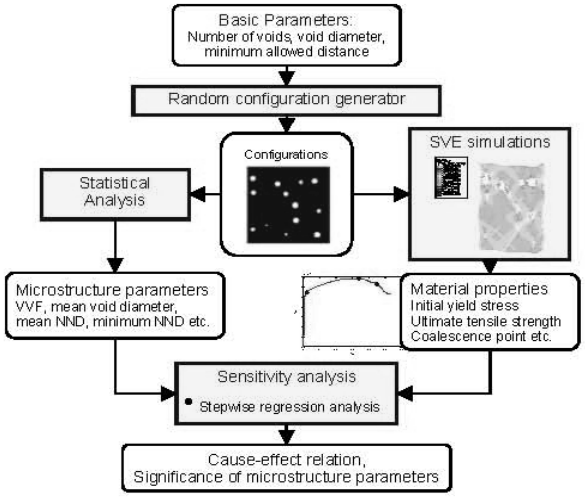

Figure 30. Statistical analysis study of material microstructure-constitutive property relation.

Within the proposed approach, statistically significant microstructure parameters are first identified based on their linear impacts on material constitutive properties. Global sensitivity analysis is then employed to provide a more comprehensive importance ranking of these critical microstructure parameters considering both main and interaction effects. The uncertainties in material constitutive properties due to random microstructure configurations are quantified in terms of distributions, statistical moments, and correlations, as shown in Figure 31. The obtained probabilistic constitutive relations are used to calibrate the model parameters in a constitutive relation model following a statistical calibration process. As shown in Figure 32, with the statistical calibration approach the obtained probabilistic constitutive relation can be reproduced through a calibrated Bammann-Chiesa-Johnson (BCJ) constitutive model.

Although our approach is currently demonstrated for a single-scale microstructure material model, our proposed techniques are generic enough to be applied to more sophisticated multiscale material models in either a hierarchical or a fully coupled (all-in-one) manner. The calibrated material constitutive models that incorporate the uncertainties propagated from random material microstructure will facilitate probabilistic analyses of material performance at the continuum level in

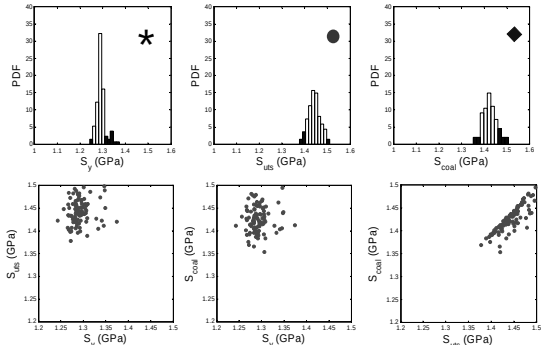

Figure 31. Distributions and correlation plots of stresses.

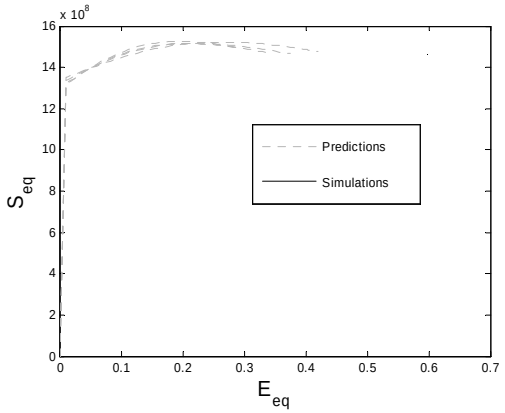

Figure 32. Random predictions/reproductions of the calibrated BCJ model compared to the SVE simulation results

multiscale design and analysis. Furthermore, the capability of deriving probabilistic material constitutive relations is essential in model validation process where the statistical computational results will be compared against random experimental results following the similar statistical model calibration procedure. The capability will also allow designers to assess the reliability of product performance by introducing the statistical representation of material constitutive relations.

A Multiscale Design Approach with Random Field Representation of Material Uncertainty (NWU)

To facilitate product design considering the impact of manufacturing process and material on product performance, a multiscale design approach is developed in our research with an emphasis on the treatment of material uncertainty across a product

domain as random field. By integrating manufacturing simulations, multiscale material models, and product models in a multiscale framework, the proposed approach allows either hierarchical or concurrent designs of manufacturing process, material and product in a multiscale content. A control-arm-design problem considering the spatial variation of initial porosity level due to casting process is used to demonstrate the applicability of the proposed approach.

For designing reliable products, uncertainty propagation under the proposed multiscale framework poses a significant computational challenge. An efficient procedure for uncertainty propagation from material random field to end product performance is developed (Figure 33). Material random field is discretized based on the product finite-element mesh and a reduced-order Karhunen-Loeve representation is derived from the covariance matrix of the discretized random field, which significantly reduces the dimensionality of random-field representation. The univariate dimension-reduction method and the Gaussian quadrature formula are applied to efficiently evaluate the statistical moments of the end-product performance.

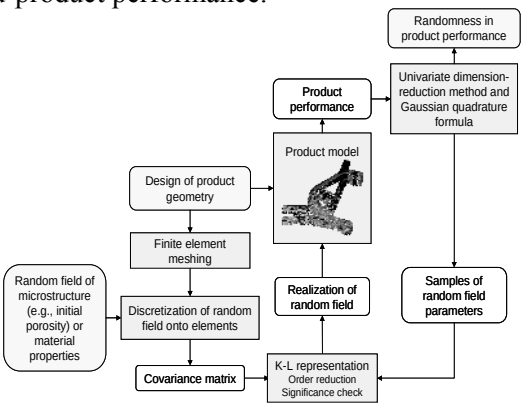

Figure 33. Efficient random field uncertainty propagation in design using multiscale analysis

The impact of a material microstructure random field with different correlation lengths on the statistical moments of product performance is studied. It is found that when the correlation parameter approaches infinity, the random field degenerates to a random variable which is uniform across the spatial domain. Based on the empirical study of the control-arm-design problem, it is discovered that the correlation parameter of input random field has a larger impact on the higher-order moments of product performance than on its mean value. Meanwhile, the correlation parameter has a monotonic negative effect on the mean product performance while a larger correlation length causes a greater standard deviation of the product performance.

A reliability-based design of the control arm is demonstrated with the consideration of uncertainty propagation across multiple scales from the material domain to the product domain. Reliable geometry designs of the control arm in terms of wall thicknesses are achieved to minimize the control-arm volume while keeping the damage level of the product under specified values. The control-arm-design example demonstrates the feasibility of the proposed approach with the random field representation of material uncertainty.

Robust Design with Arbitrary Distribution Using Gauss-Type Quadrature Formula

As a rigorous method of uncertainty propagation, the Gauss-type quadrature formula is investigated and applied to robust design formulated in terms of statistical moments of system performances. Due to the highest precision it provides, the Gauss-type quadrature formula is a well known method in the field of numerical integration. However, it has not been extensively used for uncertainty propagation involving various types of random variables. In this work, we developed a systematic procedure to find the nodes and weights of the Gauss-type quadrature formula for arbitrary input distributions and examined its mathematical meaning. It is shown that the nodes and weights of a m-node Gauss-type quadrature formula for a continuous random variable X are the samples and probability mass function of a discrete distribution, respectively, which is equivalent to X in terms of moments up to $2m-1$ order. Thus, those nodes and weights can be found from the moments of input random variables with various numerical approaches (Figure 34). Multidimensional quadrature formula can be built from the one-dimensional quadrature formula, and the tensor product formula and univariate dimension-reduction method are adopted in our work.

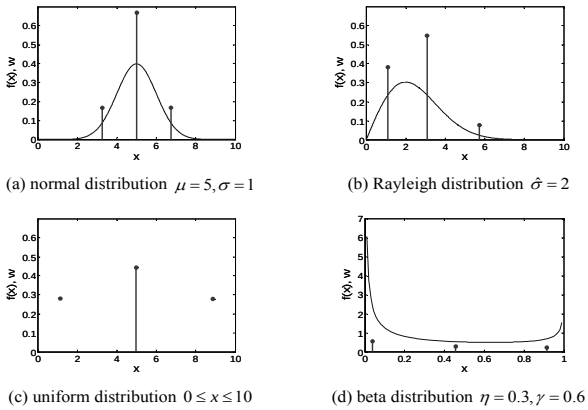

(a) normal distribution $\mu = 5, \sigma = 1$ (b) Rayleigh distribution $\hat{\sigma} = 2$

(c) uniform distribution $0 \le x \le 10$ (d) beta distribution $\eta = 0.3, \gamma = 0.6$

Figure 34. Nodes and weights in 3-node quadrature formulas for four different distributions. The vertical axis represents the values of probability distribution functions (PDF) and weights.

A procedure for robust design optimization using the Gauss-type quadrature formula is proposed with an emphasis on the efficient calculation of design sensitivity. Since one evaluation of statistical moments requires multiple function evaluations, the design sensitivity evaluation using approximate schemes such as finite-difference method will increase the computational cost of optimization significantly. In our research, formulas for semi-analytic design sensitivity of statistical moments are derived for tensor product and univariate dimension-reduction method, which utilize the sample data obtained during the moments estimation. It is shown from our case studies that the proposed design sensitivity analysis reduces the computational cost of robust design up to 40% when compared to the finite-difference method.

Conclusions

During 2008, the project has continued to make good progress on the activities planned. Also, new activities have been added to the work plan, in particular aspects related to the extrusion of Mg alloys. On the experimental part, the main focus has been on annealing studies to characterize recrystallization in Al and Mg alloys, uniaxial mechanical tests to study twinning effects in pure Mg, laboratory-scale experiments to learn about specific aspects of the extrusion process, and mechanical tests to capture the hardening behavior of sheet metals. On the material modeling part, the focus has been on MD simulations for mobility studies of hcp structures, enhancements of a crystal plasticity model to model deformation twinning, and developing a new nucleation model for recrystallization of fcc crystal structures using Monte Carlo techniques. Finally, on the design/optimization part, a probabilistic framework with its numerical aspects has been developed to quantify/propagate uncertainties due to different sources when designing/optimizing deformation processes. All this work will contribute to the development of robust TMP models and design methodologies for improving manufacturability and forming technology of lightweight materials, in particular, Al and Mg alloys.

Presentations/Publications/Patents

1. S. Groh, E. B. Marin, M. F. Horstemeyer, and H. Zbib (2008), "Multiscale Modeling of the Plasticity in Aluminum Single Crystal," *International Journal of Plasticity*, in press.
2. S. Groh, E. B. Marin, D. J. Bammann, and M. F. Horstemeyer, "Implementation of Deformation Twinning in a Crystal Plasticity Code: Application to Mg Single Crystal," CAVS internal report, under review.
3. J. Cao, W. Lee, H. S. Cheng, H. Wang, and K. Chung (2008), "Experimental and Numerical Investigation of Combined Isotropic-kinematic Hardening Behavior," to appear International *Journal of Plasticity*. doi:10.1016/j.ijplas.2008.04.007.
4. X. Yin, W. Chen, W. K. Liu, and A. To, "A Statistical Volume Element Method for Predicting Microstructure Constitutive Relations," *Computer Methods in Applied Mechanics and Engineering*, available online, January 2008.
5. X. Yin, S. Lee, W. Chen, W. K. Liu, and M. F. Horstemeyer, "A Multiscale Design Approach with Random Field Representation of Material Uncertainty," Paper No. DETC2008-49560, Proceedings of the ASME 2008 International Design Engineering Technical Conferences & Computers and Information in Engineering Conference, August 3–6, 2008, Brooklyn, New York. In press, *ASME Journal of Mechanical Design*.

6. S. Lee, W. Chen, and B. M. Kwak, "Robust Design with Arbitrary Distributions using Gauss-type Quadrature Formula," Proceedings of the 12th AIAA/ISSMO Multidisciplinary Analysis and Optimization Conference, September 10–12, 2008, Victoria, British Columbia, Canada, in press, Structural and Multidisciplinary Optimization.

References

1. [Mordike, 2001] B. L. Mordike, and T. Ebert, "Magnesium—Properties—applications—potential," *Materials Science and Engineering A*, 12 (2001) 37–45.
2. [Groh, 2008] Groh, S., Marin, E. B., Horstemeyer, M. F., and Zbib, H. M., 2008. *Int. J. Plast.,* in print.
3. [Plimpton, 1995] Plimpton, S. J., 1995. *J. Comp. Phys.* 117, 1–19.
4. [Sun, 2006] Sun, S. L., Mendelev, M. I., Becker, C. A., Kudin, K., Haxhimali, T., Asta, M., Hoyt, J. J., Karma, A., and Srolovitz, D. J., 2006. *Phys. Rev. B.,* 73, 024116-1-12.
5. [Hirth and Lothe, 1992] Hirth, J. P., and Lothe, J., *Theory of dislocations*, Krieger Publishing Company, Malabar, Florida.
6. [Conrad, 1957] Conrad, H., and Robertson, W. D., *AIME* 209 (1957) 503.
7. [Reed-Hill, 1957] Reed-Hill, R. E., and Robertson, W. D., 1957. *Acta Metall.,* 5, 717–727.
8. [Staroselsky, 2003] Staroselsky, A., and Anand, L., 2003. *Int. J. Plasticity.* 19, 1843–1864.
9. [Liu, 1996] X.-Y. Liu, J. B. Adams, F. Ercolessi, and J. A. Moriarty, *Modelling. Simul. Mater. Sci. Eng.* 4 (1996) 293–303.
10. [Kelley, 1968] Kelley, E. W., and Hosford, Jr., W. F., 1968. Trans. Metal. Soc. *AIME*, 242, 5–13.
11. [Kelley, 1968] Kelley, E. W., and Hosford, Jr., W. F., 1968. Trans. Metal. Soc. *AIME*, 242, 5–13.
12. [Kelley, 1968] Kelley, E. W., and Hosford, Jr., W. F., 1968. Trans. Metal. Soc. *AIME,* 242, 5–13.
13. [Marin, 2006] Marin, E. B., 2006 Sandia National Laboratories, CA, SAND2006-4170.
14. [Kalidindi, 1998] Kalidindi, S. R., 1998. *J. Mech. Phys. Solids.* 46, 267–271.
15. [Kelley, 1968] Kelley, E. W., and Hosford, Jr., W. F., 1968. *Trans. Metal. Soc. AIME*, 242, 5–13.
16. [Nave, 2004] Nave, M. D., and Barnett, M. R., 2004. *Scripta Mater.,* 51, 881–885.
17. [Barnett, 2007] M. R. Barnett, *Mat. Sc. Eng.* A, 464 (2007) 1–7.
18. [Salem, 2005] Salem, A. A., Kalidindi, S. R., and Semiatin, S. L., 2005. *Acta Mater.* 53, 3495–3502.
19. [Kocks, 1998] U. F. Kocks, C. N. Tomé, and H.-R. Wenk, *Texture and Anisotropy,* Cambridge University Press, Cambridge, 1998.
20. [Sarma, 1998] G. B. Sarma, B. Radhakrishnan, and T. Zacharia, Comput. *Mater. Sci.* 12 (1998) 105–123.
21. [Radhakrishnan, 1998] B. Radhakrishnan, G. Sarma, and T. Zacharia, *Acta Mater.* 46 (1998) 4415–4433.
22. [Radhakrishnan, 2000] B. Radhakrishnan, G. Sarma, H. Weiland, and P. Baggethun, *Model. Simul. Mater. Sci. Eng.* 8 (2000) 737–750.
23. [Radhakrishnan, 2004A] B. Radhakrishnan, G. Sarma, *Phil. Mag.* A22 (2004) 2341–2366.
24. [Radhakrishnan, 2004B] B. Radhakrishnan, G. Sarma, JOM 56 (2004) 55–62.
25. [Crumbach, 2004] M. Crumbach, M. Goerdeler, G. Gottstein, L. Neumann, H. Aretz, and R. Kopp, *Model. Simul. Mater. Sci. Eng.* 12 (2004) S1–S18.
26. [Radhakrishnan] B. Radhakrishnan and G. Sarma, *Mater. Sci. Eng.* A494 (2008) 73–79.
27. [Theyssier, 1999] M. C. Theyssier and J. H. Driver, *Mater. Sci. Eng.* A272 (1999) 73–82.

28. [Ridha, 1982] A. A. Ridha and W. B. Hutchinson, *Acta Metall. Mater.* 30 (1982) 1929–1939.

29. [Humphreys, 1995] F. J. Humphreys, M. Hatherly, *Recrystallization and Related Annealing Phenomena,* first ed., Elsevier, New York, 1995, pp. 335–337.

30. [Barnett, 1999] M. R. Barnett and L. Kastens, ISIJ International 39 (1999) 923–929.

31. [Yoshinaga, 1998] N. Yoshinaga, D. Vanderschueren, L. Kestens, K. Ushioda, and J. Dilewijns, *ISIJ International* 38 (1998) 610–616.

32. [Liu, 1998] Q. Liu, D. Juul Jensen, and N. Hansen, *Acta Mater.* 46 (1998) 5819–5838.

33. [Sarma, 1996] G. Sarma and P. R. Dawson, Int. J. Plast. 12 (1996) 1023-1054.

34. [Cazacu, 2005] Cazacu, O., Plunkett, B., and Barlat, F., "Orthotropic yield criterion for hexagonal closed packed metals," *Int. J. Plasticity*, 2005.

35. [Kim, 2008] Kim, J., Ryou, H., Kim, D., Kim, D., Lee, W., Hong, S. H., and Chung, K., "Constitutive Law for AZ31B Mg Alloy Sheets and Finite Element Simulation for Three Point Bending," 2008.

B. Development of High-Volume Warm Forming of Low-Cost Magnesium Sheet (AMD602*)

Principal Investigator: Peter Friedman
Ford Motor Company
Ford Research and Innovation Center
2101 Village Road, MD 3135
Dearborn, MI 48121-2053
313-248-3362; fax: 313-390-0514; e-mail: pfriedma@ford.com

Principal Investigator: Paul Krajewski
General Motors Corporation
General Motors R&D and Planning
Mail Code 480-106-212
30500 Mound Road
Warren, MI 48090-9055
586-986-8696; fax: 586-986-9204; e-mail: paul.e.krajewski@gm.com

Principal Investigator: Jugraj Singh
Chrysler Corporation LLC
Body Materials Engineering
Mail Code 482-00-11
800 Chrysler Drive
Auburn Hills, MI 48326-2757
(248) 512-0029; fax: (248)576-7490; e-mail: js329@chrysler.com

Technology Area Development Manager: Joseph A. Carpenter
(202) 586-1022; fax: (202) 586-1600; e-mail: joseph.carpenter@ee.doe.gov

Field Project Officer: Aaron D. Yocum
(304) 285-4852; fax: (304) 285-4403; e-mail: aaron.yocum@netl.doe.gov

Contractor: United States Automotive Materials Partnership
Contract No.: FC26-020R22910 through the DOE National Energy Technology Laboratory

Objective

Develop the technology and material supply base for cost-effective lightweight body panels fabricated from sheet magnesium (Mg). A warm-forming system will be designed and built to develop a suitable process for forming Mg sheet as well as a test bed to evaluate potential low-cost Mg sheet from various global producers. Specific deliverables from this project will include the following:

- Design and build a warm-forming die and demonstrate a deep-draw capability on conventional direct chill (DC) material.
  - — Demonstrate pan forming of at least 100 mm.
- Evaluate materials and compare the formability of continuous cast (CC) and DC materials.
  - — Evaluate high-temperature elongation, which is equal or greater in CC material compared to DC material.

*Denotes project 602 of the Automotive Materials Division of the United States Automotive Materials Partnership, one of the formal consortia of the United States Council for Automotive Research set up by Chrysler, Ford, and General Motors to conduct joint, precompetitive research and development (see www.uscar.org).

- Demonstrate high-volume cycle times with CC material on an integrated forming cell.
  - Part-to-part cycle time with CC material of 5–10 jobs per minute (jpm).

Approach

Continuous casting is a key technology for enabling the development of low-cost Mg sheet. This project will drive material development in the supply base by giving them a mechanism for evaluating materials. The project will receive material from major global Mg suppliers including Magnesium Elektron, CSIRO, ThyssenKrupp, LY Copper, and POSCO. These materials will be characterized via tensile testing at the University of Virginia, biaxial forming at Canada Centre for Mineral & Energy Technology (CANMET), and through stamping trials at Troy Tooling Technologies.

- Novel die systems will be designed and constructed that enable the use of warm forming in conventional single-action presses. The die will be used to determine critical forming parameters for Mg sheet, including lubricant thickness, preheat temperature, die temperature, forming speed, etc. The forming windows for the different materials will be determined to see the effect of processing via different methods, e.g., CC vs ingot (DC) casting.
- Full automation including loading of pre-heated sheet and part extraction will be developed to achieve acceptable cycle times (5–10 jpm) demonstrating the high-volume feasibility of warm forming.

Accomplishments

- Completed the material characterization work through microscopy, elevated temperature tensile testing and formability experiments on alloys from four suppliers.
- Demonstrated the formability of the CC alloys with both tensile testing, lab-scale formability experiments, and full warm-forming trials. Developed forming-limit curves at CANMET for all test alloys at two different temperatures.
- Completed first full-scale forming trial and determined a forming window for Mg sheet with respect to temperature, binder pressure, lubricant, and blank size.
- Developed a strategic approach to automating the warm-forming system based on existing equipment donated to the project from General Motors (sheet pre-heater) and Ford (robot).
- Established the feasibility of using a new, lower-cost synthetic oil lubricant for forming at temperatures up to 275°C.

Future Direction

- Forming trials on newer materials.
- Post-form analysis
- Develop automated system to pre-heat sheets and deliver them to the die to support the goal of 5 to 10 parts per minute.
- Full-scale trials on automated system

Introduction

The major barrier to the application of Mg sheet components in vehicle structures is a combination of two factors: the limited formability of Mg sheet and the cost of producing the sheet itself. Warm-forming processes similar to what was demonstrated in aluminum with the USAMP Warm Forming Project (AMD 307) can be used to significantly improve the formability of Mg sheet. This project is leveraging the accomplishments of AMD 307 to develop equipment, lubricant, simulation and forming equipment for the cost-effective forming of Mg sheet. A warm-forming cell based on the lessons learned of AMD 307 will be designed and built to demonstrate the efficient forming of Mg sheet. The target application for this process is deep-draw panels with specific interest in door inners.

The cost of Mg sheet is driven by the high conversion costs of rolling an ingot into sheet form. This is a direct result of the hexagonal close-packed (HCP) structure of Mg that requires the sheet to be rolled in small increments often with annealing steps between rolling passes. CC is a technology with the potential to reduce this cost dramatically. By casting directly into sheet form, CC offers a higher production rate, a smaller capital investment, and significantly less energy and labor as compared with the conventional DC ingot-casting process. The opportunities for decreasing the cost of Mg sheet via continuous casting have been described by Hunt et al. in their 2005 report to the DOE. Suppliers globally are working on developing CC technology. In this project, all of the major global Mg suppliers will be included to determine if their materials are suitable for the warm-forming process. The new warm-forming system will be used as a standard test bed for the evaluation of these materials as well as new Mg sheet materials produced in the future.

Low-Cost Magnesium Sheet

The project includes Mg sheet from five major global Mg suppliers. This includes two DC casters (Magnesium Elektron and ThyssenKrupp) and three continuous casters (CSIRO, LY Copper, and POSCO). Four suppliers have provided 100 blanks of 1 mm × 600 mm × 600 mm of AZ31B-O material. All of the materials will be used at three locations, The University of Virginia, CANMET, and Troy Tooling Technologies.

Materials in this work have been coded so that the technical results can be shared with all the material suppliers without providing company information. Samples of all the materials have been provided to Professor Sean Agnew at the University of Virginia and Dr. Kevin Boyle at CANMET.

Deliverable:

- Determine best AZ31 alloy for warm forming and provide guidance to the materials community on how CC materials compare with DC cast materials.

Material Characterization

The University of Virginia

In this work, the microstructure and tensile properties of four different materials of nominally the same composition but produced by distinct processing routes were characterized. While such comparative studies are often conducted in a blind or double-blind fashion in the biological, medical, and social sciences, it is rather atypical to do so within the field of metallurgy. The experimentalists in this study were unaware of the processing route, and as such were able to probe the fundamental microstructure–property relationships without any bias associated with knowledge of the processing history.

Experimental Procedures

Four heats of Mg alloy, AZ31B, sheet were examined in this study. Each of the sheets was received in the O temper (fully annealed) with a nominal thickness of 1 mm and a length and width of approximately 600 mm whose compositions are presented in Table 1. Some of the alloys were produced by strip casting and warm/cold rolling to the finish gage and some were DC cast as thick slabs, hot rolled, and finally warm/cold rolled to finish gage.

Table 1. Sample designations and compositions

Sheet	Al	Zn	Mn	Mg
M	2.6	0.71	0.32	Balance
N	3.0	0.74	0.35	Balance
O	3.0	0.74	0.32	Balance
X	2.9	0.95	0.53	Balance

The microstructures of the sheets were analyzed using optical and scanning electron microscopy. Standard metallographic sample preparation was employed, with a requirement that oil-based lubrication be used (rather than water) for all polishing steps. An acetal-picric etchant was used which revealed grains and grain boundaries. The average grain size was determined using a computer-aided linear intercept measurement.

Texture measurements were performed on the sheet surfaces and midplanes. A Scintag X1 X-ray diffractometer equipped with a CuK_{α} sealed tube source, energy-dispersive detector and a 4-circle

goniometer was employed to measure pole figures to a sample tilt of 80°. The (00.2), (10.0), and (10.1) pole figures were measured and the preferred orientation package of Los Alamos (popLA) software was used to calculate the complete orientation distribution which, in turn, allowed the recalculation and presentation of complete pole figures. Standard X-ray powder diffraction was also used to determine the phase content.

An Instron universal testing machine, equipped with a clam-shell cylindrical furnace, was used for tensile testing over a range of temperatures, from room temperature to 350°C, and a range of constant true strain rates, from 5×10^{-5} to 1 s^{-1}. Samples were tested with the stress axis aligned with two orthogonal directions: the rolling direction (RD) and the transverse direction (TD). The sample geometry was a compromise between the American Society for Testing and Materials (ASTM) standard for the characterization of sheet superplasticity [1] and a similar sample developed at General Motors (GM) Research and Development Center. The sample has a straight gage length of 32 mm, sharp radius of 1.25 mm, and large grip tabs. The sample is pulled by the grip shoulders, which enables quick loading, to avoid large temperature transients in the furnace, and quick unloading which allows rapid quenching following testing. A small number of tests were conducted in an MTS screw-driven testing machine within an ATS convection furnace, which is capable of sustaining more uniform temperature distribution, even at large deformations. Finally, because sheet-metal formability can be influenced by strain anisotropy, the Lankford coefficient r was calculated as

$$r = \varepsilon_w / \varepsilon_t \quad , \qquad (1)$$

where ε is the logarithmic true plastic strain along the sample width *w* and thickness *t*. The variation in *r* was determined as a function of strain at specific temperatures and strain rates relevant to warm forming.

Results and Discussion

Typical optical sections of the sheets, looking along the rolling direction, are shown in Figure 1.

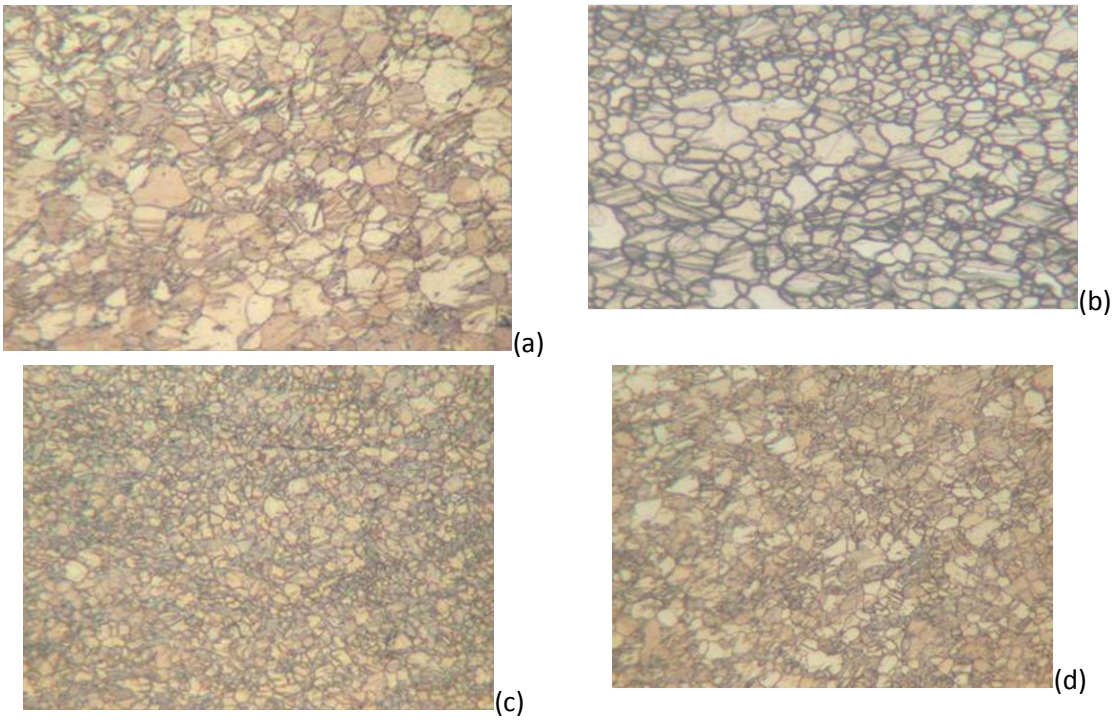

Figure 1. Optical micrographs (at right) illustrate the similarities and distinctions among the four alloys (a) M, (b) N, (c) O, and (d) X.

The grain sizes were measured using the Heyn intercept method, as described by Vander Voort [2] with measurements obtained using lines oriented parallel to the three orthogonal axes, RD, TD, and the normal direction (ND). Measurements were made on faces perpendicular to each of the three orthogonal directions. The results show that all of the sheets, without respect for the gross differences in processing history, acquired equiaxed microstructures (Table 2.), with the presence of twins more obvious in the samples with coarser grain sizes. A summary of the data is contained in Tables 2 and 3. It was found that sample M had the coarsest average grain size, samples N and X were very similar, and sample O had the finest grain sizes.

Table 2. Linear intercept grain size (in μm) measured along various directions and the corresponding aspect ratios

Sheet	d_{RD}	d_{TD}	d_{ND}	RD/TD	RD/ND	TD/ND
M	11.1	12.2	10.1	0.91	1.10	1.20
N	8.3	8.1	8.0	1.03	1.04	1.01
O	5.8	6.2	5.6	0.93	1.04	1.11
X	8.0	8.8	8.2	0.92	0.98	1.06

Table 3. Overall grain size (again in μm, and assumed equiaxed) and statistics, including standard deviation of the mean (**Σ)**, 95% confidence interval, and %-relative accuracy (RA)

Sheet	d_{avg}	Σ	95%	% RA
M	11.0	0.4	0.9	8.4
N	8.2	0.2	0.3	4.6
O	5.8	0.1	0.3	5.3
X	8.3	0.1	0.3	3.8

Additionally, while all the alloys did contain second phase particles, most notable are the large (~10 μm) particles within sheet X. Figure 2 is an SEM micrograph of a typical cracked particle. Energy-dispersive X-ray spectra (EDS) were collected to determine their chemistry. On average, the precipitates contain approximately 80% Mn, 8% Al, 5% Fe and 0–2% Mg, Na, Cr, O, Si, Cl. The presence of Fe is not surprising given that one role of the Mn additions is to scavenge such transition metal impurities.

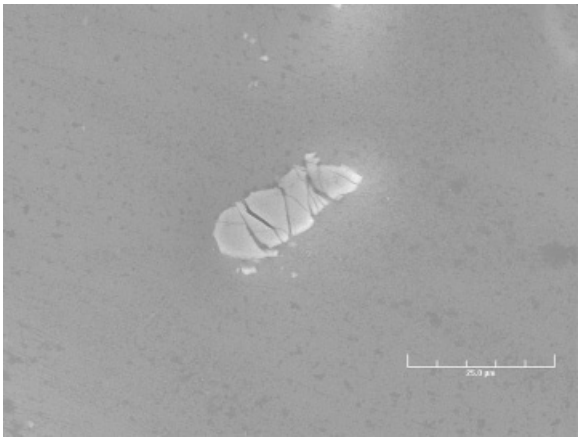

Figure 2. Scanning electron microscope image of a typical large particle in sheet X.

X-ray powder diffraction was used to determine the phase of these particles. Given that the volume fraction of second-phase particles is low, the only phase that could be unquestionably identified using initial XRD scans of monolithic samples was the α-Mg phase. Different chemical methods were explored which would digest the Mg phase, and enhance the signal from the particles. An aggressive etch of the surface, which exposed a larger fraction of particles, proved successful in confirming that the particles are the α-Mn phase. The presence of large Mn particles is consistent with the fact that sheet X had the highest Mn content. Although space precludes presentation of the images, metallography of tensile-tested samples has demonstrated that these particles initiate cavities, although this does not result in an overall lowering of the ductility with respect to the sheets which have smaller particles.

Texture:

Recalculated (00.1)- and (10.0)-pole figures are presented in Figure 3 showing that all of the sheets have a basal texture characteristic of Mg alloy AZ31B sheet, regardless of whether they were processed by DC casting and heavy reduction by hot rolling or by strip casting. This suggests that the texture is most heavily influenced by the final warm/cold reduction and annealing steps. Only the mid-plane textures are presented, since they are characteristic, although the texture was measured at the surface-, 1/8-, 1/4-, 3/8-, and mid-thickness planes of each sheet. There is no significant gradient in the texture between the 1/8- and mid-planes. Rather, the gradients are restricted to the

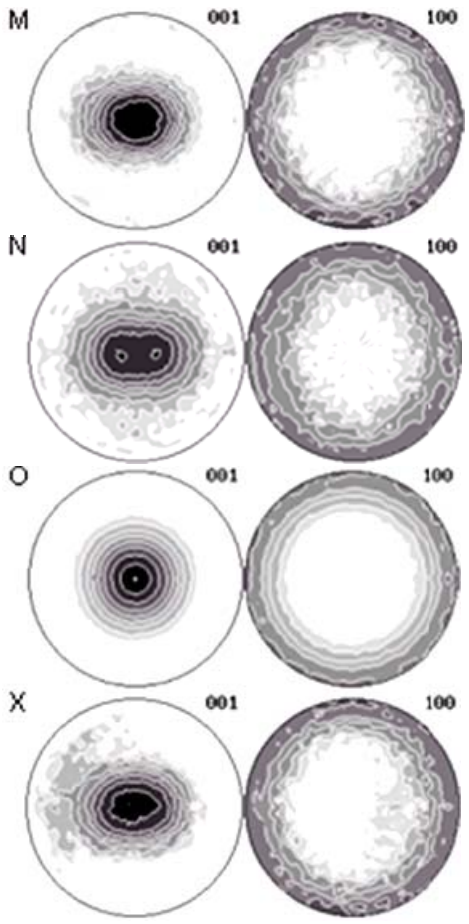

Figure 3. Textures of the 4 alloy sheets measured at the mid-plane (RD to the right, ND normal to the page, and intensity contours on a log scale: 0.21, 0.35, 0.50, 1.0, 1.7, 2.8, 4.8, 8.0).

near-surface region, which is influenced most heavily by the shear stresses imposed by contact with the rolls.

Only sheet N shows the splitting of the basal pole intensity toward the rolling direction, which is characteristic of Mg alloy AZ31B sheet in the H24 temper (e.g., [3]). Although the O temper was specified for each of the sheets, it appears that a larger volume fraction of material retained the deformation texture components in this sheet than in the others. The other sheets show a surprising level of radial symmetry about the sheet ND, which is characteristic of sheets with the O temper [4], and presumably characteristic of the recrystallization texture. Curiously, the mechanical properties (strengths) of sheet N are not distinct, although it will be shown that the Lankford coefficient, r, does show a stronger in-plane variation in this alloy than the others.

Mechanical Properties:

Figures 4 and 5 show representative flow curves out of ~235 tests performed over the temperature and rate regime of interest. None of the alloys exhibit significant strength anisotropy. Thus, only data from RD samples are presented in order to avoid cluttering the plots. In general, the four alloy sheets behave quite similar to one another, in terms of flow strength, strain hardening, and ductility.

As reported previously by Jiang et al. [5] and the present group [6], wrought Mg alloys undergo a plateau or even a decrease in ductility with increasing temperature within the temperature range examined. Note the decrease in flow stress *and ductility* as the temperature is increased from 150 to 200°C [e.g., Figure 4(a)]. This anomaly also occurs with respect to strain rate, whereby the ductility can decrease with decreasing strain rate [e.g., Figure 5(b)]. These anomalies can be predicted using a continuum mechanical model of plastic instability, if one accounts for the simultaneous changes in strain and strain rate hardening behaviour [6], and it has been mechanistically ascribed to incomplete (heterogeneous) dynamic recrystallization, which occurs within the same rate and temperature regime [5].

Figure 6 shows multiple engineering stress vs strain curves obtained from samples of each sheet at a temperature of 300°C and a strain rate of 0.005 s^{-1} within a convection furnace that ensures a uniform temperature distribution, even at large elongations. This presentation emphasizes the similarity of the flow curves, e.g., each have a "knee" in their flow curve at about 50% elongation, and exhibit plastic instability at a low strain, which means that most of the elongation is "post-uniform" and due to the finite rate sensitivity of the alloys. It is observed that the three curves with the highest peak stresses are from sheet M, which has the largest grain size, and the curves with the lowest peak stress are from sheet O, with the finest grain size.

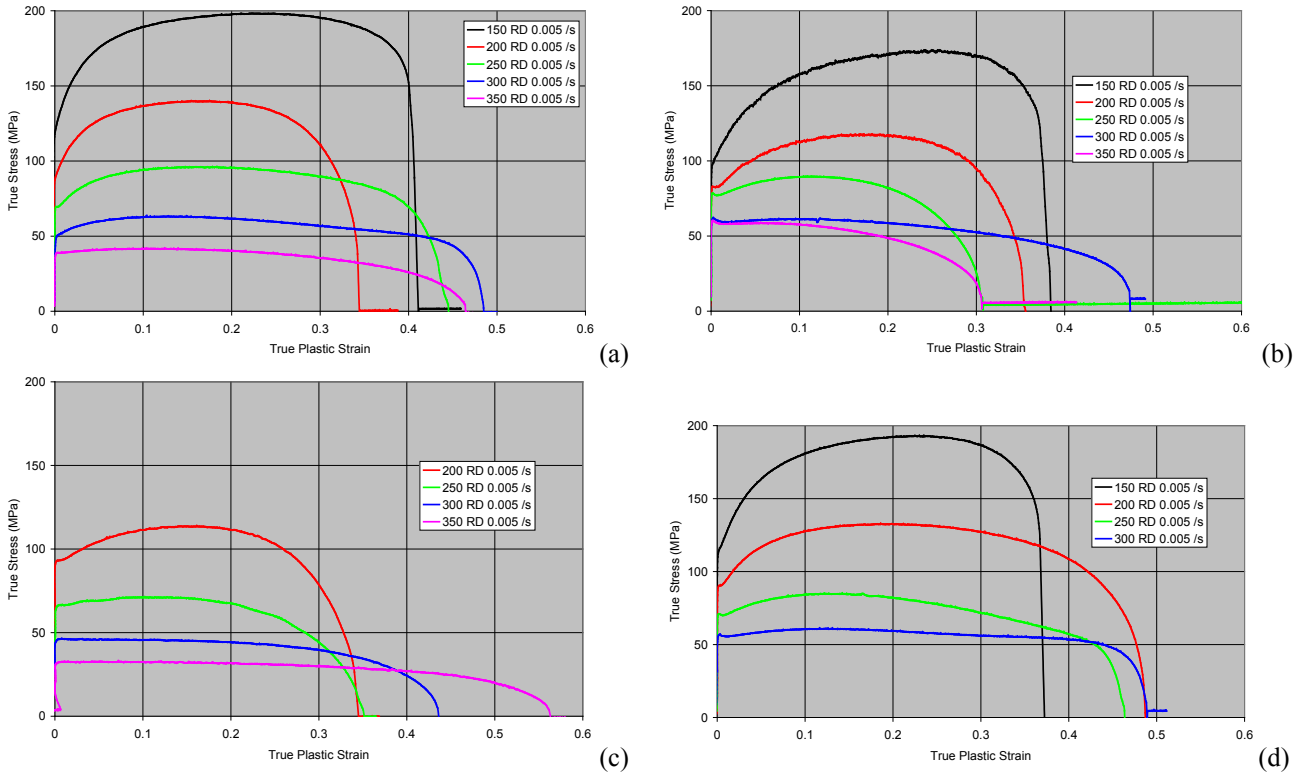

Figure 4. Temperature dependence of the RD tensile flow curves of sheets a) M, b) N, c) O, and d) X at a constant true strain rate of $.5 \times 10^{-3}$ s^{-1}.

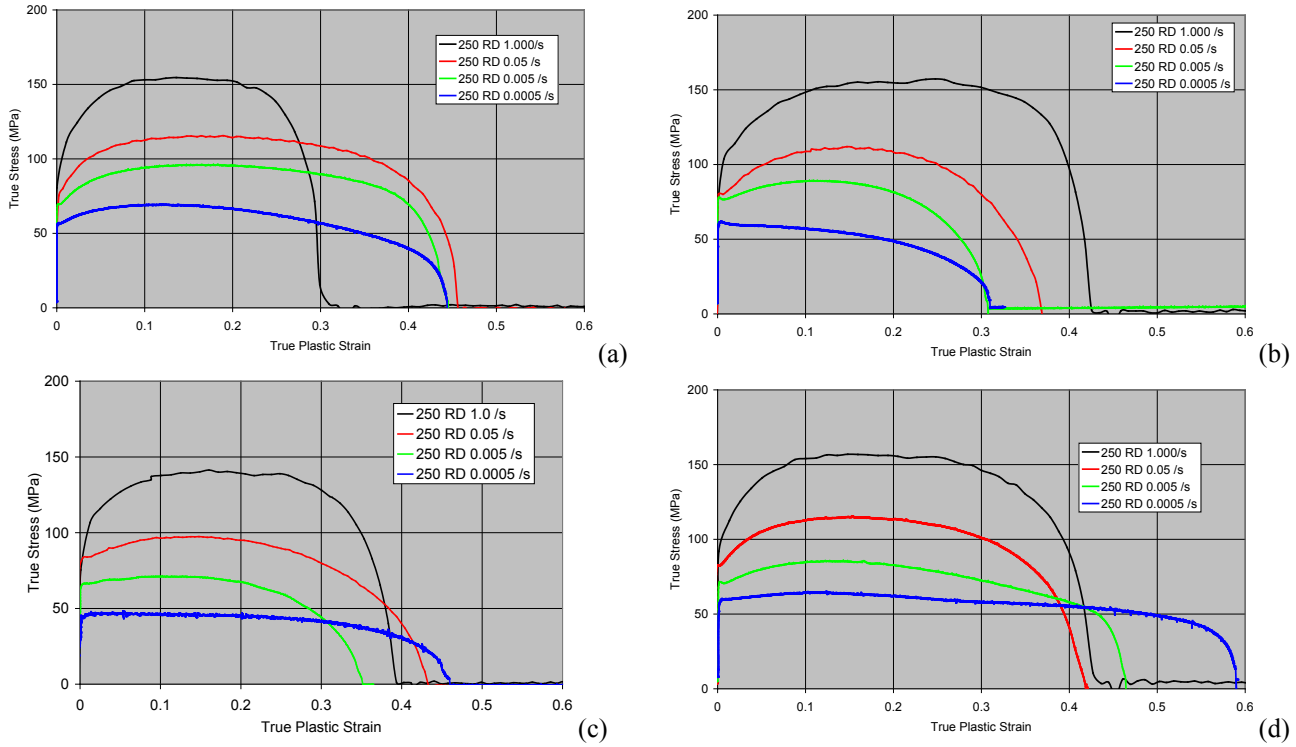

Figure 5. Strain-rate dependence of the RD flow curves of sheets (a) M, (b) N, (c) O, and (d) X at a temperature of 250°C.

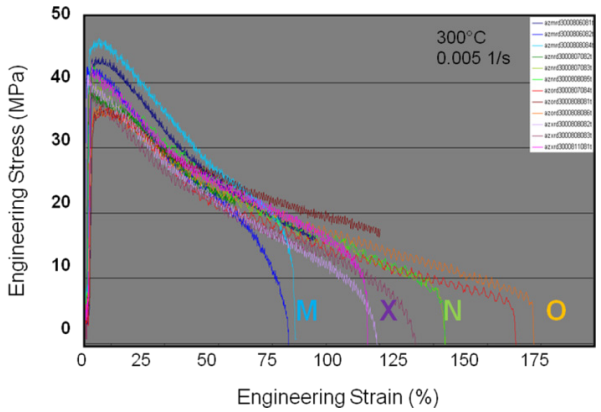

Figure 6. Engineering stress vs engineering strain at a temperature of 300°C and strain rate of 5×10^{-3} s^{-1}.

Samples of sheets N and X exhibit intermediate flow strengths in keeping with their intermediate grain sizes. At this temperature, finer grains promote easier flow and higher strain-rate sensitivity. This helps explain why samples of sheet O have the highest elongation to failure, and M samples the lowest, at this temperature.

Constitutive Modeling:

Sellars & Tegart [7] suggested the use of a hyperbolic sine function to describe the relationship between rate and flow stress over a wide range of hot-working and creep conditions.

$$\dot{\varepsilon} = A \exp\left(\frac{-Q}{RT}\right)\left[\sinh(\alpha\sigma)\right]^n \quad . \qquad (2)$$

This equation is often expressed [8,9] in terms of the Zener-Holloman parameter, Z or temperature-compensated strain rate,

$$Z = A\left[\sinh(\alpha\sigma)\right]^n = \dot{\varepsilon}\exp\left(\frac{Q}{RT}\right) \quad . \qquad (3)$$

The relationship approaches a simple power law flow stress, which is typical of high-temperature creep, and asymptotes to an exponential function at high stresses, which is typical of thermally activated slip. We determined the parameters A, α, n, and Q for each of the alloys independently, and obtained activation energies, $Q \sim 120$–160 kJ/mol. While it is possible that the fundamental controlling mechanisms could be distinct between the different sheets, it was noted that these values are close to the activation energies of Mg self-diffusion and Mg-Al interdiffusion [10]. A value of $Q = 140$ kJ/mol provides a high goodness of fit (R^2 value) for all the sheets, and the use of a single value more readily allows for comparisons, since a given temperature-strain rate pair corresponds to a single value of Z for all the sheets.

Figure 7 presents the experimentally-measured flow stresses at a strain of $\varepsilon = 0.1$ for the RD of all the sheets examined and the best fit curves corresponding to Eq (3), with an activation energy of 140 kJ/mol. Table 4 presents the fit parameters and goodness-of-fit measures for each of these curves, as well as the corresponding curves from the TD samples. It is noted that the equation does not accurately describe lower temperatures ($T < 150$°C) behavior, and this is believed to be a

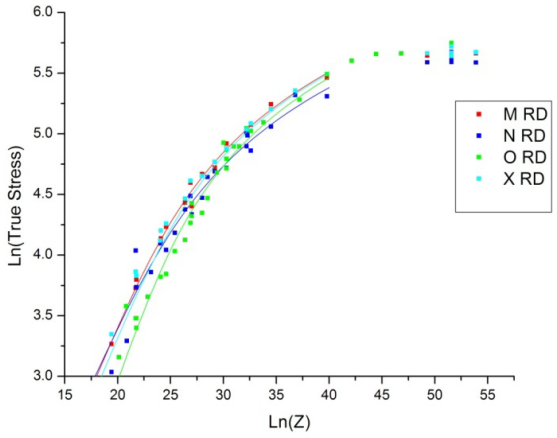

Figure 7. Best fits of the Sellars-Tegart Eq (3) to the flow stresses at a strain of 0.1 of the four sheets over a wide range of deformation conditions, Z (assuming Q = 140 kJ/mol).

Table 4. Fit parameters with the grain size.

Alloy	Grain size	ln *(A)*	*n*	*α*	R^2
M RD	11.0	22.95	4.69	0.017	0.993
M TD		22.1	4.67	0.019	0.997
N RD	8.2	21.37	3.53	0.027	0.982
N TD		23.4	4.87	0.017	0.991
O RD	5.8	22.83	3.66	0.023	0.975
O TD		24.35	3.80	0.020	0.996
X RD	8.3	23.55	4.64	0.012	0.993
X TD		25.41	5.46	0.013	0.998

result of a mechanistic transition whereby the flow stress at lower temperatures is controlled by the thermally activated slip of <a> type dislocations on non-basal planes (e.g., [3]). In summary, the overall behavior is very similar between the four heats, and that Eq (3) accurately captures the change in apparent stress exponent at high *Z*.

Focusing on the low *Z* end of the curves, a trend toward linearity is observed, i.e., the data asymptote to a power law typical of high-temperature creep. Under these conditions, alloy O has the lowest flow stresses and while the other sheets typically have power-law exponents in the range of n = 4-5 typical of diffusion-controlled climb and glide, alloy O has a lower exponent. This suggests that it may be undergoing a transition to another mechanism, such as grain-boundary sliding, characterized by n = 2. The finer grain size of sheet O would promote such a transition.

Anisotropy:

The final behavior examined is the strain anisotropy, or r-value. The r-values were measured as a function of strain from 0.1–0.3 (provided the samples underwent sufficient uniform straining to allow accurate measurements at the higher strain levels). For the present report, typical values at a strain of 0.15 are reported for tests performed along the RD and TD (Figure 8). The r-values of all the sheets tend toward 1 (isotropy) as the temperature is raised from 250 to 300°C. It has been previously reported by one of the authors [3], that this could be due to the promotion of another deformation mode at high temperatures, such as the slip of dislocations with a <c+a> Burgers vector. While this is plausible, the evidence increasingly suggests a role of a diffusion controlled process, such as dislocation climb, grain-boundary sliding, or dynamic recrystallization.

The distinct anisotropy exhibited by the four alloys (Figure 7) is readily understood in terms of their textures presented earlier (Figure 2). Sheets M and X show the highest r-values overall, and this is presumably linked with the higher over strengths of the basal textures in these sheets. Sheets N and X show greater in-plane anisotropy

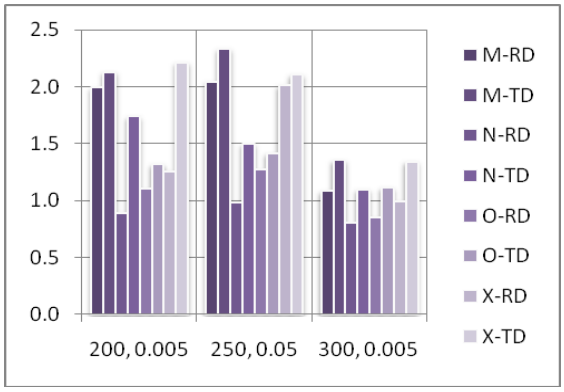

Figure 8. Comparison of r-values at a strain of ε = 0.15 show that the strain anisotropy dimishes at the highest temperatures.

than the others, and this can be explained in terms of the lower symmetry in the pole figures of these two sheets. This connection between texture and r-value was reported previously by Kaiser et al. [11] and simulated using a polycrystal plasticity model by Agnew et al. (e.g., [6,7]). The lower r-value along the RD is due to the tilt of basal poles toward the RD, which in turn allows basal slip to accommodate a large portion of the strain, while the high r-value along the TD is due to the promotion of prismatic slip, which does not produce significant strain along the thickness direction.

Summary and Conclusions

The four sheets examined in this blind study were either DC cast and hot-rolled or strip cast prior to warm/cold rolling to final gage. Neither the metallographic nor mechanical characterization made the processing history immediately apparent. Rather, simple structure property relationships were shown to describe the behaviors observed. Samples with the finest grain size exhibited the lowest flow stress and highest elongation at high temperatures (T ~ 300°C). Samples with the most asymmetric textures showed the most in-plane anisotropy in the Lankford coefficient (r-value). These results provide the process engineer with confidence that control of measurable microstructure characteristics will provide the desired control of properties, and that the details of processing history are not so important.

CANMET

The potential for warm forming was quantified by determining forming limits for strain paths including stretch, draw and bending conditions. Optical microscopy was used to determine the microstructure evolution during the warm-forming testing. General tasks included in this work consisted of:

- Determination of warm-forming limits for stretch and draw strain paths
- Establishing warm bendability (e.g., Figure 9)
- Investigating microstructural evolution during warm forming using optical metallography

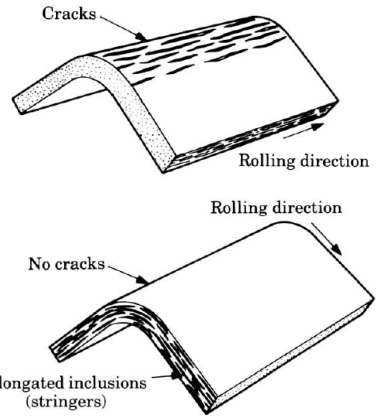

Figure 9. Bendability of sheet showing planar anisotropy.

Technical Progress

Warm-forming limits were constructed for 1.3 mm thick commercially-supplied AZ31B sheet.

- Warm FLDs are shown in Figure 10(a) for temperatures of 200°C and 250°C
- Warm-forming limits for two strain paths ($\beta = 0.8$ and -2.0, where $\beta = E_{22}/E_{11}$) were determined for range of temperatures 100 to 300°C in 25°C increments [Figure 10(b)]

Microstructural Characterization

Optical microscopy of the bulk sample reveals microstructure evolution at the limit strain for samples deformed with strain path $\beta = 0.8$. Limit strains for each temperature are given in Figure 10(b). Significant dynamic recrystallization (DRX) is observed at between 150°C and 250°C inclusive. However, DRX is most uniform and complete at 200°C [Figure 11(c)].

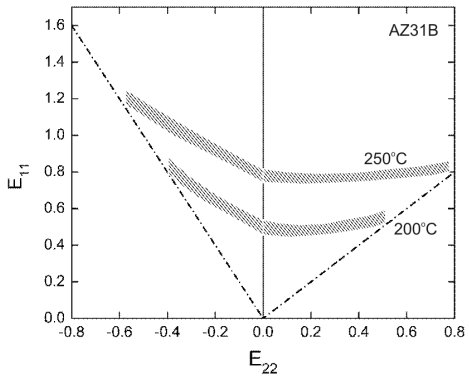

(a)

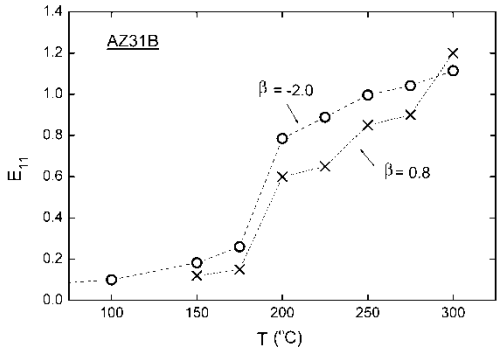

(b)

Figure 10. (a) Warm-forming limit diagrams for 1.3-mm thick AZ31B sheet and (b) forming limits for strain path $\beta = 0.8$ and -2.0 for 100 to 300°C in 25°C increments.

Inhomogeneously flow is observed at 150°C [Figure 11(b)].

At 300°C, a more equiaxed microstructure with a grain size comparable to the undeformed microstructure [Figure 11(e)] is observed, which suggests possible grain growth or the lack of DRX. The microstructure near the fracture area is compared for samples deformed at 150°C and 300°C [Figure 12(a) and 12(b)].

Planning and Deliverable for the Next Period

- Warm-forming limits will be determined for $\beta = 0.8$ for three remaining Mg sheets for temperature between room temperature and 300°C.
- Warm bending of Mg sheet will be investigated with V-notch bending for 100–300°C.

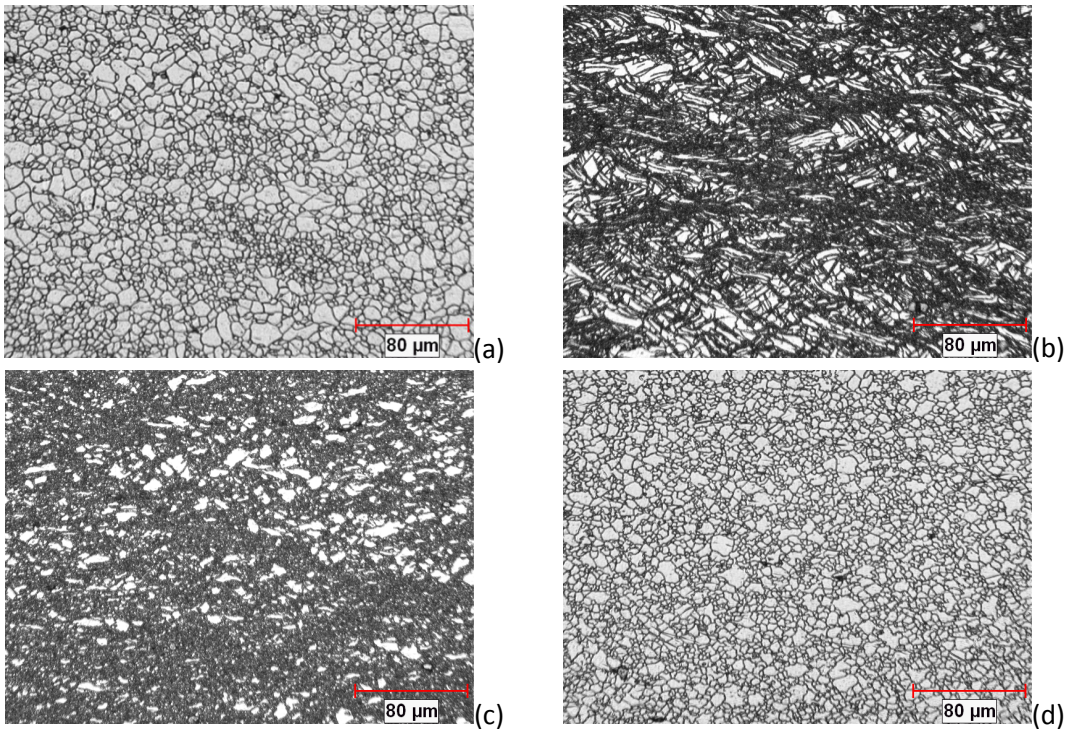

Figure 11. Optical Microscopy of RD-ND sections with strain path β = 0.8 at forming limit strain for (a) undeformed, (b) 150°C, (c) 200°C, (d) 250°C, and (e) 300°C.

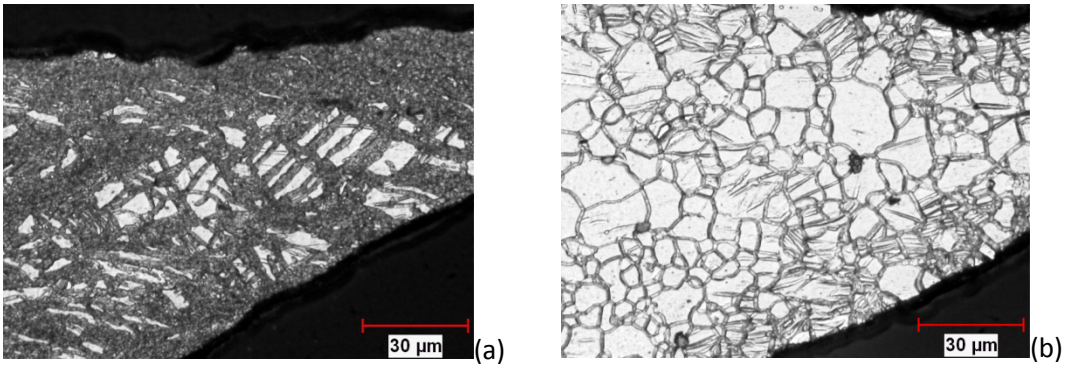

Figure 12. Optical microscopy of RD-ND sections for strain path β = 0.8 at forming-limit strain near fracture surface for a) 150°C and b) 300°C.

- A methodology for characterizing small dynamically-recrystallized grains will be investigated.
- Optical characterization of all Mg sheet at the forming limit will be completed.

Design and Build Warm Forming Tool

The previous Warm Forming Project (AMD 307) provided a great deal of information about the design and fabrication of a die for warm forming. This current project is leveraging these lessons learned and the existing equipment to create an optimized die system for warm forming.

Key elements of this optimization are using advanced simulation techniques for both thermal control (GM) and formability (Ford). A photograph of the warm-forming die is shown in Figure 13.

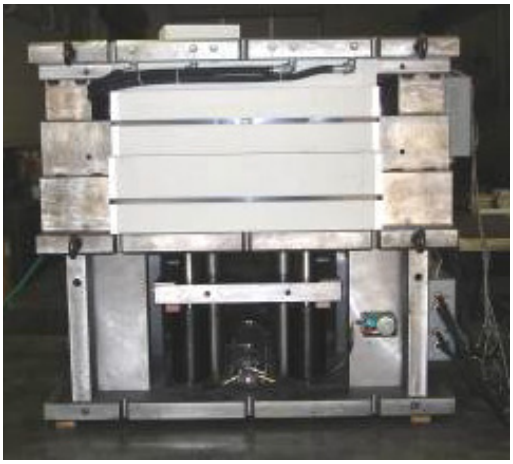

Figure 13. Modified warm forming die.

As noted in a previous report, successful pans from DC-Cast material were produced during the first forming trial to a full depth of 125 mm as shown in Figure 14. This established the feasibility to form conventional DC-cast material to a minimum of 100 mm depth which in turn achieved Gate 1 of the project.

Figure 14. Rectangular pan formed to full depth from DC-Cast AZ31.

More recently, the die has been modified to allow for the capture of both thermal and forming data through a new data-acquisition system. Data such as temperature across the tool, pressing force and forming rate will now be recorded for each formation.

Press tonnage will be measured in four locations with new load cells positioned in the die system. These load cells in cooperation with the linear potentiometer will allow for the detection of splitting as a function of both the draw depth and location. A schematic of the new cushion system re-designed to accommodate the load cells is shown in Figure 15.

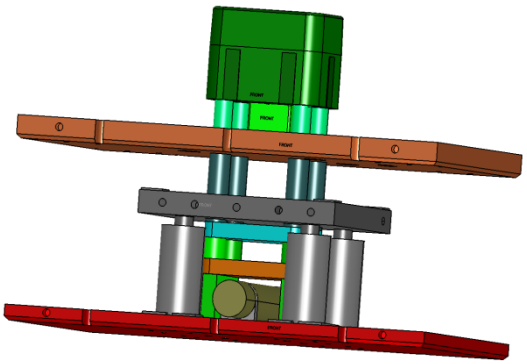

Figure 15. Schematic of the lower cushion system showing the new design to accommodate the four load cells.

The data-acquisition system designed and purchased in the previous Warm Forming Project (AMD 307) will be used to record the data from the load cells, linear potentiometer and the thermocouples.

Deliverables:

- Warm-forming die with improved thermal control and instrumented to record critical forming data such as temperature, press tonnage and deformation rate.
- Established feasibility to form conventional DC-cast material to a minimum of 100 mm depth. (Gate 1 Achieved)

Press Design and Optimization

A hydraulic press, shown in Figure 16, was chosen for the development and modified to perform the required strokes per minute and operate at different travel speeds. The press in its original state was relatively slow with a maximum down-speed of 43 mm per second and an up-speed of 56 mm per second. In order to achieve the targeted cycle times, new hydraulics were designed and implemented on the press to achieve significantly faster speeds.

The study done to modify the press hydraulic system showed that by adding a second pump and motor, modifying the existing cylinder and adding a larger oil tank, the following range of speeds could be obtained.

Down Pressing Speed 1	42.3 mm per second
Down Pressing Speed 2	80.4 mm per second
Down Pressing Speed 3	152.4 mm per second
Rapid Down Speed	311.1 mm per second
Rapid Up Speed	296.3 mm per second

Figure 16. Photograph of new dedicated press and pre-heater for the development of the fully automated warm-forming cell.

The next forming trial will be conducted using the range of speeds to determine optimal pressing speed and temperature. Subsequent trials will be performed to quantify the formability of all of the test alloys under identical forming conditions.

Deliverables:

- Dedicated hydraulic press for the AMD 602 project capable of achieving the targeted production rate of 5 to 10 jobs per minute.

Forming Trials

The aim of the first full forming trial on the newly-modified press system at Troy Tooling was to develop baseline formability data on a commercially-available Mg sheet alloy. Variables such as draw depth, binder load, forming temperature and lubricant were all investigated to determine a suitable forming window for this material as well as to develop metrics to compare the formability of all the test alloys. In this section, the results of this first full forming trial are presented and discussed.

Experimental Procedure

To minimize variation, a standard process of heating the blanks in the die was used for this trial. All experiments were conducted at a pressing speed of 80.4 mm per second which is approximately half the full speed of the press. Two lubricants were used in this investigation—the solid lubricant containing boron nitride developed in the previous project (AMD 307) which has been shown to be an effective lubricant and a new oil-based lubricant available from Fuchs called Stabylan 600HT. Interest in a new oil-based lubricant stems from two issues with the currently used solid lubricant. The first of these has to do with the cost of applying the lubricant to the sheet as well as the cost of the lubricant itself. The second issue is related to the potential for the lubricant to build up in the die and the cost of cleaning off the lubricant from the formed panels. Hence, the target for an oil-based lubricant is to be compatible with down-stream processes such that cleaning of formed panels would not be necessary. The Stabylan 600HT lubricant used in this work has a flash point around 300°C so it could not be used at all of the test temperatures of interest.

The pan formed in this work (Figure 14) is a significant test of material drawability. Each corner can be viewed as a unique experiment during the forming process, with two failure modes: splits and wrinkles. Wrinkling occurs when insufficient binder pressure is applied so that the material buckles rather than compresses in the corners. Splits occur when there is insufficient ductility in the material to be stretched into the desired shape.

Results and Discussion

A forming window based on a wide range of temperatures and binder pressures is shown in Figure 17. In this plot, panels with one or two successfully formed corners are binned together as well as panels with three and four successfully-formed corners. All of these panels were formed with the solid lubricant and binned in terms of the number of successfully-formed corners. As predicted, the forming window becomes wider in terms of binder pressure at the higher temperatures. Insufficient binder pressure results in wrinkles and failure. The forming window collapses at approximately 275°C which indicates a minimum temperature to achieve a successfully forming.

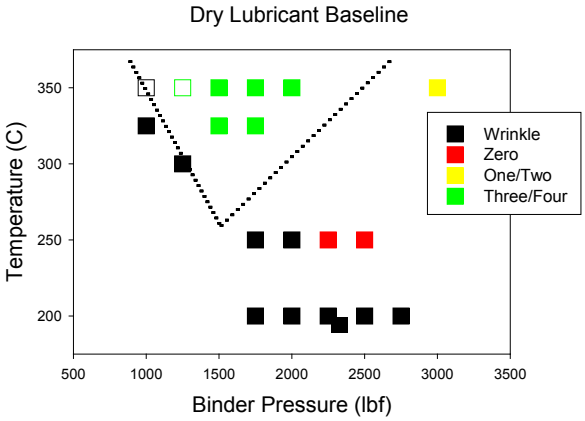

Figure 17. Forming window as a function of temperature and binder force. The successful number of corners made have been lumped in to two groups (3&4 and 1&2).

Lubricant

The Stabylan 600HT lubricant has a flash point at approximately 300°C so experiments were performed at a maximum of 290°C. As shown in Figure 18, no pans were successfully formed and a distinct border between wrinkling and splitting developed. While the results of Figure 17 indicate that some level of forming success is possible at temperatures in this range, there were no successful corners recorded for the pans formed with oil. This is most likely a result of lubricant breakdown as the temperatures approached the flashpoint. Further investigations into this lubricant (shown below) reinforce this conclusion.

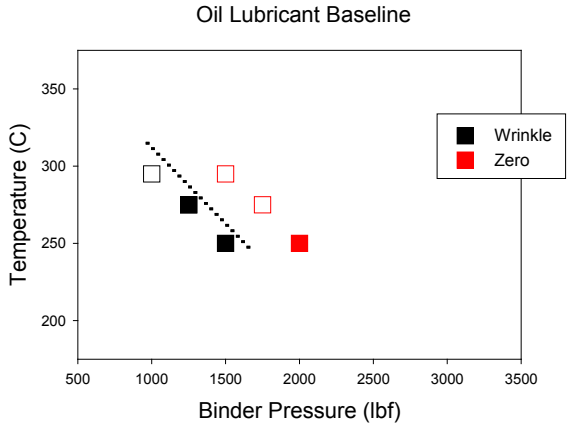

Figure 18. Plot shows a distinct transition from wrinkling to complete splitting for pans formed with oil-based lubricant up to 290°C.

Pan Depth

While the metric of successfully-formed corners has led to the development of the forming window shown in Figure 17, a more robust metric with improved resolution was sought. The chosen metric was pan depth. That is, the maximum depth a pan could be formed before splitting of any of the corners. In order to determine this value for a given set of forming parameters (temperature, binder pressure, etc.), a large number of pans would need to be formed. Since this method was impractical given the large number of variables under study, a method was developed to estimate maximum forming depth.

Pan depth was estimated by measuring the opening height of the largest corner crack (Figure 19) and subtracting that value from the full pan depth of 70 mm. This approach has been validated on a number of panels by re-configuring the press to draw to this target pan depth. In each of these tests a distinct neck was formed on the corner indicating the onset of splitting. Once splitting occurs, the material around the crack does not continue to deform and hence the crack opens the remaining stroke of the press.

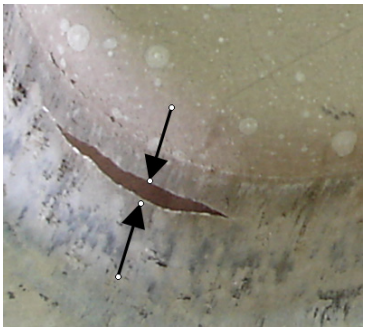

Figure 19. An example of a corner split measured for the estimation of pan depth.

This crack-measuring method was used to further evaluate the forming behavior of this baseline material under a number of different conditions. The first investigation was on the effect of temperature at various binder pressures.

As shown in Figure 20, the pan depth increases with increasing temperature. The straight line at 350°C is due to the fact that the die bottomed out at 70 mm and it was not possible to draw the

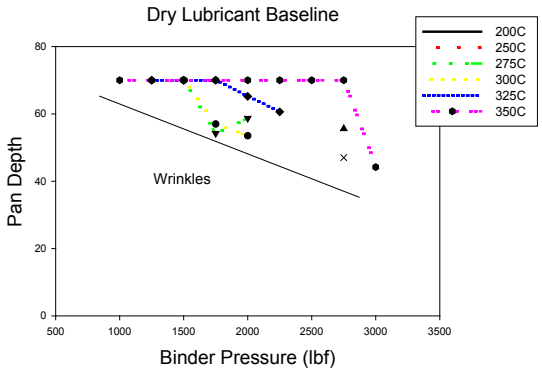

Figure 20. Plot of estimated pan depth as a function of binder force for various temperatures.

material further. If the tool were re-worked to allow for deeper forming, the suspicion is that there would be a series of parallel lines with a similar slope to the wrinkle line.

The pan-depth analysis approach was also used to compare the performance of the two lubricants used in this study. Pan depth as a function of binder pressure for temperatures ranging from 250°C to 290°C are plotted in Figure 21. For all conditions, use of the solid lubricant (dry) improves estimated pan depth. This shows a clear benefit of the dry lubricant even at lower temperatures of 250–295°C.

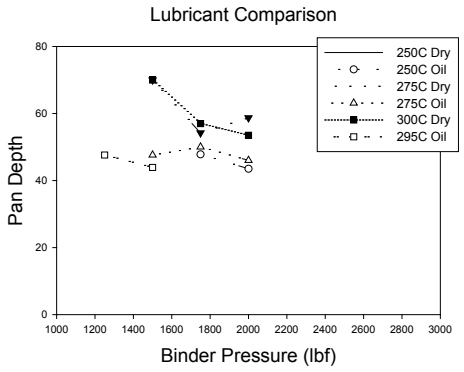

Figure 21. Estimated pan depth as a function of binder force for various temperatures for both lubricants.

Non-Isothermal Conditions

One method of improving the forming depth that has been demonstrated by several researchers is to slightly cool the punch. While the research to date on this approach has been mostly limited to laboratory-scale experiments, the concept is based on having hotter material on the binder to flow into the cavity while colder and hence stronger material in the cavity to resist necking and rupture. Preliminary experiments were attempted with the current pan die in an effort to reproduce the results from lab-based experiments. The method used was simply to turn off the heat in the punch and leave the binder in the lowest position to minimize heat transfer from the ring to the punch. While this did not offer precise control of the punch temperature, it did give a first approximation of what could be achieved in a non-isothermal system.

As noted in Figure 22, it appears that a cooler punch results in an increase in pan depth. The potential of non-isothermal warm forming will be studied further under more controlled conditions in the next forming trial.

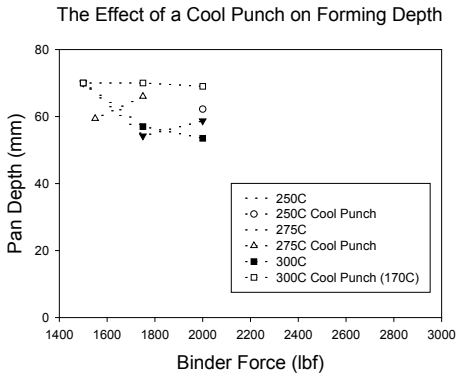

Figure 22. Estimated pan depth as a function of binder force for both isothermal and non-isothermal conditions.

Materials

A final study in this forming trial was conducted by comparing the formability of all four of the test materials at various temperatures. This preliminary study was limited to the use of the oil-base lubricants. In the next forming trial, the solid lubricant will used on all of the materials.

As noted in Figure 23, the estimated pan depth decreases with increasing temperature. While this is surprising since all of the previous data indicate improved formability with increasing temperature, this anomaly is most likely due to the further deterioration of the oil-based lubricant with increasing temperature. Follow-on studies using

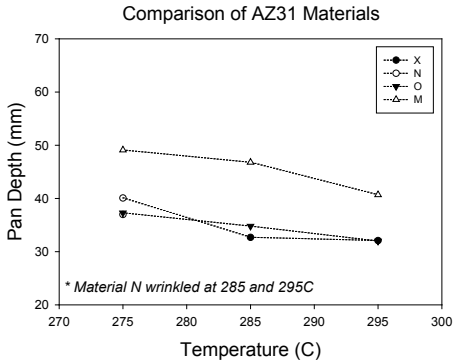

Figure 23. Estimated pan depth for all four materials in this study as a function of temperature.

the previously-developed solid lubricant will offer a better comparison of material formability.

Automated Cell and Demonstration

The final phase of the project will involve constructing a fully-automated warm-forming cell using the optimized pan die. Troy Tooling Technologies will integrate the conduction preheater and die using automated material handling to create a warm-forming cell that can produce a formed pan at a rate of 5 to 10 a minute. The process will be demonstrated to the OEM's and DOE.

Conduction Pre-Heater

A conduction preheater originally developed at GM was loaned to the AMD 602 project. This preheater was developed to rapidly heat metal sheets by conduction from two hot, steel platens placed in very close proximity to the sheet, without making intimate contact. Maintaining a small gap between the platens and the sheet is essential for achieving a very high rate of heat transfer. In this situation, the majority of the heat is transferred from the hot steel platen through a thin layer of open space (air) to the Mg sheet. For small gaps, conduction heat transfer is more dominant than either radiation or convection.

Modeling of heat transfer by conduction from solid heated platens through a controlled clearance gap of 0.5 mm on each side to a 1 mm thick Mg sheet indicate that the sheet can be heated to 400°C in less than 40 seconds (Figure 24).

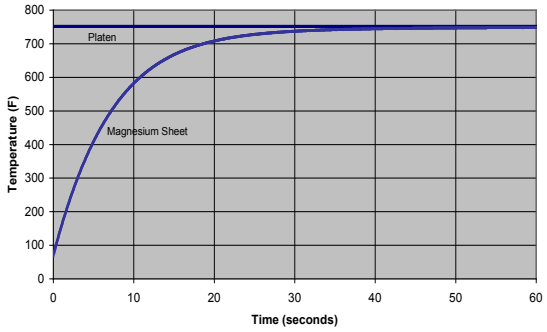

Figure 24. Heating curve of 1mm Mg sheet in the 400°C preheater with a 0.5 mm air gap on both sides of the sheet.

By placing three sheets in the preheater at once and then removing one sheet every 12 seconds and replacing it with a cold sheet, a production preheat cycle of 5 parts per minute can be achieved with the preheater. A photograph of the preheater is shown in Figure 25.

All subsequent forming trials will utilize this preheater.

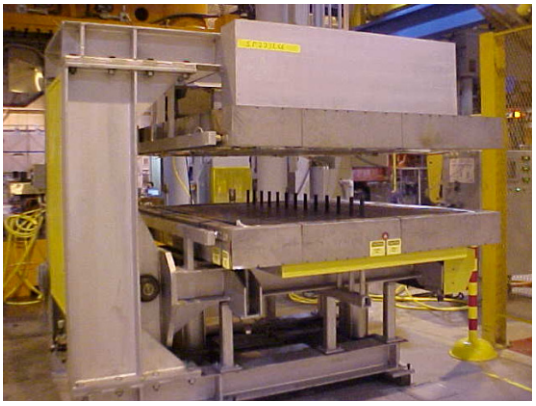

Figure 25. Photograph of the GM conduction preheater.

Deliverable:

- A heating system capable of producing blanks at target temperature at a rate fast enough to support the targeted production rate.

Cost Model

AMD 307 developed a cost model for warm forming in cooperation with Camanoe Associates. This model will be modified to understand the costs of warm forming of Mg sheet and to

establish the benefits of using lower-cost CC materials

References

1. "Standard Test Method for Determining the Superplastic Properties of Metallic Sheet Materials," *ASTM E 2448–06,* ASTM International, West Conshohocken, PA, 2006.
2. G. Vander Voort, in *Metallography Principles and Practice*, ASM International, Materials Park, OH (1984), pp. 447–449.
3. S. R. Agnew and O. Duygulu, "Plastic anisotropy and the role of non-basal slip in magnesium alloy AZ31," *Inter. J. Plasticity*. 21 (2005), pp. 1161–1193.
4. A. Jain and S. R. Agnew, "Modeling the temperature dependent effect of twinning on the behavior of magnesium alloy AZ31B sheet," *Mater. Sci. Eng. A*, 462 (2007), pp. 29–36.
5. L. Jiang, "Effect of twinning on texture and strain hardening in magnesium alloys subjected to different strain paths." Ph.D. dissertation, McGill University, Montreal, Canada (2007), pp. 46–66.
6. S. R. Agnew et al., "Constitutive behavior of four wrought magnesium alloys under warm forming conditions," in *Magnesium Technology 2008*, Ed. Pekguleryuz et al., TMS, Warrendale, PA (2008), pp. 159–164.
7. C. M. Sellars and W. J. Tegart, "Relationship between strength and structure in deformation at elevated temperature," *Mem. Sci. Rev. Metall.*, 63 (1967), pp. 731–745.
8. H. Takuda, H. Fujimoto, and N. Hatta, "Modeling on flow stress of Mg-Al-Zn alloys at elevated temperatures," *J. Mater. Proc. Tech.* 80–81 (1998), pp. 513–516.
9. M. R. Barnett, "Influence of deformation conditions and texture on the high temperature flow stress of magnesium AZ31," *J. Light Met. 1,* (2001), pp. 167–177.
10. S. S. Vagarali and T. G. Langdon, "Deformation mechanisms in h.c.p. metals at elevated temperatures—II. Creep behavior of a Mg-0.8% Al solid solution alloy," *Acta Metall.,* 30 (1982), pp. 1157–1170.
11. F. Kaiser et al. "Anisotropic Properties of Magnesium Sheet AZ31," *Mat. Sci. Forum.* 419–422 (2003), pp. 315–320

C. Electromagnetic Forming of Aluminum Sheet

Principal Investigator: Richard W. Davies
Pacific Northwest National Laboratory
P.O. Box 999, Richland, WA 99352
(509) 375-6474; fax: (509) 375-5994; e-mail: rich.davies@pnl.gov

Technical Coordinator: Sergey Golovashchenko
Ford Motor Company
Ford Research Laboratory, Dearborn, MI 48121-2053
(313) 337-3738: fax: (313) 390-0514; e-mail: sgolovas@ford.com

Technology Area Development Manager: Joseph A. Carpenter
(202) 586-1022; fax: (202) 586-1600; e-mail: joseph.carpenter@ee.doe.gov

Field Technical Monitor: Mark T. Smith
(509) 375-4478; fax: (509) 375-4448; e-mail: mark.smith@pnl.gov

Participants:
Nick Bessonov
EMF Simulations
University of Michigan-Dearborn

Jeffrey Johnson
EMF System and Control
Pacific Northwest National Laboratory

Vladimir Dmitriev
EMF R&D
Ford Motor Company

Contractor: Pacific Northwest National Laboratory (PNNL)
Contract No.: DE-AC06-76RL01830

Objective

- Develop electromagnetic forming (EMF) technology that will enable the economic manufacture of automotive parts made from aluminum sheet. EMF is a desirable process because the dynamic nature of the deformation results in benefits, including increased forming limits and reduced springback. These benefits would result in increased use of aluminum and therefore more fuel-efficient vehicles due to mass reduction.

Approach

- The project will address four main technical areas:
— Analysis methods for forming system design
— Development of durable actuators (coils)
— Industrial embodiment of the EMF process
- Modeling tools for simulation of the EMF forming process.

Accomplishments

- During the last year of this project, remaining funds were directed at completing documentation of the EMF modeling code approaches for reduced computational run times. This work was funded through a subcontract with Oakland University, and final work will be completed in early fiscal year (FY) 2009.
- Modeling of sheet-die interaction during EMF was completed during the reporting period, and results of this work were presented (and published) at the Third International Conference on High Speed Forming.
- A subcontract with Pennsylvania State University-Erie to evaluate the effects of electrical pulsing on the deformation characteristics of 5000-series aluminum alloys was completed. This work focused on evaluating whether the tensile ductility of the 5000-series aluminum alloys can be increased with the application of high energy electrical pulsing. This work resulted in a recent publication.

Future Direction

- This project will be finished with the completion of a final subcontract report documenting the EMF modeling code development and benchmarking computational efficiency improvements. A related high rate forming project has been initiated with participation by Chrysler, Ford, and General Motors. This project, titled "Pulse Pressure Forming of Lightweight Materials" (see report 2.E) is focused on the forming characteristics of aluminum, advanced high-strength steels, and magnesium sheet under electrohydraulic forming conditions.

Introduction

In the EMF process, a transient electrical pulse of high magnitude is sent through a specially designed forming coil by a low-inductance electric circuit. During the current pulse, the coil is surrounded by a strong transient magnetic field, the transient nature of which induces current in a nearby conductive workpiece that flows opposite to the current in the coil. The workpiece and coil act as parallel currents through two conductors to repel one another. The force of repulsion can be very high, equivalent to surface pressures approximately tens of thousands of pounds per square inch. Thin sheets of material can be accelerated to high velocity in a fraction of a millisecond.

A recent interest in understanding the EMF of metals has been stimulated by the desire to use more aluminum in automobiles. The high workpiece velocities achievable using this method enhances the formability of materials such as aluminum. In addition, the dynamics of contact with the forming die can help reduce or mitigate springback, an undesired effect that cannot be avoided in other forming techniques such as stamping. The commercial application of this process has existed since the 1960s, with the large majority of applications involving either the expansion or compression of cylinders (tubes). The forming of sheet materials is considerably more complex and receives relatively little attention.

Approach

This project addresses three main technical areas. The first involves establishing analysis methods for designing forming systems. These methods are based on developed knowledge of forming limits and relations between electrical system characteristics and deformation response for specific aluminum alloys of interest. The second area is coil durability. Existing EMF and relevant knowledge from pulsed power physics studies will be combined with thermomechanical analyses to develop durable coil designs that will be tested experimentally. The third technical area involves the industrial embodiment of the EMF process. In this project, EMF is expected to be hybridized with conventional sheet metal stamping. Different approaches to hybridization will be analyzed for issues affecting the economic implementation in a modern stamping plant, and different system concepts will be developed and studied. Existing knowledge of the EMF process and technical achievements in this project will be combined to establish a methodology for designing hybrid-forming systems that can be readily integrated into modern manufacturing facilities for the economic production of automotive sheet aluminum

components. Some of the project focus areas and results are discussed in the following sections.

PNNL EMF System

The EMF system at PNNL has been operational since 2001. The system typically operates at 6,500 volts, and current levels in excess of 225 kiloamperes (kA) have been demonstrated. Figure 1 shows a typical response of the EMF system during a 15 kilojoule discharge of the capacitor bank. The half-current of the system (measuring half the total system current) is approximately 86 kA so that a total current of 172 kA passed through the load coil is within 26 microseconds.

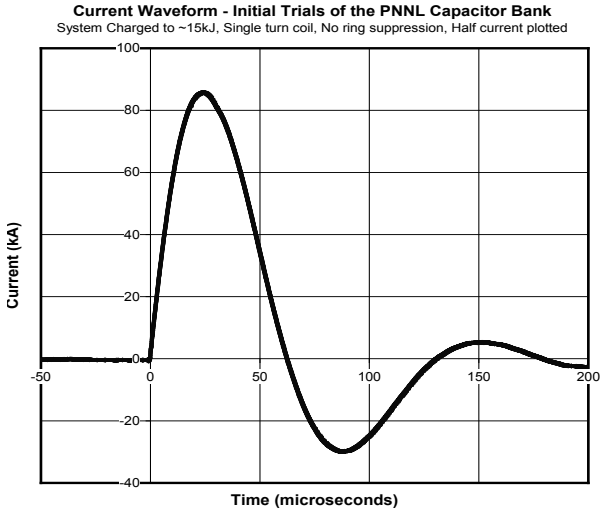

Figure 1. Typical EMF system waveform.

The system has also been cycled several thousand times at high current levels, while supporting our coil durability experimental work. The custom-designed control system was successfully demonstrated in automated cyclic loading operating modes. In the second half of FY 2007, a new power supply was installed and operationally validated. The supply has a significantly faster charge rate capacity that allowed faster recharging of capacitor banks so that the coils can be fired at higher cycle rates. This reduces the experimental run times required to test coil designs for coil durability.

EMF Process Simulation Tool Development

The first half of FY 2008 was primarily spent on further development of an EMF process simulation tool that will allow us to design the process by predicting the EMF field, stresses and strains in the blank and temperature distribution in the coil. Another focus area was the continued development of the flat coil design. Improvements were made to simplify and lower the manufacturing cost of flat coils. Further, the packaging of the flat coil assembly has been improved for robustness and ease of handling. Efforts were initiated to modify the code to run on Unix-based workstation clusters and to investigate advantages in parallelizing the code for faster run times.

EMF Process Numerical Simulation Results

The EMF process is challenging to simulate due to the need to model electromagnetic, thermal and elastic-plastic deformation of materials simultaneously. Many of the commercial research codes have serious limitations and an inability to predict EMF process results accurately. Originally, this project focused on integrating portions of existing commercial research codes to predict the important characteristics of a three-dimensional EMF process accurately. However, recent work focused on more accurate custom process simulations. The current modeling work involves collaboration with Dr. Nick Bessonov in cooperation with Oakland University and Dr. Sergey Golovashchenko at Ford.

During the last half of FY 2008, modelling focused on the interaction between the aluminium sheet formed at high velocity and the die into which it is being formed. The modelling of the sheet/die interaction requires development of the contact interaction, the most popular method of which is based on the geometrical analysis of the mutual position boundary nodes of each mesh. At every integration step, it is verifying whether a boundary node of the blank has penetrated through the certain element of the die surface mesh. If this happens, it would be necessary to make certain corrections to bring back the node to the die surface, along which the node could slide. A significant drawback of this approach is an occasional penetration of the node through the

surface, which can happen due to inaccurate calculations. As soon as the blank's node penetrates the die's surface, it is unable to return, so further calculations are useless. Therefore, a different approach was employed based on mild contact, which is popular in molecular dynamics where it is employed to model thousands of colliding atoms. The contact force is in inverse proportion to the distance between interacting surfaces. From a mathematical viewpoint, mild contact is some variable boundary of an unknown shape where the nonpenetration condition and equilibrium of forces between both surfaces must be satisfied. This idea is based on the introduction of acting-in-vicinity forces repelling the surfaces to be in contact. As a result, the surfaces do not come in contact but stay at a brief distance from each other. The force is localized in a small neighborhood of mesh elements, and it increases to infinity when the distance between them approaches zero.

In other words, when the blank and die are in geometrical contact, the force between them is localized on their joint surface. Mathematically, it can be considered as continuous functions where the absolute value of the force F is given by

$$F = \begin{cases} k\left(\frac{1}{h} - \frac{1}{h_0}\right) & \text{at} \quad h < h_0 \\ 0 \quad \text{at} \quad h \geq h_0 \end{cases},$$

where h is the actual distance from the node of the blank to the die surface and h_0 is the width of the layer where the force is different from zero. The direction of the force F is aligned along the local normal to the die surface. The described algorithm takes into account the Coulomb friction and other contact effects. Indeed, when the interaction of the node with an object of the other mesh is computed, the mutual positions and velocities are known. It is sufficient to find the friction directed along the tangent to the surface and opposite to the tangential part of the relative velocity vector.

Effect of Electrical Pulsing on Deformation Behavior of Various Aluminum Alloys

Under a subcontract with Pennsylvania State University-Erie, research was conducted to evaluate the effects of electrical pulsing on the deformation behavior of selected aluminum tensile test samples. Previous studies have shown that the presence of a pulsed electrical current applied during the deformation process of an aluminum specimen can significantly improve the formability of the aluminum without heating the metal above its maximum operating temperature range. This research extends these findings by examining the effect of electrical pulsing on 5052 and 5083 aluminum alloys. Two different parameter sets were used while pulsing three different heat treatments (as is, 398°C and 510°C) for each of the two aluminum alloys. For this research, electrical pulsing is applied to the aluminum while the specimens are deformed without halting the deformation process. The analysis focuses on establishing the effect of electrical pulsing on the aluminum alloy's various heat treatments by examining the material displacement throughout the testing region of dog-bone shaped specimens.

The results from this research show that pulsing significantly increases the maximum achievable elongation of the aluminum compared to baseline tests conducted without electrical pulsing. Significantly reducing the engineering flow stress within the material is another beneficial effect produced by electric pulsing. The pulses also cause the aluminum to deform nonuniformly such that the material exhibits a diffuse neck where the minimum deformation occurs at the ends of the specimen (near the clamps), and the maximum deformation occurs near the center of the specimen (where fracture ultimately occurs). This diffuse necking effect is similar to what can be experienced during superplastic deformation. However, when comparing the presence of a diffuse neck in this research, electrical pulsing does not create as significant a diffuse neck as superplastic deformation. Electrical pulsing has the potential to be more efficient than traditional methods of incremental forming because the deformation process is never interrupted.

Overall, with the greater elongation and lower stress, the aluminum can be deformed quicker, easier, and to a greater extent than is currently possible. Figure 2 shows the load/displacement record for the as received 5052 specimens tested

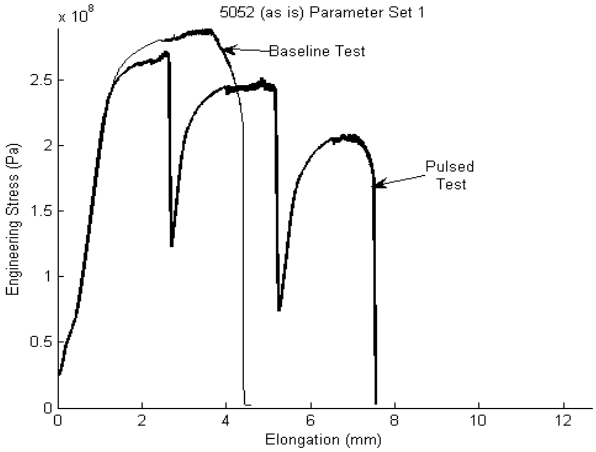

Figure 2. 5052 (as is) load/displacement results.

in baseline static tensile conditions and the same 5052 material subjected to parameter set 1 electrical pulsing. The pulsed specimens displayed significantly higher elongations prior to failure.

The test results show that electrical pulsing of the specimen results in significantly greater displacements (higher apparent formability) than that of the baseline test conditions. Similar results were observed for 5052 and 5083 aluminum alloys, and the subcontract effort resulted in publication of the results for the 2008 International Manufacturing Science and Engineering Conference.

Figure 3 shows summary displacement analysis data for 5052 aluminum deformed in tension under

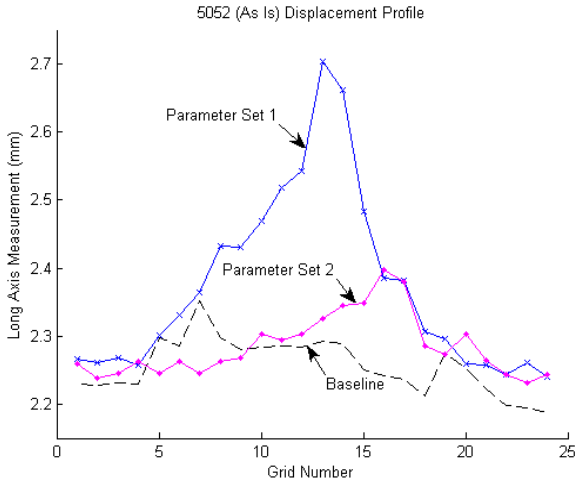

Figure 3. 5052 (as is) displacement analysis.

regular static test conditions and then with electrical pulsing using two different parameter sets.

Conclusions

This work has developed numerical models that describe three critical elements of the EMF process: propagation of the electromagnetic field through the coil-blank system and generation of pulsed electromagnetic pressure in specified areas, high-rate deformation of the blank and heat accumulation, and transfer through the coil with an air cooling system. The process models provide capability to analyze EMF restrike processes from the perspective of coil design, blank deformation, and coil cooling systems.

Presentations/Publications

1. W. Salandro, J. Jones, T. McNeal, J. Roth (Penn State-Erie), S. T. Hong, and M. Smith. 2008. *Effect of Electrical Pulsing on Various Heat Treatments of 5XXX Series Aluminum Alloys,* Proceedings of the 2008 International Manufacturing Science and Engineering Conference, Pacific Northwest National Laboratory, October 7–10.
2. R. W. Davies, N. M. Bessonov, and S. F. Golovashchenko. 2007. "Prototype Coil Performance during Electromagnetic Forming of Aluminum Sheet." Abstract submitted to *Materials Science & Technology*, Detroit, MI. PNNL-SA-54918.
3. S. Golovashchenko, N. M. Bessonov, and R. W. Davies. 2008. *Analysis of Blank-Die Contact Interaction in Pulsed Forming Processes.* Third International Conference on High Speed Forming. PNNL-SA-59420.
4. S. F. Golovashchenko, N. M. Bessonov, and R. W. Davies. 2008. *Modeling of Pulsed Electromagnetic Forming.* Numisheet 2008. PNNL-SA-60489.

D. Pulse Pressure Forming of Lightweight Materials

Principal Investigator: Richard W. Davies
Pacific Northwest National Laboratory
P.O. Box 999, Richland, WA 99352
(509) 375-6474; fax: (509) 375-5994; e-mail: rich.davies@pnl.gov

Technical Coordinators: Sergey Golovashchenko
Ford Motor Company
Ford Research Laboratory, Dearborn, MI 48121-2053
(313) 337-3738; fax: (313) 390-0514; e-mail: sgolovas@ford.com

John Bradley
General Motors Corporation
General Motors Research Laboratory, Warren, MI 48090-9055
(586) 986-0590; fax: (586) 986-3091; e-mail: john.r.bradley@gm.com

Jerry Olszewski
Chrysler LLC
Applied Materials Technology, Auburn Hills, MI 48326
(248) 512-8531; fax: (248) 512-7915; email: go5@chrysler.com

Technology Area Development Manager: Joseph A. Carpenter
(202) 586-1022; fax: (202) 586-1600; e-mail: joseph.carpenter@ee.doe.gov

Field Technical Monitor: Mark T. Smith
(509) 375-4478; fax: (509) 375-4448; e-mail: mark.smith@pnll.gov

---

Contractor: Pacific Northwest National Laboratory
Contract No.: DE-AC06-76RL01830

Objective

- Develop pulse pressure forming (PPF) sheet metal forming technologies [e.g., electromagnetic forming (EMF), electrohydraulic forming (EHF), laser shock forming (LSF) and other similar technologies] and manufacture cost effectively body-in-white and closure panels made from aluminum alloys, magnesium alloys, and high-strength and advanced high-strength steel (HHS and AHSS, respectively).

Approach

- Develop and enable a class of high strain rate metal forming processes to cost-effectively manufacture body-in-white and closure panels made from aluminum alloys, magnesium alloys, and HSS/AHSS.
- Overcome three technical barriers to using PPF processing for more cost-effective lightweight vehicles:
  - lack of understanding of the formability and strain rates that develop during PPF processing
  - lack of validated constitutive relations for lightweight materials during PPF processing
  - lack of validation of finite element simulation of PPF processing

Accomplishments

- Design, development, and fabrication of a PPF chamber and electrode system and development of experimental procedures, including validation of high-speed camera imagining and forming of test samples in the free-forming mode.
- Implementation of a high-speed camera and image analysis system to record the forming of electrohydraulic aluminum sheet specimens and electromagnetic forming of aluminum samples. Efforts will be made to provide higher resolution of the sheet specimen forming surface in future experiments.

Future Direction

- Complete equipment development and characterize forming of aluminum and steel sheet specimens.
- Characterize real-time strain rates during PPF using the high-speed camera and image analysis system.
- Investigate mechanisms for enhanced formability at elevated strain rates.

Introduction

The ultimate goal of the project is to extend the formability of high strength light metals and AHSS through the application of high forming rate PPF techniques. The deliverables for the project will be the understanding and quantification of the effects of high-rate forming on the formability, residual stress state and formed properties of several high strength lightweighting metal sheet materials, facilitating the extended forming of complex, lightweight automotive sheet components.

PPF is emerging as an attractive alternative to both conventional stamping processes and forming methods that are more advanced, such as superplastic forming and EMF. Previous project work on EMF has demonstrated enhanced formability for aluminum sheet, but the process is limited to high-conductivity materials. Because the high energy discharge develops a rapid high pressure forming pulse, PPF is not limited by the inherent conductivity of the sheet material and can therefore be used to form AHSS, titanium, aluminum, magnesium and stainless steel sheets. As with EMF, PPF offers the ability to develop extended ductility, allows the use of less expensive, single-sided tooling and results in little or no springback after forming. Although there are a number of established methods for generating the forming pressure pulse, little is understood about how PPF interacts with the forming material and what the practical forming limits are for such metal alloys as magnesium, aluminum, titanium, and AHSS. This project will conduct a series of PPF experiments to determine basic PPF operational requirements and capabilities and to generate material formability/property relationships for a series of selected sheet materials. PPF will be demonstrated on materials having significantly lower electrical conductivity than aluminum, which can be electromagnetically formed. Results from the project will include an enhanced understanding of PPF effects and the impact PPF can have on basic metal formability, design properties and forming limits as well as material property data on post-PPF materials.

Approach

The purpose of this project is to develop a formability database and more fundamental understanding of the behavior of automotive sheet materials during PPF. PPF presents a number of important variables, including generation of the pressure pulse, transmission of the pulse to the working material and the displacement path of the sheet material within the tooling or die. The project will focus on the behavior of the sheet materials during PPF and will generate biaxial forming limit data, post-formed properties, and pressure-time-displacement relationships for selected sheet materials.

The deliverables of the project include the following.

1. Fundamental relationship between pulse-generated pressure forming of selected sheet

materials, including development of biaxial forming limit relationships for variable levels of pulse pressure, rate and duration.

2. Development of pre- and post-formed property relationships for selected sheet materials, including AHSS, titanium, and magnesium.
3. Development of a strain-path based forming relationship that can be used to guide PPF component and tooling design.
4. Validation of springback behavior as a function of PPF process parameters.
5. Demonstration of the technical basis for combining warm forming capability with the PPF process.

Results

Project work to date has focused on the design and fabrication of a suitable PPF chamber capable of forming sheet metal specimens under high strain-rate forming conditions. Figure 1 shows the hemispherical PPF chamber containing the two electrodes used to discharge the high voltage charge from the capacitor bank. The chamber is filled with water and the forming sheet specimen sealed to the top of the chamber, with a bolted hold down ring pictured alongside the PPF chamber. Discharge of the electrical pulse between chamber electrodes generates a rapid high-pressure event within the chamber, resulting in the formation of the sheet specimen under high strain rate conditions. Initial test firings of the chamber have confirmed general function and demonstrated suitable strain rates in the formed sheet samples. The use of a high-speed camera system based around Correlated Solutions, Inc. image analysis software was also completed during mid-September PPF tests.

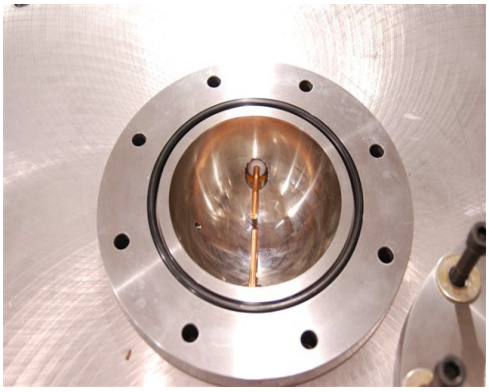

Figure 1. PPF chamber with discharge electrodes. Sheet specimen hold-down ring is shown to the right.

Conclusions

1. A survey of existing high strain rate testing and associated material constitutive modeling approaches was completed during the last quarter of fiscal year (FY) 2008.
2. The design, fabrication and testing of the PPF chamber and electrode system were completed in late FY 2008 using the PNNL capacitor bank.
3. A system of high-speed cameras was demonstrated in FY 2008, and resulting images were used by the Correlated Solutions system to determine specimen strain rates during PPF tests.

Presentations/Publications/Patents

1. R. W. Davies, E. Stephens, and M. T. Smith. 2008. *Pulse Pressure Forming of Lightweight Materials,* Project Review Meeting. October 28.

E. Ultrafine Grained Foils and Sheets by Large Strain Machining Processes

Principal Investigator: Mark T. Smith
Pacific Northwest National Laboratory
P.O. Box 999, Richland, WA 99352
(509) 375-4478; fax: (509) 375-4448; e-mail: mark.smith@pnl.gov

Principal Investigators: S. Chandrasekar and K. P. Trumble
Purdue University
West Lafayette, Indiana
(765) 494 3623; chandy@ecn.purdue.edu

Technology Area Development Manager: Joseph A. Carpenter
(202) 586-1022; fax: (202) 586-6109; e-mail: joseph.carpenter@ee.doe.gov

Field Technical Manager: Mark T. Smith
Pacific Northwest National Laboratory
P.O. Box 999, Richland, WA 99352
(509) 375-4478; fax: (509) 375-4448; e-mail: mark.smith@pnl.gov

---

Contractor: Pacific Northwest National Laboratory (PNNL)
Contract No.: DE-AC06-76RL01830

Objective

- Demonstrate the feasibility of producing magnesium (Mg) sheet and shaped products having superior formability and strength properties through the application of severe plastic deformation (SPD) developed by large-strain extrusion machining and peeling techniques.
- Evaluate the commercial economics of the candidate SPD techniques for production of fine-grained Mg alloy sheet.

Approach

- Establish the process and tooling capabilities for large strain extrusion machining (LSEM) and peeling in the context of creating bulk foil/sheet from Mg alloys. Specific attention will be paid to design of process conditions (e.g., pre-heating of sample, avoiding shear localization) to realize continuous chip formation.
- Carry out preliminary optimization of process conditions for foil/sheet production.
- Characterize the hardness and microstructure of the foil/sheet as a function of strain, using Vickers indentation, nano-indentation, optical microscopy and transmission electron microscopy (TEM). Microstructure characterization will involve examination of grain size and dislocation substructures. Note: Uniaxial strength measurements and electron back scatter diffraction (EBSD) characterization (for grain size distribution) will be done at PNNL.
- Identify the best processing conditions based on the property and microstructure characterization.
- In conjunction with PNNL, assess process scale-up, conduct cost-analysis, and suggest guidelines for process development for specific automotive applications.

Accomplishments

- Segmentation observed in preliminary experiments was overcome by tuning machining conditions to produce continuous AZ31 foils ~1 cm wide x 0.2 mm thick by both LSEM and peeling.
- A test matrix of ~20 different sets of machining conditions systematically varying strain, strain rate, and temperature showed segmentation could be suppressed for large positive rake angles, higher cutting speeds and preheating the workpiece.
- Up to a five-fold decrease in grain size was observed for the machining-based SPD processing with the smallest grain size of ~3 μm comparable to that observed in other types of SPD processing of AZ31.
- Modest hardness increases were measured, but preliminary tensile testing showed the foils exhibit strengths comparable to equal channel angular extrusion (ECAP) processed AZ31 together with large uniform tensile elongation, suggesting good formability.

Future Direction

- Samples of the large strain-processed materials will be supplied to PNNL for grain size and mechanical property evaluations. PNNL and Purdue will develop a cost model for scale-up of the process at the conclusion of the project.

Introduction

Shear strains in the 1–10 range can be imposed in a variety of materials, including those of moderate to high initial strength, in a single pass of a machining operation. Two variants of the chip formation process—LSEM and peeling—appear to be particularly attractive for the direct production of foil and sheet with ultrafine grain (UFG) microstructures. LSEM combines microstructure refinement by large-strain machining with simultaneous shape and dimensional control of the chip by "extrusion." *Peeling* is removal of material in the form of a strip (chip) with superimposed tension applied to the chip. The strain (hence the microstructure of the resulting strip) are controlled by the tool rake angle and applied tension. These approaches were used in preliminary experiments to create foils, which showed considerable segmentation that result in less than adequate mechanical strength. To overcome the segmentation challenge, pre-heating samples in the deformation zone of chip formation will be performed. A machining set-up has been devised for this purpose.

Results and Discussion

LSEM and peeling methods were applied to study the creation of foils by chip formation from Mg alloy AZ31. The preliminary experiments showed considerable segmentation of the chips, preventing realization of continuous foils. Subsequently, by using tools with large positive rake angles (15–45 deg) and higher machining speeds (100–1000 m/min), it was possible to create foils (chips) that were macroscopically continuous. While this indicated that the processing conditions were apparently accurate, microscopic observations still revealed segments in the foils. In addition, foil strength was not significant, consistent with the segmentation observed in the chips.

To overcome the segmentation challenge, pre-heating of the bulk Mg alloy sample up to 200°C in the deformation zone was employed to activate additional slip systems. This approach was based in part on work in the 1960s at the Atomic Energy Establishment in Saclay, France. A test matrix employing 11 different sets of peeling conditions (stain, strain rate, and temperature) and 8 different sets of LSEM conditions established the conditions for continuous foil production. Continuous foils ~1 cm wide and 200 μm thick were produced by both the LSEM and peeling processes. By adjusting conditions, continuous foils could be produced at ambient temperature using the LSEM process.

With grain refinement down to ~3 μm, a five-fold decrease from the starting bulk ("extruded") condition was observed (Figure 1). The grain size

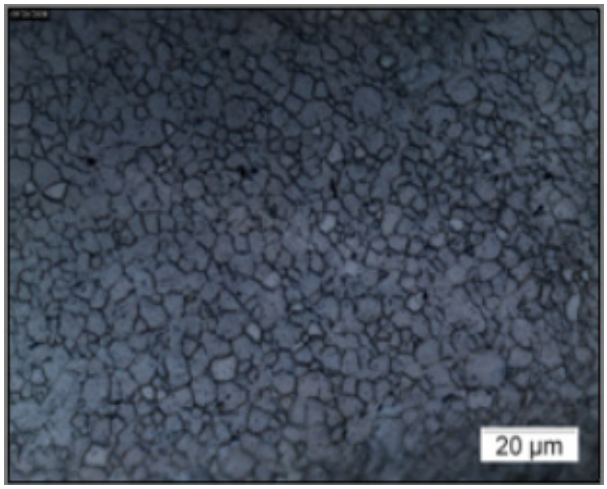

Figure 1. Continuous foil microstructure produced by LSEM at shear strain = 2, 25°C and cutting speed = 70 m/min. The means intercept grain size measured 4 µm with a uniform distribution through the foil cross-section.

distribution is uniform through the foil cross-section.

Only modest hardness increases of 5–10% were measured for the continuous foils, whereas hardness increases up to ~50% were observed in the segmented foils.

Preliminary tensile testing was conducted using test specimens cut from the continuous foils having 5.7 mm long × 2 mm wide (~0.2 mm thick) gage sections. Yield strength of ~160 megapascal (MPa) and tensile strengths up to 240 MPa with over 15% uniform elongation have been measured thus far. These properties are comparable to those reported for ECAP processed AZ31. Further testing is required to establish statistically significant tensile properties, but the results are certainly promising with respect to the anticipated forming characteristics.

Continuous foil production with UFG microstructures has been demonstrated successfully using the machining SPD approach in another hexagonal close-packed (HCP) system (titanium [Ti]) with similar deformation characteristics as Mg. Both ultra purity Ti (99.999%) and CP Ti (Grades 2 and 4) have been produced in foil form, with hardness values approximately twice that of the bulk microcrystalline material. The foils were in excess of 150 mm in length. Transmission electron microscopy showed the UFG microstructure to be composed of ~100 nm size grains. Stress-strain curves will soon be measured for these Ti foils and the resulting properties correlated with microstructure condition.

F. Formability of Continuous Cast Magnesium Sheet

Principal Investigator: Darrell Herling
Pacific Northwest National Laboratory
P.O. Box 999, Richland, WA 99352
(509) 375-6905; fax: (509) 375-4448; e-mail: darrell.herling@pnl.gov

Technology Area Development Manager: Joseph A. Carpenter
(202) 586-1022; fax: (202) 586-1600; e-mail: joseph.carpenter@ee.doe.gov

Field Technical Monitor: Mark T. Smith
(509) 375-4478; fax: (509) 375-4448; e-mail: mark.smith@pnl.gov

---

Contractor: Pacific Northwest National Laboratory (PNNL)
Contract No.: DE-AC06-76RL01830

Objective

- Characterize the post-formed properties of continuous cast magnesium sheet provided by the United States Automotive Materials Partnership (USAMP) Warm Forming Team (AMD 602).
- Evaluate the effects of tooling lubricant type on friction and formability under warm forming conditions.
- Determine the forming limits under biaxial conditions (limited dome height [LDH]) at warm forming temperatures.

Approach

- Mechanical testing of post-formed panels was received from original equipment manufacturers (OEMs) to characterize properties of continuous cast magnesium sheet, including ultimate strength and elongation to failure.
- A method was developed to evaluate the effects and down-select tooling lubricant types for warm forming magnesium sheet. Results will include coefficient of friction data for lubricant type as a function of temperature and formability under biaxial forming conditions.
- PNNL's warm biaxial forming equipment will be utilized to assist CANMET (Canada Centre for Mineral & Energy Technology) in developing biaxial forming limit diagram data and disseminate to the USAMP Warm Forming Team.

Accomplishments

- Initiated the project in late fiscal year (FY) 2008.
- Established a test plan for post-formed property characterization.
- Established both a plan and method to evaluate forming lubricants.

Future Direction

- Initiate and conduct mechanical property characterization on post-formed magnesium panels received from OEMs and the stamping supplier.

- Perform metallography on continuous cast magnesium sheet and post-formed panels in order to document microstructural and texture evolution during the warm forming process.
- Initiate biaxial formability testing and compare results with CANMET.

Introduction

The automotive industry is working continually toward reducing vehicle emissions and fuel consumption. A substantial portion of these efforts is focused on reducing overall vehicle weight. Magnesium technology gives automotive producers the ability to apply this low-density structural material selectively to automobiles ultimately to reduce cost, weight and fuel consumption. Magnesium sheet has potential application in body-in-white (BIW), body closures, interior frames/brackets and tubular components. A major barrier to use magnesium sheet is the cost of conventional wrought processing due to the hexagonal crystal structure and poor hot-short characteristics. Continuous casting of magnesium using twin-roll casting techniques offers the potential to reduce the cost of magnesium alloy sheet.

The work scope for this agreement was developed in conjunction with the USAMP Warm Forming Team (USAMP project AMD 602) and is directed at developing a fundamental understanding of the microstructure/formability relationship and post-formed properties of continuous cast sheet materials currently being considered for use by the domestic OEMs. The work focuses on a collaborative contribution to AMD 602 and is intended to work in conjunction with other program participants at the University of Virginia and CANMET.

PNNL will receive as-processed and as-formed samples from the USAMP project, will perform microstructural evaluations and analysis of failure modes and will relate these features to the formability measurements and experiments conducted collaboratively by USAMP and CANMET. Where needed, PNNL will conduct limited formability tests to complement work to be performed at the University of Virginia and CANMET.

Objectives

Currently, global suppliers are developing low-cost magnesium sheet. In this project, magnesium sheet from various suppliers and process variations will be tested to determine the warm formability and mechanical properties, hence suitability for automotive applications. The post-formed mechanical response of the supplied magnesium test panels will be characterized by room temperature tensile testing and endurance screening (fatigue). The microstructure will be documented primarily with optical microscopy and correlated to the processing methods and formability.

Formability is dependent on the friction characteristics between the sheet and tooling. As such, an evaluation of lubricants will be conducted to determine the most appropriate product that yields good formability and adequate surface finish. This testing will be conducted initially using the unique uniaxial friction test fixture at PNNL. This test rig will be set up with representative warm forming tool materials and both dry and synthetic lubricants. This uniaxial test will be used to screen lubricants for down-select, and further supplemental biaxial formability testing will be performed.

Finally, assistance will be provided to CANMET in developing forming limit diagram (FLD) data utilizing the heated-LDH test capabilities at PNNL. This work is designed to be synergetic to the effort led by CANMET in FLD development. CANMET is focused on FLD development using Marciniak in-plane stretching methods; biaxial stretching data will be complementary to this effort and will help establish a complete FLD.

Fiscal Year 2008 Activities

Activities at PNNL commenced in the latter part of 2008 and focused on establishing test matrices for post-formed property testing and lubricant evaluation. This included teleconference calls with

the USAMP Warm Forming Team to finalize the scope of work, schedules and define material sets of interest for evaluation and characterization.

Several post-formed magnesium panels have been received from the OEM participants, and test coupon schedules have been drafted. Mechanical testing of post-formed properties will commence in December 2008 and carry through the remainder of FY 2009.

In preparation for receiving magnesium samples for biaxial testing, heated LDH and Marciniak tooling was set up on an Interlaken, Inc. formability machine. The heated tooling will allow for warm formability experimentation to evaluate sheet deformation as well as lubricants. This testing will provide input into modeling and formability simulations led by the OEMs as well as the down-selection of adequate lubricant types for forming conditions up to 350°C.

Future Work

Fiscal year 2009 will be the first full year for PNNL activities in support of the magnesium warm forming program. With the receipt of materials from OEMs, PNNL can initiate the scope and conduct mechanical property characterization on post-formed magnesium panels as well as microstructural documentations. Also, a lubrication evaluation will be initiated with multiple types identified and planned for tribological evaluation. Finally, biaxial formability testing will be initiated and the results compared with work being performed at CANMET.

G. Development of High-Strength Superplastic Forming Aluminum Sheet for Automotive Applications

Principal Investigators: Curt A. Lavender, Daniel Edwards, Elizabeth Stephens
Pacific Northwest National Laboratory
P.O. Box 999, Richland, WA 99352
(509) 372-6770; fax: (509) 375-2186; e-mail: curt.lavender@pnl.gov
(509) 376-4867; fax: (509) 375-4448; email: dan.edwards@pnl.gov
(509) 375-6836; fax: (509) 375-4448; e-mail: elizabeth.stephens@pnl.gov

Technology Area Development Manager: Joseph A. Carpenter
(202) 586-1022; fax: (202) 586-1600; e-mail: joseph.carpenter@ee.doe.gov

Field Technical Monitor: Mark T. Smith
(509) 375-4478; fax: (509) 375-4448; e-mail: mark.smith@pnl.gov

---

Contractor: Pacific Northwest National Laboratory (PNNL)
Contract No.: DE-AC06-76RL0 1830

Objective

- Develop a cost-effective superplastic sheet with a post-formed strength greater than that of the commonly-used 5083 alloy.

Approach

- Identify candidate 5XXX, 6XXX, and 7XXX alloy systems.
- Establish operating limits for automotive pre- and post-superplastic forming (SPF) processes (such as heat-up rates and paint bake cycles) and assess alloy heat-treat response.
- Collaborate with aluminum (Al) suppliers to mill-process sheet materials with SPF microstructures based on selected 5XXX, 6XXX, or 7XXX alloy compositions.
- Demonstrate SPF of a high-strength sheet under simulated automotive manufacturing conditions.

Accomplishments

- A series of teleconferences were held with Sooho Kim and Paul Krajewski of General Motors (GM) and Peter Friedman of Ford to establish the automotive-specific objectives and processing constraints.
- Processing constraints were determined for:
  - Alloy superplasticity
  - Heating and cooling conditions
  - Forming rate and temperature
  - Post-SPF formability
  - Post-SPF heat-treat response during paint bake
- Two alloy systems were identified based on high-rate superplasticity developed by solute-drag (5XXX) and fine-grain size (6XXX), respectively.
- A biaxial forming die was fabricated with radii and forming depths consistent with expected automotive parts.

Future Direction

- Cast, homogenize, forge, and roll a series of alloys for evaluation for superplasticity by tensile testing using experimental heats.
- Form Al sheet materials using a biaxial forming die and evaluate the post-SPF mechanical properties using a test matrix of cooling rates and simulated paint bake cycles.
- Identify industrial Al mill to support process scale up.

Introduction

The objective of this project is to develop a cost-effective superplastic sheet with a post-formed strength >250 megapascal (MPa). Superplastic forming of Al alloys has been used in the forming of automotive outer body panels and closures. Because SPF involves forming of the Al sheet at elevated temperatures, the final formed material strength is similar to that of an annealed (soft) Al sheet. Current automotive SPF applications have focused on the use of Al 5083 alloy that, with relatively high magnesium content, develops a post-formed strength of ~150 MPa. The use of 5XXX-series Al alloys with magnesium (Mg) levels above 3% introduces the potential for stress-corrosion cracking (SCC) when exposed to an elevated temperature environment. The net result of these factors is that SPF 5083 alloys have been largely restricted from use in body-in-white (BIW) and under-hood applications where higher strength and resistance to SCC are required.

The current project is planned for three years and will evaluate a series of 5XXX-, 6XXX-, and 7XXX-series Al alloys to develop a modified alloy and mill processing methods to produce a high-strength SPF Al sheet with a post-formed strength of >250 MPa. The technical approach will evaluate modifications to existing heat-treatable alloys combined with thermo-mechanical processing methods to produce a fine-grained SPF sheet with a post-formed heat-treat response. The development of a fine-grain microstructure that remains stable at SPF temperatures generally requires a combination of alloy chemistry adjustment with hot and cold rolling into sheet. In the Al alloy system, individual alloy specifications contain significant ranges for many of the key alloying elements; from previous PNNL SPF development work, alloy modifications within the set alloy ranges can be used to optimize SPF microstructures. The focus of the project will be to develop a heat-treatable alloy that has a post-forming age-strengthening response compatible with automotive BIW thermal cycles (E-coat, paintbake). The result of the project will be development of a cost-effective SPF Al alloy sheet that can be used in higher-strength and elevated-temperature automotive applications, extending the use of SPF Al to BIW and underhood sheet components.

Automotive Superplastic Processing

Superplasticity

In order to meet the high-volume part production required for the automotive industry, it is unlikely that forming will be performed under ideal superplastic conditions (i.e., maximum strain-rate sensitivity or m-value). The criteria for superplasticity will be established by forming trials where the tray part (Figure 1) must be formed in less than 240 seconds (sec) or at an approximate strain rate of 1×10^{-3} sec^{-1}. Given that only very high-cost, rapidly-solidified powder metallurgy alloys have demonstrated fine-grained superplasticity at high rates, stable forming for this alloy will likely be achieved with a combination of solute drag and grain boundary sliding [1]. Temperatures for forming must be as low as possible in order maximize die life and minimize sheet oxidation; as a result, forming temperatures will be held below 515°C. Therefore, adequate "superplasticity" for this project has been defined as an alloy that can form to a minimum of 150% elongation at a strain rate greater than 1×10^{-3} sec^{-1} and at temperature less than 515°C.

Superplastic Forming Process

The automotive work-cell approach to superplasticity requires that the sheet blank be heated rapidly and the formed part cooled as

Figure 1. Superplastically-formed tray to be used as evaluation part for the high SPF alloy development project.

quickly as possible without excessive distortion in order to minimize production cost [2]. The fine grain size required for superplasticity in the conventional 5083 alloy is stabilized by a high level of second-phase eutectic constituent particles formed during ingot solidification and subsequent rolling. However, for Al alloys which harden by aging, the precipitate phases will dissolve during heating and therefore will provide no effective pinning of grains. In order to achieve fine grain sizes in age-hardenable alloys, a technique called particle stabilized nucleation (PSN) has been employed [3]. In PSN, an aged and cold-worked sheet is heated at high rates to maximize the number of grains nucleated while minimizing growth time. Fast heating rates are beneficial for both superplasticity and production rate; therefore, this parameter will be closely controlled.

Maximum age-hardening response in Al alloys is achieved from a solute-rich metastable solid solution formed by water quenching from a temperature where virtually all constituents are dissolved. However, when water quenches a complex shape such as an automotive panel, excessive distortion will require the use of re-strike tool, eliminating one of the most important advantages of SPF: low-cost tooling. Therefore, although high cooling rates are desirable for post-SPF paint-bake response properties, part distortion will determine that maximum cooling rate, like heating rate, will be a closely-controlled parameter.

Post-Superplastic Forming Properties

Post-SPF panel properties must be separated into two requirements: post-SPF formability and final part properties. For post-SPF formability, the panel must be ductile enough for secondary operations such as hemming and, therefore, must not exit the SPF die in the fully-hardened condition. The final part properties will be achieved after paint bake. If the strength level is greater than 250 MPa, a vehicle mass reduction of greater than 20% could be realized. However, typically high-strength Al alloys are susceptible to accelerated corrosion, particularly after cold work such as hemming. Alloying constituents known to promote accelerated corrosion such as copper (Cu) and zinc (Zn) will be avoided.

Superplastic Alloy Selection

The preceding section was a qualitative and quantitative analysis of the automotive SPF process in order to define the requirements of a high-strength SPF alloy. This analysis was required because many high-strength 2XXX and 7XXX SPF alloys have been developed for use in aerospace; however, the unique cost-sensitivity, corrosion and processing requirements (primarily production rate) of automotive prevent their use. The low-cost, high-strength SPF automotive sheet must be adapted to the existing low-cost SPF process.

The low-cost SPF process requires that the alloy be soft after SPF and achieve the 250 MPa strengths during the paint bake so that the panel can be subjected to secondary processing such as hemming, thereby eliminating alloys that might harden during the SPF process. This important requirement determines that the alloy must exit the SPF process with a metastable solid solution with adequate solute for precipitation. Therefore, the alloying elements must dissolve at 515°C or less and be retained in solution without a water quench. Previously, PNNL had demonstrated that this was possible with the 6013 alloy; however, the primary hardening phase was the AlMgCu, theta precipitate [4]. Given that Cu additions produce unacceptable corrosion resistance for automotive applications, the new alloy must rely on a silicon (Si) addition for precipitation hardening. A study similar to the previous 6013 alloy development will be undertaken, focusing on the precipitation hardening associated with Si rather than Cu.

The low-cost superplastically formable alloy composition can be summarized as follows:

1. Maximum eutectic constituent to minimize grain size (i.e., Manganese [Mn])
2. Minimum additions of Cu
3. Solution temperature less than 515°C
4. Age response consistent with a paint-bake cycle
5. Maximum solid-solution strengthening (Mg)
6. Maximum Si content.

The alloy development activity will focus on two base alloys: a 3.5% Mg 5XXX and a low Mg 6XXX. Each alloy will be modified to maximum Mn content to minimize grain size by nucleation and Mg/Si ratio to achieve maximum paint bake response. Commercially available compositions will be used, where possible. Elements such as Si, Mn, and the like will be skewed within the existing commercial tolerances to avoid development of alloys difficult to produce on an industrial basis.

Conclusions

During this reporting period, the following conclusions were derived:

- The high-strength SPF alloy must develop elevated strength by a post-forming aging treatment during the paint bake.
- The metastable solid solution required for paint bake response must be formed during the SPF process and subsequent cooling.
- The primary constituent for hardening during paint bake will be the Mg_2Si precipitate.
- Given the forming rates desired for automotive production, stable deformation will likely require a combination of fine-grained superplasticity and solute-drag.

Presentations/Publications/Patents

DOE Vehicle Technologies Program Annual Merit Review. February, 2008.

References

1. E. M. Taleff, “An Overview of Creep Deformation Behaviors in 5000-Series and Al-Mg Alloys,” 2004. *Advances in Superplasticity and Superplastic Forming*. Eds. E. M. Taleff, P. A. Friedman, P. E. Krajewski, R. S. Mishra, and J. C. Schroth, TMS (The Minerals, Metals & Materials Society).
2. J. C. Schroth, “General Motors Quick Plastic Forming Process,” 2004. *Advances in Superplasticity and Superplastic Forming.* Eds. E. M. Taleff, P. A. Friedman, P. E. Krajewski, R. S. Mishra, and J. C. Schroth, TMS (The Minerals, Metals & Materials Society).
3. N. E. Paton and C. H. Hamilton, “Method of Imparting A Fine Grain Structure to Aluminum Alloys Having Precipitating Constituents,” U.S. Patent No. 4,092,181, May 30, 1978.
4. C.A. Lavender, *Enhanced Plasticity in AA6013 at Elevated Temperatures,* Presentation at THERMEC 2006, Vancouver, British Columbia. July, 2006.

H. Aluminum Automotive Closure Panel Corrosion Test Program

Project Co-Chair: Tracie Piscopink-Jafolla
General Motors Corporation
3300 General Motors Road
MC: 483-370-101
Milford, MI 48380-3726
(248) 676-7014; fax: (248) 685-5279; e-mail: tracie.l.jafolla@gm.com

Project Co-Chair: Francine Bovard
Alcoa Technical Center
100 Technical Drive
Alcoa Center, PA 15069
(724) 337-3249; fax: (724) 337-2044; e-mail: Francine.Bovard@alcoa.com

Technology Area Development Manager: Joseph A. Carpenter
(202) 586-1022; fax: (202) 586-1600; e-mail: joseph.carpenter@ee.doe.gov

Contractor: United States Automotive Materials Partnership (USAMP)
Contract No.: FC26-020R22910 through the DOE National Energy Technology Laboratory

Objective

- Develop a standardized cosmetic corrosion test for finished aluminum automotive body panels that provides a good correlation with in-service testing and field performance.

Approach

- Conduct laboratory testing, outdoor exposures, test track exposures, and in-service testing.
- Evaluate test data to determine which accelerated tests correlate with in-service testing.
- Conduct iterative laboratory testing to improve correlation between lab tests and on-vehicle exposures.

Accomplishments

- Test track exposures, on-vehicle exposures, and outdoor exposures have been completed.
- Many laboratory tests have been conducted and compared with service-relevant exposures.
- Corrosion product analyses conducted for some laboratory tests and exposures on vehicles.
- Key environmental parameters have been identified as important for inclusion in an accelerated test for painted aluminum.

Future Direction

- As this program draws to a close, the remaining work will be focused on repeatability and reproducibility of the American Society for Testing and Materials **(**ASTM) G85-09 A2 and G85-09 A4 tests, the two accelerated corrosion tests that have shown the greatest promise at replicating in-service aluminum corrosion.

Introduction

All original equipment manufacturers (OEMs) and their suppliers rely on various laboratory tests to assist in prediction of real life service performance, even though it is well recognized that many of these lab tests do not fully represent observed corrosion behavior. Part of the difficulty lies in the large number of variables in service that influence corrosion rates and how to fully take all of these factors into account with one single test procedure. OEMs have also developed elaborate test tracks or proving ground tests in attempts to more closely simulate service conditions but in general the proving ground tests also have not correlated well with on-vehicle performance for painted aluminum [1–4].

In addition to real life corrosion conditions, there are also many factors in the OEM production process that influence the aluminum surface condition, chemical treatment and paint performance of a closure panel that are difficult to fully control on lab prepared panels. Nonetheless, the potential for time and cost savings that could be achieved by having a general agreement on a lab test capable of closely mimicking real life performance was highly desirable and in 2000 resulted in the formation of a group of representatives from the U.S. automotive manufacturers, aluminum industry, and coating and other suppliers to establish that correlation. Since then, a number of papers have been presented at the Society of Automotive Engineers (SAE) Congress [1–4] to disseminate the findings of this group to the automotive corrosion community.

In this progress report, the results of the past year's experimentation are reviewed. The latest results cover not only correlation of lab tests with the extent and morphology of in-service corrosion, but also an analysis of corrosion products to help determine whether the mechanisms of corrosion propagation are the same in lab and field exposure.

Experimental

Materials

The painted panels used in this program are listed in Table 1. The substrate materials, metal finish, and paint processing variables were selected to give a range of cosmetic corrosion performance.

Several aluminum alloys used in the Unites States and in Europe, both current and historical, were included, with two alloys processed to simulate metal finishing in an automotive assembly plant body shop. Panels made from electro zinc coated steel and uncoated cold rolled steel were included as reference materials [5].

Table 1. Materials

Panel code	Alloy substrate	Metal finish	Paint system
A or 1	AA6111-T4PD	Mill	Standard
B or 2	AA6111-T4PD	Mill	Low F^-
C or 3	AA6111-T4PD	Mill	Ecoat
D or 4	AA6111-T4PD	Sanded	Standard
E or 5	AA6016-T4	Mill	Standard
F or 6	AA6022-T43	Mill	Standard
G or 7	AA2036-T4	Sanded	Standard
H or 8	EG 60 steel	Mill	Standard
I or 9	CR steel	Mill	Standard

Two sizes of panels, 2 in. × 4 in. and 4 in. × 6 in., of each of the materials were painted with a typical automotive paint system. This paint system included zinc phosphate pretreatment, medium-build cathodic electrophoretic priming (E-coating), and spray painting with a primer surfacer and white basecoat/clear topcoat system for a total paint film thickness of approximately 100 μm. One set of 6111 panels (Panel Code B) was processed through the phosphate pretreatment with lower fluoride concentration (comparable to the fluoride level used for steel only vehicles which results in lower phosphate coating weight). Also, since qualification testing is often done on panels that are processed only through the electrophoretic primer (E-coat) step, another set of 6111 panels (Panel Code C) was processed only through the E-coat step (i.e., standard fluoride for Al but no basecoat or clear coat applied). Panel code C was evaluated in lab tests only (no on-vehicle or proving ground exposures).

Panels were prepared as needed for testing with two parallel scribes penetrating through the coatings to the substrate. The panels were provided to the testing laboratories as fully

prepared painted and scribed panels. Triplicate sets of the painted and scribed samples have been exposed in a variety of environments, including: laboratory, static outdoor exposure, proving ground, and on-vehicle exposure.

Evaluation Method

For this study, an optical imaging system developed by Atlas Material Testing Technology, LLC was employed to quantitatively interpret the degree of cosmetic corrosion. The imaging system employs controlled illumination conditions, high-resolution digital image capture, and advanced algorithm-based image and data analysis methodologies [6].

Four geometrical attributes of the cosmetic corrosion were measured: area of corrosion, maximum length, minimum length, and average length. The area of corrosion was found to be the most representative and comprehensive measurement. Because the size of the panels and therefore the scribe lengths for the lab tests were different from the other tests, the corrosion area was normalized to the length of the scribe (i.e. area per length). The normalized corrosion areas for triplicate panels (two scribes per panel) were then averaged and the results are reported as "normalized average area."

On-Vehicles Exposures

It is critical when developing a laboratory based test that test-to-field correlation be performed. In an effort to capture real-world data in developing this test, it is preferable to expose these panels to severely corrosive environments that represent "worst case" real-world service environments. Suitable environments exist in the northeastern United States, southeastern coastal areas of the United States, and southeastern Canada. Two of these environments (northeastern United States and southeastern Canada) were part of this program. The sites selected for this study were: (1) Detroit, Michigan, (2) St. John's, Newfoundland, (3) Montreal, Quebec, and (4) Cleveland, Ohio, to Buffalo, New York, truck route. Two sets of 2 in. × 4 in. test panels are exposed on each vehicle (two vehicles per site). Each set of 24 (three each of eight material variables) were attached to a mounting panel (16 in. × 12 in.) using double-backed tape prior to mounting on the vehicle. At the Detroit, St. John's, and Montreal sites, one set is mounted on the hood of each vehicle (horizontal orientation) and one set on the right front door of each vehicle (vertical orientation). For the Ohio-New York (OH/NY) truck route the panels were mounted beneath the trailer frame behind the front wheels (vertical orientation only). Each panel contains two diagonal scribe lines which are 2 in. long and 1 in. apart. The panels were exposed for a total of 4 years of in-service exposure. Intermediate evaluations were conducted when possible. Upon completion, the panels were removed and sent to Atlas Material Testing Technology, LLC for evaluation.

Laboratory Tests

Several rounds of laboratory testing have been conducted to date [1–4]. All of the accelerated laboratory tests that have been evaluated thus far are listed in Table 2.

Table 2. Laboratory tests evaluated in this program

	Test Procedure	Duration
1	SAE J2334	40, 60, and 80 cycles
2	ASTM D2803 (80% RH)	6 weeks
3	Modified ASTM D2803 (60% RH)	6 weeks
4	Modified ASTM D2803 (100% RH)	6 weeks
5	ASTM G85-09 A 2	1, 2, and 3 weeks
6	VDA 621-415	10 cycles/ 70 days
7	ASTM B117	500 and 1,000 hours
8	CCT IV	35 and 70 cycles
9	KWT	6 weeks
10	Ford Arizona Proving Ground Exposure (APGE) (Manual)	35 and 70 cycles
11	Ford APGE (Automated)	35 and 70 cycles
12	HCl Dip	3, 6, and 8 weeks
13	GM9511P	4 weeks
14	GM9682P	4 weeks

Table 2. (continued)

	Test Procedure	Duration
15	ASTM G87	20 cycles
16	ASTM G85-09 A5	500 hours
17	ASTM G85-09 A4 (continuous spray)	500 hours
18	ASTM G85-09 A4 (intermittent spray)	500 hours
19	Modified ASTM G85-09 A4 (continuous spray)	500 hours
20	Modified ASTM G85-09 A2	500 hours

Subsequent to comparison of the results from several rounds of laboratory tests (performed in the preceding years) with preliminary results from on-vehicle exposure; the list of lab tests of interest has been narrowed to the following for 2008 and beyond:

- ASTM G85-09 A2—Cyclic Acidified Salt Spray Test [7]
  - Test Cycle: 6 hour repetitive cycle with 3 steps/cycle:
    - 45 min. *Spray*
    - 2 hour dry-air *Purge*
    - 3 hour + 15 min *Soak* (RH gradually increases during soak)
  - Test Solution: 5% NaCl acidified to pH = 2.8–3.0 with acetic acid
  - Temperature: 49°C (120°F)
- ASTM G85-09 A4—Salt/SO_2 Spray Test (Continuous) [8]
  - Test Cycle: 6 hour repetitive cycle Continuous *Spray*; *w*ith introduction of SO_2 gas for 1 hour each cycle
  - Test Solution: 5% NaCl acidified to pH = 2.5–3.2
  - Temperature: 35°C (95°F)
- ASTM G85-09 A4—Salt/SO_2 Spray Test (Intermittent) [8]
  - Test Cycle: 3 hour repetitive cycle with 3 steps/cycle:
    - 30 min *Spray*
    - 30 min SO_2
    - 2 hour *Soak*
  - Test Solution: 5% NaCl acidified to pH = 2.5–3.2
  - Temperature: 35°C (95°F)
- HCl Dip Test
  - Test Cycle: 1 week cycle with 3 steps/cycle:
    - Immersion for 2 minutes at 35°C
    - Drip dry for 28 minutes in lab air
    - 143.5 hours at 40°C and 85% RH
  - Test Solution: 3.1% HCl
- APGE Simulation Test
  - Test Cycle: 24 hour repetitive cycle with 3 steps/cycle:
    - Immersion for 15 minutes at 23°C
    - Drip dry for 1.25 hours in lab air
    - 22.5 hours at 50°C and 85–90% RH
  - Test Solution: 5% NaCl pH = 6–8

Although the HCl Dip and APGE tests had shown some degree of correlation with the on-vehicle exposure results and they continue to be of some interest, they were not the focus of the work done in 2008. This work concentrated on the ASTM G85-09 A2 and A4 (including their variants) accelerated tests and corrosion product analysis.

Corrosion product analysis of panels from preliminary on-vehicle testing indicated that sulfur and chloride are significant components in aluminum corrosion products. Prior to 2007, none of the tests evaluated incorporated any form of sulfur. Another factor that has influenced the lab test selection process is that on-vehicle exposures tended to produce higher corrosion levels than the results seen in the many lab tests. Generally, the solutions used for lab tests that showed little or no corrosion were neutral pH and it became evident that more acidic environments in the lab tests increased the extent of the corrosion observed.

ASTM G85-09 A2 and ASTM G85-09 A4 (continuous spray) were previously identified as lab tests that most closely mimicked in-service corrosion performance in terms of the type and extent of the corrosion. The ASTM G85-09 A4 (continuous spray) test with SO_2 and NaCl in the exposure environment was the only test that had exhibited sulfur in the corrosion products.

Therefore, testing in 2008 was conducted to determine reproducibility of this test. The alternate cycle of the ASTM G85-09 A4 (intermittent) was also evaluated.

OEM Test Track Exposure

Completed OEM test track results were published previously [3] and are not repeated in this report.

Outdoor Exposure

Completed outdoor exposure test results were published previously [3] and are not repeated in this report.

Corrosion Product Analysis

Corrosion product analysis was performed on panels A, D, G, and I removed from 4-year long exposures on vehicles in St. John's and Montreal. In addition, panels from ASTM G85-09 A4 test (incorporating SO_2 gas) have also been examined in this study. For the top down analysis of the corrosion products, the paint layer was stripped in 1-methyl-2-pyrrolidone solvent. Water was not used during the stripping procedure so as to preserve any chloride/sodium species present within the corrosion product.

The panels were examined using a Leo 440 Scanning Electron Microscope (SEM) equipped with a Quartz XOne Energy Dispersive X-ray (EDX) analysis system. SEM/EDX technique was chosen for this examination because the amount of corrosion product on aluminum closure panels is very small, making more traditional analytical procedures impractical. In addition, the use of SEM/EDX allows not only for a measurement of the chemical species present, but also for an analysis of the distribution of these species in and around the corroded area on the panel. This technique is relatively sensitive with detection limits sometimes less than 0.1% w/w for most elements including sulfur and chlorine, which are the species of interest in this study.

Results and Discussion

On-Vehicle Exposures

Although the extent of corrosion in the on-vehicle exposures varied considerably from vehicle to vehicle for the various sites, panels D, G, and I typically exhibited significantly more corrosion than the other substrates, as illustrated by the images in Figure 1. The aluminum panels with metal finishing (D and G) generally have more corrosion than the other aluminum substrates, and cold rolled steel (I) has more corrosion than the electro-galvanized steel (H). Normalized average area from on-vehicle service relevant exposures in Detroit, Montreal, St. Johns, and the OH/NY Truck route are plotted in Figure 2. In this plot the results for the aluminum panels with metal finishing (D + G) have been averaged and the results from the other aluminum panels with standard paint system (A + E + F) have been averaged. Where possible, the results for the hood (H = horizontal) and door (V = vertical) locations are also indicated. For the 4-year exposures in Montreal the traceability of the locations was not certain so the results for H and V locations have been combined into a single average area. In the Detroit and St. Johns exposures the corrosion was more severe in the H location, but in the Montreal exposures the corrosion tended to be more severe in the V location. For the OH/NY highway trailers, panels were exposed in a vertical position only. Based on these on-vehicle results, only those accelerated tests that show a significant difference between the aluminum substrates with metal finishing (i.e., sanding) and those without metal finishing are currently being considered.

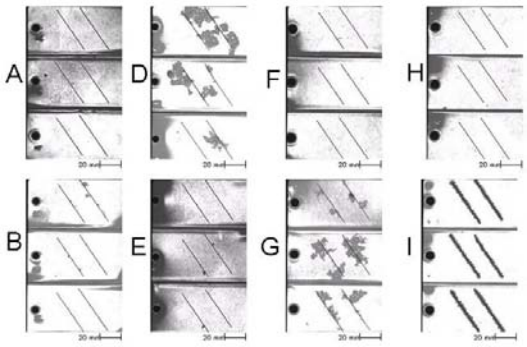

Figure 1. Images of the 3 replicate panels of each substrate from a Detroit on-vehicle exposure with ~2 years' exposure.

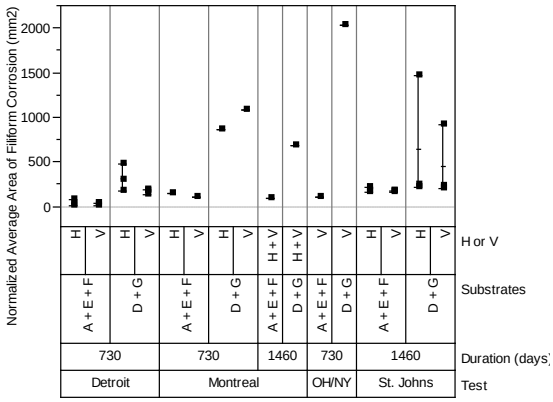

Figure 2. Compiled results from on-vehicle exposures with 2 and 4 years' exposure.

Regardless of position on the vehicle, the aluminum panels with metal finishing (D + G) exhibited more corrosion than the other aluminum panels with standard paint system (A + E + F) at all of the different exposure sites. This is consistent with other reports in the literature which indicate that metal finishing significantly impacts the susceptibility to filiform corrosion [9,10]. In 1997 Colvin et al. [9] evaluated the filiform corrosion performance of sanded vs. mill finish aluminum surfaces with zinc phosphate pretreated and painted panels in several different service environments. They observed that sanded surfaces exhibited significantly more corrosion and paint delamination in both seacoast and on-vehicle exposures. In this same study, an in depth evaluation of the impact of sanding on the deposition and growth of zinc phosphate crystals on aluminum surfaces was conducted [10]. The impact of the sanding on the filiform corrosion was attributed to localized inhibition of zinc phosphate precipitation which resulted in inconsistency of the zinc phosphate pretreatment layer on sanded surfaces.

Figure 3 presents the optical micrographs of the panels from a St. John's on-vehicle test with ~4 years' exposure. These panels were placed in the hood (horizontal) location and indicate that the aluminum panels with metal finishing (D + G) exhibited greater corrosion than the standard aluminum panel (A). In addition, the steel panel (I) also exhibited significant blistering around the scribe marks. The panels from the door (vertical)

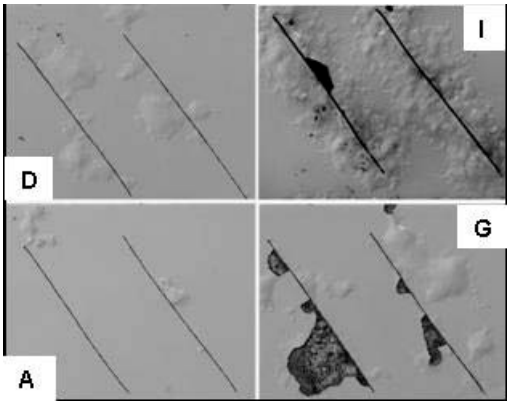

Figure 3. Images of the panels of four substrates from a St. John's on-vehicle exposure (hood) with ~4 years' exposure.

location and the panels from 4-year Montreal exposures also exhibited a similar trend.

Figure 4 presents the secondary electron micrograph and the elemental distribution maps for chlorine, sulfur, and aluminum for the G panel from the hood location at 4 years' exposure in St. John's. In the elemental distribution maps, the brighter regions qualitatively represent the greater presence of the element of interest. The white arrow in this figure indicates the scribe mark. The elemental distribution maps indicate the presence of sulfur species at the scribe mark and at the coarse corrosion product regions. Chloride species were observed at the tip of the filiform filament.

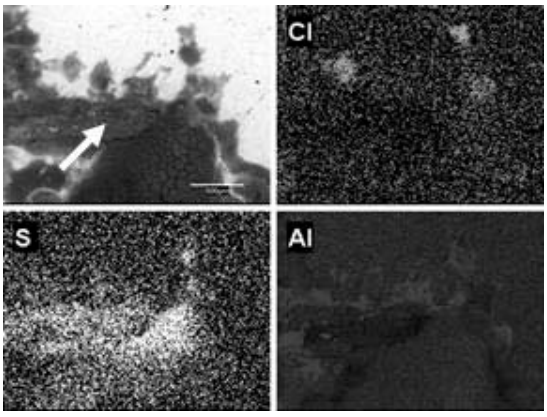

Figure 4. Secondary electron micrograph (top left) and elemental distribution maps for sulfur, chlorine, and aluminum from panel G of 4-year St. John's exposure (hood). In these images, brighter regions represent greater presence of the element of interest. Scribe mark is indicated by the arrow in this figure.

This trend is consistent for all panels from St. John's exposure including those from hood and door locations.

It should also be mentioned that while filiform corrosion was observed on the aluminum panels, the steel panel (I) exhibited a more uniform corrosion attack. Corrosion products in the steel panel also exhibited greater presence of chlorides compared to sulfur species. Finally, the corrosion product morphology and its composition on the 4-year exposure panels are similar to those observed from the 2-year exposure panels [2].

Table 3 presents the results from the EDX spot analysis of the corrosion products on the 4-year St. John's exposure panels (hood). Composition of the corrosion products was determined at three different locations. The results indicate that the aluminum panels, in general, exhibited sulfur species at more locations than the chloride species. In addition, as discussed previously, the steel panels did not exhibit sulfur enrichment to the same extent as the aluminum panels. Besides sulfur and chlorine, sodium, potassium and calcium were also detected, mostly at the scribe marks. These could arise from the presence of de-icing salts. Finally, other elements like magnesium (Mg), silicon (Si), phosphorous (P), manganese (Mn) and titanium (Ti) (not shown in the table) were also detected within the corrosion products.

Table 3. Composition of corrosion products from 4-year St. John's exposure (hood)

Panel ID	Number of Spots	Elements Detected (wt. %)									
		C	O	Na	Al	S	Cl	K	Ca	Fe	Zn
A (Hood)	4	11.3	51.1	0.2	23.8	1.7	0.2	0.1	4.9	0.4	1.9
D (Hood)	6	10.1	44.0		36.1	0.7	2.4		0.1		2.5
G (Hood)	9	9.0	51.9		25.9	0.8	1.3	0.2	0.1	0.2	4.3
I (Hood)	3	8.4	32.8	1.0	3.2	0.0	0.1	0.9	0.5	41.3	

Figure 5 presents the secondary electron micrograph and the elemental distribution maps for chlorine, sulfur, and aluminum for the G panel from 4 years of exposure in Montreal. As before, in the elemental distribution maps, the brighter regions qualitatively represent the greater presence of the element of interest. The scribe mark and the corrosion originating from the scribe mark could be clearly seen in this figure. In general, the Montreal panels qualitatively appeared to exhibit

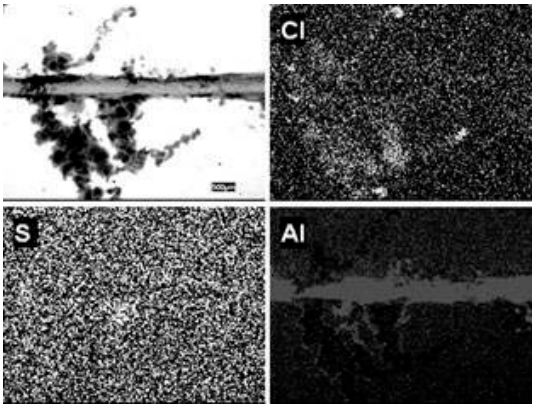

Figure 5. Secondary electron micrograph (top left) and elemental distribution maps for sulfur, chlorine, and aluminum from panel G of 4-year Montreal exposure.

less corrosion than the St. John's panels. The elemental distribution maps indicate the presence of chloride species within the corroded regions. Sulfur was detected at very few locations within the scribe mark. This is consistent with the results from the 2-year Montreal exposures [2]. This is also in contrast with the results from the St. John's exposures in which greater amounts of sulfur species could be detected within the corrosion products.

Unlike the aluminum panels, the steel panel (I) from Montreal exposure did not exhibit filiform corrosion, a trend consistent with the results from previous exposures [1,2]. Also, similar to the St. John's 4-year exposures, the steel panel exhibited greater levels of chloride species compared to the sulfur species.

The results presented in Figure 5 are also confirmed by the EDX spot analysis performed at various locations within the corrosion products. The results from these measurements are presented in Table 4. This table shows that chloride species were detected at greater locations on the aluminum panels compared to the sulfur species. In addition, the steel panel exhibited fewer sulfur-containing locations compared to the aluminum panels.

To determine the source of sulfur and chloride species, aluminum wire-containing CLIMAT units were exposed to atmospheric conditions in Montreal for a period of 3 months. Analysis of the

deposit on the aluminum wires indicated the presence of both sulfur and chlorine species with concentrations ranging from 0.3 to 2.6% by wt. for sulfur and 1.9 to 6.8% by wt. for chlorine. Thus, the results from the atmospheric corrosion exposures are consistent with those from the corrosion product analysis reported in Table 4. A similar exercise is being performed in St. John's in which the deposits on the aluminum wire exposed for a certain period will be examined by SEM/EDX technique. It is expected that results from the CLIMAT sample will be useful in explaining the trends observed in the corrosion product analysis from St. John's location.

Table 4. Composition of corrosion products from 4-year Montreal exposure

Panel ID	Number of Spots	Elements Detected (wt. %)									
		C	O	Na	Al	S	Cl	K	Ca	Fe	Zn
A	5	18.7	33.9	0.1	39.7	0.1	1.2				3.4
D	7	14.0	21.1	0.3	28.8	0.1	0.2	0.2	1.2		1.2
G	6	15.8	29.7		26.5	0.1	0.5	0.3	1.0		4.0
I	3	15.4	32.2	0.3	1.8	0.3	0.2	1.0		43.0	3.1

Laboratory Test Results

The normalized average area results from the ASTM G85-09 A2, the ASTM G85-09 A4 (constant spray) and the ASTM G85-09 A4 (intermittent spray) tests are shown in Figure 6.

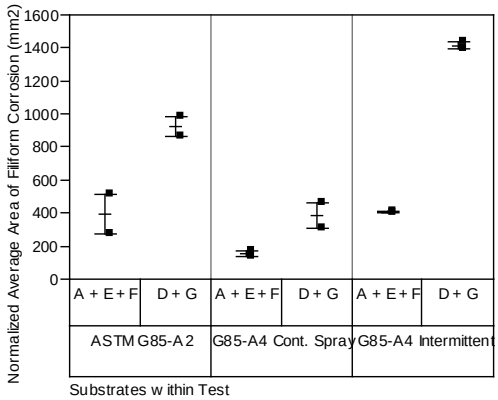

Figure 6. Normalized average area results from the ASTM G85-A2, the ASTM G85-09 A4 (constant spray) and the ASTM G85-09 A4 (Intermittent spray) tests. Duration for all 3 tests = 21 days (~500 hours).

All three tests show more corrosion area on the aluminum panels with metal finishing (D + G) than the other aluminum panels with standard paint system applied to the mill finish (nonsanded) substrates (A + E + F). The intermittent spray cycle for the ASTM G85-09 A4 test is more severe than the constant spray test and therefore appears to better differentiate between the sanded and mill finish panels. However, relative to the on-vehicle exposures, the intermittent ASTM G85-09 A4 and the ASTM G85-09 A2 test slightly over-predicted the corrosion for the mill finish substrates.

The lab test results are compared with the on-vehicle results in Figure 7. The diagonal line in the plot represents a 1:1 correlation between "D + G" and "A + E + F". All of the data for both the on-vehicle and the three lab tests are above the line reflecting the fact that the more corrosion occurred on the sanded panels (D + G) than on the nonsanded panels (A + E + F). The numbers next to the symbols on the plot are the actual ratios of (D + G) to (A + E + F). For the on-vehicle exposures the ratios range from 6:1 to 26:1. The ratios are lower for the lab tests (for example, the ASTM G85-09 A4 intermittent spray test has the highest ratio for the lab tests at 3.5:1).

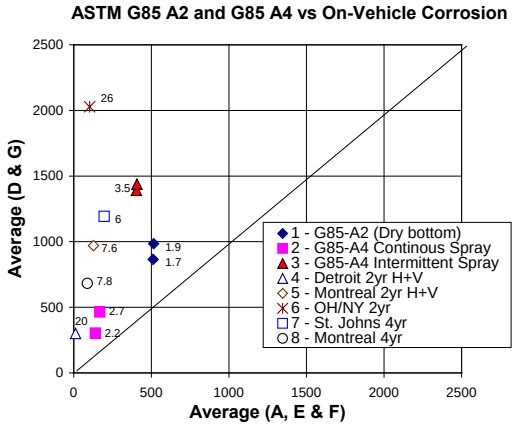

Figure 7. Average normalized corrosion area (mm^2) for substrates "A + E + F" versus that for substrates "D + G" for on-vehicle exposures and lab tests: ASTM G85-09 A2, ASTM G85-09 A4 (constant spray) and ASTM G85-09 A4 (intermittent spray).

Figure 8 shows representative images of substrate D after the ASTM G85-09 A2 and ASTM G85-09 A4 accelerated tests. Comparison of the morphology of the corrosion in these tests with those on substrate D from the on-vehicle exposures (Figure 1) shows that the corrosion

tends to be more continuous along the scribe line in the lab tests than is observed in the on-vehicle exposures. Of these three lab tests the morphology of the corrosion in the ASTM G85-09 A4 (continuous spray) appears to be more similar to that from the service relevant exposures on vehicles.

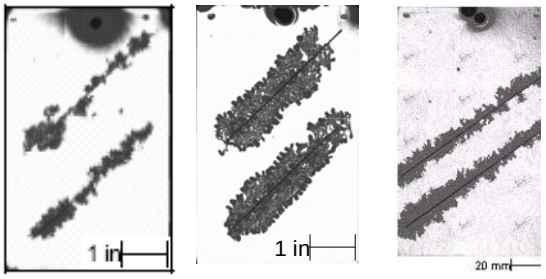

Figure 8. Images of corrosion on substrate D after accelerated corrosion testing.

Corrosion product analysis was also performed on the aluminum and steel panels exposed to G85-09 A4 (constant and intermittent) and G85-09 A-2 tests. The results from the G85-09 A2 tests have been reported previously [1] and hence only the results from G85-09 A4 tests will be presented here.

Visual examination of the G85-09 A4 test panels indicated that the intermittent salt spray exposure resulted in a more extensive corrosion along the scribe mark for the aluminum panels. However, the lengths of a few individual filiform tracks were greater for the continuous salt spray tests. For the steel panels, both tests produced similar corrosion behavior, though a slightly greater amount of corrosion was observed for the intermittent salt spray exposures. Corrosion product analysis indicated that the corrosion product composition was similar in both cases and, hence, only the results from the constant spray tests will be presented here.

Figure 9 presents the secondary electron micrograph and the elemental distribution maps for chlorine, sulfur, and aluminum for the panel D exposed to ASTM G85-09 A4 constant spray salt test. In the elemental distribution maps, the brighter regions qualitatively represent the greater presence of the element of interest. The scribe mark is at the bottom of the figure, running parallel to the bottom edge. Sulfur species were observed to be present at the scribe mark and at the coarse corrosion product regions. Chloride species were detected at the edge of the corrosion products and at the tip of the filiform filament. Thus, the results presented in this figure show that this test closely mimics the results from the St. John's 4-year exposure panels.

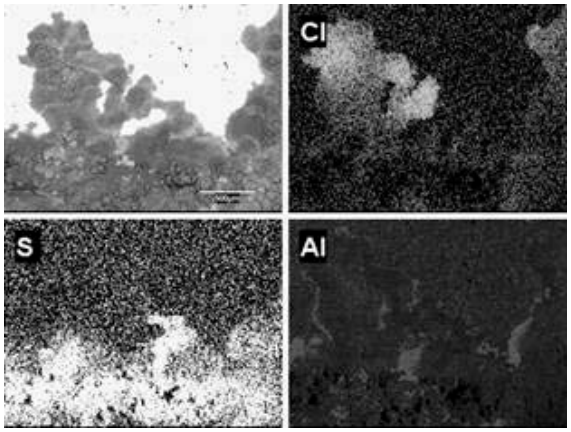

Figure 9. Secondary electron micrograph (top left) and elemental distribution maps for sulfur, chlorine and aluminum from panel D exposed to ASTM G85-09 A4 (constant spray) salt spray test.

EDX spot analyses were also performed at selected locations within the corrosion products on panels A, D, G, and I. The results from the EDX analysis are presented in Table 5. It should also be noted that, in addition to the elements shown here, Mg, Si, P, and Mn were also detected within the corrosion products. The results presented in this table indicate that sulfur and chloride species could be detected in significant quantities at most of the regions analyzed. Thus, this test appears to encompass the features observed from the 4-year on-vehicle exposures at St. John's and Montreal.

Table 5. Composition of corrosion products from ASTM G85-09 A4 (constant spray) laboratory salt spray test

Panel ID	Number of Spots	Elements Detected (wt. %)									
		C	O	Na	Al	S	Cl	K	Ca	Fe	Zn
A	7	10.8	49.9	0.6	30.6	1.5	2.1				2.6
D	6	13.8	46.1	0.9	30.4	1.4	1.6				3.4
G	8	11.2	48.8	0.6	26.2	1.3	1.3				6.1
I	6	11.2	29.3	0.2	0.8	2.4	4.2			46.8	2.9

Conclusions

An evaluation of the 4-year, in-service panel exposures shows that all of the panels that were exposed to metal finishing (sanding) prior to paint application exhibit a significantly higher level of filiform corrosion than those that were not sanded. Although a detailed understanding of the mechanism for the higher level of corrosion for sanded aluminum is outside the scope of this project, this result is consistent with the results of other studies [9, 10]. Because of this observation, the sanded panels were considered as a separate group from the nonsanded (mill finish) panels in comparisons of accelerated corrosion test results to the in-service exposure results.

Another observation from the in-service panel exposures was the presence of sulfur along with chloride in the corrosion product on aluminum panels. It is interesting to note that sulfur was found only in the corrosion products on the aluminum panels and not in the corrosion products on steel panels that were exposed to the same environment. The presence of sulfur in the corrosion products of in-service aluminum exposure panels led to an evaluation of accelerated corrosion tests that include sulfur in the exposure. It is unclear what the mechanistic role of sulfur is in the corrosion (beyond the scope of this project), but to mimic corrosion products observed on in-service aluminum sheet corrosion in certain atmospheric environments, sulfur may need to be included in the accelerated test exposure.

The accelerated corrosion tests that show the greatest promise at mimicking in-service aluminum corrosion are ASTM G85–09 A2 and ASTM G85–09 A4. Both of the accelerated tests were acidified to a pH of 2.5–3.2. An acidic exposure environment appears to be a key parameter when trying to mimic in-service corrosion performance with an accelerated test. However, many of the industry accepted standards for accelerated corrosion tests of steel are run in neutral environments. Neutral environments evaluated in this program induced little or no corrosion on the painted aluminum panels. While the ASTM G85—Annex 2 does not include sulfur in the exposure, the acidic exposure provides the necessary environment to induce corrosion on aluminum that replicates the morphology of corrosion on the in-service panels. ASTM G85-09 A4 provides both the acidic exposure and the exposure to sulfur, but can be a difficult test to run due to the use of sulphur dioxide (SO_2) gas. Although attempts were made to modify both of these tests using sulfuric acid in the exposure, it was found that sulfuric acid in the exposure was not as effective at inducing corrosion on the painted aluminum panels as either acetic acid in ASTM G85–A2 or with the SO_2 in ASTM G85–A4.

Presentations/Publications/Patents

SAE 2002B-203
SAE 2003-01-1235
SAE 2005-01-0542
SAE 2006 Oral Only
SAE 2007-01-0417
SAE 2008-01-1156

References

1. F. S. Bovard, J. Tardiff, T. Jafolla, D. McCune et al., “Development of an Improved Test for Finished Aluminum Autobody Panels,” SAE Paper No. 2008-01-1156, SAE 2008, April 2008.

2. F. S. Bovard, J. Tardiff, T. Jafolla, D. McCune, et al., “Update on the Development of an Improved Test for Finished Aluminum Autobody Panels,” SAE Paper No. 2007-01-0417, SAE 2007, April 2007.

3. F. S. Bovard, J. Tardiff, T. Jafolla, D. McCune, et al., “Development of an Improved Test for Finished Aluminum Autobody Panels,” SAE Paper No. 2005-01-

0542, SAE 2005 Transactions Journal of Materials and Manufacturing, March 2005.

4. G. Courval, K. Smith, C. Meade, F. Lutze, et al., "Development of an Improved Test for Finished Aluminum Autobody Panels," SAE Paper No. 2003-01-1235, Proceedings of SAE World Congress, March 2003.
5. SAE J2334, "Cosmetic Corrosion Lab Test," Society of Automotive Engineers, Warrendale, PA, June 1998.
6. Lee, F., B. Pourdeyhimi, and K. Adamsons, "Analysis of Coatings Appearance and Surface Defects Using Digital Image Capture/Processing/Analysis," The International Symposium on a Systems Approach to Service Life Prediction of Organic Coatings, Breckenridge, CO, Sept. 14–19, 1997.
7. ASTM G85-09 98 Annex 2, "Cyclic Acidified Salt Fog Testing," Annual Book of ASTM Standards, Vol. 3.02, 2005.
8. ASTM G85-09 98 Annex 4, "Salt/SO2 Spray Fog Testing," Annual Book of ASTM Standards, Vol. 3.02, 2005.
9. E. L. Colvin et al., "Filiform Corrosion of Aluminum Auto Body Sheet in Accelerated and Outdoor Environments," SAE Paper No. 970735, Proceedings of SAE World Congress, Feb. 1997.
10. L. F. Vega et al. "Influence of Surface Treatments on Durability of Painted Aluminum Alloys," SAE Paper No. 970731, Proceedings of SAE World Congress, Feb. 1997.

3. AUTOMOTIVE METALS—CAST

A. Improved Automotive Suspension Components Cast with B206 Alloy

Principal Investigator: Richard Osborne
General Motors Corporation
30001 Van Dyke Ave., Warren, MI 48090
(586) 575-7039; fax: (586) 575-7039; e-mail: richard.osborne@gm.com

Technology Area Development Manager: Joseph A. Carpenter
(202) 586-1022; fax: (202) 586-1600; e-mail: joseph.carpenter@ee.doe.gov

Field Project Officer: Aaron D. Yocum
(304) 285-4852; fax: (304) 285-4403; e-mail: aaron.yocum@netl.doe.gov

Contractor: United States Automotive Materials Partnership (USAMP)
Contract No.: FC26-02OR22910 through the National Energy Technology Laboratory

Objective

- The objective of this program is to establish the commercial viability of B206 alloy for suspension components by providing needed fundamental information on this alloy system and by overcoming technical issues that limit the lightweighting applications of this alloy. The B206 alloy has the potential to provide near net-shaped castings with mechanical properties equivalent to forged aluminum suspension components and ferritic ductile iron.

Approach

- Four major technical focus points have been identified for this project. Accordingly, the work will be conducted in four separate phases:
    1. Determine the effect of alloy composition on mechanical properties in the T4 and T7 heat-treated conditions and establish the feasibility of using less-expensive versions of the alloy.
    2. Study heat treatment of B206 alloy and establish combinations of solution and aging time and temperatures which produce desirable strength with stress-corrosion immunity. This portion of work will also determine the feasibility of using improved T7 heat treatment cycles to increase elongation in this temper.
    3. Create cost models for automotive suspension components produced by different processes and different materials.
    4. Produce control-arm castings using two different casting processes. Test components produced in the T4 and T7 tempers, to provide required CAE and design information and establish the feasibility of using cast B206 alloy components to replaced forged aluminum parts.

Accomplishments

- The project was officially initiated October, 2005.
- Mr. Richard Osborne accepted project leadership responsibilities in November 2008 after Mr. Eric McCarty left Chrysler LLC. Efforts are on-going for the project to hire a new independent technical consultant (ITC) to assist in completing the project by December 31, 2009.
- Phases 1, 2, and 3 have been completed.

- Phase 4 is on-going with semi-permanent mold and ablation castings delivered the third quarter of 2008. Ballard Brass & Aluminum, Inc. produced semi-permanent mold castings, an economically favorable process that is typically used for the 206 alloy. Eck Industries/Alotech produced castings using the ablation process, a direct-chill process that is well suited to the B206 which responds better to fast solidification rates. Castings were delivered with optimum T4 and T7 chemistries and heat-treatment conditions. Comprehensive mechanical testing is planned for the second quarter of 2009.

PHASE 1:

Phase 1 is complete and consists of two separate studies. The first study was to identify the optimum chemistries for the T4 and T7 tempers, and the second study was to evaluate the effect of solidification rate on the properties of B206 in the T4 and T7 tempers.

Phase 1, Part 1:

A study of tensile properties versus alloy composition was conducted by researchers at Alcan International. These results show that best results for the T4 and T7 tempers are obtained with two separate alloy compositions. The two alloy compositions and expected properties are provided below (in wt %):

T4 Temper
The alloy contains 4.7 to 4.9% Cu, 0.35 % Mg, and 0.2 % Mn. The expected tensile properties are (Yield Strength [YS], ultimate tensile strength [UTS], elongation): 250–260 MPa, 430–450 MPa, and 18 to 22%.

T7 Temper
For a ductile T7 version, the alloy contains 4.2 to 4.4% Cu, 0.15% Mg, 0.2% Mn, 0.10% Fe, 0.10% Si. The expected average tensile properties would be (YS, UTS, elongation): 370–390 MPa, 445–455 MPa, and ~9% elongation.

In addition to the above results, a set of casting guidelines has been prepared for foundrymen who want to pour B206 alloy.

Phase 1, Part 2

A second stage of phase one casting trials was completed in September 2005 by Nemak researchers at their Central Development and Technology Center near Monterrey, Mexico. Several different alloy compositions were prepared and ‘wedge’ castings were made. The ‘wedge’ castings were poured to establish the tensile properties of the alloy as the solidification rate varied from 30 seconds to 30 minutes. In addition, hot-crack test castings were poured to determine the effect of alloy composition on castability.

PHASE 2

Phase 2 was conducted at the University of Windsor under the direction of Prof. Jerry Sokolowski. Alcan International also assisted this phase of the project by providing additional testing. A survey study of the aging of B206 alloy was completed. Samples were aged at temperatures between 125 and 225°C for times ranging from two to forty eight hours. The hardness and electrical conductivity were measured, and the samples were subjected to a corrosive medium to establish their vulnerability to intergranular attack. A report of these experiments was issued in October 2005. Additional studies were conducted to establish the kinetics of the solution heat-treatment process. Attempts to develop an alternative T7 aging process to increase elongation in that temper were mostly unsuccessful.

PHASE 3

Phase 3 has been completed. A cost model was developed by A. Edmund. P. E. Herman, of Creative Concepts Company, Inc. in March 2006. A Microsoft Excel spreadsheet was developed which can be used to compare costs of producing castings using A356-T6, B206-T4 and B206-T7 alloys.

PHASE 4

Phase 4 is in progress. The intent of Phase 4 was to produce and test B206 castings using green sand Hayes Lemmerz and precision sand at Nemak Mercury Castings was added in September 2005 to produce castings using their Slurry-on-Demand process.

Hayes Lemmerz

The design work for the castings was completed in April 2006. However, Hayes Lemmerz closed their Ferndale, Michigan facility and discontinued their involvement in the program before castings could be made.

Mercury Castings

Mercury Marine attempted to make semi-solid castings but was unable to produce acceptable quality castings. No further work with Mercury Marine is planned.

Nemak

The gating system design concepts proposed by Dr. Tiryakioğlu and Prof. John Campbell were adopted by Nemak, and the final gating system design, as shown in Figure 1, was developed with the assistance of Prof. Campbell. Mold-filling simulations using Magma software showed significant improvement over previous designs.

Figure 1. The gating and feeding system design used by Nemak.

Initial trial castings poured at Nemak with complete sand cope and drag showed extensive porosity and metal-mold reaction problems. Consequently, the mechanical properties, especially elongation, and surface finish of castings did not meet expectations (YS = 270 MPa, UTS=310 MPa, el = 10%). Based on Phase 1 results, the project team concluded that the slow solidification rate in the full sand mold was the primary reason why the castings did not achieve the desired properties.

To increase the solidification rate, Nemak machined an aluminum drag, poured 30 castings and heat treated castings in the T4 and T7 tempers. The results were encouraging but neither temper fully achieved the targeted mechanical properties. The T4 temper missed the target yield stress by 5%. The T7 temper greatly exceeded the UTS and YS targets but failed to achieve the targeted 10% elongation. Unfortunately, due to business conditions, Nemak had to withdraw from the program. Nemak delivered the metal drag and sand cope to Chrysler in the event that another supplier may be able to cast the parts.

Ballard Brass & Aluminum, Inc.

Ballard was selected to produce 50 castings using an optimized semi-permanent mold process. Castings have been produced using both T4/T7 chemistry and each group heat treated to the T4/T7 condition, respectively. Finished castings have been delivered to Chrysler and are being inspected and processed for material property testing.

Eck Industries/Alotech

Eck Industries and Alotech produced 50 castings, 25 of the T4 temper and 25 of the T7 temper, with the ablation casting process, which generates high cooling rates and low levels of porosity. Castings were poured and delivered in July 2008 using the same T4 and T7 chemistries and heat-treat schedules as the semi-permanent mold castings. Preliminary tensile results from specimens excised from castings heat treated to the T7 condition are promising and shown in Table 1.

Table 1. Preliminary tensile results for samples excised from semi-permanent mold and ablation castings in the T7 heat treatment condition

Preliminary Av. Tensile Properties, B206-T7

Casting	YS (MPa)	UTS (MPa)	Elong. (%)
Semi-Perm. Mold, n=4	289	360	11.0
Ablation, n=10	309	374	9.5
Min. Req.	270	310	10.0

Component Testing

- Semi-permanent mold and ablation castings are being delivered to both General Motors and Westmoreland Mechanical Testing and Research. General Motors will conduct bench durability testing in accordance with forged 6061-T6 control-arm components. Westmoreland will complete tensile, compression, fracture toughness and corrosion testing from samples excised from both processes and heat treatment tempers.
- In addition to component and material testing, a select group of cast control arms will be subjected to load-deformation failure testing to determine whether any casting structural defects exist and can be avoided with better melt quality and improved mold filling system design. A full project report will be available in December 2009.

Future Direction

- The project team believes that it is possible to achieve the targeted properties and is currently investigating a lean chemistry to boost the T4 yield and direct cooling (ablation) or heat-treat optimization to improve the T7 elongation. The two casting processes selected for the production of the control arm castings, semi-permanent mold and ablation are expected to meet the target mechanical properties. The project will be completed in December 2009.

Aluminum B206 Cast Component Rationale

The 206 alloy is significantly stronger than the 356 alloy and has mechanical properties approaching some grades of ductile iron. It also has excellent high-temperature tensile and low-cycle fatigue strength. Consequently, this material could be used in a number of applications to reduce vehicle weight. Cost savings may also result, because less material would be required to provide the strength needed for the application. In spite of its excellent properties, however, 206 alloy is seldom used because of its propensity for hot cracking. GKS Engineering has discovered a better method to grain refine this alloy, which reduces the tendency for hot cracking. This material has a number of potential applications, but its high strength and excellent ductility make it an ideal candidate for suspension components. Consequently, in the first stage of work (Project AMD305—completed in May 2002) control arms were produced via a tilt-pour/permanent-mold

casting process to establish the viability of this material for these safety critical components. The work completed under AMD305 showed that extremely high mechanical properties can be obtained. The tensile properties of permanent-mold B206 alloy control arms were nearly the same as (or slightly better than) those found with many forged aluminum components, and the low-cycle fatigue life of B206 alloy is ten times that of A356 alloy castings for an equivalent stress level. AMD305 also showed that the permanent-mold casting process, although suitable, may not be the best manufacturing process for 206 alloy. Traditional sand-casting and composite casting methods (such as Nemak´s semi-permanent mold precision sand casting process) are more forgiving of hot cracking. The additional work proposed in this project will examine the technical feasibility of producing B206 alloy suspension components in three other casting processes. Other important technical and commercial issues related to B206 will also be addressed. The object is to provide the technical and economic data needed to justify commercial use of this material in suspension components.

Justification

Automakers are under increased pressure to reduce CO_2 emissions and improve fuel economy through increased CAFE standards. Because of its higher strength, B206 alloy structures have the potential to reduce vehicle mass, which is directly linked to improved CAFE and vehicle performance. There is also a potential for cost savings, because less material would be required when compared to conventional aluminum castings.

Program and Deliverables

This project was initially planned to be completed in 30 months and proceeded in four stages. Below is a description of the deliverables for each of the four phases of the project.

Phase 1

The main alloying elements in 206 alloy (Cu, Mg, Mn) will be varied in a series of statistically-designed experiments. Test bars will be cast at each composition and heat treated to the T4 and T7 tempers. Hot-crack test castings will be made to study the effect of alloy composition on castability, and 'wedge' castings will also be poured to determine the effect of solidification rate on tensile properties. These tests will determine the effect of alloy composition on mechanical properties and castability, and will allow design and casting engineers to better tailor mechanical properties for any specific application. The minor impurity elements (Fe and Si) will also be varied to determine the effect of these elements on mechanical properties. It appears that the maximum limits for Fe and Si, presently listed in the AA specifications for the 206 alloys, are lower than necessary for most automotive applications. Increasing these limits by a modest amount would reduce the cost of the alloy. These tests will be conducted at the Research and Development Center of Alcan International, and at Nemak.

Phase 2

Parts made in 206 alloy are immune to stress corrosion in the T4 and T7 tempers. Parts that have been aged to peak strength (T6), however, are susceptible. Published information on other Al-Cu-Mg alloys suggests that relatively short aging times may induce stress corrosion, and that the susceptibility to stress corrosion may occur before any change in hardness is found. For example, the temperatures and times used in powder coating may cause a problem. This part of the study will map out the dangerous areas which must be avoided. It will also examine alternative T7 treatments to see if there is a way to improve material properties (especially elongation) in this temper. The use of alternative methods to test for stress-corrosion resistance will also be evaluated. The standard test is cumbersome and takes 30 days to complete. A simpler, more rapid, test is desirable. This phase of work will be carried out at the University of Windsor in Windsor, Ontario and at Westmoreland Mechanical Testing Laboratories. Additional support will be provided by the laboratories of Alcan International.

Phase 3

A cost model will be constructed for suspension components manufactured using different processes and materials. A General Motors FLCA forged in 6xxx alloy will serve as a mule for this

economic study. The following component cases will be considered:

–forged 6xxx alloy
–sand-cast B206 alloy
–semi-permanent mold cast B206 alloy
–permanent mold cast A356 alloy

Creative Concepts will assist the project group in formulation of the cost models in this portion of the study. Sync Optima will also do FEM studies of the different cases, to determine changes required in the design (and weight) of the control arm as the material is changed from the base condition (forged 6xxx alloy).

Phase 4

In this final stage of work, control arm 'Mule' castings will be manufactured by the composite precision sand casting process at Nemak. Semi-solid cast parts will also be made at Mercury Castings.

In AMD305 parts were made and heat treated to the T4 temper. In this new work, additional castings will be made and tested in both the T4 and T7 tempers. In this way, a complete set of mechanical property data will be obtained for the castings. For this portion of the project, the compositions used to produce castings will be the optimum alloy compositions mapped out in phase 1 of the project.

Westmoreland Mechanical Testing and Research will do testing of castings made in this phase of work.

Measurable Success Indicators

The successful results desired from each of the four phases of work are outlined below:

Phase 1

Mechanical properties as a function of cast material composition will be provided, allowing automotive design engineers to optimize component properties at lowest possible cost. Information will be provided, which may allow us to increase upper limits for dissolved Si and Fe, and reduce costs in 206 alloy.

Phase 2

Optimum heat treatment schedules, which avoid stress-corrosion problems, will be established and recommended. Simple and rapid tests for stress corrosion susceptibility will also be evaluated.

Phase 3

Cost models will be provided for the production of suspension components using several manufacturing processes and different materials. This model will assist automotive design engineers to optimize component performance, and at the same time to help realize production cost savings.

Phase 4

Control-arm castings will be produced using two different casting processes, and a complete battery of material property tests of the components will provide the technical database needed to design, manufacture and use suspension components cast in B206 alloy.

Technical Results

The results of the phase 1 casting trials have been used to map out the range of mechanical properties that can be obtained from B206 alloy castings. For permanent-mold test bars, which have a relatively rapid solidification rate (20–30 seconds), the tensile properties found in the T4 temper are shown in Figure 2. The irregular polygon in these figures indicates the variation of tensile properties UTS, YS in MPa, and elongation) that one may expect as the composition is varied between the upper and lower limits for this alloy in the Aluminum Association specifications. The amounts of Cu, Mg, Mn, Fe, and Si in the alloy were all allowed to vary. The corresponding range of mechanical properties available in the T7 temper is indicated below in Figure 3.

In addition to the above results, two of the Alcan alloy compositions were poured into an end-chill mold. Tensile samples were cut at three distances from the chill (ranging from 12.5 to 50 mm (½ to 2 in.). The tensile properties obtained from these castings are shown Figure 4, together with data published for the more commonly used aluminum casting alloys.

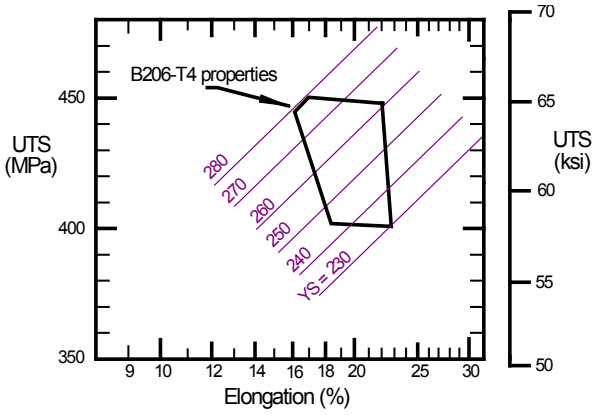

Figure 2. B206-T4 tensile properties.

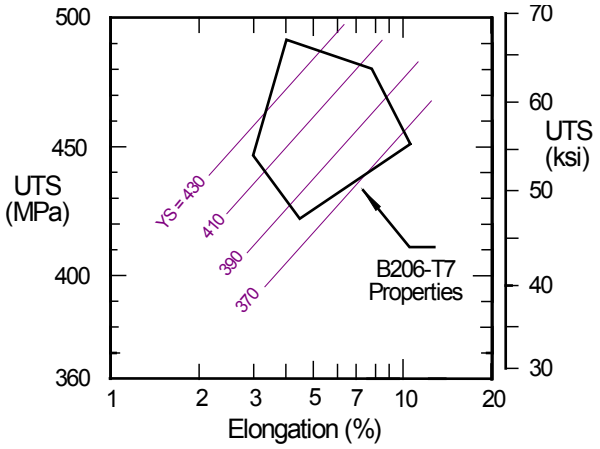

Figure 3. B206-T7 tensile properties.

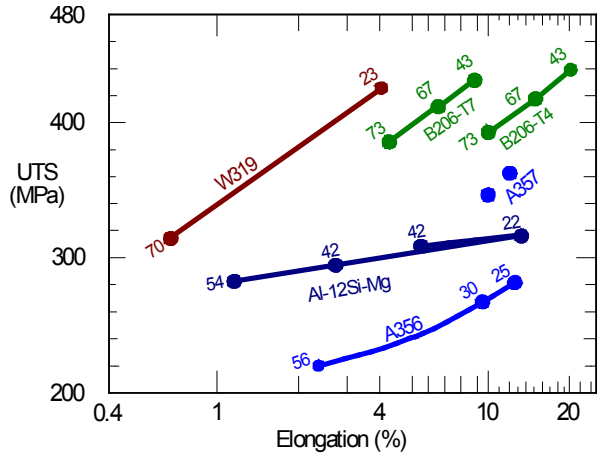

Figure 4. Range of mechanical properties in five aluminum casting alloys.

The solidification time is indicated in this figure by numerical values for the secondary dendrite arm spacing (SDAS), or the cell size in the case of B206 alloy. (The data for A357 alloys are for heavily chilled sections of aerospace castings only.) It can be seen that B206 alloy exhibits mechanical properties superior to the conventional Al-Si-Mg and Al-Si-Cu casting alloys.

A number of B206 alloy samples were aged and tested for intergranular attack by corrosion. A test procedure outlined in Mil Spec MIL-H-6088 and ASTM specification G110 was used. This procedure correlated well with the results of a standard alternate immersion test in 201 alloy,* and so it was adapted for use in phase 2 of this study. The average depth of the intergranular attack by corrosion (in microns) is plotted in Figure 5, as a function of aging time and aging temperature. In Figure 5, the safe aging conditions are indicated by the hatched areas. (These areas indicate aged samples where the average intergranular corrosion depth was less than 20 μm deep.) The areas of worst corrosion attack are 'in between' the safe areas, at aging temperatures between 100 and 180°C.

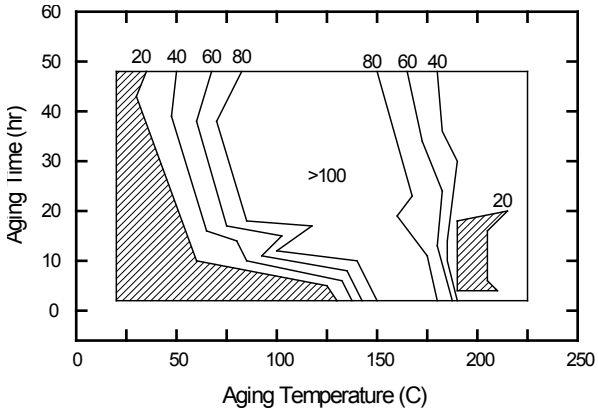

Figure 5. Average Depth of Corrosion.

In Phase 2 of our program, immersion stress-corrosion tests were conducted in accordance with ASTM G47-98 standard. Specimens were all naturally aged for 3 days and artificially aged for different durations at temperatures between 100 and 225°C. The stress-corrosion cracking (SCC) life contour plot is provided in Figure 6 as a function of artificial aging temperature (T) and time. The worst stress-corrosion life occurred between 100 and 175°C, which is consistent with intergranular corrosion results outlined in

*M. S. Misra and K. J. Oswalt: "Corrosion Behavior of Al-Cu-Ag (201) Alloy," *Metals Engineering Quarterly*, **16**, pp. 39–44 (1976).

Figure 6. More analysis will be conducted for possible correlation between the results from the two test methods.

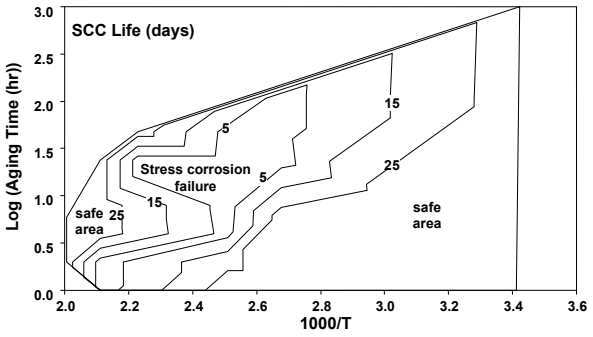

Figure 6. Stress-corrosion cracking life contours as a function of artificial aging time and temperature.

Contour plots of tensile properties after artificial aging at temperatures between 100 and 225°C for various durations are presented in Figure 7. Highest UTS and elongation are obtained at an artificial aging for 12–24 hours at 125°C. A small set of experiments are planned at Alcan Laboratories to obtain more detailed results.

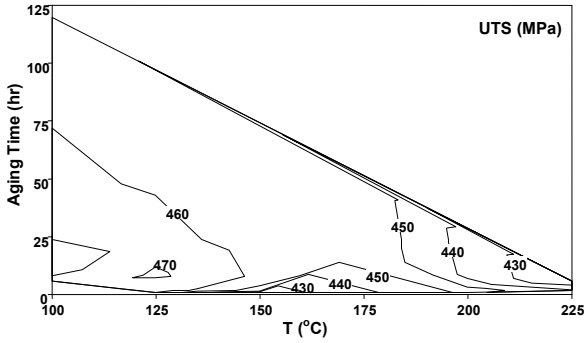

(a)

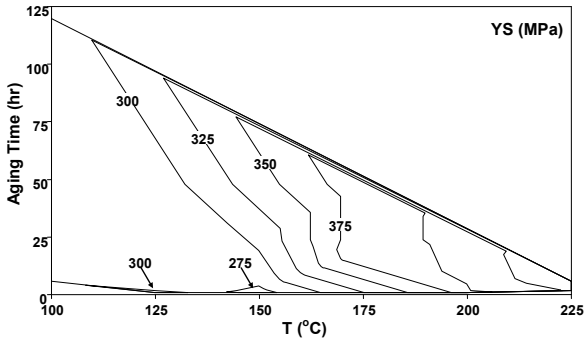

(b)

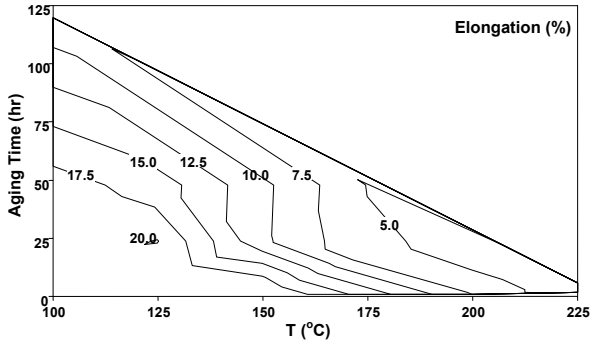

(c)

Figure 7. Contour plots for (a) ultimate tensile strength, (b) yield strength, and (c) elongation as a function of artificial aging time and temperature.

Two castings produced by the semi-permanent mold process (with an aluminum drag) at Nemak were tested by excising tensile coupons from three locations in each casting. The tensile properties are summarized in Figure 8. The desired level of each property is indicated by a dashed line.

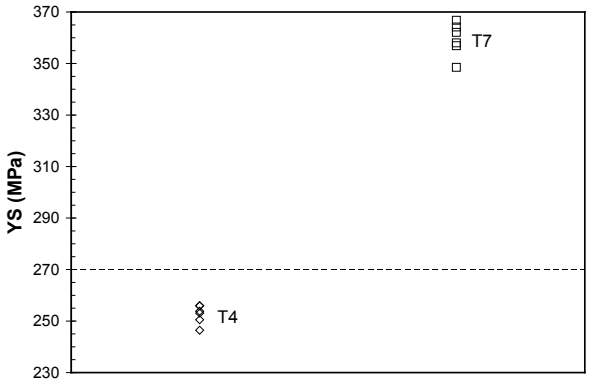

(a)

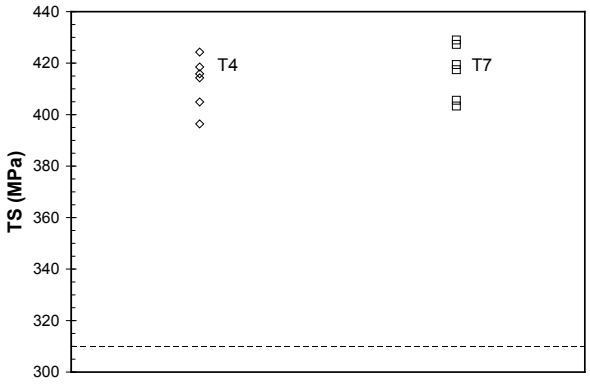

(b)

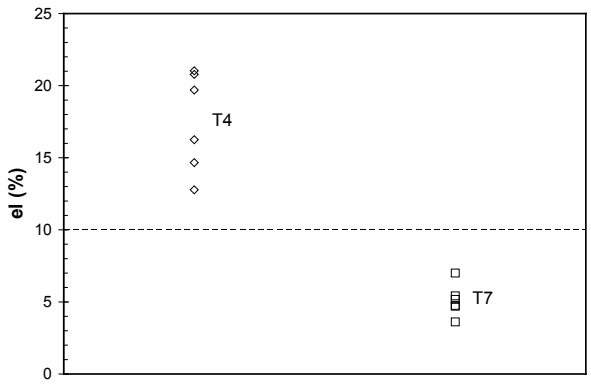

(c)

Figure 8. The tensile properties of semi-permanent mold castings in T4 and T7 tempers produced by Nemak.

Note that the yield strength for T4 and the elongation for T7 tempers are barely below the desired levels. It is the believed by the entire project group that these properties can exceed the desired levels by the optimization of the heat treatment process.

Presentations and Publications

The results from this project so far have generated two presentations and papers:

1. G. K. Sigworth and J. F. Major. "Factors Influencing the Mechanical Properties of B206 Alloy Castings," Light Metals 2006, pp. 795–799, 2006 (presented at 2006 TMS Annual Meeting).
2. J. F. Major and G. K. Sigworth, "Chemistry/Property Relationships in AA 206 Alloys," paper 06-029, AFS Transactions (presented at 2006 AFS Congress).

B. Magnesium Powertrain Cast Components (AMD304*)

Principal Investigator: Bob R. Powell
General Motors Research & Development Center
30500 Mound Road, Mail Code 480-106-212
Warren, MI 48090-9055
(586) 986-1293; fax: (586) 986-3091; e-mail: bob.r.powell@gm.com

Technology Area Development Manager: Joseph A. Carpenter
(202) 586-1022; fax: (202) 586-1600; e-mail: joseph.carpenter@ee.doe.gov

Field Project Officer: Aaron D. Yocum
(304) 285-4852; fax: (304) 285-4403; e-mail: aaron.yocum@netl.doe.gov

Contractor: United States Automotive Materials Partnership (USAMP)
Contract No.: FC26-02OR22910 through the DOE National Energy Technology Laboratory

Objective

- Demonstrate and enhance the feasibility and benefits of using magnesium alloys in place of aluminum in structural powertrain components, and achieve at least 15% mass reduction of the cast components.
- Note: the final engine achieved a cast component mass reduction of nearly twice the original target, 28%.

Approach

- Identify, benchmark, and develop a design database of the potentially cost-effective, high-temperature magnesium alloys and, using this cast-specimen database, select the alloys that are most suitable for the magnesium components. (Task 1)
- Design, using finite-element analysis (FEA), an ultra-low-mass engine containing potentially four magnesium components (cylinder block, bedplate, structural oil pan, and front engine cover) using the most suitable low-cost, recyclable, creep- and corrosion-resistant magnesium alloys. (Task 2)
- Create a cost model to evaluate alloy, manufacturing, and technology costs to predict the cost-effective performance of the engine. (Task 2)
- During the execution of Tasks 1 and 2, identify and prioritize the critical gaps in the fundamental science of magnesium alloys and their processing that are barriers either to the progress of the project or to the use of magnesium in future powertrain applications. Seed-fund the most critical research, and promote additional identified needs to support further development of the magnesium scientific infrastructure in North America, thereby enabling more advanced powertrain applications of magnesium. This will be one aspect of the technology transfer deliverables of the Magnesium Powertrain Cast Components (MPCC) Project. (Task 3)
- Note: before addressing Tasks 4–6 and funding Task 3 research, an in-depth review of the engine design, including performance and durability predictions, alloy requirements and measured alloy properties, cost model, and predicted mass reduction will be conducted. Passing this gate review is necessary for entry into the second-half of the project, which has the goal of demonstrating/validating the engine design with respect to castability, manufacturability, performance, durability, and cost.

*Denotes project 304 of the Automotive Materials Division of the United States Automotive Materials Partnership, one of the formal consortia of the United States Council for Automotive Research set up by Chrysler, Ford, and General Motors to conduct joint, precompetitive research and development (see www.uscar.org).

- Refine the engine component designs as necessary (updating to match the properties of the alloy selected for each component), design and build tools and patterns, and cast the engine components. (Task 4)
- Excise specimens from the cast components and develop a full mechanical and corrosion design database for the alloys. Create an original equipment manufacturer (OEM)—common material specification for magnesium powertrain alloys. (Task 5)
- Assemble complete engines, dynamometer-test the components, and conduct end-of-test teardowns. Refine the cost model to support determining the cost-effective performance of the engine. (Task 6)

Accomplishments

- In the fiscal years (FYs) 2001 to 2007, Tasks 1 through 4 were completed. At the Phase II gate review it was announced that the achieved mass reduction for the magnesium components was 28 percent, nearly twice that of the original target. Alloys were selected for each magnesium engine component; component designs were revised accordingly; casting tooling was designed and built; and all four magnesium components were cast, machined, and delivered for component and engine testing. The five basic research projects in support of the objectives of Task 3 were also completed.

FY 2008 Accomplishments:

- Passed pulsator testing of the head gasket which had been designed by Dana Victor Reinz Corp. specifically for the requirements of the MPCC magnesium cylinder block and aluminum cylinder heads. The head gaskets and the rest of the bill of materials for engine assembly were delivered to Roush Industries and several test engines were assembled.
- Completed and passed bench-top Thermtronic testing of the cylinder block: thermal cycling and thermal soak.
- Completed calibration of the engine dynamometer and demonstrated with the successful operation of an aluminum production Duratec engine. Passing this test was an essential requirement for starting magnesium engine testing.
- Completed and passed the Hot Scuff Engine Test, which is a measure of piston/ring/bore design compatibility as well as the adhesion and durability of the thermal sprayed, wear-resistant coating that was applied to the cylinder bores in lieu of cast-in-place or pressed-in-place liners.
- Completed and passed the Cold Scuff Engine Test, which is a much more severe test of the bore coating adhesion and wear resistance. It a very critical and difficult test to pass. Hot and Cold Scuff Engine Tests are gateway tests to engine durability testing.
- Initiated the Deep Thermal Shock Engine Test. However, during break-in operation of the engine, bulkhead numbers 2 and 3 broke and cracks were detected propagating across the remaining bulkheads (1 and 4). Testing was stopped and root cause analysis was conducted. The apparent cause of failure was identified and finite element analysis was initiated to demonstrate the ability to predict the failure.
- Completed High Speed Durability Engine Test of an aluminum block with magnesium oil pan and front cover and demonstrated durability of these two components.
- Completed a Coolant Corrosion Engine Test of the complete MPCC magnesium-intensive engine. Run at low load to protect the bulkheads, this 672-hour test (based on a Ford industry standard) provides a good measure of the effectiveness of the Honeywell coolant, which contained an additive to protect the magnesium. Analysis of the coolant samples and teardown analysis of the engine are ongoing.
- Completed tensile testing of specimens excised from each of the four cast components (cylinder block, oil pan, front engine cover, and rear seal carrier). The results compared favorably with the results of the cast specimens tested in Phase 1 of the Project. The results were placed in the Lightweighting Materials electronic database.
- Completed cost analysis of the magnesium-intensive engine. This involved putting manufacturing and economic data into the cost model for each magnesium part (cylinder block, oil pan, and front engine cover). This yielded the cost per pound (or kg) saved and the identification of the major cost contributors. In general, the mass reduction was cost effective, relative to the cost of gasoline; $3.89 per pound of mass reduced vs a

current gasoline price of nearly $4.00 per gallon. The original target of $2.00 per pound mass reduced was not achieved, primarily due to increases in the cost of magnesium ingot from approximately $1.30 to $1.92 per pound between 2003 and 2008.

- The patent application for the structural details of the magnesium cylinder block was accepted and US Patent No. 7,284,528 was issued on October 23, 2007. The rights of the patent were assigned to USAMP.

Future Direction

- Complete the FEA analysis of the bulkhead failures in the Deep Thermal Shock Engine Test.
- Complete teardown and analysis of the Coolant Corrosion engine.
- Complete the final report for the Magnesium Powertrain Cast Components Project by March 31, 2009.

Introduction

The MPCC project team's vision is of a magnesium-intensive engine that is cost-effective, lightweight, and meets the manufacturability and durability requirements of the automotive industry. The approach taken was the redesign of an aluminum production engine (2.5L Ford Duratec) to a magnesium-intensive version; that is, to convert the cylinder block, bedplate, oil pan, and front engine cover to magnesium. All other parts of the engine were production carryover. The design, materials testing, tooling design, and casting of the parts were accomplished in prior years. Summaries can be found in previous progress reports. In 2008 component and engine testing was completed and is summarized in this, the FY 2008 Progress Report. The original aluminum block and MPCC magnesium blocks are shown in Figures 1 and 2, respectively. An assembled MPCC engine with its magnesium front cover and oil pan are shown in Figure 3.

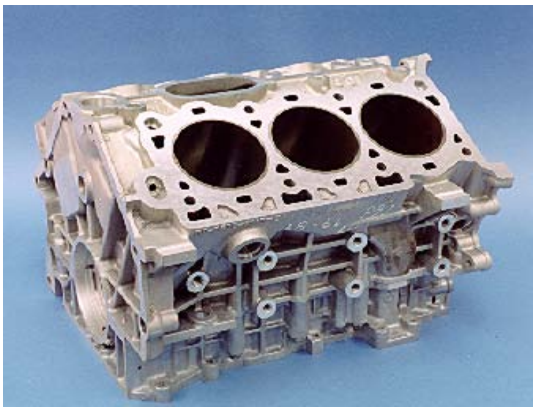

Figure 1. Aluminum production V6 cylinder block and bedplate.

Figure 2. MPCC magnesium cylinder block.

Figure 3. MPCC magnesium-intensive engine with valve covers removed.

Though initially intended to contain a magnesium bedplate, the final design became that of a deep skirt block without a bedplate, which necessitated also adding a magnesium rear seal carrier to the design.

All component testing and Hot Scuff and Cold Scuff engine dynamometer testing was completed in 2008. However, the original engine durability

test plan was changed because of a bulkhead failure that occurred in the first of the durability tests. Root cause analysis of the failed block was completed. Based on the results, the MPCC team revised the engine test program and two durability tests were completed; a 675-hour High Speed Durability test of the magnesium front cover and oil pan, which were mounted on the aluminum cylinder block and a 672-hour Coolant Corrosion test, which was run at low load to protect the bulkheads. A summary of the results of the completed component and engine testing is provided. Tensile test results for specimens excised from the cast magnesium components are also presented. Finally, a summary of the cost model application is presented. The MPCC project team is completing the final report and will complete the project in early 2009.

Head Gasket Design and Pulsator Testing

Many parts for the magnesium-intensive engine were carry-over from the production aluminum Duratec. This was not possible for the head gaskets. Differences in material properties of magnesium relative to aluminum (modulus, yield strength, coefficient of thermal expansion) required a new design. The Dana Victor Reinz Corporation designed a 4-layer, selectively-coated 301 stainless steel gaskets, based on Dana's Wave-Stopper Technology. A schematic is shown in Figure 4.

Figure 4. A schematic of the Dana Victor Reinz-MPCC head gasket cross section.

Sealing was assessed at 100% bolt load and 70% bolt load, the latter load case being done to anticipate the effect of possible bolt load loss due to magnesium creep and/or gasket relaxation. FEA predicted acceptable performance of the gasket, but pulsator testing was required to confirm this. Deep thermal shock testing was also done before releasing the gaskets for the magnesium-intensive engine. Testing was done on a magnesium block with an aluminum head and the test gasket between. Pulsator testing comprised 10,000,000 cycles to 70 bars. Thermal shock testing comprised subjecting the block to 278 cycles from –18 to 115^{o}C. The head gaskets passed both tests; e.g., there was no loss of coating, sealing stress transfer was as predicted, and there were no signs of leakage or Brinelling into the deck face of the cylinder block.

Cylinder Block Component Testing

The objective was to determine effects of thermal cycling and thermal soak on cylinder bore and crank bore distortion due to permanent growth of the magnesium alloy. The magnesium alloy used for the MPCC cylinder block is AMT-SC1, which requires heat treatment. Testing was required to determine if the high engine operating temperatures would further "heat treat" the alloy and cause permanent growth (expansion) of the cylinder block. We were also interested in critical fastener clamp load retention, specifically the head bolts and the bulkhead bolts. Detroit Testing Laboratory conducted the testing. A block configured for testing is shown in Figure 5.

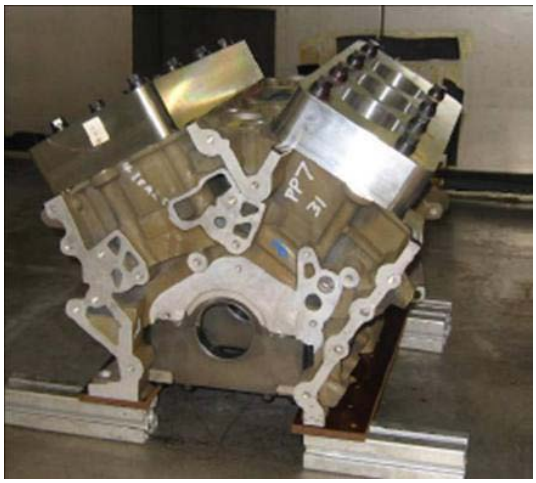

Figure 5. Magnesium block assembled for thermal testing.

Thermal Cycling

The block was cycled from -40^{o}C to 150^{o}C for 100 cycles. Cylindricity (bore out-of-roundness) increased slightly, but less than is typical of production aluminum blocks with iron liners. There was head bolt clamp load loss, but also within acceptable ranges.

100-Hour Thermal Soak

A second magnesium block was held for 100 hours at 150°C. Initial measurements suggest no growth, but the complete set of measurements is in progress.

Engine Testing—Hot and Cold Scuff

The MPCC magnesium-intensive engine used thermal-sprayed cylinder bores in place of iron or aluminum liners. There were several reasons for this: avoidance of the extra mass of the liner, minimizing bore distortion (cylindricity) by strengthening and stiffening the bore walls, and simplifying head gasket design. This significant change to the magnesium engine required that scuff testing be done to determine the fit and compatibility of the pistons and rings with the new bore, and to ensure that bore wear and coating adhesion were acceptable. Scuff testing was conducted at Roush Industries on fully assembled magnesium-intensive engines.

Hot Scuff Engine Test

This test consisted of running the Ford test protocol, high engine rpm for thirty minutes. Subsequently the engine was disassembled and the bores, pistons, and rings inspected for wear. Inspection confirmed normal wear of the bore coating and normal wear of the piston skirt (see Figure 6).

Figure 6. Post-hot scuff tested piston showing acceptable wear of the piston skirt coating.

Cold Scuff Engine Test

This test required 120 cycles of sub-zero cold starts at light load and low engine speed. It simulates low lubrication conditions because the oil has drained from the bore surface and is cold enough to take time to recoat the surface. This is generally a very demanding test and failure would be an indicator of future problems on the engine durability tests planned for the magnesium-intensive engines.

Both the pistons and bores looked excellent at the end of test. There was no scuffing of the rings or pistons, or in the bores. A ring tip scratch occurred in one bore, but this was not indicative of scuff, and is not unusual in engine testing. A typical bore after cold scuff testing is shown in Figure 7.

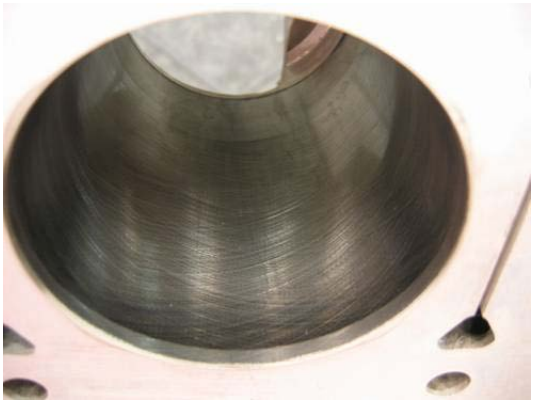

Figure 7. Cylinder bore at end of cold scuff test. Honing marks are evident.

Deep Thermal Shock Test—Bulkhead Failure and Root Cause Analysis

The Deep Thermal Shock Test (DTS) was to have been the first of four durability tests for the magnesium-intensive engine. However, during break-in runs the behavior of the engine showed higher blow-by than the production engine and leakage past the crank seals and the oil fill cap. Subsequently, the engine oil pressure dropped and the engine began making bottom-end noises. Inspection revealed complete failure of the two interior bulkheads, numbers 2 and 3, and cracks propagated partially across bulkheads 1 and 4 (see Figure 8).

An intensive root cause analysis was launched by the MPCC project team. It included both failure analysis of the engine and a reevaluation of the FEA work done during engine design. Results point to the interface between the cast iron inserts

and the magnesium bulkheads which were cast around them. FEA modeling is being done to include this possibility in the safety factor predictions. If confirmed, then preventing this failure mode should be possible in future engine designs.

Figure 8. Fracture of DTS engine bulkhead 3.

Anticipating the correctness of root cause analysis, the MPCC project team changed the engine durability test plan. Two engines durability tests were adopted and completed: a 675-hour High Speed Durability Test and a 672-hour Coolant Corrosion Test.

675-Hour High Speed Durability Test

Because the root cause analysis of the DTS engine test failure did not indicate a method to prevent bulkhead failure in the already-cast cylinder blocks, the magnesium front cover and oil pan were mounted on a production aluminum engine in place of the aluminum cover and pan. Then the intended High Speed Durability Test was run.

The 675-hour test consisted of 75 cycles through over 200 power/torque conditions and a 1-hour soak. Checks of all fasteners, including RIBE's Aluform aluminum fasteners which were used on the front cover and oil pan, were performed every nine hours. At the end of test, break-away toques for all bolts were measured and parts were inspected for signs of damage, including corrosion. Standard coolant (no protective additive) was used for this test.

The front cover bolts went the full 675 hours and showed no loosening during testing; neither the RIBE bolts nor the carry-over production bolts. The oil pan developed a small leak during testing, which was determined to be due to a casting defect, either a hot crack or hot tear. It was repaired with epoxy and the pan completed the test without further incident. No evidence of corrosion was seen on either the cover or the oil pan.

During the test, an assessment of the noise level of the engine was made. It was concluded that there was no evidence of unusual noise or vibration due to the magnesium parts. It was recommended that more systematic testing be done to quantify this promising result.

672-Hour Coolant Corrosion Test

An important objective of this project was to determine the corrosion behavior of the magnesium cylinder block in the presence of ethylene glycol water-based coolant. Extensive bench testing was done of all considered magnesium alloys in the earlier phase of the Project. After testing, the Honeywell experimental coolant was selected for the engine dynamometer coolant.

Because the intended durability testing could not be done, the team chose to do a different durability test which was based on the Ford BL 102-02 standard for screening coolant behavior. The major change to the test protocol was to run the engine at low load, low enough to protect the bulkheads but high enough to achieve the necessary coolant temperatures to effectively test the coolant/component interfaces. The engine was run at 2,000 rpm at 50 kN with periodic high and low temperature soaks.

Testing went well and no issues were reported. Coolant samples were drawn before and after the test and at 96-hour intervals. Analysis is ongoing and the results are promising.

Tensile Testing of Excised Specimens

In Phase 1 of the MPCC Project, an extensive mechanical and thermo-physical property database was created of the several die-casting and sand-casting magnesium alloys considered by the

project team. Test specimens were cast to size. In Phase II, having cast the magnesium components for engine testing, specimens were excised from these components and tensile tested at room temperature and at 150°C. A comparison of these results with those of cast specimens will be helpful to design engineers using the database. This work has been completed. All mechanical testing was done at Westmoreland Mechanical Testing & Research. Figure 9 shows an example of locations from which specimens were excised from the structural oil pan. Specimens were excised from the sand-cast cylinder block, the high-pressure die-cast front cover, and the thixomolded rear seal carrier.

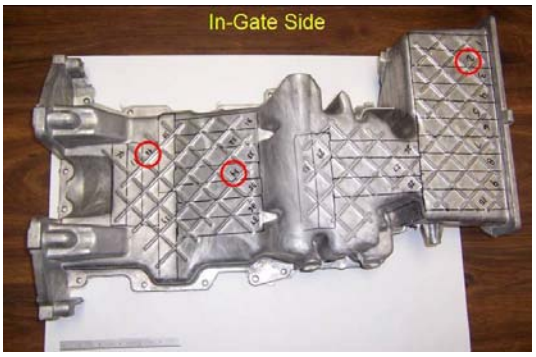

Figure 9. Structural oil pan showing locations of excised specimens.

Comparison of the tensile properties of the cast specimens and the excised specimens showed them to be in relatively close agreement, which suggested that it was possible to obtain good materials properties even in complex castings. Although, it should be noted that extensive effort was made by the team members to make good castings for component and engine testing. In addition, excised specimens were X-rayed and screened at ASTM E505 Level 1 quality at Chrysler.

The North American Die Casting Association (NADCA) invited the MPCC project team to include a summary of the tensile test results in the next edition of the NADCA Product Specification Standards for Die Castings. The data were provided and will be available to the public in 2009.

Determination of Cost-Effective Mass Reduction

A final criterion for a cost-effective, magnesium-intensive engine is that it indeed be cost effective. In Phase 1 of the MPCC Project, technical cost models were created for both the sand-cast and high-pressure die-cast magnesium components. In Phase 2 of the Project, we revisited the technical cost models, revised as necessary, and populated the models with "manufacturing" data collected during the casting trials and obtained calculated costs per unit of mass reduction and breakdowns of the various factors contributing to the overall cost of the components.

Figure 10 shows the calculated cost breakdown for the manufacturing costs of the structural oil pan. It compares the costs of the production aluminum pan with those of the magnesium pan. The terms "old" and "new" in the figure indicate the results of the Phase 1 and Phase 2 calculations, respectively. The Phase 2 calculations reflect the actual manufacturing data that were not available for Phase 1. It also reflects the recent "short term" increase in the cost of magnesium ingot.

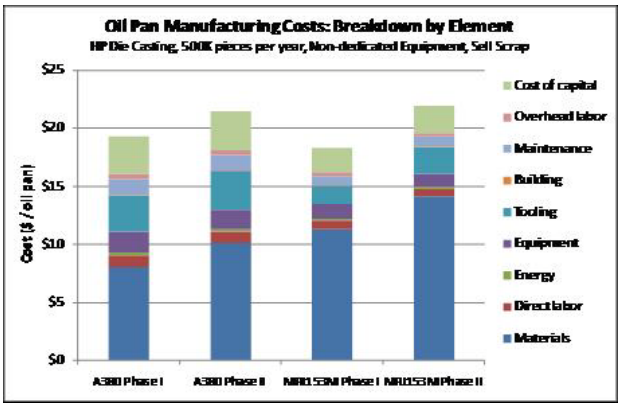

Figure 10. Cost elements in the manufacturing of the structural oil pan.

The overall results indicate that when the models were run using the current magnesium prices, the cost of 28% mass reduction for the engine with the components converted from aluminum to magnesium was less than $4 per pound, approximately that of the then-current price of gasoline in dollars per gallon. Most of the cost was attributable to the cost of the cylinder block. The costs of mass reduction of the oil pan and front

engine cover were essentially zero. Nevertheless, the primary cost contributor for all of the magnesium components was the cost of magnesium ingot, which increased 50% between 2003 and 2008, from an estimated $1.30 to $1.92.

Conclusions

In 2008, we were able to physically test major magnesium engine components based on the excellent progress the MPCC project has made since its inception in 2001. The significant challenge for the Mg-intensive engine has been identified as designing around the thermal expansion coefficient of magnesium, which is greater than that of aluminum. This mismatch drove numerous final design attributes and probably contributed to the failure of the bulkheads in the Deep Thermal Shock engine test. If analysis confirms our hypothesis, it appears that the thermal expansion mismatch problem can in fact be avoided through redesign.

Our results indicate that cost, corrosion, and creep behavior do not appear to be showstoppers in the implementation of magnesium engine components. However, field performance and robustness have yet to be demonstrated.

Over the course of this project, our collaborations have yielded considerable valuable information about creep-resistant magnesium alloys, their castability, designing with them, and the cost factors entering into achieving cost-effective mass reduction.

Presentations/Publications/Patents

1. B. R. Powell, "Automotive Applications of Cast Magnesium," presented to the American Foundry Society, Saginaw Valley Chapter Education Series, Saginaw, MI, February 13, 2008.
2. B. R. Powell, W. L. Miller, L. J. Ouimet, J. A. Hines, J. E. Allison, R. S. Beals, and P. P. Ried, "Performance of Creep-Resistant Magnesium Alloys in Component and Dynamometer Testing of the USAMP Magnesium-Intensive V6 Engine," presented at the 2008 TMS Magnesium Technology Symposium, New Orleans, LA, March 10, 2008.J. A. Hines, J. E. Allison, B. R. Powell, W. L. Miller, L. J. Ouimet, R. S. Beals, and P. P. Ried, "USAMP Magnesium Powertrain Cast Components Project: Engine Test Results," presented in the Magnesium Technologies Session of the 2008 SAE Congress, Detroit, MI, April 14, 2008.
3. R. S. Beals, L. Kopka, J. A. Hines, J. E. Allison, R. M. McCune, B. R. Powell, W. L. Miller, and P. P. Ried, "USAMP Magnesium Powertrain Cast Components Project: Engine Test Results," presented at the 19th Annual Magnesium in Automotive Seminar, International Magnesium Association, Livonia, MI, April 30, 2008.
4. J. A. Carpenter, J. Jackman, R. J. Osborne, B. R. Powell, N. Li, and P. Sklad, "Automotive Research and Development in North America," *Die Casting Engineer*, [**3**] 54–9, (2008).
5. R. J. Natkin, B. Oltmans, T. J. Heater, J. E. Allison, J. A. Hines, G. K. Tappen, and D. Peiskammer, "Crank Shaft Support Assembly," US Patent No. 7,288,528 B2, October 23, 2007.

Acknowledgments

The success of this project is due to the dedicated efforts of a large number of team members at Ford, Chrysler, and General Motors. The many other companies and organizations making up the project team are listed in Table 1. The continuing support of our respective companies and the U.S. Department of Energy is gratefully acknowledged.

Table 1. The MPCC Project Team

Core Team	J. Allison, R. Beals, J. Hines, L. Kopka, R. McCune, W. Miller, L. Ouimet, B. Powell, J. Quinn, P. Ried
Alloy Suppliers	AMT, Dead Sea Magnesium, General Motors (GM), Noranda, Norsk-Hydro, Solikamsk, VSMPO-Avisma
Bore Treatment	Gehring, Flame Spray
Casters	Eck, Gibbs, Intermet, Lunt, Meridian, Nemak, Spartan, Thixomat
Casting Modeling	EKK, Flow Science, MAGMAsoft, Technalysis
Coolants	Ashland/Valvoline, ChevronTexaco, Honeywell/Prestone, CCI International
Fasteners	RIBE
Friction Stir Welding	Hitachi
Gaskets	Dana/Victor Reinz
Product Design	Ford, GM, Chrysler, Magna Powertrain
Professional Organizations	International Magnesium Association, North American Die Casting Association
Project Administration	Ried and Associates
Testing Labs	Amalgatech, CANMET, Stork, Westmoreland, Quasar
Tooling	Becker, Delaware Machinery, EXCO, HE Vannatter

C. Ultra-Large Castings of Aluminum and Magnesium (AMD406*)

Principal Investigator: Michael H. Maj
Ford Motor Company
Research and Advanced Engineering
2101 Village Road
Dearborn, MI 48121
(313) 337-6700; fax: (313) 390-0514; e-mail: mmaj@ford.com

Project Administrator: Thomas N. Meyer, Ph.D.
TNM Contract Engineering and Consulting Services
3987 Murry Highlands Circle
Murrysville, PA 15668
(412) 860-7946; e-mail: tnmeng@aol.com

Technology Area Development Manager: Joseph A. Carpenter
(202) 586-1022; fax: (202) 586-1600; e-mail: joseph.carpenter@ee.doe.gov

Field Project Officer: Aaron D. Yocum
(304) 285-4852; fax: (304) 285-4403; e-mail: aaron.yocum@netl.doe.gov

Contractor: United States Automotive Materials Partnership (USAMP)
Contract No.: DE-FC26-020R22910 through the DOE National Energy Technology Laboratory

Objective

- Assess the manufacturing feasibility, economics, and mass reduction potential of thin-wall structural castings of aluminum and magnesium applied to automotive weight reduction.

Approach

- The Ultra-Large Casting (ULC) project builds on the findings of a DOE funded contract to the American Foundry Society (Project ORNL-12401) which benchmarked various casting processes to assess their suitability to manufacture large light-metal castings. This annual report will address three technical areas focusing on the ULC objective. These include demonstration and evaluation of two semi-solid processes: the Sub-Liquidus Casting (SLC) process for magnesium and aluminum, and a multiple hot-runner direct injection Thixomolding process for magnesium. In addition, the project has been expanded to include a study of a new large thin casting (LTC) concept which examines reducing total casting cycle times by a factor of four. The SLC and Thixomolding efforts focus on mechanical properties suitable to thin-wall structural parts while the LTC effort emphasizes low cycle time, and hence, cost for thin-wall parts of modest properties. A "real world" application of a ULC made from one of the casting processes is intended to demonstrate the weight savings potential and other benefits of ULCs. Based on this background work and continuing research, the ULC project approach is described.
- Further describe and substantiate the rationale for using light-metal castings in place of conventional stamped and welded steel automotive body structures to reduce vehicle weight.

* Denotes project 406 of the Automotive Materials Division of the United States Automotive Materials Partnership, one of the formal consortia of the United States Council for Automotive Research set up by Chrysler, Ford, and General Motors to conduct joint, precompetitive research and development.

- The project will be executed in two concurrent phases. *Phase I* is focused on process selection and capability analysis. Pha*se II* is focused on designing, analyzing, and testing a "real-world" vehicle application meeting the ULC team's criteria of a ULC.
- The main objective for *Phase I* is to utilize the selected processes to improve the quality of cast components vs conventional casting processes by achieving homogeneous distribution of properties and demonstrate consistent and predictable mechanical properties with improved strength and ductility.
  - The major tasks for *Phase I* will consist of Flow and Solidification Modeling, Tool Design/Analysis/Fabrication, Correlation with Casting Trials, Material Characterization, Process Capability Studies, and an Economic Analysis.
- The main objective for *Phase II* is a "Real-World" application of a ULC that will demonstrate a mass reduction of 40% to 60% at a competitive cost compared to conventional steel construction. Additionally, it is desired to demonstrate parts consolidation, reduced investment cost in tooling and dies, and improved energy absorption.
  - The major tasks supporting *Phase II* are Finite Element Analyses (FEA) for Static, Durability, Noise, Vibration, and Harshness (NVH), and Crash Analyses; System Level and Full Vehicle Prototype Fabrication; Durability Testing; Dynamic Crash Testing; and an Economic Analysis.
- In addition, the ULC project initiated the exploration, analytical development, and engineering evaluation of a process concept to establish the process parameters and machine configurations required to produce LTCs with thicknesses as low as 1 mm at production rates of 240 pieces per hour.

Accomplishments

Large Thin Casting

- On a theoretical basis, the process technical feasibility of making large (e.g., automotive door inner panels) magnesium, and aluminum castings 1.00 mm thick was established.
- Determined processing requirements.
- Developed concepts for the necessary engineering methods, equipment, tooling, and controls.
- Preliminary assessment of the potential cost competitiveness of LTC castings.
- Submitted project "close-out" report.

The Sub-Liquidus Casting Process

- All coupons and test parts were produced in 2007 with evaluation and final report to be completed in June of this year. There has been significant difficulty obtaining a "close-out" report from the staffs at Cosma and the Promatek Research Centre. Appeals to the upper management at Cosma and Promatek will be submitted for assistance in bringing the "close-out" report to completion.

Thixomolding Process to Produce "Shotgun"

- Based upon previous trials, the part was redesigned to be more compatible with the Thixomolding process. Consequently, the tooling was modified accordingly.
- Two significant trials were conducted in 2008 yielding several hundred parts with the expectation that the second trial recently completed will show consistent elongation of 10% or better in critical areas of the "shotgun."
  - The improved design provided major improvement in part ejection.
  - Statistical analysis of data from first trial in 2008 indicates elongation is significantly better than High Pressure Die Casting (HPDC) parts (e.g., 7.01% vs 5.68%). The goal for elongation remains 10% minimum in critical areas of the part. An assessment of this will be determined for the parts produced in the recent second trial.
  - This first trial demonstrated the value of x-ray in assessing the quality of parts in specific areas of interest.

- An economic analysis was completed and is being reviewed and developed.
- The hot runner has been a focus of continued development.

Future Direction

Large Thin Casting

- Integrate the "Project Close-out Report" for LTC into the AMD406 project "close-out" report.

SLC Process

- As noted, the casting trials are complete with the remainder of the work focused on:
  - Characterizing the mechanical properties of the castings.
  - Completing a statistical analysis of Design of Experiments results to determine process capability.
  - Developing conclusions and recommendations for further process improvements.
  - Obtaining a "close-out" report from the project manager at Cosma and at the Promatek Research Centre. Will seek assistance from upper Cosma management and Promatek Research Centre.

Thixomolded Shotgun

- Parts were produced in two trials in 2008. The parts produced during the second trial recently completed will be evaluated first by G-Mag and then by Ford, General Motors (GM), and Canada Centre for Mineral and Energy Technology (CANMET).
- Document all findings in a "Project Close-out Report" which will include assessment:
  - Part design
  - Economics
  - Part properties
  - Full component testing

Introduction

Ultra-Large Casting Rationale

The majority of mass-market automobile and light truck body structures are constructed of sheet metal stampings fastened together with resistance spot welding. This method of construction tends to increase the weight of the body because it introduces structural redundancies. For example, an outer panel requires an inner panel for stiffness, which in turn might require local reinforcements. The casting process enables all of these structural elements and features to be integrated into a single piece, and thus has the potential to significantly reduce weight. This logic is illustrated with the example in Figure 1, which shows how a multi-piece stamped steel liftgate inner structure could be integrated into a single casting. There are numerous examples in the industry literature to be cited (e.g., final reports of references 1, 2, and 3); however, the basic justification for ULCs is the ability to *reduce cost* by integrating components and *reduce weight* by taking advantage of the

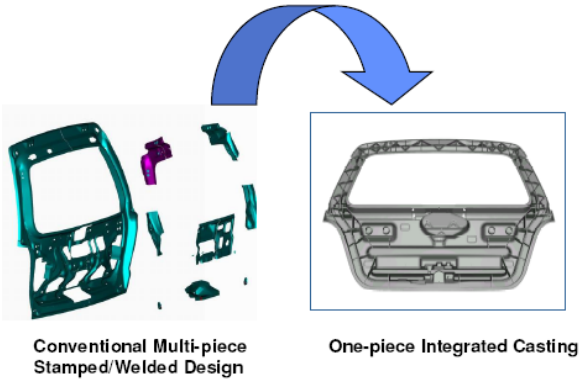

Figure 1. Example of parts integration.

casting process to eliminate structural redundancies, and additionally, using lower density material such as magnesium or aluminum. Preliminary studies indicate large castings can be cost competitive with conventional stamped steel; however, a comprehensive, definitive case study comparing a true structural casting to conventional multi-piece stamped and welded construction has yet to be completed. Such a case study is essential

for substantiating the rationale for ULCs and is undertaken by the ULC team.

Existing Applications of Large Light-Metal Castings

There are many examples in the industry of what are considered ULCs such as die-cast magnesium instrument panel structures, seat structures, closure inner structures, etc. However, it is more appropriate to describe these applications as quasi-structural because they are not totally integrated into the body structure. These quasi-structural components demonstrate the lightweighting potential of large castings replacing conventional stamped steel structures.

A notable example of an ultra-large structural casting is the current Ford F-150 radiator support structure. It is a one-piece, thin-walled magnesium casting (see Figure 2) that replaces seven major stamped steel parts for a 25 lbs weight savings. It is integrated into the body structure where it contributes to torsional stiffness and plays a role in crash. If applications of ultra-large structural castings like the F-150 radiator support and other large quasi-structural parts already exist, why is there a need for a ULC project? These particular components are manufactured using the conventional High Pressure Die Casting (HPDC) process, which has some inherent limitations in achieving consistent mechanical properties.

Figure 2. Cast magnesium radiator support.

Current Manufacturing Processes for Producing Large Light-Metal Castings

The F-150 radiator support and most large quasi-structural automotive light metal castings are manufactured with the HPDC process. While they perform adequately in many applications, HPDCs may not be suitable for other primary structures like pillars, rails or body sides that have to manage large amounts of crash energy. HPDCs lack the level of ductility and other desirable mechanical properties for these structural applications. Therefore, further uses of HPDCs beyond today's applications are limited by the process capabilities and by the mechanical properties achievable with conventional die-casting.

Utilizing a relatively simple process such as HPDC to make structural parts is highly desirable by the industry. Unfortunately, the presence of porosity in HPDCs has a detrimental effect on mechanical properties. A plethora of countermeasures have been developed to combat porosity (and other shortcomings) of the HPDC process by introducing into the process vacuum, non-turbulent filling of the shot sleeve, "squeezing" during solidification. There are also expensive specialty heat-treatable alloys that are used along with one or more of the countermeasures to lower porosity levels and improve quality but not without significant increase in cost. In spite of these enhancements and spin-off HPDC based processes, HPDCs continue to be challenged by tradeoff between quality and cost. This inhibits the wide use of HPDCs as primary structural parts.

Besides porosity and non-uniform mechanical properties, adapting HPDC to ultra-large castings presents other challenges, such as low yield. In some cases, over 50% of the shot weight consists of biscuits, runners, and overflows. This has an effect on economics, especially for magnesium die-castings since magnesium is not able to be recycled in-process. As casting size increases, runner systems become larger and more complex, increasing tooling cost and necessitating the use of larger tonnage die-casting machines. This significantly increases the cost of capital equipment.

Large Thin Castings

There have been significant developments in die casting machines and processes over the past 30 years (1975–2005). Nearly all of that development has focused on making castings that are more structurally sound. Squeeze casting and several semisolid processes such as "thixocasting," Thixomolding, and "rheocasting" are examples.

There have been a few examples of moderately large thin castings, but large thin (1 mm) aluminum castings have not become common in the market place. Thin magnesium castings (such as cell telephone housings) are common, but they are small. The design freedom intrinsic with castings leads one to believe that there must be a market for large thin aluminum and magnesium castings if they can be made with consistently high quality and at a low enough cost.

This is not a study of the costing and pricing dynamics of the industry. If the castings can be made 1 mm thick and cast at 240 castings per hour from a single cavity die, requirements for mass reduction and cost parity should be satisfied.

A casting process concept has been proposed and this engineering evaluation is to determine its technical and economic feasibility. For demonstration, a large thin panel (e.g., pickup truck door inner) was chosen for a full analysis. The procedure follows the North American Die Casting Association (NADCA) 23 step ***"Process Engineering and Design for Die Casting"*** flow chart[4]. Questionable, missing data and physical relationships are identified. Concept designs for a casting machine die and work cell to meet the processing requirements are created and is described in the NADCA paper[5]. Following this engineering analysis, the economics of operation are developed.

Finally, detailed descriptions of possible follow-on projects were developed and are described in a separate section of this report. At this point, the following conclusions can be stated:

- It is feasible to pressure cast components having a projected area of 1 m^2 and a substantial area having a thickness of 1 mm. A door inner for a full size pickup truck is an example.
- Cast such panels at a rate of 240 per hour.
- High investment cost and unproven technology are significant barriers.
- Cost model shows that such castings may be cost competitive with stamped steel door inner panels.
- Direct material remains the largest single cost factor accounting for over half of the part cost without considering the amortized cost of tooling.

The paper, "USCAR/USAMP Large-Thin Casting Project," presented by E.H. Herman won "Best Paper" at the Cast Expo 08 NADCA Casting Congress held May 17-20, 2008 in Atlanta, Georgia. This was followed by a paper published in the July, 2008 issue of *Die Casting Engineer*.

SLC Process Development/ Demonstration

Although the SLC process[6] has been described in previous annual reports, some review is provided here. It is a unique process that offers the potential to produce thin-wall aluminum castings having greater properties (i.e., no heat treatment) than typically achieved by conventional sand, permanent-mold, or die-casting processes. The THT hardware system offers the possibility to operate as many as four injectors; thus, the metal flow length can be kept low while producing large parts. The machine operates as a vertical casting machine at elevated pressures with the injectors providing metal with a vertical stroke. The time that molten metal is held in the injector determines the solid fraction of metal injected.

SLC Approach

To conduct this evaluation, a test part was designed that met the following criteria:

- Producable on an existing 1,000 ton machine.
- Part reflects the flow length for a ULC.
- Part casting features/challenges are representative of a structural ULC.
- Enables the assessment of knit line quality.
- Same tool set can be readily used for fluidity test part (Figure 3), geometric features of rib section (Figure 4), step section (Figure 5), and knit line node (Figure 6) evaluation.

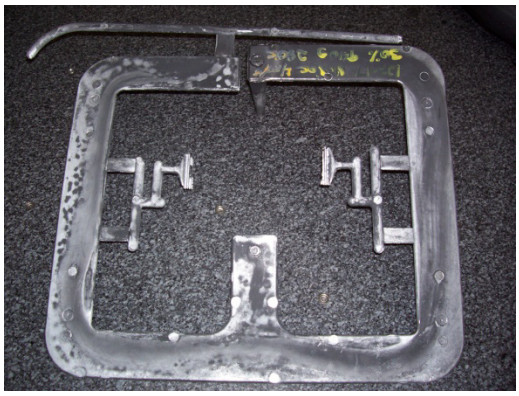

Figure 3. Fluidity test part.

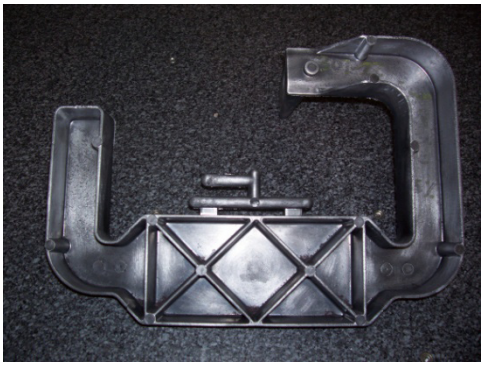

Figure 4. Rib/Waffle geometry.

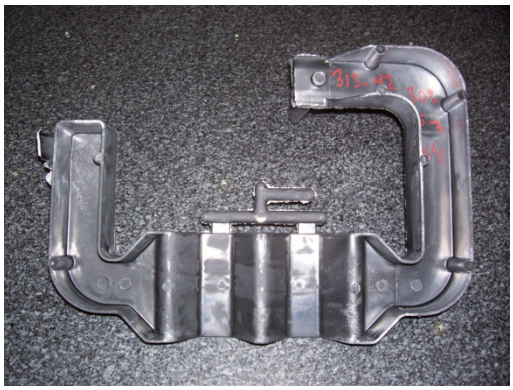

Figure 5. Step geometry.

- Fluidity picture frame (Figure 3) measures 395 mm by 395 mm.
- Flow length from gate through the rib section (Figure 4) is 580 mm and the same holds for the step section. For example, the metal flows from the gate through the grid section and exits the grid section after flowing approximately 580 mm.

Figure 6. Knit line node geometry.

- Flow length from the gate to the far side of the knit line node is approximately 530 mm. The node is a cylinder 50 mm high with a 63.5 mm ID and 6.5 mm wall. NOTE: the runners for the grid, step, and node are primarily a U-section with the width 53.6 mm, height 40 mm, and nominal wall thickness of 3 mm.

SLC Experimental Results

No new results have been reported since 12/31/07, but the conclusions previously established will be repeated below.

SLC Conclusions

- Low flow velocity and short flow distances; thus, hot runner technology (Mg) and multiple in-gates for aluminum are desirable for quality parts.
- Stable die temperatures yield consistent casting quality and reduced process scrap.
- Elevated die temperatures enable manufacture of components having reduced cross section.

The remaining effort will include:

- Property determinations
- Process assessment for aluminum and magnesium parts with economics
- Project Close-out Report

Thixomolded Shotgun

G-Mag is modifying tooling in preparation for one more casting trial utilizing the Thixomolding process to produce a magnesium shotgun. The Thixomolding process has the potential to produce magnesium ULCs with properties compatible with

structural applications at costs competitive with steel components. The effort exploits the semi-solid process licensed by Thixomat Inc. of Ann Arbor, Michigan. It can be best described by its similarity to plastic injection molding. Magnesium is prepared in chip form and supplied to the casting machine where the chips are partially melted and injected into the mold cavity.

To evaluate and develop the process, a shotgun for a Ford F-Series vehicle was chosen. The shotgun (see Figure 7) joins the A-pillar to the radiator support structure. The radiator support structure is a magnesium casting produced by the HPDC process. For such a part, a full evaluation of the component can be conducted.

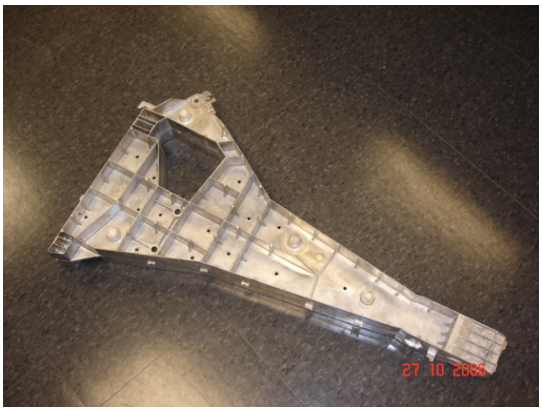

Figure 7. F-Series "Shotgun".

Several trials have been performed in a continuous effort to improve operation (e.g., part ejection difficulties) and part quality (e.g., elongation). For 2008, the part design was significantly modified to reach the project objectives.

Casting Trials

As a result of the trials conducted in 2007, the part design and the tooling were significantly modified to provide:

- Improved part ejection.
- Better metal flow.
- Reduction in total metal required for the part such that metal may be available for overflows and charge cylinder is not required to near end of stroke.

The part design prior to 2008 is shown in Figure 7 with the modified design shown in Figure 8 and

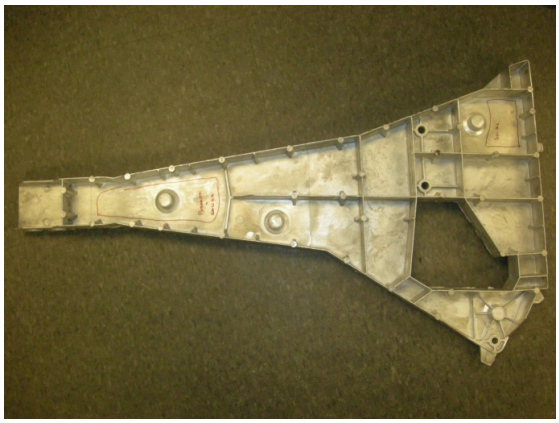

Figure 8. F-Series "Shotgun" revised.

Figure 9. Note that ribs have been eliminated on one side to reduce charge. It should be noted that

Figure 9. F-Series "Shotgun" revised.

the ribs for the modified shotgun only exist on one side. The shotguns installed in cab and prepared for testing are shown in Figure 10. During the first trial the following conclusions were made:

- Part ejection and process interruptions greatly improved.
- Cycle times changed from 90 seconds to 70 seconds with opportunity to further improve.
- Part-to-part consistency improved.
- Packing pressure increased from 2,000 to 5,000 psi.
- Overflows were not utilized.
- Further improvements in the design must be made to be more favorable to magnesium molding.

Figure 10. Full cab with magnesium shotguns.

- Shorter fill times increased difficulty for firing 4 drops simultaneously.
- Entrapped die lube and air were not fully expelled.
- Location of hot drops is not optimized for providing best quality in crumple zone.

For the parts produced in this first trial, Ford conducted a statistical analysis comparing observed elongation with x-ray quality. This analysis confirmed that x-ray is an effective tool to identify acceptable parts/unacceptable parts. For the samples examined, it was shown that the mean elongation for parts having an x-ray quality of level 1 exhibited a mean elongation of 9.6%, level 2 a mean elongation of 6.2%, and level 3 a mean elongation of 3.7%.

Based upon the results of this first trial, it was clear that overflows provide a major advantage in removal of entrapped air. Although some significant improvements to the part are preferred to minimize air entrapment, overflows will be opened for this second run and are expected to improve part quality. Over 300 parts were produced during this second run conducted in December and they are undergoing analysis first at G-Mag and Husky, followed by evaluation at Ford, General Motors (GM), and CANMET. It also must be noted that overflows were considered at the beginning of the effort but so much material was required in the part design that none was available for overflow.

Conclusions

As a result of the effort expended this year the following conclusions are provided:

- During 2007, dimensional control was shown to be very acceptable.
- Critical property (elongation) fell short of expectations (i.e., seeking 10%) in 2007, with some improvement noted in the first trial of 2008 working with the revised shotgun design.
- The revised part design enabled much improved ejection of parts.
- X-ray can clearly distinguish between acceptable and unacceptable parts.
- Solids content varies significantly over a relatively small area of the part and around the same drop. This is an indication that the drops do not always open to flow.

In this second trial, the die overflows were opened. These parts will be evaluated at G-Mag/Husky using x-ray, porosity, and tensile, yield and elongation measurements. A group of 65 parts will be sent to Ford for x-ray evaluation. These same parts will be distributed to GM, Ford, and CANMET for a more thorough evaluation of tensile, yield, and elongation. It is anticipated that like all previous trials, properties will continue to improve and presumably hit the 10% elongation target in buckling zone. A production cost analysis was submitted but further changes are required before data can be communicated. Cost analysis was done for 115k, 178k, and 268k parts per year volume.

After receiving the final “close-out” reports for Thixomolding and SLC efforts, an integrated “close-out” report will be prepared for all of AMD406 efforts.

Presentations/Publications/Patents

1. E. Herman, “USCAR/USAMP Large Thin Casting Project,” Cast Expo 08 NADCA, Atlanta, Georgia, May 17–20, 2008. “Best Paper” award.
2. E. H. Herman, USCAR/USAMP Large-Thin Casting Project, Die Casting Engineer, pp. 52–55, July 2008.

3. Ultra Large Casting (USCAR), "Shotgun," awarded 1st Place in the Process Category, IMA 2007 Awards Competition, Vancouver, BC, May 15, 2007.
4. M. Maj, "Ultra Large Castings for Lightweight Vehicle Structures," IMA Automotive Seminar, Laurel Park Manor, Livonia, MI, March 28, 2007.
5. M. Maj. "Ultra Large Castings for Lightweight Vehicle Structures," TMS 2007 Annual Meeting, Orlando, FL, 2/21–3/1, 2007.

References

1. *Development of a Casting Process for Ultra-Large Automotive Components,* Final Report, Subcontract No. 86X-SU545C, April 28, 2000.
2. American Foundry Society (AFS) Project ORNL-ULC, July 16, 2002.
3. AFS Project ORNL-ULC-II, July 30, 2003.
4. Education Program Master Plan, NADCA.
5. USCAR/USAMP Large-Thin Casting Project NADCA, *Die Casting Engineer*, July 2008, pp. 52–55.
6. "Sub-Liquidus Casting: Process, Concept and Product," J. Jorstad, M. Thieman, R. Kamm, M. Loughman, and T. Woehlke, 2003 *AFS Transactions*, No. 03-162

D. High Integrity Magnesium Automotive Castings (AMD 601*)

Principal Investigator: Richard J. Osborne
General Motors Corporation
Mail Code 480-210-3B1
30001 Van Dyke Road
Warren, MI 48090-9020
(586) 575-7039; fax: (586) 575-8163; e-mail: Richard.osborne@gm.com

Technology Area Development Manager: Joseph A. Carpenter
(202) 586-1022; fax: (202) 586-1600; e-mail: joseph.carpenter@ee.doe.gov

Field Project Officer: Aaron D. Yocum
(304) 285-4852; fax: (304) 285-4403; e-mail: aaron.yocum@netl.doe.gov

Contractor: United States Automotive Materials Partnership (USAMP)
Contract No.: DE-FC26-02OR22910 through the National Energy Technology Laboratory

Objective

- Develop and validate casting process technologies needed to manufacture squeeze and low-pressure cast magnesium (Mg) automotive suspension components.
- Address critical technology barriers inhibiting Mg application and component affordability.
- Deliver Mg control-arm components for static and/or vehicle testing.
- Evaluate potential of emerging Mg castings technologies, specifically the ablation and T-Mag processes.

Approach

- The approach of the High Integrity Magnesium Automotive Castings (HIMAC) Project is to develop the metal casting process technologies necessary to cost effectively manufacture high integrity (high ductility and strength, low porosity, free of objectionable oxides and inclusions) cast Mg automotive chassis components.
- This project will develop existing aluminum low-pressure permanent-mold and squeeze-casting processes for the production of Mg structural castings.
- Two new emerging casting processes (ablation and T-Mag) will be investigated.
- The project aims to facilitate production of Mg components requiring geometries and properties not possible with existing high pressure die casting (HPDC) process limitations.
- The project will also develop enabling technologies critical to increased cast Mg automotive applications, microstructure control, porosity and hot-tearing computer models, thermal treatments, and controlled mold filling.

*Denotes project 601 of the Automotive Materials Division (AMD) of the United States Automotive Materials Partnership (USAMP), one of the formal consortia of the United States Council for Automotive Research (USCAR) set up by Chrysler, Ford, and General Motors (GM) to conduct joint, pre-competitive research and development. See www.uscar.org.

Accomplishments

- Cost expenditures match original budget numbers, and in-kind support meets or exceeds forecasted numbers.
- The HIMAC Project team has 43 active participants from the Big 3; industry, academia, and Canada Centre for Mineral and Energy Technology (CANMET).
- Project participants support the project functions including visits to project member's facilities and universities, and participation in conference calls and quarterly review meetings (QRM).
- Four new Mg casting processes have been or are being developed. Rear lower control arms have already been produced from three of the processes.
- Seven different universities are actively involved in the HIMAC Project, including students from undergraduate to Ph.D. levels.
- Microstructure properties and modeling techniques are being identified for the different types of Mg alloys that have already been cast.
- The typical Mg control arm that is being evaluated is shown in Figure 3.
- The Magnesium Vision 2020 document (developed by the Structural Cast Magnesium Development [SCMD] Project) is used as reference by the HIMAC Project team as the new Mg casting processes are developed.
- The electromagnetic pump (Task 6) is completed and is being fitted for the low-pressure permanent mold (LPPM) machine at CMI Equipment.

Future Direction

- Accomplishment of the four new Mg casting processes will provide industry with higher-integrity Mg automotive castings that can be manufactured at a more economical initial set-up cost than is currently used by industry.
- Installation and use of the electromagnetic pump in the LPPM system will be a new innovation in the manufacture of Mg castings.
- The HIMAC Project team will provide Mg control arm castings from all four new casting processes by the end of the June 2009 for testing and evaluation.
- All original statement of work (SOW) tasks will be completed in accordance with the original project timeline and budget figures. However, the HIMAC Project team has discovered some important R&D atures of these three processes that could use additional funding to develop them to their full potential, especially in the understanding of grain refinement and modeling characteristics.

Introduction

The overall introduction for this project changed when the original SOW was revised to include additional information on the T-Mag process. As each report is submitted to DOE, various aspects within the introduction will be mentioned as progress is made in the completion of tasks. Perhaps the quickest near-term path to increased Mg content in automobiles is through increased use of metal castings, and the HIMAC Project is well on its way to support this goal.

The HIMAC Project addresses near- and mid-term technical barriers that currently inhibit Mg casting production that will move the automotive industry into a better position to realize emerging automotive Mg component needs, build needed Mg industry infrastructure, and develop tools that will be required to reduce the cost of Mg components and enable sustainable production requirements. The HIMAC Project has already started to address various aspects of these three key issues.

Development of Casting Tools

Developed technologies and tools required for sustainable long-term procurement of cast Mg

automotive components (Tasks 3, 4, 5, and 6). These tasks will address the science and technological barriers that currently inhibit metal casting development needs identified in the published *Magnesium Vision 2020* document. Understanding and eliminating production barriers that affect the affordability of cast Mg components.

Casting Process Development

Developed casting processes to facilitate production of cast Mg automotive chassis components that cannot be manufactured using current process limits (Tasks 1, 2, and 7). A new Squeeze Casting Cell (Figure 1) was built and operated briefly by CONTECH. However, they recently closed the facility due to economic conditions.

Figure 1. CONTECH squeeze casting cell.

An existing Squeeze Cast Production machine at Meridian Technologies Inc. (Figure 2) was activated to support the HIMAC Project.

Figure 2. Meridian squeeze casting cell.

Magnesium control arms have already been produced at Meridian and are being evaluated.

A low pressure casting cell (Figure 3) was built by CMI E & E for the HIMAC Project.

Figure 3. CMI E & E low pressure casting cell.

Magnesium control arm castings (Figure 4) have been produced from this cell and are being evaluated.

Figure 4. Magnesium control arm.

Tooling is currently being built for the T-Mag Casting Process located in Australia (Figure 5). Casting will be available for testing and evaluation by June 2009.

Figure 5. T-Mag casting cell.

Infrastructure Development

Development of all four casting processes and tools will include industry participation by automotive suppliers currently producing aluminum components (Tasks 1, 2, 7); include the development of equipment uniquely suitable for the production of Mg components (Task 2, 6); and provide for the development of a broader research and science base (Tasks 3, 4, 5, 8).

New casting processes and tool development will be demonstrated by production of an Mg control arm by low-pressure cast, squeeze cast, and two new emerging casting processes (ablation and T-Mag). Control arms will be delivered for static and/or vehicle testing from these processes by June of 2009.

To support the achievement of these processes, the project is divided into eight tasks. These tasks will address key technology barriers that limit casting of Mg automobile suspension, chassis applications, and affect the manufacturing costs of these components as they are defined today.

Task 1: Squeeze-casting process development
Task 2: Low-pressure casting process development
Task 3: Thermal treatment of castings including research into stepped heat treatment and fluidized beds
Task 4: Microstructure control during casting including grain refining and property improvement
Task 5: Computer modeling and properties to enable prediction of casting quality and microstructure
Task 6: Controlled Molten Metal Transfer and Filling
Task 7: Emerging Casting Technologies
Task 8: Technology Transfer

Note: Steering committees within the HIMAC Project have been formed to independently assist the core project team in the achievement of these tasks.

Conclusions

The HIMAC Project addresses the critical barriers to Mg casting implementation, as stated in the *Magnesium Vision 2020* document. The four new casting processes will provide industry with higher-integrity Mg automotive castings for applications such as control arms, knuckles, and wheels that may ultimately enable weight savings of 35 to 60%. The new enabling technologies will reduce Mg component processing, facility costs, and enable the production of high integrity Mg castings. The use of controlled molten metal transfer and filling (electromagnetic pump) will eliminate many of the production and environmental issues associated with the standard cover gas over Mg melts and yield higher quality castings. In addition to all of the above, the HIMAC Project will provide technical support to the Magnesium Front End Research and Development Project (AMD 604). (See report 6.C.)

Presentations/Publications/Patents

1. Beckermann, “Prédiction of Porosity and Hot Tears in Magnesium Casting.” Materials Science and Technology (MS&T), 2007 Conference, Detroit, MI, September 2007.
2. Y. Xue, M. F. Horstemeyer, D. L. McDowell, H. El Kadriri, and J. Fan. “Microstructure-based multistage fatigue modeling of cast

AE44 magnesium alloys," *Int. J. of Fatigue* **29,** 666–76 (2007).

3. El Kadiri, Y. Xue, M. F. Horstemeyer, B. Jordan, and P. Wang. "Fatigue Crack Growth Mechanisms in a Die Cast AM50 Alloy." *Acta Materialia* **54,** 5061–76 (2006).
4. Greg Woycik, CMI Equipment & Engineering. "Low Pressure Casting of Magnesium Alloys for Automotive Components." American Foundry Society-111th Metalcasting Congress, May 15–18, 2007.
5. David Weiss, Eck Industries, Inc. "Magnesium Casting Technology Update." American Foundry Society-111th Metalcasting Congress, May 15–18, 2007.
6. Brian Szymanowski, CONTECH. "HIMAC Magnesium Squeeze Casting Update." American Foundry Society-111th Metalcasting Congress, May 15–18, 2007.
7. Bruce Cox, DaimlerChrysler NA. "High Integrity Magnesium Automotive Components (HIMAC)." American Foundry Society-111th Metalcasting Congress, May 15–18, 2007.
8. M. Pokorny, C. Monroe, C. Beckermann, L. Bichler, and C. Ravindran. "Prediction of Hot Tear Formation in a Magnesium Alloy Permanent Mold Casting." *Int. J. Metalcasting*, Vol. 2, No. 4, 41–53 (2008).
9. American Foundry Society (AFS) 6th International Conference on Permanent Mold Casting of Aluminum and Magnesium, Frisco, TX, February 11–12, 2008.
10. G. G. Woycik, CMI Equipment and Engineering, Inc., AuGres, MI; M. Marlatt, Marlatt Technologies, Three Lakes, WI. "Low Pressure Permanent Mold Casting of a Magnesium Lower Control Arm." (Publication and Presentation).
11. Randy Sheng, Sarah Chen, and Jagan Nath, General Aluminum, Madison Heights, MI. Sponsored Research: "Low Pressure Casting Process Simulation and Tooling Design for HIMAC's Magnesium Automotive Control Arm (08-148)." CastExpo '08, May 17, 2008, Atlanta, GA. (Publication and Presentation).
12. Leonard Winardi, Preston Scarber, and Robin Griffin, University of Alabama-Birmingham, Birmingham, AL; David Weiss, Eck Industries Inc., Manitowoc, WI. "Comparison of Gas Evolution Results from Chemically Bonded Cores In Contact with Magnesium and Aluminum Melts (08-048)." (Publication and Presentation).
13. Richard Jacques, CONTECH U.S. LLC, Portage, MI; John Jekl, Meridian Magnesium, Strathroy, ON, Canada (2 Presentations). "Development of the Squeeze Cast Process for the USCAR HIMAC Project. (08-165)."
14. Michael Marlatt, Marlatt Technologies, Three Lakes, WI; Gregory Woycik, Woycik Metallurgical Consulting LLC, Lapeer, MI; Chung-Whee Kim, EKK Inc., Farmington Hills, MI: (2 Presentations). "Low Pressure Casting of a Magnesium Control Arm (08-166)."

Acknowledgements

The HIMAC Project team has cast Mg castings from all four of the new casting processes, and completed the casting of the Mg control arms from three of the processes. This success would not have been possible without the support and help from: the DOE; the U.S. Council for Automotive Research (USCAR) steering committee; the U.S. Automotive Materials Partnership (USAMP) Automotive Metals Division (AMD) Board; the Big 3; the Canada Centre for Mineral and Energy Technology (CANMET); and the technical societies, and industrial and academia teams that support this project.

In addition, the USCAR office and American Foundry Society staff members were available to assist our project team during monthly and quarterly review meetings that were held at their respective facilities. The project chairman appreciates the support from all of the teams mentioned above.

E. Casting/Solidification of Magnesium Alloys

Principal Investigator: Sergio Felicelli
Associate Professor, Mechanical Engineering
Carpenter Engineering Bldg., Rm. 210
Mississippi State, MS 39762
(662) 325-1201; e-mail: felicelli@me.msstate.edu

Co-Principal Investigator: J. Berry
Professor, Mechanical Engineering
Mississippi State University, 210 Carpenter Bldg.
Mississippi State, MS 39762
(662) 325-7309; e-mail: berry@me.msstate.edu

Postdoctoral Associate: Liang Wang
Center for Advanced Vehicular Systems, CAVS 2181
Mississippi State University, P.O. Box 5405
Mississippi State, MS 39762-5405
(662) 325-9235; Home: (662) 325-5421; e-mail: liangw@cavs.msstate.edu

Adrian S. Sabau
Senior Research Staff Member
Oak Ridge National Laboratory
Materials Science and Technology Division
1 Bethel Valley Road, Oak Ridge, TN 37831-6083
(865) 241-5145; fax: (865) 574-4357; e-mail: sabaua@ornl.gov

Contractor: *Mississippi State University*
Contract No.: *4000054701*

Objective

- Identify the root causes for porosity, segregation, and other defects in magnesium (Mg) cast parts, and propose practical solutions for the improvement of casting processes.

Approach

- Mg alloy cast parts are gaining increasing attention from the automotive sector, aiming at weight saving. However, the casting of Mg alloys is still plagued with problems that are difficult to solve: porosity, macrosegregation, oxide entrainment, irregularity of microstructure, corrosion, machining safety, etc. This research project addresses the fundamental behavior of solidification phenomena that lead to undesired defects (e.g., porosity, macrosegregation, mushy zone) in Mg cast parts with the objective of developing new or improved casting methods (considering gravity-poured method first) for these alloys.

Accomplishments

- Conducted Mg alloy gravity-poured casting experiments at Oak Ridge National Laboratory.
- Performed microstructural analysis of cast Mg alloys (AZ91 and AE42).
- Developed a model for porosity formation during solidification of Mg alloy AZ91.
- Developed a model for dendrite growth during solidification of AZ91 Mg alloy.

Future Direction

- Complete analysis of porosity and secondary dendrite-arm spacing (SDAS) in cast samples and correlate with cooling rate.
- Obtain physical properties of AE42 for modeling purposes.
- Model development for porosity formation for AE42.
- Obtain second dendrite-arm spacing for different cooling rates using optical microscopy.
- Complete validation of AZ91 and AE42 models through experimental results.

Introduction

Magnesium cast alloys, such as AZ91 and AE42, are gaining increasing attention in the struggle for weight saving in the automobile industry [1]. However, in many cases the consistent production of sound Mg castings is marred by the stubborn persistence of some defects that are difficult to remove: porosity, macrosegregation, oxide entrainment, irregularity of microstructure, etc. The formation of microporosity in particular is known to be one of the primary detrimental factors controlling fatigue lifetime and total elongation in cast light-alloy components.

Much effort has been devoted to modeling and experiments on porosity formation in the last 20 years. More recently, rather sophisticated models have been developed to include the effect of pores on fluid flow (three-phase transport) [2], multiscale frameworks that consider the impingement of pores on the microstructure [3], and effects of finite-rate hydrogen (H) diffusion in the formation of pores [4]. A recent review on the subject of computer simulation of porosity and shrinkage-related defects has been published by Stefanescu [5]. New mechanisms of pore formation based on entrainment of oxide films during the filling of aluminum (Al) alloy castings have been identified and documented [6–11]. Oxide film defects are formed when the oxidized surface of the liquid metal is folded over onto itself and entrained into the bulk liquid. A layer of air is trapped between the internal surfaces of the oxide film, which leads to the porosity formation in the solidified castings. The entrainment process due to surface turbulence is usually rapid, on the order of milliseconds; therefore, the time is very limited to form new oxide film on the fresh surface, so the entrained oxide film can be very thin, on the order of nanometers [6].

Four parts are included in this work: (1) gas porosity model in Al and Mg alloys; (2) porosity and oxide films in AZ91, (3) porosity and oxide films in AE42, and (4) dendrite growth model in Mg alloy solidification.

The results presented in this report are relevant to a gravity-pour casting process for which we develop a porosity model. This model is not applicable to high-pressure die casting, which involves flow conditions and a time scale vastly different from the one treated by the current solidification model. The role of oxide films in adding porosity formation could carry over to other low-pressure permanent mold and direct chill casting processes.

Gas Porosity Model in Al and Mg Alloy

A numerical model of H porosity formation during solidification was developed and applied to Al alloy A356 and Mg alloy AZ91. The model (named MULTIA) solves the conservation equations of mass, momentum, and energy and each alloy component within a continuum framework in which the mushy zone is treated as a porous medium of variable permeability. To predict whether microporosity, the solidification shrinkage due to different phase densities, occurs, the concentration of gas-forming elements and their redistribution by transport during solidification were later added to the model. In this form, the model was able to predict regions of possible formation of porosity by comparing the Sievert's pressure with the local pressure, but it lacked the capability of calculating the amount of

porosity. This model has already been presented in detail (references [12] and [13]).

Modeling results of the distribution of pore volume fraction and pore size in A356 are compared with published works. In view of the limited availability of experimental data for Mg alloy gravity-poured castings, the model is used to make a comparison study of porosity formation between Al alloy A356 and Mg alloy AZ91, assuming similar casting conditions. The minimum initial H content that leads to the formation of gas porosity is compared for both alloys. The two parameters of the porosity model, initial pore size and concentration of inclusions, are taken from the A356 data. We acknowledge that these are rather arbitrary assumptions, but in view of the lack of more suitable data, our purpose is only to observe how porosity in AZ91 would form and evolve under these conditions and make a side to side comparison with A356.

Figure 1 shows the variation of pore volume fraction and pore diameter versus cooling rate in the solidified casting of A356 Al alloy for an initial H content of 0.11 cc/100g.

In Figure 1, the small dots are calculated values that span throughout the casting; each dot represents the pore volume fraction or pore diameter calculated at a mesh node in the casting. A least squares fit of the calculated values is also shown as a solid black line. The experimental data of Fang and Granger [14] are indicated as larger circular dots; these were taken by manual reading from their paper, so bars estimating possible reading error are added. The experimental dots represent average values measured at a certain section of the casting, while the simulation shows the space variation within the entire casting. Certainly, the pore volume fraction and diameter are affected by other solidification variables in addition to cooling rate, but an average trend can be identified which is that they both decrease for higher cooling rates. The quantitative agreement of simulated results with the experimental data is reasonable considering that we are using a relatively simple two-dimensional continuum model.

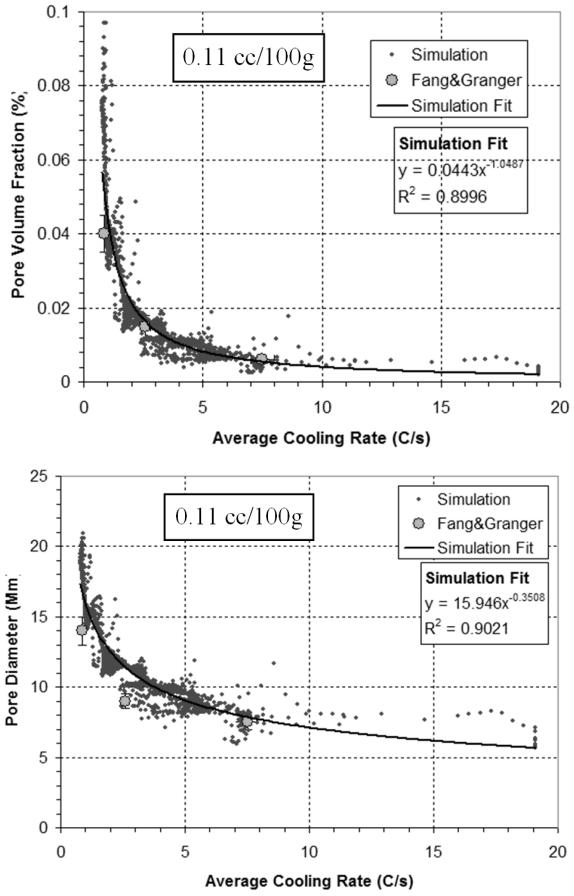

Figure 1. Pore volume fraction and pore diameter vs cooling rate for A356 (H content: 0.11 cc/100g).

Figure 2 shows the variation of pore volume fraction and pore diameter vs cooling rate in the solidified casting of AZ91 Mg alloy for an initial H content of 17.72 cc/100g. Similarly to Figure 1, the small dots are calculated values that span all the casting; each dot represents the pore volume fraction or pore diameter calculated at a mesh node in the casting. A least squares fit of the calculated values is also shown as a solid black line. Both pore volume fraction and pore diameter show a similar trend between AZ91 and A356, suggesting that porosity develops similarly in both alloys. However, the minimum initial concentration of H to form pores in AZ91 is much higher than in A356. The high initial H content (~16 ppm) needed to form porosity in AZ91 is attributed to the high solubility of H in this alloy.

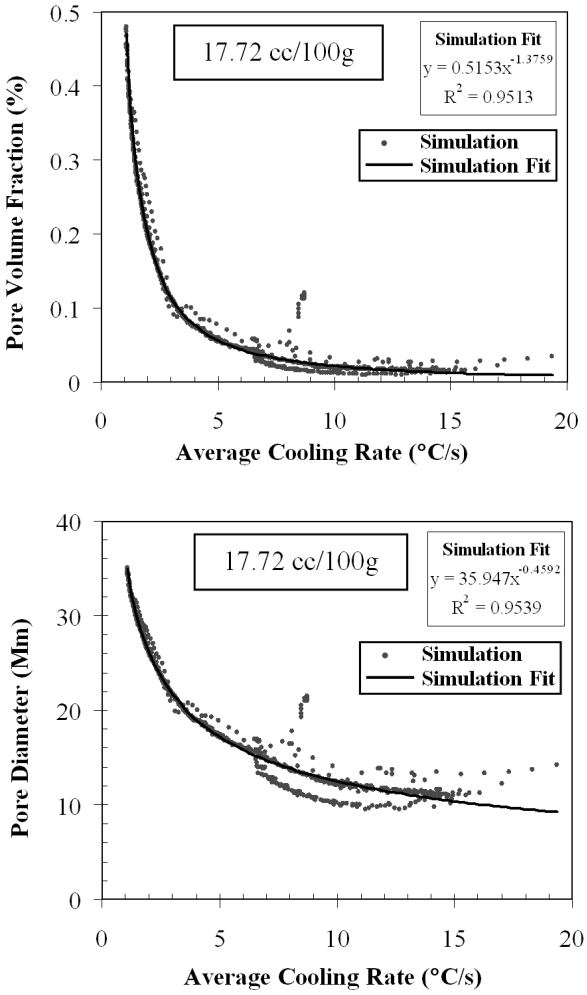

Figure 2. Pore volume fraction and pore diameter vs cooling rate for AZ91 (H content: 17.72 cc/100g).

The porosity growth rate, R_p (in microns per cubic centimeter per hundred grams), due to the change of the initial H content in the liquid alloy is defined as

$$R_p = \frac{d_1^p - d_2^p}{C_1^H - C_2^H} \quad , \qquad (1)$$

where d_1^p and d_2^p are the pore diameters at a certain cooling rate for different initial H content, C_1^H and C_2^H, respectively. Figure 3 shows the porosity growth rate as a function of the average cooling rate when the initial H content increases in the amount of 0.14 cc/100g for A356 and AZ91 under the same casting conditions. It is observed that the porosity growth rate for AZ91 is much smaller than for A356, which is expected because

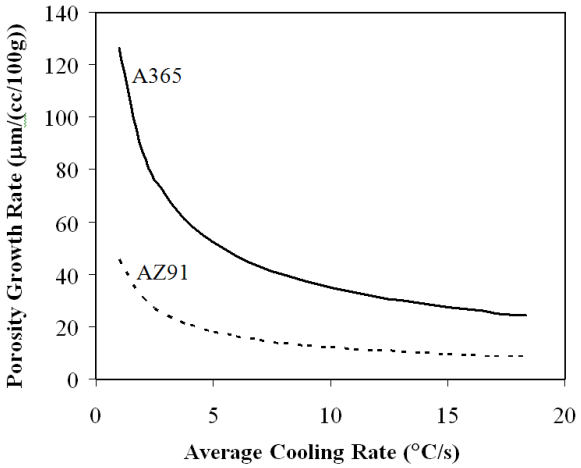

Figure 3. Porosity growth rate vs cooling rate when the initial H content increases in the amount of 0.14 cc/100g for A356 (from 0.11 to 0.25 cc/100g) and AZ91 (from 17.72 to 17.86 cc/100g).

the diffusion coefficient of H in liquid Mg is smaller than that in liquid Al, as shown in Figure 4.

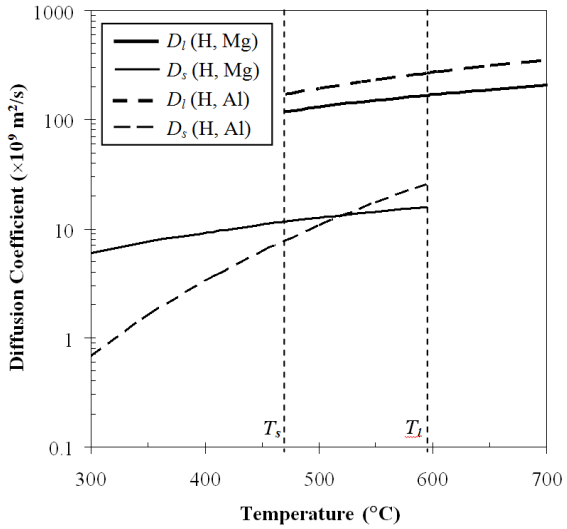

Figure 4. Diffusion coefficient of H in Mg and Al as a function of temperature [16].

Porosity and Oxide Films in AZ91

In this study, we examined the microstructure of Mg alloy AZ91 ingots gravity poured in plate graphite molds. Temperature information during cooling was acquired with type K thermocouples at 60 Hz in two locations for each casting. The microstructure of samples extracted from the

regions of measured temperature was then characterized using optical metallography, tensile tests, and scanning electron microscopy (SEM) of the fracture surfaces. The nature of oxide film and porosity defects in AZ91 was investigated.

Porosity was the major defect observed in the tested specimens. Pores ranging in size from 100 μm to 500 μm were found in many of the polished surfaces. Figure 5 shows typical pore morphology at a location close to the thermocouple in the AZ91 C1 sample [Figure 5(a)]. A magnified view [Figure 5(b)] reveals dendrites protruding into the pore as well as pieces of oxides on the surface of the pore. Energy-dispersive X-ray (EDX) spectroscopy shows a threefold increase of the oxygen content inside the pore compared with the surrounding matrix. [15]

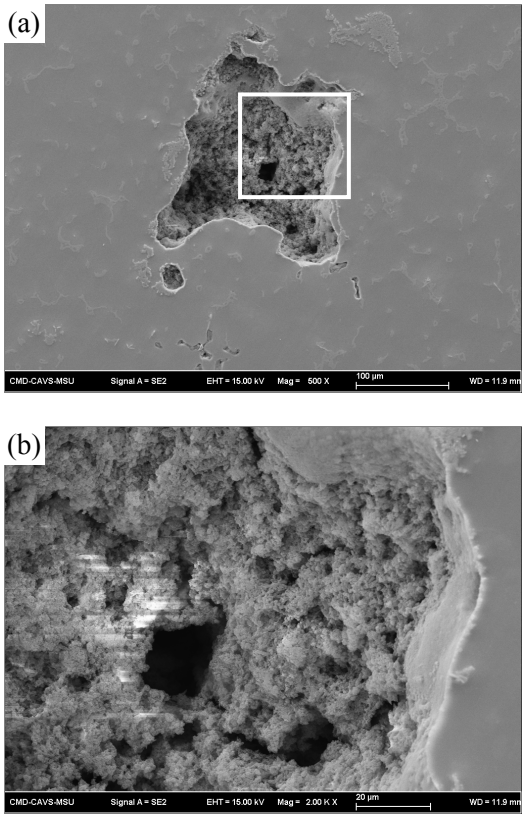

Figure 5. (a) Typical pore morphologies formed at the location close to the thermocouple in casting AZ91, sample C1; (b) higher magnification (2000×) of image (a).

This pore was most probably caused by interdendritic shrinkage; however, the presence of oxides might suggest also a pore formed by an entrained double oxide that was torn apart by shrinkage-induced shear forces. The details of fracture surfaces of tensile test AZ91 samples are shown in Figures 6 and 7. Figure 6 shows two symmetrical oxide films on either side of a fracture surface. This agrees well with the observation by Griffiths and Lai [17] for pure Mg castings. A magnified view of the oxide region (Figure 7) reveals a pleated surface similar to that observed in double oxide films in Al alloys.

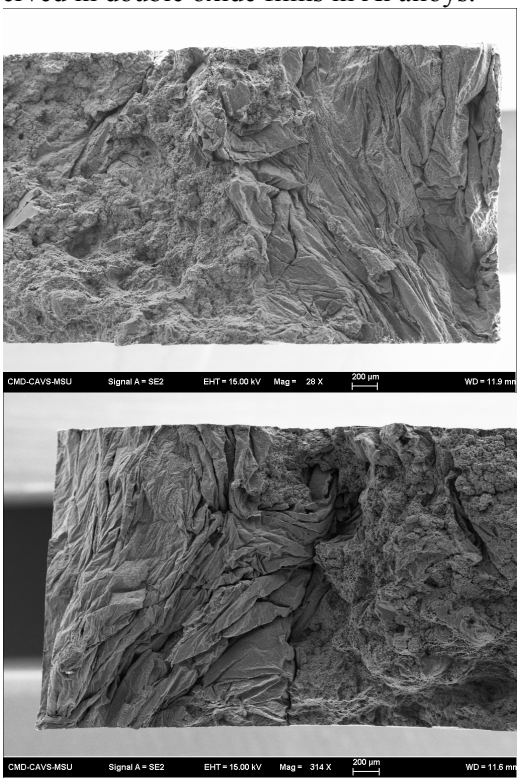

Figure 6. Scanning electron microscope images of oxide films on the two sides of the fracture surfaces of a tensile test specimen taken from AZ91, sample C1.

Porosity and Oxide Films in AE42

In this study, we examined the microstructure of Mg alloy AE42 ingots gravity poured in plate graphite molds. Two graphite plate molds and a ceramic cylindrical mold were selected to produce a wide range of cooling rates. Temperature information during cooling was acquired with type K thermocouples at 60 Hz in two or three locations for each casting. The microstructure of samples extracted from the regions of measured temperature was then characterized with optical

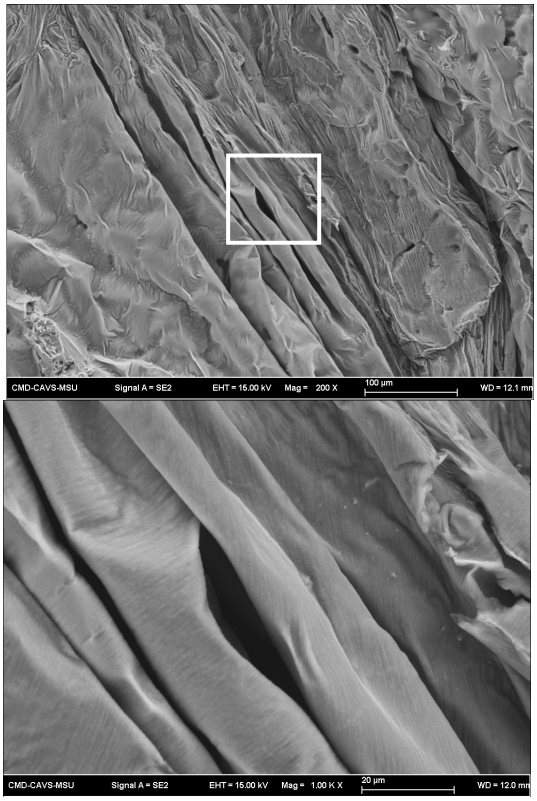

Figure 7. Higher magnification views of the oxide film found on the fracture surface shown in Figure 6.

metallography. This work investigated the nature of oxide film and porosity defects in AE42 for different cooling rates.

The tested AE42 alloy composition was Mg, 3.96% Al, 0.35% Mn, 0.01% Si, 0.001% Ni, 0.007% Zn, 0.0003% Fe, 0.0008% Cu, and 8 ppm Be. The furnace charge was in the form of prealloyed ingot. The weight of the melt was 8 kg, and the alloy was melted in an electrical resistance furnace. For protection, Ar and CO_2 + 3% SF_6 were used as cover gases. The pouring temperature for AE42 was roughly 680 to 700°C. No degassing procedures were used. All castings were poured from one melt. The melt was poured directly from the crucible to minimize temperature decrease during pouring.

The pouring temperature was about 715, 695, and 725°C for casting types C, A, and E. All the molds were not preheated and were coated with boron nitride. To assess the reproducibility of the results, two molds were used for each type of casting.

Temperature information was acquired with type K thermocouples at approximately 60 Hz. The cooling curves are shown in Figure 8. The cooling curves are labeled in the following format: xn_m, where x is a letter, indicating the mold type; n indicates casting number (1 or 2); m indicates thermocouple (1 or 2) for molds A and E and position of thermocouples for molds type C (b—bottom of casting, c—center of casting). The cooling curves show an excellent reproducibility. The temperature information measured by the thermocouple near the top of the casting was discarded because of turbulence in this region. As shown in Figure 8, the cooling rates for AE42 alloy castings were approximately 20, 5, and 1°C/s for molds A, C, and E.

A common feature found in all the samples is that the pores were observed to be smaller at higher cooling rates. Porosity was the major defect observed in the tested specimens. Figure 9 shows long pieces of oxide films, some longer than 1 mm in the sample E1-1 from the mold type E with cooling rate of 1°C/s. The distinct precipitation upon both sides of the film might suggest the former existence of a double oxide that was later torn open, with the higher precipitation occurring on the wetted side. It is interesting to note that oxide films were found only in the samples from ingots cast at the lowest cooling rate. This fact needs confirmation by examining more samples.

Dendrite Growth Model in Mg Alloy

In this work, a coupled cellular automaton–finite element model was developed to simulate dendrite growth during the solidification of Mg alloy AZ91. The model was applied to the simulation of small specimens with equiaxed and columnar grain growth. The influence of cooling rate and some kinetics parameters on the grain morphology were also discussed as follows.

A single nucleus is set at the calculation domain center to start the grain growth process during solidification. The calculation domain has uniform initial temperature and composition. Constant heat flux (10 kw/m^2) is imposed at the four walls. The nucleus has an initial composition kC_0 and preferred growth orientation of zero degree with

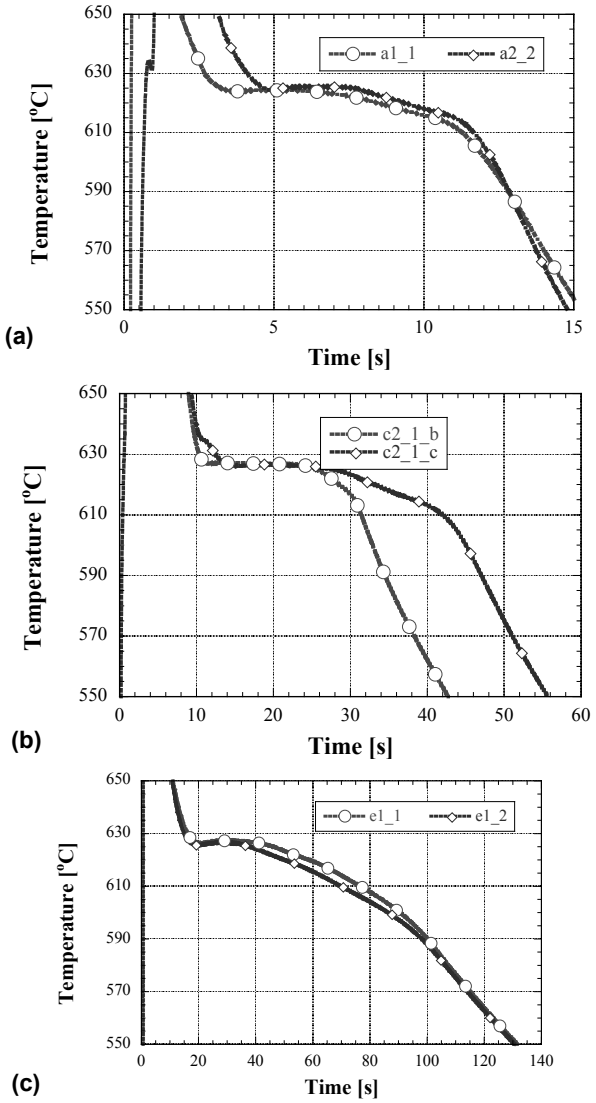

Figure 8. Cooling curves for Mg alloy AE42 castings. (a) mold type A, (b) mold type C, and (c) mold type E.

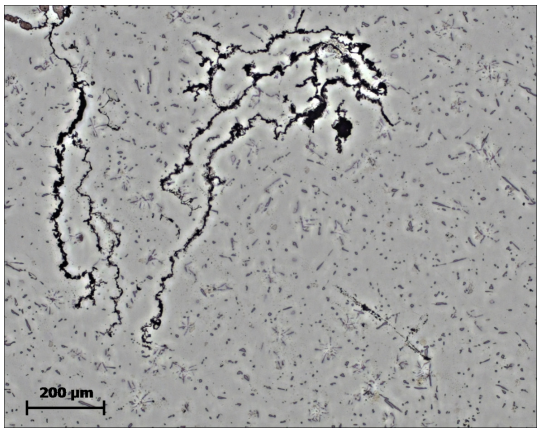

Figure 9. Typical micrographs for Mg alloy AE42, sample E1-1, showing porosity and oxide films.

respect to the horizontal direction. The square domain has a 400 × 400 mesh and a side length of 200 µm. Figures 10(a), (b), and (c) present the simulated evolution of equiaxed dendrite growth at different holding times of 0.0212s, 0.0424s, and 0.0636s, respectively. It can be seen that in the early stage of solidification, the dendrite develops the primary arms which follow the crystallographic orientations [Figure 10(a)]. As solidification proceeds, the primary arms become larger and the secondary arms begin to occur [Figure 10(b)]. With further solidification, some tertiary dendritic arms form from the secondary arms [Figure 10(c)].

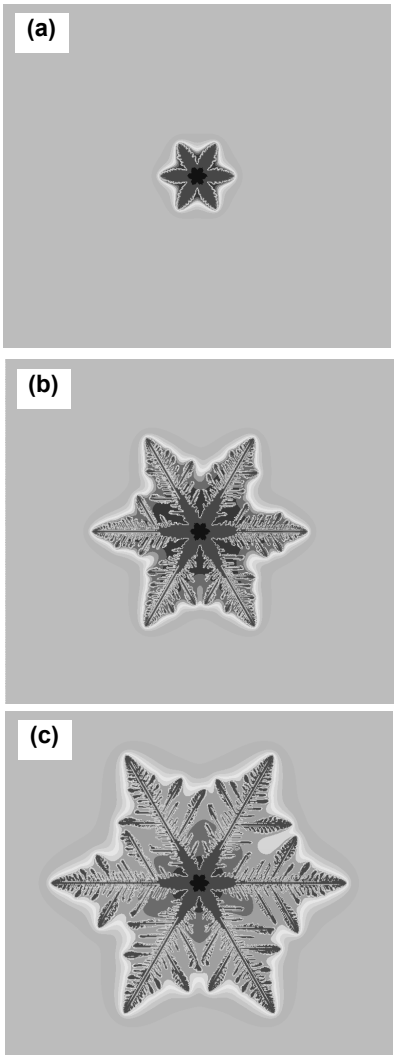

Figure 10. Solute map at different holding times. (a) 0.0212s, (b) 0.0424s, and (c) 0.0636s.

Two different heat flux boundary conditions were imposed on the walls to study the influence of cooling rate on dendrite morphology (Figure 11). Large heat flux corresponds to high cooling rate [Figure 11(a)]. An increase of the heat flux makes the dendrite grow faster and the secondary arms longer. As Figure 11(b) shows, when the heat flux is 5 kW/m^2, only a few secondary arms occur. In addition, a large heat flux makes the grain grow faster, so more solute is released from the solid and there is less time for solute diffusion, which produces a high solute composition in the liquid. The growth of columnar dendrites was also simulated for the same Mg alloy directionally solidified with heat flux applied on the left wall. The calculation domain has a 400 × 200 mesh and dimensions of 100 × 50μm. Two nuclei were placed at the left wall with crystallographic orientation aligned with the temperature gradient.

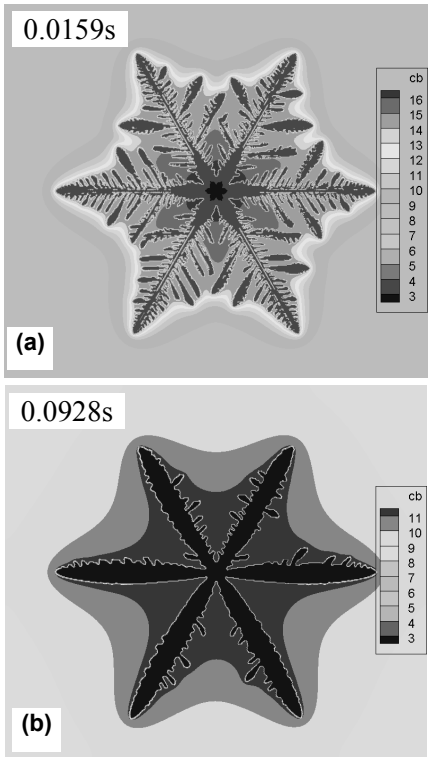

Figure 11. Solute map with heat flux of 20kW/m^2 (a) and 5kW/m^2 (b).

Figures 12 (a) and (b) present the simulated evolution of columnar dendrites with heat fluxes of 80kW/m^2 and 20kW/m^2, respectively. A larger heat flux produces a steeper temperature gradient, which leads to thinner dendrites. The primary

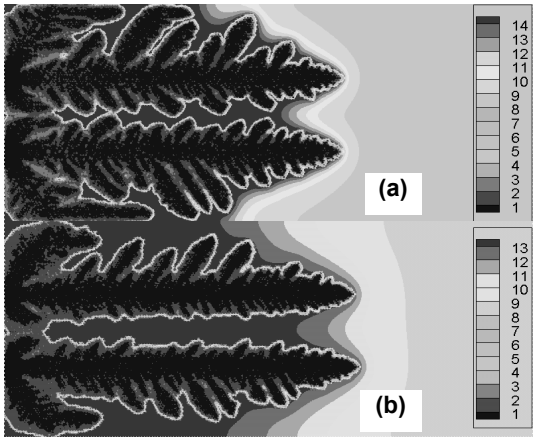

Figure 12. Solute map with heat flux of 80kW/m^2 and holding time 0.0339s (a) and 20kW/m^2 with holding time 0.1166s (b).

arms whose morphology orientation is not parallel to the heat transfer direction will be stopped by the growth of the arm parallel to temperature gradient. The growth of some main arms can also be stopped by nearby dendrites. High liquid composition between the two columnar grains due to the small separation between them makes the secondary arms comparatively short.

Conclusions

The following conclusions were derived in this study.

- A solidification-porosity model was developed based on transport of inclusions and H diffusion pore growth. The model was validated for A356, and simulations were performed for AZ91.
- A dendrite growth model based on the cellular automaton technique was developed which shows good potential to deal with the still unsolved problem of mesh-induced anisotropy in hexagonal systems like Mg alloys.
- Gravity poured castings of AZ91 and AE42 were prepared in graphite and ceramic molds of various sizes. Analysis of microstructural data (in progress) should provide an estimate of correlation of porosity with cooling rate, useful for model verification (though no H content data are available).
- Microstructural analysis of AZ91 and AE42 samples revealed the presence of oxide films

similar to those found in Al castings, including some in the interior surface of pores.

Presentations/Publications/Patents

1. S. D. Felicelli et al., "A model for Gas Microporosity in Aluminum and Magnesium Alloys," *Metallurgical and Materials Transactions B* (accepted).
2. L. Wang et al., "Oxide Film and Porosity Defects in Magnesium Alloy AZ91," 2009 TMS Annual Meeting & Exhibition, Shaping Casting: Third International Symposium, San Francisco, California, February 15–19, 2009 (accepted).
3. L. Wang et al., "Interdependence between Cooling Rate, Microstructure and Porosity in Mg alloy AE42," 2009 TMS Annual Meeting & Exhibition, Magnesium Technology, San Francisco, California, February 15–19, 2009 (accepted).
4. H. Yin and S. D. Felicelli, "Simulation of microstructure evolution during solidification of magnesium alloys," *Materials Processing Fundamentals*, 2009 TMS Annual Meeting & Exhibition, San Francisco, California, February 15–19, 2009 (accepted).
5. J. C. Heinrich et al., "Projection method for flows with large local density gradients. Application to dendritic solidification," *International Journal for Numerical Methods in Fluids*, **57**(9), pp. 1211–1226 (2008).
6. S. Poola et al., "A re-examination of factors affecting porosity gradients in unidirectionally solidified samples," *Transactions of the American Foundry Society,* **116**, pp. 157–168 (2008).
7. S. D. Felicelli, E. Escobar de Obaldia, and C. M. Pita, "Simulation of hydrogen porosity during solidification," *Transactions of the American Foundry Society*, **115**, paper 07-078, pp. 1–13 (2007). (BEST PAPER AWARD.)
8. S. Felicelli et al., "An International Collaboration for the Study of Defects in Castings," *2008 ASEE Annual Conference & Exposition*, Pittsburgh, Pennsylvania, June 22–25, 2008.

References

1. C. H. Caceres et al., "Effects of solidification rate and ageing on the microstructure and mechanical properties of AZ91 alloy," *Materials Science and Engineering A*, **325**, pp. 344–355 (2002).
2. A. S. Sabau and S. Viswanathan, *Metall. Mater. Trans. B*, **33B**, pp. 243–255 (2002).
3. P. D. Lee et al., *Mater. Sci. Eng. A*, **365B**, pp. 57–65 (2004).
4. K. D. Carlson, Z. Lin, and C. Beckermann: *Metall. Mater. Trans. B*, **38B**, pp. 541–555 (2007).
5. D. M. Stefanescu, *Int. J. Cast Met. Res*., **18**, pp. 129–143 (2005).
6. John Campbell, *Castings 2nd ed.* (Butterworth-Heinemann, London, 2003), pp. 17–69.
7. X. Yang et al., "Quantitative characterization of correlations between casting defects and mechanical strength of Al–7Si–Mg alloy castings," *Materials Science & Technology*, **22**, pp. 561–570 (2006).
8. J. Campbell, "Entrainment defects," *Materials Science & Technology*, **22**(2), pp. 127–145 (2006).
9. J. Knott et al., "Commentaries on 'entrainment defects' by J. Campbell," *Materials Science & Technology*, **22**, pp. 999–1008 (2006).
10. R. Raiszadeh and W.D. Griffiths, "A method to study the history of a double oxide film defect in liquid aluminum alloys," *Metallurgical and Materials Transactions. B*, **37**, pp. 865–871 (2006).
11. J. Mi et al., "entrained oxide films in TiAl castings," *Intermetallics*, **11**, pp. 377–385 (2003).
12. S. D. Felicelli, D. R. Poirier, and P. K. Sung, *Metall. Mater. Trans. B*, **31B**, pp. 1283–1292 (2000).
13. S. D. Felicelli, J. C. Heinrich, and D. R. Poirier, *Int. J. Numer. Meth. Fluids*, **27**, pp. 207–227 (1998).

14. Q. T. Fang and D. A. Granger, *AFS Trans*., **97**, pp. 989–1000 (1989).

15. L. H. Rhee Wang et al., "Oxide Film and Porosity Defects in Magnesium Alloy AZ91," 2009 TMS Annual Meeting & Exhibition, Shaping Casting: Third International Symposium, San Francisco, California, February 15–19, 2009 (in review).

16. S. D. Felicelli et al., "A model for gas microporosity in aluminum and magnesium alloys," *Metallurgical and Materials Transactions B* (in review).

17. W. D. Griffiths and N. W. Lai, "Double oxide film defects in cast magnesium alloy," *Metallurgical and Materials Transactions A*, **38**, pp. 190–196 (2007).

F. Multi-Material Metallurgical Bond Joining to Steel

Principal Investigator: Qingyou Han
Purdue University
Mechanical Engineering Technology Department
401 North Grant Street
Knoy Hall, Room 107
West Lafayette, IN 47907-2021
(765) 494-7528; fax: (765) 494-6219; e-mail: hanq@Purdue.edu

Technology Area Development Manager: Joseph A. Carpenter
(202) 586-1022; fax: (202) 586-6100; e-mail: joseph.carpenter@ee.doe.gov

Field Project Officer: Aaron D. Yocum
(304) 285-4852; fax: (304) 285-4403; e-mail: aaron.yocum@netl.doe.gov

Participants:
This project is being conducted as a partnership with the United States Automotive Materials Partnership (USAMP-MMV) with participation that includes the following automotive company representatives:
Bill Charron, Ford Motor Company; e-mail: wcharron@ford.com (Project Leader)
Bruce Cox, Chrysler Corporation; e-mail: bmc8@chrysler.com
Larry Ouimet, General Motors Corporation; e-mail: larry.j.ouimet@GM.com

---

Contract No.: DE-FC26-02OR22910

Objectives

- The primary objective of this concept feasibility project is to verify that the proposed technology can achieve a true metallurgical bond between cast aluminum (Al) and steel and between cast magnesium (Mg) and steel. There are no known alternative, economically attractive processes that can achieve a true metallurgical bond.
- The metallurgical bond between Mg and Al will also be assessed.
- Technical hurdles to implementation will be identified for potential follow-on work.

Approach

- The project team will create test criteria and identify potential target applications.
- Test piece castings will be designed for selected inserts that meet the test criteria.
- Dr. Han will develop the process for and manufacture the test castings.
- The cast components will be tested according to the test procedure and analyzed by the team.
- Technical hurdles to implementation will be identified for potential follow-on work.
- Information and data will be distributed to the participating companies.

Accomplishments

- The test criteria team was established with OEM and supplier participants.
- The test criteria team identified potential applications for the technology to be developed for joining Al to steel, Mg to steel, and Al to Mg. Included in the potential components list were the anticipated cast materials and insert descriptions.
- In light of the first potential components list exercise, the team identified the casting materials, and insert materials to be considered for the test castings to be produced by Dr. Han.
- The team established the testing criteria.
- Three casting designs were created to meet all the test criteria established.
- Early stage development has shown that a strong metallurgical bond can be achieved with this technology for steel pins in cast Al.
- Technical hurdles to implementation have been identified for potential follow-on work.

Future Directions

- Remaining test piece castings will be manufactured with selected inserts that meet the test criteria.
- The cast components will be tested according to the test procedure and analyzed by the team.
- The final technical hurdles to implementation list will be completed for potential follow-on work.

Introduction

The pressure to reduce weight and improve fuel economy has resulted in increased numbers of cast Al and Mg components that need to be attached to the existing steel architectures. The joining of these multi-material components requires traditional bolted connections, mechanical locking strategies, or other non-traditional welding processes. These joining solutions result in added costs and potential offsetting mass (bolts, bosses, flanges, etc.) This project proposes to develop and evaluate a new concept in bonding cast Al and Mg components to steel. The new concept creates a metallurgical bond when ultrasound is applied to a steel insert (sheet, tube, rod, etc.) during the casting process without significant alteration to the casting cycle time or process. It is envisioned that the development of this technology could result in cast components with weldable steel inserts that could be joined to today's steel architectures by currently available, economical production processes like spot welding.

The development approach will build upon preliminary work done at Oak Ridge National Laboratory. Test castings will be made with this new technology, tested and evaluated. In addition, technical hurdles to implementation will be identified for potential follow-on work.

Background

The processes for joining multi-material components (Al, Mg, and steel) into vehicle structures often add cost and offset weight saved from the use of the lighter weight materials. Capital costs may be increased to implement nontraditional welding processes, machining processes, fastener assembly stations, associated material handling systems, etc. Operating costs also increase due to these added processes and parts. In addition, some of the mass reduced by using the lighter weight materials is offset by added locking features, bolts, bolt bosses, flanges, and other features.

Recent investigative development at Oak Ridge National Laboratory has shown that it is possible to achieve a metallurgical bond between Al and steel or Mg and steel by applying ultrasound to steel inserts in molds for casting of the lighter metals. The initial work seemed to indicate that there was no significant loss in productivity due to the introduction of the insert or ultrasound. However, significant development and testing is

needed to verify these assumptions and identify the risks and opportunities for application of this technology.

Work Completed

Task 1: Establish Team, Confirm Target Applications, and Create/Identify Test Criteria

Approach:

- Establish team
- Define potential applications for the technology to be developed for joining Al to steel and Mg to steel.
- Select an Al and Mg alloy.
- Define metrics of success and attributes of a good bond (physical properties, metallurgical properties, and corrosion performance). Criteria to be considered:
  - Features required for test piece
  - Bond line interface quality
  - Diffusion layer distance
  - Brittleness
  - Raw Strength
  - Key life testing
  - Pull-out/shear
  - Peel
  - Fatigue
  - Porosity
  - Corrosion performance
  - Process parameters (i.e. time to produce metallurgical bond, ultrasonic control and measurement aspects, etc.)
  - Requirements for steel sample preparation, etc.

Deliverables:

- Team established
- Potential application(s) (flanges, tubes, etc.) defined.
- Testing criteria and metrics of success defined.
- Requirements for the casting design and insert(s) defined.

Results:

- The test criteria team was established and functioning with active participation from:
  - Chrysler
  - Ford
  - General Motors
  - Purdue
  - TechKnowledge
- The test criteria team identified potential applications for the technology to be developed for joining Al to steel, Mg to steel, and Al to Mg. Included in the potential components list were the anticipated cast materials and insert descriptions. The potential components list is included in the appendix to this report.
- The team settled on the following testing criteria for analyses of the test castings:
  - Cross sectioning
  - Torsional force
  - Pull or push force (depending on bond to be tested)
  - Die penetrent
  - Stress/strain
  - Peel
- Based upon the work completed in the first task, the team identified the casting materials and insert materials to be considered for the test castings to be produced by Dr. Han.

Casting Material	Insert
Mg AZ91E	Mild steel weldable flange
Al 356	Mild steel weldable flange
Mg AZ91E	Steel rod
Al 356	Steel rod
Mg AZ91E	Al 6061 rod
Mg AZ91E	Al 356 cast material

Task 2: Design Test Casting and Steel Inserts:

Approach:

- Design the test casting and steel insert(s) to satisfy testing criteria establish in Task 1.

Deliverables:

- Casting design completed.
- Insert(s) design completed.

Results:

- The test criteria team identified three casting designs that would achieve all the objectives established in Task 1.

The three designs are:

Design 1

The design 1 is illustrated in Figure 1. An insert will be cast in with a cylindrical casting. The test casting will be tested for shear strength and fatigue. Three combinations of metals will be made: steel insert in Mg casting, steel insert in Al casting, and Al insert in Mg casting. For each combination, 15 samples will be made and shipped to the United States Council for Automotive Research (USCAR) for testing.

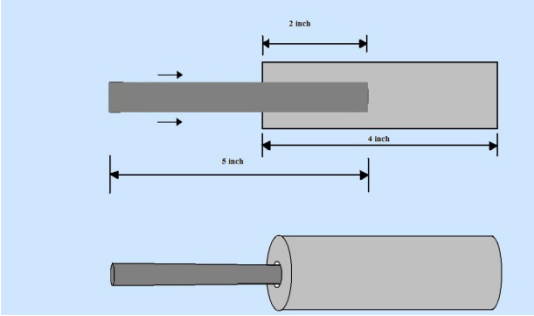

Figure 1. Test Casting Design 1.

Design 2

Design 2 is illustrated in Figure 2. A steel or Al strap will be joined to an Al or Mg disc casting. Testing will be carried out to determine the interfacial strength between the strap and the 2 inch diameter puck. Three combinations of metals will be made: steel strap with Mg casting, steel strap with Al casting, and Al strap with Mg casting. For each combination, 15 samples will be made and shipped to USCAR for testing.

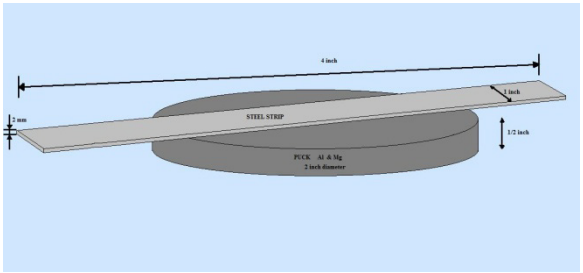

Figure 2. Test Casting Design 2.

Design 3

Design 3 is illustrated in Figure 3. This design will be used to test mi-metal casting. An Al casting (half a disc) will be made in a mold. Molten Mg alloy will then cast to make a disc half Al and half Mg. The joint between the Al half and the Mg half will be tested. 15 specimens will be made and shipped to USCAR for further testing.

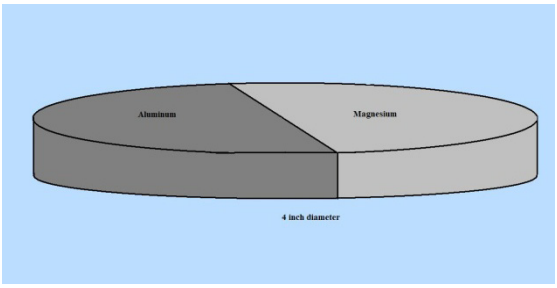

Figure 3. Test Casting Design 3.

Task 3: Develop Process and Make Test Pieces

Approach:

- Prepare mold and ultrasonic tooling (simple molds will be used during this task)
- Procure materials
- Prepare inserts
- Develop the process for manufacturing the test pieces
- Manufacture test pieces
- Document process data

Deliverables:

- Mold and ultrasonic tooling prepared and ready for casting process.
- Samples ready for material and property evaluations.
- Data set captured.

Results:

- Design 1 test castings, steel pin in Al and steel pin in Mg, were manufactured and distributed for testing.
- Design 2 test castings, steel strip on Al, were manufactured and distributed for testing.

Task 4: Test and Evaluate Test Pieces

Approach:

- Test, evaluate, analyze and verify that the new casting/joining process can achieve metallurgical bond between Al to steel and Mg to steel as defined in Task 1. Evaluations will consider physical/ mechanical and metallurgical properties and corrosion performance.

Deliverables:

- Test results and analysis of the capability of this technology to bond multi-material structures.

Results:

- Design 1 test castings, steel pin in Al, were tested by Ford and Casting Technologies Company. Micrographs and physical testing indicated a metallurgical bond was achieved with evidence of tearing of Al during the push out (shear stress) testing. Micrographs indicated a transitional zone between the Al and steel at the joint.
- Design 1 test castings, steel pin in Mg, were tested at Purdue and did not indicate a metallurgical bond was achieved. It was concluded an additional step might be required like pre-coating the steel pin with Al prior to casting into the Mg.

Task 5: Information Dissemination and Reporting:

Approach:

- Identify technical hurdles to implementation
- Disseminate technology to team members

Deliverables:

- Final reports
- Identification of hurdles to implementation

Results:

- Technical hurdles list created and maintained and included in appendix to this report.
- All results distributed to team and maintained on USCAR V-Room secured virtual information site.

Work to be Completed

Task 3: Develop Process and Make Test Pieces

- Complete test castings for:
  - Design 1 steel rod in cast Mg
  - Design 1 Al rod in cast Mg
  - Design 2 steel strip to cast Mg
  - Design 3 cast Al to cast Mg

Task 4: Test and Evaluate Test Pieces

- Complete testing and analyses of all cast test pieces

Task 5: Information Dissemination and Reporting:

- Complete dissemination of all information to team
- Provide final report

Conclusions

Early stage results indicate the concept is a viable means to bond steel to cast Al. The remaining tasks to be completed will determine if similar success can be achieved with Mg to steel and Mg to Al. The team has identified a broad number of potential applications for this technology that could result in weight and cost reductions in the fastening of lightweighting materials to vehicle structures. With the successful development of this technology it is clear that lightweighting materials such as Mg will be enabled for increased usage.

Appendix

Multi-Material Metallurgical Bond
Joining to Steel
MMV 704*

Potential Component List
March 20, 2008

Interior Components:

Component	Cast Material	Inserts
Steering column support	Magnesium	Cast-in steel nuts and studs
	Aluminum	Cast-in steel nuts and studs
Steering wheel arm	Magnesium AM 50 or 60	Cast-in steel bushings
	Aluminum	Cast-in steel bushings
I/P (cross car beam)	Magnesium AM60	Cast-in steel nuts and studs and steel support structures
Seat structures	Magnesium AM 50 or 60	Cast-in steel nuts and studs and steel support structures
Center consuls	Magnesium AM60	Cast-in steel nuts and studs
Knee bolsters	Magnesium AM60	Cast-in steel nuts and studs
Door handles	Magnesium AZ91D	Cast-in steel nuts and studs

* Denotes project 704 of the Multi-Material Vehicle (MMV) focus area of the United States Automotive Materials Partnership (USAMP), one of the formal consortia of the United States Council for Automotive Research (USCAR) set up by Chrysler, Ford and General Motors (GM) to conduct joint, pre-competitive research and development. See www.uscar.org.

Multi-Material Metallurgical Bond
Joining to Steel
MMV 704*

Potential Component List

Body Components:

Component	Cast Material	Inserts
Roof components	Magnesium AM60/AZ91D	Cast-in nuts and studs
	Aluminum 356	Cast-in nuts and studs
Shot guns	Magnesium AM60	Cast-in nuts and studs and weldable steel flanges
Radiator supports	Magnesium AM60	Weldable steel flanges
	Aluminum 5754	Weldable steel flanges
Door Inners	Magnesium AM60	Cast-in nuts, tapping plates, studs, and weldable steel flanges
	Aluminum 356	Cast-in nuts, tapping plates, studs, and weldable steel flanges
Lift gate inners	Magnesium AM60	Cast-in nuts, tapping plates, studs, and weldable steel flanges
	Aluminum356	Cast-in nuts, tapping plates, studs, and weldable steel flanges
Magnesium front end	Magnesium	Cast-in nuts, tapping plates, studs, weldable steel flanges, and aluminum isolation plugs, plates and flanges
Mirror brackets	Magnesium AM60	Aluminum isolation plugs and flanges

Multi-Material Metallurgical Bond
Joining to Steel
MMV 704*

Potential Component List

Chassis Components:

Component	Cast Material	Inserts
Sub frames (cradles and Cross members)	Magnesium AM60	Cast-in nuts and tapping plates, and aluminum isolation plugs, plates and flanges
Control arms	Magnesium	Cast-in nuts and tapping plates
Wheels	Magnesium	Hybrid design with aluminum hub area and magnesium tire rim
ABS brackets	Magnesium AZ91D	Aluminum isolation plugs, plates, and flanges
Steering racks	Magnesium AZ91D	Aluminum isolation plugs, plates, and flanges
Steering knuckles	Magnesium AM60	Aluminum isolation plugs, plates, and flanges
Covers	Magnesium AZ91D	Aluminum isolation plugs, plates, and flanges
Boxes	Magnesium AZ91D	Aluminum isolation plugs, plates, and flanges
Brake Pedals	Magnesium AM60	Cast-in nuts and tapping plates

Power Train Components:

Component	Cast Material	Inserts
FEAD	Magnesium AZ91D	Aluminum isolation plugs, plates, flanges and cast-in steel nuts and studs
	Aluminum 380	Cast-in steel nuts and studs
Transfer Cases	Magnesium AZ91D	Aluminum isolation plugs, plates, and flanges
	Aluminum 380	Cast-in steel nuts and studs
Oil Pans	Magnesium AZ91D	Aluminum isolation plugs, plates, and flanges
	Aluminum 380	Cast-in steel nuts and studs
Brackets	Magnesium AZ91D	Aluminum isolation plugs, plates, and flanges
	Aluminum 380	Cast-in steel nuts and studs
Front Covers	Magnesium AZ91D	Aluminum isolation plugs, plates, flanges and cast-in steel nuts and studs
	Aluminum 380	Cast-in steel nuts and studs

* Denotes project 704 of the Multi-Material Vehicle (MMV) focus area of the United States Automotive Materials Partnership (USAMP), one of the formal consortia of the United States Council for Automotive Research (USCAR) set up by Chrysler, Ford and General Motors (GM) to conduct joint, pre-competitive research and development. See www.uscar.org.

4. AUTOMOTIVE METALS—TITANIUM

A. Low-Cost Titanium Powder for Feedstock

Principal Investigators: Curt A. Lavender and K. Scott Weil
Pacific Northwest National Laboratory
P.O. Box 999, Richland, WA 99352
(509) 372-6770; fax: (509) 375-4448; e-mail: curt.lavender@pnl.gov
(509) 375-6796; fax: (509) 375-4448; e-mail: scott.weil@pnl.gov

Technology Area Development Manager: Joseph A. Carpenter
(202) 586-1022; fax: (202) 586-1600; e-mail: joseph.carpenter@ee.doe.gov

Field Technical Monitor: Mark T. Smith
(509) 375-4478; fax: (509) 375-4448; e-mail: mark.smith@pnl.gov

---

Contractor: Pacific Northwest National Laboratory
Contract No.: DE-AC06-76RLO1830

Objectives

- Investigate alternate powder and melt processing methods for low-cost titanium (Ti) materials.
- Evaluate processing methods to produce powder metallurgy Ti products with International Titanium Powder, Inc. (ITP) powder.
- Evaluate the suitability of emerging Ti technologies for the production of low-cost Ti products for automotive applications.

Approach

- Perform characterization and analysis of the sintering behavior of the ITP powder. Provide feedback of results to ITP for use in process design.
- Develop low-cost feedstocks for powder metallurgy (P/M) use in automotive applications from low-cost Ti tetrachloride ($TiCl_4$).
- Survey the emerging technologies for the low-cost production of Ti powders and evaluate for use in automotive applications.

Accomplishments

- A Ti powder containing only vanadium as a beta stabilizer produced using the ITP process was obtained, characterized by scanning electron microscope and X-Ray diffraction and evaluated for sinterability.
- Developed press-and-sinter cycles that produced greater than 97% dense plates of cold-pressed Ti from the ITP powder.
- Developed sintering cycles that produced 95+% dense bars of commercial purity (CP) Ti that exhibit ductility of up to 14% in selected samples from standard tensile tests using low-cost $TiCl_4$.
- A low-cost precursor for the alloying addition of iron to the ITP process has been identified.
- A series of die and powder lubricants based on aromatic hydrocarbons was evaluated and increased green density of the Hunter fines powder, resulting in an increase from 90 to 94+% of theoretical as-sintered density.

Future Direction

- Perform cost analysis on two new emerging Ti production processes and update the ITP process cost model.
- Perform laboratory trials of sodium reduction of an iron precursor as a low-cost beta stabilizer for the ITP process.
- Produce a beta stabilized alloy bar for use in automotive applications using a powder produced by a low-cost process.
- Measure tensile and fatigue properties of low-cost beta alloy bar stock.
- Continue the development of sintering cycles for the ITP powder with an emphasis on understanding the sintering mechanisms of the powder to increase ductility.
- The Ti4V alloy powder is to be evaluated and processed powder will be characterized for tensile properties.

Introduction

This project is a collaborative effort between Ford, General Motors, Chrysler, Pacific Northwest National Laboratory (PNNL) and the Ti raw material producers and is focused on the development and evaluation of low-cost feedstock materials produced by emerging low-cost Ti production technologies. The purpose of this project is to develop and demonstrate materials and processing methods for producing low-cost Ti feedstock materials and automotive components. The project will evaluate and validate all processing steps necessary to produce low-cost Ti materials capable of meeting automotive property requirements.

Metal products fabricated from Ti possess a combination of properties that could substantially increase the performance and reduce the mass of automobiles. Although Ti has been used in low production volume specialty and racing automobiles, widespread use of Ti in higher volume production vehicles has been prevented by the high expense of producing Ti components. The cost to extract Ti metal from beach sand by the conventional Kroll process alone exceed the cost targets needed for most automotive uses. Several new processes for the production of Ti metal have been developed in recent years and are projected to meet the cost targets of the automotive industry. This project will survey the Ti industry for emerging technologies and evaluate their suitability as feedstock for automotive applications through technical cost studies and characterization.

Many of the newly developed processes produce Ti in a powder product ready for use in the solid-state consolidation processes. Solid-state Ti consolidation by P/M methods will substantially reduce the secondary processing costs by the elimination of energy intensive and low yielding conventional ingot processing technology. Because each new process produces a powder with unique processing requirements and because there is virtually no commercial Ti P/M industry, PNNL will perform processing trials on each powder product that has been projected to satisfy the automotive cost goals.

Approach

The earlier phase of this project was focused on the selection of low-cost powder and secondary processing development. The current phase will be directed at the production of semi-finished products of automotive interest.

Results and Discussion

Due to its relatively high strength, Ti alloys are the most likely materials to be substituted for high-strength steels in applications such as fasteners and suspension components [1]. To date, this project has focused on the development of low-cost feed materials for use in the emerging power production technologies. Although low-cost interstitial elements such as carbon, oxygen and nitrogen are used to strengthen commercial purity Ti, corresponding decreases in ductility, fracture toughness and fatigue strength require the use of an alloy. Using conventional ingot metallurgy processing, commercial purity Ti sponge is

blended with master alloy chunks, which are then pressed into a compact that is vacuum arc or electron beam melted. The ingots are then forged to refine the as-cast microstructure and processed to a semi-finished shape such as a bar or rod. The production of this semi-finished product from ingot usually results in a yield loss on the order of 50%. This process is costly, requiring the development of expensive raw material feedstocks and high purity master alloys. The primary advantage of the newly developed processes is that they produce Ti in a powder form that can be used in solid-state consolidation at a near-net shape and in the case of P/M, net-shape products.

During this reporting period, the project focused on the challenges associated with development of high-yield low-cost beta Ti alloy processing, and evaluation of die and pressing friction associated with direct P/M processing.

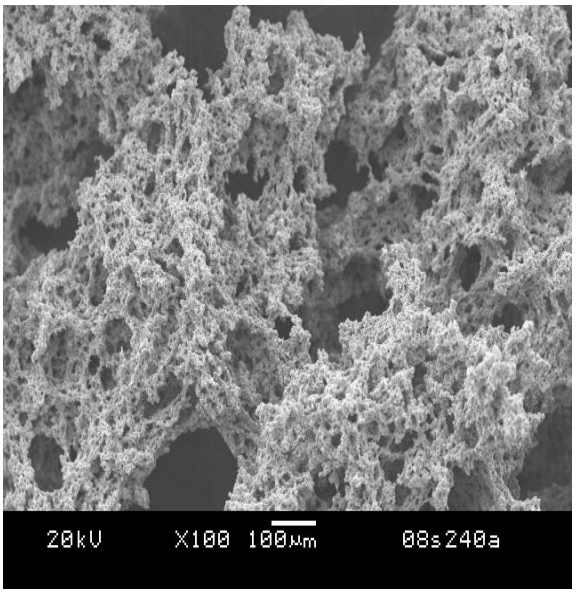

Figure 1. Low-cost Ti4V powder morphology as produced by ITP.

Beta Titanium Alloys

Beta Ti alloys are made by alloying with an element that allows the retention of body centered cubic beta phase at room temperature after rapid cooling from above the beta transus [2]. Beta alloys are normally "age" hardened to high strength (i.e., above 1400 megaPascals (MPa) by the low temperature transformation of beta to the alpha phase [3]. Typically, alloying elements such as molybdenum that stabilize beta are costly, but an effective beta stabilizer is iron, which would be a low-cost addition, possibly lowering the overall alloy cost. As a beta stabilizer, iron presents several challenges; therefore, for ease of processing at ITP the initial trial of beta alloy production was a binary alloy containing only 4 weight percent vanadium (Ti4V). The vanadium was added using a halide that co-reduced efficiently with $TiCl_4$ and produced the pre-alloyed powder shown in Figure 1.

The Ti4V as shown in Figure 2(a) appeared similar in morphology to the commercial purity powders (CP Ti) produced previously and shown in Figure 2(b). The powders were characterized by energy dispersive x-ray (EDX) in the scanning electron microscope (SEM) to evaluate the distribution of the vanadium. As determined by EDAX analysis, the vanadium appears to be

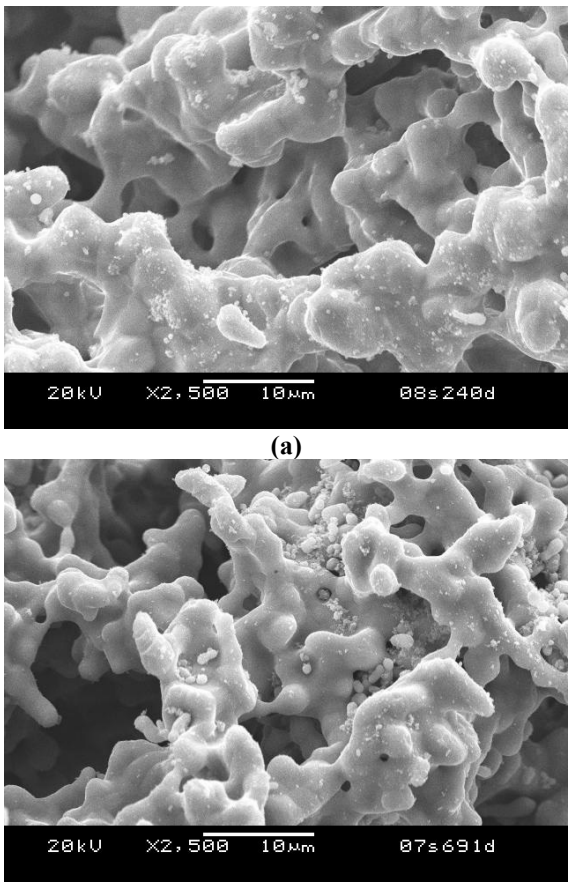

Figure 2. (a) SEM micrographs of low-cost commercial purity and (b) low-cost Ti4V powder showing similar morphology.

uniformly distributed, and it would be expected that the alloy is relatively homogeneous given the amount of vanadium solid solution. The powder was then X-rayed to determine which phase (alpha or beta) had been produced during cooling from the reduction process. The x-ray peaks shown in Figure 3 indicate that both alpha and beta were stabilized [4].

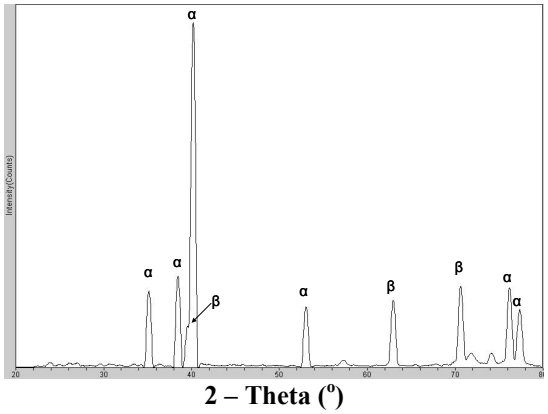

Figure 3. X-Ray of as-produced Ti4V powder, showing the presence of both alpha and beta phase.

The sinterability of the Ti4V was found to be superior to commercial purity powder. In like sinter conditions, the Ti4V consistently sintered to greater than 97% dense, compared to 91% for the CP Ti. This result is likely related to the same mechanism observed in low purity $TiCl_4$, where the vanadium raises the onset of sintering and allows deleterious species to off-gas prior to closing porosity as shown in the dilatometry presented in Figure 4. Although the shrinkage curves shown by Figure 4 show only slight difference, the distinction is in a critical region where many Na compounds tend to decompose, allowing gases to escape prior to a closed porosity condition. Heat treatment studies and tensile testing will be performed, and the sintered Ti4V tensile bars will be measured.

Beta Alloy Bar Stock

Ti is projected to replace high-strength steel fasteners and suspensions components in automotive applications; therefore, a low-cost method to produce bar stock must be developed.

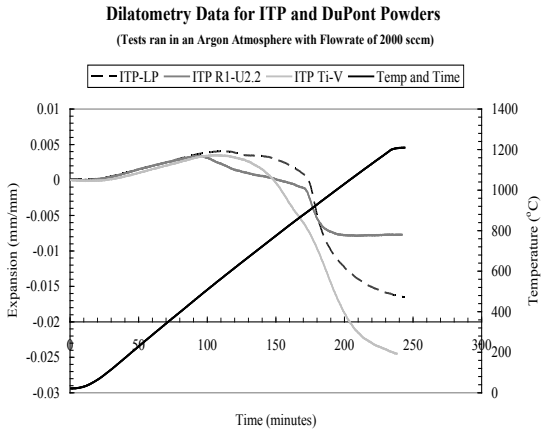

Figure 4. Sintering shrinkage curves powders produced from low-cost $TiCl_4$ (ITP-LP), refined $TiCl_4$ (ITP-R1-U2.2) and Ti with 4 weight percent vanadium.

Conveniently, the new Ti production processes produce powders that can be consolidated by solid state processing. Several studies have looked at solid state consolidation by extrusion; however, the studies are primarily driven by aerospace applications that use irregular cross-section. For the automotive industry, the primary shape of interest will be a round bar stock made by a low-cost rod-rolling method. Therefore, a study has been initiated to produce alloys Ti64 (Ti6Al4V), Ti5553 (Ti5Al5V5Mo5Cr) and Ti185 (Ti1Al8V5Fe) by hot rod-rolling.

The Ti64 alloy was selected as a moderate strength baseline material. Although Ti5553 is not a low-cost composition, there are many extrusion studies that can be used for comparison for this high-strength alloy. Developed in the 1950s by Mallory-Sharon Titanium Company, the Ti185 alloy is a unique composition that when heat treated properly could develop strengths in excess that of Ti5553 with a low-cost composition that can be produced by the ITP process. The Ti185 development was stopped due to iron segregation that occurred during solidification, which may be prevented by using a low-cost P/M solid-state consolidation method resulting in a homogeneous high-strength alloy. The rods produced by this study will be characterized for fatigue, tensile strength and double shear compared to ingot-processed materials.

Low-cost Iron Precursor

Iron can be an effective beta stabilizer; however, iron can segregate during melting, leaving an inhomogeneous microstructure. The addition of iron to Ti by P/M can avoid the segregation and lead to homogeneous low-cost beta alloys. Although iron can be reduced during the ITP process, it is a more difficult element to add to the ITP process. An iron precursor that may be incorporated easily into the ITP process has been identified and is under evaluation. Conceptually in the ITP process, the iron precursor would be vaporized along with $TiCl_4$ to form a mixed-vapor steam. When injected into a spray of molten sodium, the $TiCl_4$ will react with the sodium to form Ti and NaCl, and the heat of reaction will cause the iron precursor to decompose thermally into zero valent iron, thus simultaneously generating the metal species needed to form a Ti-Fe alloy powder. PNNL researchers plan to carry out small-scale proof-of-principle experiments to validate the concept and to understand the variables involved in the overall reaction prior to attempting the process on a larger scale at ITP.

Powder Processing

Powder/Die Lubrication

Ti powders create many challenges for high-volume die pressing due to a high tendency to gall. Using a previously developed instrumented die and newly developed aromatic hydrocarbon lubricants, the coefficient of friction for the low-cost Ti powder has been reduced to below copper powders that are used in high volume production. In addition to decreased friction to levels that can be used in high-volume P/M die pressing, the green density of the compacts increased to levels greater than 90%, resulting in higher as-sintered densities and increased ductility. The progress in the die pressing is summarized in Figures 5 and 6, which show that Ti powders with admixed lubricant and die wall lubrication can be pressed with a coefficient of friction less than that of a copper alloy without issue in high-volume P/M processing and sintered to greater than 93% of theoretical density. As shown in Figure 5, the use of a powder lubricant can reduce the die wall friction to levels near those of high-production volume iron and copper powders and will allow

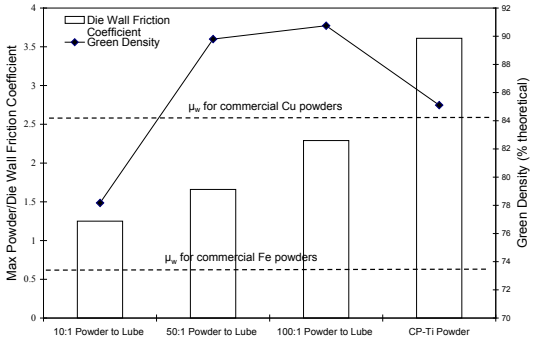

Figure 5. Summary pressing results using a double acting instrumented pressing die with anthracene. With proper lubrication, the low-cost Ti powders can behave similar to copper and iron powders used in high-volume P/M processing.

the use of Ti powders in automotive volume die pressing. Continued development of the powder lubrication is summarized in Figure 6, which shows that the preferred lubricant of Ti is camphor, an aromatic hydrocarbon whose complete removal occurred during sintering leaves behind no residual contamination.

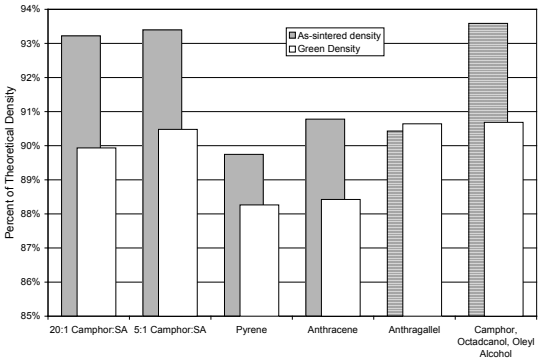

Figure 6. Density effects of various lubrication schemes mixed at a 50:1 with Ti powder.

Conclusions

The conclusions reached during this reporting period are as follows:

- As shown by the investigation of the Ti4V alloy, small alloying additions to the ITP powder process result in substantial differences in the sintering behavior of Ti powder. Combined with the previous results using the low-cost $TiCl_4$, this significant

conclusion suggests that an alloy could be tailored to produce low-cost Ti P/M components.
- Solid-state consolidation for beta bar stock will allow the use of low-cost alloys and processes previously not possible with ingot metallurgy processing.
- Powder lubrication with aromatic hydrocarbons will allow the use of Ti powder in high-volume die pressing applications. Friction can be reduced by a factor of 3 while raising the as-sintered density from 90 to 94%.

Presentations/Publications/Patents

1. S. Hong, Y. Hovanski, C. A. Lavender, and K. S. Weil. 2008. "Investigation of Die Stress Profiles during Powder Compaction using Instrumented Die." *J Materials Engineering and Performance* 17(3):382–386. DOI:10.1007/s11665-008-9229-1.
2. C. A. Lavender. 2008. "Titanium Recycle." USCAR Recycling Working Group Meeting, Detroit, MI. September 24.
3. M. Sadayappan, M. Sahoo, C. A. Lavender, and P. Jablonski. 2008. "Permanent Mold Casting of Titanium Alloy TI-6AL-4V." *Intl J of Metalcasting* 2(1):69–74.
4. K. S. Weil, Y. Hovanski, and C. A. Lavender. "Effects of TiCl4 purity on the sinterability of Armstrong-processed Ti powder." *J Alloys Compd*, DOI:10.1016/j.jallcom.2008.06.09.

References

1. Personal communication from Dr. Andrew Sherman, Ford Motor Company.
2. P. J. Bania. 1994. *J Met* 41:16–19.
3. Weiss and S. L. Semiatin. 1998. *Mat Sci A* A243:46–65.
4. J. W. Elmert et al. 2003. *J Appl Phys* 93(4):15. February.

B. Production of Heavy Vehicle Components from Low-Cost Titanium Powder

Principal Investigator: Seong Jin Park
Associate Research Professor
Center for Advanced Vehicular Systems, CAVS, 2215
Mississippi State University, P.O. Box 5405
Mississippi State, MS 39762-5405
(662) 325-8565; e-mail: sjpark@cavs.msstate.edu

Co-Principal Investigator: Haitham El Kadiri
Assistant Research Professor
Center for Advanced Vehicular Systems
Mississippi State University, P.O. Box 5405
Mississippi State, MS 39762-5405
(662) 325-5568; Cell: (662) 617-4790; e-mail: elkadiri@cavs.msstate.edu

Co-Principal Investigator: Youssef Hammi
Center for Advanced Vehicular Systems
Mississippi State University, P.O. Box 5405
Mississippi State, MS 39762-5405
(662) 325-5452; e-mail: yhammi@cavs.msstate.edu

Contractor: Mississippi State University (MSST)
Contract No.: 4000054701

Objective

- Design and produce titanium (Ti) structural components by using math-based, experimentally validated, powder compaction and sinter models.

Approach

- Examine lower cost blended elemental (BE) and prealloyed Ti powders that are responsive to the powder metallurgy process and synthesize new combinations and innovations in powders composition. Recent developments, such as using hydride powders, have enabled the fabrication of BE parts to over 99% of full density, resulting in significantly improved properties. Additives such as carbon or boron then can generate carbide or boride reinforcing phases—dispersed phase composites. Further studies and developments show that this approach may be well suited to reduce the cost of producing automotive parts, making titanium more cost competitive with other materials commonly used.
- Explore powder modifications, novel organometallic lubricants (the composition is proprietary), finite element analysis of compaction to minimize wall friction and wear, and evaluation of novel tooling materials and coatings. New computer tools for modeling porosity and size change during both compaction and sintering will be tailored to titanium systems with the ability of performing computer aided design for the tooling and processes to attain dense and net-shaped final products.

Accomplishments

- Completed a literature survey for low-cost Ti powder and Ti alloys for automotive application, including cost analyses and processing techniques.
- Designed new Ti alloys and proposed three Ti alloy candidates.

- Evaluated and selected Ti alloys including boride Ti alloys based on mechanical properties, liquid phase sinterability, and cost-effectiveness.
- Performed powder injection molding (PIM) experiment.
- Developed simulation tool for PIM, die compaction, sintering, and hot isostatic pressing (HIPing) with some optimization.

Future Direction

- Continue PIM experiment.
- Develop modeling and simulation for die compaction, sintering, and HIPing using Oak Ridge National Laboratory (ORNL) experimental data.
- Produce a real component for automotive use.

Introduction

Lower cost Ti could be the catalyst for titanium to break into the automotive industry. The goal is to have a competitively priced Ti component produced by cost-competitive manufacturing methods. The research on Ti and Ti-matrix composites is the first stage in a sequence of powder metallurgy (P/M) efforts geared to infuse net-shape production of lightweight materials into the domestic automotive industry. P/M techniques afford designers the ability to produce significantly complex near-net shape parts at potentially significant cost savings, with very little wasted material.

Table 1 shows the overall structure of Task 1 with ORNL collaboration.

Table 1. Overall structure of Task 1.

	Experiment	Simulation
Die compaction	ORNL	MSST
PIM	MSST	MSST
Sintering	ORNL	MSST
HIPing	ORNL	MSST

Work Schedule

Table 2 shows the current progress based on the schedule planned. Subtasks related to the experiment are at risk now because we need experimental data for die compaction, sintering, and HIPing for modeling. For the PIM, we need to find a sponge powder supplier or support from ORNL.

Table 2. The proposed schedule of Task 1 with marks of progress.

Subtasks	Year 1				Year 2			
	Q1	Q2	Q3	Q4	Q1	Q2	Q3	Q4
1.1 literature review, first simulation	100							
1.2 powder evaluation	100							
1.3 microstructure and interfacial study	100							
1.4 processing evaluation	100							
1.5 modeling and simulation		100						
1.6 optimization		75						
1.7 experimental verification		50						
1.8 mechanical properties					50			
1.9 process verification								

Summary of Progress

Task 1 consists of four research categories: literature survey, Ti alloy design and evaluation, PIM experiment, and modeling and simulation for Ti powder processing.

Literature Survey

The literature was surveyed for Ti powder production methods for gas atomized, hydride-dehydride (HDH), and sponge Ti powders; Ti alloys; P/M processes; and previous uses of Ti alloys for automotive applications. The cost of Ti alloys is at least 10 times higher than the cost of aluminum (Al) alloys and 30 times higher than the cost of steels. Table 3 summarizes the consumption of Ti alloys in the automotive market between 1998 and 2002. It can be seen that Ti alloys were never used in massive production mode but were limited only to components

Table 3. Ti alloy use in automotive applications.

Year	Component	Material	Manufacturer
1998	Brake guide pins	Grade 2	Mercedes
1998	Sealing washers	Grade 1s	Volkswagen
1998	Gear shift knob	Grade 1	Honda
1999	Connecting rods	Ti-6Al-4V	Porsche
1999	Valves	Ti-6Al-4V	Toyota
1999	Turbocharger rotor	Ti-6Al-4V	Mercedes
2000	Suspension spring	LCB	Volkswagen
2000	Valve cups	ß-Ti alloy	Mitsubishi
2000	Turbocharger rotor	γ-TiAl	Mitsubishi
2001	Exhaust system	Grade 2	GM
2002	Valves	Ti-6Al-4V	Nissan

requiring extra high stiffness and superior maximum strength and fatigue strength scaled to density. However, manufacturers show a preference for the more expensive Ti alloys over Al in powertrains if rotating and oscillating masses are to be substantially reduced.

We also analyzed the cost for the candidate Ti alloys, as shown in Figure 1. This analysis indicates that the Ti powder type is the most important factor in cost among gas atomized, HDH, and sponge Ti powders.

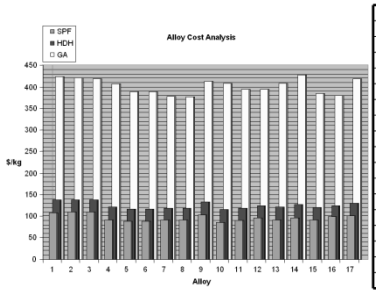

ID	Alloy Composition
1	Ti-6Al-4V
2	Ti-6Al-4V-1Mo
3	Ti-6Al-4V-1Mo-0.2B
4	Ti-8Al-1V-1Mo
5	Ti-6Al-2Sn-4Zr-2Mo
6	Ti-6Al-2Sn-4Zr-2Mo-0.2Si
7	Ti-6.5Al-4.6Sn-4.6Zr-1Nb-0.3Si-1Mo
8	Ti-6.6Al-4.6Sn-4.6Zr-0.9Nb-1Mo-0.35Si
9	Ti-4.5Al-3V-2Fe-2Mo
10	Ti-6Al-1.7Fe-0.1Si
11	Ti-4.5Fe-6.8Mo-1.5Al
12	Ti-1.5Fe-6.8Mo-4.8Al-1.2Nb
13	Ti-1Fe-1Mo-6.3Al-1.2Nb
14	Ti-1.5Fe-2.25Mo-1.2Nb-0.3Al
15	Ti-6Al-4Sn-4Zr-1Nb-1Mo-0.2Si
16	Ti-4.3Fe-7Mo-1.4Al-1.4V-5.4B
17	Ti-2Co-2Mo-1.4Al-1.4V-1.8B

Figure 1. Cost analysis plot for candidate Ti alloys.

Ti Alloy Design

Ti alloys can be a predominant monophase structure; hexagonal close-packed (hcp) or body-centered cubic (bcc), or a dual phase structure $\alpha + \beta$, depending on the composition strength ratio between the hcp stabilizing elements and bcc stabilizing elements. Figure 2 schematically illustrates the main properties of potential Ti alloys falling in different crystallographic classes. Alpha alloys only enclose traces of beta phase. Near-alpha alloys contain predominantly alpha,

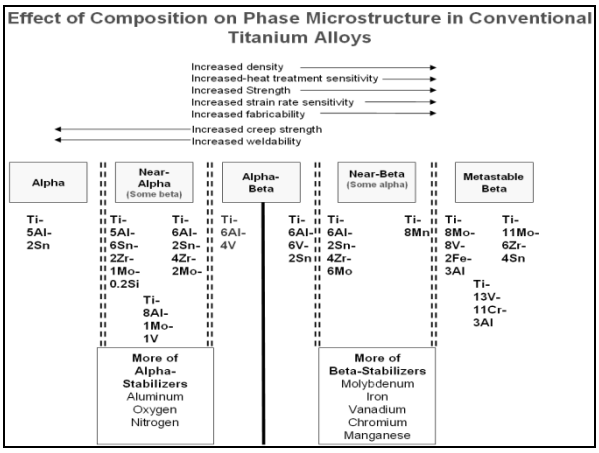

Figure 2. General classification of titanium alloys with respect to properties and microstructure.

and the microstructure may appear similar to that of an alpha alloy. A dual phase alpha-beta alloy consists of alpha and retained or partially transformed beta phases. Metastable beta alloys consist of predominantly retained beta, which is susceptible to a fine transformation upon post-heat treatments. All of these alloys are used for applications where temperatures are less than 600°C, although the melting temperature is higher than that of typical steel. The thermal expansion coefficient is less than half that of Al.

Based on our research, we recommend starting with the following three alloy compositions for generating the eutectic systems.

1. Ti- (2 to 3%)Fe- (3% to 6%)Zr- (2% to 4%)Sn- (1% to 3%)Mo- (0% to 1%Cr)
2. Ti- (2 to 3%)Fe- (3% to 6%)Zr- (2% to 4%)Sn- (2% to 3%)Mn- (1 to 2%)Mo- (0% to 1%Cr)
3. Ti- (2 to 3%)Fe- (3% to 6%)Zr- (2% to 4%)Sn- (2% to 3%)Mn- (1 to 2%)Mo- (2% to 5%)Cr3C2

Currently we have purchased these powders for evaluating the proposed Ti alloy compositions. The evaluation will be performed through powder mixing, die compaction, sintering, and mechanical property measurement. Figure 3 shows the optimization algorithm for liquid phase sintering of Ti alloy powder.

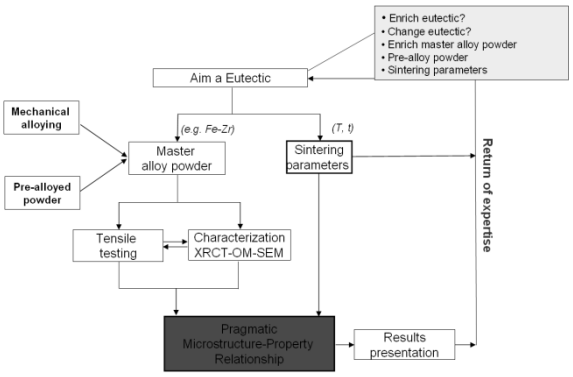

Figure 3. Composition optimization algorithm for liquid phase sintering of Ti alloy powder.

As for the PIM, we prepared PIM feedstock based on the standard wax-polymer binder system with 50% solid loading percentage. Now we are measuring the viscosity using a homemade capillary rheometer to obtain the material properties for the simulations.

Experimental Evaluation of Designed Ti Alloys

In this research, three different Ti powers are used as shown in Figure 4: (1) sponge (DuPont), (2) HDH (Phelly Materials), and (3) gas-atomized powders (Sumitomo Corporation). To evaluate the designed Ti alloys described in the previous section, we also purchased additive elements such as iron (Fe), molybdenum (Mo), zirconium (Zr), tin (Sn), manganese (Mn), chromium (Cr), and chromium carbide (Cr_2C_3).

We evaluated 15 Ti alloys as shown in Table 4 and selected 6 Ti alloys according to the following criteria (in order).

1. Higher sintered density using liquid phase sintering (LPS) cycle.
2. Clear endothermic peak for LPS (see Figure 5).
3. Cost of Ti alloys.

Based on the 6 selected Ti alloys, we proposed 16 Ti alloys with more/different combinations of additive elements. We measured the mechanical properties of the 16 Ti alloys, including sintered density, hardness, ultimate tensile strength, and

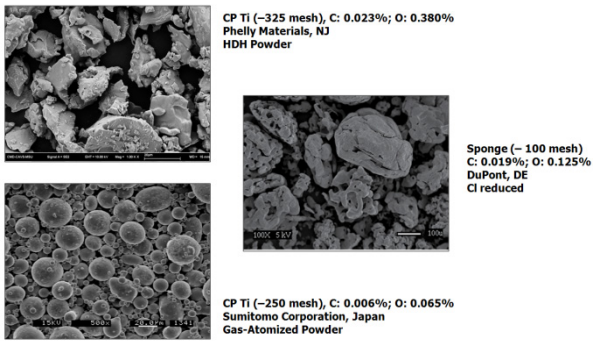

Figure 4. SEM images for three Ti powders used in this research.

Table 4. Ti alloys evaluated and selected.

ID No.		Ti	Fe %	Mo %	Zr %	Sn %	Mn %	Cr %	Cr_2C_3 %
1		97.0	1.5	1.5					
2		94.0	3.0	3.0					
3	selected	94.5	1.5	1.5	2.5				
4		89.0	3.0	3.0	5.0				
5	selected	93.0	1.5	1.5	2.5	1.5			
6		86.0	3.0	3.0	5.0	3.0			
7		91.5	1.5	1.5	2.5	1.5	1.5		
8	selected	83.0	3.0	3.0	5.0	3.0	3.0		
9		90.5	1.5	1.5	2.5	1.5	1.5	1.0	
10	selected	81.0	3.0	3.0	5.0	3.0	3.0	2.0	
11	selected	89.5	1.5	1.5	2.5	1.5	1.5	1.0	1.0
12		79.0	3.0	3.0	5.0	3.0	3.0	2.0	2.0
13	selected	83.0	3.0	3.0	6.0	4.0		1.0	
14		81.0	3.0	2.0	6.0	4.0	3.0	1.0	
15		76.0	3.0	3.0	6.0	4.0	3.0		5.0

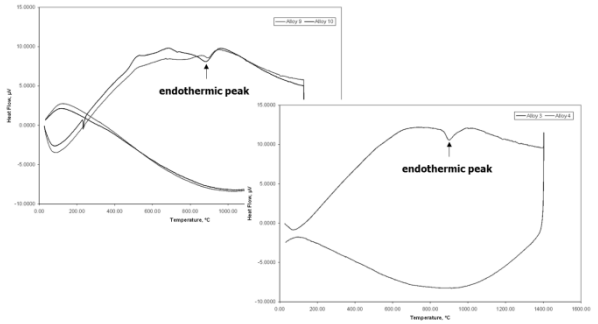

Figure 5. Differential scanning calorimetry experiment for LPS evaluation.

elongation, as shown in Table 5. Finally, we selected Ti-Fe-Zr combinations as candidate Ti alloys.

We focused on microstructural analysis of Ti-Fe-Zr alloys produced by the press and sinter process. Samples were produced by mixing of initial pure metallic powders followed by uniaxial pressing with subsequent densification by sintering at 1,275°C in vacuum. Scanning electron microscopy (SEM) and optical microscopy were used to study

Table 5. Mechanical properties for selected Ti alloys.

Alloy	Density (g/cm³)	Green Sample		Sintered Sample (1275 °C, 60 min, 10 mtorr)				
		Density (g/cm³)	Relative Density (%)	Density (g/cm³)	Relative Density (%)	Hardness (HRB)	elongation (%)	UTS (MPa)
Pure Ti	4.51	3.24	71.8	4.14	91.8	88.1	3.13	643
Ti-5Fe-2.5Zr	4.64	3.26	70.2	4.41	94.9	103.9	3.54	1025
Ti-5Fe-5Zr	4.68	3.29	70.3	4.40	94.0	104.3	2.50	1227
Ti-10Fe-2.5Zr	4.75	3.21	67.6	4.54	95.6	108.1	0.60	611
Ti-10Fe-5Zr	4.79	3.43	71.6	4.77	99.6	112.9	0.00	281
Ti-5Fe	4.61	3.39	73.6	4.30	93.3	101.7		
Ti-10Fe	4.71	3.26	69.2	4.40	93.4	104.5		
Ti-10Fe-2.5Zr-1Cr	4.77	3.21	67.3	4.37	91.7	102.6		
Ti-10Fe-5Zr-1Cr	4.81	3.34	69.5	4.43	92.2	104.4		
Ti-10Fe-2.5Zr-1.5Mo	4.79	3.44	71.8	4.59	95.8	104.8		
Ti-10Fe-2.5Zr-3Mo	4.83	3.41	70.5	4.45	92.0	105.4		
Ti-10Fe-2.5Zr-2Sn	4.79	3.31	69.1	4.44	92.7	104.1		
Ti-10Fe-2.5Zr-4Sn	4.83	3.55	73.5	4.46	92.4	103.4		
Ti-10Fe-2.5Zr-2Cr_2C_3	4.78	3.16	66.1	4.38	91.6	105.2		
Ti-10Fe-2.5Zr-4Cr_2C_3	4.81	3.28	68.1	4.53	94.1	108.3	1.40	373
Ti-10Fe-2.5Zr-1.5Mn	4.78	3.19	66.7	4.32	90.4	101.4		
Ti-10Fe-2.5Zr-3Mn	4.81	3.19	66.3	4.37	90.9	103.7		

the microstructure of the sintered samples. Figure 6 shows the importance of vacuum level in Ti alloy sintering. Hardness and tensile tests were performed for each sample. The results show that as Fe and Zr increase, the theoretical density and mechanical properties increase, as listed in Table 6. The maximum properties of samples were obtained with the addition of 5Fe-5Zr wt % at 1,275ºC for 60 min.

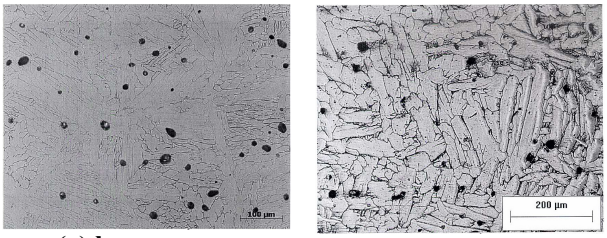

(a) low vacuum **(b) high vacuum**

Figure 6. SEM images of microstructures.

Table 6. Mechanical properties of Ti-Fe-Zr alloys.

Powder	Composition	Density (%)	Strength (MPa)	Elongation (%)	Vacuum (mtorr)
HDH	Pure Ti	91.8	643	3.13	10
	5Fe-2.5Zr	95.0	1025	3.54	
	5Fe-5Zr	94.0	1127	2.50	
Sponge	Pure Ti	94.8	524	4.52	0.3
	5Fe-2.5Zr	96.6	983	3.91	
	5Fe-5Zr	96.4	1067	3.20	

Evaluation of Boride Ti Alloys

As we proposed, the boride Ti alloy is one of the possible candidates for structural materials. We investigated the sintering behavior, the microstructure, and the mechanical properties of Ti-5Fe alloy with boron additions for structural applications, as shown in Figures 7 and 8. Samples were produced by mixing of initial pure metallic powders followed by uniaxial pressing with subsequent densification by sintering at 1,200°C

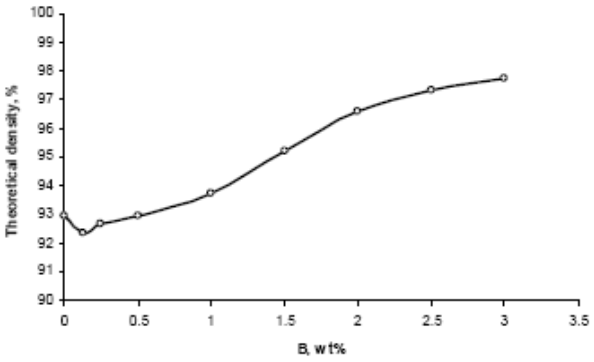

(a) density

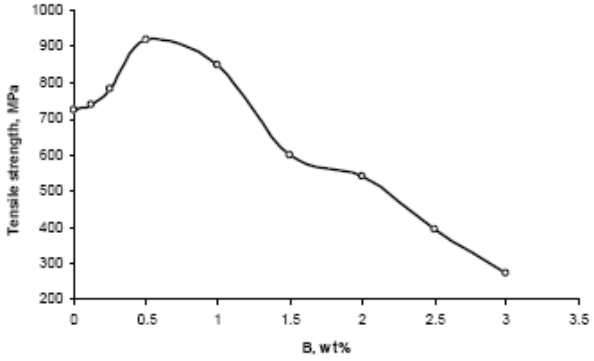

(b) tensile strength

Figure 7. Sintering behavior and mechanical properties of Ti-Fe alloys with boron additions.

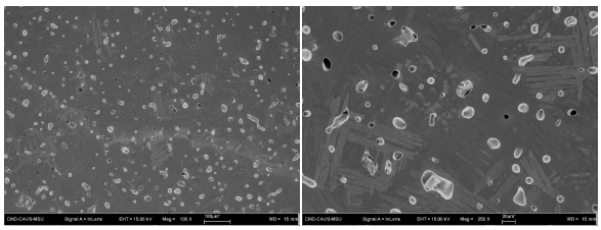

Figure 8. SEM images of Ti-5Fe-0.5CrB_2.

and 1,300°C, in vacuum. SEM was used to study the microstructures of the sintered samples. Hardness and tensile testing were performed for different samples. The results show that with increases of boron the theoretical density and tensile strength and hardness increase but the ductility decreases.

PIM Experiment

Initial trials on injection molding were conducted with the 17-4PH stainless steel feedstock that was readily available (Figure 9). We used a new binder formulation for sponge and HDH Ti powder

Figure 9. Molding trial by Ryer Feedstock (Stainless Steel).

injection molding to avoid formation of TiC as follows:

- 65 wt % paraffin wax,
- 25 wt % low density polypropylene,
- 9 wt % Fusabond,
- 1 wt % stearic acid, and
- 50 vol. % solid loading of –325 mesh Ti-HDH powder as determined by torque rheometer.

Modeling and Simulation

We first compared flow behavior of three different Ti powders, gas atomized, HDH, and spheroidized HDH Ti powders, as shown in Figure 10(a). We obtained the material properties from the literature on HDH Ti powder PIM for PIM simulation using donated PIMsolver, CetaTech, Inc. We selected the tensile specimen as the first geometry. We performed the first analysis simulation [Figure 10(b)], found possible processing windows [Figure 10(c)], and optimized the filling time for minimum injection pressure [Figure 10(d)].

Die Compaction

We obtained all material properties from a compressibility curve [Figure 11(a)] in the literature on commercial purity (CP) Ti powder for die compaction simulation using ABAQUS. We selected the gear as the first geometry. We performed the first analysis simulation [Figure 11(b)]. We have the optimization algorithm for loading schedule for uniform green compact density.

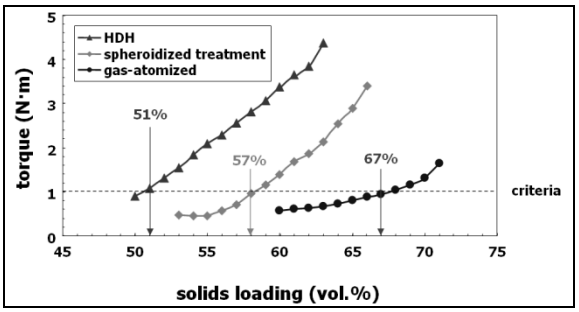

(a) Torque vs solid loading

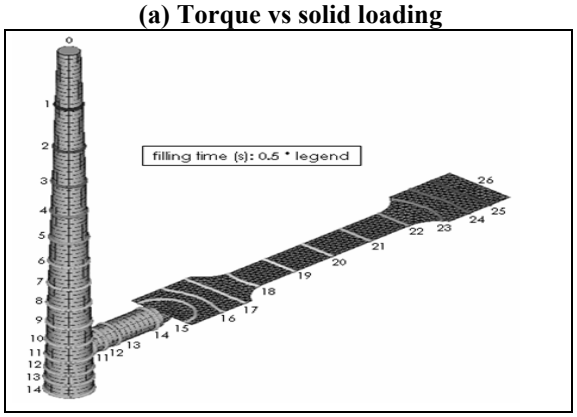

(b) Filling pattern

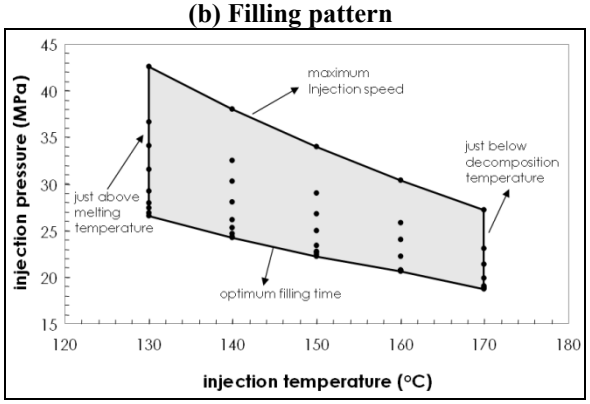

(c) Processing window

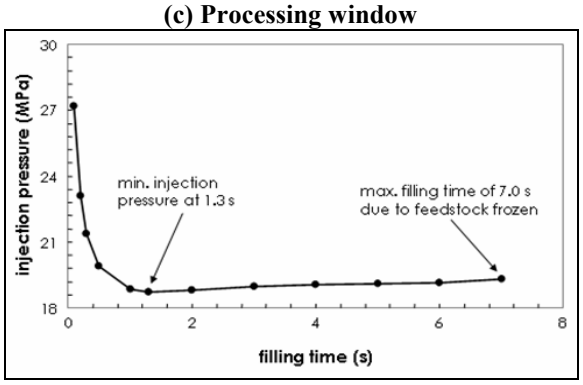

(d) Optimum filling time

Figure 10. The first trial of PIM simulation and optimization with HDH Ti powder.

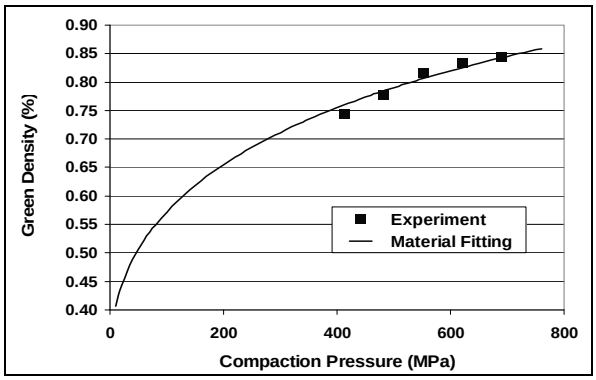

(a) Compressibility curve

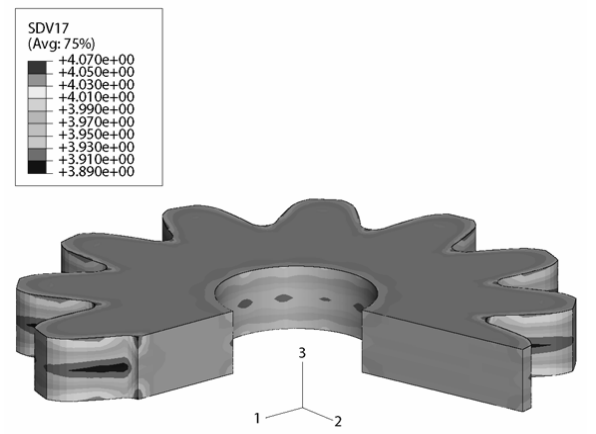

(b) Density distribution after compaction

Figure 11. The first trial of die compaction simulation with CP Ti powder.

Sintering and HIPing

We also have the capability to simulate sintering and HIPing processes. As for the HIPing, we obtained all material properties from creep test with pressure and temperature dependency of Ti-6Al-4V powder and performed simulation for powder and can. In addition, we also have developed the algorithm to optimize can geometry to obtain accurate final HIPed component dimension. But we could not find any Ti powder or Ti alloy powder material properties for simulations for the sintering in the literature.

Conclusions

In the last 6 months, we have accomplished the following:

- completed literature survey for low-cost Ti powder, Ti alloys for automotive application with cost analysis, and their processing techniques;
- designed and evaluated new Ti alloys including boride Ti alloy;
- performed PIM experiment; and
- developed simulation tool for PIM, die compaction, sintering, and HIPing, with some optimization.

Presentations/Publications/Patents

1. S. J. Park et al., "Rheological and Thermal Debinding Behaviors of Titanium Powder Injection Molding," *Metallurgical and Materials Transactions A*, 2008 (accepted).
2. O. Gulsoy et al., "Microstructure and Mechanical Properties of Sponge Ti and Its Alloy Powders with Various Powder Metallurgical Processes," *TMS 2008*, New Orleans, March 9–13, 2008.
3. O. Gulsoy et al., "Investigations on Novel Titanium Alloys for Structural Applications," *PM 2008*, Washington, D.C., June 8–12, 2008.
4. H. O. Gulsoy et al., "Effect of boron additions on microstructural and mechanical properties of Ti-5Fe alloy for structural applications," *5th International PM Conference*, Ankara, Turkey, October 8–12, 2008.
5. O. Gulsoy et al., "Development of Powder Injection Molding Process for Sponge Ti Alloy," *TMS 2009*, San Francisco, February 15–19, 2009.
6. O. Gulsoy et al., "Development of Powder Injection Molding Process for Sponge Ti Alloy," *PIM 2009*, Orlando, Florida, March 2–5, 2009.
7. Patents (in preparation): Three Ti alloy compositions.

C. Powder-Metal Performance Modeling of Automotive Components (AMD410*)

Project Manager: Howard Sanderow
Management & Engineering Technologies
4337 Oaks Shadow Drive
New Albany, OH 43054
(614) 775-0218; fax: (614) 775-0163; e-mail: metgroup@earthlink.net

Principal Investigator: Mark F. Horstemeyer (Paul T. Wang, Youssef Hammi)
Center for Advanced Vehicular Systems Chair in Solid Mechanics & Professor, Mechanical Engineering
Mississippi State University
206 Carpenter Bldg., P.O. Box ME
Mississippi State, MS 39762
(662) 325-7308; fax: (662) 325-7223; e-mail: mfhorst@me.msstate.edu

Russell Chernenkoff (retired from Ford Motor Company)
Metaldyne Sintered Component, Inc.
Metaldyne Powertrain Global Operations and Technical Center
47603 Halyard Drive
Plymouth, MI 48170
(734) 582-6227 ; fax: (734) 582-6250; email: russellchernenkoff@metaldyne.com

Paulo Rosa, Materials Development Engineer
Chrysler LLC
800 Chrysler Drive, CIMS 484-01-07
Auburn Hills, MI 48326
(248) 576-3197; fax: (248) 576-2177; e-mail: pr31@chrysler.com

Shekhar G. Wakade, Technical Specialist Materials Engineering
GM Powertrain
823 Joslyn Ave.
Pontiac, MI 48340
(248) 568-1143; fax: (248) 857-4425; e-mail: shekhar.g.wakade@gm.com

Glen Weber, Technical Specialist Engine Metals
Ford Motor Company
Building #1, Cube 12A037
Dearborn, MI
(313) 322-0175; e-mail: gweber@ford.com

Technology Area Development Manager: Joseph A. Carpenter
(202) 586-1022; fax: (202) 586-1600; e-mail: joseph.carpenter@ee.doe.gov

Field Project Officer: Aaron D. Yocum
(304) 285-4852; fax: (304) 285-4403; e-mail: aaron.yocum@netl.doe.gov

* Denotes project 410 of the Automotive Materials Division of the United States Automotive Materials Partnership, one of the formal consortia of the United States Council for Automotive Research set up by Chrysler, Ford, and General Motors to conduct joint, precompetitive research and development (see www.uscar.org).

Contractor: United States Automotive Materials Partnership (USAMP)
Contract No.: FC26-020R22910 through the DOE National Energy Technology Laboratory

Objective

- Our objective is to develop and experimentally validate math-based models for powder metallurgy component design and performance prediction. We will extend an existing USAMP microstructure-property model from casting to powder metallurgy (PM) for practical application in low strain-rate (design and durability) and high strain-rate (toughness-driven impact-strength) environments. We will use this model to evaluate and optimize an automotive component design (main bearing cap) as affected by materials (ferrous and non-ferrous) and manufacturing processes (compaction and sintering). We will implement this model into various software platforms such as ABAQUS [1]. This model will be robust enough to facilitate the insertion of various lightweight materials (such as aluminum and titanium) for future component applications.

Approach

- Determine current PM standards publications, component design guidelines, manufacturing, and evaluation methodologies. Provide a selection of metal powders that can satisfy design performance requirements, component design guidelines, and manufacturing and testing specifications across industry participants (Task 1).
- Evaluate and develop numerical modeling techniques to predict mechanical properties throughout PM component sections. The transition of current materials/design requirements to advanced structural PM components has created a need to predict the properties of components in all sections of design. In addition, the design processes should consider the least-cost, lowest-mass product designs and reduced development lead-time. We will extend an existing math-based framework with the abilities to predict PM component structures and properties accurately throughout the compaction and sintering processes (section size, density variation, dimensional tolerances, potential for cracking), and with the input of alloys and process parameters (machine functions, tool and powder temperatures, friction and pressure). We will capture the history of a PM part through its pressing, sintering, and life-cycle performance using the developed multiscale methodology. (Task 2).
- Develop component- and vehicle-level testing to validate durability, quality control and performance of PM parts. We will determine quality control process factors (powder properties, press settings, tooling design, and furnace conditions) for PM parts production in terms of their impact on process variations and quality improvement. We will use optimization and statistical techniques to help determine the main factors affecting the final component. We will perform validation experiments considering actual boundary conditions from real processes to fracture the components. (Task 3).
- Manage and report program activities. We will incorporate bi-weekly teleconferences, have two technical review sessions per year and have intermittent meetings throughout the year to report progress and discuss issues. Proper execution of this task will greatly enhance the visibility and the value of this program. Reports generated from this program will follow the guidelines suggested by the Department of Energy (DOE) and United States Council for Automotive Research (USCAR). (Task 4).
- Perform Technology/Commercial transfer throughout the product value chain. To date, there exists limited accountability for major research and development (R&D)/technical institutions to foster the infrastructure to support large-scale applications of PM components. If the auto industry wishes to take advantage of PM's potential weight and cost reduction opportunities, they must nurture PM development through programs sponsored and directed by USCAR. The project team will request the professional support of societies to publish notices of meetings and project information, as released by the project team. (Task 5).

Accomplishments

- Determined the cap eccentricity parameter to complete the powder characterization (represented by a p-q plot) of FC-0205 Ancorsteel powder provided by Hoeganaes and 205Q powders provided by Metaldyne. (Task 2).
- Measured the density distributions of the green and sintered main bearing caps provided by Metaldyne using Immersion Density and Image Analysis. Measured the density distribution of the sintered main bearing cap (MBC) using two-dimensional (2D) X-Ray Computed Tomography. (Task 3).
- Performed springback analysis of the MBC after compaction to measure the dimensional changes and to determine the density distribution out of the die. (Task 2).
- Performed experiments on notched Bridgman specimens to determine the damage at failure using computed tomography. (Task 3).
- Performed an MBC monotonic performance test (loaded to failure) to determine the tensile strength and failure location of the MBC. (Task 3).
- Validated the plasticity/fatigue model on the MBC with the information provided by Metaldyne. (Task 3).
- Performed sensitivity and uncertainty analysis to identify which input parameter contributes more to the overall uncertainty in the compaction model. (Task3).
- Submitted three conference papers at Metal Powder Industries Federation Powder Metal 2008 Conference (MPIF-PM2008). (Task 4).
- Developed several software programs with graphical interfaces to calibrate the model constants for compaction, sintering, performance and fatigue. (Task 4).
- Held a Technology Transfer Training Session for PM end users at Ford Research Laboratory, Dearborn, MI. (Task 4).
- Used the model to optimize the compaction process for a MBC. (Task 4).
- Completed the 2008 semi-annual and annual reports for release to USCAR and DOE. (Task 4).

Work Plan for Remainder of the Project

- Perform sintering analysis of the MBC for the FC-0205 and 205Q powders using experimental data and for an Al alloy using literature data. (January, 2009)
- Correlate the FC-0205 and 205Q sintering data with the models. (January, 2009)
- Validate the sintering simulation results with the experimental results on the MBC. (January, 2009)
- Apply the modeling to lightweight material such aluminum powder using literature data and predict the performance and fatigue property in a MBC. (January, 2009)
- Perform optimization simulations of the MBC. (January, 2009)

Introduction

The objective of this project is to develop and experimentally validate math-based models for powder metallurgy component design and performance prediction.

During the last twelve months, the remaining closed-die compaction tests were conducted on the FC-0205 and 205Q powders to determine the cap eccentricity parameter, which was optimized to determine the shape of the yield surface during powder densification. The completed compaction data were used to generate p-q plots, which define the density value for any stress state and graphically represent the yield surface evolution during compaction. An uncertainty analysis was performed to quantify the overall uncertainty of the outputs due to uncertainties in the input parameters. To identify which input parameter's uncertainty contributes more to the overall

uncertainty, a sensitivity analysis was also conducted.

Regarding the model development, the springback analysis has been performed on the MBC to determine the density distribution out of the die. The density distribution after springback was used as the initial state for the sintering model, as well as the initial state for the performance and fatigue analysis because the density variation during sintering is almost insignificant for steel-based powders.

Performance tests have also been completed for notched Bridgman and MBC samples to determine the damage failure of the sintered MBC under monotonic loading. The performance model material constants were validated by comparing the plastic and damage prediction of the Bridgman notch tensile specimens to the experimental results. A finite-element analysis (FEA) simulation of the monotonic testing of the MBC was completed and validated with the experimental test results.

As such the model correlation and validation for the life cycle analysis will take the information from the after compacted and after sintered processes. The fatigue failure and life was determined using the multistage fatigue (MSF) model developed at the Center for Advanced Vehicular Systems (CAVS).

A preliminary design optimization study was conducted on the MBC to improve density distribution and increase mechanical properties. Some results from this study are included. The compaction model implementation for aluminum MBC was also completed and the results presented.

Finally, several software programs have been developed at CAVS to provide the PM end users a graphical interface for calibrating the model parameters for the compaction, sintering, performance and fatigue processes. This software, along with the experimental and computational work, was presented to PM end users during a technology transfer session in May, 2008.

Powder Characterization

A number of experimental tests were performed to gather the data necessary for characterization and validation of the constitutive equations of the compaction and sintering processes.

To determine the cap eccentricity parameter in the Modified Drucker/Prager Cap Model [2], closed-die compaction tests were performed on cylindrical samples. Compaction tests were performed on several FC-0205 powder cylinders of 0.5-inch diameter with four different fill depths. The cap eccentricity parameter, R, which can be derived from the ratio of axial and radial stresses, was determined with an inverse method by comparing the numerical hoop strains to the measured hoop strains at different location on the die. The radial stress, exerted by the powder on the die wall, was calibrated by modifying the cap eccentricity parameter R in order to fit the strain gage with the highest hoop strain.

By combining the cap eccentricity results with the previous Brazilian, compression and compressibility test results, the failure line and cap surface at different densities were determined. Figure 1 shows the equidensity lines in the hydrostatic pressure (p)—von Mises (q) stress space for the FC-0205 and 205Q powders, which correspond to the evolution of the Modified Drucker/Prager compaction model during densification.

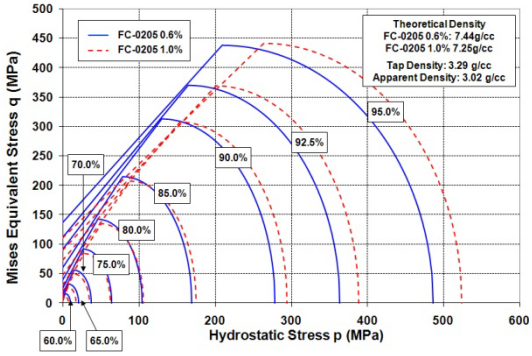

Figure 1. Isodensity curves in the p-q plane representing the evolution of the Cap Model with respect to relative density (% theoretical).

Sensitivity and Uncertainty Analysis

Sensitivity analysis aims to identify which input parameter, such as initial density ρ0, maximum plastic volumetric strain W, or material parameters c1, c2, d1, d2, ρd, R1, R2, ρc and k, contributes more to the overall uncertainty. In the compaction model, we obtain the sensitivities by simply computing the derivatives of the output variables, namely the green density, the interparticle friction, the material cohesion, the cap eccentricity, and the elastic modulus.

Figure 2 shows the sensitivity of the compressibility curve for FC-0205 with 0.6% wax. For all of the output variables, we notice that the most dominant parameter is the initial (or tap) density.

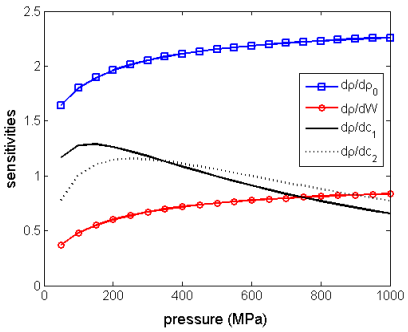

Figure 2. Sensitivity of compressibility curve for FC-0205 with 0.6% Acrawax.

Uncertainty analysis quantifies the overall uncertainty of the output due to uncertainties in the input parameter. To quantify the effect of uncertainties on the material constitutive model, we use uncertainty propagation based on first order Taylor series expansion [3] as given in Eq. (1):

$$VAR(Y) = \sum_{i=1}^{N} \left(\frac{dY}{dX_i} \right)^2 VAR(X_i) \quad , \qquad (1)$$

where *VAR* stands for variance (a measure of uncertainty, square of standard deviation), X_i is the ith input uncertainty, N is the number of uncertain input variables and Y is the output. Since the analytical formulations exist, the uncertainty analysis is computationally inexpensive. If the analytical formulation did not exist and the output parameter calculations were expensive, then we would perform the uncertainty analysis using more efficient techniques {e.g., Dimension Reduction (DR) method + Extended Generalized Lambda Distributions (EGLDs) technique proposed by Acar et al. [4]}.

Figure 3 shows that the most of the FC-0205 material test data falls between the 95% confidence bounds. Notice that the uncertainty in the compressibility curve reduces as the pressure is increased.

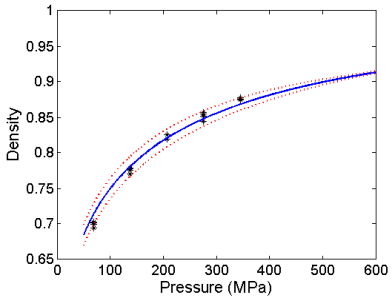

Figure 3. Uncertainty in the compression curve for FC-0205 with 0.6% Acrawax.

Figure 4 depicts the variation of uncertainties in the interparticle friction of FC-0205 as the green density changes. We notice that the effect of the input uncertainties on the interparticle friction is more profound when 1.0% Acrawax is used in the powder. Identically, the increase of the wax in the powder from 0.6% to 1.0% results in a huge uncertainty in the material cohesion.

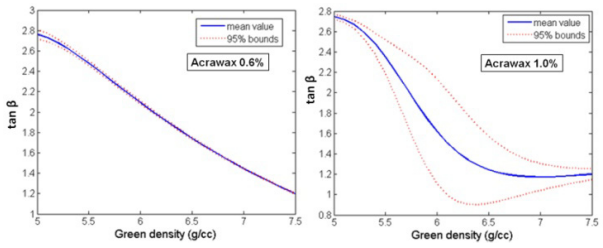

Figure 4. Uncertainty in the interparticle friction for FC-0205 with different Acrawax amounts.

The reason for the significant difference between the results of powder with 0.6% and 1.0% acrawax is due to the higher scattering of failure stress data points in the compression tests of the FC-0205 1.0% Acrawax.

Compaction Modeling

Springback Analysis

Ejection is an important part of the compaction process because it determines the final shape of the unloaded part, with or without cracks. Due to three-dimensional contact nonlinearities between the powder and tools that lead to convergence issues in ABAQUS/Standard, the ejection results presented were obtained by simply removing the tools from the compacted powder to obtain the dimensional and density changes after springback.

For the springback analysis, the material solution of the compacted model (without the tools) was exported from ABAQUS/Explicit, and the appropriate boundary conditions were applied. In this simulation, no further powder densification was considered and the powder compact was assumed elastic at any material point. During the springback analysis, it was calculated that the volume grew approximately 0.6% with most of the dimensional changes occurring along the compacting direction. These results are consistent with the non-uniform density measured in the real PM component after compaction.

Performance Testing and Modeling

Notch Bridgman Test

Monotonic loading of notch Bridgman specimens was performed up to failure. The use of the notch geometry creates stress triaxiality gradients in the specimens allowing for both experimental and numerical methods to be validated. Two different notch radii are chosen for the analysis and labeled as R60 and R150 for notch radii of $R = 0.060$ in and $R = 0.150$ in, respectively. By analyzing the tested Bridgman specimens we studied how different triaxiality conditions influence the damage behavior of the material. Strain-controlled experiments on the notch Bridgman specimens were performed to failure and to 98%, 95%, and 90% of the failure load using an Instron 5882 testing machine with a $\pm$100 kN maximum loading capacity. After testing, the damage in the specimen was analyzed. Results from the tests for the Bridgman specimens revealed that the larger notch root radius exhibited more plasticity than the smaller radius specimens.

Notch Test Validation

The performance model material constants were validated by comparing the plastic and damage behavior of the material with the Bridgman notch tensile specimens to the experimental results. The ratio between one half of the cross-sectional diameter of the specimen at the centre of the notch, a, respect to the notch radius, r. Therefore, R60 has a ratio a/r=0.142/0.06 =2.367 and for R150, a/r=0.142/ 0.075=1.893. Figure 5 presents a comparison between the load- displacement curves obtained experimentally and computationally using the FEA model.

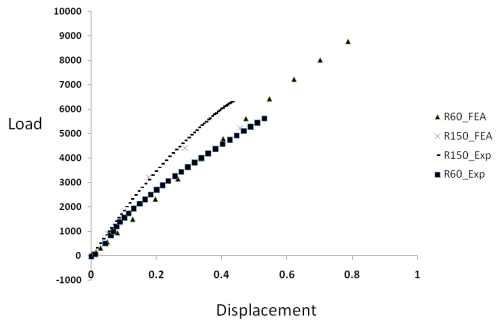

Figure 5. Load displacement comparison for notch Bidgman specimens of the experiment and FEA results.

The model predicts the maximum load and fracture displacement for the R60 specimens. All modeled curves show a very slight variation in the elastic slope, while in the experiments the variation is more noticeable. The stress-strain curves take into account the initial cross-sectional area of the specimen, as well as the area reduction after passing the ultimate strength point. In comparison, the load-displacement plots only reflect the displacement applied to the specimen at certain load. The model predicts satisfactorily the elongation at fracture for the R60 and R150. Damage levels are directly proportional to triaxiality magnitude. Thus, larger levels of triaxiality will not only translate in a greater area where the voids nucleate and evolve, but also these voids will have a larger fracture diameter.

MBC Performance Tests

The tensile strength of a sintered MBC was determined experimentally for validation of the internal state variable (ISV) plasticity-damage

model developed for powder metallurgy materials. The load was applied on both legs of the bearing cap as indicated in Figure 6.

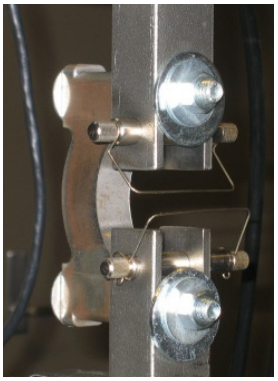

Figure 6. Test fixture and loading application of the MBC.

Initial tests based on strain control indicated some plasticity occurring in the region of test fixture component that connects through the bolt holes of the MBC. Therefore, subsequent tests based on displacement control were performed using a test fixture of a higher stiffness. The MBCs were tested on a 20 kip MTS load frame at a rate of 0.25 mm/s and at room temperature (~273 K) in laboratory air with relative humidity (RH) near 45–60. The MBCs were preloaded to 30 lbf, which ensures the load is applied at the end of the bearing caps. Programming the test, controlling the experiment, and collecting data were performed by using the MTS controller application, Multipurpose Test Ware (MPT). Data acquisition was recorded every 100 ms by MPT with extension, load, and displacement recorded.

The load-displacement data for the monotonic tensile tests of the MBCs is reported in Figure 7. The failure location was basically the same for all the MBCs tested and agrees favorably with test results by Metaldyne [5].

MBC Performance Test Validation

A finite element model for the monotonic load testing of the bearing cap was developed to study the damage state of the bearing cap. Using ISV theory, damage-dependent material parameters are used to capture the location of failure. The material parameters are obtained from the

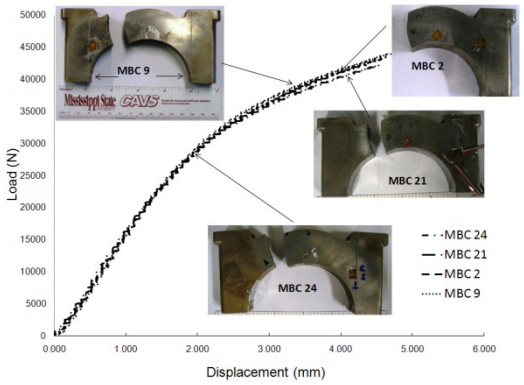

Figure 7. Experimental load-displacement results for MBC and corresponding fractured MBCs.

experimental data and applied to the Bammann-Chiesa-Johnson (BCJ) ISV model. Figure 8 provides a comparison of the FEA simulation results of the monotonic testing with the experimental results. The comparison indicates that the FEA results were very close to those of the experimental results when comparing the strains measured from applied strain gages in the region noted.

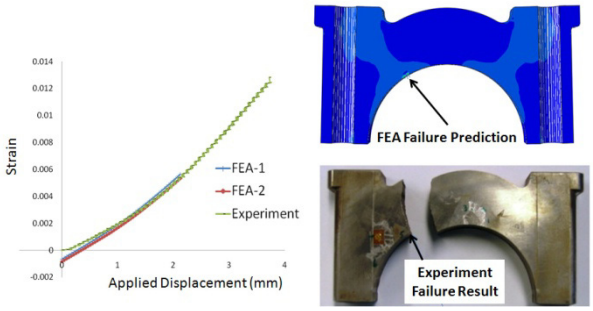

Figure 8. Comparison of strain-displacement results for the FEA model and the experiment test results for the MBC.

Figure 8 shows that the model predicted the exact location where damage initiated in the MBC and not where the greatest von Mises stress existed, as shown in Figure 9. The reason the classical Mises stress does not correctly capture the damage is because it does not account for the heterogeneities arising from the porosity distribution and because damage nucleates, grows, and coalesces more with the stress triaxiality. As discussed previously, the proposed ISV plasticity-damage model captures this effect and therefore correctly predicts the failure location.

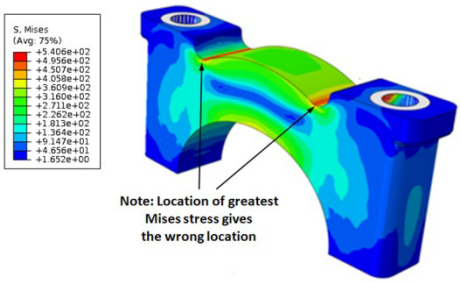

Figure 9. Mises stress distribution for the MBC after performance testing.

Fatigue Modeling

The fatigue analysis is performed on the MBC by modeling the Metaldyne experimental fatigue fixture. A cyclic sine waveform loading was applied onto a shaft, which is connected to the MBC through a half-circular ring. Different maximum loads, from 20,000 to 23,000 lbs, were tested up to 10 million cycles, with a minimum load of 1,000 lbs. The lower and upper bounds of the fatigue life were determined from strain-controlled, low-cycle fatigue tests on samples of, respectively, high and low porosities (Figure 10). The MSF model was applied to predict the fatigue life of the MBC in the FEA [6,7]. Using the fatigue software MSFfit, developed at CAVS, the fatigue parameters were calibrated on the low-cycle fatigue curve and on its extrapolation for the high-cycle regime. The MSF model was implemented into the user subroutine UVARM to generate element output within ABAQUS/Standard.

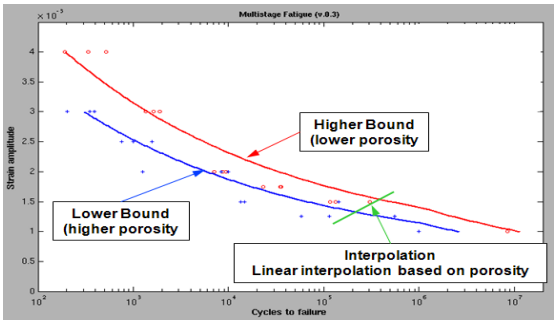

Figure 10. Strain Amplitude vs. Cycle to failure curve for the lower and higher bounds.

Multistage Fatigue (MSF) Model

The MSF approach decomposes fatigue life into four consecutive stages based on the microstructural details of fatigue crack growth based upon, i.e.,

$$N_{Total} = N_{Inc} + N_{MSC} + N_{PSC} + N_{LC} = N_{Inc} + N_{MSC/PSC} + N_{LC} \quad , \qquad (2)$$

where N_{Total} is the total fatigue life. Here, N_{Inc} is the number of cycles to incubate a crack at a micronotch; N_{MSC} is the number of cycles required for propagation of a Micro-structurally Small Crack (MSC); N_{PSC} is the number of cycles required for propagation of a physically small crack (PSC), during the transition from MSC status to that of a dominant long crack (LC). In Equation (2), for simplicity the MSC and PSC regimes are combined into one mathematical form. The number of cycles required for LC propagation is given by N_{LC}, applicable to growth in the range $a >$ 200-800 µm, where a is the crack length, and the crack propagation depends on the amplitude of loading and the corresponding extent of microplasticity ahead of the crack tip.

Fatigue Analysis

The density distribution was mapped from the PM process analysis to define the elastic mechanical properties for each material point of elements. Because the stresses throughout the MBC are within the elastic domain, the MBC is defined by density-dependent elastic properties only. Figure 11 shows the effective strain amplitude Δε

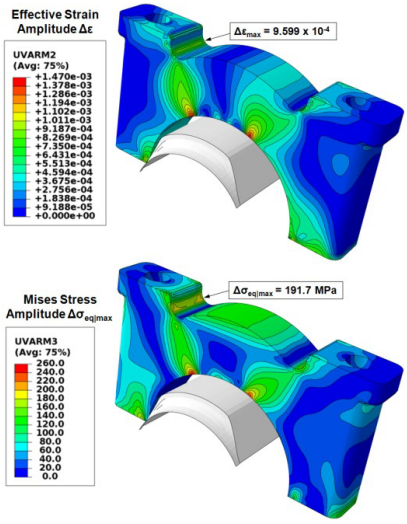

Figure 11. Effective strain and Mises stress amplitudes for a shaft load of 23,000 lb.

and Mises stress amplitude $\Delta\sigma_{eq}$ that are considered in the fatigue model.

The fatigue lives N_{Inc}, N_{SC}, N_{LC} and N_{Total} were calculated using the interpolation based on density of either the fatigue parameters (Interpolation I) or the fatigue lives (Interpolation II) of the lower and upper bounds (Figure 10). The fatigue life N_{Total} is predicted to be near 7.2 million cycles at the location shown on Figure 12 for a shaft load of 23,000 lbs. Low values of N_{Total} around the arch were ignored due to the fact that the contact nodes leads to a certain strain localization.

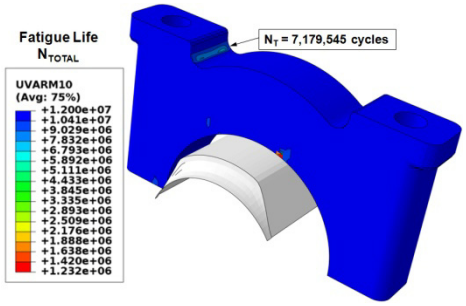

Figure 12. Fatigue life N_{Total} and its location for a shaft load of 23,000 lb.

Table 1 shows the fatigue lives for different shaft loads. Only the solution with heterogeneous density was able to capture the correct prediction. The fatigue test is considered to be successful when the fatigue life is greater than 10 million cycles.

Compaction Modeling for Al MBC

To evaluate material substitution and lightweight materials in the MBC parts, the compaction modeling of a MBC was performed with aluminum material parameters that were calibrated using literature data [8]. The simulation was performed using the exact same tool geometries and motions as the FC-0205 MBC. The density distribution shows the same pattern as for the steel MBC (Figure 13) but the density values are quantitatively much lighter.

Table 1. Fatigue lives for Interpolation I and II at different shaft loads

Higher Bound (Low Homogeneous Porosity)				
Fatigue Life	Shaft Loading (lbs)			
	20,000	21,000	22,000	23,000
N_{INC}	> 10,000,000	> 10,000,000	> 10,000,000	> 10,000,000
N_{SC}	2	2	2	1
N_{LC}	142,942	106,044	79,826	60,890
N_{TOTAL}	> 10,142,944	> 10,106,046	> 10,079,828	> 10,060,891
Failure	PASS	PASS	PASS	PASS

Lower Bound (High Homogeneous Porosity)				
Fatigue Life	Shaft Loading (lbs)			
	20,000	21,000	22,000	23,000
N_{INC}	2,399,554	1,658,665	1,176,098	778,410
N_{SC}	1	1	1	1
N_{LC}	173,956	129,105	97,223	74,187
N_{TOTAL}	2,573,511	1,787,771	1,273,322	852,598
Failure	FAIL	FAIL	FAIL	FAIL

Interpolation I (Heterogeneous Porosity)				
Fatigue Life	Shaft Loading (lbs)			
	20,000	21,000	22,000	23,000
N_{INC}	> 10,000,000	9,902,806	8,341,563	7,109,965
N_{SC}	1	1	1	1
N_{LC}	163,212	121,115	91,194	69,579
N_{TOTAL}	> 10,163,213	10,023,922	8,432,758	7,179,545
Failure	PASS	CRACK	FAIL	FAIL

Interpolation II (Heterogeneous Porosity)				
Fatigue Life	Shaft Loading (lbs)			
	20,000	21,000	22,000	23,000
N_{INC}	> 10,000,000	> 10,000,000	8,553,476	7,485,101
N_{SC}	1	1	1	1
N_{LC}	163,212	121,115	91,194	69,579
N_{TOTAL}	> 10,163,213	> 10,121,116	8,644,671	7,554,681
Failure	PASS	PASS	FAIL	FAIL

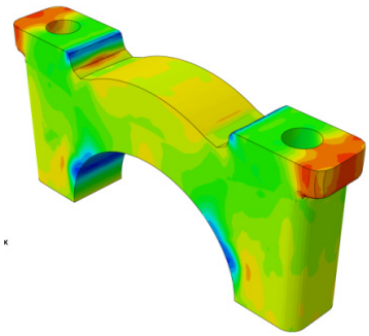

Figure 13. Density distribution for an Al-MBC.

Technology Transfer

Several software programs have been developed at CAVS to provide the PM end users a graphical interface for calibrating the model parameters for the compaction, sintering, performance and fatigue processes.

The software utility for the Modified Drucker-Prager Cap model was developed using experimental data (compressibility, material cohesion, interparticle friction, cap eccentricity, Young's modulus and p-q data) to calibrate the model constants. The software allows the influence of each constant on the P-Q plot to be interactively investigated.

A software utility for calibrating the master sintering curve from dilatometry data was also developed. The software utility for the performance and fatigue processes will be made available to the PM end users after additional verification procedures are completed.

Conclusions

For the Powder-Metal Performance Modeling of Automotive Components project, determination of the microstructure-property relations and parameter calibration was completed for compaction model. The ejection feature represented by a springback analysis was performed on a MBC, giving the initial density distribution that was used for the preliminary fatigue fixture analysis of the MBC. Model simulation of the fatigue failure and life of the MBC were also evaluated and validated based on favorable comparison to the experimental test results. These results will be considered for better design, performance and mass optimization. Regarding the sintering model, additional dilatometer tests were performed to measure the dimensional changes of green compacts that have relatively the same green density as the green MBC. Finally, the compaction and sintering property database on aluminum was collected from another DOE project in order to evaluate material substitution and lightweight materials in the MBC parts, and the compaction model prediction was presented.

Publications

1. P. Allison, M. Horstemeyer, Y. Hammi, and H. Brown. 2008, "Stress-State Dependence of FC-0205 Steel Powder," MPIF/APMI 2008 World Congress on Powder Metallurgy & Particulate Materials, June 8–12, Washington, D.C.
2. Y. Hammi, T, Stone, L. Arias-Meza, P. Allison, and M. Horstemeyer. 2008, "Modeling for Powder Metallurgy Component Design and Performance Prediction," MPIF/APMI 2008 World Congress on Powder Metallurgy & Particulate Materials, June 8–12, Washington, D.C.
3. T. W. Stone, L. Arias-Meza, T. N. Williams, Y. Hammi, H. El Kadiri, and M. Horstemeyer. 2008, "Comparison of Density Measurement Techniques for Large PM Components," MPIF/APMI 2008 World Congress on Powder Metallurgy & Particulate Materials, June 8–12, Washington, D.C.

Acknowledgements

The authors would like to acknowledge funding from the Center for Advanced Vehicular Systems at Mississippi State University and from USAMP Advanced Materials Division (AMD) 410. We thank Michael O'Neill, Ernie Bertolasio and Edmund Ilia from Metaldyne Sintered Components for all the information and material samples they provided us.

References

1. Abaqus, User's Manual, Version 6.7, Hibbit, Karson & Sorensen, Inc., 2006.
2. O. Coube and H. Riedel. 2000, "Numerical Simulation of Metal Powder Die Compaction with Special Consideration of Cracking", Powder Metallurgy, Vol. 43, No. 2, pp. 123–131.
3. H. S. Ang and W. H. Tang. 2006, "Probability Concepts in Engineering: Emphasis on Applications to Civil and Environmental Engineering," 2nd Edition, Wiley.
4. E. Acar et al. 2008, "Uncertainty analysis of damage evolution computed through microstructure property relations," Proceedings of the ASME IDETC/CIE 2008, August 3–6, New York City, New York, USA.
5. E. Ilia et al. 2003, "Development of a Main Bearing Cap For an Inline 6 Cylinder Engine," Proceedings of the 2003 International Conference on Powder Metallurgy &

Particulate Materials, June 8–12, Las Vegas, NV, USA.

6. D. L. McDowell et al. "Microstructure-Based Fatigue Modeling of Cast A356-T6 Alloy," Engineering Fracture Mechanics, Vol. 70, pp. 49–80, 2003.
7. Y. Xue et al. 2007, "Microstructure-based multistage fatigue modeling of a 7075-T651 aluminum alloy," Engineering Fracture Mechanics, Vol. 74, pp. 2810–2823.
8. S. C. Lee and K. T. Kim. 2002, "Densification behavior of aluminum alloy powder under cold compaction", International Journal of Mechanical Sciences, Vol. 44, pp. 1295–1308.

D. Examining Fundamental Mechanisms of Tooling Wear for Powder Processing

Principal Investigator: Seong Jin Park
Associate Research Professor
Center for Advanced Vehicular Systems, 2215
Mississippi State University, P.O. Box 5405
Mississippi State, MS 39762-5405
(662) 325-8565; fax: (662) 324-4001; e-mail: sjpark@cavs.msstate.edu

Co-Principal Investigator: Youssef Hammi
Center for Advanced Vehicular Systems
Mississippi State University, P.O. Box 5405
Mississippi State, MS 39762-5405
(662) 325-5452; e-mail: yhammi@cavs.msstate.edu

Co-Principal Investigator: Haitham El Kadiri
Assistant Research Professor
Center for Advanced Vehicular Systems
Mississippi State University, P.O. Box 5405
Mississippi State, MS 39762-5405
(662) 325-5568; fax: (662) 617-4790; e-mail: elkadiri@cavs.msstate.edu

Co-Principal Investigator: Paul T. Wang
Manager, Computational Manufacturing and Design
Center for Advanced Vehicular Systems
Mississippi State University, P.O. Box 5405
Mississippi State, MS 39762-5405
(662) 325-2890; fax: (662) 325-5433; e-mail: pwang@cavs.msstate.edu

Co-Principal Investigator: Anthony Antonyraj
Assistant Research Professor of Materials Science
Center for Advanced Vehicular Systems
Mississippi State University, P.O. Box 5405
Mississippi State, MS 39762-5405
(662) 325-8558; email: aanton@cavs.msstate.edu

Technology Area Development Manager: Joseph A. Carpenter
(202) 586-1022; fax: (202) 586-1600; e-mail: joseph.carpenter@ee.doe.gov

Field Project Officer: Aaron D. Yocum
(304) 285-4852; fax: (304) 285-4403; e-mail: aaron.yocum@netl.doe.gov

---

Contractor: Mississippi State University (MSST)
Contract No.: 4000054701 through the National Energy Technology Laboratory

---

Objective

- Develop an innovative design of tooling surfaces and novel lubricants for processing ferrous and lightweight materials.

Approach

- Productivity and performance of powder metallurgy (P/M) parts rely on the behavior of a surface oxide, which by nature is a dispersion-strengthened product. This work plans to use coated powders to provide an opportunity to control tool friction, surface reactions, and component strength. This research will apply new tools to the old problem of aluminum P/M. It relies on powder changes, alloying and processing optimization to produce nearly full-density products with complex shapes and dimensional precision. The work is fundamentally new, since very little efforts have been focused on moving forward the lightweight automotive components fabricated by P/M for meeting desirable property levels, as comparable with traditional ferrous P/M. Significant progress is expected in the key areas, such as the optimal particle size distribution, powder coatings, active lubricants, and computer simulations.

Accomplishments

- Developed a new methodology to quantify tool wear for die compaction in the mold using silicon rubber.
- Proposed a new integral equation to quantify tool wear from numerical simulation results.
- Characterized the effect of lubricant on tool wear.
- Obtained industry sponsor in-kind support, including CetaTech and CM Furnaces.
- Published six journal papers and eleven conference papers related to this task.
- Produced two students with Master degree through this task.
- Worked with Oak Ridge National Laboratory (ORNL) wear test facility, through the High Temperature Materials Laboratory (HTML)/ORNL user program
- Developed full design and optimization algorithms

Introduction

P/M techniques are widely used to fabricate complex automotive components from ferrous powders. The energy efficiency and cost attributes of P/M are recognized by the domestic automotive industry. With the push for lighter-weight, higher-strength and more- durable structures, the barriers to lightweight P/M in domestic automobiles needs to be addressed. Besides economics, the technical barriers are: tool wear, performance and ductility at high strain rates (related to crashworthiness). In this work, we use aluminum (Al) powders to demonstrate the development of tooling wear control technology. Similar methodology could be applied to other lightweight powders such as titanium (Ti).

Current Progress Based on Schedule Planned

Table 1 shows the current progress based on the schedule planned. All subtasks have been accomplished, and the final report is presented here.

Table 1. The proposed project schedule with marks of progresses.

Subtasks	Year 1				Year 2			
	Q1	Q2	Q3	Q4	Q1	Q2	Q3	Q4
5.1 Perform thorough literature review to strengthen the quantitative goals in terms of materials and processes	100							
5.2 Create first FEM simulations to establish a context for the research	100							
5.3 Design Experiment in terms of Al powders, additives, lubricant for tool wear and high strength alloy	100							
5.4 Perform compaction and sintering trials to evaluate whole processes with new alloys		100						
5.5 Develop experimental techniques for quantifying tool wear		100						
5.6 Develop a constitutive relation for tool and FEM simulation tool					100			
5.7 Perform mechanical testing including tensile test, three-point bending, and hardness					100			
5.8 Perform microstructure evaluation by SEM testing of the final sintered product and fracture surface analysis						100		
5.9 Employ computer simulations to optimize learning and rapidly advance research						100		

Summary of the Progress

This project (referred to as Task 5 within the MSST lightweighting materials projects) comprises three research categories: die-wear measurement, aluminum-alloy evaluation, and modeling and simulation for tool wear.

Characterization Tool Surface Quality

We established a new methodology to quantify tool wear during die compaction (Figure 1a) through a nondestructive method using RepliSet

(Figure 1b) and a TalySurf profilometer (Figure 1c).

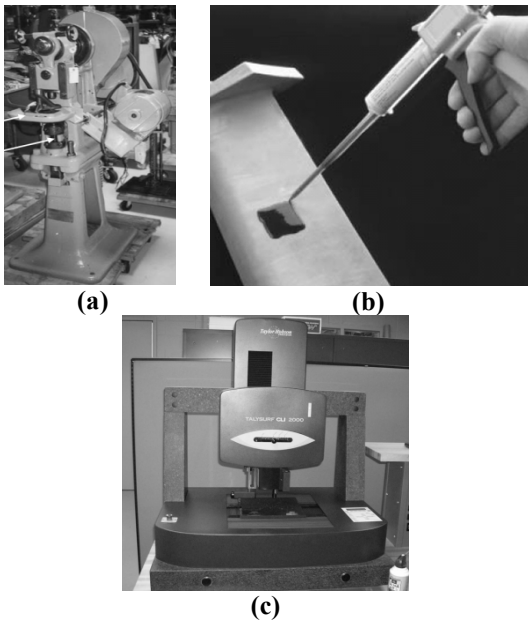

Figure 1. Establishment of new methodology to quantify tool wear: (a) compaction machine with die for wear measurement, (b) RepliSet (silicon rubber and shot gun) and (c) TalySurf profilometer for surface measurement.

Once the methodology was set up, we calibrated a silicon rubber technique and found that its resolution was ±0.5 μm. We measured tool wear with three die-tool materials and four different powders including die diameter, die weight, surface roughness and so on for quantifying tool wear. In addition, the microstructure was evaluated using scanning electron microscopy (SEM), as shown in Figure 2.

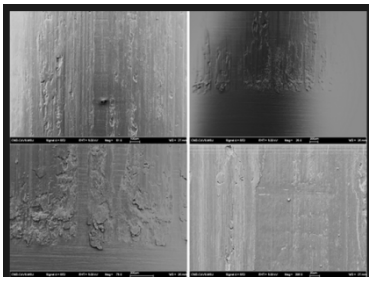

Figure 2. SEM image of silicon rubber surface to investigate ability of transcription of RepliSet.

Tribological Measurement for Tool Wear

By collaborating with ORNL, tribological experiments were designed to obtain specific material properties within minimized time and cost. In this study, two methods (1) a modified pin-on-flat test and (2) a continuous-loop abrasion test, were employed to observe wear occurring on die materials, as shown in Figure 3. Figure 4 shows microscopic images from these tribological

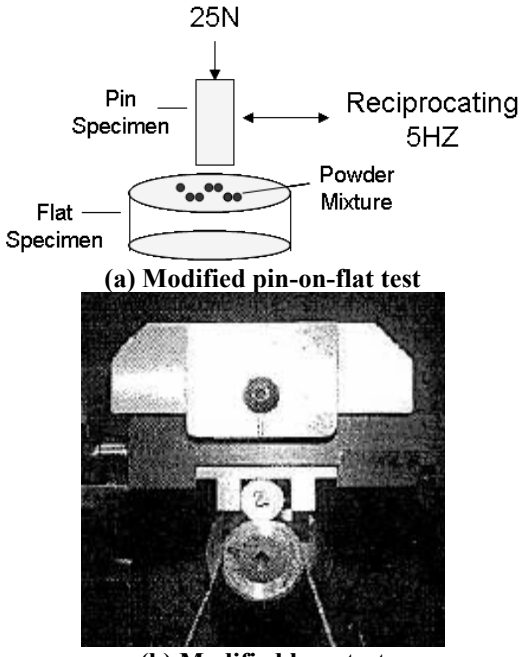

Figure 3. Tribological experiments.

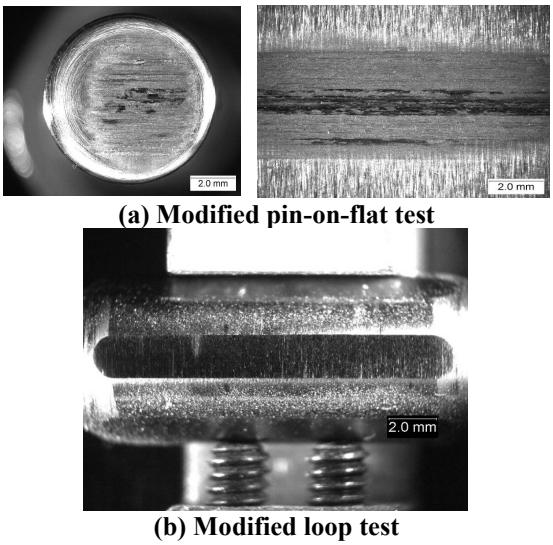

Figure 4. Microscopic images from tribological experiments.

experiments. The quantification of wear was based on the mass-loss measurement, dimensional-change measurement, and dimensional-change calculation. From these measurement results, we obtained *k* values for Archards' Law of wear as shown in Figure 5, which was used for finite-element model (FEM) simulations.

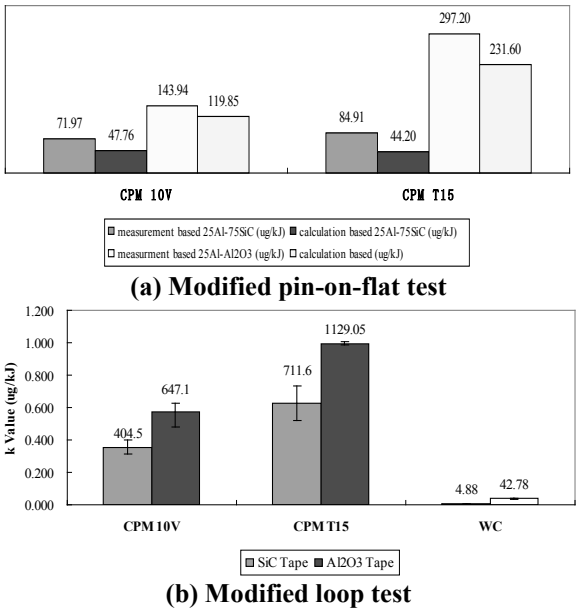

Figure 5. *k* values for Archards' Law of wear from tribological experiments.

Automatic Compaction Experiment for Tool Wear

Automatic compaction was used to simulate the industrial production process. To observe the effect of wear of the Al-SiC and Al-Al_2O_3 powder mixtures on tooling in an industrial environment, a table-size press was used with a tungsten carbide BC-14S die, while top and bottom punches were made from M4 tool steel. Cylindrical compacts with a diameter of 6.35 mm and a height of approximately 4.5 mm were compacted at a rate of approximately 70 compacts per minute. The bottom punch was adjusted to hold a filling height of 7.8 mm. The upper punch stroke length was calibrated to achieve green compact relative densities of 80% theoretical. For each of the powder mixture compositions, 30,000 samples were compacted. We then evaluated the effects of the amount of hard additives, the number of operations, and the amount of lubricants as shown in Figure 6.

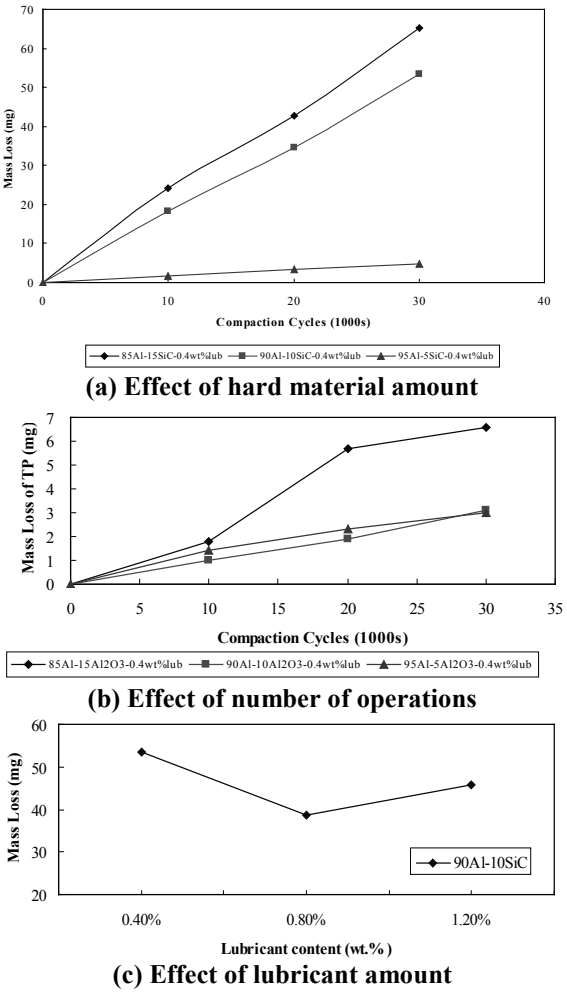

Figure 6. Tool wear measurement through automatic die compaction.

Material Design for Al alloys

We tried to improve mechanical properties of Al alloys. We designed eight Al-based alloys and added Al 6061 powder (Atmix, Japan), recently commercialized using rapid solidification technology. Physical and mechanical properties were measured (density, hardness, tensile strength, elongation and transverse rupture strength) after alloyed samples went through press and sinter processes. We used four control parameters: die compaction pressure, heating rate, sintering temperature, and holding time. Figure 7 shows comparison of transverse rupture strength (TRS) for all Al alloys used in this study.

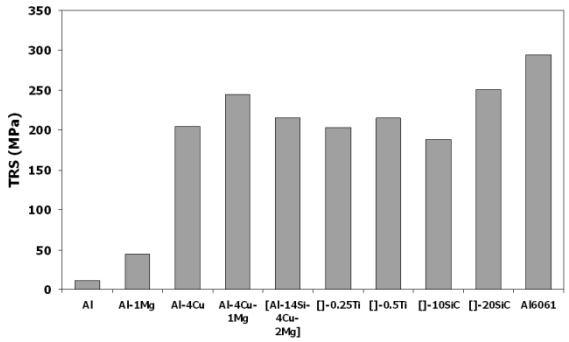

Figure 7. TRS for all Al alloys used in this study.

Bio-Inspired Design for P/M Materials

We developed a new material design by mimicking bamboo, which has a cellular, layered, and fibrous microstructure. These features offer lightweight, high compressive strength and flexibility, which are pre-requisites for superior performance of any automotive component. A finite-element simulation model was developed for three-point-bending test of aluminum alloy with consideration of the effect of porosity on Young's modulus. The results show the bio-inspired design with 30% of porosity has the most beneficial in the strength-to-weight ratio, as shown in Figure 8. We tried several experiments for feasibility study, as shown in Figure 9.

Modeling and Simulation

We used Shima and Oyane model and PMsolver (Cetatech, Inc., Sacheon, Korea) to determine a curve fit for compressibility experimental data of green density versus compaction pressure and simulate die compaction process. The model employs a generalized form of the yield criterion for compaction as follows:

$$\Phi = \left(\frac{q}{\sigma_m}\right)^2 + \alpha(1-D)^{\gamma}\left(\frac{p}{\sigma_m}\right)^2 - D^m$$

where D is the relative density, q is the effective stress, p is the hydrostatic pressure, σ_m is the flow stress of the fully-dense material and α, γ, and m are material parameters. Parameters α, γ, and m are determined by fitting yield-stress data from uniaxial cylindrical compression tests over a range of relative densities. The flow stress, σ_m, of the fully-ense material includes work hardening via a

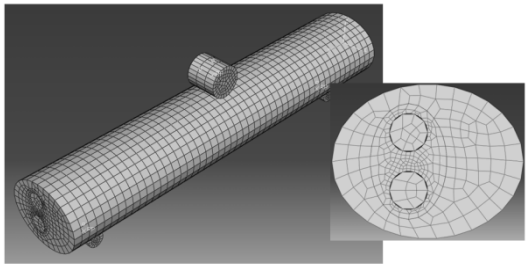

(a) Mesh for three-point bending

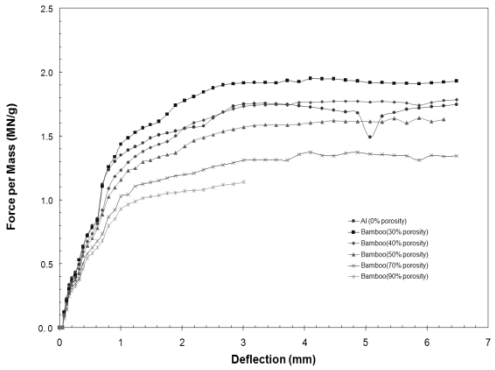

(b) Force per mass plot

Figure 8. Three-point-bending simulation with bamboo-like microstructure.

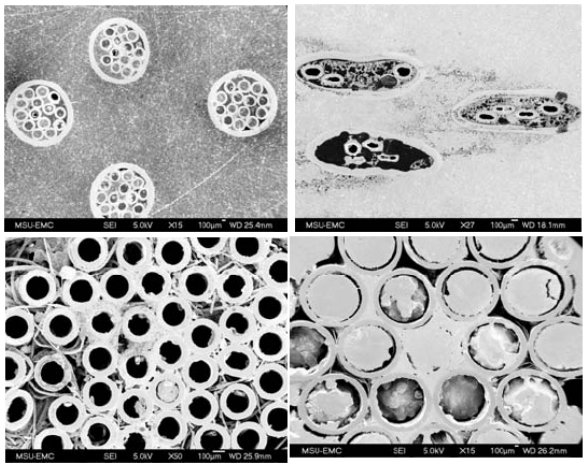

Figure 9. Bamboo-like microstructure of Al and stainless steel.

simple power-law strain relation defined as follows:

$$\sigma_m = a + b\bar{\varepsilon}_m^n$$

where a, b, and n are material parameters and $\bar{\varepsilon}_m$ is the effective strain of the fully-dense material. Figure 10 shows the curve-fitted model for FEM simulation with the amount of lubricant effect.

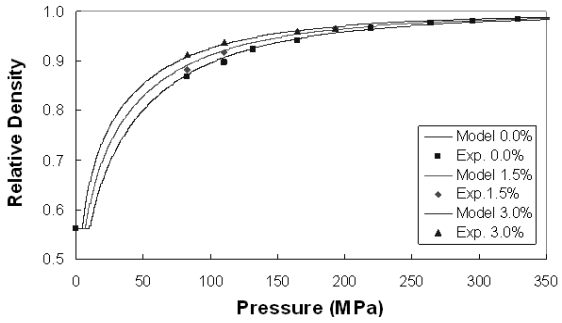

Figure 10. The effect of the amount of lubricant on compressibility of die compaction.

In order to take advantage of our simulation capability, we proposed a new concept of wear work in an integral form based on FEM simulation results of die compaction and ejection.

$$M = H(k_1 S_1 + k_2 S_2)W$$

and

$$W = \int_t \mu \int_A \sigma_n dA v dt$$

where M is the amount of tool wear, H is the Vickers hardess number of tool material, k is the proportional constant, S is the surface area of compact contacted with die tool, subscript 1 is for Al powder and 2 is for hard additives such as alumina (Al_2O_3) or silicon carbide (SiC), W is the wear work, μ is the friction coefficient, σ_n is the normal stress to die tool surface, A is the surface area, v is the velocity of the powder compact and t is the time. We applied this wear work definition to develop FEM simulation tools for die compaction and ejection with experiment validation to investigate the effect of friction coefficient as shown in Figures 11 and 12.

Sensitivity Analysis and Optimization

We performed sensitivity analysis to wear work for five design variables:

- The amount of SiC as hard additives: 2 to 10 kJ/wt%
- The amount of Al_2O_3 as hard additives: 2 to 14 kJ/wt%
- The amount of lubricant: -80 to -150 kJ/wt%
- A fixed friction coefficient: 12 kJ/wt%
- The punch speed of die compaction: 10 to 40 kJ/(m/s)

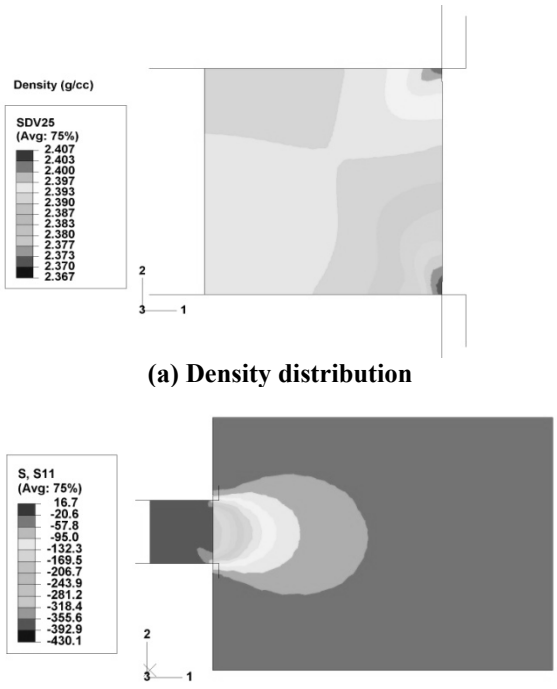

(a) Density distribution

(b) Stress distribution with die tool deformation

Figure 11. FEM simulation result.

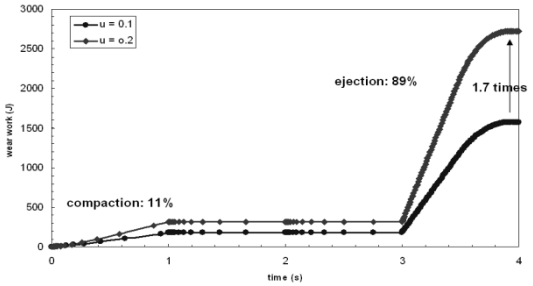

Figure 12. The effect of die compaction and ejection stage with different friction coefficient on tool wear.

To perform the optimization, we need a multi-objective function, including minimization of tool wear, maximization of mechanical property, and minimization of density uniformity; those could be defined based on the user's interest. For each objective function, we needed material parameters to quantify it. Figure 13 shows one example of die-compaction process optimization to maximize density uniformity.

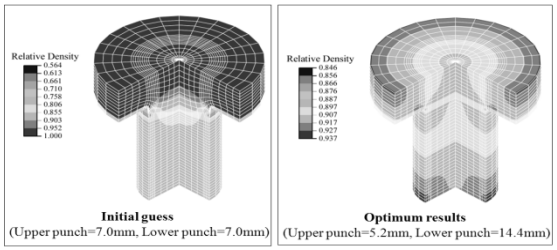

Figure 13. Loading schedule optimization for maximizing density uniformity.

Conclusions

We have accomplished the following tasks:

- Developed a new nondestructive methodology to quantify tool wear for die compaction in the mold using silicon rubber.
- Proposed a new integral equation to quantify tool wear from numerical simulation results.
- Verified the proposed new integral equation to quantify tool wear by automatic compaction experiments and tribological experiments.
- Further studied the impact of lubricant on tool wear.
- Published six journal papers and eleven conference papers related to this task.
- Graduated two students with Master's degrees through this task.

Presentations/Publications/Patents

Journal papers:

1. S. H. Chung, Y.-S. Kwon, S. J. Park, and R. M. German, "Sensitivity Analysis by the Adjoint Variable Method for Optimization of the Die Compaction Process in Particulate Materials Processing," Submitted for publication to ASME J. Eng. Mater. Tech., 2007. (submitted)
2. F. Findik, A. Antonyraj, S. J. Park, and R. M. German, "Investigation of Sintering Behavior and Mechanical Properties of Al P/M Alloys by the Addition of Cu and Mg," *Powder Technology*, 2008. (submitted)
3. F. Findik, A. Antonyraj, S. J. Park, and R. M. German, "Mechanical Properties of Sintered Aluminum Alloys Containing Si, Cu, Mg, Ti, and SiC," *Powder Technology*, 2008. (submitted)
4. J. K. Thompson, W. Li, S. J. Park, A. Antonyraj, F. Findik, and R. M. German, "Utilization of Silicon Rubber to Characterize Tool Surface Quality During Die Compaction," *Powder Metallurgy*, 2008. (accepted)
5. W. Li, P. J. Blau, J. Qu, S. J. Park, and R. M. German, "Tribological Behavior of Die Tool Materials for Powder Metallurgy ," *Powder Metallurgy*, 2008. (under preparation)
6. A. Antonyraj, S. J. Park, and Randall M. German, "Viscoelastic Behavior of Porous Sintered Steels Compact," *Research Letters in Physics*, 2008. (in press)

Conference Presentations:

1. J. K. Thompson, S. J. Park, R. M. German, F. Findik, and A. Antonyraj, **"**Novel Methodology to Quantify Tool Wear in Powder Metallurgy," *Proceedings of the 2007 International Conference on Powder Metallurgy & Particlate Materials (PowderMet 2007)*, complied by John Engquist and Thomas F. Murphy, Metal Powder Industries Federation and APMI International, Princeton, NJ, USA, Part 1, pp. 50–59, Denver, CO, USA, May 13–16, 2007.
2. A. Antonyraj, S. J. Park, and R. M. German, "Thermal Expansion and Viscoelastic Properties of Sintered Porous Ferrous Components," *Proceedings of the 2007 International Conference on Powder Metallurgy & Particlate Materials (PowderMet 2007)*, complied by John Engquist and Thomas F. Murphy, Metal Powder Industries Federation and APMI International, Princeton, NJ, USA, Part 1, pp. 60–69, Denver, CO, USA, May 13–16, 2007.
3. F. Findik, J. K. Thompson, A. Antonyraj, S. J. Park, and R. M. German, **"**Mechanical and Physical Properties of Titanium and Silicon Carbide Containing Mixed Powder Sintered Aluminum," *Proceedings of the 2007 International Conference on Powder Metallurgy & Particlate Materials (PowderMet 2007)*, complied by John

Engquist and Thomas F. Murphy, Metal Powder Industries Federation and APMI International, Princeton, NJ, USA, Part 10, pp. 103–113, Denver, CO, USA, May 13–16, 2007.

4. F. Findik, A. Antonyraj, S. J. Park, and R. M. German, "Investigation of Sintering Behavior and Mechanical Properties of Al P/M Alloys by the Addition of Cu and Mg," *5th International PM Conference*, Ankara, Turkey, October 8–12,.2008.
5. A. Antonyraj, P. Suri, S. J. Park, G. Thibaudeau, R. M. German, B. Brain, and K. Cho "Development Novel Bio-Inspired Design Ferrous Components," *Bio Inspired Design 2008 Conference*, August 19–22, Mississippi State, MS.
6. A. Antonyraj, S. J. Park, G. Thibaudeau, R. M. German, and B. Brain "Fabrication of Bio-Inspired Design Engineering Components by Powder Metallurgy," *Bio Inspired Design 2008 Conference*, August 19–22, Mississippi State, MS.
7. A. Antonyraj, P. Suri, S. J. Park, and R. M. German, "Development and Analysis of Bio-inspired Design Aluminum Composites," *PM 2008*, Washington, D.C., USA, June 8–12, 2008.
8. W. Li, P. J. Blau, J. Qu, S. J. Park, Y. Hammi, and R. M. German, "Prediction of Tool Wear and Tool Life by Experiment/ Modeling/ Simulation of the Die Compaction Process," *PM 2008*, Washington, D.C., USA, June 8–12, 2008.
9. S. Lee, H. Singh, S. J. Park, S. Atre, and R. M. German, "Mapping between Material Design and Properties Using Material Informatics for P/M Simulation," PM 2008, Washington, D.C., USA, June 8–12, 2008.
10. Antonyraj, S. J. Park, R. M. German, P. Suri, W. Morgan, T. Pelletiers, Y. Kato, and I. Otsuka, "Mechanical Properties of Various Aluminum Alloys by Powder Metallurgy," TMS 2008, New Orleans, LA, USA, March 9–13, 2008.
11. A. Antonyraj, S. J. Park, R. M. German, P. Wang, T. Pelletiers, Y. Kato, and I. Otsuka, "Mechanical Properties of Aluminum 6061 Alloys by Powder Metallurgy," TMS 2009, San Francisco, CA, USA, February 15–19, 2009.

5. AUTOMOTIVE METALS—STEEL

A. High-Strength Steel Joining Technologies

Project Manager: Michael S. Bzdok
Auto/Steel Partnership
2000 Town Center, Suite 320
Southfield, MI 48075-1123
(248) 945-4778; fax: (248) 356-8511; e-mail: mbzdok@a-sp.org

Co-chair: John C. Bohr
General Motors Corporation—Conveyors, Controls, Robotics, and Welding
30300 Mound Road, Mail Code 480-109-164
Warren, MI 48090-9015
(810) 602-8276; fax: (586) 947-1039; e-mail: johnc.bohr@gm.com

Co-chair: Eric Pakalnins
Chrysler LLC
800 Chrysler Drive, CTC-CIMS 482-00-11
Auburn Hills, MI 48326-2757
(248) 576-7454; fax: (248) 576-7490; e-mail: ep18@chrysler.com

Technology Area Development Manager: Joseph A. Carpenter
(202) 586-1022; fax: (202) 586-1600; e-mail: joseph.carpenter@ee.doe.gov

Field Project Officer: Aaron D. Yocum
(304) 285-4852; fax (304) 285-4403; e-mail: aaron.yocum@netl.doe.gov

---

Contractor: United States Automotive Materials Partnership (USAMP)
Contract No.: DE-FC05-02OR22910 through the National Energy Technology Laboratory

---

Objective

- Provide welding and joining expertise to support Auto/Steel Partnership (A/SP) project teams in developing lightweight automotive body structures.
- Supplement the existing welding and joining technical knowledge with applied research to facilitate an increased use of Advanced High-Strength Steel (AHSS).
- Utilize A/SP research data to prepare industry weldability and weld quality acceptance standards.

Approach

- Anticipate needs of the A/SP lightweighting projects and conduct applied research to address identified technology gaps.
- Determine welding parameters to produce quality welds, then statically and dynamically test welds produced at these parameters to quantify individual weld structural performance (see Figure 1). Tensile shear strength, impact energy and fatigue life are typically evaluated.

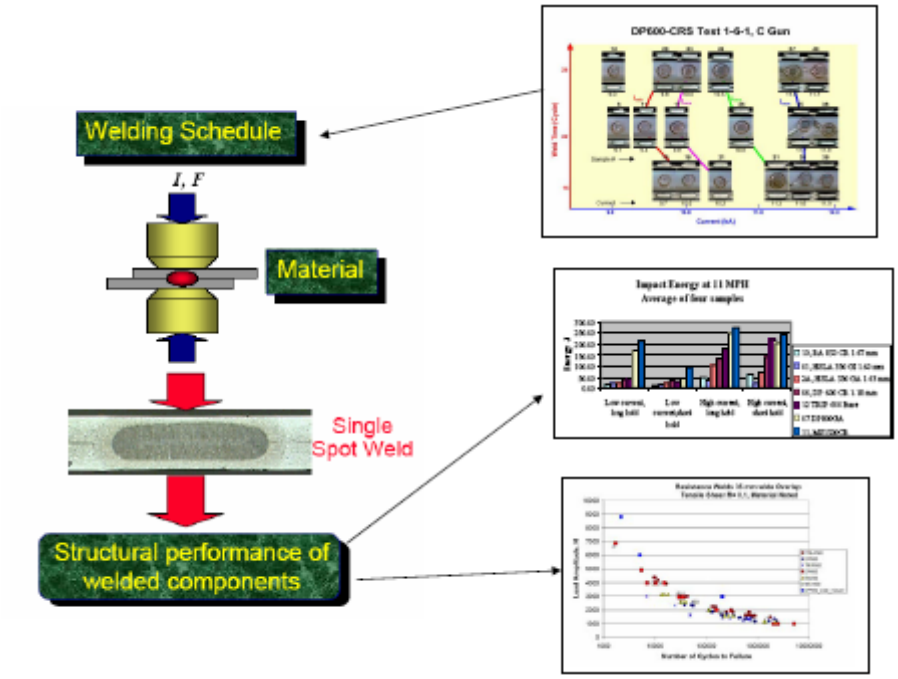

Figure 1. Resistance spot welding (RSW).

- Utilize commercially-available equipment or equipment typically found in existing manufacturing facilities for AHSS feasibility assessments. Utilize other, new technologies as necessary for lightweighting implementation.
- Focus on materials classified as Group 3 and 4 (see Figure 2) as well as specific materials recommended by the A/SP member companies.

Group: Tensile Strength (MPa)	1. Low Strength < 350	2. Intermediate Strength 350–500	3. High Strength > 500–800	4. Ultra High Strength > 800
Typical Materials	Mild 140YS/270TS BH 180YS/300TS BH 210YS/320TS BH 240YS/340TS	BH 260YS/370TS HSLA 280YS/350TS HSLA 350YS/450TS DP 300YS/500TS	DP 350YS/600TS TRIP 350YS/600TS DP 500YS/800TS TRIP 500YS/800TS CP 700YS/800TS	DP 700YS/1000TS MS 950YS/1200TS MS 1150YS/1400TS MS 1250YS/1520TS HS 950YS/1300TS

Note: Steels with a minimum tensile strength above 500 MPa (Groups 3 and 4) are generally considered advanced high-strength steels (AHSSs).

Acronyms: YS = yield strength, TS = tensile strength, BH = bake hardenable, DP = dual phase, HSLA = high-strength, low-alloy, TRIP = transformation-induced plasticity, MS = martensitic steel, CP = complex phase.

Source: International Iron and Steel Institute (IISI), *Advanced High Strength Steel (AHSS) Application Guidelines, 6 June 2006*

Figure 2. IISI steel classifications for welding.

- Investigate the use of process finite-element modeling to predict weld quality characteristics and optimize weld process parameters (see Figure 3). Utilize simulation for future projects to develop weld process optimization and weldability assessments. Validate simulation results with experimental data.

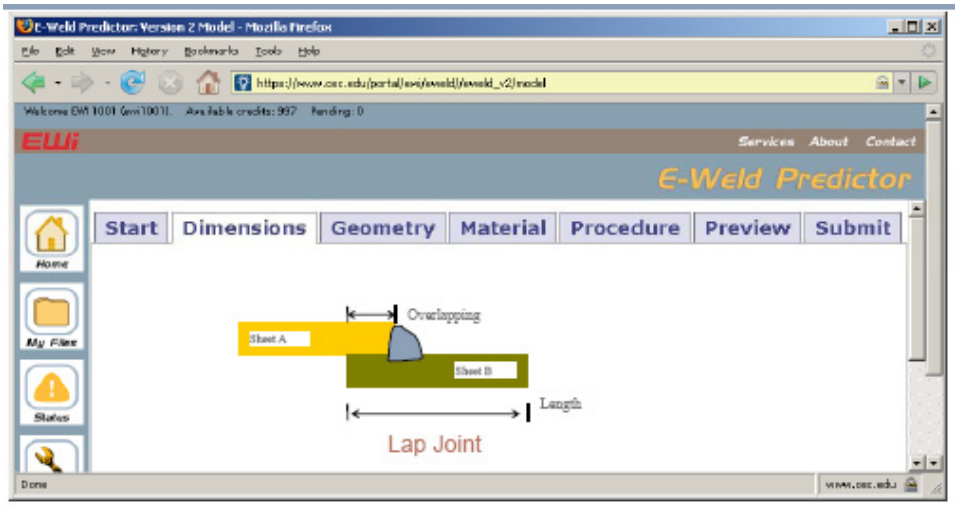

Figure 3. Gas metal arc weld (GMAW) process simulation input.

Accomplishments

- Completed a comprehensive study on joint efficiency that will allow joining process comparisons for weld repair or substitution. Joint efficiency is defined as joint strength/parent material strength. The Joint Efficiency project is intended only to compare processes. Data are also available for energy comparisons and for stiffness comparisons (see Figure 4).

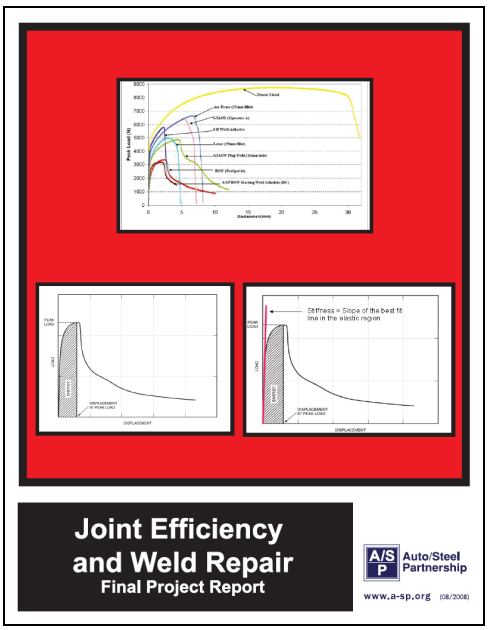

Figure 4. A/SP Joint Efficiency—Phase I final report.

- Created and published a set of arc weld design rules for the Lightweight Chassis Project Team (see Figure 5).

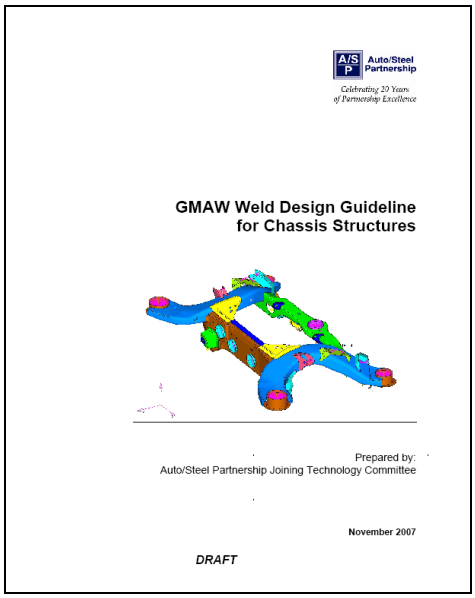

Figure 5. GMAW Weld Design Guideline for Chassis Structures.

- Supported development of an automotive industry AHSS resistance spot weld material characterization [American Welding Society (AWS) D8.9M:200X] and provided technical support for development of a software application to support common deployment and analysis of the AHSS Design of Experiment test method. This American National Standard has started the balloting process heading towards publication (see Figure 6).

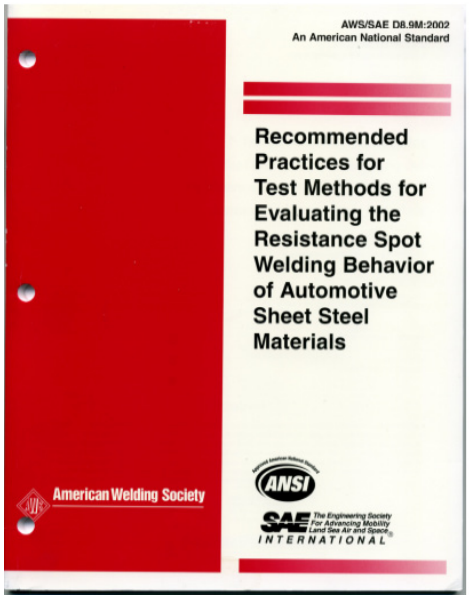

Figure 6. AWS D8.9M:200X.

- Created and published Weld Bond Adhesive Guidelines for the Lightweight Chassis Project Team (see Figure 7).

Figure 7. A/SP Weld Bond Adhesive Guidelines.

- Completed extensive finite-element modeling (FEM) and laboratory experimentation to develop and validate starting resistance spot weld schedules for advanced high strength steel applications (see Figure 8).

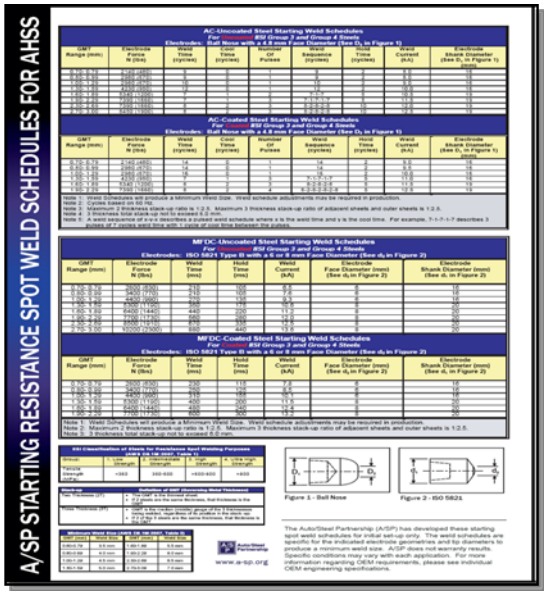

Figure 8. Starting RSW Weld Schedules for AHSS.

Future Direction

- Future team activities include supporting welding development for the A/SP AHSS Application Guidelines Project Team and developing welding parameter and joint performance data for specific applications on AHSS automotive body prototypes. Future project work also includes:
- Develop arc weld procedures for various weld filler metals and AHSS joints, including determining the hot-cracking susceptibility and filler metal compatibility of sheet AHSS materials.
- Develop an FEM application for automotive arc welding utilizing the E-Weld Predictor tool developed by the Edison Welding Institute and the Ohio Super-Computer Center.
- Initiate a weld bonding applied research project to study adhesive effects on between spot weld buckling.
- Initiate a Phase 2 of the Weld Repair and Joint Efficiency Study to expand the assessment of the various joining processes in coach peel applications.

Introduction

The purpose of this project is to evaluate the weldability of the new AHSS currently being considered by the automotive companies as a solution to lightweighting without compromising cost or structural strength. The project intent is to evaluate various grades, thicknesses, and joining processes.

Initially, resistance welding was evaluated. Subsequent projects extended to Metal Inert Gas (MIG), laser-assisted MIG, and plasma- assisted MIG joining processes. Additional evaluations have included projection nut welding and drawn arc stud and nut welding to AHSS.

Weld Repair and Joint Efficiency Project

A study of joint efficiency for various joining processes does not currently exist for AHSS. These materials are considered for future automotive production. The objective of this project is to demonstrate weldability and joinability of AHSS by various processes. This work is a comprehensive study on various grades of steels, which quantifies peak load, joint efficiency, energy up-to-peak load, and joint stiffness for a variety of joining methods. The data allow comparisons to be made for production welding/joining processes and repair substitutions. Processes studied include:

- Resistance spot welding (RSW)
- Conventional, alternating current (ac) and direct current (dc) schedules, RSW with adhesives
- Gas metal arc welding (GMAW)
- Lap fillet, plug weld, fillet in slot, arc spot, cold metal transfer
- Gas metal arc brazing (GMAB)
- Lap fillet, plug weld, fillet in slot
- Laser welding/brazing
- Lap, lap fillet, laser/MIG, braze, staple geometry mechanical fasteners
- Hemlok rivet, Henrob self-pierce rivet, Tog-L-Loc mechanical clinch, rivet with adhesive bonding
- Dow Betamate 1484, Henkel 4555B, Henkel 5087, JB Weld, 3M VHB tape
- Other processes including Arplas, Spot Fast, Supersonic Spray Transfer, Fronius Delta Spot, Friction Stir Spot Welding

Welding/joining processes were performed on mild steel and four advanced high strength steels.

Materials:

- 0.7 mm electro-galvanized mild steel
- 1.2 mm hot-dip galvannealed 590R
- 1.2 mm hot-dip galvanized Dual Phase (DP) 600
- 1.15 mm hot-dip galvannealed DP 780
- 1.0 mm electro-galvanized TRIP 800

Tensile shear tests were performed for a minimum of two test specimens for each material/process combination. If the variation in peak load of the first two samples was within 5%, a third sample was not tested. Load/displacement curves were generated using an MTS 810 Material Test System. Joint efficiency was calculated as the

peak load of the joint divided by the peak load of the parent material, expressed as a percentage. Energy was calculated as the area under the load/displacement curve up to the peak load. Joint stiffness was calculated as the slope of the best fit line in the elastic region of the load/displacement curve. Normalized stiffness was calculated as the joint stiffness divided by the parent material stiffness, expressed as a percentage. Normalized energy was calculated as the joint energy divided by the parent material energy, expressed as a percentage.

The average joint efficiency for all material/joining combinations was 48%. The average normalized energy for all material/joining combinations was 6%. Several observations can be made regarding joint efficiencies and normalized energy for all categories of welding/joining processes studied.

- Joint efficiencies for resistance spot welds ranged from 29% to 54%. Normalized energies ranged from 2% to 9%.
- GMAW and laser processes generally produced higher joint efficiencies than resistance spot welds for all materials.
- The highest joint efficiency for GMAW processes was obtained with the double fillet weld in a slot. Joint efficiency ranged from 61% to 90%. This process also produced the highest normalized energy for AHSS within GMAW welds.
- The laser staple geometry generally produced some of the highest joint efficiencies and normalized energies for all materials. Joint efficiencies ranged from 61% to 73%. Normalized energies ranged from 9% to 23%.
- Very high joint efficiencies were obtained with several fracture toughened adhesive/rivet combinations, which produced joint efficiencies between 51% and 87% and normalized energies between 2% and 18%. Normalized energy was exceptionally high for mild steel, but relatively low for AHSS.

It is observed that AHSS are weldable and joinable by all of the processes studied in this project. Several processes had joint efficiencies less than 10% and energies of almost 0% for AHSS, which may limit their applications in automotive structures.

Various joining processes result in different strength metrics. There appears to be no correlation between joint efficiency, energy, and stiffness for the material/process combinations tested. Processes which produce high joint efficiency can produce very low energy values. Processes producing similar joint efficiencies can result in very low or very high energies. For mild steel, an AWS D8.1M resistance spot weld produced a joint efficiency of 34% and normalized energy of 3%. A Hemlok Rivet in mild steel produced a joint efficiency of 27%, and normalized energy of 11%, which is almost four times greater than that of the spot-welded joint. Similar observations can be made for a number of material/process combinations for both mild and AHSS.

It is observed that joint efficiency decreases as material strength increases for most processes studied. This shows that peak load and corresponding joint strength does not generally increase in proportion to parent material strength increase.

For most processes, normalized stiffness tends to increase from mild to advanced high strength steels. Within the AHSS, normalized stiffness does not vary significantly.

Joint energy in this study is considered only up to peak load. In general, the entire area under the load/displacement curve is equal to the energy input required to cause joint fracture. A joint may have high tensile strength but short displacement under load. High tensile strength increases the peak load and, therefore, joint efficiency. Shorter displacement corresponds to low energy input. This is observed by the decreased area under the load/displacement curve. Increasing the energy required to cause fracture may improve joint performance under various loading conditions. Because joints may have very different efficiencies and energies depending on material and process, all factors should be considered when choosing joining processes. For both mild and advanced high strength steels, acceptable welding and joining processes can be selected from those

tested in this project, based on application and loading requirements.

Lightweight Rear Chassis and Arc Weld Design Guidelines

The Lightweight Rear Chassis team of the A/SP requested assistance in welding a lightweight design from DP 600, 800, and 980 materials. After obtaining the various materials, the Joining Team proceeded to evaluate the weldability of these materials, and to test weld the combinations prescribed for a rear-end structure. The Joining Team established the weld parameters, and assisted the prototype source in making the structure. Weld parameters were delivered to the Lightweight Rear Chassis Team along with mechanical and chemical properties of the test materials.

The Lightweight Rear Chassis team requested assistance for developing future designs requiring arc welded joints. The Joining Team then established a project to do the following.

- Develop and publish an A/SP GMAW Weld Design Guideline for Chassis Structures.
- Utilize a methodology to use existing Original Equipment Manufacturer (OEM) Design Standards to create a comparison matrix of product design rules applicable to arc welded chassis structures.
- Utilize the comparison matrix, assess requirements, and create a consensus set of A/SP design guidelines applicable to arc-welded chassis structures.

The results of the project are published as the GMAW Weld Design Guideline for Chassis Structures by the Auto/Steel Partnership.

Evaluation of Starting Resistance Spot Weld Schedules

The OEM's currently have starting point resistance spot weld (RSW) schedule matrices for resistance spot welding mild and High-Strength Low Alloy (HSLA) production materials (steels classified as IISI Groups 1 and 2) that are based on Governing Metal Thickness (GMT) and type of material coating. These starting-point weld schedules are used for material weldability testing as well as during product launch for set-up of resistance spot welding equipment.

The purpose of this A/SP Joining Technologies Project was to determine whether these existing ac and dc weld schedules were suitable for Advanced High Strength Steels (AHSS) classified as IISI Group 3 and 4 materials. Verification of these weld schedules for Group 3 and 4 steels was accomplished by

1. finite-element modeling via Simulation and Optimization of Resistance Projection and Spot Welding Processes (SORPAS), Version 7.0, software and
2. limited welding of two-thickness (2T) and three-thickness (3T) stack-ups with available material.

2T and 3T stack-up combinations were considered. The IISI Group 3 and Group 4 steels included; TRIP 800, DP 600, DP 980, and uncoated hot-stamped boron. Mild steels were used in 3T stack-up modeling including AISI 1006 and BH 210. Finite- element modeling for both ac and dc RSW consisted of the following 3 types of thickness combinations:

1. 2T stack-up, Group 3 and 4 steel welded to itself.
2. 2T stack-up, Group 3 and 4 steel welded to itself with a thickness ratio of 1:2.5.
3. 3T stack-up, Group 3 and 4 steel welded to itself along with a 0.64 to 1.08 mm mild steel.

The test constraints for verification were as follows: maximum 6.0 mm total stack-up thickness, 2.1 mm maximum gage for a coated steel, 3.0 mm for uncoated steel, and a worst-case thickness ratio equal to 1 to 2.5. The governing metal thickness was the 2nd thickest sheet. Additionally, for 3T stack-ups, the worst-case welding situation was thin to thick to thick. The criteria was that the Minimum Weld Size (MWS) as per AWS D8.1M:2007 (Specification for Automotive Weld Quality-Resistance Spot Welding of Steel) was obtained.

The results from finite-element modeling indicated that the ac starting-point weld schedules met the MWS requirement stated above. The initial dc weld schedules proved to be "hot" and required adjustments which were then simulated. The final dc weld schedules also met the MWS requirement.

The following materials at various gages were scheduled to be welded using the ac and dc weld schedules that were verified through finite element modeling: DP 600, DP 590R, DP 750, DP780, DP 980, and TRIP 800. Welding with actual steel consisted of the following:

1. 2T stack-up, Group 3 and 4 steel welded to itself.
2. 2T stack-up, Group 3 and 4 steel welded to itself at different thicknesses.
3. 3T stack-up, Group 3 and 4 steel welded to itself along with thinner mild steel.

Testing of the welded samples included destructive peel, shear tension, cross tension, and metallography. Results were compared to the requirements of AWS D8.1M:2007.

The results will be published as a one-page set of tables entitled, "A/SP Starting Resistance Spot Weld Schedules."

Conclusions

Additional welding issues will be addressed during 2009, by the Joining Technologies Team, funded by USAMP Lightweighting Initiatives and as member company in-kind contributions.

Presentations and Publications

1. John C. Bohr, General Motors Corporation, "Joint Efficiency of Advanced High-Strength Steel Joints made by Various Joining Processes," *Presented at the Sheet Metal Welding Conference in Livonia, Michigan on May 14–16, 2008*.
2. Chonghua Jiang, AET Integration, "Resistance Spot Welding of Advanced High-Strength Steel (AHSS); A Comparative Study of Joint Efficiency" *Presented at the 5th International Seminar on Advances in Resistance Welding in Toronto, Ontario, Canada on September 24–26, 2008*.
3. Michael L. Kuntz, University of Waterloo, "Development of Starting Weld Schedules for AHSS—SORPAS Modeling of Starting Point Weld Schedules with Experimental Evaluation and Validation," *Presented at the 5th International Seminar on Advances in Resistance Welding in Toronto, Ontario, Canada on September 24–26, 2008*.

B. Hydroforming Materials and Lubricants

Project Manager: Bart Clark
Auto/Steel Partnership
2000 Town Center, Suite 320
Southfield, Michigan 48075-1123
(248) 945-4776; fax: (248) 356-8511; e-mail: bclarke@a-sp.org

Chairperson: Ronald Soldaat
ArcelorMittal USA
1330 Burlington Street East
P.O. Box 2460
Hamilton, Ontario, Canada L8N 3J5
(905) 548-7200 ext. 2664; fax: (905) 548-4250; e-mail: ronald.soldaat@arcelormittal.com

Technology Area Development Manager: Joseph A. Carpenter
(202) 586-1022; fax: (202) 586-1600; e-mail: joseph.carpenter@ee.doe.gov

Field Project Officer: Aaron D. Yocum
(304) 285-4852; fax (304) 285-4403; e-mail: aaron.yocum@netl.doe.gov

---

Contractor: United States Automotive Materials Partnership (USAMP)
Contract No.: DE-FC05-02OR22910 through the National Energy Technology Laboratory

---

Objective

- Develop mechanical test procedures and forming limit diagrams (FLDs) for tubes.
- Improve the accuracy and confidence in finite-element modeling (FEM) of tubular hydroforming.
- Investigate the fabricating and performance characteristics of tailor-welded tubes (TWTs).
- Develop an understanding of steel and lubricant requirements for hydroforming using a combination of experiments and FEM.
- Develop an improved understanding of the structural and cost benefits of hydroformed components.
- Support the work of other Auto/Steel Partnership (A/SP) project teams when they investigate hydroformed structural components.
- Validate the performance benefits of hydroforming in automotive structures.

Approach

The approach taken on this project is to initially gain a basic understanding of the hydroforming process and potential issues and to then extend learning to real-world applications of increasing complexity. The investigation encompasses various steel grades with a focus on Advanced High Strength Steel (AHSS) and gauges of steel tubing, including TWTs, in free expansion and corner-fill processes using several types of lubricants. Project plans are developed based on identified knowledge gaps, barriers to implementation and technology needs as follows.

- Limited in-depth understanding of hydroforming and associated processes.
  - — Effect of process variables such as lubrication at each operation on subsequent operations. Forming operations prior to hydroforming include tube making, prebending and preforming.
  - — Forming limits (e.g., FLDs) and other failure criteria.

- Limited experience with AHSS in hydroforming applications.
- Attitude is conservative toward new materials and envelope-pushing applications.
  - — Need to demonstrate the benefits of tube hydroforming through projects focused on real-world applications.
- Limited computer modeling knowledge and lack of validated tools for automotive design process.

Accomplishments

During the report period from October 1, 2007, to September 30, 2008, the following objectives were accomplished.

- Hydroforming of DP600 and Interstitial Free (IF) Steel Bent Tubes with Welded End Caps
  - — Completed work on the final report on the Influence of Bending parameters on Hydroforming of IF and DP600 Tubes.
- Technology Transfer Deliverables and Rewrites of FLD and Influence of Bending on Hydroforming Reports
  - — Completed technology transfer of FLD and Influence of Bending on Hydroforming reports and presentations to be used for dissemination of the learning.
- Study on the Forming Characteristics of TWTs.
  - — Completed a project to obtain strain and thickness measurements during the hydroforming process of the above TWTs.
  - — The final report has been prepared and is being reviewed by the A/SP Hydroform team.
- AHSS Hydroform TWT Lightweight Front Rails
  - — In March 2005 the team was challenged to demonstrate the manufacturability of AHSS hydroform TWT lightweight automotive front rails.
  - — Successfully completed bending the TWTs to fit in the hydroform dies. This process proved to be a significant challenge due to the high strength, multiple thicknesses and high diameter to thickness (d/t) ratio. Wrinkling and splitting of the tubes was a major problem. Various experts from the industry were recruited to assist in resolving the tube bending issues. Bending issues have been resolved. Tubes have been successfully bent.
  - — Hydroform dies remain ready for use at Schuler, Inc. These dies are being used by Schuler to pursue the next phase of the project, hydroforming tailor-welded front rails.
  - — Technical issues pertaining to the hydroforming process have been encountered and are being pursued by Schuler.
  - — In light of the difficult technical issues encountered throughout the project, the team is evaluating whether or not the expenditure of further cost and effort on this project is warranted.
- Investigation of Fabricating Dual Phase and Transformation-Induced Plasticity (TRIP) Steel Tube from an Electric Resistance Welding (ERW) Production Line
  - — This project has been undertaken by CANMET using their laboratory high-frequency induction tube welding draw bench. Work on this project is on schedule and is nearing completion.
- Investigation of Fabricating Dual Phase and TRIP Steel Tube from a Laser Production Line
  - — This project has been deleted.
- Numerical Modeling of Straight TWT Hydroforming and Pre-Bent Tubular Hydroforming
  - — This project has been deleted.
- Characterizing Material Response during Tube Hydroforming
  - — The costs of proposals received for an initial demonstration project were greater than expected. The Statement of Work (SOW) was revised to include more test conditions, but fewer repeats.
  - — A revised Request for Quotation (RFQ) was issued and revised bids were received.

— Further evaluation of this project led to the conclusion that it would be more appropriate for this project to be undertaken by a new, stand-alone A/SP project team rather than have the Hydroform Team continue with it. A new project team is being formed. If sufficient support for this project can be generated, then the new project team will be formalized and will begin work.

Future Direction

During fiscal year (FY) 2009, the Hydroforming Materials and Lubricant Team plans to accomplish the following.

- Continue work to fabricate the Hydroformed Lightweight Front Rails project which was initially undertaken in support of the Lightweight Front Structure project, A/SP110.
  - — Evaluate the components and quantify the manufacturing parameters of the hydroformed components.
  - — If the rails can be successfully manufactured, they will be further tested by the Strain Rate Characterization project, A/SP190 (see report 5.F).
  - — Summarize lessons learned from the fabricating, bending and hydroforming work done on the front rail components.
- Transfer the revised project Characterize Material Response During Hydroforming to a new A/SP project team if there is sufficient support for the project.
- Issue the final report on the Hydroforming of DP600 and IF Bent Tubes with Welded End Caps and take appropriate technology transfer steps.
- Complete the project, "Investigation of Fabricating Dual Phase and TRIP Steel Tube from an ERW Production Line" and take appropriate technology transfer actions.
- It is anticipated that after the Hydroform Materials and Lubricants project team completes their current projects, the team will disband in FY 2009.

Introduction

Hydroformed steel tubes have been used in the automotive industry to form components that meet structural objectives, particularly strength and rigidity, at optimal mass. One of the most significant advantages of tubes is that they are monolithic closed sections and, as such, exhibit many times more stiffness in torsion than conventional open sections, such as "C" and "hat" shapes. Their use is limited largely by a lack of knowledge about the capabilities and parameters of hydroforming processes and the effects of the processes on the tubes.

This project was undertaken to investigate and quantify the capabilities and parameters of various hydroforming processes so that automotive designers and engineers can utilize the tube configurations that are available and predict the performance of components made by hydroforming. Hydroformed tubes and TWTs made from high-strength steel and AHSS are of particular interest because of the potential reduction of mass associated with materials of higher strength and optimal thickness.

The Hydroforming Process

Hydroforming is a process in which a tube is placed into a die which is shaped to develop the desired configuration of the tube. Water is introduced into the tube under very high pressure causing the tube to expand inside the die. The tube ends can be held stationary or moved inward during the process to end feed material into the die cavity.

The process has two distinct stages, shown in Figure 1. The first stage is free expansion, [Figure 1(a)]. The free expansion phase continues until the tube contacts the die wall [Figure 1(b)]. In the second stage, the corner filling phase, the tube is in contact with the surface of the die which constrains subsequent deformation [Figure 1(c)]. During this stage, the tube expands into the corners of the cavity, accomplishing corner fill. A tube that has been hydroformed is shown with the die in Figure 2. Note that the test was continued until the tube failed.

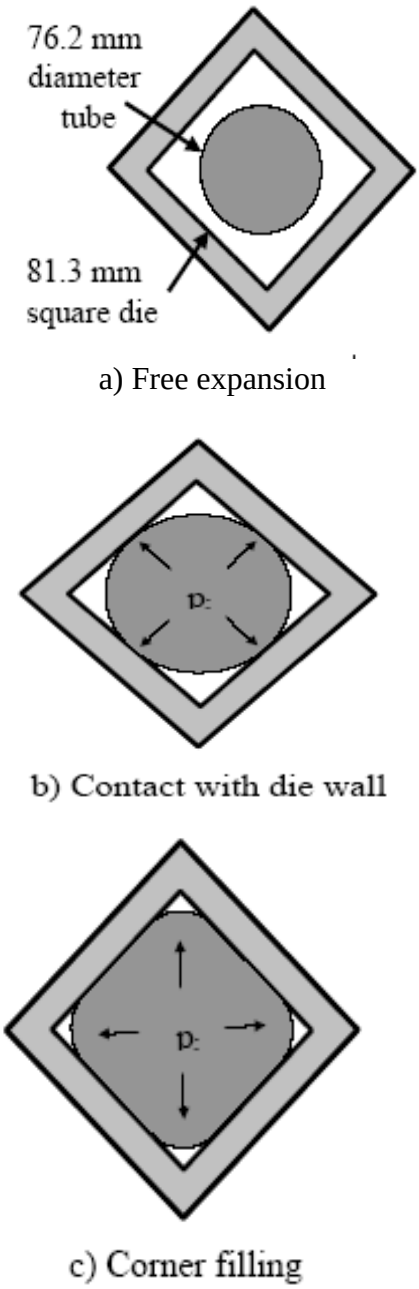

Figure 1. (a) Free expansion stage, (b) contact with the die wall, and (c) corner filling.

During corner fill, the tube slides against the die. Friction between the tube and die affects the process. The lubricant used in the process is a significant parameter.

Figure 2. Hydroformed Tube and Die (the test was run to failure of the tube).

During both stages, the tube undergoes plastic strain. The amount of plastic strain that can occur before the material fractures is predicted in stamping processes that utilize flat sheet steel by using a FLD. The FLD is determined by the properties of the material. The hydroforming process is preceded by tube forming and sometimes pre-bending of the tube, both of which induce strains in the material and alter its properties. Before an FLD can be developed for the hydroforming process, the strain history, that is, the strain induced in the material prior to hydroforming, must be known.

Project Discussion

Tailor-Welded Tubes

Tailor-welded blanks are used for sheet steel stampings in numerous automotive applications. Their use enables the development of components with varying material thicknesses and mechanical properties to achieve the required structural performance at optimal mass. These same advantages can be achieved in tubes by utilizing the expertise currently available for producing tailor-welded blanks.

The Hydroforming Team recognized that optimal performance can be achieved only when the

parameters of fabricating and hydroforming tubes with varying thicknesses and/or material properties are understood. For example, when a sheet steel blank of a given thickness and grade is joined to a blank with greater thickness and/or strength, the former sheet will tend to expand farther than the latter. The tendency for differential expansion imposes loads on the interface of the sheets, namely, the weld, where there can be no differential expansion.

Tubes are usually formed before hydroforming in bending operations which progressively bend the tube to the desired radius along its length. Bending parameters may need to be adjusted to move progressively over tube sections with varying thickness and material properties.

To assess the parameters associated with these conditions, the Hydroforming Team developed a test plan that will allow direct comparison of TWT characteristics by forming five sets of tubes, 12 tubes per set. The first set is a baseline tube made from one blank. The other four are made from two laser-welded blanks, as follows.

1. One-piece tube as a baseline: 1.5 mm DP 600.
2. Same material, same thickness: 1.5 mm DP 600 welded to 1.5 mm DP 600.
3. Same material, different thickness: 1.2 mm DP 600 welded to 1.5 mm DP 600.
4. Different material, same thickness: 1.5 mm HSLA 350 welded to 1.5 mm DP 600.
5. Different material, different thickness: 1.5 mm HSLA 350 welded to 1.2 mm DP 600.

Hydroforming with Welded End Caps

During hydroforming operations, expansion of the tubes causes "end feeding", wherein the ends of the tube move inward toward the expanding area due to metal flow in the workpiece. End feeding affects the strain patterns in the tube. In some hydroforming operations, deliberate end feeding is performed under controlled parameters in relationship to other parameters, such as water pressure, to enhance metal flow. End feeding can be prevented by welding the tubes to the end caps (interface between the tube and the area where water is introduced) and fixing the caps rigidly in the hydroforming tool. The Hydroforming Team determined that the effects of end feeding on strain patterns in the hydroformed tubes could be better understood by performing tests with no end feeding. Welded end caps were used in all tests.

Conclusions

Work conducted during this reporting period indicated the following:

- the interior surface condition of dies to be used in hydroforming is an important characteristic,
- tooling used to fabricate the TWTs must be carefully tuned to achieve acceptable circularity of the tubes,
- tooling used to bend TWTs into the desired shapes for hydroforming must take into account the differing tube metal thicknesses, and
- hydroforming TWTs presents many significant engineering challenges.

Presentations and Publications

1. "Hydroforming Group," Auto/Steel Partnership Program Review, Department of Energy, September 21, 2005.

2. "Hydroforming Committee," A/SP SPARC financial planning review, July 18, 2006.

3. "Hydroforming Materials and Lubricants," Auto/Steel Partnership Department of Energy Peer Review meeting was conducted on Friday, December 1, 2006.

4. "Influence of Lubricant in Bending & Hydroforming Evaluations" presentation by Jean Reid at ASTM D02 Petroleum Products and Lubricants Committee workshop/ symposium on Tribological Challenges of Metal Deformation Fluids, Florida, June 17, 2007.

5. "Tube Hydroforming Phase V: Experimental Forming Limits of Steel Tubes" IRDI report, March 2007 (awaiting publication by A/SP Technology Transfer Team).

6. "Influence of Bending Parameters on the Hydroforming of IF and DP 600 Tubes" IRDI report, March 2007 (awaiting publication by A/SP Technology Transfer Team).

7. "Hydroforming Materials and Lubricants (A/SP060)—Project Description Sheet, Statement of Project Objectives and Presentation," A/SP Project Review and Budget meeting, July 17, 2007.

8. "Hydroforming Materials and Lubricants (A/SP060)—Project Description Sheet, Statement of Project Objectives and Presentation," A/SP Project Review and Budget meeting, August 19, 2008.

C. Sheet Steel Fatigue Characteristics (A/SP160*)

Project Manager: Bart Clark
Auto/Steel Partnership
2000 Town Center, Suite 320
Southfield, Michigan 48075-1123
(248) 945-4776; fax: (248) 356-8511; e-mail: bclark@a-sp.org

Chair: Raj Mohan Iyengar, PhD.
Severstal North America Inc
3001 Miller Road
P.O. Box 1631
Dearborn, MI 48121-1631
(313) 317-1303; fax: (313) 337-9372; e-mail: rmohan@severstalna.com

Technology Area Development Manager: Joseph A. Carpenter
(202) 586-1022; fax: (202) 586-1600; e-mail: joseph.carpenter@ee.doe.gov

Field Project Officer: Aaron D. Yocum
(304) 285-4852; fax: (304) 285-4403; e-mail: aaron.yocum@netl.doe.gov

Contractor: United States Automotive Materials Partnership (USAMP)
Contract No.: DE-FC05-02OR22910 through the National Energy Technology Laboratory

Objectives

- Compile the test data generated in the previous phases of the program into a user-friendly database that can be used in all phases of design and structural analysis of sheet steel vehicle bodies.
- Investigate the fatigue life of joints formed by spot welding, adhesive bonding and weld bonding (a combination of spot welding and adhesive bonding).
- Explore the fatigue response of advanced high-strength steels (AHSSs) after being subjected to metal inert gas (MIG) and laser-welded joining and compare this behavior with that of standard automotive steels.
- Assist the Joining Technology team in identifying the optimum welding parameters for laser and MIG welded joints, and develop a fatigue test program.
- Study durability issues pertaining to the use of AHSS in automotive applications

Approach

- Investigate the fatigue characteristics of resistance spot welding, a fusion process in which the metal pieces to be joined are melted and re-solidified via a brief high voltage electrical pulse, forming an alloy with a distinctly different microstructure than that of the parent metals. At the intersection of the weld nugget, or button, and the faying surfaces a crack-like discontinuity is formed which is often the site of initial crack growth. In addition, the weld nugget itself may contain discontinuities (such as porosity), which can also become sites at which fatigue cracks form. The amount and type of discontinuities, and thus the fatigue properties, can be affected to a

* Denotes Project 160 of the Auto/Steel Partnership (A/SP), the automotive-focus arm of the American Iron and Steel Institute (AISI) (see www.a-sp.org). The A/SP cofunds projects with DOE through a cooperative agreement between DOE and the United States Automotive Materials Partnership, one of the formal consortia of the United States Council for Automotive Research set up by Chrysler, Ford, and General Motors to conduct joint, precompetitive research and development (see www.uscar.org).

considerable extent by the welding process. The microstructures of the joined metals are also changed in the area adjacent to the weld, which is known as the heat-affected zone (HAZ).

- Investigate the fatigue characteristics of adhesive bonding, which substitutes an entirely different material in place of the weld to act as the load-bearing connection. The adhesive must adhere to the metals being joined and resist interfacial fatigue failure at the adhesive/metal interface and within itself (cohesive failure).
- Investigate the fatigue characteristics of weld bonding, which is a combination of adhesive bonding and spot welding.
- Investigate the previously unknown, or at best little known, factors that are expected either to improve impact durability or facilitate their modeling and simulation.
- Reduce the spot weld, adhesive bonded and weld bonded test data to a form that is useful to design engineers who perform vehicle structural analysis.
- Develop a test program to investigate the fatigue performance of gas metal arc welding (GMAW) – a fusion welding process which results in continuous joints. However, under GMAW or MIG welding, a third "filler" metal is introduced under an arc and shielding gas, and, akin to spot-welding, alloys and microstructures are formed which are different from the metals being joined.
- Identify the parameters, including metal grades, metal thicknesses, coatings, and joint configurations that impact the fatigue performance of GMAW welded joints.
- Evaluate durability performance of AHSS components in automotive applications.

Accomplishments

- Completed testing of spot welds in mild steel and ultrahigh strength boron steel, and placed online the knowledge base developed from the results.
- Completed a detailed study of effect of geometric parameters on fatigue lives of spot-welded specimens.
- Developed a specification for fabricating MIG and laser-weld specimens, submitted a request for quotation, selected a contactor and awarded a contract.
- Completed fatigue testing of MIG welded specimens created by the Joining Technologies Team, A/SP070 (see report 5.A).
- Completed fabrication of test specimens for Phase 1A MIG weld fatigue testing.
- Completed weld fatigue testing for MIG welded Phase 1A test specimens. The team is evaluating the results of the testing.
- Began work to resolve technical questions pertaining to test specimens for Phase 1B fusion weld fatigue testing.

Future Direction

- Specimens for Phase 1B testing will be designed and fabricated.
- The project team will complete the Phase 1B of its program of fatigue testing MIG and laser welds in fiscal year (FY) 2009.
- Detailed analyses and interpretations of the test results will be conducted to develop appropriate parameters that capture the effect of weld and specimen geometry on fatigue performance.
- Preliminary projects will be undertaken to determine if there is sufficient support for the Fatigue Team to shift their focus to durability studies. If so, then subsequent projects will focus more deeply into understanding durability issues with the use of AHSS in automotive applications.

Introduction

Future and near-future vehicle designs are faced with several stringent requirements that impose conflicting demands on the vehicle designers. Safety, particularly crash-energy management, must be improved while vehicle mass and cost are contained.

AHSSs, judiciously selected and applied, are currently the best candidates to achieve a low-cost solution, compared with aluminum, magnesium, and plastics that meets these mandates. As structural components are optimized and thinner gauge, higher strength materials are assessed, the fatigue lives of the areas where loads are transferred become increasingly important considerations. To assess the performance of a component in the design phase, the fatigue characteristics of not only the base material but the joints, where loads are transferred, must be known. This project has essentially completed testing various grades of steel and steel coupons that have been spot welded, adhesively bonded, and weld bonded. Testing of GMAW and laser-welded joints is under way.

Discussion

The effort to evaluate the fatigue characteristics of spot-welds began in the 2002 fiscal year with presentations by key researchers on the current state of the work at Chrysler Corporation, Ford Motor Company, and General Motors Corporation. Based on these presentations, the Sheet Steel Fatigue Project Team has produced results beneficial to all three companies in achieving light weight designs. Early in the planning, the Auto/Steel Partnership (A/SP) Joining Technologies Team was consulted and that team prepared the samples that were tested. This interaction ensured that the samples were joined using consistent procedures that were properly controlled and in adherence to the best current practices in sheet metal joining in the automotive industry.

The following fatigue test parameters were agreed upon and carried out:

- Two modes of testing: tensile shear (Figure 1) and coach peel (Figure 2).

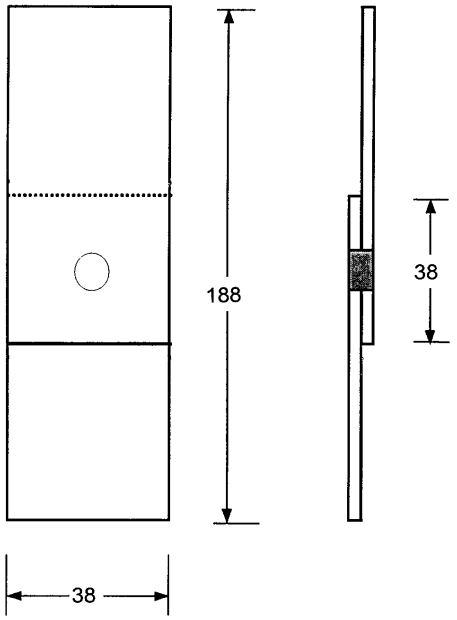

Figure 1. Spot-welded lap shear test specimen (dimensions in millimeters).

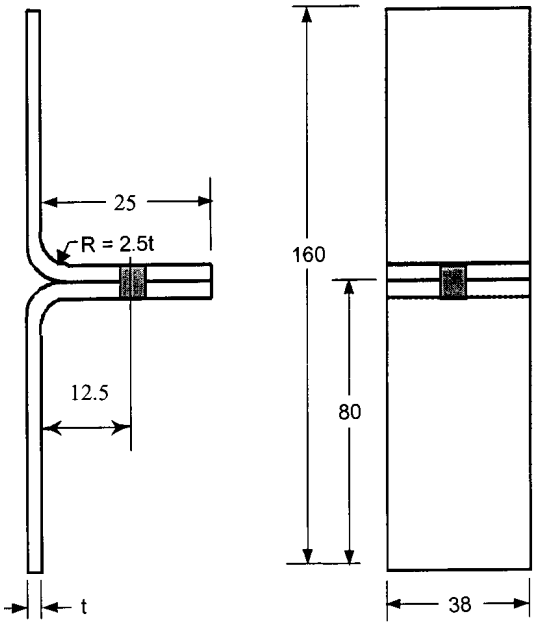

Figure 2. Coach peel test specimen (dimensions in millimeters).

- A single thickness (1.6 mm) was selected to ensure that results were comparable between steel grades. A thinner gage (0.8mm) was selected for a small satellite study [one AHSS

and one high-strength low-alloy (HSLA)] on the effect of gage thickness on fatigue.
- Because no such data was available for advanced high strength steels, several grades in this class were tested.
- Testing was done at two R ratios: 0.1 and 0.3. The stress ratio R is defined as the ratio of the minimum stress to the maximum stress in the test cycle. Maximum and minimum values are algebraic, with tension designated as positive and compression negative.
- Eleven steel grades were tested.
- While the majority of testing was performed on spot welded joints, the fatigue performance of adhesive-bonded and weld-bonded joints was explored in several tests series.

Two testing sources, of the nine invited to submit testing proposals, were selected to perform the fatigue experiments: The University of Missouri at Columbia, Missouri, and Westmoreland Mechanical Testing and Research, Inc. in Youngstown, Pennsylvania.

As the testing progressed and results were analyzed, the following tests were added for comparison purposes:

1. Testing at specified R ratios means that the maximum and minimum loads are constant throughout a given test. However, as the maximum load is increased to generate fatigue curve data, the minimum loads also increase. This process is valuable for establishing baseline data. However, in the real world, loads amplitudes can be expected to be variable. For this reason, automotive spectrum load tests, set to two different predetermined scalings, were run.
2. To investigate the effect of button size, fatigue studies were performed on specimens with a welding schedule that produced a smaller weld button.
3. At the request of the Joining Technologies Team, three test series were run using wide samples (125 mm vs. the standard 38 mm). The wider samples minimize rotation of the weld under load and allow negative R-ratios to be explored.

Gas Metal Arc Welded (GMAW) Joints

GMAW welding is the second most common welding process used on vehicle structures, with the rate of applications increasing yearly. GMAW or MIG welds are used not only on body members and sub-frames in passenger cars, but also in frames for larger passenger vehicles, light trucks and Sport-Utility Vehicles (SUVs). Therefore, the test samples will be made from two thickness groups: a thinner gage of 1.6 mm for body applications and a thicker gage of 3.4 mm for frame applications. These target thicknesses, primarily based on material availability, represent typical as-welded material thicknesses found in body and frame applications, respectively.

Frame members do not generally require as much formability as do body members and they offer excellent opportunities for mass reduction through downgaging. Therefore, tests on frame joints will ultimately employ higher strength materials than those specific to body members, but often result in similar numbers of welds and amount of weld area.

The team agreed to four specimen designs for testing. Each explores a different loading mode and reveals different information about the material/joint performance: butt weld (Figure 3), single lap shear (Figure 4), double lap shear (Figure 5), and perch mount (Figure 6).

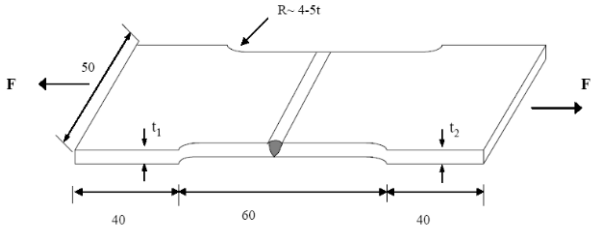

Figure 3. MIG butt-welded specimen (dimensions in millimeters).

Results—Spot Welds

Plotted in Figure 7 are all the tensile shear and coach-peel fatigue results for all nominal 1.6 mm gage materials with 7 mm diameter spot weld, conventional steels and AHSS included. Data labels ending in R0.1 indicate R=0.1 loading and data labels ending R0.3 indicate R=0.3 loading.

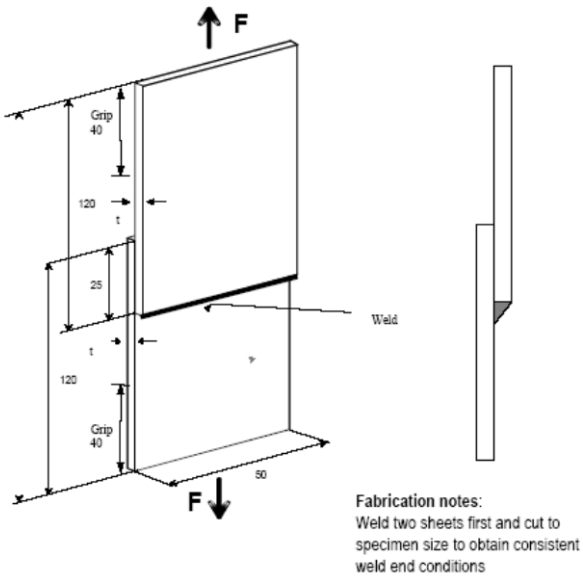

Figure 4. MIG welded single-lap shear specimen (dimensions in millimeters).

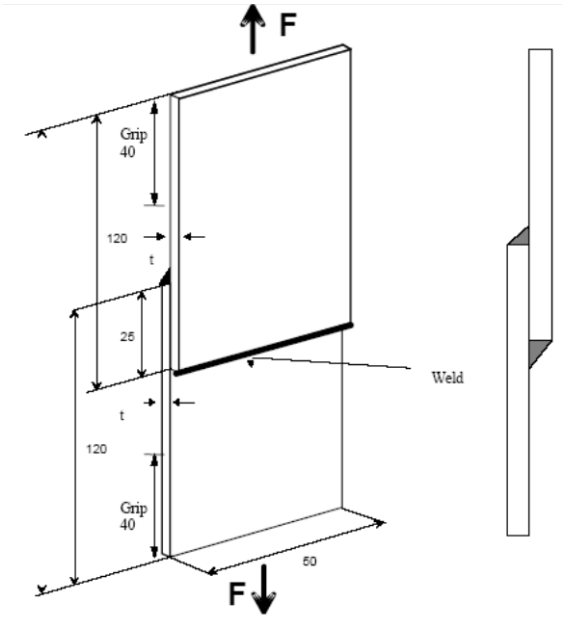

Figure 5. MIG welded double-lap shear specimen (dimensions in millimeters).

Runouts are plotted but not otherwise indicated in this figure.

Two thicknesses of HSLA340 (1.0 mm and 1.78 mm) and two thicknesses of DP600 (1.53 mm and 0.83 mm) are compared in Figure 8. The nominal button size for all specimens was 7.0 mm, and the welding parameters were held as similar as possible between the gages/grades without

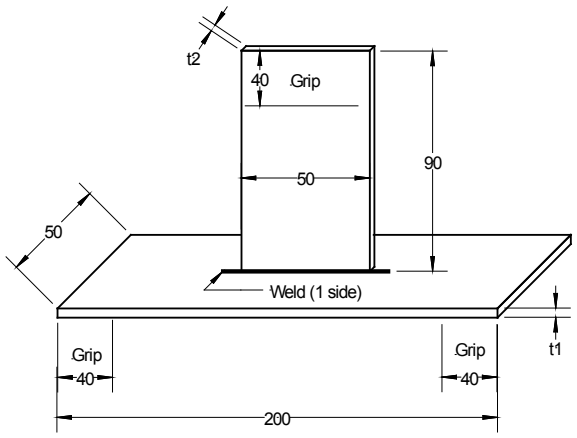

Figure 6. MIG welded perch mount specimen (dimensions in millimeters).

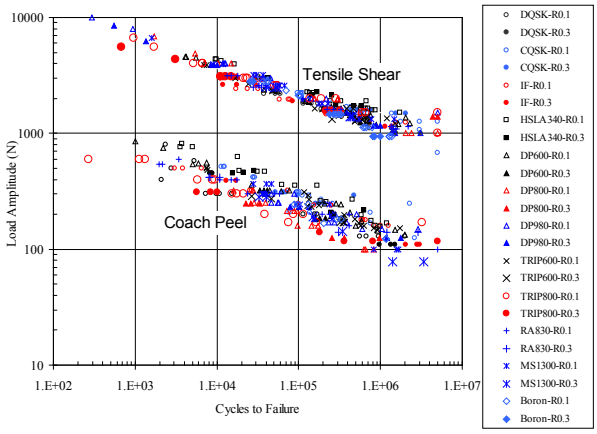

Figure 7. Fatigue results for all 1.6 mm thick, 7 mm diameter nugget spot-welded materials.

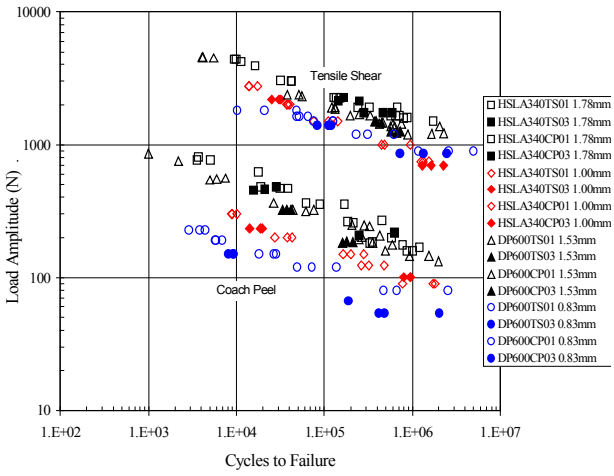

Figure 8. Effect of thickness on fatigue performance.

compromising strength. It was expected that the thinner gages would show shorter life because of

the intrinsically higher stresses in the joint, and this result was indeed found in both materials.

Results—Fusion Welds

Fatigue testing of specimens containing the fusion weld-line within the width of the specimen was conducted to assist the Joining Technology team in identifying the optimum welding parameters for laser and MIG welded joints. The dimensions of the specimens are shown in Figure 9a and 9b. The weld location was centered between the edges of the sample and the robot travel was 25 mm total. This produced a weld with a start and a stop within the gage section of each specimen. GMAW welding of the DP780 AHSS was performed with 70 ksi and 90 ksi filler wires while GMAW welding of the DP600 AHSS was performed with only 70 ksi filler wire. No filler was used with the laser welds.

The DP600 results of the fatigue, shown in Figure 10a, indicate no significant difference in performance between the alternating current (ac), direct current (dc) or laser-assisted GMAW welding processes. Similarly, the performance of the DP780 GMAW welds (Figure 10d) was not influenced by either the process type or the strength of the filler material used. Similar observations may be made concerning the laser processing presented in Figure 10b and 10c. The mean stress appears to be an insignificant factor in the fatigue performance of fusion welded joints. This behavior can be seen in all of the graphs in Figure 10.

Conclusions

Analysis of test results indicates that, for the specimen geometries and steel grades selected for this study, the fatigue performance of a spot weld is independent of the base metal strength. This finding supports the initial understanding that the melting and resolidifying processes associated with spot welding form new alloys and make the properties and coating of the material(s) being joined, and the welding parameters, insignificant contributors to fatigue performance.

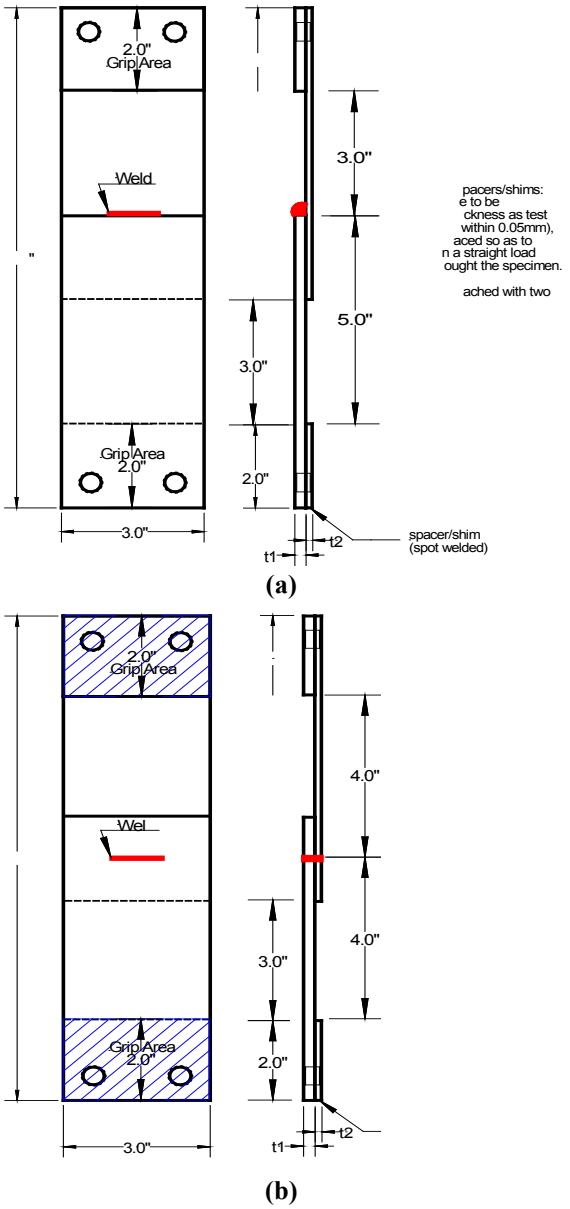

Figure 9. (a) Schematic of specimens for GMAW (dimensions in mm) and (b) Schematic of specimens for laser weld fatigue tests (dimensions in millimeters).

Similarly, the results clearly indicate that, within either the GMAW or laser weld groups, the type of weld does not seem to influence the fatigue performance (e.g., for GMAW it does not matter if the weld is ac, dc, or laser-assisted).

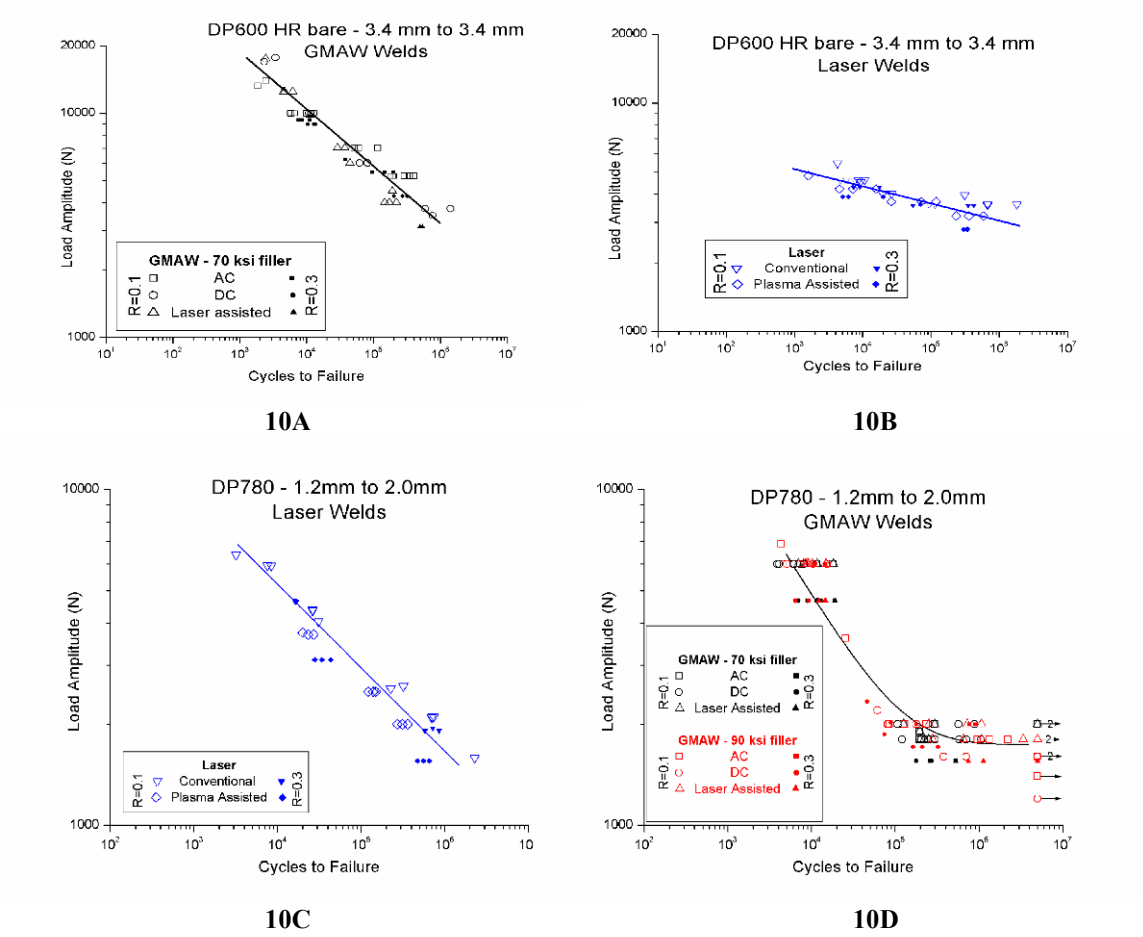

Figure 10. Fatigue performance evaluation of GMAW and laser welds in two advanced high strength steels, DP600 hot rolled, bare, and DP780 coated. Specimens for DP600 are 3.4 mm to 3.4 mm while the specimens for DP780 are 1.2 mm to 2.0 mm.

Presentations and Publications

1. "Sheet Steel Fatigue Group", Auto/Steel Partnership Program Review, Department of Energy, September 21, 2005.

2. "A/SP Sheet Steel Fatigue Committee", Joint Policy Board, Feb. 1, 2006.

3. J.J.F. Bonnen, Hari Agrawal, Mark A. Amaya, Raj Mohan Iyengar, Hong Tae Kang, A. K. Khosrovaneh, Todd M. Link, Hua Chu Shih, Matt Walp, Benda Yan, "Fatigue of Advanced High Strength Steel Spot Welds," 2006, Society of Automotive Engineers, SAE-2006-01-0978, pp. 19. *Republished in 2006 SAE Transactions.*

4. Kang, HongTae, "Evaluation of Spot Weld Fatigue Damage Parameters" 2006, Society of Automotive Engineers, SAE-2006-01-0978, pp. 19. *Republished in 2006 SAE Transactions.*

5. "Spot Welds, MIG Welds and their effect on the fatigue of AHSS steels," Mar. 10, 2006 (A/SP Frame group).

6. "Sheet Steel Fatigue Committee," A-S/P SPARC financial planning review, July 18, 2006.

7. "Spot Welds, MIG Welds and their effect on the fatigue of AHSS steels," Mar. 10, 2006 (Joining group).

8. "Fatigue of MIG Welds" AISI Wheel Task force meeting, Nov 18, 2005.

9. A/SP Team Review, Dec. 15, 2005.

10. "Fatigue of AHSS SpotWelds," 2nd Annual Ford AHSS Conference, Oct. 18, 2005.

11. J.J.F. Bonnen and R. Mohan-Iyengar, "Fatigue of Spot Welds in Low-Carbon, High-Strength Low-Alloy, and Advanced High-Strength Steels and Fatigue of Fusion Welds in Advanced High-Strength Steels," 2006 Proceedings of the International Automotive Body Congress (IABC 2006), pp 12, 2006.

12. H.-T. Kang, J. J. F. Bonnen, and R. Mohan Iyengar, "Sources of Variability in the Fatigue Strength of Spot Welded Specimens," Proceedings of Materials Science & Technology Conference, Detroit, September 2007.

13. J. J. F. Bonnen and R. Mohan Iyengar, "Fatigue Performance of Conventional and Advanced High-Strength Steel Spot Welds," presented at the special symposium marking the 20th Anniversary of A/SP, held as part of the Materials Science & Technology Conference, Detroit, September 2007.

D. Tribology (A/SP230*)

Project Manager: Pat V. Villano
Auto/Steel Partnership
2000 Town Center Drive, Suite 320
Southfield, Michigan 48075-1123
(248) 945-4780; fax: (248) 356-8511; e-mail: pvillano@a-sp.org

Project Chairperson: David Meuleman (disability leave)

Project Chairperson: Connie Yao (retired)

Acting Chairperson: Tareena Mulholland
General Motors Corporation
Manufacturing Engineering
30001 Van Dyke Avenue, Mail Code 480-210-Y25
Warren, Michigan 48090
(586) 575-5255; e-mail:tareena.mulholland@gm.com

Technology Area Development Manager: Joseph A. Carpenter
(202) 586-1022; fax: (202) 586-1600; e-mail: joseph.carpenter@ee.doe.gov

Field Project Officer: Aaron D. Yocum
(304) 285-4852; fax (304) 285-4403; e-mail: aaron.yocum@netl.doe.gov

Contractor: United States Automotive Materials Partnership (USAMP)
Contract No.: DE-FC05-02OR22910 through the National Energy Technology Laboratory

Objective

- The ability to fully realize the benefits of advanced high-strength steels depends upon the ability to aggressively form these steels into challenging parts. These steels have been shown to cause die failures in early implementations. This project is intended to improve the tribological understanding of the interaction among advanced high-strength steels (AHSSs), tooling, coatings, lubricants and the forming process so that the proper system can be selected to successfully manufacture automotive parts.
- Effective trimming of advanced high-strength steel parts has recently been noted as among the most challenging manufacturing operations for these materials particularly those steels with tensile strengths greater than 750 MPa. Accelerated wear of trim steels has lowered productivity and adversely affected part quality. There are many developments occurring in trim steel materials, but no effective method of screening the newly-available material is available.
- The work-hardening effects of advanced high-strength steel has also introduced excessive temperatures and wears on the forming and flanging operations. The challenge arises to determine what materials, surface treatments, lubrications, and die conditions are optimal for producing high quality, cost-effective parts.

*Denotes Project 230 of the Auto/Steel Partnership (A/SP), the automotive-focus arm of the American Iron and Steel Institute (see www.a-sp.org). The A/SP cofunds projects with DOE through a cooperative agreement between DOE and the United States Automotive Materials Partnership, one of the formal consortia of the United States Council for Automotive Research set up by Chrysler, Ford, and General Motors to conduct joint, precompetitive research and development (see www.uscar.org).

Approach

- Previously in this project, a continuous friction/die wear test had been developed for evaluating friction and wear during a long term (up to 100,000 strokes) simulation of the stamping process.
- This year's work was to extend the analysis of data already obtained, to fully extract information on heat generation during forming advanced high-strength steels, as well as, to further analyze the initiation and development of wear as it pertains to the metallurgy of the tooling material, tool coatings and sheet steel coating.
- Additional testing of specific form, flange, trim, and pierce steel materials/coatings will be conducted. However, as a result of delayed and unsatisfactory results from the previous methods of testing, a progressive die will be constructed and used to test several materials, coatings, angles, and clearances in form, flange, trim, and pierce functions in a production-type environment.

Accomplishments

- Completed Technical Paper—"Comparison of Friction Results Between Draw Bead Simulator & Twist Compressor Tester."
- Completed Technical Paper—"Effect of Process & Material Variables on Temperature Increase in Draw Bead Test."
- Completed Technical Paper—"Effect of Stroke Length and Penetration on Wear of Male Draw Beads."
- Completed design and construction of progressive die that tests 17 pierce, 12 flanging, 15 trimming, and 6 forming conditions.
- Completed 60,000 hits with dual phase (DP) 980 providing results for all operations.

Future Direction

- Further develop die to account for new materials and coatings in the completion of Phase 1 and Phase 2.
- Stamp 3.5 remaining coils of DP980 to complete Phase I of the Progressive Die Test with additional materials and coatings.
- Correlate results of progressive die test with production data as AHSS is implemented into production.
- Develop and begin Phase II of Progressive Die Test, vary current conditions, including findings from Phase I, and evaluate different grades of AHSS.

Introduction

Auto/Steel Partnership (A/SP) Tribology Team members designed a progressive die in which each operation is inserted in a way that the die can be designed to test a myriad of different conditions and materials. The team's interest is to determine the optimal die material and surface treatments for stamping AHSS.

Phase 1 Progressive Die Project

Phase 1 of the project has eleven stations of operation and two idle stations. Three of the piercing stations tested a range of pierce clearances. The trim and flange stations each tested seven different materials. Two-thirds of the DP980 bare sheet material has been stamped. While there is still ongoing work to complete Phase 1, the following conclusions are already apparent:

- There is a definitive clearance range from 5–15% where pierce is acceptable for part quality, burr height increases with clearance.
- The key-hole shaped pierce had a much larger burr than the other shaped pierce.
- The pre-strain from the bead accelerated trim steel wear significantly.
- Hardness of the trim steels directly impacted the failure mode of the insert.

- The bare materials in the flange operation failed quickly regardless of type of material.
- The low-temperature coating wore quickly in the flange operation, while the high-temperature coating proved superior.
- Higher trim angles result in a higher burr, and the "flange-out" pierce shape resulted in the largest burr.
- The coated flange steels ran at lower temperatures; however, flange steel temperature is not a good indicator of failure.
- Hardness of the flange steels has little impact on performance, whereas coating had high impact on performance.

The materials and coatings failed before we completed the stamping run. The team plans to complete Phase 1 utilizing the same operation design with additional materials and coatings.

When Phase 1 is complete, several parts and all die materials will be analyzed to determined exact mode of failure. At this time, the final report will be completed.

Publications/Presentations

1. One technical paper will be written from Phase 1 work and expected to be made available to various trade publications.

2. Phase 1 results are to be presented at the 2009 Great Designs in Steel Conference.

E. Advanced High-Strength Steel Stamping (A/SP050*)

Project Manager: Michael S. Bzdok
Auto/Steel Partnership
2000 Town Center, Suite 320
Southfield, Michigan 48075-1123
(248) 945-4778; fax: (248) 356-8511; e-mail: mbzdok@a-sp.org

Co-chair: James Fekete
General Motors Corporation
Body Manufacturing Engineering
30001 Van Dyke Avenue
Warren, Michigan 48090
(586) 201-9520; e-mail: jim.fekete@gm.com

Co-chair: Changqing Du
Chrysler LLC
800 Chrysler Drive
Auburn Hills, Michigan 48326
(248) 576-5197; fax: (248) 576-0230; e-mail: CD4@chrysler.com

Technology Area Development Manager: Joseph A. Carpenter
(202) 586-1022; fax: (202) 586-1600; e-mail: joseph.carpenter@ee.doe.gov

Field Project Officer: Aaron D. Yocum
(304) 285-4852; fax (304) 285-4403; e-mail: aaron.yocum@netl.doe.gov

Contractor: United States Automotive Materials Partnership (USAMP)
Contract No.: DE-FC05-95OR22363 through the National Energy Technology Laboratory

Objectives

- Determine how to accurately predict and control the amount of springback and other deviations from the desired stamping geometry for parts made from advanced high-strength steel (AHSS) prior to construction of production tooling.
- Develop part design and manufacturing process guidelines that can be recommended to automotive design and manufacturing engineers for the purpose of reducing springback and other part distortions.
- Investigate and analyze fractured materials for the purpose of understanding the fracture mechanism in terms of material properties and processing effects. Develop the ability to predict the onset of shear fracture in stamping processes.

Approach

- Predict AHSS stamping springback through finite-element analysis (FEA).

*Denotes Project 050 of the Auto/Steel Partnership (A/SP), the automotive-focus arm of the American Iron and Steel Institute (see www.a-sp.org). The A/SP cofunds projects with DOE through a cooperative agreement between DOE and the United States Automotive Materials Partnership, one of the formal consortia of the United States Council for Automotive Research set up by Chrysler, Ford, and General Motors to conduct joint, precompetitive research and development (see www.uscar.org).

- Control AHSS stamping springback by developing knowledge of part design geometries that affect flange springback and die processes that control springback.
- Develop predictive tools related to fracture in AHSS based upon an investigation and analysis of fractured material properties and microstructural characterization.

Accomplishments

- Modified tooling for stretch-forming processes of AHSS auto body structural components to neutralize the residual stresses that cause springback and sidewall curl. Predictable results have been shown for high-strength, low-alloy (HSLA) 350, DP600 MPa, DP780 MPa and DP980 MPa. Panel measurements and data analysis have been reported. The use of stiffening beads and other part shape modifications as well as control of key process variables are being recommended to product designers for control of twist, undercrown and springback based upon these results.
- Began a study to evaluate springback compensation technology developed in the DOE-supported "Die Face Engineering" project. A previously evaluated part (GM B-Pillar) was reevaluated, and numerical technology was used to develop a new die face which is expected to compensate for springback and lead to a dimensionally acceptable part.
- Completed five additional case studies of AHSS part developments by working through the original equipment manufacturers (OEMs). Applications guidelines studies were completed on roof rail reinforcement, three "B" pillar reinforcements, two "A" pillar reinforcements, and a rear rail. The volume "Advanced High-Strength Product and Process Applications Guidelines" was published, using the information developed from the case studies and other project activities.
- Made significant progress in an investigation of shear fracture of AHSS with the Edison Welding Institute, in cooperation with The Ohio State University (OSU), to perform analyses directed at understanding the basic characteristics of fractures at a microstructural level and predicting their onset.
- Completed an investigation of shear fracture in dual phase (DP) and transformation-induced plasticity (TRIP) steels at Wayne State University. The investigation included measuring the key material parameters needed to predict fracture; proposal of a new fracture criteria based on these material parameters; and preliminary guidelines to develop predictive tools and develop a standardized test for predicting failures in sheared edge stretching and breakage on a radius.
- Modified and tried out "15-Flange Die" for use in evaluating stretch-flanging capability of dual phase and other AHSS materials. Results were used in the Wayne State University study.
- Completed an evaluation of the mechanical properties of DP and TRIP steels in biaxial stretching through the OSU Center for Precision Forming. This forming mode allows data to be taken at higher strains than conventional tensile testing, resulting in more robust material models for forming and springback simulations.

Future Direction

- Additional material characterization work is required to evaluate material behavior at deformation levels beyond uniform elongation and close to failure. The team has identified mechanical testing with strain measurement accomplished with digital image correlation as a key method in this characterization. The team also recognizes that microstructural inhomogeneity has significant influence in the fracture performance of AHSS materials, and will be performing experiments to understand the effect of test direction as an additional step in understanding these phenomena.
- The B-Pillar springback compensation trials will be completed and the results analyzed for the purpose of evaluating the effectiveness of the technique.
- Additional applications guidelines case studies are being compiled.

Introduction

AHSS combining high-strength and superior formability compared to conventional high-strength steels are increasingly being used to deliver superior vehicle safety performance, while at the same time provide opportunities for mass reduction. AHSS have high initial work hardening rates as well as high tensile strengths. These characteristics, which make the material attractive to design engineers, also create challenges in the stamping and manufacturing processes; especially in terms of dimensional control and fracture prediction.

FEA has been widely used in automotive industry for vehicle designs and manufacturing feasibility. Over a period of 20 years, a high level of confidence has been achieved using FEA to predict splits and wrinkling in metal- forming processes. However, it remains a challenge to accurately predict springback, particularly for those parts with twists and sidewall curls. Numerous studies have been carried out to correlate computer prediction to experimental results. The material model, element formulation, friction and contact algorithm are important parameters affecting simulation accuracy. Other studies have also demonstrated the sensitivity of springback predictions to other numerical parameters, such as mesh size, number of through-thickness integration points, tooling travel speed, contact interface parameters, etc. During the last decade, FEA software developers and users have been investing much effort into the solution of springback prediction problems. A steady improvement has been seen in the prediction capability and methodology.

Prediction of splits using FEA has also been complicated with the emergence of shear fracture in AHSS stamping. Shear fractures are not predicted using conventional FEA analysis techniques, and this has resulted in significant issues during tryout of AHSS parts.

To address these issues, the A/SP initiated enabler projects, focusing on stamping experiments using production-intent tooling, with the results being compared to analyses using computer (FEA) models. To date, various classes of automotive parts have been studied, which were fabricated from AHSS with tensile strengths varying from 600 to 980 MPa. Stamping experiments included various forming process variables, including pad forces, blank holder forces and die configurations (drawing versus crash forming). Simulations were carried out using various numerical parameters (mass scaling, adaptive levels and mesh coarsening) in order to study their effects on the prediction accuracy. Experimental results were compared to the corresponding FEA simulations.

Discussion

Most experiments have been conducted with a multi-process research die with sub-die inserts (Figure 1) to produce various automotive structural components by a variety of processes. This die has the necessary higher holding pressures and controlled processes required for working the higher-strength materials. A programmable, hydraulic pressure cushion is the main component of this system that provides the means of stretch-forming the metal and controlling springback.

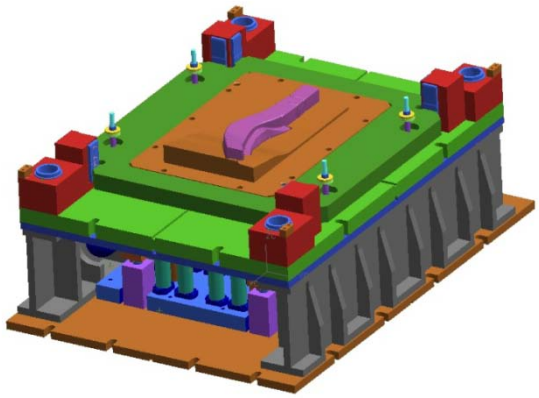

Figure 1. Lower half of multi-process die.

Sub-die inserts in the multi-process master shoe die enable stamping of underbody, cross-car and body side structural components with a variety of stamping processes.

The latest results of the experiments are described below.

Rear Longitudinal Rail Sub-Dies

Tryout utilized three different stamping processes: draw action, with part on post or part on binder; and form die with upper pad. Figure 2 shows examples of parts produced with these processes.

Figure 2. Rail stampings form three processes (from left to right: draw process– part on post; draw process– part on binder; form process).

Materials included 1.6 mm and 2.2 mm DP600 MPa steel and 1.6 mm DP780 MPa and DP980 MPa steel. Tryout resulted in identification of a forming process that lowered press forces and used material more efficiently, with springback comparable to the other processes. However, part dimensions were still outside acceptable ranges, so efforts continued with the higher strength grades to improve the springback control with a Four Break Bead, added to the forming process. Figure 3 shows a cross section of this die process.

This process feature was shown in previous work to be effective at controlling sidewall curl. The experiments were completed in this reporting period, with the following results:

- The amount of springback increases with the material strength;

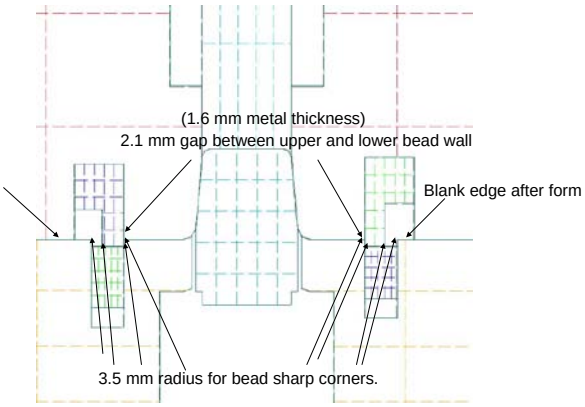

Figure 3. Cross-section of four break-bead evaluated in this reporting period.

- Trimming increases the amount of springback;
- Four Break-Bead produces less springback than the crash form with developed blanks. However, the amount of springback after trimming is almost the same as that by crash form;
- Four Break-Bead produces more variations in springback than crash form;
- Four Break-Bead produces less twist than crash form;
- Four Break-Bead produces more side wall curl than crash form;
- Four Break-Bead produces less flange opening angle than crash form

LS-DYNA simulation results were compared to the experimental results. The following conclusions are obtained:

- Both the experimental and the simulation results showed that the draw form process produced more springback than the crash form process; and the amount of springback increased with the material strength.
- The FEA-predicted springback match to the experiments was seen to be dependent upon material strength. Reasonably good prediction accuracy was obtained for the DP600 parts.
- The correlation between the predicted and the experimental results for DP780 and DP980 parts is not as good as that for DP600 (Figure 4). Further study is needed to improve the predictability for higher strength materials.

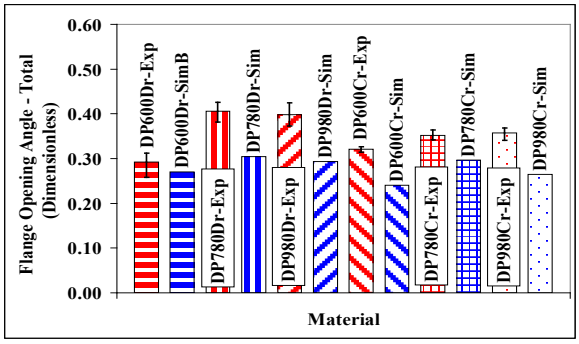

Figure 4. Correlation simulation vs experimental.

- Increasing mass scaling and reduced adaptive levels will deteriorate the prediction accuracy. Mesh coarsening prior to springback analysis does not greatly affect the prediction results.

Body Side Center Pillar Sub-Die

A sub-die for a Body Center Pillar was modified through tryout to optimize results (Figure 5). This part is crucial to the body side structure for meeting side impact requirements. It is also typically difficult to stamp in medium strength grades due to springback, twist and undercrown. The higher-strength grades increased the manufacturing difficulties.

Figure 5. Body side center pillar.

During tryout, several features were added to the part to enable stamping in DP780 material. Changes were made to the product shape to take up excess metal and features were added to stiffen the part. Split- and fracture-free stampings were then made from both DP780 and DP980 material. Parts have been scanned and dimensional analysis has been completed.

Phase two of the project is utilizing the dimensional evaluation of both untrimmed and trimmed parts. This information, FEA analysis, and computer-guided compensation were used to recut the die to achieve dimensional accuracy of the part. The recut die is complete and awaiting tryout upon receipt of appropriate steel material.

Viscous Bulge Mechanical Testing

Materials models for formability and springback simulation have weaknesses that compromise the quality of the results. One of the weaknesses is the limitations of data from tensile tests, since true stress-strain data can be easily extracted only at strains below the end of uniform elongation. In practical stamping processes, this level of effective strain is often exceeded. For this reason, the team contracted researchers at the OSU Center for Precision Forming to test a range of DP and TRIP steels using a viscous pressure bulge test, which allows data to be collected at significantly higher strains than can be achieved with tensile testing. This contract was successfully completed in this reporting period, and the data have been distributed to the team. An example is shown in Figure 6.

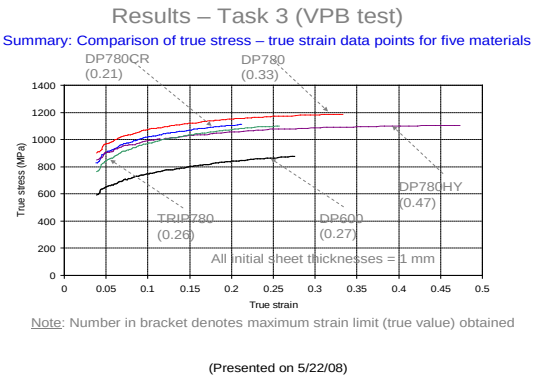

Figure 6. Results of viscous pressure bulge testing of DP and TRIP steels.

Shear Fracture Project

Beginning in 2007 the A/SP AHSS Stamping Team contracted with Edison Welding Institute (EWI), in association with OSU, to conduct a

three year project for shear fracture characterization, Draw Bend Formability (DBF) testing and fracture criteria development of AHSS. Shear fracture has emerged as a common and unpredictable failure mechanism in production of AHSS parts. An example is shown in Figure 7.

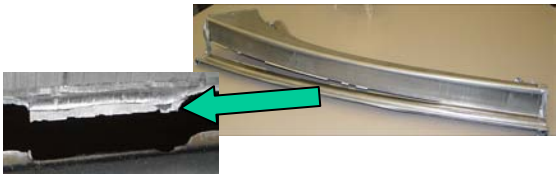

Figure 7. AHSS shear fracture phenomenon.

DBF testing to date has focused upon DP 590 and DP780 steel in 1.4 mm and 1.75 mm gauges. Work has also started developing constitutive equations for AHSS and finite-element simulation of AHSS deformation.

The results to date have indicated that the type of fracture (shear fracture vs conventional tensile-type failure) can be predicted based on knowledge of the material properties and test parameters (Figure 8). Further, the results have shown that the heat generated during the deformation of the sample has a significant influence on the hardening behavior of the material, and should be taken into account for the most accurate simulations.

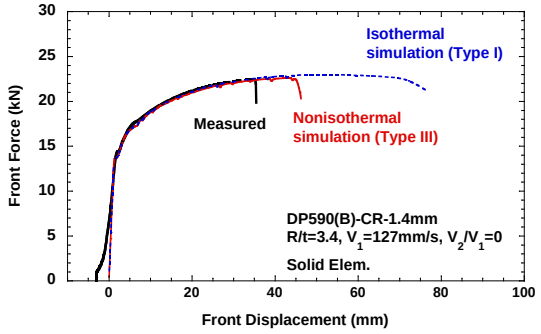

Figure 8. Comparison of predicted vs measured fracture behavior in a stretch-draw test.

Significant progress has also been made in characterizing microstructural damage that occurs during the stretch bending process. This information will be used in conjunction with microstructural-level FEA modeling to determine the relative influence of microstructural damage and thermal characteristics on the bending failures.

Flange Shear-Affected Zone Study

In October 2007 the A/SP AHSS Stamping Team contracted with Wayne State University in Detroit, Michigan to characterize the nature and extent of the shear-affected zone of shear-trimmed and subsequently flanged DP steel features (Figure 9).

Figure 9. Example of performance of DP980 in flanging a 5 mm diameter hole.

This project was completed during this program period. The tasks of this project were two fold: (a) experimentally characterize the shear-affected zone and material and edge microstructures for three DP steels: DP600, DP780 and DP980; (b) perform computer simulation on flanging two specially designed parts made of three DP steels and with three flange lengths: 1 mm, 3 mm, and 5 mm.

The report describes the results of edge characterization of mechanically-pierced part edges, and makes a comparative study with samples containing laser-cut edges. A new technique, based on flow-line analysis commonly used in evaluation of deformation in forging processes, was used to calculate the strain in the pierced samples as a function of distance from the sheared surface.

Based on the experimental finding, a new computing technique was proposed that takes into account the non-uniform microstructure of materials. The model uses constituent properties as input, similar to that in microstructure-based

micromechanics method, but the phase particles are modeled at the element level. The technique considers statistical features of the microstructure and the pierced edge characteristics are to be used as the input of FEA. Further work is necessary to fully develop this proposed technique.

AHSS Case Studies and Applications Guidelines

The work of this team was leveraged with evaluations of actual production parts. These detailed case studies include part designs, materials selections, stamping processes, analysis results, and lessons learned. Five case studies were completed this reporting period. They are available at http://www.a-sp.org/publications.htm.

In addition, this combined work was summarized and compiled into a volume entitled "Advanced High Strength Steel Applications Guidelines", which is also available as a download at the above website, or as a paperback book.

Summary and Conclusions

Evaluations of production parts and processes continued in this reporting period. The Four Break-Bead was again shown to have some positive effect on dimensional control. Further, FEA evaluation using current state-of-the-art techniques showed that though progress has been made, improvements were still required for robust dimensional prediction.

The team is in the process of evaluating the latest generation of FEA technology for springback prediction. The B-pillar die face has been recut based on FEA technology. The resulting tool is expected to deliver a dimensionally-correct part. The evaluation will be completed in the next reporting period.

Elements of the experimental work, combined with the results of the case studies, have been compiled into a volume entitled "Advanced High-Strength Product and Process Applications Guidelines."

Evaluation of shear fracture in bending and edge stretching are ongoing. Preliminary results show that fracture type can be predicted with knowledge of material and process variables. Microstructural damage occurs as a result of these processes, and its influence on fracture is currently under investigation. FEA modeling at the microstructural level is also being investigated to determine if it provides value in predicting these fractures.

Presentations and Publications

1. Ken D. Schmid, General Motors Corporation "Evaluation of DP780 and DP980 for B-Pillars," *Presented at the 2008 Great Designs in Steel Seminar, April 9, 2008, Livonia, Michigan.*
2. Changqing. Du, Chrysler LLC "Correlation of FEA Prediction and Experiments on Dual-Phase Steel Automotive Rails," *Presented at the 2008 Great Designs in Steel Seminar, April 9, 2008, Livonia, Michigan.*
3. "Advanced High-Strength Product and Process Applications Guidelines" manual prepared by the Auto/Steel Partnership Applications Guidelines Team, November, 2007.
4. The team held a one-day Shear Fracture Technical Progress Review on Sept. 10, 2008. All project contributors and some invited guests presented the status of their work to a group of researchers from the member companies of the Auto/Steel Partnership. The presentations can be made available.

F. Strain-Rate Characterization (A/SP190*)

Project Manager: Pat V. Villano
Auto/Steel Partnership
2000 Town Center Drive, Suite 320
Southfield, Michigan 48075-1123
(248) 945-4780; fax: (248) 356-8511; e-mail: pvillano@a-sp.org

Chairman: Kathy Wang
General Motors Corporation
2000 Centerpoint Parkway
Pontiac, Michigan 48341
(586)-986-1173; fax: (586) 986-8722; e-mail: kathy.wang@gm.com

Lead Scientist: Srdjan Simunovic
Oak Ridge National Laboratory
Oak Ridge, Tennessee 37831-6359
(865) 241-3863; fax: (865) 574-7463; e-mail: simunovics@ornl.gov

Technology Area Development Manager: Joseph A. Carpenter
(202) 586-1022; fax: (202) 586-1600; e-mail: joseph.carpenter@ee.doe.gov

Field Project Officer: Aaron D. Yocum
(304) 285-4852; fax (304) 285-4403; e-mail: aaron.yocum@netl.doe.gov

Contractor: United States Automotive Materials Partnership (USAMP)
Contract No.: DE-FC05-02OR22910 through the National Energy Technology Laboratory

Objectives

- Develop new experimental setups for characterization of crashworthiness and strain-rate sensitivity of both advanced high-strength steels (AHSS) and structural designs.
- Replicate impact conditions that occur in automotive impact by simpler and more manageable experiments in order to generate meaningful data for computer modeling.
- Initiate new, robust spot weld finite-element formulation procedures for modeling various modes of spot-weld failure as a function of impact, welding conditions and materials while maintaining the current computational efficiency.
- Establish an experimental database on the performance of resistance spot welds in AHSS components during impact.

Accomplishments

- Developed procedure for new crashworthiness characterization test based on parallel-plates buckling.
- Developed and conducted constant-velocity crash experiments on circular tubes.

*Denotes Project 190 of the Auto/Steel Partnership (A/SP), the automotive-focus arm of the American Iron and Steel Institute (see www.a-sp.org). The A/SP cofunds projects with DOE through a cooperative agreement between DOE and the United States Automotive Materials Partnership, one of the formal consortia of the United States Council for Automotive Research set up by Chrysler, Ford, and General Motors to conduct joint, precompetitive research and development (see www.uscar.org).

- Developed hydraulic tests for strain rate characterization of High Strength Steels (HSS).
- Developed web-based database for display and analysis of coupon, spot weld, and tube crush experiments
- Develop test method for investigation of strain-rate effects of spot welds.

Future Direction

- Develop experiments for characterizing fracture in HSS in forming and crash.
- Provide high-quality data for material and Finite-Element Modeling (FEM) development.
- Expand tests to other welding processes (weld bonding, friction stir spot welding, etc.).

Introduction

Crashworthiness characterization of AHSS requires testing of materials and structures under increased strain rates, large plastic strains, and large displacements that are characteristic of actual impact events. The AHSS characterization involves testing at several different length scales. The intrinsic material properties are investigated using the coupon-level specimens where the material is exposed to simple stress states that can be reduced to the equivalent stress and strain measures used in formulation of constitutive models. The coupon tests involve uniaxial tension and compression in plane-stress conditions. High-speed hydraulic equipment is used to impose constant velocity in order to determine material response to different loading rates. At a higher length scale, the characteristic plastic hinge mechanism responsible for crash energy absorption in AHSS structures is investigated using the double-plate test. This test has shown that the strain-rate sensitivity of AHSS in bending under out-of-plane compression exhibit trends that cannot be fully explained using the plate bending models derived from material behavior under uniaxial plane stress. At the component level, AHSS properties in tubular structures are investigated using specialized hydraulic equipment that allows constant crush speeds up to 8 m/s. In automotive design, the structural integrity of AHSS components is primarily provided by spot welds. The response of spot welds under different loading velocities and loading states have also been characterized in this project.

The above experiments provide high-quality data for development of material and structural FEM models for AHSS and thereby enable more accurate modeling and design of lightweight, crashworthy vehicles. The developed experiment technology is also directly relevant to other automotive materials as it provides a systematic approach to characterization and comparison of crashworthiness of new automotive materials.

Design of Experiments

The experiments conducted under this project have been compiled into interactive databases that are accessible over the World Wide Web. The portal page for the experiments is shown in Figure 1.

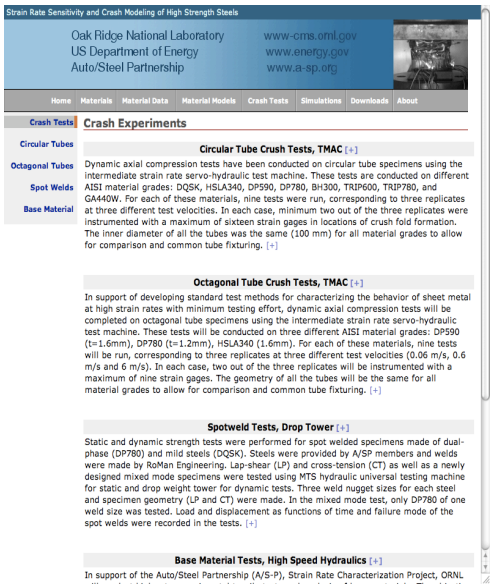

Figure 1. Web portal for AHSS experiments.

The experimental data is integrated with the other project components and provides mechanisms for

data analysis and collaboration between project participants.

Strain-Rate Characterization in Sub-Hopkinson Regime

In support of the Auto/Steel Partnership (A/SP), Strain-Rate Characterization Project, Oak Ridge National Laboratory researchers are conducting high-rate experimental tests and analysis of base material specimens in uniaxial tension configuration. The objective of the test program is to provide the necessary experimental data in support of the A/SP efforts to determine high-strain-rate mechanical properties of AHSS. The test program consists of testing tensile specimens under strain rates of quasi-static, 0.1/s, 1/s, 10/s, 100/s and maximum strain rates achievable in full open-loop configuration (1000/s) and the selected gage length. Among the unique features of the current approach is the ability to conduct tests across all speeds on the same apparatus and, thereby, eliminate variability associated with using different testing methods and actuators. The equipment allows for testing at speeds from quasi-static to 700 in/sec (18.5 m/s) over a range of 4 inches (100 mm) at maximum loads of 9000 lbf (40 KN). If an effective gage length for the chosen specimen is known, the equipment can run non-linear velocities in the drive file to achieve global strain control (engineering or true strain rate as desired). The test equipment is shown in Figure 2.

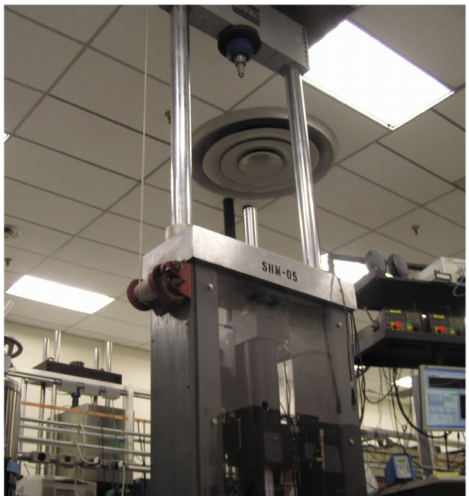

Figure 2. High-speed hydraulic tester. The test stage is elevated to allow for actuator acceleration to desired test speed.

The dynamic testing procedures from recent studies sponsored by International Iron and Steel Institute [1,2] and published literature [3,4] are followed and further enhanced using the new measurement techniques and synchronization. The multiple measurement methods of both forces and displacements allow for correlation of the results and verification of the different instrumentation techniques. Schematic representation of the test specimen and the measurement locations is shown in Figure 3.

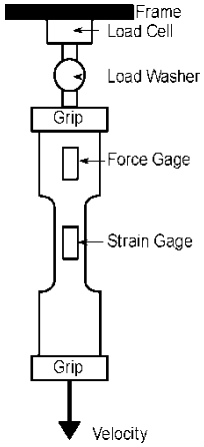

Figure 3. High strain-rate rate test setup.

The specimen geometry for dual phase 780 MPa (DP780) steel is shown in Figure 4.

Figure 4. High strain-rate specimen geometry.

The horizontal lines in the gage area were added to allow for optical-measurement correlation with the data from actuator displacement and electrical resistance strain gage in the gage area. All the measurements are synchronized using the central trigger. High-speed video recording is used to provide detailed record of the test and to correlate optical measurement with the mechanical output data. An output of the program from tracing multiple markings in the high-speed movie developed for optical measurement is shown in Figure 5. The measurement is based on the variations in color intensity along the prescribed

scan lines. The pixel location of the found gage marks is shown in the images for increasing displacement.

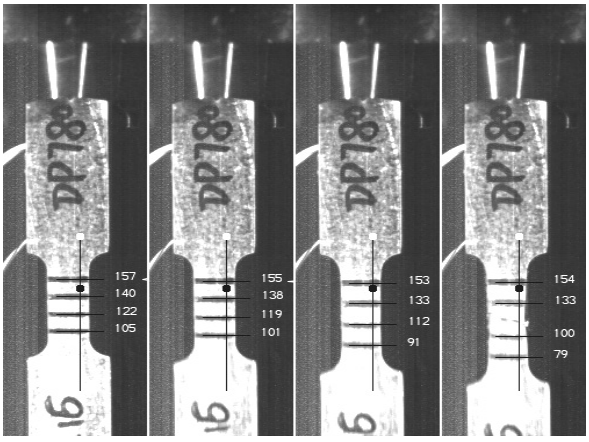

Figure 5. Optical strain measurement output for increasing strain. Horizontal black lines denote found gage mark based on color intensity. The test is conducted on DP780 material under 1000/s strain rate.

White numbers on the image denote vertical mark location in pixels. The distance between the lines can be used to determine uniformity of strain and the onset of localization. Figure 6 shows the output of the optical measurement and strain derived from the locations of the top (Line 1) and bottom (Line 4) marks.

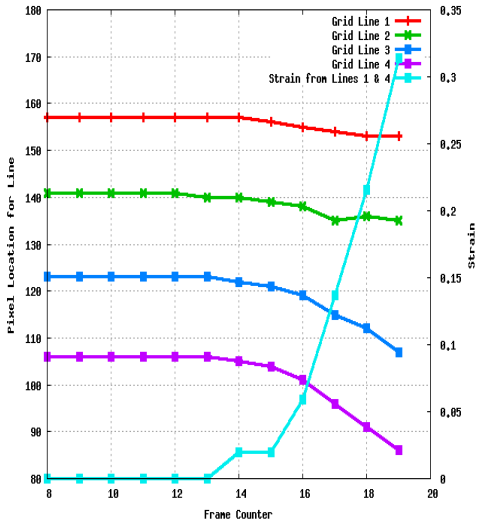

Figure 6. Analysis of the optical strain measurement output for increasing strain (Frame Counter). Divergence of the green (Line 2) and blue (Line 3) lines indicates onset of localization. Overall strain in the gage is calculated from the location of the top (Line 1) and bottom (Line 4) lines.

The multiple-measurement methods of both forces and displacements allow for correlation of the measurements, identification of test areas for further improvement, and verification of the method. All the measurements are synchronized using the central trigger. A Web-based database for the experiments has been created. The database is used to disseminate test results to the A/SP partners. A user can dynamically select and analyze tests results for different materials and strain rates. The main interface to the tests database is shown in Figure 7.

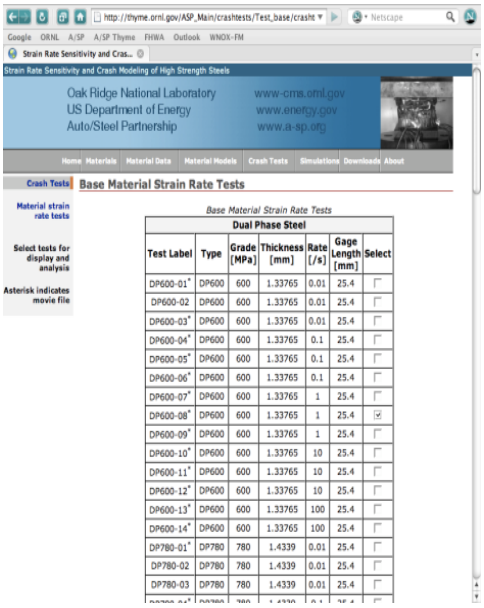

Figure 7. Web interface to the experimental data. Users select materials and proceed to the analysis phase.

The selected data is further analyzed and provided for download. It includes raw measurement data from multiple sources and high-speed video of the test. The stress-strain curves calculated from different sources for DP600 material are shown in Figure 8.

Figure 8. DP600 test at 1 /sec strain rate. The lower two lines (Red and yellow) denote measurement from load washer and force strain gage on specimen tab, respectively.

Conclusions

A new method for characterization of strain-rate sensitivity under automotive strain rates has been developed. This method uses multiple measurements of material response in a single testing apparatus. It enables the correlation of the measurements and identification of test areas for further improvement. The developed method allows for determination of material parameters to be used in computational modeling and design, and enabling of more-effective use of new materials and structures under impact loads.

Acknowledgments

Support from the Auto/Steel Partnership Strain Rate Characterization Team is acknowledged.

Future Work

Future work on the project will focus on the following.

1. Improvement of accuracy of strain and force measurements at strain rates larger than 100/s.
2. Development of integrated measurement system that automatically processes and correlates measurements.
3. Development of the specification for the testing of materials in the automotive strain rates regime.
4. Strain-rate sensitivity measurements for the new AHSS.
5. Development of new coupon-level crash characterization experiments for AHSS fracture under impact.

References

1. Recommendations for Dynamic Tensile Testing of Sheet Steels, International Iron and Steel Institute, 2005.
2. C. Wong, IISI-AutoCo Round-Robin Dynamic Tensile Testing Project, International Iron and Steel Institute, 2005.
3. D. Matlock, J. Speer, Constitutive Behavior of High Strength Multiphase Sheet Steels Under High Strain Rate Deformation, AISI/DOE Technology Roadmap Program, Report TRP 9904, 2005.
4. D.M. Bruce, “Dynamic Tensile Testing of Sheet Steels and Influence of Strain Rate on Strengthening Mechanisms in Sheet Steels”, Ph. D. Thesis # MT-SRC-003- 018, Colorado School of Mines, 2003.

G. Future Generation Passenger Compartment—Validation (A/SP241*)

Project Manager: Pat J. Villano
Auto/Steel Partnership
2000 Town Center Drive, Suite 320
Southfield, Michigan 48075-1123
(248) 945-4780; fax: (248) 356-8511; e-mail: pvillano@a-sp.org

Co-Chairman: Jody R. Shaw
Manager, Automotive Marketing
United States Steel Corporation
5850 New King Court
Troy, Michigan 48098-2608
(248) 267-2608; fax: (248) 267-2580; e-mail: jrshaw@uss.com

Co-Chairman: Joe Polewarczyk
General Motors Corporation
Body Systems & Closures
Engineering West
Mail Code 480-11-W13
30200 Mound Road
Warren, Michigan 48092-2025
(586) 986-2157: fax: (586) 986-8592; e-mail: joseph.m.polewarczyk@gm.com

Co-Chairman: Shawn Morgans
Ford Motor Company
Body Structure—Technical Leader
Product Development Center
20910 Oakwood Boulevard
Cube-2F-C11
Dearborn, Michigan 48121
(313)805-3596: fax:313-845-5634; e-mail: smorgans@ford.com

Technology Area Development Manager: Joseph A. Carpenter
(202) 586-1022; fax: (202) 586-1600; e-mail: joseph.carpenter@ee.doe.gov

Field Project Officer: Aaron D. Yocum
(304) 285-4852; fax (304) 285-4403; e-mail: aaron.yocum@netl.doe.gov

---

Contractor: United States Automotive Materials Partnership (USAMP)
Contract No.: DE-FC05-02OR22910 through the National Energy Technology Laboratory

---

Objective

- Validate the findings of the Future Generation Passenger Compartment (FGPC) Phase 1 project on a 5-passenger, 4-door, high production volume donor vehicle reducing passenger compartment mass by 25% or

*Denotes Project 241 of the Auto/Steel Partnership (A/SP), the automotive-focus arm of the American Iron and Steel Institute (see www.a-sp.org). The A/SP cofunds projects with DOE through a cooperative agreement between DOE and the United States Automotive Materials Partnership, one of the formal consortia of the United States Council for Automotive Research set up by Chrysler, Ford, and General Motors to conduct joint, precompetitive research and development (see www.uscar.org).

greater with cost parity relative to baseline while maintaining the structural performance in crash safety, stiffness and durability.

- Mass Efficient Architecture for Roof Strength, (MEARS) project is the concept development of a large truck cab with no B-pillar that comprehends the increase from 1.5 to 2.5 times vehicle curb mass roof-strength criteria with weight parity.
- Comprehend manufacturing feasibility in advanced manufacturing.
- Comprehend opportunities and influence of mass compounding.

Approach

- Aggressive use of Advance High-Strength Steels (AHSS), advanced manufacturing and computer- aided topology, grade, gauge, and geometry optimization techniques.
- Comprehend secondary mass reduction of vehicle systems with empirical regression analysis of production vehicle data.
- Assemble production-intent vehicle structure and conduct crash testing.

Accomplishments

- Developed concepts for reducing sedan donor vehicle passenger compartment mass by 12% while maintaining baseline structural performance criteria, passenger requirements, and vehicle architecture.
- Developed three concepts for a truck cab with no B-pillar that satisfy Federal Motor Vehicle Safety Standard (FMVSS) 216 (3.0 times roof strength criteria) with minimal mass gains of 7.5 to 10.5 kg and $80 cost increase.
- Identified possible secondary mass reductions on the order of 1.5 times the primary mass savings in clean-sheet vehicle architectural executions due to mass compounding.

Future Direction

- Develop vehicle structure with radical architectural changes and mass compounding to achieve structural mass reductions up to 50%.

Introduction

The FGPC project will incorporate current propulsion systems and fuel-cell technologies into concept architectures. This project will reduce passenger compartment mass by 25% or greater with cost parity relative to FreedomCAR baseline while meeting the structural crash performance objectives in meeting Insurance Institute for Highway Safety (IIHS) tests and also in anticipation of future crash requirements for the FMVSS pole side- impact test and FMVSS 2.5x vehicle weight roof-strength test. Further, it will maintain performance in static and dynamic stiffness, durability and front and rear crash requirements and also comprehend passenger and component packaging constraints. The project addresses concept development and validation on a donated 5-passenger, 4-door sedan; concept development of a large truck cab with no B-pillar comprehending 2.5 times roof- strength criteria; and comprehends opportunities and influence of mass compounding.

Project Status

FGPC—Validation

This project was initiated in February 2007 using a current (OEM) production vehicle and applying the FGPC Phase 1 integrated solutions. This study will develop a new safety cage by benchmarking, developing and documenting proven integrated solutions that will balance the interaction of geometry, material, manufacturing and performance costs effectively.

The project has completed Task 1, which establishes the performance baseline for the donor vehicle and sets performance targets for the project. For Task 2, the initial investigations

indicated that critical load paths identified in Phase 1 can be implemented in the donor vehicle. In addition, Task 2 shape-optimization work has been completed. Task 3 objectives were to perform design optimization of the final gauges and confirm that the final design met all performance objectives. This task has also been completed. Task 4 investigates impact of mass on vehicle performance in the side pole test. A study to investigate the sensitivity of seat alignment with the new cross-car load path and its impact on the side crash performance is currently underway. Also in progress is an investigation of the potential for additional mass savings with continuous joining methods such as laser welding and weld/bonding. Task 5 will establish a cost analysis against the baseline design. Task 6 will complete the engineering report and technology transfer of the findings.

Mass Efficient Architecture for Roof Strength (MEARS)

Passenger compartment concepts for large vehicles [trucks and sport utility vehicles (SUVs)], where the structure is driven by 2.5 times vehicle curb mass roof-strength criteria, were completed in 2007. The project focused on developing three different concepts: stamping-intensive (termed Concept 1), hydroforming-intensive (termed Concept 2), and stamped with composite structural inserts (termed Concept 3). All three concepts used AHSS steels.

Extensive optimization was carried out for each concept using HEEDS (optimization software tool).

In the stamping intensive design (Concept 1), structural changes including panel geometry, part thickness, and material grades were proposed. The major reinforcements in A-pillar, roof rail and C-pillar were proposed to be made from hot-stamped Boron steel. The inner parts of these sections were proposed to be of DP600 and DP800 steels. The body side outer material was not changed, but its thickness was increased. The most mass efficient design from several concepts was optimized as a final design for Concept 1.

In the hydroform-intensive design (Concept 2), the reinforcements in the A-Pillar, roof rail and C-Pillar were replaced with hydroform tubes made from DP780. Tubes were also investigated for the roof header and roof bow. A total of four concepts were proposed with different tube configurations, with the most mass-efficient design being optimized to obtain the final design for Concept 2.

In the stamped configuration with composite structural inserts (Concept 3), the thickness of major load-carrying members was reduced in the baseline model while materials were up-graded to AHSS to make the structure lighter and to take advantage of the stiffness provided by the lighter inserts. A total of four concepts was proposed with different types of inserts (i.e., steel-concepts 3A and 3B, Nylon-Concept 3B, and Beta foam-Concept 3C). Optimization was not carried out for these basic concept levels.

A comparative study of all concepts was done from the perspective of mass, cost, manufacturability, and reparability. The concept with the nylon inserts was selected as the final design. Further studies were carried out on the design to optimize the size of nylon inserts and the design of the sheet- metal parts. Formability studies were carried out on the major structural parts to ensure that there were no major issues.

Phase 2 has been approved and will focus on improving the modeling of the nylon inserts, adhesive materials, and validating the predictions with physical testing to validate the performance of the models.

Mass Compounding

Vehicle design engineers intuitively know that an unplanned mass increase in a component during vehicle design has a ripple effect throughout the vehicle; other components need to be resized increasing vehicle mass even more. The phrase *mass begets mass* describes this phenomenon. A more-encouraging view of this behavior considers a reduction in the mass of a component enabled by a new technology resulting in a greater mass reduction ripple effect throughout the vehicle. Published data on this effect are sparse and based on 1975-1981 model years. The purpose of the

project was to update the data using contemporary vehicles.

The secondary mass change is the additional mass reduction resulting from primary mass reduction by the implementation of mass-reduction technology. When all subsystems can be resized, the secondary mass savings is from 0.8 to 1.5 kg/kg (1.25 kg/kg is the estimate for the *all* vehicle group). When the powertrain has been fixed and is not available for resizing, the secondary mass savings is from 0.4 to 0.5 kg/kg (0.5 kg/kg is the estimate for the all vehicle group).

The initial study is complete for D-segment sedans and SUV vehicles with the deliverable being a report and a calculator for estimating secondary mass savings.

The Project is currently extending the vehicle segments to include B and C class vehicles and is still in progress.

Conclusions

FGPC—Validation

The 2004 production donor vehicle baseline structure had aggressively used AHSS and was shown to be 6% lighter than a typical comparable 2004 vehicle. The final optimized design demonstrated a 39.8 kg mass reduction from the baseline, as summarized in Figure 1. This represents a 15% mass savings for the parts modified and a 12% mass savings for the full passenger compartment as compared to the baseline design, while meeting all structural performance objectives. The concept design is constrained by maintaining the existing architecture of the donor vehicle. The results were achieved by using more AHSS grades (thus increasing the average strength level of the vehicle structure), improving structural load paths (such as a cross car load path through the seat structure), and conducting shape optimization of the major structural components.

Additional findings will be made available with the completion of Tasks 4, 5 and 6.

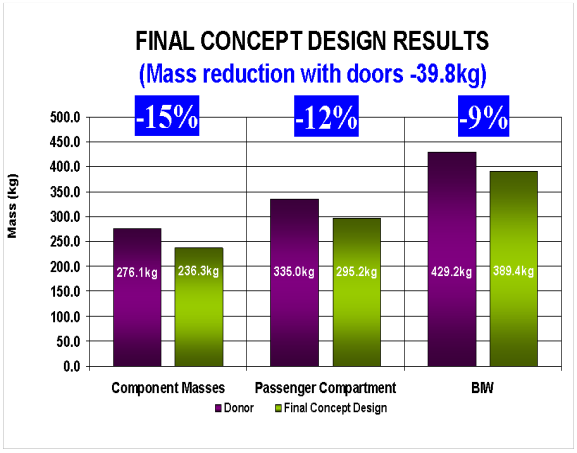

Figure 1. Final concept design results.

MEARS

The baseline design of the donor vehicle (large truck cab with no B-pillar) roof strength performance was improved from 1.5 times vehicle curb mass to 3.0 times vehicle curb mass with design optimization. Several concept design solutions were investigated and evaluated for mass, cost, manufacturability and reparability as shown in Table 1.

Table 1. Summary of concept design solutions.

S.No	Concept	Load Factor	Mass [kgs]	Cost	Rating				Weighted Rating
					Mass	Cost	Manufacturability	Repair	
Weight Factor ---------->					4	3	2	1	
1	Stamping Intensive	3.06	17.6	$108	1	1	4	3	18
2	Hydroform intensive	3.00	10.5	$79	4	3	3	3	34
3 A1	Steel Inserts-Tube in C-Pillar	3.00	14.9	$79	2	3	3	4	27
3 A2	Steel Inserts-Stamped C-Pillar Rnf	3.06	13.8	$67	3	5	4	4	39
3. B	Nylon Inserts (Drop-in)	3.06	7.5	$80	5	3	4	2	39
3. C	BetaFoam (Injected)	2.95-3.82*	8.4	$78	5	3	2	2	35

Design 3B provides a 7.5 kg mass increase and $80 cost increase relative to the baseline donor vehicle design. The results were obtained with use of AHSS and hot-stamped boron steel, advance design optimization and use of nylon inserts to improve section stability.

Mass Compounding

When all subsystems can be resized, the secondary mass savings is from 0.8 to 1.5 kg/kg (1.25 kg/kg is the estimate for the *all* vehicle group). When the powertrain has been fixed and is not available for resizing, the secondary mass savings is from 0.4 to 0.5 kg/kg (0.5 kg/kg is the estimate for the all vehicle group).

The study indicates that optimized steel structure can meet the FreedomCAR mass reduction targets when mass compounding is considered. Realizing this objective requires additional technology development and is challenged by mass increases resulting from increased safety requirements, alternative powertrains and additional passenger amenities.

Presentations/Publications/Patents

There are no patents or publications associated with this project.

FGPC—Validation

This project is still being completed and final results being documented. No results have been formally communicated to date.

MEARS

This project is still being completed and final results being documented. No results have been formally communicated to date.

Mass Compounding

Phase 1 results of the study have been presented to engineers at automotive companies and steel partnerships and the USAMP Steering Committee and Multi-Material Vehicle Task Force.

Phase 2 of project is still being completed and final results are being documented. No results have been formally communicated to date.

H. Lightweight Rear Chassis Structure (A/SP601*)

Project Manager: Jim Cran
Auto/Steel Partnership
2000 Town Center, Suite 320
Southfield, MI 48075
(905) 385-8276; fax: (905) 383-3200; e-mail: jim.cran@sympatico.ca

Co-Chair: Jamal Alghanem, PhD
Chrysler LLC
800 Chrysler Drive—CIMS 484-01-09
Auburn Hills, MI 48326
(248) 576-0849; fax: (248) 576-2197; e-mail: ga5@chrysler.com

Co-Chair: Michael Gulas
ArcelorMittal USA
P.O. Box 2460
1330 Burlington St. E.
Hamilton, ON, Canada L8N 3J5
(905) 548-4719; fax: (905) 548-4250; e-mail: michael_gulas@arcelormittal.com

Technology Area Development Manager: Joseph A. Carpenter
(202) 586-1022; fax: (202) 586-1600; e-mail: joseph.carpenter@ee.doe.gov

Field Project Officer: Aaron D. Yocum
(304) 285-4852; fax: (304) 285-4403; email: aaron.yocum@netl.doe.gov

---

Contractor: United States Automotive Materials Partnership (USAMP)
Contract No.: DE-FC05-02OR22910 through the National Energy Technology Laboratory

---

Objectives

- Obtain a minimum mass reduction of 25% for a baseline passenger car rear chassis structure with no more than a 9% cost premium.
- Develop and document integrated solutions that balance the interaction of materials, manufacturing, and cost. The solutions will focus on high-volume production (200,000 plus vehicles per year).
- Demonstrate the successful use of advanced high-strength steel (AHSS) in a passenger car rear chassis structure.
- Address corrosion and durability issues associated with reduced-thickness AHSS.

Approach

- Phase 1: Material optimization. Through material substitution and minimal size and shape changes, the mass of the baseline chassis was reduced 15% noting limited reduction in stiffness. Prototypes have been fabricated and

*Denotes Project 601 of the Auto/Steel Partnership (A/SP), the automotive-focus arm of the American Iron and Steel Institute (AISI) (see www.a-sp.org). The A/SP cofunds projects with DOE through a cooperative agreement between DOE and the United States Automotive Materials Partnership, one of the formal consortia of the United States Council for Automotive Research set up by Chrysler, Ford, and General Motors to conduct joint, precompetitive research and development (see www.uscar.org).

physically tested. The lessons learned are being used in Phase 2. Phase 1 completion is scheduled for February 2009.

- Phase 2: Design optimization. Through a clean-sheet redesign, the primary goal is to obtain a minimum mass reduction of 25% with no reduction in stiffness. A secondary goal is to obtain no more than a 9% cost premium. However, the cost goal may be relaxed to achieve mass reduction provided the design remains competitive in cost with any aluminum alternative. A Phase 2 final design has been prepared, and manufacturing feasibility and a cost analysis are underway. Phase 2 completion is scheduled for February 2009.
- Phase 3: Communications. The goal is to transfer the technology developed in the project to original equipment manufacturer (OEM) and Tier 1 chassis structure designers. Phase 3 completion is scheduled for April to June 2009.

Accomplishments

- Verified a fatigue methodology for validating the durability of the Phase 2 final design.
- Established a Phase 2 final design, which offers a 27% mass reduction.
- Completed a one-step forming analysis for all parts in the Phase 2 final design.
- Prepared a preliminary cost analysis for the Phase 2 final design.
- Determined the mass-compounding effect for a rear chassis associated with a 20% lighter vehicle.

Future Direction

- Conduct an incremental forming analysis for three parts in the Phase 2 final design.
- If required for manufacturing feasibility, modify the Phase 2 final design.
- Finalize the cost analysis for the final design.
- Evaluate the results from the 100 trailer test corrosion cycles.
- Prepare Final Reports for Phases 1 and 2.
- Transfer the technology through road shows to Auto/Steel Partnership (A/SP) member companies and key Tier 1 suppliers.

Introduction/Overview

Phase 1 is almost completed. Four of the five technology gaps have been addressed (AHSS Availability, AHSS Forming, AHSS Welding and Fatigue Resistance). Work on the remaining gap (Corrosion Resistance) will be completed by February 28, 2009.

By mutual agreement, due to changing the timing and scope of the project, Martinrea ceased contract work after completing the Phase 2 Preliminary Design in September of 2007. However, Martinrea graciously continued to support the project through in-kind work until December 2007. At that time, the team set a new direction, which meant that a Request for Quote (RFQ) was required to take the Phase 2 preliminary design to a Phase 2 final design. The new direction included a new baseline, the elimination of Phase 2 prototypes, and the addition of a fatigue analysis on the final design, a mass-compounding exercise and an extended project completion date.

In February 2008, Altair was awarded a contract to complete Phase 2 and conduct Phase 3. Altair reviewed the Martinrea Phase 2 Preliminary Design using the loads and stiffnesses associated with the new baseline (Figures 1 and 2). Altair concluded the preliminary design was solid. Optimization work led to a Phase 2 final design that is 27% lighter than the new baseline. However, modifications required to overcome

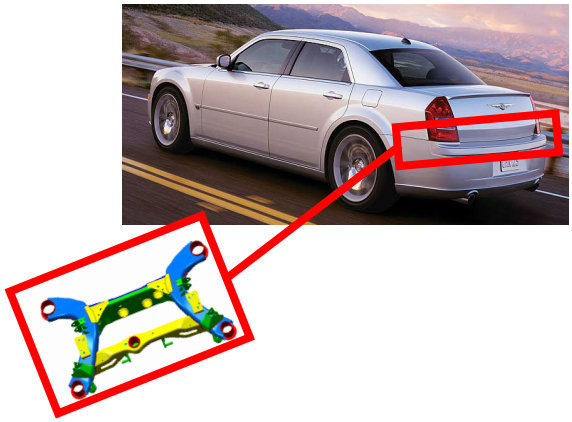

Figure 1. Donor vehicle and new baseline structure.

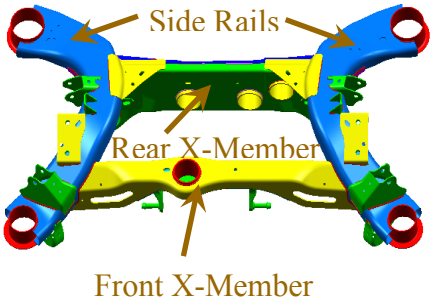

Figure 2. Baseline structure detail.

stamping issues associated with three parts might reduce this mass saving.

Phase 1: Material Optimization

Ten prototypes were fabricated using DP590 and TRIP780 steels. The last two prototypes built (9 and 10) have a mass of 21.74 kg compared to the 25.81 kg mass of the baseline. Thus, a mass reduction of 15% was achieved. However, it should be noted that the prototype design was a material substitution exercise. Thus, the prototypes have a limited reduction in stiffness compared to the baseline. Computer-aided design (CAD) and finite-element analysis (FEA) models of the as-built prototypes were constructed.

The prototypes were allocated as follows: two for show pieces (Figure 3), one for modal testing (Figure 4), three for bracket fatigue testing (Figure 5), two for corrosion testing (Figure 6) and two (9 and 10 with gusset plates) for subsystem fatigue testing (Figure 7).

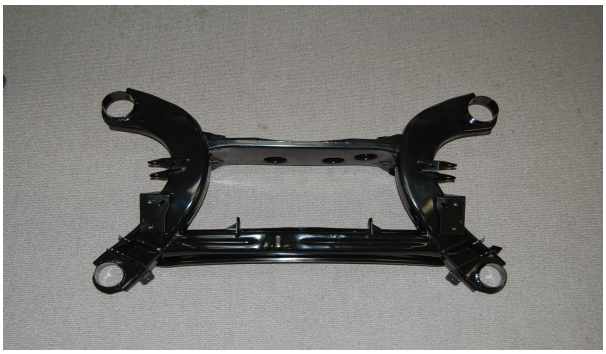

Figure 3. Phase 1 prototypes 1–8 without gusset plates.

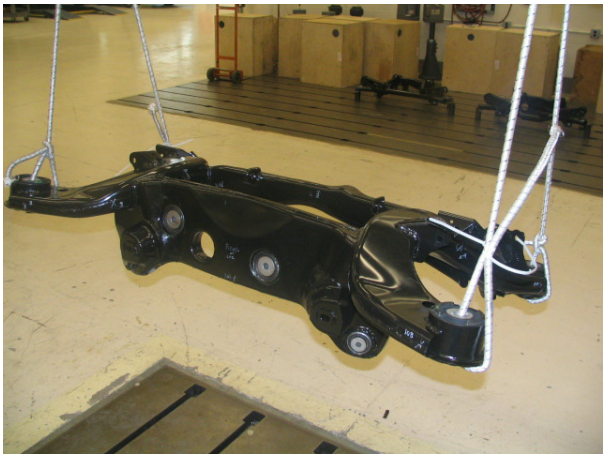

Figure 4. Modal test.

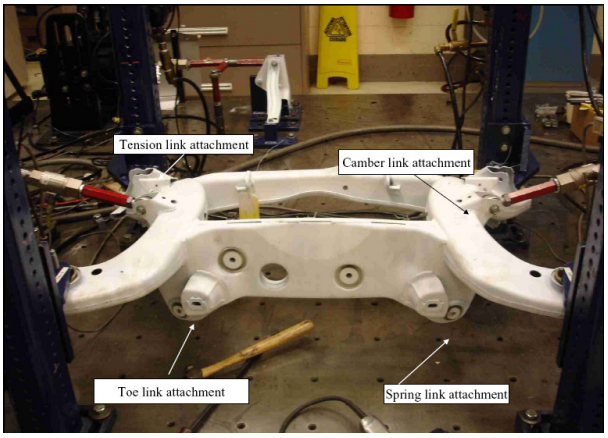

Figure 5. Bracket fatigue test.

Phase 1 completion is scheduled for February 2009.

Figure 6. Corrosion trailer test.

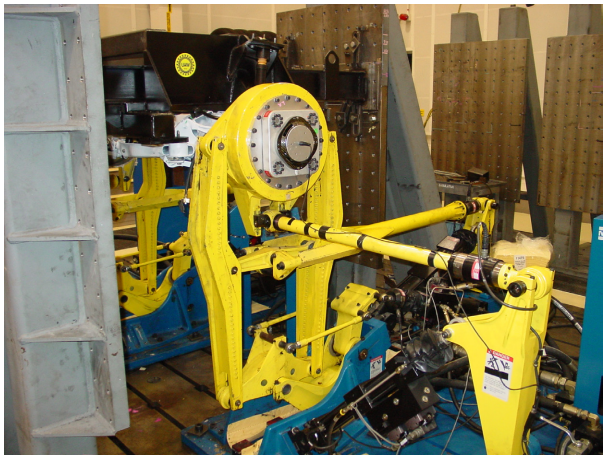

Figure 7. Subsystem fatigue test.

Phase 1 Technology Gap Analysis

Availability of AHSS

The team believes that the lack of a table showing the global availability of AHSS is hindering the use of AHSS for mass reduction in chassis structures. The team pursued the development of a global table but discovered that the steel producers, for commercial reasons, do not want the availability of their AHSS in the public domain. Thus, the team has reluctantly agreed that it is unable to address this technology gap.

Forming of AHSS

As discussed in the FY 2007 Annual Report, the team has concluded that commercially-available AHSS grades may be formed into satisfactory chassis structure parts. However, for dual phase steels, strain kicks off strain hardening even at room temperature. Thus, as much work as possible should be done during the first draw. Also, stampings need to be processed immediately from stage to stage.

Welding of AHSS

Heat-Affected Zone (HAZ) softening, which depends on steel chemistry, is more pronounced in higher strength steels. This softening reduces joint efficiency and must be taken into account when designing a chassis structure.

To address the softening issue, the team collaborated with A/SP's Joining Team (see report 5.A) to develop a Gas Metal Arc Welding *(GMAW) Weld Design Guideline for Chassis Structures*. The Joining Team finalized the Guideline in December 2007. It covers both conventional and AHSS steels.

Oak Ridge National Laboratory (ORNL) is developing a model to predict the effects of welding on AHSS microstructure. The model predicts softening in the HAZ. The Chassis Team is interacting with ORNL to ensure a simplified model. That is, a model suitable for inclusion into automotive FEA.

Corrosion Resistance

Downgaging with AHSS means thinner steel. In chassis structures, the thickness of the steel is used as the second line of defense against corrosion. Thus, there is a concern that thinner steel may cause corrosion problems.

The team's Corrosion Working Group has concluded that the performance of E-Coat over parts made from galvanized steel is a known technology for chassis applications. Hence, it can be used to protect thin AHSS chassis structure members (thickness less than 2.0 mm). However, the Group feels it is desirable to have an alternate corrosion protection method. Thus, it is evaluating the Electropoli hot-dip galvanizing method used in Europe to coat chassis structures after fabrication. Two baseline rear chassis structures and two Phase 1 prototypes have been coated with Electropoli in France. One baseline structure with E-coat, one baseline structure with Electropoli and one Phase 1 prototype with Electropoli were

sectioned by Ford to evaluate coating coverage. The baseline structure with both E-coat and Electropoli had good coating coverage inside and out. However, the Phase 1 prototype with Electropoli had no coating on the inside corners. Insufficient holes to ensure good coverage or weld flux might be the reason.

One baseline structure with E-coat, one baseline structure with Electropoli and one Phase 1 prototype with Electropoli were subjected to 100 cycles of the General Motors corrosion trailer test. This test is an indicator of long term exterior cosmetic corrosion. It is also an indicator of interior/crevice corrosion; but, interior/crevice corrosion is accelerated to a much lower degree than exterior cosmetic corrosion.

Examination of the three chassis structures, sectioned after 100 cycles, showed that Electropoli offers more protection than E-coat. Pit depth measurements are being taken in order to establish the benefits of Electropoli.

Fatigue Resistance

Durability is a major criterion in chassis design. AHSS brings not only mass reduction but higher stresses, which may reduce fatigue resistance if not properly accommodated.

The team has addressed the fatigue issue with the A/SP Sheet Steel Fatigue Team (see report 5.C). There is ample evidence that the fatigue strength of sheet steel is proportional to tensile strength. Thus, even though design stresses are higher in AHSS, the higher tensile strength of AHSS results in higher fatigue strength. The end result is the fatigue strength of AHSS material is not an issue. There is little data on the fatigue strength of metal inert gas (MIG) welded joints made with AHSS. However, fatigue experts agree that the fatigue strength of all MIG welded joints depends on weld process and joint geometry. That is, the fatigue strength of MIG welded sheet steel joints is independent of steel grade. To verify this conclusion, the A/SP Fatigue Team has launched a test program using DP590, DP780, DP1000, and TRIP780 AHSS joined by MIG and laser welds. The program should be completed in 2009.

The team wished to develop an appropriate analytical method to evaluate the fatigue resistance of chassis structures and the Phase 2 final design. To this end, Altair evaluated the use of finite element (FE)-safe software with the Verity module and the use of FE-safe software with the British Standard (BS) 5400 module. Analytical results using these two methods were compared to the results from bracket fatigue tests on Phase 1 prototypes. Both methods predicted the fatigue crack locations. However, the Verity module gave a better prediction of fatigue life. The BS 5400 module, due to a built-in safety factor, gave an overly conservative fatigue life.

Analytical results using FE-safe and the Verity module were compared to results from subsystem fatigue testing conducted on Phase 1 prototype 9. The first crack in the analysis appeared at 1.9 lives compared to 1.4 lives in the test. There was no catastrophic failure in either the analysis or the test. For these reasons, the team concluded that the FE-safe and the Verity module may be used to validate the durability of the Phase 2 final design.

Phase 2: Design Optimization

Martinrea prepared a Phase 2 preliminary design in FY 2006, which had a 12% mass reduction compared to the new baseline. However, in order to properly incorporate the lessons learned from Phase 1 into Phase 2, work on Phase 2 was put on hold until February 2008. At that time, Altair commenced work to finalize the preliminary design. Its first activity was to evaluate the preliminary design using the loads associated with the new baseline. The preliminary design is superior to the baseline from the maximum stress point of view. Further, it has a stiffer response than the baseline for virtually all of the load cases. The team concluded it was not necessary to match the baseline stiffness in all directions. The team identified the stiffnesses to be matched. Also, the team decided that the lesser of a 10x bushing rate and the actual baseline bushing rate should be used in the redesign.

Altair explored numerous alternatives in order to increase the 12% mass reduction of the Phase 2 preliminary design. In fact, over 20 gage

optimizations were prepared in order to evaluate material selection, the use of patches and the use of tailored blanks. The team detected that an inefficient bracket was adding unnecessary mass to the chassis structure. Altair optimized this bracket. The end result of all this activity is the Phase 2 final design (Figures 8 and 9). The mass of the Phase 2 final design is 18.83 kg compared to 25.81 kg for the baseline. Thus, a mass reduction of 27% was achieved while meeting all stress and stiffness targets. Using the correlated fatigue methodology (see *Phase 1 Technology Gap Analysis—Fatigue Resistance*), Altair compared the fatigue resistance of the Phase 2 final design to the fatigue resistance of the new baseline chassis structure. The fatigue life of the Phase 2 final design is as good as or better than the fatigue life of the baseline.

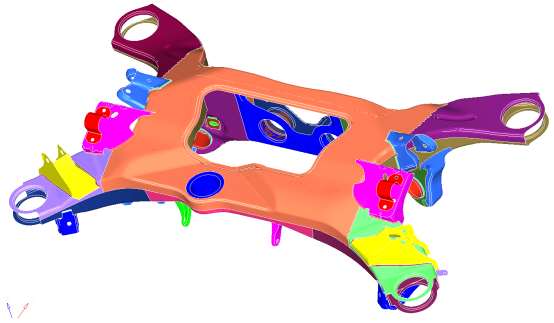

Figure 8. Phase 2 final design.

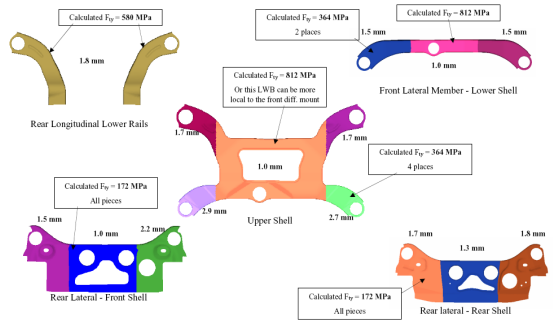

Figure 9. Exploded view of Phase 2 final design.

A one-step forming analysis was used to check the manufacturability of all parts in the Phase 2 final design. It disclosed that there are forming issues with three of the parts. The team has agreed to extend the Altair contract to allow Altair to conduct an incremental forming analysis for the three parts. If necessary, the Phase 2 design will be modified to overcome the stamping issues associated with the three parts. Any modifications might reduce the 27% mass saving associated with the present Phase 2 final design.

The Massachusetts Institute of Technology (MIT) Cost Model has been used to establish a greenfield site cost for the baseline chassis structure and the Phase 2 final design chassis structure. The costs will be finalized after the stamping issues associated with the three parts are resolved.

Phase 2 completion is scheduled for February 2009.

Mass Compounding

To determine the mass compounding effect for a rear chassis structure, the Phase 2 design was modified through gage optimization to suit a vehicle, similar in size to the baseline, but having a 20% lower gross vehicle weight. The team assumed that a 20% reduction in gross vehicle weight results in 20% lower stiffness targets. Thus, the gage optimization was conducted using 20% higher deflection constraints. Stresses were not checked because the design is stiffness driven. Stresses only affect the choice of steel grades. A 20% reduction in gross vehicle weight results in an 8% mass reduction of the rear chassis structure.

Phase 3—Communications

Phase 3 communications activity is scheduled for January–March 2009.

Conclusions

The technology gaps that prevent mass reduction in chassis structures through the use of AHSS have been addressed. The team is confident that the project objectives will be accomplished and the results will facilitate the use of AHSS by chassis engineers to achieve mass reduction.

Presentations/Publications/Patents

To date, no presentations or publications have been placed into the public domain.

I. Characterization of Thermomechanical Behaviors of Advanced High-Strength Steels (AHSS): Formability, Weldability, and Performance Evaluations of AHSS Parts for Automotive Structures

Principal Investigator: Mohammad A. Khaleel
Pacific Northwest National Laboratory
P.O. Box 999, Richland, WA 99352
(509) 375-2438; fax: (509) 375-4392; e-mail: moe.khaleel@pnl.gov

Technology Area Development Manager: Joseph A. Carpenter
(202) 586-1022; fax: (202) 586-1600; e-mail: joseph.carpenter@ee.doe.gov

Field Technical Monitor: Mark T. Smith
(509) 375-4478; fax: (509) 375-4448; e-mail: mark.smith@pnl.gov

---

Contractor: Pacific Northwest National Laboratory
Contract No.: DE-AC06-76RL01830

Objective

- Investigate the formability of advanced high-strength steels (AHSS) with emphases on loading temperature, loading paths and secondary deformation effects on part residual strength and microstructure.
- Develop a fundamental understanding of transformation kinetics of AHSS steels by analyzing the crystallographic and morphological features of the phase transformations subject to different thermal and mechanical loading paths from forming and welding.
- Provide performance data and constitutive models for formed AHSS parts.
- Investigate the weldability of AHSS under various welding processes and parameter conditions applicable to auto-production environment.
- Generate weld performance data including static strength, formability, impact strength and fatigue life as function of welding processes and parameters.
- Investigate welding techniques for improved AHSS weld performance and benchmark the performance against the current welding practices for roll- and hydro-formed AHSS frame and underbody structure applications.
- Develop design guidelines on AHSS to assist rapid structure design and prototyping.

Approach

- Investigate formability and weldability of AHSS. This task includes forming under complex loading paths (uniaxial and biaxial); quantification of formability and weldability for various grades of AHSS based on their chemistries and corresponding thermal-mechanical process.
- Investigate the interdependency of manufacturing processes: both weldability of a formed part and formability of a welded part.
- Develop transformation kinetics model and macroscopic constitutive relationships for AHSS (dual phase [DP], transformation-induced plasticity [TRIP] and complex phase [CP]).
- Systematically evaluate the effects of various welding process and process parameters on the microstructure and weld property. Welding processes include gas metal arc, laser, hybrid laser-arc, and resistance spot. Metallurgical and process models will be used to analyze the microstructure evolution. The properties will be

measured as a function of geometry, composition, process and process parameters. A performance evaluation procedure will be developed that allows for quantifying the performance improvement, weight and cost savings associated with use of AHSS.

- Evaluate structural performance evaluation of formed and welded parts made of AHSS. This task will provide the automotive design engineers with accurate material performance data for design verification of AHSS structural parts.

Accomplishments

- Completed micromechanics-based failure analysis and stress versus strain predictions for DP800/DP980.
- Completed quantifying individual phase stress and strain partition in TRIP800 in transverse direction.
- Completed micromechanics-based failure analysis and failure mode prediction modeling for TRIP800.
- Completed examining effects of martensite mechanical properties on failure mode and ductility of DP800/DP980.
- Completed examining effects of martensite volume fraction on the failure of DP steels.
- Completed examining potential sources for shear fracture of DP steels during stamping process using microstructure-based representative volume element (RVE).
- Completed preliminary fracture toughness prediction of TRIP800 using microstructure-based RVE.
- Started preliminary studies on three grades of twinning induced plasticity (TWIP) steels and a nano-precipitate-strengthened steel (NPSS).
- Performed advanced photon source tests in an attempt to quantify the evolution of micro-twin volume fraction during deformation of TWIP steels, data analyses underway.

Future Direction

- Complete the micromechanics based cyclic and fracture toughness modeling of TRIP800.
- Complete preliminary evaluations of three TWIP steel grades with various manganese compositions.
- Complete microstructure and mechanical property characterizations of NPSS.

Introduction

This project is a collaborative effort between the Department of Energy, Pacific Northwest National Laboratory (PNNL), Oak Ridge National Laboratory and the United States (U.S.) Automotive Materials Partnership of the U.S. Council for Automotive Research. The work began in October 2005.

Because of their excellent strength and formability combinations, advanced high-strength steels (AHSS) are being used in vehicle body structures to reduce vehicle weight and improve crash performance. Currently, technical barriers hindering wider applications of AHSS in the domestic auto industry are as follows:

- The fundamental behaviors of AHSS parts subject to different thermal and mechanical loading paths (forming and welding) are not fully understood and quantified.
- The constitutive behaviors for the formed parts are not available to computer-aided engineers for rapid prototyping.
- Welding-induced complex microstructures and the effects of different welding processes and welding parameters on weld performance are not well understood.

To address these issues, PNNL's role in this project includes investigating the formability of AHSS with emphases on loading temperature, loading paths and secondary deformation effects on part residual strength and microstructure. The

project also develops a fundamental understanding of transformation kinetics of AHSS steels by analyzing the crystallographic and morphological features of the phase transformations subject to different thermal and mechanical loading paths from forming. The goal is to provide the automotive design engineers with accurate material performance data and constitutive models for design evaluations and verification of AHSS structural parts.

Approach

Prediction of Failure Modes and Ductility for DP980 Using Plastic Strain Localization

Ductile failure of metals is often treated as the result of void nucleation, growth and coalescence. Throughout this study, ductile failure of dual-phase steels is predicted in the form of plastic strain localization resulting from the incompatible deformation between the harder martensite phase and the softer ferrite matrix.

Failure modes and ultimate ductility of DP980 steels are analyzed using finite element analyses (ABAQUS) based on the actual steel micro-structure. Figure 1 shows an actual micro-structure of DP980 obtained using scanning electron microscopy (SEM) and the corresponding finite-element model used for the representative volume element (RVE) in this study. For the finite element analysis, the mechanical properties of the constituent phases (ferrite and martensite) are determined by the *in-situ* synchrotron-based high energy X-ray diffraction (HEXRD) technique

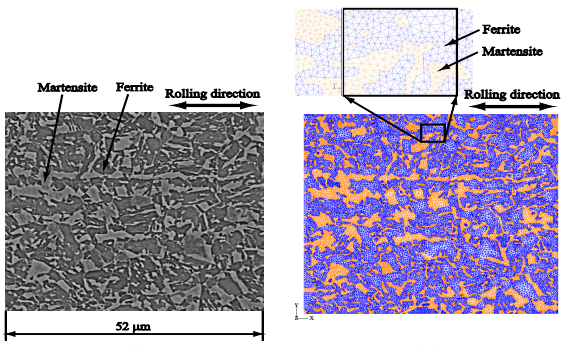

Figure 1. (a) An actual microstructure of DP980; (b) the corresponding finite element model used for the RVE of DP980 ($V_{f,M}$=38%). ($V_{f,M}$ = *Volume* fraction of martensite).

together with the RVE prediction for the uniaxial tension. The *in situ* experiments were performed at the 11-ID-C beamline of Advanced Photon Source (APS) at Argonne National Laboratory.

Under different loading conditions, different failure modes and ultimate ductility are predicted in the form of plastic strain localization. It is found that the local failure mode and ultimate ductility of dual-phase steels are closely related to the stress state in the material. Under plane-stress condition with free lateral boundary (Figure 2, Region A), one dominant shear band develops and leads to final failure of the material. However, if the lateral boundary is constrained (Figure 2, Region B), splitting failure perpendicular to the loading direction is predicted with much reduced ductility. On the other hand, under plane-strain loading condition (Figure 2, Region C), commonly-observed necking phenomenon is predicted that leads to the final failure of the material. Figure 3 shows three different failure modes predicted in the RVE under the different loading conditions corresponding to the three regions shown in Figure 2. These predictions are in reasonably good agreement with experimental observations shown in Figure 4.

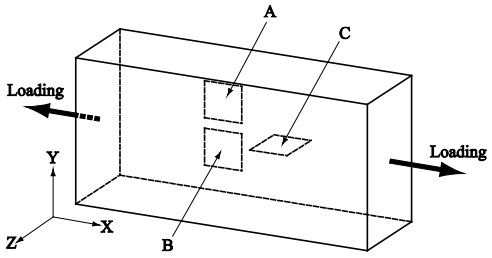

Figure 2. Three different locations of a sheet specimen under tension.

The methodology developed in this study can be used as a tool in studying the effects of the various factors on the ductile failure mechanisms of dual-phase (DP) steels.

Martensite Mechanical Property Effects on DP980 Failure Mode and Ductility

In this section, the effects of the mechanical properties of the martensite phase on the failure mode and ductility of DP980 under uniaxial tension are investigated using the microstructure-

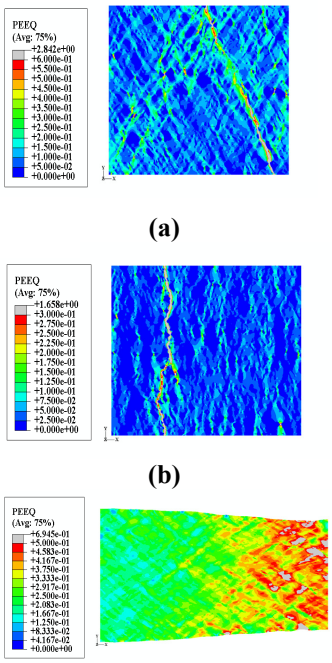

Figure 3. Different failure modes in the RVE for the three Figure 2 locations. Engineering strains for (a), (b), and (c) are 12.5%, 3.6% and 30.2%, respectively.

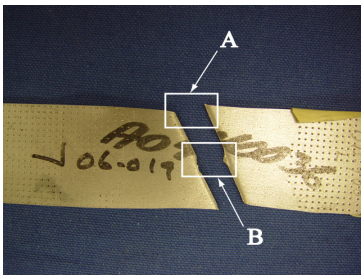

Figure 4. A failed DP980 sheet specimen.

based modeling methodology presented in the previous section. The reference mechanical properties of the constituent phases in DP980 are the same as those obtained in the previous section. Computations are then conducted on the RVE in Figure 1. Various reasonable combinations of initial yield strength ($\sigma_{y,M}$) and linear hardening rate (K_M) for the martensite phase are considered for this purpose. Figure 5 shows the input stress-strain curve for the ferrite phase and the examined

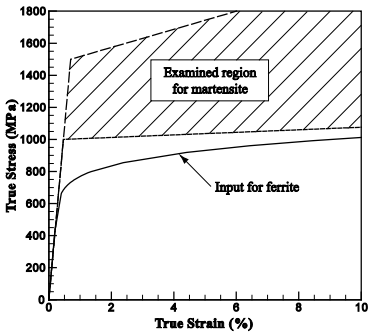

Figure 5. Examined region for the mechanical properties of the martensite phase to investigate its effects on the RVE macroscopic response.

region for the mechanical properties of the martensite phase in this investigation. Figure 6 shows an example of the effects of the mechanical properties of the martensite phase on the macroscopic response of the RVE. The computations show that, as the strength of the martensite phase increase, the ultimate tensile strength (UTS) of DP980 steels increases but UTS strain and failure strain decrease.

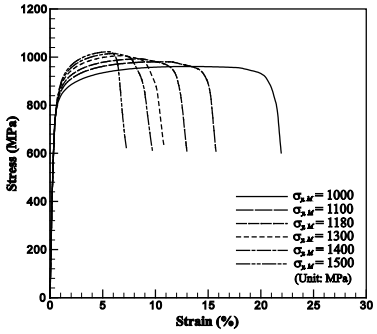

Figure 6. Effects of the initial yield strength of the martensite with K_M=1740 megapascals (MPa) on the macroscopic response of the RVE.

The computations also show that shear-dominant failure modes usually develop for DP980 with lower martensite strengths, whereas split failure modes typically develop for DP980 with higher martensite strengths. These trends are well presented in Table 1, which shows a clear diagonal band separating the shear and split modes. Figure 7 shows the predicted different failure modes in the RVE for different mechanical

Table 1. Predicted failure modes in the RVE of DP980 under tensile loading for different mechanical properties of the martensite phase. (PS=pure shear failure, SD=shear dominant failure, SSC=split and shear combined failure, S=split failure)

K_M / $\sigma_{Y,M}$	800	1740	2800	3800	4800	5800
1000	PS	SD1	SD1	SD2	SD3	SSC1
1100	SD1	SD1	SD2	SD3	SSC1	SSC3
1180	SD1	SD2	SD3	SD3	SSC3	S
1300	SD2	SD3	SD3	S	S	S
1400	SD2	SD3	S	S	S	S
1500	SSC2	S	S	S	S	S

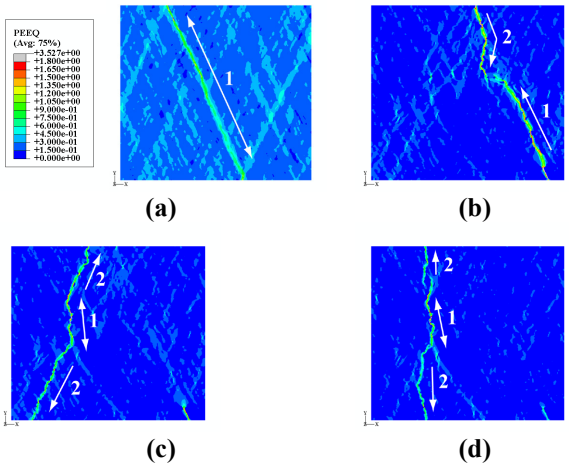

Figure 7. Different failure modes in the RVE depending on the mechanical properties of the martensite phase: (a) PS, (b) SD3, (c) SSC1, and (d) S.

properties of the martensite phase. The information based on these investigations can be used as a quantitative design guideline for DP steels.

Effects of Martensite Volume Fraction on Failure of DP Steels

For the DP steels with lower martensite volume fractions, ultimate failure can be dominated by the ductility of the ferrite phase through the conventional void nucleation, growth and coalescence process. There may be some range of martensite volume fraction where the failure of DP steels may depend on the inhomogeneity among the various constituent phases, rather than on the ductility of the individual constituent.

The approximate range of martensite volume fraction controlled by initial phase inhomogeneity is determined in this section. For this purpose, various micromechanics-based finite-element models are generated based on the actual microstructures of DP and TRIP steels. Figure 8 shows two examples of the various finite-element models with different martensite volume fractions, used in this investigation. The mechanical properties for the ferrite and martensite phases are the same as those determined for the DP980 in the previous section.

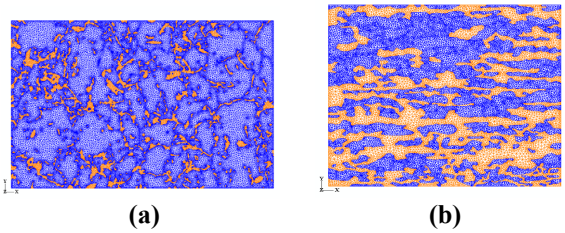

Figure 8. Finite-element models based on different microstructures of DP and TRIP steels. $V_{f,M}$ percentage in the models are (a) 14 and (b) 44.

First, the influence of ductility of the constituent phases on the overall ductility of DP steels was examined. Figure 9 shows the failure strains (ultimate ductility) as function of martensite volume fraction for different input strain ranges of the ferrite phase. Similar trends are observed when varying the input strain ranges of martensite. The results in Figure 9 indicate that the phase inhomogeneity dominant region appears to be with

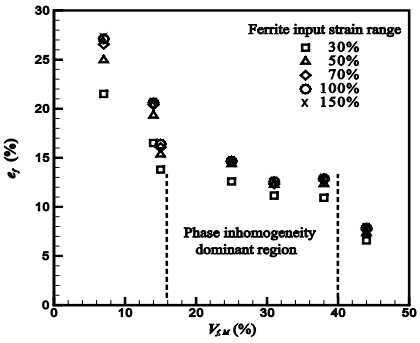

Figure 9. Ultimate ductility as function of martensite volume fraction for different input strain ranges of ferrite.

the martensite volume fraction between 15% and 40% since in this region, the failure strains of DP steels shows no dependence on the ductility of the constituent phases.

Additionally, the effects of voids on the overall ductility of single phase (SP) and DP steels were examined. Figures 10 and 11, respectively, show the engineering stress-strain curves and failure modes of selected RVEs with and without voids for the cases of SP and DP steels. Based on these figures, it seems that voids do not have noticeable influence on the failure strain and/or mode of DP steels when the martensite volume fraction in DP steels is larger than about 15%, which is similar to the effects of ductility of the constituent phases. This is also because the phase inhomogeneity becomes a dominant factor for the failure of RVE (rather than voids) in this range of martensite volume fraction. Therefore, based on actual micro-structures of DP steels, the methodology can be applied to DP steels with the martensite volume fraction within the phase inhomogeneity region in tailoring the DP steel design without serious consideration of the ductility of the constituent phases.

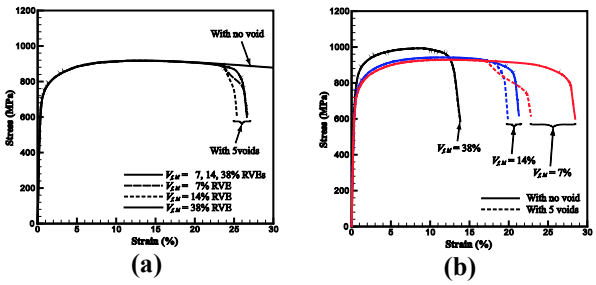

Figure 10. Engineering stress-strain curves based on three different RVEs with and without voids: (a) single- and (b) dual-phase materials.

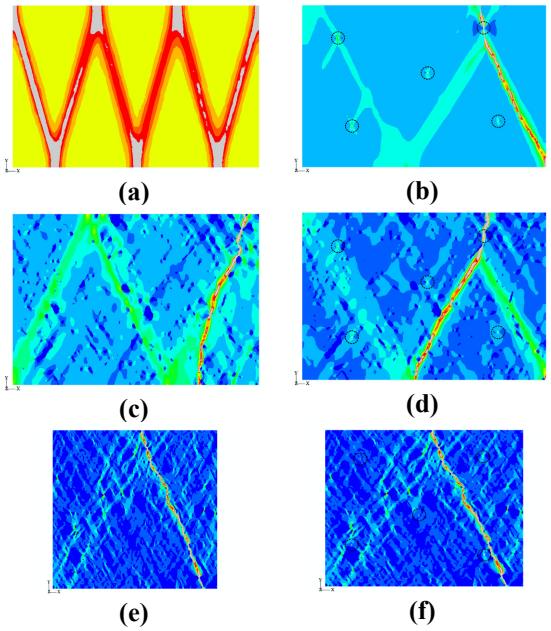

Figure 11. Failure modes of RVEs: (a) SP w/o voids, (b) SP with 5 voids, (c) DP ($V_{f,M}$=7%) w/o voids, (d) DP ($V_{f,M}$=7%) with 5 voids, (e) DP ($V_{f,M}$=38%) w/o voids, and (f) DP ($V_{f,M}$=38%) with 5 voids. Dotted circles represent the void positions.

Simulation of Shear Fracture in Stamping Process of DP Steels

DP steels appear to exhibit shear fracture during stamping of a variety parts that are not normally experienced with conventional drawing quality steel and high-strength low-alloy (HSLA) steel. Figure 12 shows DP980 steel sheets after a stamping process. Note that the sheet in Figure 12(b) is fractured by shear. Figure 13 shows the corresponding micro-structures of the two DP980 steel sheets. Note that the DP980 in Figure 13(a) has an evenly distributed microstructure whereas that in Figure 13(b) has a banded structure.

In this section, the possibility of using the developed micromechanics models to simulate the tendency for shear fracture in DP steels and understand the fundamentals of the driving forces for the observed shear fracture during stamping

Figure 12. Fractured B-pillar, made of DP 980, during stamping process: (a) Type A and (b) Type B.

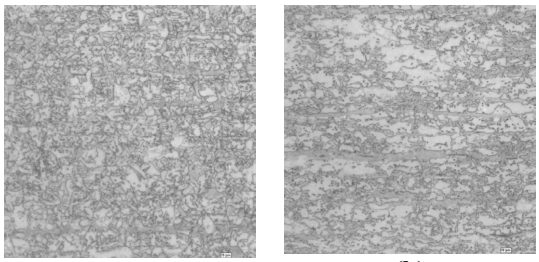

(a) (b)

Figure 13. Microstructures of (a) Type A and (b) Type B. RVE in Figure 8(b) was used, which is developed based on the actual microstructure in Figure 13(b). The input stress-strain curves for the ferrite and martensite phases are newly calibrated within the reasonable variation range from the mechanical properties of the DP980 determined in the previous sections.

was examined. For this purpose, Figure 14 shows the distributions of equivalent plastic strain under uniaxial tension based on the plane-strain elements (CPE3) at engineering-strain level of 32%. From the figure, the predicted failure mode seems to be a shear failure mode under plane-strain state. In order to simulate the shear fracture during stamping process, an indentation to the RVE was applied in addition to a tension. Figure 15 shows the distribution of equivalent plastic strain in the homogeneous material and DP980 under tension and indentation. For homogeneous material, the strain distribution shape is symmetric with respect to the center line and, therefore, a shear fracture is hard to be predicted. However, for DP980, high strain-localization area is developing from under the contact and propagating in the inclined downward direction, which may lead to a shear fracture. This is naturally due to the combined effects of contact and tension. The strain distributions shown in Figure 15(b) may explain the shear fracture which usually occurs near the corner area during stamping process as shown in Figure 12(b). This type of shear strain localization seems to be originated mainly from the microstructures and/or its uniformity in DP steels. More detailed investigation may be needed on the effect of morphology on the overall behavior and failure behavior of DP steels.

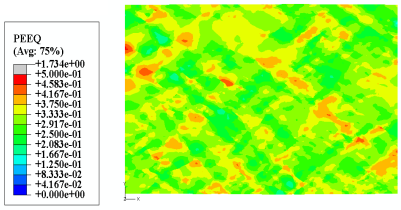

Figure 14. Distribution of equivalent plastic strain in DP 980 of type B under tension, based on the RVE in Figure 8(d).

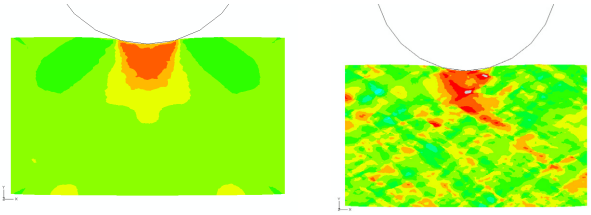

(a) (b)

Figure 15. Distribution of equivalent plastic strain under tension and indentation for (a) homogeneous material and (b) DP980 of type B.

Prediction of Failure Mode and Ductility for TRIP800 Based on Micromechanical Model with Consideration of Phase Transformation

In this section, a micromechanical finite-element model is developed based on an actual microstructure of TRIP800 steel to capture the complex deformation behavior of TRIP steels. A transformation yield function considering the stress-state effect is employed to model the martensite transformation kinetics.

Figure 16 shows an actual microstructure of TRIP800 obtained from SEM and the corresponding finite-element model used for the RVE in this study. Here, the RVE is composed of three different phases as shown in Figure 16 with the initial volume fraction of 15% of austenite. The mechanical properties of the constituent phases of TRIP800 steel and the fitting parameters describing the martensite transformation kinetics are determined using the synchrotron-based *in-situ* HEXRD experiments performed under a uniaxial tensile deformation together with the RVE prediction of the evolution of the volume fraction of austenite phase under different loading

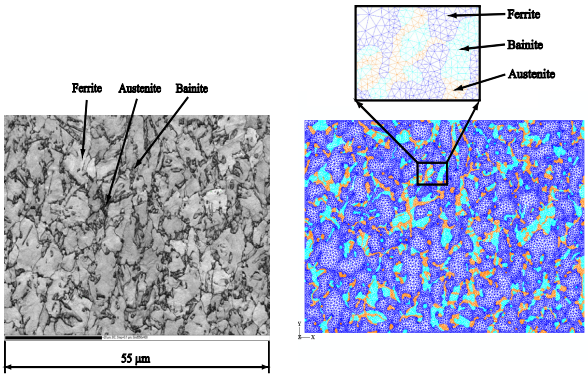

Figure 16. (a) An actual microstructure of TRIP800 and (b) the corresponding finite element model used for the RVE.

conditions. Figure 17 compares the RVE prediction and test results for uniaxial tension based on the determined material parameters, which shows a good agreement with each other.

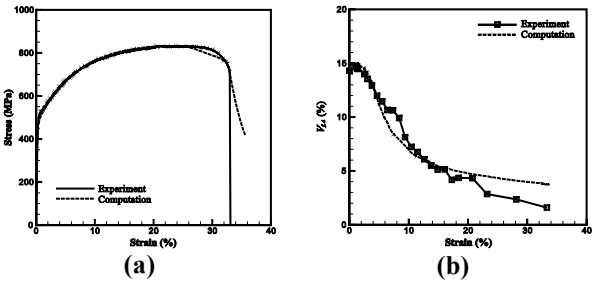

Figure 17. Macroscopic responses of the RVE under uniaxial tension based on the fitted input stress-strain curves for the four constituent phases: (a) engineering stress-strain curves and (b) volume fractions of austenite phase as function of applied strain.

Figure 18 shows a martensite distribution in the RVE under uniaxial tension. The ability of the current model to predict the martensite distribution in the RVE is helpful to obtain information on the better morphology in TRIP steels under different loading conditions. Figure 19 shows the volume fractions of austenite phase as functions of the macroscopic equivalent plastic strain of the RVE under different loading conditions. This figure indicates that the phase transformation and the failure of the RVE depend on the overall stress triaxiality in the RVE, which shows the similar trends reported in other experimental researches. Figures 20 and 21 show a failed TRIP800 sheet specimen and the predicted failure modes in the

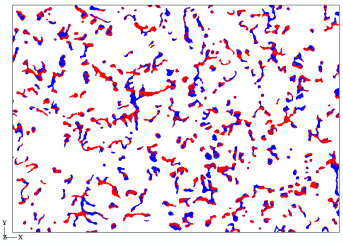

Figure 18. Martensite distribution in the RVE under uniaxial tension at strain of 10.6%. (Black: austenite; Grey: martensite; White: ferrite and bainite).

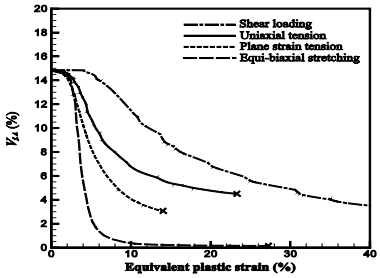

Figure 19. Volume fractions of austenite phase as functions of the macroscopic equivalent plastic strain of the RVE under different loading conditions.

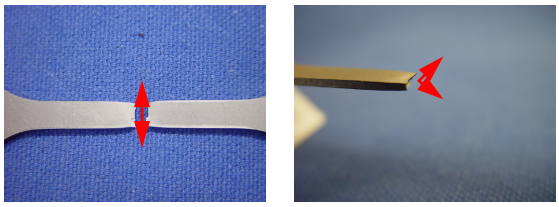

Figure 20. A failed TRIP 800 specimen under uniaxial tension: (a) plane-stress state and (b) plane-strain state.

RVE under plane stress and plane strain states, respectively. In Figure 21, the predicted failure under plane stress state is rather vertical failure mode whereas the predicted failure under plane strain state seems to lead to the shear failure mode, which correlates well with the experimental observations in Figure 20. The methodology adopted in this investigation may be a first step in predicting optimum processing parameters in TRIP steel productions.

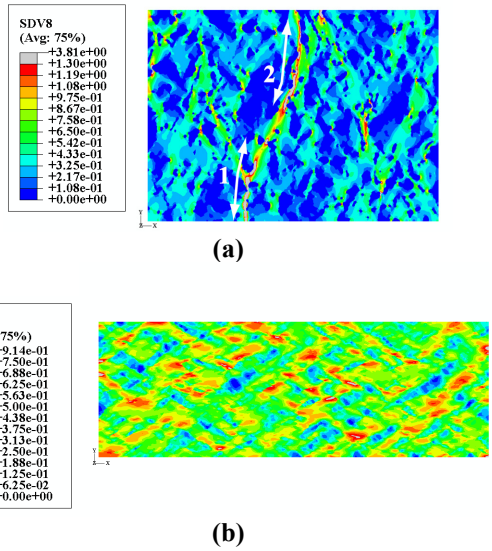

Figure 21. Different failure modes in the RVE: (a) plane-stress state and (b) plane-strain state.

Prediction of Crack Growth and Fracture Toughness of TRIP800

In this section, the fracture toughness of TRIP steels is investigated using both experiments and micromechanics-based finite-element analysis. Uniaxial tensile tests on TRIP800 notched sheet specimens were first conducted in order to determine the fracture resistance curve. The micromechanics-based finite-element model of TRIP800, shown in Figure 22, was then employed to predict the crack initiation and propagation and determine the resistance curve at the microstructure level.

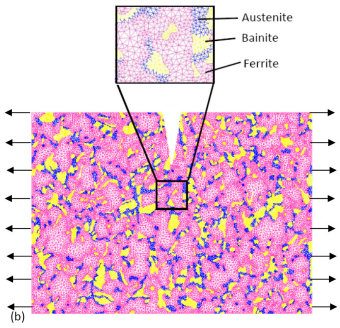

Figure 22. Finite-element model used for the RVE.

The same mechanical properties for the constituent phases and the same fitting parameters for the transformation kinetics, introduced for TRIP800 steel in the previous sections, were adopted for this simulation. A strain-based failure criterion is also adopted to model the damage and crack growth in the RVE and the levels of strain-to-failure for each phase are calibrated in order to fit the overall behavior of the RVE with the experimental data.

Figure 23 shows the comparisons of experiments and simulations for stress-strain curves and resistance curves. As shown in this figure, the predicted results based on the RVE are generally in good agreement with those of experiments despite some over-constrained boundary

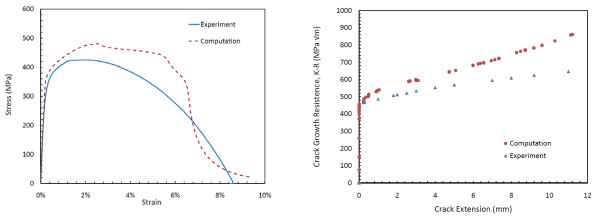

Figure 23. Comparison of experiments and simulations: (a) engineering stress-strain curves and (b) resistance curves.

conditions on the RVE. Figure 24 shows the distribution of the martensite phase in the RVE under uniaxial tension at different engineering strain levels. As the crack tip advances, more area of the retained-austenite phase transforms to the martensite phase as shown in the figure. This freshly-formed martensite has high strength and thus increases the fracture resistance of TRIP steels. Figure 25 shows the predicted crack-propagation path in the microstructure. The predicted crack-propagation path is not straight, and it tends to be along the grain boundaries between ferrite-bainite and ferrite-martensite, consistent with most experimental observations for multiphase materials. Future work in this area includes the implementation of some mesh-insensitive techniques (i.e., energy-based failure criterion or strain gradient plasticity theory).

Preliminary Studies on Twinning-Induced Plasticity (TWIP) and Nano-precipitate Strengthened (NPSS) Steels

In this section, results based on preliminary TWIP and NPSS steel studies are discussed. The goal is

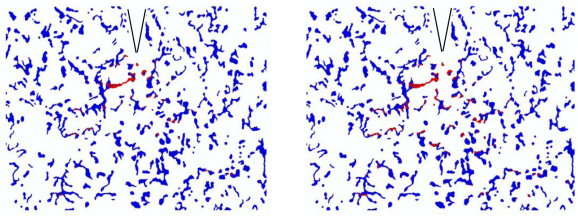

(a) **(b)**

Figure 24. Martensite distributions in the RVE under uniaxial tension at the strains of (a) 3% and (b) 5%. (Black: austenite; Grey: martensite; White: ferrite and bainite).

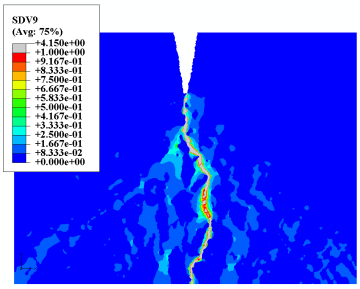

Figure 25. Predicted crack growth: distributions of equivalent plastic strain in the RVE.

to explore the possible directions for development of third-generation AHSS.

Three different grades of TWIP steels and a NPSS were covered in this preliminary investigation. Tables 2 and 3 and Figure 26 show the chemical compositions and the engineering stress-strain curves of two TWIP steels and the NPSS, respectively. Note that the Mn content in TWIP Steels B is considerably lower than 27–30%, which is typically observed in second-generation AHSS. The results in Figure 26(a) show that TWIP Steel B with lower Mn content has much higher ductility and almost equivalent UTS as TWIP Steel A with higher Mn content. These preliminary results indicate a possible direction for the development of third-generation AHSS: cost-effective low Mn TWIP steel. The examined NPSS also demonstrates good combinations of UTS and ductility due to the presence of nano-precipitates. To understand the basic attributes of these steels, various experimental approaches are still planned and underway, including the interrupted tensile test, dynamic tensile test and SEM/TEM analyses. Molecular Dynamics (MD) simulation is also considered for NPSS to get more fundamental understanding of the nanoparticles strengthening mechanisms.

Table 2. Chemical composition of two different TWIP Steels, A and B.

	C	*Mn*	*P*	*S*	*Si*	*Cr*
A	0.05	22.47	0.007	<0.001	1.90	<0.01
B	0.52	17.53	0.007	0.008	0.98	<0.01
	Ni	*Mo*	*Cu*	*Co*	*Nb*	*Ti*
A	<0.01	0.11	0.02	<0.01	0.02	0.01
B	<0.01	0.05	0.02	<0.01	0.01	0.01

Table 3. Chemical composition of NPSS.

C	Mn	P	S	Si	Cr	Ni
0.04	1.25	0.012	0.001	0.06	0.03	<0.01
Mo	Cu	Ti	V	Al	Co	Nb
0.18	0.01	0.08	0.015	0.048	0.006	0.011

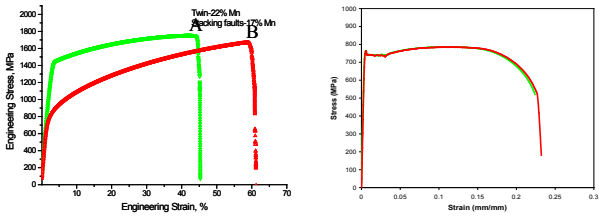

(a) **(b)**

Figure 26. Stress-strain curves for (a) two different TWIP steels and (b) NPSS.

Presentations/Publications/Patents

1. K. S. Choi, W. N. Liu, X. Sun, and M. A. Khaleel. 2008a. "Influence of Martensite Mechanical Properties in Failure Mode and Ductility of Dual Phase Steels." To appear in *Metallurgical and Materials Transactions A*.

2. ---. 2008b. "Micromechanics-Based Constitutive Modeling of TRIP Steel–Prediction of Ductility and Failure Modes." Submitted for publication in *Journal of the Mechanics and Physics of Solids*.

3. K. S. Choi, W. N. Liu, X. Sun, M. A. Khaleel, Y. Ren, and Y. D. Wang. 2008. "Advanced Micromechanical Model for TRIP Steels with Application of In-Situ High-Energy X-ray

Diffraction Method." *Metallurgical and Materials Transactions A* 39:3089-3096.

4. K. S. Choi, A. Soulami, W. N. Liu, X. Sun, and M. A. Khaleel. 2009. "Applicability of Micro-mechanics Model Based on Actual Micro-structure for Failure Prediction in DP Steels." SAE Technical Paper 09M-0176. To be presented in SAE 2009 World Congress, April 20–23, Detroit, MI.
5. A. Soulami, K. S. Choi, W. N. Liu, X. Sun, and M. A. Khaleel. 2009. "Characterization of the Fracture Toughness of TRIP 800 Sheet Steels Using Microstructure-Based Finite Element Analysis." SAE Technical Paper 09M-0174. To be presented in SAE 2009 World Congress, April 20–23, Detroit, MI.
6. X. Sun, K. S. Choi, W. N. Liu, and M. A. Khaleel. 2008. "Predicting failure modes and ductility of dual phase steels using plastic strain localization." *International Journal of Plasticity*, doi:10.1016/j.ijplas.2008.12.012.

J. Characterization of Thermomechanical Behavior of Advanced High-Strength Steels (AHSSs): Task 2—Weldability and Performance Evaluations of AHSS Parts for Automotive Structures

Principal Investigator: Zhili Feng
Oak Ridge National Laboratory
P. O. Box 2008, Oak Ridge, TN 37831-6095
(865) 576-3797; fax: (865) 574-4928; e-mail: fengz@ornl.gov

Participants:
Wan C. Woo, Eliot D. Specht, and Stan A. David
Oak Ridge National Laboratory
John Chiang
Ford Motor Company
Cindy Jiang
AET Integration, Inc.
Min Kuo
ArcelorMittal Steel

Technology Area Development Manager: Joseph A. Carpenter
(202) 586-1022; fax: (202) 586-1600; e-mail: joseph.carpenter@ee.doe.gov

Field Technical Monitor: C. David Warren
(865) 574-9693; fax: (865) 574-6098; e-mail: warrencd@ornl.gov

---

Contractor: Oak Ridge National Laboratory (ORNL)
Contract No.: DE-AC05-00OR22725

Objective

- Develop fundamental understanding and predictive capability to quantify the effects of welding and service loading on the structural performance of welded AHSS auto-body parts.
- Investigate welding techniques and practices to improve structural performance of AHSS welded auto-body components.
- Establish design guidelines and computer-aided engineering (CAE) methodology to assist rapid structure design validation and prototyping for vehicle weight reduction and safety enhancement through knowledge-based selection and use of AHSSs.

Approach

- Develop fundamental understanding of phase transformations in AHSSs during welding through thermodynamic analysis, advanced microstructure characterization, and in situ neutron and synchrotron phase transformation measurement.
- Develop integrated thermal-mechanical-metallurgical predictive models to predict the microstructure and mechanical property gradients in the weld region that potentially govern the performance of welded AHSS parts.
- Conduct comparative welding experiments on various AHSSs to develop the correlations between the joint properties, welding process conditions, and steel chemistry.

- Characterize and rank the factors controlling the weld geometry, weld microstructures, and weld joint performance.
- Investigate welding techniques for improved AHSS weld performance and benchmark them against the current welding practices.
- Generate weld performance data including static strength, impact strength, and fatigue life as a function of welding processes/parameters and steel chemistry.
- Develop design guidelines and CAE methodology for AHSSs to assist rapid structure design and prototyping.

Accomplishments

- Identified the fundamental metallurgical mechanisms causing the complex microstructure variations and the heat-affected zone (HAZ) softening phenomenon of current-generation AHSS welds.
- Developed an integrated thermal-mechanical-metallurgical welding process model capable of simulating the microstructural changes and the softening in the HAZ of AHSS welds. The initial version of the integrated model is being licensed and transferred to the auto and steel industry.
- Developed the correlation between the static structural performance and the microstructural changes of AHSS welds. A practical design parameter—joint efficiency—was introduced to quantify the effect of welding on the strength of AHSS welds.
- Revealed the influence of HAZ softening on the impact strength of AHSS joints.
- Demonstrated considerable fatigue-life improvement by refining welding conditions (within industry's acceptable welding practices).
- Developed a weld fatigue-life prediction model relating the fatigue life of a weld joint to weld geometry and local weld properties.
- Applied in situ neutron and synchrotron diffraction experiments to understand the phase changes during welding of AHSSs and the stress partitioning among different phases in transformation-induced plasticity (TRIP) steel.
- Developed close interactions with the industry including different Auto/Steel Partnership (A/SP) technical committees and the auto and steel companies to exchange research progress, to collaborate on related research projects, and to transfer and commercialize the technology developed in this project.

Future Direction

- Continue to investigate key factors controlling weld joint performance under static, fatigue, and impact loading conditions.
- Further investigate weld-joint performance under impact/crash loading conditions.
- Investigate the structural performance of AHSS weld joints under complex loading conditions (component level behavior).
- Continue to investigate welding techniques and practices to improve weld performance.
- Complete CAE analysis methodology to assist rapid design and prototyping of AHSS structures.
- Support the third generation AHSS initiative (see reports 5.K–5.T), focusing on new steel alloying and design concepts to avoid/minimize welding-induced thermal instability and microscopic deformation behavior of the new steels.

Introduction

This report describes an ORNL-Pacific Northwest National Laboratory (PNNL; see report 5.I) collaborative research project on characterization of thermomechanical behavior of AHSSs. This joint project aims at developing fundamental

understanding and predictive modeling capability to quantify the effects of auto-body manufacturing processes (forming, welding, paint baking, etc.) and in-service conditions on the performance of auto-body structures made of AHSSs. ORNL's research (designated as Task 2 in this project) focuses on welding AHSSs and the influence of welding parameters on the structural performance of weld joints.

The specific relation of Task 2 to the mission of the DOE Lightweighting Materials efforts and the needs of the automotive industry for accelerated use of AHSSs for body structure lightweighting has been given in previous annual reports and will not be repeated here.

Task 2 has a technical steering committee with representatives from Chrysler, Ford, General Motors (GM), A/SP technical committees, and steel companies.

Since initiation of the project in fiscal year (FY) 2006, considerable progress has been made toward obtaining a basic understanding of microstructural changes and their influence on the structural performance (static, fatigue, and impact) of AHSS welds and potential practical welding techniques/methods to effectively use AHSSs in auto-body structures. The progress has been summarized in the previous DOE project reports, review meeting presentations, and publications and presentations [1–4]. Following are highlights of previous research findings.

- The static tensile strength of the lap-weld joint made by the gas metal arc welding process (GMAW) increases as the base-metal steel strength increases. However, the joint efficiency (the ratio of weld strength to the base-metal strength) is influenced by the HAZ softening in the AHSS weld. Ultra-AHSSs such as martensitic and boron steels have the most noticeable HAZ softening and therefore lower joint efficiency. The lower grade AHSSs without HAZ softening exhibit high joint efficiency. Nevertheless, AHSS welds typically exhibit considerably higher absolute static strength than mild-steel welds.
- The HAZ softening phenomenon is inherently associated with the thermal instability of the hardened phases (such as martensite or bainite) subjected to welding heat, the existence of the intercritical temperature range in Fe-C alloy, and the allotropic phase transformation and solution strengthening used in the current AHSS steelmaking practice.
- Microstructural changes in the weld region of AHSS welds and the degree of HAZ softening have been quantified in an integrated thermal-mechanical-metallurgical weld process model. The initial version of this model has been licensed and transferred to several industry collaborators of the project.
- The HAZ softening does not appear to be a major factor affecting the fatigue life of GMAW joints. However, AHSS welds do not exhibit improved fatigue life over the mild-steel welds. New and/or improved welding practices specific for weld fatigue-life enhancement are required to realize the potential of using AHSSs to "down-gauge" (and thus "lightweight") the steels in a vehicle.
- It is feasible to improve the weld fatigue life of AHSS by manipulating welding process conditions. It has been demonstrated that, by adjusting the welding parameters (within the process window acceptable to the auto industry), the weld geometry profile can be improved to reduce the stress concentration at the fatigue crack initiation site. This has resulted in drastic improvement of weld fatigue life, especially at the high-cycle fatigue regime.

FY 2008's research and development (R&D) efforts focused on the following major activities.

Predictive Models for Fatigue Life of AHSS GMAW Lap Joints

The predictive model for weld fatigue life of AHSSs initially developed in FY 2007 has been further extended to cover a wide range of loading conditions and grades of steels. We also improved prediction of weld fatigue life in the fatigue crack propagation part of the model. More detailed description of the fatigue-life model is given in citation [5] in the project presentations list at the end of this report.

Our fatigue prediction model uses the notch strain approach for crack initiation and the Paris law for fatigue crack propagation. The total fatigue life (N_t) consists of the crack initiation part (N_i) and the subsequent cracking propagation (to failure) part (N_p):

$$N_t = N_i + N_p \quad . \qquad (1)$$

The notch strain approach was based on the Coffin-Manson-Morrow equation [1–3]:

$$\frac{\Delta\varepsilon}{2} = \frac{(\sigma_f' - \sigma_m)}{E}(2N_i)^b + \varepsilon_f'(2N_i)^c \ (N_i \le N_E) \quad .(2)$$

The fatigue initiation life N_i was solved iteratively using the solution scheme proposed by Darcis et al. [4]. The stress concentration factor used in the fatigue initiation was determined using the finite-element method.

The crack-propagation equation developed by Paris and Erdogan [5] was used to describe the relationship between the fatigue crack propagation rate, *da/dN*, and the stress intensity factor range, *ΔK*:

$$\frac{da}{dN} = C(\Delta K)^m (\Delta K_{th} << \Delta K << K_{IC}, R = 0) \quad . \qquad (3)$$

The crack-propagation life, N_p, is obtained by integration of Eq. (3) with crack-depth-dependent *ΔK* values calculated by finite-element method over the entire crack-propagation range:

$$N_p = \int_{a_i}^{a_f} \frac{da}{C(\Delta K)^m} \quad . \qquad (4)$$

The model developed in this project relates the weld fatigue life to the three major governing factors: (1) the stress state, including the weld residual stress; (2) the local stress concentration due to weld geometry and discontinuity; and (3) the local material strength, which is a function of the microstructure in the weld region. Therefore, our fatigue-life prediction model is capable of including the experimentally observed effect of weld geometry and the local microstructure and material strength gradients of the weld region on the fatigue life of welded joints.

The fatigue crack life prediction model has been evaluated against the experimental testing data for nine steels and two different weld geometries. The comparison and evaluation are summarized in Figure 1 for three different characteristic loading regimes (low-stress, high-cycle; medium-stress, medium-cycle; and high-stress, low-cycle) of nine steels.

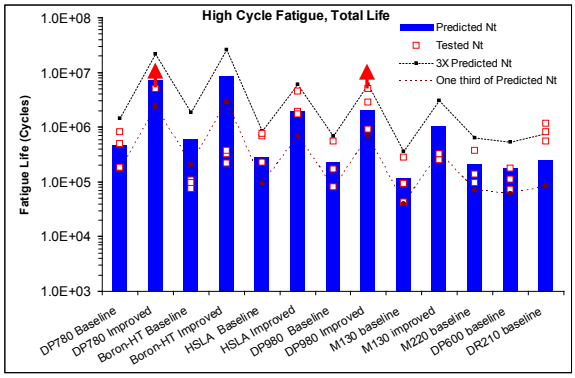

(a) low-stress, high-cycle fatigue

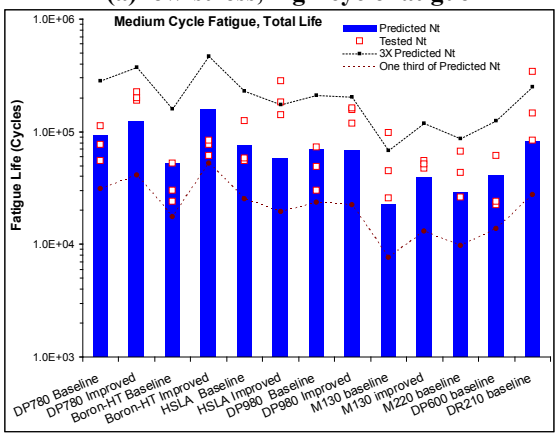

(b) medium-stress, medium-cycle fatigue

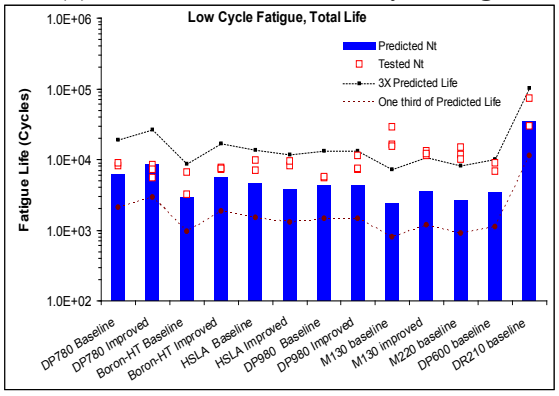

(c) high-stress, low-cycle fatigue

Figure 1. Comparison between predicted total fatigue lives and the experimental results for GMAW lap joints [Arrow in (a) represents test runout].

Overall, the model reasonably predicts the experimentally observed influences of steel grade (local mechanical property in the weld and HAZ) and the weld geometry for the steel grades investigated. With a few exceptions (e.g., hardened boron steel under high-cycle fatigue), the experimental data fall within a narrow band bounded by the 3× and 1/3× lines of the predicted data in the figure. The discrepancies between the model prediction and the testing results are on the same order as the scatter of the testing data. The few exceptions where the discrepancies are significant appeared to be related to the dramatic material property change in the weld region in boron steel. Further improvement in the prediction model is being developed.

Impact Testing of AHSS Weld Joints

Preliminary impact tensile testing was conducted in FY 2008 to investigate the effects of weld microstructure changes on the tensile strength of AHSS welds under loading rates relevant to auto-body crash conditions. The tests were performed using ORNL's hydraulic high-strain-rate test machine. A high-speed camera was used to record the dynamic deformation and failure processes during the test. Strain gages were attached on selected specimens to record the dynamic load changes during high-strain-rate testing.

Three types of steel (DP 780, hardened boron steel, and DP 210) were tested under three loading rates (5, 15, 25 mph). A lap-shear tensile coupon with reduced cross section was used (Figure 2). DR 210, a mild steel with nominal static tensile strength of 350 MPa, did not exhibit noticeable HAZ softening. It was used for reference in the remaining tests. For both AHSSs (DP 780 and boron steel), all specimens failed in the softened HAZ region under all loading rates. On the other hand, all DR 210 welds failed in the base-metal region of the specimen, as shown in Figure 3.

Our preliminary study indicated that, similar to the behavior observed during static testing, the impact strength of AHSS welds is generally higher than that of mild steels. However, the HAZ softening phenomenon will play an important role in determining the level of strength reduction

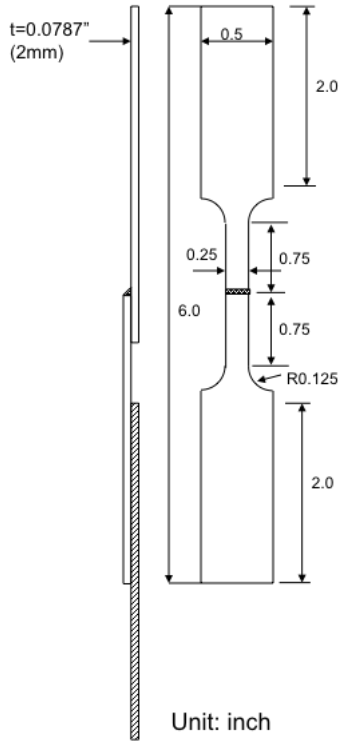

Figure 2. Dimensions of lap-shear tensile specimen used in impact testing of GMAW joint.

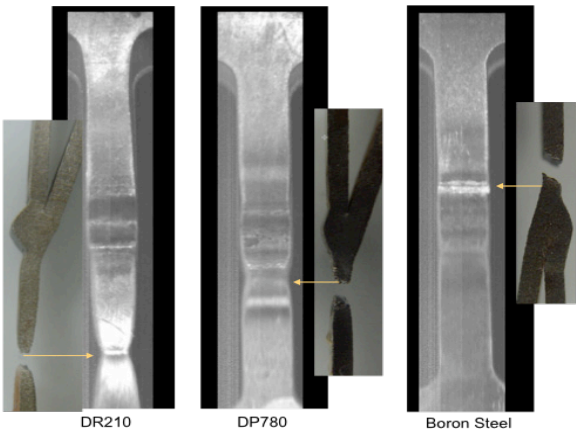

Figure 3. Failure location of GMAW joints during impact tensile testing. The effect of HAZ softening on localized deformation failure is evident in both DP 780 and boron steel.

(compared to the base metal strength) of AHSS welds.

In-depth study of the impact behavior of AHSS welds is planned in FY 2009.

In Situ Phase-Transformation Study Using High-Energy X-Ray Synchrotron Source

The high-energy X-ray synchrotron source at the Advanced Photon Source of Argonne National Laboratory was used to study the kinetics of phase transformations of current generation AHSSs under the rapid heating and cooling conditions associated with welding. Four types of steels were included in the study. They were boron steel, DP 980, TRIP 700, and DR 210.

A miniature electric-resistance-heating device built specifically for this study was used to provide Joule heating to the steel sample during the in situ experiment. The heating rate was closed-loop controlled during the experiment. The experimental principles and setup are shown in Figure 4.

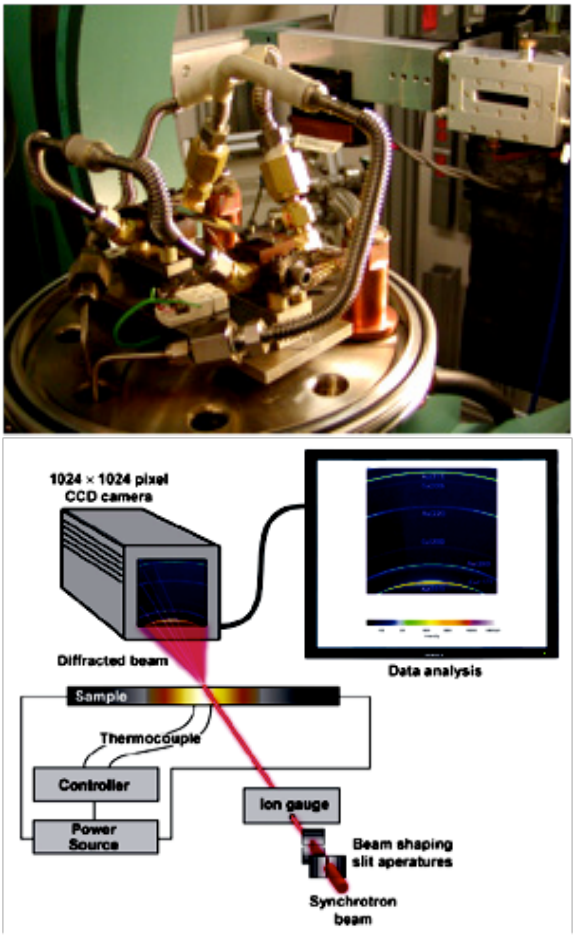

Figure 4. In situ synchrotron X-ray diffraction experiment to study phase transformation kinetics of AHSSs.

The in situ synchrotron diffraction measurements focused on elucidating the phase transformation kinetics during heating in the intercritical temperature range (i.e., between the A_1 and A_3 temperatures of the Fe-C phase diagram) and its impact on the phase transformation during cooling, as the intercritical temperature region is most critical to the HAZ softening observed in the current generation of AHSSs.

The heating rates varied from 3ºC to 150ºC per second during the in situ synchrotron diffraction experiments. The measurement data are still being analyzed, but preliminary results suggest a noticeable dependency of phase-transformation kinetics on the heating rate. In addition, aluminum-bearing TRIP steel showed very different phase-transformation behavior than the other two AHSSs.

Additional neutron and synchrotron experiments are planned in FY 2009. We expect to report the detailed findings of this work in the FY 2009 progress report.

Interactions with the Auto and Steel Industry

The weldability task (Task 2) has received strong industry support from the start of the project. We have maintained active interactions with the auto and steel industry through the technical steering committee and various A/SP committees. Such interactions have been mutually beneficial to the project and to the industry. We were invited to attend meetings of A/SP's Joining Technologies Team (see report 5.A), Sheet Steel Fatigue Committee (see report 5.C), and Lightweight Chassis Structures Team (see report 5.H) to exchange research results. We were also invited to Chrysler, Ford, and GM to discuss our research progress and learn more about the needs of the industry. Several collaborative efforts have come out of these interactions. For example, the A/SP Joining Technologies Team has used the joint efficiency index to characterize the static joint strength of a much wider range of steels, gage thickness, and other welding processes. The Sheet Steel Fatigue Committee is interested in incorporating our findings on fatigue-life improvement into their studies. The integrated

weld model, weld fatigue-life prediction model, and weld fatigue improvement techniques developed in this project have been licensed and transferred to several automotive and steel companies for their internal R&D applications. A/SP's joining and lightweight chassis design committees are looking into the feasibility of incorporating our weld microstructure model in some of their CAE design and research activities. We plan to maintain the strong interactions with the industry in this program.

Plan for FY 2009

The R&D activities in FY 2009 will be built on the progress of the program, focusing on completing the following tasks.

1. **Welding and mechanical performance testing of AHSS weld joints.** Continue to study the effects of microstructural changes in the weld region on the dynamic (crash) behavior of AHSSs. Techniques to further improve the weld fatigue life will be investigated.
2. **Microstructural Characterization.** Conduct in situ neutron and/or high-energy X-ray (synchrotron) diffraction measurements to better understand the phase transformation behavior of AHSSs.
3. **Strengthening Mechanisms and Phase Stability in Third Generation AHSSs.** Explore new steel design and alloying approaches to mitigate the detrimental effects of welding on the current generation of AHSSs. A close collaboration with universities is anticipated.
4. **Weld Process and Performance Model.** Complete development of the integrated thermal-mechanical-metallurgical welding process and performance model with emphasis on integrating damage-mechanics-based failure prediction under dynamic-loading conditions.

Presentations/Publications/Patents

1. Z. Feng et al., "A New Perspective on Fatigue Performance of Advanced High-Strength Steels (AHSS) GMAW Joints" *Sheet Metal Welding Conference XIII* (Livonia, Michigan, American Welding Society, 2008).
2. Z. Feng. et al., "Fatigue Performance of Advanced High-Strength Steels (AHSS) GMAW Lap Fillet Welds," *8th International Symposium of The Japan Welding Society*, Kyoto, Japan, 2008.
3. S. Cheng et al., "Probing the Characteristic Deformation Behaviors of Transformation-Induced Plasticity Steels," *Metallurgical and Materials Transactions A*, **39A**(8), pp. 3105–3112 (2008).
4. Z. Feng et al., "Weldability and Performance of Advanced High-Strength Steels (AHSS) in Automotive Structure," (invited) SAE World Congress (Society of Automotive Engineers, Detroit, 2007).
5. Z. Feng, et al., "Weldability and Performance of GMAW Joints of Advanced High Strength Steels," *Great Designs in Steel 2007* (American Iron and Steel Institute, Livonia, Michigan, 2007).
6. Z. Feng et al., "Fatigue Performance of Advanced High-Strength Steels (AHSS) GMAW Joints," paper 09M-0256, *SAE 2009 World Congress,* Detroit, April 20–23, 2009 (to be presented).

Acknowledgements

We would like to acknowledge the following individuals and A/SP committees who contributed to this project.

Chrysler: W. Marttila
Ford: J. Chiang, P. Geck
GM: S. Gayden, J. Bohr, C. Chen
Mittal Steel: M. Kuo
US Steel: M. F. Shi
Severstal N. A.: R. M. Iyengar, Y.-W. Wang
AK Steel: T. Montroy
Dofasco: W. Bernert
OTC: P. Mosquera

A/SP Joining Technologies Team
A/SP Sheet Steel Fatigue Committee
A/SP Lightweight Chassis Structure Team

References

1. J. D. Morrow, "Cyclic plastic strain energy and fatigue of metals," *ASTM STP 378* (American Society for Testing and Materials, Philadelphia, 1965), pp. 45–87.
2. L. F. Coffin, "A study of the effects of cyclic thermal stresses on a ductile metal," *Transactions ASME*, **76**, pp. 931–950 (1954).
3. S. S. Manson, "Fatigue-a complex subject-some simple approximations," *Experimental Mechanics*, **5**, pp. 193–226 (1965).
4. P. Darcis, T. Lassen, and N. Recho, "Fatigue behavior of welded joints part 2: physical modeling of the fatigue process," *Welding Journal*, **112**, pp. 19s–26s (2006).
5. P. C. Paris and F. Erdogan, "A critical analysis of crack propagation law," *Trans. ASME, J. Basic Eng.*, **85**, pp. 528–539 (1963).

K. Fundamental Study of the Relationship of Austenite-Ferrite Transformation to Austenite Retention in Carbon Steels

Principal Investigator: Michael L. Santella
Oak Ridge National Laboratory
P.O. Box 2008, Oak Ridge, TN 37831-6096
(865) 574-4805; fax: (865) 574-4928; e-mail: santellaml@ornl.gov

Technology Area Development Manager: Joseph A. Carpenter
(202) 586-1022; fax: (202) 586-1600; e-mail: joseph.carpenter@ee.doe.gov

Field Technical Monitor: C. David Warren
(865) 574-9693; fax: (865) 574-6098; e-mail: warrencd@ornl.gov

Contractor: Oak Ridge National Laboratory (ORNL)
Contract No.: DE-AC05-00OR22725

Objective

- Support the development of the Generation (Gen) III advanced high-strength steels (AHSSs) through fundamental studies of the ferrite-austenite phase transformation during steel finishing operations and its relationship to stabilizing and retaining austenite in finished microstructures.
- Characterize in situ the austenite-ferrite phase transformation behavior of carbon steels under the rapid heating/cooling conditions that typify modern sheet steel production.
- Determine the extent to which retained austenite can be increased in commercial and experimental low-carbon (<0.2 wt %) steels.

Approach

- The majority of the experimental part of this work will be done using the DOE Office of Science, Advanced Photon Source (APS) to provide synchrotron radiation for high-speed diffraction. Diffraction patterns can be collected at rates of one every second, possibly even higher. Capabilities exist for integrating diffraction with rapid heating/cooling cycles. Control of temperatures and heating/cooling rates are sufficient for replicating most of the processing steps used to produce existing AHSS. Analysis of the diffraction data can determine volume fractions of the ferrite and austenite phases, their lattice parameters, and how they vary under dynamic temperature/time conditions.

Accomplishments

- Held discussions about potential collaborations with several universities with National Science Foundation (NSF) funding to support development of Gen III AHSSs.
- Prepared and submitted a proposal for access to the APS. It received a high score in the proposal review process, but due to the overall level of demand, it was rejected for access in the October–December 2008 time frame.
- Secured an allocation of beam time from APS as part of a standing allocation available to ORNL.
- Prepared specimens for the first round of experiments in November 2008.
- Contacted beam-line scientists at APS for input on future proposal submissions.

Future Direction

- Revise and resubmit the proposal for access to APS, incorporating input from APS scientists. (Note: In the mean time, an allocation of beam time has been secured from a standing allocation available to ORNL.)
- Continue to seek university partners for collaboration.

Introduction

Project Background

Metals comprise about 80% of all the materials used for light vehicle construction and, by a wide margin, the largest fraction of the metals are steels [1, 2]. Steels represent about 62% of average vehicle weight. Of the various steel mill products used for auto construction, about 70% of the total, or 839 kg of the 1,970 kg average light vehicle weight, is supplied as flat-rolled carbon steel for chassis parts and body panels. The dominance of carbon steels, in terms of total vehicle weight, results from a variety of factors. The metallurgy of carbon steels creates broad boundaries for manipulating important properties such as strength and ductility, as indicated in Figure 1. Carbon steels are relatively inexpensive and they have excellent potential for recycling (e.g., the recycle rate for automotive steels is about 100% [3]).

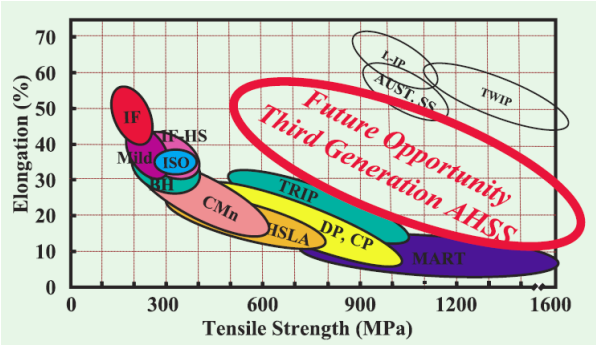

Figure 1. General variation of tensile elongation with strength showing how these properties characteristically balance in various grades of steel (*Source:* Steel Recycling Institute Website [3]).

The traditional sheet steels used for chassis and body constructions are the so-called "mild" steels. The alloying and processing of mild steels are relatively simple, and their microstructures consist principally of ferrite (the equilibrium iron phase at room temperature that has a body-centered cubic crystal structure) and iron carbide (cementite, Fe_3C). Examples of mild steel grades are the interstitial-free, bake-hardenable, and solid-solution-strengthened steels.

The combined interests of improving crash worthiness and reducing vehicle weights were at least partially responsible for the development of the first generation (Gen I) of AHSSs. Included in this group are the dual-phase (DP), complex-phase, martensitic, and transformation-induced plasticity (TRIP) steels. Metallurgically, a characteristic of this group is the development of properties, in part, from more specialized processing that results in the retention of various amounts of nonequilibrium ferrite constituents such as martensite and bainite or metastable phases such as retained austenite (an equilibrium form of iron that is stable above about 700°C and has a face-centered cubic crystal structure). As Figure 1 shows, remarkable strength levels can be developed in the Gen I AHSSs. However, these strength levels are obtained at the expense of reduced ductility and increased alloying. The more limited ductilities complicate forming operations. Increased alloying increases materials cost and complicates other essential processing operations such as welding.

The need to maintain high ductilities while simultaneously developing high strength led to development of the second generation (Gen II) of AHSSs, indicated on the upper right region of Figure 1. The Gen II AHSSs are much more highly alloyed to either completely stabilize the austenite phase or to retain much higher fractions of metastable austenite than in Gen I AHSSs. For example, steels containing 25–30 wt % of manganese are austenitic and capable of developing very high strengths and ductilities. Some of their ductility derives from a metallurgical mechanism known as twinning, which is the source of the term, twinning-induced plasticity (TWIP). Based on raw materials costs, TWIP steels are cheaper than standard austenitic stainless steels, but they are much more expensive

than ferrite-based carbon steels. There are concerns about whether they can be produced reliably with the existing primary steelmaking infrastructure. Also, their responses to fabrication processes like forming and welding are virtually unknown.

What is now desired is a third generation (Gen III) of AHSSs that borrows from the Gen I and Gen II steels to achieve intermediate strengths and ductilities, as indicated in Figure 1, but at costs that would make acceptance for automotive construction feasible. Controlling cost will likely require that Gen III AHSSs be no more than modestly alloyed compared to Gen I AHSSs and capable of being produced within existing steel mill infrastructures. This project was initiated in late 2008 to address those desires.

Approach

Developing the Gen II AHSSs required developing completely new alloys that, in a commercial sense, did not exist at the time. In terms of their properties this was successful, as illustrated in Figure 1. In terms of costs and processing, however, this approach appears to have been unrealistic. Consequently, a more productive approach to identifying Gen III steels is to emphasize better understanding of processing in existing Gen I-type steels (e.g., DP 600, DP 780) and to supplement this with work on experimental steels having chemical compositions specifically modified to promote retained austenite. Emphasizing development based on Gen I-type steels is also likely to ensure that acceptable forming and welding properties will be maintained.

There are two temperature ranges where improved understanding is crucial to achieving these goals. One is the so-called intercritical temperature range. This is the range from about 700–850°C where, depending on chemical composition, the ferrite and austenite phases coexist at equilibrium. The time and temperature of intercritical annealing during sheet production controls both the relative fractions and chemical compositions of ferrite and austenite in the microstructure. These properties, combined with cooling rate, will determine how the austenite behaves during subsequent cooling. In other words, these factors determine whether austenite transforms to martensite, bainite, or ferrite and whether any austenite is retained in the microstructure. The second critical range is from about 200–500°C where austenite can be maintained in a metastable condition due to the partitioning of alloying elements like carbon, manganese, and silicon. As is well known, retaining austenite can markedly improve ductility at high strength through the TRIP effect.

Because of their commercial significance, there is considerable practical knowledge about how steels behave in these temperature ranges. However, there is a lack of scientific underpinnings that limits progress on improving properties to the limits of experience. Better fundamental understanding of austenite-ferrite transformations will enable a more scientific approach to improving properties through novel processing that can be achieved with existing infrastructure.

Technical Challenges

1. Making direct, in situ observations of the time dependence of austenite-ferrite transformation behavior at elevated temperatures, during rapid heating/cooling, and during low-temperature treatments designed to maximize retained austenite.
2. Measuring partitioning of carbon between austenite and ferrite during processing.
3. Understanding effects of critical alloying elements such as carbon, manganese, and silicon on transformation behavior and retention of austenite.

The technical activities of this task are complementary to and will be coordinated with those of NSF-funded Gen III AHSS projects at universities (see reports 5.L–5.T).

Materials and Experimental Details

Initial work will be done using two uncoated high-strength steels: the DP steel DP 780 (ArcelorMittal) and a hot-stamp boron steel (HSBS) sourced from a Swedish supplier, the parent of U.S. HardTech. The analyzed compositions of the steels are as follows.

- DP 780 (wt %): Fe-0.11C-1.93Mn-0.24Si
- HSBS (wt %): Fe-0.20C-1.26Mn-0.27Si-0.22Cr-0.002B

Specimens with dimensions of 5 mm × 1.25 mm × 110 mm were machined from sheets of both steels. The surfaces of these strips were ground by machining to remove oxides.

The thermal cycles shown in Figure 2 will be used for the initial experiments. We will heat specimens through these conditions while simultaneously collecting X-ray diffraction spectra at the rate of about 1/s. The data will be analyzed to measure the relative fractions of ferrite and austenite phases. The lattice parameters of these phases will also be determined and analyzed for possible relationships to chemical compositions.

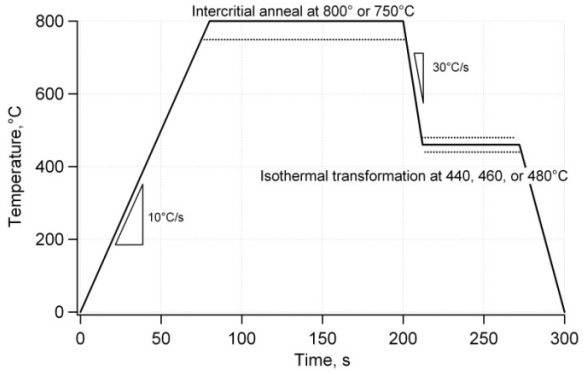

Figure 2. Schematic representation of thermal cycles used for initial diffraction experiments.

Conclusions

Because this was a start-up activity during the second-half of FY 2008, we do not have any conclusions to report at this time.

Presentations/Publications/Patents

None

References

1. Richard A. Schultz, "Metallic Material Trends for North American Light Vehicles," *Great Designs in Steel* seminar presentation, 2007; available: American Iron and Steel Institute website (http://www.autosteel.org/AM/Template.cfm?Section=GDIS&CONTENTID=24666&TEMPLATE=/CM/HTMLDisplay.cfm).
2. John Schnatterly, "Steel Content in North American Vehicles," *Great Designs in Steel* seminar presentation, 2007; available: American Iron and Steel Institute website (http://www.autosteel.org/AM/Template.cfm?Section=GDIS&CONTENTID=24666&TEMPLATE=/CM/HTMLDisplay.cfm).
3. Steel Recycling Institute Website (www.recycle-steel.org).

L. National Science Foundation Funding for the Development of Third Generation Advanced High-Strength Steels (A/SP 280*)

Project Manager: Roger A. Heimbuch
Auto/Steel Partnership
2000 Town Center Drive, Suite 320
Southfield, Michigan 48075-1123
(248) 945-4770; fax: (248) 356-8511; e-mail: rheimbuch@a-sp.org

Chairman: Ronald Krupitzer
American Iron and Steel Institute
2000 Town Center Drive, Suite 320
Southfield, Michigan 48075-1123
(248)-945-4761; fax : (248) 352-1740; e-mail: krupitzerr@autosteel.org

Technology Area Development Manager: Joseph A. Carpenter
(202) 586-1022; fax: (202) 586-1600; e-mail: joseph.carpenter@ee.doe.gov

Field Project Officer: Aaron D. Yocum
(304) 285-4852; fax: (304) 285-4403; e-mail: aaron.yocum@netl.doe.gov

Contractor: United States Automotive Materials Partnership (USAMP)
Contract No.: DE-FC05-02OR22910 through the National Energy Technology Laboratory

Objectives

- Conduct the fundamental research required to develop a third generation advanced high-strength steel (AHSS) that is higher in strength and more formable than currently available commercial grades of AHSS with the potential of being more cost-effective than stainless steels and twinning-induced plasticity (TWIP) steels.

Approach

- Conduct fundamental steel research at universities that can lead to the development of a cost-effective family of third generation AHSS that can be applied for mass reduction in the auto body.
- Utilized National Science Foundation (NSF) processes to manage the research.
- Provide a portion of the funding (25%), through this project, for fundamental research required to develop a third generation AHSS.
- Additional funding will be provided directly by DOE (25%) and the NSF (50%).

Accomplishments

- NSF AHSS Workshop held October 22–23, 2006, Arlington, Virginia.

*Denotes project 280 of the Auto/Steel Partnership (A/SP), the automotive-focus arm of the American Iron and Steel Institute (see www.a-sp.org). The A/SP cofunds projects with DOE through a cooperative agreement between DOE and the United States Automotive Materials Partnership, one of the formal consortia of the United States Council for Automotive Research set up by Chrysler, Ford, and General Motors to conduct joint, precompetitive research and development (see www.uscar.org).

- NSF AHSS Proposal Panel Review held April 10–11, 2007, Arlington, Virginia. Eight proposals, from 30 submitted, were selected for funding, using the NSF process, and a budget allocation prepared by NSF. The research projects will be carried out over 3 years.
- NSF will notify the appropriate principal investigators (PIs) and universities of their grants and track and document the research projects following NSF standard practices.
- An NSF/DOE Steel Research Program Review was held April 10, 2008. Participants included the university professors that are conducting the NSF research; DOE national laboratory researchers working on steel research; Canada Centre for Mineral & Energy Technology (CANMET) steel researchers; and personnel from NSF, DOE, and Auto/Steel Partnership (A/SP) member companies.
- An industry-based steering committee has been formed.

Future Direction

- The industry-based steering committee will work to provide the requested additional support to the researchers.
- A web-based site will be developed for researchers to store and share information.
- An annual review of the NSF/DOE Steel Research Program will be held in spring 2009.

Introduction

One of the tasks of the A/SP241 Future Generation Passenger Compartment Project (see report 5.G) was to run the structural optimization codes with unrestricted strength limitations to define the upper strength bound for auto body steel for optimized mass reduction. Several areas of the body were found that would benefit from higher strength.

An additional 5% to 8% mass reduction is possible in those areas of the vehicle. Based on the specific areas of the body, estimates were made of the forming characteristic needed to make those types of parts. A window of opportunity was defined ranging from 600 MPa/40% elongation to 1,600 MPa/20% elongation for a cost-effective third generation AHSS family. It was recognized fundamental steel research would be required to develop steels in that property range. A collaborative effort by NSF, DOE, American Iron and Steel Institute (AISI), and A/SP has been put together to fund eight university research proposals, using the NSF processes, to fund the supporting fundamental research to develop steels with the desired properties.

Objective

The objective of this project is to provide a portion of the funding (25%) for the fundamental research required to develop a cost-effective family of third generation AHSS that can ultimately be applied for mass reduction in the auto body. Additional funding will be provided directly by DOE (25%) and NSF (50%). The research will be done utilizing the processes of the NSF. If the research is successful, it will provide the basis for the commercial development of cost-effective third generation AHSS by the A/SP steel members.

Project Status

An NSF AHSS Workshop was held October 22–23, 2006, in Arlington Virginia. As a result of that workshop, the NSF requested proposals for basic research to support the development of a family of third generation AHSS. An NSF AHSS Proposal Panel Review was held April 10–11, 2007, in Arlington, Virginia. Eight proposals, from 30 submitted, were selected for funding, using the NSF process, and a budget allocation was prepared by NSF. The research projects will be carried out over 3 years starting the academic year 2007–2008. The following table shows the PIs, institutions, and titles.

University	Professor	Topic
Carnegie Mellon University	Warren Garrison	AHSS through microstructure and mechanical properties
Case Western Reserve University	Gary Michal	AHSS through C partitioning
Colorado School of Mines (CSM), Ohio State University (OSU)	David Matlock (CSM) and Robert Wagoner (OSU)	Collaborative GOALI Project Formability and Springback of AHSS
Drexel University	Surya Kalidindi	FEM using crystal plasticity simulation modeling tools
OSU	Ju Li	Multi-scale modeling of deformation for design of AHSS
Texas A&M University	Abu Al-Rub Rashid	AHSS through particle size and interface effects
University of Missouri-Rolla	David C. Van Aken	AHSS through nano-acicular duplex microstructures
Wayne State University	Susil K. Putatunda	High strength high toughness bainitic steel

An industry-based steering committee has been formed with members from A/SP member companies. They include representatives from steel research centers, mills, and automotive applications centers and advanced materials representatives from the automotive companies. The steering committee will help coordinate additional support for the NSF researchers and become the technology transfer interface for the research back into industry.

An NSF/DOE Steel Research Program Review was held April 10, 2008, in Southfield, MI in conjunction with AISI's Great Designs in Steel (GDIS) event April 9, 2008. GDIS provided the steel researchers the opportunity to see the need for a third generation AHSS. Overviews of each of the NSF sponsored research programs were presented. In addition, related research being conducted at Pacific Northwest National Laboratory, Oak Ridge National Laboratory, and Canada's CANMET Laboratory was reviewed. Eleven representatives from the steel industry; seven representatives from the automotive industry; and staff from A/SP, AISI, NSF, and DOE participated. There was active discussion during the reviews among the participants.

Opportunities for future interactions among the attendees, areas needing additional support, and gaps in the research were identified and are being addressed.

The researchers requested a web-based system where information could be stored and shared. A system was developed and became available in May 2008.

Conclusions

NSF has initiated the research contracts with the eight selected Universities. Reporting of the research will follow the normal processes of NSF.

Future Work

The industry-based steering committee will work to provide the additional support requested by the researchers**.** A second annual progress review of third generation AHSS research is being planned for spring 2009. The intent is to share progress, identify gaps in the research program, and identify areas where additional support would be valuable. A web site debuted in May 2008 to store and share data among the researchers.

Acknowledgments

The support and guidance of Drs. Mary Lynn Realff and Joyceleyn Harrison of NSF, Dr. Joseph Carpenter of DOE, and Ronald Krupitzer of AISI in developing and implementing this research initiative are greatly appreciated.

References

1. The NSF Report "Advanced High Strength Steel Workshop Oct.22–23, 2006, Arlington, Virginia" by Professor Robert Wagoner, Department of Material Science and Engineering, The Ohio State University, Columbus, Ohio.

M. A Multiresolution Analysis of the Particle Size and Interface Effects on the Strength and Ductility of Advanced High-Strength Steels

Principal Investigator: Rashid K. Abu Al-Rub
Texas A&M University
3136 TAMU, College Station, TX 77843-3136
(979) 862-6603; fax (979) 845-6554, e-mail: rabualrub@civil.tamu.edu

Technology Area Development Manager: Joseph A. Carpenter
(202) 586-1022; fax: (202) 586-1600; e-mail: joseph.carpenter@ee.doe.gov

Field Project Officer: Aaron D. Yocum
(304) 285-4852; fax: (304) 285-4403; e-mail: aaron.yocum@netl.doe.gov

Contractor: Texas Engineering Experiment Station
National Science Foundation Contract No.: CMMI 0728032, jointly funded by NSF and DOE

Objective

- Identification of the role of dispersed micro- and nano- particles (inclusions) on enhancing the yield strength, ultimate strength, and ductility of advanced high strength steels (AHSSs) reinforced with inclusions at decreasing microstructural length scales.
- Development of a multiresolution (multiscale) computational framework that can be used effectively in the design of AHSS with superior strength and ductility.

Approach

- Development of a robust, multiresolution theoretical framework for the multiscale modeling of inelastic-deformation processes of evolving multiphase AHSS.
- Development of a non-local strain gradient theory coupled with the developed multiresolution analysis.
- Implementation of the developed theoretical models in a multiscale hierarchal computational framework.
- Conduct of a parametric study of the effect of microstructural features (e.g., particle size, interfacial properties, particle volume fractions and distribution) on the strength and ductility of AHSS.

Accomplishments

- A theoretical model based on nonlocal strain gradient plasticity has been developed and successfully validated. This model can be used in predicting the increase in yield strength and strain-hardening rates of AHSS with decreasing the particle (inclusion) size and by increasing the stiffness of these second-phase particles.
- It is found that there is an optimum combination between hard and soft particles that can be dispersed within the matrix of AHSS to achieve a simultaneous increase in both strength and ductility.

Future Direction

- Incorporate micro-damage nucleation and growth laws that can simulate micro and nano crack evolution within the matrix material of AHSS and at internal interfaces of second-phase materials and particles.
- Incorporate phase-transformation laws that can be used to explain additional strengthening besides the strengthening due to dispersed particles.

- Implement the proposed multiresolution framework and conduct a parametric study of the effect of microstructural features on the strength and ductility of AHSS.

Introduction

With the introduction of stronger safety legislation and increased dependence on foreign oil, auto manufacturers must respond with higher car-body stiffness for safety and lower body weight for fuel efficiency. The fields of materials development, engineering, and manufacturing are working together to achieve autobody weight reduction with improved crash characteristics [1]. For that reason, the use of advanced high-strength steels (AHSS) [steels with tensile strength ≥ 500 MPa and tensile elongation ≤ 20% in car bodywork has spread in recent years [2]. The American Iron and Steel Institute (AISI) is forecasting a dramatic increase in the use of AHSS in the automotive industry. As shown in Figure 1, the second generation of AHSS offers superior combinations of strength (performance) and ductility (formability) over the other types of steels. This is attributed to their elevated strain hardening capacity as a result of a lower yield strength/ultimate tensile strength ratio. Therefore, the main advantage of these types of steels is a higher impact resistance, which allows reducing the weight of the bodywork components by using thinner metallic sheets. However, the cost of the second generation AHSS is prohibitive for widespread adoption because of costly alloy content (e.g., nickel or manganese). The to-be-developed third generation AHSS are envisioned as affordable alternatives to second generation AHSS, but will trade some mechanical properties, still being much more effective than current and first generation AHSS.

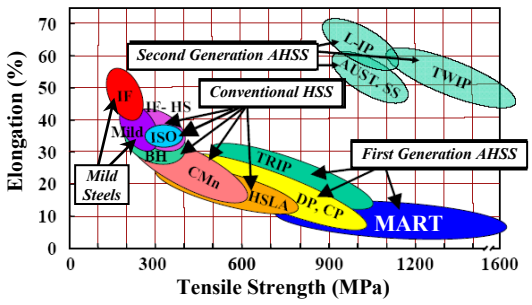

Figure 1. Comparison between different grades of steels for strength and ductility [3].

Work-hardening is one of the primary reasons for the enhanced strength and ductility of AHSS over other types of steels. Work-hardening can be enhanced by second phase particles (inclusions) of different sizes at distinct length scales. The main objective of this study is the development at different nested length scales (i.e., multiresolution) a fundamental understanding of the particle size and interface effects on the strengthening (strain hardening) and micro-damage (strain softening) mechanisms that lead to drastic increase/decrease in the strength and ductility of AHSS. This will ultimately lead to design of modern AHSS with desirable micro/nanostructures and optimized properties through alloy component/phase selection. Therefore, the AHSS that we are interested in display strong particle size and interface effects. It is well known that conventional steels contain soft iron matrix and hard inclusions. For the AHSS that will be the core of this study, the iron matrix comprised of martensite and austenite that is designed to be transformable into body-centered-cubic (BCC) martensite, which is a desirable hard substance. The inclusions, which are distributed in a non-homogeneous manner, are divided into two groups (see Figure 2): the primary particles with diameters around several microns and the secondary particles in the range of 1 to 0.1 microns. It is argued until now that the secondary particles increase the strength by strain-hardening mechanisms whereas primary particles lower the fracture toughness by strain- softening mechanisms. Therefore, by optimizing the volume fractions, sizes, shapes, interfacial strength, and distribution of these constituents, one may be able to increase the strength and ductility of AHSS simultaneously.

Approach

Theoretical modeling and multiscale computational simulations are necessary for the design of new generations of AHSS. Therefore, it is imperative to develop a constitutive model and a multiscale framework that can be used

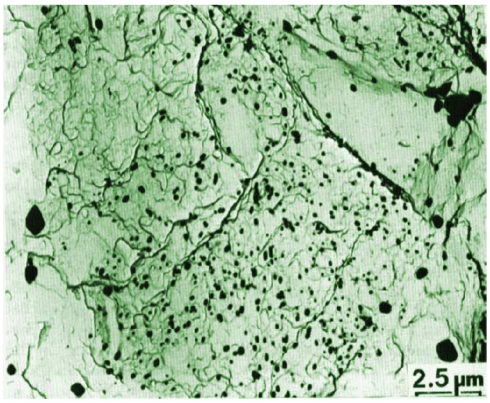

Figure 2. A TEM micrograph of the microstructure of an AHSS showing the different levels of dispersed small particles [4].

successfully in incorporating the strengthening effects due to the reduction in particle (inclusion) size and the effects of the interfacial hardening by incorporating the particle-matrix interfacial mechanical properties (e.g., interfacial strength and hardening). Unfortunately, the classical continuum plasticity theories (e.g., von Mises or Drucker-Prager) are unable to predict the influence of particle size due to the absence of a microstructural length scale parameter in their constitutive equations [4]. Therefore, within a classical continuum mechanical framework, the mechanical properties of multiphase materials only depend on the volume fraction of particles while the particle size is not accounted for. However, the mechanical properties of lightweight advanced materials, with a typical distance D between particles and particle size d, depend on how these geometrical parameters interfere with other characteristic distances such as the mean-free path of dislocations. Reducing the size of particles, while keeping the volume fraction constant, significantly improves the material macroscopic mechanical properties.

Since the increase in strength with decreasing scale can be related to proportional increase in the plastic strain gradients that evolve at the particle-matrix interfaces due to dislocation pileups (see Figure 3), the gradient plasticity theory has been successful in addressing the size effect problem [5]. This success stems from the incorporation of a microstructural length scale parameter through functional dependencies on the plastic strain gradient of nonlocal media [5]. The gradient-

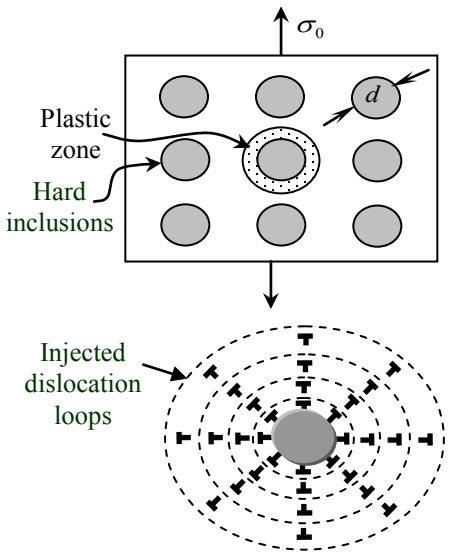

Figure 3. Plastic strain gradients are caused by evolution of geometrically necessary dislocations (GNDs) around spherical inclusions of size d under uniaxial loading.

dependent theory abandons the assumption that the stress at a given point is uniquely determined by the history of strain at this point only. It takes into account possible interactions with other material points in the vicinity of that point.

As an initial effort, in order to include the size effect of dispersed particles within the AHSS matrix, a higher-order gradient plasticity theory have been developed and validated. This nonlocal theory takes into account the plastic strain gradient (i.e., heterogeneous distribution of plasticity) around the second-phase inclusions (see Figure 3). Also, the interfacial mechanical properties of the particle-matrix interface (e.g., interfacial yield strength and interfacial hardening) are explicitly incorporated in the formulated theory. Depending on the interfacial properties, the effect of hard, stiff, or soft inclusions are incorporated.

Also, in this theory, two plasticity yield conditions are formulated, one for the bulk (i.e., the matrix) and one for particle-matrix interface and grain boundaries. Therefore, two length scale parameters are incorporated. The bulk length scale parameter, ℓ, is related to the average spacing between dislocations within the matrix material; whereas, the interfacial length scale, ℓ_I, is related to the boundary layer thickness at the particle-

matrix interface. Both length scales can be identified from nanoindentation tests.

Results

The formulated nonlocal strain gradient plasticity theory has been implemented in the commercial finite-element program ABAQUS through its user material subroutine UMAT and used to demonstrate the ability of the model in predicting particle size effects on the strength of AHSS. The direct and simple numerical implementation method for gradient-dependent theories as presented in [6] has been utilized for calculating the plastic strain gradients.

Figure 4 shows that strain gradient plasticity is successful in predicting the inclusion size effect for a constant volume fraction unlike the classical plasticity theory. Moreover, Figure 5 shows mesh dependent results when simulating strain localization due to particle debonding when using the classical theory of plasticity which can be largely corrected when using the proposed strain gradient plasticity theory.

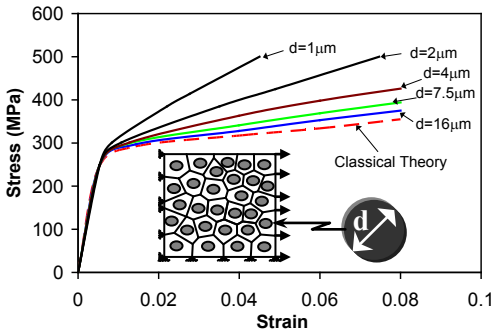

Figure 4. Finite-element computational comparisons between the predictions from strain gradient plasticity theory and the classical plasticity theory for inclusion size effect on strain hardening at a constant volume fraction.

Moreover, it is shown that the proposed nonlocal strain gradient plasticity theory can predict the increase in the initial yield strength (i.e., onset of plasticity) characterized by the ratio of the average yield strength of AHSS σ_Y to the matrix size-independent yield strength σ_y as shown in Figure 6. This increase in the initial yield strength is shown for different particle sizes d

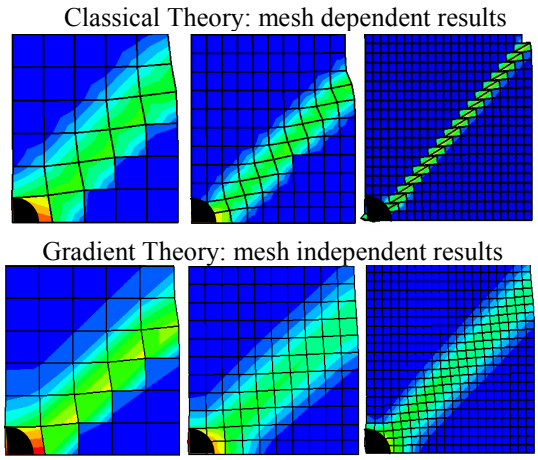

Figure 5. Finite element computational comparisons between the predictions from strain gradient plasticity theory and the classical plasticity theory for strain localization induced particle debonding.

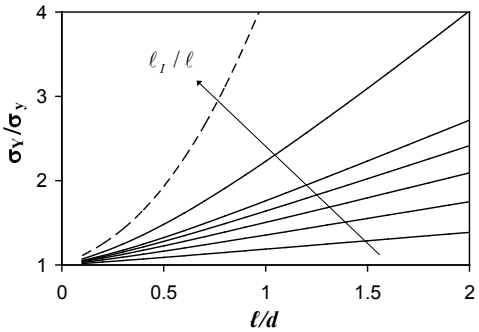

Figure 6. Normalized macroscopic yield strength of AHSS σ_Y versus particle size d for different particle-matrix interfacial strength increases. The dashed line is for a rigid particle.

(characterized by the ratio ℓ/d where ℓ is the material length scale) and for different particle-matrix interfacial strengths (characterized by the ratio ℓ_I/ℓ, where ℓ_I is the interfacial length scale parameter). As ℓ_I/ℓ increases, the hardness of the particle increases. Similarly, Figure 7 shows the particle size effect on the strain hardening rate characterized by the normalized ratio of the hardening tangent modulus E^T to the Young's modulus E. It can be seen that as the particle size decreases or as the particle hardness increases, the strain hardening rate increases. In other words, the smaller the particle size and the larger the particle hardness, the larger the ultimate strength. However, it is noteworthy that the above

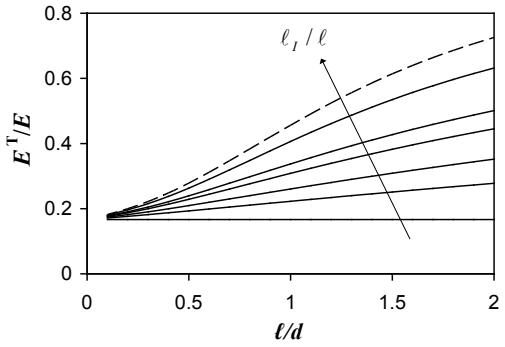

Figure 7. Normalized macroscopic hardening modulus of AHSS E^T versus particle size d for different particle-matrix interfacial strength increases. The dashed line is for a rigid particle.

conclusions and observations are valid only in the case wherein the particle debonding and fracture effects are not considered. These effects will be incorporated in the subsequent development of the current study.

Conclusions

It is concluded that a nonlocal strain gradient plasticity theory can be used to qualitatively predict the particle size effect in AHSS reinforced with particles (inclusions) at decreasing microstructural length scales. These particles can range in size from few hundreds of nanometers to few microns.

It is shown that as the particle size decreases or particle hardness increases both the onset of plasticity (yield strength) and strain hardening rate (or ultimate strength) increases. This is a crucial conclusion for the design of AHSS with improved yield and ultimate strengths. However, these conclusions are only valid in the case wherein both debonding and fracture of particles are not considered. Future extensions of the current study will consider damage evolution in the matrix, particle, and particle debonding which are very important to validate the aforementioned conclusions and for assessment of the effect of particle size and hardness on the ductility of AHSS.

Moreover, future work will be concerned with incorporating the formulated nonlocal strain gradient plasticity theory in a multiscale hierarchal computational framework ranging from the nano scale to the macro scale. This is important to study the effect of each scale on the other and how the microstructural changes within each scale affect the overall macroscopic strength and ductility of AHSS or low-density materials. Furthermore, phase transformation of austenite to the hard phase martensite will also be incorporated into the proposed multiscale framework. One of the important aspects of this study that will be investigated thoroughly is the calibration, validation, and verification of the proposed theoretical models and computational tools. The proposed frameworks will be validated and verified against available experimental results for specific material systems or microstructures.

Presentations

1. Abu Al-Rub, R. K. “Non-local Strain Gradient Plasticity and Damage: A Multiresolution Framework for Bridging the Material Length Scales,” Computational Sciences & Mathematics Division, Pacific Northwest National Laboratory (PNNL), Richland, Washington, September 4, 2008.
2. Abu Al-Rub, R. K., “Nonlocal Gradient-dependent Plasticity and Damage: An Approach for Bridging the Material Length Scales,” Symposium of Predictive Science and Technology of Mechanics and Materials, Center for Advanced Vehicular Systems (CAVS), Mississippi State University, June 24, 2008.
3. Abu Al-Rub, R. K., “AHSS through Particle and Interface Effects,” NSF/DOE Steel Research Program Review, Auto/Steel Partnership Offices, Southfield, MI, April 10, 2008.
4. Abu Al-Rub, R. K., “On the Higher-Order Nonlocal Gradient-Dependent Theory and its Non-classical Microscopic Boundary Conditions,” In. 2008 ASME International Mechanical Engineering Congress and Exposition, Session on Nonlocal Methods and Length-Scale Effects, Boston, Massachusetts, November 2–6, 2008.
5. Abu Al-Rub, R. K., “Interfacial Gradient Plasticity Governs Scale-Dependent Yield Strength and Strain Hardening Rates at

Decreasing Microstructural Length Scales," In. 2008 ASME International Mechanical Engineering Congress and Exposition, Session on Multiscale Constitutive Modeling, Boston, Massachusetts, November 2–6, 2008.

6. Abu Al-Rub, R. K., "Multiresolution Modeling of Size and Interfacial Effects in Metal Matrix Composites with Dispersed Particles at Decreasing Microstructural Length Scales," In. 2008 ASME International Mechanical Engineering Congress and Exposition, Session on Mechanics of Composites with Coupled Mechanical and Nonmechanical Behaviors, Boston, Massachusetts, November 2–6, 2008.
7. Abu Al-Rub, R. K., "Prediction of Nanoindentation Size Effect from Conical or Pyramidal Indentation," In. 2008 ASME International Mechanical Engineering Congress and Exposition, Session on Modeling and Experiments in Nanoindentation, Boston, Massachusetts, November 2–6, 2008.
8. Abu Al-Rub, R. K., and Kim, S.-M., "Nonlocal Framework for Simulating the Micromechanics of Localized Damage and Fracture in Metals at High-Speed Impact," In. 2008 ASME International Mechanical Engineering Congress and Exposition, Symposium Honoring John W. Hutchinson, Boston, Massachusetts, November 2–6, 2008.
9. Abu Al-Rub, R. K., Voyiadjis, G. Z., Bammann, D. J., and Aifantis, E. C., "On the Higher-Order Gradient Plasticity Theory and its Non-classical Boundary Conditions," In. 45th Annual Technical Meeting of the Society of Engineering Science (SES), Symposium on Plasticity and Damage Size Effects at the Micron and Nano Length Scales, Champaign, Illinois, October 12–15, 2008.
10. Abu Al-Rub, R. K., "Prediction of Micro and Nano Indentation Size Effects from Pyramidal and Spherical Indentation," In. 45th Annual Technical Meeting of the Society of Engineering Science (SES), Symposium on Plasticity and Damage Size Effects at the Micron and Nano Length Scales, Champaign, Illinois, October 12–15, 2008.
11. Abu Al-Rub, R. K., "Interfacial Gradient Plasticity Governs Scale-Dependent Yield Strength and Strain Hardening Rates at Decreasing Microstructural Length Scales," In. 45th Annual Technical Meeting of the Society of Engineering Science (SES), Session in Honor of Professor Subra Suresh, Champaign, Illinois, October 12–15, 2008.
12. Abu Al-Rub, R. K., "Multi-scale Prediction of Micro and Nano Indentation Size Effect," In: First American Academy of Mechanics Conference, Session on Multi-scale Modeling and Simulation of Nano Structured Materials, New Orleans, Louisiana, June 17–20, 2008.
13. Abu Al-Rub, R. K., "Prediction of Size Effects at the Micron and Submicron Length Scales," In: First American Academy of Mechanics Conference, Session on Modeling Inelastic Deformation at Varying Length Scales, New Orleans, Louisiana, June 17–20, 2008.
14. Abu Al-Rub, R. K., "Surface/Interfacial Effects on Size Dependent Strength of Micro/Nano Systems," In. 49th AIAA/ASME/ASCE/AHS/ASC Structures, Structural Dynamics and Materials Conference, AIAA 2008, Session on Multiscale Material Analysis, Schaumburg, Illinois, April 7–10, 2008.

Publications

1. Abu Al-Rub, R. K., "Modeling the interfacial effect on the yield strength and flow stress of thin metal films on substrates," Mechanics Research Communications, Vol. 35, No. 1-2, pp. 65–72, 2008.
2. Abu Al-Rub, R. K., "Interfacial gradient plasticity governs scale-dependent yield strength and strain hardening rates in micro/nano structured metals," International Journal of Plasticity, Vol. 24, No. 8, pp. 1277–1306, 2008.
3. Abu Al-Rub, R. K., Voyiadjis, G. Z., and Aifantis, E. C. "On the thermodynamics of higher-order gradient plasticity for size-effects at the micron and submicron length scales," International Journal of Materials and Product

Technology, Vol. 34, Nos. 1/2, pp. 172–187, 2009.

4. Abu Al-Rub, R. K., "Surface/interfacial effects on size dependent strength of micro/nano systems," In. Collection of Technical Papers AIAA/ASME/ASCE/ AHS/ASC Structures, Structural Dynamics and Materials Conference, AIAA 2008-1946 (5 pages).

References

1. Marsh, M., 2000. "Development of autobody sheet materials for crash performance," In: Proc. of Conf. Materials and Structures for Energy Absorption, IMech, London, May 9, 2000, 55–64.
2. Baker, M. A., 2004. Proceedings of the International Conference on Advanced High Strength Sheet Steels for Automotive Applications. Association for Iron and Steel Technology, Warrendale, PA, USA.
3. Wagoner, R. H., and Smith, G. R., 2006. Advanced High-Strength Steels (AHSS) Workshop. October 22–23, 2006, Arlington, Virginia, USA.
4. Abu Al-Rub, R. K., 2008. "Interfacial gradient plasticity governs scale-dependent yield strength and strain hardening rates in micro/nano structured metals," International Journal of Plasticity, 24, 1277–1306.
5. Voyiadjis, G. Z., and Abu Al-Rub, R. K., 2009. Nonlocal Continuum Damage and Plasticity: Theory and Computation. World Scientific Publishing Co Pte Ltd., UK.
6. Abu Al-Rub, R. K., and Voyiadjis, G. Z., 2005. A direct finite element implementation of the gradient plasticity theory. Int. J. Numer. Meth. Engng. 63, 603–629.

N. Study of the Effects of Microstructure on the Mechanical Properties and Failure Mechanisms of Advanced High-Strength Steels

Warren M. Garrison Jr., Anthony Rollett, Sridhar Seetharaman
Carnegie Mellon University
5000 Forbes Avenue
Pittsburgh, PA 15213
(412) 268-3593; fax: (925) 268-7596; e-mail: wmg@andrew.cmu.edu

Technology Area Development Manager: Joseph A. Carpenter
(202) 586-1022; fax: (202) 586-1600; e-mail: joseph.carpenter@ee.doe.gov

Field Project Officer: Aaron D. Yocum
(304) 285-4852; fax: (304) 285-4403; e-mail: aaron.yocum@netl.doe.gov

---

Contractor: Carnegie Mellon University, Pittsburgh, Pennsylvania
National Science Foundation (NSF) Award CMMI 0726949, jointly funded by NSF and DOE

Objectives

- To understand the effect of complex, multiphase microstructures on the mechanical behavior and formability of advanced high-strength sheet steels.
- To investigate the effect of void nucleation resistance at inclusion particles on the mechanical behavior and formability of high-strength sheet steels.

Approach

- Develop microstructures consisting of lower bainite mixed with 0%, 25%, and 50% ferrite and assess the mechanical behavior and formability of these microstructures.
- Develop microstructures consisting of martensite mixed with 0%, 25%, and 50% ferrite and assess the mechanical properties and formability of these microstructures and compare the behavior of these martensite structures with those of the lower-bainite structures.
- Prepare heats of steel which are identical except for the sulfide type with one sulfide type having low resistance to void nucleation and the other sulfide type being resistant to void nucleation. Sulfide particles which have a low resistance to void nucleation are achieved by gettering the sulfur as particles of manganese sulfide. Sulfide particles which are very resistant to void nucleation are achieved by gettering the sulfur as particles of titanium carbo-sulfide.

Accomplishments

- Defined four steel compositions to be used in investigating mixtures of lower bainite and ferrite and mixtures of martensite and ferrite on mechanical behavior and formability.
- Defined two steel compositions to be used to assess void nucleation resistance of inclusions on mechanical behavior and formability.
- Melted the six heats corresponding to the six selected compositions and processed some of each composition to one-half-inch-thick plate. This was done at US Steel research facilities in Pittsburgh.
- Investigated the effect of solution treatment temperature on the amount of ferrite, hardness, and Charpy impact energy for the four compositions used to explore effects of mixed microstructures on mechanical behavior and formability.

- Obtained Charpy impact toughness and tensile properties of the two compositions to be used to assess the effect of void nucleation resistance on formability of sheet steels.

Future Directions

- Decide on heat treatments to be used to obtain the mixed microstructures.
- Prepare sheet material which have the desired mixed microstructures and begin to carry out studies of formability.
- Prepare sheet material from the two heats which represent inclusions resistant to void nucleation and inclusions not resistant to void nucleation and begin to carry out studies of formability.

Introduction

The purpose of this work is to examine the effects of heat treatment and composition on the microstructure and mechanical properties of high-strength steels with the ultimate goal of producing microstructures which would have ultimate tensile strengths of at least 1,200 megapascals (MPa) and which would be suitable for use in automotive applications, especially for steel sheet to be used in forming operations.

There are several factors to consider in assessing the formability of steel. The first is that the work-hardening capacity and characteristics be sufficient to ensure formability in the sense that strain localization and/or local thinning do not take place in the forming process; thus, the strains which can be tolerated prior to local thinning increase with work-hardening rate [1]. The uniform strain is often taken as measure of this characteristic, thus high uniform strains are desired in steels which are intended for applications in which they must be formed. The second is that the material has sufficient ductility that fracture does not take place during the forming operation. The latter characteristic is important because it has been found that as the strength levels of steels for forming applications are increased, there is a tendency for fracture to take place before the forming operation is complete, at least for some forming operations [2–7]. Thus, not only are the work-hardening characteristics important, in that the work-hardening rates should be high and remain high even at large strains, but that resistance to fracture should also be high. Thus, in assessing sheet materials for forming using a tensile test, one would want both high uniform strains and high true strains to fracture. That is, the behavior of the material after necking is also of importance. Coupled with the requirements for high formability there are interests in steels of higher strength in order to reduce weight and the ability of the structures produced of these materials to absorb energy under impact conditions [8].

Our approach is strongly influenced by two papers concerning Transformation Induced Plasticity (TRIP) [2-5, 9-15] steels developed for steel sheet applications. These TRIP steels contain several microstructure features, including ferrite, bainite, martensite, and retained austenite which, through control of composition and heat treatment, is mechanically stable. In the TRIP steels developed for sheet applications, it is believed that the carefully controlled transformation of the retained austenite to a high-carbon martensite during deformation is critical to achieving high rates of work hardening and high uniform strains, which are important to good formability.

The first paper is a note by Bhadeshia [16] which was inspired by a paper by Jacques et al. [17]. Jacques et al. found that one could obtain excellent uniform elongations in multiphase steels which did not contain silicon or aluminum to promote the existence of mechanically stable retained austenite which is free from carbide formation. Badheshia suggested, based on these results, that the 8 to 15 volume % retained austenite commonly found in TRIP steels contributed about 2% to a total uniform elongation of say 25%. Badheshia suggested that the high work-hardening rates in the multiphase steels typical of TRIP steels might be instead due to a mixture of soft and hard phases. In his discussion, Badheshia suggested

that the high work- hardening rates might be associated with initial deformation of the ferrite which would not work harden at a high rate but, at some point, the as-quenched martensite in the microstructure would start to deform and the high work-hardening rate of the as-quenched martensite is what determines the high work-hardening rate of the structure and the high uniform elongations. (The high work-hardening rate of as-quenched martensite is related to not only the distribution of the carbon [18] in the martensite but also, we believe, to the amount of retained austenite in the as-quenched martensite).

The second paper is one by Lee et al. [19] in which void generation in multiphase steels was investigated. They found that voids are generated during plastic deformation not only at inclusions and carbide particles but at interfaces between strong and weak microstructural elements; for example, voids could be generated at interfaces between ferrite and martensite. The rate at which voids are formed during deformation can have important consequences in terms of tensile ductility and possibly on formability. The slower the rate at which voids are generated the greater the chance that tensile ductility can be improved. The rate of void generation will be influenced by the rate at which the volume fraction of voids increases and by the strain at which voids is nucleated. The goals would be to minimize the volume fraction of voids at each point of the deformation process and to make void nucleation as difficult as possible.

As a consequence of these observations, we view the proposed work to be primarily an examination of the effects of complex, multiphase microstructures on strength, work-hardening behavior, and ductility or toughness. In the end, of course, the objective would be to examine the formability of such steels, particularly in applications where ductility as measured by, for example, the true strain to fracture in a tensile test or toughness, are important. The microstructure to be examined will be essentially dual phase steels, which we can control through heat treatment and composition, the amounts of ferrite and martensite, and the amount of retained austenite, and TRIP steels. Thus, we would be examining the effects of mixtures of ferrite and martensite or of ferrite and bainite on mechanical behavior. In both systems we have the possibility of introducing different amounts of retained austenite. In this work, we will adhere to one melt practice and aim to maintain constant inclusion types and inclusion volume fractions. We also propose a separate study of the effect of inclusion resistance to void nucleation on formability.

Statement of Objectives

The primary objective of this work is to understand the effects of complex, multi-phase microstructures on the mechanical properties of such steels. To be specific, we are assessing the effect of ferrite in combination with either a martenstic structure or with a bainitic microstructure on mechanical properties. And, we will be comparing the properties of bainitic structures and martensitic structures at the same amounts of ferrite. Furthermore, at each ferrite level the bainitic and martensitic structures should have very similar strength levels. The mechanical properties of interest will be the tensile properties, including strength, work-hardening behavior, the associated uniform strain, and the tensile ductility, which is taken as the true strain to fracture. An important issue is the strain to fracture after reaching the uniform strain. Also, the toughness of the microstructures will be assessed and formability assessed, primarily for forming operations in which ductility and or toughness appears to be an issue. This work will be done using materials which should have the same inclusion characteristics.

In addition, we will explore the effect of the void-nucleation resistance of inclusions on tensile properties and toughness of a low-alloy martensitic steel and assess the effect of inclusion void-nucleation resistance on formability.

Proposed Compositions

We will employ the compositions given in Table 1. The first four compositions will be used in the development of complex microstructures and the assessment of the mechanical properties and void-generating characteristics of these microstructures and the effects of void generation and the fine-scale microstructure on tensile ductility, toughness, and formability. The last two

Table 1. Compositions of proposed heats in weight percent.

Alloy	C	Mn	Ni	Al	Si	Cr	Mo	Ti
MP1	0.2	4.0	–	–	–	–	–	–
MP2	0.2	4.0	–	1.5	–	–	–	–
MP3	0.2	4.0	–	–	1.5	–	–	–
MP4	0.2	4.0	–	–	3.0	–	–	–
M1	0.15	0.5	3	–	2.0	1	0.25	–
M2	0.15	–	3	–	2.0	1	0.25	0.04

compositions are for the assessment of martensitic steels to be used to study the influence of inclusion void-nucleation resistance on formability.

First, we will discuss the heats labeled MP for multiphase. We have pushed the carbon from a more typical 0.15 wt. % primarily to increase the potential strength level and to reduce the martensite-start temperature. The manganese is added to make sure that we can completely austenitize the samples. The manganese is also critical to hardenability. Use of Thermo-Calc indicates that the alpha and gamma two-phase region will be sufficiently large that we will be able to achieve the desired levels of ferrite. The aluminum and silicon are there to delay to higher tempering temperatures the decomposition of retained austenite in martensite on tempering and to repress the precipitation of carbides in the bainite laths and in the austenite during isothermal heat treatments to form bainite. The latter reason is why they are added to low-alloy TRIP steels. Aluminum is preferred to silicon by manufacturers of these steels because silicon promotes the formation of a scale which makes galvanizing difficult. Heat treatments planned for these four compositions to obtain multiphase microstructures will be discussed in the next section.

The last two heats will be given quenched and tempered heat treatments (tempering at 200°C), so that the microstructure will be tempered martensite. The silicon is added to promote higher strength and to promote retained austenite on air-cooling from the austenitizing temperature. The sulfide particles in the first martensitic heat will be small, closely spaced particles of manganese sulphide (MnS). The sulfide particles in the second martensitic heat will be small, closely spaced particles of titanium carbo-sulfide. We have found in highly alloyed steels such as HY180 [20] and AF1410 [21] and in high-strength, low-alloy steels that gettering sulfur as titanium carbo-sulfide can substantially improve fracture toughness because the particles of titanium carbo-sulfide are much more resistant to void nucleation than the particles of MnS. These two martensitic steels will be used to investigate the effect of inclusion resistance to void nucleation on ductility, toughness, and formability. We have previously investigated this composition and have achieved excellent levels of toughness at a carbon content of 0.35 wt. % [22].

Proposed Heat Treatments and Microstructures

Multiphase Microstructures

Current low-alloy TRIP steels are heat treated and processed by hot rolling to obtain a microstructure of pro-eutectoid ferrite and pearlite. They are then cold rolled with the main purpose of the cold reduction to form sheet but the cold rolling does provide the stored energy for the re-crystallization of ferrite in the next step. They are then held in the α-γ two-phase field to form a mixture of about 50% ferrite and 50% austenite. The carbon content of the ferrite is quite low whereas the carbon content of the austenite is on the order of 0.3 wt. %. The material given the inter-critical anneal is then quenched to a reaction temperature during which low-carbon bainite forms, and the remaining austenite is continuously enriched in carbon reaching carbon contents of about 1.3 wt. %. The material is then quenched to room temperature so that the microstructure consists of ferrite, some form of bainite, martensite formed from some of the high- carbon austenite on quenching from the reaction temperature to room temperature and some regions of retained austenite. The martensite would be primarily plate martensite and would itself contain some retained austenite. The austenite could exist as retained austenite associated with the martensite, as finely distributed austenite associated with the bainite and perhaps as large pools of retained austenite not associated with either the martensite or the bainite. The retained austenite would have a high carbon content, and this high carbon content would make it resistant to transforming to martensite during straining. Presumably, the more

finely distributed retained austenite associated with the martensite and the bainite would have its mechanical stability further enhanced due to mechanical constraint. It is believed that this mechanically stable austenite is what gives rise to the high work-hardening capacity of these TRIP steels as the retained austenite would continuously transform to untempered plate martensite with increasing strain. However, as Bhadeshia has pointed out, the large volume fraction of the ferrite may be critical to achieving the high work hardening rates and a high uniform strain [16].

Using the four compositions designated for the formation of multiphase microstructures, we plan, broadly speaking, two different types of heat treatments. We will describe these heat treatments and the types of microstructures we expect to see.

Obtaining Mixed Microstructures Consisting of Martensite and Ferrite

Here, it is proposed to obtain microstructures containing ferrite and martensite. The first microstructure will consist of martensite which will be formed by directly quenching to room temperature from a temperature at which the alloy is completely austenitic. The next microstructure will be obtained by using an inter-critical anneal to form 25% ferrite and 75% austenite. This structure will then be quenched to room temperature, and the final microstructure would consist of 25% ferrite and 75% martensite. The third heat treatment would be to form 50% ferrite and 50% austenite in the inter-critical anneal. On quenching to room temperature, the structure would consist of 50% ferrite and 50% martensite. In all cases the martensite would be expected to be lath martensite and with inter-lath films of retained austenite. However, the martensite carbon content will be only about 0.2 wt. % in the wholly martensitic structure. It would be higher for the microstructure obtained by quenching the material held at the first inter-critical anneal in which 25% ferrite would be formed. The martensite formed on quenching the material held at the inter-critical anneal designed to form 50% ferrite would be about 0.4 wt. %. Thus, the three martensites would differ significantly in strength and in the amount of inter-lath retained austenite. The microstructures could be altered by tempering the as-quenched structures at 200°C. This would have the effect of increasing the yield strength of the martensite and lowering its ultimate tensile strength. The mechanical stability of the retained austenite in the martensite would be substantially increased by this tempering treatment. The tempered martensite should have considerably higher ductility and toughness than the as-quenched martensite. The strength of the martensite in the final microstructure would be high indeed, approaching a hardness of 550 Vickers.

We will outline in the next section how we will obtain microstructures containing 0, 25, and 50% ferrite and 100, 75, and 50% bainite. The bainite formed in the three microstructures will have strength levels comparable to those of the martensite formed at 0, 25, and 50% ferrite. Thus, differences in the ductility of the bainitic and martensitic structures for a given amount of ferrite will not be influenced by strength but by details of the microstructure. We can vary the amount of retained austenite in the ferrite-martensite structures by slowing the cooling rate from the austenitizing or inter-critical annealing temperatures (this will increase the amount of retained austenite), by refrigeration of retained austenite to reduce the amount of retained austenite or by using heat treatments to stabilize the retained austenite to increase the amount of retained austenite.

Obtaining Mixtures of Bainite and Ferrite

Here, we will use three basic heat treatments. In the first, the material will be austenitized and then quenched to a series of reaction temperature in which bainite would be formed. There would be no ferrite. In the second, the material would be given an inter-critical anneal to form 25% ferrite, and then samples would be quenched to a series of isothermal hold temperatures in which bainite would be formed. In the third set of experiments, the material would be given an inter-critical anneal in which the ferrite formed would be 50% and then the material would be quenched to a range of isothermal- transformation temperatures in which bainite would be formed. At each isothermal reaction temperature, the effect of isothermal hold time on the microstructure will be evaluated. From what we understand of bainite formation, during

the isothermal holds it is expected that the bainite formed would be carbide free and the carbon content of the retained austenite would reach levels approaching 1.3 wt. %, at least with the addition of silicon or aluminum. On quenching from the isothermal hold temperature, we would expect to have a microstructure consisting of low-carbon bainite laths, films of retained austenite interspersed through the bainite laths, pools of high-carbon retained austenite, and some plate martensite, which is formed from the high-carbon austenite on quenching from the isothermal hold temperature [23–27]. The plate martensite formed from this high-carbon austenite would, of course, contain retained austenite. The possibility of carbide precipitation cannot be excluded either in the bainite laths or associated with the retained austenite. However, the aluminum and silicon additions are believed to stabilize the structure with respect to cementite formation. These microstructures could also be tempered. For example, it might be interesting to temper at 200°C in order to increase the mechanical stability of the austenite, at least the austenite within the bainite laths and the martensite.

Whether or not such tempering would improve the mechanical stability of the austenite in pools in the microstructure is not known. We note that it has been reported that the quench rate from these isothermal holds can significantly increase the amount of total retained austenite in the structure. Thus, retained austenite could be varied by varying the cooling rate from the reaction temperature. Miihkinen and Edmonds [23–25] found that refrigeration in liquid nitrogen had no effect on the amount of retained austenite in their bainitic microstructures.

The Effect of Inclusion Void- Nucleation Resistance on Formability

The two martensitic steels will be heat treated in the following manner. They will be austenitized at 900°C for one hour, oil- quenched to room temperature, and tempered at one hour at 200°C. The microstructures will consist of lath martensite and a small amount of inter-lath retained austenite. The microstructures of the two steels will differ in that the titanium-modified steel will contain some small titanium carbides which might have an effect on prior austenite grain size and a different type of sulfide. In the titanium-modified heat, the sulfides will be titanium carbo-sulfides and in the other heat the sulfides will be MnS. Our expectation is that the titanium-modified heat will have a substantially higher true strain to fracture and a substantially higher toughness as the particles of titanium carbo-sulfide are much more resistant to void nucleation than the particles of MnS. We intend to compare the formability of the two heats. Primarily we will be interested in forming operations where ductile fracture has precluded use of other high-strength sheet steels. However, we have found in previous studies of the deformation and forming of sheet steels that voids at inclusions were nucleated well before reaching the forming limit and the extent of void growth was considerable before the forming limit was reached, as defined by a strain at which local thinning of the sheet was observed. There are theoretical studies in support of the idea that void generation can influence formability by hastening the onset of local thinning [28–30], and we will use these materials to test this idea in more conventional forming operations.

Results

We have accomplished the following. First, we have melted heats of the six desired compositions. Second, we have begun processing these materials into one-half-inch plate and into sheet. Third, we have begun to establish the heat treatment for the compositions MP1, MP2, MP3, and MP4 to obtain the desired mixtures of ferrite and martensite and the desired mixtures of ferrite and bainite in each of these four compositions. Fourth, we have heat treated Charpy impact specimens and tensile specimens for the two heats of the compositions M1 and M2 which are to be used in the assessment of void-nucleation resistance of inclusions on the formability of steel sheet.

Melting and Composition of Heats

The heats having the composition of MP1, MP2, MP3, MP4, M1, and M2 have been prepared in the following by vacuum induction melting using aluminum additions to deoxidize the heats. The compositions of the six heats are given in Table 2.

Table 2. Compositions of experimental heats in weight percent.

Alloy	C	Mn	Ni	Cr	Mo	Ti	Al	Si	P	S	O_2	N_2
MP1	0.188	3.84	<0.002	0.01	0.002	<0.002	0.021	0.015	0.005	0.0037	0.0021	0.0041
MP2	0.183	3.73	<0.002	0.01	0.021	<0.002	1.437	0.021	0.005	0.0024	0.0033	0.0041
MP3	0.197	4.22	<0.002	0.011	0.003	<0.002	0.030	1.461	0.005	0.0031	0.0013	0.0056
MP4	0.205	4.27	<0.002	0.010	0.003	0.002	0.033	2.837	0.004	0.0025	0.0027	0.0055
M1	0.180	0.49	3.013	0.983	0.244	<0.002	0.031	1.979	0.003	0.0027	0.0015	0.0018
M2	0.158	0.007	2.927	0.971	0.248	0.038	0.025	1.945	0.002	0.0034	0.0013	0.0014

Processing to Plate and Sheet

From each of material, we wanted 1.27 cm thick flat plate as well as sheet material with a thickness of 0.1397cm.

The ingots after melting were 12.7 cm × 27.9 cm × 45.72 cm. Each ingot was hot rolled from a thickness of 12.7 cm to a thickness of 2.54 cm using a reheat temperature of 1,250°C and a finishing temperature of 870°C. They were then air- cooled to room temperature. Each of the slabs thus produced were cut into four 30.5 cm lengths. One of these four slabs was rolled from a thickness of 2.54 cm to a thickness of 1.27 cm using three passes and a reheat temperature of 1,100°C and a finishing temperature of 920°C. The finished plates were then air-cooled to room temperature. This resulted in the 1.27-cm- thick plate to be used in initial studies.

To prepare sheet material, two of the slabs of a thickness of 2.54 cm were further hot rolled to a thickness of 0.457 cm. This was done in five passes using a reheat temperature of 1,250°C and a finishing temperature of 920°C. The strip thus produced was water-spray cooled to 650°C, placed in a furnace set at 600°C, and then furnace-cooled to room temperature. Beginning with the two strips of a thickness of 0.457 cm, the sheet material is being produced by two different routes. The two different routes are used to obtain two different surfaces. The two different routes are termed Process A and Process B. In process A, one of the hot- rolled strips is sheared into five pieces each having a length of 25.4 cm and a thickness of 0.457 cm. Two of these pieces were sent to the machine shop and surface ground to a thickness of 0.3175 cm. Then, after the surface grinding they were cold rolled from 0.3175 cm to a thickness of 0.1397 cm. This results in two sheets of a thickness of 0.1397 cm and a width of 27.94 cm and a length of 50.8 cm. In process B a hot-rolled strip of a thickness of 0.457 cm is sheared into five pieces of a length of 25.4 cm and a thickness of 0.457 cm. Then, two of these pieces are grit blasted and pickled to remove scale. Then the pieces are cold rolled from the thickness of 0.457 cm to a thickness of 0.201 cm. This will result in two sheets of a thickness of 0.201 cm and a width of 27.94 cm and a length of 50.8 cm. Thus, the sheet produced by process B is thicker and it would be possible to grind surfaces of pieces of this sheet which have been heat treated and still arrive at a final thickness of 0.1397 cm.

Determining Solution Treatment Temperatures for Compositions Used to Produce Multiphase Microstructures

For the compositions MP1, MP2, MP3, and MP4, we want to obtain structures which are 100% martensite, 25% ferrite and 75% martensite, and 50% ferrite and 50% martensite, and we also want microstructures which are 100% bainite, 25% ferrite and 75% bainite, and 50% ferrite and 50% bainite. Thus, we need to determine for each of the four compositions the temperatures at which we have 25% ferrite and 75% austenite and 50% ferrite and 50% austenite. To do this we began with using Thermo-Calc to determine the phase diagrams relevant to our compositions.

Based on these phase diagrams, we have selected a number of temperatures spaced 20°C apart for each of the four alloys and have held samples at these temperatures for one hour and then oil-quenched. The austenite which was present at a given temperature will transform to martensite on quenching, and the ferrite present at that temperature will remain ferrite on quenching. Thus by determining the volume fractions of

ferrite and martensite in a quenched sample, we can determine the volume fractions of austenite and of ferrite present at the temperature of interest prior to quenching.

For the alloy MP1, the temperatures selected were 900°C, 800°C, 780°C, 760°C, 740°C, 720°C, 700°C, 680°C, and 660°C. For the alloy MP3, which contains 1.5 wt. % silicon, the same temperatures were selected. For the alloy MP4, which contains 3 wt. % silicon, the temperatures selected were 900°C, 800°C, 780°C, 760°C, 740°C, 720°C, and 700°C. The temperatures selected for the composition MP2, which contains 1.5 wt. % aluminum, were 1,000°C, 950°C, 900°C, 880°C, 860°C, 840°C, 820°C, 800°C, 780°C, 760°C, and 740°C. Samples from each temperature selected for each alloy are now being mounted for metallography. From these specimens we will obtain a plot of the amount of ferrite as a function of temperature for each of the four alloys, and we can then decide on the solution treating temperatures which result in 25% ferrite and 50% ferrite for each of the four alloys. In addition, we have mounted samples of the hot-rolled plate for each of the compositions to determine the initial microstructure for each of the alloys.

We have also prepared Charpy impact specimens for each of the selected temperatures for each of the four alloys which were tempered at 200°C for one hour From these we have obtained the Charpy impact energy and hardness for each alloy as a function of solution treating temperature, at least for the ferrite-martensite mixed microstructures.

The hardness levels for all four heats were about 72 Rockwell-A at higher solution treating temperatures. The hardness of the alloy containing 1.5 wt. % aluminum begins to decrease with decreasing solution treatment temperature for solution treatment temperatures less than 800°C. This decrease begins at 780°C for the alloy containing 3 wt. % silicon and begins at a solution treating temperature of 740°C for the alloy with 1.5 wt. % silicon and for the alloy containing no aluminum or silicon. The Charpy impact values also change with solution treating temperature. At high hardness levels the Charpy impact energy of the alloy containing 1.5 wt. % silicon is the highest of the four alloys and is about 70 J. However, this Charpy impact energy is less than those of the two high-nickel steels being used to assess the effect of inclusion void nucleation resistance on formability.

Once we have established the appropriate solution treating temperatures for the four alloys, we will be able to heat treat test specimens which contain 100% martensite, 25% ferrite and 75% martensite, and 50% ferrite and 50% martensite. However, before we can produce the structures which are bainitic, 25% ferrite and 75% bainite and 50% ferrite and 50% bainite, we will need to determine for each solution treatment temperature for the four alloys the martensite-start temperature, and this will be done by dilatometry.

Mechanical Properties of Alloys to be Used to Investigate Effect of Inclusion Void-Nucleation Resistance on Formability

Charpy impact and tensile specimens have been tested for the two alloys M1 and M2. The sulfides in M1 are manganese sulfides, and the sulfides in M2 are titanium carbo-sulfides. The heat treatment was austenitizing at 900°C, oil quenching and then tempering at 200°C. The yield strengths and ultimate tensile strengths for the two heats were about 1,100 MPa and 1,400 MPa, respectively. The tensile percent reduction-in-areas were 64.2% for the heat in which the sulfur was gettered as MnS and 66.2% for the heat in which the sulfur was gettered as titanium carbo-sulfide particles. The Charpy impact energies were 124 J for the heat in which the sulfur was gettered as MnS and 113 J for the heat in which the sulfur was gettered as titanium carbo-sulfide.

References

1. W. F. Hosford and R. M. Caddell. *Metal Forming: Mechanics and Metallurgy*, Prentice-Hall, Englewood Cliffs, N.J., 1983, p. 299.
2. K. Sumimoto, J. Sakaguchi, T. Iida, and T. Kashima, Stetch-flangeability of High-strength TRIP Type Bainitic Sheet Steel, ISIJ international, Vol. 40, 2000, 920.

3. K. Sumimoto, A. Kanda, R. Kikuchi, S. Hasimoto, T. Kashima, and S. Ikeda, Ductility and Formability of Newly Developed High Strength Low Alloy TRIP-aided Sheet Steels with Annealed Martensite Matrix, ISIJ international, Vol. 42, 2002, 910.
4. K. Sugimoyo, B. Yu, Y. Mukai, and S. Ikeda, Microstructure and Formability of Aluminum Bearing TRIP-Aided Steels with Annealed Martensite Matrix, ISIJ international, Vol. 45, 2005, 1194.
5. K. Yamazaki. M. Oka, H. Yasuda, Y. Mizuyama, and H. Tsuchiya, Recent Advances in Ultrahigh-Strength Sheet Steels for Automotive Structural Use, Nippon Steel Technical Report No. 64, January 1995, 37.
6. Y. J. Park, A. P. Coldren, and J. W. Morrow, Effect of Martensite Bands and Elongated Manganese Sulfide Inclusions on the Formability of Dual-Phase Steels, Proceedings on the Conference on the *Fundamentals of Dual Phase Steels*, held at Chicago, 1981, p. 485.
7. Nishimoto, Y. Hosoya, and K. Nakaoka, Relation Between Hole Expansion Formability and Metallurgical Factors in Dual-Phase Steel Sheets, Proceedings on the Conference on the *Fundamentals of Dual Phase Steels*, held at Chicago, 1981, p. 447.
8. C. D. Horvath and J. R. Fekete, Opportunities and Challenges for Increased Usage of Advanced High Strength Steels in Automotive Applications, International Conference on Advanced High Strength Sheet Steels for Automotive Applications Proceedings, Winter Park, Colorado, 2004, p. 3.
9. J. Van Slycken, P. Verleysen, J. Degrieck, L. Samek, and B.C. De Cooman, High-Strain-Rate Behavior of Low-Alloy Multiphase Aluminum and Silicon Based Transformation Induced Plasticity Steels, Metall. and Mat. Transactions A, Vol. 37A, 2006, 1527.
10. S. Traint, A. Pichler, K. Hauzenberger, P. Stiaszny, and E. Werner, Influence of Silicon, Aluminum Phosphorus and Copper on the Phase Transformations of Low Alloyed TRIP Steels, Steel Research, Vol. 73, 2002, 259.
11. T. Lung, J. Drillet, A. Couturier, and C. Olier, Detailed Study of the Transformation Mechanisms in Ferrous TRIP Aided Steels, Steel Research, Vol. 73, 2002, 218.
12. H. Matsuda, F. Kitano, K. Hasegawa, T. Urabe, and Y. Hosoya, Metallurgy of Continuously Annealed High Strength TRIP Steel Sheet, Steel Research, Vol. 73, 2002, 211.
13. B. Ehrhardt, T. Gerber, and T.W. Schaumann, Approaches to Microstructural Design of TRIP and TRIP Aided Cold Rolled High Strength Steels, International Conference on Advanced High Strength Sheet Steels for Automotive Applications Proceedings, Winter Park, Colorado, 2004, p. 39.
14. K. Sugimoto, S. Hashimoto, and S. Ikeda, Ultra High Strength Low Alloy TRIP-Aided Sheet Steels With Bainitic Ferrite Matrix, International Conference on Advanced High Strength Sheet Steels for Automotive Applications Proceedings, Winter Park, Colorado, 2004, p. 63.
15. Y. R. Cho, S. K. Kim, H. N. Han, Y. S. Jin, and J. H. Jung, Development of Hot Rolled High Strength TRIP Steel With a Tensile Strength of 780MPa Grade, International Conference on Advanced High Strength Sheet Steels for Automotive Applications Proceedings, Winter Park, Colorado, 2004, p. 71.
16. H.K.D.H. Bhadeshia, TRIP-Assisted Steels. ISIJ international, Vol. 42, 2002, 1059.
17. P. J. Jacques, E. Girault, Ph. Harlet, and F. Delannay, The Developments of Cold-rolled TRIP-assisted Multiphase Steels. Low Silicon-assisted Multiphase Steels, ISIJ international, Vol. 41, 2001, 1061.
18. M. Saeglitz and G. Krauss, Deformation, Fracture, and Mechanical Properties of Low-Temperature-Tempered Martensite in SAE 43xx Steels, Metall. and Mat. Transactions A, Vol. 28A, 1997, 377.

19. S. B. Lee, J. G. Speer, and D. K. Matlock, The Influence of Phase Distributions and Interfaces on Fracture and formability of High Strength Sheet Steels, International Conference on Advanced High Strength Sheet Steels for Automotive Applications Proceedings, Winter Park, Colorado, 2004, p. 383.
20. J. L. Maloney and W. M. Garrison Jr., The Effect of Sulfide Type on the Fracture Behavior of HY180 Steel, Acta Materialia, Vol. 53, 2005. 533.
21. L. E. Iorio and W. M. Garrison Jr., The Effects of Titanium Additions on AF1410 Ultra-high Strength Steel. Metallurgical and Materials Transactions A, Vol. 37A, 2006, 1165.
22. W. M. Garrison, Jr., The Effect of Silicon and Nickel Additions on the Inclusion Spacing and Fracture Toughness of a 0.4 Carbon Low Alloy Steel, Metall. Trans. A, Vol. 17A, 1986, 669.
23. V.T.T. Miihkinen and D. V. Edmonds, Microstructural Examination of Two Experimental High Strength Bainitic Low-Alloy Steels Containing Silicon, Mat. Sci. and Eng., Vol. 3, 1987, 422.
24. V.T.T. Miihkinen and D. V. Edmonds, Tensile Deformation of Two Experimental High Strength Bainitic Low-Alloy Steels Containing Silicon, Mat. Sci. and Eng., Vol. 3, 1987, 432.
25. V.T.T. Miihkinen and D. V. Edmonds, Fracture Toughness of Two Experimental High Strength Bainitic Low-Alloy Steels Containing Silicon, Mat. Sci. and Eng., Vol. 3, 1987, 441.
26. H.K.D.H. Bhadeshia and D. V. Edmonds, Bainite in Silicon Steels: New Composition-Property Approach, Part 1, Metal Science, Vol. 17, 1983, 411.
27. H.K.D.H. Bhadeshia and D. V. Edmonds, Bainite in Silicon Steels: New Composition-Property Approach, Part 2, Metal Science, Vol. 17, 1983, 420.
28. Z. Narciniak and K. Kuczynski, Limit Strains in the Processes of Stretch-Forming Sheet Metal, Int. J. Mech. Sci. Vol. 9, 1967, 609.
29. J. H. Schmitt and J.M. Jalinier, Damage in Sheet Metal Forming-I. Physical Behavior, Acta Metall., Vol. 30, 1982, 1789.
30. J. H. Schmitt and J. M. Jalinier, Damage in Sheet Metal Forming-II. Plastic Instability, Acta Metall., Vol. 30, 1982, 1799.

O. Development of Novel Finite-Element Simulation Tools that Implement Crystal-Plasticity Constitutive Theories Using an Efficient Spectral Framework

Principal Investigator: Surya R. Kalidindi
Drexel University
Department of Materials Science and Engineering, Philadelphia, PA 19104
(215) 895-1311; fax: same; e-mail: skalidin@coe.drexel.edu

Technology Area Development Manager: Joseph A. Carpenter
(202) 586-1022; fax: (202) 586-1600; e-mail: joseph.carpenter@ee.doe.gov

Field Project Officer: Aaron D. Yocum
(304) 285-4852; fax: (304) 285-4403; e-mail: aaron.yocum@netl.doe.gov

---

Contractor: Drexel University
National Science Foundation (NSF) Award CMMI 0727931, jointly funded by NSF and DOE

Objective

- Develop spectral crystal-plasticity-based, finite-element tools for simulating deformation-processing operations and final mechanical performance of advanced high-strength steel (AHSS) components. A salient feature of these tools is that they can be executed with computational times that are comparable to the tools currently used by the industry, which largely employ phenomenological material models.
- Systematically introduce the inherent complexities of the physics of plastic deformation at multiple length scales in the spectral crystal-plasticity framework. The goal is to start with crystallographic slip and then proceed to deformation twinning. From the perspective of length scales, the goal is to start with grain-scale deformation and then proceed to incorporating explicitly the mechanics of dislocation networks.
- Develop computationally-efficient spectral approaches for higher-order homogenization theories that utilize local spatial correlations for a rigorous quantification of the interactions at the lower length scales in the material.
- Critical validation of the tools and methodologies developed in this work by comparisons with experiments and numerical predictions obtained by other approaches.

Approach

- Capture solutions at the lower length scales in an efficient spectral database. Although building the database requires substantial effort, it is a one-time activity. Once an appropriate database is built, all subsequent computations requiring solutions at the lower length scales can be accomplished with minimal computational effort and resources.
- Explore the use of discrete Fourier transforms (DFTs) for building such databases, as they offer tremendous computational efficiency.

Accomplishments

- Demonstrated that it is possible to speed up the crystal-plasticity calculations in cubic metals that deform by crystallographic slip by two orders of magnitude using a compact database of DFTs. Observed that a relatively small number of dominant transforms adequately captured the dependence of the stresses, the lattice spins, and the strain hardening in individual crystals on their lattice orientation and the applied-deformation mode.

- The feasibility of the basic concepts underlying the spectral approaches for capturing higher-order structure-to-structure evolution linkages at the lower length scales has been demonstrated by taking a specific example in dislocation dynamics. In particular, it was demonstrated that the dislocation dynamics solutions from a previously-developed code at the Indian Institute of Science (Bangalore, India) can be captured efficiently in a spectral database. This database is now capable of providing solutions that are equivalent to the original formulation for a very broad set of initial conditions and strain rates, but with significantly-reduced computational effort. The main advantage of our approach is that it is now feasible to explore a rigorous multiscale simulation involving multiple length scales with very reasonable computational resources.

Future Direction

- Incorporate the spectral crystal-plasticity tools developed for cubic metals deforming by crystallographic slip in a finite-element code used in simulating metal-forming operations. In particular, we will focus our efforts on FORGE3 and ABAQUS.
- Extend the spectral linkages to incorporate deformation twinning and details of dislocation networks and their evolution during plastic deformation.
- Extend the spectral linkages to include grain-scale interactions using a framework newly developed by our research group.

Introduction

Crystal-plasticity theories [1–6] are used extensively in understanding and predicting the evolution of the underlying microstructure (mainly texture-related aspects) and the concomitant anisotropic stress-strain response in polycrystalline metals subjected to finite plastic strains. Such physics-based constitutive theories are highly desirable for conducting more accurate simulations of various metal manufacturing/fabrication processes, since they provide better understanding and predictions of the material behavior [7–9]. The main deterrent in the more widespread use of these theories (in place of the highly simplified phenomenological isotropic plasticity theories typically used) is the fact that the implementation of the crystal-plasticity theories in a finite-element modeling framework demands substantial computational resources and highly- specialized expertise.

In recent work [10, 11], we have identified that the crystal-plasticity solutions for face-centered cubic (fcc) polycrystals experiencing rigid-viscoplastic deformations can be organized efficiently as a set of functions that describe the dependence of the stresses, the lattice rotations, and the total slip rates in individual crystalline regions on their lattice orientation and the imposed velocity gradient tensor (quantifying the deformation mode) on those regions. The domain of these functions was defined to be the product space comprising all possible crystal orientations and all possible isochoric deformation modes.

In this work, we have explored the representation of all of the functions capturing the crystal-plasticity solutions in their complete respective domains using DFTs. The most remarkable discovery in this new direction was the recognition that only a limited number of the dominant DFTs were adequate to recover the functions of interest on their entire respective domains. This new approach was found to be able to speed up the crystal-plasticity computations by about two orders of magnitude compared to the traditional approaches used in crystal plasticity computations. A particularly attractive feature of this new approach is that it provides the user with tremendous flexibility in making trade-offs between accuracy and computational speed. In other words, the new spectral database described here will allow the user to perform a large number of very quick simulations at a lower than desired accuracy, identify the specific ones that appear to produce promising results, and redo these much more accurately (at a higher computational cost).

The above approach has been applied here initially to rigid-plastic Taylor-type (full constraints) model calculations for fcc polycrystals with equal hardening of all slip systems, where it is assumed that all constituent crystals experience the same

deformation history. Development of higher-order models requires a more sophisticated approach that partitions the imposed deformation on the polycrystal to each of the constituent grains while taking into account the details of its neighborhood. With the goal of extending the spectral crystal plasticity framework to include details at lower length scales as well as higher-order interactions, we have a novel spectral approach in this work. This new approach and its potential for facilitating physics-based, multiscale models will be discussed in this report.

Spectral Crystal Plasticity Framework

The crystal-plasticity computations typically demand significant computational resources because of the low value of strain-rate sensitivity parameter denoted by *m* in the rate-dependent crystal-plasticity formulations [1] (which makes the resulting system of algebraic equations numerically extremely stiff). Moreover, the same computations are likely to be repeated several times in simulations performed by the conventional approach because the results of computations in any one time step are immediately forgotten when the computations advance to the next time step. In the spectral crystal-plasticity approach [10, 11], we have established efficient spectral representations for the essential functions capturing the solutions to the traditional crystal-plasticity theory. In other words, we have established the functions $\sigma'_{ij}(g,\mathbf{L})$, $W^*_{ij}(g,\mathbf{L})$, and $\sum_\alpha \left|\dot{\gamma}^\alpha\right|(g,\mathbf{L})$, where g is the crystal lattice orientation and L is the applied velocity gradient tensor. In any given time step in the simulation of the deformation process, these functions are then used to compute all of the needed microscale and macroscale field quantities that would be typically computed by the traditional crystal-plasticity approach.

In the approach developed here, the functions mentioned above are stored as their DFTs. It is typically observed that only a small fraction of the DFTs are numerically significant compared to the others. The numbers of numerically-significant DFTs (henceforth referred to as dominant DFTs) varied for the different field variables. In particular, it was noted that by retaining only about 500 dominant transforms for the stress tensor, the spin tensor and the total shearing rate, the average error was well below 5%.

In order to demonstrate the validity of the new DFT-based spectral approach developed in this work, we simulated plane strain compression on polycrystalline face-centered cubic (fcc) metals to a true strain of $\varepsilon = -1.0$ along the compression axis. The polycrystal was assumed to possess a random initial texture that was captured by a set of 1000 discrete crystal orientations. We computed the deformed textures and the anisotropic stress-strain curves using the Taylor-type model, both by the traditional approach and the new DFT spectral approach based on the dominant transforms described here. The predicted textures from the traditional approach are compared against those obtained from the DFT method using a minimal set of dominant transforms (134 for stress, 255 for lattice spin, and 182 for shearing rate) in Figure 1(a), while the corresponding predictions of the stress-strain responses are shown in Figure 1(b).

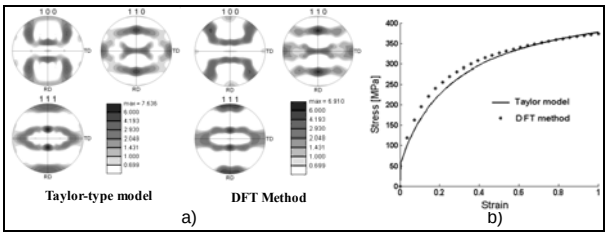

Figure 1. Comparison of the predictions from the DFT-spectral method using a minimal set of dominant transforms against the corresponding predictions from the conventional Taylor-type model for plane strain compression of oxygen-free high-conductivity (OFHC) copper: (a) pole figures, and (b) stress-strain curves.

Another calculation was performed using more of the dominant DFTs (500 for stress and shearing rate and 3000 for lattice spin) and its comparison with predictions from the traditional approach is presented in Figure 2 (note the slight improvement in the accuracy of the spectral approach between Figure 1 and Figure 2). It is seen that the DFT method described here accurately reproduced all of the features of the Taylor-type model predictions. This simulation took 108 seconds on a regular Pentium 4 desktop personal computer

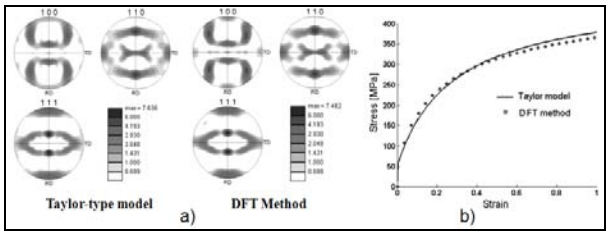

Figure 2. Comparison of the predictions from the DFT-spectral method, using more dominant transforms against the corresponding predictions from the conventional Taylor-type model for plane strain compression of OFHC copper: (a) pole figures, and (b) stress-strain curves.

using the conventional crystal-plasticity algorithms and only 0.7 seconds using the minimal set of the dominant DFTs, and 2.3 seconds using the larger number of dominant DFTs. This establishes that the spectral approach developed in this work has the potential to accelerate the computations by about two orders of magnitude.

Higher-Order Spectral Linkages

There have been several notable accomplishments in the development and validation of physics-based numerical models (e.g., atomistic simulations, finite- element models, phase-field models) for exploring structure-property-processing relationships at various length scales of interest in a given material system. It is now possible to incorporate very complex physics in these models that accurately accounts for the anisotropy inherent to the local behavior at any selected length scale. However, there is a critical need to couple these simulations over several length scales to predict macroscale performance characteristics, which tantamounts to executing sophisticated numerical models within other sophisticated numerical models in a hierarchical manner. Currently no computationally- efficient algorithms to accomplish a robust and accurate scale-transition exist.

As a specific example to demonstrate the potential of spectral approaches, we have studied the phenomenon of the Portevin-Le Châtelier (PLC) effect. This problem is of major interest to automobile manufacturers. The PLC effect is characterized by a stress-strain curve that exhibits repeated yield drops that are dependent on strain rate and temperature along with undesirable deformation bands on the surface of panel. The PLC effect is a plastic instability that is caused by dynamic strain aging (DSA), i.e., the interaction of mobile dislocations with diffusing solute atoms. During plastic deformation, mobile dislocations become arrested at solute atoms. When a sufficient stress is applied, the arrested dislocations become mobilized again until they encounter another obstacle. The remobilization of the dislocations occurs on a very fast time scale resulting in the drops in the stress-strain curve, resulting in the PLC effect.

A well-established model proposed by Ananthakrishna et al. [12] simulates the spatio-temporal details of the PLC effect. The model captures the cooperative behavior of the dislocations for the different band types while capturing the slow and fast time scales associated with the phenomenon. The governing set of differential equations in this model describe the kinetics of the evolution of the mobile dislocation densities (ρ_m), the immobile dislocation densities (ρ_{im}), the Cottrell-type dislocation densities (ρ_c), and the effective stress (ϕ). These equations can be expressed as:

$$\frac{\partial \rho_m(x,t)}{\partial t} = -b_o\rho_m - \rho_m\rho_{im} + \rho_{im} - a\rho_m + \phi^m_{eff}\rho_m + \frac{D}{\rho_{im}}\frac{\partial^2\left(\phi^m_{eff}(x)\rho_m(x)\right)}{\partial x^2}$$

$$\frac{\partial \rho_{im}(x,t)}{\partial t} = b_o\left(b_o\rho_m^2 - \rho_m\rho_{im} - \rho_{im} + a\rho_c\right)$$

$$\frac{\partial \rho_c(x,t)}{\partial t} = c\left(\rho_m - \rho_c\right)$$

$$\frac{\partial \phi(t)}{\partial t} = d\left(\dot{\varepsilon} - \frac{1}{L}\int_0^L \phi^m_{eff}(x)\rho_m(x)\,dx\right)$$

$$\phi^m_{eff}(x) = \left(\phi - h\rho_m^{1/2}\right)^m$$

where a, b_o, c, d, D, and h are parameters that are empirically fit to experimental observations. Varying the value of the imposed strain rate, $\dot{\varepsilon}$, results in three different types of bands that are experimentally verified. A stiff differential solver is required to solve this equation.

Casting the interactions between each of the dislocation densities and their spatial variations

will dramatically improve the computational efficiency of solving these equations. For this purpose, we seek spectral linkages that can be expressed as:

$$\Im[\dot{\rho}_m] = \sum_H \sum_K A_k^h M_k^h(\rho_m, \rho_{im}, \rho_c)$$

$$\Im[\dot{\rho}_{im}] = \sum_H \sum_K B_k^h M_k^h(\rho_m, \rho_{im}, \rho_c)$$

$$\Im[\dot{\rho}_c] = \sum_H \sum_K \Gamma_k^h M_k^h(\rho_m, \rho_{im}, \rho_c)$$

where A, B, and Γ are the spectral influence coefficients, and $\Im[\ ]$ denotes the DFT operation. M describes the DFT of the microstructure function that captures the dislocation densities discretized into H bins (h enumerates these bins).

After the database of coefficients is built, the instantaneous changes in dislocation densities can be reasonably well predicted using these computationally-efficient linkages as shown in Figure 3. Figure 4 shows the evolution of the mobile dislocations using the Euler Forward method in conjunction with spectral influence coefficients.

Conclusions

It has been demonstrated that it is possible to speed up the crystal-plasticity calculations by two orders of magnitude in fcc metals using a compact database of DFTs. It was seen that a limited set of dominant transforms adequately captured the dependence of the stresses, the lattice spins, and the strain hardening in individual crystals as a function of their lattice orientation and the applied-deformation mode. A computationally-efficient spectral interpolation scheme was devised and implemented to recover values of these functions for any selected combination of crystal orientation and deformation mode using only the dominant DFTs. The case studies conducted thus far revealed tremendous savings in the computational time and provide a significant incentive for incorporation into the finite- element simulations of bulk deformation-processing operations.

It has also been demonstrated that spectral approaches can be used to capture the complex

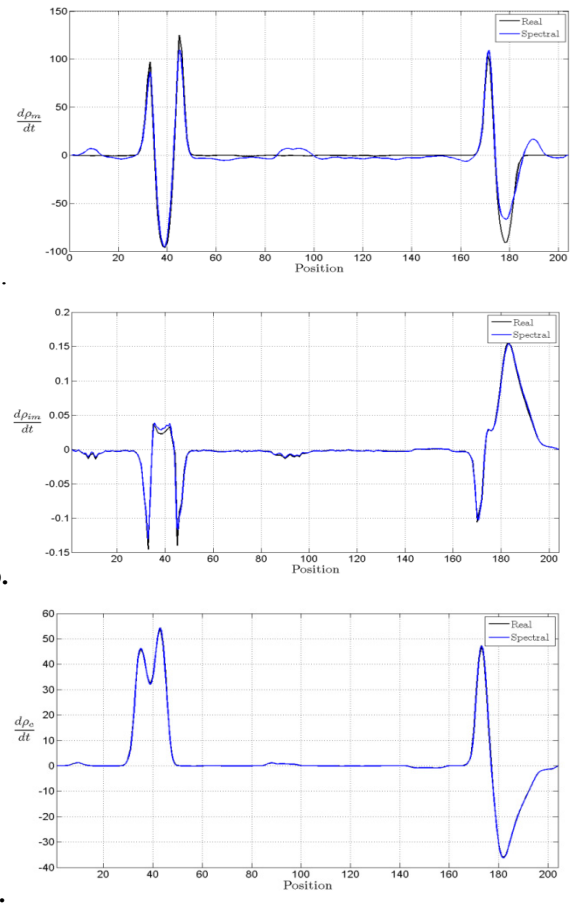

Figure 3. A comparison between the predictions from solving the dynamical system of equations and those from the spectral methods at an intermediate time step in the evolution. a. Mobile, b. Immobile, and c. Cottrell-type components.

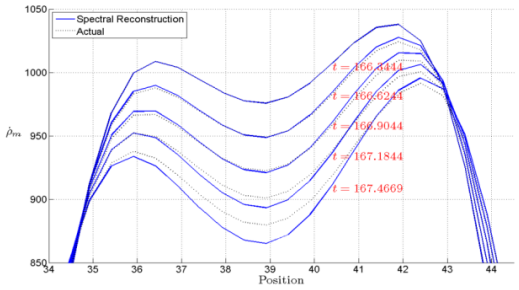

Figure 4. Comparison of the predictions for the temporal evolution of the mobile dislocations from actually solving the governing equations and those predicted by the spectral database coefficients.

interactions that occur in a higher-order composite system. In particular, it was demonstrated that it is possible to capture the complex physics of the

dynamics of dislocation systems controlling the PLC effect in a suitable spectral database. The broad range of strain rates and the complex description of the microstructural states involved in this problem provide unambiguous testament to the potential of the spectral approaches in multiscale materials modeling.

Publications

1. M. Knezevic, H. F. Al-Harbi, S. R. Kalidindi, "Crystal Plasticity Simulations Using Discrete Fourier Transforms," submitted to Acta Materialia (2008).

References

1. R. J. Asaro and A. Needleman, Acta Metallurgica et Materialia 33 (1985) 923–953.
2. C. A. Bronkhorst, S. R. Kalidindi, and L. Anand, Philosophical Transactions of the Royal Society of London Series A-Mathematical Physical and Engineering Sciences 341 (1992) 443–477.
3. S. R. Kalidindi, C. A. Bronkhorst, and L. Anand, Journal of the Mechanics and Physics of Solids 40 (1992) 537–569.
4. L. Delannay, S. R. Kalidindi, and P. Van Houtte, Materials Science and Engineering A 336 (2002) 233–244.
5. P. Van Houtte, L. Delannay, and S. R. Kalidindi, International Journal of Plasticity 18 (2002) 359–377.
6. B. S. R. Kalidindi and R. Doherty, Proceedings of the Royal Society of London: Mathematical, Physical and Engineering Sciences. (2004).
7. D. Raabe, Z. Zhao, and F. Roters, Steel Research 72 (2001) 421–426.
8. D. Raabe, Y. Wang, and F. Roters, Computational Materials Science 34 (2005) 221–234.
9. W. F. Hosford and R. M. Caddell, Metal forming mechanics and metallurgy, Prentice-Hall, Inc, 1993.
10. S. R. Kalidindi, H. K. Duvvuru, and M. Knezevic, Acta Materialia 54 (2006) 1795–1804.
11. M. Knezevic, S. R. Kalidindi, and D. Fullwood, International Journal of Plasticity 24 (2008) 1264–1276.
12. G. Ananthakrishna and M. S. Bharathi, Physical Review E 70, 02611.

P. Advanced High-Strength Steel through Paraequilibrium Carbon Partitioning and Austenite Stabilization

Principal Investigator: Gary M. Michal
Case Western Reserve University
Department of Materials Science and Engineering
Cleveland, OH 44106
(216) 368-5070; fax: (216) 368-3209; e-mail: gmm3@case.edu

Co-Principal Investigator: Arthur H. Heuer
Case Western Reserve University
Department of Materials Science and Engineering
Cleveland, OH 44106
(216) 368-3869; fax: (216) 368-3209; e-mail: ahh@case.edu

Technology Area Development Manager: Joseph A. Carpenter
(202) 586-1022; fax: (202) 586-1600; e-mail: joseph.carpenter@ee.doe.gov

Field Project Officer: Aaron D. Yocum
(304) 285-4852; fax: (304) 285-4403; e-mail: aaron.yocum@netl.doe.gov

---

Contractor: Case Western Reserve University
National Science Foundation (NSF) Contract No.: CMMI 0727583, jointly funded by NSF and DOE

Objective

- The development of a third generation of advanced high-strength steel (AHSS) possessing:
  - strength and ductility combinations exceeding those of ferritic first-generation AHSS.
  - the ability to be manufactured much more economically than austenitic second-generation AHSS.
- Establish a steel chemistry that fulfills the three transformational characteristics required to achieve a double-stabilization thermal-processing scheme:
  - the steel can be completely austenitized at 900°C.
  - the hardenability of the steel is great enough that the bainite transformation can be avoided during a liquid-metal quench to 450°C.
  - carbide formation is suppressed during aging somewhere in the range of 300 to 500°C during which carbon will partition from the martensite phase to the austenite phase.

Approach

- The strength/ductility goal of a third-generation AHSS can be achieved by employing a microstructure comprised of martensite and a significant volume fraction of austenite.
- The austenite must have sufficient stability such that it transforms to martensite only at progressively higher levels of strain, so that the work-hardening rate of the steel concurrently increases in a continuous fashion.
- A high volume fraction of austenite must be obtained within the constraints of:
  - a carbon content low enough that weldability is not severely compromised.
  - the alloy levels in the steel do not greatly increase its price.
  - the processing route for the steel is consistent with current sheet-steel commercial production practice.
- Use of a double-stabilization thermal-processing scheme to increase the amount of austenite:
  - the steel will be held for a brief time at approximately 450°C for its first stabilization.

— the second stabilization will be an aging of the steel at a temperature at which carbides will not form while carbon partitions from the martensite phase to the austenite phase.

Accomplishments

- A thermal-processing facility was constructed based upon four crucible furnaces that will maintain the four key temperatures associated with a double-stabilization thermal-processing scheme:
  — austenitization in a molten salt bath at 900°C.
  — the initial quench temperature of approximately 450°C using liquid tin.
  — the final quench temperature of 20 to 200°C using oil or Wood's metal.
  — the aging temperature of 300 to 500°C during which carbon partitioning from martensite to austenite occurs and comprises the second stabilization.
- Interstitial solid solution models for ferrite and austenite phases were constructed using the compound energy (CALPHAD) formalism to:
  — determine austenitization temperatures for various candidate alloy chemistries.
  — compare predictions of the models with those made by standard Thermo-Calc software.
- Four laboratory induction air melted heats of steel have been processed at AK Steel Corporation—Research:
  — carbon contents vary from 0.092 to 0.29 wt. %.
  — the heats were boron treated to increase their hardenability.
  — manganese contents vary from 2.0 to 4.1 wt. %.
  — the alloy levels for silicon and aluminum were nominally 2 wt. %. and 1.5 wt. %., respectively.
- Final processing of the laboratory heats was a cold reduction of 67% to a final thickness of 1.02 mm (0.040 inch).

Future Direction

- Perform austenitization thermal cycles with the initial series of cold-rolled steels:
  — followed by an immediate rapid quench to room temperature.
  — determine the volume fraction of austenite that was present at 900°C.
- Carry out two-step austenitization followed by a liquid-metal quench to 450°C thermal cycles:
  — finish with a rapid quench to room temperature.
  — determine if bainite formed during the liquid metal quench.
- Do complete double-stabilization thermal-processing procedures using the most promising alloy chemistries.
- Determine the amount of retained austenite present in thermally-processed samples using an x-ray technique.
- Prepare thin foil samples and conduct transmission electron microscopy (TEM) analyses of the retained austenite contained in select samples.

Introduction

Efforts are aimed at the development of a third generation of advanced high-strength steel (AHSS) with strength and ductility combinations exceeding those of ferritic first-generation AHSS and can be manufactured much more economically than austenitic second-generation AHSS. The strength/ductility goal of a third-generation AHSS can be achieved employing a microstructure comprised of martensite and a significant volume fraction of austenite. The austenite must have sufficient stability to transform to martensite only at progressively higher levels of strain, so that the work-hardening rate concurrently increases in a continuous fashion. The key to a viable third-generation AHSS is obtaining a high volume fraction of such austenite within the constraints of a carbon content low enough to not severely compromise weldability, alloy levels that do not greatly increase the cost of the steel, and a processing route consistent with current sheet steel production practice.

Initial activities on the project have proceeded along two parallel routes. One undertaking has been the design and construction of a thermal-processing facility. Such a facility will enable a steel strip to track the rapid temperature changes associated with a double-stabilization thermal cycle. The second effort has pursued the design and production of the first series of candidate heats of steel. The steels were designed with the aid of CALPHAD-based interstitial solid-solution models for the ferrite and austenite phases. The initial group of three steel chemistries already has been produced by AK Steel Corporation—Research.

Thermal Processing Requirements

The core design requirement for the thermal-processing facility was to be able to achieve the thermal cycle illustrated in Figure 1.

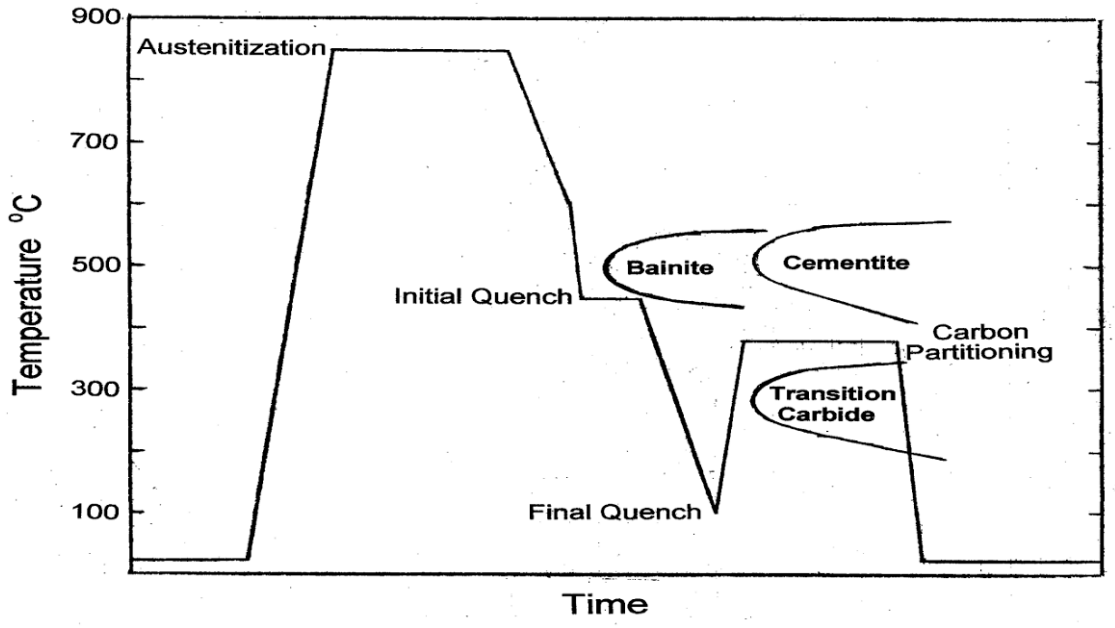

Figure 1. A schematic representation of a double stabilization thermal cycle.

The thermal cycle contains four brief isothermal holds corresponding to (1) austenitization, (2) initial quench and stabilization, (3) final quench, and (4) carbon partitioning for final stabilization. The hold times at the four relevant temperatures are anticipated to vary from as little as two seconds to several minutes. The demand for rapid temperature changes associated with movement from one isothermal hold to another prompted the use of liquid media to establish the isothermal hold temperatures. For austenitization the temperature will be in the range of 800 to 900°C, and the chosen medium will be a neutral salt. For the initial quench and the carbon partitioning, the temperature will be in the range of 300 to 500°C and the medium will be liquid tin. For the final quench, the temperature will be in the range of 20 to 200°C, and the medium will be oil.

Four crucible furnaces were purchased to establish the core of the thermal-processing facility. Funding for the furnaces was obtained through a grant from the Ohio Department of Development. The austenitization furnace is equipped with a high-alumina cylindrical crucible 190 mm (7.5 inch) deep with an inside diameter of 102 mm (4 inch). The other three furnaces contain KIMAX cylindrical crucibles 184 mm (7.25 inch) deep with an inside diameter of 83 mm (3.25 inch). Each furnace has a primary control thermocouple and a second over-temperature control thermocouple. A third thermocouple is inserted directly into the liquid media in each crucible. These latter four thermocouples and a set of two thermocouples constructed with very fine chromel-alumel wires for an extremely fast response time will all be read with an eight-place

analog-to-digital board with output to a laptop computer for data display and storage. The set of fast-response thermocouples will be embedded in the test samples. The thermal-processing facility comprised of furnaces, crucibles, liquid media, and control and analysis thermal couples has been assembled and is now operational. The facility is currently undergoing a series of tests to assess it performance characteristics.

Modeling

Interstitial-solid-solution models for ferrite and austenite phases were constructed using the compound energy (CALPHAD) formalism. The free energy of both phases defined with the conventional method of one mole of formula units was transformed to a one-mole-of-atoms basis to allow examination of molar free-energy diagrams as a function of temperature. The anticipated austenitization times will be less than 60 seconds. The brief time will limit partitioning of the substitutional alloying elements during austenitization. As such, the thermodynamic modeling evaluated the molar free energies of the ferrite and austenite phases under paraequilibrium conditions.

Candidate Steels Chemistry

The chemical compositions of candidate steels were strongly influenced by the requirements of the double-stabilization thermal cycle. To maintain a completely austenitic microstructure during cooling to the initial quench temperature, the steel must have sufficient hardenability to avoid the formation of bainite as shown schematically in Figure 1. To enhance hardenability, boron was chosen as an alloying element in all of the candidate steels. In order to reliably achieve boron levels of 0.001 to 0.003 wt. %, titanium also must be added to the steel to prevent the formation of BN. Manganese increases the hardenability of steel. Conventional steel-making practices limit the manganese content to a maximum of 2 wt. %. That level of manganese provides substantial hardenability and was chosen as a baseline value for the candidate steels. A manganese content of 4 wt. %. was chosen for a more highly-alloyed heat. To suppress the formation of carbides during the carbon-partitioning isothermal hold, the candidate steels must contain ample concentrations of silicon or aluminum. The decision was made to make a combined addition of silicon and aluminum to the candidate steels at concentrations commonly used for electrical steel grades. The chosen alloying levels for the silicon and aluminum were nominally 2 wt. % and 1.5 wt. %, respectively.

Carbon is the alloying element that has by far the greatest potency with respect to increasing the stability of the austenite phase and the strength of the martensite phase. Carbon also is a very low-cost alloying element. The primary restraint to having high carbon contents in candidate alloys is provided by a loss of weldability. To maintain good spot-welding performance, sheet steels typically have less than 0.1 wt. % carbon. Other forms of welding steel can tolerate carbon contents several times that value. The decision was made to have nominally 0.3 wt. % carbon in the most highly-alloyed candidate steel and half that level of carbon in the baseline candidate steel. As carbon partitions from martensite to austenite, the austenite's resistance to transformation to martensite increases and the strength of the martensite decreases. To bolster the strength of the martensite phase, the decision was made to nominally add 0.5 wt. % chromium to the highly-alloyed candidate steel. As an example of the effect of chromium, the tensile strength of martensite containing 0.02 wt. % carbon has been shown to increase from 525 to 625 MPa due to an increase in its chromium content from essentially zero to 0.5 wt. %. [1]

A total of three candidate steel chemistries were selected for initial preparation and evaluation. The chemical compositions of these first three candidate alloys are listed in Table 1.

Production of Laboratory Heat of Steel

AK Steel Corporation-Research has produced four laboratory induction air-melted heats of steel using high purity materials. Each heat yielded one 14 Kg (30 lb) ingot 9.5 × 9.5 × 19 cm (3.75 × 3.75 × 7.5 inch) in size. One heat of the baseline (A) and one heat of the intermediate (B) alloy chemistries were melted. Two heats of the highly-alloyed (C) chemistry were melted. To prevent excessive

Table 1. Proposed chemical compositions (in weight percent) for the initial candidate steels.

Alloy	C	Mn	Si	Al	S	P	B	Cr
A	0.13/0.17	1.95/2.05	2.0/2.30	1.50/1.70	0.015 max	0.010 max	0.001/0.003	0.12 max.
B	0.18/0.22	1.95/2.05	2.0/2.30	1.50/1.70	0.015 max	0.010 max	0.001/0.003	0.12 max.
C	0.28/0.32	3.90/4.10	2.0/2.30	1.50/1.70	0.015 max	0.010 max	0.001/0.003	0.45/0.55

oxidation and losses during melting, the liquid steel surface was shrouded with argon.

After solidification was complete, the ingots were removed from their molds and their hot tops were sawn off and discarded. A 13 mm (0.5 inch) thick slice was sectioned from the top of each ingot and submitted for chemical analysis. The measured chemical compositions are listed in Table 2. The ingots were then machined so that their faces were made parallel. The ingots were reheated to 1,205°C (2,200°F) for three hours in a nitrogen-enriched atmosphere, then hot rolled in five passes to produce billets 25 mm (1 inch) thick. After this initial hot rolling, the temperature of the billets was still above 900°C (1,650°F). The billets were subsequently air-cooled to room temperature.

Table 2. Ingot analysis of the chemical compositions (in weight percent) of the initial candidate steels.

Heat	C	Mn	P	S	Si	Ni	Cr	Cu	Mo	N	Nb	V	Ti	Al	B
3	0.12	2.18	<0.002	0.0011	2.14	0.002	<0.002	<0.002	<0.002	0.0039	<0.002	0.002	0.003	1.47	0.0028
4	0.29	4.16	0.002	0.0014	2.16	0.003	0.48	<0.002	<0.002	0.0068	<0.002	<0.002	0.002	1.57	0.0036
5	0.28	1.96	0.002	0.0008	2.07	0.004	0.014	<0.002	<0.002	0.0027	<0.002	0.002	0.002	1.48	0.0024
6	0.32	4.0	0.002	0.0012	2.1	0.003	0.49	<0.002	<0.002	0.0045	<0.002	0.002	0.023	1.52	0.0018

The billets were sectioned to a length of 18 cm (7.1 inch) to ensure that after hot rolling the steel strips would fit inside of the 152 cm (60 inch) deep furnace used for coiling simulations. The billets were reheated to 1,250°C (2,275°F) in a nitrogen-enriched atmosphere, then hot rolled in five passes to a thickness of 3 mm (0.12 inch). The finishing temperature prior to the last pass was maintained near 900°C (1,650°F), excluding the two hot bands from heat #3. The hot bands from heat #3 cobbled during the last rolling pass resulting in their finishing temperature being below 815°C (1,500°F). All of the hot bands were subsequently placed inside of a coiling simulation furnace set at 593°C (1,100°F) and cooled at a rate of 28°C (50°F) per hour to room temperature. The hot bands were then descaled by shot blasting.

The two hot bands from each of the heats #3 and #5 (hot bands 3A, 3B, 5A, and 5B) were sectioned into 14 cm (5.5 inch) long pieces which were cold-reduced 67% to a final thickness of 1.02 mm (0.040 inch) using a laboratory cold mill. One hot band from each of the highly alloyed chemistry heats (hot bands 4B and 6B) was sectioned into 14 cm (5.5 inch) long and 2.5 cm (1 inch) wide pieces. The highly-alloyed steel was sectioned into narrow pieces to decrease rolling loads. However, attempts to cold reduce these pieces of hot band in their as-hot-rolled and "coiled" condition resulted in edge cracks and fracture of the samples. To circumvent this problem, the pieces of hot band were given an additional thermal treatment at 704°C (1,300°F) for 40 minutes then air-cooled to room temperature. After this annealing, the edges

of the pieces were ground flat. Cold reductions of 67% to a final thickness of 1.02 mm (0.040 inch) using a laboratory cold mill were then readily achieved. One hot band from each of the highly-alloyed chemistry heats (hot bands 4A and 6A) has been retained for evaluation and possible alternative processing to a cold-rolled thickness.

Results

Chemical compositions obtained from cold-rolled samples derived from all six hot bands are listed in Table 3. Comparison of the chemical compositions measured in the samples obtained from the original four ingots to those from the final cold-rolled samples reveals a consistent loss of approximately 0.03 wt. % carbon due to reheating and hot working of the steels. For the ingot samples boron was analyzed by acid dilution followed by inductively-coupled plasma (ICP) spectroscopy. High levels of manganese in the steels caused interference with the determination of the boron signal and yielded values significantly higher than the actual boron levels. For the cold-rolled samples, a more time-consuming and accurate extraction and back-extraction followed by ICP analysis procedure was employed. The final boron contents fell within the range of 0.001 to 0.002 wt. %. Table 3 shows that the manganese, silicon, aluminum, and chromium contents of the cold-rolled samples essentially met the proposed concentration levels as listed in Table 1. Only heat #6 had an extra titanium addition to prevent the boron from combining with nitrogen.

Table 3. Chemical compositions (in weight percent) of cold reduced samples of the initial candidate steels.

Hot Band	C	Mn	P	S	Si	Ni	Cr	Cu	Mo	N	Nb	V	Ti	Al	B
3A	**0.10**	**2.16**	<0.002	0.0008	**2.15**	0.004	**<0.002**	<0.002	<0.002	0.0049	<0.002	0.002	**0.003**	**1.48**	**0.0018**
3B	**0.092**	**2.17**	<0.002	0.0008	**2.17**	0.002	**<0.002**	<0.002	<0.002	0.0046	<0.002	0.002	**0.003**	**1.48**	**0.0016**
4B	**0.26**	**4.12**	0.002	0.0008	**2.12**	0.002	**0.47**	<0.002	<0.002	0.0080	<0.002	0.002	**0.002**	**1.58**	**0.0014**
5A	**0.25**	**1.95**	0.002	0.0007	**2.08**	0.002	**0.013**	<0.002	<0.002	0.0055	<0.002	0.002	**0.002**	**1.46**	**0.0016**
5B	**0.25**	**1.95**	0.002	0.0008	**2.06**	0.003	**0.014**	<0.002	<0.002	0.0039	<0.002	0.002	**0.002**	**1.44**	**0.0015**
6B	**0.29**	**3.99**	0.002	0.0008	**2.12**	0.002	**0.48**	<0.002	<0.002	0.0047	<0.002	0.002	**0.022**	**1.50**	**0.0011**

The baseline chemistry "A" carbon level was supposed to be realized in heat #3. The carbon contents attained in the cold-rolled samples from hot bands 3A and 3B are only two-thirds of the aim value of 0.15 wt. %. Initial CALPHAD-based solution-thermodynamic modeling predicts that the low carbon content of the 3A and 3B steels will prevent them from achieving complete austenitization at any temperature. The intermediate chemistry "B" carbon level was supposed to be realized in heat #5. The carbon contents attained in the cold-rolled samples from hot bands 5A and 5B are 0.05 wt. % above the aim values of 0.20 wt. %. The additional carbon will enable these steels to achieve complete austenitization at lower temperatures than initially anticipated. The highly alloyed chemistry "C" carbon level was supposed to be realized in heats #4 and #6. Only the cold-rolled samples from the hot band 6B have essentially the aim carbon concentration value of 0.30 wt. %. Preliminary examination of the microstructure produced in the hot band 6B found that the steel possesses a high degree of hardenability based upon the presence of a substantial volume fraction of bainite/martensite/retained austenite constituent.

The sum total of the cropping, machining, sectioning, and descaling applied to the original 13.6-Kg (30-lb) ingots resulted in a yield of the final cold-rolled steel of about 24%, i.e., 3.2 Kg (7 lb). Each hot band produced approximately 0.2 m^2 (310 $inch^2$) of cold-rolled steel 1.02 mm (0.040 inch) thick. That amount of steel will provide an ample number of test coupons to enable exploration of an extensive range of time/temperature parameters associated with double-stabilization thermal cycles.

Conclusions

Initial modeling results indicate that substantial carbon and manganese contents will be required in steels that are to be fully austenitized that have silicon and aluminum concentrations of nominally 2 wt. % and 1.5 wt. %, respectively. There is a distinct tradeoff between the competing goals of lowering the carbon content for enhanced weldability and raising the aluminum and silicon levels to suppress carbide formation and promote carbon partitioning.

Presentations

1. G. M. Michal, "AHSS through Paraequilibrium Carbon Partitioning and Austenite Stabilization," Special seminar at AK Steel Corporation—Research, Middletown, Ohio, August 30, 2007.
2. G. M. Michal and A. H. Heuer, "Increasing the Austenite Content of AHSS by Dual Stabilization Processing," MS&T'07 Conference and Exhibition, Detroit, Michigan, September 17, 2007.
3. G. M. Michal, "AHSS through Carbon Partitioning," NSF/DOE Steel Research Program Review, Southfield, Michigan, April 10, 2008.
4. G. M. Michal and A.H. Heuer, "Use of Dual Stabilization Thermal Processing to Increase the Austenite Content of AHSS," MS&T '08 Conference and Exhibition, Pittsburgh, Pennsylvania, October 6, 2008.

Reference

1. E. G. Bain and H. W. Paxton, "Alloying Elements in Steel," ASM, Metals Park, OH, 1966, P. 126.

Q. Development of a High-Strength, High-Toughness Bainitic Steel

Principal Investigator: Susil K. Putatunda
Chemical Engineering and Material Science, Wayne State University, Detroit, MI- 48202
(313) 577-3808; fax: (313) 577-3810; e-mail: sputa@eng.wayne.edu

Technology Area Development Manager: Joseph A. Carpenter
(202) 586-1022; fax: (202) 586-1600; e-mail: joseph.carpenter@ee.doe.gov

Field Project Officer: Aaron D. Yocum
(304) 285-4852; fax: (304) 285-4403; e-mail: aaron.yocum@netl.doe.gov

Contractor: Wayne State University
National Science Foundation (NSF) Contract No.: CMMI 0727004, jointly funded by NSF and DOE

Objective

- The primary objective of this investigation was to develop a new bainitic steel with simultaneous high yield strength, ductility, and fracture toughness by applying the novel concept of an adiabatic deformation and two-step austempering process.
- The secondary objective was to examine the influence of austempering temperature on the microstructure and mechanical and physical properties of this new steel.

Approach

- In the preliminary investigation under a seed grant, a new low-alloy steel has been designed and austempered by single-step austempering process. The alloy steel has been designed such that its M_s (martensite start) temperature is below 315°C, because 315°C is the general position of the boundary line between upper and lower bainite. The steel with the following composition has been designed for this investigation: C=0.50%, Si=2.0%, Cr=1.0%, Mn=0.60% and Mo=0.20% and Cu = 0.50%, with S and P as low as possible. The M_s temperature of such steels can be expressed as $M_s = 1000 – (650 \times \% C) – (70 \times \% Mn) – (35 \times \% Ni) – (70 \times \% Cr)$.
- The calculated M_s temperature of the steel was 296°C. Inclusion of high silicon helped in the prevention of cementite formation during the transformation to upper bainite. The addition of chromium helped in reducing graphitization and improving hardenability. This also depressed the M_s temperature. The carbon content has been selected as 0.50% because we need sufficient carbon to depress the M_s temperature and inhibit pearlite formation during austempering. Carbon also helped to depress the upper to lower bainite boundary transition line. This allowed us to initially quench the steel to a lower austempering temperature and thus achieve refinement of bainitic ferrite-austenite structure. Addition of a small amount of molybdenum helped to attain higher hardenability. We added copper, recognizing the fact that while it is not normally a very desirable element in commercial steel because of the formation of pearlite phase, it can improve corrosion resistance. We show that even with copper added, we did not find evidence for any pearlite phase formation in this steel during the austempering.

Accomplishments

- A new low-alloy, medium-carbon steel with high silicon content has been developed.
- By austempering this steel in the temperature range of 260°C–400°C, considerable strength, toughness, and ductility were produced in the steel.

- After austempering this steel in the temperature range of 315°C–400°C, a mixed microstructure consisting of bainitic ferrite and austenite was obtained in this steel. However, presence of some martensite was also observed.
- Exceptionally high fracture toughness of 116 MPa√m was obtained in this steel after austempering at 315°C.
- The steel had relatively large magnetization compared to traditional low-alloy steels.
- This steel is an inexpensive alternate to maraging steel in applications requiring very high fracture toughness.
- This steel has high ductility and very good strength and toughness. Therefore, it can be used in automotive components to reduce weight and increase fuel efficiency.

Future Directions

- In the future, we propose to apply adiabatic deformation and a novel concept of two-step austempering in this steel. Applying adiabatic deformation and two-step austempering will result in an extremely fine-scale microstructure (nano-scale region) and very high carbon in the austenite. Further, higher density of nucleation at the same growth rate will cause the austempering reaction (stage 1) to occur very fast; i.e., the end point of reaction one will be achieved quickly. The purpose of step austempering is to momentarily force the material into the lower bainitic region to increase nucleation, and we intend to raise the temperature of transformation into the upper bainitic region to grow the ferrite austenite structure. In our opinion, single-step austempering will not produce as fine a structure as the two-step austempering. When we do the initial quench to a temperature just above the M_s temperature of the steel, we expect to be in the region below the bainitic nose of the IT diagram. Therefore, we do not expect a significant amount of lower bainite to be formed in the material.
- Thus, the overall new process will include the following steps:
  - Heat up the material to an initial austenitizing temperature (T_1) (i.e., just below and above A1)
  - Enclose in an insulated chamber with heated rolls maintained at the same temperature.
  - Adiabatically deform it by rolling to a final temperature (T_2) (i.e., about 871°C)
  - This will be followed by two-step austempering, i.e., immediate quenching to first austempering temperature T_3 in a salt bath (above M_s temperature) and then raising the temperature of the salt bath to the final austempering temperature (T_4) and holding and finally air cooling .
- This processing will result in a steel with very fine-scale ausferritic microstructure (nano-scale region) and will also result in exceptional combination of mechanical and physical properties.

Introduction

The primary focus of this investigation was to create a high-strength, high-toughness bainitic steel. This was achieved by austempering medium-carbon low-alloy steel with high silicon content.

Steels with bainitic structure have several advantages including high strength, high toughness, and high ductility. In conventional steels, the fracture toughness generally decreases as yield strength increases. On the other hand, the fracture toughness will be high when the yield strength is low. Thus the combination of high strength and high fracture toughness cannot easily be obtained in most conventional steels. In this investigation, new bainitic steel with simultaneous high yield strength and high fracture toughness was developed. This novel steel was synthesized using the concepts of austempered ductile cast iron (ADI) technology.

Austempered Ductile Cast Iron

ADI has emerged as a major engineering material in recent years because of its excellent properties, such as high strength with good ductility [1–3], good wear resistance [4], good fatigue properties [5–9], and good fracture toughness [10]. It is widely used in manufacturing components as diverse as gears [11], crankshafts [12], locomotive wheels [13], connecting rods, brake shoes, etc. ADI has other advantages, such as low production cost arising from its good castability, excellent

machinability resulting in consequently longer tool life, and shorter heat-treatment processing cycles.

ADI is an alloyed and heat-treated nodular cast iron. It has a unique acicular matrix structure [14] that consists of high carbon austenite (γ_{HC}) and ferrite (α) with dispersed graphite nodules. This unique microstructure, the product of the austempering process, provides the excellent mechanical and physical properties of ADI. The chemical composition of ADI is similar to that of conventional ductile cast iron [15]. However, some alloying elements, such as nickel, copper and molybdenum, are usually added to increase its heat treatability, i.e., to delay austenite decomposition to pearlite and ferrite upon cooling. Proper austempering heat treatment will avoid [16] the formation of unwanted microstructural constituents such as martensite, carbides, and pearlite.

ADI Processing

The development of ADI involves a two-stage process. The first step is the melting and casting of alloyed nodular (ductile) cast iron. This is followed by heat treatment. The casting is heated and held in the austenitizing temperature range of 815°C -927°C for one to two hours. At this stage, the structure becomes fully austenitic (γ). After austenitizing, the alloy is quenched in a molten-salt bath and cooled to an austempering temperature range between 260°C and 400°C. The casting is maintained at this temperature range for about two to four hours and then air- cooled to room temperature.

During austempering, ADI goes through a two-stage phase-transformation process [15–18]. In the first stage, the austenite (γ) decomposes into ferrite (α) and high carbon austenite (γ_{HC}):

$$\gamma \rightarrow \alpha + \gamma_{HC} \qquad (l)$$

If the casting is held at the austempering temperature for too long, a second reaction takes place [15–18], during which the high-carbon austenite γ_{HC} can further decompose into ferrite and carbide:

$$\gamma_{HC} \rightarrow \alpha + \varepsilon \qquad (2)$$

In this case, the structure will contain ε carbide, which makes the material brittle. Therefore, this reaction must be avoided. The best combination of mechanical properties (tensile strength and ductility) is obtained in ADI after the completion of the first reaction but before the onset of the second reaction. This time period between the completion of the first reaction and the onset of the second reaction is termed the "process window." This process window can be enlarged by addition of alloying elements such as nickel, molybdenum and copper. Proper austempering produces a unique bainitic structure that consists of high-carbon or transformed austenite (γ_{HC}) and acicular ferrite with dispersed graphite nodules.

The exact morphology of the ferrite phase and the relative amounts of ferrite and austenite determine [19–22] the mechanical properties of ADI and can be controlled by austempering temperature and time. For example, when ADI is austempered at a lower temperature (e.g., 260°C), it has a very high yield strength. On the other hand, when it is austempered at higher temperature (e.g., 385°C), it has a lower yield strength. This higher yield strength (for ADI processed at lower temperatures) is due to the presence of fine ferrite and austenite in the matrix [15–18]. On the other hand, at higher austempering temperature, ferrite and austenite become feathery or coarse and this causes a decrease [19] in the yield strength of ADI. This higher yield strength at lower austempering temperature develops from a smaller grain size and a lattice mismatch effect [15–18].

The term austempered ductile iron therefore describes a family of materials whose properties can be varied over a wide range by the correct choice of heat-treatment variables (temperature and time) and chemical composition. Austempered ductile irons can have tensile strengths up to 260 Ksi (1600 MPa) with 1 percent elongation and high hardness (in excess of 60 R_c) for applications in which wear resistance is of primary importance. Materials of lower hardness having tensile strengths of [120–170 Ksi (800 to 1200 MPa)] and elongation up to 14% can also be produced when higher ductility is required.

Another interesting possibility exists with ADI. Generally, in almost all materials, fracture toughness decreases as yield strength increases and vice versa. However, ADI is an exception. This investigator [20–21] and others [23–25] have observed that fracture toughness is higher in ADI when its yield strength is also high. Thus, it is possible to produce simultaneous high yield strength and high fracture toughness in ADI, something that cannot be obtained in most other materials.

Austempering Reaction in ADI

During austempering of nodular or ductile cast iron, acicular ferrite grows from austenite by a nucleation and growth [2, 16, 26–28] process. While the ferrite phase grows, the remaining austenite becomes enriched with carbon. When ADI is austempered at lower temperatures (i.e., in the lower-bainitic region), it develops a microstructure that consists of acicular ferrite with precipitated carbide [16, 26] and retained austenite. This is similar to a lower-bainitic structure in steel. However, when ADI is austempered in the upper-bainitic region, it produces a microstructure that consists of carbide-free ferrite and austenite [16, 26]. Due to the high silicon content, the formation of cementite phase, which is normally associated with the bainitic reaction in steel, is suppressed in ADI. Consequently, the remaining austenite continues to be enriched with carbon as the reaction proceeds. As the austenite becomes enriched with carbon, the growth of bainitic ferrite platelets is inhibited [17] and the reaction is arrested. Depending upon the transformation temperature and time, it can contain large amounts [26] (up to 50%) of austenite. Presence of this high-carbon austenite (γ_{HC}) increases the work-hardening rate [25–28] of ADI. This, in turn, contributes to the good fatigue strength and fracture toughness in ADI.

Austempering Reaction in Steel

When steel is austempered at temperatures below the nose of the time-temperature-transformation (TTT) curve, a structure is produced in which ferrite and iron carbide are not lamellar. This transformation product is called bainite. Bainite in steel has a needle-like (acicular) microstructure. Whereas pearlite is nucleated by iron carbide [29, 30] and is accompanied by the subsequent formation of ferrite, bainite is nucleated by ferrite and followed by the precipitation of iron carbide. This process leads to the dispersion of iron carbide in a ferrite matrix. With a lower transformation temperature, the distribution of carbide is finer and the ferrite needles are thinner [29–32]. This product is called lower bainite. The transformation product at relatively higher temperatures consists of lath- or plate- shaped ferrite units arranged in packets and interlath carbide precipitates. This product is called upper bainite [35]. In steel, lower bainite produces higher yield strength but lower toughness. While the austempering reaction in ADI is a two-step reaction process, it is a one-step reaction process [29–32] in the case of steel. During austempering in steel, austenite directly decomposes into acicular ferrite and carbide (bainite). Austempering of steel offers the advantages of increased ductility, reduced distortion, and a short overall time cycle to harden thoroughly. Generally, upper-bainitic temperatures are above 316°C (600°F) in the case of steels and cast iron. Temperatures between 232°C (450°F) to 316°C (600°F) are the lower-bainitic temperature range.

However, when steels contain sufficient silicon or aluminum (exceeding 2.0%) and are austempered in the upper-bainitic temperature range, a unique microstructure similar to ADI develops. The carbon that is partitioned into residual austenite does not precipitate but remains stable to ambient temperature. The microstructure obtained consists of fine plates of bainitic ferrite separated by a carbon-enriched region of austenite. The potential advantages of this mixed microstructure can be listed as follows:

- Cementite is responsible for initiating fracture in high-strength steels. Its absence is expected to make the microstructure more resistant to cleavage failure and void formation.
- The bainitic ferrite is almost free of carbon, which substantially strengthens the ferrite [42].
- The microstructure derives its strength from the fine grain size of the ferrite plates, which

are less than 1 micrometer (μm) in thickness. It is the thickness of these plates, which determines the mean free-slip distance, so that the effective grain size is less than a μm. This cannot be achieved by any other commercially-viable process. Grain refinement is the only method available for simultaneously improving the strength and toughness of steels.

- The ductile films of austenite, which are intimately dispersed between the plates of ferrite, have a crack-blunting effect. They further add to toughness by increasing the work of fracture as the austenite is induced to transform to martensite under the influence of the stress field of a propagating crack. This is the transformation-induced plasticity (TRIP) effect.
- The diffusion of hydrogen in austenite is slower than in ferrite. The presence of austenite can therefore improve the stress-corrosion resistance.
- Steels with the bainitic ferrite and austenite microstructure can be obtained without the use of expensive alloying elements. All that is required is that the silicon or aluminum concentration should be large enough to suppress the cementite formation.

In spite of these appealing features, the microstructure does not always give the expected good combination of strength and toughness. This is because the relatively large, blocky regions of austenite between the sheaves of bainite readily transform into high-carbon martensite under the influence of stress. This untempered, hard, and coarse martensite regions severely embrittle the steel. Therefore, we argue that if the austenitic and ferrite can be made in very fine-grained structure and austenite sufficiently enriched with carbon so that its M_s temperature is sufficiently depressed [39–41], then the strength and other mechanical properties will increase significantly.

A novel concept of adiabatic deformation and two step austempering process has been conceived by this investigation to produce extremely fine-scale microstructure consisting of ferrite and austenite. This is expected to produce an exceptional combination of strength, ductility, and fracture toughness in this steel.

Results

This investigator was awarded a seed grant to establish the proof-of-principle for this project. With this seed grant, we melted and cast a medium-carbon, low-alloy steel with high silicon content of the following composition (C-0.5%, Si-2%, Mn-0.4%, Ni-1%, Cr-0.8% and Mo-0.3%). After hot rolling and annealing, the steel was austenitized at 926°C for 2 hours and then austempered at several temperatures between 260°C and 398°C. Figure 1 shows the typical

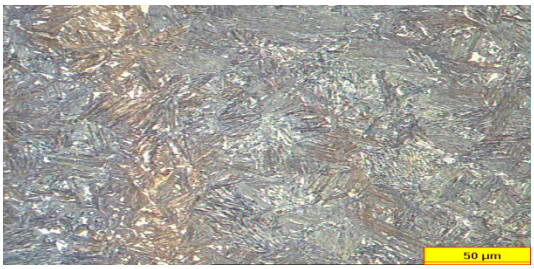

Figure 1. Microstructure of the steel after austempering at 700°F.

microstructure of the steel after austempering at 371°C .This microstructure shows a fine-scale ausferritic structure, i.e., a mixture of ferrite and high-carbon austenite. X-ray diffraction confirmed the microstructure consisting of ferrite and high-carbon austenite. Table 1 below reports the mechanical properties of the steel including the fracture toughness .We obtained exceptionally high strength (1336 MPa) and high fracture toughness (116 MPa√m, comparable to maraging steel) in this material after austempering at 315°C. The ductility of the material is also significantly high (11.5% elongation). We also processed a few samples by adiabatic deformation and single-step austempering and this resulted in an extremely fine-scale microstructure. Thus, we have already established the proof-of-principle for this project. We now propose to apply the novel concept of adiabatic deformation and two-step austempering in this steel to produce an extremely fine (nearly nano crystalline) microstructure with austenite and ferrite together with a very high carbon content in the austenite. We expect to have properties significantly higher than maraging steels. As

Table 1. Mechanical Properties of Steels Investigated in Initial Proof-of-Concept Project

Austempering Temp (°C)	Yield Strength (MPa)	Ultimate Tensile Strength (Mpa)	Ductility (% elongation)	Fracture Toughness (MPa√m)
As-cast	507	882	16.8	42.8
260	1423	1779	10.1	84.5
315	1336	1653	11.5	116.2
343	1244	1381	12.7	96.3
371	1103	1408	14.9	75.8
398	864	1384	18.5	62.6

mentioned earlier, such high-strength, high-toughness steel will have major applications in defense, automotive and other manufacturing industries because it will result in significant weight savings. Another potential application of this steel will be in armored plates and combat tanks. This steel will have extremely high fracture toughness, impact resistance, and ballistic mass efficiency (BME). Moreover, they will have major applications in automotive components, reducing weight and improving fuel economy and reducing pollution.

Once this steel of the above-mentioned composition has been developed, we will concentrate on developing other ausferritic steels with lower carbon content and different alloying composition using the same basic principle; i.e., designed with a lower M_s temperature and processed by adiabatic deformation and two-step austempering.

Conclusions

A new low-alloy, medium-carbon steel with high silicon content has been developed. By austempering this steel in the temperature range of 260°C–400°C, considerable strength and ductility were produced in the sample. After austempering this steel in the temperature range of 315°C–400°C, a mixed microstructure consisting of bainitic ferrite and austenite was obtained in this steel. The steel had properties comparable to maraging steel. Adiabatic deformation produced very fine-scale ferrite and austenite.

Presentations/Publications/Patents

1. Two papers were presented at M.S and T conferences in October 2007 and October 2008.
2. One paper has been accepted for publication in Materials Science and Engineering A.
3. One patent application has been filed with U.S. Government.

References

1. J. Dodd, “High Strength, High Ductility Ductile Irons,” Modern Casting, Vol. 68, No. 5, pp. 60–66 (1978).
2. R. B. Gundlach and J. F. Janowak, “Development of a Ductile Iron for Commercial Austempering,” AFS Transaction, Vol. 94, pp. 377–388 (1983).
3. R. A. Harding and G.N.J. Gilbert, “Why the Properties of Ductile Irons Should Interest Engineers,” British Foundryman, Vol. 79, pp. 489–496 (1986).
4. I. Schmidt and A. Schuchert, “Unlubricated Wear of Austempered Ductile Cast Iron,” Zeitschriftjbr Metalkunde, Vol. 78, pp. 871–875 (1987).
5. M. Johansson, “Austenitic Bainitic Ductile Iron,” AFS Transaction, Vol. 85, pp. l 17122 (1977).
6. S. K. Putatunda et. al., “Influence of Microstructure on High Cycle Fatigue Behavior of Austempered Ductile Cast Iron,” Materials Characterization, Vol. 30, pp. 22l-234 (1993).
7. P. Shanmugam, P. P. Rao, K. R. Udupa, and N. Venkataraman, “Effect of Microstructure on the Fatigue Strength of an Austempered Ductile Iron,” J of Materials Science, Vol. 29, pp. 4933–4940 (1994).
8. L. Bartosiewicz, S. Duraiswamy, A. Sengupta, and S. K. Putatunda, “Near Threshold Fatigue

Crack Growth behavior of Austempered Ductile Cast Iron," Morris Fine Symposium, TMS, Detroit, pp. 135–138 (1991).

9. L. Bartosiewicz, A. R. Krause, A. Sengupta, and S. K. Putatunda, "Relationship between Fatigue Threshold and Fatigue Strength in Austempered Ductile Cast Iron." International Symposium for Testing and Failure Analysis, ISTFA, ASM Vol. 16. pp. 323–336 (1990).
10. G. Wilkinson and C. Grupke, "Design Consideration and Product Applications of Casting," 2nd International Conference on Ductile Iron, Ann Arbor, Michigan. pp. 349–358, (March 1986).
11. J. Panasiewicz, C. Grupke, and J. Huth, "Chrysler's Experience with Austempered Ductile Iron," World Conference on Austempered Ductile Iron, Bloomingdale, IL, pp. 176–194 (March, 1991).
12. K. Okazaki, H. Asai, M. Tokuyoshi, H. Kusonoki, and H. Sakahara, Proceeding World Conference on Austempered Ductile Iron, Bloomingdale, IL, pp. 288–299 March, 1991.
13. B. V. Kovacs, "Austempered Ductile Iron, Facts and Fiction," Modern Casting, Vol. 36, pp. 38–41, (1990).
14. T. Shiokara, "On the Austempered Ductile Cast Iron, Their Mechanical properties and Some Practical Applications," 59th Japan Ductile Cast Iron, Association conference, Tokyo, Japan, pp. 138–150 (1978).
15. J. F. Janowak and P. A. Norton, "A Guide to Mechanical Properties Possible by Austempering, 1 Spercent Ni, 0.3 percent Mo Iron," AFS Transaction, Vol. 88. pp. 123–135, (1985).
16. R. B. Gundlach and J. F. Janowak, "Austempered Ductile Irons Combine Strength with Toughness and Ductility," Metal Progress, Vol. 12, pp. 231–236 (1985).
17. J. F. Janowak, R. B. Gundlach, G. T. Eldis, and K. Rohrting, "Technical Advances in Cast Iron Metallurgy," AFS International Cast Metal Journal, Vol. 6, pp. 28–42 (1982).
18. D. J. Moore, T. B. Noun, and K. B. Rundman, "The Relationship between Microstructure and Tensile Properties in Austempered Ductile Cast Iron," AFS Transaction, Vol. 87, pp. 165–174, (1987).
19. L. Bartosiewicz, A. R. Krause, B. V. Kovacs, and S.K. Putatunda, "Fatigue Crack Growth Behavior of Austempered Ductile Cast Iron," AFS Transaction, Vol. 92, pp. 135–142, (1992).
20. S. K. Putatunda and I. Singh, "Fracture Toughness of Unalloyed Austempered Ductile Cast Iron," Journal of Testing and Evaluation, Vol. 23, No. 5, pp. 325–332, (September 1995).
21. S. K. Putatunda, I. Singh, and L. Bartosiewicz, "Influence of Chromium on Mechanical Properties of Austempered Ductile Cast Iron," Journal of Materials Engineering and Performance, Vol. 4, No. 1, pp. 90–101, (Feb.1995).
22. I. Singh, "Fatigue and Fracture behavior of ADI," Ph. D. Thesis, Wayne State University, June 1996, Advisor S.K. Putatunda.
23. J. L. Doong and C. Chen, "Fracture Toughness of Bainitic-Nodular Cast Iron," Fatigue Fracture of Engineering Material and Structure, Vol. 12, pp. 155–165 (1989).
24. E. Dorazil and M. Holzman, "Fracture Behavior of Austempered Ductile Iron," Proceeding World Conference on Austempered Ductile Iron, Bloomingdale, IL, March, 1991, pp. 32–66.
25. M. Grech, P. Bowen, and J. M. Young, "Effect of Austempering Temperature on the Fracture Toughness and Tensile Properties of an ADI alloyed with Copper and Nickel," Proc. World Conference on Austempered Ductile Iron Bloomingdale, IL, March, 1991, pp. 338–374.
26. D. J. Moore, T. N. Rouns, and K. B. Rundman, "The Effect of Heat Treatment, Mechanical Deformation and Alloying Elements on Rate of Bainitic Formation in Austempered Ductile Cast Iron," J of Heat Treating, Vol. 4, No. 1, June 1985, pp. 7–24.

27. S. K. Putatunda and P. P. Rao, "Influence of Microstructure on Fracture Toughness of Austempered Ductlie Cast Iron," Metallurgical and Materials Transaction, Vol. 28A. No. 7, pp. 1457–1470, July 1997.
28. S. K. Putatunda, R. Gupta, and P. P. Rao, "Influence of Austempering time and temperature on Fracture Toughness of Austempered Ductile Iron," Microstructural Sciences, ASM International, Vol. 24, pp. 103–110, (1996).
29. R. E. Reed Hill, "Physical Metallurgy Principles 2nd Edition, D. Van Nostrand Company New York, 1973.
30. D. A. Porter and K. E. Easterling, "Phase Transformations in Metals and alloys," Chapman and Hall, 2nd Edition, 1992.
31. P. G. Shewmon, "Phase Transformations in Metals," McGraw Hill, 1986.
32. W. F. Smith, "Structure and Properties of Engineering Alloys," McGraw Hill (1981).
33. B.P.J. SandVik, "Bainitic Transformation in High Silicon Steel," Metallurgical Transactions, Vol. A13, pp. 777–787, 1982.
34. H.D.K.H. Bhadeshia, "Bainite in Steels," Second Edition, The University Press, Cambridge, IOM communication Ltd., London, pp 373–375, 2001.
35. J. Aranzabal et al., "Influence of Heat Treatment on the Microstructure of an Austempered Ductile Iron," Materials Science and Technology, Vol. 20, pp. 36–46, 1994.
36. S. K. Putatunda, "Development of a High Carbon and High Silicon Steel," Journal of Materials Processing and Technology, pp. 335–358, August 2001.
37. S. K. Putatunda, "Fracture Toughness of a High Carbon and High Silicon Steel," Materials Science and Engineering, Vol. A297, pp. 31–43, January 2001.
38. H.K.D.H Bhadeshia et al., "Very Strong Low Temperature Bainite," Material Science and Technology, Vol. 18, pp 279 – 284, March 2002.
39. S. K. Putatunda and P. P. Rao, "Comparative Study of Fracture Toughness of Austempered Ductile Iron with Upper and Lower Ausferritic Microstructure," Materials Science and Technology, Vol. 14, pp 1257–1263, December, 1998.
40. P. P. Rao and S. K. Putatunda, "Investigations on Fracture Toughness of Austempered Ductile Iron Alloyed with Chromium," Materials Science and Engineering, Vol. A346, pp. 254–265, 2003.
41. P. P. Rao and S. K. Putatunda, "Dependence of Fracture Toughness of Austempered Ductile Cast Iron on Austempering Temperature," Metallurgical and Materials Transaction, Vol. 29A, pp. 3005–3016, December 1998.
42. S. Yazdani and A. Firouzi, "Influence of Heat Treatment on Fatigue Behavior of a Cu-Ni Alloyed Austempered Ductile Iron," Material Science Forum, Vols. 426–432, pp. 925–930, 2003.
43. K. L. Harynen, D. J. Moore, and K. B. Rundman, "Tensile Properties and Microstructure of a Clean Austempered Ductile Iron," AFS Transaction, Vol. 98, pp. 471, 1990.
44. A.S.H. Ali, K. I. Uzlov, N. Darwish, and R. Elliot, "Austempering of a Low Manganese Ductile Iron, Part 4 Relationship between Mechanical Properties and Microstructure," Materials Science and Technology, Vol. 70, pp. 35–48, 1994.
45. S. K. Putatunda and P. Gadicherla, "Influence of Austenitizing Temperature on Fracture Toughness of a Low Manganese Austempered Ductile Cast Iron, "Materials Science and Engineering, Vol. A268, pp. 15–31, August 1999.
46. S. K. Putatunda, "Development of Austempered Ductile Cast Iron (ADI) with Simultaneous High Yield Strength and Fracture Toughness by a Novel Two-step Austempering Process," Materials Science and Engineering, Vol. A 315, pp. 70–80, September (2001).

47. ASTM E-8, "Standard Test Method for Tensile Testing of Metallic Materials," Annual Book of ASTM Standards, ASTM Philadelphia, Vol. 03.01, pp. 506–536, 1992.

48. C. S. Roberts, "Effect of Carbon Content on Lattice Parameter of Austenite," Transaction TMS-AIME, Vol. 230, pp. 373, 1964.

49. B. D. Cullity, "Elements of X-Ray Diffraction," Addison-Wesley, Reading, MA. 1974, pp. 411–412.

50. ASTM E-399, "Standard Test Method for Plane Strain Fracture Toughness testing of Metallic Materials," Annual Book of ASTM Standard, PA, Vol. 3.01, p.745, (1992).

R. Development of Nano-Acicular Duplex Steels

Principal Investigator: David C. Van Aken
Missouri University of Science and Technology
Materials Science and Engineering, 1400 N. Bishop, Rolla, MO 65409-0340
(573) 341-4717; fax: (573) 341-6934; e-mail: dcva@mst.edu

Co-Principal Investigator: Julia E. Medvedeva
Missouri University of Science and Technology
Physics, 1315 N. Pine St., Rolla, MO 65409-0640
(573) 341-4789; fax: (573) 341-4715; e-mail: juliaem@mst.edu

Co-Principal Investigator: Von L. Richards
Missouri University of Science and Technology
Materials Science and Engineering, 1400 N. Bishop, Rolla, MO 65409-0340
(573) 341-4730; fax: (573) 341-6934; e-mail: vonlr@mst.edu

Technology Area Development Manager: Joseph A. Carpenter
(202) 586-1022; fax: (202) 586-1600; e-mail: joseph.carpenter@ee.doe.gov

Field Project Officer: Aaron D. Yocum
(304) 285-4852; fax: (304) 285-4403; e-mail: aaron.yocum@netl.doe.gov

---

Contractor: Missouri University of Science and Technology
National Science Foundation (NSF) Contract No.: MMI 0726888, jointly funded by NSF and DOE

Objective

- Develop a third-generation advanced high-strength steel (AHSS) that is both lighter and stronger than current automotive steels. The new steel is to be stronger than first-generation AHSS that is based upon ferritic microstructures and less expensive than the high-manganese (Mn), austenitic grades that are second- generation AHSS.
- Improve automotive crashworthiness by producing a microstructure that is similar to acicular $\alpha+\beta$ titanium (Ti) alloys that have high fracture toughness. The new steel will be a duplex microstructure of acicular ferrite and austenite.
- Develop a physics-based understanding of phase stability with respect to alloying. Use first-principles calculations to determine appropriate alloy additions to strengthen the austenitic phase. This knowledge can then be used in the formulation of steel alloys to produce nano-scale, acicular ferrite microstructures.
- Develop an acoustic-emission facility for studying bainitic phase transformation.

Approach

- To address the questions related to the structural, electronic, and magnetic properties of steels, we have performed a thorough density-functional investigation of the electronic structure, magnetic properties, and stability for α (body-centered cubic, bcc) and γ (face-centered cubic, fcc) iron (Fe) phases, their solid solutions with interstitial carbon and substitutional manganese, as well as for cementite with 2*p* and 3*p* impurities. A projector augmented wave (PAW) method was implemented in the Vienna *ab initio* simulation package within the generalized gradient approximation (GGA). We considered the octahedral interstitial sites for carbon (C) which are the most preferable in both bcc and fcc Fe phases, and the nearest substitutional positions of manganese. In cementite, to determine the most energetically-preferable location of the 2*p* or 3*p* impurity

(nitrogen, N; oxygen, O; boron, B; or silicon, Si; aluminum, Al; sulfur, S; phosphorous, P), we compared the formation energies of either carbon or iron substitution by the impurity. For all the structures investigated, we optimized the lattice parameters and the internal positions of all atoms in the supercells via the atomic force and the total-energy minimization.

- The solution enthalpy is calculated as ΔH_s = E(Fe32C)-E(Fe32)-E(C) for carbon and ΔH_s = E(Fe31MnC)-E(Fe32C)+E(Fe)-E(Mn) for manganese, where supercells were taken with the same magnetic states and E(C), E(Fe) and E(Mn) are the total energies of carbon as graphite, iron and α-Mn, respectively.
- Steelmaking will be performed at Missouri University of Science and Technology with the aim of producing steel microstructures similar to the acicular α+β titanium alloys, which have high fracture toughness. Of particular interest will be alloys containing manganese, aluminum, and silicon, where the addition of aluminum and silicon promotes the formation of bainitic ferrite, but discourages the formation of cementite. Aluminum has the added benefit of lowering the overall density of the steel. Initial steel heats will be used to verify the thermochemical database for Fe-Mn-Al-Si-C steel compositions using FactSage (a free-energy minimization modeling program). Alloy and phase-composition studies will then be performed to narrow the range in steel compositions explored.

Accomplishments

- A charge-density distribution plot for the (110) plane reveals the formation of a Mn-C-Fe (180°) defect structure. Other Mn positions result in higher total energy by ~50-230 millielectron volt (meV). Previously-reported Mn-C complexes based on a solid-mechanics model place the carbon atom in the next nearest octahedral position relative to the Mn atom.
- The phase stability and physical properties of Fe_3C can be varied within a wide range by substitutional or interstitial additions of appropriate elements. We found that ΔH is negative only for cementite with boron addition $Fe_3C_{0.75}B_{0.25}$, i.e., boron stabilizes orthorhombic cementite and prevents the graphitization (dissociation of metastable cementite with the formation of bcc Fe and graphite).
- Three types of steels have been produced at Missouri University S&T: 5%Mn steel with nitrogen, a hard, bainitic steel with composition Fe-2.1Mn-4Co-1.2Si-0.6C-0.2Mo, and a lightweight steel with composition Fe-13Mn-4Al-1Si-0.1C. Steel compositions are reported in weight percent. Transformation in the 5% Mn steel was too sluggish to be practical in steelmaking practice. Microstructures similar to acicular α+β titanium alloys were produced in the Fe-2.1Mn-4Co-1.2Si-0.6C-0.2Mo steel by austempering 3 days at 300°C. The high cost of cobalt and the sluggish transformation kinetics also make this steel impractical for automotive steels. The Fe-13Mn-4Al-1Si-0.1C steel appears promising. The addition of aluminum and silicon reduced the density by 5-7% and slow cooling the steel from 1000°C produced a microstructure of degenerate Widmanstätten ferrite and retained austenite.

Future Direction

- Ferrite and austenite Fe-Mn-N alloys. We will perform comparative investigations of the electronic structure, magnetic properties, and stability of α- and γ-Fe with interstitial nitrogen and substitution manganese. The main goal is to determine the ground states of the Fe-N, and Fe-Mn-N phases with small manganese and nitrogen concentration and to understand how these impurities affect the lattice parameters, local crystal structure, magnetic interactions and phase stability. The results will be compared to those obtained for Fe-Mn-C alloys.
- Austenite Fe-Mn-(C,N)-(Al,Si) alloys. We will study the distribution of the light impurities (N, C) with respect to the substitutional 3*d* (Mn) or 3*p* (Al, Si) atoms, as well as the distribution of the latter two with respect to each other.
- Phase-stability maps will be constructed to determine a composition near the Fe-13Mn-4Al-1Si-0.1C steel that produces a fully-austenitic microstructure at hot-rolling temperatures. First, a chemical analysis will be performed on regions in the experimental Fe-13Mn-4Al-1Si-0.1C steel that are austenitic. FactSage will be used to determine vertical sections of the phase diagram near the measured composition of the austenite to formulate new steel compositions.

- Three to four experimental heats will be produced based upon compositions derived from the thermodynamic studies. These steels will be hot rolled to produce sheet product and metallurgically characterized.
- Mechanical-property tests will be conducted on the derivative steel compositions. Both static tensile tests and instrumented impact testing will be performed.
- The role of displacive relaxation and strength in the transformation of the parent phase will be examined using acoustic emission. Initial studies will examine the melting of indium inclusions embedded in aluminum. Inclusions that are embedded within crystalline grains are known to require superheating prior to melting, since the melting is inhibited by the additional pressure produced by the matrix confining the volume expansion. Acoustic-emission studies of the bainitic reaction will be conducted using the Fe-2.1Mn-4Co-1.2Si-0.6C-0.2Mo steel produced at Missouri University S&T.

Introduction

Recent developments in steels have resulted in first-generation advanced high-strength steels (AHSSs) with ferritic microstructures and second-generation high-strength steels with austenitic microstructures. The research performed here is to develop steels with duplex ferrite and austenite microstructures that will be analogous to acicular microstructures developed in α+β titanium which have high fracture toughness (see Figure 1).

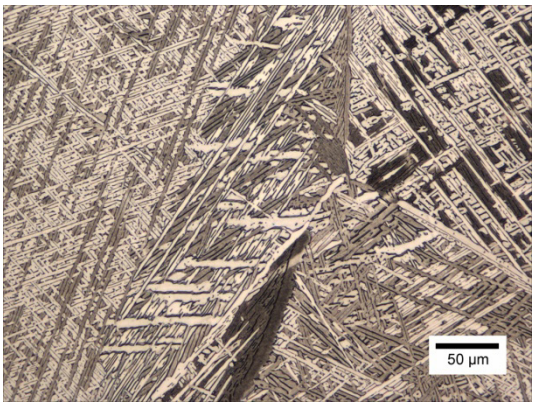

Figure 1. A titanium α+β microstructure of acicular α plates with retained β developed for high toughness.

These new steels will have strengths greater than first-generation advanced high-strength steels, but cost less than the ultra-high- manganese second-generation twinning-induced plasticity (TWIP) and transformation-induced plasticity (TRIP) steels (see Figure 2). These new third-generation steels will have nanometer-size acicular ferrite microstructures with metastable austenite, which results in steels both high in strength and toughness. These steels are expected to maintain steel as the preeminent high-strength structural

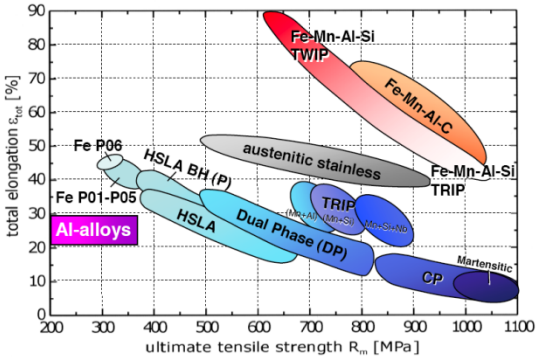

Figure 2. Property distribution plot for first- and second-generation AHSS.

material in designing low-weight automobiles with exceptional crashworthiness.

The complex structural and magnetic properties of iron (Fe) make it a challenge to determine the effect of impurities on the microstructure of steel, as well as its electronic structure, which is critical for the fundamental understanding of the observed macroscopic properties.

A physics-based approach to alloy design is being pursued to understand the role of Mn in the defect formation with interstitial atoms. Systematic calculations of the electronic structure and lattice distortions are being performed using the highly-precise, first-principles, full-potential linearized augmented plane wave (FLAPW) method with the structure-optimization capabilities. This allows us to calculate the dependence of the lattice parameters on carbon and nitrogen concentrations for austenite and ferrite. Similar calculations will be performed for the transition metal additions including manganese (Mn), chromium (Cr), and molybdenum (Mo). The interaction between

solutes and interstitials is the most important part of our investigations. The total- and formation -energy calculations allow us to analyze the possibility of clustering and the effect of solutes on the diffusion of interstitial impurities (C, N, and B).

As distinct from the Fe and Fe-Mn phases, less-theoretical studies exist for the Fe-C and Fe-Mn-C alloys. The structural and magnetic properties of fcc Fe-C and Fe-Mn-C alloys were suggested to differ from those in pure fcc Fe. The observed anomalies in magnetic susceptibility indicate the occurrence of inhomogeneous ferromagnetic and spin-glass-like regions in the Fe-Mn-C alloys. Recent *ab initio* calculations show that interstitial carbon favors local ferromagnetic coupling, but the results for the ground state (both magnetic and crystal structure) are inconclusive. This calls for in-depth, accurate investigations of Fe, Fe-C and Fe-C-Mn systems.

Besides ferrite and austenite, carbon steels and white cast iron contain iron carbide, Fe_3C (cementite), which may substantially affect the resulting mechanical properties. The Fe-C phase diagram exhibits complex interplay of many factors including carbon concentration, temperature, treatment processes (solidification), etc. To shed light on the microscopic role of impurities in electronic and magnetic properties of cementite and its stability, we have studied Fe_3C doped with 2*p* (N, O, B) and 3*p* (Si, Al, S, P).

Theoretical Modeling of Ferrite and Austenite with Manganese: Crystal Structure, Local Distortions and Magnetic Instability

Using an *ab initio* density-functional approach, we performed calculations of α-Fe (bcc) and γ-Fe (fcc), Fe-C, Fe-Mn, and Fe-Mn-C phases (with carbon and/or manganese content of 3 atomic (at.) % in order to determine the ground states in α-Fe and γ-Fe with small manganese and carbon concentration and to understand how these impurities affect: (1) the lattice parameters, (2) local crystal structure, (3) magnetic interactions, and (4) thermodynamic stability. All α-Fe, Fe-C and Fe-Mn-C phases were found to exhibit ferromagnetic (FM) ground states and carbon in octahedral interstitial sites, which leads to tetragonal distortion. Manganese had little effect on the local and bulk crystal parameters. For Fe-Mn-C, we obtained only one stable state where manganese has ferromagnetic coupling with iron. On the other hand, two stable configurations with opposite magnetic moments of manganese (1.05 and -1.90 μ_B) differibg in energy by only 3 meV, were found for bcc Fe-Mn alloy. Thus, we demonstrate that carbon stabilizes the ferromagnetic Fe-Mn coupling in the Fe-Mn-C alloys (Figure 3).

For γ- Fe, Fe-C and Fe-Mn-C phases, the calculations were performed with fixed cubic or tetragonal symmetry for nonmagnetic (NM), FM, single-layer antiferromagnetic (AFM1), and double-layer antiferromagnetic (AFMD) states. Our results reveal that the AFMD state (which is a good collinear approximation for spiral magnetism) is the most stable in all γ- Fe, Fe-C and Fe-Mn-C phases. For every magnetic phase, the tetragonal equilibrium structure was found to have larger volume and larger magnetic moment and is lower in energy by 27–45 meV than the corresponding cubic phase, in agreement with the $c/a>1$ tetragonality of all magnetic fcc Fe states.

We predict that among two FM γ- Fe states, the tetragonal equilibrium high-spin (HS) state (FM/HS) has much lower energy, whereas the low-spin (LS) state is the most unfavorable magnetic state. Hence, the anti-Invar transition involves AFMD and FM/HS states, but not the low-spin FM state. Analyzing the α- γ transition, we show that the total energy difference between the ground magnetic states of α and γ phases corresponds to the experimentally-observed temperature, while the energy difference between the nonmagnetic phases is more than three times larger and has an opposite sign, pointing out the crucial role of magnetism in this transition.

Local tetragonal distortions around interstitial carbon strongly depend on the magnetic state, being the largest in the tetragonal FM state and much smaller in the antiferromagnetic states. We predict the frustration of ideal magnetic order for the AFM1 state in the interstitial Fe-C alloy, where the region of the Fe atoms with the opposite

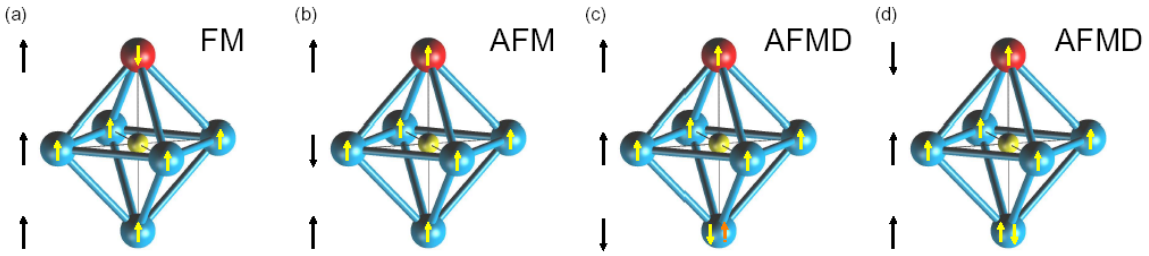

Figure 3. Local magnetic coupling of the Fe (blue) and Mn (red) atoms, which are nearest to the interstitial carbon (yellow). Black arrows at left show bulk magnetic ordering. In the double-layer configuration (AFMD), Mn and C may belong to the layers of the same (c) or opposite (d) spin. These configurations differ by only a few meV in total energy.

intra-layer coupling arises locally near the octahedral site of carbon. So, we demonstrate that carbon favors short-range ferromagnetism in γ-Fe. For the AFMD structure, we find two, nearly-degenerate, stable AFMD states which correspond to the cases where either five or all six nearest Fe atoms have ferromagnetically aligned spins. It is a competition between the intra-layer and inter-layer FM coupling that results in spin flip of the magnetic moments (–2.0/1.9 μ_B) at the Fe atoms near carbon. Thus, we show that carbon introduces FM coupling of the nearest Fe atoms and leads to magnetic instability.

For fcc Fe-Mn-C alloy, we find that manganese is antiferromagnetically coupled with the host iron atoms in FM state, but shows the ferromagnetic intra-layer coupling in both antiferromagnetic ground states. Further, the moments of planar Fe atoms may be either antiferro- or ferromagnetically coupled with the moments of the other Fe atoms in the layers to which they belong to for the ground antiferromagnetic or AFMD states, respectively. In the first case, the moments of all six nearest Fe atoms are ferromagnetically coupled. This behavior in local magnetic ordering is similar to that found in the Fe-C alloy.

Thus, we find that the nearest manganese and iron atoms may be FM or antiferromagnetic coupled with the host iron in the fcc Fe-Mn-C alloy and the energies for spin flip are very small, which should result in magnetic instability of both manganese and iron. Furthermore, for cubic structures, we show that the short-range ferromagnetism of the nearest iron atoms is compensated by the appearance of antiferromagnetic order of the iron atoms in the neighbor layers.

These results provide an understanding of the origin for the observed spin-glass behavior in Fe-Mn-C.

Finally, we estimated the solution enthalpy ΔH for carbon and manganese in α-Fe and γ- Fe. For the bcc FM Fe-3%C alloy, we found positive solution enthalpy of +0.79 electron volt (eV) for carbon in octahedral sites that is in good agreement with experimental value 0.6-0.8 eV. The positive solution enthalpy corresponds to low carbon solubility in bcc Fe. For fcc Fe-3%C, we obtained ΔH to be +0.02, -0.05 eV, -0.06 and -0.07 eV for NM, FM, AFM1 and AFMD states, respectively. The negative solution enthalpy was obtained for magnetic states and this result demonstrates the crucial role of magnetism in the solubility of interstitial impurities.

For manganese, the solution enthalpy is +0.39 eV for bcc FM Fe-Mn-C, and –0.29, –0.37 and –0.40 eV for fcc FM, AFM1 and AFMD Fe-Mn-C states, respectively. Thus, manganese and carbon destabilize α-Fe, but give a strong stabilizing effect in γ-Fe. This fact explains the shift of the α-γ phase transition to lower temperatures caused by manganese in austenite.

Electronic Structure, Stability and Magnetic Properties of Fe_3C (Cementite) with 2*p* and 3*p* Impurities.

Cementite as a bulk compound in the Fe-C system is metastable with respect to α-Fe and graphite at all temperatures, and this graphitization process

plays an important role for iron alloys with high carbon content e.g., cast irons. Alloying impurities may dissolve in Fe and (or) in Fe_3C and may favor or prevent the graphitization. The phase stability and physical properties of Fe_3C can be varied within a wide range by substitutional or interstitial additions of appropriate elements. Here, we study the electronic structure, enthalpy of formation and magnetic properties of cementite Fe_3C doped with 2*p* (N, O, B) and 3*p* (Si, Al, S, P) impurities. We predict that all 2*p* elements, phosphorus and sulfur replace carbon and have a small effect on the values of the magnetic moments of the nearest iron atoms, while aluminum and silicon substitute for iron in special positions and reduce the iron magnetic moments as well as the total magnetization.

All 2*p* and 3*p* impurities have a small effect on the location of the Fermi level, which is in the region of almost-filled Fe3$d\uparrow$ states and local minimum of partially-occupied Fe3$d\downarrow$ states, similar to the undoped cementite and γ-Fe. The main changes occur near the bottom of the hybrid band, and we find that the total density of states increases for all 2*p* and 3*p* impurities except for oxygen (Table 1). All impurities mainly contribute in the spin-up density of states $N^{\uparrow}(E_F)^{imp}$, while $N^{\downarrow}(E_F)^{imp}$ remains much lower.

Each impurity (except for oxygen) substituted for carbon has a small negative magnetic moment and slightly changes the magnetic moments at the nearest iron atoms in special (Fe_s) and general (Fe_g) positions (Figure 4). The total magnetization is also little affected. The impurities, which substitute for iron (Al, Si) have antiferromagnetic coupling with iron, but they essentially decrease the magnetic moments of the nearest iron atoms and magnetization (Table 1).

The positive formation energy ΔH = 0.06 eV/atom was obtained for the unalloyed cementite. The experimental finding (0.05–0.07 eV/atom) also gave the positive value testifying that Fe_3C is a metastable bulk compound. To estimate the effect of 2*p* and 3*p* impurities on the stability of cementite, we analyzed the enthalpy of formation energies ΔH, which were calculated as the difference of total energies Fe_3C-X, where impurity X was substituted in the preferable site, iron, carbon, and impurity in their ground states.

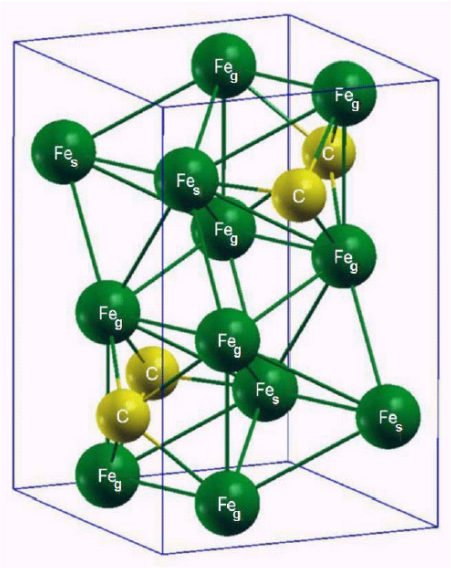

Figure 4. Unit cell of cementite showing general (Fe_g) and special (Fe_s) lattice positions.

We found that ΔH is negative only for cementite with boron addition $Fe_3C_{0.75}B_{0.25}$, i.e., boron stabilizes orthorhombic cementite and prevents the graphitization (dissociation of metastable cementite with the formation of bcc Fe and graphite).

A small stabilizing effect was obtained for nitrogen, while oxygen and sulfur slightly destabilize cementite. Aluminum and especially silicon lead to strong destabilization of cementite, which explains their effects on the promoting of graphitization. Thus, our results reveal that among 2*p* and 3*p* impurities, only aluminum and silicon may completely suppress the formation of cementite.

Production of Third-Generation High-Strength Steels

Development of a third-generation AHSS based upon a nano-acicular duplex microstructure will require new strategies in alloy chemistry to produce nano-scale microstructures in continuously-cooled wrought steel products. The important issues in developing nano-acicular duplex steels of high strength are (1) understanding the fundamental alloy effects in Fe-X-C and Fe-X-N systems, (2) predicting physical properties of these alloys, (3) eliminating

Table 1. Total density of states at the Fermi level $N^{\uparrow}(E_F)$ and $N^{\downarrow}(E_F)$ and the contribution of impurity states ($N^{\uparrow}(E_F)$ and $N^{\uparrow}(E_F)^{imp}$ (states/eV*f.u.); the averaged local magnetic moment (m, in μ_B), the total magnetization (M, in μ_B) and the formation energy ΔH (eV/f.u.) for cementite with 2*p* and 3*p* impurities.

	$Fe_3C_{0.75}B_{0.25}$	Fe_3C	$Fe_3C_{0.75}N_{0.25}$	$Fe_3C_{0.75}O_{0.25}$
$N^{\uparrow}(E_F)$	1.24	1.19	1.26	0.78
$N^{\downarrow}(E_F)$	1.83	1.78	1.92	1.54
$N^{\uparrow}(E_F)^{imp}$	0.011	0.012	0.036	0.029
$N^{\downarrow}(E_F)^{imp}$	0.004	0.005	0.009	0.012
m(X) μ_B	–0.14	–0.12	–0.06	0.14
$m(Fe_s)$ μ_B	2.10	1.96	1.98	2.19
$m(Fe_g)$ μ_B	1.89	1.86	1.88	2.09
M, μ_B	1.90	1.85	1.89	2.05
ΔH, eV	–0.06	0.22	0.18	0.33
	$Fe_{2.75}Al_{0.25}C$	$Fe_{2.75}Si_{0.25}C$	$Fe_3C_{0.75}P_{0.25}$	$Fe_3C_{0.75}S_{0.25}$
$N^{\uparrow}(E_F)$	1.44	1.27	1.06	1.08
$N^{\downarrow}(E_F)$	1.94	2.02	2.19	2.31
$N^{\uparrow}(E_F)^{imp}$	0.006	0.014	0.013	0.022
$N^{\downarrow}(E_F)^{imp}$	0.002	0.003	0.004	0.005
m(X), μ_B	–0.04	–0.04	–0.08	–0.03
$m(Fe_s)$ μ_B	1.34	1.33	2.02	2.08
$m(Fe_g)$	1.70	1.48	1.87	1.89
M, μ_B	1.55	1.54	1.88	1.90
ΔH, eV	0.65	1.29	0.21	0.29

precipitation of ferrite along prior austenite grain boundaries, (4) inoculating the steel to produce intragranular precipitation of the acicular ferrite, (5) controlling the ferrite subunit width during transformation to produce nanometer scale microstructures, and (6) reducing silicon levels to produce steel of better surface finish.

The starting point for many high-strength bainitic alloys is Fe-2Si-2Mn-C, which has sufficient hardenability to reach the bainite start temperature, which avoids allotriomorphic ferrite and pearlite microstructures. The bainite start temperature is largely controlled by the carbon content and decreases with increasing carbon content. Manganese is the next most effective alloy addition with respect to reducing the bainite start temperature and the program of study is examining steel chemistries with higher Mn contents than the first-generation AHSS, ferritic alloys, but substantially less Mn than that used in the second-generation AHSS, austenitic alloys. We expect to utilize manganese in the range of 2 to 14 weight % (wt %) for the nano-acicular duplex steels. The total interstitial content will be reduced to 0.10 wt % to maintain a high chemical driving force for the formation of ferrite. Additions of aluminum, rather than cobalt, will be employed to encourage transformation to ferrite upon continuous cooling. Aluminum has the added benefit of lowering the steel density and as shown in the theoretical studies of this report, aluminum destabilizes the cementite. Thus, the addition of aluminum may lower the required amount of silicon to inhibit cementite formation and encourage incomplete transformation, i.e., retention of austenite.

Missouri University S&T has a strong and active steelmaking program. We have the ability to cast up to 200 pounds of steel of a single chemistry. Steelmaking was performed by melting high-purity charge materials under argon using a coreless induction furnace (see Figure 5). Active oxygen is measured in the ladle using a Hereaus Electronite oxygen probe. Steels are deoxidized by measured additions of aluminum or titanium and subsequently cast into no-bake sand molds. Molds

Figure 5. Photograph of casting steel in the Missouri University S&T foundry.

were designed to produce sound slabs for hot rolling.

An initial study was performed to examine Fe-5Mn-1.5Si-0.35C-0.3Mo steel alloyed with and without nitrogen. The first heat was divided into two casts: the base composition and the base steel modified by the addition of nitrided ferromanganese. Each of these steels was deoxidized with either aluminum or a combination of aluminum and titanium. When both aluminum and titanium were used, the initial addition of aluminum was insufficient to fully deoxidize the melt and deoxidation was finished with titanium. The expectation was that the initial Al_2O_3 formed would act as a nucleation site for Ti_2O_3, which then serves as an inoculant for acicular ferrite.

We discovered very quickly that these nitrided manganese steels were very resistant to bainitic transformation. Indeed, annealed specimens that were furnace cooled had microstructures that were fully martensitic. Figure 6 shows an example of the steel austempered 7 days at 400°C, which was partially transformed. The figure shows that degenerate Widmanstätten ferrite nucleated on TiN particles. The scale of the ferrite width could be measured in microns and the steel composition was deemed unworkable for automotive steel.

A traditional, hard bainitic steel was cast to study nanometer-scaled ferritic microstructures. The steel composition was Fe-0.63C-3.99Co-2.1Mn-1.35Si-0.34Cr-0.21Mo-0.61Al. The steel was

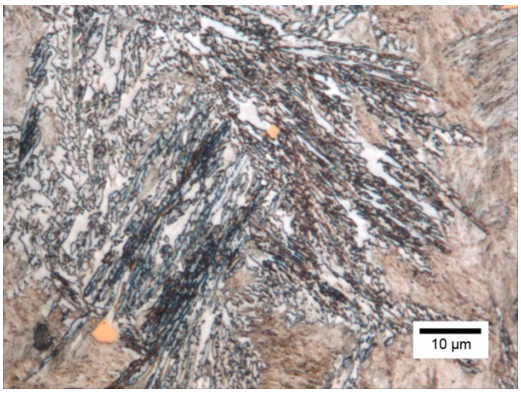

Figure 6. Austempered microstructure of steel alloy with composition Fe-5.01Mn-1.34Si-0.29Mo-0.075Al-0.80Ti-0.029N. Nital etch.

austenitized at 920°C and isothermally transformed at 300°C to produce a classic "basket-weave" microstructure (see Figure 7). This microstructure compares favorably with the α+β titanium alloys developed for high fracture toughness. The scale of the bainitic ferrite was measured by x-ray diffraction to be 10–20 nanometers (nm). The retained austenite was also determined to be less than 10%.

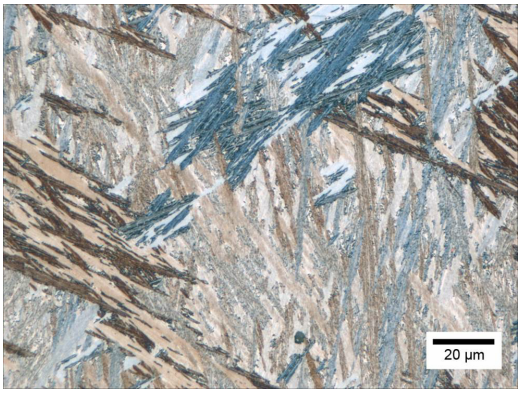

Figure 7. A basket-weave microstructure produced by austempering a Fe-0.63C-3.99Co-2.1Mn-1.35Si-0.34Cr-0.21Mo-0.61Al steel at 300°C for 3 days. Nital etch and imaged with cross-polarized light and ¼ wavelength filter.

The high cost of cobalt makes the hard bainitic type steel impractical for automotive applications. However, we will use this steel in our acoustic-emission studies of bainitic transformation. There are three definitions of bainite currently in use. The surface-relief theory states that a displacive transformation produces a surface-relief distortion and that this transformation occurs at velocities

fast enough to produce acoustic emissions. Thus far, these emissions have only been observed in continuously-cooled steels. We are building a facility to measure the emissions during isothermal transformation and will study this phenomenon. It is also possible that these emissions are a displacive relaxation in the parent phase and these relaxations occur as a dynamic strain-aging effect with sudden dislocation multiplication. Understanding this reaction will be fundamental in the design of new steels.

Aluminum is the only other addition to steel that is known to increase bainitic transformation kinetics. Aluminum has the added benefit of reducing the density of steel. Aluminum has a lower mass and produces lattice dilatation; both contribute to reducing the density. Manganese will also reduce the density, but to a lesser degree. A new steel was formulated with the following nominal composition: Fe-13Mn-4Al-1Si-0.1C. The steel was produced at Missouri University S&T. These high-manganese compositions require wet chemical analysis and this information was not available at the time of this report. The density of the cast steel was measured to be 7.2 g/cm^3 and this would be approximately a 7% decrease in density relative to typical automotive steels. This low density is similar to that of TWIP steels. The cast microstructure was a combination of ferrite and austenite. When slowly cooled from an elevated temperature, the austenite transformed producing a degenerate Widmanstätten ferrite (see Figure 8). Degenerate structures are produced by sympathetic nucleation of small subunits of ferrite and are often associated with the phenomenon of incomplete transformation.

FactSage, a free-energy minimization modeling program, was used to predict the equilibrium phase stabilities of this alloy system. The simulation is shown in Figure 9. There was good agreement between the observed and calculated ferrite and austenite content. Based on these results, we will use FactSage to determine appropriate alloy content to produce steel that can be fully austenitized at typical hot-working temperatures. This composition will also be measured directly from the austenitic regions of our cast steel.

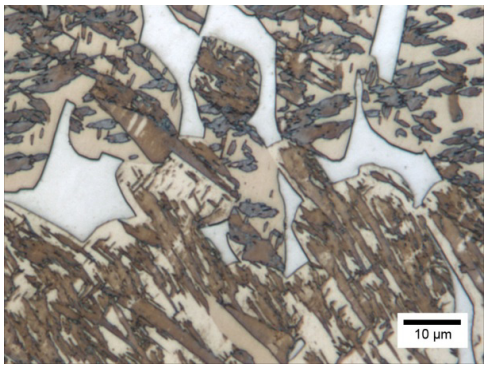

Figure 8. Microstructure of Fe-13Mn-4Al-1Si-0.1C alloy that was heated to 1000ºC then slowly cooled to ambient temperature. Interdendritic ferrite appears as the light contrast feature and degenerated Widmanstätten ferrite appears as the darkest contrast feature. Etched with 10% $Na_2S_2O_5$.

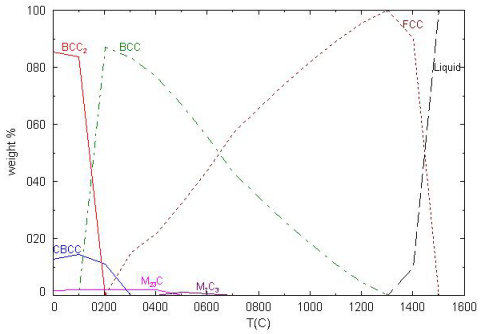

Figure 9. FactSage predictions of phase composition as a function of temperature for the Fe-13Mn-4Al-1Si-0.1C alloy. A duplex mixture of ferrite and austenite is predicted at typical hot working temperatures between 900 and 1100°C.

The transformed austenite shown in Figure 8 has many of the qualities desired for a third-generation advanced high-strength steel: a basket-weave microstructure of ferrite plates in a matrix of retained austenite. Future experiments on this steel will examine hot working of the steel, grain-size control, controlled cooling, microstructural characterization, and mechanical properties.

Presentations/Publications/Patents

1. M. C. McGrath, D. C. Van Aken, J. Medvedeva, S. N. Lekakh, and V. L. Richards. "Advanced High Strength Steels (AHSS) with Duplex Ferrite and Austenite Microstructures," MS&T 08 Conference and Exhibition, Pittsburgh, PA October 5–9, 2008.

S. Sheet Formability and Springback of Advanced High-Strength Steels—CSM

Principal Investigator: David K. Matlock
Advanced Steel Processing and Products Research Center
Department of Metallurgical and Materials Engineering
Colorado School of Mines
Golden, CO 80401
(303) 273-3775; fax: (303) 273-3016; e-mail: dmatlock@mines.edu

Co-Principal Investigator: John G. Speer
Advanced Steel Processing and Products Research Center
Department of Metallurgical and Materials Engineering
Colorado School of Mines
Golden, CO 80401
(303) 273-3897; fax: (303) 273-3016; e-mail: djspeer@mines.edu

Co-Principal Investigator: James G. Schroth
General Motors
R & D Center
30500 Mound Road
M/C 480-106-212
Warren, MI 48090-9055
(586) 986-0977; fax: (586) 986-9204; e-mail: james.g.schroth@gm.com

Principal Investigator: Robert H. Wagoner
Department of Materials Science and Engineering
The Ohio State University
2041 College Road
Columbus OH 43210
(614) 292-2079; fax: (614) 292-6530; e-mail: wagoner.2@osu.edu

Technology Area Development Manager: Joseph A. Carpenter
(202) 586-1022; fax: (202) 586-1600; e-mail: joseph.carpenter@ee.doe.gov

Field Project Officer: Aaron D. Yocum
(304) 285-4852; fax: (304) 285-4403; e-mail: aaron.yocum@netl.doe.gov

---

Contractor: Colorado School of Mines (CSM)
National Science Foundation (NSF) Award CMMI 0729114, jointly funded by NSF and DOE

Objective

- Identify new processing routes and microstructures which lead to economical steels with properties characteristic of third-generation advanced high-strength steel (AHSS).
- Experimentally and theoretically evaluate properties of new AHSS materials.

Approach

- Utilize theoretical predictions developed by the authors and others to predict ideal microstructures that lead to potential strength/ductility combinations characteristic of the third-generation AHSS.

- Evaluate and develop novel laboratory processing methods to produce materials with controlled variations in phase volume fractions, distributions, and properties.
- Produce sample material for use in this project as well as in the companion springback study at the Ohio State University, a partner with CSM through the NSF GOALI program.
- Experimentally evaluate the mechanical properties, including formability, of the experimental steels.
- Compare experimentally-measured properties to predictions of the theoretical models.
- For materials which appear promising based on laboratory data, assess potential paths to process materials on a larger scale.

Accomplishments

- Supported Senior Design Project at the CSM. The project entitled "Design Concepts to Produce the Next Generation of Advanced High Strength Sheet Steels," was completed during the spring semester, 2008.
- Successfully recruited a PhD graduate student, Mr. Paul Gibbs.
- Research plan was reviewed in March 2008 with the sponsors of the Advanced Steel Processing and Products Research Center at the CSM.
- Initial materials for evaluation have been received and initial heat-treat experiments have begun.

Future Direction

- Identify and obtain additional materials for analysis.
- Evaluate the microstructures and properties of heat-treated manganese (Mn) steels.
- Evaluate the mechanical properties of austenitic stainless steels with controlled volume fractions of deformation-induced martensite.
- Initiate discussions about the applicability of including duplex stainless steels in the study.
- Assess predictions of theoretical models for the deformation behavior of multi-constituent steels and compare to predictions based on simplified composite model.
- Support a senior design project at CSM for the spring semester of 2009.

Introduction

This project is in the early stages of development and has concentrated on literature review and analysis of the composite models on which the original research proposal was based. The project was budgeted for 3 years, and DOE/NSF funded the project over 4 years. The PhD graduate student, Mr. Paul J. Gibbs, initiated his graduate studies in August 2008, after completing his BS in Metallurgical and Materials Engineering at CSM in May 2008. In this report, the background for the project is highlighted, along with the materials and processing approaches that have been identified for the first phase of the research program.

Background

Recently, significant interest has been expressed by steel-producing and steel-using industries for development of the next generation of advanced high-strength steels (AHSSs) sheet to meet the demanding requirements for strength, formability, toughness, cost, etc [1–3]. To produce the new AHSS sheet steels, unique processing schemes will be required. It is anticipated that these will be initially based on modifications to routes currently employed to produce dual phase (DP) and transformation-induced plasticity (TRIP) steels. To produce materials with the desired final properties, several microstructural features must be simultaneously and independently controlled. These include: number of constituents (e.g., phases) and constituent volume fractions, sizes,

and distributions, along with the mechanical properties (e.g., strength and strain-hardening behavior) of the individual constituents.

A methodology to assess effects of microstructural variables in new AHSS grades has been demonstrated [2, 3] based on the composite model approach of Mileiko [4]. Figure 1 compares predicted effects of systematic microstructural variations, obtained by increasing the martensite volume fraction (up to 70 pct), in hypothetical, two-component composite materials of ferrite plus martensite or stable austenite plus martensite [2, 3]. These predictions are superimposed on a strength-ductility map often used to compare sheet-steel properties [1] and identify property bands associated with first- and second-generation AHSS. For these calculations, specific properties for each phase were assumed based on literature data and predictions utilized a composite model for two ductile constituents assuming iso-strain [2]. Figure 1 shows that the properties of a wide variety of sheet-steel families, including the first-generation AHSS steels, are reasonably predicted with a two-component system based on ferritic steels and that steels in the third-generation band may be modeled by various combinations of martensite with stable austenite. Similar calculations based on metastable austenite have shown that the resulting composite properties depend sensitively on austenite stability against deformation-induced transformation to martensite [3].

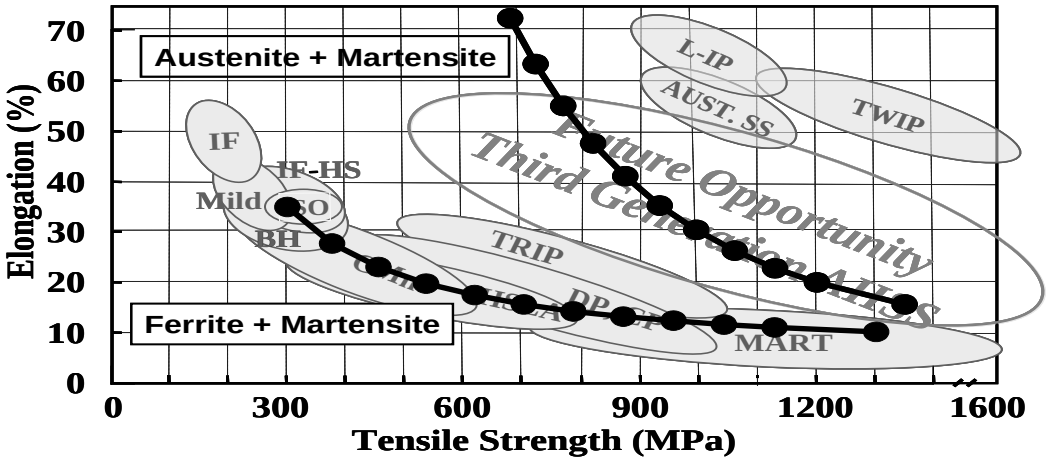

Figure 1. Predicted [2, 3] strength/ductility combinations for two hypothetical steel families with systematically-varied martensite volume fractions with property bands for various classes of conventional and AHSS steels [1]. Predictions shown are for composites consisting of ferrite + martensite or stable austenite + martensite.

The analysis summarized in Figure 1 successfully predicted strength-ductility properties for existing ferritic-based steels from low-strength interstitial free (IF) to high-strength martensitic steels. While predictions from the composite analyses provide insight into microstructural combinations required for the new AHSS, the simplifying assumptions (each constituent was assumed to deform independently and iso-strain was assumed) embedded in the composite model [4] and consideration of actual deformation behavior of and interactions between constituents will be required to predict optimal microstructures. Nonetheless, it appears clear that the third generation of AHSS will consist of complex microstructural combinations, with significant use of both high-strength constituents (e.g., martensite, bainite, ultrafine-grained ferrite, etc.) and high-ductility constituents with significant strain-hardening capacity (e.g., austenite with controlled stability against deformation-induced transformation to martensite) [2, 3]. The methodology has been applied, as illustrated in the following sections, to predict properties of steels of interest here.

Predictions of AHSS Microstructures and Properties

The predictions presented in Figure 1 depend on variations in the mechanical properties of the individual constituents used in the model. Figure 2 presents one example which shows the significance of increasing the strength of the stable austenite from 640 MPa used in Figure 1 to 850 MPa with a corresponding decrease in uniform strain from 0.6 to 0.4. These property changes are consistent with a mechanism such as temper rolling or refinement of the austenite grain size. For Figure 2, the volume fraction of martensite was varied from 0 to 0.7, and the martensite properties were assumed constant. An increase in austenite strength with a corresponding *decrease* in the true uniform strain, is shown to lead to an *increase* in ductility of the composite at a given strength level. The observation that increasing the strength of one phase leads to a ductility increase is interesting, counterintuitive, and illustrates the importance of phase interactions on the overall properties of multi-phase steels.

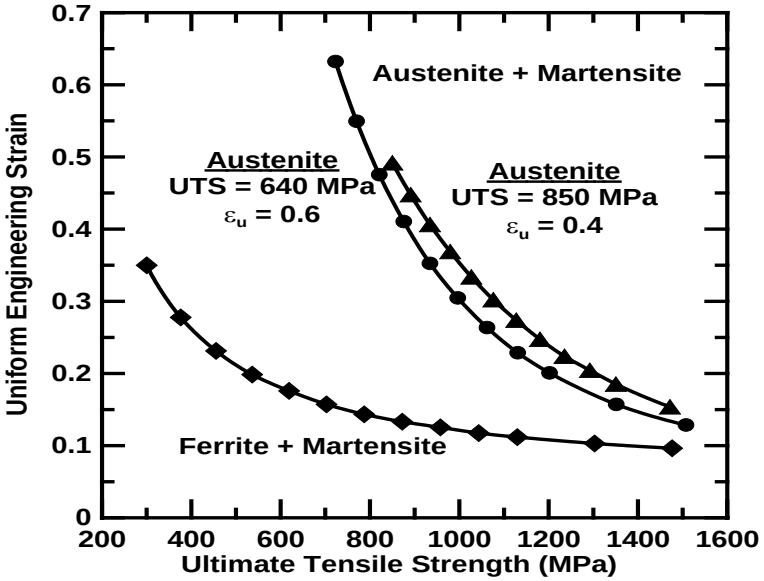

Figure 2. Influence of austenite properties on the predicted strength/ductility combinations shown in Figure 1 obtained by applying Mileiko's analysis [4]. The effect of increasing the austenite ultimate tensile strength (UTS) to 850 MPa with a corresponding decrease in ductility are shown. For each material, the ferrite + martensite data used in the calculations are UTS and true uniform strain, ε_u. The specific data used are: ferrite UTS = 300 MPa, ε_u = 0.3 [5, 6]; stable austenite, UTS = 640 MPa, ε_u = 0.6 [7]; and martensite, UTS = 2000 MPa, ε_u = 0.08 [5, 6].

The importance of metastable austenite transformation to martensite with strain and variations in austenite stability have been evaluated with predictions based on the Mileiko model for steels with hypothetical microstructures containing up to 85% austenite [2, 3]. Following the composite modeling approach used to generate Figures 1 and 2, the results with metastable austenite highlight the importance of controlling the austenite stability. Specifically, low austenite stability leads to rapid (with strain) austenite transformation to martensite resulting in properties similar to dual phase steels while relatively high austenite stability delays martensite formation, improving work hardening at high strains leading to suppression of necking and higher ductilities. These predictions suggest that the next generation of AHSS may consist of complex microstructural combinations, with significant contents of high-strength phases, which could be martensite as considered here, bainite, or ultrafine-grained or cold-worked ferrite, and highly-ductile phases

with significant capacity for strain-hardening phases (e.g., austenite). Once a desirable combination of properties and microstructure is identified, then novel techniques must be identified to produce microstructural constituents with the necessary deformation response.

Evaluation of Methodologies to Produce Third-Generation AHSS

Recently, there has been considerable research interest in cold-rolled steels annealed at temperatures greater than A_3 or at an intercritical temperature and then rapidly cooled to a temperature below the martensite-start temperature, M_s, but above the martensite-finish temperature, M_F. This sequence is akin to a modified martempering process as employed in quenched and tempered steels, but is designed to modify the microstructure rather than the thermal stresses. After cooling, the material is held at the quench temperature (QT) or is reheated slightly and held for a specified time prior to cooling to room temperature. Materials produced by this interrupted quenching process have been referred to by a variety of terms including "quenching and partitioning (Q&P)" [8, 9], "TRIP-dual" [10], "TRIP aided bainitic ferrite (TBF)" [11], "isothermal quench and tempering (IQ+T)" [12], and "quenching, partitioning, and tempering (Q-P-T)" [13]. For the discussion that follows, steels from these studies are referred to as "Q&P" steels, although Q&P processing usually implies quenching temperatures meaningfully below the martensite-start temperature (M_s). On quenching, the amount of initial martensite that forms depends on the M_s for the austenite present during annealing, and the difference between the M_s and QT. Subsequent changes in the microstructure on isothermal holding prior to cooling to room temperature depend on alloy content, temperature, and holding time.

To illustrate the potential for the Q&P process to produce AHSS materials of interest, Streicher et al. evaluated the heat-treating response of a 0.19C, 1.59Mn, 1.63Si (wt %) alloy processed with Q&P temperature-time histories as well as thermal histories designed to simulate more conventionally heat-treated Q&T and austempered TRIP steels [9, 14]. Figure 3 correlates ultimate tensile strengths with total elongations for one-step and two-step Q&P materials annealed from both above and below the A_{c3}, with similar data on dual phase, TRIP, and martensitic steels. In addition to steels processed by Streicher et al., Figure 3 also includes data from the literature [9, 14]. The Q&P materials included samples with austenite volume fractions up to 16 pct. The dual phase steels included here were of relatively high strength, owing to the effects of relatively high martensite fractions.

The data in Figure 3 show that strength/ductility combinations characteristic of the third generation of AHSS were obtained, indicating that Q&P processing may be a viable route to producing new steel grades. Clearly, the data obtained to date are promising, but significantly more work is required to optimize Q&P processing and design alloys and process histories compatible with current and future production constraints.

Recently, two studies designed to extend current production technologies to higher strength-ductility regimes have been shown to produce materials with properties in the third-generation AHSS property band in Figure 1. Wakita et al. [15], in their study on thermomechanically-controlled processing (TMCP), evaluated ultrafine TRIP-aided multi-phase microstructures in a 0.19C, 1.96Si, 2.01Mn (wt pct) low-carbon steel. They found that heavy deformation at low austenite rolling temperatures led to the formation of 2 micrometer (μm) ferrite, a high volume fraction of retained austenite (on the order of 25 pct), and a modification of the retained-austenite morphology from film-like to granular. The resulting ultra-fine TRIP microstructure exhibited a tensile strength of 1080 MPa and total elongation of 26.9 pct. The high ductilities were attributed to austenite which was partially stabilized by the ultrafine microstructure and only transformed at higher strains, leading to high work-hardening rates which suppressed necking.

In comparison to the work of Wakita et al.[15], Merwin [16, 17] evaluated the effects of processing on the TRIP behavior of a series of 0.1 wt pct C steels with Mn contents in the range of 5.2 to 7.1 wt pct. Data were obtained for material in the as-hot-rolled and in the cold-rolled

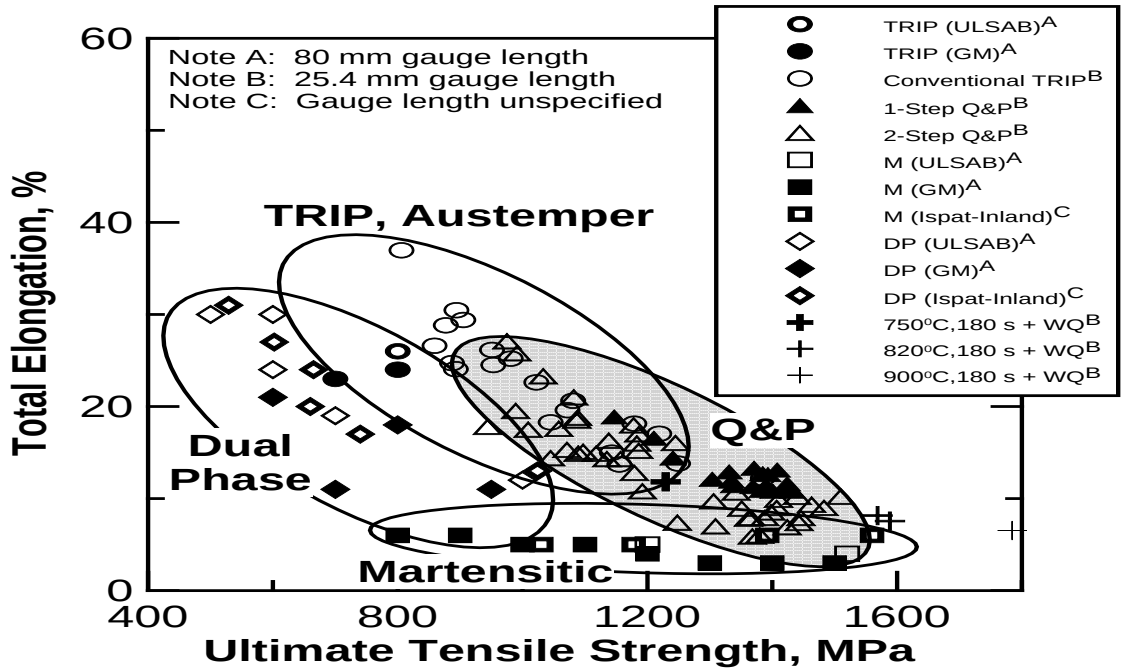

Figure 3. Total elongation vs. ultimate tensile strength for sheet steels processed with microstructures characteristic of TRIP, dual phase (DP), martensitic, Q&P materials. References for the individual data are summarized elsewhere [9, 14].

and annealed conditions. In the as-hot-rolled condition, all microstructures were martensite (i.e., the alloys were fully hardenable even at the coil cooling rates applicable to conventional hot-strip mill processing). Cold rolling and annealing of the initially martensitic structure resulted in very fine ferrite-austenite microstructures, with the amount of austenite dependent on the annealing temperatures and times chosen to simulate hot and cold spots in batch annealing. In the cold-rolled and annealed samples, retained austenite contents up to approximately 38 pct were observed. Tensile data were obtained and Figure 4 correlates UTS and total elongation values for cold-rolled and annealed materials with the desired property band for third-generation AHSS steels. Also shown is the result from the thermomechanical processing study of Wakita et al. [15]. Data for samples from Merwin [16, 17] and the data of Wakita et al. [15] that plot within the desired property band correspond to samples with high volume fractions of retained austenite. This comparison indicates that development of the next generation of steels may be possible with controlled Mn additions along with controlled thermomechanical processing to produce ultrafine-grained ferrite for strength and high volume fractions of retained austenite for ductility.

Additional processing routes have been identified based on recent results on new AHSS products published in the proceedings of the International Conference on New Developments in Advanced High Strength Sheet Steels, held in Orlando, Florida, on June 15–18, 2008 [18]. These include modifications to traditional DP, TRIP, and martensitic steel processing, and further analysis of these to produce property combinations of interest are underway.

Status of Current Research Activities

Several alloying and processing approaches that have been identified to assess the predictability of the composite model that has been developed and to assess microstructural combinations that lead to strength-ductility combinations characteristic of the third generation of AHSS currently under study. Following the work of Merwin [16, 17], a processing methodology to increase austenite stability via Mn partitioning is currently being evaluated at CSM. Hot- and cold-rolled materials

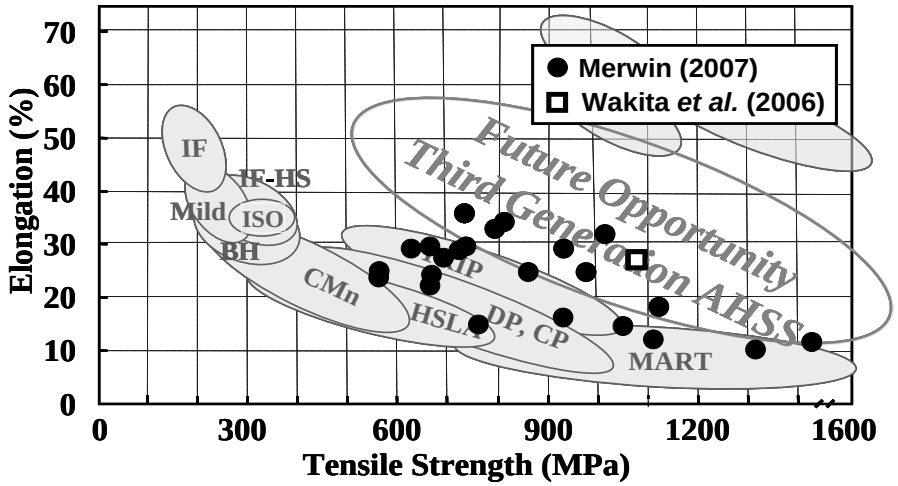

Figure 4. A comparison of tensile strength and tensile elongation data for thermomechanically controlled processed, Mn-modified, low-carbon steels with fine microstructures, some with significant amounts of retained austenite compared to the opportunity band for third-generation AHSS. Data shown from Wakita et al. [15] and Merwin [16, 17].

have been obtained from US Steel Corporation from the same heats used by Merwin.

Metastable austenitic stainless steels, prestrained a constant amount at various temperatures below room temperature to produce a series of samples with different initial martensite volume fractions, are being used to directly evaluate the predictability of the composite modeling. Specifically, tensile tests on these materials at and above room temperature provide data on materials with different austenite stabilities (the austenite stability against deformation-induced transformation increases with test temperature). Initial data on metastable austenitic stainless steels were obtained as part of the spring 2008 senior design project at the CSM. A follow-up senior design project is being planned for 2009. Initial evaluation of duplex stainless steels as an "ideal material" to assess deformation fundamentals in two-constituent materials has also been completed.

Conclusions

The composite methodology based on iso-strain deformation, while simplistic, can be used to predict the effects of microstructural, property, and testing variables including grain size; second-phase volume fraction, size and distribution; imposed strain rate; strain-hardening behavior of the martensite; etc. Potential approaches to develop new steels with microstructures that produce mechanical properties characteristic of the third generation of AHSS have been identified. The importance of combining an understanding of fundamental deformation mechanisms with predictions based on appropriate composite models to describe the deformation behavior of multiphase materials has been illustrated. From these analyses, it is predicted that the third generation of AHSS will require significant amounts of a high-strength constituent (e.g., martensite or ultrafine-grained ferrite) and significant amounts of austenite. Furthermore, the austenite must be designed with controlled deformation-induced transformation behavior to modify the work-hardening response. While the required microstructures are complex, alloying and processing approaches, particularly involving Q&P processing or Mn-modified low-carbon steels, might be used to produce the desired microstructures. It is also clear that significant research is still required to design alloying and processing methodologies to optimize third-generation AHSS material properties.

Presentations/Publications/Patents

1. David K. Matlock (Speaker) and John G. Speer, "Third Generation of AHSS: Microstructure Design Concepts," presented at Materials and Textures in Steels

(MATS2008), Jamshedpur, India, February 6, 2008 (invited presentation).

2. David K. Matlock, "Collaborative Proposal: GOALI: AHSS: Sheet Formability and Springback of Advanced High Strength Steels—An NSF/DOE Funded Program," Presented at the Advanced Steel Processing and Products Research Center Semi-Annual Review Meeting, Golden, CO, March 18, 2008.
3. David K. Matlock, "Summary: International Conference on New Developments in Advanced High Strength Sheet Steels," Conference Closing Keynote Lecture, Orlando, Florida, June 18, 2008.
4. David K. Matlock, "Advanced High Strength Sheet Steels: Microstructures, Properties, and Formability," 20th Posco Conference on Iron and Steel Technology, Postech University, Pohang, Korea, August, 27, 2008, keynote lecture.
5. Paul J. Gibbs, "Development of the Third Generation of Advanced High Strength Sheet Steels," Presented at the Advanced Steel Processing and Products Research Center Semi-Annual Review Meeting, Golden, CO, September 23, 2008.
6. David K. Matlock, "Advanced High Strength Sheet Steels: Microstructures, Properties, and Formability," invited lecture to the Saudi ASM Chapter; meeting held at the SABIC Technology Center in Jubail, Saudi Arabia on November 9, 2008.
7. D. K. Matlock and J. G. Speer, "Third Generation of AHSS: Microstructure Design Concepts," *Proceedings International Conference on Microstructure and Texture in Steels*, ed. by A. Haldar, Springer-Verlag, London, 2008, in press.
8. D. K. Matlock and J. G. Speer, "Processing Opportunities for New Advanced High Strength Sheet Steels," *Proceedings of the 2nd International Conference on Thermo-Mechanical Simulation and Processing of Steels*, ed. by S. K. Chaudhuri, B. K. Jha, S. Srikant, P. K. Maini, A. Deva, and R. Datta, Allied Publishers Ltd., New Dehli, India, 2008, pp. 169–179.

References

1. "Third Generation Advanced High Strength Steel (AHSS)," Research and Development Solicitation, AISI, Washington, D.C., 2006.
2. D. K. Matlock and J. G. Speer, *Proceedings of the 3rd International Conference on Structural Steels*, ed. by H. C. Lee, The Korean Institute of Metals and Materials, Seoul, Korea, 2006, pp. 774–781.
3. D. K. Matlock and J. G. Speer, *Proceedings International Conference on Microstructure and Texture in Steels*, ed. by A. Haldar, Springer-Verlag, London, 2008, in press.
4. S. T. Mileiko, *J. of Mat. Sci.*, vol. 4, 1969, pp. 974–977.
5. R. G. Davies, *Metall. Trans. A*, vol. 9A, 1978, pp. 451–455.
6. R. G. Davies, *Metall. Trans. A*, vol. 9A, 1978, pp. 41–52.
7. G. Frommeyer, U. Brüx, and P. Neumann, *ISIJ Int*., vol. 43, no. 3, 2003, pp. 438–446.
8. J. G. Speer, A. M. Streicher, D. K. Matlock, F. Rizzo, and G. Krauss, *Austenite Formation and Decomposition*, ed. by E.B. Damm and M. J. Merwin, TMS, Warrendale, PA, 2003, pp. 505–522.
9. A. M. Streicher, J. G. Speer, D. K. Matlock, and B.C. De Cooman, *International Conference on Advanced High Strength Sheet Steels for Automotive Applications Proceedings*, edited by J. G. Speer, AIST, Warrendale, PA, 2004, pp. 51–62.
10. H. J. Jun and N. Fonstein, in *Proceedings, International Conference on New Developments in Advanced High-Strength Sheet Steels*, ed. by J. G. Speer, B. Nelson, and R. Pradhan, AIST, Warrendale, PA, 2008, pp. 155–168.
11. J. W. Jin, S. H. Byun, S. B. Lee, S. I. Kim, C.S. Oh, N.K. and K.M. Cho, in *Proceedings, International Conference on New Developments in Advanced High-Strength Sheet Steels*, ed. by J. G. Speer, B. Nelson, and R. Pradhan, AIST, Warrendale, PA, 2008, pp. 169–178.

12. S. Cobo, C. Colin, and S. Allain, *Proceedings, New Developments on Metallurgy and Applications of High Strength Steels*, edited by Teresa Perez, published by Tenaris, Ternium, and Argentina Association of Materials, Buenos Aires, Argentina, 2008, Paper #65.
13. T. Y. Hsu and Z. Xu, *Mat. Sci. Forum*, vols. 561–565, 2007, pp. 2283–2286.
14. A. Clarke, Ph.D Thesis, *Carbon Partitioning Into Austenite From Martensite In A Silicon-Containing High Strength Sheet Steel*, Colorado School of Mines, Golden, CO, 2006.
15. M. Wakita, Y. Adachi, and Y. Tomota, *Materials Science Forum*, vols., 539–543, 2007, pp. 4351–4536.
16. M. J. Merwin, SAE Technical Paper #2007-01-0336, SAE, Warrendale, PA, 2007.
17. M. J. Merwin, *Proceedings of Steel Properties and Applications Conference*, edited by L. C. Oldham, AIST, Warrendale, PA, 2007, pp. 1017–1038.
18. J. G. Speer, B. Nelson, and R. Pradhan, editors, *Proceedings, International Conference on New Developments in Advanced High-Strength Sheet Steels*, AIST, Warrendale, PA, 2008.

T. Sheet Formability and Springback of Advanced High-Strength Steels—OSU

Principal Investigator: Robert H. Wagoner
Distinguished Professor of Engineering, George R. Smith Chair, and Professor, Department of Materials Science and Engineering, Ohio State University
484 Watts Hall, 2041 N. College Rd, Columbus, OH 43210
(614) 292-2079; fax: (614) 292-6530; e-mail: wagoner.2@osu.edu

Co-Principal Investigator: James G. Schroth
General Motors R & D Center, 30500 Mound Road, M/C 480-106-212, Warren, MI 48090-9055
(586) 986-0977; fax: (586) 986-9204; e-mail: james.g.schroth@gm.com

Principal Investigator: Partner University: David K. Matlock
Advanced Steel Processing and Products Research Center
Department of Metallurgical and Materials Engineering, Colorado School of Mines
Golden, CO 80401
(303) 273-3775; fax: (303) 273-3016; e-mail: dmatlock@mines.edu

Technology Area Development Manager: Joseph A. Carpenter
(202) 586-1022; fax: (202) 586-1600; e-mail: joseph.carpenter@ee.doe.gov

Field Project Officer: Aaron D. Yocum
(304) 285-4852; fax: (304) 285-4403; e-mail: aaron.yocum@netl.doe.gov

---

Contractor: The Ohio State University Research Foundation
National Science Foundation Award CMMI-0727641, jointly funded by NSF and DOE

Objectives

- Process Development: formability and springback of existing and new advanced high- strength steels (AHSSs)
- Material Development: identification of new processing routes and microstructures upon which to base a 3rd generation of AHSS
- Educational Program: attraction of promising and diverse students to related technical areas at both undergraduate and graduate levels

Approach

- Measure strain hardening in complex paths
- Devise advanced constitutive equations, implement in finite-element (FE) model
- Measure springback
- Simulate springback
- Simulate draw-bend tests

Accomplishments

- Three characteristics are found in reverse loading tests: Bauschinger effect, transient behavior near re-yielding domain, and permanent softening
- Two-path tests show complicated but systematic directional-hardening behaviors

- Developed a novel one-dimensional (1-D) constitutive equation which can predict post-uniform behavior well based on total elongation.
- Developed a thermomechanical FE model and used it with 1-D constitutive law to predict AHSS failure without damage mechanics.
- Developed three-dimensional (3-D) constitutive equations which have good agreement with tension/compression (T/C), compression/tension (C/T) test.
- As the back-force increases, the springback angle can drop quickly with increasing material strength. This behavior is pronounced at low bend radius (R) to thickness (t) (R/t) ratios.
- Anticlastic curvature and curl radius have direct implication on the springback angle in the draw-bend specimen.
- Constructed a new formability test for a draw-bend test and identified the importance of thermal effect.

Future Direction

- Develop 1-D constitutive equation for transformation-induced plasticity (TRIP) steels
- Compare constitutive equation with balanced biaxial bulge test at elevated temperatures
- Simulate springback with 3-D constitutive equations
- Springback test of AHSS at various roller sizes

Introduction

There is a growing need to conserve energy, reduce environmental impact, and increase energy for the performance of transportation vehicles. Based on the requirement of the marketplace, advanced high-strength steels (AHSS) are produced and provide outstanding mechanical properties in strength and ductility. Among the fundamental technical questions which need to be addressed before AH SS are widely used, sheet formability and springback are the most crucial ones. In this report, springback and formability are investigated and experiments and simulations are applied to the AHSS.

Springback Objective

"Springback" is the elastically driven recovery after forming material into a useful shape and releasing the forming force. The inability to accurately predict springback is a major cost factor in industry. To provide enough knowledge and tools to obtain reliable, precise prediction of springback, the following steps are taken for AHSS.

1. Conduct T/C, C/T, two-path, and biaxial-bulge tests.
2. Devise accurate constitutive equations.
3. Conduct draw-bend springback tests.
4. Develop simulations of springback.

Measure Strain Hardening for Complex Paths

Tension/Compression and Compression/Tension Tests

Springback is sensitive to transient hardening and stabilized T/C and C/T tests are necessary for accurate springback prediction. The laboratory equipment (Figure 1) developed by OSU is used to obtain accurate experimental results. T/C and C/T tests are applied to three grades of dual phase (DP) steels and one grade of transformation-induced plasticity (TRIP) steels: DP590, DP780, DP980, and TRIP780. Figure 2 shows the results of C/T tests with different compression strain compared with the monotonic tension test for DP590. From the experimental results, three characteristics are found: (a) Bauschinger effect, (b) transient behavior near re-yielding domain, and (c) permanent softening. Taking into account the behavior of Figure 2 in the simulations of springback will massively reduce error.

Figure 1. T/C and C/T test device developed by OSU.

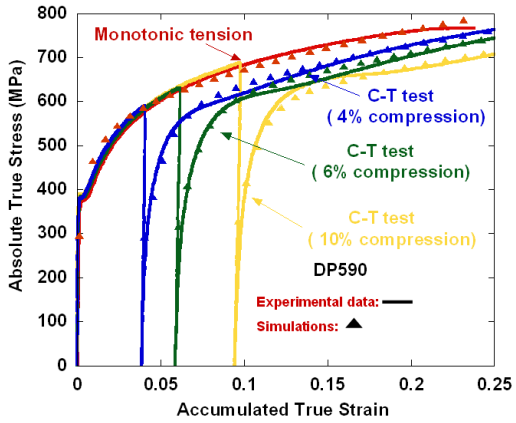

Figure 2. C/T tests and monotonic tension test compared with 3-D constitutive equations (DP590).

Two-Path Tensile Tests

Non-proportional loading results are important for devising precise 3-D constitutive equations for the AHSS. During two-path tensile tests for DP980, the specimens are preloaded along the rolling direction (RD) followed by different loading paths (RD, transverse direction (TD), and 45-degree direction). The different material- hardening behaviors are observed in Figure 3. It shows that the directional-hardening behaviors are complicated but systematic.

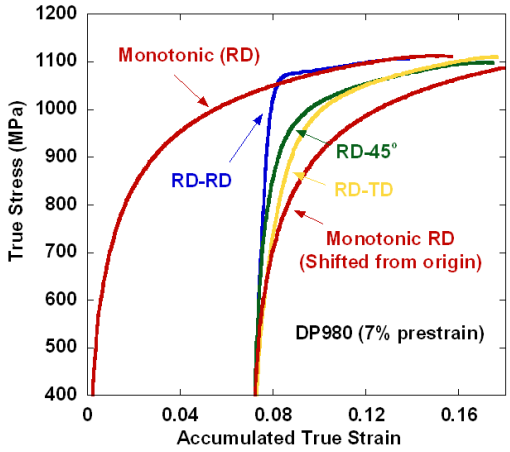

Figure 3. Two-path tensile tests compared with monotonic tension (DP980).

Balanced Biaxial Bulge Tests

Balanced biaxial bulge tests are conducted in cooperation with the Alcoa Research and Development (R&D) Center. In-plane membrane stress, σ_b and the magnitude of thickness strain, ε_b are transformed to effective stress and strain using '79 Hill's criterion and measured normal anisotropy value, $\bar{r}$. The results of biaxial bulge tests for DP590, DP780, and DP980 are shown in Figure 4.

Constitutive Equations

1-D Constitutive Equation

A new empirical work-hardening constitutive model for DP steels, Holloman/Voce (H/V) model, is proposed as three multiplicative functions, Eq. (1). Each function represents the effects of strain hardening, strain rate, and temperature, respectively. This model differs from other models in that the strain hardening is a function of strain and temperature.

$$\sigma = \sigma(\varepsilon, \dot{\varepsilon}, T) = f(\varepsilon, T) \cdot g(\dot{\varepsilon}) \cdot h(T) \qquad (1)$$

Coefficients of the constitutive equation are found by fitting Eq. (1) to tensile-test results at various conditions: various temperatures and speeds.

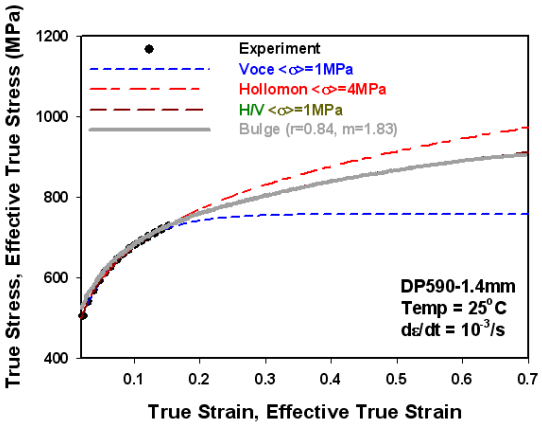

(a) DP590

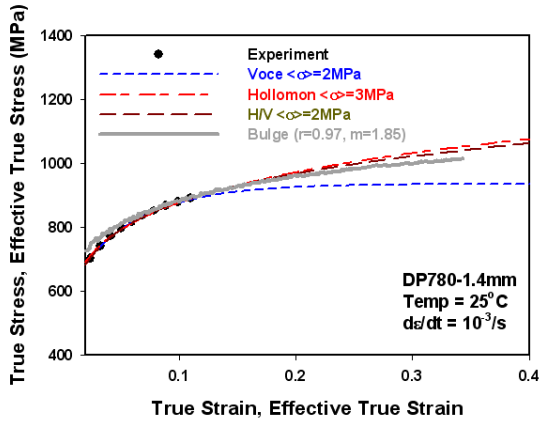

(b) DP780

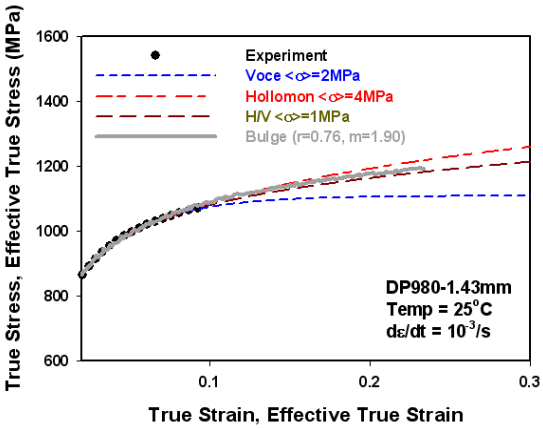

(c) DP980

Figure 4. Biaxial bulge test compared with 1-D constitutive equations.

Strain Hardening Function, $f(\varepsilon,T)$

It has been reported that the Hollomon model predicts better at room temperature conditions and the Voce model does better at elevated temperature for DP steels [1]. Therefore, a strain-hardening function $f(\varepsilon,T)$ is proposed as Eq. (2) represented by a novel linear combination of the Hollomon and Voce equations with a temperature-dependent proportion, $\alpha(T)$.

$$\begin{aligned} & f(\varepsilon,T)=\alpha(T)f_{Hollo}+(1-\alpha(T))\cdot f_{Voce} \\ & ,where\ \alpha(T)=\alpha_1-\alpha_2(T-T_{RT}) \\ & f_{Hollo}=K\varepsilon^n \\ & f_{Voce}\ =y_0(1-Ae^{-B\varepsilon}) \end{aligned} \tag{2}$$

Where T is current temperature, T_{RT} is room temperature, and α_1, α_2, K, n, y_o, A, B, are material constants. The function $\alpha(T)$ allows a more Voce-like curve at higher temperatures and a more Hollomon-like curve at lower temperatures. $\alpha(T)$ and $h(T)$ (see below) are obtained by fitting the constitutive equations to tensile-test results carried out at various temperatures.

Strain-Rate Sensitivity Function, $g(\dot{\varepsilon})$

Strain-rate sensitivity is an important parameter influencing plastic instability of many materials, so it must be included in the constitutive equation for accurate failure prediction. The strain-rate sensitivity is incorporated into constitutive equations by multiplicative form, Eq. (3). It was observed that the strain-rate sensitivity index, m increased with increase of strain rate. Therefore, the strain-rate sensitivity index m is expressed as a linear form of logarithmic value of strain rate, Eq. (4).

$$\sigma=f(\varepsilon,T)_{\dot{\varepsilon}_0}\left(\frac{\dot{\varepsilon}}{\dot{\varepsilon}_0}\right)^m \text{ [multiplicative]} \tag{3}$$

$$m=a[\log\dot{\varepsilon}]+b \tag{4}$$

where a and b are material constants.

Temperature-Dependent Function, $h(T)$

The temperature term included in the strain-hardening function, Eq. (2), represents the change of strain-hardening curve with temperature, while the temperature function, $h(T)$, represents the change of strength with temperature as a simple multiplicative form, Eq. (5).

$$h(T) = (1 - C \cdot (T - T_{RT})) \quad (5)$$

where C is a material constant which can be found by fitting to tensile-test data at various temperatures.

The constitutive equations developed for three grades of DP steels, DP590, DP780, and DP980, are compared with the effective stress-strain curves obtained from balanced biaxial bulge tests, Figure 4.

FEM Simulations for 1-D Constitutive Laws

The proposed constitutive equations are investigated using a recently developed, thermomechanical, finite-element model (FEM), C3D8RT, of a tensile test with the same specimen geometry as in the experiments. ABAQUS Stand version 6.7 [2] is utilized for this analysis, Figure 5.

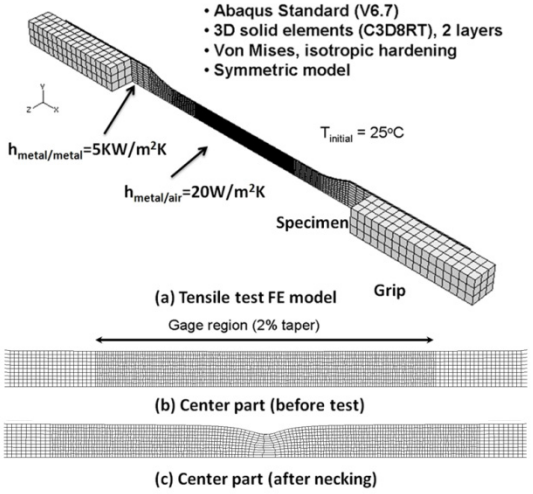

Figure 5. FE model for tensile test.

A series of FEM simulations of tensile tests are conducted using the three constitutive equations, Hollomon, Voce, and H/V model for the three DP steels, and thermal coefficients shown in Figure 6. The results are compared in terms of total elongation where the total elongation in the simulation is determined based on a fractional load drop that is measured in the experiment. As shown in Figure 6, the Hollomon model predicts fracture well at room temperature but shows big error in the elevated temperatures, and vice versa for Voce. The H/V model, however,

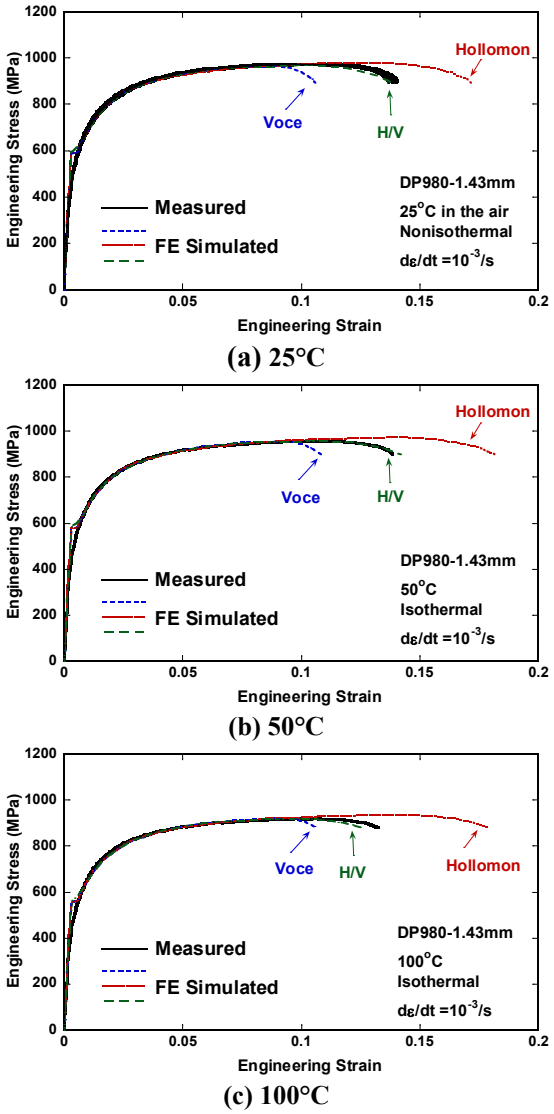

Figure 6. Comparison of FE simulation and experiments of uniaxial tensile test using different 1-D constitutive laws at various temperatures for DP980.

shows good agreement with the experimental results in the temperature range from 25 to 100 °C for all three materials. "Damage" localization resulting from the growth of voids is unlikely to play a significant role in tensile localization and failure for DP steels based on the comparison results between FE simulation and experiments.

3-D Constitutive Equations

Accurate 3-D constitutive equations have been developed to describe the T/C and C/T tests. The Von Mises yield surface is assumed and a non-

linear kinematic hardening model, the Chaboche model, is proposed as follows,

$$\boldsymbol{\alpha} = \boldsymbol{\alpha}_1 + \boldsymbol{\alpha}_2$$

$$d\boldsymbol{\alpha}_1 = \frac{2}{3} C_1 d\boldsymbol{\varepsilon}_p - \gamma \boldsymbol{\alpha}_1 dp \qquad (6)$$

$$d\boldsymbol{\alpha}_2 = \frac{2}{3} C_2 d\boldsymbol{\varepsilon}_p$$

where $\boldsymbol{\alpha}$ is the back stress, $\boldsymbol{\varepsilon}_p$ is the plastic strain, and p is the effective strain. C_1, C_2, and γ are constants. The backstress is divided into two parts, a linear component $\boldsymbol{\alpha}_1$ which represents permanent softening, and a non-linear variable for transient behavior near the re-yielding domain.

Isotropic hardening is taken as an exponential function

$$R = R_s(1 - \exp(-bp)) \qquad (7)$$

where R is the yield surface size, and R_s and b are constants. Figure 2 represents a good agreement between the C/T tests and 3-D constitutive laws simulations.

Draw-Bend Springback

A draw-bend springback (DBS) test is conducted to investigate the relationship between springback and the retaining force, as shown in Figure 7. Three grades of dual phase steels, namely DP590, DP780, and DP980, are used in this study. The specimen is cut along the rolling direction for 710-mm length and 25.4-mm width. The back force is varied between 50% yield strength of the material to 110 % yield strength at regular intervals of 10%. The specimen is drawn to a distance of 127 mm at a rate of 25.4 mm per second over two roller radii, 6.4 and 11.1 mm.

As the normalized back-forces (F_bs) increased, the springback angle reduced (Figure 8). The reduction in springback angle increased with increasing material strength. The springback angle at high F_b's is controlled by anticlastic curvature [3]. Higher F_bs accentuate anticlastic curvature which in turn increased the moment of inertia of the specimen cross-section, thus reducing springback. At F_bs, the springback angles for

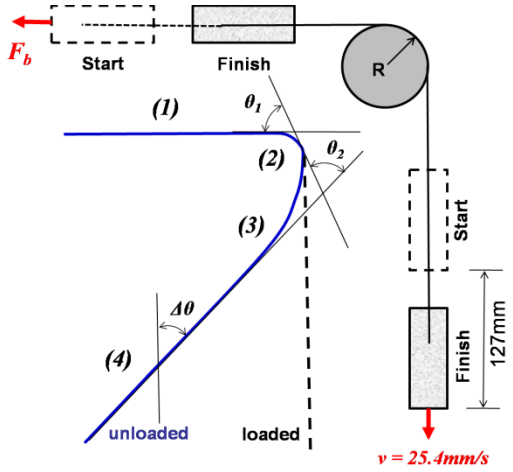

Figure 7. Schematic of the stages of the draw-bend test and unloaded specimen geometry

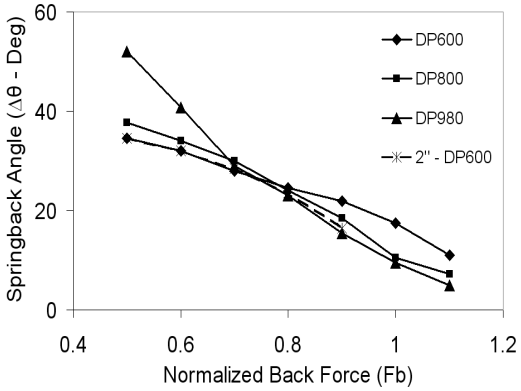

Figure 8. Springback angle obtained using R=6.4 mm.

increasing material strength are higher. Beyond Fb = 0.8 this trend reversed and the springback angles for increasing material strength became smaller.

AHSS (DP 590, DP 780, DP 980, and TRIP 780) show time-dependent springback at room temperature, while standard autobody steels such as draw-quality semi-killed (DQSK), aluminum-killed draw-quality (AKDQ), and high-strength low-alloy (HSLA) steels showed no such time-dependent springback up to seven years following deformation.

Springback Simulations

As schematically shown in Figure 9, 300 shell elements with 51 integration points (IP) through the thickness are used for FE simulation of

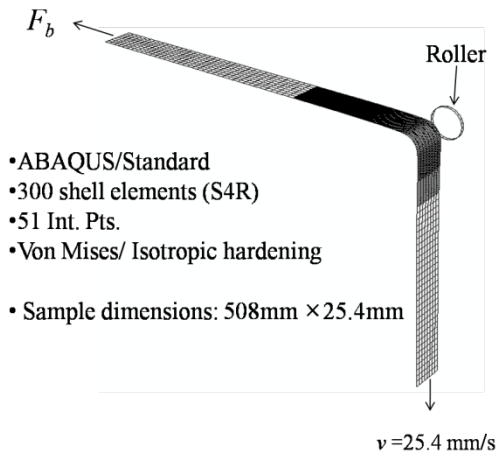

Figure 9. Simulation of springback.

springback using ABAQUS/Standard [2]. Von Mises yield function and isotropic hardening are used as a simple material model that showed good agreement with experiments in previous works [4] for F_b <0.7. As can be seen in Figure 10, simulated initial springback angle shows relatively good agreement with the experiment even though a simple material model is used.

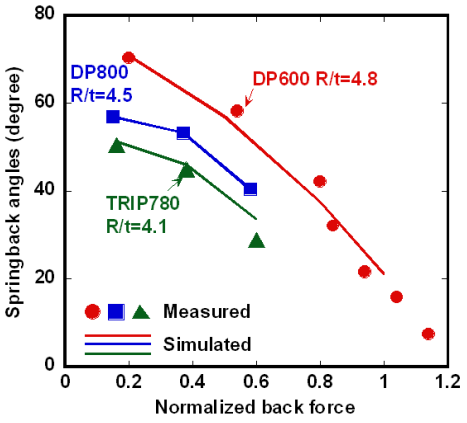

Figure 10. Comparison of the measured and simulated springback.

Formability Objective

Depending on the application and the grade, failures in AHSS are not always able to be predicted by the usual forming simulation and application of forming-limit diagrams. Such diagrams represent the forming limit based on localized deformation, or necking, which has proven successful in predicting failures for conventional sheet steels. The new type of failure, so-called "shear fracture", is observed at sharp radii where bending and unbending under tension during forming occurred [5].

The draw-bend test mimics the mechanics of deformation of sheet metal as it is drawn, stretched, bent, and straightened over a die radius entering a typical die cavity [6]. The test can produce both normal plastic localization/necking and shear fracture. For AHSS, the flow stress is affected significantly by deformation-induced heating at even modest strain rates, so the constitutive equations must take into account these effects [7]. Deformation- induced heating is usually expected to have a detrimental effect on ductility [8].

The objective of this research is to develop a FE model of the draw-bend test, and to improve predictability by taking into account thermal effect with a new 1-D constitutive equation relating flow stress to strain, strain rate, and temperature for three dual phase steels.

Thermomechanical Finite-Element Analysis for Draw-Bend Test

A thermomechanical finite element model of draw-bend tests is developed to investigate the failure mechanisms of AHSS. The model accounts for deformation heating and heat transfer and is capable of representing softening and altered strain hardening of materials measured at elevated temperatures. Such capability is required because temperatures increase much beyond room temperature during draw-bend tests by deformation heating. A symmetric 3-D solid model (C3D8RT) is used with five layers through thickness in ABAQUS 6.7 Standard. Isotropic yield and isotropic hardening are assumed for simplicity. Thermal coefficients are measured from independent experiments or obtained from the literature. The friction coefficient is based on a comparison of forces of front grip and back grip between FE simulation and draw-bend fracture test using Coulomb's friction law.

As can be seen from Figures 11–13, all three types of failure are predicted accurately (Type I—tensile, Type II—mixed, Type III—shear) and the

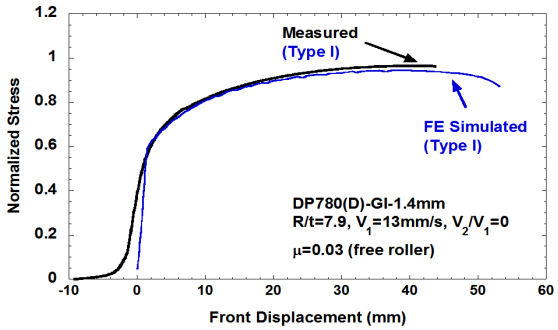

Figure 11. Thermomechanically FE simulated and measured stress-displacement curves, Type I.

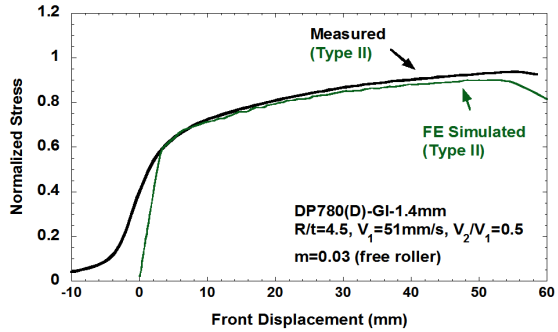

Figure 12. Thermomechanically FE simulated and measured stress-displacement curves, Type II.

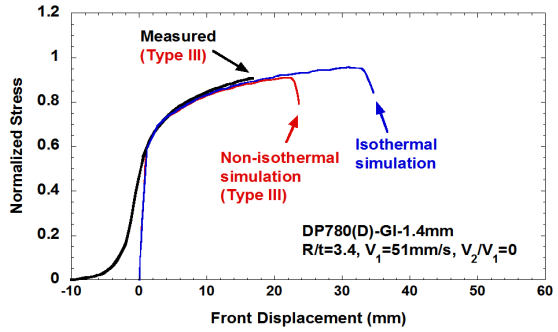

Figure 13. Thermomechanically FE simulated and measured stress-displacement curves, Type III.

draw distances to failure are predicted within 5–20 percent of the measured results. Isothermal simulations significantly over-predicted the draw distances to failure, by up to 100 percent (Figure 13).

The normalized maximum stresses are compared as a function of strain rates in Figure 14. While the normalized stress to failure changes little, the failure type changes from Type I to Type III (tensile localization to shear failure) as the strain

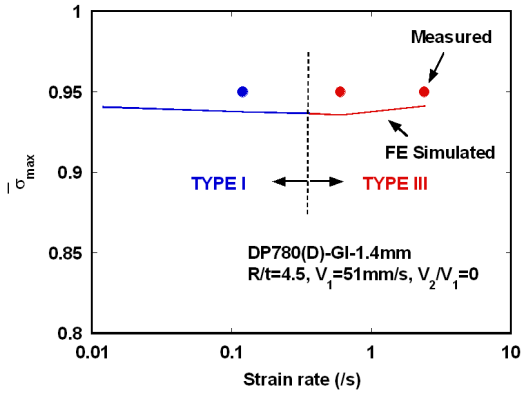

Figure 14. Comparison of simulated and measured maximum stresses at various strain rates.

rate increases. This result suggests that shear failure is a consequence of thermally assisted strain localization, in agreement with Figure 14.

Conclusions

Measure Strain Hardening

(1) T/C and C/T tests show: (a) Bauschinger effect, (b) transient behavior near re-yielding domain, and (c) permanent softening.

(2) From two-path tensile tests, directional-hardening behaviors are complicated but systematic.

Constitutive Equations

1-D and 3-D constitutive equations are developed.

1. 1-D constitutive equation has a remarkable agreement of the thermomechanical tensile test FE model simulation with experimental results. Using the proposed constitutive equation lends confidence that the constitutive equations are valid well beyond uniform elongation in tension within the temperature range of 25–100°C and predict correctly AHSS failure without damage mechanics.
2. "Damage" is unlikely to play a significant role in tensile localization and failure for DP steels based on the comparison results between FE simulation and experiments.
3. Accurate strain-hardening description beyond uniform elongation is critical.

4. 3-D constitutive law had a good agreement with T/C and C/T tests.

Springback

1. As the back-force increases, the springback angle can drop quickly with increasing material strength and this behavior is pronounced at low R/t ratios.
2. Draw restraining force has significant influence on the springback; higher forces result in less springback and consequently produce dimensional stability in the formed part.

Draw-Bend Test

A new formability test and FE model of the draw-bend tests are developed. Maps of failure type and normalized maximum sheet tensions have been measured and simulated with good accuracy as functions of R/t and strain rate for dual phase steels. Deformation induced heating and consequent material softening is a critical part of the failure process at typical strain rates. The results suggest that damage is not an important component of "shear" failures observed, at least with these alloys under these conditions.

Presentations/Publications/Patents

1. R. Padmanabhan, Jihyun Sung, H. Lim, M. C. Oliveira, L. F. Menezes, and R. H. Wagoner, "Influence of Draw Restraining Force on the Springback in Advanced High Strength Steels," International Journal of Material Forming, 3 April, 2008.
2. H. Lim, M. G. Lee, J. H. Sung, and R. H. Wagoner, "Time-Dependent Springback," International Journal of Material Forming, 3 April, 2008.
3. Ji Hoon Kim, Ji Hyun Sung, and R. H. Wagoner, "Finite Element Simulation of DP590 Draw-Bend Tests," NADDRG 2008, May 14–15, 2008, Windsor, Canada.
4. Ji Hyun Sung, Ji Hoon Kim, and R. H. Wagoner, "Constitutive Equation of AHSS," NADDRG 2008, May 14–15, 2008, Windsor, Canada.
5. H. Lim, Ji Hyun Sung, M. G. Lee, and R. H. Wagoner, "UPDATE: Time-Dependent Springback of AHSS," NADDRG 2008, May 14–5, 2008, Windsor, Canada.
6. M. Amitesh and R. H. Wagoner, "Draw Bend Failure of AHSS," NADDRG 2008, May 14–15, 2008, Windsor, Canada.

References

1. J. H. Sung, J. H. Kim, and R. H. Wagoner, "Constitutive Equation of AHSS," 2008 Spring NADDRG, May 14–15, Windsor, Canada.
2. ABAQUS, User's manual for version 6.7.1. Hibbit, Karlson & Sorensen Inc.
3. L. Geng and R. H. Wagoner, "Role of Plastic Anisotropy and its Evolution on Springback," International Journal of Mechanical Sciences 44, 123–148, 2002.
4. J. F. Wang, R. H. Wagoner, D. K. Matlock, and F. Barlat, "Anticlastic Curvature in Draw-Bend Springback," International Journal of Solids and Structures 42, 1287–1307, 2005.
5. R. H. Wagoner, "Fundamental Research Issues," Proc. Of NSF Workshop, Arlington, VA, Oct. 22–23, 2006.
6. F. F. Damborg, R. H. Wagoner, J. Danckert, and D. K. Matlock, "Stretch Bend Formability," Ph.D. Dissertation, Aalborg University, Aalborg, Denmark, 1997.
7. S. I. Kim, Y. Lee, and S. M. Byon, "Study on Constitutive Relation of AISI 4140 Steel Subject to Large Strain at Elevated Temperatures," J. Mat. Proc. Tech., 140:84–89, 2003.
8. Y. Gao and R. H. Wagoner, "A Simplified Model of Heat Generation During the Uniaxial Tensile Test." Metall. Trans. A, 18A:1001–1009, 1987.

6. AUTOMOTIVE METALS—CROSSCUTTING

A. Magnesium Research and Technology Development

Principal Investigator: Eric A. Nyberg
Pacific Northwest National Laboratory
P.O. Box 999, Richland, WA 99352
(509) 375-2103; fax (509) 375-2766; e-mail: Eric.Nyberg@pnl.gov

Technology Area Development Manager: Joseph A. Carpenter
(202) 586-1022; fax: (202) 586-1600; e-mail: joseph.carpenter@ee.doe.gov

Field Technical Monitor: Mark T. Smith
(509) 375-4478; fax: (509) 375-4448; e-mail: mark.smith@pnl.gov

---

Contractor: Pacific Northwest National Laboratory (PNNL)
Contract No.: DE-AC06-76RL01830

Objective

- Support the DOE-United States Automotive Materials Partnership (USAMP) Magnesium Front End Research and Development (MFERD) project (see report 6.C) in collaboration with China and Canada.
- Increase awareness and familiarity of magnesium (Mg) as a viable option for automotive applications.
- Compile, document and evaluate state-of-the-art research and development (R&D) in Mg research around the world as a resource to best determine where United States (U.S.) government resources should be directed.

Approach

- As MFERD Project Technical Committee (PTC) Cochair, provide the Project Steering Committee (PSC) member, who is the DOE Technology Area Development Manager, with relevant information as it relates to funding or significant technical developments and challenges of the MFERD project. Review the monthly U.S. MFERD Task Leaders' progress and note issues that may arise relevant to funding or DOE concern.
- Attend and evaluate both the semiannual and annual U.S. MFERD Task Leaders' review meetings and assess effectiveness of the nine U.S. tasks of the MFERD project. Attend and be cognizant of progress/issues with the associated USAMP front-end design project, Magnesium Front End Design and Development MFEDD (see report 6.B).
- Through quarterly teleconferences, collaborate with the Chinese and Canadian PTC Cochairs for the organization of the annual report and annual review meeting.
- Submit an updated report on the gaps in international research related to Mg R&D.
- Promote a consorted effort for international non-competitive Mg R&D.
- Develop and maintain the Mg R&D Bibliographic Database located at magnesium.pnl.gov.

Accomplishments

- **MFERD**: In fiscal year 2008, Eric Nyberg was the MFERD PTC Cochair responsible for the coordination of the quarterly PTC teleconferences, developing the agenda for the annual review and coordinating the U.S. portion of the annual report in both English/Chinese. It has been critical to maintain frequent and open

communication with PTC members in Canada and China. This has resulted in significant technical progress in a relatively short time. As a DOE-funded program, the U.S. tasks are driven by the USAMP representatives. Through monthly teleconferences, the USAMP Task Leaders were able to provide frequent updates to progress and issues. Specifically from the MFERD Cochair, activities have included the following.

— Coordinated and reviewed progress by the nine U.S. Task Leaders.

— Participated in quarterly international conference calls with other PTC members from China and Canada.

— Edited the 2008 U.S. and International Semi-Annual and Annual MFERD Project Reports.

— Reviewed the U.S. Task Leaders' annual presentations held at USCAR headquarters on October 2007.

— Established a central repository for electronic project files available to all project members.

— Co-organized the annual Task Leaders' and PSC/PTC meeting held in Hangzhou, China.

— Coauthored a paper with other PTC members published in the October 2008 issue of *Advanced Materials and Processes* titled "Magnesium for Future Autos: Magnesium-intensive vehicles and enabling technologies are under development through an international collaboration," which highlights a model for international collaborative success.

- Other Magnesium Research and Technology Development activities included the following.

  — Expanded the publicly available Mg bibliographic database located at www.magnesium.pnl.gov to over 1,700 publications and presentations on Mg R&D.

  — Served as the 2008–2009 The Minerals, Metals & Materials Society (TMS) Magnesium Committee Chairman organizing the 2009 Magnesium Technology Symposium and editing the associated technical proceeding.

  — Attended the 2008 International Materials Research Conference where Mr. Nyberg organized a meeting in Chongqing, China with over 20 leaders from the international Mg R&D community to discuss ways to increase international collaboration on basic, fundamental research of Mg in precompetitive areas.

  — Updated the 2007 research report "International Experience and Gaps in Magnesium Research and Development in the Automotive Industry."

  — Submitted a proposal for Mg composites in response to the DOE Energy Efficiency Renewable Energy research call on Nanomanufacturing for Energy Efficiency titled "Solidification processing and development of metal matrix nanocomposites fabricated by ultrasonic cavitation particle dispersion."

  — Served on the International Program Committee for the 8th International Conference on Magnesium Alloys and their Applications, Weimar, Germany, October 2009.

Future Direction

- For the MFERD, coordinate the U.S. Year 2 annual report and evaluate Phase 1 progress. This evaluation will be used as part of the Phase 1 Gate Review to recommend when and if the second three-year phase of the project should commence.
- Develop collaboration with the U.S. Army, the National Science Foundation, and DOE on efforts for fundamental Mg R&D.
- Continue to evaluate and propose Mg R&D activities that are unique and necessary.
- Serve as the TMS Magnesium Light Metals Committee Chairman and Symposium organizer.

Introduction

The primary purpose of this project is to support the Canada-China-U.S. collaborative project entitled "Magnesium Front End Research and Development" (MFERD), the goal of which is to develop key enabling technologies for a

lightweight Mg front-end structure and other body applications. The MFERD project is developing enabling technologies in high-integrity casting, wrought Mg processing, Mg and dissimilar metal joining and corrosion, and in generating scientific understanding in corrosion science, crash-energy management, fatigue and noise, vibration and harshness (NVH) performance. The project also provides a platform for Mg research in collaboration with Canada, China, and the United States.

Background

As mentioned above, the goal of the MFERD project is to develop key enabling technologies (body casting, extrusion, sheet and joining) and knowledge base (crashworthiness, NVH, durability and corrosion) for primary (load-path) body applications of Mg alloys. The following are some specific objectives.

- Define materials and develop manufacturing processes for Mg body castings, extrusions, sheet, and joining technologies.
- Develop knowledge base and define Mg body technical requirements in crashworthiness, NVH, durability, corrosion, and surface finishing.
- Enhance the infrastructure for integrated computational materials engineering for Mg applications, including alloy design/ development, process optimization, and component manufacturing.
- Develop a total life-cycle analysis showing the net benefit of vehicle lightweighting using Mg vs energy consumption, emission, and pollution in Mg production.
- Promote high-quality professionals and students educated in materials science, engineering, and Mg R&D infrastructure in Canada, China, and the United States.
- Establish automotive original equipment manufacturer/supplier/academia collaboration in Mg body applications.

PNNL Approach to Supporting the MFERD Project and Database Development

Eric Nyberg continues as the 2009 U.S. PTC Chairman as a liaison to the PSC representative at DOE. Through continued participation in all project-related meetings since the initial three-country meeting held in Dearborn, Michigan, in October 2005, a sense of continuity has developed. This enables frank and open communication with the other PTC members, especially those in China, where the professional relationship is critical to workable progress. This participation has made technical issues or cultural complexities less of a hindrance than otherwise might be. *During the annual review meeting, the PSC members expressed appreciation to the PTC and Task Leaders for work that has been completed during the project's relatively short existence.*

With the assistance of software engineers at Mississippi State University, Mr. Nyberg has developed a MFERD SharePoint website. At this site, the nonproprietary project information is collected at a central location/depository for the international task teams to access these documents easily. This type of coordination is an effort to make communication and sharing of information more efficient to all of the team members around the world.

The Mg bibliographic database was updated this year to include over 1,700 referenced papers and presentations. This database is linked at both the TMS Magnesium and the International Magnesium Association websites. This makes the database an increasingly available tool to researchers exploring state-of-the-art Mg R&D around the world.

At the 3rd International Conference on Magnesium at the June 2008 International Materials Research Conference in Chongqing, China, Mr. Nyberg organized the meeting for developing international collaboration on fundamental Mg R&D.

Highlights of the positive benefits and productive results of the three-country international MFERD

project are included in the October issue of *Advanced Materials and Processes*.

Current and Future Work

For MFERD, future work will be to evaluate progress of the nine U.S. tasks, participate in Task Leader review meetings and PTC quarterly teleconferences, and report results/make recommendations to the U.S. PSC Chairman. The PTC is currently planning the 3rd Annual Task Leaders' meeting that will be held in Canada starting May 11, 2009, and will be followed by a joint PSC/PTC meeting. This will be an important review, as it is the intention of the PTC to provide a recommendation to the PSC on the future direction of the MFERD project.

Mg research opportunities inside and out of PNNL will be reviewed and proposed to DOE in consideration for future funding opportunities. In addition, we will continue to manage and update the publicly available Mg R&D Database at www.magnesium.pnl.gov.

Conclusions

This technical support project is aimed primarily at assisting the management of the U.S. portion of the three-country MFERD project. To date, the second full year of the MFERD project is nearly complete, and the annual report is being prepared for release at the annual meeting in May 2009.

Efforts continue to develop coordinated research between countries and among U.S. agencies (i.e., Army, National Science Foundation, and DOE).

Presentations/Publications/Patents

1. Luo A., E. Nyberg, K. Sadayappan, and W. Shi. 2008. "Magnesium Front End Research and Development: A Canada-China-USA Collaboration," Magnesium Technology: Proceedings from the TMS 2008 Annual Meeting and Exhibition, New Orleans, Louisiana, March 9–13, pp. 3–10.
2. Nyberg E., A. Luo, K. Sadayappan, and W. Shi. 2008. "Magnesium for Future Autos: Magnesium-intensive vehicles and enabling technologies are under development through an international collaboration," *Advanced Materials and Processes,* October, pp. 35–37.
3. Nyberg, E. (PNNL), to J. Carpenter (DOE EERE), 2008. Research Report: International Experience and Gaps in Magnesium Research and Development in the Automotive Industry, Revision 1. October.

B. Magnesium Front-End Design and Development (AMD603*)

Principal Investigator: Alan A. Luo
General Motors Research & Development Center
MC 480-106-212
30500 Mound Road
Warren, MI 48090-9055
(586) 986-8303; fax: (586) 986-9204; e-mail: alan.luo@gm.com

Program Technical Administrator: Robert C. McCune
Robert C. McCune and Associates, LLC
5451 S. Piccadilly Cir.
West Bloomfield, MI, 48322-1446
(248) 661-0085; fax: (248) 661-8718; robert.mccune@sbcglobal.net

Technology Area Development Manager: Joseph A. Carpenter
(202) 586-1022; fax: (202) 586-1600; e-mail: joseph.carpenter@ee.doe.gov

Field Project Officer: Aaron D. Yocum
(304) 285-4852; fax (304) 285-4403; email: aaron.yocum@netl.doe.gov

Contractor: United States Automotive Materials Partnership (USAMP)
Contract No.: FC26-02OR22910 through the National Energy Technology Laboratory

Objectives

- Engineering design, computer-aided analysis, and technical cost modeling of exemplary magnesium-intensive front-end structures for selected "unibody" and body-on-frame (BOF) vehicle architectures having the following design stretch targets.
  - — Mass reduction target: 60% lighter than comparator steel baseline structures and 35% lighter than comparator aluminum (Al) structures for mid-size passenger car, with comparable strength and crashworthiness.
  - — Vehicle mass distribution: Shift the front-to-rear mass ratio by -1/+1 toward 50/50 for the rear-wheel drive, unibody donor architecture.
  - — Demonstration via technical cost modeling of a maximum of $8/kg (of mass saved) cost penalty (100,000 vehicles/year production volumes), via part consolidation using large magnesium (Mg) castings (e.g., dash panel, shotguns) and attractive pricing of Mg in world markets.
  - — Matched or improved key performance characteristics such as stiffness, durability, and NVH (noise, vibration, and harshness) of the multi-material vehicle (MMV) "donor" vehicle via simulation.

Approach

The organizational structure of AMD603 has been described in detail in the prior progress report [1]. The project consists of two tasks: (1) Design and (2) Technical Cost Modeling. The designs are predicated on two vehicle structural archetypes: a body-frame-integral (BFI, also known as a unibody), principally used for passenger vehicles, and a BOF, which incorporates a separate (presumably steel) frame to which the body structure is attached

*Denotes Project 603 of the Automotive Materials Division (AMD) of the United States Automotive Materials Partnership (USAMP), one of the formal consortia of the United States Council for Automotive Research (USCAR) set up by Chrysler, Ford, and General Motors to conduct joint, precompetitive research and development (see www.uscar.org).

in final assembly. This latter structure is used primarily for light trucks and sport-utility vehicles (SUVs). Both tasks have been commissioned to contractors with design and manufacturing data made available from the original equipment manufacturers (OEMs) as required. There are no other supplier participants.

- Task 1. Design. The design task was originally divided into stages to incorporate data being simultaneously developed with regard to materials and processes as part of AMD604 (Magnesium Front End Research and Development). The initial (Phase 1) design was intended to utilize handbook properties of materials, and such general design information as was available at the outset from the relevant OEMs. Phase 2 was intended to incorporate refinements to material properties occurring through AMD604, and Phase 3 projects designs are to be predicated on optimized properties and manufacturing methods presumably having been developed throughout the course of AMD604. The design task also incorporates computer-aided engineering (CAE) techniques to explore such features as crashworthiness, modal analysis, and durability. These critical topics are amenable to computer modeling when knowledge of deformation characteristics of the materials, including their strain-rate behaviors, cyclic deformation characteristics, and fracture are understood.
- Task 2. Technical Cost Modeling. The approach uses process-based technical cost modeling [2] to provide the following deliverables for the two front-end designs (unibody and BOF):
  - — Determine primary Mg production costs and market impact of the electrolytic vs. direct thermal reduction (Pidgeon) processes.
  - — Provide a detailed cost analysis and report for all the components and assembly identified by the Design Task for both the unibody and BOF designs.
  - — Assessment of current steel designs for both the unibody and BOF as comparators for weight and cost.

The cost-modeling task is also divided into phases. Phase 1 includes the primary Mg production analysis and the component cost of individual parts for each design. Phase 2 includes the assembly of the components to each other and to the remainder of the body structure. Phase 2 also incorporates any updates to the front-end design determined by design changes or information gathered by AMD604. The cost analysis includes part manufacture, corrosion protection treatment, as well as any surface finishing, machining, or any other process each component requires to allow it to be attached or integrated with the rest of the front-end assembly. The overall cost of the assembly including components is provided for each design as compared to the steel baseline.

Accomplishments

- Phase 1 Final Design Review conducted on Dec. 10, 2007. Accomplishments included initial determination of piece part designs, vehicle stiffness, bill-of-materials, mass reductions, and estimate of concept-level (i.e., lacking complete physical model) crash assessments. Ongoing design reviews (Phase 1 addenda and Phase 2) conducted during 2008.
- Phase 2 Progress: Evolving mechanical property data and manufacturing technology information have been transmitted to the Design contractor (Cosma Engineering, Troy, Michigan) by the various AMD604 U.S. Task Teams. The contractor has participated in many Task Team functions and worked with suppliers to gain firsthand knowledge useful in the design process (e.g., joining, part fabrication, and surface treatment).
- Mechanical Property Status: To date, the projected processing methods for vacuum die casting show that while the ultimate tensile strength of 220 MPa for AM60B is attainable, as is desirable elongation minimum of 6%, that the initial designs based on the anticipated yield strength of 140 MPa are not aligned with presently measured yield strength values of 125 MPa from the advanced die-casting processes. Studies are underway to determine if minor alloy modification of AM60B may permit higher yield strength to be achieved, or alternately that designs may require modification in section thickness (and concurrent mass) based on lower yield strengths actually measured.
- Cost Modeling Review: A comprehensive review of the initial component cost model was conducted by the contractor, Camanoe Associates (Cambridge, Massachusetts) as part of the yearly project review on October 21, 2008. The extractive metallurgy models are still under development; however, the models for basic part fabrication using die casting (both high-vacuum and Thixoforming processes), sheet fabrication, and extrusion were presented at that review.

- The status of specific design targets includes the following.
  - — Part count reduction: 57 pieces (42 Mg front end (MFE) vs 99 steel baseline—or 58%).
  - — Mass reduction: 45 kg (47%) (with equivalent global body stiffness to the steel baseline, but prior to meeting full requirements of crash, NVH, and durability performance).
  - — Materials technologies: 15 castings, 3 extrusions, 15 formed Mg sheets, and 9 Al stampings.
  - — Initial joining strategy developed include friction stir welding, metal inert gas (MIG) welding, self-piercing rivets (SPRs), tungsten inert gas (TIG)/laser welding, and adhesive bonding.
  - — Crashworthiness: Using the latest material properties (including cracking), the crash performance of the current MFE design falls short of the steel baseline vehicle in Insurance Institute for Highway Safety (IIHS) Deformable Barrier and the New Car Assessment Program (NCAP) 35 mph full frontal impact.
  - — Modal analysis: Full body, structure-only modes occur at higher frequencies than the baseline, indicating generally greater structural stiffness. However, some of the local front-end stiffness metrics and some of the engine-cradle attachment point stiffness metrics of the Mg design are currently below the baseline steel vehicle.
  - — Assembly sequence has been identified for the initial design, permitting prospective plant layout and more focused cost modeling.
  - — The preliminary corrosion prevention strategy is to precoat all the parts, join the parts into the front-end assembly, and further coat the entire assembly before the paint shop.

- Specific progress in the Technical Cost Modeling project includes the following.
  - — Completed preliminary technical cost models for Thixomolding, super vacuum die casting (SVDC), extrusion, and modifications to the previously developed warm-forming model.
  - — Preliminary results, based on available information, indicated that while Thixomolding and SVDC have different process parameters, the end costs are similar within the fidelity of the preliminary models.
  - — Determined preliminary piece cost for Mg-designed components. This information was used to identify high-cost components which are in the process of being redesigned for alternate manufacturing technologies.
  - — Determined cost-sensitive process parameters for individual technologies such as extrusion rate, lubricant type and heat-treatment requirements. Task teams are refining these numbers using manufacturing trials.
  - — Developed framework for primary Mg production cost models.

Future Direction

- Crashworthiness: Validation of CAE methods used to predict crash behavior, including use of computer codes such as LS-DYNA, is progressing via Task 1.1 in AMD604. In particular, this parallel task seeks to establish validation of crash performance of the materials and processes of interest (castings, extrusions, and sheet parts) when Mg is fabricated into a generic rail structure, viz. the “double top hat” which is amenable to both computer analysis and experimental validation. Such analysis is intended to incorporate the materials in such states as would actually be manufactured in practice (e.g., vacuum die casting). Once crashworthiness validation is completed in AMD604, the front-end design will be modified to match the crash performance of the baseline steel vehicle.
- To date, strain-rate effects for the various forms of Mg are less problematic than deformation anisotropy associated with wrought Mg materials. This material property dependence on local manufacturing directions (i.e., longitudinal direction for extrusion and rolling direction for sheet) presents a challenge for incorporating the most accurate material descriptions in the finite-element analytical methods.
- Manufacturing: While an initial build sequence has been proposed by the contractor, certain specifics such as corrosion protection surface treatment and joining methodologies have not been fully developed and included as specifics and continue to emerge from the AMD604 research and development project. This development is expected to continue throughout Phase 2.
- Cost Modeling: Conclude comparative analysis of primary production processes.

- Refinement of the process cost models and interaction between the design team and technical cost modeling team will continue to provide insight and direction to the front-end design to improve the component and assembly costs.
  - — Refine manufacturing type for projected piece parts to reflect knowledge of process limitations and cost structures (e.g., sheet parts become castings; press size limitations on castings).
  - — Continue to seek weight-reduction opportunities through down-gauging, part consolidation, or other means to more closely approach design stretch target.

Introduction

Background for AMD603, Magnesium Front End Design and Development (MFEDD), has been provided in a prior annual progress report [1]. MFEDD is complementary to both AMD604, Magnesium Front End Research and Development, and the USAMP MMV. Whereas AMD604 is predicated on development of enabling Mg technologies via leveraging with Canadian and Chinese Mg experts on a collaborative basis, AMD603 is confined to the OEM partners of USAMP [i.e., Ford, General Motors (GM) and Chrysler] and two selected suppliers focused on design (Cosma Engineering, Troy, Michigan) and technical cost modeling (Camanoe Associates, Cambridge, Massachusetts).

The front-end structures envisioned as the objectives of the project include two structural archetypes: (1) a unibody (or BFI) structure as illustrated in Figure 1 and (2) a BOF approach as shown in Figure 2. The former structural type is associated with light passenger vehicles, whereas the latter is incorporated in light trucks and SUVs. The traditional unibody structure is assembled typically from individually stamped steel parts which are then joined together by resistance spot welding, and often incorporate adhesive bonding or "weld bonding" in combination with resistance welding for improved strength, stiffness, and performance. The attraction for use of Mg in the unibody structure arises from both weight reduction opportunity at comparable stiffness, and the prospects of combining individual piece parts into entire subassemblies, via large-scale die casting. Such large cast parts, of which present-day instrument panels and radiator supports are exemplary, have excellent dimensional properties and reduced costs over assemblies of steel stampings.

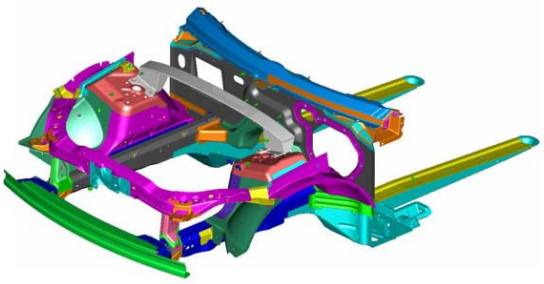

Figure 1. Unibody steel front-end baseline structure for the donor vehicle.

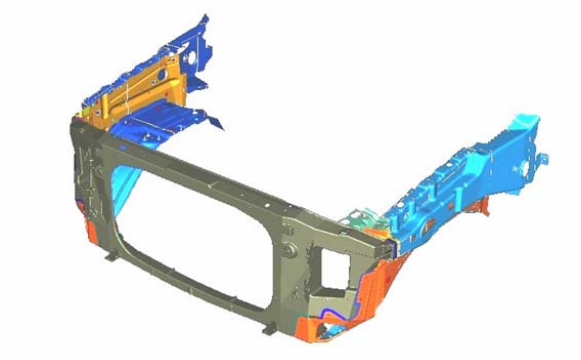

Figure 2. Baseline BOF donor vehicle steel structure with existing Mg radiator support.

Similarly, the baseline steel structure for the BOF donor vehicle is illustrated in Figure 2. The remainder of this report describes the status of the design exercise and generalized outcomes of the cost-modeling exercise.

Design Status

The "design review" is a traditional mechanism among OEMs for presentation, analysis, and discussion of new or ongoing designs of vehicles and subsystems. The format of the design review discussions for the MFE follows the itemized agenda of Table 1.

Table 1. Design attributes for magnesium front end from the agenda for the design review process.

1. Design CAD – structural design to match specified envelope.
2. CAE – crash studies by LS-DYNA analysis, durability.
3. Bill of Materials – parts listing, manufacture method and drawings.
4. Mass and part count summary.
5. Vibration modal analysis and structural stiffness by CAE.
6. Frontal crash analysis for NCAP and IIHS protocols.
7. Typical cross sections of major structures and substructures.
8. Joining strategy for magnesium components.
9. Magnesium-to-steel interface strategy.
10. Manufacturing implications.
11. Assembly protocol.
12. Corrosion prevention strategy.
13. Stress/durability evaluation – static and dynamic loading of structure.

This section considers each of the major design attributes of Table 1 and provides a brief report of the status of that item. Most of the design effort in FY 2008 focused on the unibody design because of the complexity therein; however, progress was also made on the BOF, which relies more on several large-scale castings and less on part integration.

1. Computer-Aided Design. Front-end envelopes, including vehicle “hard points” and attachment points, are now implemented in physical designs and individual components for the Mg-intensive BOF and unibody designs of Figures 1 and 2. For the unibody, the original design envelope was expanded to include a multipiece Al floor pan and cowl extension brackets, also addressing item 9 regarding interfacing strategies to steel components. The unibody Mg-intensive design is indistinguishable from the baseline in terms of surfaces, cut-outs, and hard points.
2. Computer-Aided Engineering. Phase 1 material properties used for initial crash simulations and nodal analysis, and refined (Phase 2) properties incorporated in follow-on models indicating performance deficit in comparison to steel baseline (cf, item 6). Additional mass-reduction and nodal analysis studies were completed.
3. Bill of Materials. Unibody: Original design envelope extended to include floor pan and cowl extension brackets. BOF: No change.
4. Mass and Part Count. Unibody: Part count original (steel) is 99 with mass of 96.07 kg; Mg-intensive front end is 42 parts (58% reduction), and mass of 51 kg (47% reduction). BOF: 16 steel parts with mass of 70.7 kg, reduced to 3 castings with mass of 37.5 kg (81% part reduction; 47% mass reduction).
5. Vibration modal analysis and structural stiffness (Unibody). Current steel design structural modes are maintained for the entire body-in-white implemented with Mg-intensive front end. However, some of the front-end stiffness metrics and some of the engine-cradle attachment point stiffness metrics of the Mg design are currently below the baseline steel vehicle.
6. Frontal Crash (Unibody). NCAP 35 mph full frontal and IIHS deformable barrier. Initial projections using handbook mechanical properties, and absent any cracking (or material failure criteria) of the material (Phase 1), showed acceptable approximation to the baseline steel structure. However, upon incorporation of updated material properties measured in AMD604 and incorporation of the material-cracking criterion assumptions in LS-DYNA, the Mg-intensive design crash performance fell short of the baseline steel structure in both NCAP and IIHS protocols based on the current materials models and assumptions. Design updates and improvements in material properties and selection to attempt to bring the crashworthinesss performance of the MFE to match that of the steel baseline are pending results from the research and development efforts in the companion project AMD604.
7. Typical Sections. All typical cross sections at various points on both structures are visible through the CAD programs and a compendium of such sections (unibody) has been generated for the design reviews.
8. Joining Strategy for Magnesium Components (Unibody). Structural adhesive bonding is called for at most joint lines, requiring metal pretreatment in advance of the assembly process and accommodation of in-place adhesive for any secondary joining processes (e.g., rivets, welds, etc.). SPRs were prescribed predominantly in Phase 1, although it appears that friction stir welds may be

utilized in some number of cases (to be determined). To date, a supplier for SPRs has not been enrolled to the AMD604 project. A more limited number of MIG or TIG fusion welds are indicated at several positions of the structure. A complete mapping of all joining processes and manufacturing scenario has been produced as a "bill of manufacture."

9. Magnesium-to-Steel Body Interface Strategy. The bill of materials has been modified in the case of the unibody structure to permit a number of Al interface parts as isolators between the predominant MFE and the remainder of the steel unibody. Isolation through use of Al is a practice in the industry. Additionally, the design team has challenged the AMD604 Corrosion and Surface Treatment (Task 1.4) group to address the interface issue with alternatives to Al spacers such that part counts are kept low.
10. Manufacturing Implications (Unibody). Each component part has been assessed for manufacturing capability by the relevant AMD604 subteam, and recommendations were provided regarding optimal choice of process and capabilities. The BOF side support or "shotgun" structure has been the subject of a separate USAMP project on ultra-large castings and manufacturing considerations thereof. An exemplary "shotgun" structure implemented as a single Mg casting is illustrated in Figure 3.

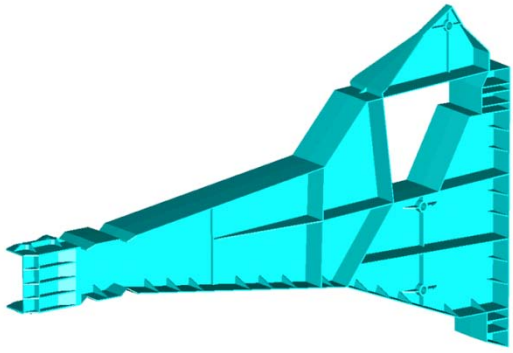

Figure 3. Structural Mg alloy shotgun structure designed for the Ford donor vehicle.

11. Assembly Protocol. An assembly sequence for the 42 component pieces of the unibody has been configured as part of the design and includes relevant joining methods or any ancillary items (e.g., rivets). A hypothetical manufacturing layout has also been devised to permit factory floor plans and further cost modeling to be developed. Exemplary manufacturing cells were shown at the November 2008 design review.
12. Corrosion Prevention Strategy. The AMD604 Task 1.4 (Corrosion and Surface Treatment) team has provided much of the background for this activity. Current assumptions are based on requisite metal pretreatment for adhesive bonding and also for accommodation of any additional polymeric topcoats, either prior to or as part of the normal body and paint shop.
13. Stress/Durability Analysis (CAE). Relevant static load cases have now been provided to Cosma Engineering for the unibody structure and will become the basis for CAE analysis of applied loads to the structure.

Cost Modeling Status

Primary Mg Production. Figures 4 and 5 show schematizations from the literature [3] depicting the silicothermic reduction (i.e., Pidgeon) process and electrolytic extraction process respectively. Further development of the task relative to cost modeling of extraction will continue based on these process models.

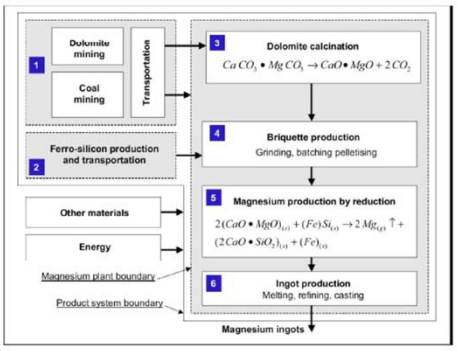

Figure 4. Block diagram of silicothermic reduction (Pidgeon) process after reference [3].

Magnesium Piece Part Cost Models. Each of the approximately 33 Mg pieces of the designed Mg-intensive front-end structure has been subjected to a process-based, technical cost model using one of

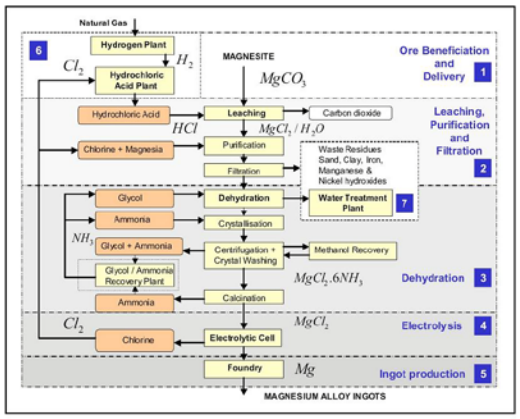

Figure 5. Block diagram of electrolytic extraction process for Mg after reference [3].

the candidate forming technologies (SVDC, warm sheet forming, or extrusion). Additionally, models were developed to permit comparison of SVDC and Thixomolding. A portion of the international research covered by AMD604 involves production of larger-scale parts using the Thixomolding process.

Each cost model and associated component is unique (with the exception of left- and right-hand versions of the same part), and the overall model accounts for the basic factors attributed for each aspect of the basic part fabrication, including: material, labor, equipment, tooling (unique to each part), and the category of "other," which includes such items as energy, process-related materials (e.g., special lubricants), overhead, building costs, and maintenance.

While it is beyond the scope of this report to detail such cost models for all the componentry under consideration, Figure 6 shows an exemplary breakdown for the case of an arbitrary-shape Mg die casting.

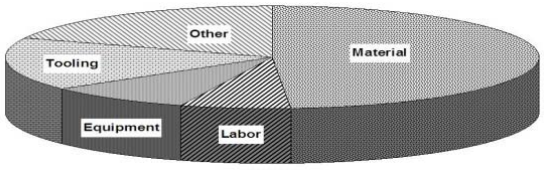

Figure 6. Approximate cost-element breakdown for a Mg casting of arbitrary shape.

In this particular instance, it can be seen that the cost of material represents the single largest element of the component cost. The individual models for each forming technology and each piece part are again different from each other, although several common features have begun to emerge: (1) a general tendency for the material cost to be among the largest single factors contributing to overall component cost and (2) a tendency for extrusion to show a generally lower cost of the individual forming tool, as is well-known for the comparable Al extrusion process.

It should be reiterated here that at this phase of the project, the cost models do not consider surface finishing of the as-formed part, joining, or final finish of the projected assembly.

Conclusions

At the end of the second fiscal year of its operation, the project has concluded a Phase 1 design based on handbook and anecdotal data and is midway through Phase 2, in which property values for the materials of consideration from the companion AMD604 project are included in the performance evaluations. The current design level must be improved and updated to have the performance of the MFE match the performance of the baseline steel vehicle. Piece-part technical cost models have been derived for SVDC, extrusion, and warm-sheet forming. The cost modeling results are influencing the design choices.

Acknowledgments

The success of this project is due to the dedicated efforts of team members at Chrysler, Ford, and GM, as well as the suppliers Cosma Engineering and Camanoe Associates. David Wagner of Ford, Theresa Lee of GM, and Steve Logan of Chrysler are specifically acknowledged for their significant contributions and tireless efforts. The continuing support of our respective organizations and the U.S. Department of Energy is gratefully acknowledged.

References

1. A. Luo, R. C. McCune, J. A. Carpenter, A. D. Yocum, and P. S. Sklad, "AMD603

Magnesium Front End Design and Development," FY 2007 Progress Report to DOE, (2008).

2. R. Kirchain and F. R. Field III, "Process-Based Cost Modeling: Understanding the Economics of Technical Decisions," *Encyclopedia of Materials Science and Engineering* (2001).

3. S. Ramakrishnan and P. Koltun, "A Comparison of the Greenhouse Impacts of Magnesium Produced by Electrolytic and Pidgeon Processes," pp. 173-178, in A. A. Luo, et al , eds., *Magnesium Technology* 2004, TMS, Warrendale, Pennsylvania (2005).

C. Magnesium Front End Research and Development (AMD604*)

Principal Investigator: Alan A. Luo
General Motors Research & Development Center
MC 480-106-212
30500 Mound Road
Warren, MI 48090-9055
(586) 986-8303; fax: (586) 986-9204; e-mail: alan.luo@gm.com

Program Technical Administrator: Robert C. McCune
Robert C. McCune and Associates, LLC
5451 S. Piccadilly Circle
West Bloomfield, MI, 48322-1446
(248) 661-0085; fax: (248) 661-8718; e-mail: robert.mccune@sbcglobal.net

Technology Area Development Manager: Joseph A. Carpenter
(202) 586-1022; fax: (202) 586-6100; e-mail: joseph.carpenter@ee.doe.gov

Field Project Officer: Aaron D. Yocum
(304) 285-4852; fax (304) 285-4403; email: aaron.yocum@netl.doe.gov

Contractor: United States Automotive Materials Partnership (USAMP)
Contract No.: DE-FC05-02OR22910 through the National Energy Technology Laboratory

Objective

- The concurrent development of key enabling materials and manufacturing technologies and the accompanying performance knowledge base to permit design and implementation of magnesium- (Mg-) intensive automotive-body front-end structures having greatly reduced mass, but with performance and cost comparable to sheet-steel baseline structures. Figure 1 illustrates an exemplary baseline unibody front-end structure implemented in sheet steel, which then serves as the design envelope for the proposed Mg-intensive structure. A second vehicle structure using a "body-on-frame" archetype of many light trucks is also under consideration by the project. The following two aspects of this project are unique within USAMP.
  - — The focus is on entire front-end structures as the developmental object, in contrast to individual components, thereby offering critical vehicle-level benefits in terms of mass distribution and performance while challenging the technical community to devise materials and manufacturing approaches to permit mass production of such structures at reasonable cost.
  - — Implementation of an international effort enlisting the best scientific and engineering expertise in Mg technology from the United States, Canada, and China in a first-of-its-kind, global collaboration.

Approach

- Organization and Administration: Establishment of organizational and technical steering committees and systematic management of information and activities in a global environment including web-based platforms.
- Partitioning of Projects: Separation of the design function into a separate USAMP project (AMD603) as well as Integrated Computational Materials Engineering—ICME (AMD702 and 703)—to facilitate handling of original

*Denotes Project 604 of the Automotive Materials Division (AMD) of the United States Automotive Materials Partnership, one of the formal consortia of the United States Council for Automotive Research set up by Chrysler, Ford, and General Motors to conduct joint, precompetitive research and development (see www.uscar.org).

equipment manufacturer- (OEM-) sensitive design data and to permit a broader, more universal approach to ICME. The international project, additionally, has a task for life-cycle analysis, in which USAMP is not participating.

- Enabling Technologies: Assessment of the state-of-the-art and development of emerging technologies in primary forming, joining, and finishing that would permit the manufacture of the envisioned structures.
- Knowledge Base: Understand the current awareness and knowledge gaps with regard to materials and structural performance in the intended application, particularly with regard to crashworthiness, noise-vibration harshness (NVH), fatigue, and durability (including corrosion).
- Technical Gateways: Provide for rigorous assessment of progress against pre-determined metrics at sub-levels of the project assuring that functional targets are achieved or, alternatively, that further efforts are discontinued if required metrics cannot be achieved. Gateways exist for both the design stage and also for the enabling technologies, such that efforts for an envisioned prototype build (Phase 2) only occur upon successful accomplishment of Phase 1. Overall timing and conceptual flow for projects AMD603 and AMD604 are illustrated in Figure 2, which also illustrates the positioning of the ICME project AMD703.

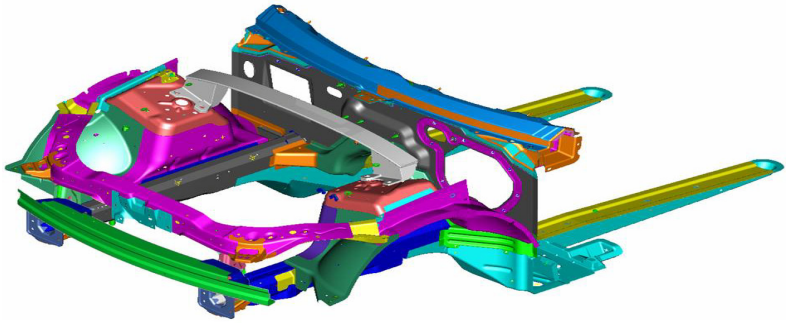

Figure 1. Exemplary unibody front-end design envelope as presently implemented in sheet steel.

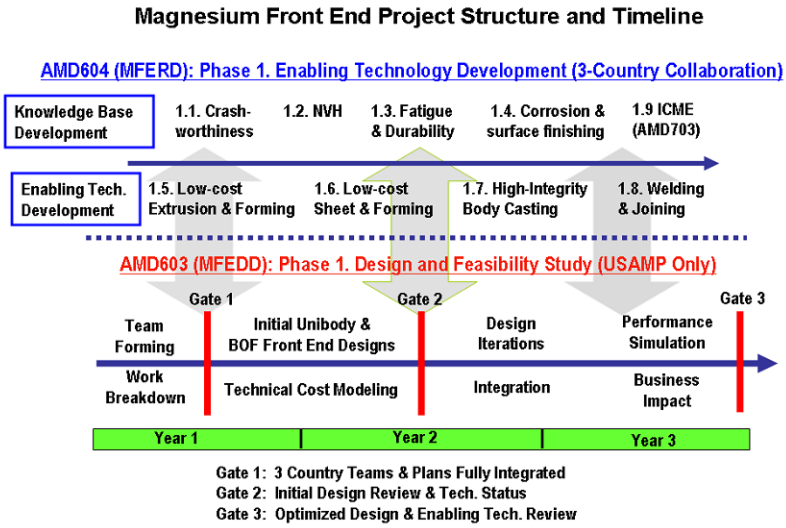

Figure 2. Schematization of AMD603 and AMD604 partitioning, timing, and technical gateways.

Accomplishments

The relationship between activities of the individual task areas and overall project objectives is shown in the fishbone diagram of Figure 3. Targets for knowledge-based and enabling technologies are illustrated therein. General project accomplishments for FY 2008 are summarized below.

- Participated in 2nd International Review Conference held in Hangzhou, PRC, from April 1–4, 2008.
- Contributed to a 366 page proceedings volume detailing work on the project up to the review date.
- Conducted an agenda of individualized visits within the People's Republic of China to specific institutions conducting task-related project work. Such visits included travel to Shanghai, Hangzhou, Chongqing, Xi'an, Louyang, Dalian, Shenyang, and Beijing.
- Conducted meetings of the Project Steering Committee (PSC) and Project Technical Committee (PTC) in conjunction with the review in Hangzhou. Additionally, PTC conference calls were held on July 30 and November 19, 2008.
- The Mississippi State University (MSST) "SharePoint" web site for project information sharing between international groups became operational in March 2008 and was rolled out at the Hangzhou meeting.
- The USAMP annual review of Project AMD604 was held on October 20, 2008, and participants from the Canadian and Chinese teams were in attendance. A group of U.S. participants attended the Canada annual review at the University of Sherbrooke, Quebec, on September 23–24.
- Conducted individual Task Team international conference calls at various times during the project year.
- The next annual international review meeting for the project will occur from May 11–13, 2009, at Niagara-on-the-Lake, Ontario, Canada.
- The USAMP AMD604 Project presented its "Gate 2" review to the AMD Board of Directors on July 18, 2008, and after some refinement of status reporting and metrics was given approval for continuation of Phase I.
- Thirty-six individual supplier companies or institutions have provided work plans and received USAMP contracts.
- USAMP AMD604 task area highlights are as follows.
  - Task 1.1 Crashworthiness—Acquisition and analysis of deformation characteristics of selected coupon materials over a range of agreed-upon strain rates and temperatures. Devised and manufactured standardized "box" crush sections for comparison of physical testing and computer simulation of deformation. Conducted initial simulations and deformations for the extruded and sheet formed box section structures.
  - Task 1.2 Noise, Vibration and Harshness (NVH)—Completed requisite documentation to enlist U.S. supplier (IAC) to support and complement Canadian and Chinese works and to provide two-layer panel samples. Reporting of initial transmission loss data from supplier IAC for exemplary Mg-intensive Chrysler prototype vehicle.
  - Task 1.3 Fatigue and Durability—Completed round-robin fatigue testing of extruded AM30 by all participants. Obtained initial fatigue data on AZ91D super vacuum die casting (SVDC) shock towers and AS31 sheet. Additional fatigue studies including piece fabrication and prototypical joint structure are underway.
  - Task 1.4 Corrosion and Surface Treatment—Prototype surface treatments received from China for analysis. First round of U.S.-based pretreatments concluded. Protocol for fastener galvanic corrosion established. Proposals for assessment of complete coating systems developed. Assembly protocol proposed to accommodate metal pretreatment prior to adhesive bonding.
  - Task 1.5 Extrusion—Conducted extrusion trials of AM30 and AZ61 alloys for the "double top hat" crush box prototype. Conducted texture measurement and mechanical properties of extruded AM30 to ascertain anisotropy of mechanical properties. Extrusion simulation studies conducted at Lehigh University. Coordination with ICME Extrusion task at MSST.
  - Task 1.6 Sheet Forming—Various AZ31 sheet materials show similar constitutive behaviors approximating the Sellars-Tegart model. For pan forming, the binder pressure was found to be critical to forming

capability as well as temperature. Sheet interaction with lubricant and the tool surface was found to override microstructural differences among alloys evaluated. Exemplary continuous cast sheet material has now been received from China for evaluation.

— Task 1.7 High-Integrity Body Castings—Prototype shock tower castings were produced in both AZ91D and AM60B using the novel SVDC process. An alternative vertical vacuum die casting process was also used to produce coupon pieces for properties determination. Initial mechanical property data suggests superior elongations achievable with such processing and strength levels approaching, but not exceeding, the anticipated design levels.

— Task 1.8 Joining—Completed guidelines for structural and nonstructural breakstem rivets. Completed assessment of the strength, durability, and corrosion performance of 10 pretreatments applied to AZ31 sheet, AM60B casting, and AM30 extruded Mg. Performed preliminary nondestructive evaluation (NDE) assessment of X-ray and ultrasonic evaluation of self-piercing rivet (SPR) joints.

— Task 1.9 ICME—(International nomenclature) Reported separately as USAMP project AMD703.

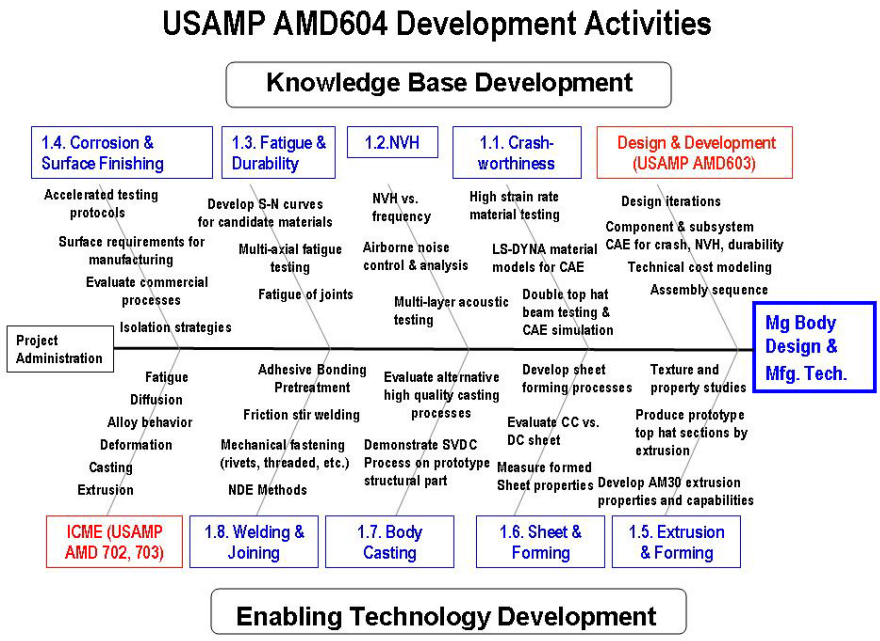

Figure 3. Magnesium front-end project/task structure fishbone diagram.

Future Direction

- Continuation of international discussions and progress reports via next annual meeting at Niagara-on-the-Lake, Ontario, Canada (May 11–13, 2009).
- U.S. Task Teams to provide updated physical property, material performance, and manufacturing recommendations to AMD603 Design Team as such data becomes available.
- Gate review and potential development of Phase II International project to be conducted prior to and during the next International Project Review meeting in Canada.
- "Knowledge-base" information to be collated and recorded in media accessible to the participants (e.g., via USCAR Vroom for U.S. or MSST SharePoint web site for international participants.

Introduction

Details of the AMD604 (MFERD) project, including its background and rationale, were included in the prior annual reviews and are not repeated here for reasons of brevity [1]. This report emphasizes achievements of the second full

year of the project with a focus on those task items accomplished through the USAMP AMD604 Project. Accomplishments of the international partners during this period are detailed in a separate report [2]. The overarching objectives of the effort are (1) the development of a knowledge base for use in eventual design and (2) the realization of enabling manufacturing technologies for Mg componentry, as may be assembled into durable vehicle substructures. These broad objectives collectively support design and potential manufacture of Mg-intensive automotive structures such as the "front end" portrayed in Figure 1. Technical obstacles to the realization of structurally sound and durable Mg-intensive assemblies are well known and itemized in USAMP's roadmap document for Mg technology [3]. The agenda for the various project tasks as detailed in Figure 3 support the overarching technical challenges of the project as a whole.

During FY 2008, substantial progress was made in all task areas, not only in the U.S., but in Canada and China as well, as had been demonstrated at both the international review in Hangzhou, and the Canadian annual meeting in Sherbrooke. Sample materials are now being distributed to the various laboratories and measurements are being reported through the international task teams. The "knowledge" tasks 1–4 are regularly reporting results and sharing sample materials as they become available. Some international task teams are also progressing to the point of regular international conference calls and web meetings to review status and discuss various results. The "SharePoint" web site, maintained by MSST, is being populated with project reports and data.

The overarching project philosophy, dating back to initial discussions of such an extensive collaborative effort, encompasses both a set of extraordinary opportunities in vehicle design and performance, and concomitantly, a set of grand challenges for the scientific and technological underpinnings of such a concept. The opportunities arise from the theoretical potential for an approximate 50% (or better) mass savings as compared to a mild steel baseline for components of comparable stiffness. Additionally, the die casting process, and its derivatives, for Mg alloys could readily permit considerable piece-part consolidation and thereby systemic cost reduction. Design targets such as mass redistribution and mass-loss compounding are also realizable. The grand challenges derive principally from the basic materials science of Mg metal and its various commercial alloys: (a) exceedingly temperamental mechanical properties fundamentally attributable to its hexagonal close-packed crystal structure and (b) extraordinarily large electrochemical oxidation potential, rendering it anodic to virtually all other engineering materials to which it may be coupled. While scientific and technical approaches to these grand challenges exist, principally through alloying, microstructural control, thermomechanical processing, and protective surface treatments, it is not clear that any of the scientifically accepted remedies might become so commonplace as to be readily accepted into the automotive manufacturing environment where cost, availability, and performance are paramount.

ICME has the potential to address the grand challenges from the standpoint of orchestration of the basic physical metallurgy of Mg and its processing into a less formidable undertaking [4]. Mg alloys could be among the first engineering materials to benefit from ICME. The companion projects (AMD702 and 703) seek to take advantage of the ICME approach and worldwide community of practitioners.

The following sections describe key technical attributes of the project and accomplishments occurring during federal fiscal year (FY) 2008.

2008 Progress and Accomplishments

Project Management and Organization. The project managerial structure as originally set forth is fully operational, and requisite meetings of the PSC and PTC are ongoing. All project documentation is received and archived. The second annual review meeting was held in Hangzhou, PRC, in April 2008, and a bound proceedings volume was concurrently published for use by team members [2]. All task area committees are functional and work flows are progressing according to the initial project work statement or amended versions as agreed upon by the task teams. The USAMP companion design project (AMD603) has generated a number of

outcomes, from which generalized design guidelines can flow into the relevant committee structures, short of actual complete design details. The next international review meeting is scheduled to occur at Niagara-on-the-Lake, Ontario, Canada, from May 11–13, 2009.

Task 1.1—Crashworthiness. The Crashworthiness task includes material testing, computer-aided engineering (CAE) analyses, and testing of beams in bending and axial compression. During 2008, approximately 85% of the material testing was completed on the five Mg alloys of interest: AM30 and AZ31 extrusions, AZ31 sheet, AM60 and AM50 die castings. AM30 extruded box-section beams were tested in slow four-point bend, slow axial compression, and fast axial compression. LS-DYNA models predicted beam response. The high speed axial crush test involves local corner and flat section buckling, local plastic deformation, high local strains, locally high strain rates, material cracking, and separation. The LS-DYNA model predicted a peak axial load 50 kN higher than the peak load measured in the six tests. The overprediction of the peak load and the overprediction of the continuing collapse load results in more than a 100% overprediction in the calculated energy absorbed during the first 200 mm of deformation. The initial LS-DYNA predictions did not include cracking. The tested parts all exhibited significant material cracking and fracture as shown in Figure 4.

Figure 4. Final deformed shape of the extruded Mg AM30 beam after an axial compression test.

Continuing efforts of the task are aimed at reconciling differences between predicted and observed crush behaviors, as well as extending the measurements and calculations to the other materials of interest, once an acceptable CAE formalism has been determined.

Task 1.2—NVH. The U.S. team enlisted the participation of supplier company IAC, and acquired sound transmission loss (STL) data for 1 mm and 2 mm sheet Mg materials as employed in an exemplary Chrysler Mg-intensive vehicle dash structure. These data are shown in Figure 5, where it can be seen that the 2 mm material approximates loss values from 0.8 mm steel sheet. Additionally, IAC provided data for Mg sandwich structures employing structural foams as acoustic resistance between flat-panel elements. The U.S. team also supplied generic NVH materials information to support the CAE modeling activities internationally.

Task 1.3—Fatigue and Durability. Subtasks for this topic include the international round-robin fatigue testing of excised coupons from an extruded AM30 Mg structure, originally devised by one of the OEMs. Strain-life data from these coupons has now been collected and typical results from 0.3% and 0.6% strain are summarized in Figure 6.

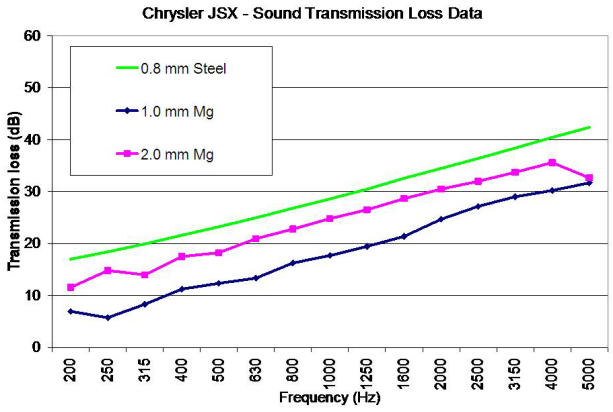

Figure 5. STL for 0.8 mm steel sheet and 1 mm and 2 mm Mg sheet as determined by IAC Corporation.

Monotonic stress-strain data collected to date from the particular AM30 extruded material show an average ultimate tensile strength of 245 MPa, yield strength of 170 MPa, and elongation in the

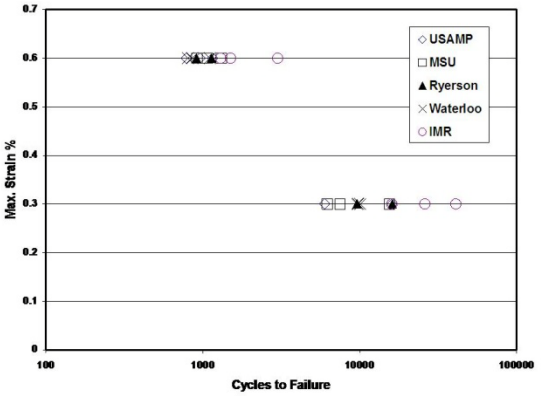

Figure 6. Strain-life data points from extruded AM30 structural piece by laboratory.

range of 15–20%. Fatigue testing to date has not taken into account the large plastic deformation anisotropy associated with extruded materials, and such data will eventually need to be obtained. The crush tube extrusions employed by the crashworthiness task, however, have wall thicknesses too thin (ca 2 mm) for idealized fatigue test geometries. MSST has provided recommendations for specific joint geometries for fatigue testing of weldments.

Task 1.4—Corrosion and Surface Treatment. The Task 1.4 Team assessed various pretreatments including conversion type treatments and anodized surfaces for application with both paint and adhesive overlayers. Additionally, a statistically designed experiment (DOE) was conducted to evaluate sensitivities for a proposed VDA-based protocol for measuring the resistance of coatings on steel fasteners to galvanic coupling to adjacent Mg alloy structures. An experimental approach to the assessment of completed coating systems including metal pretreatment and polymeric topcoat layers was developed by Eastern Michigan University. This methodology, known as AC/DC/AC, utilizes electrochemical impedance spectroscopy (EIS) as the primary measurement technique, with provision for a cathodic direct current stress applied to the specimen to force undercut corrosion of the polymer layer, as is expected to occur with Mg. Typical results from this approach are illustrated in Figure 7, which shows initial Bode plots (modulus vs frequency) for the AZ31 sheet and AM60B die casting and subsequent plots revealing a more severe degradation of the coating system for the AZ31 sheet in comparison to the AM60B die casting. The approach greatly reduces the time required to make an assessment of the total coating system by approximately a factor of ten. The international team has also discussed the matrix of expected test protocols for the various situations as may exist on a hypothetical front-end structure, ranging from coating durability and corrosion resistance to fastener studies and evaluation of environmentally-assisted fractures, either stress-corrosion crack or corrosion fatigue.

Task 1.5—Low-Cost Extrusion. Although the initial conceptual design for the unibody front-end structure suggests a relatively small number of extrusions, these components are crucial insofar as providing among the higher specific strengths observed for structural Mg alloys and expectation of use in critical positions such as bumper beams and crush rails. The traditional limitation to greater use of Mg extrusions is the generally high cost of manufacture, dictated in part by the relatively low rate of production due to the intrinsically poor formability of the material. An emerging concern is also the large degree of mechanical property anisotropy (in particular, yield strength) being observed for shapes such as the crush tube for Task 1.1 as illustrated in Figure 8. Efforts underway include expanded use of modeling software such as DEFORM 3-D to predict and optimize extrusion behavior for specific cross-sections. The Institute for Metal Forming of Lehigh University has conducted modeling and microstructural evaluations of the extrusion process. The topic is similarly linked to AMD702 (ICME) efforts at MSST to understand the influence of microstructure on the extrusion process. First-year results also include initial measurement of crystallographic textures of extruded shapes at key locations. A major U.S. supplier of extrusions, Timminco Inc., has been enlisted to produce experimental shapes as shown above for the project in both AM30 and AZ61 alloys. Extruded tubes of alloys AM30, AZ31, and AZ61 from China have been chemically analyzed and material properties determined.

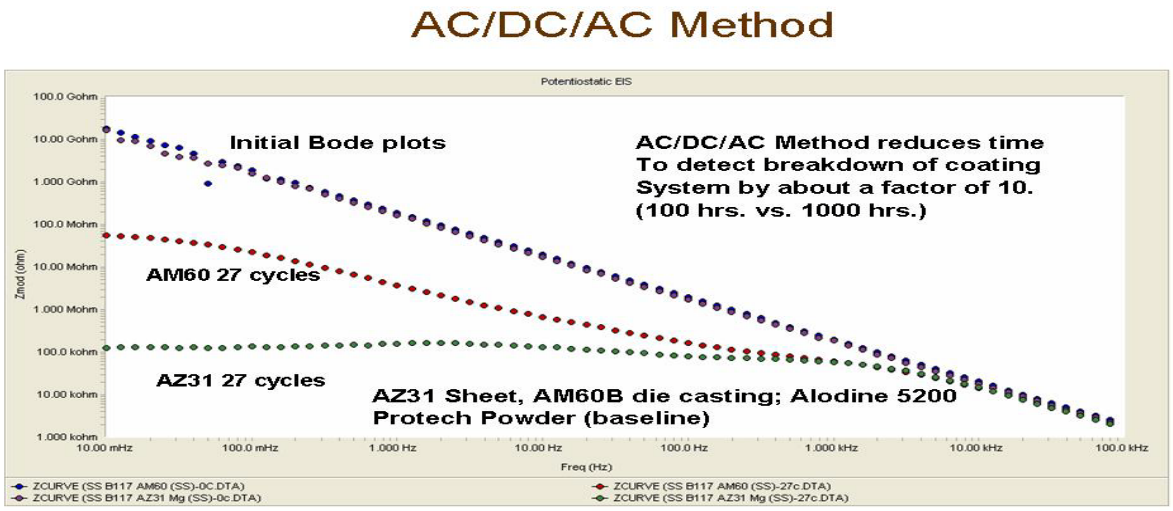

Figure 7. Before and after EIS evaluation of AZ31sheet and AM60B die casting with comparable surface treatments.

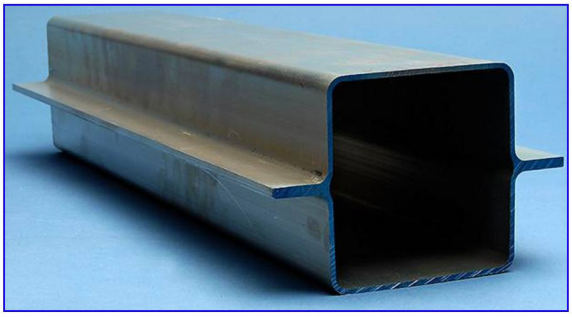

Figure 8. AM30 alloy extruded as a "crush tube" for crashworthiness and mechanical property studies of deformation anisotropy.

Task 1.6—Low-Cost Sheet and Forming. Efforts on low-cost sheet forming of Mg are incorporated in USAMP project AMD602, and only differentials requisite for the "front end" structure are considered here. To date, a variety of commercially available sheet materials of both direct chill and continuous cast materials are available and comparative sheet forming results were obtained. The various sheet materials all showed similar deformation behavior, generally capable of constitutive modeling using the Sellars-Tegart equation [5]. In "pan" forming (which has been the principal approach of AMD602), binder pressure is critical for forming deeper pans without wrinkling. The interaction of the sheet material with the lubricant and die surface tends to override any microstructural differences in the starting materials. The lowest temperature for successful pan forming was found to be 275ºC. Figure 9 illustrates the acceptable forming regime plotted as number of acceptable "corners" of the pan, in terms of binder pressure and forming temperature.

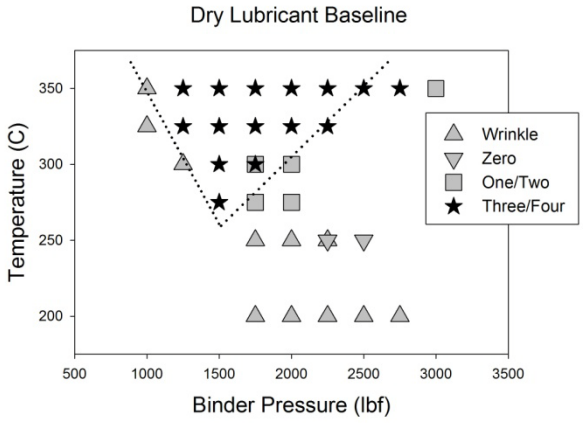

Figure 9. Regime of acceptable forming of a pan structure from AZ31 sheet, in terms of sheet preheat temperature and binder pressure.

Task 1.7—High-Integrity Body Castings. The companion design project (USAMP AMD603) suggests a strong reliance on large Mg alloy castings which simultaneously achieve both weight reduction and part integration, contributing to lowering of manufacturing cost. The casting process also permits adjustment of section thickness at various locations in the component,

which is generally not achievable in sheet forming processes. The traditional high-pressure die casting process, presently used to form large structures in Mg, can suffer from substantial reductions in localized strength and elongation when compared to the maximum theoretical values for the material. These variations are primarily due to incorporation and distribution of porosity resulting from the turbulent nature of the die-casting process itself. ICME is expected to play a major role in addressing those physical attributes of the metal flow and solidification which can lead to improved properties. Vacuum-based processes have also been found to reduce the quantity of entrained gas and permit generally improved metal flows into the die cavity. International efforts are aimed at exploring alternative casting processes [e.g. Thixoforming (Canada), squeeze casting (China)] as remedies to challenge at hand. Additionally, heat treatments may be a remedy to improve performance of the as-cast structures.

In FY 2008, initial trials have been conducted with two vacuum processes, including a horizontal process (SVDC—Contech, LLC) and vertical (Gibbs Die Casting) approaches. Figure 10 illustrates a shock tower component of a front-end structure as implemented in SVDC.

Figure 10. AM60B shock tower produced by the horizontal SVDC process.

Although yield strengths of excised coupons appear marginally below isolated coupon or handbook values, improvement may be possible through minor alloy modifications. Elongation, indicative of the influence of porosity, is markedly improved by the vacuum processes.

Task 1.8—Joining: The U.S. Task 1.8 team is focused on the following subtask areas: (a) adhesive bonding, including pretreatment and degradation; (b) NDE of all joint types; (c) friction stir welding; and (d) fasteners, including threaded fasteners, breakstem rivets, and SPRs. Hitachi America was enlisted as a project participant in 2008 to provide developmental friction-stir welding of both spot and linear welds. A supplier is still being sought for development of SPR technology as this technology is expected to have substantial use in manufacture of unibody Mg front-end structures.

A major achievement in 2008 was the assessment of various metal pretreatments available either developmentally or in the marketplace, including several representative treatments from participating organizations in China. Several key design factors surround the selection and performance of metal pretreatments: (a) current design considerations for the unibody assembly suggest widespread use of adhesive bonding in concert with other techniques, hence the requirement that metal surfaces receive some form of pretreatment prior to the build process, (b) corrosion undercutting of the adhesive is an undesirable failure mode of the bond, and also a concern for painted surface degradation in other areas of the structure, and (c) design for durability must take into account any degradation of adhesively bonded joints with regard to structural integrity in service.

Figure 11 shows adhesive bond fracture appearance and strength degradation data obtained from lap-shear tensile pull testing of pretreated, bonded, and corrosion-exposed joints. Comparative before/after strength values for two different metal pretreatments (denoted “A” and “B”) and resultant fracture paths after 30 cycles of a standardized cyclic corrosion test (Ford APGE) are shown. For pretreatment “A” the fracture is characterized by complete undercutting of the bond and substantial loss in lap-shear strength, while in “B” the joint was seen to fail through the adhesive material as is desirable for adhesive bonding. Similar measurements were conducted

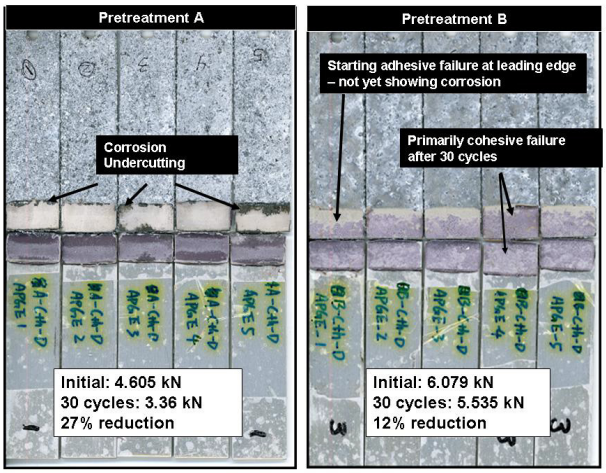

Figure 11. Typical locus of fracture experiment results for tensile lap-shear coupons for comparative assessment of pretreatment durability.

over a matrix of 10 different pretreatments, permitting levels of acceptance to be established. Assessment of general corrosion resistance of the same pretreatments was also undertaken by Task 1.4 (Corrosion).

Conclusions

At the end of its second full year, AMD604 continues to demonstrate progress toward objectives for all of the individual task areas, with considerable challenges remaining in many of them. The organizational framework, both nationally and internationally, is functional; despite impediments of time, space, and language, the collaborative approach is proving to be both scientifically and culturally gratifying to the participants. Materials, data, and discussions are regularly transcending the obstacles once imagined. New friendships and networks are developing.

The pivotal milestone of FY 2009 will be the collective decision by the participants regarding the future of the project. Factors both scientific and otherwise will surely make this discussion both exciting and challenging for those involved

Presentations/Publications

1. A. A. Luo, E. A. Nyberg, K. Sadayappan, and W. Shi, "Magnesium Front End Research and Development: A Canada-China-USA Collaboration," pp 3–10 in M. O. Pekguleryuz, N. R. Neelameggham, R. S. Beals, and E. A. Nyberg, eds. *Magnesium Technology 2008,* TMS Annual Meeting, New Orleans, Louisiana, March 9–13, 2008, TMS, Warrendale, Pennsylvania (2008).
2. E. A. Nyberg, A. A. Luo, K. Sadayappan, and W. Shi, "Magnesium for Future Autos," *Advanced Materials & Processes,* **166**(10), 35–37 (2008).

Acknowledgments

The success of this project is due to the dedicated efforts of a large number of team members at Chrysler, Ford, and General Motors; the various supplier organizations listed below; and the international counterparts in Canada and China. The current and past USAMP core team members, Steve Logan, Randy Beals, and Eric McCarty of Chrysler; John Allison, David Wagner, Mike Maj, Joy Hines Forsmark, and Jake Zindel of Ford; James Quinn, Dick Osborne, Larry Ouimet, Ravi Verma, and Theresa Lee of General Motors, are acknowledged for their significant contributions and tireless efforts. Continuing support from our respective organizations and DOE is gratefully acknowledged.

University of Dayton Research Institute
Troy Tooling Technologies
Cosma Engineering
Contech U.S., LLC
IAC Group North America
Westmoreland Mech.Testing & Research
Metokote Corporation
Henkel Corporation
PPG Corporation
Chemetall-Oakite Corporation
Keronite
International Hardcoat Corporation
MacDermid, Incorporated
The Magni Group, Inc.
Atotech Corporation
Kamax LP
Ohio State University
Eastern Michigan University
University of Michigan - Dearborn
North Dakota State University
Luke Engineering & Mfg. Corp.
Technical Applications Group
Timminco Corporation
Lehigh University
Scientific Forming Technologies Corp.
Magnesium Elektron North America
Contech Global, LLC
EKK Corporation
U.S. Magnesium
North American Die Casting Assn.
Gibbs Die Casting
Hitachi
ATF
REMINC
Visteon
MNP Corp.
Dow Automotive

References

1. A. Luo, R. C. McCune, J. A. Carpenter, A. D.Yocum and P. S. Sklad, "Mg Front-End Research and Development (AMD604)," FY 2007 Progress Report, U.S. DOE, 2008.

2. A Canada-China-USA Collaborative Research and Development Project, "Magnesium Front End Research and Development (MFERD)," 2007 Annual Progress Reports, Project Technical Committee, Hangzhou, China, April 2008.
3. USAMP, "Mg Vision 2020: A North American Automotive Strategic Vision for Mg," Nov. 1, 2006.
4. "Integrated Computational Materials Engineering: A Transformational Discipline for Improved Competitiveness and National Security," Committee on Integrated Computational Materials Engineering, National Research Council, ISBN: 0-309-12000-4 (2008).
5. http://www.nap.edu/catalog/12199.html.
6. M. Sellars and W. J. Tegart, "Relationship between Strength and Structure in Deformation at Elevated Temperature," *Mem. Sci. Rev. Metall.* **63**, 731–745 (1967).

D. Nanotechnology-Based Self-Healing Coating System to Enable Use of Magnesium Alloys in Automotives

Principal Investigator: Dr. Jiong Liu
Alternate POCs: Mr. Shekhar Bafna and Dr. Ganesh Skandan, CEO
NEI Corporation
400 Apgar Drive, Suite E
Somerset, NJ 08873
732-868-3141; fax: 732-868-3143; E-Mail: JLiu@neicorporation.com; gskandan@neicorporation.com

Technology Area Development Manager: Joseph A. Carpenter
(202) 586-1022; fax: (202) 586-1600; e-mail: joseph.carpenter@ee.doe.gov

Contractor: NEI Corporation
Contract No.: DE-FG02-08ER85204 through the Small Business Innovation Research and Small Business Technology Transfer Program

Objective

- To develop chromate-free self-healing coating systems, including pretreatment and primer, which exhibit damage-responsive corrosion protection to magnesium substrates.

Approach

- The pretreatment was based on a polymer which reacts with the magnesium cations formed under mildly acidic conditions. This reaction in turn leads to the formation of a thin and dense protective film on the metal surface.
- Nanoscale corrosion inhibitors added to the pretreatment matrix were based on a functionalized nanoparticle. Active components leach out from the nanoparticle and retard the cathodic corrosion reactions of magnesium by forming a dense protective film on the surface.
- Chromate-free corrosion inhibiting particles that can be added into primer formulations mimic the self-healing behavior of chromate-based corrosion inhibitors which can diffuse through the coating matrix to defect sites and transition from higher to lower valence state by undergoing reduction to form a protective and stable film on the metal surface.

Accomplishments

- Demonstrated the ability of a waterborne inorganic-organic hybrid pretreatment (hereafter NEI pretreatment) containing functionalized nanoparticles to passivate the surface of AZ91D magnesium alloy. The NEI pretreatment forms a coherent barrier layer, with corrosion inhibition provided by the functionalized nanoparticles.
- Demonstrated that the NEI pretreatment is compatible with commercial automotive e-coat and powder coat, and that the coatings applied on the surface treated substrate do not have any defects.
- Demonstrated self-healing behavior of the NEI pretreatment through direct current (dc) polarization studies: the corrosion current of AZ91D was reduced and the corrosion potential was increased by the NEI pretreatment;
- Developed a novel, chromate-free corrosion-inhibiting particle based on a transition metal. Electrochemical tests showed the ability of this particle to result in a passivating film on AZ91D, mimicking that of a chromate pigment.
- Formulated a corrosion-inhibiting automotive epoxy primer and powder coat containing the newly developed chromate-free particle and demonstrated self-healing corrosion protection.

Future Direction

- The Phase I project is complete.
- Phase II, if awarded, will be focusing on the development of a self-healing pretreatment and powder coat to mitigate galvanic and general corrosion of magnesium components.

Introduction

This Phase I project was completed in April 2008. The overall purpose of this study was to search for effective chromate-free self-healing coating systems to protect lightweight magnesium die-cast alloys from corrosion.

NEI Corporation demonstrated self-healing characteristics in a newly developed pretreatment and primer applied on the most commonly used magnesium structural alloy, AZ91D. Corrosion tests showed that the pretreatment with nanoscale particles has the ability to provide damage-responsive corrosion protection to the magnesium substrate. A corrosion-inhibiting epoxy spray primer and powder coat were also formulated in the Phase I program. It was found that the corrosion-inhibitor particles have the ability to leach out from the coating to active corrosion sites on the magnesium substrate and provide self-healing. Hence, the combination of a corrosion-inhibiting pretreatment and powder coat has the potential to provide enhanced corrosion protection to magnesium compared to the current coatings. The coating formulations used in the Phase I program are significantly different from the state-of-the-art, and are enabled by nanotechnology. The pretreatment and primer formulations contain functionalized nanometer-sized particles (hereafter nanoparticles) with corrosion-inhibiting ions incorporated directly into a polymer matrix. These ions readily leach out and form a protective insoluble film at the active corrosion sites. Excellent adhesion and barrier properties are attributed to the formulation chemistry, which also enables efficient transport of the corrosion-inhibiting species. The formulations are stable suspensions and the coatings are homogeneous systems at the micro- and macro-scale, since they contain well-dispersed nanoparticles.

Development of a Waterborne Pretreatment Formulation Containing Nanoparticle Corrosion Inhibitor

The NEI pretreatment formulation has a hybrid inorganic-organic matrix containing functionalized nanoscale particles. The hybrid matrix not only acts as an adhesive forming strong bonds with the metal surface, but also provides corrosion protection by forming an insoluble barrier film. The functionalized nanoparticles enable the corrosion inhibition of AZ91D alloy.

Figure 1 shows dc polarization curves of different commercial and NEI pretreatments on AZ91D alloy. The data show that the alloy has a high activity with an open-circuit potential of -1.5 V.

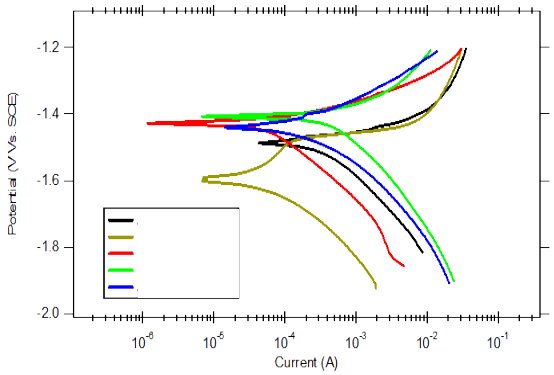

Figure 1. Polarization curves of different pretreatments on AZ91D in 3% salt-water solution.

Application of the NEI pretreatment, nonchromate II pretreatment and chromate conversion coating (Dow 7) shifts the polarization curve to a more noble value of about -1.4 V, indicative of a passivation coating which is less reactive to the salt solution compared to the

AZ91D alloy. The corrosion current of NEI pretreatment, non-chromate II pretreatment is lower by an order of magnitude compared to the AZ91D alloy, implying durability and protective properties of the pretreatments. With the NEI pretreatment, there is a positive shift in the E_{corr} similar to the chromate conversion coating (Dow 7).

Deposition of Commercial E-coat on Pretreated AZ91D Panels

During the Phase I program, we performed e-coating of NEI and commercially pretreated AZ91D coupons at a commercial E-coat company who showed keen interest in our research efforts and allowed the use of their e-coating line for our panels at no charge. Panels were tested in the salt fog test to determine the corrosion resistance of the e-coat applied on NEI and other commercial pretreatments.

Figure 2 shows photographs of e-coats applied over untreated AZ91D panels and panels after NEI pretreatment with and without corrosion inhibitors. The photographs were taken after four weeks of salt fog testing. Untreated panels undergo severe delamination of the e-coat and corrosion products form along the scribe (Figure 2a). NEI pretreatment without nanoscale corrosion inhibitors showed significant improvement in the scribe creep indicating strong adhesive properties of the pretreatment (Figure 2b). Addition of functionalized nanoparticles into the pretreatment further decreased the scribe-creep and showed no corrosion along the scribe lines (Figure 2c). However, e-coat applied over NEI pretreatment containing nanoparticle corrosion inhibitors show some defects over the surface. This is presumably due to the aggregation of nanoparticles which led to defects on the coating surface. The Phase II effort will optimize the pretreatment formulation to eliminate these defects.

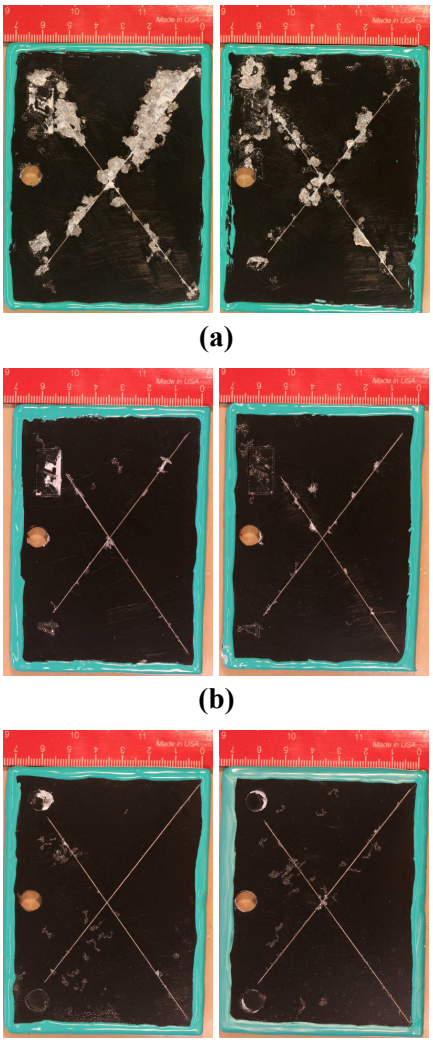

(a)

(b)

(c)

Figure 2. Photographs of epoxy e-coat applied over AZ91D panels having different pretreatments after 4 weeks of American Society for Testing and Materials B-117 salt fog test. (a) Untreated AZ91D, (b) NEI pretreatment without nanoparticle corrosion inhibitor, and (c) NEI pretreatment with nanoparticle corrosion inhibitor.

Synthesis of Chromate-Free Corrosion Inhibitor Particles for Powder Coat

A new corrosion-inhibiting compound containing transition metal was synthesized. This particle mimics the self-healing behavior of chromate-based corrosion inhibitors which can diffuse through the coating matrix to defect sites and transition from higher- to lower-valence state by undergoing reduction to form a protective and stable oxide film on the metal surface. The ability of the chromate-free particle to change valence state was confirmed by X-ray photoelectron spectroscopy (XPS) and ultraviolet-visible (UV-Vis) spectroscopy. Figure 3 shows that the corrosion current is lowered by an order of magnitude by the NEI chromate-free particle compared to a blank AZ91D sample, indicating that the inhibitor particle led to the formation of a passivating film on the AZ91D surface.

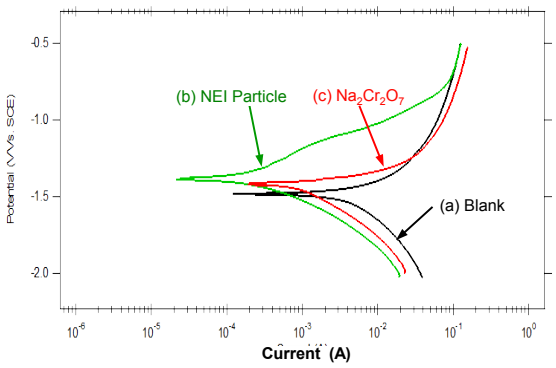

Figure 3. The dc polarization of AZ91D exposed to (a) 3% NaCl solution, (b) 3% NaCl + 0.2% NEI chromate-free particle solution, and (c) 3% NaCl solution + 0.2% sodium dichromate. Panels were exposed to the solutions for 3 hours before the anodic and cathodic scans were performed.

Development of Corrosion-Inhibiting Powder Coat and Liquid Epoxy Primers to Achieve "Self-healing" Corrosion Protection

The newly developed, chromate-free particles were successfully incorporated into an epoxy powder coat and an automotive refinish epoxy primer with excellent dispersive properties (Figure 4). Figure 5 shows photographs of micrometer-sized artificial defects made in the epoxy primer before and after immersion in salt water for 48 hours. It demonstrates that the defect in the primer without NEI corrosion inhibitors is completely corroded indicating the high propensity of the Mg alloy to corrode. On the other hand, the defect in the primer containing 5 wt% NEI particles does not corrode and shows the appearance of a protective film on the surface.

(a) **(b)**

Figure 4. Photographs of (a) epoxy powder coat with 4 vol % NEI chromate-free inhibitor and (b) epoxy liquid spray primer with 5 vol % NEI chromate-free inhibitor.

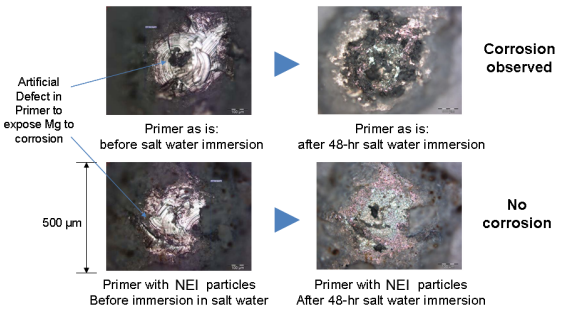

Figure 5. Optical micrographs of artificial defect made in epoxy primer with and without NEI chromate-free particles. AZ91D test coupons before immersion in 3 % NaCl solution and after 48 hours immersion are shown.

Conclusions

A self-healing pretreatment and a self-healing powder coat for corrosion protection of magnesium alloy AZ91D have been developed in Phase I. Electrochemical and salt-water immersion tests showed that an organic-inorganic hybrid pretreatment containing functionalized nanoparticle passivates AZ91D and lowers its rate of corrosion. A transition-metal-based corrosion-inhibiting particle was synthesized in the program. Preliminary tests in salt-water immersion and potentiodynamic polarization showed the ability of the inhibitor to mimic inhibiting properties of chromium salt. Further confirmation of inhibitive properties of the particles was detected by UV-Vis

spectroscopy and XPS. The Phase I program has demonstrated the feasibility of inhibiting corrosion of magnesium by the proposed pretreatment and primer/powder coat process.

Presentations/Publications/Patents

1. J. Liu, S. Bafna, F. Allen, and G. Skandan, "Chromate-free Corrosion Resistant Nanocomposite Pretreatments for Structural Metals", Mega Rust Navy Corrosion Conference, Norfolk, Virginia, June 2009.
2. J. Liu, S. Bafna, F. Allen, and G. Skandan, "Chromate-free Corrosion Resistant Nanocomposite Pretreatments for Light-weight Metals", 215th ECS meeting, San Francisco, California, May 2009.
3. F. Allen, S. Bafna, J. Liu, and G. Skandan, "Corrosion Inhibiting Chromate-free Nanocomposite Pretreatments for Structural Metals", U.S. Army Corrosion Summit, Clearwater Beach, Florida, February 2009.
4. S. Bafna, J. Blair, and G. Skandan, "Corrosion Resistant Coatings for Light Metal Alloys", 236th ACS National Meeting, Philadelphia, Pennsylvania, August 2008.

E. High-Strain-Rate Characterization of Magnesium Alloys

Principal Investigator: Srdjan Simunovic
Oak Ridge National Laboratory
P.O. Box 2008, Oak Ridge, TN 37831-6164
(865) 241-3863; fax: (865) 241-0381; e-mail: simunovics@ornl.gov

Co-Principal Investigator: J. Michael Starbuck
Oak Ridge National Laboratory
P.O. Box 2009, Oak Ridge, TN 37831-8048
(865) 576-3633; fax: (865) 574-8257; e-mail: starbuckjm@ornl.gov

Co-Principal Investigator: Don Erdman
Oak Ridge National Laboratory
P.O. Box 2009, Oak Ridge, TN 37831-8048
(865) 576-4069; fax: (865) 574-0641; e-mail: erdmandl@ornl.gov

Technology Area Development Manager: Joseph A. Carpenter
(202) 586-1022; fax: (202) 586-1600; e-mail: Joseph.Carpenter@ee.doe.gov

Field Technical Monitor: C. David Warren
(865) 574-9693; fax: (865) 574-6098; e-mail:warrencd@ornl.gov

---

Contractor: Oak Ridge National Laboratory
Contract No.: DE-AC05-00OR22725

Objectives

- Characterize mechanical material properties of magnesium (Mg) alloys for automotive applications.
- Determine material model parameters for various constitutive models available in crash codes.
- Develop methods for interrupting strain-rate test at the prescribed strain.
- Experimentally determine evolution of material properties for various loading situations and strain rates.
- Formulate experimental findings into constitutive models based on continuum damage mechanics.
- Establish test and property database for automotive Mg alloys.

Accomplishments

- Performed initial strain-rate test in tension for Mg AM60 alloy.
- Developed preliminary design of the fixture for interrupted strain-rate tests in tension
- Developed database for test data analysis.

Future Direction

- Improve accuracy of strain measurements for Mg alloys.
- Integrate faster high-speed video into measurement system.
- Test and improve method for interrupted strain-rate tests.

Introduction

The low density and excellent machinability of Mg alloys make them good candidates for light-weight construction of automotive components. However, they also exhibit much more complex mechanical behavior than more common automotive materials. The mechanical response of Mg alloys involves notable anisotropy, nonisotropic hardening, yield asymmetry, lower ductility than other automotive materials, and significant degradation of effective properties due to formation and evolution of microdefects. Figure 1 shows a Mg alloy tube being crushed at 0.5 m/s. The intense fracturing is notably different behavior from the progressive folding observed in conventional automotive steel structures and requires in-depth material and structural understanding for automotive application.

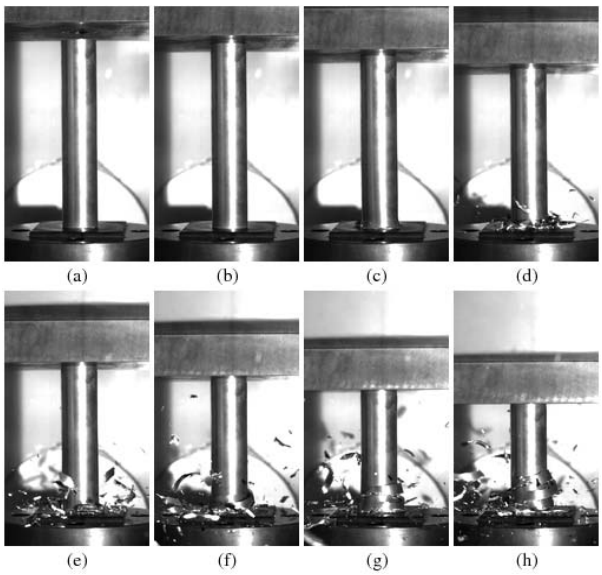

Figure 1. Crush of Mg alloy tube at 0.5 m/s.

Accordingly, the necessary characterization procedures and constitutive models are more complex than commonly used uniaxial tests and isotropic plasticity for steel. Another issue of concern for automotive designers is the strain-rate sensitivity of various properties of Mg alloys. Preliminary tests indicate there is significant strain-rate sensitivity in certain Mg alloys. In Mg alloys, strain-rate sensitivity is manifested by an increased hardening rate that is beneficial for diffusing and postponing the onset of localization and fracture. However, the lack of strain-rate sensitivity information coupled with the lack of understanding of loading-induced property degradation for Mg alloys adds to the concerns typically associated with using a new material. The strain-rate sensitivity in Mg alloys is not only linked to yield strength but to other effective material properties such as effective elastic modulus, while internal structure evolution is important to the onset of ductile fracture. Experiments on several wrought and cast Mg alloys reported in the literature show the considerable effect of manufacturing conditions on alloy properties. Correlation of the properties of Mg alloys in manufactured parts with those of specimens made under optimal conditions is needed to avoid lengthy testing for numerous manufacturing situations.

Technical Approach

In support of the U.S. Automotive Materials Partnership project AMD604, Magnesium Front End Research and Development, we are investigating rate-dependent properties of automotive Mg alloys. The results will be used in the framework of different modeling approaches such as continuum damage mechanics and mechanics of plastic voided solids. The experiments are conducted under various strain rates ranging from quasi-static to rates of 500/s on the same equipment. The main scientific and technical advances anticipated are (1) the development of detailed information about Mg alloy response to impact loading, (2) characterization of property degradation by the control of imparted strain for high strain rates that will allow for detailed investigation of evolution of internal state as a function of loading rate, (3) development of tightly controlled compressive and shear high-speed tests, and (4) correlation of manufactured and ideal material properties.

The deliverables for the project are the documented rate-sensitive properties for the selected Mg materials, microstructural characterization and damage data from the tests, and material model data for selected constitutive model formulations.

High-Strain-Rate Experiments

During fiscal year 2008, we conducted several preliminary experiments and compiled them into an interactive database that is accessible over the World Wide Web (http://thyme.ornl.gov/Mg_Main/description). The home page for the database is shown in Figure 2.

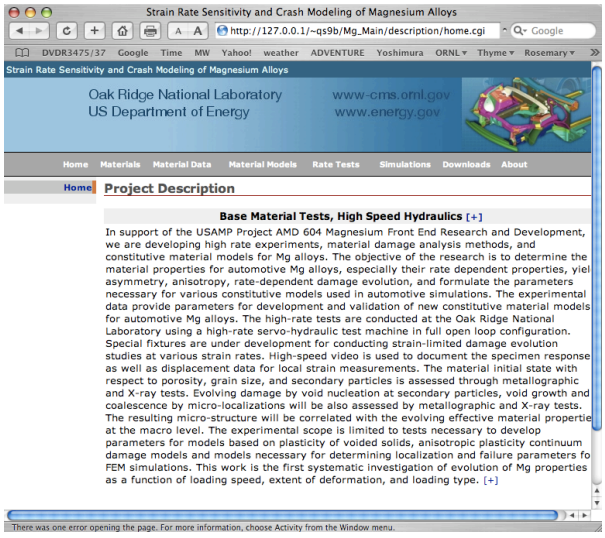

Figure 2. Home page for Mg alloy tests database.

The web interface allows for experimental data to be integrated with the other project components and provides mechanisms for data analysis and collaboration between project participants.

Tensile High-Strain-Rate Tests on Hydraulic Equipment

For tensile loading, different variations of the dog-bone style tensile specimen configurations for sheet and solid materials are used (see specimens from laboratories labeled B and C from reference [2]). Specimens are machined to accommodate a strain gage attachment in the load measurement section for sheet specimens. A similar arrangement is used for testing bar specimens from cast samples. Figure 3 is a schematic for sheet tensile tests.

Tests are conducted at six actuator speeds to achieve strain rates of quasi-static (0.001/s), 0.1/s, 1/s, 10/s, 100/s, and maximum strain rates on the order of 500/s. At high loading speeds, specimen gage lengths are shortened to provide sufficient time for specimen equilibration under the highest

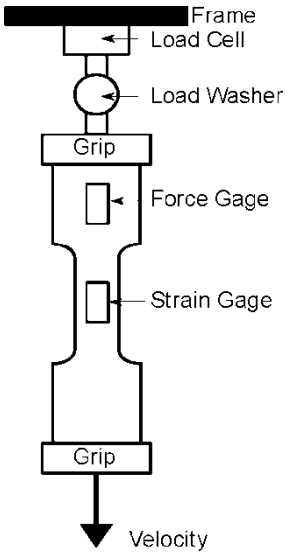

Figure 3. Tensile specimen configuration.

loading speeds [2, 3]. A slack adapter is incorporated in the load train and its initial position controlled to allow the actuator to reach constant velocity before the specimen is loaded. Also, low mass grip concepts are used to minimize inertia effects and machine resonance on the measured specimen response.

The instruments listed below are used for measurement of forces, displacements, stresses, and strains. Tests at rates higher than 1/s will be recorded with high-speed video. To ensure consistency among the various test rates, several lower-rate tests are recorded during the test development.

Forces are measured by the following.

1. Strain gage, full bridge DC load cell.
2. Piezoelectric load washer.
3. Calibrated strain gage on the specimen tab [3].

Strains are measured by the following.

1. Actuator displacement.
2. Optical measurements from high-speed video.
3. Strain gages located in the test gage region.

Multiple measurement of both forces and displacements allows for correlation of the results and verification of the methods.

Characterization of Damage Evolution in Mg Alloys

For realistic description of the mechanical response of Mg alloys and to characterize the onset of failure it is essential to identify and understand the initiation and progression of damage leading to material property degradation, instability, and failure. To this end, test methods must be able to incrementally load specimens to intermediate levels on the stress-strain curve and evaluate the magnitude of the damage evolution at each level. To accomplish this task at high strain rates, novel test fixtures must be used to limit strain and/or load levels for a series of single specimens and evaluate the damage state using microscopy/metallographic techniques on the sectioned specimens.

Figure 4 schematically depicts the method to introduce a desired strain level at high rate [4] into a specimen by attaching a strengthened pull-rod to the bottom end of the specimen with a mechanical fuse. The pull-rod passes through a hole in the fixed plate and is attached to the test machine actuator. When the actuator moves downward, the specimen elongates until it contacts the fixed rigid plate and the mechanical fuse breaks and detaches from the specimen.

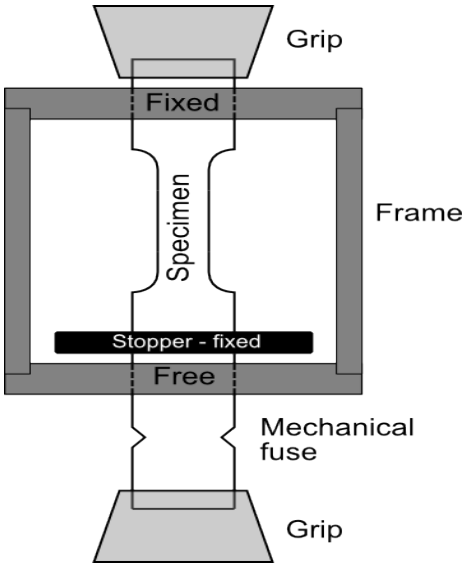

Figure 4. Strain-limiting fixture schematic.

We have designed a preliminary fixture based on the above idea and adapted it to the current high-speed testing setup. The fixture design will be further evolved as we conduct the tests and develop more experience with the process.

Material damage will be assessed through measurement of effective elastic modulus, and measurement of evolving microstructural features (e.g., void distribution and size) will be accomplished through a combination of metallographic and X-ray examinations. Evolving stages of damage (e.g., void nucleation, void growth, and void coalescence) will be characterized.

Conclusions

A new project for characterization of strain-rate sensitivity of Mg alloys under automotive strain rates has been initiated. The test methods are being modified to account for characteristic Mg response under impact conditions. When fully developed, the tests will provide needed data for more effective design with Mg alloys and lightweight automotive designs.

Future Work

Future project tasks include the following.

1. Specimen design for high-rate tests for Mg alloys.
2. Refinement of the interrupted strain-test method.
3. Development of high-strain-rate tests for compression and shear.
4. Measurement of material properties for Mg alloys.
5. Measurement of evolving damage in Mg alloys under loading.
6. Constitutive models for Mg alloys.

References

1. E. A. Nyberg, A. A. Luo, and K. Sadayappan, “Magnesium for Future Autos, Advanced Materials, and Processes,” ASM International, October 2008, pp. 35–37 (2008).
2. C. Wong, “IISI-AutoCo Round-Robin Dynamic Tensile Testing Project, International Iron and Steel Institute,” 2005.

3. D. Matlock and J. Speer, "Constitutive Behavior of High Strength Multiphase Sheet Steels Under High Strain Rate Deformation," AISI/DOE Technology Roadmap Program, Report TRP 9904, 2005.

4. Choi et al., "Strain Control during High Speed Tensile Testing," *Journal of Testing and Evaluation*, **34**(5), pp. 1–4 (September 2006).

F. High-Rate Damage and Fracture, Experimentation, Simulation, and Visualization

Principal Investigator: Philip Gullett
Assistant Professor, Civil and Environmental Engineering
Mississippi State University
Walker Bldg., Rm. 235 M
Mississippi State, MS 39762
(662) 325-5486; fax: (662) 325-7189; e-mail: pmgullett@engr.msstate.edu

Co-Principal Investigator: Mark F. Horstemeyer
Center for Advanced Vehicular Systems Chair in Solid Mechanics and Professor, Mechanical Engineering,
Mississippi State University
206 Carpenter Bldg., PO Box ME
Mississippi State, MS 39762
(662) 325-7308; fax: (662) 325-7223; e-mail: mfhorst@me.msstate.edu

Co-Principal Investigator: Tomasz Haupt
Center for Advanced Vehicular Systems, Mississippi State University
Box 5405
Mississippi State, MS 39762
(662) 325-4524; fax: (662) 325-5433; e-mail: haupt@cavs.msstate.edu

Research Associate II: David Oglesby
Center for Advanced Vehicular Systems, Mississippi State University
200 Research Blvd.
Mississippi State, MS 39762
(662) 325-6854; fax: (662) 325-5433; e-mail: doglesby@cavs.msstate.edu

Co-Principal Investigator: Srdjan Simunovic
Oak Ridge National Laboratory
P.O. Box 2008, Oak Ridge TN 37831-6164
(865) 241-3863; fax: (865) 241-0381; e-mail: simunovics@ornl.gov

Co-Principal Investigator: J. Michael Starbuck
Oak Ridge National Laboratory
P.O. Box 2008, Oak Ridge, TN 37831-6053
(865) 576-3633; fax: (865) 574-8257; e-mail: starbuckjm@ornl.gov

Co-Principal Investigator: Don Erdman
Oak Ridge National Laboratory
P.O. Box 2008, Oak Ridge, TN 37831-6091
(865) 576-4069; fax: (865) 574-0641; e-mail: erdmandl@ornl.gov

Technology Area Development Manager: Joseph A. Carpenter
(202) 586-1022; fax: (202) 586-1600; e-mail: joseph.carpenter@ee.doe.gov

Field Technical Manager: Philip S. Sklad
(865) 574-5069; fax: (865) 576-4963; e-mail: skladps@ornl.gov

Contractor: Mississippi State University (MSST)
Contract No.: 4000054701

Objective

- Evaluate the strain rate failure of AZ31 magnesium (Mg) for various stress states.
- Develop a damage model for stress-state dependence of dynamic damage evolution.
- Evaluate numerical procedures for the modeling of monotonic fracture of Mg.

Approach

- Characterize material behavior using split-Hopkinson pressure bar (SHPB) experiments in compression, tension, and torsion.
- Characterize damage nucleation using molecular dynamics.
- Develop damage-evolution-based fracture.

Accomplishments

- Examined anisotropic, high strain rate compression, metallurgical evaluation, of Mg AZ31.
- Evaluated the effects of grain orientation and stress states on void nucleation at triple junctions in aluminum (Al) using molecular dynamics.

Future Direction

- Complete high strain rate torsion and tension testing of AZ31.
- Develop a void nucleation model based on nanoscale simulations.
- Implement microstructure-property damage-based fracture criteria in fracture-simulation code.

Introduction

This report summarizes the state of the experimental and numerical simulation study of fracture mechanisms in metallic alloys at various size scales. This is a joint effort between Oak Ridge National Laboratory and MSST. The aim is an enhanced, multiscale microstructure-property model that can be implemented into commercial codes and be used in high-fidelity crash simulations for the design and optimization of structural Mg components. The development effort will focus on the AZ31 Mg alloy, and a complementary experimental effort will provide experimental data for other Mg alloys that can be used for the development of microstructure-property model parameters.

Experimental Results: Anisotropic Response of AZ31B

The anisotropic response of AZ31B under high-rate compressive loading has been examined. To fully quantify the effect of the loading orientation and strain rate on the stress-strain behavior of AZ31B, compression tests at quasi-static and high strain rates were performed in all three directions as indicated by Figure 1. All of the specimens were tested to fracture. The specimens were obtained from an as-received 19.05 mm thick plate in the H24 condition. Tests under quasi-static conditions were performed using an Instron 5882 electromechanical machine under constant strain rate controlled at 0.001/s. The high strain rate tests were conducted using a maraging steel SHPB apparatus.

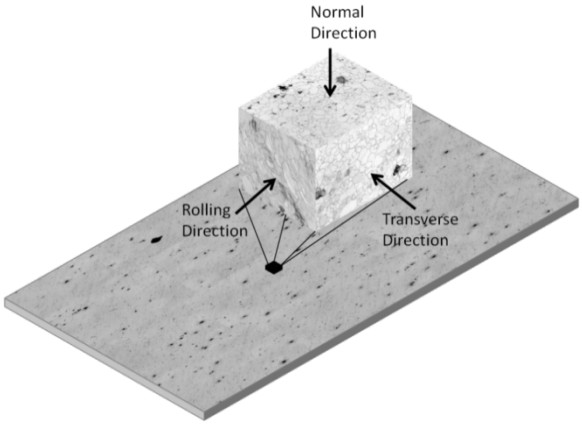

Figure 1. Orientations of testing and microstructural analysis relative to the as-received AZ31B plate.

Figure 2 shows the results of tests performed at quasi-static (10^{-3}/s) and high strain rates (3,400/s–4,300/s). When tested in the normal or short transverse direction, a strong rate dependence on the yield strength was evident. The initial hardening rate at high strain rate was similar to that at quasi-static rates, but the high strain rate specimen began to exhibit softening at a strain of approximately 0.08 which continued until the specimen fractured at a strain of approximately 0.18. This constituted a significant increase in the strain-to-failure compared to the quasi-static conditions and is likely due to either thermal softening or the onset of dynamic recrystallization during the adiabatic conditions of the high-rate test.

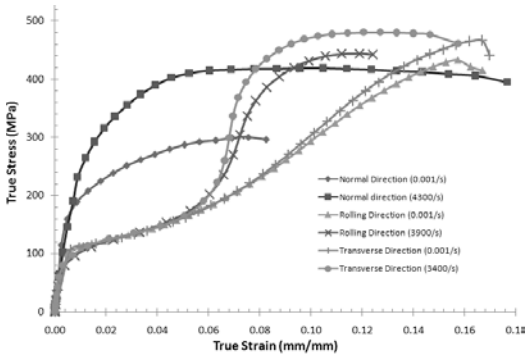

Figure 2. Compressive stress–strain behavior of AZ31B-H24 showing the anisotropic effects on the strain rate dependence.

Microstructural analysis was conducted on the specimens before and after each test and image analysis was conducted to calculate the particle-size distribution, the particle nearest-neighbor distance distribution, the aspect-ratio distribution, and the total particle area fraction. The number and percentage of fractured particles was also determined. Each specimen was then etched so that grain size and twin density analysis could be performed.

Figure 3 shows optical microscope images of the polished and etched specimens. This particular specimen was oriented in the normal direction and tested in quasi-static compression. Note that image 3(a) is a mosaic of 16 smaller images so that a representative area could be analyzed. The grain

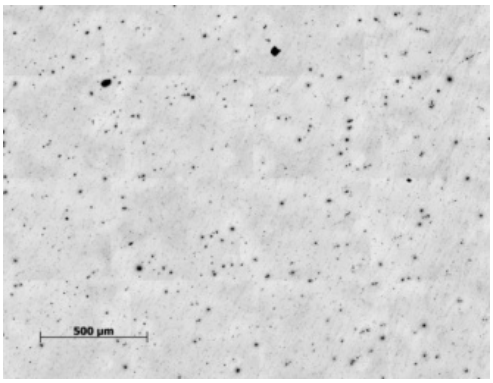

(a)

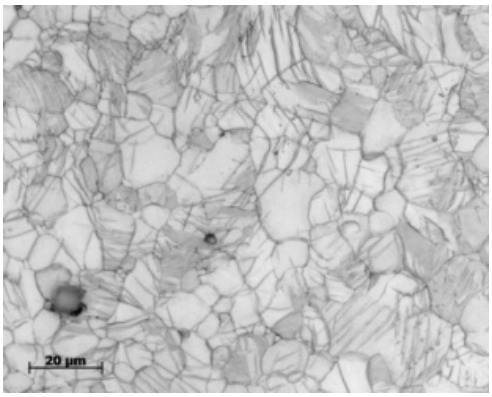

(b)

Figure 3. Specimen images after quasi-static compression orientated in the normal direction. Figure 3(a) shows the specimen after polishing and before etching to allow for the characterization of the parameters related to the second-phase particles. Figure 3(b) shows the same specimen after etching with grain boundaries and deformation twins evident. Note the difference in scale.

size, particle information, and twin information were each averaged from a total of nine individual images that were separately analyzed. Analysis indicates that energy absorption increased with an increased strain rate in the normal direction while the energy absorption in the rolling and transverse directions was within the level of testing uncertainty. The level of strain-to-failure increased as the strain rate increased in the normal direction; however, the strain-to-failure slightly decreased in the rolling and transverse directions as the strain rate increased. The twin density and particle fracture density increased as the strain rate increased in all three orientations.

Nanoscale Simulation: Void Nucleation Modeling and Visualization

Isolated triple junctions in Mg have been examined using molecular dynamics to determine the effects of grain orientation and stress states on void nucleation. A pseudo-two-dimensional system isolates a single triple junction and examines the factors controlling void nucleation. Each simulation consists of three grains in a simulation cell of 40 nm × 40 nm × 2.3 nm with ~250,000 atoms (see Figure 4).

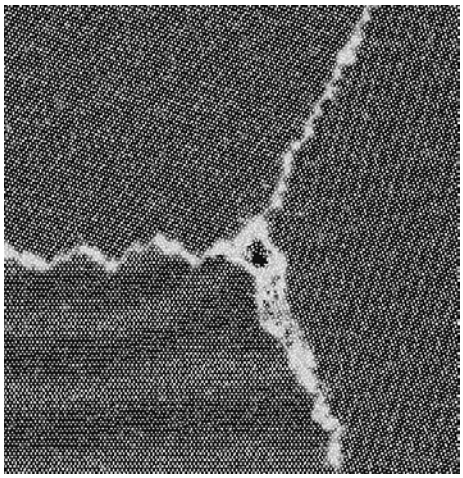

Figure 4. Atomic structure and centro-symmetry values of triple junction that nucleated a void.

The atoms comprising the exterior boundary are held fixed in the direction of the surface normal but are allowed to move in the direction of the thickness to accommodate Poisson effects. A total of 15 different initial structures are examined with grain orientations incremented in 15° counter-clockwise rotations about the z-axis from the reference orientation, 0°, defined as $x = (\bar{1}10)$, $y = (010)$ and $z = (110)$. Since all grains will have a common (110) texture, each grain in effect is a columnar structure with four active slip systems capable of capturing the necessary plasticity for this length scale. The grains are loaded by applying a constant strain rate of $10^{\wedge 9}$/s in the *x* and *y* directions. The modified embedded-atom method (MEAM) is used to determine the energetics of the Al-Al interaction.

The focus of this work is to study void nucleation; thus, we will begin with examining only biaxial loading since it has previously been shown that loading atomistic triple junctions uniaxially will result in significant plasticity and no void nucleation up to 30% strain. For all simulations loaded biaxially, voids begin to nucleate at stresses of $\sigma_{xx} = \sigma_{yy} \approx$ 6–7 GPa and strains of $\varepsilon_{xx} = \varepsilon_{yy} \approx$ 6.7–7.8%. Only 2 of the 15 simulations nucleate voids directly at the triple junctions and the others nucleate voids along one of the three grain boundaries. At this point there is no clear grain boundary characteristic that leads to the failure of one particular grain boundary over another. Yet for the case of adjacent grains with orientations of 0° and 30°, a (233)/(211) grain boundary forms and is always the location for void nucleation independent of the other two boundaries. This boundary is not a perfect (233)/(211) boundary as a result of the method used to generate the initial structures, but it does have similar characteristics. One characteristic of this particular grain boundary is that there is a larger amount of "free volume" located along the (233)/(211) boundary relative to the others.

The centro-symmetry parameter measures the degree of local shear and disorder, which is similar to the local volume increase associated with nonhydrostatic stresses. The centro-symmetry values further show that the grain boundaries that nucleate voids tend to have larger local free volumes relative to the other grain boundaries. This simple visual analysis requires more quantitative support, which will be performed soon.

While analysis of grain orientation on void nucleation is critical, the stress-state dependence is also very important. It is well documented that a critical factor of void nucleation and void growth is triaxiality. Here triaxiality is defined as the hydrostatic/mean stress divided by the von Mises/effective stress,

$$\chi = \sigma_m / \sigma_{eff} \quad ,$$

for a perfect biaxial loading $\chi = 0.67$ and approaches infinity for a perfectly hydrostatic loading.

To elucidate stress-state dependence a single simulation, which nucleated a void at the triple junction, is selected and deformed under several different stress states. The results of varying the stress triaxiality on the strain to failure, or the strain to nucleate a void, are shown in Figure 5. As expected, the strain to failure increases with decreasing triaxiality. For the (110) texture, at higher triaxiality slip is inhibited because of low shear stresses that do not activate the slip systems. Slip and dislocation activity is the natural form of dissipation in a metal; if critical tensile stress is necessary for void nucleation and dislocations reduce the stress in the system, some sort of hardening must occur at higher strains in order to reach the critical stresses necessary for void nucleation. For the highest triaxiality, $\chi = 35$, the remote hydrostatic stress is ~8 GPa. This high triaxiality case has nearly homogenous stress throughout the simulation, which means this is most likely the critical hydrostatic stress necessary for void nucleation. In the cases with lower triaxiality, it is necessary to increase the local stress near the point of void nucleation.

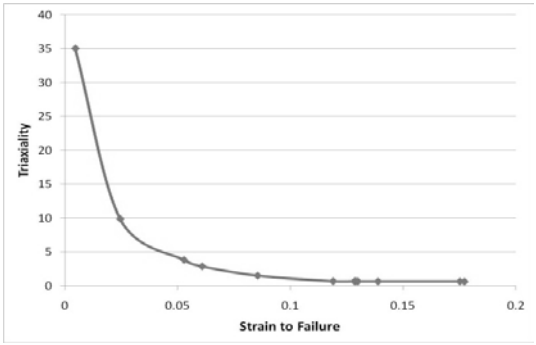

Figure 5. Graph of stress triaxiality vs the strain to failure or strain to void nucleation. The higher the triaxiality the lower the strain to failure and vice versa.

To completely understand the void nucleation, an analytic model should be developed to describe the energetics of the system. This model will focus on the simulations that do not nucleate any dislocations before void generation, $\chi > 0.5$. The simplest system to study is the purely biaxial case, $\chi = 0.67$, beginning by analyzing the elastic response of this particular case. Since Al is fairly isotropic, the stress strain curves for all 15 grain orientations under biaxial stress lie relatively on top of each other up to failure. Since all of the stress strain curves are similar, the same orientation used in Section 2 is selected for analysis. The first step is to capture the elastic response under different stress states.

Applying Hooke's law reproduces the elastic regions of all the stress strain curves for varying triaxialities. Following the elastic analysis a yield/nucleation criterion must be developed. The yield/nucleation criterion has not been developed, yet, but is being considered.

Macroscale Modeling and Visualization

Visualization of fracture propagation is complete. The previous visualization tool only allowed analysis of an individual step, while the revised implementation displays evolution of all field values throughout the simulation history. This was accomplished through integration with the visualization software EnSight, which was chosen due to its robustness and portability. The framework was established that will allow the user to view various entities as the simulation progresses.

This particular example is of a compact specimen with the properties of steel being pulled in the top hole upward and the bottom hole downward, each with the same amount of force (Figure 6). The top and bottom right corners of the specimen are fixed in the horizontal direction, and the midpoint of the right side is fixed in the vertical direction.

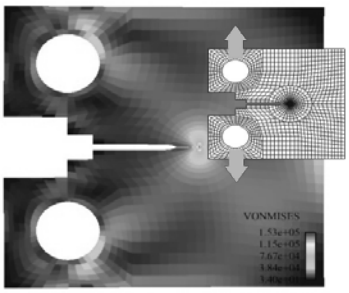

Figure 6. The loading of a compact tensile specimen is shown. Color variation reflects the von Mises stress level. Note the highly localized stress gradient near the region of the crack tip.

Figure 7 shows the von Mises stress levels near the crack tip. The steep stress gradients are resolved by a high resolution mesh that follows the crack as it grows through the specimen. At that tip of the crack [Figure 7(b)] is an "exclusion region" in which crack growth may be modeled using a variety of physically based models. Fracture modeling may be performed using a concurrent multiscale approach in which microstructural details are used to establish crack direction and extension. Information is passed between the exclusion region and the standard finite-element mesh by a weak momentum balance between the exclusion region and the surrounding finite elements. Current efforts are focused on implementation of the microstructure-property and damage model into the simulation frame work.

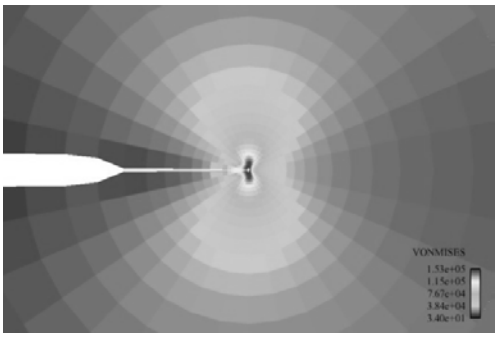

(a)

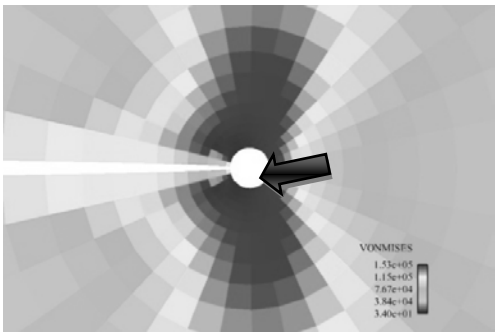

(b)

Figure 7. Steep stress gradients are resolved by a high resolution mesh that follows the motion of the crack tip. The circular zone at the tip of the crack, called the "Exclusion Region," is modeled independently, allowing for physically based fracture criteria, including lower scale simulations.

Conclusions

We have completed high-rate testing of AZ31 Mg in compression and have begun testing in torsion. Once testing is completed, modeling of the behavior will be incorporated into our existing multiscale, microstructure-property model. Simulations of void nucleation have provided detailed information related to the nucleation of voids at triple points. Data will be incorporated into the nucleation term of the damage model. The damage model is currently being incorporated into the fracture simulation code. Once this has been completed, fracture simulations will be evaluated against experimentally observed results.

Presentations/Publications/Patents

Matthew T. Tucker et al., "Anisotropic effects on the strain rate dependence of a wrought magnesium alloy," *Scripta Materialia*, **60**(3), pp. 182–185 (2009).

G. Integrated Computational Materials Engineering for Magnesium in Body Applications (Mg ICME) (AMD702 and 703*)

Principal Investigator: John E. Allison
Ford Motor Company Research and Innovation Center
Mail Drop 3182
2101 Village Road
Dearborn, MI 48124
(313) 845-7224; fax: (313) 323-1129, e-mail: jalliso2@ford.com

Program Technical Administrator: Robert C. McCune
Robert C. McCune and Associates, LLC
5451 S. Piccadilly Cir.
West Bloomfield, MI, 48322-1446
(248) 661-0085, fax: (248) 661-8718, robert.mccune@sbcglobal.net

Technology Area Development Manager: Joseph A. Carpenter
(202) 586-1022; fax: (202) 586-6100; e-mail: joseph.carpenter@ee.doe.gov

Field Project Officer: Aaron D. Yocum
(304) 285-4852; fax (304) 285-4403; email: aaron.yocum@netl.doe.gov

---

Contractor: United States Automotive Materials Partnership (USAMP)
Contract No.: FC26-02OR22910 through the National Energy Technology Laboratory

---

Objectives

The primary goal of this project is the development of an Integrated Computational Materials Engineering (ICME) infrastructure for optimization of magnesium (Mg) manufacturing processes and automotive body components and for Mg alloy development. This is a key enabling technology for future Mg applications, including the Mg front-end architectures of companion programs AMD603—Magnesium Front End Design and Development (MFEDD) and AMD604—Magnesium Front End Research and Development (MFERD). The following are specific objectives.

- Establishment of an international ICME infrastructure (including contributor network, knowledge-base, and cyberinfrastucture) for Mg alloys in automotive structural body applications, specifically:
  - — Product and manufacturing process optimization (processes include extrusion, sheet forming, and high-pressure die casting)
  - — Microstructural engineering
  - — Future alloy development
- Development of a web-based cyberinfrastructure to serve as a hub for exchanging high quality data and models between global collaborators in academia and industry.
- Use ICME infrastructure for MFERD Phase II product and process optimization.
- Attract materials researchers into the Mg field and leverage their efforts by providing a collaborative, virtual workplace for coupling high-quality data and models.

*Denote projects 702 and 703 of the Automotive Materials Division of the United States Automotive Materials Partnership, one of the formal consortia of the United States Council for Automotive Research set up by Chrysler, Ford, and General Motors to conduct joint, precompetitive research and development (see www.uscar.org).

- Advance scientific understanding in various aspects of Mg cast and wrought alloys for structural body applications including development of quantitative processing-structure-property relationships for crash energy management and fatigue performance as well as design optimization.
- Incorporate the contributions of high-quality professionals and students educated in materials science and engineering in the U.S., Canada, and China.

Approach

The project is divided for contractual purposes into two separate projects, AMD702 and AMD703, within the Automotive Metals Division of USAMP. AMD703 is a conventional USAMP project, funded by the Automotive Lightweighting Materials technology area of DOE, and subject to the cooperative agreement between the organizations. In AMD702, work conducted by USAMP Original Equipment Manufacturer (OEM) companies is provided on an "in-kind" basis in support of a separate DOE cooperative agreement with Mississippi State University (MSST), wherein ICME is only one part of a broader research agenda. In addition, DOE is directly funding Mg diffusion research at Oak Ridge National Laboratory (ORNL). The overall ICME for Mg in Body Applications (Mg ICME) project is structurally linked to AMD604 which has a Phase 1 duration of 3 years; however, the initial projected duration of the Mg ICME Project is 5 years. The USAMP Mg ICME project is an integral component (Task 1.9) of the Three Countries (USA, China, Canada) Mg Front End Research and Development (MFERD) enabling technologies project. The plan of work is outlined as follows.

- Develop a web-based electronic "community of practice" allowing development and integration of multi-scale, physics-based, open-source materials models for selected properties and processes.
- Establish and verify a web-accessible, "first principles" and calculated phase diagram (CALPHAD)/diffusion database and computational infrastructure. Development of a user-friendly extensible, self-optimizing phase equilibrium program and graphical user interface (GUI) for a wide range of wrought and cast Mg alloys.
- Establish physics-based and/or empirical relationships for microstructural evolution and similarly-based relationships between microstructures and mechanical response of materials under stress in tension, compression (at varying strain rates), and fatigue loading. This formalism would apply to:
  - Extruded Mg components
  - Sheet Mg components
  - High-integrity, high-pressure die-cast Mg components
- Establish and demonstrate the capability for multi-attribute optimization. Demonstrate the capability to optimize Mg alloys, processes, and components for cost and performance on one or more extruded components. Extend such capability to MFERD Phase II efforts (should they occur).
- Coordination, information dissemination, and reporting. Establish overall coordinated work structure between AMD702, AMD703, AMD604 and Canadian and Chinese suppliers involved in the Three Countries MFERD Program.

Accomplishments

USAMP AMD 702/703, Integrated Computational Materials Engineering for Mg in Body Applications, was approved by USAMP on February 14, 2007. Accomplishments for the included time period of this report (October 1, 2007–September 30, 2008) are summarized as follows.

- The project "kick-off" meeting was held at USCAR in Southfield, MI, January 29, 2008. Details of this meeting are posted on USCAR Vroom web site for USCAR partners.
- The first Project Review meeting was held August 27, 2008, at USCAR.
- Detailed program plans, work statements, and USAMP contracts for all participants were developed, including:
  - Three U.S. universities contributing specifically to AMD703 (Northwestern, University of Michigan, and University of Virginia)
  - Mississippi State University (MSST) via AMD702

  - — Four companies or other organizations contributing to AMD703 (MaterialsGenome, TMS (The Mining, Metals and Materials Society), Thermo-Calc, Magma Foundry Technologies)
- Legal agreement between USAMP and MSST was completed.
- Interdependent plans with Canadian and Chinese participants were developed via MFERD Task 1.9.
- Magnesium alloys were identified for ICME developments (AZ91D—casting, AM30—extrusion and AZ31—sheet).
- Materials for experimental work at various universities were obtained and distributed. (e.g., super vacuum die-cast "shock towers" for University of Michigan.)
- MSST SharePoint web site became operational (March 2008) and was announced at the Hangzhou meeting in China in April 2008.

Future Direction

- Continue to define appropriate initial examples and populate the SharePoint web-based "cyberinfrastructure" platform at MSST.
- Provide high quality materials (e.g., super vacuum die castings, extrusions, sheet) for analysis.
- Demonstrate linkage between first-principles calculations, calculated phase diagrams, and microstructural evolution.
- Make significant progress in developing quantitative processing-structure-property relationships for Mg extrusions, sheet formed parts, and super vacuum die casting (SVDC) castings.
- Convene two review meetings of project participants in spring and late-summer 2009 time frame.
- Strengthen international collaboration via careful planning, frequent electronic networking, and next annual meeting at Niagara-on-the-Lake, Ontario, Canada (May 2009).

Introduction

The background for the Mg ICME project was discussed in the 2007 Annual Report to DOE [1]. Additionally, a broader review of ICME principles and approach has recently been prepared by the National Research Council [2]. The focus of this progress report will be on the accomplishments of USAMP Projects AMD702 and AMD703 during the federal fiscal year 2008 period from October 2007 through September 2008.

In the sections that follow, the overall project status is first reviewed, followed by specific sections devoted to the accomplishments of the individual Task areas during the reporting interval.

General Project Accomplishments for the Reporting Period

All organizational and contractual aspects of the project as pertain to the participants, suppliers, and relationship between USAMP and Mississippi State University (MSST) are now complete. The working agreement with MSST was approved by all parties on February 27, 2008. The USAMP project "kick-off" was held at USCAR on January 29, 2008, and the first collective review meeting was held on August 27, 2008. Details of these meetings may be found either on the USCAR 'Vroom' web site (for USCAR and DOE partners only) or on the Mississippi State University SharePoint web site [3] for the three countries participants. An ICME project is also part of the U.S.-Canada-China MFERD project as international Task 1.9, and results of that work have been reported in the project annual review [4].

The following sections detail accomplishments in the various project tasks over the reporting period.

Task 1 Cyberinfrastrucure

Mississippi State University

MSST is responsible for establishment of the Mg ICME Cyberinfrastructure. MSST presently hosts

two independent portals: one for project information sharing for the overall Three Countries MFERD Project, and the other for specialized purposes of the Mg ICME task. The ICME portal will enable sharing scientific data and models between the project participants in the USA, Canada, and China. The MSST Cyberinfrastructure development leader attended the MFERD meeting in Hangzhou, China, and conducted discussions on the requirements for the Cyberinfrastructure for the overall MFERD project and for the ICME task. The SharePoint server at MSST has been filled with content, in collaboration with Eric Nyberg (PNNL) and Robert McCune (USAMP), who are managing the Web Sites for MFERD and ICME, respectively. Eventually, the server will provide a single point of access to all services rendered by the cyberinfrastructure, through the contents aggregation. The current and future activity focuses the maintenance of the servers. As of October 2008, the MFERD/ICME (http://carload.hpc.msstate.edu) portal has 100+ registered users from USA, Canada, and China.

Development of specific services supporting online repository of material properties, design optimizations, and multiscale simulations: A repository of material properties has been developed and made available to test users (both at MSST and ICME).

The repository is online at http://ccg.hpc.msstate.edu/ccgportlets and through the ICME site. The repository comprises a database of experimental data (stress-strain, strain-life, and microstructure images), a database of material constants (for damage and multistage fatigue models), and is seamlessly integrated with online tools (Damage Fit, Multistage Fatigue Fit, and Microstructure Analyzer) for extracting the material constants from experimental data. The seamless integration means a full support for searching experimental data directly from the tools interfaces, transferring analysis results from one tool to another (e.g., grain statistics to damage or fatigue model), and storing the analysis results into the material constants database so that they can be retrieved a latter time, perhaps by a different user, and formatted according to specification of a finite-element analysis (FEA) application, such as the commercial program ABAQUS.

In summary, a basic infrastructure has been created that forms a solid foundation for creating the cyberinfrastructure for engineering virtual organizations. During 2008, the infrastructure has been used to develop and deploy two integrated applications: the repository of material properties and FAME (a system for adaptive metamodeling).

The Minerals, Metals and Materials Society (TMS)

As a professional society, TMS is providing programming and a web-based portal to aid in the creation of a communications network among professionals dedicated to the subject matter of Mg science and technology and ICME. A special joint symposium with the American Physical Society regarding this topic was conducted at the 2008 TMS Annual Meeting [5]. The TMS website presently contains links to Mg and ICME [6].

Task 2 Calculated Phase Diagrams (CALPHAD), Diffusion Infrastructures and Database

Northwestern University

The first-principles portion of this project focuses on phases relevant to precipitation in the AZ91 (Mg-Al-Zn) example system. Work to date has concentrated on phase stability, defects, and site substitution in the $Mg_{17}Al_{12}$ (β) phase, which is significant for this particular alloy. These calculations should aid in more predictive, physics-based CALPHAD thermodynamic database construction. Additionally, calculation of key unknown parameters related to Mg diffusion (e.g., solute-vacancy binding across a wide variety of solutes) is being conducted in order to help construct better diffusion databases for Mg alloys.

a. First-principles study of β-Mg17Al12 phase. Previous experimental observations have shown that the solubility of β-Mg17Al12 extends to Mg-Al-Zn, thus Zn has to be introduced in the sublattice model within the CALPHAD framework. First-principles calculations of end-members in the β-phase for the Mg-Al binary system show good agreement with previous

CALPHAD databases (which were fit to first-principles data). However, in the Mg-Al-Zn system, the addition of Zn to the end-member energetic for β show that the most recent CALPHAD assessment needs to be further improved. Table 1 shows these end member energetics, and should be useful in constructing a new CALPHAD description of β.

Table 1. Comparison of formation enthalpies for selected end members of the β- phase as calculated by first principles and by CALPHAD

ΔH_f (end-members)	First-principles (J/mol)	CALPHAD (J/mol)	Difference (J/mol)
$Mg_{17}Zn_{12}$ (Mg:Mg:Zn)	-8051	-5000	3051
Mg_{29} (Mg:Mg:Mg)	4490	4602	112
Mg_5Zn_{24} (Mg:Zn:Zn)	-5879	10000	15879
$Mg_{17}Zn_{12}$ (Mg:Zn:Mg)	1127	3000	1873

b. Defects and off-stoichiometry of β-$Mg_{17}Al_{12}$. Additionally, a calculation of off-stoichiometric defects of β-$Mg_{17}Al_{12}$ in binary and ternary systems has been initiated. These defect energies will be used to understand the unusual asymmetry of the phase boundaries in Mg-Al, and will aid in future CALPHAD database construction. Native point defects, i.e., vacancy and anti-sites in β-$Mg_{17}Al_{12}$, have been calculated and are shown in Figure 1.

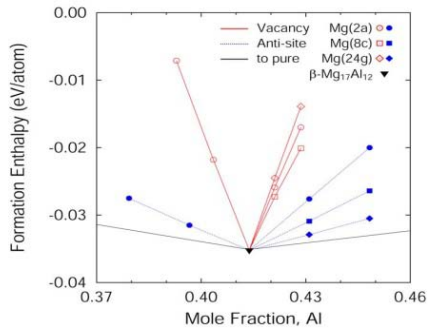

Figure 1. Calculated native point defects in β-$Mg_{17}Al_{12}$.

MaterialsGenome, Inc.

During this reporting period, the data infrastructure for storing input data used for thermodynamic modeling and output data was established, and the feasibility of this data structure to be implemented by database software (e.g., SQL) was demonstrated. Figure 2 shows the

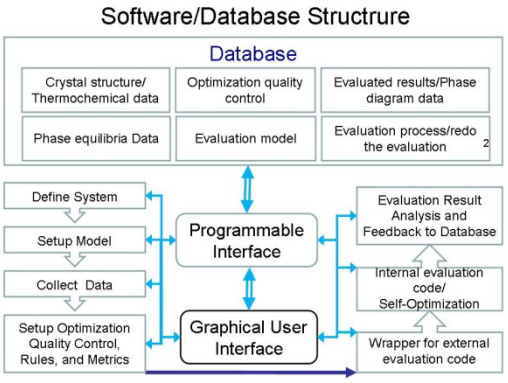

Figure 2. Organization of database structure for thermodynamic data.

overall structure of the software/database to be developed in this project. In the database, crystallographic, thermochemical, and phase-equilibrium data based on available measurements and predictions will be collected and stored. Additionally, the most common or frequently used thermodynamic models will be stored in the database. Secondly, rules for optimization quality control, e.g., the weight of each thermodynamic datum and the optimization order during thermodynamic modeling will be established. There rules are heuristic and will be treated as part of the database. Thirdly, the key data created in the optimization processes will also be saved in the database in order to redo or continue a selected thermodynamic model. Finally, the modeled results, i.e., the self-consistent thermodynamic functions, will be stored. In the GUI part, the user has the option to connect the whole database and change partial data through the database management. The GUI will let the user model a system (e.g., Al-Mg, Al-Mg-Zn, etc.) based on available thermodynamic and crystallographic data. As shown in Figure 2, the main steps to model a system will be as follows: (i) Define a new system or select an existing one to be studied, e.g., Al-Mg-Zn system. (ii) Select a thermodynamic model (or use the default sublattice model) to describe different phases. (iii) Collect available data needed for modeling from the database or user input. (iv) Set rules for optimization quality control suggested by software or selected by user. (v) The self-optimization procedure will work, and the final results will be generated. The last step (v) will not require interactions with the user; however, it will depend

on the internal-evaluation, self-optimization code (yet to be developed).

Additionally, MaterialsGenome has devised a number of the operational features and definitions that will become part of the developing software package. These features include a nomenclature system which will work in concert with the SQL database to determine the base metals and phases from established source identifications, and corresponding parameters (e.g. crystal structures). Additionally, a formalism has been established to name and identify parameters that would be employed by the user in setting up any particular analysis within using the software system.

ThermoCalc Software, Inc.

Thermo-Calc Software provided technical support and advice to partnering organizations as needed, specifically, evaluation and use of thermodynamic data and use of CALPHAD-related tools including Thermo-Calc and DICTRA, both directly within the project and also in the context of a broader cyberinfrastructure. Thermo-Calc expects to support calculations made by OEM partners and also the development of a user-friendly, self-optimizing, phase equilibrium computer program and accompanying GUI for a wide range of wrought and cast Mg-based alloys; such an interface is being developed separately by MaterialsGenome, Inc. as part of this project.

During this reporting period, the supplier met with OEM partners to assess the current state-of-the-art, specifically for Al and Mg alloys, and to establish requirements for ultimately constructing a database, verifying and validating the same, and addressing challenges of automating this task and incorporating CALPHAD-type tools into a broader cyberinfrastructure. Additionally, calculations and comparisons were made using different commercially-available thermodynamic databases for Mg alloy AZ91D which demonstrated that there inadequacies in the present modeling of this alloy.

Thermo-Calc Software has cooperated with MaterialsGenome, Inc. regarding the automation of phase diagram assessments and the development of the software and graphical user interface to make this task more accessible. The initial focus was on the general approach to automate the binary and ternary assessments and sharing experience of past attempts to accomplish this task. While the automation of binary assessments is novel, there has for many years been software tools built into applications such as Thermo-Calc that enable the expert to perform much of the numerical optimization associated with a thermodynamic assessment, directly within the code, in a semi-interactive/semi-automated manner. MaterialsGenome will take this fundamental approach further towards a novel, fully-automated methodology which also supports better archiving of the experimental data that is the foundation of the thermodynamic evaluation. There is a hurdle in going from a collection of binary and ternary assessed systems to a database that has been optimized and validated for specific alloys. Part of the development of such a database includes the validation of predictions (but not fitting of the data) to thermodynamic data available for higher-order commercial alloys. In situations where the fit is poor, the expert database developer will use their judgment to improve the data assessments and even apply estimated data required to improve the fit and accuracy of the database. It is the automation of this heuristic approach to thermodynamic modeling that presents the greatest challenge and opportunity. Incorporation of first principles ‘ab initio’ calculations of thermodynamic quantities, as being determined by the work at Northwestern University, is also expected to increase the accuracy models and improve the quality of estimations for unmeasured quantities.

Oak Ridge National Laboratory (direct DOE funding)

This recently-initiated project is funded directly from DOE and, although it is not a formal part of the USAMP AMD703 project, is providing essential information for modeling microstructural evolution in Mg alloys. The ORNL project aims at developing a tracer diffusion database in Mg-based light material alloy systems. The safety issues that have hampered previous tracer diffusion measurements based on radioactive tracers are somewhat avoided in this project with the use of *stable isotopes* for most elements in this

study (except Al and manganese (Mn) for which radioactive isotopes are needed). Homogeneous single phase samples in the Mg-Al-Mn system will be prepared using conventional techniques; stable isotopes of these elements will be deposited in the form of thin films on these samples, and the measurement of isotopic diffusion profiles of stable isotopes in these samples after diffusion annealing will be conducted using automated secondary ion mass spectrometry (SIMS) facilities either at ORNL or University of Central Florida.. The combination of a tracer diffusion and thermodynamic database, which is being continually updated by other participants during the course of the Mg-ICME program, will provide the required interdiffusion information for the other modeling tasks in this program. The first year of this study will focus on isotopic diffusion measurements in the Mg-Al-Zn system which is the base system for commercial AZ alloys. Future work beyond these ternaries will include studies in Mg-Al-Zn and Mg-Al-Zn-Mn alloy systems. Additionally, various diffusion formalisms will be evaluated for the test Cu-Ni-Zn system (for which a tracer diffusion database already exists). The formalisms will be then evaluated for the Mg tracer diffusion database when completed.

The primary progress in 2008 centered on upgrades to the Secondary Ion Mass Spectrometry (SIMS) facility at ORNL. The SIMS instrument (Cameca ims4f ion microscope, Figure 3) is being upgraded for the high sample load of this project initially with hardware improvements, to be followed by method and automated software developments. Completed upgrades include improved pumping of the secondary ion source, permitting a vacuum of 10^{-11} torr. This level of vacuum virtually eliminates interferences caused by formation of secondary ion hydrides, which in fact are the principle interferent in isotope ratio measurements. Pending upgrades include integration of optical and electronics microscopic systems with the secondary ion microscope systems of the Cameca. These upgrades will permit automated determination of exactly where on a sample measurements are being made at any given time.

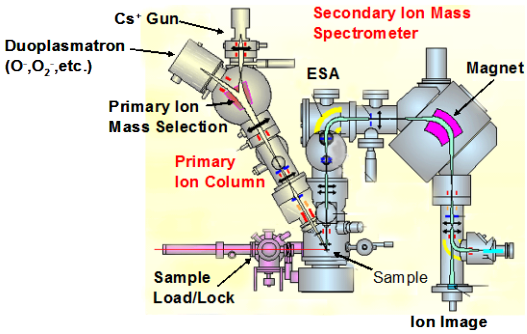

Figure 3. Schematic of ORNL Cameca ims-4f SIMS system that is ideally suited for isotope ratio diffusion depth profile measurements.

Task 3 Processing-Structure–Property Relationships for Extruded Magnesium Components

The team has selected alloys AM30 and AZ61 as the model alloys for this task. Extrusions are being supplied by the AMD604 extrusion task team in the form of crush columns.

Mississippi State University

MSST is developing experimental characterization techniques and fundamental knowledge of the extrusion process for Mg alloys to understand their processing-structure-property relationship (see report 6.H). Particular alloys being studied are AZ61 and AM30. Main research activities are focused on performing microstructural / mechanical characterization of automotive components to build a material database for model development; carrying out lab-scale extrusion experiments to learn about the process and validate material and numerical models; developing a multiscale materials modeling approach using molecular dynamics, discrete dislocations, and crystal plasticity to generate a robust internal variable model for large scale simulations; and constructing experimentally validated finite element models of the extrusion process for process design and optimization.

Figure 4 presents results of the microstructural studies (texture and grain morphology) performed on an extruded component (GM crash rail, AM30). Besides being used for modeling purposes, such information helps to gain insights

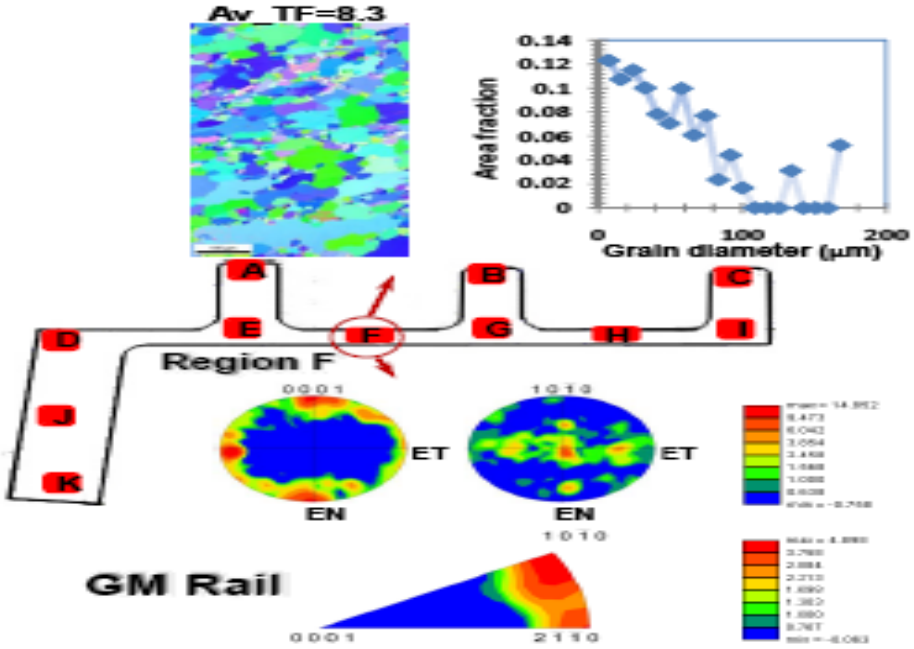

Figure 4. Microstructural characterization at specific locations of GM crash rail. The material is Mg alloy AM30.

into how the process parameters may relate to the extrudate mechanical properties (e.g., anisotropy), an aspect strongly linked to the product performance.

Figure 5 shows a preliminary finite-element model for the lab-scale extrusion experiments being designed and performed at MSST. There are a number of numerical issues that need to be addressed when modeling extrusion (e.g., finite-element formulation and numerical integration of material models). In particular, modeling the extrusion process with fully Eulerian and Arbitrary-Lagrangain-Eulerian finite-element formulations helps avoid the large mesh distortion problems typically exhibit by Lagrangian formulations.

Fractographic analyses on the strain-life specimens were completed. The *in-situ* scanning electron microscopy SEM fatigue specimens are being prepared so that the fatigue damage can be observed at microscale.

Constitutive Modeling: Progress has been made at all scales of simulation. MSST has developed a new nested internal state variable (ISV) theory that

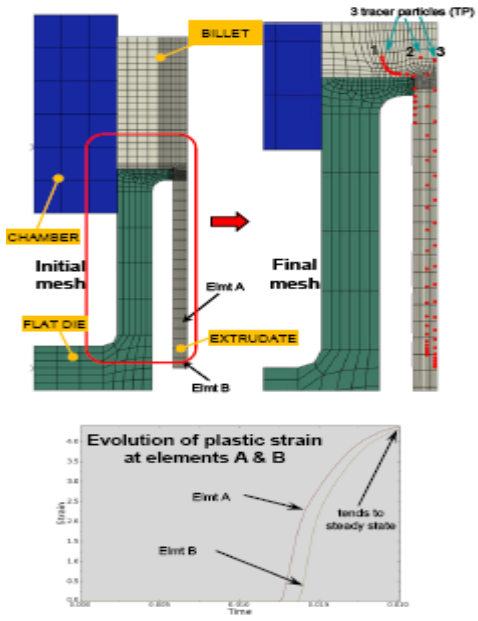

Figure 5. Finite-element model of preliminary lab-scale indirect extrusion experiments using ABAQUS.

physically and strongly couples deformation and internal defects. A methodology related to a higher order tensorial rank of damage for void nucleation and void growth has been developed. Uncertainty

related to material heterogeneities that facilitated new optimized material development has been quantified. With this new nested macroscale ISV theory, MSST is conducting some materials-processing studies that capture the structure-property relations in the model correlation and model validation stages. At lower scales, they have implemented and tested kinematics, kinetics, and hardening rules for twinning deformation in a crystal plasticity code. They analyzed dislocation/twin activities in a Mg single crystal under different loading conditions and used that information to identify the parameters of slip hardening rules. This multiscale material model of Mg alloys reproduced well the anisotropic responses reported in the literature.

Lehigh University

Modeling of the extrusion process for Mg alloys of interest (e.g., AZ31, AM30 and AZ61) is a subtask of the AMD604 project, being conducted by Lehigh University and is closely aligned with objectives of the ICME project. MSST has also conducted modeling of the extrusion process as part of the ICME project, using alternative methodologies. Lehigh's current approach utilizes a "modified" Barrett flow-stress model for the deformation of magnesium as elevated temperature and various strain rates, incorporating an added contribution from dynamic recovery and recrystallization [7]. Agreement between theory and experiment for AZ31 at 350ºC and 0.01 sec^{-1} strain rate is shown in Figure 6.

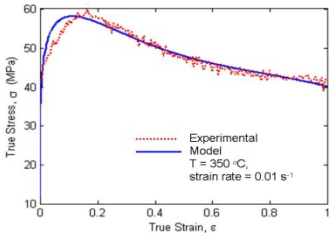

Figure 6. Agreement between theory and experiment for extrusion of AZ31 as determined by Lehigh University.

Task 4 Processing-Structure–Property Relationships for Sheet Magnesium Components

The team has chosen alloy AZ31 as the model alloy for this task. The alloy will be provided in the form of a formed box sample and will be provided by the AMD602 Warm Forming of Mg project team (see report 2.B).

The University of Virginia

The University of Virginia is presently a participant in the AMD602 (Warm Forming of Magnesium) project, and its tasks under AMD703 are coordinated with those efforts, specifically with regard to modeling and the development of constitutive equations for the warm-forming of Mg sheet alloys (typically AZ31). One role in the AMD703 program is to provide guidance in model selection and parameter identification. Two basic approaches are being examined:

a. Phenomenological/continuum approach. A literature review of the models that have been developed to simulate the flow of metals (including Mg) undergoing dynamic recovery (DRV) and recrystallization (DRX) has now been completed. The relevant equations were identified and shared with the ICME team. Initial constitutive modeling focused on the pseudo steady-state viscoplastic response of the magnesium alloy, AZ31, at elevated temperatures. Results presented in Figure 7 show that the Sellars-Tegart [8] hyperbolic sine relation accurately models the flow stress at a fixed strain as function of strain rate and temperature within the regime of interest (i.e., T = 150 – 350°C) for all four of the sheet materials examined within the AMD602 project (designated here as O, M, N, and X). The deformation condition is described by the temperature compensated strain rate parameter, $Z = \dot{\varepsilon}\exp(Q/RT)$, where Q is an apparent activation energy, strain rate, R is the gas constant and T is temperature.

The technical partner at GM has used the derived Sellars-Tegart constitutive model for alloy O to perform sheet forming simulations at 200, 250,

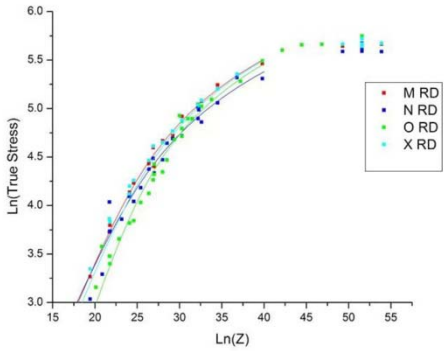

Figure 7. Best fits of the Sellars-Tegart relation [8] to the flow stresses at a strain of 0.1 of the four sheets (O,M,N,X) over a wide range of deformation conditions, Z (assuming Q = 140kJ/mol).

and 300°C using the PAMSTAMP 2G computer code. The geometry and boundary conditions of the simulations were designed to conform to those of the warm forming trials being performed within the context of the AMD602 project. Figure 8 shows the results of the simulation performed at 300°C, which highlight the fact that the most sheet thinning occurs at the corners of the pan wall where actual failure was observed to occur during the forming trials.

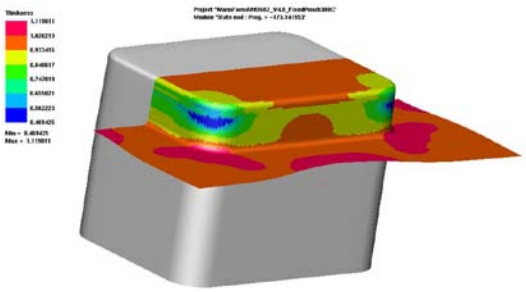

Figure 8. PAM-STAMP 2G simulation of warm forming of AZ31 material 'O' using constitutive model provided by the University of Virginia.

More recent modeling efforts have exploited the ICME network through collaboration with partners at MSST. They have made the GUI, DMGfit, available to us and provided guidance in how to develop an accurate parameter set for modeling not only the temperature and strain-rate dependence of the flow stress, but also the strain hardening using an internal state variable model developed by Bammann, Chiesa, and Johnson [9]. While the actual strain hardening exhibited by the alloy AZ31 under conditions of adequate warm formability is marginal, the internal state variable modeling approach provides a platform upon which to develop the desired DRX modeling capacity. This is viewed as a critical goal of Task 4, since DRX is known to induce strain softening, which can have a negative impact upon the formability.

The advantage of the phenomenological approach outlined above has been the ability to quickly integrate within the finite-element modeling context. However, it is well known that the crystallographic texture of magnesium alloy sheets can render the material anisotropic and that the texture itself can evolve rapidly with strain, particularly in cases where mechanical twinning is active. Thus, a second, more fundamental approach based upon crystal plasticity, is also being investigated.

b. Crystal plasticity/mechanistic approach. This aspect of the project is very new. While polycrystal plasticity models exist, they have primarily been developed to describe room temperature flow of Mg alloy sheets. Although, various *ad hoc* approaches to incorporate temperature dependence have been explored, it has been concluded that a more rigorous approach incorporating the effects of "creep mechanisms" of climb and/or dynamic recrystallization must be developed. The University of Virginia team is presently examining viscoplastic creep models that activate the climb of dislocations using a modified version of the generalized Schmid law that is used to activate slip. Similarly, the effect of the nucleation of new grains during the process of dynamic recrystallization is being considered. The team believes that this may be another means by which lack of strong texture evolution during flow at elevated temperatures can be explained. Finally, prediction of forming limit curves (FLCs) and post-formed room temperature stress/strain properties will further serve to validate the models being considered. A crystal plasticity-based forming limit code was written during a prior project and will be used in simulations once the appropriate constitutive models are validated.

Inputs and outputs will be coordinated with companion USAMP projects.

Task 5 Processing-Structure–Property Relationships for Die-cast Magnesium Components

The team has selected alloy AZ91D as the model alloy for this task. Limited work may also be conducted in alloy AM50. Super vacuum die-cast shock towers from the AMD604 casting task team have been provided for use in this project Task.

The University of Michigan

The goal of this particular study is the development of experimentally-validated models that account for the influence of microstructure on monotonic tensile properties and low-cycle fatigue response of high-pressure die-cast Mg alloys. Seventy SVDC AZ91D shock tower castings have been received and a metallographic survey of five key casting regions (Figure 9) has been completed

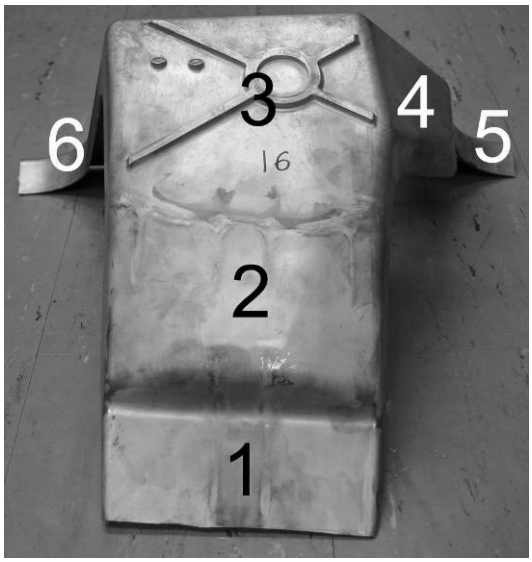

Figure 9. SVDC shock tower showing locations of microstructural and heat treatment studies.

to characterize variation in the as-cast microstructure with location and to provide a baseline for subsequent heat treatment and low cycle fatigue investigations. Vickers microhardness is being used as an indicator of mechanical properties as a function of aging treatment. The influence of aging time up to 500 hours and aging temperature (168 and 216°C), as well as the influence of time (up to 25 hours) at the solution treatment temperature of 413°C have been examined. As-cast microhardness is shown for three locations in Figure 10, and the significant response to heat treatment is shown in Figure 11.

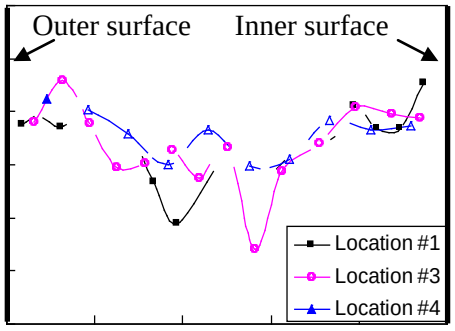

Figure 10. Baseline microhardness as a function of casting location showing variation across casting thickness.

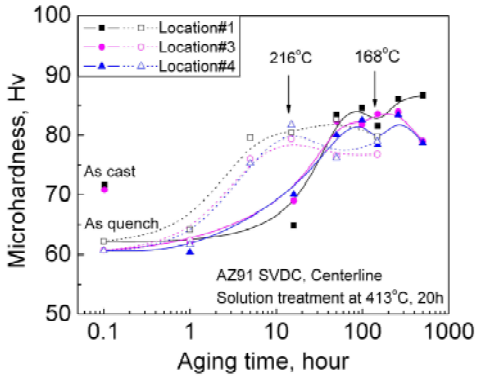

Figure 11. Response to heat treatment for three different locations in shock tower.

Tensile tests are ongoing and initial results are consistent with the results of the microhardness studies. X-Ray Powder Diffraction has been used to assess changes in phase fraction with heat treatment, and the variation of the fraction of β-$Mg_{17}Al_{12}$ with aging time at 168°C is shown in Figure 12. This technique will be used to evaluate, to the extent possible, the kinetics of phase changes during heat treatment. Low-cycle fatigue tests are underway on as-cast sheet coupons extracted from specific locations in the SVDC shock towers, and the preliminary results are

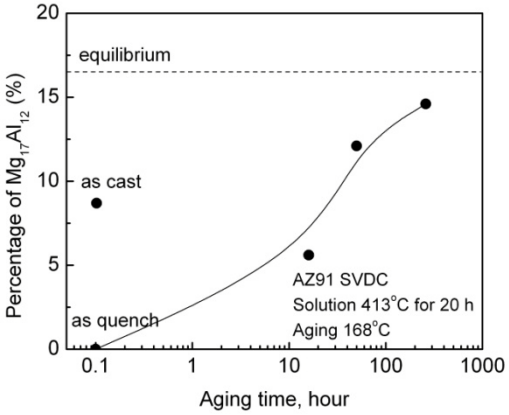

Figure 12. Variation of beta phase fraction with aging time determined by x-ray powder diffraction.

shown in Figure 13. Low-cycle fatigue work will continue in the coming year with tests on heat-treated materials.

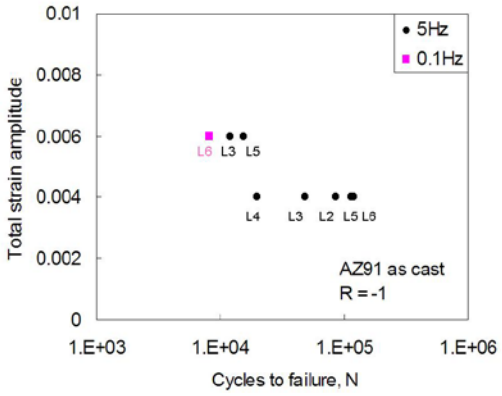

Figure 13. Fatigue life versus total strain range for different locations in SVDC shock towers in the as-cast condition.

Magma Foundry Technologies, Inc.

MAGMA Foundry Technologies, Inc. has participated in this project to aid in the development of computer mapping tools for the prediction of mechanical properties in large magnesium castings. MAGMA has focused on transferring information from the casting process simulation tool MAGMASOFT to finite-element meshes. Additional result transfers have been conducted to verify the transfer capabilities of different result files (i.e., temperatures and stress distributions). The development of models to predict the microstructure of die-cast magnesium components is continuing. The main focus is now placed on the simulation of the filling and solidification of the demonstrator component and the comparison of the simulation results with observer/measured casting defects and properties to develop quality and property maps for Mg castings produced by the SVDC process. Figure 14 illustrates a typical calculation of residual stresses in the SVDC shock tower as shown in Figure 9.

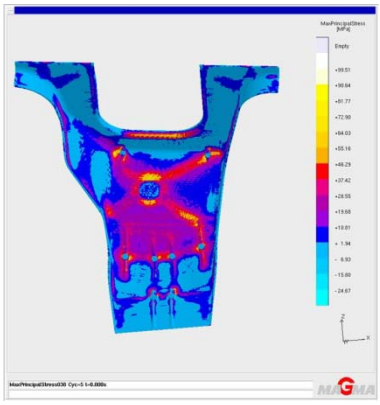

Figure 14. Residual stress pattern in SVDC magnesium shock tower (Figure 9) as determined by MAGMASOFT CAE simulation.

Task 6 Multi-Attribute Design Optimization

Mississippi State University

MSST developed a new technique based on optimum ensemble of metamodels, examined the performance of five different metamodeling techniques, and established a framework for Flexible Advanced Metamodel Estimator (FAME) with the code currently under development with the ICME Cyberinfrastructure. MSST investigated a single-level reliability-based design optimization (RBDO) methodology and its application to an automotive structural component (e.g., side rail). In collaboration with the MSST Multiscale Material Modeling group, they initiated this objective ahead of the original schedule. Using the available ABAQUS UMAT subroutine for A356 cast Al, they were able to integrate multiscale material modeling, uncertainty analysis, design optimization, and metamodeling technologies, and demonstrate the new capability in design

optimization of an automotive control arm. Work on this task is currently on hold pending development of the appropriate multi-scale modeling knowledge base for Mg alloys.

Task 7 Fatigue

Mississippi State University

MSST has also conducted literature surveys on fatigue and small-crack growth in Mg alloys. They developed a test matrix and test specimens for tensile and fatigue tests on the Mg alloys to determine material parameters for the multi-stage fatigue (MSF) and Small-Crack Theory models. In anticipation of receiving AM30 and AM61 extrusion, MSST acquired two AZ31D extrusions from GM. Monotonic tension and compression tests were conducted as well as uniaxial low cycle fatigue tests. The framework of MSF modeling was developed for AZ31 Mg alloy. Typical loading spectra for automotive applications were reviewed. FASTRAN was used to calculate the fatigue behavior using crack growth. The shape of the calculated strain-life curve was very similar to the test data (see Figure 15).

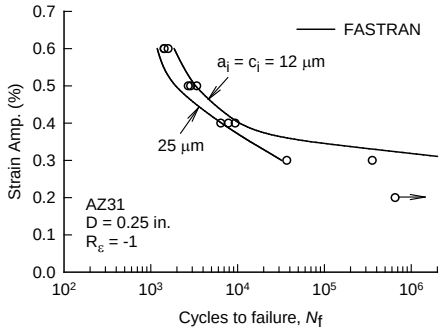

Figure 15. Strain-life curve for AZ31 magnesium alloy.

Conclusions

The Integrated Computational Materials Engineering for Mg in Body Applications project was launched in 2007 and incorporates interfaces with the AMD604 project. All work plans have now been adopted, contracts issued and both "kick-off" and first review meetings conducted. Substantial progress has been made in all task areas as evidenced by the individual report areas. The TMS "Magnesium" and "ICME" web portals are operational.

Acknowledgments

The success of this project is due to the dedicated efforts of team members at Chrysler, Ford, and General Motors, as well as The University of Michigan, The University of Virginia, Northwestern University, MaterialsGenome, Inc., Magma Foundry Technologies, Inc., ThermoCalc Software, Inc., and The Minerals, Metals and Materials Society (TMS). The project leadership also acknowledges the ongoing collaboration with colleagues at Mississippi State University. The USAMP ICME project management team is comprised of Randy Beals, Chrysler; Lou Hector, GM; John Allison, Ford; and Robert McCune, Project Administrator. The continuing support of our respective organizations and the US Department of Energy is gratefully acknowledged.

References

1. Integrated Computational Materials Engineering, Annual Report to DOE, J.E. Allison, Principal Investigator, USAMP, 2007.
2. Integrated Computational Materials Engineering: A Transformational Discipline for Improved Competitiveness and National Security," Committee on Integrated Computational Materials Engineering, National Research Council, ISBN: 0-309-12000-4 (2008). http://www.nap.edu/catalog/12199.html
3. http://mferd.hpc.msstate.edu/_layouts/login.aspx
4. A Canada-China-USA Collaborative Research and Development Project "Magnesium Front End Research and Development (MFERD)" 2007 Annual Progress Reports, Project Technical Committee, Hangzhou, China, April 2008.
5. Joint APS/TMS Symposium "Frontiers in Computational Materials: Session I" held in New Orleans, LA, TMS Annual Meeting, March 10, 2008.
6. http://iweb.tms.org/forum/default.aspx?forumid=15
7. M. Barnett, Z. Keshavarz, and X. Ma. "A Semianalytical Sachs Model for the Flow Stress of a Magnesium Alloy." *Metallurgical*

and Materials Transactions A, 37(7), 2283–2293 (2006).

8. C. M. Sellars and W. J. Tegart, 1967. "Relationship between strength and structure in deformation at elevated temperature," Mem. Sci. Rev. Metall. 63, 731–745.

9. D. J. Bammann, M. L. Chiesa, and G. C. Johnson, "Modeling large deformation and failure in manufacturing processes," pp. 359–376 in R. Tatsumi, E. Watanabe, and T. Kambe, eds., *Theoretical and Applied Mechanics*, London: Elsevier (1996).

H. Multiscale Microstructure-Property Plasticity Considering Uncertainty

Principal Investigator: Mark F. Horstemeyer
Chair in Solid Mechanics & Professor, Mechanical Engineering
Center for Advanced Vehicular Systems
Mississippi State University
206 Carpenter Bldg., P.O. Box ME
Mississippi State, MS 39762
(662) 325-7308; fax: (662) 325-7223; e-mail: mfhorst@me.msstate.edu

Co-Principal Investigator: Douglas J. Bammann
Professor, Mechanical Engineering
210 Carpenter Bldg.
Mississippi State, MS 39762
(662) 325-3260; Home: (662) 294-2585; fax: (662) 325-5433; e-mail: bammann@cavs.msstate.edu

Co-Principal Investigator: Esteban B. Marin
Senior Structural Analyst, Center for Advanced Vehicular Systems
Mississippi State University
200 Research Blvd.
Mississippi State, MS 39762
Office: (662) 325-6696; fax: (662) 325-5433; e-mail: ebmarin@cavs.msstate.edu

Co-Principal Investigator: Kiran Solanki
Research Associate, Center for Advanced Vehicular Systems
Mississippi State University
200 Research Blvd.
Mississippi State, MS 39762
Office: (662) 325-5454; fax: (662) 325-5433; e-mail: kns3@cavs.msstate.edu

Technology Area Development Manager: Joseph A. Carpenter
(202) 586-1022; fax: (202) 586-6100; e-mail: joseph.carpenter@ee.doe.gov

Field Project Officer: Aaron D. Yocum
(304) 285-4852; fax: (304) 285-4403; e-mail: aaron.yocum@netl.doe.gov

---

Contractor: *Mississippi State University*
Contract No.: *4000054701*

Objective

- Develop a multiscale nested internal state variable (ISV) modeling methodology that includes statistical variations from the material microstructure for lightweighting designs, made of various structural alloys.

Approach

- The approach is to quantify structure-property relations through multiscale modeling and multiscale experiments, so the macroscale ISVs can capture the lower length-scale effects. Once the cause-effect relations are quantified for various engineering metal alloys, then statistical methods can be used in the context of the ISVs and used for constitutive models in finite-element analysis (FEA). As such, the FEA can be used for a simulation-based design methodology as manufacturing processes and in-service life are accurately modeled.

Accomplishments

- Progress has been made at all scales of simulation. In doing so, we have developed a new nested ISV theory that physically and strongly couples deformation and internal defects. We established a methodology related to a higher order tensorial rank of damage for void nucleation and void growth. We then developed and quantified uncertainty related to material heterogeneities which would facilitate the optimization of lightweight material development. With the newly developed macroscale ISV theory, we conducted some materials-processing studies that capture the structure-property relations in model correlation and validation stages.

Calibration, Validation, and Verification Including Uncertainty of an ISV Plasticity and Damage Model

The rationale and motivation of this study are to understand the effect of material internal heterogeneity and boundary conditions on localized damage and its progression mechanism. The failure mechanism studied here is a result of void-nucleation, growth, and coalescences, which are modeled using a physically-based ISV form of microstructure-property model (Horstemeyer et al. 2000a), based from the plasticity of Bammann et al. (1993) and later modified to incorporate damage due to void-nucleation, growth and coalescences by Horstemeyer et al. (1999, 2000a). The overall procedure to study the effect of material microstructural variability and boundary conditions on the material response and failure mechanism can be outlined as depicted in Figure 1. First, the experimental uncertainties due to both systematic and bias are calculated along with uncertainties in the microstructure features in the model. Then, the microstructure features with their variability, the experimental stress-strain curves with their variability and the model-calibrating routine is used to calibrate material parameters along with their variability. The calibrating routine used here is a material point simulator. Finally, a user material subroutine is developed, implemented, and used to predict material mechanical responses and material failure mechanisms along with their respective uncertainties. One of the most important contributions the authors believe is to show how internal microstructural clustering affects strain to failure.

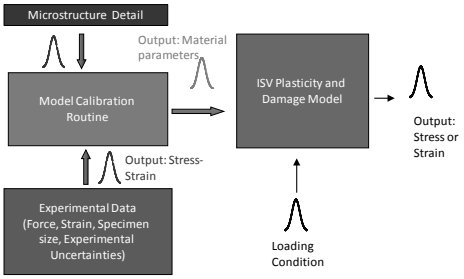

Figure 1. Procedure for studying the effect of material microstructure variability and loading conditions on material response and their failure mechanisms.

Material Mechanical Responses, Microstructure Characterizations, and Their Uncertainties

The microstructure of a typical metallic material contains a large number of microdefects such as microcracks, dislocations, pores, and decohesions. Some of these defects are induced during the manufacturing process and are present before the material is subjected to mechanical loads and thermal fields. In general, these defects are small and distributed throughout most of the volume.

In this report, we focus on a wrought 7075-T651 aluminum (Al) alloy. The 7075-T651 aluminum is a wrought product with a relatively high yield strength and good ductility. As displayed by the triplanar optical micrographs of the plate concerned in the current investigation shown in Figure 2, the grains of this wrought alloy were found to be pancake shaped and aligned in the rolling direction of the wrought plate.

An optical microscope image of the wrought alloy, as shown in Figure 3, displays typical 7075-T651 aluminum microstructure in the untested condition. The alloy contains two main types of primary particles: iron (Fe)—rich particles, [Al_6(Fe,Mn), Al_3Fe, αAl(Fe,Mn,Si) and

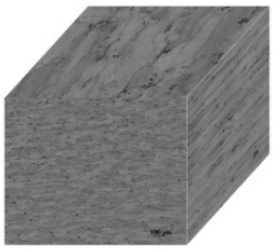

Figure 2. Triplanar optical micrograph illustrating the grain structure and orientation of 7075-T651 aluminum alloy.

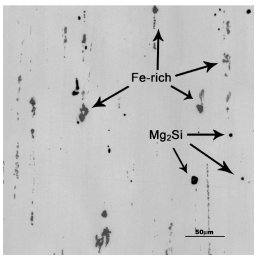

Figure 3. Microstructure of unstrained 7075-T651 aluminum alloy (Harris, 2006).

Al_7Cu_2Fe] and silicon (Si) compound particles Mg_2Si). The iron-rich intermetallic particles are seen in the optical micrograph (Figure 3) as light grey particles, and the Mg_2Si intermetallics are shown as the dark particles. The particle size, nearest-neighbor distance and aspect ratio for the primary distributions for the iron-rich and Mg_2Si intermetallics in the untested condition were tabulated from a 5.75 mm^2 area of material for each of the orientations and are shown in Figure 4. Figure 4(a) displays the area size of the particles, Figure 4(b) displays the nearest neighbor distance of the particles and Figure 4(c) displays the aspect ratio distributions of the particles. The mean values of the particle area, area fraction, aspect ratio, and nearest neighbor distances are displayed in Table 1. In addition to the intermetallic particle stereography, the average grain size was determined by electron backscatter diffraction (EBSD) analysis taken in each of the directions and the results listed in Table 1. Figure 5 displays the grain morphology of the 7075-T651 aluminum alloy along with its orientation distributions (Figure 6).

To properly model the 7075-T651 alloy, standard monotonic experiments were performed (American Society for Testing and Materials [ASTM] E8). Three different types of monotonic experiments (tensile, compression and torsion) were performed along the longitudinal direction. All experimental specimens were machined 2.54 mm from the rolling surface of the plate. The tension, compression and torsion tests were performed with a strain rate of 0.001/sec in an ambient laboratory environment.

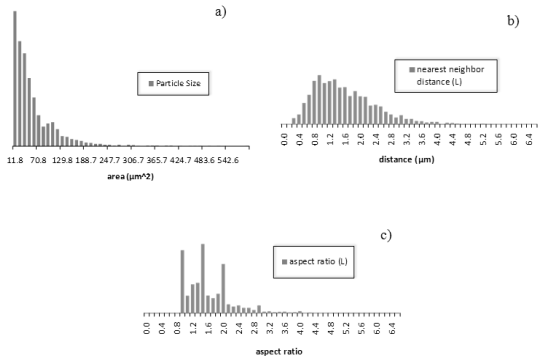

Figure 4. Stereological distributions of intermetallic particles (large) in the longitudinal (L) direction: (a) particle area, (b) nearest-neighbor distance, (c) aspect ratio.

Table 1. Metallographic analysis of virgin aluminum 7075-T651 alloy

Particle Area Fraction	Avg. Particle Size (μm²)	Avg. Nearest Neighbor Distance (μm)	Avg. Grain Size (μm)
0.025	68.2	18.7	18.9

Figure 5. Microstructural grain orientation and size analysis for 7075-T651 aluminum alloy in the longitudinal direction.

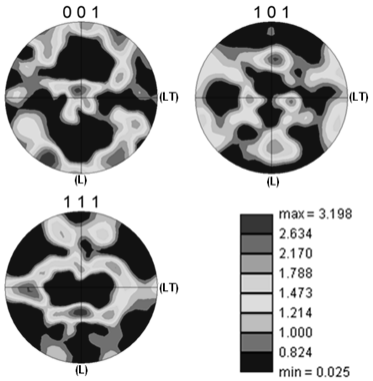

Figure 6. Crystal orientation of the wrought 7075-T651 alloy.

The experimental stress/strain curves were tabulated by taking load and strain values and by using the nominal cross-sectional area. In order to quantify random uncertainties of measured quantities, three specimens for each direction of the alloy were tested. Table 2 shows the accuracy related to different instruments used to measure load-strain curve. The experimental uncertainties are calculated based on systematic and random uncertainties in the measured quantities such as force, strain, and specimen sizes, Eqs. (1)–(3) (see Coleman and Steele, 1999).

$$U_E = \sqrt{U_r^2 + U_s^2} \quad (1)$$

where U_r is random uncertainty and U_s is systematic uncertainty.

Table 2. Accuracy of instruments used to measure load-strain in monotonic tension, compression, and torsion tests

	Accuracy
Load Cell	1%
Extensometer	1%
Micrometer	0.001 in
Data Acquisition Load Reading	0.25%
Data Acquisition Strain Reading	0.25%

The random uncertainty in experimentally measured quantities r_i (force and strain) for M different tests is given by

$$U_r = 2\sqrt{\frac{1}{M-1}\sum_{i=1}^{M}(r_i - r_{mean})^2} \quad (2)$$

The systematic uncertainty in experimentally measured quantities r_i (force and strain) for M different tests is given by

$$U_s = r_i\sqrt{U_L^2 + U_{daq}^2} \quad (3)$$

where U_L is uncertainty in the load cell or extensometer or strain gauges, and U_{daq} is the uncertainty in the data acquisition. The tensile tests were conducted using a Tinuis Olson type tensile machine. The tests were conducted in constant cross-head control, with a speed of 5 inches per minute. An MTS knife-blade axial extensometer with a 2-inch gage length was used for the strain measurement and was set at a full scale of 25% strain and calibrated to better than 0.25% through the full-scale range. The load cell was calibrated to within 0.25% error reading through the full-scale range. The stress-strain data were collected on a System 5000 Data Acquisition system. Similarly, compression and torsional tests were also performed. Figure 7 shows mechanical responses of wrought 7075 aluminum alloy under tension, compression, and torsional loadings with their variability from mechanical experiments. From experimentally measured mechanical response, it was found that the variations in elongation to failure are about ±5.2%, ±6.3%, and ±6.5% for torsion type loading, tensile loading, and compressive loading, respectively.

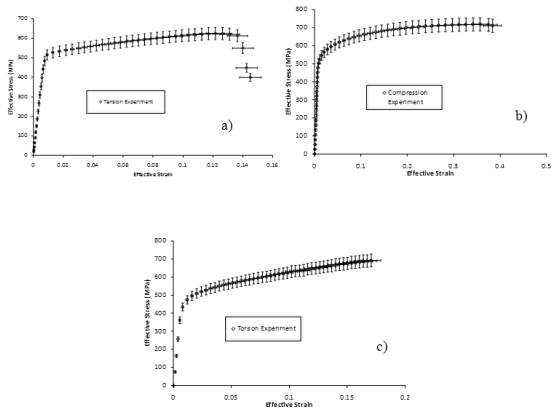

Figure 7. Material mechanical response under (a) tension, (b) compression, and (c) torsion loadings with their variability.

Additional tests were performed to further characterize the mechanical behavior (Bauschinger effects) of the wrought alloy. The Bauschinger effect is interpreted as anisotropic "yielding" that arises upon reverse loading from internal backstresses that are attributed to dislocations accumulating at obstacles. To quantify the Bauschinger effect, cylindrical low-cycle fatigue-type specimens with a uniform gage length based on ASTM standard E606 were used. Specimens with an outer diameter of 10.135 mm were used to test the 7075-T651 and were machined from the longitudinal direction of the two-inch-thick plate. The strain rate was 0.001/sec and the temperature was ambient. Two types of experiments to observe the Bauschinger effect were conducted. First, the cylindrical specimens were prestrained in tension and then uniaxially

reloaded in compression. The second type included a different set of specimens that were prestrained in compression and then uniaxially reloaded in tension. Figure 8 shows the Bauschinger behavior of the wrought 7075 aluminum alloy for tension followed by compression, and compression followed by tension with their variability from mechanical experiments.

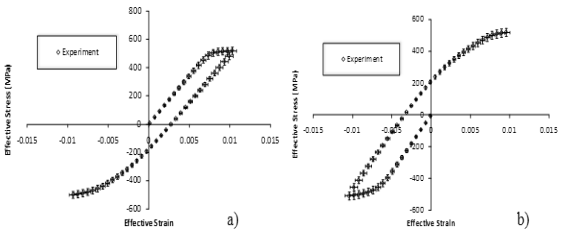

Figure 8. Material Bauschinger behavior under (a) tension followed by compression and (b) compression followed by tension with their variability.

Further experimental tests for the model calibration included interrupted tensile experiments in the longitudinal direction to determine the primary void nucleation rate and damage constants for the ISV model. As confirmed by Dighe et al. (2002), obtaining interrupted cracked or debonded sub-micron particles is not feasible and as such, the damage rate was assumed to be the same as the primary particles. Tensile specimens were loaded monotonically to pre-determined strain levels and sectioned for void and/or crack density quantification. The cracked and debonded primary particles were then quantified as a function of effective strain similar to Dighe et al. (2002).

Model Calibration, Validation, and Verification

In this section, we develop a model calibration technique for the structure-property ISV model (Horstemeyer 2001), with its associated variabilities. The model calibration technique used here differs from the classical uncertainty calibration technique. Here model calibration means fitting model parameters using a material point simulator and calculating associated uncertainty using a Monte-Carlo technique with a sample size of 10^6. The material model will be calibrated with different stress states, Bauschinger effect and material microstructure details. Then the calibrated model will be implemented, using a user material model routine in commercially available finite element code ABAQUS. The verification simulations will be performed using ABAQUS and compared with the experimental data. Finally, a series of validation simulations will be performed for validation and prediction capability.

Model Calibration

A nonlinear regression algorithm in conjunction with Monte-Carlo technique was used to calibrate the above mentioned microstructure-property ISV model, Eqs. (1) to (3). The internal state variable model was calibrated with experimentally-measured mechanical responses from tension, compression, torsion, tension followed by compression and compression followed by tension and their variabilities. Along with mechanical responses, the material microstructure characteristics (particle size, particle orientation, void size, void orientation, grain size, and nearest-neighbor distance) and their variability were also used in the model calibration process (see Figure 1). First, uncertainty in calibration data was calculated, then through Monte Carlo simulations with a sample size of 10^6 and a nonlinear regression algorithm, we calibrated the physically-motivated material model for a given set of mechanical responses and microstructural detail. The sampling distributions for microstructural features are shown in Figures 4 to 6. For mechanical responses, we used a normal distribution with three standard deviations derived from the uncertainty calculations using the propagation rule (see Coleman and Steele, 1999).

The microstructure-property-based ISV model includes plasticity material parameters related to the yield stress, kinematic hardening, isotropic hardening, and the shear and the bulk moduli, along with their temperature and strain-rate dependencies, all of which were calibrated using experimentally-measured mechanical responses and microstructural features, as shown in Table 3. It includes the damage progression, which is multiplicatively decomposed into void-nucleation,

Table 3. Microstructure-property (elastic-plastic) model parameters for 7075-T651 aluminum alloys

ID #	Constants (Units)	Mean	ID #	Constants (Units)	Mean
1	G (MPa)	26426	15	C_{10} (°K)	5.0
2	A	1.0	16	C_{11} (sec/MPa)	0.0
3	K (MPa)	68915	17	C_{12} (°K)	0.0
4	B	0.0	18	C_{13} (1/MPa)	0.323
5	The melt temp (°K)	1400	19	C_{14} (°K)	0.0
6	C_1 (MPa)	0.0	20	C_{15} (MPa)	3625
7	C_2 (°K)	0.0	21	C_{16} (°K)	12
8	C_3 (MPa)	360	22	C_{17} (sec/MPa)	0.0
9	C_4 (°K)	110	23	C_{18} (°K)	0.0
10	C_5 (1/MPa)	1.0	24	C_a	3.99
11	C_6 (°K)	0.0	25	C_b	-0.627
12	C_7 (1/MPa)	0.07581	26	init.temp (°K)	297
13	C_8 (°K)	0.0	27	heat gen. Coeff.	0.0
14	C_9 (MPa)	2937			

void-growth, and void-coalescence variables. The microstructure characteristic parameters are calibrated in conjunction with plasticity parameters using mechanical response and microstructure features as shown in Table 4.

Table 4. Microstructure-property (damage) model parameters for 7075-T651aluminum alloys

ID #	Constants (Units)	Mean
28	M	0.3
29	R_o (mm)	0.00931
30	an	3.187e-7
31	bn	16737.2
32	cn	1250
33	C_{coeff}	0.00837
34	K_{ic} MPa(m$^{1/2}$)	29.
35	d (mm)	0.00931
36	F	0.027598
37	cd1	0.108
38	cd2	0.93373
39	DCS0 (mm)	40
40	DCS (mm)	40
41	Z	0.01
42	initial void volume fraction	0.0001
43	NTD	-850
44	CTD	-0.0172
45	NND	8.0E-5

The uncertainty distributions calculated during the calibration process using the Monte Carlo method related to the material and microstructural parameters of microstructure-property model are shown in Figures 9 to 15. Several observations can be drawn from these results. One can see that in almost every case the material mechanical

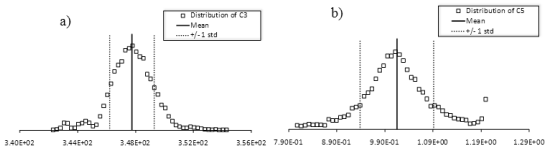

Figure 9. Uncertainty distribution of material parameters related to the yield stress (a) yield stress parameter which determines the rate independent yield stress and (b) yield stress parameter which determines the transition strain rate from rate independent to dependent.

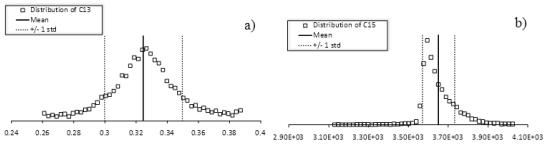

Figure 10. Uncertainty distribution of material parameters related to the isotropic hardening (a) isotropic hardening parameter which describes the isotropic dynamic recovery and (b) isotropic hardening parameter which describes the isotropic hardening modulus.

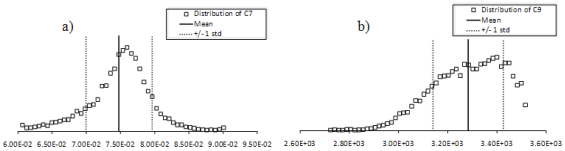

Figure 11. Uncertainty distribution of material parameters related to the kinematic hardening (a) kinematic hardening parameter which describes the kinematic dynamic recovery and (b) kinematic hardening parameter which describes the kinematic hardening modulus.

response and microstructural parameters have the same distribution shape (Gaussian), but different uncertainty levels (the spread of distribution). This could be due to the different sensitivity levels of each model parameter in the constitutive relationship for this material.

Having calibrated the model parameters and quantified the uncertainty associated with these parameters, comparisons were made of the stress evolution as a function of strain for different stress states to predict strain-to-failure and the work-hardening behavior. Figures 16–17 show the effective stress–strain response comparisons for different stress states and the associated

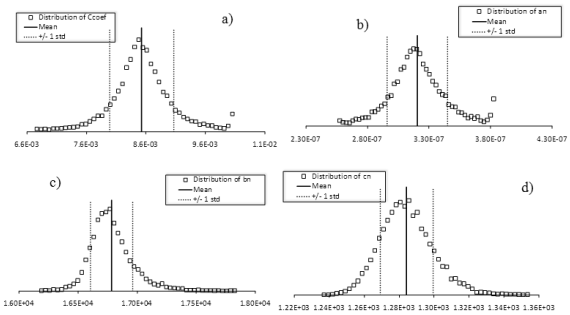

Figure 12. Uncertainty distribution of material parameters related to the void nucleation (a) void-nucleation exponent coefficient, (b) void-nucleation parameter which related nucleation density under torsion, and (c–d) are void-nucleation parameters related to tension and compression void nucleation densities.

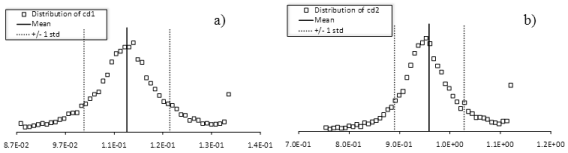

Figure 13. Uncertainty distribution of material parameters related to the void coalescence (a) void coalescence parameter related to void sheeting, and (b) void coalescence parameter related to void impingement.

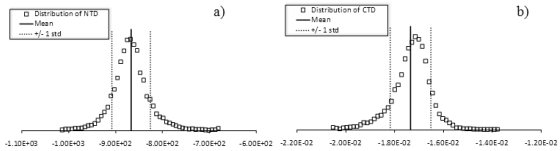

Figure 14. Uncertainty distribution of material parameters related to (a) the temperature dependency on the void nucleation, and (b) the temperature dependency on the void coalescence.

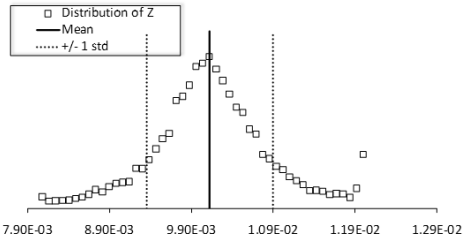

Figure 15. Uncertainty distribution of material parameters related to the material texture.

variability. As Figures 16–17 show, the model is able to compare/predict the elongation to failure with a given level of uncertainty in initial microstructural clustering. It was found that the variations in elongation-to-failure are about ±7.0%, ±8.1%, and ±9.75% for torsion loading, tensile loading, and compressive loading, respectively, due to initial material microstructural heterogeneities.

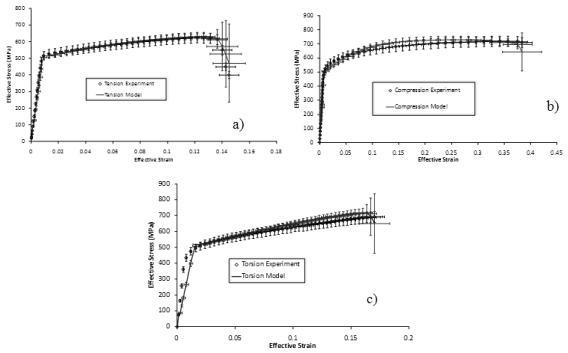

Figure 16. Comparison of experimental tension, compression and torsion data with a microstructure-property model under (a) tension, (b) compression, and (c) torsion loadings with their associated variability.

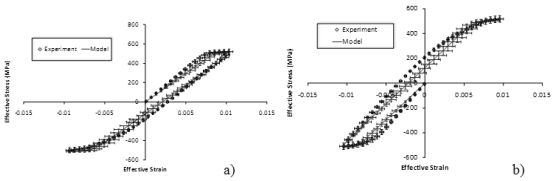

Figure 17. Comparison of experimental measure material Bauschinger behavior with a microstructure-property model under (a) tension followed by compression, and (b) compression followed by tension with their variability.

After good initial correlations with monotonic stress state responses, next the damage progression was plotted for different stress states, as shown in Figure 18. From Figure 18, we can observe that the rate of damage is higher for tension, followed by torsion, and then compression. This may be a material characteristic because with the same microstructure-property model, Horstemeyer et al. (1999) noted that for an A356 cast aluminum alloy, the damage rate was higher for torsion, followed by tension, and then compression. The evolution of damage distributions at different

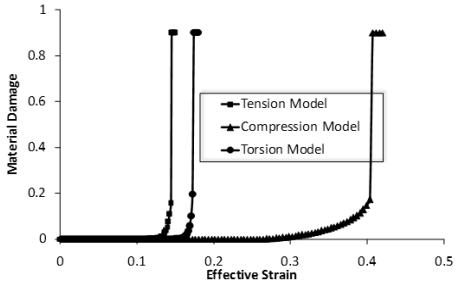

Figure 18. Damage progressions of aluminum alloy 7075-T651 for different stress states.

tensile strains are shown in Figure 19. It is interesting to note that initial isotropic damage (symmetric) evolved into an anisotropic form (asymmetric) as applied strain is increased. Another interesting observation is that as the applied strain is increased, the spread of evolution of damage distribution increased even though the uncertainty in the input microstructure remained the same.

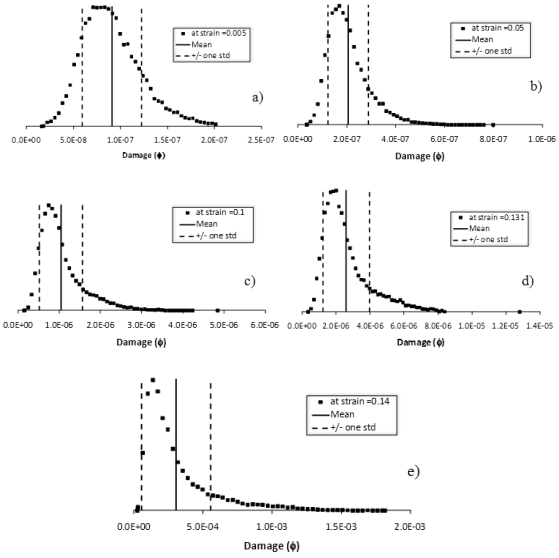

Figure 19. Evolution of damage distributions at different tensile strain: (a) at strain = 0.005, (b) at strain = 0.05, (c) at strain = 0.1, (d) at strain = 0.131, and (e) at strain = 0.14.

In the present study, the material damage was modeled through a multiplicative decomposition into void-nucleation, void-growth, and void-coalescence. It is important to understand why initially isotropic damage distributions evolved into an anisotropic form. For that, we plotted nucleation density distribution evolutions for tensile strains as shown in Figure 20. It is interesting to remember that the initial microstructural distributions (for example, the particle size) are asymmetric and the particle aspect ratio is symmetric. Because the loading directions would be different along the short and long axis of the particles, the physical behavior observed by Jordon et al. (2008) showed an anisotropic response.

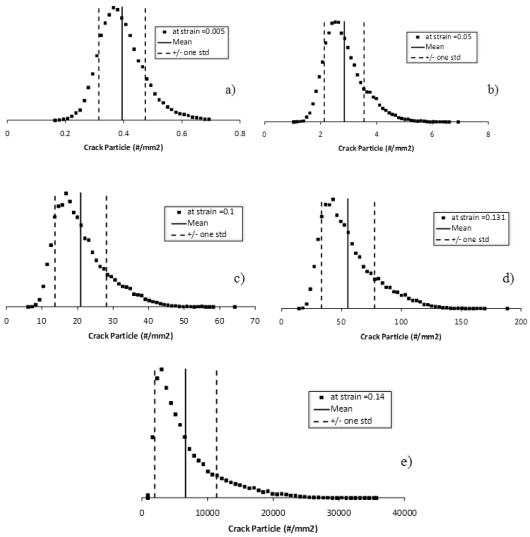

Figure 20. Evolution of nucleation density distributions at different tensile strain: (a) at strain = 0.005, (b) at strain = 0.05, (c) at strain = 0.1, (d) at strain = 0.131, and (e) at strain = 0.14.

Finally, it should be noted that the results presented here include initial distributions and correlation effects of material mechanical responses and microstructural parameters. The use of other probability distributions may have a strong effect on the quantitative values of the results, while the qualitative values still hold.

Model Verification

For model verification (ensuring that the model is implemented correctly in the finite element codes), simulations were performed using ABAQUS finite-element software under different loading conditions (tension, compression, torsion, tension followed by compression and compression followed by tension). Figures 21 and 22 show the stress-strain curves comparing the finite-element

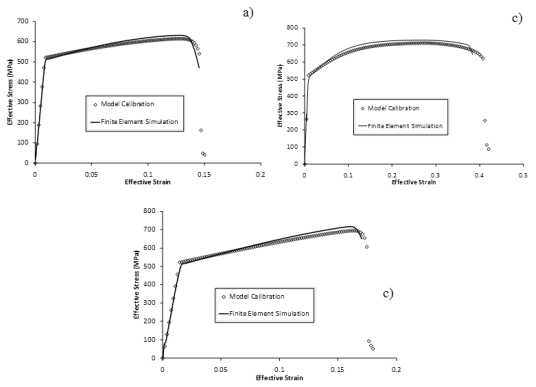

Figure 21. Comparison of finite element simulated mechanical responses under (a) tension, (b) compression, and (c) torsion.

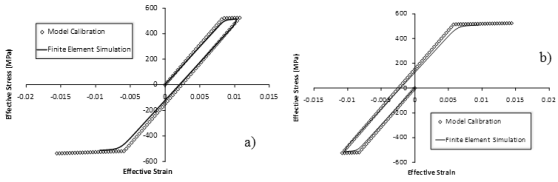

Figure 22. Comparison of finite element simulated Bauschinger under (a) tension followed by compression and (b) compression followed by tension.

simulations results to the results obtain through calibration processes at different stress states.

Figures 21 and 22 show good correlation and how the model captured the differences between the work-hardening rate in tension, compression, and torsion, which express the importance of a physically motivated internal state variable plasticity and damage continuum model for modeling microstructural details. The model is able to capture the history effects arising from the boundary conditions and load histories, the microstructural defects and progression of damage from these defects and microstructural features such as second- phase particles and intermetallics.

Model Validation

For model validation (ensuring that the model captures the correct physics/mechanics), notch tensile tests were conducted as shown in Figure 23. The stress triaxiality is the primary driving factor for damage in ductile materials. In a uniform material, the notch geometry induces a

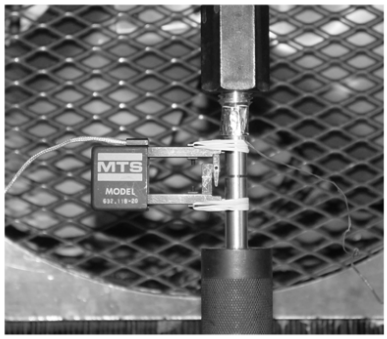

Figure 23. The 0.025-inch-radius notched Bridgmen specimen made of AA7075-T651 shown with the 1-inch axial extensometer placed across the notch to measure displacement.

smooth stress triaxiality field with a maximum value near the center of the specimen. In a damaged medium, stress concentrations induced by the presence of pores may cause local regions of high stress triaxiality. The notch tests were conducted with constant cross-head speed of 5 inches per minute. However, a MTS knife-blade axial extensometer with a 1-inch gage length was used for the strain measurement and was set at a full scale of 25% strain and calibrated to better than 0.25% for the full scale range. The load cell was calibrated to within 0.25% error reading through the full-scale range. The data were collected on a System 5000 Data Acquisition system. Figure 24 shows a good comparison of notch specimen experiment data with finite-element simulation result.

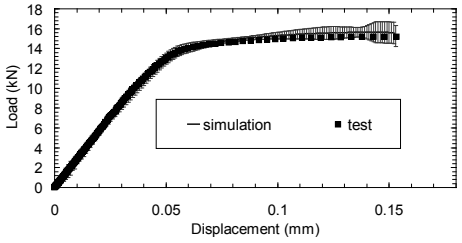

Figure 24. Comparison of experimental measured load-displacement response of aluminum alloy 7075-T651 with a calibrated microstructure-property model for a notch radius of 0.025 inch.

Sensitivity of Damage Uncertainty at Different Strain Values

In this section, we calculate the sensitivity of the damage uncertainty to multiscale material parameters. We measure the sensitivity of damage, S_i, to an input mechanical response and microstructural parameters (see Tables 3 to 4) X_i by using

$$S_i = \frac{\partial \phi}{\partial C_i} \frac{X_i}{\phi} \quad (4)$$

where C_i is the coefficient of variation of X_i. Notice that the second term is used for normalization purposes. Sensitivity of damage uncertainty to the uncertainties of the mechanical responses and microstructural parameters are depicted in Figure 25 for tension. For instance, Figure 25(a) shows that at the very beginning of the damage evolution the initial radius of a void, r_o, and nucleation coefficient are the most influential parameters. Figures 25(b-c), on the other hand, show that as damage progresses the initial temperature, the fracture toughness as the void started to nucleate and void growth are more important. Finally, Figure 25(d) displays the effect of coalescence and growth parameters on the last stages of damage progression. A similar observation was noted for the compressive and torsional loading case. The sensitivity plots are shown in Figure 25 for tension and are also consistent with the physics of the damage progression for this particular type of material. At the very beginning, the initial defect size and number density of cracked particles are important. As the damage evolves, more voids nucleate and grow. Finally, voids combine with each other and coalescence becomes the main driver.

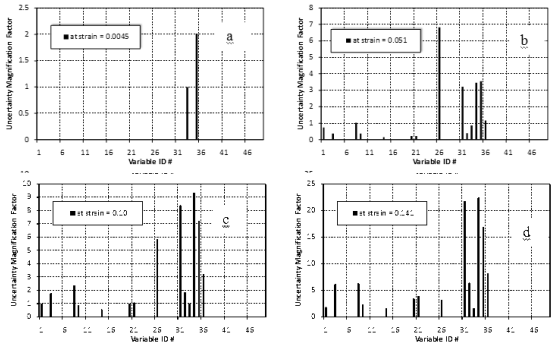

Figure 25. Sensitivity of uncertainty of damage under tension type loading to the uncertainties of the microstructure-property material model parameters: (a) at strain =0.0045, (b) at strain = 0.051, (c) at strain = 0.1, and (d) at strain = 0.141.

Summary

The rationale and motivation of this study are to understand the effect of material internal heterogeneity and boundary conditions on localized damage and its progression mechanism. We analyzed the effect of uncertainty in microstructural features (i.e., voids, cracks, inclusions), along with uncertainties in loading and boundary conditions on the mechanical response and damage evolution (or accumulation) of a wrought aluminum alloy. We first calibrated the microstructure-property relationship model with monotonic mechanical responses (tension, compression, torsion, tension followed by compression and compression followed by tension) and material microstructure features. Based on the calibration results, we quantified the influence of uncertainty of various material model parameters in the constitutive equations on uncertainty in damage. During the calibration process, we have also shown that a physically-motivated material model was necessary to understand and predict the stress states and damage states associated with rolled aluminum containing large intermetallics. The uncertainty distribution related to material parameters associated with the plasticity and microstructural features were also tabulated during the calibration processes and show that almost every material mechanical response and microstructural parameters have the same distribution shape (Gaussian), but different uncertainty level (the spread of distribution).

Having calibrated the model with monotonic loadings, validation and verification simulations and tests were performed using different types of loading, geometrical, and boundary conditions. The modeling result shows good correlation with experimental data. This study demonstrates a method of calibrating, verifying, and validating a microstructure-property relationship based on an internal state variable form material model. However, this chapter's important contribution is

the approach of modeling and quantifying uncertainties associated with the damage from particles. Thus, this approach could be used to model composites and other heterogeneous materials. The authors believe that the good correlation of the internal state variable plasticity and damage continuum model to the experimental results, along with sensitivity analysis, support the physically-based modeling of void nucleation, growth, and coalescence resulting from large and small particles.

The following conclusions are drawn from the results of this work.

- Better correlation with experimental compression, tension, and torsional stress-strain curve was demonstrated.
- Uncertainty calculations revealed that the distribution of material damage, void nucleation, and growth changes related to the applied strain path. It also revealed that small variations in experimental data could lead to significant variations in strain-to-failure.
- Uncertainty calculations revealed that the initial isotropic damage (symmetric) evolved into an anisotropic form (asymmetric) as applied strain is increased, consistent with experimentally-observed behavior for 7075 aluminum alloy in the literature.
- The spread of damage-evolution distribution increases with the applied strain, even though the uncertainties of initial microstructure distributions remain the same.
- The sensitivities of the uncertainty of damage to the uncertainties of the input material responses and microstructural parameters were found to be dependent on the strain values. As the strain value changed (that is, as the damage evolved), the importance of these material responses and microstructural parameters changed.
- The sensitivities were found to be consistent with the physics of the damage progression for this particular type of material. At the very beginning, the initial defect size and number density of cracked particles are important. As the damage evolves, more voids are nucleated and grow. Finally, voids combine with each other and coalescence becomes the main driver. It also shows that the damage evolution equations provide an accurate representation of the damage progression due to large intermetallic particles.
- Finally, we have shown that the initial variation in the microstructure clustering lead to about ±7.0%, ±8.1% and ±9.75% variation in the elongation to failure strain for torsion, tension, and compression loading, respectively.

Magnesium Extrusion

At present, our efforts are focused on developing a reliable experimental procedure for crystallographic data collections of extruded magnesium alloys. A sample-preparation procedure was developed that showed a good repeatability. Figures 27 and 28 display [0002], [1010] and [1120] pole and inverse pole figures together with ODF maps of a sample machined from the center of Section F of an extruded AM30 bumper beam. The entire section is schematized in Figure 26 with highlight on locations that will be analyzed for this component. In the pole figures, the normal direction coincides with the extrusion direction. The texture in Figure 27 was obtained from crystallographic data collected at 0.1 µm step size, while in Figure 28 the step size was 0.5 µm. The difference in step size was intended to reveal the effect of twinning on texture by modifying the statistical contribution of the associated disorientation. A typical width of a fully-grown twin in extruded AM30 alloy measures approximately 2 µm.

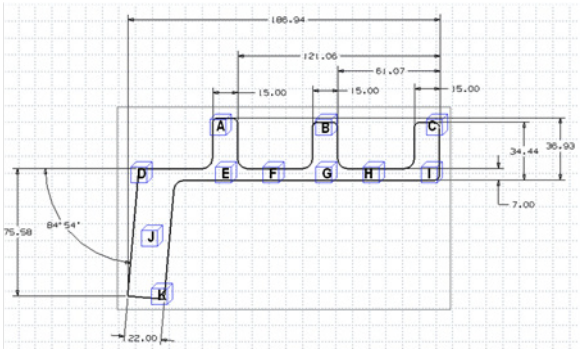

Figure 26. Cross-section of an AM30 bumper beam highlighting the sub-sections to be analyzed.

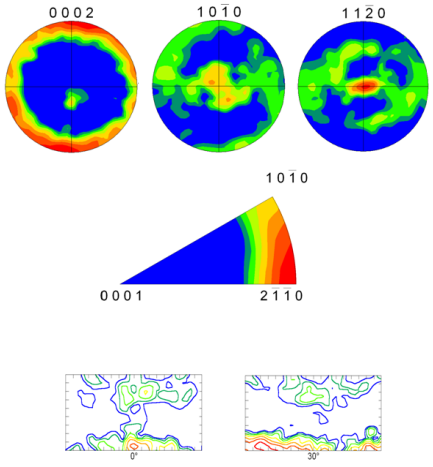

Figure 27. Extrusion texture at the center of Section F obtain after collection at 0.5 µm step-size showing, (a) [0002], [1010] and [1120] pole figures, (b) inverse pole figure of the extrusion axis, and (c) ODF in φ_2-sections.

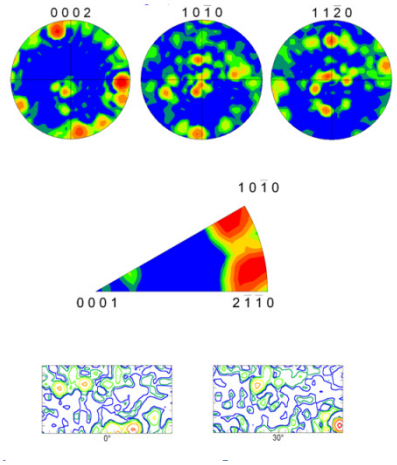

Figure 28. Extrusion texture at the center of Section F obtain after collection at 0.1 µm step-size showing, (a) [0002], [1010] and [1120] pole figures, (b) inverse pole figure of the extrusion axis, and (c) ODF in φ_2-sections.

For both scans the extrusion axis tends to concentrate in the vicinity of the [1010] pole, which is typical for deformed hcp metals by mean of extrusion. This rod texture is sharper for the scan obtained at the larger step-size, where the basal pole [0002] rotated to scatter uniformly around the normal of the extrusion axis. In contrast, for the scan with a smaller step-size, the texture develops secondary fibers that may be related to the [1010] peak through a twinning relationship. The formation of these secondary fibers is consistent with the increased statistical contribution of twinning expected for finer scans.

Macro-Texture Analyses

Texture analyses of the AM30 based bumper beam have been performed by means of X-ray diffraction using a Rigaku system. The pole figure data are being collected and the purchase of friendly commercial software for ODF calculation is being investigated.

Metal Forming of Magnesium Sheet

To represent the unusual stress-strain material responses of magnesium alloys compared with other conventional cubic crystalline metals, appropriate constitutive equations that reflect viscoplasticity, anisotropy, damage, strain sensitivity, temperature dependence, grain size, and twinning need to be developed. These mechanical properties are also needed to accurately predict strain-field evolution, thinning, and localization in the sheet-metal forming. Currently, an existing DMG microstructure-plasticity model is calibrated to the material responses of Mg AZ31 uniaxial tensile tests at different strain rates and temperatures (Figure 29). This model will be modified and extended to include the aforementioned mechanical responses. Also, a stress-integration algorithm that accounts for plane stress conditions needs to be developed

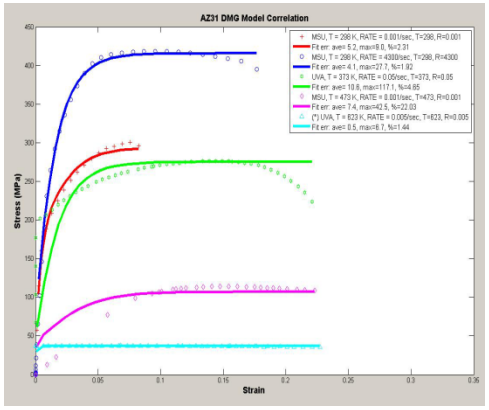

Figure 29. Material fitting of Mg AZ31-O with DMG model.

and implemented in a general finite-element code such as ABAQUS, in order to take advantage of the shell elements, which have been proven to be very time efficient compared to three-dimensional (3D) solid elements.

Sheet-Metal Forming Simulations

The forming limit diagram depicts the maximum strains that can be sustained by sheet materials prior to the onset of localized necking, which is a common failure mode in metal forming. Generally, this failure process is controlled not only by external loading but also by internal microstructures. The major mechanical material properties controlling the formability (i.e., the forming limit diagram) of sheet metals are the work hardening, the rate sensitivity, and the plastic anisotropy of the sheet material. To evaluate the mechanical properties of Mg AZ31 magnesium alloys and study their formability, warm-forming finite-Element (FE) simulations of pan forming of magnesium sheets (Figure 30) are performed at various conditions (temperature, tool speed, friction, binding pressure, etc.) using the current version of the DMG model.

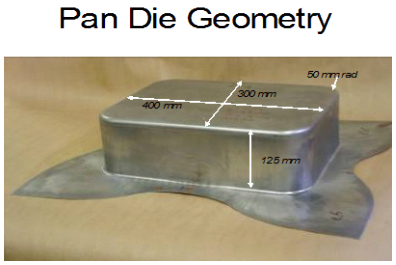

Figure 30. MgAZ31 warm-forming pan geometry for FE simulations.

In this analysis, the punch is assumed stationary, while the die moves down after the sheet is clamped with a given binder force and the sheet is then formed around the stationary punch. The coefficient of friction varies within a range of 0.16 and 0.20. The sheet and die temperatures are set to be equal, starting at 250ºC, and the run simulations at 25ºC increments to 350ºC. Regarding the binder pressure, arbitrary values are chosen until data will be measured from the forming tests. Different results will be post-processed (Figure 31), and the prediction of

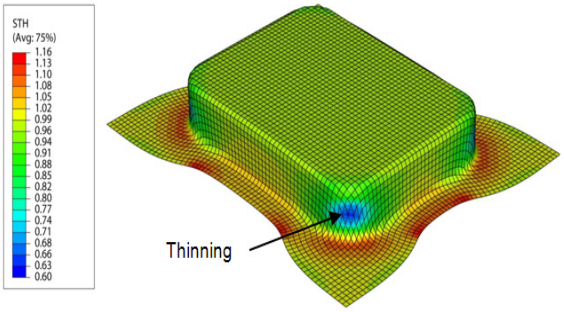

Figure 31. Thickness distribution after warm forming of a pan box.

forming limit curves and post-formed stress/strain properties will serve to validate the models.

References

1. H. Agarwal, A. M. Gokhale, S. Graham, S., and M. F. Horstemeyer (2002), "Quantitative Characterization of Three-Dimensional Damage Evolution in a Wrought Al-Alloy under Tension and Compression," Metallurgical and Materials Transactions A, 33(8), 2599–2606.
2. D. J. Bammann, M. L. Chiesa, M. F. Horstemeyer, and L. I. Weingarten (1993), "Failure in Ductile Materials Using Finite Element Methods," eds. N. Jones and T. Weirzbicki, Structural Crashworthiness and Failure, Applied Science.
3. D. J. Bammann (2001), "A Model of Crystal Plasticity Containing A Natural Length Scale," Mat. Sci. Engr., A309–310, 406–410.
4. Budiansky and O'Connell, (1976), "Elastic Moduli of a Cracked Solid," Int. J. Solids Struct., 12, 81–97.
5. J. L. Chaboche (1993), "Development of Continuum Damage Mechanics for Elastic Solids Sustaining Anisotropic and Unilateral Damage," Int. J. Damage Mech., 2 (4), 311–329.
6. B. D. Coleman and M. E. Gurtin (1967), "Thermodynamics with Internal State Variables," J. Chem. Phys., 47, 59.
7. B. D. Coleman and W. Noll (1963), "The Thermodynamics of Elastic Materials with

Heat Conduction and Viscosity," Arch. Ration. Mech. Anal., 13, 167–178.

8. H. W. Coleman and W. G. Steele (1999), "Experimentation and Uncertainty Analysis for Engineers," 2nd Edition, John Wiley, New York, NY.
9. J. P. Cordebois and F. Sidoroff (1979), "Damage Induced Elastic Anisotropy", Euromech 115, Villard de Lens.
10. Y. F. Dafalias (1985), "The Plastic Spin," Journal of Applied Mechanics, 52 (44), 865–871.
11. M. D. Dighe, A. M. Gokhale, and M. F. Horstemeyer (2002), "Effect of Strain Rate on Damage Evolution in a Cast Al-Si-Mg Base Alloy," Metall. Mat. Trans A, 33A, 555–565.
12. Gangalee and J. Gurland (1967), "On the Fracture of Silicon Particles in Aluminum–Silicon Alloys," Transactions of the Metallurgical Society of AIME, 239, 269–272.
13. W. M. Garrison Jr. and N. R. Moody (1987), "Ductile Fracture," J. of Physics and Chem. of Solids, v 48 (11), 1035–1074.
14. Y. Hammi and M. F. Horstemeyer (2007), "A Physically Motivated Anisotropic Tensorial Representation of Damage with Separate Functions for Void Nucleation, Growth, and Coalescence," Int. J. Plast., 23, 1641–1678.
15. C. R. Harris (2006), "Particle Cracking Damage Evolution in 7075 Wrought Aluminum Alloy under Monotonic and Cyclic Loading Conditions," M.S. Thesis, Georgia Institute of Technology.
16. M. F. Horstemeyer, D. L. McDowell, and D. J. Bammann (1995), "Torsional Softening and the Forming Limit Diagram," SAE Tech. Ser. 960599, ed. K. Chen, Analysis of Autobody Stamping Technology.
17. M. D. Horstemeyer and A. M. Gokhale (1999), "A Void-Crack Nucleation Model for Ductile Metals," Int. J. Solids and Structures, 36, 5029–5055.
18. M. F. Horstemeyer, J. Lathrop, A. M. Gokhale, and M. Dighe (2000a), "Modeling Stress State Dependent Damage Evolution in A Cast Al-Si-Mg Aluminum Alloy," Theory and Appl. Fract. Mech., 33, 31–47.
19. M. F. Horstemeyer and S. Ramaswamy (2000b), "On Factors Affecting Localization and Void Growth in Ductile Metals: A Parametric Study," Int. J. Damage Mech., 9, 6–28.
20. M. F. Horstemeyer (2001), "From Atoms to Autos A New Design Paradigm Using Microstructure-Property Modeling, Part 1: Monotonic Loading Conditions," Sandia National Laboratories, Sand2000-8662, March 2001.
21. M. F. Horstemeyer and P. Wang (2003), 'Cradle-to-Grave Simulation-Based Design Incorporating Multiscale Microstructure-Property Modeling: Reinvigorating Design with Science," Journal of Computer-Aided Materials Design, 10, 13–34, 2003.
22. L. M. Kachanov (1958), "Time of the Rupture Process under Creep Conditions," Izvestiya Akad. Nauk USSR, Otd. Tech. Nauk, 8, 26–31.
23. N. Kanetake, M. Nomura, and T. Choh (1995), "Continuous Observation of Microstructural Degradation During Tensile Loading of Particle Reinforced Aluminum Matrix Composites," Materials Science and Technology, 11 (12), 1246–1252.
24. J. Kratochvil and O. W. Dillon Jr. (1969), "Thermodynamics of Elastic-Plastic Materials as a Theory with Internal State Variables," J. Appl. Phys., 40, 3207.
25. J. Lemaitre (1985), "Continuous Damage Mechanics Model for Ductile Fracture," Transactions of the ASME Journal of Engineering Materials, 107, 83–89.
26. M. P. Miller and D. L. McDowell (1992), "Stress State Dependence of Finite Strain Inelasticity," ASME Summer Applied Mechanics Meeting, Tucson, AZ, ASME AMD-Vol. 32, Microstructural Characterization in Constitutive Modeling of Metals and Granular Media, 27–44.
27. M. P. Miller, P. R. Dawson, and D. J. Bammann (1995), "Reflecting Microstructural

Evolution in Hardening Models for Polycrystalline Metals," Simulation of Materials Processing: Theory, Methods, and Applications, eds. Shen and Dawson, Balkema, Rotterdam.

28. S. Murakami (1988), "Mechanical Modeling of Material Damage," J. Appl. Mech., 55, 280–286.
29. V. C. Prantil, J. T. Jenkins, and P. R. Dawson (1993), "An Analysis of Texture and Plastic Spin for Planar Polycrystals", Journal of the Mechanics and Physics of Solids, 41 (8), 1357.
30. T. Park and G. Z. Voyiadjis (1998), "Kinematic Description of Damage," J. Appl. Mech., 65, 93–98.
31. M. Ortiz and E. P. Popov (1985), "Accuracy and Stability of Integration Algorithms for Elastoplastic Constitutive Relations," International Journal of Numerical Methods in Engineering, 21, 1561–1576.
32. J. Rice and D. M. Tracey (1969), "On the Ductile Enlargement of Voids in Triaxial Stress Fields", Journal Mechanics Physics Solids, 17, 201–217.

I. Materials Design for Magnesium Alloys

Principal Investigator: Seong-Gon Kim
Associate Professor, Department of Physics and Astronomy
Mississippi State University
Hilbun Hall, Room 237, P.O. Box 5405
Mississippi State, MS 39762-5405
(662) 325-8031; fax: (662) 325-8898; email: kimsg@hpc.msstate.edu

Co-Principal Investigator: Mark F. Horstemeyer
Chair in Solid Mechanics and Professor, Department of Mechanical Engineering
Center for Advanced Vehicular Systems
Mississippi State University
206 Carpenter Bldg., P.O. Box ME
Mississippi State, MS 39762
(662) 325-7308; fax: (662) 325-7223; email: mfhorst@me.msstate.edu

Co-Principal Investigator: Hongjoo Rhee
Postdoctoral Associate
Center for Advanced Vehicular Systems
Mississippi State University
P.O. Box 5405
Mississippi State, MS 39762-5405
(662) 325-9221; fax: (662) 325-5433; email: hrhee@cavs.msstate.edu

Co-Principal Investigator: Sungho Kim
Postdoctoral Associate
Center for Advanced Vehicular Systems, CAVS 2182-C
Mississippi State University
Mississippi State, MS 39762-5405
(662) 325-9241; fax: (662) 325-5433; email: sk5@msstate.edu

Co-Principal Investigator: Shengjun (Dennis) Zhang
Postdoctoral Associate, Department of Material Science and Engineering
Robert R. McCormick School of Engineering and Applied Science
Northwestern University
2220 Campus Dr.
Evanston, Illinois 60208-3108, USA
(847) 491-5887; fax: (847) 491-7820; email: shengjun-zhang@northwestern.edu

Co-Principal Investigator: Greg Olson
Winson-Cook Chaired Professor in Engineering Design
The Steel Research Group at Northwestern
Department of Mechanical Engineering
Northwestern University
2145 Sheridan Road
Evanston, Illinois 60208-3111
(847) 491-2847; fax: (847) 491-7820; email: g-olson@northwestern.edu

Co-Principal Investigator: Qingyou Han
Mechanical Engineering Technology Department
Purdue University
401 North Grant Street
Knoy Hall, Room 107
West Lafayette, Indiana 47907-2021
(765) 494-7528; fax: (765) 494-6219; email: hanq@purdue.edu

Contractor: Mississippi State University
Contract No.: 4000054701

Objective

- Investigate the effect of nanoscale precipitates and novel additives to the overall strength and ductility in magnesium (Mg) alloy systems.

Approach

- In support of the collaborative materials design effort proposed here aimed at lightweight components for automotive applications, a systems approach to materials design [1] will be applied. Working within a multiscale hierarchy of microstructural subsystems governing desired property combinations for structural performance, key microstructural elements will be identified for the calibration, application, and validation of process/structure and structure/property design models defining key theoretical parameters and critical experiments enabling parametric design of novel alloy compositions.
- At the electronic level, quantum-mechanical first-principles simulations based on density functional theory (DFT) [2, 3] will be performed to elucidate the origin of the alloying effects. A fundamental understanding of solidification, dislocation, creep, fatigue, crack nucleation and failure of Mg-based alloy systems also requires accurate atomistic modeling of nanoscale systems containing up to hundreds of thousand atoms. We will perform large-scale atomistic simulations using efficient and reliable empirical interatomic potential methods such as the modified embedded-atom method (MEAM) [4, 5, 6] and force-matching-embedded-atom-method (FMEAM) potentials.
- Various state-of-the-art experimental techniques will also be employed in this project. Scanning electron microscopy (SEM) and transmission electron microscopy (TEM) will be used to obtain microscale as well as nanoscale structural information of Mg alloys. The structure and energies of dislocation cores and planar defects, including stacking faults and twin boundaries, determine the mechanical behavior of the Mg alloys. Electron backscatter diffraction (EBSD) and X-ray diffraction (XRD) measurements will be used to keep track of texture evolution during deformation. An in-situ chemical analysis and mapping of alloying elements can be used to keep track of these elements. Three-dimensional atom probe (3DAP) is capable of resolving the chemical identity and position of individual atoms in 3D with atomic resolution in the z-direction and sub-nanometer resolution in the lateral direction. Furthermore, fundamental thermo-mechanical experiments to measure creep resistance and ductility will be carried out under various loading conditions. Experimental failure analysis will be performed to understand the microstructure-driven mechanism of plasticity and damage growth under monotonic and cyclic loadings. X-ray computed tomography (CT) will be used to quantify the 3D morphological and topological evolutions of voids and microstructural features relevant to material damage. Depth-sensing microindenters and nanoindenters will also be used to evaluate the micromechanical properties of each microstructural phase present in the Mg alloys. These measurements will be used to validate and, in turn, guide the computational material design of new Mg alloys.

Accomplishments

The objectives for the second year were met by accomplishing the following.

- Developed a new zinc (Zn) FMEAM potential using the multi-objective optimization method. The potential parameters and validation data have been compiled into a manuscript for publication (see reference 5 in the "presentations/publications/patents" section at the end of this report).
- Developed a new Mg-Zn FMEAM potential using the multi-objective optimization method. The potential is being applied to study the adsorption of Mg atoms on Zn surfaces and vice versa, and the data are being compiled into a manuscript to be submitted to a peer-reviewed journal (see reference 6 in the presentations/publications/patents section).
- Performed first-principles calculation of the crystal structure of φ phase in Mg-Zn-aluminum (Al) casting alloys. The results have been compiled into a manuscript for publication (see reference 7 in the presentations/publications/patents section).
- Performed materials/mechanical properties characterization on the die-cast base alloys (AZ91D, AM50A, AM60B, and AE44) to provide information for design and simulation efforts.
- Performed chemical analysis using a spectrometer, microstructure observation using optical and scanning electron microscopes, nanoindentation and microindentation tests, room temperature tensile tests at different strain rates, elevated temperature tensile tests, and creep tests by using Oak Ridge National Laboratory (ORNL) facilities.
- Investigated the strengthening precipitates in a Mg-7 wt % Zn-3 wt % Al alloy at peak hardness using 3DAP. The chemical compositions of the matrix and precipitates were measured by local-electrode atom probe spectrometry and compared with the results calculated by the Thermo-Calc software based on the COST2 database. Ternary nanosize precipitates have been found. The precipitates have compositions consistent with the ternary φ or τ phase including its metastable extension. The equivalent sphere diameter of the precipitates at peak strengthening is measured as 20–50 nm, providing an important strength model calibration for materials design. The experimental results are available as a preprint (reference 3 in the presentation/publications/ patents section of this report).

Future Direction

- Develop a new FMEAM potential for Al-Zn alloy systems to study Mg-Zn-Al ternary phases of Mg-based alloys.
- Validate Mg-Zn-Al FMEAM alloy potentials with DFT calculations.
- Perform quantum mechanical first-principles DFT calculation for Mg-Zn-Al casting alloys in the ternary τ phase.
- Perform large-scale molecular dynamics (MD) simulations to study the effect of additive elements on material properties of Mg-based alloys using Mg-Zn-Al FMEAM alloy potentials.
- Carry out microstructure and mechanical properties characterization of new Mg-based alloys with novel additives.

Introduction

Mg alloys are currently used in relatively small quantities for automotive components, generally limited to die castings. Two main barriers to wider use of Mg alloys in the automotive industry are poor creep resistance at temperatures above 150°C for powertrain applications and poor ductility for structural body parts, engine components, engine cradles, and control arms.

To achieve the goal of improving the fuel efficiency of cars built in the future, the automobile industry needs to have lightweight, high-strength materials with better materials properties. We need to perform compositional design of Mg-based alloys in a manner that

increases creep resistance and ductility while keeping production costs low.

The future state of this technology will be the development of Mg-based alloys that have lower mass densities and increased strength compared to Al-based alloys, better creep resistance than that of AE44 grade Mg alloy, and costs comparable to that of AZ91D grade Mg alloy. The new Mg-based alloys should also exhibit sufficiently high ductility to allow conventional fabrication processes to be used, but generate adequate strength after the fabrication process.

Approach

At the electronic level, quantum-mechanical, first-principles total-energy calculations are performed within DFT [2, 3] using Blöchl's all-electron projector augmented wave method [7] as implemented by Kresse et al. [8]. For the treatment of electron exchange and correlation, we use either local-density approximation [9, 10] or generalized gradient approximation [11] depending on the accuracy required. The Kohn-Sham equations are solved by using a preconditioned band-by-band conjugate-gradient minimization [12].

At the atomistic level, accurate atomistic simulations are performed using efficient and reliable empirical interatomic potentials such as MEAM [4, 5, 6] or FMEAM [13, 14] potentials. The interatomic potentials are constructed by optimizing the potential parameters to reproduce various experimental materials properties and atomic force data from DFT calculations.

Various state-of-the-art experimental techniques are used in this project. The chemical analysis is performed by using a spectrometer. Microstructures of the alloys are investigated by optical microscopy and SEM. SEM and TEM are used to obtain microscale as well as nanoscale structural information for Mg alloys. EBSD and XRD measurements will be used to keep track of texture evolution during deformation. The quantitative as well as qualitative chemical compositions of each phase present in the alloys will be individually analyzed by an energy dispersive X-ray spectroscopy technique. An in situ chemical analysis and mapping of alloying elements can be used to keep track of these elements. A 3DAP is capable of resolving the chemical identity and position of individual atoms in 3D with atomic resolution in the z-direction and subnanometer resolution in the lateral direction. Conventional hardness tests will be conducted to gain overall properties of the alloys, while depth-sensing microindentation and nanoindentation tests are performed to obtain micromechanical properties of each microstructural phase present in Mg alloys. Thermomechanical experiments to evaluate creep resistance and ductility are carried out under various conditions. X-ray CT will be used before and after the creep tests to quantify the 3D morphological and topological evolutions of voids and microstructural features relevant to material damage. Experimental failure analysis will be performed to understand the microstructure-driven mechanism of plasticity and damage growth under monotonic and cyclic loadings. (For a more detailed description of our experimental and computational approach, see the 2007 annual report [15].)

Interatomic Potentials for Mg-Based Alloys

In addition to the Mg, Al, and Mg-Al interatomic FMEAM potentials we developed in the first year [15, 16], we developed two additional interatomic potentials this year: Zn and Mg-Zn FMEAM potentials.

It is quite a challenge to develop a successful embedded-atom-method (EAM) potential for Zn [17] and only a few EAM potentials are available for Zn to date. Ramprasad and Hoagland developed an EAM potential for Zn and applied it to study the thermodynamic properties of small Zn clusters [18]. Recently, challenging the prevalent opinion of inadequateness of the EAM for hexagonal close packed (hcp) metals, Liu and coworkers developed a set of EAM potentials for the Mg-Al alloy system that give much more improved results than currently available MEAM potentials [14, 19]. Sun et al. further improved this EAM potential to get better equilibrium melting properties and high-temperature phase stability [20]. We prefer the EAM potential since we are interested in eventually developing related semiempirical potentials for alloy systems

involving Zn, such as the φ-phase of Al-Mg-Zn [21]. EAM is much better suited for multicomponent systems than MEAM since EAM requires a separate potential for each pair of elements while MEAM requires a separate potential for each combination of triplets of atoms. Therefore, we choose Liu's EAM potential as a template to develop an EAM potential for Zn.

The multi-objective optimization procedure [22] was used to develop the Zn FMEAM potential [23]. We used the Mg potential by Liu et al. [14] as an initial potential. We used zero temperature configurations with fixed positions for various calculations except force calculations. We calculated the forces on Zn atoms in structures obtained by thermal equilibrium at six different temperatures. More than 18 objectives including equilibrium lattice constant, cohesive energies, and elastic constants are used to construct the EAM potential parameters for Zn. The cohesive energies of Zn atoms in hcp, face-centered cubic, and body-centered cubic crystal structures were calculated for several atomic volumes near the equilibrium atomic volumes. Figure 1 is the plot of cohesive energies of Zn crystals in hcp structure as a function of atomic volume. The minimum of this curve determines the equilibrium lattice constant a_0 and equilibrium cohesive energy $E_{coh} = E_{hcp}$. Hexagonal crystals have five independent elastic constants: C_{11}, C_{12}, C_{13}, C_{33}, and C_{44} [24]. The elastic constants are calculated numerically by

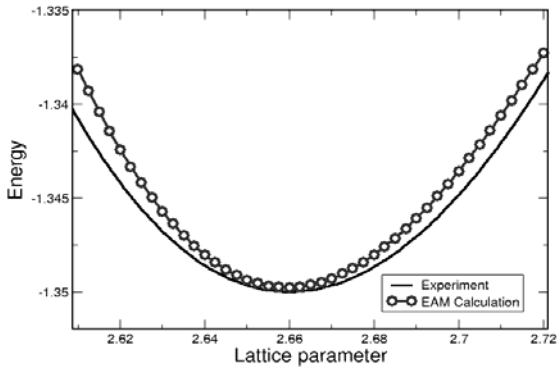

Figure 1. The energy per atom of Zn crystals in hcp structures as a function of atomic volume. The Rose's equation of state is constructed from experimental values of bulk modulus equilibrium volume and cohesive energy.

applying small strains to the lattice. We follow the procedure described by Mehl et al. [25] and apply several different strains ranging from −2.0% to +2.0%. The elastic constants are obtained by fitting the resultant curves to quadratic functions.

To obtain the force data, initial atomic structures that contain 192 Zn atoms were created from the bulk hcp crystal structure. The positions of atoms are randomly disturbed from their equilibrium positions and 10,000 steps of MD simulations with a time step Δt = 1.0 fs were performed to equilibrate each structure for different temperatures. If no FMEAM potential is available for MD simulations, one could use an intermediate FMEAM potential that is generated. The potential should be adequate enough to obtain a reasonable set of structures.

The energy-volume curve for three basic structures has been evaluated with the present EAM potential and compared with DFT calculations. Figure 1 shows that our new Zn FMEAM potential reproduces the Rose's universal equation of state constructed from the experimental parameters rather well. Whenever possible, the experimental values are chosen as the target values. If the experimental values are not available or known to be unreliable, the computed values from the first-principles method are used.

We note that the present FMEAM potential reproduces the experimental lattice constant and the cohesive energy correctly. The sequence of the structures is also predicted correctly in the order of stability by the present Zn FMEAM potential. The five elastic constants for hexagonal crystal structure are in good agreement with the experimental values.

The force-matching against the ab initio forces database has also been performed. The DFT and FMEAM calculations were done with 192 atoms, at six different temperatures. It shows that the FMEAM potential from the present work reproduces the forces in close agreement with DFT calculations.

Mg-Zn-Al Ternary Phase Structure

The structure of $Mg_{84}(Al_xZn_{1-x})_{68}$ alloy in ternary φ phase has been determined from the first-principles calculations. Bourgeois et al. characterized the crystal structure of the equilibrium intermetallic φ-phase formed in a Mg–Zn–Al casting alloy from electron diffraction patterns obtained using TEM [21]. Despite these experiments and a few simulations to reproduce the diffraction patterns, the equilibrium structure of φ phase in a Mg–Zn–Al casting alloy is not fully determined and the identity of some of the ambiguous sites are yet to be determined [21, 26]. For the first time, we obtained the equilibrium structure and determined the identity of all atomic sites of φ phase based on the first-principles method based on DFT [2, 3]. The structure and identity of atoms are determined by minimizing the heat of formation of $Mg_{84}(Al_xZn_{1-x})_{68}$ alloy as a function of x. The heat of formation is evaluated from:

$$H_f = E\left[Mg_{84}(Al_xZn_{1-x})_{68}\right] - xE\left(Mg_{84}Al_{68}\right) - (1-x)E\left(Mg_{84}Zn_{68}\right) \quad . \qquad (1)$$

There are 10 sites which Al and Zn atoms can occupy interchangeably. Figure 2 shows the heat of formation values obtained from Eq. (1) for all possible combinations (2^{10} = 1,024). Figure 3 shows the structure of $Mg_{84}(Al_xZn_{1-x})_{68}$ alloy in φ phase with x = 0.4725 that has the lowest heat of formation in Figure 2.

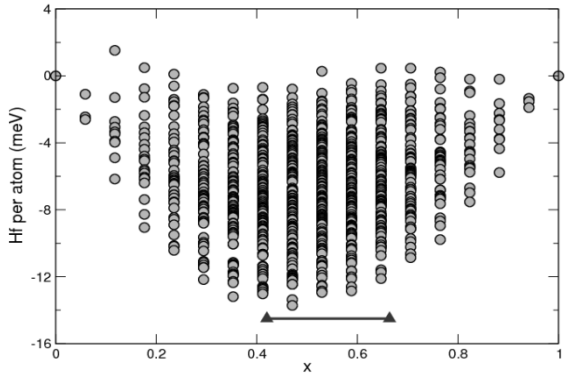

Figure 2. The heat of formation per atom of $Mg_{84}(Al_xZn_{1-x})_{68}$ alloy as a function of x. The dark grey line indicates the range of x values consistent with previous experiments [21].

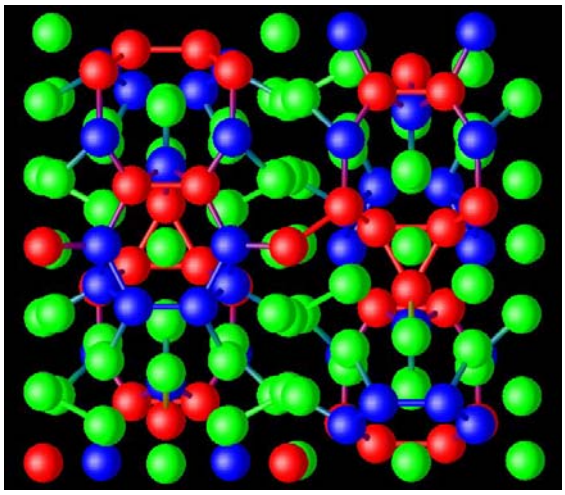

Figure 3. The structure of $Mg_{84}(Al_xZn_{1-x})_{68}$ alloy in φ phase with x = 0.4705. The green spheres represent Mg atoms, blue spheres Zn atoms, and red spheres Al atoms.

Mechanical Properties of Mg-Based Alloys

To obtain fundamental mechanical properties and attain proper stress levels for creep tests, tensile tests were carried out in the quasi-static strain rate regime. The tensile tests were performed at various strain rates of 0.0001, 0.001, and 0.01 per second, with different testing temperatures of room temperature and 150°C. The stress versus strain plots of the various base alloys under such test conditions are shown in Figure 4. The ultimate tensile stress and the flow stress level of the alloys strongly depend on the alloy composition, testing temperature, and strain rate. Not surprisingly, AZ91D possessed the highest tensile strength and the worst ductility among tested alloys. AM series Mg alloys are developed for and characterized by slightly reduced strengths with higher ductility and impact strength compared to AZ91D grade [27, 28, 29, 30], while AE series Mg alloys are developed for good ambient and elevated temperature properties and creep resistance [31, 32, 33, 34, 35]. The test results showed such characteristics.

Figure 5 provides fracture surfaces of the tensile tested specimens observed by SEM. The fractography reveals that fractures occurred in a brittle manner in all cases. The absence of shear lips on the edges of fracture surfaces, indicating a general lack of ductility, is noted. The features of the fracture surfaces are associated with shrinkage

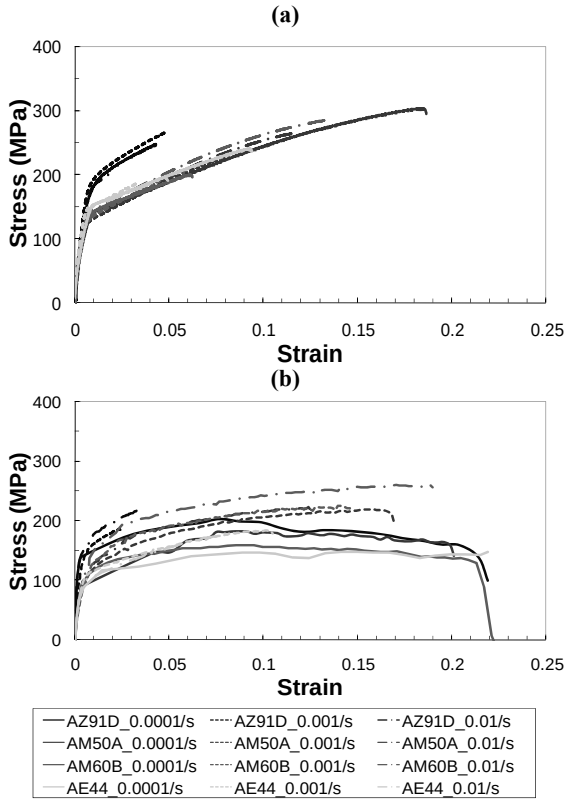

Figure 4. Stress versus strain plots of the Mg-based alloys obtained from quasi-static tensile tests at (a) room temperature and (b) 150°C.

cavities. Fracture surfaces contained many pores ranging from a few tens of microns to hundred microns in size. These cavities could have resulted from entrapped air being carried into the mold by undue turbulence during casting. In addition, granular secondary arms of dendrites can be seen on the fracture surfaces.

The creep behaviors of the base alloys were investigated to determine better ways for developing novel Mg alloys with improved creep resistance. Two experimental approaches, stress relaxation and creep tests, were used to obtain creep properties of the base alloys. The stress relaxation tests were carried out on an Instron machine at various temperatures (120, 150, and 200°C) after imposing prestrain of 0.02 and prestrain rate of 0.001/s before the stress relaxation process. Stress versus time plots of the base alloys obtained from the stress relaxation tests are given in Figure 6. For a given test condition, the peak stress obtained from AZ91D before the stress relaxation tests is the highest

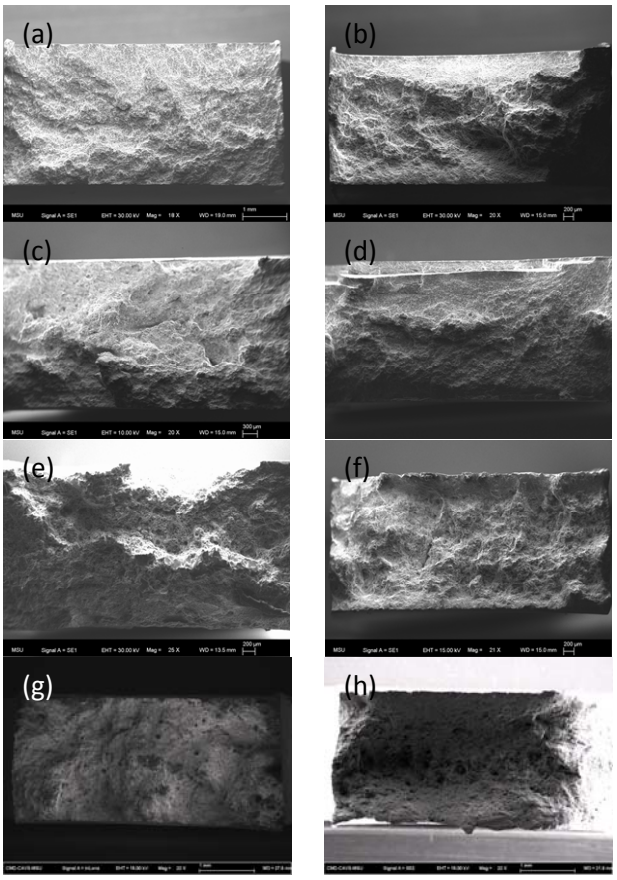

Figure 5. SEM fractography on the tensile tested specimens. (a) AZ91D, (b) AM50A, (c) AM60B, and (d) AE44 tested at room temperature; (e) AZ91D, (f) AM50A, (g) AM60B, and (h) AE44 tested at 150°C.

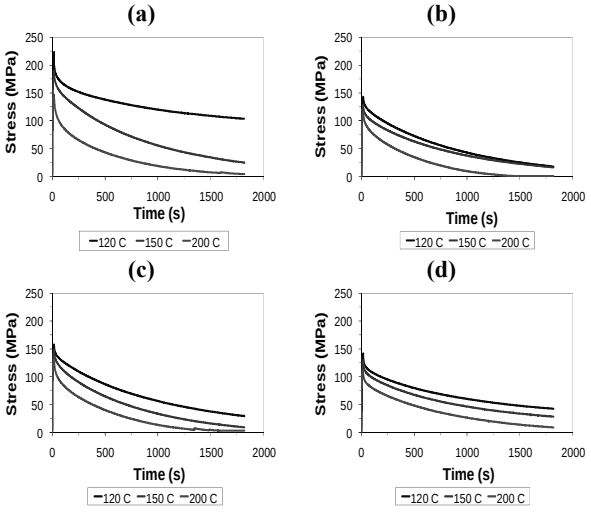

Figure 6. Stress versus time plots obtained from stress relaxation tests at various temperatures: (a) AZ91D, (b) AM50A, (c) AM60B, and (d) AE44.

among tested alloys, and this result is comparable to tensile test results. The peak stress and residual stress levels decrease with increasing testing temperature for any given test conditions.

The creep parameters for the base alloys obtained from stress relaxation tests can be extracted by fitting the data to a power-law creep equation [36]:

$$\dot{\gamma} = A\tau^n \exp\left(-\frac{Q_c}{RT}\right) , \qquad (2)$$

where $\dot{\gamma}$ is the steady-state strain rate in creep, A is the material constant, τ is the stress, n is the stress exponent, Q_c is the creep activation energy, R is the gas constant, and T is the absolute temperature. The relationship between strain rate and stress of the base alloys obtained from the stress relaxation part of the tests is depicted in Figure 7. The stress exponents that depend on the operating creep mechanisms are provided, and they are comparable to the stress exponents reported in the literature [37, 38, 39].

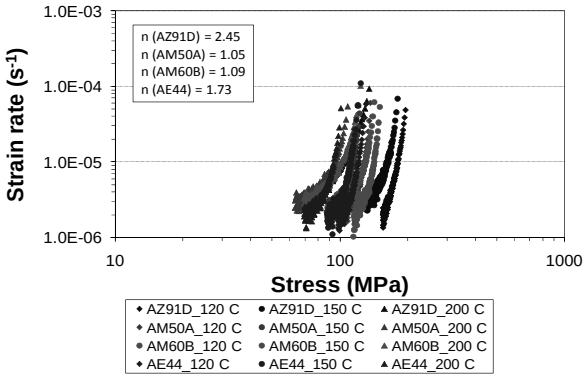

Figure 7. Relationship between strain rate in creep and stress obtained from the stress relaxation tests of various base alloys.

Figure 8 shows the relationship between peak stress and testing temperature using the data from Figure 7. The creep activation energy values obtained from stress relaxation tests are varied with respect to different compositions of the alloys. The dominant creep mechanism of the tested condition can be identified by comparing the experimentally obtained values of n and Q_c with those predicted because each creep mechanism predicts a unique range of those values [40, 41].

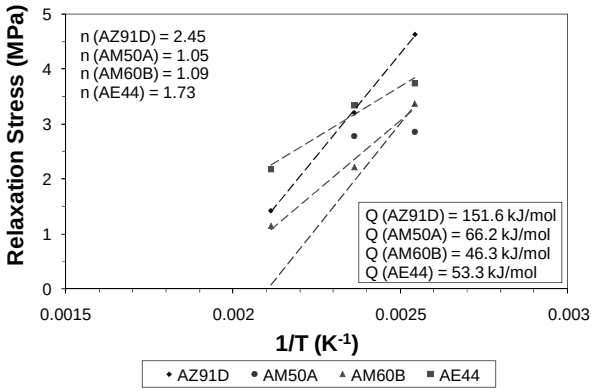

Figure 8. Relationship between peak stress and testing temperature obtained from the stress relaxation tests.

Creep test results obtained from ORNL creep test facilities are shown in Figure 9. Creep tests were performed at three different temperatures (120, 150, and 200°C) with three different stress levels (20, 40, and 80 MPa). Four creep tests (two low stress tests at 120 and 150°C) for AZ91D were discontinued after 500 hours of testing as the apparent steady state condition was achieved, whereas six tests were discontinued for AE44

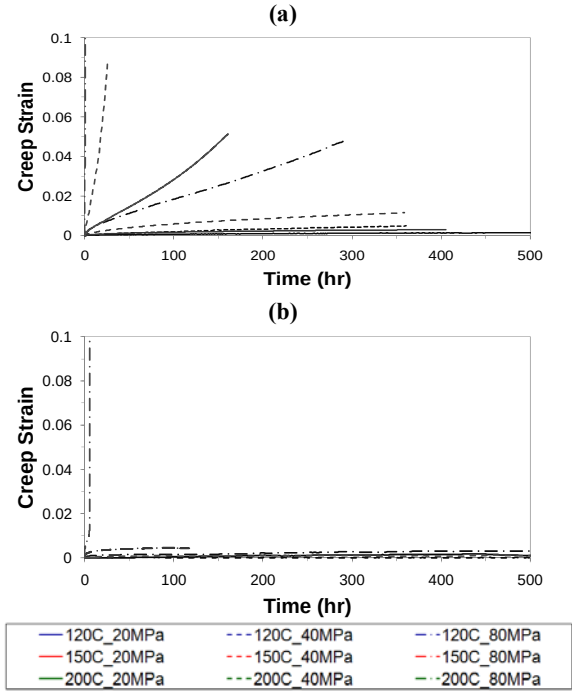

Figure 9. Creep curves obtained from ORNL creep test facilities under various test conditions: (a) AZ91D and (b) AE44.

creep tests because no detectable creep deformation was observed under such test conditions.

Figure 10 provides a comparison of creep curves between AZ91D and AE44 tested at 200°C under stress of 80 MPa. Steady-state creep rate of AZ91D is much higher than that of AE44, and the rupture lifetime of AE44 is dramatically longer than that of AZ91D.

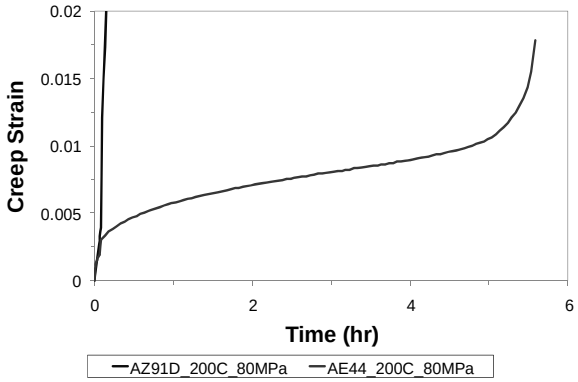

Figure 10. Comparison of creep curves between AZ91D and AE44 tested at 200°C under 80 MPa.

As to strengthening mechanisms of Mg-based alloy systems, to strengthen the Mg-Zn system, the alloy must be aged to increase hardness. The yield strength increases with hardness as the aging temperature increases. Using results for Mg-7 wt % Zn, the strength increases by 29.3% to 199.8 MPa at an aging temperature of 40°C.

Figure 11 shows the plot of aging temperature against composition of Zn. The data points in the plot correspond to peak hardness values found through literature review. The solvus lines were estimated by tracking the phases of the precipitates present at each of the data points. For instance, if the β1' and β2' phases both exist at a certain aging temperature and composition, this data point was assumed to lie between the solvus lines of β1' and β2'. Points lying on the solvus lines for the β1' and β2' phases were found in the literature for Mg-5 wt % Zn, and a point on the solvus line for the Guinier-Preston (GP) zone precipitates was found for Mg-5.53 wt % Zn. It should be noted that peak hardness is controlled by the β1' and β2' phases. These points were used as reference points

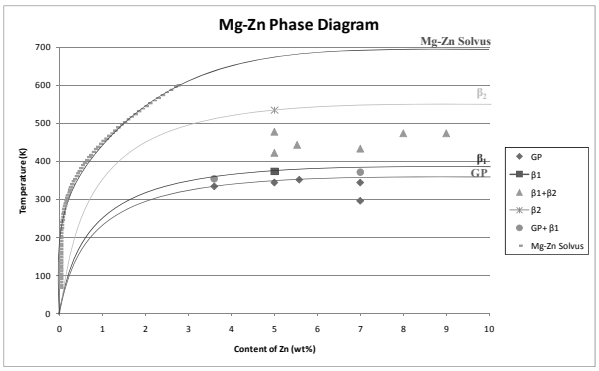

Figure 11. Metastable phase diagram for Mg-Zn: Aging temperature versus composition of Zn.

to draw the estimated solvus lines in Figure 12. We investigated the strengthening mechanisms of the Mg-Zn and Mg-Zn-Ca systems based on the experimental data in the literature. To strengthen the Mg-Zn system, the alloy must be aged to increase hardness. The yield strength increases with hardness as the aging temperature increases. Using results for Mg-7 wt % Zn, the strength increases by 29.3% to 199.8 MPa at an aging temperature of 40°C.

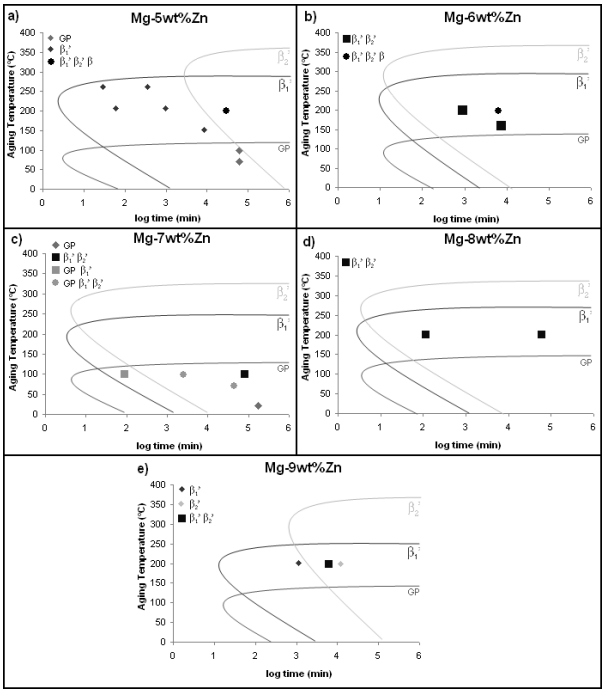

Figure 12. TTT diagrams for (a) Mg-5 wt % Zn, (b) Mg-6 wt % Zn, (c) Mg-7 wt % Zn, (d) Mg-8 wt % Zn, and (e) Mg-9 wt % Zn.

To characterize the time-temperature transformation (TTT) diagrams, data from the literature on the phases present at certain aging temperatures and aging times were plotted. Based on which phases were present at each point, the appropriate phase transformation lines were drawn.

Figure 12 shows the TTT diagrams for several compositions of the Mg-Zn system. In general, in the Mg-Zn system, at lower temperatures, GP zones form first, followed by the metastable β1' and β2' phases, and the stable β phase. The transformation lines were estimated using this general trend.

As shown in Figure 12(a), for the Mg-5 wt % Zn alloy, at lower temperatures the β1' and β2' phases do not seem to develop even after extended periods of aging. Also, it is reasonable to conclude that the β1' phase will build up at aging temperatures higher than 150°C. At 200°C, the β2' and β phases appear after 30,000 minutes of aging. It is clear as to when the β1' phase is dominant.

The Mg-6 wt % Zn alloy is shown in Figure 12(b). The β1' and β2' phases were present in this alloy at an aging temperature of 200°C and an aging time of 900 minutes, which corresponds to peak hardness. As the alloy is overaged, the stable β phase begins to accumulate, resulting in decreased hardness.

For the Mg-7 wt % Zn alloy in Figure 12(c), after aging at a temperature of 98°C for 90 minutes, GP zones and the β1' phases were observed. After aging for 2,400 minutes, the β2' phase appears in addition to the GP zones and the β1' phase. As the alloy is aged even more, at 84,000 minutes, the GP zones disappear leaving only the β1' and β2' phases present. It should also be noted that at ambient temperature aging, even after extended periods of aging, the β1' and β2' phases do not appear and only the GP zones are observed. Due to limited resources, only two data points were plotted for the Mg-8 wt % Zn alloy. The phases present in both data points were the β1' and β2' phases, as shown in Figure 12(d). The GP zone transformation line should lie below 200°C while the β1' and β2' lines should lie above 200°C.

Conclusions

We applied the multi-objective optimization procedure to develop two new interatomic potentials for Zn and Mg-Zn based on FMEAM.

The structure of $Mg_{84}(Al_xZn_{1-x})_{68}$ alloy in ternary φ phase has been determined from first-principles calculations.

The creep behavior of the Mg-based alloys was investigated using stress relaxation and long-time creep tests. We found that steady-state creep rate of AZ91D is much higher than that of AE44, and the rupture lifetime of AE44 is dramatically longer than that of AZ91D.

The strengthening mechanisms of the Mg-based alloy systems were investigated. The metastable phase diagrams with GP solvus and metastable precipitate solvus have been constructed. Preliminary TTT diagrams of Mg-based alloys have been estimated according to experimental information. These diagrams provide the basis for calibration of thermodynamic and kinetic modeling of precipitation strengthening in the Mg-based alloy systems.

Presentations/Publications/Patents

1. B. Jelinek et al., "Modified embedded-atom method interatomic potentials for the Mg-Al alloy system," *Phys. Rev. B*, **75**, 054106 (2007).
2. J. Houze et al., "A multi-objective optimization procedure to develop modified-embedded-atom-method potentials: an application to magnesium," submitted to *Phys. Rev. B.*, arXiv:0708.0075.
3. Shengjun Zhang and Gregory B. Olson, "3D-atom probe investigation of strengthening precipitates in a Mg-7Zn-3Al alloy," Preprint.
4. S. Groh et al., "Mobility of <**a**> dislocations in Mg and Mg/Al alloys by molecular dynamic simulations," submitted to *Computational Materials Science*.
5. Amitava Moitra et al., "Force-matching embedded-atom-method potential for Zinc," to be submitted to *Phys. Rev. B*.

6. Amitava Moitra et al., "Adsorption of Zn atoms on Mg(0001) surface," in preparation.
7. J. Houze et al., "First-principles calculation of the crystal structure of Phi phase in Mg-Zn-Al casting alloys," in preparation.

References

1. G. Olson, "Systems design of hierarchically structured materials: Advanced steels," *Journal of Computer-Aided Materials Design*, **4**, p. 143 (1998).
2. G. Kresse and J. Furthmüller, "Efficient iterative schemes for ab initio total-energy calculations using a plane-wave basis set," *Phys. Rev., B* **54**, p. 11169 (1996).
3. W. Kohn and L. J. Sham, "Self-consistent Equations Including Exchange and Correlation Effects," *Phys. Rev.,* **140**, p. A1113 (1965).
4. M. I. Baskes, "Modified embedded-atom potentials for cubic materials and impurities," *Phys. Rev. B*, **46**, p. 2727 (1992).
5. M. S. Daw and M. I. Baskes, "Embedded-atom method: Derivation and application to impurities, surfaces, and other defects in metals," *Phys. Rev. B*, **29**, p. 6443 (1984).
6. M. S. Daw and M. I. Baskes, "Semiempirical, Quantum Mechanical Calculation of Hydrogen Embrittlement in Metals," *Phys. Rev. Lett*., **50**, p. 1285 (1983).
7. P. E. Blöchl, "Projector augmented-wave method," *Phys. Rev. B*, **50**, p. 17953 (1994).
8. G. Kresse and D. Joubert, "From ultrasoft pseudopotentials to the projector augmented-wave method," *Phys. Rev. B*, **59**, p. 1758 (1999).
9. D. M. Ceperley and B. J. Alder, "Ground State of the Electron Gas by a Stochastic Method," *Phys. Rev. Lett*., **45**, p. 566 (1980).
10. J. P. Perdew and A. Zunger, "Self-interaction correction to density-functional approximations for many-electron systems," *Phys. Rev. B*, **23**, p. 5048 (1981).
11. J. P. Perdew, K. Burke, and M. Ernzerhof, "Generalized Gradient Approximation Made Simple," *Phys. Rev. Lett*., **77**, p. 3865 (1996).
12. G. Kresse and J. Hafner, "Ab initio molecular dynamics for liquid metals," *Phys. Rev. B*, **47**, p. 558 (1993).
13. Youhong Li et al., "Embedded-atom-method tantalum potential developed by the force-matching method," *Phys. Rev. B*, **67**, p. 125101 (2003).
14. Xiang-Yang Liu et al., "EAM potential for magnesium from quantum mechanical forces," *Modell. Simul. Mater. Sci. Eng*., **4**, p. 293 (1996).
15. Seong-Gon Kim et al., "Task 4: Materials Design for Mg Alloys," ORNL FY 2006–2007 Annual Report, Chaps. 4, pp. 28–45 (2007).
16. B. Jelinek et al., "Modified embedded-atom method interatomic potentials for the Mg-Al alloy system," *Phys. Rev. B*, **75**, p. 054106 (2007).
17. R. Pasianot and E. J. Savino, "Embedded-atom-method interatomic potentials for hcp metals," *Phys. Rev. B*, **45**, p. 12704 (1992).
18. R. Ramprasad and R. G. Hoagland, "Thermodynamic properties of small zinc clusters based on atomistic simulations," *Modell. Simul. Mater. Sci. Eng*., **1**, p. 189 (1993).
19. X.-Y. Liu et al., "Anisotropic surface segregation in Al-Mg alloys," *Surf. Sci*., **373**, p. 357 (1997).
20. D. Y. Sun et al., "Crystal-melt interfacial free energies in hcp metals: A molecular dynamics study of Mg," *Phys. Rev. B*, **73**, p. 24116 (2006).
21. L. Bourgeois, B. C. Muddle and J. F. Nie, "The crystal structure of the equilibrium φ phase in Mg–Zn–Al casting alloys," *Acta Mater*., **49**, pp. 2701–2711 (2001).
22. J. Houze et al., "A multi-objective optimization procedure to develop modified-embedded-atom-method potentials: an application to magnesium," Preprint, arXiv:0708.0075.
23. Amitava Moitra et al., "Force-matching embedded-atom-method potential for Zinc," to be submitted to *Phys. Rev. B*., (2008).

24. H. M. Ledbetter, *Journal of Physical and Chemical Reference Data*, **6**, p. 1181 (1977).

25. M. J. Mehl, B. M. Klein, and D. A. Papaconstantopoulos, in "Intermetallic Compounds: Principles and Applications," edited by J. H. Westbrook and R. L. Fleischer John Wiley & Sons Ltd., London, 1994.

26. P. Lianga et al., "Experimental investigation and thermodynamic calculation of the Al-Mg-Zn system," *Thermochimica Acta*, **314,** pp. 87–110 (1998).

27. W. Blum et al., "Independent deformation of the magnesium alloys AS21 and AZ91," *Zeitschrift für Metallkunde*, **88**, p. 636 (1997).

28. W. K. Miller, "Creep of die cast AZ91 magnesium at room temperature and low stress," *Metall. Trans. A*, **22**, p. 873 (1991).

29. K. Pettersen and S. Fairchild, "Stress relaxation in bolted joints of die cast magnesium components," SAE Tech. Paper 970326 (1997).

30. B. R. Powell et al., "Microstructure and creep behavior in AE42 magnesium diecasting alloy," *J. Electrochem. Soc*., **54**, p. 34 (2002).

31. I. A. Anyanwu, Y. Gokan, A. Suzuki, S. Kamado, Y. Kojima, S. Takeda, and T. Ishida, "Effect of substituting cerium rich mischmetal with lanthanum on high temperature properties of die-cast Mg-Zn-Al-Ca-RE alloys," *Mater. Sci. Eng. A*, **380**, 93 (2004).

32. P. Bakke, K. Pettersen, and H. Westengen, "Improving the strength and ductility of magnesium die casting alloys via rare earth addition," *JOM*, **46** (2003).

33. B. Mordike, "Development of highly creep resistant magnesium alloys," *J. Mater. Process. Technol*., **117**, p. 391 (2001).

34. I. P. Moreno et al., "Microstructural characterization of a die cast magnesium-rare earth alloy," *Scr. Mater*., **45**, p. 1423 (2001).

35. L. Y. Wei and G. L. Dunlop, "The solidification behavior of Mg-Al-rare earth alloys," *J. Alloys Compd*., **232**, p. 264 (1996).

36. T. H. Courtney, *Mechanical Behavior of Materials,* McGraw-Hill, Inc., New York, 1990.

37. *Metals Handbook,* 9th ed., ASM, Metals Park, Ohio, 1985.

38. F. von Buch and B. L. Mordike, "Microstructure, mechanical properties and creep resistance of binary and more complex magnesium scandium alloys," Mg Alloys & their App. Conf. 1998, 145, Wolfsburg, Germany (1998).

39. V. Sklenicka, M. Pahutova, and T. G. Langdon, "Creep of reinforced and unreinforced AZ91 magnesium alloys," *Key Eng. Materials*, **171–174**, p. 593 (2000).

40. M. F. Ashby and D. R. H. Jones, *Engineering Materials: an Introduction to Their Properties and Applications,* (Pergamon Press, Oxford, 1982).

41. G. E. Dieter, *Mechanical Metallurgy,* McGraw-Hill, Inc., London, 1988.

J. High Throughput Isotopic Diffusion Databases for Integrated Computational Materials Engineering

Nagraj S. Kulkarni
Research Assistant Professor
Department of Materials Science & Engineering
Center for Materials Processing
University of Tennessee,
Knoxville, TN 37996-0816

Monolithic Systems Development Group
Oak Ridge National Laboratory
Measurement Science & Systems Engineering Division
Oak Ridge, TN 37831-6006
(865)576-0592; fax: (865)576-2813, e-mail: kulkarnins@ornl.gov

Technology Area Development Manager: Joseph A. Carpenter
(202) 586-1022; fax: (202) 586-1600; e-mail: joseph.carpenter@ee.doe.gov

Field Technical Monitor: C. David Warren
(865) 574-9693; fax: (865) 574-6098; e-mail: warrencd@ornl.gov

Participants:
Peter Todd
Oak Ridge National Laboratory

Professor Yongho Sohn
University of Central Florida

Contractor: Oak Ridge National Laboratory (ORNL)
Contract No.: DE-AC05-00OR22725

Objectives

- Develop a tracer-diffusion database for magnesium-rich phases in the magnesium-aluminum-zinc-manganese (Mg-Al-Zn-Mn) system using secondary ion mass spectrometry (SIMS) for measurements of diffusion depth profiles of isotopes. Initial year focus will be on the Mg-Al-Zn system.
- Upgrade the SIMS instrument (Cameca IMS 4f ion microscope) at ORNL for automated and reliable isotopic ratio depth-profile measurements.
- Use an intrinsic diffusion simulation to assess diffusion formalisms needed for obtaining practical interdiffusion information from tracer-diffusion and thermodynamic databases. Diffusion formalisms include the Darken, Manning, and Moleko formalisms.

Approach

- Establish procedures for thin-film isotope deposition and SIMS measurements of diffusion depth profiles in a few select Mg alloy samples annealed at different temperatures. Analyze diffusion profiles to determine tracer diffusivities.

- Prepare homogeneous single-phase compositions in the Mg-rich phase of ternary subsystems such as Mg-Al-Zn and Mg-Al-Mn and a few in the quaternary Mg-Al-Zn-Mn. Deposit thin films of stable isotopes (Mg, Zn) of the primary elements and anneal at different temperatures and times. Analyze diffusion data using SIMS to obtain Mg and Zn tracer-diffusion coefficients for various compositions as a function of temperature.
- Construct a tracer-diffusion database for Mg and Zn in this system by fitting tracer-diffusion data as a function of composition and temperature using polynomial or other suitable functions.
- Conduct interdiffusion and intrinsic diffusion measurements using diffusion couples.
- Further develop intrinsic diffusion simulations that can take tracer-diffusion and thermodynamic data as input and provide interdiffusion and intrinsic diffusion data as output in order to compare them with experimental interdiffusion and intrinsic diffusion measurements. Collaborate with leading theoreticians in diffusion to further refine formalisms.

Accomplishments (since July 2008)

- **Initiated upgrade of Cameca IMS 4f ion microscope for SIMS.** A primary requirement of our project is the capability to quickly and accurately measure isotopic ratios in Mg samples using SIMS. The SIMS instrument at ORNL (Cameca IMS 4f ion microscope) is being upgraded for the high sample load of this project (initially with hardware improvements, to be followed by method and automated software improvements).
- **Initiated assessment of diffusion formalisms.** To use tracer-diffusion databases for prediction of interdiffusion behavior in the presence of concentration or chemical potential gradients, the connection between tracer and interdiffusion as embodied in the Darken-Manning formalisms needs to be utilized. Recently, the Darken-Manning formalisms for a test copper-nickel-zinc (Cu-Ni-Zn) system at 900^{o}C were evaluated using the intrinsic diffusion simulation. Preliminary simulations indicated that the Manning formalism was slightly better than the Darken formalism though none of these formalisms provided an ideal fit. More detailed simulations and analyses are in progress at the present time.

Future Direction

- Complete initial upgrade of ORNL SIMS system (Cameca IMS 4f), and test the University of Central Florida (UCF) SIMS system (Cameca IMS 3f) for isotopic ratio measurements in select Mg alloy samples.
- Once preliminary SIMS measurements are confirmed, begin sample preparation in Mg-rich phase of Mg-Al-Zn system and proceed with tracer-diffusion database construction for ternary systems.
- Assess the Darken and Manning formalisms at various temperatures in face-centered cubic (fcc) Cu-Ni-Zn. Incorporate Moleko formalism in the diffusion simulation if results in the test Cu-Ni-Zn system show improvement over the Darken-Manning formalisms.
- Evaluate project and funding requirements for tracer-diffusion measurements of radioactive isotopes of Al and Mn in the Mg-Al-Zn and Mg-Al-Mn ternary systems.

Introduction

The vision of the Department of Energy Integrated Computational Materials Engineering (ICME) project (see report 6G) is to initiate and coordinate a multiorganizational effort whose goal is to develop an integrated suite of validated computational materials modeling tools that are linked to analysis systems used in manufacturing as well as engineering design [1]. In short, the goal is to provide a quantitative linkage between the processing, microstructure, and properties of a material for the desired application (e.g., Mg-based light-metal alloys used in the automotive industry). Improvement in the ICME approach will require continued improvement both in theory and in the associated modeling within the vast array of tools currently available and those still in need of development. Knowledge of fundamental materials properties, thermodynamics, and kinetics in the form of reliable databases are the foundations on which the ICME approach is based. These are expected to be incorporated in the task on cyber infrastructure within the ICME project. A gap in the

understanding of any one of these may dramatically reduce the effectiveness of, adaptability of, and confidence within the engineering community in the ICME effort. While great strides have been made in the development of reasonably robust thermodynamic databases over the course of the past 25 years, the same cannot be said for diffusion databases. The reasons have partly to do with the lack of fundamental (tracer) measurements of diffusion in binary or multicomponent systems; the limited research resources available for such studies; and the lack of clarity in using the appropriate theoretical, experimental, and modeling tools necessary for developing robust diffusion databases that are valid regardless of the driving forces (e.g., concentration, temperature, stress gradients) causing diffusion.

This project aims at developing a tracer-diffusion database in Mg-based light-metal alloy systems. The safety issues that have hampered previous tracer-diffusion measurements based on radioactive tracers are somewhat avoided in this project with the use of *stable isotopes* for most elements in this study (except Al and Mn for which radioactive isotopes are needed). Homogeneous single-phase samples in the Mg-Al-Mn system will be prepared using conventional techniques, stable isotopes of these elements will be deposited in the form of thin films on these samples, and the measurement of isotopic diffusion profiles of stable isotopes in these samples after diffusion annealing will be conducted using automated SIMS facilities either at ORNL or UCF. A combined tracer-diffusion and thermodynamic database, which is continually updated by participants during the course of the Mg-ICME project, will provide the required interdiffusion information for the other modeling tasks in this program. More rigorous application of the phenomenological theory connecting tracer and interdiffusion or intrinsic diffusion behavior can be obtained using the Manning random alloy model [2], rather than the Darken model [3], or using the more recent Moleko formalism [4].

The first year of this study will focus on isotopic-diffusion measurements in the Mg-Al-Zn system, which is the base system for commercial AZ (i.e., Mg-Al-Zn) alloys. Future work beyond this ternary will include studies in the Mg-Al-Mn ternary and Mg-Al-Zn-Mn alloy systems. Additionally, various diffusion formalisms will be evaluated for the test Cu-Ni-Zn system (for which a tracer-diffusion database already exists). The formalisms will then be evaluated for the Mg tracer-diffusion database.

Project Background

Current diffusion database efforts are based on an approach developed by John Agren and others as part of the diffusion software DICTRA (Diffusion Controlled TRAnsformations) [5]. The foundation of this approach is the Darken version of the intrinsic diffusion flux in a multicomponent system with n components:

$$J_k = -\sum_{i=1}^{n} L_{ki}\frac{\partial \mu_i}{\partial x} = -L_{kk}\frac{\partial \mu_k}{\partial x}$$
$$J_k = -c_k M_k \frac{\partial \mu_k}{\partial x} \quad .....(L_{ki} = 0, k \neq i)(k = 1,2,..,n) \qquad (1)$$

By ignoring the cross terms in the matrix of phenomenological diffusion coefficients L_{ki}, the above simplified version of the formalism used by DICTRA is obtained. In this expression, the flux J_k of a component is dependent only on the diagonal term L_{kk}, which in turn is related to the "mobility" of component k, M_k. In the simplified form of the above equation, the driving force for the intrinsic flux of a component is provided by the chemical potential gradient $\partial\mu_k/\partial x$ of that component. From the Darken theory, the connection between L_{kk} or M_k and the tracer-diffusion coefficient D_k^* is

$$L_{kk} = c_k M_k = \frac{c_k D_k^*}{RT} \qquad (2)$$

Originally, the Darken theory connecting the mobility to the tracer-diffusion coefficient was proposed for binary systems. In Eq. (2), it has been extended to multicomponent systems as well. In principle, if the tracer-diffusion coefficients (i.e., the diffusion of an isotope of a component in a homogeneous system) in a system are known, the entire matrix of phenomenological coefficients for that system can be determined (*without ignoring the cross terms—i.e., with no assumptions*) provided the thermodynamics of that

system are known, which is expected to be the case for the current Mg alloy system because a thermodynamic database is already available and is being continually updated. However, because tracer-diffusion experiments are difficult to perform (tracers typically used are radioactive isotopes) and such data are not readily available, the above Darken assumption [Eq. (2)], inherent in the DICTRA formalism, is needed to determine unknown mobilities from diffusion data obtained through conventional interdiffusion experiments. The combination of mobilities obtained from tracer-diffusion data and those obtained from interdiffusion and intrinsic-diffusion experiments are typically used in an optimization process to develop a functional form of a mobility database within the DICTRA formalism [5, 6]. While the assumptions inherent in the DICTRA formalism are well known, the approach nevertheless appears to have provided a practical path toward developing diffusion databases within acceptable margins of error [6]. However, for developing reliable diffusion databases using this formalism, tracer-diffusion information is still necessary for most compounds and phases in the system of interest. This means for compounds or phases in new systems that have not been previously studied, the limiting factor in the development of dependable diffusion databases is the availability of tracer-diffusion data. Additionally, because the DICTRA approach is dependent upon a thermodynamic database for the construction of a mobility database (because converting interdiffusion information to mobilities requires thermodynamic information), the mobility database is not independent of the thermodynamic database. This means that alternate thermodynamic databases cannot be straightforwardly used for diffusion analysis and modeling with the existing mobility database.

Approach

The approach proposed at ORNL offers a robust procedure for developing tracer-diffusion databases using SIMS measurements of the concentrations or concentration ratios of stable isotopes in homogeneous Mg-based light-metal alloy systems. The important point to be noted here is that, unlike tracer-diffusion studies in the past where the use of radioactive isotopes meant that such studies required several years of effort and considerable expense even for limited data, in the present case stable isotopes are used instead, and their diffusion profiles are measured using SIMS techniques [7] whose resolution and accuracy have improved significantly within the past 5–10 years. The advances in SIMS techniques that now permit trace amounts of stable isotopes to be detected enable the use of thin-film or Fick's type solutions to determine the tracer diffusivity that are only valid for trace amounts of isotopes in homogeneous phases.

Unfortunately, the elements Al and Mn do not have any known stable isotopes; hence, for these elements, radioactive isotopes have to be used. However, SIMS can still be used for the tracer-diffusion measurements as before. One advantage of using SIMS over radiation measurement techniques for the radioactive isotope of Al is that the reduced activity of the isotope is actually not a hindrance for SIMS measurements [8]. In addition, safety requirements are likely to be less severe though a more detailed analysis remains to be performed. Because of the high costs of the Al radioactive isotope and the associated safety requirements for handling radioactive isotopes, a separate program request for such experiments will be needed.

An important advantage of a tracer-diffusion database over a mobility database is that the former is independent of the thermodynamic database; hence, the same tracer-diffusion database can be used with a variety of thermodynamic databases for analyzing diffusion problems.

Progress in Fiscal Year 2008 (July–September)

SIMS Upgrade

An important requirement of our project is the ability to measure isotope ratio depth profiles using the SIMS facility at ORNL. Therefore, the ORNL SIMS instrument (Cameca IMS 4f ion microscope, Figures 1 and 2) is initially being upgraded for the high sample load of this project with hardware improvements, to be followed by method and automated software improvements. Completed upgrades include improved pumping of

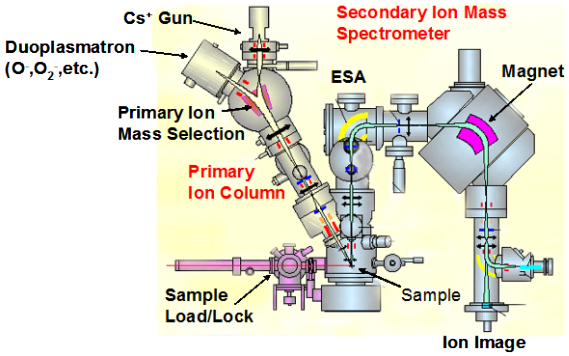

Figure 1. Diagram of ORNL Cameca IMS 4f SIMS system that is ideally suited for isotope ratio diffusion depth-profile measurements.

Figure 2. ORNL Cameca IMS 4f SIMS system currently being upgraded for rapid isotopic ratio diffusion depth-profile measurements.

the secondary ion source, permitting a vacuum of 10^{-11} torr. This level of vacuum virtually eliminates interference caused by formation of secondary ion hydrides, which in fact are the principle interferants in isotope ratio measurements. Pending upgrades include integration of optical and electronics microscopic systems with the secondary-ion microscope systems of the Cameca. These upgrades will permit automated determination of exactly where on a sample measurements are being made at any given time.

Assessment of Diffusion Formalisms

A test of different diffusion formalisms connecting tracer diffusion to interdiffusion requires reliable tracer-diffusion and thermodynamic databases. The Cu-Ni-Zn system is one of the few systems where an excellent tracer-diffusion database is available [9]. A thermodynamic model for this system is also available [10]. Thus, the system was chosen as a test case to evaluate the diffusion formalisms, including the Darken and Manning formalisms. An intrinsic-diffusion simulation [11] that can take the available tracer and thermodynamic information as input and provide the required interdiffusion and intrinsic-diffusion information (e.g., concentration profiles, composition paths, lattice or Kirkendall shifts) as output was used for this assessment.

Darken

In the extended version of the Darken or mobility formalism to multicomponent systems, the cross terms in the matrix of phenomelogical coefficients are ignored [see Eq. (1)]. The mobility of a component is related to its tracer-diffusion coefficient as shown in Eq. (2). The resultant multicomponent intrinsic flux expression for a component is

$$J_i = \frac{-D_i^*}{V} X_i \frac{\partial \ln a_i}{\partial x} \quad , \qquad (1)$$

where D_i^* is the tracer-diffusion coefficient, X_i is the mole fraction, V is the molar volume, and a_i is the activity of component i in this system. In terms of the thermodynamic factors, the flux is expressed as

$$J_i = \frac{-D_i^*}{V} X_i \left(\frac{\Phi_{ii}}{X_i}\frac{dX_i}{dx} + \sum_{j=1\neq i}^{c-1} \frac{\Phi_{ij}}{X_j}\frac{dX_j}{dx} \right) \quad , \qquad (2)$$

where the thermodynamic factors Φ_{ij} are defined by

$$\Phi_{ij} = \frac{d \ln a_i}{d \ln X_j} \quad . \qquad (3)$$

The thermodynamic factors in turn can be obtained in analytical form using the excess Gibbs energy function for face-centered cubic (fcc) Cu-Ni-Zn as a function of composition and temperature. The tracer-diffusion coefficients are available in a convenient form at 900°C [10]:

$$\begin{aligned} \ln D_{Cu}^* &= -3.53 X_{Ni}^{1.16} + 3.6 X_{Zn}^{1.02} - 9.46 \\ \ln D_{Ni}^* &= -4.05 X_{Ni}^{1.3} + 3.28 X_{Zn}^{1.07} - 9.96 \\ \ln D_{Zn}^* &= -3.2 X_{Ni}^{1.16} + 5.21 X_{Zn}^{1.25} - 9 \end{aligned} \quad . \qquad (4)$$

Using the above tracer functions and thermodynamic data as input to the diffusion simulation [11], the outputs of the diffusion simulation were compared with the experimental measurements in diffusion couples prepared by Wan [9]. A few experimental and simulated composition paths are provided in Figures 3 and 4.

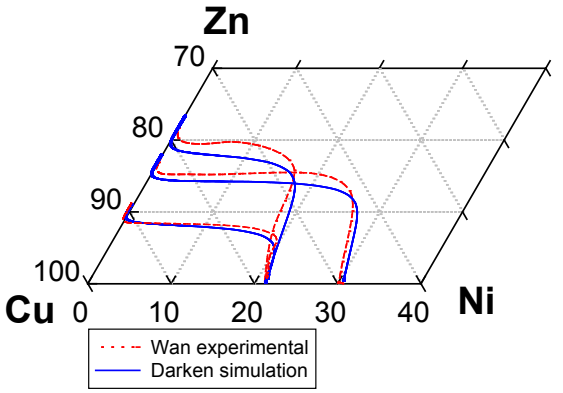

Figure 3. Experimental and simulated composition paths in fcc Cu-Ni-Zn at 900°C using the Darken formalism.

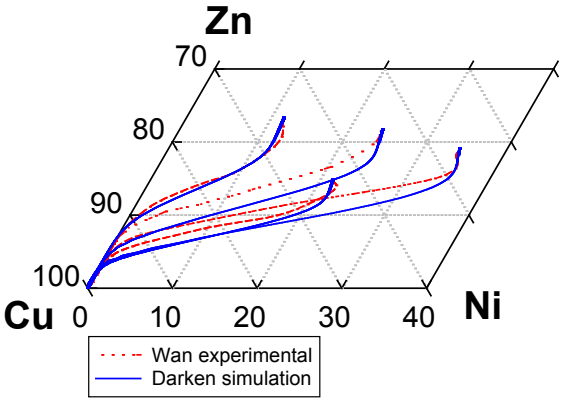

Figure 4. Additional experimental and simulated composition paths in fcc Cu-Ni-Zn at 900oC using the Darken formalism.

Manning

For a multicomponent system consisting of n components, the intrinsic flux can be expressed in terms of the phenomenological coefficients (L_{ij}'s) as follows:

$$J_i = -L_{ii}\frac{\partial \mu_i}{\partial x} - \sum_{j=1\neq i}^{n} L_{ij}\frac{\partial \mu_j}{\partial x} \quad . \qquad (5)$$

The diagonal and the nondiagonal phenomenological coefficients are related to the tracer-diffusion coefficients by the relations provided by Manning [2]:

$$L_{ii} = \frac{X_i D_i^*}{VRT}\left(1 + \frac{2X_i D_i^*}{M_o \sum_{k=1}^{n} X_k D_k^*}\right) \quad , \qquad (8)$$

$$L_{ij} = \frac{X_i D_i^*}{VRT}\frac{2X_j D_j^*}{M_o \sum_{k=1}^{n} X_k D_k^*} \ldots\ldots (i \neq j)$$

where M_o is a geometric constant for the given crystal structure (7.15 for fcc structures) and R is the universal gas constant. The chemical potential gradients in Eq. (7) can be expressed in terms of the thermodynamic factors as in the Darken case. The resultant expression can then be used to test the Manning relations for the fcc Cu-Ni-Zn system at 900°C as was done previously for the Darken relations.

The simulated composition paths using the Manning relations were found to be very similar to those obtained with the Darken simulation and are hence not shown here. The Kirkendall shifts for various diffusion couples using both the Darken and Manning formalisms are compared in Figure 5. Though more simulations are needed to confirm the present findings, it is evident from the preliminary simulations that the Manning relations appear to be slightly better than the Darken

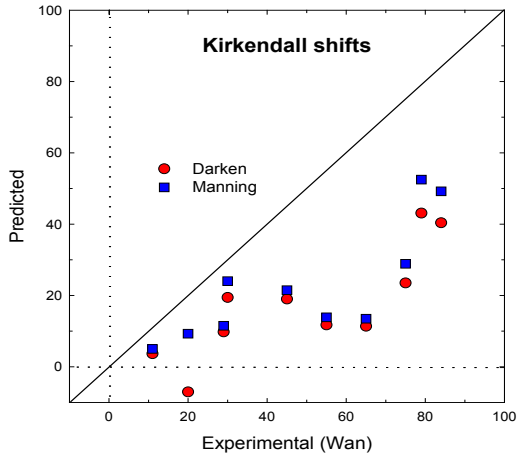

Figure 5. Experimental and simulated Kirkendall shifts in fcc Cu-Ni-Zn at 900°C using the Darken and Manning formalisms.

relations, especially for the Kirkendall shifts. However, neither the Darken nor Manning formalisms could provide a good match to the experimental Kirkendall shifts. Thus there appears to be a need to explore alternate formalisms such as the Moleko formalism [4] in the future. Additionally, a test of diffusion formalisms in hexagonal close-packed systems, such as the current Mg alloy systems, will provide further evidence for the choice of the most suitable diffusion formalism.

Conclusions

A Cameca IMS 4f SIMS system is currently being upgraded at ORNL for reliable automated isotopic ratio depth profile measurements in Mg alloy systems.

Preliminary tests of diffusion formalisms in the Cu-Ni-Zn system indicated that while the predicted composition path profiles provided a reasonable representation of experimental composition paths, the simulated Kirkendall shifts were underestimated in comparison to the experimental ones.

Presentations/Publications/Patents

1. N. S. Kulkarni, P. J. Todd, and Y. H. Sohn, "Assessment of Diffusion Formalisms for Databases," invited talk presented at the *Symposium on Fundamentals & Characterization: Phase Stability, Diffusion Kinetics & Their Applications (PSDK-III)* at the Materials Science & Technology Conference (MS&T08), Pittsburgh, Pennsylvania, October 5–9, 2008.
2. N. S. Kulkarni, P. J. Todd, Y. H. Sohn, "Diffusion Databases for Mg-ICME," presented at the TMS 2008 Annual Meeting, New Orleans, Louisiana, March 12, 2008.

References

1. J. Allison, D. Backman, and L. Christodoulou, *J. Met.*, p. 25 (Nov. 2006).
2. J. R. Manning, *Met. Trans.* **1**, p. 499 (1970).
3. L. S. Darken, *Trans. AIME* **175**, p. 184 (1948).
4. L. K. Moleko, A. R. Allnatt, and E. L. Allnatt, *Phil. Mag.* A **59**, p. 141 (1989).
5. J. O. Andersson et al., *Calphad* **26**, p. 273 (2002).
6. C. E. Campbell, W. J. Boettinger, and U. R. Kattner, *Acta Mat*. **50**, p. 775 (2002).
7. R. A. De Souza et al., *Sol. State Ionics* **176**, p. 1465 (2005).
8. P. Fielitz et al., *Sol. State Ionics* **177**, p. 493 (2006).
9. C. C. Wan, Ph.D. dissertation, University of Florida, Gainesville, 1973.
10. M. Jiang et al., *J. Phys. Chem. Sol*. **66**, p. 246 (2005).
11. N. S. Kulkarni and R. T. DeHoff, *Acta Mat.* **53**, p. 4097 (2005).

K. Cyberinfrastructure

Principal Investigator: Tomasz Haupt
Center for Advanced Vehicular Systems
Mississippi State University
P.O. Box 5405, Mississippi State, MS 39762
(662) 325-4524; fax: (662)325-5433; email: haupt@cavs.msstate.edu

Co-Principal Investigator: Ricolindo Carino
Center for Advanced Vehicular Systems
Mississippi State University
P.O. Box 5405, Mississippi State, MS 39762
(662) 325-5579; e-mail: rlc@cavs.msstate.edu

Co-Principal Investigator: Anand Kalyanasundaram
Research Associate, Center for Advanced Vehicular Systems
Mississippi State University
P.O. Box 5405, Mississippi State, MS 39762
(662) 325-5458; e-mail: anand@cavs.msstate.edu

Technology Area Development Manager: Joseph A. Carpenter
(202) 586-1022; fax: (202) 586-1600; e-mail: joseph.carpenter@ee.doe.gov

Field Project Officer: Aaron D. Yocum
(304) 285-4852; fax: (304) 285-4403; e-mail: aaron.yocum@netl.doe.gov

---

Contractor: Mississippi State University (MSST)
Contract No.: DE-FC26-06NT42755

Objective

- Design and develop a cyberinfrastructure to exploit the recent transformative research in material science involving multiscale physics-based predictive modeling, multiscale experiments, and design. More specifically, the creation of the cyberinfrastructure will result in the development of the "community of practice" portal that allows development and integration of multiscale physics-based materials models for selected properties and processes, in the context of United States Automotive Materials Partnership (USAMP) three-nation Magnesium Front-End Research and Development pilot project.

Approach

- The development of the cyberinfrastructure to support the capabilities described above will leverage tools, technologies, and software approaches developed by other large-scale scientific cyberinfrastructures, in particular GEONGrid (http://www.geongrid.org/) and NEESit (http://it.nees.org/). Much of the foundation of the infrastructure is common across domains (security, grid integration, etc) and can serve to bootstrap this project to delivering an initial working solution in a relatively short time frame. Some initial customization was needed to support the unique aspects of this project. After the initial system had been developed, many of the advanced capabilities of the system required additional software development and customization and entirely new development to support additional features. Hence, we are proceeding with a two-stage development model: phase one was to initial leverage of existing software and tools to bring up a working software infrastructure, and phase two was to evaluate and further develop missing or insufficient software, as needed, to support the project requirements.

- The actual development and deployment of the cyberinfrastructure was driven by the requirements and early feedback generated by the engineering community, composed of MSST researchers performing other tasks of this project, as well as researchers and engineers involved in the MFERD/ICME project. Frequent interactions between researchers and students developing the cyberinfrastructure with the community (as defined above) resulted in modifications of the initial plans, such as adding new elements to the cyberinfrastructure and changing the priorities of the development and deployment of the cyberinfrastructure components. The changes reflect a close collaboration between tasks and the pursuit to maximize the benefits of the cyberinfrastructure to the end user.

Accomplishments

- **Task 1**: Identify, acquire, and deploy servers supporting simple object access protocol (SOAP), Web Services Description Language (WSDL), and integrating Message Oriented Middleware. This task has been completed. We selected and installed: Globus Toolkit 4 grid computing (remote access to resources, security); Apache/Tomcat Web Server with support for J2EE (Java Server Pages), GridSphere (portlet container), JBoss (Enterprise JavaBeans container), Axis (SOAP and WSDL container), ServiceMix (Java Business Integration—Service Bus) and Microsoft's SharePoint Server for the deployment of USAMP community portal. This subtask has been completed during year 1 of this project. Year 2 activities were limited to the maintenance of the deployed serves and fine-tuning of their configurations.

- **Task 2:** Create a virtual organization encompassing all partners involved in the project research and implement authentication, authorization, and auditing mechanisms according to policies negotiated with the system administrators. This task has been modified. At this phase of the project there is no need for resource sharing (e.g., running jobs on machines outside MSST campus or allowing non-MSST employees or students to run jobs on MSST systems). On the other hand, the USAMP project mandates the development of an electronic "community of practice" web site, which allows for the development and integration of multi-scale physics-based material models for selected properties and processes. To this end, we deployed the Microsoft's SharePoint Server configured to be accessible from any place in the world, with all necessary security settings protecting against misuse and cyber-vandalism. The portal has been made available to the users participating in the USAMP MFERD project. Most of this effort has been completed during year 1. During year 2, the SharePoint server has been filled with contents, closely collaborating with Eric Nyberg and Robert McCune, who are managing the Web Sites for MFERD and ICME, respectively. Eventually, the server will provide a single point of access to all services rendered by the cyberinfrastructure, through the contents aggregation. The current and future activity focuses the maintenance of the servers. As of October 2007, the MFERD/ICME (http://carload.hpc.msstate.edu) portal has 100+ registered users from the U.S., Canada, and China.

- **Task 3:** Develop and deploy services for secure access to remote resources (job submission to high performance platforms, job monitoring, access to file systems and databases). Most of the services have been developed and utilized in Task 5. This task has been essentially completed in year 1 (back-end and middle-tier support). In year 2, the job submission service has been extended for running MATLAB-based applications, as required by the modified task 5 described below.

- **Task 4:** Develop support for service orchestration and workflows. In year 1, the service orchestration is achieved by employing the Service Bus and used in Task 5. The interfaces for composing workflows remain to be implemented. This means that Task 4 is 50% completed. Since the direct support for multiscale simulations has been postponed to the later phases of the project, no progress has been achieved in year 2.

- **Task 5:** Develop specific services supporting online repository of material properties, design optimizations, and multiscale simulations. This builds on the results of activities within Tasks 1, 3, and 4, and is the subject for the integration efforts in Tasks 2 and 7. Most of the year 2 achievements have been accomplished within this task and task 7, even though the direct support for multiscale simulations has been postponed to the later phases of the project. Based on the metadata and storage services developed during year 1 (presented at 7th International Conference on Grid Computing, Barcelona 2006 and International Conference on Grid Computing and Applications, Las Vegas 2007), a repository of material properties has been developed and made available to test users (both at MSST and ICME). The repository is online at http://ccg.hpc.msstate.edu/ccgportlets and through ICME site. The repository is comprised of a database of experimental data (stress-strain, strain-life, and microstructure images), a database of material constants (for damage and multistage fatigue models), and is seamlessly integrated with online tools (Damage Fit, Multistage Fatigue Fit, and Microstructure Analyzer) for

calibrating model constants from experimental data. The seamless integration means a full support for searching experimental data directly from the tools interfaces, transferring analysis results from one tool to another (e.g., grain statistics to damage or fatigue model), and storing the analysis results into the material constants database so that they can be retrieved a latter time, perhaps by a different user, and formatted according to specification of a finite element analysis (FEA) application, such as ABAQUS. The concept and implementation of the repository has been presented and discussed during ICME meetings and The Minerals, Metals, and Materials Society (TMS) annual meetings in Orlando (2007) and New Orleans (2008). Independently, a preview of the Flexible Advanced Metamodeling Estimator (FAME) for automatic generation of best metamodel-based surrogate model has been developed and made available for testing and validation (see report 6.L, FY 2008 Progress Report on "Simulation-Based Design Optimization"). FAME is comprised of integrated web services for the creation of metamodels applying different algorithms, such as radial basis functions (RBFs) or response surface methodology (RSM), and web services for aggregating the metamodels into metamodel assembles.

- **Task 6:** Develop a resource management system for multiscale simulations. During year 1, we have developed an overlay scheduler to support adaptive multiscale simulations (presented at TMS 2006). No further development has been made during year 2.
- **Task 7:** Integrate all components into a single system (cyberinfrastructure). Verify and validate the system and improve the graphical user interfaces (GUIs), performance, and robustness. The year 2 achievement here is applying a service oriented architecture (SOA) involving web services and service bus (cf, task 1), for a seamless integration of independent, loose-coupled back-end services, including MATLAB-based modules, into integrated sub-systems: the repository of material properties and FAME. The initial Java-based GUI has been abandoned and replaced by lightweight, rich user interfaces implemented in AJAX (asynchronous Java Script and XML), promoting service aggregations (mashups), and enhancing the end user experience (faster response, more context sensitivity) on one hand and simplifying the maintenance, as well as extensibility of the systems.

Future Direction

- During the first year, the basic infrastructure has been created that forms a solid foundation for creating the cyberinfrastructure for engineering virtual organizations. Furthermore, preliminary implementation of vital components has been done, in particular support for design optimizations and service-based repository of material properties. During year two, the infrastructure has been used to develop and deploy two integrated applications: the repository of material properties and FAME.
- The planned activities for year three include the following.
  - Maintenance of all servers comprising the cyberinfrastructure, including MFERD/ICME portals.
  - Repository of Material Properties: Transition to production mode, making it widely accessible to the researchers within the MFERD/ICME project, in particular making it the project-wide platform for the exchange of magnesium data and material models. Populate the database with experimental data, generated at MSST and through collaborators and data taken from literature. Enhance access control mechanisms (group and/or project based) to support protection of intellectual properties, thus making it possible to open the database to the general public in the future, perhaps in collaboration with TMS. Collect the user feedback and enhance the repository by supporting more data types and more types of material models, as requested by the user community and the project objectives.
  - Support for Design Optimizations: Collaborate with Task 4 to verify and validate FAME, collect the user feedback, and improve/enhance the GUI according to the user requests. Merge FAME with job submission and job monitoring services into a single system supporting the complete process of design optimizations starting with the design-of-experiment service. Through automated job submissions, generate the responses of the simulated system while using the adaptive environment for creating metamodel ensembles to the support of the actual design optimizations with user-friendly interfaces all while developing flexible resource management techniques to minimize the turnaround time for generation metamodels. In the later phases, the subsystem for design optimizations will be integrated with the subsystem for multiscale simulations.
  - Repository of computational modules: Create the prototype of a repository of computational modules needed for multiscale simulations including manufacturing processes, fatigue and design optimizations. The repository will allow exchange codes between the collaborators, and for authorized users, submit jobs

on the computational resources at MSST. The initial targets are: Vienna Ab-initio Simulation Package (VASP), Molecular Dynamics Simulator LAMMPS, Micro-3D, ABAQUS, and LS-DYNA.

— Gather community requirements for support for multiscale simulations, and design the cyberinfrastructure components to meet these requirements.

Introduction

The objective of this cyberinfrastructure is the establishment of an engineering virtual organization (EVO) to exploit the recent transformative research in material science involving multiscale physics-based predictive modeling and multiscale experiments and design, in conjunction with robust design and manufacturing process optimizations with uncertainty and cyberinfrastructure development (Figure 1). The information, data, and software tools generated by the virtual organization will enable closing the significant knowledge gaps in a unifying physics-based modeling theme that captures a broad range of materials, admits structure-property relations, can be used in simulation-based design, can be implementable into finite-element codes, can be experimentally validated, can capture historical effects, and can morph into a metamodel for rapid use prognostics. The knowledge and data will come from many sources across organizational boundaries (distributed databases of geometries, material properties, manufacturing processes, experimental results coming from different labs, etc.), allowing experts from different disciplines (such as bio-inspired material models, models at different length scales, metamodeling, and optimizations) to work together toward a common goal.

The implementation will follow the Service-Oriented Architecture paradigm.

More specifically, the creation of the cyberinfrastructure will result in the development of the "community of practice" portal that allows for the development and integration of multiscale physics-based materials models for selected properties and processes in the context of USAMP's three-nation Magnesium Front-End Research and Development pilot project (MFERD), in particular task 1.9: Cyberinfrastructure for Integrated Computational Material Engineering (ICME).

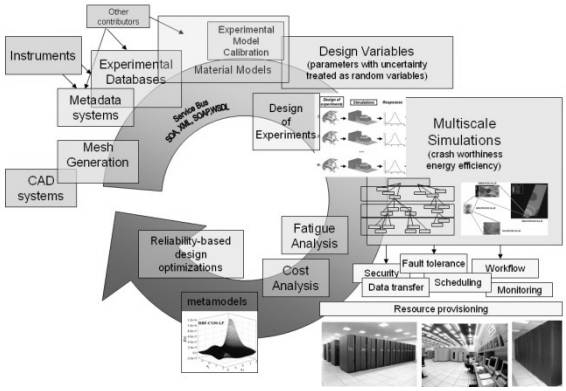

Figure 1. The vision of the cyberinfrastructure will integrate distributed databases of engineering knowledge and computational workflows for multi-objective, multiscale design optimizations under uncertainty.

The Portal manages the user credentials and user sessions and hosts portlets implementing rich GUIs for services rendered by the infrastructure (database queries, remote job submission, etc.). The GUI is being implemented using the combination of Java Applets, Java Script, and AJAX. In addition, the Portal will enable accessing the services from Grid-enabled standalone applications. For example, modules for MATLAB and ABAQUS are planned to allow these applications to access the material properties databases directly from the native GUI (MATLAB, ABAQUS, respectively) and submit jobs to remote high-performance platforms.

The portals delegate the actual processing of the user requests to services implemented in Java. The services will form a façade for the Grid fabric services, such as Globus grid resource allocation management (GRAM)—remote job submission, direct access interface system (DAIS)—remote database access, and gridFTP (file transfer and remote file system access). The overall architecture of the proposed Cyberinfrastructure for engineering Virtual Organization is shown in Figure 2.

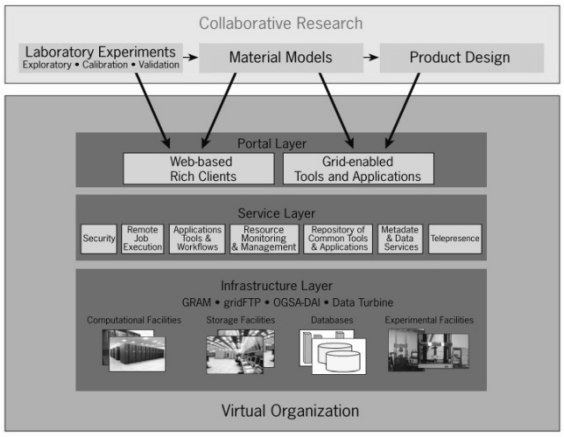

Figure 2. Architecture for MFERD/ICME portal.

Finally, the software integration is accomplished by applying the Java Business Integration (JBI) approach, using an open-source Service Bus implementation, as shown in Figure 3.

Figure 3. Horizontal software integration based on the service bus concept (as opposed to currently used centralized "hub and spoke" architectures) leading to vertical silos and stovepipes.

Repository of Material Properties

Introduction

The goal for this cyberinfrastructure component is threefold as shown in Figure 4. It serves as a repository for experimental data (stress-strain, strain-life, and microstructure images), a repository for material constants (for plasticity-damage models, the multistage fatigue models, and models of the material microstructure), and a suite of online tools for extracting the material constants from the experimental data (damage fit, multistage fatigue, and microstructure analyzer). The seamless integration of those otherwise disparate functionalities is achieved by implementing all back-end ("server-side") support as web services and mashing them up using AJAX on the client-side (Web browser).

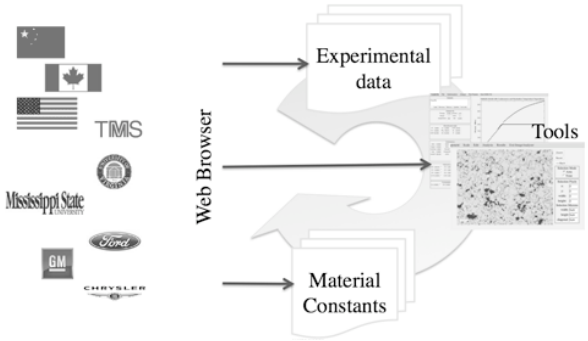

Figure 4. The concept of the Web-based Repository of Materials Properties.

Design of the Repository

Experimental Data

The system is designed to support the sharing of thousands of data sets of a small to moderate size (gigabytes). The large number of the data sets mandates a support for metadata describing these data sets thus allowing for queries. The manner of how the data is described, that is, the metadata schema, may vary for different types of experimental data and in addition, it may change in time, adapting to the evolving user needs. Therefore, it is necessary to introduce a very flexible metadata system without compromising the performance of queries. The data may be stored at different locations that support different mechanisms or interfaces for data access. Finally, strong authentication and group-based authorization mechanisms are required.

The metadata catalog and the storage are deliberately organized independently from each other. The storage is implemented as a flat collection of files and the physical location of a particular file is determined by the storage. The user can access it only by its logical name. The resolution from the logical name to the physical location is performed dynamically by an independent service—the replica locator. The metadata catalog is conceptually implemented as a single "business" structured query language (SQL) table. The columns of the table represent the attributes of the metadata, with the logical name of the file as one of the attributes. The user may query the catalog to retrieve a set of logical names of files that match the selection criteria constructed as Boolean expressions involving the

values of the metadata attributes—equivalent of SQL queries. In addition, the metadata system supports capturing the parent-child relationships between the metadata entries, adding to the flexibility creating different views on the catalog, and consequently, allowing the user to customize the interfaces for the data selection.

The data stored in the repository are meant to be consumed by the user applications (as input files). It is a well known fact that hardly ever any two applications accept the data in the same format. It is thus imperative that the repository provides support for data transformations. The transformation can be simple, such as format translations (e.g., the parameters of a stress-strain curve needs to be formatted differently for ABAQUS and LS-DYNA finite analysis simulations) or may involve more complex processing, such as performing model fits.

The repository of experimental data is thus implemented as an aggregate of independent services: metadata service, replica locator, data storage and authorization service, and transformation services, all integrated using Apache's ServiceMix—an Open Source implementation of an enterprise service bus (ESB) compliant to the Java Business Integration (JBI) specification. A more detailed description of the repository of the experimental data has been given in the last year annual report.

Material Constants

The material constants are stored as metadata records without associated data files. The same metadata service is used for managing the constants (without orchestration with the replica locator and storage services).

Integration of the Repository of Experimental Data and the Repository of Material Constants

The integration is achieved by the association of the experimental data entries in the metadata catalog and, independently, material constants entries in the catalog with particular material. To make the navigation of the metadata catalog easier for the end user, the materials (typically understood as a particular alloy) are grouped into "material classes" representing the dominant component of the alloy. For example, the class "Magnesium" represents all alloys of magnesium. As shown in Figure 5, to find all experimental data pertaining to material hy130steel, the metadata catalog is queried to find all metadata records corresponding to experimental data with material name "hy130steel."

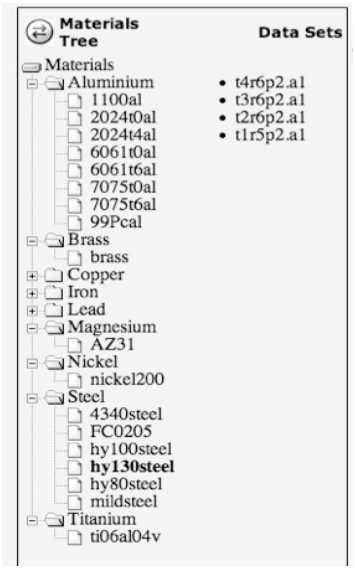

Figure 5. A screenshot of the user interface for browsing the contents of the repository.

To narrow the search, the query may be limited to data sets corresponding to a particular data type, such as stress-strain, or by specifying the values of a set of metadata attributes to be matched. Note the GUI of the repository automates the process of generating queries; the user navigates the tree of materials as if the repository was just a hierarchy of folders and files on the local disk, accessible through familiar File Explorer (Microsoft's Windows) or Finder (Mac) interfaces. The result of the query—the list of the available data sets—is displayed under the "data set" header (Figure 5). By selecting a particular element in the list, the user may display the metadata record (Figure 6), see the data displayed as a plot (Figure 7), or invoke a tool (damage fit for stress-strain data). Note that in order to display the plot, the replica locator needs to be queried to localize the data set, the data must be retrieved from the storage, the stress-strain curve must be calculated from the raw data, and a plot must be generated and sent to the

browser. All this happens automatically as a result of pressing the "Plot" button.

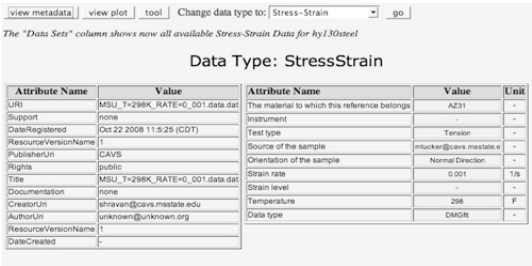

Figure 6. A screenshot of the user interface displaying the metadata record for a selected experimental data set.

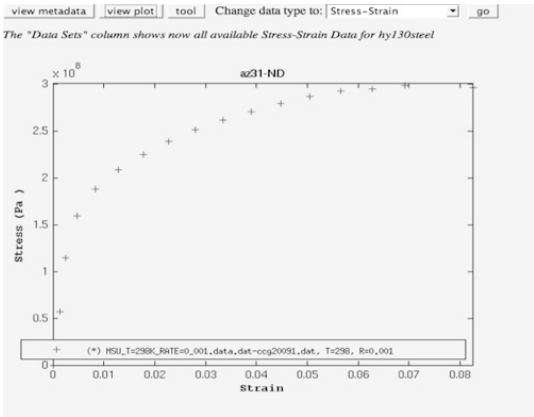

Figure 7. A screenshot of the user interface displaying a stress-strain curve computed from the selected data set.

To get material constants for a given material, a similar catalog query needs to be executed: "find all metadata records representing material constants with material name 'hy130steel'."

Online Tools

The tools are implemented as MATLAB modules running on the server side, invoked via a job submission service.

The job submission service, as any other WSDL service, is stateless and designed to support running jobs in batch mode, which is in clear conflict with statefull and inherently interactive MATLAB applications. This problem has been solved by re-engineering the MATLAB code for a tool into a series of short, stateless batch operations executed as the result of the user clicking on GUI widgets and delegating the responsibility of maintaining the MATLAB session to the Portal middleware (the session object). This solution not only creates an illusion of interactivity for the end user, but also allows for several independent users using the MATLAB of the same tool. Figures 8, 9 and 10 are screenshots to demonstrate the available tool.

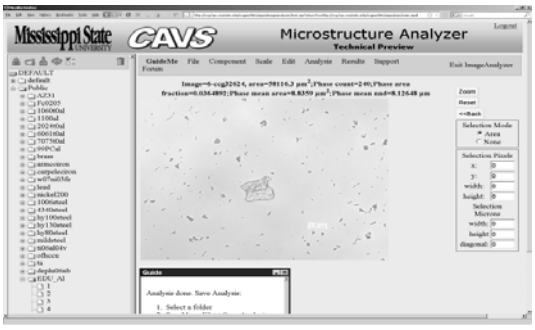

Figure 8. A screenshot of the user interface for the tool to extract microstructure information from a high-resolution image of a material sample.

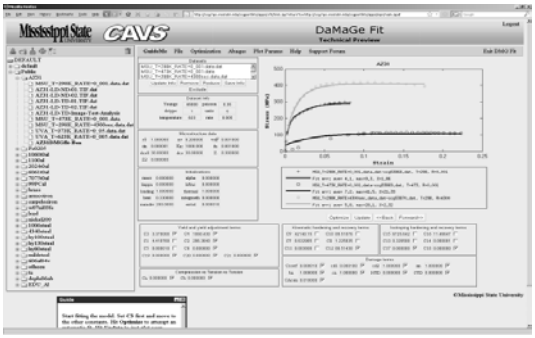

Figure 9. A screenshot of the user interface for the damage model calibration tool.

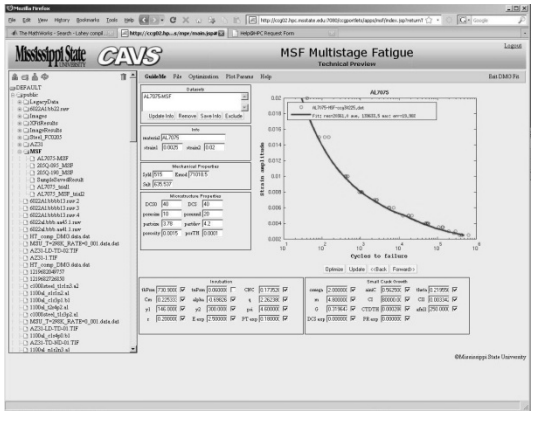

Figure 10. A screenshot of the user interface for the multistage fatigue model calibration tool.

Data Service Façade

Construction of the repository from the independent services has many advantages. On the other hand, it is difficult for the end user (or the user agent) to use such a distributed system. Many conceptually simple operations, such as retrieving a file, require making multiple requests to different services. The above mentioned flexibility of the system adds to the complexity of using the repository: the user must not only know the right order of service invocations, but also needs to know interfaces of the particular services and the communication protocols used by these services. Furthermore, since all services act independently from each other, maintaining repository consistency becomes difficult (e.g., each metadata record corresponds to at least one data resource and each data resource has associated metadata records).

To ease these difficulties, all constituent services of the repository are hidden from the user behind a façade, which is the middle-tier service that orchestrates the services and exposes a simple, intuitive interface for the end user. Now, given the Uniform Resource Identifier (URI) of the resource (from querying the metadata service or otherwise), there is a single method of the façade to retrieve the file. The invocation of this method results in all actions needed to get the authorization assertions, resolving URI to the physical locations and returning the data stream. To achieve that, the façade employs the business delegate pattern that delegates the actual implementations of the back-end service clients to service providers, which understands the transport and assertion requirements of the corresponding services. In addition, the provider-based architecture makes it easy to retarget the repository to a different implementation of any of the constituent services; it requires just replacing the service provider without the need for modifications of the façade interface. The business logic of the façade also enforces the integrity of the repository. For example, a request to remove a data resource from the storage automatically triggers appropriate actions of replica locator and metadata services initiated by the façade.

Data Transformations

Hardly ever have any two applications accepted the data in the same format. It is thus imperative that the repository provides support for different data transformations. There are two basic types of data transformations. One type facilitates relatively simple operations, such as format translations or processing data headers that can be performed on-the-fly. The other type supports the processing of large files or making complex transformations. These transformations are delegated to high-performance platforms. The data transformations are independent from the metadata catalog, or file repository services, and need to be implemented as independent services (the loose coupling principle) and invoked either prior to the data uploading or after retrieving the data from the file repository, but before returning the data to the end user.

Several data transformations have been developed. Among the purposes of the material properties repository is the collection of data coming from the measurement of stress-strain curves. The data coming from different instruments are, very expectably, in different formats. A transformation service hides these differences from the instrument operator who uploads the data to the repository. The service creates a metadata record by combining the information from the header automatically generated by the instrument from the system (e.g., time and the operator identifier), and the data typed in by the operator (the instrument has no way to know what material and in what manufacturing stage, e.g., after rolling or stamping), and then from the measured values of the displacements and loads, calculates the true stress and strain values. Once this "transformation" is complete, the metadata and data pair are uploaded to the repository. When retrieving the data from the repository, the user may specify the desired format (e.g., raw data, data formatted to match the syntax of the ABAQUS FEA package, or others). Such format translation is delegated to another transformation service, which is invoked automatically after retrieving the data from the repository and before sending the data to the user.

Integration of Data Repository Services Using the Enterprise Service Bus

The primary functionality of the service bus is to route messages between services associated with it. There are two base types of associations. The service can be plugged into the bus container as a so-called service engine to be directly invoked through a Java message service (JMS). Alternatively, a service may be deployed in a separate container and be invoked through a web service interface (WSDL). The web service invocation is facilitated by a binding service bus component.

The incoming requests, generated by a web portal or a standalone client, are accepted by a custom developed hypertext transfer protocol (HTTP) input component. The input components effectively act as service brokers, forwarding the requests to the target services that generate the actual responses to the client requests. To make it possible, the client's request must provide a signature of the target service. In order to invoke the service (i.e., to forward the request), the signature must be resolved into the service endpoint reference (EPR). To this end, the broker uses a service directory—another custom service engine. The service signature is a collection of the service attributes. In the simplest case, it could be just the service name. The service WSDL interface could serve as the service signature; however, for this data repository, most of the transformation services implement the same WSDL interface making it easy to "bind" the actual transformation late, depending on the context of the request. The EPR may refer to an "atomic" service (either a service engine or a binding component) or refer to an orchestrating service (e.g., a Business Process Execution Language (BPEL) engine, or a service façade) that aggregates several services in order to generate the final response the client requested.

Architecture of the Repository

The architecture of the repository is shown in Figure 11. The clients, implemented in asynchronous JavaScript, communicate with the service bus through the ubiquitous Hypertext Transfer Protocol (HTTP). The Input Component/Service Broker accepts three types of requests: metadata query, data upload (that may or may not involve the data transformations), and data download (that may or may not involve the data transformations). The metadata query allows the user to search the metadata catalog to locate the data set of interest, create custom views on the data repository, as well as uploading and downloading of data. Consequently, the client requests to perform these operations are simply forwarded by the service broker to the façade service engine. The data façade invokes the constituent service services as needed through the binding components.

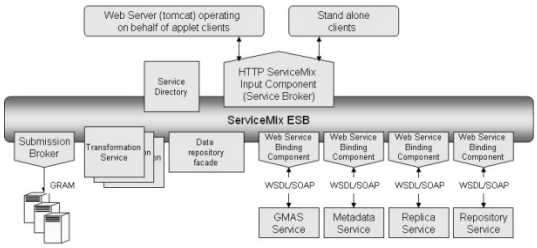

Figure 11. Architecture of the data repository integrated by an enterprise service bus (ESB).

The data transformations, on the other hand, are dynamically bound. If the repository operation requires a transformation, the name of the transformation is passed as the request argument. The broker resolves the transformation name into the service EPR using the service directory and invokes the service before or after invoking the data façade services, depending whether data are uploaded to or downloaded from the repository, respectively. Simple transformations are implemented as ESB service engines, while complex transformations are executed by the submission broker—a binding ESB component. The submission broker is responsible for setting the runtime environment (setting the environmental variable, creating a working directory, etc.), staging in data, executing and monitoring jobs on remote systems and finally passing the results to the requested destination (typically through a third-party data transfer). Since all transformations implement the same WSDL interface (the transformation specific parameters are grouped as a single array of strings), the dynamic binding allows seamless adding or replacing existing transformations.

FAME: Flexible Advanced Metamodeling Estimator

Simulation-Based Design Optimizations

Simulation-based design optimization is playing an increasingly important role in engineering product development. It enables engineers to make optimal product design and manufacturing process decisions, reduce or eliminate the need for physical prototyping, and increase the quality of manufactured products. This importance is also evident in the development and marketing of several commercial optimization software tools (e.g., Vanderplaats R&D, Inc.'s Design Optimization Tool, Dassault Systemes' iSIGHT) that can be interfaced with computer-aided design (CAD) or computer-aided engineering (CAE) and engineering simulation programs to accommodate a paperless product design activity.

The rapid development of computer technology and commercial simulation tools has enabled engineers to solve more complex problems and obtain more details to enhance knowledge. For example, it is now possible to perform full-scale, finite-element (FE) simulations of vehicle crashes with commercial FE codes and parallel computers. However, the increased complexity has significantly increased the computational cost that in turn prevents engineers from combining the simulation tool with an optimization method, which is an iterative procedure and requires hundreds or even thousands of simulations to perform one design. To alleviate the high computational cost of full-scale simulations, yet maintain the level of complexity, the metamodeling approach has been widely adopted in simulation-based design optimization.

In the metamodeling approach, the expensive simulation tool is replaced with a surrogate approximation model (metamodel) that is in explicit form and efficient to evaluate. The metamodel is created from the results of some predefined simulations determined by Design of Experiments (DoE) methods. Figure 12 illustrates the procedure of simulation-based design optimization using DoE and metamodeling. There are four major components in this procedure: DoE, simulation, metamodeling, and optimization, which serve as four independent functional blocks.

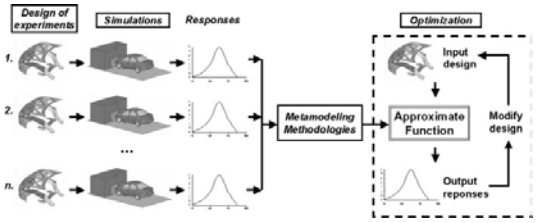

Figure 12. Workflow for simulation-based optimization using DoE and metamodeling.

Since a limited number of simulations are used in creating the metamodel, the model accuracy will depend on how well the selected designs represent the design space. To this end, the DoE methods such as factorial design, central composite design, Taguchi orthogonal array, and Latin hypercube sampling are typically used to create the samples and referred to as the response surface methodology (RSM). For high-order nonlinear responses, other metamodeling methods using high-order nonlinear functions, particularly the RBFs, work best.

With the created metamodels representing responses within the design space, the optimization can be carried out using existing optimization methods such as gradient-based or direct search algorithms. As pointed out by the no-free-lunch theory, there is no single optimization method that is good for all types of problems. Therefore, it is preferred to apply different optimization methods at this stage to obtain the best solution.

FAME Design

The purpose of FAME is to provide the environment for the creation of metamodels given a set of input (design) points and the corresponding system responses. The flexibility refers to the capability of FAME to generate many different metamodels by selecting different metamodeling techniques and adjusting their parameters. Once created, the metamodel can be quickly verified by computing the residuals between the metamodel predictions and the actual responses obtained by a measurement and/or by a direct numerical simulation. Advanced refers to the capability of FAME to combine several metamodels into a metamodel ensemble, by applying different ensemble techniques (from

simple average to methods weighting the contributions from constituent metamodels, based on the accuracy of their predictions). The metamodels (and metamodel ensembles) are persistent [i.e., they can be accessed (be modified or used to generate predictions)] across the user sessions and shared between users.

This functionality has been achieved by orchestrating several loose-coupled web services, as illustrated in Figure 13. The metamodeling service provides a uniform interface for creating, customizing, evaluating, and getting predictions of metamodels, given the values of the input variables and the system responses (typically two sets: one for the metamodel creation and the other for the metamodel validation). The ensemble service provides a uniform interface for creating, customizing, evaluating, and getting predictions of ensembles, given a vector of existing metamodels together with a set of test points (the value of the input variables and the corresponding responses).

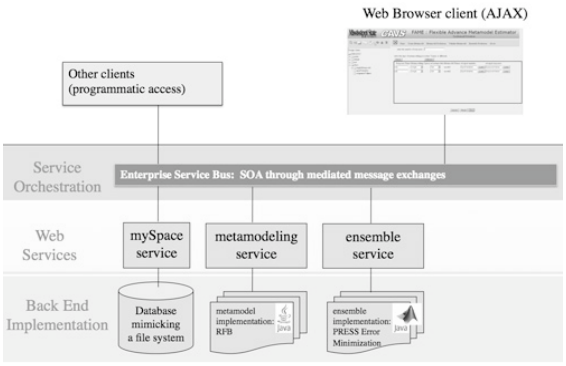

Figure 13. The architecture of FAME.

The design based on uniform interfaces guarantees extensibility of FAME. Each metamodeling (or ensemble) technique is an independent software component (a Java class), implementing a common (i.e., uniform) service interface. This allows the adding of new metamodeling techniques at a later time, without the need of modifying the existing components. The uniform interface provide methods for the metamodel (or ensemble) creation, validation, and getting predictions, as well as methods for querying the service about the parameters needed by a particular implementation of the interface. The FAME GUI implementation extensively uses the queries in order to dynamically create the user interface custom tailored for a particular metamodeling (or ensemble) technique to be used (cf Figure 14).

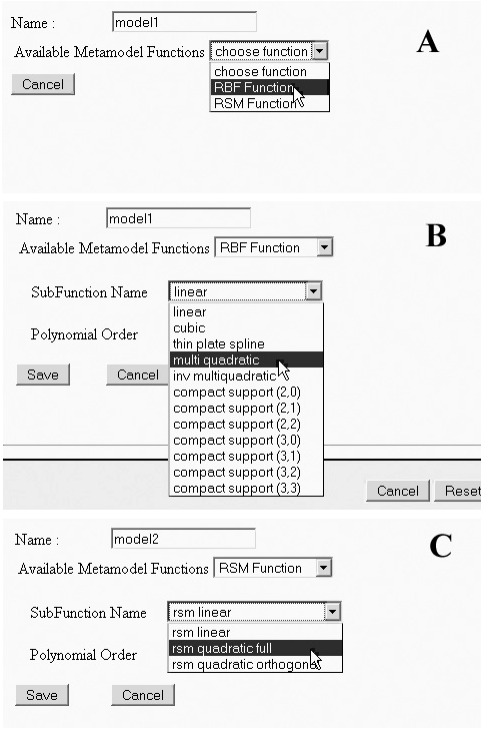

Figure 14. A composite of three screenshots of a fragment of FAME user interface. Depending on the selection of the metamodel type (A), the GUI displays a custom form for providing metamodel parameters (B or C).

The metamodeling and ensemble services operate on data (values of input variables and responses) provided by the user. Therefore, it was necessary to develop a support for uploading and maintaining the data on the server side. This has been accomplished by developing MySpace service. MySpace reuses the services used for the repository of experimental data with metadata record, comprising the name of the data set, the name of the user who uploaded it and the date and time of the upload. The GUI for the MySpace service is similar to Microsoft's File Explorer and Mac's Finder (cf Figure 15). MySpace is used not only to store and manage user-provided data set; the results of FAME—metamodels, ensembles, and results of validation are stored there as well.

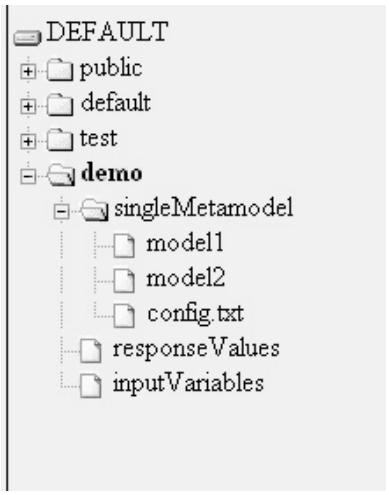

Figure 15. A screenshot of MySpace user interface.

Presentations/Publications/Patents

1. T. Haupt and M. Horstemeyer, "Cyberinfrastructure for Design Optimizations," 2008 TMS Annual Meeting, New Orleans, LA, March 9–13, 2008
2. T. Haupt, "Cyberinfrastructure for multiscale Simulations," 2007 TMS Annual Meeting, Orlando, FL, Feb 25–March 1, 2007.
3. T. Haupt, A. Voruganti, A. Kalyanasundaram, and I Zhuk. "Grid-Based System for Product Design Optimization," *2nd IEEE International Conference on e-Science and Grid Computing*, Amsterdam, the Netherlands, Dec 4–6, 2006.
4. T. Haupt, A. Kalyanasundaram, and I. Zhuk "Architecture for a Secure Distributed Repository," *7th IEEE/ACM International Conference on Grid Computing*, Barcelona, Spain, Sept 27–28, 2006: IEEE/ACM Press, 170–177.
5. T. Haupt, A. Kalyanasundaram, G. Singh, and I. Zhuk, "Data Repository for Ad-Hoc Collaborations Horizontally Integrated with Transformation Services," *The 2007 International Conference on Grid Computing and Applications*, Las Vegas, NV, June 25–28, 2007.

L. Simulation-Based Design Optimization

Principal Investigator: Masoud Rais-Rohani
Professor, Aerospace Engineering
Mississippi State University
318c Walker Bldg.
Mississippi State, MS 39762
(662) 325-7294; fax: (662) 325-7730; e-mail: masoud@ae.msstate.edu

Co-Principal Investigator: Chris Eaman
Assistant Professor, Civil Engineering
Mississippi State University,
235F Walker Bldg.
Mississippi State, MS 39762
(662) 325-9839; fax: (662) 325-7189; e-mail: eamon@engr.msstate.edu

Technology Area Development Manager: Joseph A. Carpenter
(202) 586-1022; fax: (202) 586-1600; e-mail: joseph.carpenter@ee.doe.gov

Field Project Officer: Aaron D. Yocum
(304) 285-4852; fax: (304) 285-4403; e-mail: aaron.yocum@netl.doe.gov

---

Contractor: Mississippi State University
Contract No.: 4000054701

Objective

- Develop computational design technologies (methods and tools) that can be used for the analysis and optimization of automotive structural design concepts made of lightweight materials. The selected research topics are directed towards the principal attributes, lightweighting and safety, in presence of design uncertainties and are investigated while pursuing the following objectives.
  - — Development of novel approaches for deterministic and probabilistic (reliability-based) design optimization of automotive structures.
  - — Investigation of various metamodeling and mechanics-based analytical techniques as viable surrogates for expensive, high-fidelity finite-element simulations.
  - — Development of mathematical models for efficient uncertainty quantification and structural reliability analysis.
  - — Integration of advanced constitutive models in simulation-based design optimization of automotive structures.
  - — Application of the developed methods and tools in design optimization of example problems involving automotive structural components, subsystems, and systems.

Approach

- The activities in this task are separated into the following areas: (1) design optimization, (2) structural mechanics, (3) surrogate modeling, (4) uncertainty quantification, and (5) structural reliability. The research scope and plan of action in each area are outlined as follows.
  - — Investigate different approaches for reliability-based design optimization (RBDO) of automotive structural components. Develop RBDO formulations and solution techniques consistent with the complexity of vehicle structures. Investigate novel approaches for topology optimization of continuum structures and multilevel optimization of hierarchical systems, with deterministic and reliability-based design constraints.

- — Since crashworthiness is a major requirement in design of automotive structures, investigate the mechanics of progressive collapse in dynamically-loaded thin-walled structures to explore opportunities for design of lightweight and energy-absorbent components. Perform nonlinear static and nonlinear transient dynamic finite-element simulations of vehicle components and systems made of different lightweight materials. Compare the response predictions with traditional plasticity and the internal state variable (ISV)-based constitutive models.
- — Evaluate the performance of modern metamodeling techniques as low-cost surrogates for high-fidelity response simulations. Study the accuracy and efficiency of stand-alone and ensemble of metamodels for estimation of nonlinear response functions. Investigate the accuracy and efficiency of mechanics-based analytical models for estimation of structural responses, such as energy absorption under impact loading.
- — Investigate the accuracy and efficiency of the different techniques used for the quantification of random uncertainties and their propagation in the design optimization process.
- — Develop new approaches to increase the efficiency and accuracy of failure probability/safety index estimations for the evaluation of component, as well as system reliability.
- — Apply the techniques developed or examined in the different research areas to simulation-based design optimization of automotive structural problems ranging from a single component to a multi-component system.

Accomplishments

- Developed a new stochastic method for topology optimization of continuum structures and compared its performance with some other stochastic, as well as gradient-based, techniques reported in the literature.
- Investigated the application of alternative approaches for multilevel optimization of hierarchical (product-material) systems under uncertainty.
- Performed nonlinear transient dynamic finite-element simulations to investigate the progressive collapse and energy-absorption characteristics of extruded multi-cell tubes as design concepts for automobile side rail. Also developed a mechanics-based analytical model for estimation of mean crush force of multi-cell tubes.
- Developed an analytical technique for uncertainty quantification and investigated its use in uncertainty analysis of damage based on an internal state variable constitutive model.
- Developed a simulation-based technique for component and system reliability analysis and compared its performance with several analytical and simulation-based techniques reported in the literature.
- Collaborated with cost-share partners, Alpha STAR Corporation and Wade Services, on topics related to finite-element modeling and simulation of joint concepts for composite structures and optimum designs for trailer components.
- Wrote several conference papers and journal publications as listed at the end of this chapter. However, the journal manuscripts that are still under review are not included.

Future Direction

- Investigate the energy-absorption characteristics of crush tubes made of fiber-reinforced polymer composite materials.
- Investigate multilevel optimization of integrated material-product / process-product systems, using multiscale material models.
- Conduct an optimization study, using full-vehicle simulations with ISV-based material models under multiple design criteria, such as damage and fatigue.

Introduction

This report provides a summary of major activities conducted in the second year of the Department of Energy's Southern Regional Center for Lightweight Innovative Design project as part of the simulation-based design optimization task. The areas of emphasis include topology optimization,

energy absorption under impact loads, uncertainty quantification, and structural reliability. In each of the following sections, a major focus area is briefly discussed with highlights of pertinent results.

Other activities not reported here include the application of multilevel optimization techniques to hierarchical systems with deterministic and reliability-based design constraints. Also, as a result of collaboration with two cost-share providers, Alpha STAR Corporation and Wade Services, members of this task had the opportunity to apply some of the developed techniques to an industrial problem and to explore the capabilities of the progressive failure analysis software GENOA for the analysis of structural design concepts made of advanced composite materials.

Topology Optimization Using Element Exchange Method

Topology optimization of continuum structures is aimed at finding the optimum distribution of a specified volume fraction of material in a selected design domain that would result in the minimization of structural compliance or strain energy and provide an optimal load path between the loading points and the structural supports.

Topology optimization is often used as a first step in identifying the general layout of the material in a specific domain before performing sizing and/or shape optimization to find the optimal geometry.

Previous efforts in topology optimization have, for the most part, been based on the gradient-based solid isotropic material with penalization (SIMP) method (Bendsoe 1989, Zhou and Rozvany 1991). SIMP is computationally efficient and easy to integrate with most general-purpose FEA codes. However, SIMP-based solutions show mesh-dependency and the clarification of final topology requires the use of one of several filtering techniques.

Besides the gradient-based methods, several stochastic methods have also been developed for topology optimization. Two notable approaches are the particle swarm optimization (PSO) (Fourie and Groenwold 2001) and enhanced genetic algorithms (GAs) (Wang et al. 2006). Although these methods may not require any filtering of the optimum layout, they tend to be very computationally expensive.

As part of this project, we developed a new stochastic approach called the Element Exchange Method (EEM) for compliance minimization. Named after the principal operation in the topology optimization strategy, EEM solution procedure is simple to implement and easy to integrate with any existing FEA code.

In this section of the report, we provide a brief description of the EEM algorithm and compare the performance of this method with some others using two- and three-dimensional example problems.

The EEM algorithm starts with a random distribution of a specified number of solid isotropic elements consistent with the desired volume fraction, V_o, in the design domain. While the solid elements are given a nondimensional density of 1.0, the void elements have a small nondimensional density (0.001). Similarly, the Young's modulus of void elements is taken as 0.001 times that of the solid elements. The non-zero properties for the void elements are meant to prevent numerical ill conditioning of the stiffness matrix in FEA.

With the initial topology identified, a static FEA is performed to find the strain energy distribution among the solid and void elements, as well as the strain energy of the structure as a whole. Based on the selected value for the number of exchange elements, N_{EE}, the algorithm performs a so-called *element exchange* operation. The N_{EE} solid elements with the lowest strain energy amongst the solid elements are converted into void elements (density and Young's modulus set to respective minimum values), while a volumetrically-equivalent number of void elements with the highest strain energy amongst the void elements are converted into solid elements (density and Young's modulus set to respective maximum values), such that the volume fraction remains fixed. This step is followed up by another static FEA and the exchange operation procedure is continued until convergence is reached.

Although the EEM algorithm pushes the topology towards minimum-compliance, the basic element exchange operation alone may not prevent the development of undesirable checkerboard patterns or the possibility of back-and-forth oscillation in a subset of elements from solid to void, back to solid in repeated iterations.

However, with the help of additional operations introduced as part of EEM algorithm, these two problems are eliminated. One such operation identifies and eliminates the checkerboard regions in the topology, whereas another involves a random redistribution or shuffling of a limited number of solid elements after the completion of a set number of exchange iterations. This move is similar to a mutation operation in GAs and craziness in PSO, and is found to improve the final topology by eliminating the possibility of entrapment at a locally optimum design point. Additional details about EEM can be found in Rouhi and Rais-Rohani (2008).

Two-Dimensional Example Problems

The cantilevered beam model and corresponding optimum topology results are shown in Table 1.

Table 1. Comparison of EEM and enhanced GAs

Design domain & Boundary conditions			
	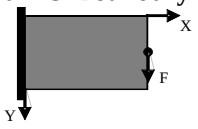		
n_X, n_Y, V_o	**24, 12, 0.5**		**48, 24, 0.5**
Method	**EEM**	**Enhanced GA[a]**	**EEM**
SE	**66.1**	**64.4**	**63.5**
N	**150**	**4x10^4**	**250**
Topology		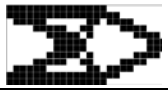	

[a]Wang et al. (2006).

Each design domain is defined according to n_X, n_Y, and V_0 values, representing the number of finite elements in the horizontal and vertical directions and the required volume fraction, respectively. The final value for the nondimensional strain energy (SE), total number of iterations (N) and the resulting topology are also shown in Table 1. Two different mesh densities are considered for EEM, resulting in slightly different topologies. The results reported by Wang et al. (2006) based on the enhanced GA approach are also shown in Table 1 for comparison. Although the final geometry and strain-energy values are nearly the same, the EEM solution converges much faster.

With the beam dimensions modified, the EEM solutions are compared with those based on PSO in Table 2. As in the previous model, the EEM approach converges much faster with no loss of accuracy.

Table 2. Comparison of EEM and PSO

Design domain & Boundary conditions				
	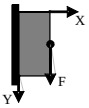			
n_X, n_Y, V_0	**20, 47, 0.5**		**40, 94, 0.5**	
Method	**EEM**	**PSO[*]**	**EEM**	**PSO[a]**
SE	**2.96**	**Not reported**	**5.1**	**Not reported**
N	**100**	**10^5**	**103**	**10^3**
Topology		**Continuous Density**		**Binary Density**

[a]Fourie and Groenwold (2001).

Three-Dimensional Example Problems

A cubic domain shown in Figure 1(a) is simply supported at its four bottom corners and is loaded by four concentrated vertical forces at the top surface. Using the EEM procedure with n_x, n_y, n_z, V_0 = 20, 20, 20, 0.08, the optimum topology in Figure 1(b) is obtained after 178 iterations. For comparison, the results obtained by Olhoff et al. (1998) using the optimum microstructure (OM) method is shown in Figure 1(c). The grey regions in Figure 1(c) imply intermediate density, since the OM method is gradient-based. Also, elements with density less than the threshold value are filtered out to arrive at the final topology.

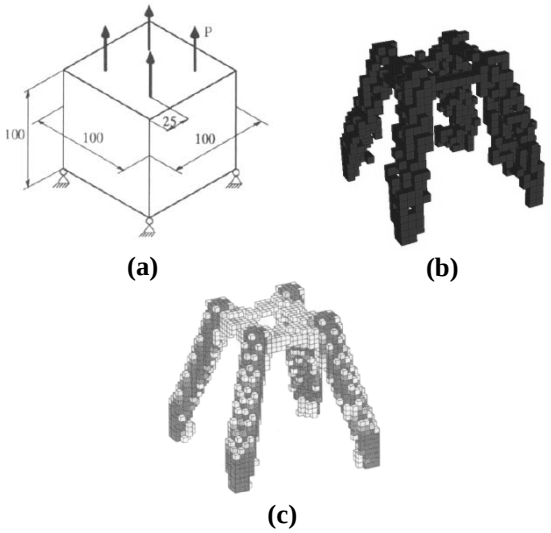

Figure 1. (a) Design domain and boundary conditions, (b) EEM, and (c) Optimum microstructures.

Therefore, the final topology of OM may not match the pre-specified volume fraction.

The geometry shown in Figure 2(a) is a generic model of an automobile control arma. While the triangular region in the middle can be altered through topology optimization, the three-corner regions (knuckles) are held fixed with the specified boundary conditions. The EEM solution based on n_x, n_y, n_z, V_0 = 26, 40, 12, 0.1 is shown in Figure 2(b). Since the design domain is symmetric, only the upper half of the final topology is considered and shown for clarity. The optimization result in Figure 2(c) is obtained using commercial software Optistruct,* where elements with density less than 0.15 are removed and the resulting geometry is post-processed to obtain a smoother shape.

The conclusions that can be drawn from this work are that unlike the gradient-based methods, EEM requires no filtering of the final topology and the resulting solid-void solution satisfies the imposed volume fraction. Also, the checkerboard control and the random shuffle algorithms help increase the solution fidelity and accuracy. Although EEM is not as efficient as the SIMP method, it is found to be significantly more efficient than the stochastic methods found in the literature.

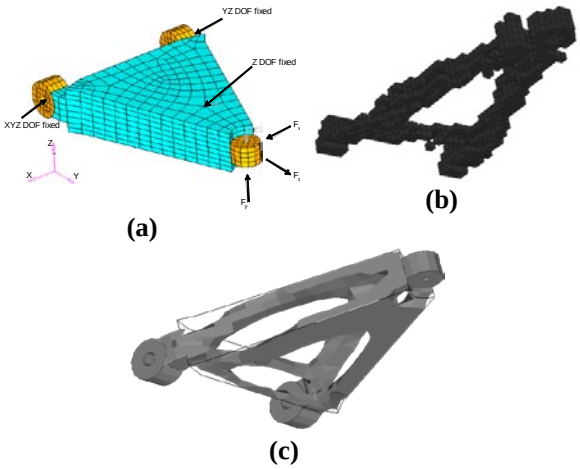

Figure 2. (a) Design domain and boundary conditions, (b) EEM, and (c) Optistruct.

Energy Absorption Assessment of Axially Loaded Multi-Cell Tubes

There is a growing interest in the use of lightweight materials (e.g., magnesium alloys) combined with the extrusion process for the future production of automotive components, such as the side rails. One desirable feature of the extrusion process is that it accommodates the fabrication of multi-cell tubes with varying degrees of geometric complexity, as dictated by the design requirements.

Besides the material properties, the cross-sectional geometry (shape and size) of the side rails has a significant influence on its collapse mechanism and energy-absorption capacity in frontal collisions. Hence, the ability to evaluate multiple rail design concepts in an efficient manner can help improve the overall design process of automotive structures.

As part of our research in simulation-based design optimization, we investigated the mechanics of progressive collapse in thin-walled, angular, multi-cell tubes using the nonlinear transient dynamic FE simulations and studied the influence of cross-sectional geometry on the energy absorption of such tubes made of ductile materials.
We performed a series of FE simulations to evaluate the force-displacement response, specific

* http://www.kxcad.net/Altair/HyperWorks/ostutorials/ostut.htm#os2010.htm

energy absorption (SEA), crush pattern and crush distance for different multi-cell, multi-corner models. As part of this work, we also investigated the merits of adaptive meshing, the effect of using different shell-element formulation, the effect of friction at the barrier contact surface, the role of trigger mechanism and initial imperfection on crush response and the used hourglass energy as means of verifying the accuracy of the simulation results.

The multi-cell models investigated are shown in Figure 3(a). The principal feature of these models is that they consist of two square tubes that are connected together in four different forms: corner-to-corner (A), web-to-corner (B), corner-to-web (C) and web-to-web (D). Although the different forms of connection do not drastically change the weight of the tube, it can alter the collapse response under dynamic axial loading.

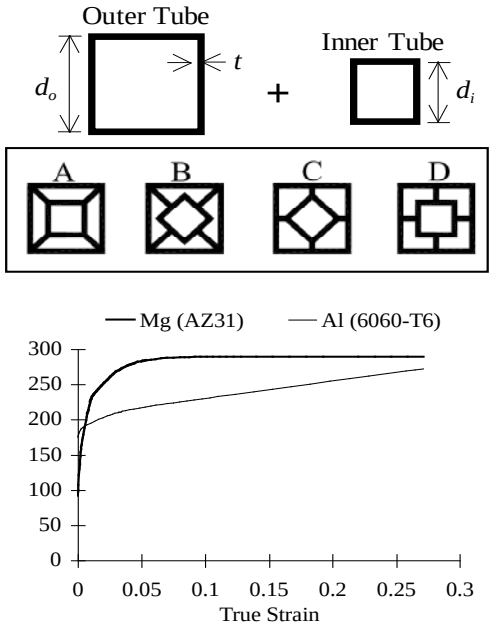

Figure 3. (a) Alternative cross-sectional models and (b) Tensile stress-strain curves of aluminum and magnesium alloys.

We developed an FE shell model for each tube in Figure 3(a) and used them for crush simulations using LS-DYNA. All tubes are 400 mm in length with (d_o, d_i, t) = (80, 40, 2) mm. The tube is treated as a clamped-free column that is impacted on its free end by a rigid block of 300-kg mass traveling at a speed of 15.6 m/s (35 mph). The material model used for preliminary investigations is AA6060-T6 with E = 70 GPa, ν = 0.3, and ρ = 2.7e-6 kg/mm^3, and the true stress-strain curve as shown in Figure 3(b).

Figure 4 shows the simulated collapse of the four aluminum tube models at various time increments up to 30 ms. All FE models are based on Hughes-Liu shell elements and have an indentation trigger mechanism placed on two opposite walls of the outer tube near the impacted end.

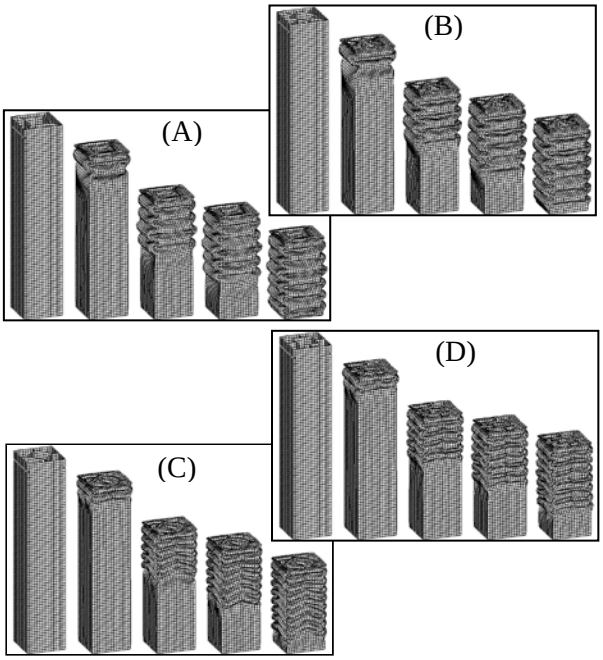

Figure 4. Collapse behavior of multi-cell tubes.

All models show a fairly symmetric progressive collapse with repeated folding deformation that extends to nearly 75% of the length in model D and the entire length in model A. Clearly, model A demonstrates less resistance to axial deformation as compared to model D, indicating the difference between corner-to-corner and web-to-web connections. Also, models B and C appear to have nearly the same crush distance, although the folding geometries are distinctly different. While the trigger mechanism reduces the maximum peak force shortly after impact, it helps to stabilize the crush deformation.

The plots of the crush force versus crush distance are shown in Figure 5.

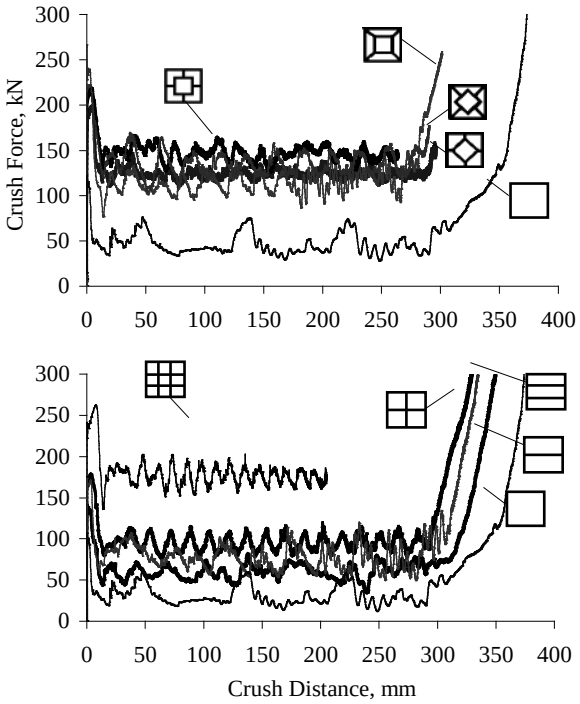

Figure 5. Crush force versus crush distance for different cross-sectional shapes.

Besides the models introduced earlier, other configurations (with uniform cell geometry), as reported in the literature, are also shown for comparison. Using the cell divisions in the horizontal and vertical directions as the distinguishing feature, these models are labeled as 2 × 1, 3 × 1, 2 × 2, and 3 × 3. The response of a single-cell square tube is also shown in Figure 5 for reference purposes.

The larger oscillatory pattern in each curve is due to the changes in tube stiffness as a result of repeated formation and closure of folds in the tube walls (see Figure 4). The maximum peak load varies from a low of 107 kN for the single-cell tube, to a high of 263 kN for the 3 × 3 model. For models A through D, the average maximum peak value is approximately 215 kN. The rapid rise at the end of some curves indicates complete collapse that results in solidification (end of plastic deformation) in the tube.

The bar chart in Figure 6 compares the impact energy absorption as a measure of efficiency of the tube models considered. SEA is the ratio of internal energy to mass. The energy values used for the calculation of SEA in Figure 6 correspond to the point where solidification begins. The models with the minimum and maximum SEA values are the square tube and the multi-cell model C, respectively. With an average SEA of 28.2 kJ/kg, models A through D appear to absorb more energy than the other four multi-cell shapes with an average SEA of 25.8 kJ/kg. The mass of each tube in units of kg is shown parenthetically in Figure 6.

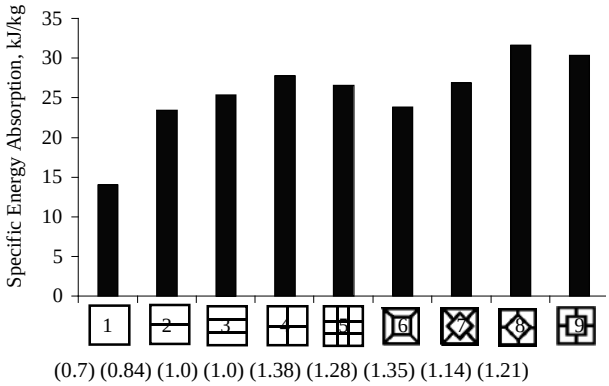

Figure 6. Specific energy absorption and mass (kg) for different cross-sectional shapes.

Crushing deformation of ductile thin-walled, multi-corner tubes under quasi-static and dynamic axial loads is principally governed by the collapse mechanism of the corner sections. In their study of rectangular tubes, Wierzbicki and Abramovicz (1983) pointed out that the generalized folding collapse of the corner sections involves four separate mechanisms described as rigid-body translation and rotation along with inextensional, quasi-inextensional, and extensional deformation. Although a large portion of the material undergoes rigid-body translation and rotation due to propagating hinge lines, it is the smaller region of toroidal and conical surfaces that is responsible for plastic deformation and energy absorption.

Figure 7 shows the predicted mean crush force for the four multi-cell models A through D based on three different analytical models, one developed here and two others as reported in the literature. The prediction accuracy of these models is judged by the relative difference with the values found by FE simulations using LS-DYNA. With an average

error of 8% for the four tube models, the present analytical model is found to be more accurate than the other two. Detailed description of this study appears in Najafi and Rais-Rohani (2008), with some of the key findings presented in this section of the report.

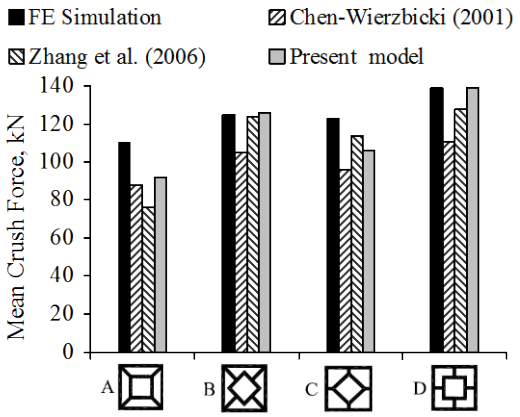

Figure 7. Comparison of numerical and analytical predictions for the mean crush force.

The crush simulations were repeated by switching the material to a magnesium alloy (AZ31) (E = 45 GPa, ν = 0.33, and ρ = 1.8e-6 kg/mm^3), with the true stress-strain curve as shown in Figure 3(b). Using the mean crush force and SEA values, the bar charts in Figure 8 show the difference in performance as a result of material selection. It is worth noting that the material models used here do not consider damage. Therefore, the comparison of different materials is solely based on the plasticity models in Figure 3(b).

Uncertainty Analysis Using Dimension Reduction and Distribution Fitting

Random uncertainties in the material properties and boundary conditions can lead to uncertainties in structural responses, such as stress, strain, and damage. Generally speaking, the probability theory can be used to capture the influence of random or stochastic uncertainties in the basic parameters on uncertainty of the resulting random response.

In this section an analytical approach is described and applied to uncertainty analysis of damage as predicted by an internal state variable (ISV) plasticity-damage model (Horstemeyer 2001). ISV evolution equations, which are formulated at the macroscale level, offer an effective method to capture the microstructure-property relationships. The ISVs reflect the lower spatial size-scale microstructural rearrangements, so that history effects can be modeled. With the help of such a material model, it would be possible to relate structural responses of interest, such as damage, to key material parameters such as particle size, interfacial strength, and spacing at each length scale.

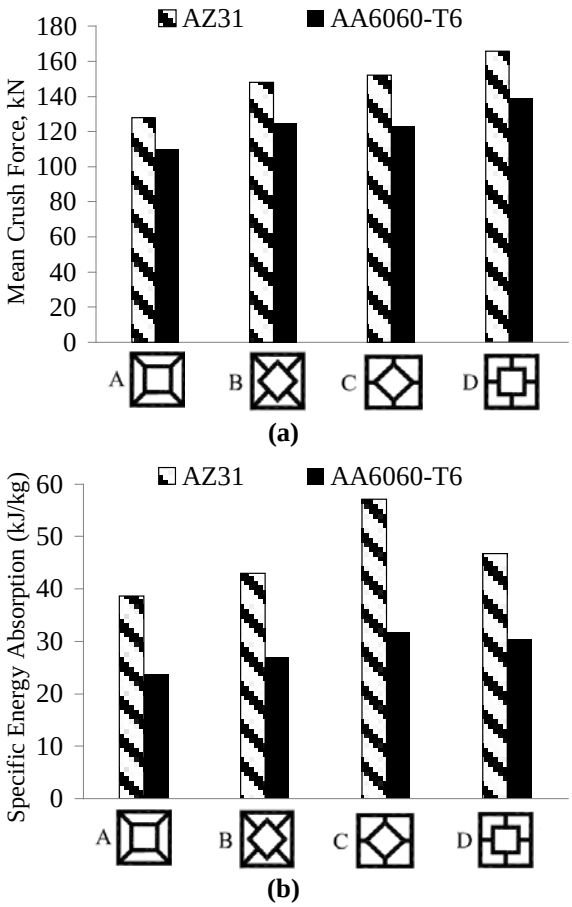

Figure 8. (a) Mean crush force and (b) Specific energy absorption using two different lightweight materials.

Horstemeyer et al. (2005) used a first-order Taylor series expansion to investigate the effects of uncertainty in microstructure features and the boundary conditions that characterize damage evolution in A356 cast aluminum alloy. In particular, void-nucleation, void-growth, and void-coalescence equations were evaluated and

quantified in terms of the sensitivity and uncertainty of various parameters in the constitutive equations. However, the accuracy of a Taylor expansion method largely depends on the scale of uncertainty in the random parameters and the nonlinearity in the corresponding random response.

Recently, Rahman and Xu (2004) proposed the dimension reduction (DR) technique to evaluate a multidimensional integral of a random function by solving multiple one-dimensional integrals. This technique offers an efficient approach for the evaluation of statistical moments such as the mean, variance, skewness, and kurtosis of a random response.

To fully characterize the uncertainty in a random response, such as damage, the estimated moments can be used to find its probability distribution using a suitable probability distribution fitting technique.

Commonly-used distribution fitting techniques include the Pearson and Johnson families of distributions, Saddlepoint approximations, and generalized lambda distributions (GLDs). In this work, we used the extended generalized lambda distribution (EGLD), which combines the GLD with the generalized beta distribution (GBD). The efficiency and accuracy of distribution fitting via GLD and GBD can be found in Karian et al. (1996), Karian and Dudewicz (2000), Lampasi et al. (2005), and King and MacGillivray (2006). After the first four statistical moments of damage are calculated, the parameters of the EGLD are estimated by minimizing the differences between the moments of EGLD and those obtained through DR.

As an illustrative example, we considered the FE simulation of an un-notched A356 aluminum alloy tension specimen loaded at a strain rate of 10^{-3} s^{-1} until the point of failure. Using an ISV-based constitutive model (Horstemeyer 2001) in the FE simulations, DR+EGLD technique is used to study the influence of uncertainty in the individual parameters of the ISV model on the uncertainty in damage.

The microstructure of a typical metallic material contains a large number of microdefects such as microcracks, dislocations, pores, and decohesions. Some of these defects are induced during the manufacturing process and are present before the material is subjected to mechanical loads and thermal fields. In general, these defects are small and distributed throughout the material. For A356 cast aluminum alloy, scattered electron microscope images suggest that the material is more isotropic in nature with the secondary constituent particles within the matrix ranging from 3 to 6 μm, with an average size of 4 μm and particle volume fraction of approximately 7%.

Using the experimental data obtained from the testing of A356 specimens, a nonlinear regression algorithm (Horstemeyer, 2001) is used to calculate the ISV model constants. Moreover, the experimental data and associated uncertainties are propagated through a model correlation routine to predict uncertainties in the ISV model parameters. The calculated first-order coefficients of variation (COV) of the plasticity parameters related to the yield strength (C_1 to C_6), the kinematic hardening and recovery terms (C_7 to C_{12}), the isotropic hardening and recovery terms (C_{13} to C_{18}), and the shear and the bulk moduli (G and K), along with their temperature and strain-rate dependencies ($a1$ and $b1$) are as shown in Table 3. In addition, C_a and C_b are the material plasticity parameters related to dynamic recovery and anisotropic hardening terms, respectively. Similarly, the microstructure damage parameters and associated uncertainties are given in Table 4, where m is void growth constant, R_0 is the initial void radius, a, b, and c are the stress state-based void nucleation constants, C_{coeff} is the void-nucleation coefficient parameter, K_{ic} is the fracture toughness, d is the particle size, f is the particle volume fraction, cd1 and cd2 are the coalescence factors, z, DCS and DCS_0 are parameters related to grain size and C_{CT} and $C_{\eta T}$ are the void-coalescence and the void-nucleation temperature-dependent parameters, respectively. The excluded parameters, with mean and COV of zero, are also shown in Tables 3 and 4 for completeness sake.

The calculated COVs are assumed to be normally distributed and rounded off, due to limited test data. These COVs indicate the scatter in the given

parameters that enable the study of their influences on damage uncertainty.

Table 3. Elastic-plastic model constants for A356-T6 aluminum alloys

ID #	Constants (Units)	Mean	COV
1	G (MPa)	25920	0.05
2	$a1$	1.0	0.05
3	K (MPa)	67630	0.05
–	$b1$	0.0	0.0
4	Melting temperature (°K)	5556	0.08
5	C_1 (MPa)	53.09	0.08
6	C_2 (°K)	945.3	0.08
7	C_3 (MPa)	155.9	0.08
8	C_4 (°K)	110.5	0.08
9	C_5 (1/MPa)	0.00001	0.08
–	C_6 (°K)	0.0	0.0
10	C_7 (1/MPa)	0.00087	0.08
11	C_8 (°K)	–1877	0.08
12	C_9 (MPa)	4820	0.08
13	C_{10} (°K)	10.94	0.08
14	C_{11} (s/MPa)	0.01369	0.08
15	C_{12} (°K)	2000	0.08
16	C_{13} (1/MPa)	0.0000165	0.08
17	C_{14} (°K)	–1000	0.08
18	C_{15} (MPa)	2818	0.08
19	C_{16} (°K)	4.622	0.08
–	C_{17} (s/MPa)	0.0	0.0
20	C_{18} (°K)	235.4	0.08
21	C_a	–7.0	0.05
22	C_b	–0.3776	0.05
23	Initial temperature (°K)	297	0.10
–	Heat generation coefficient	0.0	0.0

The plot of damage, ϕ as a function of strain, ε is shown in Figure 9. Damage values range from zero to one, with a rapid growth beyond the value of ~0.01. Here, the uncertainty in damage depends on the random uncertainties in the ISV model parameters and the strain value selected.

The overall uncertainty analysis procedure using DR+EGLD technique is as follows. First, damage calculations are performed at some selected points in the random variable space. Next, the first four statistical moments of damage are estimated using DR. Then, the probability distribution of damage is approximated with EGLD. Detailed description of this technique is provided in Acar et al. (2008).

Table 4. Damage model constants for A356-T6 aluminum alloys

ID #	Constants (Units)	Mean	COV
24	m	0.3	0.15
25	R_o (mm)	0.0002	0.25
26	a	615369	0.15
27	b	58630	0.15
28	c	30011	0.15
29	C_{coeff}	90.6	0.15
30	K_{ic} (MPa-m$^{1/2}$)	17.3	0.20
31	d (mm)	0.000004	0.25
32	f	0.07	0.25
33	$cd1$	1.0	0.15
–	$cd2$	0.0	0.0
34	DCS_0 (mm)	20	0.15
35	DCS (mm)	20	0.15
36	z	0.0509	0.15
37	Initial void volume fraction	0.0001	0.15
38	$C_{\eta T}$	0.6	0.15
–	C_{CT}	0.0	0.0

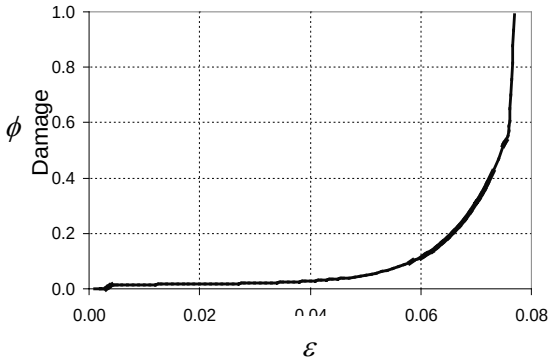

Figure 9. Damage vs. strain for A356 aluminum alloy.

The DR+EGLD-based probability density function (PDF) plots of damage at different points along the damage-strain curve (Figure 9) are shown in Figure 10. The mean value and scatter (C_ϕ) in damage appear to increase as the strain value increases.

For comparison, the PDF plots based on the direct Monte Carlo simulation (MCS) with a sample size of 10^4 and those based on a Gaussian (normal) estimation of damage, are also shown. Since the number of random variables is large (38 random variables), in view of the central limit theorem, the

probability distribution of damage can also be represented reasonably well with a normal distribution.

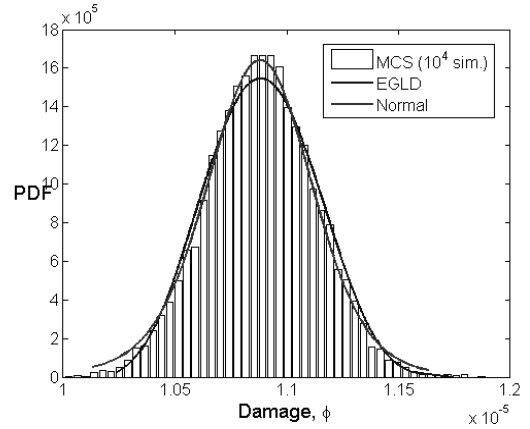

ε = 0.001, C_ϕ = 0.022

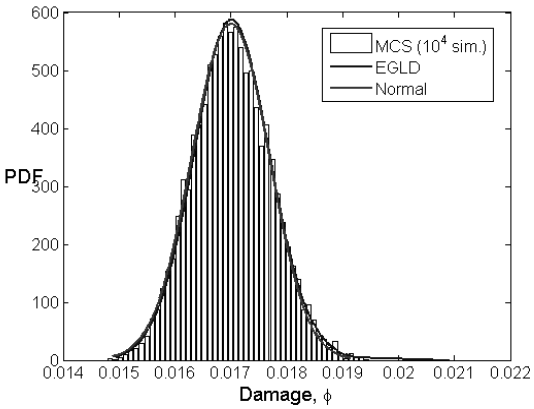

ε = 0.01, C_ϕ = 0.040

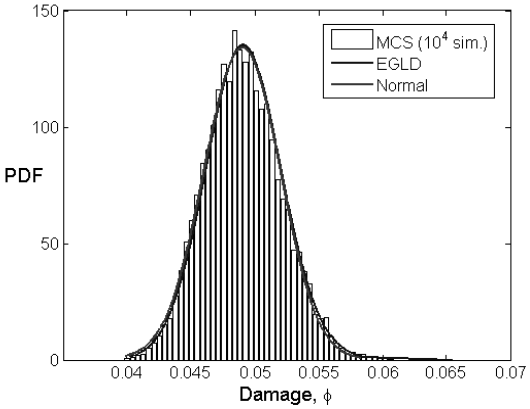

ε = 0.05, C_ϕ = 0.061

Figure 10. Probability distributions of damage at different strain levels.

In addition to uncertainty analysis, the sensitivity of damage to the random variables in Tables 3 and 4 were also investigated. Initially, at ε = 0.001, damage is found to be most sensitive to the initial radius of spherical void R_0, and void-nucleation coefficient C_{coeff}. With increasing values of strain (ε = 0.01) and corresponding damage in the tensile specimen, the initial temperature, coalescence factor cd1 and initial void volume fraction become more important, and finally, at ε = 0.05, the most influential parameters are found to be the fracture toughness K_{ic}, initial temperature and void-coalescence temperature dependent parameter, $C_{\eta T}$.

From the results obtained in this study, we can draw the following conclusions.

1. The scatter in damage, as measured by the coefficient of variation of damage, can increase with strain even though the uncertainties in the input variables are kept fixed.
2. The sensitivities of damage uncertainty to the uncertainties in the input random variables are dependent on the strain values. As the strain value changes (as damage evolves), the importance of the random variables changes.
3. The sensitivities are found to be consistent with the physics of the damage progression. At the very beginning, the void properties (initial size and growth parameters) are found to drive the damage evolution. Then, void coalescence becomes the main driver and finally near the failure condition, macroscopic properties such as fracture toughness, dominate the damage evolution process.

Reliability Analysis Using Failure Sampling

The reliability assessment of a structural component requires the evaluation of the failure probability of one or more possible failure modes. If the limit state or safety margin for a particular mode is defined by the function $g(\boldsymbol{X})$, where $\boldsymbol{X}$ denotes the vectors of random variables, then safety is defined as $g(\boldsymbol{X}) > 0$ and failure as $g(\boldsymbol{X}) \le 0$. The probability of failure is computed according to the multi-integral equation

$$P_f = P(g < 0) = \int_{g(\boldsymbol{X}) \le 0} f_x(\boldsymbol{X}) d\boldsymbol{X} \quad , \qquad (1)$$

where $f_X(\boldsymbol{X})$ is the joint PDF of random variables. For most engineering problems, the analytical integration of Eq. (1), or the full distributional approach is not possible. Hence, alternate techniques are often used to find an estimation of P_f or its corresponding safety index, β.

Popular simulation based methods include Monte Carlo simulation (MCS) and associated variance reduction techniques, such as importance sampling (Rubinstein 1981) and adaptive importance sampling (Wu 1992). Analytical methods such as first- and second-order reliability methods (FORM, SORM) (Madsen et al. 1986) and fast probability integration (Wu and Wirsching 1987) tend to be more efficient than simulation methods, but often with reduced accuracy. Recently, we showed that it is also possible to use the DR+EGLD technique, as discussed in the *Uncertainty Analysis using Dimension Reduction and Distribution Fitting* section, for analytical estimation of failure probability. Details of that study can be found in Acar et al. (2008).

As part of this project, we developed a computationally-efficient simulation-based method that does not rely on a most probable point of failure (MPP) search, such as importance sampling, but can generate accurate results for difficult limit states of relatively high-reliability. We refer to the method as failure sampling (FS). The method is based on a combination of Conditional Expectation and the cumulative distribution function (CDF) or PDF of a portion of the limit state, g, by direct MCS. If the CDF, or PDF, of g can be accurately developed, failure probability can be easily calculated by numerical integration over the failure region. The difficulty of developing this curve by MCS is that most samples fall close to the mean of g, which may be far from the failure region, making accurate integration of this region difficult or impossible. For complex, implicit problems, such as some practical nonlinear engineering problems, requiring an incremental FEA solution for evaluation of the limit state is a realistic concern.

FS solves this problem by reformulating the initial limit state, $g(\boldsymbol{X})$, into a new limit state, g_{fs}, which is expressed in terms of a control random variable (X_k, $k \neq i$), representing the 'load', q, and all the remaining random variables, which will collectively represent a 'resistance' function, $R(X_i)$, with

$$g_{fs} = R(X_i) - q \quad , \qquad (2)$$

g_{fs} is mathematically equivalent to g, hence, failure probability is identical.

Other than statistical independence from the remaining random variables, there is no theoretical limitation to the selection of the control variable; thus, X_i and q are not required to be the actual resistance and load random variables of the problem. However, some choices of the control variable may cause FS to fail, though these cases are often easy to identify based on some understanding of the mechanics of the problem. Note that g_{fs} can be completely implicit and there is no need for an analytical or closed-form formulation.

The value of $R(X_i)$ at the MPP of g_{fs} is generally closer to the central region of the PDF of $R(X_i)$, f_r than $g(X_j) = 0$ is to the central region of the PDF of g, f_g. Therefore, if f_r is generated by MCS, for instance, the calculation of P_f of g_{fs} becomes less sensitive to the tail region of f_r, than is the P_f of g to the tail of f_g. This allows a more accurate computation of P_f of g_{fs}, than the P_f of g, with the same number of simulations.

The samples needed to estimate F_R or f_r, are taken while the condition $g_{fs} = 0$ is imposed on the process. Practically, this involves conducting MCS to generate values x_i, then $R(x_i)$ is evaluated. The value of q required to set $g_{fs} = 0$ is then found. Since $R(x_i) = q$ at failure, q, therefore, represents a sample of $R(X_i)$. With sufficient samples of $R(X_i)$ obtained, a good estimation of F_R or f_r can be obtained and P_f or β can easily be computed from Eq. (2), using a large variety of available reliability techniques. For many practical (i.e., nonlinear and implicit) problems, imposing $g_{fs} = 0$ generally requires a higher computational cost per FS sample than MCS sample, as each FS sample requires solution of $g_{fs} = 0$ for q. For an implicit, nonlinear problem, this may require multiple iterations. However, as will be shown, this cost is greatly outweighed by the savings in overall

number of samples required, especially as P_f decreases.

We applied the FS technique to a large number of example problems, two of which are included in this report. Most problems considered have a range of β from 2 to 5, which is a realistic range for most structural reliability problems, although some β beyond this range have also been considered.

Ten-Bar Nonlinear Truss

The truss shown in Figure 11 is subjected to a random load, *P*, at joint 2. The material model is steel (elastic modulus 29,000 ksi), with a bi-linear stress-strain curve. Yield stress of all members is taken as a single random variable (i.e., yield stress fully correlated), with mean of 50 ksi and COV of 10%. Post-yield (tangent) modulus, E_t, of all members is also taken as a single random variable, with mean of 1200 ksi and COV of 25%. Thus, including load, there are only three random variables in this problem. Mean value of P is varied from 40 to 60 kips, with COV of 10%. All random variables are normally distributed. Failure is defined as the state when the vertical displacement, *d*, of joint 2 reaches 1.5 inches.

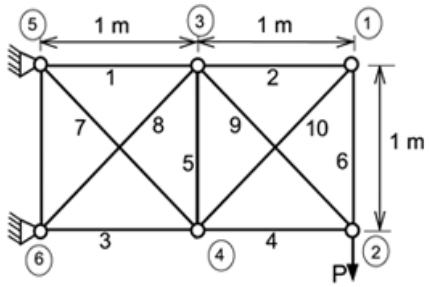

Figure 11. Ten-bar Truss.

The limit state is expressed as

$$g = 1.5 - d(\sigma_y, E_t, P) \quad , \qquad (3)$$

with *P* treated as the control variable. The nonlinear truss problem is analyzed using the FEA code MSC Nastran with Newton-Raphson solution. For FS, P is selected as the control variable and the bisection method is used to find the value for which $g_{fs} = 0$ (error tolerance taken as 0.01). Results are given in Table 5 for a mean load of 50 kips.

Table 5. Comparison of results for the truss example

Method	No. of calls	CPU time (hr)	β	% err
Exact	10^5	43	2.35	–
FS (NI)	1000	3	2.36	0.5
FS (FORM)	1000	3	2.35	0.3
FORM (RF)	15–239	0.017–0.17	7.85	235
SORM	25–444	0.034–0.25	5.67	142
MCS	7000	3	2.27	3.4
LHS	7000	3	2.43	3.7
IS	7000	3	2.34	0.3

In Table 5, the "Exact" result is based on 10^5 MCS samples, with each requiring a separate FE solution. FS (FORM) refers to calculating β from Eq. (2) with FORM once f_r was estimated with FS results, whereas FS (NI) refers to calculating P_f from FS results by numerical integration.

$$p_f = \int_{-\infty}^{\infty} F_R(x)\, f_q(x) dx \quad . \qquad (4)$$

Equation (4) is a 2-random variable form of Eq. (1), once F_R is estimated from FS results.

Then, using the standard normal transformation $\beta = -\Phi^{-1}(P_f)$, generalized β is reported in the table. FORM (RF) applies the Rackwitz-Fiessler (1978) search algorithm to locate the MPP, while SORM refers to the common parabolic approximation of Breitung (1984). LHS refers to Latin Hypercube sampling. Using the correlation reduction technique as described by Inman and Conover (1982), it was generally found that MCS is equally if not more effective than LHS with only 1000 samples, though LHS can provide significant improvements over MCS with a larger number of simulations (Eamon et al. 2005). The simple version of importance sampling (IS) considered the uses of the MPP found from FORM (RF), while the importance sampling function is taken as the joint probability density function of the original limit state, with the random variables' means shifted to the MPP.

The simulation methods were given equal CPU time, rather than equal number of calls. This is because an FS call is more costly than the others for this type of implicit problem due to the need to satisfy the constraint $g_{fs} = 0$ for each sample. This resulted in the other simulation methods, acquiring seven times the number of samples as FS. Even so, FS out-performed the comparison methods, resulting in a more accurate solution for the same overall CPU time. This is particularly apparent at the highest β level.

Crush Tube

A square tube, 400 mm long and 80 mm wide, with an end mass, m, and initial velocity, V, strikes a rigid wall. Random variables are the tube density, ρ_t, end mass, m, tube thickness, t, initial velocity, V, Young's modulus, E, yield stress, σ_y, and tangent modulus, E_t. Statistical properties of the random variables are given in Table 6.

Table 6. Properties of the random variables

RV	Mean	COV	Distribution
ρ	2.70×10^{-6} kg/mm^3	0.05	normal
m	800 kg	0.15	normal
t	4 mm	0.01	normal
V	11 m/s	0.10	normal
E	69 GPa	0.10	lognormal
σ_y	0.175 GPa	0.15	normal
E_t	0.265 GPa	0.15	normal

Failure is defined as the crush distance exceeding 50% of the tube's original length, or 200 mm at 20 ms after impact. The limit state is given as

$$g = 200 - d(\rho_t, m, t, V, E, \sigma_y, E_t) \quad . \qquad (5)$$

The limit state is evaluated with the FEA code LS-DYNA, using a (explicit) central difference integration scheme for solution. The tube is modeled using quadrilateral shell elements. Due to the computational cost of this problem, only 100 FS samples are considered. As each FS sample takes approximately three times as long as an MCS sample, the other simulation methods each achieve approximately 300 samples for the same CPU time. Results are given in Table 7. The MCS samples were plotted on probability paper to verify results. Here only FS was able to provide a solution and was very accurate. By contrast, FS (FORM), SORM and IS methods could not converge to an acceptable solution.

Table 7. Comparison of results for the crush tube example

Method	No. of calls	CPU time	β	% err
Exact	60,000	10 days	2.28	–
FS (NI)	100	25 hrs	2.23	–2.3
FORM	104	9 hrs	2.54	11
MCS	300	25 hrs	2.11	7.1
LHS	300	25 hrs	2.22	–2.8

The results of this investigation show that the new FS approach can provide accurate results for a wide range of reliability problems at considerable computational savings.

Conclusions

A summary of research activities under the general area of simulation-based design optimization were presented. Good progress was made in a number of areas, including topology optimization, energy absorption characterization of extruded multi-cell crush tubes, uncertainty quantification, and reliability analysis.

Presentations/Publications/Patents

1. E. Acar and M. Rais-Rohani, "Ensemble of Metamodels with Optimized Weight Factors," *Structural and Multidisciplinary Optimization*, **37,** No. 3, 2008, pp. 279–294.
2. E. Acar, K. Solanki, M. Rais-Rohani, and M. Horstemeyer, "Uncertainty Analysis of Damage Evolution Computed Through Microstructure-Property Relations," *Proceedings of the ASME 2008 International Design Engineering Technical Conferences & Computers and Information in Engineering Conference (IDETC/CIE)*, New York City, NY, Aug 3–6, 2008.
3. A. Najafi and M. Rais-Rohani, "Influence of Cross-Sectional Geometry on Crush Characteristics of Multi-cell Prismatic Columns," *Proceedings of the 49th AIAA/ASME/ ASCE/AHS/ASC Structures, Structural Dynamics, and Materials Conference*, Schaumburg, IL, Apr 7–10, 2008.

4. M. Rouhi and M. Rais-Rohani, "Topology Optimization of Continuum Structures Using Element Exchange Method," *Proceedings of the 4th AIAA Multidisciplinary Design Optimization Specialist Conference*, Schaumburg, IL, Apr 7–10, 2008.
5. E. Acar, M. Rais-Rohani, and C. Eamon, "Reliability Estimation using Dimension Reduction and Extended Generalized Lambda Distribution," *Proceedings of the 10th AIAA Non-Deterministic Approaches Conference*, Schaumburg, IL, Apr 7–10, 2008.
6. E. Acar and M. Rais-Rohani, "Ensemble of Metamodels with Optimized Weight Factors," *Proceedings of the 4th AIAA Multidisciplinary Design Optimization Specialist Conference*, Schaumburg, IL, Apr 7–10, 2008.
7. B. Charumas, "A New Technique for Structural Reliability Analysis," MS Thesis, Mississippi State University, May 2008.

References

1. E. Acar, K. Solanki, M. Rais-Rohani, and M. F. Horstemeyer, "Uncertainty Analysis of Damage Evolution Computed Through Microstructure-Property Relations," Proceedings of the ASME 2008 International Design Engineering Technical Conferences & Computers and Information in Engineering Conference (IDETC/CIE 2008), New York, NY, Aug 3–8, 2008.
2. E. Acar, M. Rais-Rohani, and C. Eamon, "Reliability Estimation using Dimension Reduction and Extended Generalized Lambda Distribution," Proceedings of the 10th AIAA Non-Deterministic Approaches Conference, Schaumburg, IL, Apr 7–10, 2008.
3. M. P. Bendsoe, "Optimal Shape Design as a Material Distribution Problem," *Journal of Structural and Multidisciplinary Optimization*, **1**, No. 4, 1989, pp. 193–202.
4. K. Breitung, "Asymptotic Approximations for Multinormal Integrals," *Journal of Engineering Mechanics*, ASCE, **110**, No. 3, pp. 357–366, 1984.
5. W. Chen and T. Wierzbicki, "Relative Merits of Single-Cell, Multi-Cell and Foam-Filled Thin-Walled Structures in Energy Absorption," *Thin-Walled Structures,* **39**, No. 4, 2001, pp. 287–306.
6. C. Eamon, M. Thompson, and Z. Liu, "Evaluation of Accuracy and Efficiency of some Simulation and Sampling Methods in Structural Reliability Analysis," *Journal of Structural Safety*, **27**/4, pp. 356–392, 2005.
7. P. C. Fourie and A. A. Groenwold, "The Particle Swarm Algorithm in Topology Optimization," Proceedings of the Fourth World Congress of Structural and Multidisciplinary Optimization, Dalian, China, 2001.
8. M. F. Horstemeyer, "From Atoms to Autos, A New Design Paradigm Using Microstructure-Property Modeling, Part 1: Monotonic Loading Conditions," Sandia National Laboratories, Sand2000-8662, Mar 2001.
9. M. F. Horstemeyer, K. Solanki, and W. G. Steele, "Uncertainty Methodologies to Characterize a Damage Evolution Model," Proceedings of International Journal of Plasticity Conference, Kauai, Hawaii, Jan 2005.
10. R. L. Inman and W. J. Conover, "A distribution-free approach to inducing rank correlation among input variables," *Communications in Statistics*, **11**, No. 3, pp. 311–334, 1982.
11. Z. E. Karian, E. J. Dudewicz, and P. McDonald, 'The Extended Generalized Lambda Distribution System for Fitting Distributions to Data: History, Completion of Theory, Tables, Applications, the "Final Word" on Moment Fits', *Communications in Statistics—Computation and Simulation*, **25**, No. 3, 1996, pp. 611–642.
12. Z. Karian and E. Dudewicz, "Fitting Statistical Distributions to Data: The generalized Lambda Distribution and the Generalized Bootstrap Methods", CRC Press, Boca Raton, FL, 2000.
13. R.A.R. King and H.L. MacGillivray, "Fitting the Generalized Lambda Distribution with Location and Scale-Free Shape Functionals," Proceedings of the Symposium on Fitting

Statistical Distributions to Data, Auburn, AL, Mar 2006.

14. D. A. Lampasi, F. D. Nicola, L. Podesta, "The Generalized Lambda Distribution for the Expression of Measurement Uncertainty," IEEE Instrumentation and Measurement Conference, Ottawa, Canada, May 2005.
15. H. O. Madsen, S. Krenk, and N. C. Lind, Methods of Structural Safety, Prentice Hall, Englewood Cliffs, NJ, 1986.
16. A. Najafi and M. Rais-Rohani, "Influence of Cross-Sectional Geometry on Crush Characteristics of Multi-cell Prismatic Columns," Proceedings of the 49th AIAA/ASME/ASCE/AHS/ASC Structures, Structural Dynamics, and Materials Conference, Schaumburg, IL, Apr 7–10, 2008.
17. N. Olhoff, E. Ronholt, and J. Scheel, "Topology Optimization of three-dimensional structures using optimum microstructures," *Structural Optimization*, **16,** No. 1, 1998, pp. 1–18.
18. R. Rackwitz and B. Fiessler, "Structural Reliability Under Combined Random Load Sequences," *Computers and Structures*, **9**, No. 5, pp. 484–494, 1978.
19. S. Rahman and H. Xu, "A Univariate Dimension-Reduction Method for Multi-dimensional Integration in Stochastic Mechanics," *Probabilistic Engineering Mechanics*, **19**, No. 4, 2004, pp. 393–408.
20. M. Rouhi and M. Rais-Rohani, "Topology Optimization of Continuum Structures Using Element Exchange Method," Proceedings of the 4th AIAA Multidisciplinary Design Optimization Specialist Conference, Schaumburg, IL, Apr 7–10, 2008.
21. R. Y. Rubinstein, Simulation and the Monte Carlo Method, John Wiley & Sons, New York, 1981.
22. S. Y. Wang, K. Tai, and M. Y. Wang, "An Enhanced Genetic Algorithm for Structural Topology Optimization," *International Journal of Numerical Methods in Engineering*, **65,** No. 1, 2006, pp. 18–44.
23. T. Wierzbicki and W. Abramowicz, "On the Crushing Mechanics of Thin Walled Structures," *Journal of Applied Mechanics*, **50**, 1983, pp.727–734.
24. Y. T. Wu, "An Adaptive Importance Sampling Method for Structural Systems Analysis," Reliability Technology, edited by T.A. Cruse, ASME Winter Annual Meeting, Vol. AD 28. Anaheim, CA, pp. 217–231, 1992.
25. Y. T. Wu and P. H. Wirsching, "New Algorithm for Structural Reliability Estimation," *Journal of Engineering Mechanics*, ASCE, **113**, No. 9, pp. 1319–1336, 1987.
26. X. Zhang, G. Cheng, and H. Zhang, "Theoretical Prediction and Numerical Simulation of Multi-Cell Square Thin-Walled Structures," *Thin-Walled Structures*, **44**, No. 11, 2006, pp. 1185–1191.
27. M. Zhou and G.I.N. Rozvany, "The COC algorithm, part II: Topological, Geometry and Generalized Shape Optimization," *Computer Methods in Applied Mechanics and Engineering*, **89**, No. 1–3, 1991, pp. 197–224.

M. Fatigue of Lightweight Automotive Materials

Principal Investigator: Mark F. Horstemeyer
Chair in Solid Mechanics and Professor, Dept. of Mechanical Engineering
Center for Advanced Vehicular Systems
Mississippi State University
206 Carpenter Bldg., P.O. Box ME
Mississippi State, MS 39762
(662) 325-7308; fax: (662) 325-7223; e-mail: mfhorst@me.msstate.edu

Co-Principal Investigator: Paul T. Wang
Manager, Computational Manufacturing and Design
Center for Advanced Vehicular Systems
Mississippi State University
P.O. Box 5405
Mississippi State, MS 39762-5405
(662) 325-2890; fax: (662) 325-5433; e-mail: pwang@cavs.msstate.edu

Co-Principal Investigator: Adrian Pascu
Postdoctoral Associate, Engineering
Center for Advanced Vehicular Systems
Mississippi State University
P.O. Box 5405
Mississippi State, MS 39762-5405
(662) 325-3812; email: ap326@msstate.edu

Co-Principal Investigator: Yibin Anna Xue
Assistant Professor, Mechanical and Aerospace Engineering
Utah State University
4130 Old Main Hill
Logan, UT 84322
(435) 797-2867, e-mail: http://www.mae.usu.edu/personnel/faculty.php

Technology Area Development Manager: Joseph A. Carpenter
(202) 586-1022; fax: (202) 586-1100; e-mail: joseph.carpenter@ee.doe.gov

Field Project Officer: Aaron D. Yocum
(304) 285-4852; fax: (304) 285-4403; e-mail: aaron.yocum@netl.doe.gov

---

Contractor: Mississippi State University (MSST)
Contract No.: 4000054701

Objective

- Develop and experimentally validate prognostic tools for in-service life prediction and fatigue design of lightweight automotive materials and components. An extensive test program is being conducted for AZ31D and AM30 magnesium (Mg) extrusion alloys. A multistage fatigue (MSF) model, which considers fatigue life to comprise incubation, microstructurally small crack growth, and large crack growth, will be developed for Mg alloys.

Approach

- Develop methodologies for simulating microstructurally-small cracks in selected magnesium alloys. Observation of the incubation lives for the selected magnesium alloys, measurement and correlation of the growth of microstructurally small cracks and large-crack behavior will be conducted for development of the physics-based models. (Task 1)
- Perform a literature survey on fatigue and small-crack behavior in magnesium alloys; conduct fatigue and crack-growth tests on selected magnesium alloys; conduct monotonic and cyclic stress-strain tests, uniaxial, and multi-axial fatigue tests on AZ31; conduct fatigue tests for the United State Automotive Materials Partnership (USAMP) round robin; and use data from the Fatigue and Durability Research Program to validate the models. (Task 2)
- Perform in situ scanning electron microscopy (SEM) fatigue tests on selected alloy(s) to identify crack initiation site(s) and metallurgical features. We will conduct in situ studies on the fatigue and crack behavior of the selected magnesium alloy. (Task 3)
- Correlate the influence of grain boundaries, crack shapes, and plasticity effects on the fatigue models. We will conduct microstructural studies on the influence of grain boundaries on crack growth, the effects of plastic deformations on the fatigue, and fatigue crack-growth behavior. (Task 4)
- Experimentally validate the models with a selected material and non-proprietary automotive component tested under in-service loading specified by sponsors. (Task 5)

Accomplishment

- Conducted literature surveys on fatigue and small-crack growth in magnesium alloys. (Task 2)
- Developed a detailed Statement of Work on "Development of Microstructure-Based Multistage Fatigue Models for Alloys Utilized in Automotive Mg Front End Project." (Task 2)
- Developed test matrix and test specimens for tensile and fatigue tests on the magnesium alloys to determine material parameters for the MSF model. (Task 2)
- Conducted MultiStage Fatigue (MSF) analyses of cast AZ91 material and components. (Task 1)
- Conducted preliminary fatigue crack-growth analyses and correlations of crack-growth rates for AZ91E to determine material parameters for Small-Crack Theory model. (Task 1)
- Conducted fatigue analyses on unnotched strain-controlled tests on AZ91E coupons using Small Crack Theory. (Task 1)
- Acquired AZ31D and AM30 extrusions from General Motors (GM). (Task 2)
- Determined composition and particle morphology and distributions for AZ31D and AM30 Mg alloys from GM. (Task 2)
- Developed a detailed test plan for the tensile and fatigue specimens to be machined from AZ31D and AM30 extrusions. (Task 2)
- Initiated tensile testing on the extruded AZ31D and AM30 alloy. (Task 2)
- Published a conference paper on MTS 2008 on fatigue of Mg AZ31. (Task 1)

Future Direction

- Evaluate and model fatigue behavior of self-piercing rivet (SPR) lap joint configuration
  - — Develop candidate SPR specimen
  - — Uniaxial tensile strain-life testing ($R > 0$)
  - — Microstructural evaluations

- Evaluate and model fatigue behavior of Mg AZ31D and AM30 extrusions
  - Evaluate grain size, orientation, and distribution for given Mg alloys
  - Complete the monotonic and cyclic stress-strain tests on the given extrusion samples
  - Conduct uniaxial strain-life tests with mean stress effects (R = -1, and R = 0.1)
  - Evaluate fractographs of fatigue specimens, identify incubation site(s) and fatigue stages
  - *In situ* SEM tests on AZ31 and AM30 coupons to study fatigue incubation and crack-growth behavior (collaboration with Chinese partners)
  - Perform MSF analyses of the uniaxial, strain-controlled fatigue tests on unnotched Mg coupons
- Fatigue components design
  - Obtain in-service spectrum loading sequences from automotive industry
  - Conduct MSF analyses under in-service variable-amplitude loading.
- Publications and reports
  - Submit a paper on the fatigue analysis of the AZ91E alloy using Small Crack Theory to the *International Journal of Fatigue*.
  - Complete a full report on fatigue analyses of AZ31D and AM30 under constant and variable amplitude loading.

Introduction

Prognostic tools for in-service life prediction of lightweight automotive materials and components are being developed and validated for magnesium alloys. Stress-strain tests and fatigue tests under low- and high-cycle fatigue conditions are being conducted. Detailed observations of the fatigue failure process will guide development of the physics-based models.

Quasi-static Tensile Tests for AM30 Mg Alloy

We ran the tensile tests with strain rate 10^{-3} /sec, at T1 = 300K, using the Instron 5869 machine and the Epsilon extensometer (Epsilon 3542-0100-025-ST). The tensile true stress-strain curves are presented in Figure 1. The tensile tests and elastic results are summarized in Table 1. The initial linear modulus were obtained using the least square regression technique from the tensile curve; however, this value is smaller than the elastic modulus obtained from unloading (unloading is more correct).

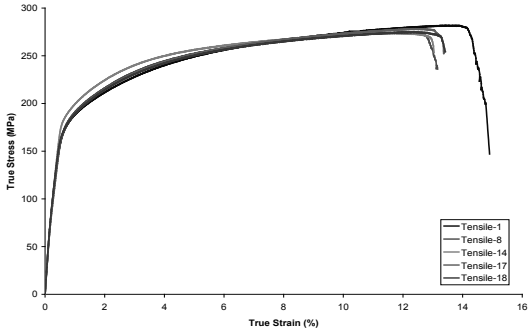

Figure 1. True stress-true strain curves for tensile tests at TI = 300K and strain rate 10^{-4} /sec for AM30 Mg alloy.

Table 1. Tensile properties of AM30 Mg alloy at a strain rate of 10^{-3} /s at T1 = 300K

Sample ID	Initial dimension	Linear modulus	Elastic modulus	Yield stress	Ultimate stress	Failure strain
	b x h [mm x mm]	[GPa]	[GPa]	[MPa]	[MPa]	[%]
Tensile-1	6.4 x 5.1	33.59	42.00	167.8	276.4	14.20
Tensile-8	6.4 x 5.1	32.49	42.00	170.2	268.4	12.83
Tensile-14	6.4 x 5.1	36.35	42.00	183.3	264.7	12.89
Tensile-17	6.4 x 5.1	32.69	42.00	168.9	272.1	13.19
Tensile-18	6.4 x 5.1	34.36	42.00	169.7	268.4	13.29
Average		**33.90**		**172.0**	**270.0**	**13.30**
SDV		**1.56**		**6.39**	**4.45**	**0.54**
CoV (%)		**4.61**		**3.72**	**1.65**	**4.02**

Figure 2(a) shows one specimen (Tensile-18) before the test and Figure 2(b) shows the same specimen after the tensile test at T1= 300K.

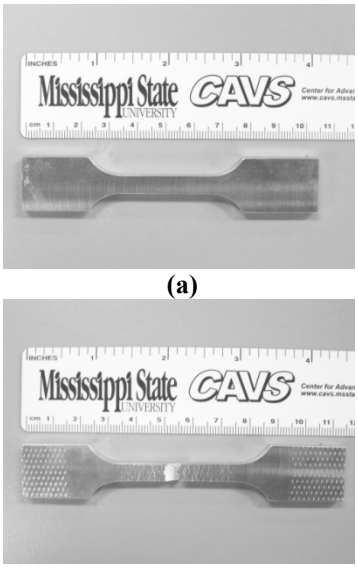

(a)

(b)

Figure 2. AM30 Mg alloy specimen (a) before test and (b) after the test at TI = 300K.

Using the same Instron machine and an Instron extensometer (Instron 263-107 GL 25 mm), we ran the tensile tests with strain rate 10^{-3} /sec, at T2=400K. The tensile tests and elasticity results are summarized in Table 2. The tensile true stress-strain curves are presented in Figure 3.

Table 2. Tensile properties of AM30 Mg alloy at a strain rate of 10^{-3} /s at a T2=400K

Sample ID	Initial dimension	Linear modulus	Elastic modulus	Yield stress	Ultimate stress	Failure strain
	b x h [mm x mm]	[GPa]	[GPa]	[MPa]	[MPa]	[%]
Tensile-1	6.4 x 5.1	30.42	42.00	147.51	197.6	33.42
Tensile-8	6.4 x 5.1	29.75	42.00	136.67	214.0	36.57
Tensile-14	6.4 x 5.1	27.63	42.00	124.76	173.5	47.09
Tensile-17	6.4 x 5.1	27.38	42.00	119.72	208.3	39.45
Tensile-18	6.4 x 5.1	23.98	42.00	120.44	208.2	33.86
Average		**27.81**		**129.8**	**200.3**	**38.28**
SDV		**2.56**		**11.99**	**16.14**	**5.39**
CoV (%)		**9.19**		**9.24**	**8.06**	**14.09**

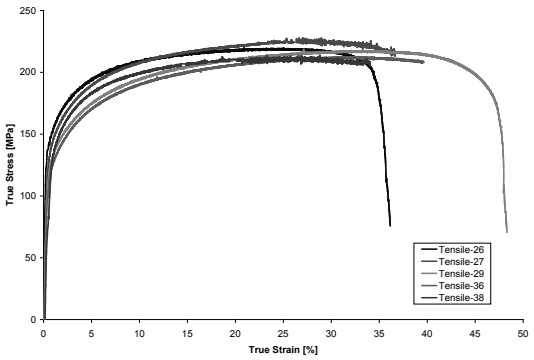

Figure 3. True stress-true strain curves for tensile tests at T2 = 400K and strain rate 10^{-3} /sec for AM30 Mg alloy.

Figure 4(a) shows one specimen (Tensile-26) before the test and Figure 4(b) shows the same specimen after the tensile test at T2=400K. Figure 2(b) shows one specimen after the tensile test at T1=300K and Figure 4(b) shows the similar specimen after the tensile test at T2=400K. Figure 5 presents a comparative plot.

(a)

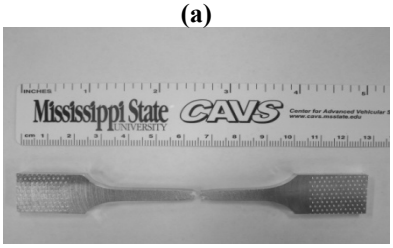

(b)

Figure 4. AM30 Mg alloy specimen (a) before test and (b) after the test at T2 = 400K.

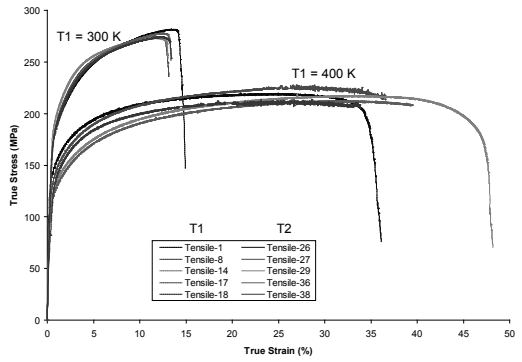

Figure 5. Comparative plots true stress-true strain curves for AM30 Mg sample tested in uniaxial tensile tests at TI = 300K and T2 = 400K.

After these tests, we observed a decrease in the failure stress for testing at 400K with approximately 38% (σ_{fHT}=200.3 MPa, σ_{fRT}=268.4 MPa) compared to the tests at 300K, and an increase of failure strain at 400K with approximately 187% (ε_{fHT}=38.2%, ε_{fHT}=13.30%) compared with the same tests at 300K. Typical scanning electron microscope (SEM) images of the fracture surfaces of the AM30 tensile specimens tested at 300K and 400K is shown in Figure 6(a) and 6(b), respectively.

Quasi-static Compression Tests at T1=300K for AZ31 Mg Alloy

We ran compression tests with strain rate 10^{-3}/sec, at T1=300K using the Instron 5869 machine and the Instron extensometer (Instron 263-107 GL 25 mm). The compression tests results were summarized in Table 3. The stress-strain behavior is presented in Figure 7 for the extruded and transverse directions. The tests were run for three specimens, cutting one in the transverse direction (CT-2, CT-5) and cutting two specimens in the extruded direction (CE-1, CE-3, CE-4). Figure 8 shows the compression specimen after the test at T1=300K.

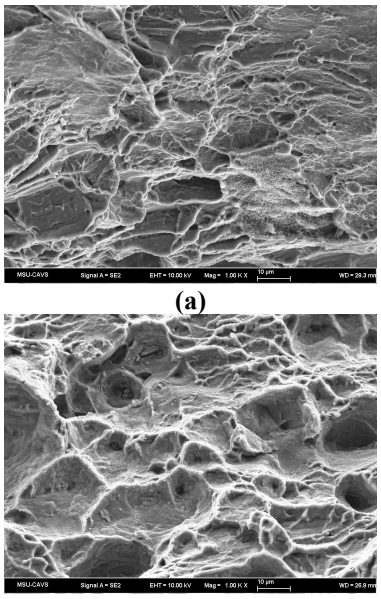

Figure 6. SEM fracture surface images with different magnification of the AM30 tensile specimens at (a) TI = 300K tested with 10^{-3}/sec strain rate and (b) T2 = 400K with 10^{-3}/sec strain rate.

Table 3. Compression properties of AZ31 Mg alloy at a strain rate of 10^{-3} /s at T1 = 300K

Sample ID	Initial dimension b x h [mm x mm]	Failure strain [MPa]	Failure stress [MPa]	Maximum stress [MPa]
CE-1	12.75 x 25.50	53.81	293.96	334.82
CE-3	12.75 x 25.50	55.06	336.24	355.65
CE-4	12.75 x 25.50	62.08	319.17	354.64
Average		**56.98**	**316.46**	**348.37**
SDV		**4.46**	**21.27**	**11.75**
CoV (%)		**7.82**	**6.72**	**3.37**
CE-3	12.75 x 25.50	35.44	235.61	271.70
CE-4	12.75 x 25.50	36.37	244.65	276.30
Average		**35.91**	**240.13**	**274.00**
SDV		**0.66**	**6.39**	**3.25**
CoV (%)		**1.83**	**2.66**	**1.19**

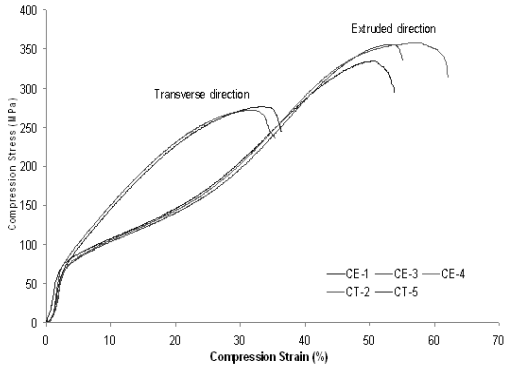

Figure 7. Compression stress-strain curves of five AZ31 Mg alloy samples, tested at a strain rate of 10^{-3} /s and temperature T1 = 300K.

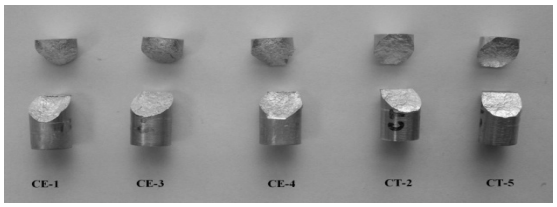

Figure 8. Compression specimens (AZ31) after the test at T1 = 300K.

Fatigue Tests for AM30 Mg Alloy

The fatigue tests for AM30 Mg alloy were performed using a MTS machine (model MTS-810) with a 100 kN capacity. Also used was an extensometer (MTS model no.: 634-31F-25, gauge length: 10 mm) in order to control strain signal and measure strain (Figure 9). The fatigue tests were performed at room temperature for a fully reversed loading cycle ($R = \varepsilon_{min}/\varepsilon_{max} = -1$) and for two strain amplitudes of 0.6 % and 0.3 % (there are more planned at different strain amplitudes). Figure 10 shows the experimental strain-life for AM30 Mg alloy. The number of failure cycles for each specimen is shown in Table 4 and the hysteresis for the first, middle, and last cycles for a few tests are presented in Figure 11.

Figure 9. Fatigue tests setup.

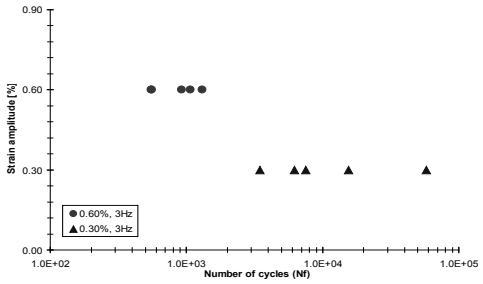

Figure 10. Experimental AM30 Mg strain life curve.

Table 4. Number of failure cycles for each specimen tested

Strain amplitude [%]	Frequency [Hz]	Nf Specimen 1	Nf Specimen 2	Nf Specimen 3	Nf Specimen 4	Nf Specimen 5
0.3	5	6,212	15,488	3,459	57,891	7,491
Strain amplitude [%]	Frequency [Hz]	Nf Specimen 6	Nf Specimen 7	Nf Specimen 8	Nf Specimen 9	Nf Specimen 10
0.6	3	919	1,310	558	1,071	553

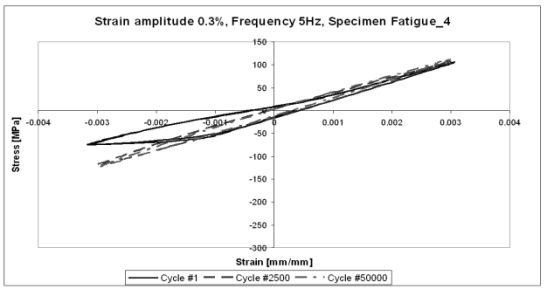

(a)

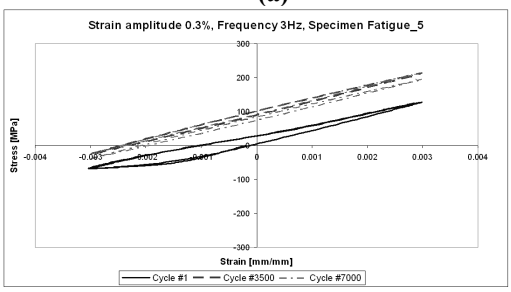

(b)

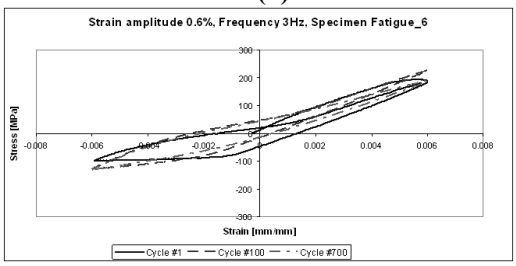

(c)

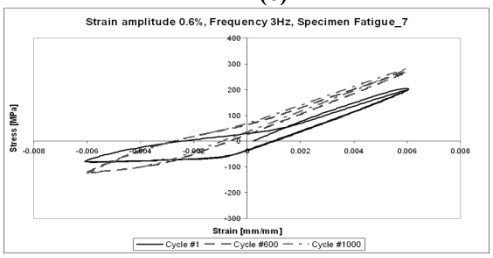

(d)

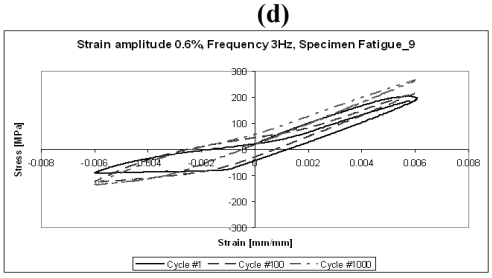

(e)

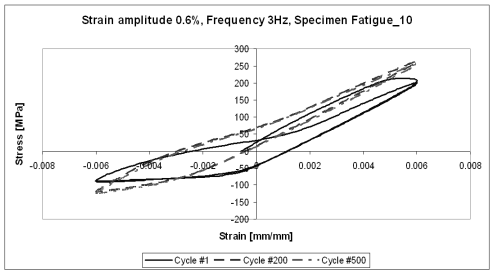

(f)

Figure 11. Hysteresis for different AM30 Mg alloy specimen at first, middle, and last cycle.

Using these test results, we have a preliminary model-experiment correlation for the extruded AM30 magnesium alloy. In Figure 12, the correlation between experimental results and MSF model results are presented.

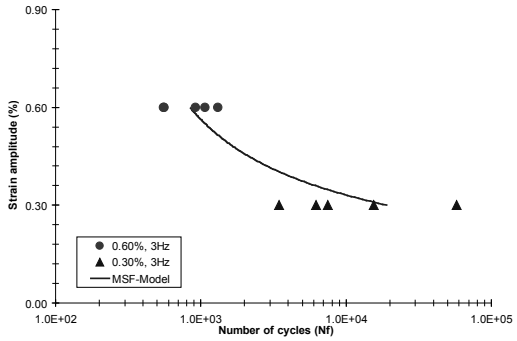

Figure 12. MSF model-experiment correlation showing the strain-life behavior for AM30 Mg alloy.

Fatigue Tests for AZ31 Mg Alloy

Fatigue tests for the AZ31 Mg alloy were performed using the same MTS machine (model MTS-810) with 100 kN capacity and the same extensometer (MTS model no.: 634-31F-25, gauge length: 10 mm) for controlling the strain signal and to measure strain. Also, the fatigue tests for these materials were performed at room temperature for a fully reversed loading cycle ($R = \varepsilon_{min}/\varepsilon_{max} = -1$) and for seven strain amplitudes: 0.2%, 0.25%, 0.3%, 0.4%, 0.5%, 0.6%, and 0.7%. In Figure 13, the experimental strain-life for AZ31 Mg alloy is presented. The number of failure cycles for each specimen is shown in Table 5.

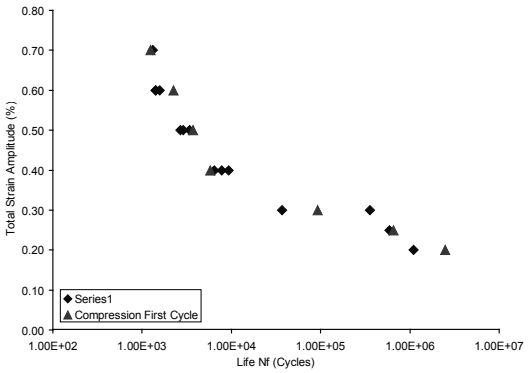

Figure 13. Experimental strain-life behavior for AZ31 Mg alloy.

Table 5. Number of failure cycles for each AZ31 Mg alloy specimen tested.

Sample ID	Diameter [mm]	Area [mm²]	Strain amplitude [%]	Frequency [Hz]	Cycles failure [#]	Comments
UF2-12	6.10	29.19	0.70	1	1,308	
UF-6	6.10	29.19	0.70	1	1,246	compression first cycle
UF-2	6.32	31.42	0.60	1	1,583	
UF-11	6.30	31.16	0.60	1	1,426	
UF-10	6.32	31.42	0.60	1	1,424	
TL2-5	6.29	31.04	0.60	1	2,258	compression first cycle
UF-7	6.35	31.67	0.50	2	2,698	
UF-3	6.32	31.42	0.50	2	3,380	
UF-5	6.35	31.67	0.50	2	2,875	
UF2-11	6.32	31.42	0.50	1	3,697	compression first cycle
UF-14	6.32	31.42	0.40	3	6,400	
UF-4	6.34	31.54	0.40	3	9,381	
UF-12	6.32	31.42	0.40	2	7,831	
UF-9	6.32	31.42	0.40	2	5,786	compression first cycle
UF-13	6.35	31.67	0.30	3	36,852	
UF-1	6.34	31.54	0.30	3	356,043	
UF2-7	6.32	31.42	0.30	3	92,084	compression first cycle
UF2-TL2-6	6.18	30.04	0.25	4	591,620	
UF2-5	6.29	31.04	0.25	3	657,005	compression first cycle
UF-8	6.32	31.42	0.20	3	1,099,874	
UF2-TL2-4	6.32	31.42	0.20	4	2,486,100	compression first cycle

Using these test results, we started the model—experimental correlation for the AM30 magnesium alloy. In Figure 14, the correlation between experimental results and MSF modeling results are presented.

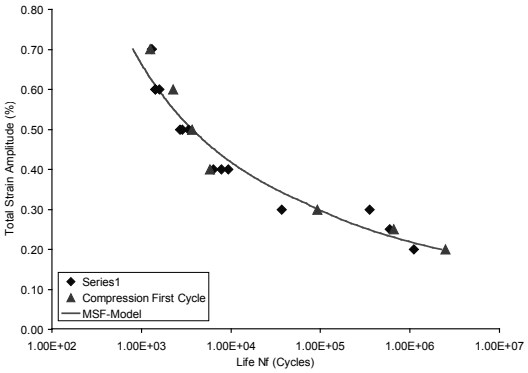

Figure 14. Model/Experimental correlation showing the strain life curve for AM30 Mg alloy.

Conclusions

Two magnesium extruded alloys, AZ31 and AM30, provided by our automotive sponsors, were investigated. Tensile and fatigue tests were conducted to generate mechanical properties for calibrating a physics-based MultiStage Fatigue (MSF) model. Fatigue lives under strain-controlled loading conditions were obtained. Preliminary results of AM30 and AZ31 extruded alloys were used to calibrate the MSF model. The MSF model could account for the influence of the manufacturing process of the strain-life behavior. Model development will be continued in Phase II of the program.

Presentations/Publications/Patents

1. Y. Xue, M. Lugocamarena, M. F. Horstemeyer, and J. C. Newman Jr., *Multistage Fatigue Model for an Extruded AZ31 Mg Alloy,* TMS 2008.

7. LOW-COST CARBON FIBER

A. Low-Cost Carbon Fibers from Renewable Resources

Project Contacts: F. S. Baker, N. C. Gallego, D. A. Baker, A. K. Naskar
Oak Ridge National Laboratory
P. O. Box 2008, Oak Ridge, TN 37831-6087
(865) 241-1127; fax: (865) 576-8424; e-mail: bakerfs@ornl.gov

Technology Development Manager: Joseph A. Carpenter
(202) 586-1022; fax: (202) 586-1600; e-mail: joseph.carpenter@ee.doe.gov

Field Technical Manager: C. David Warren
(865) 574-9693; fax: (865) 574-6098; e-mail: warrencd@ornl.gov

Contractor: Oak Ridge National Laboratory (ORNL)
Contract No.: DE-AC05-00OR22725

Objective

- Carbon fiber-resin composite materials could substantially reduce the weight of passenger vehicles, increase vehicle fuel economy, and result in lower CO_2 emissions. Carbon fibers have the potential for substantial weight saving in vehicles because of their remarkable high strength, high modulus, and low density; each 10% reduction in vehicle weight would translate into an increase in vehicle fuel economy of about 6%, with concomitant reduction in emissions. To place the potential increase in fuel economy into perspective, body-in-white modeling indicates that more than 60% of the steel in a vehicle could be replaced with carbon fiber composite materials without impacting vehicle crashworthiness. However, carbon fiber is currently too expensive for large scale automotive use, which will necessitate a large reduction in cost of appropriate strength fiber (from about $20/lb to about $5/lb) before we see significant use in the automotive industry. The cost of the precursor material currently accounts for about 50% of the cost of manufacturing carbon fibers, and therefore, emphasis in the ORNL research work is being placed on the development of processes using low-cost precursor materials, notably textile-grade polyacrylonitrile (PAN) and lignin, a renewable resource material. The goal of this project is to identify at least one precursor formulation, comprising both renewable and recycled materials, which could be used to produce industrial grade carbon fiber at a cost in the range of $5–7/lb. In addition to precursor, cost savings will also be achieved through advanced processing techniques, including plasma oxidation, carbonization, and graphitization of the precursor fiber, to obtain more efficient use of energy resources.

Approach

- Derive the fundamental data required to establish melt-spinning conditions for the continuous production of lignin-based carbon fiber meeting target properties.
- Using research- and pilot-scale carbon-fiber production lines, construct the technical database necessary to facilitate commercial production of lignin-based carbon fiber, including knowledge of the following respects.
  - — Isolation and purification of lignin to obtain appropriate precursor properties for carbon-fiber production.
  - — Melt-spinning technology, including extruder and spinneret configuration, spinning conditions, copolymers, and plasticizing agents.
  - — Thermal processing of precursor fiber into carbon fiber.
  - — Advanced processing of lignin-based carbon fiber.
  - — Mechanical properties of lignin-based carbon fibers.

— Surface treatment and sizing technology for relevant resin systems.
— Economics of lignin purification and processing of precursor fiber into finished carbon fiber.

- Development of intellectual property for the production of lignin-based carbon fibers.

Accomplishments

- Demonstrated continuous melt spinning of multifilament fiber from a 50-50 blend of unpurified kraft softwood lignin (SWL)—a notable first—using a purified kraft hardwood lignin (HWL) as the plasticizer.

  — The SWL was produced by Kruger Wayagamack (Quebec, Canada) using the LignoBoost process (developed by STFI-Packforst in Sweden) to isolate the lignin from kraft black liquor under process conditions that were more carefully controlled than currently practiced for the production of commercial kraft lignin products. The lignin still contained a very small proportion of cellulose fibers, which impacted the structural integrity of the spun fiber (as revealed by scanning electron microscope imaging) and subsequent processing into carbon fiber. Nevertheless, this demonstrated that it is possible to isolate lignin from a kraft chemical pulping operation which is very much cleaner than current commercial kraft lignin, and that with refinement of the isolation process, kraft lignin meeting the target specifications for carbon fiber production could be produced without the need for an additional purification process. Such a development would enhance the economics of lignin-based carbon fiber production; a reduction of lignin cost from 50 to 30¢/lb would reduce carbon fiber cost by 60 to 80¢/lb.

- Demonstrated stabilization, carbonization, and graphitization of 50-50 softwood-hardwood lignin fibers.

  — The mechanical properties of the carbonized fibers (1,000°C treatment) were about 60% of the milestone target for fiscal year (FY) 2008, an encouraging result for the first successful melt spinning of blends incorporating an SWL and, furthermore, a lignin that had not been subjected to a purification procedure. Further heat treatment of the carbon fiber at 1,700°C decreased mechanical properties, a probable consequence of the defects created in the fiber through volatilization of the cellulose fiber contaminant in the SWL. Kruger Wayagamack is working to refine the lignin isolation procedure to produce a kraft lignin product meeting the target purity specifications.
  — On a related note, through a meeting at ORNL (October 10), contact was established with key personnel at STFI-Packforst, Swedish Research Institute, where the LignoBoost process for isolating lignin from kraft black liquor was developed. As a result, a preliminary agreement has been reached whereby STFI and ORNL will collaborate on further development work on the use of lignin for carbon-fiber production; specifically, STFI will provide kraft lignin meeting the purity specifications and, based on results obtained at ORNL, will modify the lignin chemistry as appropriate to enhance the properties of carbon fiber produced from the lignin. STFI-Packforst is the world's leading institution with respect to lignin materials, and bringing it onboard the project will help to accelerate progress on the development of lignin-based carbon fibers as well as promote the ORNL research effort to a larger and more diverse industry base of potential lignin suppliers.

- Implemented work on Alcell, a lignin material produced by the Organosolv process in which waste wood materials are pulped with solvents to produce cellulose (for ethanol fuel production) and lignin. The Alcell lignin (200 lb) was furnished by Lignol Innovations (Vancouver, Canada), the leading company with respect to the production of cellulosic ethanol (recently awarded a $30M Department of Energy [DOE] contract to build a biorefinery in Colorado). The Organosolv process produces a much cleaner lignin than current commercial kraft lignin products and more than meets the purity specifications for carbon-fiber production.

  — Conditions were established for devolatilization of the Alcell lignin to remove residual solvents, and rheological and thermal analysis measurements were made to help establish melt-spinning conditions. Fibers were readily melt spun on the multifilament equipment (without the need for a plasticizing additive), and conditions for processing the precursor fibers into carbon fibers were established. The mechanical properties of the Alcell lignin-based carbon fibers are currently falling well short of the target properties (approaching 50% of target), but each new spinning run on the Alcell material has resulted in a greater understanding of the properties of this very different but promising type of lignin. One important characteristic of the Alcell lignin is its higher glass transition temperature (T_g) and melt spinning temperature, which enable the fiber stabilization stage of processing to be carried out at a significantly higher temperature (i.e., faster rate) than

possible for the high-purity kraft HWL (solvent extracted) on which much of the process development efforts this fiscal year were focused.

- Melt-spinning speed trials confirmed that the spinning speed of lignin can be increased to at least 2 times the Kline economic model baseline speed of 600 meters/minute (m/min), the speed for commercial mesophase pitch-based fiber. Alcell lignin fibers of the target diameter of 10 microns (μm) were successfully spun and wound at a winding speed of 1,200 m/min. For this demonstration, a suitable spinning die was manufactured to accommodate the required increase in mass throughput of the lignin melt and to achieve the required fiber draw-down ratio of 25 : 1 (instead of 15 : 1). Spinning speed is one of the most important process parameters with respect to the economics of carbon-fiber production from lignin (precursor cost and carbon yield are the most important material considerations). Demonstration of further increases in spinning speed is dependent on upgrading the melt-spinning equipment, notably installation of a higher-speed winder.
- Demonstrated that ultraviolet (UV) irradiation of lignin fibers facilitates subsequent thermal stabilization of the fibers.
  - — Thermal stabilization-differential scanning calorimetry (DSC) studies on high purity kraft HWL fibers confirmed that UV irradiation of the fibers greatly enhanced (20-fold) the rate of stabilization during subsequent thermal treatment of the fibers at about 130°C, a temperature dictated by the melting point of the lignin but too low to obtain an acceptable rate of stabilization through thermal treatment alone. The studies to date indicate that a short (<1 minute) UV irradiation of the HWL fibers increases the rate of stabilization of the fibers at 130°C to an acceptable level. As resources and higher priority work permit, further work will be carried out to determine whether other lignin fibers (e.g., Alcell) could be stabilized through UV irradiation alone.
- A comprehensive thermal analysis database was compiled to facilitate carbon-fiber conversion processing.
  - — Thermal analysis (DSC, thermogravimetric analysis [TGA]), rheometry, and molecular weight characterizations were made on selected lignin materials representing different species of wood (hardwood and softwood), different methods of pulping (kraft, soda, and Organosolv), and different methods of purification (aqueous, organic, none). The extensive database provides insight into the relationships between lignin chemistry, method of isolation/purification, purity, and melt spinnability, and facilitates more efficient evaluation of a lignin material for suitability for carbon-fiber production. Similarly, to facilitate conversion of lignin fiber into carbon fiber, the thermal analysis data provide information on T_g and melting points; volatiles content; rates of stabilization at selected temperatures; and the influence of atmosphere and UV-irradiation treatment, temperature range of carbonization, carbon yield (at 1,000°C), and ash content of the carbon (relates to initial salt content of the lignin). Ultimately, the database will help correlate the engineering properties of lignin-based carbon fibers with the fundamental properties of the lignin precursor material and conversion conditions.
- A research paper on the use of lignin as a precursor material for carbon fiber production was written.
  - — This particular paper covers only the production of melt-spun fibers, not details of conversion into carbon fiber. When the manuscript has passed through the ORNL approval process, the paper will be submitted for publication in a major materials journal, possibly the *Journal of Materials Science*. Similarly, a section on lignin-based carbon fibers was written for a paper on the low-cost carbon fiber (LCCF) project as a whole ("Multitask Research Program to Develop Commodity Grade, Lower Cost Carbon Fiber") to be presented by Dave Warren at the SAMPE Fall Technical Conference 2008 in Memphis, Tennessee (September 8–11).

Future Direction

- Development of a technically and economically viable process for the commercial production of industrial-quality carbon fiber from lignin feedstock. Key tasks will include the following.
  - — Down-selection of key sources of lignin (upwards of three) suitable for carbon-fiber production without purification and procurement of large batches for process development work.
  - — Selection of appropriate copolymers and/or plasticizing agents as needed to facilitate melt spinning of precursor fibers from specific sources of lignin.

- — Installation and commissioning of an extrusion compounding-pelletizing line to facilitate production of lignin feedstock pellets for melt spinning into precursor fibers (with or without copolymers and plasticizers).
- — Design of extruder and spinneret die to obtain high spinning speeds of target diameter fiber with good structural characteristics.
- — Establishment of conditions for continuous melt spinning of lignin fiber tow at speeds of at least 1,200 m/min (i.e., twice the Kline economic model baseline spinning speed of 600 m/min).
- — Development of techniques for spooling and rewinding of lignin-based precursor fiber tow.
- — Establishment of conditions for batch-scale thermal processing of lignin-based precursor fiber into carbon fiber meeting target engineering properties.
- — Establishment of conditions for continuous thermal processing of lignin-based precursor fiber tow into carbon fiber.
- — Identification of methods for surface treatment of lignin-based carbon fibers to enhance compatibility with relevant resin systems.
- — Production of a suitable quantity of finished lignin-based carbon fiber for composite testing by the Automotive Composites Consortium (ACC) and other entities.

- Collaboration with industrial, government, and academic partners to do the following.
  - — Clearly establish sources of lignin suitable for carbon fiber production, including lignin derived from the production of ethanol fuel from biomass resources (e.g., waste wood and switchgrass).
  - — Resolve any outstanding issues regarding the isolation and purification of lignin from different sources.
  - — Address knowledge gaps with respect to the use of recycled polymers as alloying agents for melt spinning of lignin-based precursor fibers.
  - — Complete identification of melt-spinning conditions and fiber winding technology for continuous production of lignin-based precursor fiber tow.
  - — Demonstrate carbon-fiber production from lignin-based multifilament tow using a pilot-scale process line.
  - — Achieve target engineering properties of lignin-based composite materials incorporating lignin-based carbon fibers (with the ACC).
  - — License and transfer lignin-based carbon fiber production technology to industry.

Introduction

The DOE FreedomCAR-funded work at ORNL is directed toward the development of processes for the low-cost production of carbon fibers including the use of advanced processing techniques such as plasma oxidation, carbonization, and graphitization of the precursor fiber (see reports 7.B and 7.C). The objective of the FreedomCAR project is to develop more energy-efficient, cost-effective processes for production of carbon fibers for use in composite materials for vehicles, which would substantially reduce vehicle weight, increase vehicle fuel economy, and result in lower CO_2 emissions (e.g., each 10% reduction in vehicle weight would translate into an increase in vehicle fuel economy of about 6%, with concomitant reduction in emissions). Carbon fibers have the potential for substantial weight saving in vehicles because of their remarkable high strength, high modulus, and low density.

To place the potential increase in fuel economy into perspective, body-in-white modeling indicates that more than 60% of the steel in a vehicle could be replaced with carbon-fiber composite materials without impacting vehicle crashworthiness. However, carbon fiber is currently too expensive for large-scale automotive use, and the supply is far too limited to meet the projected demand. Thus, a large reduction in the cost of appropriate strength fiber (from about $40/kg to about $10/kg) and an increase in supply must take place before we will see substantial increases in carbon fiber use in the automotive industry. The cost of the precursor material currently accounts for about 50% of the cost of manufacturing carbon fibers, and therefore emphasis in the ORNL research work is being placed on the development of processes using low-cost precursor materials, notably textile-grade PAN and lignin, a renewable resource material.

Lignin has a significant potential cost advantage over even textile-grade PAN as a precursor material for LCCF production. Whereas the cost of PAN is almost directly proportional to the cost of oil, the cost of lignin is largely independent of oil price, essentially being based on its fuel value of about 5¢/lb. On the downside, however, relatively little is known about how to transform lignin into carbon fiber. Furthermore, as currently isolated from the chemical pulping of wood for paper production (using either the kraft or soda processes), the lignin by-product is not suitable for carbon-fiber production and requires purification before it can be properly used for this purpose, which increases its cost, although not prohibitively.

Currently, chemical pulping of wood is the only immediate source of lignin in the United States, but as biomass refineries come onstream, the lignin by-product from cellulosic ethanol fuel production will represent a valuable resource material for carbon-fiber production. Work on biomass lignins produced from the Organosolv pulping of wood, the first step in cellulosic ethanol production, has already demonstrated that such lignins are readily melt-spinnable as isolated and are of a much higher purity level than lignins derived from the chemical pulping of wood for paper production.

Lignin is one of the main components of all vascular plants and the second most abundant polymer in nature (after cellulose). It is an amorphous, polyphenolic material arising from the enzymatic dehydrogenative polymerization of three phenyl propanoid monomers; namely, coniferyl alcohol, sinapyl alcohol, and *p*-coumaryl alcohol. The biosynthesis process leads to the formation of a complex, three-dimensional polymer that lacks the ordered, repeating units found in other natural polymers such as cellulose and proteins. Lignin plays a significant role in the carbon cycle, sequestering atmospheric carbon into the living tissues of woody perennial plants. It fills the spaces in the cell wall between cellulose, hemicellulose, and pectin components of wood. It is covalently bound to hemicellulose and thereby cross links different plant polysaccharides, conferring mechanical strength to the cell wall and thus to the plant as a whole.

An example of the complex structure of lignin is shown in Figure 1 for lignin isolated from beech hardwood. HWL is composed of coniferyl alcohol and sinapyl alcohol units in varying ratios, whereas SWL predominantly comprises coniferyl alcohol (>90%) and a small proportion of *p*-coumaryl alcohol.

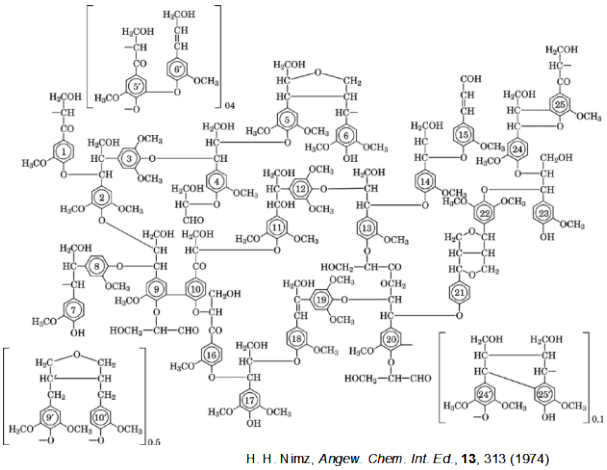

Figure 1. Chemical structure of HWL.

Because it is almost impossible, certainly very difficult, to isolate lignin from wood without degradation, the true molecular weight of native lignin is a subject of debate. However, the weight-average molecular weight of SWL isolated by mechanical milling of the wood (low degradation process) is about 20,000. Milled HWL exhibits significantly lower molecular weights. These and other differences between the chemistries of HWLs and SWLs influence the use of lignin for carbon-fiber production.

Depending on species, wood is about 15-25 wt % lignin, compared to about 38-48 wt % cellulose (on a dry wood basis); switchgrass has a similar content of lignin. Thus, wood and switchgrass contain significant amounts of lignin (about 50% of the proportion of cellulose), which if used for the production of value-added products, such as carbon fiber, could effectively offset the high cost of producing cellulosic ethanol from biomass (a relatively small proportion of the lignin would be used as a fuel in the ethanol production process). Furthermore, use of the lignin by-product for carbon-fiber production (and other value-added chemicals) would result in real benefits in the contexts of increased energy efficiency, reduced

environmental pollution, and enhanced national security (e.g., reducing dependence on imported fossil fuels).

Worldwide, more than 200 million metric tons of lignin pass through pulp mills annually, of which about 1.2 million tons are isolated for the production of lignin-based products. Lignin is not a waste product of the pulp and paper industry, but a coproduct that is used in modern, highly integrated pulping operations as a fuel (and reducing agent) in the pulping chemicals recovery process (it has about 70% of the calorific value of number 2 fuel oil). In fact, many modern mills have cogeneration facilities to produce electrical energy for sale to utility companies.

Lignin is already used on a large scale in transportation applications (e.g., as an emulsifying agent for asphalt road surfaces and as a dispersing agent for cement and concrete mixes, used in the construction of roads). Lignin is used as an "expander" (of active species surface area) in the negative plates of lead-acid batteries, the large majority of which are used for starting, lighting, and engine ignition functions on vehicles. Lignin derivatives are used as economical adhesives for carbon black, 70% of the world production of which is used in the compounding of rubber for vehicle tires. Other large-scale uses include textile dye dispersants; oil drilling muds; pesticide surfactants; sequestrants for micronutrients (agricultural and forestry uses); water treatment for boilers and cooling systems; and binders for plywood, particle board, fiberglass insulation, and animal feed.

Use of Lignin for LCCF Production

Most (>90%) carbon fiber is currently produced from PAN precursor fiber, which is made using a wet (solvent-based) process. This first unit operation of carbon-fiber production is one of the most intensive operations of the overall process, involving many stages of washing to remove residual traces of solvent which would otherwise adversely impact carbon-fiber properties, especially of the high-end and expensive grade fibers for aerospace applications (upwards of $150/lb). The associated solvent recovery and purification operations also add to the complexity and cost of PAN precursor fiber production. Melt spinning of a precursor fiber is much preferred over the wet-spinning process, but currently is only used in the spinning of pitch-based carbon fibers, which account for a relatively small proportion of worldwide carbon-fiber production. PAN cannot be melt spun, at least as formulated to achieve the engineering requirements of PAN-based carbon fibers, because it rapidly decomposes close to its melting point.

Certain types of lignin, notably hardwood-derived, can be melt spun providing that the contaminants in lignin isolated from the black liquor in chemical pulping operations can be reduced to acceptable levels. Impurities include nonmelting particulates (clays and sand, which block the very fine holes in the spinneret), inorganic salts (e.g., sodium sulfate), rosin, and residual carbohydrates (both in the form of fibers and bound to the lignin). The contaminated HWL could be melt spun in principle, but the spinning operation could not be maintained for any useful length of time to produce continuous fibers before the spinneret was blocked. Also, we found that the contaminants in the spun fibers degraded the engineering properties of the carbon fiber subsequently produced from the small quantities of lignin fiber. Nevertheless, the demonstration that even single carbon fibers could be produced from lignin was an encouraging development and represented a milestone achievement in the project.

A dedicated effort in earlier carbon-fiber project work at ORNL led to the development of laboratory-scale techniques to purify kraft lignins to the targeted levels. Ironically, because the melting point of the purified lignins, notably HWLs, was above their decomposition temperatures, they could not be melt spun. Chemically-pulped lignin is a heterogeneous material that includes a wide range of molecular weights, and it is the presence of some of the lowest molecular weight fractions that appears to impart melt spinnability to the HWL as a whole. Unfortunately, the lower molecular weight lignin fractions, which in essence serve as plasticizing or alloying agents for the higher molecular weight fractions, were selectively removed during the purification process. As so often happens in

research, progress was made in one area at the expense of another.

Thus, solutions to this unexpected challenge had to be found, which included the development of alternative methods of purifying the lignin to retain its desirable properties for melt spinning. This was tackled on several fronts, including the funding of fundamental work at Pacific Northwest National Laboratory (PNNL) and collaborative efforts with several large paper manufacturers, notably MeadWestvaco Corporation (MWV) of Charleston, South Carolina, the only current producer of kraft lignin-based products worldwide. At the same time, work was also implemented to identify suitable plasticizing agents for purified lignins, including SWL, which, because of its chemistry, is not readily melt spinnable. These efforts led to the development of a radically different process for purifying lignins, both hardwood and softwood and, more significantly, the first demonstration (in FY 2007) of continuous and uninterrupted spinning of multifilament lignin fiber tow over a period of many hours.

To support the efforts on the lignin-based carbon fiber project, melt-spinning equipment was custom designed and built for the project and installed at ORNL. The equipment, shown in Figure 2, is the main workhorse for establishing appropriate process conditions for melt spinning of lignin fiber tows and for producing precursor fiber for thermal processing into carbon fiber. The equipment includes a draw frame which permits fibers to be tensioned and hot stretched through a series of rollers to both obtain the desired filament diameter and help align the molecular structure of the precursor fiber to facilitate development of the desired engineering properties in the subsequent carbon fiber.

Before attempts are made to melt spin a lignin material on this equipment, however, it is characterized with respect to its rheological properties, most notably its viscosity and thermal stability at temperatures close to its melting point (above and below). Thermal analysis measurements are carried out to determine the T_g and melting point of the lignin and the temperature range for carbonization and the carbon yield, a very important factor with respect to the economics of carbon-fiber production. When an acceptable understanding of the fundamental properties of a candidate lignin material has been obtained, it is examined for melt spinnability on small, single fiber spinning equipment. If a candidate lignin shows promise for fiber spinning, it is examined on the larger and more effort-intensive multifilament spinning equipment. It is on this equipment that the process boundary limits will be defined for a given lignin and larger quantities of precursor fiber for processing into carbon fiber will be produced.

Figure 2. Multifilament melt-spinning equipment.

Lignin Purification and Fiber Spinning

As noted previously, a laboratory-scale process was developed at ORNL to purify kraft HWL to the required level. However, the laboratory process was not readily scalable to either pilot scale or commercial production, and therefore a joint program of work was implemented by PNNL and MWV to develop an economically viable process for lignin purification (based on the ORNL findings). As laid out in the timeline and tasks for the project, PNNL would focus on the use of combinatorial chemistry techniques to examine the key variables of the proposed process to establish appropriate processing conditions, MWV would scale up the PNNL findings to produce larger samples of purified lignin for melt spinning studies and perform the economic

analysis of the proposed process, and ORNL would carry out the melt-spinning studies.

The first approach to lignin purification at PNNL using an aqueous method proved to be problematic, and MWV was unable to scale up the process and furnish the purified lignin needed by ORNL to move its lignin-based carbon-fiber efforts forward. To overcome this hurdle in the short-term, MWV agreed to reexamine an alternative approach to the purification of kraft lignin that it had investigated several years earlier; namely, extraction of the lignin with organic solvents to dissolve the lignin components away from the insoluble salts, carbohydrates, and other impurities—essentially the opposite approach to the aqueous method.

Early in the fourth quarter of FY 2007, a small sample of the solvent-extracted lignin (SEL) was received from MWV. The rheometry measurements made on the material indicated that it exhibited the desired viscosity-temperature-time relationships and that it should be readily melt spinnable. Examples of the rheometry test data are shown in Figure 3, in which the stability of the MWV SEL product is exemplified by the horizontal line for the plot (circular symbols) of transient viscosity as a function of holding time at a given temperature.

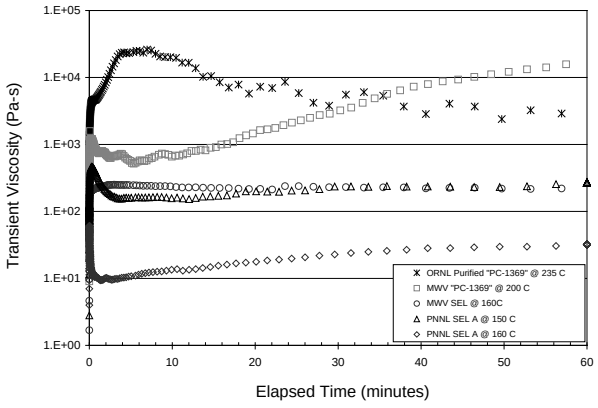

Figure 3. Viscosity of HWL as a function of time (at a given temperature).

In contrast, undesirable rheometry data are exemplified by the upper plot (square symbols) for the MWV HWL (PC-1369) as received, which exhibits an unstable (rising) viscosity as a function of residence time. It was this HWL material that was solvent extracted to produce the SEL product.

The suitability of the MWV SEL product for melt spinning was confirmed through single-fiber melt-spinning tests during which lignin fiber was continually spun onto small spools; in fact, the lignin was the most readily melt spinnable of all the lignin materials examined in the ORNL work to that date. On the basis of these positive findings, MWV committed to the production of kilogram quantities of the purified lignin for testing at ORNL on the multifilament spinning equipment.

The first "large" batch of MWV solvent-extracted (organic-purified) lignin was melt spun in late FY 2007 (August 2007), with very positive results. Once steady-state conditions were established in the extruder, metering pump, and spinneret, 12-filament fiber was continuously spun over several hours without interruption (other than to change take-up spools) and without the need for addition of alloying or plasticizing agents. An example of a spool of the lignin fiber is shown in Figure 4. Emphasis in this first run was placed on establishing the relationship between fiber winding speed and filament diameter, the results of which are summarized in Figure 5.

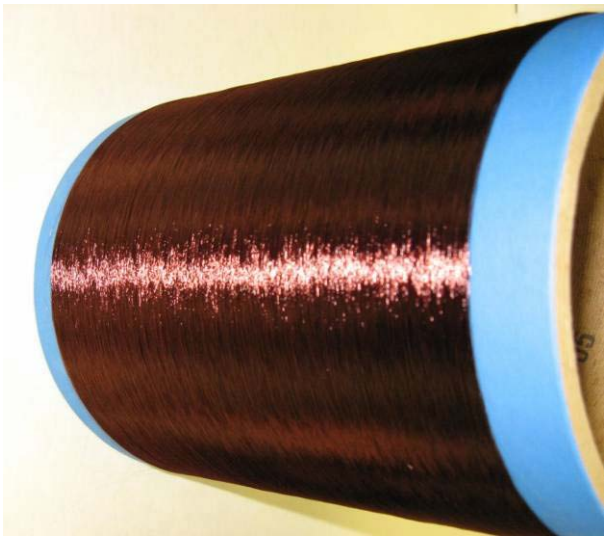

Figure 4. Lignin fiber tow comprising 12 filaments, each 11 μm in diameter.

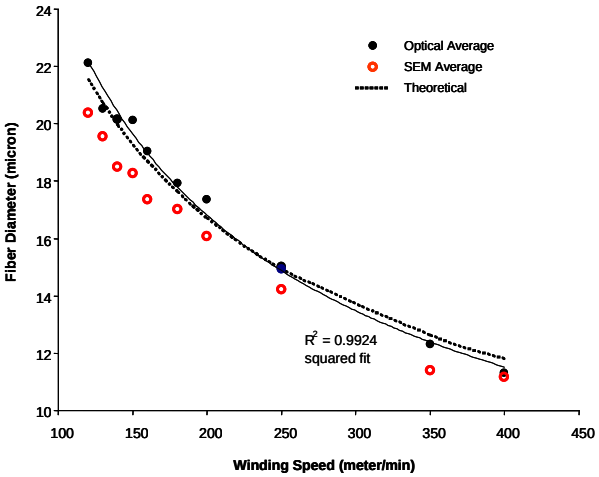

Figure 5. Lignin filament diameter as a function of winding speed.

The maximum fiber winding speed achieved in this first multifilament spinning run was 400 m/min (i.e., 67% of the preliminary target speed of 600 m/min). This was a significant first-time accomplishment. In fact, it was apparent that fiber winding speed could have been increased to at least the preliminary target industrial rate of 600 m/min, but the subsequent increase in draw-down ratio would have resulted in filament diameters substantially below the target of 10 µm (i.e., entering the upper end of the region of filament diameters that present a potential respiratory hazard). In the interest of safety, this particular study of spinning speed was terminated after 5 hours of continuous spinning when the lignin filament approached a visually estimated diameter of 10 µm; optical microscopy and scanning electron microscopy (SEM) measurements of filament diameter were made after the fact.

Representative SEM images of lignin filaments about 15 µm in diameter are shown in Figure 6.

The SEM images revealed that, regardless of filament diameter, the filaments exhibited very uniform diameters, smooth outer surface, and a cross-section structure that was totally devoid of air-entrapment, impurity particles, or other observable defects that could impact the engineering properties of carbon fiber subsequently produced from the precursor fiber. SEM magnifications as high as 20,000× were made, confirming the structural uniformity of the lignin fibers.

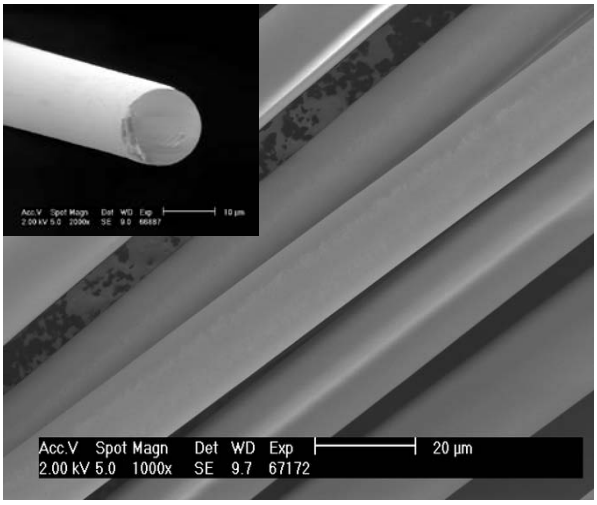

Figure 6. SEM images of lignin precursor fibers.

Subsequent studies of spinning speed targeted a twofold increase in spinning speed over the baseline speed assumed in the Kline economic model (i.e., 1,200 m/min instead of 600 m/min, the spinning speed of commercial mesophase pitch-based fiber). The target speed was achieved using (unpurified) Alcell lignin (q.v.) as the feedstock. This necessitated increasing the mass throughput in the melt extruder and spinneret and increasing the fiber draw-down ratio from 15 : 1 to 25 : 1 so that the target filament diameter of 10 µm could be achieved at the much higher winding speed. Further studies of spinning speed will target yet higher winding speeds and also spinning of 24-filament tow at high rates.

The first of the samples expected from the PNNL-MWV lignin purification program arrived from PNNL in mid-September, too late to make a significant impact on our efforts in FY 2007. However, the initial evaluation indicated that it was readily melt spinnable without an additive. In fact, its thermal and rheological characteristics were very similar to those of the MWV SEL that was so readily melt spinnable. The similarity of the MWV SEL product and the first PNNL material is exemplified by the rheometry data shown in Figure 3, in which the viscosity data for the PNNL lignin are represented by triangle symbols, which are almost directly superimposed

on the plot for the MWV SEL product (circular symbols).

PNNL subsequently confirmed that its first sample of purified lignin was not only produced from the same PC-1369 HWL (i.e., not from black liquor per se) but also was purified by a solvent-extraction approach (not aqueous). Thus, given these commonalities, it is not surprising that the MWV and PNNL purified HWL samples exhibited similar viscosity characteristics and were each readily melt spinnable without the need for a plasticizing additive. Apparently PNNL has refined its solvent-extraction procedure to produce a higher melting point material (a desirable feature) that will be sent to ORNL in the near future for evaluation.

In the meantime, PNNL also scaled up production of an aqueous-purified HWL, an approach that, as mentioned previously, had been problematic through most of the year. A 1-lb sample of the aqueous-purified lignin, produced from the same PC-1369 batch of HWL, was received in the first quarter of FY 2008 (11/9/07). The initial tests indicate that its melting point is in the desired ballpark, namely, around 220°C. However, the rheometer tests indicate that it is not sufficiently stable at this temperature and begins to decompose within a short time span.

Single fiber tests confirmed that the first sample of the PNNL aqueous-purified lignin was not melt spinnable without the aid of a plasticizing agent. Further tests indicated that it may be melt spinnable when blended with an SEL (e.g., either the MWV or PNNL SEL products). These preliminary findings on the PNNL sample of aqueous-purified lignin are consistent with earlier findings on the same batch of HWL purified by ORNL using a similar aqueous approach.

The aqueous approach yields a clean lignin that meets the purity specifications and also exhibits a melting point (at least a “softening point”) at a desirable temperature (around 230°C). However, the purified HWLs produced to date through use of an aqueous procedure are not melt spinnable without a plasticizing agent. Nevertheless, it is a positive development that HWL purified through an aqueous procedure can be melt spun by inclusion of a minor proportion of a readily spinnable SEL. The positive attributes of each are reinforced and the negative aspects essentially eliminated.

Apart from its good purity, a positive attribute of the aqueous-purified HWL is high carbon yield. This is highlighted in Figure 7(a), in which TGA data are shown for ORNL aqueous-purified HWL together with the corresponding data for the unpurified lignin as received. TGA data for an unpurified SWL are included for the purpose of comparison.

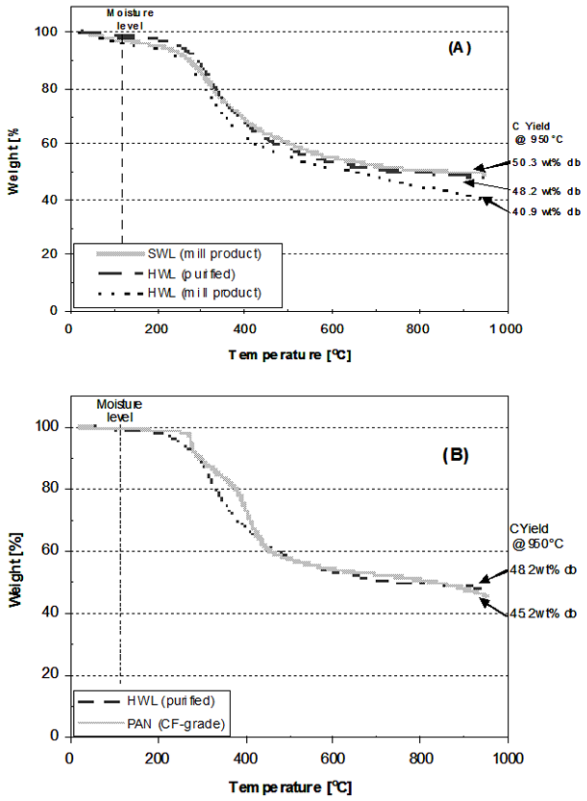

Figure 7. TGA data for lignins (a) and PAN (b).

In Figure 7, carbon yields obtained at 950°C are compared on a dry basis (adjusted for the initial moisture content of the starting material). The beneficial effect of purifying the HWL using an aqueous procedure is discerned from the fact that carbon yield increased from 40.9% to 48.2%. The theoretical carbon content of HWL is about 55–60% (Table 1). For comparison, the yield of carbon obtained from carbon-fiber-grade PAN under the same TGA conditions was 45.2 % [Figure 7(b)]. The negative attribute of the

aqueous-purified lignin is that it is not melt spinnable without the addition of a plasticizing agent.

Table 1. Carbon contents of lignin and PAN

Precursor Material	Theoretical Carbon Content	ORNL TGA Measurement
Hardwood lignin mill product	50–55	40.9
Hardwood lignin (aqueous-purified)	55–60	48.2
Softwood lignin mill product	55–60	50.3
Softwood lignin (aqueous-purified)	60–65	*55* ?
PAN (carbon-fiber grade)	68	45.2

Conversely, the positive attribute (in addition to high purity) of the organic-purified SEL is the fact that it is very readily melt spinnable and can also be used as a plasticizing agent for lignins that are not melt spinnable. The negative aspect of the SEL is relatively low carbon yield. This is apparent from the TGA data shown in Figure 8 for SEL samples.

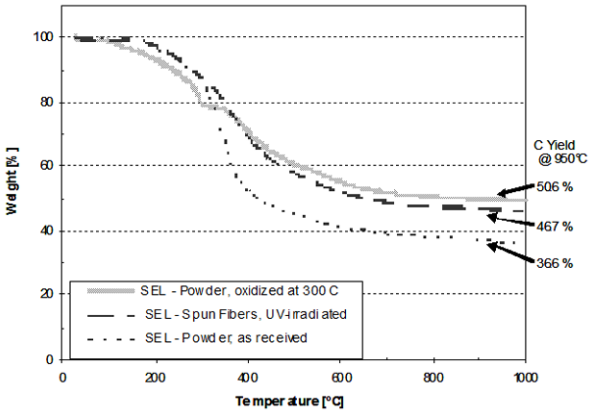

Figure 8. TGA data for fibers produced from MWV SEL.

As received, the SEL powder exhibited a carbon yield of 36.6% at 950°C. Encouragingly, though, when the SEL powder was oxidized with air, in situ at 300°C in the TGA instrument, the carbon yield increased to a respectable 50.6%. This demonstrated that the SEL material is cross-linkable (i.e., there is no thermodynamic barrier to stabilizing the SEL or to achieving high carbon yield from the material). However, the temperature at which the SEL powder was oxidized to obtain a meaningful rate of cross-linking (300°C) was about twice that of the melting point of the lignin (about 140°C) and, therefore, impractical with respect to the production of carbon fibers from the SEL material.

Thus, for SELs to be of practical use with respect to the production of carbon fibers, a viable, alternative approach to stabilization of SEL materials must be identified. Very recent preliminary data in this context are summarized in Figure 8, which shows the TGA data for SEL fibers irradiated with UV light at ambient temperature (25°C) in air. Melt-spun fibers obtained from the multifilament spinning run discussed above were UV irradiated for different lengths of time; the data shown in Figure 8 are those for SEL fibers irradiated for 16 minutes. The carbon yield at the reference temperature of 950°C was 46.7%, indicating that the SEL lignin had cross-linked (oxidized) under the treatment conditions. Although this is a very preliminary finding and must be confirmed through more detailed work, it nevertheless is encouraging that a relatively simple UV treatment of a lignin material will facilitate stabilization of the material in fiber form.

Based on the data obtained to date with respect to the purification and subsequent melt spinnability of kraft HWL, the following general conclusion can be drawn. Aqueous purification procedures are based on the separation of water-soluble contaminants and lignin (alike) at high pH and the subsequent separation of the contaminants and lignin through selective precipitation of the different species upon careful reduction of solution pH. The purified lignin so obtained is a higher molecular weight material in which the lower molecular weight lignin fractions are retained in solution with the salt and other mineral impurities. The lower molecular weight lignin fractions appear to be the plasticizing agent for the

lignin as a whole, and their elimination from the HWL negatively impacts the melt spinnability of the purified lignin.

In marked contrast, organic solvent extraction of lignin purifies the lignin by dissolving the lignin away from the contaminants (mineral and carbohydrate). However, lower molecular weight lignin fractions are preferentially dissolved over higher molecular weight fractions, at least through the organic solvents and process conditions examined to date. Thus, the organic-purified lignin contains a large proportion of the low molecular weight lignin fractions that are plasticizing agents for the lignin as a whole, thereby retaining the melt-spinnability characteristics in the purified lignin. However, because of their lower molecular weight, these fractions depress the average molecular weight of the purified lignin, which is reflected by a melting point too low to permit stabilization of the subsequent fiber at an acceptable rate through conventional thermal processing techniques alone.

Melt Spinning and Production of Carbon Fiber from Unpurified Lignin Materials

The recent commercialization of the LignoBoost process for isolating lignin from kraft black liquor has resulted in much cleaner unmodified kraft lignin material becoming available (i.e., compared to current commercial, unmodified lignin products). The process was developed by STFI-Packforst (Swedish Research Institute) and its partner companies in the project over a 4-year period. The process was developed primarily for the production of lignin fuel pellets, thereby helping to increase paper mill productivity, but is also attracting increasing interest as a means of isolating lignin for production of chemicals and related materials, including carbon fiber. Several large pulp and paper companies around the world are evaluating the process for both purposes. One of these companies, Kruger Wayagamack in Ontario, Canada, has furnished kraft SWL for evaluation for carbon-fiber production.

The work carried out on the Kruger lignin to date has demonstrated that the quality of the SWL is close to the target specification for carbon-fiber production and that the material can be melt spun as-received, at least with the aid of a plasticizing agent (a prerequisite for all unmodified, kraft SWL materials). In the initial work, a 50–50 blend of the Kruger lignin with the solvent-extracted kraft HWL (produced by MWV) as the plasticizing agent was readily melt spun on the multifilament equipment. The carbon fiber produced from the lignin precursor fiber exhibited mechanical properties approaching 50% of target. This was the first time that an unpurified kraft lignin, and more notably an SWL material, had been successfully spun on the multifilament equipment, albeit with the addition of a high proportion of a purified lignin to serve as the plasticizing agent. This represented a significant development with respect to the economics of carbon-fiber production from lignin materials, with the potential for reducing the cost of a lignin-based carbon fiber by 60-80¢/lb. Further work on this lignin material to greatly reduce the proportion of plasticizing agent was placed on hold to permit evaluation of a second source of unpurified lignin materials; namely, the Alcell lignin by-product of the production of cellulosic ethanol fuel.

So-called biomass-derived lignins will become increasingly available from cellulosic ethanol manufacturers as biorefinery programs ramp up to produce ethanol fuel from lignocellulosic materials, such as wood and switchgrass, instead of corn. As mentioned in more detail below, Lignol Innovations is a leading company in this respect and was recently awarded a $30M DOE contract to build a demonstration biorefinery in Colorado. Lignol Innovations uses the Organosolv pulping process to separate cellulose and lignin in lignocellulosic materials; this process uses a small proportion of the ethanol that is subsequently produced from the cellulose through enzymatic hydrolysis as the pulping solvent. Lignol Innovations was contacted, and the company furnished 200 lbs of its Alcell lignin product to the FreedomCAR program for evaluation for carbon-fiber production.

Conditions were established to remove traces of residual solvents from the Alcell lignin, and rheology and thermal analysis measurements were made to establish melt-spinning conditions. Fibers were readily melt spun on the multifilament

equipment, from the lignin as-received and without the need for a plasticizing additive, and conditions were established for processing the precursor fibers into carbon fibers. The mechanical properties of the Alcell lignin-based carbon fibers are currently falling well short of the target properties (approaching 50% of target), but each new spinning run on the Alcell material has resulted in a greater understanding of the properties of this very different but promising type of lignin. One important characteristic of the Alcell lignin is its higher T_g and melt-spinning temperature, which enable the fiber stabilization stage of processing to be carried out at a significantly higher temperature (i.e., faster rate) than possible for the high-purity kraft HWL (solvent extracted) on which much of the process development efforts this fiscal year were focused.

Pending further improvements in the quality of the Kruger SWL, the efforts in the second half of FY 2008 were focused on the Alcell lignin, the quality of which more than met the specifications for carbon-fiber production. These efforts included melt-spinning speed trials in which it was demonstrated that the melt-spinning speed of lignin can be increased to at least twice the baseline speed assumed in the Kline economic model [i.e., 1,200 m/min vs the baseline speed of 600 m/minute (the spinning speed of commercial mesophase pitch-based fibers)]. Thus, in addition to the advantage of being able to use a lignin material without the need for (relatively expensive) purification, increases in the spinning speed of this magnitude will also have a beneficial impact on the economics of carbon fiber from lignin materials. Demonstration of spinning speeds greater than 1,200 m/min is dependent on upgrading the winder on the multifilament spinning equipment.

Finally, to place into perspective the quality of the key lignin materials examined in the work during FY 2008, some of the elemental analysis data obtained on each of the relevant lignin materials are summarized in Table 2.

The elemental analysis and ash data in Table 2 clearly demonstrate the superiority of the Alcell (Organosolv) lignin, as-received, with respect to purity, most notably in contrast with the commercial kraft HWL product. When discussing lignin quality, however, it should be noted that the commercial kraft lignin product in question is an unmodified lignin (i.e., in the form as isolated from black liquor). Relatively little of the lignin is sold in this form, and that which is sold for commercial applications meets the quality needs of the customers. The majority of kraft lignin products are chemically modified forms of the lignin isolated from black liquor (e.g., sulfonated derivatives for use as dispersants). The processes of modification result in very much higher quality kraft lignin products with much lower residual salt contents. From both chemistry and cost standpoints, however, the modified kraft lignins are not suitable for carbon-fiber production.

Table 2. Elemental analysis of lignins

Lignin Material	C (%)	S (%)	Na (ppm)	K (ppm)	Ca (ppm)	Ash (%)
HWL	59	2.45	19,000	1770	650	2.8
HWL-Aq	65	1.48	73	70	255	0.05
HWL-SE	65	1.40	1,160	104	76	0.01
SWL-K2	67	1.18	2,390	100	78	0.2
Alcell	66	0.05	17	44	163	0.001

HWL = MWV hardwood lignin as received
HWL–Aq = Hardwood lignin aqueous purified by ORNL
HWL–SE = Hardwood lignin solvent extracted by MWV
SWL-K2 = Kruger softwood lignin as received (2nd sample)
Alcell = Lignol Innovations (Organosolv) lignin as received

Summary of Progress on the Lignin Project in FY 2008

Progress made on the lignin project over the past year included the following.

- For the first time, multifilament lignin fiber tow was successfully melt spun, continuously and for extended periods of time, from unpurified lignin materials, including SWL and Organosolv lignin (i.e., from lignin materials which, as isolated from biomass, were either close to or exceeded the purity specifications for melt spinning and carbon fiber production).
- Target diameter fiber (10 μm) was produced at the Kline economic model baseline speed of 600 m/min. Melt-spinning speed was successfully increased to 1,200 m/min, the limit of the winding equipment, producing a fiber diameter less than 10 μm.

- Preliminary data obtained indicate that melt-spun lignin fibers can be quickly stabilized through UV irradiation in air at 25°C.
- It was demonstrated that kraft HWL purified using an organic solvent-extraction procedure is not only readily melt spinnable but can also be used as a plasticizing agent for other lignins that are not inherently melt spinnable.
- A sounder understanding of the factors that influence the melt spinnability of lignin materials was achieved.
- Thermally-processed precursor fibers melt spun from different types (and sources) of lignin were processed into carbon fiber. Mechanical properties of the carbon fibers currently fall in the range of 45–60% of target, but several possible causes have been identified, including inadequate compounding of powder lignin into the pellets required as the feedstock for the spinning operation.
- Additional sources of lignin materials were identified, including kraft SWL from Kruger Wayagamack and STFI-Packforst (Sweden), and Organosolv lignin from Lignol Innovations (a by-product of cellulosic ethanol production).

Lignin Sources for Continued Development Work

Following the merger of Mead and Westvaco in 2002, the business direction of the new corporation has been toward packaging and land development and away from the production of paper and specialty chemicals. Many of the new corporation's pulp and paper operations have been sold (including the Charleston, South Carolina mill that is the company's sole source of kraft lignin), and divestiture of its specialty chemicals business is possibly part of MWV's long-term business strategy. Thus, even before the company's decision toward the end of FY 2007 to terminate all its long-term research efforts, including its support of the LCCF project, it was clear that an alternative industrial partner would need to be found.

Kruger Wayagamack, Inc., Quebec, Canada

Kruger Wayagamack is a large Canadian-based pulp and paper producer that also uses the kraft process for the pulping of wood (predominantly softwood in Canada). Almost 2 years ago, Kruger made it clear that it was interested in isolating lignin for much the same reason as Weyerhaeuser; namely, to "debottle" its recovery-constrained mills and increase pulp production. To increase small profit margins and stave off competition from China, many pulp and paper companies wish to increase pulp production and throughput of paper in their mills but are largely unable to do so because the mills concerned are not able to also increase recovery of the pulping chemicals (new recovery boilers are very capital intensive). Thus, some mills are seeking to isolate lignin from the black liquor, largely for use as a fuel in other operations but also as a potential source of valued-added products. Kruger, for example, is initially targeting the production of fire logs, an application that has a value of about 20¢/lb of lignin. At a potential price of 50¢/lb, sale of lignin for LCCF production is of substantial interest to Kruger. Kruger is evaluating the LignoBoost lignin isolation technology from STFI-Packforsk, the Swedish Research Institute. As a point of information, the LignoBoost process was developed to produce a lignin-based biofuel, and Weyerhaeuser is one of the industrial stakeholders in LignoBoost process development efforts under a 4-year (2005–2008) research and development program titled, "Future Resource Adapted Pulp Mill—step 2" ("FRAM 2"). Thus, both Weyerhaeuser and Kruger may well be producing lignin from kraft black liquor using the same lignin isolation technology.

Kruger senior management gave the forma1 go-ahead for mill trials this year, a significant financial commitment. As part of this effort, the company is constructing a pilot-scale lignin-isolation plant with a capacity of 100 kg/day, which is expected to be onstream in 2009. Thus, we have another pulp and paper manufacturer on-board that is willing to furnish ORNL with kraft lignin for the LCCF efforts. Needless to say, this will not be without its own challenges, not the least of which is that the lignin is softwood-based (as is Weyerhaeuser's lignin) and thus is not melt spinnable without the aid of a plasticizing agent (or chemical modification). However, we have learned a great deal about spinning lignin materials over the past year, which will help us to

continue to move forward with new sources of lignin as a precursor material for carbon-fiber production, notably those lignins that do not require purification for this purpose.

We have already demonstrated that the first two samples of Kruger's lignin (the solvent-extracted HWL discussed above) are melt spinnable with a plasticizing additive. Furthermore, based on an analysis of the second sample received from the company (5 kg), the purity of the Kruger lignin is approaching the desired specifications and is certainly much better than that of the commercial, unmodified kraft lignin product from MWV with which we have worked to date. Refinement of the isolation procedure (e.g., through incorporation of additional washing stages) is expected to result in a lignin material meeting the purity specifications without the need for subsequent purification. This would represent a very distinct economic benefit with respect to LCCF production.

Weyerhaeuser Company, Washington

Under a Cooperative Research and Development Agreement for a separate project, Weyerhaeuser has sent sample kraft SWL to ORNL for evaluation for LCCF production. Apparently, it has been demonstrated that the Weyerhaeuser SWL is melt spinnable with the addition of a plasticizing agent, at least on a single fiber scale, and that carbon fibers can be produced from the precursor lignin fiber. This is consistent with the preliminary evaluation of the Kruger SWL under the FreedomCAR program, a kraft lignin believed to have been isolated using the same LignoBoost technology. Weyerhaeuser has indicated that it is willing to provide samples of its lignin to the FreedomCAR program for multifilament melt-spinning evaluation and carbon-fiber production but has yet to furnish the material. Access by the FreedomCAR program to Weyerhaeuser lignin is considered to be an important element of future efforts on the FreedomCAR LCCF program.

STFI-Packforst (Swedish Research Institute)

STFI-Packforst developed the LignoBoost process for isolating lignin from kraft black liquor for the primary purpose of producing fuel pellets and for enhancing the productivity of kraft pulp mills. However, increasing attention is being given by several pulp and paper companies to use of the kraft lignin for production of value-added chemicals, including carbon fiber. STFI-Packforst has carried out preliminary work on the melt spinning of lignin fibers and conversion into carbon fibers. As a result, STFI is interested in collaborating with ORNL on the use of kraft lignin for LCCF production. STFI is the leading research institute with respect to the science and technology of lignin materials and will bring to the table considerable expertise in this area. This, in turn, will allow ORNL to focus on the development of processes for converting lignin into carbon fiber.

Following a recent visit to ORNL by STFI (October 10), STFI has to date identified five pulp and paper companies interested in collaborating on the project, initially through furnishing kraft lignin products (meeting the purity specification) for evaluation. STFI will carry out the detailed characterizations of the lignin materials, which will add to our current database and help to better correlate lignin properties, notably chemistry, with melt spinnability and carbon-fiber quality. Further discussions with STFI-Packforst regarding collaboration will be held during the DOE workshop on carbon fiber at ORNL, tentatively proposed for January 21–22, 2009.

Lignol Innovations Ltd., British Columbia, Canada

Lignol Innovations, a wholly-owned subsidiary of the Lignol Energy Corporation, is building biorefineries in Canada for the production of ethanol fuel and other products from lignocellulosic biomass, notably waste wood. Lignol has improved on the process originally developed by General Electric and further refined by Repap Enterprises, Inc., from which the Alcell lignin product was produced. It has been known since the earliest days of the LCCF project at ORNL that the Alcell lignin product (derived from hardwood) is relatively pure as isolated and is readily melt spinnable. However, the Alcell product was unable to compete with commercial lignin products produced from conventional chemical pulping, and Repap consequently ceased business operations. With the greatly increased emphasis on the production of cellulosic ethanol,

however, there is renewed interest in finding markets for the lignin by-products from cellulosic ethanol operations, and Lignol Innovations regards LCCF production as an attractive potential market for its lignin product.

Other Biomass-Derived Lignins

Biomass-derived lignins will become increasingly available from other cellulosic ethanol programs around the world, most notably from the University of Tennessee (UT), Knoxville joint venture with ORNL. We anticipate getting in on the ground floor of the new UT-ORNL program with respect to evaluating the lignin produced in this particular biomass-to-ethanol research work. The economics of any biomass-to-ethanol process will partially depend on what is done with the lignin by-product from the process, which could account for upwards of 35% of the mass input of the biomass. Certainly, it will not be acceptable either environmentally or economically to landfill the lignin, and burning it for energy is worth only about 5¢/lb, even based on today's oil price of nearly $70/barrel.

Purification of Lignin Materials

The need to purify lignin materials to make them suitable for melt spinning and carbon-fiber production has been superseded as a result of the project findings this year. Elimination of a purification step will significantly reduce the cost of lignin-based carbon fiber by an estimated 60-80¢/lb.

It was clearly demonstrated in FY 2008 that it is possible, under appropriate process conditions, to isolate lignin with the required state of purity from the black liquor of commercial kraft pulping of softwood for the production of pulp and paper. Furthermore, even cleaner and more readily melt-spinnable lignins are becoming available from the production of cellulosic ethanol fuel from lignocellulosic materials, such as wood and switchgrass. Thus, the following discussion of the lignin purification processes evaluated is largely included for the record.

Solvent-Extracted Lignins

Both the MWV and PNNL solvent-extracted HWL materials exhibited excellent melt-spinnability characteristics, especially the former. The downside to these particular SEL materials is their low melting point of about 140°C, which is fine from a melt-spinning standpoint but is too low to stabilize spun fiber at an acceptable rate using conventional thermal processing techniques. Nevertheless, it was demonstrated that the MWV SEL will readily crosslink at temperatures above its melting point, resulting in a substantial increase in carbon yield (from 37 to 51%). It was also demonstrated that UV irradiation of the MWV SEL fiber at ambient temperature (25°C) over a short period of time (16 minutes) resulted in a similar, substantial increase in carbon yield, indicating the potential for UV stabilization of fibers produced from such lignins. Furthermore, both the MWV and PNNL SELs were useful plasticizing agents for other, non-melt-spinnable lignins, including those purified using an aqueous procedure.

Thus, some efforts to exploit the beneficial characteristics of lignins purified using a solvent-extraction process will be continued, particularly if it is demonstrated that, through refinement of the procedure, the melting point of such lignins can be raised to near the desired level of about 250°C. However, efforts at ORNL in this respect will be limited to evaluation of SELs (i.e., the work will not encompass lignin purification per se). PNNL is considering extending its work in this respect, and other entities may be interested in picking up the MWV work.

About 5 tons of the PC-1369 HWL, produced by MWV in support of the LCCF project at ORNL, are available for sale. If new findings are developed that indicate that the molecular weight and melting point properties of an SEL could be enhanced through refinement of the solvent-extraction procedure (e.g., choice of solvents), then it would be appropriate to consider funding of a solvent-extraction purification run by the toll processor identified by MWV for this purpose. Furthermore, it would be advantageous to have SEL on hand for use as a plasticizing agent for other purified lignins that are not readily melt

spinnable (about 2 kg of SEL is currently on hand for this purpose).

Kraft lignin exhibits antioxidant properties because it is a radical scavenger (e.g., it has been tested for the treatment of certain cancers). It readily absorbs UV radiation and, as noted above, UV irradiation may be a viable route to stabilizing SELs as currently produced. In addition, an evaluation should be made of whether the SEL material could be satisfactorily stabilized using other advanced processing techniques, including plasma treatment or incorporation of a catalyst to promote oxidative stabilization of the spun fibers at temperatures below their melting point of about 140°C.

PNNL-Produced Lignin Materials

Apparently, PNNL may have overcome the difficulties encountered in the early part of the PNNL-MWV program to purify HWL using an aqueous procedure, and has produced purified material for evaluation. Similarly, PNNL may have refined its organic solvent-extraction procedure to produce a purified HWL of higher molecular weight and melting point. If so, both of these HWL materials should be evaluated for melt spinnability and production of multifilament tow. Needless to say, though, PNNL is not in a position to furnish the quantities of purified lignin required for multifilament melt spinning; someone else must scale up the PNNL process.

Project Deliverables

By the end of this multiyear program, production of carbon fibers suitable for transportation use, from one or more economically feasible, renewable resource materials, will have been demonstrated and the transfer of production technologies and related intellectual property to industry implemented.

Awards/Presentations/Publications/Patents

Awards

American Carbon Society Graffin Lecturer for 2008/2009

The American Carbon Society's Graffin Lectureship is endowed by Asbury Carbons in honor of George D. Graffin, a pioneer in the natural graphite industry. Each year, the American Carbon Society selects a lecturer who has made distinguished contributions to carbon science and engineering. The lecture is made available to North American universities, companies, and government agencies by arrangement with the lecturer, and all travel expenses for the lecture tour are picked up by the American Carbon Society. The Graffin Lecture for the 2008/2009 period is "*Nanoporous Carbon Materials—How They Benefit Our Lives and the Environment.*"

Presentations

1. Darren A. Baker, Nidia C. Gallego, and Frederick S. Baker, "Carbon Fiber Production from a Kraft Hardwood Lignin," Fiber Society Annual Meeting and Technical Conference, Boucherville, Quebec, Canada, October 1–3, 2008.
2. C. David Warren et al., "Multitask Research Program to Develop Commodity Grade, Lower Cost Carbon Fiber," SAMPE Conference, Memphis, Tennessee, September 8–11, 2008.
3. Frederick S. Baker and Nidia C. Gallego, "Lignin-based, Low-cost Carbon Fiber," Invited Paper, Boeing Fiber Workshop, Seattle, Washington, July 23–25, 2008.
4. Frederick S. Baker, "A Carbon Cycle: Use of Biomass-based Carbon Fiber Materials for Reduction of Carbon Emissions to the Environment," Invited Plenary Lecture, CARBON 2008 Conference, Nagano, Japan, July 13-18, 2008.
5. Frederick S. Baker, "Production of Carbon Fibers from Renewable Resource Materials," Invited Seminar (3-hour) at Buckeye Technologies, Inc., Memphis, Tennessee, June 20, 2008.

Publications

1. Trishelle Copeland-Johnson (student intern) et al., "Viscoelastic Properties of Alcell Lignin for Carbon Fiber Production," submitted to DOE for consideration for publication in the *Journal of Undergraduate Research*, August 2008. (Trishelle received the 2nd place award

in the SERch competition for her poster on her project at ORNL.)

United States Patents (those patents involving carbon fibers)

1. "Lightweight, Durable Lead-Acid Batteries," Edgar Lara-Curzio, Ke An, Jim Kiggans, Nancy J. Dudney, Cristian I. Contescu, Frederick S. Baker, and Beth L. Armstrong, Application filed May 2008 (UT-Battelle).
2. "Rotary Adsorbers for Continuous Bulk Separations," Baker, Frederick Stanley; US-2008-0047436, Application published February 28, 2008 (UT-Battelle).
3. "Activated Carbon Fibers and Engineered Forms from Renewable Resources," Baker, Frederick Stanley; US-2007-0142225, Application published June 21, 2007 (UT-Battelle).

B. Advanced Stabilization of Polyacrylonitrile Fiber Precursor

Principal Investigator: Felix L. Paulauskas
Oak Ridge National Laboratory
P.O. Box 2008, Oak Ridge, TN 37831-6053
(865) 576-3785; fax: (865) 574-8257; e-mail: paulauskasfl@ornl.gov

Participants:
Christopher J. Janke, Amit K. Naskar, Soydan Ozcan, and Cliff Eberle
Oak Ridge National Laboratory

Truman Bonds
Atmospheric Glow Technologies

Professor Roberto Benson
University of Tennessee

Marshall Cleland and Rick Galloway
IBA Group-Radiation Dynamics Inc.

Technology Area Development Manager: Joseph A. Carpenter
(202) 586-1022; fax: (202) 586-1600; e-mail: joseph.carpenter@ee.doe.gov

Field Technical Monitor: C. David Warren
(865) 574-9693; fax: (865) 574-6098; e-mail: warrencd@ornl.gov

---

Contractor: Oak Ridge National Laboratory (ORNL)
Contract No.: DE-AC05-00OR22725

Objectives

- Develop an improved technique for stabilizing carbon fiber (CF) precursor with increased line speed and reduced CF cost.
- Verify that finished fiber properties satisfy automotive and heavy vehicle manufacturers' requirements.
- Conduct a preliminary evaluation of the cost impact of the new stabilization technique.
- Integrate the stabilization module into an advanced technology pilot line.

Approach

- Develop plasma processing as the primary stabilization route for the conversion factory.
- Develop electron-beam (E-beam) processing as the preferred stabilization route for implementation at a precursor factory.
- Integrate plasma stabilization and plasma oxidation into a single process module.
- Conduct parametric studies to correlate processing parameters and fiber properties.
- Determine process parameters that minimize residence time.
- Characterize fibers to confirm that they satisfy program requirements.

Accomplishments

- Initiated integration of plasma stabilization and plasma oxidation into a single experimental reactor module.
- Constructed and commissioned a multi-tow plasma reactor for stabilization and oxidation.
- Commenced operation and obtained first experimental results from multi-tow plasma reactor.
- Initiated discussions with a precursor manufacturing partner regarding in-line E-beam stabilization at the precursor factory.
- Conducted experiments to characterize free radical concentration in E-beam stabilized precursor.
- Successfully developed and executed a plan for recovering from the loss of a key partner, resuming experimental operations within two fiscal quarters.

Future Direction

- Complete integration of stabilization and oxidation into one module.
- Scale the integrated plasma stabilization/oxidation process to achieve high speed, multiple large tow, semicontinuous (multiple pass) plasma stabilization-oxidation process.
- Conduct parametric studies and fiber characterization to better understand process effects and the processing window and to quantify fiber properties.
- Investigate stabilization of alternative precursors.
- Integrate plasma stabilization into an advanced technology pilot conversion line.
- Develop E-beam stabilization for implementation at a precursor factory.

Introduction

The purpose of this project is to investigate and develop a technique to rapidly and inexpensively stabilize a polyacrylonitrile (PAN) precursor. New processing techniques are being developed for the purpose of reducing the cost of CF conversion. Previous and ongoing research at ORNL demonstrated that plasma processing shows great promise for inexpensively and rapidly oxidizing, carbonizing, and graphitizing polymer precursors to convert them to CFs. Initial results indicated that the precursor needed to be lightly stabilized, or cross-linked, before it could be subjected to plasma oxidation. Stabilization and oxidation together are estimated to represent ~18% of the cost of commercial grade CF [1]. A rapid, inexpensive, and robust stabilization technique is needed to complement the aforementioned advanced processing modules and enable the development of an integrated advanced technology conversion line that converts polymer precursor fibers into CFs at significantly lower cost than conventional conversion technology.

This project therefore intends to develop an advanced stabilization module that integrates with other advanced fiber processing modules to produce inexpensive CF with properties suitable for use by the automotive industry. Critical technical criteria include (1) ≥25 Msi tensile modulus and ≥1.0% ultimate strain in the finished fiber, (2) uniform properties along the length of the fiber tow, (3) repeatable and controllable processing, and (4) significant unit cost reduction compared with conventional processing.

Project Deliverable

At the end of this project, the project team will have demonstrated satisfactory PAN precursor fiber stabilization with residence time well below that typical of conventional CF conversion lines. The project deliverable is a process specification that will enable the commencement of scaling experiments aimed at development of a subscale, multiple large tow, advanced technology pilot line.

Technical Approach

At the start of the project, a successful plasma-based stabilization process had not been discovered, so researchers investigated three other prospective PAN precursor fiber stabilization routes, E-beam processing, thermochemical processing, and ultraviolet (UV) processing, while simultaneously continuing to work on developing a plasma-based process. In fiscal year (FY) 2007, the project team finally discovered a plasma-based recipe that rapidly and effectively stabilized the virgin precursor fibers. At the end of FY 2007, plasma stabilization was selected as the preferred stabilization route, and E-beam stabilization was kept as a backup option for implementation at the precursor factory.

The selected stabilization processes must be effectively integrated with the plasma oxidation process. As shown in Figure 1, the stabilization-oxidation interface may not be precise. It can be affected by the process routes and parameters. Ideally, stabilization will require minimum residence time with the interface moved as far to the left (Figure 1) as possible to minimize the total residence time for both processes combined.

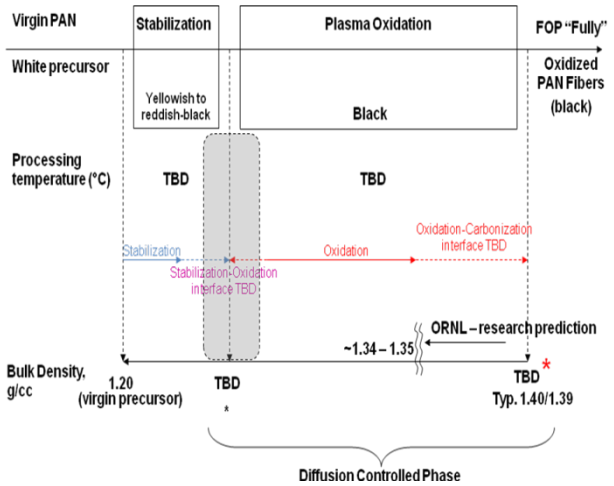

Figure 1. Stabilization-oxidation diagram showing the uncertain interface position.

Progress

Detailed design and process data are not disclosed in this report due to export control restrictions. They are periodically reported to the program managers and partners in compliance with the export control restrictions. Table 1 shows abbreviated data on the experiments with UV, E-beam, and thermochemical stabilization processes.

Table 1. Selected data from experiments with various stabilization routes

Precursor type	Density (g/cc)		Residence time (min)
	Initial	Final	
Virgin Hexcel	1.19	1.33–1.34	26
	1.33–1.34	1.37–1.38	27 (total 53 min)
Lightly prestabilized (conventionally processed) (residence time 23 min)	1.22–1.23	1.35–1.36	26 (total 49 min)
UV pretreated	~1.19	1.34–1.35	26
	~1.19	1.35–1.36	26
	~1.19	1.33–1.34	26
	~1.19	1.33–1.34	26
E-beam pretreated	~1.19	1.23–1.24	26
	1.27–1.28	1.36–1.37	27 (total 53 min)
	~1.19	1.27–1.28	26
	1.23–1.24	1.36–1.37	27 (total 53 min)
	~1.19	1.28–1.29	26
	1.28–1.29	1.37–1.38	27 (total 53 min)

Plasma Stabilization

The discovery of an effective plasma stabilization process and its selection as the baseline stabilization route enabled the seamless integration of stabilization and oxidation into a single process module. Figure 2 shows selected differential scanning calorimetry (DSC) thermograms for plasma stabilization (labeled “direct oxidized” in the figure). Based on these data, plasma stabilization was selected as the preferred stabilization route. Therefore, the major stabilization accomplishment during this reporting

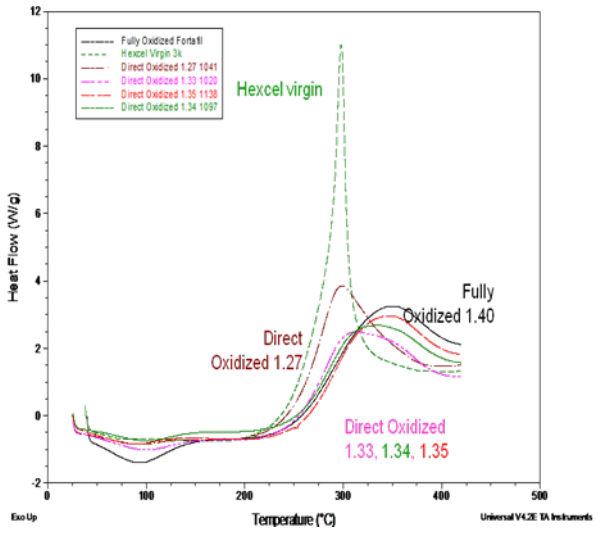

Figure 2. Selected DSC thermograms from plasma stabilization experiments.

period was the commencement of integration of the plasma stabilization and oxidation processes and equipment. Plasma stabilization seamlessly integrates with plasma oxidation and each requires less than one-third of the conventional process residence time. The researchers completed construction and initial operation of the first multi-tow reactor for the integrated plasma stabilization-oxidation module. Reactor construction was completed in early February, immediately followed by operational tests and "sweetening." By the end of March, the project team had achieved single-tow line speed in the multi-tow reactor roughly equivalent to that previously demonstrated in the single-tow reactor. Multi-tow operation has not yet been attempted.

In the preliminary series of experiments, plasma stabilized fibers were successfully oxidized at higher level in a simultaneous operation using the new reactor.

Electron Beam Stabilization

E-beam stabilization delivers very high throughput (line speed) potential, with the electron irradiation step completed in seconds. It can potentially be implemented in-line in a precursor factory. Electron spin resonance (ESR) data (Figure 3) indicate that electron irradiation generates free radicals, which are the probable source of thermal runaway when E-beam stabilized fibers are

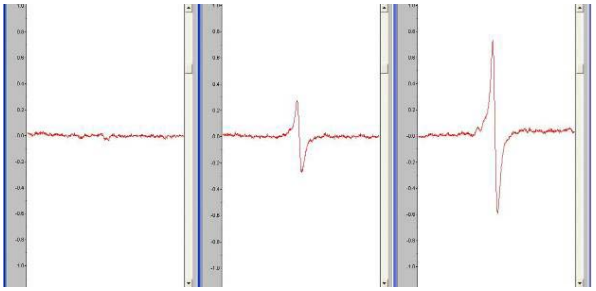

Figure 3. ESR traces, with dose increasing from left (unirradiated) to right. Higher peak indicates higher free radical concentration.

exposed to atmospheric pressure plasma or its chemically reactive exhaust. The project team is working to develop an approach to resolve, or perhaps even exploit, the free radical generation. Irradiation experiments were conducted with in situ ESR at the University of Notre Dame's Department of Energy-funded radiation laboratory to better characterize the free radical generation and test potential approaches to control it. The test results are tabulated in Table 2. Initial results based on the data obtained at the University of Notre Dame (Figure 4) indicate that the population of free radicals in E-beam irradiated PAN fiber gradually decreases with exposure of the irradiated fibers in a slightly elevated temperature environment. This supports our initial finding of a fiber annealing requirement prior to oxidation of irradiated PAN tow.

Table 2. ESR spectroscopy test matrix

Run No.	Sample ID	Irradiation	ESR scan Temperature (°C)	Environment
1	Hexcel PAN	Yes	25	Air
2	Alanine	Yes (dose calibration)	25	Air
3	Hexcel PAN	Yes	100	N_2 then Air
4	Hexcel PAN	No	100	N_2 then Air
5	PAN (homopolymer)	No	25	Air
6	Hexcel PAN	Yes	150	Air
7	Hexcel PAN	No	150	Air
8	Textile PAN	No	25	Air

Initial results were obtained on evolved gas analysis from a thermogravimetric analyzer (TGA) during aerial oxidation of neat PAN fibers and those pretreated with E-beam and UV radiation. An abrupt evolution of gases like CO_2 and NH_3 in the cases of neat PAN and UV treated PAN was observed. On the other hand, E-beam treated PAN

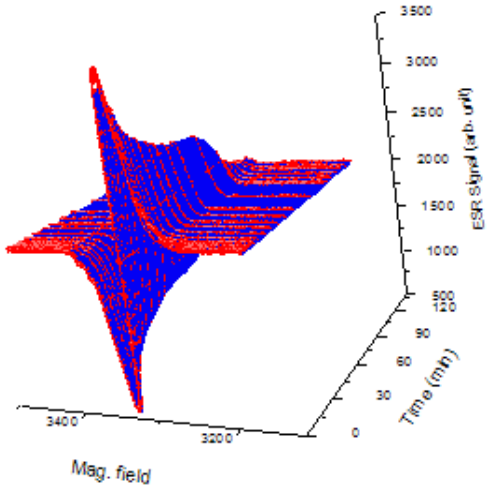

Figure 4. ESR spectra of irradiated PAN fibers during annealing at a temperature below that of oxidation.

did not show any abrupt release of gases. This result was also supported by TGA weight loss rate during the initial part of oxidation. This study proved E-beam irradiation actually stabilized the PAN molecular structure. However, E-beam caused generation of macro-free radicals which accelerated oxidation at elevated temperature. This suggests controlling the reaction by reducing dosage and using suitable additives in PAN composition. At a lower temperature than that at which vigorous oxidation takes place, the level of free radicals generated by E-beam undergoes time dependent decay. Therefore, well controlled oxidation of E-beam treated PAN will be a potential route for rapid oxidation of CF precursors.

At least one prospective precursor manufacturing partner has indicated interest in using E-beam stabilization in the precursor factory. ORNL, its irradiation partner IBA Industrial, Inc., and the precursor manufacturer met at IBA's U.S. headquarters and have begun initial discussions to assess equipment parameters and investment scenarios.

Future Direction

We will focus our primary efforts on the development of plasma stabilization, its integration with plasma oxidation, and scaling of the plasma stabilization-oxidation technique. We will also continue development of E-beam stabilization as an option that can be implemented at the precursor factory or a toll processing facility upstream of the conversion factory.

Patents and Publications

There was no new patent or publication activity during this period.

Education

University of Tennessee materials science graduate students are providing characterization and evaluative support to this project (mainly on oxidized fiber samples) under the guidance of Professor Roberto Benson.

Partners

ORNL gratefully acknowledges the following partners that have made valuable contributions to this project.

- Atmospheric Glow Technologies (AGT)—plasma equipment design and processing (subcontract).
- Automotive Composites Consortium—programmatic and technical direction (complimentary).
- Hexcel Corporation—raw materials and technical consultation (complimentary).
- IBA Industrial, Inc. (formerly Radiation Dynamics Inc.)—irradiation analysis, protocols, and beam time (complimentary).
- Sentech—plasma equipment design and processing (subcontract).
- TohoTenax America—raw materials and technical consultation (complimentary).
- University of Tennessee—characterization (subcontract).

About midyear it became apparent that our key plasma processing partner, AGT, was in a state of acute financial distress. We had previously considered courses of action in case of such an event, and it became necessary to plan and execute an alternative project approach that did not depend on AGT as a partner. Extensive inventories and documentation of assets and experimental data were completed. We investigated the following options: (1) finding another partner with atmospheric pressure plasma processing expertise,

(2) acquiring the key employees and assets to make all of the plasma oxidation research internal to ORNL, and (3) acquisition of key AGT employees and assets by another private entity that would assume AGT's former role. The second and third options were pursued in parallel, with the final solution being that Sentech, Inc., hired the key AGT employees, acquired AGT's relevant assets, and subcontracted with ORNL to assume AGT's former role. A contract with Sentech was signed at the end of FY 2008, and experimental operations were resumed at the former AGT premises. Those premises are currently shared with another company that acquired other portions of AGT's business, assets, and employees, and there are some problems with the arrangement that have to be resolved before we are able to restore fully effective experimental operations. We are currently able to conduct experimental operations, but with some inconveniences and limitations that we expect to resolve in the first half of FY 2009.

Conclusions

The plasma stabilization process has been integrated with plasma oxidation. A multi-tow reactor was constructed and commissioned, and we initiated scale-up of the integrated plasma stabilization-oxidation process. E-beam stabilization is being developed as an option for high throughput cross-linking in the precursor factory.

Reference

1. S. M. Cohn and S. Das, "A Cost Assessment of Conventional PAN Carbon Fiber Production Technology," Energy Division, Oak Ridge National Laboratory (unpublished draft, 1998).

C. Advanced Oxidation of Polyacrylonitrile Fiber Precursor

Principal Investigator: Felix L. Paulauskas
Oak Ridge National Laboratory
P.O. Box 2008, Oak Ridge, TN 37831-8048
(865) 576-3785; fax: (865) 574-8257; e-mail: paulauskasfl@ornl.gov

Participants:
Cliff Eberle, Amit K. Naskar, Soydan Ozcan, and Kenneth D. Yarborough
Oak Ridge National Laboratory

Professor Joseph Spruiell
University of Tennessee

Truman Bonds
Atmospheric Glow Technologies

Technology Area Development Manager: Joseph A. Carpenter
(202) 586-1022; fax: (202) 586-1600; e-mail: joseph.carpenter@ee.doe.gov

Field Technical Monitor: C. David Warren
(865) 574-9693; fax: (865) 574-6098; e-mail: warrencd@ornl.gov

---

Contractor: Oak Ridge National Laboratory (ORNL)
Contract No.: DE-AC05-00OR22725

Objectives

- Develop an improved technique for oxidizing carbon fiber (CF) precursor with reduced residence time, CF cost, and equipment footprint.
- Verify that finished fiber properties satisfy automotive requirements.
- Provide data for the preliminary evaluation of the cost impact of the new oxidation technique.
- Investigate interfaces and compatibility with other advanced conversion processes.

Approach

- Develop a process for polyacrylonitrile (PAN) precursor oxidation using atmospheric-pressure plasma.
- Develop fiber handling protocols for continuous processing.
- Conduct parametric studies and perform diagnostics to correlate processing parameters and fiber properties.
- Characterize fibers to confirm that they satisfy program requirements.

Accomplishments

- Characterized decomposition profiles of the key reactive oxidative species.
- Constructed and commissioned first multi-tow plasma oxidation reactor.
- Commenced operation and obtained initial experimental results from multi-tow plasma oxidation reactor.

- Commenced integrating stabilization and oxidation into a single plasma-based conversion module.
- Successfully developed and executed a plan for recovering from the loss of a key partner, resuming experimental operations within two fiscal quarters.

Future Direction

- Continue refining and scaling the reactor design and processing protocols to achieve high speed, multiple large tow, semicontinuous (multiple pass) plasma oxidation process.
- Complete integration of plasma stabilization and plasma oxidation into a single conversion module.
- Acquire and implement new diagnostic tools. Conduct parametric studies and fiber characterization to better understand process effects and the processing window and to quantify fiber properties.
- Conduct rate-effect studies and update cost analysis.
- Investigate oxidation of alternative precursors.
- Investigate interface with microwave-assisted plasma carbonization process and integrate into an advanced technology pilot line.

Introduction

The purpose of this project is to investigate and develop a plasma processing technique to rapidly and inexpensively oxidize PAN precursor fibers. Conventional oxidation is a slow thermal process that typically consumes more than 80% of the processing time in a conventional CF conversion line. A rapid oxidation process could dramatically increase the conversion line throughput and appreciably lower the fiber cost. A related project has already demonstrated the potential for greatly increasing line speed in the carbonization and graphitization stages, and rapid stabilization techniques are being developed, but the oxidation time must be greatly reduced to effect fast conversion. This project will develop a plasma oxidation technology that integrates with other advanced fiber conversion processes to produce inexpensive CF with properties suitable for use by the automotive industry. Critical technical criteria include: (1) ≥25 Msi tensile modulus and ≥1.0% ultimate strain in the finished fiber, (2) uniform properties over the length of the fiber tow, (3) repeatable and controllable processing, and (4) significant unit cost reduction compared with conventional processing.

Project Deliverable

At the end of this project, the researchers will have developed an advanced oxidation process with residence time much shorter than that typical of conventional CF conversion lines. The advanced oxidation process will be sufficiently well understood and documented that the team can commence scaling it up to develop a multiple, large-tow oxidation module for an advanced technology pilot line.

Technical Approach

The researchers are investigating PAN precursor fiber oxidation using nonequilibrium, nonthermal plasma at atmospheric pressure. Plasma processing is thought to enhance oxygen diffusion and chemistry in the PAN oxidation process. Atmospheric-pressure plasma provides better control over the thermal environment and reaction rates than evacuated plasma in addition to eliminating the sealing problems accompanying evacuated plasma processing. Various fiber characterization tools and instruments are used to conduct parametric studies and physical, mechanical, and morphological evaluations of the fibers to optimize the process.

In ORNL's conventional pilot line, which represents the baseline process, PAN stabilization and oxidation occur in four successive furnaces, in air, at temperatures increasing from about 200 to 250°C. Although there is not a precise transition from stabilization to oxidation, in general, one can consider stabilization to occur in the first furnace and (chemical) oxidation in the last three, so in

this project the researchers are working to reproduce the conversion advancement from the last three furnaces. The advancement from the first furnace is being addressed in the parallel advanced stabilization project.

Experimental Results

At the end of fiscal year (FY) 2007, a reduction in oxidation residence time of about two-thirds and 0.3 m/min single-pass line speed had been achieved in a six-zone, single-tow reactor. Initial single-fiber mechanical data were generated (Figure 1). The results fall short of property requirements but are encouraging at this stage of the development program. After the encouraging single-filament data were produced, we started oxidizing 3k tows for tow testing, following conventional carbonization. These tows were oxidized in a six-zone, single-tow reactor configuration.

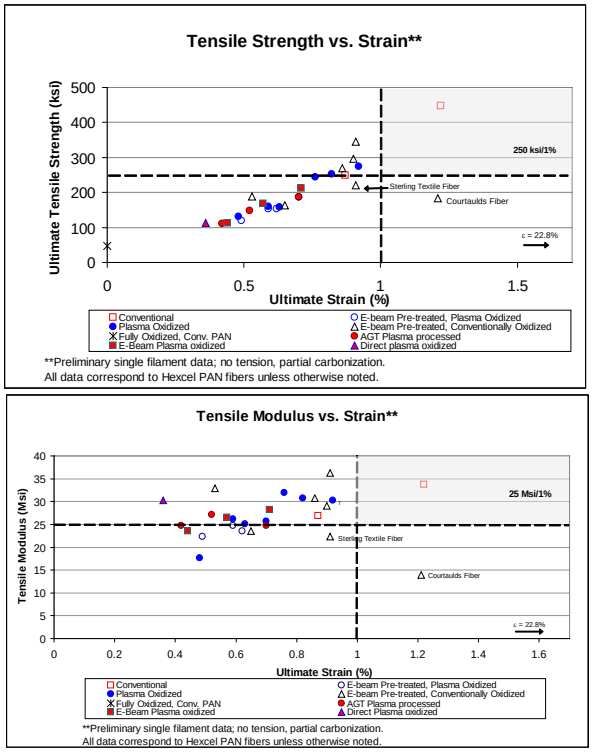

Figure 1. Mechanical properties of CFs stabilized and oxidized by various routes then conventionally carbonized at low temperature. There was no tensioning, controlled stretching, or tow spreading during conversion. Conventional data points are for thermally shocked and thermally ramped heating protocols.

There were problems with the tow tensioning system, so it was upgraded during construction of the multi-tow reactor, described later in this report. The tow production and testing were not completed during FY 2008 because of a key partner's bankruptcy (described in further detail below).The initial tow oxidation is tabulated in Table 1 and will be completed after resumption of experimental operations in FY 2009.

Table 1. Plasma oxidized 3k tow samples produced for carbonization

Sample #	Length (m)	Density (g/cc)	Tow tension during oxidation
1486	67	>1.40	No
1543	90	1.34–1.35	No
1637	53	1.36–1.37	No
1531	72	1.36–1.37	Yes
1532	66	1.37–1.38	Yes
1410	25	1.33–1.34	No
1411	21	1.34–1.35	No
1361	38	1.36–1.37	No

During FY 2008, technical efforts were primarily focused on characterizing the concentration of reactive oxidative species (ROS); better understanding the parameters that control concentration; and construction, commissioning, and initial operation of a multi-tow plasma oxidation reactor.

ROS concentration is extremely important for initiating and controlling the oxidation process. Recently acquired instrumentation and reactor modifications have enabled characterization with significantly improved spatial resolution and measurement precision. Figure 2 shows the normalized results of one set of ROS measurements for various reactor configurations and thermal conditions. Figures 3(a) and 3(b), representing data from two sets of samples run on different dates (three- or four-digit numbers given in the legend of the figures indicate sample IDs), show that the current plasma oxidation process is comparable to or better than conventional oxidation in terms of completing the exothermic oxidation reactions. Differential scanning calorimetry (DSC) thermograms are shown for a number of different samples and/or processing

protocols, and in all cases the plasma oxidation thermogram lies below the conventional oxidation thermogram.

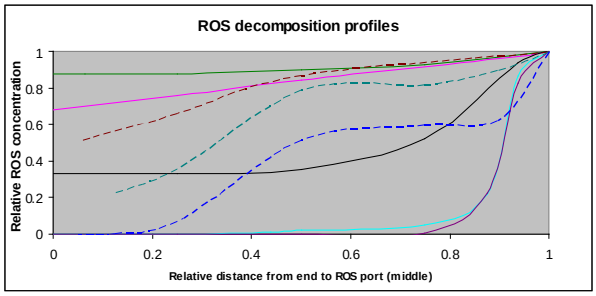

Figure 2. Normalized ROS decomposition profiles for various plasma oxidation reactor configurations and thermal conditions.

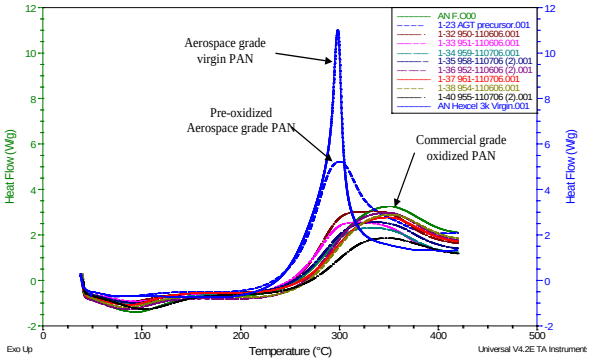

Figure 3(a). DSC thermograms of PAN tow, conventionally oxidized in a commercial factory or plasma oxidized in ORNL's multi-zone, single-tow reactor.

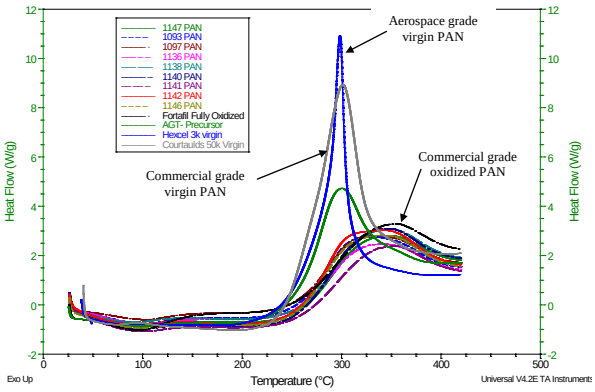

Figure 3(b). DSC thermograms of PAN tow, conventionally oxidized in a commercial factory or plasma oxidized in ORNL's multi-zone, single-tow reactor.

The project team began scaling to multiple tows with the commencement of construction of a multi-tow reactor in late FY 2007. Scaling is now a major part of this project's focus. The multi-tow reactor construction was completed, followed by initial testing and "sweetening," during this reporting period. Initial operations yielded surprisingly good results. Figure 4 shows similar data for the multi-tow reactor; again the DSC thermogram of plasma oxidized PAN fibers lies below that of conventionally oxidized PAN precursor, thus indicating that complete chemical oxidation was achieved. Figure 5 shows that, depending on the reactive species concentration and operating parameters, plasma oxidized fibers show controllable residual heat of reaction. Processing time versus density enhancement during conventional and advanced oxidation processes is presented in Figure 6. It is apparent that the rate of oxidation in plasma oxidation is significantly faster than the conventional route.

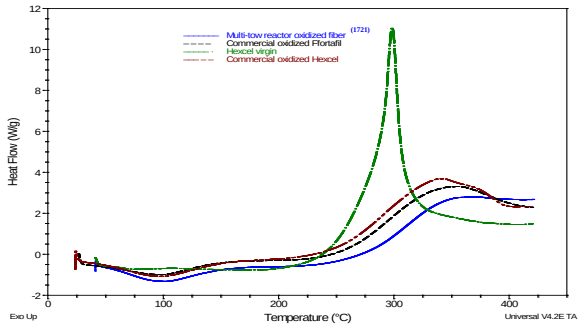

Figure 4. Representative DSC thermogram of multi-tow reactor processed oxidized precursor in comparison to those of virgin PAN and commercial oxidized precursors.

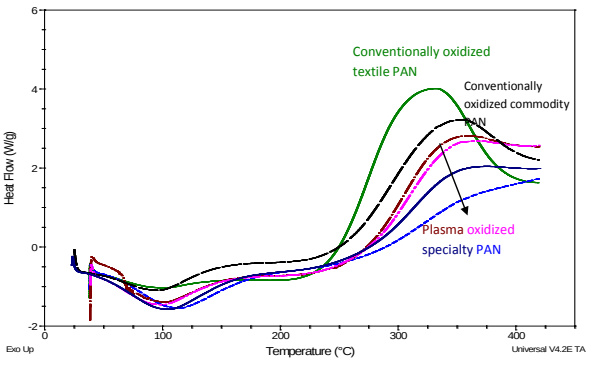

Figure 5. DSC thermograms of different PAN fibers oxidized conventionally or by plasma oxidation.

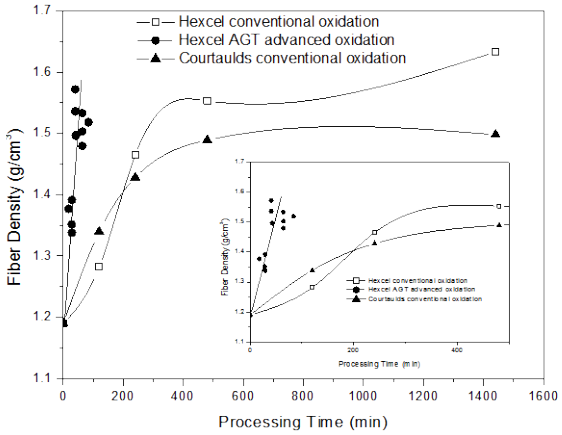

Figure 6. Processing time vs density profiles for fibers in conventional and ORNL proprietary oxidation process.

By the end of this reporting period, the project team had achieved single-tow line speed in the multi-tow reactor roughly equivalent to that previously demonstrated in the single-tow reactor. Multi-tow operation has not yet been attempted. For patent protection and export control reasons, detailed equipment design and process parameters are not published, but they are periodically disclosed to the relevant program managers in oral briefings.

Future Direction

In early FY 2009 we will restore fully effective experimental operations, possibly by moving to another facility. The future project direction will focus on scaling, achieving improved properties of carbonized fibers, oxidation of alternative precursors, process and equipment reliability, integration with other conversion process modules, and commercialization with an industrial partner.

Patents and Publications

There were no new invention disclosures, patent activities, or publications arising from this project during this reporting period.

Education

Materials characterization has been conducted in partnership with the University of Tennessee's (UT's) materials science department. UT graduate students were engaged to provide characterization support to the project.

Partners

ORNL gratefully acknowledges contributions to this project by Hexcel and TohoTenax America. Both have generously provided raw materials and offered technical consultation. Additionally, technical and programmatic consultation has been provided by the Automotive Composites Consortium.

About midyear it became apparent that our key plasma processing partner, Atmospheric Glow Technologies (AGT), was in a state of acute financial distress. We had previously discussed potential courses of action in case of such an event. It became necessary to plan and execute an alternative project approach that did not depend on AGT as a partner. Extensive inventories and documentation of assets and experimental data were completed. We investigated the following options: (1) finding another partner with atmospheric pressure plasma processing expertise, (2) acquiring the key employees and assets to make all of the plasma oxidation research internal to ORNL, and (3) acquisition of key AGT employees and assets by another private entity that would assume AGT's former role. The second and third options were pursued in parallel with the final solution being that Sentech, Inc., hired the key AGT employees, acquired AGT's relevant assets, and subcontracted with ORNL to assume AGT's former role. A contract with Sentech was signed at the end of FY 2008, and experimental operations were resumed at the former AGT premises. Those premises are currently shared with another company that acquired other portions of AGT's business, assets, and employees, and there are some problems with the arrangement that have to be resolved before we are able to restore fully effective experimental operations. We are currently able to conduct experimental operations, but with some inconveniences and limitations that we expect to resolve in the first half of FY 2009.

Conclusions

Plasma oxidation of PAN fibers continues to progress toward the goal of reducing the cost of CF manufacture. To date, researchers have reduced oxidation residence time by about two-thirds compared to conventional oxidation.

Critical process characterization was conducted during this period, and scale-up began to receive significant attention with the completion and initial operation of the first multi-tow plasma oxidation reactor.

D. Precursor and Fiber Evaluation

Principal Investigator: Felix L. Paulauskas
Oak Ridge National Laboratory
P.O. Box 2008, Oak Ridge, TN 37831-8048
(865) 576-3785; fax: (865) 574-8257; e-mail: paulauskasfl@ornl.gov

Participants: Amit K. Naskar, Soydan Ozcan, and Kenneth D. Yarborough
Oak Ridge National Laboratory

Technology Area Development Manager: Joseph A. Carpenter
(202) 586-1022; fax: (202) 586-1600; e-mail: joseph.carpenter@ee.doe.gov

Field Technical Monitor, Composites: C. David Warren
(865) 574-9693; fax: (865) 574-6098; e-mail: warrencd@ornl.gov

Contractor: Oak Ridge National Laboratory (ORNL)
Contract No.: DE-AC05-00OR22725

Objectives

- Provide capability for production of small quantities of fiber or composite material samples.
- Provide capability to test the convertibility of alternate precursors into carbon fiber (CF), and develop their conversion protocols.
- Provide capability to test new concepts that can potentially lower CF cost.

Approach

- Maintain and operate ORNL's conventional pilot line for production of fiber or composite material samples.
- Maintain, upgrade, and operate ORNL's precursor evaluation system.
- Use the aforementioned facilities to test new concepts that can potentially lower CF cost.

Accomplishments

- Evaluated textile polyacrylonitrile (PAN), polyolefin, and proprietary precursors in the precursor evaluation system.
- Ordered equipment for independently tensioning up to three tows on conventional pilot line.
- Ordered 2,500ºC furnace for precursor evaluation system.

Future Direction

- Upgrade, operate, and maintain the facilities as needed to support the Low-Cost Carbon Fiber (LCCF) initiative.

Introduction

The purpose of this project is to perform the general evaluations that support the LCCF initiative. The key aspect of this project is maintenance, intelligent upgrading, and wise use of the critical facilities that have been developed in previous projects. The "wise use" of these

facilities includes evaluation of alternate precursor convertibility, production of fibers and/or composite specimens for evaluation by the Automotive Composites Consortium and other interested parties, and new concept evaluations. The primary facilities supported by this project are the precursor evaluation system; the 1 : 20 scale, conventional, CF pilot line; and the microwave-assisted plasma (MAP) carbonization unit.

ORNL's conventional pilot line enables production on the order of 1 pound/day of 50,000 (50k) filament tow. Therefore, it is useful for making small quantities of fiber for tow and composite evaluations. It can also be used to conventionally oxidize or carbonize tows that are partially converted by advanced processes. Minimum material requirements for evaluation on the pilot line are hundreds of feet of ≥1k tow, and startup time for the high-temperature furnaces is ≥10 hours.

The precursor evaluation system is designed to complement the conventional pilot line in that it is designed for single-shift evaluation of small precursor quantities. During precursor development, initial batches tend to be a few short filaments. The precursor evaluation system is useful for evaluating the feasibility of converting alternative precursors and then determining the process parameters for converting those precursors into CFs. After the conversion process parameters are determined, the conversion protocols can be validated on the pilot line and evaluation quantities of fiber produced there. The precursor evaluation system can be used to convert a single filament or a single tow up to ~80k filaments.

The MAP carbonization unit was developed in the advanced carbonization project and continues to be maintained and operated for demonstration purposes. It is expected that at some point in the future the current MAP carbonization unit will be the starting point for development of an advanced technology demonstration line.

Project Deliverables

The primary project deliverables are samples of converted CFs or composite specimens fabricated from fibers converted at these facilities. Short lengths of tow or mechanical test data from converted fibers, would be typical deliverables from the precursor evaluation system. Small spools of fiber would be typical deliverables from the pilot line and MAP carbonization unit. On rare occasions, the deliverable may be a few kilograms of fiber or composites made from fiber converted at these facilities.

Current Status

The conventional pilot line and the precursor evaluation system are currently operational. The precursor evaluation system was used to evaluate textile PAN, polyolefin, and proprietary precursors in fiscal year (FY) 2008. A 2,500°C furnace has been ordered to replace the aging high-temperature furnace and increase the system's maximum temperature capability. The conventional pilot line was used extensively for processing textile PAN precursor obtained from Fibras Sinteticas Portugal, S.A. (Lisbon, Portugal). A tow tensioning system to independently tension three tows was ordered for the pilot line. The MAP carbonization cooling system was upgraded for improved safety. The MAP system operation was frequently demonstrated for guests, including the assistant secretary for the Department of Energy's Office of Energy Efficiency and Renewable Energy. These facilities are pictured in Figures 1–3.

Figure 1. Operation of oxidation and low-temperature carbonization furnaces in precursor evaluation system.

Figure 2. Conventional pilot-line installation at ORNL.

Figure 3. MAP carbonization unit in operation.

Future Direction

New equipment has been ordered to upgrade the precursor evaluation system's high-temperature capability and the pilot line's creeling and fiber transport/tensioning system. This equipment will be installed and commissioned in FY 2009, and these facilities will continue to be maintained and operated as needed to continue the development of low-cost CF.

Conclusions

The precursor evaluation system, conventional pilot line, and MAP carbonization unit have been upgraded, maintained, and operated to continue the development of low-cost CF.

Presentations/Patents/Publications

None.

E. Commercialization of Textile and Lignin Precursors

Principal Investigators: Felix L. Paulauskas
Oak Ridge National Laboratory
P.O. Box 2008, Oak Ridge, TN 37831-8048
(865) 576-3785; fax: (865) 574-8257; e-mail: paulauskasfl@ornl.gov

Participants:
Timothy S. Bigelow, Cliff Eberle, Stanley C. Forrester, Amit K. Naskar, Soydan Ozcan, C. David Warren, and Kenneth D. Yarborough
Oak Ridge National Laboratory

Mohamed Abdallah
MGA Advanced Composites and Engineering

Ana Paula Vidigal, Paolo Correira, José Contreiras
FISIPE, S.A.

Technology Area Development Manager: Joseph A. Carpenter
(202) 586-1022; fax: (202) 586-1600; e-mail: joseph.carpenter@ee.doe.gov

Field Technical Monitor: C. David Warren
(865) 574-9693; fax: (865) 574-6098; e-mail: warrencd@ornl.gov

---

Contractor: Oak Ridge National Laboratory (ORNL)
Contract No.: DE-AC05-00OR22725

Objectives

- Develop textile-based polyacrylonitrile (PAN) precursors for conversion into carbon fiber (CF).
- Develop all processing parameters needed for use of textile-based PAN and lignin-based precursors.
- Help current and future CF producers incorporate the new precursors into manufacturing plants.
- Assist with plant design and equipment specifications.
- Transfer time-temperature-tension (T3) profiles to users of the alternate precursors. Assist in optimization of the manufacturing parameters.
- Develop any needed surface treatment and sizing technologies for CFs made from alternative precursors as project times allow (may be handled under a separate effort).
- Provide the capability to develop and test conversion protocols for new polymer precursors.
- Produce small quantities of finished CF using the new precursors.

Approach

- Work with potential precursor manufacturers to develop alternative, lower cost precursors.
- Determine the T3 conversion profiles for converting alternative precursors into CF.
- Work with potential CF manufacturers to incorporate the alternative precursors into current or future CF production facilities.

- Assist potential CF manufacturers with specifying and designing CF plants and lines that allow the use of alternative, lower cost precursors.
- Develop sizing technologies, tow splitting technologies, and alternate final material formats to make the products from lower cost CF lines amenable to high volume industries.

Accomplishments

- Initiated work on full-scale development of a textile PAN precursor.
- Completed a technical evaluation of the pilot precursor line and laboratory capabilities of Portuguese textile PAN fiber manufacturer FISIPE, S.A., and entered into a partnership with them to scale up and commercialize textile PAN precursor technology.
- "Down selected" a preferred textile PAN-vinyl acetate (VA) chemical composition from among numerous candidate chemical compositions.
- Began developing the conversion protocols for converting the textile precursor into CF.
- Delivered spools of fully carbonized textile-precursor-based CF to Ford, General Motors, and Chrysler.
- Achieved current best fiber properties for strength of 350 ksi (kips or kilopounds per square inch) on 26,600 filament tows. Program requirement is 250 ksi.
- Achieved current best fiber properties for modulus of 31.7 Msi on 26,600 filament tows. Program requirement is 25 Msi.
- Met with and evaluated the potential for partnering with Bluestar Fibres Company Ltd. to develop a methyl-acrylate-based (MA-based) PAN textile precursor.
- Met with Owens Corning, Zoltek, Hysoung, SGL, DuPont, Great Lakes Carbon Fiber, and others protected by secrecy agreements to scope out possible collaborative efforts to commercialize textile- and lignin-based precursors.

Future Direction

- Continue to optimize the FISIPE precursor processing conditions. Will require adding differential tensioning to the pilot line to yield more precise fiber stretching during stabilization and oxidation.
- Defer any further developments with Bluestar and Owens Corning.
- Pursue commercialization of lower cost precursors with one current research partner, protected by a secrecy agreement.
- Pursue commercialization of lower cost precursors with other current industrial CF suppliers.
- Evaluate potential collaboration with new entrants into the CF market.
- Upgrade the CF pilot line to allow for more precise tensioning during oxidation and the production of larger volumes of fiber.
- Scale up textile precursor technology from pilot line scale to production line scale at the FISIPE plant in Portugal.

Introduction

During the past several years, the Lightweighting Materials (LM) thrust has been developing technologies for the production of lower cost CF for use in body and chassis applications in automobiles. Program requirements target materials that have tensile strengths in excess of 250 ksi and moduli of at least 25 Msi. Past work included the development of alternate, lower cost precursors and alternate, lower cost methods for manufacturing precursors into finished CF. The purpose of these projects was to take two

precursor technologies, textile-based and lignin-based, from the technical feasibility stage and scale up to a manufacturability demonstration. The technology being pursued for the textile-based precursor is the chemical modification of textile PAN containing either MA or VA using a proprietary solution bath while the fiber is still in the uncollapsed state. This project will result in determination of the best concentration-temperature-exposure profiles to render the fiber carbonizable by conventional processes and also readily and inexpensively manufacturable in existing textile PAN plants. Successful completion of this project will result in (1) ORNL providing project partners with specific instructions for precursor conversion, subject to export control limitations, and (2) a selected manufacturer being ready to sell products based on the new technologies to producers. The technology being pursued for the lignin precursors is the conventional conversion of melt-spun lignin fibers from other LM projects and from non-Department of Energy (DOE) projects. Deliverables include spools of fully carbonized and sized CF and composites made from that CF.

The project also includes collaborative efforts with current and potential CF manufacturers to enable them to incorporate these new precursors into their manufacturing facilities. T3 profiles for each precursor will be developed. The program researchers will then work with current CF manufacturers to modify their equipment and facilities to use these lower cost precursors. The program researchers will also work with future CF manufacturers to design factories and specify equipment for future CF lines.

Three separate efforts are described in this report: (1) work with FISIPE, S.A. (Lisbon, Portugal) to develop PAN-VA textile-based precursors, (2) potential work with Bluestar Fibres (Grimsby, United Kingdom [UK]) to develop PAN-MA precursors, and (3) work with other companies to incorporate new precursors into their current and future manufacturing facilities.

Background

Previously under a separate contract as part of the LM program, Hexcel Corporation (Connecticut, U.S.A.) developed the basic science necessary to render textile-based PAN polymers carbonizable. That science included subjecting the textile precursor to a chemical pretreatment bath while the fiber was still in the uncollapsed state. That work was conducted offline from the textile fiber manufacturing. Fiber samples were split off from the line by hand, packaged, and shipped to Hexcel's Decatur, Alabama, plant for processing. Hexcel obtained satisfactory samples but under only one set of processing conditions and with one specific textile fiber. Certain issues needed to incorporate the technology into manufacturing plants were not addressed but will be addressed for VA- and MA-containing precursors in this project. They include the following.

1. Determination of how and when in the production line to split the precursor into manageable sizes for use by the automotive industry. A specific "standard" tow size of approximately 24,000 filaments is the current program goal.
2. Determination of the necessary chemical absorption required to create a sufficient shift in the differential scanning calorimetry (DSC) curves to indicate that the precursor is stabilizable in an acceptable amount of time. The shift in the DSC curves is tied to both the absorption of the pretreatment chemical by the fiber and the diffusion of the elements into the fiber.
3. Acceleration of the chemical pretreatment to make the chemical treatment readily amenable to textile fiber production processes without slowing down the production processes and thus adding cost to the precursor.
4. Design of the chemical treatment equipment.
5. Determination of the required processing conditions for converting the precursor into finished CF. Early samples are being processed using ORNL's precursor evaluation equipment. Later materials are being processed using ORNL's 1/20th scale CF line and the precursor evaluation system (Figure 1).
6. Evaluation of conventional processing, sizing, and surface treatment technologies to ensure the finished CF will have the properties needed by the automotive industry and that those properties will translate into finished

composites. ORNL, with Automotive Composites Consortium (ACC) guidance, is testing tow samples, making composites from the finished fiber, and delivering the samples to ACC for evaluation.

7. Development of a thorough understanding of the processing temperatures, tensions, and conversion protocols for each new precursor material.
8. Provision of assistance to current and future users of the alternative precursors to help them specify equipment and design CF lines that will most efficiently convert the precursors into CF. The main goal is to reduce the risks from incorporating alternative precursors into manufacturing processes.

Figure 1. Conventional pilot line installation at ORNL.

Project Deliverables

At the end of this project, lower cost precursors will have been made from textile grade PAN in textile mills. The technologies for chemically pretreating, and converting the precursors into CF will have been fully developed integrated into commercial manufacturing facilities. Conversion protocols for lignin will be developed in a sister project in which the tasks necessary to commercialize lignin-based precursors will be accomplished in collaboration with industrial partners. To accomplish the goal of commercialization, the following tasks will have to be completed. Tasks that have been completed are indicated by (C), and those in-process are indicated by (I).

- (C) Development of suitable formulations of textile PAN.
- (C) Development of chemical pretreatment methods for textile PAN.
- (I) Design and incorporation of chemical pretreatments in textile plants.
- (C) Determination of T^3 processing profiles for textile PAN.
- (I) Determination of T^3 processing profiles for lignin precursors.
- (I) Determination of methods of splitting and/or maintaining splits in textile-based precursors during the spinning process.
- (I) Development of surface treatment technologies for CFs made from textile PAN and lignin precursors.
- (I) Development of sizing technologies for CFs made from textile PAN and lignin precursors.
- (I) Development (if necessary) of alternate material formats that may be required by higher volume industries.
- Assistance given to current CF manufacturers to incorporate alternative precursors into their manufacturing facilities.
- Assistance given to future CF manufacturers to utilize alternative, lower cost precursors in their manufacturing facilities.
- (I) Upgrade of ORNL pilot line to allow for more optimization of final CF properties from alternative precursors.
- (I) Upgrade of ORNL pilot line to allow for production of larger amounts of laboratory-scale produced fiber from alternative precursors.

Completion of these tasks should allow for the lowest risk commercialization and incorporation of alternative precursors into conventional CF manufacturing facilities.

Current Status

The efforts to commercialize alternative precursors are separated into three distinct but interrelated areas that are budgeted as three separate entities: (1) development of PAN-VA precursors, (2) development of PAN-MA precursors, and (3) commercialization of alternative precursors.

Development of PAN-VA Precursors

ORNL has established a highly interactive and mutually beneficial partnership with Portuguese textile fiber manufacturer FISIPE, S.A., which produces VA-comonomered PAN for textile applications. FISIPE is a high volume manufacturer that produces a commodity fiber that is roughly one-half the cost of conventional acrylic CF precursors. Our efforts are aimed at developing a chemical pretreatment for the FISIPE manufacturing line that will render one of its textile formulations oxidizable and carbonizable and thus satisfactory as a CF precursor.

The first step in development of the precursor was to evaluate the DSC curves of more than 30 potential formulations that FISIPE made with a variety of proprietary additives. The onset of the exotherms, seen in the DSC curves, is indicative of the onset of stabilization, and the steepness of the curves is indicative of the severity of the exotherm during oxidative stabilization. Less steep curves indicate a less severe exotherm that correspondingly could result in more rapid stabilization.

Once candidate precursors were selected, FISIPE installed a chemical treatment unit in its pilot line and began generating chemically pretreated samples. ORNL has conducted extensive characterization of chemically modified precursors and polymer samples generated by FISIPE and conversion trials on filaments and tows generated by FISIPE from selected precursor chemical compositions. An example DSC characterization is shown in Figure 2. We have selected a preferred chemical composition that is the baseline for future work. By the end of FY 2007, FISIPE was making multiple spools of chemically treated 26.6 k tow at 1–2 kg of fiber per spool. This fiber has subsequently been used for conversion trials in ORNL's precursor evaluation system and pilot line.

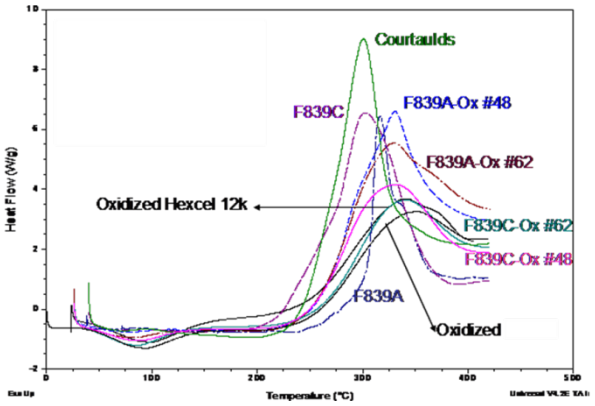

Figure 2. DSC characterization of various oxidized textile PAN precursor compositions and comparison to oxidized commercial precursors.

The next step at ORNL was to determine oxidation temperatures to obtain optimal processing conditions. This was done using the precursor evaluation line and measuring the oxidation density while targeting values that would be close to conventional CF precursors that were fully oxidized. Evolution of the oxidation profile is shown in Figure 3 with standard CF precursors used as a baseline. Oxidized densities slightly higher than industrial grade precursors and slightly lower than aerospace grade precursors have been obtained.

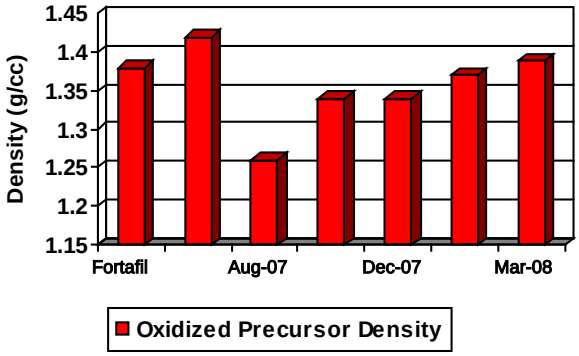

Figure 3. Oxidized density of FISIPE precursor over time when compared to conventional precursors.

For the period covered by this report, ORNL has been using both the precursor evaluation line and the pilot line to determine T^3 processing profiles for the FISIPE precursor. Program requirements are to develop fibers with strength values of at least 250 ksi and modulus values of at least 25 Msi. Figures 4 and 5, respectively, show the evolution of the strength and modulus during development of processing conditions over time. We have currently reached strength values of 363 ksi, exceeding program goals, and are also well above program goals on modulus, with a current value of 31.7 Msi. The addition of

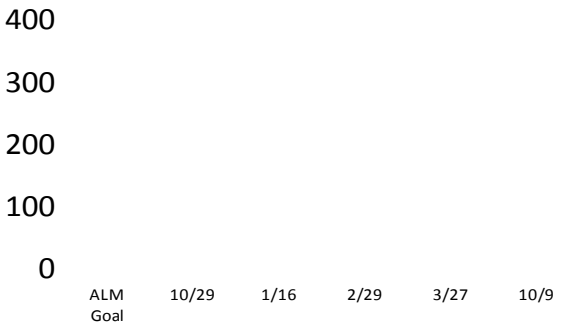

Figure 4. Obtained strength (ksi) of CF produced from FISIPE precursor during development of the processing protocol as a function of time.

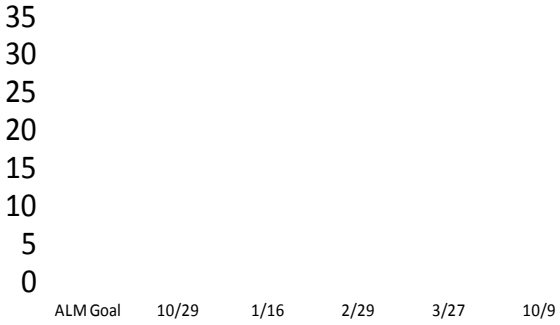

Figure 5. Obtained modulus (Msi) of CF produced from FISIPE precursor during development of the processing protocol as a function of time.

differential tensioning during upgrade of the pilot line should yield significant improvement in the ability to align grapheme planes and increase modulus. Figures 6 and 7, respectively, show manufacturing of the CF on the precursor evaluation line and the resultant carbonized fiber tows.

At the end of FY 2008, ORNL delivered spools of fully carbonized textile-precursor-based CF to Ford, General Motors, and Chrysler, meeting the program milestone and property requirements.

Development of PAN-MA Precursors

At the outset of the program, ORNL approached Fibres Worldwide in Grimsby, UK, as a potential development partner. The Grimsby plant had produced CF precursors for a wide variety of CF manufacturers worldwide, and two lines for producing textile PAN at textile costs had been installed in recent years. The textile lines were based upon an MA comonomer.

Figure 6. Processing of FISIPE precursor using ORNL's precursor evaluation line.

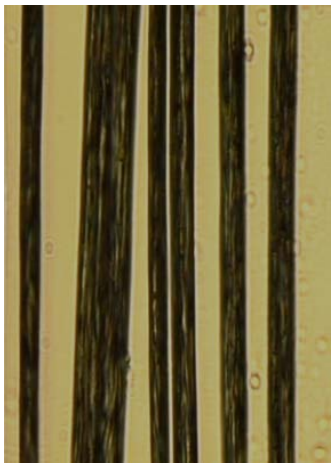

Figure 7. Carbon fibers produced from FISIPE precursor.

While personnel at the plant have remained essentially unchanged (mostly UK citizens), Fibres Worldwide was acquired by a large multinational Chinese corporation, Blue Star, in late 2006 and renamed Bluestar Fibres Company

Ltd. The Grimsby plant was visited by ORNL program management in February to assess the feasibility of continuing to develop a partnership.

During that trip it was learned that Bluestar's textile lines had been decommissioned and that its CF precursor lines were undergoing major renovations. The purpose of the renovations is to produce precursor for a CF plant being built in China. Targeted uses for the CF are reported to be windmills, power cables, and other industrial applications.

Because of the decommissioning of the textile lines, which provided the opportunity for producing lower cost precursors; U.S. competitiveness issues related to potentially enabling a foreign company to more competitively enter the market; and export control issues related to CF manufacture, Fibres Worldwide/Bluestar Fibres is no longer considered a likely partner.

We attempted to identify other likely partners in both the U.S. and the U.K.; however, this part of the project has since been terminated and funding diverted to other efforts.

Commercialization of Advanced Precursors

This portion of the project was initiated during the period covered by this report. At the start of the current fiscal year, Owens Corning and ORNL were negotiating a Cooperative Research and Development Agreement (CRADA) for the commercialization of conventionally processed textile precursor. The original plan was to develop two factories, a smaller one in the United States and a larger one in a yet to be determined location. However, as a result of a merger with Vetrotex and the associated refocusing of efforts, Owens Corning decided not to pursue the joint effort.

Subsequently, DOE and ORNL were approached by another large U.S. company to collaborate on commercializing advanced precursors by developing the technology necessary to build a large factory in the United States. ORNL and this partner are currently in discussions with DOE program management about a cost-shared CRADA. Identity of the company and specific plans are confidential at this time.

ORNL continues to field frequent inquiries about the CF technology under development. Over the past year, we have hosted about a dozen prospective industrial partners at ORNL, who were making site visits to tour our facilities and inquire about potentially licensing and commercializing CF technology. We have responded to numerous other inquiries that did not result or have not yet resulted in site visits. At this time, we are in very active discussions with multiple potential partners and are maintaining some degree of continued discussion with several other partners.

The technological advances in the program, combined with recent growth in the CF industry, are responsible for much of this interest by prospective industrial partners. Additionally, ORNL staff members routinely participate in industry conferences, including the cochairmanship at the 2008 Global Outlook for Carbon Fibers Conference, and numerous contacts have been made at these events. ORNL staff will continue to engage prospective industrial partners and work to develop partnerships that will lead to successful commercialization and deployment of the advanced CF technology.

The commercialization plans under discussion will require the capability to produce a sufficient quantity of advanced CFs for prospective end users to sample and to support downstream part manufacturing process development. Therefore, immediate upgrades to ORNL's facilities are being implemented, including a higher temperature furnace, improved tow transport and stretching/tensioning, and increased line speed for ORNL's conventional pilot line.

Future Direction

The future plans for each of the three subprojects are described below.

Development of PAN-VA Precursors

During the next few months, ORNL will refine the processing parameters for converting the FISIPE precursor into CF with the goal of increasing both the modulus and the strength of the fiber. FISIPE is in the process of developing an improved precursor formulation which should yield a better

product. Work to date has been focused on developing processing conditions using material from the FISIPE pilot line. Currently FISIPE is installing equipment in its production facility to produce textile-based precursor. Once that equipment is in place, material will be processed at ORNL to confirm that the scale-up to full industrial scale has been successfully completed. If time remains in the project, efforts will then be turned toward developing the best surface treatment and sizing technologies to allow good load transfer from the fiber to the resin systems, which is critical to making good composites with excellent properties. Once these steps are completed, fiber and composite samples will be made and supplied to ACC for composite testing. In addition, we have begun tow splitting studies with the object of making one precursor into a variety of finished CF tow sizes.

This project will be followed by an intense effort to introduce current and future CF manufacturers to the project goals and results so that the technology will be integrated into future CF production facilities.

Development of PAN-MA Precursors

No further activities are planned.

Commercialization of Advanced Precursors

Equipment capabilities will be upgraded to enable the production of sufficient quantities of advanced CFs to support property testing and process development material needs. ORNL will continue to engage prospective industrial partners and pursue CRADAs with CF manufacturers to commercialize advanced precursors. Meetings have been held and are being planned with a variety of current CF manufacturers, potential future CF manufacturers, and fiber production equipment manufacturers to develop more than one commercialization route.

Conclusions

The development of PAN-VA textile precursors is well ahead of schedule. Strength values (363 ksi) exceed program requirements (250 ksi), and modulus values (31.7 Msi) are above program requirements (25 Msi). A more refined version of the precursor is being developed, and commercialization plans are being developed.

No future efforts to develop PAN-MA precursors are planned.

A major effort to commercialize alternative precursors is being developing, and related activities are being planned.

Presentations/Patents/Publications

1. Joseph A. Carpenter et al., **"**FreedomCAR and Low Cost Carbon Fiber for Automotive Applications," Low Carbon Generation, 3M innovation Centre, London, UK, February 9, 2008.
2. C. David Warren, "The Development of Lower Cost Carbon Fiber Technologies for Automotive Applications," Proceedings of *The Global Outlook for Carbon Fiber 2007*, San Diego, California, October 23–25, 2007.
3. C. David Warren, "A Comprehensive Research Program to Develop Commodity Grade, Lower Cost Carbon Fiber," to be published in the proceedings of the *ACMA Breaking New Ground: Structural Composites Applications in Defense, Infrastructure, Transportation and Corrosion-Prevention*, University of Alabama-Birmingham, March 4–6, 2008.
4. C. David Warren et al., "Multi-Task Research Program to Develop Commodity Grade, Lower Cost Carbon Fiber," proceedings of the *2008 SAMPE Fall Technical Conference*, Memphis, Tennessee, September 8–11, 2008.
5. C. David Warren et al., "Future Lower Cost Carbon Fiber for Autos: International Scale-up & What is Needed," Proceedings of the *2008 SPE Composites Conference*, Detroit, Michigan, September 16, 2008.
6. C. David Warren and Felix L. Paulauskas, "Investment in the Carbon Fibre Business for Commercial Grade Low Cost Composites," Proceedings of the *Carbon Fibre 2008 Conference*, Hamburg, Germany, September 30–October 2, 2008.

7. Felix L. Paulauskas and C. David Warren, "Producing Low-Cost, High Volume Fibres for Commercial Applications," Proceedings of the *Carbon Fibre 2008 Conference*, Hamburg, Germany, September 30–October 2, 2008.

8. C. David Warren, "Development of Lower Cost Carbon Fiber for High Volume Applications," Proceedings of the *Composites + Polycon 2009 Conference*, Tampa, Florida, January 15–17, 2009.

8. POLYMER COMPOSITES RESEARCH AND DEVELOPMENT

A. Automotive Composites Consortium Focal Project 4 (ACC007*)

Principal Investigators: Libby Berger
General Motors Corporation
Research & Development
MC 480-106-710
30500 Mound Road
Warren, MI 48090-9055
(586) 986-1177; fax: (586) 986-1207; e-mail:libby.berger@gm.com

John Jaranson
Ford Motor Company
Vehicle Design R&A
2101 Village Road MD 3137
Dearborn, MI 48121
(313) 390-5842; fax: (313) 337-5581; e-mail: jjaranso@ford.com

Field Project Manager, Composites: C. David Warren
Oak Ridge National Laboratory
P.O. Box 2009, Oak Ridge, TN 37831-8050
(865) 574-9693; fax: (865) 574-6098; e-mail: warrencd@ornl.gov

Technology Development Manager: Joseph Carpenter
(202) 586-1022; fax: (202) 586-6109; e-mail: joseph.carpenter@ee.doe.gov

Field Project Officer: Aaron D. Yocum
(304) 285-4852; fax: (304) 285-4403; e-mail: aaron.yocum@netl.doe.gov

---

Contractor: U.S. Automotive Materials Partnership (USAMP)
Contract No.: DE-FC-59OR22545

Objectives

- Guide, focus, and showcase the technology research of the Automotive Composites Consortium (ACC) working groups.
- Design and fabricate structural automotive components with reduced mass and cost, and with equivalent or superior performance to existing components.
- Develop new composite materials and processes for the manufacture of these high volume components.

Approach

- Design, analyze, fabricate, and test a structural composite underbody, focusing on the following.
  - A 2 ½ minute cycle time (100k units per year [upa], 2 shift operation).

*****Denotes Project 007 of the Automotive Composites Consortium, one of the formal consortia of the United States Council for Automotive Research set up by Chrysler, Ford, and General Motors to conduct joint, precompetitive research and development (see www.uscar.org).

- — Methods of joining and assembly of the underbody to the vehicle.
- — Processes for fabricating oriented reinforcement within the time window.
- — Design, analyze, and fabricate a second row composite seat (with and without an integrated restraint system [SIR and STD, respectively]) which will combine the functions of a seat and a load floor.

Accomplishments

- Selected glass fabric sheet molding compound (SMC) with a high elongation core as our material and process system (M&P system) for the composite underbody.
- Developed design methodologies to achieve acceptable performance of the underbody in Full Frontal, Frontal Offset Deformable Barrier, Side, and Rear Offset Impact, and completed CAE stiffness, crash performance, and mass assessments.
- Conducted the initial testing of composite-to-steel weld-bond joints, using doubler strip (Applied for a U.S. Patent)
- Selected surrogate tool for the underbody for use in processing trials, fabric drape studies, and correlation of analytical and experimental dynamic testing. Designed appropriate test methodologies for correlations.
- Demonstrated vibro-thermography as a means of nondestructive evaluation of damaged weld-bonds.
- Achieved a seat design that meets worst-case load requirements for a vehicle seat, including front and rear impact and cargo retention with a cushion that is 30% lighter and a seat back that is up to 58% lighter than the comparator average.
- Cost modeling of the ACC seat design and a comparator thermoplastic P4 (programmable powdered preform process) (TPP4) design has been completed. While a weight save of greater than 50% can be achieved, the composite seat design is cost prohibitive due to the reliance on carbon fiber.
- A preliminary redesign of seat structure based on lessons learned in the Phase 1 work and the work done by Ecole Polytechnic Federal de Lausanne (EPFL) has been completed in carbon fiber reinforced nylon. Changes in the constraints placed on the design allow more efficient section properties.
- Constraint changes to the seat package include:
- 20% reduction in occupant body-to-metal clearance.
- Remove the kneeling feature of the seat.
- Allow trim panels.

Future Direction

- Selection of high elongation core material and demonstration of benefits to enable maximum weight savings of structural composite underbody.
- Further manufacturing demonstration of the selected M&P System, with fabric drape studies, cycle-time analysis, and determination of durability and high strain rate properties.
- Processing development and dynamic and durability characterization of composite-to-steel weld-bonded joints.
- Continued investigation of nondestructive evaluation (NDE) techniques for manufacturing quality and durability.
- Development of a manufacturing scenario for underbody and its assembly into vehicle.
- The seat redesign will continue with glass-fiber based composites to control costs while trying to achieve a goal of 50% weight reduction.

Introduction

This project encompasses two components, a composite underbody and a lightweight composite seat, with unique goals with respect to vehicle volume per annum, physical size, materials, and technology development. They both require structural performance with reduced mass and acceptable cost, and with equivalent or superior performance to existing components.

Structural Composite Underbody

The structural composite underbody is targeted to be part of the USAMP Multi-Material Vehicle (MMV) project, and will follow the MMV vehicle technical specifications. The primary research outcomes of this project are as follows.

- A 2 ½ minute cycle time (100k vehicles per year, 2 shift operation).
- Developing methods of joining and assembly of the underbody to the vehicle.
- Processes for fabricating oriented reinforcement within the time window.

Phase 1 of this project, completed in the first quarter of fiscal year 2008, was the selection of the materials and processes for the underbody, which involved the following.

- The development of a design concept, including a means of joining and assembly.
- The preliminary design of the concept using three material and process systems.
- The selection of an M&P System based on manufacturing considerations such as the following.
  - 2 ½ minute cycle time.
  - Technical feasibility of molding.
  - Joining and assembly feasibility.
- Technical cost model analysis.

Phase 2, which is now underway, is the full design of the underbody, based on a Large Rear Drive Vehicle (LRDV). This design includes the following.

- The whole underbody.
- Manufacturing plan for the component.
- Plan for joining and assembly to the vehicle structure.
- Validation of materials, processes, and analysis methodologies and assumptions.

Phase 3 will be fabrication and testing of the underbody.

In Phase 1, a preliminary composite underbody design was developed to replace the steel assembly from the donor vehicle. The preliminary design takes into account three proposed M&P System candidates, as well as the general vehicle packaging, and assembly and joining requirements. The vehicle level stiffness performance with the composite underbody is required to have equivalent performance to the donor, while crash performance is required to meet applicable government and industry requirements.

The concept design for Phase 1 must be suitable for predicting preliminary CAE-based structural performance and mass reduction, conducting technical cost modeling, and further Phase 2 detail design and development. The material and process system selected was a glass fabric sheet molding compound with a high elongation core (HEC). The glass fabric SMC has been demonstrated in several molding trials. However, the HEC is still under development. Our future processing, material evaluation, and design efforts will focus on this material system.

Our preliminary design and M&P system are based on the following set of assumptions.

- Analytical methodologies used to design the underbody for structural and crash performance are correct for this system.
- Material properties achieved with plaque testing will translate to properties in the complex underbody structure.
- Processing techniques can be developed to preform and mold the fabric SMC into the complex shapes needed.
- A high-elongation core material can be developed to maintain some continuity of the structure after crash.

- A production-feasible method of fabricating the composite-to-steel weld bonded joints will be developed, with necessary properties and durability.

Phase 2 addresses these assumptions as we move forward with the full design. Our primary means of doing this will be a structural surrogate with many of the challenges of the underbody. Chrysler has suggested a tub tool that can be used both in design and fabrication. Although this tub was designed for a Chrysler vehicle, it has not gone into production. The three-dimensional nature of this tool will allow testing of the material drape, preform and molding techniques, and property retention.

A composite-to-steel weld bonded joint has been designed and will be tested statically by the ACC, using super-lap-shear (SLS) specimens. Dynamic testing of the joint will be done at the Oak Ridge National Lab (ORNL) Test Machine for Automotive Crashworthiness (TMAC) facility; see 12.B. Physical testing methodologies for the surrogate structure, including the weld bonded joints, have been developed, to be compared with structural and crash analysis results.

One point of interest which has been raised about structural applications of composites is how to ensure quality, both after the initial manufacture and through day-to-day usage, or after low-energy crash events. This will require the development of NDE techniques that are low cost, robust, and easy to use. Examples of techniques which we will be evaluating for further development are thermal wave imaging (TWI), vibro-thermography, embedded microspheres or nanotubes encapsulating a fluorescent dye, embedded fiber optic mesh, and “coin tap” techniques.

Manufacturing a structural composite underbody and assembling it into a vehicle is a radical change in the vehicle assembly process. We are beginning to work on a scenario that will allow this assembly within a generic auto manufacturing facility.

Composite Design & CAD Model

Multimatic, the design and analysis supplier for Phases 1 and 2, examined the benchmark steel vehicle underbody [see Figure 1(a)] to determine the basic construction, attachment requirements, parts count, material selection and gage.

Based on an evaluation of the steel design, and the results of Phase 1, the preliminary Phase 2 composite underbody CAD design model was developed to assess manufacturing and tooling requirements, and for further development [see Figure 1(b)]. The composite underbody design integrates 16 stamped steel components into a single molded floor with ribs, and utilizes both carry-over and modified mating components. The model represents the proposed joining concept and component integration. The overall dimensions of the underbody are approximately 1,640 × 1,470 × 445 mm with a variable material thickness ranging from 2.0 to 5.0 mm based on the selected M&P System and Phase 1 performance requirements.

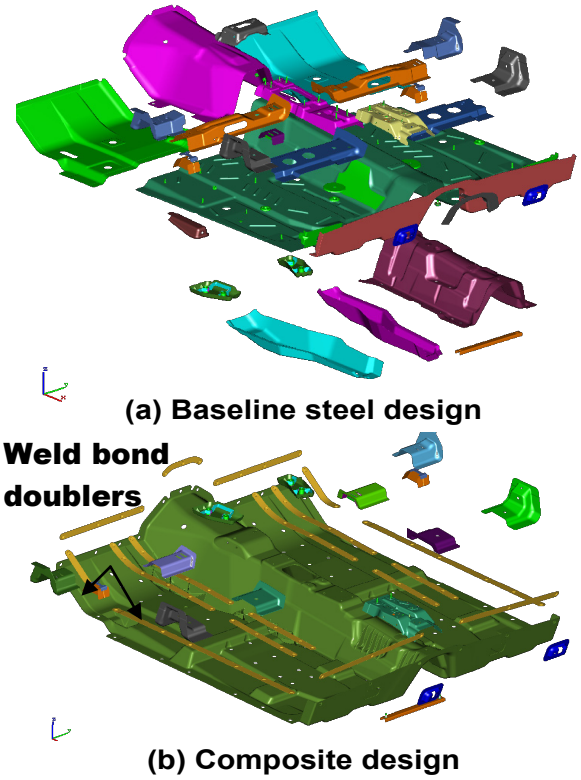

Figure 1. Baseline steel and composite design.

The expected mass savings using glass fabric SMC with a high elongation core is 14.9 kg, including 3.3 kg saved from the underbody rails, which is allowed by the increased structure of the floorpan. This translates to 33.2% mass savings.

An additional 1.6 kg could be saved by going to carbon fabric with an HEC. However, this would be at a cost of about $150/kg saved. This surprisingly high cost is due to the fact that this application is strength-driven, and must carry the crash loads. This is in contrast to most of the automotive studies of carbon-fiber composites to date, which focus on modulus-driven applications. For these, the higher modulus-to-strength ratio of carbon fiber composites is more beneficial.

Vehicle Assembly/Joining

Conceptually, the integration of structural composites into a primary metallic structure can be solved via adhesive utilization. This basic joining approach has been successfully implemented in many operations with slow builds, particular conditioning procedures and special care. In optimal, lightweight, multi-material designs, structural bonding provides enhanced seam integrity, gap bridging or tolerance functions and galvanic separation. However, for cyclic line rates and automotive body shop plant infrastructure, several process considerations and integrity qualifications present concerns and need solutions. In the high volume automotive environment, cycle time, body shop assembly process compatibility, and structural performance are all key requirements, and welding is a primary joining technique.

The combination of welding and bonding, weld bonding, is currently being implemented in some OEM body designs and assembly plants as a means of increasing stiffness, reducing mass, and improving durability. Weld bonding is currently envisioned as the primary joining process to meet the complex automotive requirements for the composite underbody. Specifically, the concept is to attach steel weld bond doublers (see Figure 1b) to the composite to enable spot welding to the surrounding steel structures as well as to attach the structural underbody rails to the composite floor (see Figure 2). The adhesive would be applied prior to spot welding. Not only would weld bonding provide compatibility with current body shop assembly and welding processes for installing the underbody itself, but the spot welds would also serve as peel stoppers in the adhesive joints, provide fixturing during adhesive cure, and enhance overall joint durability and robustness. A typical weld bond joint at the rocker location is illustrated in Figure 3.

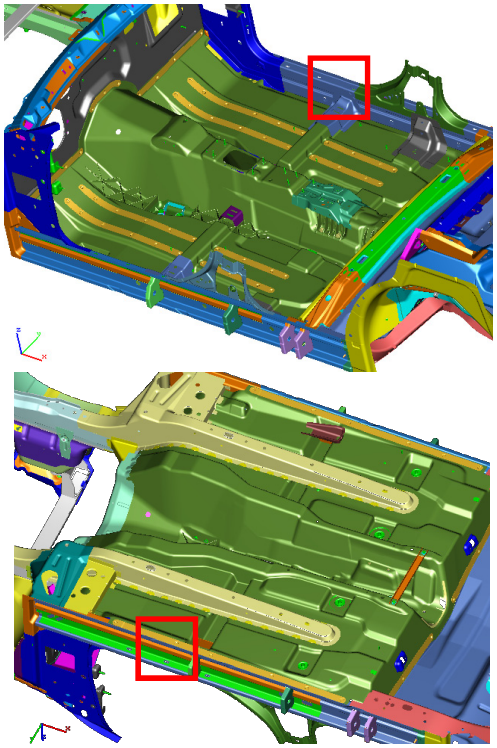

Figure 2. Composite underbody assembled into donor vehicle BIW.

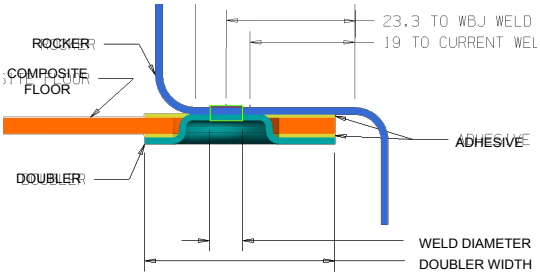

Figure 3. Typical weld bond joint section at rocker.

Phase 2 Performance Requirements

In Phase 1, the following key development load cases were considered.

- Body-in-White (BIW) static torsional and bending stiffness and modal response.
- NCAP 35 mph Full Frontal Impact.
- EuroNCAP/IIHS 40 mph Frontal Offset Deformable Barrier (ODB).

- FMVSS214 33.5 mph Side Impact.
- FMVSS301 50 mph Rear Offset Impact.

In Phase 2, additional performance requirements will need to be considered, including the following.

- FMVSS208 30 mph Frontal Impact at ±30°.
- IIHS 30 mph Side Impact.
- EuroNCAP 30 mph Side Impact.
- NCAP 38.5 mph Side Impact.
- FMVSS214 20 mph Dynamic Side Pole Impact.
- ECE R32 23 mph 100% Overlap Rear Impact.
- FMVSS207/210 Seat and seat belt anchorage strength.
- Vehicle shipping loads.
- Durability.
- Seat track modal response.

Material and Process System Development

As stated above, a glass fabric SMC with a high elongation core was selected as our material and process system. While molding trials in 2007 showed that this concept could work, further testing indicated that the originally selected HEC material would not withstand the processing temperatures needed for vehicle assembly. M&P System development in 2008 has focused on finding an acceptable core material. In a plaque molding trial, a variety of core materials were screened, including expanded mesh materials such as steel, poly ethylene terephthalate, and poly vinyl chloride, a polyester roofing fabric, a thermoplastic epoxy film, aluminum screening, and several types of cotton fabric. A number of these showed the desired failure mode of continued low level structural connectivity at high strain after failure. Several of these will be further evaluated in upcoming molding trials.

Experimental-Analytical Correlation Studies

As part of the development of the Phase 2 design input data, several experimental-analytical correlation studies are planned to develop the analytical material properties and models required for the detailed features of the Phase 2 underbody CAD design. These studies will be used to develop and validate analytical modeling techniques for materials, weld bonded joints, and structural components by correlating physical testing of coupons and surrogate components in environmental, static and dynamic loading conditions.

Surrogate Component

The surrogate tool mentioned above is illustrated in Figure 4, and has a nominal size of approximately 1365 × 785 × 285 mm with a nominal 3.5mm wall thickness and a 2.0 mm perimeter bond flange thickness. This is approximately 45% of the plan view size of the composite underbody with a similar part depth. The tool is a compression tool with shear edges designed for molding glass mat thermoplastics, which should be suitable for molding our glass fabric SMC material. The surrogate tool will be used for material and process development and to mold components for physical and analytical component level performance assessment trials.

Figure 4. Surrogate component.

Evaluation of Surrogate Tub Performance

As a first step toward assessing the impact performance of the surrogate tub, two component test configurations were developed to estimate the needed impact test mass and speed requirements to achieve “reasonable” tub deformations and loads. For this purpose, portions of the full tub were selected to represent impacted sections of the full vehicle (see Figure 5). The required initial mass and impact speeds were iteratively determined by means of a dynamic finite-element (FE) analysis

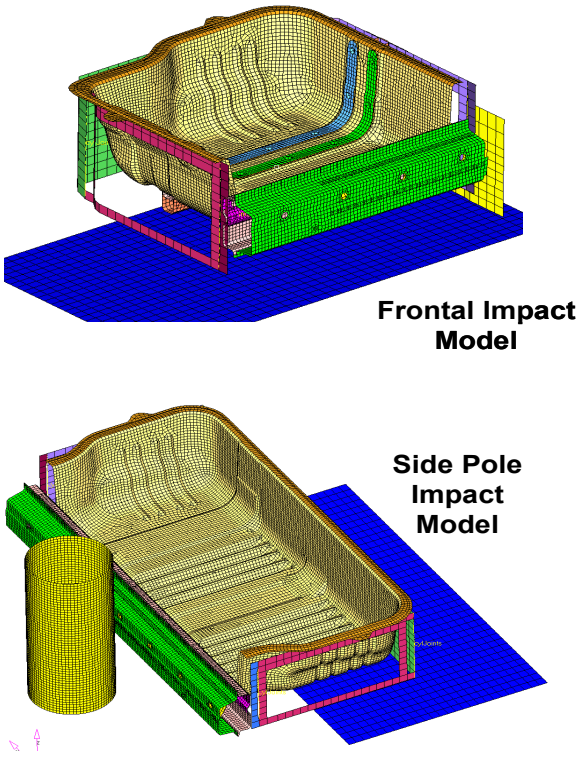

Figure 5. Surrogate component impact models.

to induce similar deformation modes (within the confines of the donor tub design) as observed in the full vehicle models.

Further analytical test development is planned once a suitable physical test facility is identified and test capabilities are established. Physical impact testing and performance validation is planned pending the availability of molded tubs. A similar approach is under development for the fatigue testing of the surrogate tub.

Material Drape Studies

One of the major issues for processing the underbody is the drape of the fabric SMC. The fabric will not deform as easily as a conventional SMC, but large deformations are possible via the shearing of the fabrics. The simulation of the complex fabric-SMC deformation behavior is possible and the drapability of the tub and the underbody has been studied. We have worked with the University of Massachusetts at Lowell to determine the drape characteristics of multiple layers of the fabric SMC, and to use this in computer models to determine appropriate layup, blank size and shape, and preform configurations for the underbody. The models are applied to a simple shape, a double-dome with a connecting tunnel, as well as the surrogate tool and the full underbody design. The double-dome shape will be molded, and the fabric orientation will be analyzed to validate the modeling. This study includes the characterization of the SMC material (i.e., the frictional, tensile, and in-plane shearing behavior).

Material characterization

Shear Frame Test

Shear frame testing was performed to measure the force generated during shearing of the SMC fabric. Compounded fabric samples of specific geometry are tightly clamped in a custom-built frame and sheared. Figure 6 displays the loading, initial and final positions of the shear frame test as well as an example of resulting data.

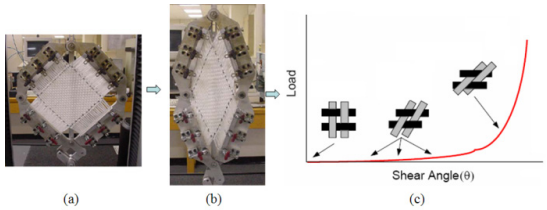

Figure 6. (a) Loading and initial position of shear frame testing. (b) Final position of sheared fabric. (c) Load vs shear angle plot and corresponding yarn positions.

Tensile testing

Conventional tensile tests on the dry yarns were performed to determine their stiffness and failure stress (Figure 7). Then, knowing the crimp ratio (the difference between the length of the fabric and the length of the yarn) and the yarn stiffness, the tensile behavior of the fabric can be assessed.

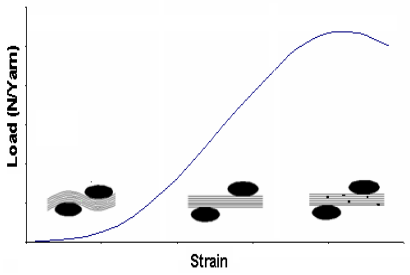

Figure 7. Typical tensile behavior of a woven fabric showing the decrimping phenomena.

Friction testing

A load-control friction test apparatus was used to capture the static and dynamic coefficients of friction at the tool/fabric and fabric/fabric interface. For the fabric/fabric friction characterization, the inner-fabric layer to be pulled out is placed between two additional layers of fabric clamped together on one end. The coefficient of friction was plotted against the pull-out displacement. Typically, these curves result in an initial peak, followed by a somewhat steady-state situation. The peak and the steady-state portions of the curves correspond to the static and dynamic friction coefficients, respectively. While the two outer layers of an SMC part will contact the heated tool, a thermal gradient will exist within the inner layers of a multilayered part. Therefore, tool temperatures of 25, 35, 45, and 90°C were selected to simulate different fabric temperatures in a multilayered part.

Figure 8 shows typical friction vs. displacement curves of the SMC material at the fabric/fabric

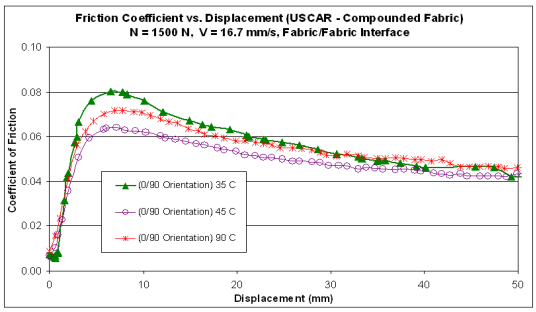

Figure 8. Coefficient of friction as a function of pull-out length.

interface, and Figure 9 compares the resulting static and dynamic friction coefficients of the SMC material at the tool/fabric interface. At high tool temperatures, as well as at the fabric/fabric interface, the lubricant resin film dominated the friction behavior and therefore, the coefficient of friction is essentially negligible for analytical modeling purposes.

Draping Simulation

A mesoscopic/discrete approach using beams to model the yarns has been used, and shell elements are associated to the beams in order to model the

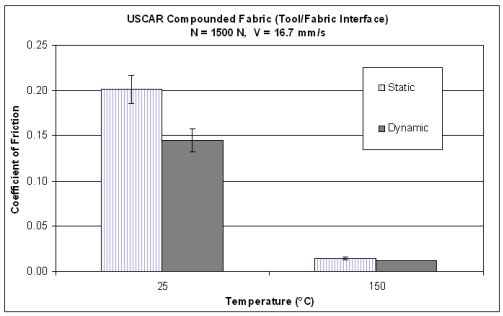

Figure 9. Coefficient of friction (tool/fabric) at low and high tool temperatures. The error bars indicate one standard deviation.

in-plane shear behavior. The drapability of both the tub and the floorpan has been studied for different fabric orientations (Figures 10 and 11). Tensile and shear properties for the beam and shell elements are provided from the materials characterization effort, as well as the friction layers and between the tool and the surface fabric layer.

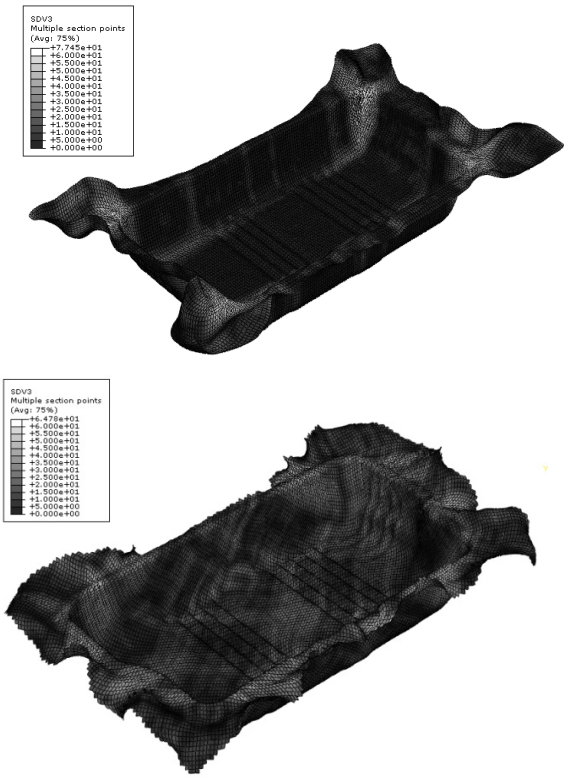

Figure 10. Forming simulation of the Tub for a 90°/0° ply orientation (top) and a +45°/-45° (bottom). Shear angle contour (lighter areas show higher angles, with white above 60°).

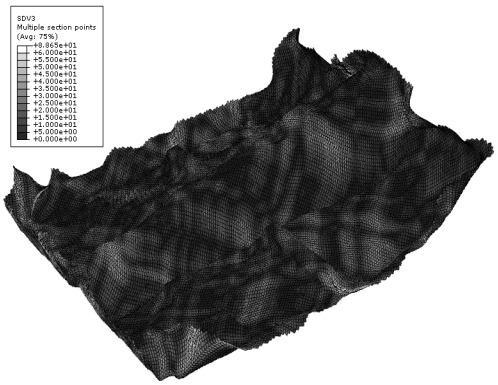

Figure 11. Forming simulation of the floorpan for a 45°/-45° ply orientation. Shear angle contour (lighter areas show higher angles, with white above 60°).

Based on these simulations, the initial orientation of a quasi-isotropic stack of plies within the mold were determined to achieve the best drapability. Valuable information was extracted from these simulations to further improve the drapability of the parts. For example it has been noted that ridges with sharp right angles lead to significant stress in the yarns that could lead to yarn failure (e.g., the flange or the bottom ridge of the tub part). A more filleted or curved edge would probably reduce this issue. In addition, the points of initial tooling contact can affect formability. For example, the corrugations at the bottom of the tub can lead to high tensions and fiber bridging across the channels if contact is first made across the peaks and the fabric must subsequently be forced into the channels. The simulation suggests that a preform that allows for more fabric in this region would improve formability.

Weld Bond Studies

A key element of the underbody design is the composite to steel weld bond joining concept as shown in Figure 3 (see joint location in Figure 2). To gain confidence in the vehicle level joint performance, quasi-static, impact, and fatigue loading conditions will be accessed via analysis and physical testing. Test-analysis correlation will be used to establish the best modeling practices and material models to be used for the prediction of weld bond joint performance.

Since it will be necessary for the underbody joints to carry dynamic loads, the adhesive used in the weld bonding must also be able to survive this loading. Two highly toughened adhesives, currently in use by the automotive industry for steel body-in-white weld bond applications, were trialed by the adhesive suppliers. In these trials, the adhesive suppliers were provided laser cut coupons of 50% random chopped glass SMC with the planned resin. They used these coupons for standard composite-to-composite lap shear testing using their adhesives. Both investigations reported positive results in that the failures noted occurred in the composite substrate and not the adhesive joint interface.

Super-Lap-Shear Coupon

The primary geometry for evaluating the joint performance is the SLS coupon. The SLS coupon was designed to evaluate quasi-static tensile joint performance, but it is also being considered as a candidate for evaluating dynamic tensile performance, as well as bending and torsional durability performance. Several SLS coupons have been fabricated to date for initial performance assessments and test method development. An early SLS coupon is shown in Figure 12.

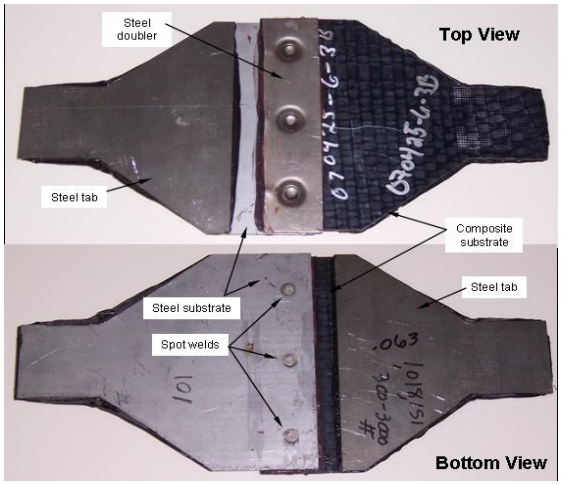

Figure 12. Super-lap-shear coupon**.**

Quasi-Static Performance

Several analytical studies were carried out to gain insight into quasi-static SLS tensile performance and to further develop the initial coupon design. The initial efforts were focused on:

- Mesh sensitivity
- Adhesive and weld modeling techniques
- Steel gage / grade effects
- Composite material effects (random and fabric SMC)
- Joint strength for tension, shear, bending, and torsion load cases

Preliminary quasi static tension, bending, and torsion testing have been carried out by ORNL and GM R&D for some early SLS coupons. Figure 13 shows the sample data for coupons made with a 7 ply 0/90 fabric and two gages of steel, 0.7mm GMW2 and 1.6mm DP590.

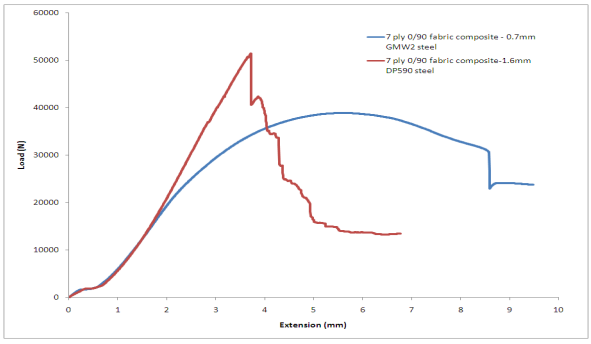

Figure 13. Load-extension curve of weld bonded composite to steel super-lap coupons in quasi-static tensile test.

The specimen with 0.7mm steel showed significant yielding of the steel before the joint failure. The specimens with 1.6mm steel, however, appeared to fail in the joint with composite shearing and tearing of weld nuggets accompanied by delamination. The sequence of the failure was unknown. A high-speed video camera will be used in the future to capture the failure sequence.

NDE found no clear evidence of cracks in the SMC, but did indicate the loss of continuity through the stacks and interply disintegration with debonds. Debonding at the steel-adhesive interface in the specimen with 0.7mm steel was found. Based on the overall results from preliminary tests, new test methods will be established for final quasi-static and dynamic evaluation.

Key variables in the matrix include grade and gage of the steel substrate, number of welds, type of adhesive, and test temperature. The data obtained from these tests will be used in structural test-analysis correlation and to develop the model for the tub tool.

Dynamic Performance

Dynamic tensile testing is planned at the TMAC facility at ORNL. The tensile tests will be carried out at higher strain rates derived from predicted rates observed in vehicle side impact. The initial test efforts will be focused on:

- Coupon, fixture and test methodology development
- Steel gage / grade effects
- Composite material effects (random and fabric SMC)
- Rate effects

To understand the general durability loading conditions in the proposed composite underbody, an early vehicle level finite element model was utilized to gain insight into the joint level loading modes. The vehicle model was subjected to simulated pothole loads and the resulting peel and shear forces were studied in the joint areas. From the analysis results, it was observed that localized mixed mode shear and peel stresses were induced in many joint areas of the underbody, but especially at the end of the weld bond joints and in the vicinity of the local geometric features.

Based on these observations, various loading conditions for the SLS coupons were investigated in an effort to generate a range of peel and shear stresses in the adhesive joint. The results of this coupon level study indicated that a range of peak shear and peel could indeed be achieved, depending on the gage of the steel substrate, and the loading condition. Preliminary tension-tension fatigue testing and quasi-static bending and torsion testing has recently been completed. The test results are being evaluated along with the analysis results and various practical considerations in an effort to select the most appropriate test methodologies and coupon configuration for further fatigue testing.

Nondestructive Evaluation

Several NDE techniques are being investigated to determine which would best fit the needs of

insuring the integrity of the composite underbody and it's joining to the rest of the vehicle structure.

Nondestructive techniques can be used to evaluate

- durability of preproduction designs,
- manufacturing operation quality, and
- possible repairs needed after a crash event.

Some of the desired attributes of NDE methods are as follows:

- robustness,
- low cost,
- ease of use,
- noncontact,
- no damage to part,
- full field,
- no or limited consumables,
- can be automated, and
- currently in use, with little technical development needed.

The level of importance for each of these criteria will be determined by where in the life of the underbody it is to be used. For example, an NDE technique for manufacturing quality assurance must be automated and high speed, but could require more capital expense than a technique that would be used to evaluate the need for repair in an independent body shop, where low cost and ease of use will predominate.

Several NDE tests were performed to analyze the failures in SLS joints, including TWI, vibro-thermography, X-ray radiography, ultrasonic scan, both through transmission (UT-TT) and pulse/echo (UT-PE). The super-lap coupons were difficult to inspect due to their geometry. The tests found no clear evidence of cracks in the SMC. UT-TT indicated the loss of continuity through the stacks and interply disintegration with debonds. UT-PE tests indicated debonding at the steel-adhesive interface in the specimen with 0.7 mm steel.

TWI was used to image the adhesive pattern as shown in Figure 14. The adhesive attached a doubling metal plate on the left side of the image. No contact to the part under test is required,

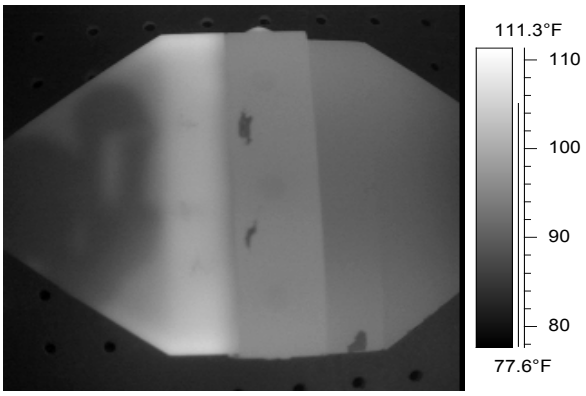

Figure 14. An example of infrared thermal wave imaging. The gray scale image shows the subsurface adhesive bead (left side of image) after construction of the composite weld bond. The construction consisted of an adhesive bead sandwiched between an SMC section and a sheet metal layer.

although line of sight to the area under test needs to be maintained.

Vibro-thermography was used to detect damage caused by striking a weld bond sample with a ball peen hammer... The three defects are easily detected, as indicated by the arrows in Figure 15.

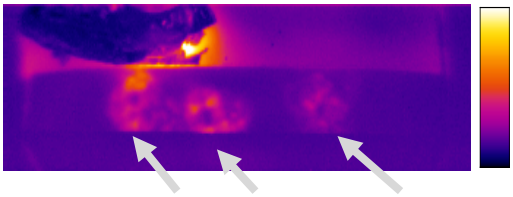

Figure 15. Arrows are pointing at each of 3 impact blows from a ball peen hammer on to the SMC layer of a composite weld bond sample.

TWI was also used to detect subsurface blistering on sheet molding compound (SMC) panels shown in Figure 16. The heat pulse in this TWI example was applied to the back side of the panel. The blisters prevented heat from reaching the front surface of the panel, thereby looking colder (darker gray scale) than the surrounding SMC material.

Other techniques which are under investigation include embedding a dye in the composite which would be visible upon fracture, coin tap methods, and enhanced visual inspection. Work is also underway to determine the degree of damage and size of damage areas that must be detected, for

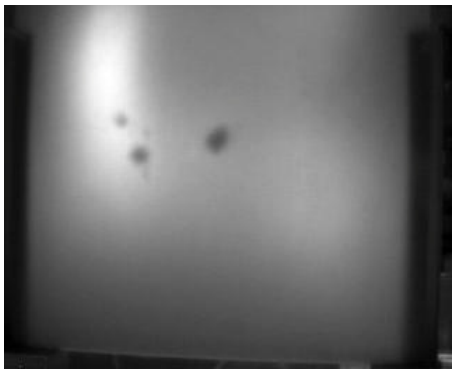

Figure 16. Infrared thermal wave image showing three blisters present in an SMC test panel.

both the weld bond joints and the composite structure itself.

The end result may be that no one NDE technique has all of the desired attributes. A combination of several techniques may be required, including different techniques for preproduction validation, manufacturing monitoring, and post crash evaluation.

Underbody Summary

In Phase 1, glass fabric SMC, with a high elongation core was selected as our material and process system. A preliminary one-piece molded composite underbody design concept was selected, and its structural performance was analytically assessed assuming surrogate material properties and several stiffness and crash development load cases. In Phase 2, additional load cases have been considered along with M&P-specific material properties, leading to an overall mass savings of 14.9 kg, or 33%, including mass saved in the sled rails. To achieve the required level of confidence in the analytical performance and mass assessments, further considerations will be made for material rate dependency and environmental effects.

Further development of the fabric SMC is necessary, particularly for the manufacture of large parts, and for joining of these parts to the steel vehicle structure. Plaque molding trials have provided several materials showing the proper failure behavior for the HEC, which will be further investigated. Fabric drape analysis has shown areas for which the design needs to be slightly modified.

A surrogate tool has been identified, to allow processing studies of a large structure and validation of design and analysis methodologies in a molded and weld bonded part. Dynamic evaluation of weld bond samples is underway, in cooperation with the ORNL TMAC facility. Investigations into NDE techniques to determine manufacturing quality and durability have shown promise and are being further developed.

Lightweight, Low-Cost Composite Seat

The primary objective of this part of FP4 is to develop materials, processes, and designs to yield a light-weight, low-cost composite seat structure.

Second row outboard stand-alone seats with volumes up to 340k upa are the target applications. Results from the comparator seat teardowns and testing have been used to develop average weights for a conventional steel seat frame that is used for comparison with the composite seats. The project will predominately investigate glass fiber reinforced composites, due to cost considerations, but will consider local reinforcement with carbon fiber and other materials, including metal, in order to achieve a 30% weight savings versus the components being replaced. Both thermoset and thermoplastic matrix material will be included. A design achieving a 50% weight savings utilizing carbon fiber reinforced composites is also being developed, although this may be cost prohibitive.

CAE Analysis

The original ACC seat design, shown in Figure 17, met the 120% loading requirements, required for the seatback to be used as a load floor, with only some minor local issues that are being addressed.

Recent activity has involved the redesign of the composite seat which began with topology optimization by Altair Engineering. Based on this redesign, only the back frame, cushion frame, and the pivoting recline/folding joint are included in the current project scope. The results of the topology optimization can be seen in Figure 18.

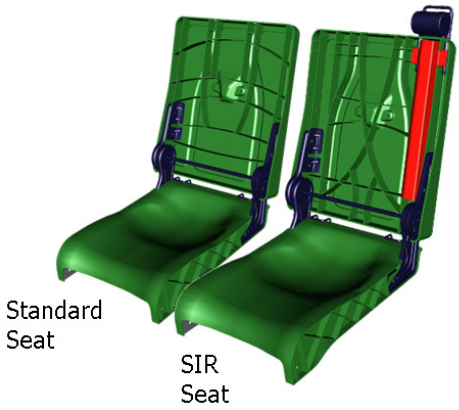

Figure 17. ACC seat designs—original.

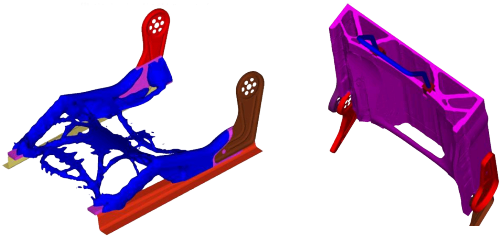

Figure 18. Seatback topology results—redesign.

The redesign resulted in inner and outer bonded shell designs for the seat back and seat cushion. This type of design allows much more geometric section modulus to be designed into the seat. Typical sections through the cushion and back are shown in Figure 19.

The design utilizes adhesive bonding to join the inner and outer shells. The adhesive paths are shown in Figure 20. The specific adhesive will not be selected until the final composite material choice has been made. The current redesign of the seat is shown in Figure 21.

Weight Status

The original design of the ACC seat achieved a 30% weight reduction for the cushion pan. The seat back achieved an 18% weight saving, although some opportunity for further weight savings may exist with thickness optimization. However, EPFL used a different design approach for the seatback with carbon fiber, and achieved a weight saving of 58%.

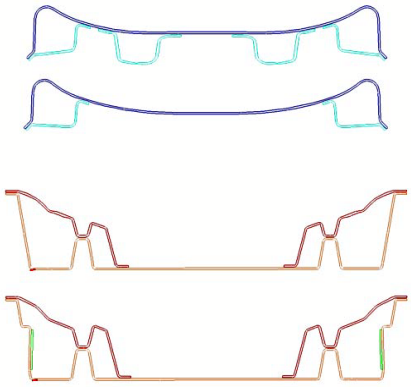

Figure 19. Redesigned seat sections

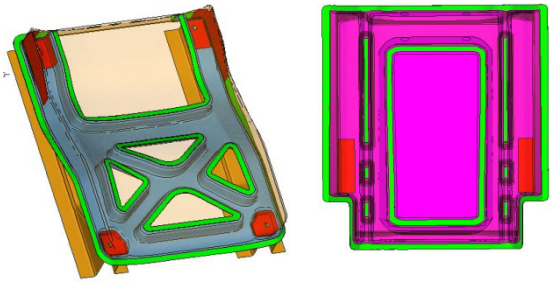

Figure 20. Adhesive paths and reinforcements.

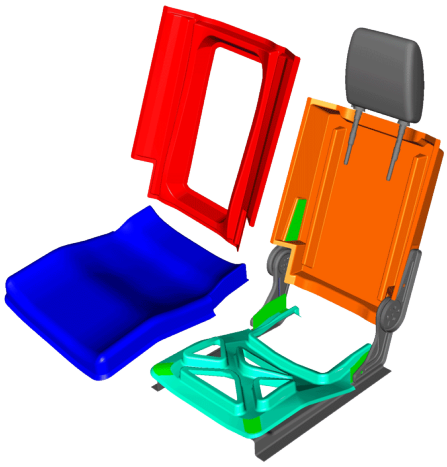

Figure 21. Redesigned composite seat.

The redesigned ACC seat shows significant opportunity to save weight with a random chopped carbon fiber/nylon composite. The seat back is currently at a 41% weight save and the cushion is at 56% weight save. Further weight savings may be possible with localized directional reinforcements.

A glass based design is being developed to reduce the cost of a composite seat. Finite element analysis is ongoing to develop the design and thickness of the glass-based seat to meet the structural requirements of the application. The weight of the glass-based design will be calculated when it meets these requirements.

The details of the weight status can also be seen in Table 1.

Table 1. Composite seat weight status

	Cushion	Back	
	Weight (kg)	Weight (kg)	Cost [1] ($)
ACC Carbon Design	2.70	2.92	$73.76
% of Steel Comparator	-30%	-18%	738%
ACC Re-Design Carbon	1.71	2.11	TBD
% of Steel Comparator	-56%	-41%	
ACC Re-Design Glass	TBD	TBD	TBD
% of Steel Comparator			
EPFL Carbon Design	na	1.50	$41.51
% of Steel Comparator		-58%	415%
EPFL Glass Design	na	2.42	$15.74
% of Steel Comparator		-32%	157%
Steel Comparator	3.88	3.56	$10.00

[1] at 260k upa

Material Assumptions

The composite seat will be comprised of nylon 6 reinforced with chopped carbon fiber for the bulk of the molded composite part. The composite parts will be compression molded using DLFT compounded material. The inserts will be preformed from blanked, pre-laminated sheet stock and heated prior to being placed in the main molding tool. Robotic transfer will be necessary to meet the cycle times for the insert transfer.

Cost Modeling

Work has been completed with EPFL on developing a cost model for the composite seat. EPFL has designed a version of the seat back that utilizes the TPP4 process and materials. EPFL has also substituted the carbon/nylon material from the ACC seat design and reduced the material thickness to account for the improved mechanical properties. All three versions of the composite seat back have been used to understand the costs of a composite seat structure. Both of the carbon-based seat backs are significantly more expensive than the steel comparator, as can be seen in Table 1. The ACC Seat back is over seven times the cost of the steel seat back. The carbon EPFL design is over four times as expensive. This cost discrepancy can be largely attributed to the material cost of the carbon fiber. The TPP4 design is the only seat that is close to the steel seat back at approximately 1.5 times the cost. This is largely attributed to the use of glass fiber reinforcement and low cost polypropylene.

EPFL's seat design can be seen in Figure 22. Additional trim parts and reinforcements may be necessary for the TPP4 seat and would need to be accounted for in a complete seat cost.

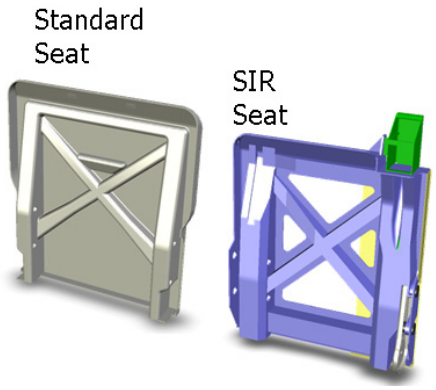

Figure 22. EPFL seat back designs.

Next Steps

The redesign of the composite seat structure will continue to be refined for carbon/nylon composites. It will also be designed with glass/PP and other glass fiber reinforced composites to reduce cost. The cost modeling exercise will need to be redone with the new designs.

Presentations/Publications/Patents

1. J. P. Fuchs, et al., “Automotive Structural Joint and Method of Making Same,” US Patent Application 12119084, 5/12/2008.
2. H. Fuchs, “Initial Design of the Automotive Composites Consortium Structural Composite Underbody,” SAMPE Fall Technical Conference, Memphis, TN, 9/10/2008.

3. L. Berger, et al., "Materials and Processes for a Structural Composite Underbody," SAMPE Fall Technical Conference, Memphis, TN, 9/10/2008.

4. L. Berger, et al., "Development of a Structural Composite Underbody," SPE Automotive Composites Conference and Exhibition, Troy, MI, 9/16/2008.

B. Composite Underbody Attachment

Barbara J. Frame (Principal Investigator), Vlastimil Kunc
Oak Ridge National Laboratory (ORNL)
P.O. Box 2008, Oak Ridge, TN 37831-6053
(865) 576-1892; fax: (865) 574-8257; e-mail: framebj@ornl.gov
(865) 574-8010; fax: (865) 574-8257; e-mail: kuncv@ornl.gov

Automotive Composites Consortium (ACC) Joining Group
United States Council for Automotive Research (USCAR)
1000 Town Center Bldg., Ste. 300, Southfield, MI 48075
(248) 223-9000; fax: (248) 223-9021; e-mail: cphilpott@uscar.org

Technology Area Development Manager: Joseph A. Carpenter
(202) 586-1022; fax: (202) 586-1600; e-mail: joseph.carpenter@ee.doe.gov

Field Technical Monitor: C. David Warren
(865) 574-9693; fax: (865) 574-6098; e-mail: warrencd@ornl.gov

---

Contractor: Oak Ridge National Laboratory (ORNL)
Contract No.: DE-AC05-00OR22725

Objective

- Develop a method to predict the effects of environmental exposures and mechanical loadings on the durability of a composite-adhesive-metal (i.e., multi-material) joint. The focus application for this project is the joining of a polymer-matrix composite (PMC) underbody to an automotive body structure.

Approach

- Develop and validate the analytical models and tools capable of predicting multi-material joint performance and durability under multiple loading scenarios.
- Generate an experimental database on the multi-material joint's performance and durability under various loading and environmental conditions to support and validate the modeling approach.
- Establish and define the bounds of validity for the methodology.

Accomplishments

- Conducted a literature review of current best practices for joining structural automotive composites that included current domestic and foreign automotive technologies and recent technologies that have been developed and implemented in nonautomotive applications.
- Prepared and distributed to the working team data files containing geometry, material property, and other information necessary to describe and model the composite underbody joint.
- Prepared a conceptual test specimen design for simulation of individual load cases expected for the composite underbody joint during service. The conceptual specimen design has an advantage that representative global thermal stresses arising due to manufacturing or environmental exposures can be "locked in" to the specimen and thereby included as a part of the multi-material joint durability evaluation.
- Identified critical load cases (tension, bending, and torsion) for evaluation in joint durability tests and model validation efforts.

- Defined the durability cycle and environmental conditions (temperatures, humidity) to be used for joint durability testing.
- Identified the weld bonded "super lap shear" specimen geometry for initial joint durability testing and model validation efforts
- Conducted analyses to identify minimum specimen dimensions necessary to adequately capture the effects of thermal loading when using the super lap shear specimen design.
- Constructed an analytical model to estimate stresses in super lap shear, weld bonded geometry arising from manufacturing process temperatures.
- Identified an existing "tub tool" for the manufacture of the composite portion of the multi-material joint specimens to be evaluated in the second phase of this project.
- Conducted infrared (IR) thermography examinations of a weld bonded composite-to-steel super lap shear specimen.

Future Direction

- Conduct durability testing with super lap shear specimens tested in tensile mode.
- Modify and adapt super lap shear specimen geometry to accommodate testing via four-point-bending and torsion test methods.
- Prepare test fixtures and equipment to evaluate a weld bonded specimen via four-point-bending and torsion test methods.
- Evaluate validity of durability analytical models with weld bonded specimen test data and make modifications to models as appropriate.
- Design specimen, tests, fixtures, and equipment for evaluating multi-material joint durability using three-dimensional (3D) composite molded from "tub tool."

Continue validation and development of durability analytical models using test data from tub tool specimens as input.

Introduction

The objective of this project is to develop a method to predict the effects of environmental exposures and mechanical loadings on the durability of a composite-adhesive-metal joint. The focus application is joining a PMC underbody to an automotive body structure and validating the assembly's long-term durability and performance.

Technologies for attaching/joining PMC parts with other metallic components enable the wide-spread integration of composites into a predominantly steel vehicle's design and manufacture. This design strategy requires reliable technologies for joining components made of dissimilar materials. Issues associated with joint design include long-term reliability (durability) and ease of assembly (manufacturing cost). Multi-material joining also requires an understanding of the compatibility of the joined members and means of attachment (adhesives, fasteners, etc.) under long-term service conditions.

Attempts have been made to characterize performance of such load-bearing joints in aerospace as well as some automotive applications in the past. However, those earlier results were specific to the geometries, materials, and joining techniques studied. Generic tools for predicting the performance of any composite design do not exist. Consequently, the joint and materials to be used in the PMC underbody must be studied for this particular application.

Because original equipment manufacturers need to minimize the number of developmental prototypes, validated modeling tools must be created to allow them to predict the durability of composite structures with the same level of

confidence as metal structures if they are to implement composite structures in vehicles intended to be produced in high volume using common program timing. This project is a step toward achieving that goal.

This project will validate the basic methodology for building computer-aided engineering (CAE) models capable of predicting the durability of composite-to-metal joints. Additional work will be required to expand the models to other types of multi-material joints. However, the tools developed as part of this project will be available for other joint designs, including other material combinations.

Technical Approach

A methodology for coupon-level testing of combined environmental and mechanical loading in a multi-material joint will be developed. The underbody geometry will be simplified to allow extraction of test data representative of the performance of this type of joint. Necessary size and scaling techniques to interpret test results will be established. CAE modeling will be conducted to aid in the design of the test specimens to best replicate real-life joint exposures and to allow for accelerated testing of environmental stressors and joint design due to differing load histories.

The validity of existing automotive CAE durability tools for this application will be evaluated. Inputs for model validation and development will be based on test results obtained as part of this project and previous research on similar materials. Test-program specifics will be determined in conjunction with the Automotive Composites Consortium (ACC) Focal Project 4, (see "Automotive Composites Consortium Focal Project 4," X.Y) design teams and relevant ACC working groups.

The key elements of this project include (1) design of the multi-material joint test, (2) material characterization, (3) test article manufacture, (4) mechanical performance of joint specimens for durability, (5) synergistic durability from multiple environmental stressors, and (6) CAE model validation. This project is a joint effort between ACC and ORNL.

Project Deliverables

Deliverables include a composite-to-metal joint coupon-testing protocol, test data, CAE model validation results, and final report. Recommendations to improve the methodology (testing and analytical) will be proposed as deemed appropriate.

Literature Review

A literature review of current best practices for joining structural automotive composites was conducted that included the current domestic and foreign automotive technologies as well as recent technologies that have been developed and implemented in nonautomotive applications (military, aerospace, industry, etc.). Technology gaps identified as part of this literature review included a general lack of durability modeling for composite-to-metal joints under automotive conditions.

Joint Specimen Concept

A multi-material joint specimen was designed incorporating previously analyzed super lap shear specimen dimensions and expected radii and flange sizes from the underbody geometry and surrogate tub (Figure 1). The specimen has the added feature of being able to "lock in" representative global thermal stresses arising due to manufacturing or environmental exposure.

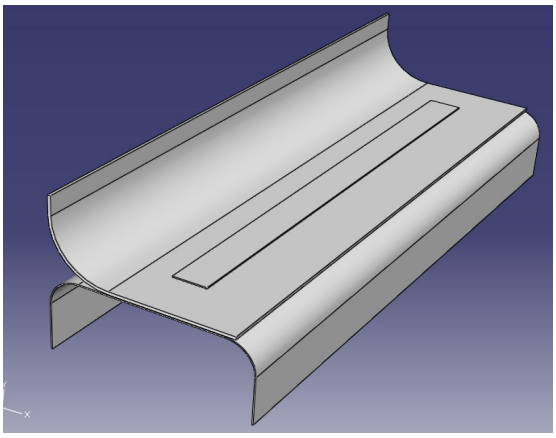

Figure 1. Conceptual design of multi-material joint specimen.

Six possible load cases were defined for the joint configuration, inducing various levels of peel and

shear along the concept joint specimen edges. Stress concentration factors, KvonMises and Kpeel, were devised to characterize the relative severity of the load cases, and are defined as

$$K_{vonMises} = \frac{\sigma_{vonMises}}{\sigma_{AJ}} \ldots K_{peel} = \frac{\sigma_{peel}}{\sigma_{AJ}} \quad .$$

In this equation, σ_{AJ} is defined as the applied load divided by the area of the joint, and $\sigma_{vonMises}$ and σ_{peel} are, respectively, the vonMises and peel stresses.

Results of this analysis are summarized in Figure 2 and indicate that the most significant load cases were associated with peel along the long (L) length of the joint and across the width (E).

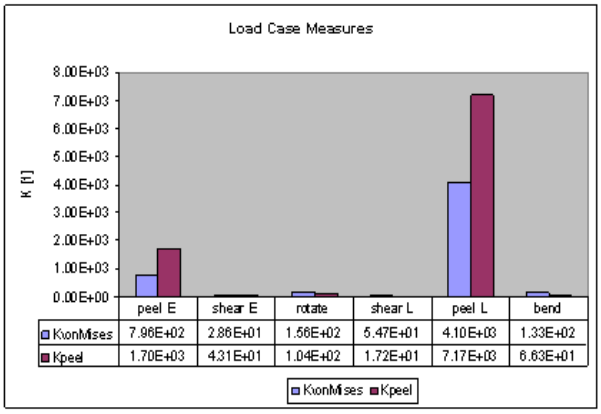

	peel E	shear E	rotate	shear L	peel L	bend
KvonMises	7.96E+02	2.86E+01	1.56E+02	5.47E+01	4.10E+03	1.33E+02
Kpeel	1.70E+03	4.31E+01	1.04E+02	1.72E+01	7.17E+03	6.63E+01

Figure 2. Analysis and severity ranking of load cases for conceptual joint specimen.

Experimental Test Parameters

Joint evaluations will be conducted through a combination of quasi-static and cyclic fatigue testing. The quasi-static tests are to determine the maximum joint strength and identify failure mechanisms. Fatigue testing will generate the S-N curves for each load case and environmental condition. The S-N curve is defined in high cycle fatigue as a graph of the magnitude of the cyclical stress (S) against the logarithmic scale of cycles to failure (N).

Fatigue-test parameters are 10% to peak load (sinusoidal) at 3 Hz. The environmental conditions include tests conducted at 25°C (ambient temperature), 80°C, −40°C, and 50°C and 85% relative humidity.

Super Lap Shear Weld Bonded Coupon Tests

The super lap shear weld bonded coupon, shown in Figure 3, was developed by General Motors for evaluating weld bonded metal joints. Since a significant amount of joint characterization has already been conducted using this geometry, this coupon was selected for the first phase of durability testing of a composite-to-metal joint.

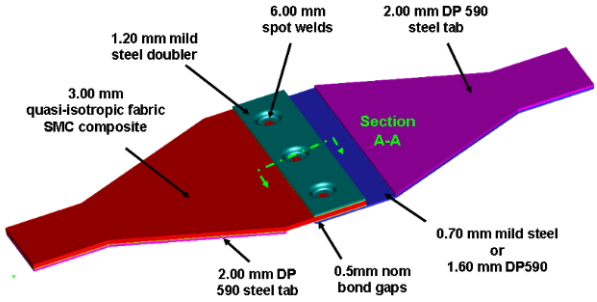

Figure 3. Super lap shear test weld bonded coupon developed by General Motors. (Image is courtesy of Multimatic Incorporated.)

Tested in tension, loading of the coupon's joint is primarily due to shear stresses (with a minor peel-stress contribution) leading (ideally) to failures that are shear dominated. The durability test data derived from these tests will therefore be used to validate simple durability models for prediction of shear dominated failures in a multi-material joint.

A goal of the project is to validate durability models for failure prediction of multi-material joints that are loaded in ways similar to what they would experience in the on-vehicle structure. In-service joints are typically subjected to mixed- or combined-loading conditions. Analyses conducted by Multimatic Incorporated show that in bending-mode tests (such as four-point bend tests), loading of the coupon joint is dominated by peel stresses. In torsion tests, loading is a combination of both shear and peel stresses.

Plans are to attempt to modify and adapt the basic components of the super lap shear specimen so that it may be used as both a four-point bend test specimen and a torsion test specimen. The data derived from these tests will be used to validate that the durability models are appropriate for

prediction of durability under these loading conditions as well.

Manufacturing Stresses Analysis

Linear finite-element analysis (FEA) was used to estimate the residual stresses in the composite-to-metal joint due to cooling after cure and spot welding.

A joint strip model was created with three welds along the length (see Figure 4) and geometry adopted from the super lap shear specimen model. The stresses were analyzed in the adhesive layer (Figure 5) of the composite.

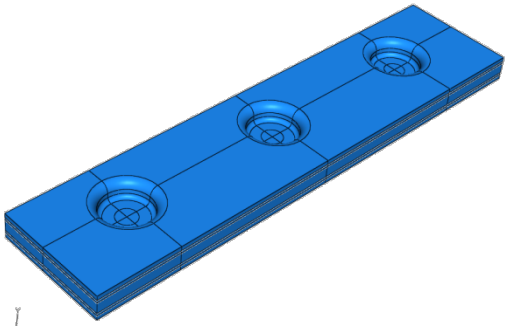

Figure 4. Representation of weld bonded joint used in residual manufacturing stress analysis.

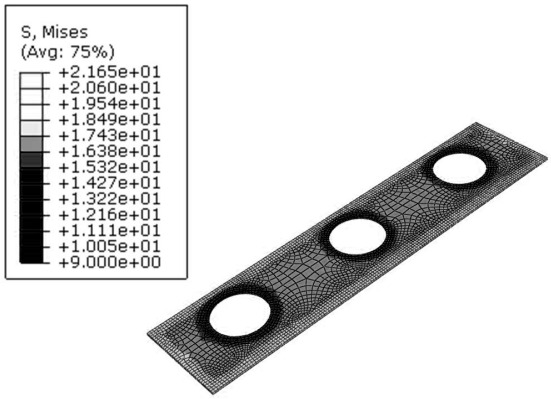

Figure 5. Analysis of residual manufacturing stresses in adhesive portion of weld bonded joint. The highest stresses are at the edges of the specimen.

Results of this analysis showed that the highest stresses were at the edges of the adhesive portion of the specimen. This type of analysis could be used to estimate an appropriate knockdown factor for a durability model.

"Minimum Length" Analysis

Analyses were conducted to establish the minimum specimen dimension required to ensure that the thermally driven stresses in a long, weld bonded, composite-to-metal joint are accurately represented by the test specimens. Stresses due to thermal loading were analyzed in flat specimens containing up to six welds. Figure 6 shows the mesh for one of the analyses and a path along which stresses were plotted in Figure 7.

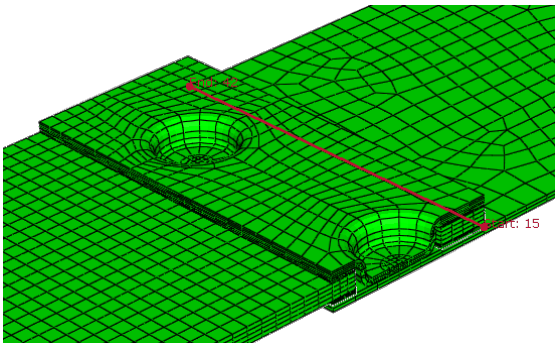

Figure 6. FEA mesh for analysis of thermally driven stresses in long weld bonded joint.

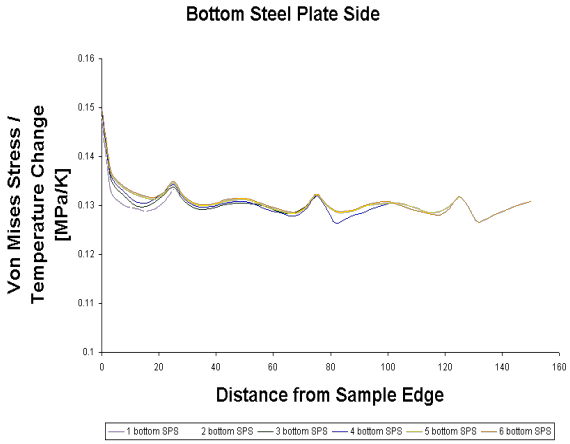

Figure 7. Thermally induced stresses versus distance from sample edge for multiple lengths of weld bonded specimens.

Upon examination of the results, it was concluded that specimens containing two or more welds experienced virtually identical stresses along the edges of the joint as those of longer specimens.

Surrogate Tub Specimens

Use of an existing tool for molding a composite tub was identified as a low cost way to obtain a

surrogate part for this project. This component will be used to provide the composite portion of the structure used in substructural-level testing in the second phase of this project. Composite tubs molded in the tub tool will possess many of the 3D features of the composite underbody design, including the flanges and corner details.

Design of the tub-tool test specimens is on hold pending results of the super lap shear coupon tests and model validation work.

Infrared Thermography Inspection of Weld Bonded Coupon

A super lap shear specimen was evaluated at ORNL using the IR thermography technique to determine whether the constituents of the joint (weld nugget, composite, and adhesive) could be examined nondestructively.

Figure 8 shows IR images of the coupon weld bonded region as a function of time following a thermal exposure applied to one side of the specimen using a xenon flash. An analysis of the measured IR intensity as a function of depth from the surface is shown in Figure 9.

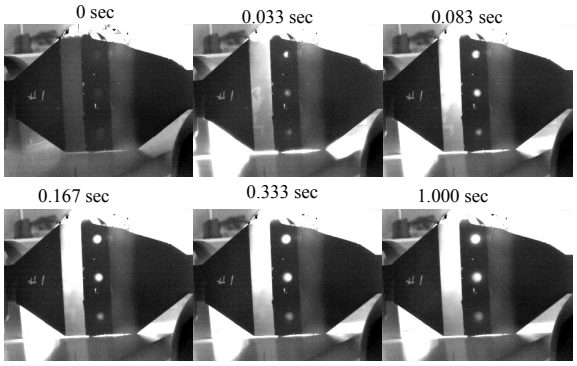

Figure 8. IR thermography images of composite-metal weld bonded coupon.

The preliminary data indicate that the details and size of the weld nugget could be deduced, and the weld nugget diameters in this specimen ranged between 5.78 and 6.50 mm (0.228 and 0.256 in.). Further work will be required to obtain information regarding the composite and adhesive.

IR thermography may provide a means to assess the quality and uniformity of weld bonded,

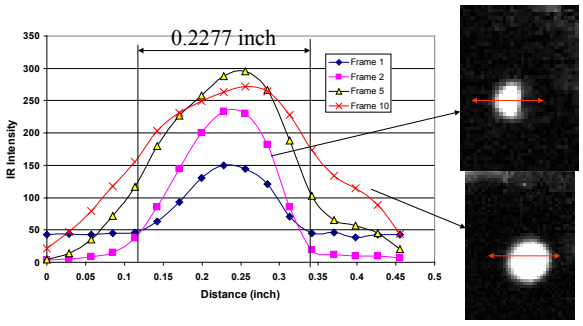

Figure 9. Estimated weld bond nugget size (0.228 in. or 5.78 mm) using IR thermography data.

composite-to-metal assemblies. It has the added potential to provide information on failure mechanisms for test specimens and structures where details of the failure (composite delaminations and cracks, weld nugget fractures, etc.) may be obscured by the outer facings of the specimen.

Summary and Conclusions

A literature review of current best practices for joining structural automotive composites was conducted. The results indicated a general lack of durability models for joints under automotive conditions, which this project addresses.

A conceptual multi-material joint specimen was designed incorporating previously analyzed super lap shear specimen dimensions as well as expected radii and flange sizes from the underbody geometry and tub tool. This concept specimen has the added feature of being able to lock in representative global thermal stresses arising due to manufacturing or environmental exposure.

Critical load cases to be studied for the joint durability test and model validation efforts have been identified, as well as the durability cycle and environmental conditions (temperatures, humidity) to be used during testing.

A super lap shear weld bonded coupon has been selected for the first phase of durability testing of a composite-to-metal joint. In addition to tensile tests, plans are to attempt to modify and adapt the basic components of the super lap shear specimen so that the weld bonded geometry can be evaluated in four-point bend and torsion.

Linear FEA was used to estimate the residual stresses in the composite-to-metal joint due to cooling after cure and spot welding. Analyses were also conducted to establish the minimum specimen dimensions required to ensure that the coupons experience thermally driven stresses during testing at temperature. Results showed that specimens containing two or more welds experienced virtually identical stresses along the edges of the joint as those of longer specimens.

An existing tool for manufacturing surrogate parts was identified. This tool will be used to manufacture the composite portion of the multi-material joint specimens to be evaluated in the second phase of this project. Design of the specimens based upon this component is on hold pending results of the super lap shear coupon tests and model-validation work.

A super lap shear specimen was evaluated using the IR thermography technique to determine whether the constituents of the joint (weld nugget, composite, and adhesive) could be examined nondestructively. Preliminary data indicate that the details and size of the weld nugget can be deduced. Additional work is required to obtain information regarding the composite and adhesive.

Acknowledgements

The principal investigators would like to acknowledge and thank Hsin Wang at ORNL for conducting the IR thermography examination and analysis presented in this report.

C. Development of Next-Generation Programmable Preforming Process

Principal Investigator: Robert E. Norris Jr.
Oak Ridge National Laboratory
P.O. Box 2008, Oak Ridge, TN 37831-6053
(865) 576-1179; fax: (865) 574-8257; e-mail: norrisrejr@ornl.gov

Technology Area Development Manager: Joseph A. Carpenter
(202) 586-1022; fax: (202) 586-1600; e-mail: joseph.carpenter@ee.doe.gov

Field Technical Monitor: C. David Warren
(865) 574-9693; fax: (865) 574-6098; e-mail: warrencd@ornl.gov

---

Contractor: Oak Ridge National Laboratory (ORNL)
Contract No.: DE-AC05-00OR22725

Objectives

- Develop the next generation of low-cost fiber-preforming technologies based on programmable, robotic-controlled, directed chopped-fiber processes for the application of
  - low-cost carbon fiber (CF),
  - reinforced thermoplastics, and
  - hybrid glass-carbon.
- Develop the supporting technologies required to successfully implement the process technology including
  - preform characterization (e.g., permeability, areal-density uniformity) and
  - perform process modeling for process-effects analysis.
- Conduct parametric process studies to investigate fundamental process effects and establish process-property relationships.
- Conduct requisite molding investigations—experimentally and through modeling—to elucidate the relationship between preform characteristics and moldability.

Approach

- Use and expand the base-research, programmable, robotic preforming system for development and evaluation of advanced capabilities (e.g., new chopper designs).
- Use a highly instrumented and controlled research molding capability to isolate and investigate the effects of process variables on moldability and mechanical properties.
- Develop new severing technologies to facilitate the implementation of low-cost carbon-reinforced thermoplastics and hybrid glass-carbon products.
- Benchmark and incorporate process modeling in experimental work to guide parameter selection and to provide tools for longer-term implementation of preforming and related technologies.

Accomplishments

- Using commercially available industrial grades of CF and glass fiber, fabricated a number of test preforms with polypropylene and blends at various ratios of carbon and glass reinforcement to evaluate potential advantages of combining these materials to achieve performance and/or economic benefits. Although the focus of this approach is to facilitate evaluation of alternative material combinations, especially looking at hybrids, in situ blending may prove economically attractive as well. Since the variety of forms of commingled materials is

extremely limited, this allows evaluation of materials not available at all in commingled form and in a much broader array of blending alternatives.
  - — Significantly improved preforming and preconsolidation processes to allow evaluation in further processing.
  - — Demonstrated molding of hybrid panels made with the above processes. Results are encouraging, with the biggest issue being uneven distribution of the polypropylene through the panel thickness.
- Procured a refurbished urethane injection system to be installed in fiscal year (FY) 2009 to enable evaluation of various materials/forms in liquid molding processes, including hybrid blends and natural-fiber preforms, and early evaluation of lower cost CF.
- Developed and demonstrated capability to control prototype Wolfangel chopper in operations representative of those used in high-throughput preforming and specifically simulating a generic liftgate pattern. Established capability limits of original hardware and necessary parameters for scaling up the system.
- Designed, built, and characterized significant upgrades to Wolfangel chopper to simulate robotic-preforming operations at speeds exceeding those of the current chopper system and meeting economic goals established from earlier work.
- Achieved apparent improvements in cutter wear of Wolfangel blades coated with a thin layer of zirconium using the C3 International Metal Infusion Surface Treatment (MIST) process.
- Initiated effort to model image projection of the laser and fiber-optic delivery system being used in laser-severing experiments.
- Modified previously developed general modeling approach to handle various fiber types and improve realistic fiber-deformation predictions leading to enhanced capability to model void space and potential flow pathways.

Future Direction

- Continue improvements in preforming and molding through studies with hybrid carbon and glass reinforcement and polypropylene materials blended in situ at the preforming machine. Expand to consider various other product forms including forms with low-cost CF as available. Implement more industry-representative and effective means of heating and transferring blanks of reinforcing fibers mingled with thermoplastic fibers into the press for compression molding.
- Develop and implement required hardware modifications and control changes necessary to use Wolfangel chopper on the ORNL preforming machine while maintaining capability to switch back to the original chopper as necessary.
- Demonstrate technical and economic feasibility of higher-speed Wolfangel chopper in representative preforming manufacturing operations using the upgraded preforming machine.
- Demonstrate more durable chopping mechanisms using alternative blade materials and coatings and other hardware as appropriate, using both standard and higher-speed choppers. Continue monitoring/evaluating alternative chopping techniques for longer-term development.
- Evaluate preform process models relative to physical preform characteristics and expand model capability as resources permit.
- Continue developing and implementing tools for more-effective characterization of process variables and effects on final products.

Introduction

Polymer-matrix composite materials offer a number of benefits in lightweighting of automotive and heavy vehicles, including greater stiffness and strength per unit weight than conventional materials, easier formability, less corrosion susceptibility, the ability to tailor properties to specific load requirements, and enhanced noise and vibration damping. However, widespread implementation of CF composites, which are among the materials with the greatest weight-saving potential, will require lower-cost

materials and manufacturing processes than are currently available. Advanced preforming processes offer opportunities to facilitate the widespread use of carbon composites.

Robotic-controlled, programmable, directed-fiber preforming processes have demonstrated exceptional value for rapidly preforming large, glass-reinforced, automotive composite structures. Due to their unique features and flexibility and to their inherently low scrap rate, they are among the most viable candidate processes for making affordable CF preforms for a variety of structural automotive components. The Automotive Composites Consortium (ACC) has very successfully implemented the programmable powdered preform process (P4) with glass fibers in its truck box program—Focal Project 2 (FP2). Prototype B-pillars were also successfully fabricated with both carbon- and glass-fiber reinforcement and tested as part of the ACC's Focal Project 3 (FP3) composite-intensive body structure program). Original equipment manufacturers have transferred the technology to commercial applications such as the General Motors Silverado pickup box and the Aston Martin Vanquish body side.

Analyses have indicated a potential for greater than 60% weight savings for a CF-intensive body-in-white under the assumption of a thickness design constraint of 1.5 mm. The analyses also indicated the potential for saving an additional 15% if the thickness constraint is reduced to 1 mm. Unfortunately, evidence suggests that 1.5 mm may be a practical limit for liquid molding. However, thermoplastics preforms, in which the matrix and fiber are both deposited in the preforming step, offer a potential path to obtaining thinner sections and, consequently, additional weight savings as well as greater potential for recyclability. Hybrid-fiber preforms that can effectively take advantage of concurrently using carbon and glass fibers offer another potential benefit in terms of economics and property enhancement and may be a good route for actually introducing more CF at somewhat lower quantities than necessary for all-carbon components in automotive applications.

Preforming Developmental Approach

The objective of this project is to advance directed-fiber preforming processes to effect a further reduction in vehicle weight—relative to metals and conventional glass-fiber composites—while maintaining the economical advantages of net-shape preforming. The project is pursuing three focus areas corresponding to three materials systems: reinforced thermoplastics, CF, and hybrid glass-CF. Each focus area consists of four main tasks: (1) materials development, including introduction and evaluation of alternative and/or new fiber product forms and binders; (2) machine development, particularly new severing technology; (3) process development, for example, to control areal-density uniformity and preform anisotropy; and (4) supporting technologies development, including modeling and characterization techniques. This project will also include developing a deeper understanding of fundamental aspects of the process and their effects on preform quality and mechanical properties in the molded part. To summarize, this project will support, augment, and facilitate the current and future research activities undertaken in related ACC projects.

A research-focused preforming system has been installed in the polymer composites laboratories at ORNL to serve as the base for hardware and associated technology developments. A number of combinations of reinforcing fibers, binders, and/or matrix fibers have been obtained to establish materials baselines for comparison with and advancement of previous P4 work conducted by ACC. The P4 machine is currently being used to build preforms for evaluation using the Twintex product (glass fiber commingled with thermoplastic fiber to serve as the matrix), glass impregnated with thermoplastic resin using the Direct Reinforcement Fabrication Technology (DRIFT) process, and various forms of carbon and glass reinforcement in alternate independent and hybrid forms. Although the near-term focus is on demonstrating advances with glass fiber and existing industrial grades of CF, the long-term goal is to establish the groundwork for large-scale introduction of low-cost CF for significant impact in automotive lightweighting.

In Situ Blending to Evaluate Hybrid Carbon and Glass Compositions

Because it is believed that hybrid-fiber preforms can effectively take advantage of concurrently using carbon and glass fibers and offer potential benefits in terms of economics and property enhancement, ORNL has obtained standard, lower-cost CF alternatives from Zoltek and Toho to evaluate in conjunction with glass- fiber reinforcement previously acquired from Owens Corning. ORNL has also procured polypropylene fiber from Fiber Science to serve as the composite matrix in initial trials to evaluate and demonstrate in situ blending of these hybrid blends at the preforming machine.

A number of preforming and molding experiments has been conducted to establish the equipment setup requirements and process parameters necessary to evaluate the potential of these hybrid blends. As previously established in cutting the Twintex materials, the polypropylene is more difficult to completely sever than the carbon- or glass-fiber reinforcement, although it is less abrasive to the cutter blades themselves. Due to current polypropylene product availability, typically only in very small tow sizes, and the desire to maintain the capability to adjust the mix ratios to a large degree, the polypropylene was combined by the vendor to a larger tow size, which was still about half the size of the smaller glass and carbon tows on hand. Currently, the only packaging found immediately available was configured for outside unwind of this product versus the inside unwind configuration that works best for preforming. These limitations necessitated use of a multiple position creel to facilitate processing and mitigate entanglement. Still not being intermixed on a filament-to-filament basis with the reinforcement fibers as with the Twintex, the polypropylene also tends to "fuzz" a little more in handling than that with the Twintex. These factors have made the in situ-blended materials a little more difficult to cut while preforming and a little more difficult to preconsolidate into a preform having structural integrity for handling.

As we continued to make adjustments (e.g., to blade and roller configurations and placement of air purges and vacuum to reduce clogs) and improve chopability, significant effort was devoted to improving the preconsolidation process and developing necessary processing conditions for molding. We determined that one of the key problems in the preconsolidation process was that we were not able to get uniform air flow into the preform during compaction. Compaction is achieved by the dead-weight loading of the upper compaction table being let down on top of the lower table until the upper table weight is sustained by the combination of the pressure on the screen by the compressed preform and weight on the lower screen frame when the upper screen frame makes contact. Assuming that the screen-frame sections make contact (which had been the case for all preforms made until experiments described below), the greater the thickness of the preform, the greater the compaction pressure within each preform. It appears that the additional fuzziness of the in situ-blended materials probably impedes air flow and leaves more clumps of fibers and fibers extending out of the two-dimensional plane of the preforming screen. The air flow into the preform during the preconsolidation process is also not a self-stabilizing process (i.e., as the air flow encounters more resistance from the more densely packed regions in the preform, it actually concentrates flow through the less dense, lesser packed regions). The net result was that the initial preforms had holes where the hot air had created separation of all materials and some regions in which the polypropylene had been totally melted and flowed into almost a solid sheet and other larger regions with no signs of any consolidation. We were able to mitigate these effects by placing shims between the upper and lower screen-frame sections, thereby reducing the compaction pressure. Although this does allow some of the hot air intended for preconsolidation to escape, the upper screen still extends into the lower frame such that the thickness of the shims can be adjusted to balance escaping air flow and compaction pressure within the preform. Although still not optimal, this approach allows us to get preforms consolidated well enough for initial molding trials and is encouraging for further development.

To conduct initial molding experiments to evaluate the preforms and establish detailed

requirements for more optimal charge heating and transfer of the charge to the press, various heating and transfer techniques are being evaluated for this process. An existing laboratory curing oven is currently being used for charge heating. Due to the oven's relatively small air-flow capability and distance from the press, an aluminum plate has been used to maintain temperature while the preform is conveyed from the oven to the press. In addition, we have been using a single sheet of high-temperature release film large enough to fold and cover both the top and bottom of the preform to mitigate air exposure during oven-to-press transfer and to facilitate transfer of the charge from the aluminum sheet into the mold. Initial experiments indicate that we are approaching an acceptable preforming/molding process but that the distribution of the polypropylene is not uniform through the thickness of the panel, with the side of the panel that corresponds to the preforming screen much "wetter" than the "sprayed-up" side. We think that this could be due to the polypropylene being melted and flowing or being forced down to the screen due to the air flow in the preconsolidation process or problems with the initial blending. Although we have conducted a limited amount of mechanical testing, tests so far have been used to identify and direct process improvements (as discussed above) as opposed to generating reportable data.

During the latter portion of this period, experiments were conducted to evaluate different techniques to improve the intermixing of reinforcing fibers with the polypropylene. Several variations of the device shown in Figure 1 were used to evaluate injection of turbulent air flow into fibers before the chopping process, similar to the approach used in textiles for intentional yarn entanglement for splicing or other purposes. Although the different fibers were obviously better intertwined, initial experiments did not show significant improvements in the final panels after molding. We plan to investigate further entanglement in the preforming and changes in air flow and temperatures in the preconsolidation process. We are also evaluating whether we will go with an improved convection oven or a combination of convection and infrared for the charge preheating; either way, the oven will be placed significantly closer to the press to minimize transfer time.

Figure 1. Prototype air injector for enhancing fiber intermixing.

As part of establishing supporting tools, a limited amount of effort was spent developing the capability to rapidly determine weight and volume ratios for mixtures of glass, carbon, and polypropylene. Typically, acid digestion processes for the composite matrix are used to determine ratios of carbon to resin in CF-reinforced composite parts. Typically, resin burn-off or acid digestion processes are used to measure glass and polypropylene ratios in glass-reinforced composite parts. Burn-off techniques are usually quicker, create fewer hazardous wastes, and are more practical for larger sections than acid digestion. However, if an inert atmosphere is not used, one has to be careful with CF to avoid oxidizing the fiber itself at high temperatures. The author and others have used combinations of acid digestions to determine resin content and then high temperatures in air (~800°C) to get the carbon : glass ratios for hybrid-type samples. We are conducting experiments to determine whether we can get ballpark numbers for resin content without oxidizing the CF at about 450–500°C. Alternatives include using an inert atmosphere and possibly higher temperatures to eliminate the resin. If so, this would be a much quicker and

more cost-effective tool for composition analysis for this work.

Although the current focus of this work is using polypropylene for demonstration purposes, the concept should also be applicable for other thermoplastic materials, including polyester and nylon. If successfully demonstrated, in situ blending would offer greater flexibility for manufacturers to tailor-blend ratios in-house to specific product needs without long lead times, inventory requirements, or dependence on the limitations of product variety from suppliers as is the case with the Twintex product manufactured by Saint-Gobain Vetrotex. It is believed that regardless of whether the in situ-blending process itself proves adequate for high-quality, thermoplastic matrix parts, the technology being developed could prove advantageous in blending glass and carbon reinforcement to a level adequate for use of hybrid reinforcement in general and could likely be extended beyond thermoplastics and applied to thermosets in sheet molding compounds or to preforming for structural reaction injection molding (SRIM). This could have significant impact on DOE and ACC goals as hybrids would appear to be an effective route for actually introducing more CF at somewhat lower quantities than necessary for all-carbon components in automotive applications and an effective means of reducing the component cost in CF by using only the minimum amount that is needed. To both expand the breadth of hybrid blend alternatives and facilitate evaluation of low-cost CFs being developed at ORNL, we have procured a refurbished urethane injection system, shown in Figure 2, to establish in-house SRIM capability for this program.

High-Speed Chopper Development and Demonstration

The ACC Materials and Processing working groups had initiated work with Ecole Polytechnique Fédérale de Lausanne (EPFL) in Switzerland to study processing effects and material properties of commingled glass and thermoplastic fibers leading to cost-model comparisons of various thermoplastic-composite processes. The focus of this work has been on the Twintex materials produced by Saint-Gobain

Figure 2. Urethane injection system capable of 110 pounds (lb)/minute and 33 lb shot sizes.

Vetrotex, incorporating glass and polypropylene fibers, but the basic evaluation process can be extended to a variety of materials and processes based on this concept. With the support of EPFL and an ACC representative, ORNL fabricated approximately 200 sample panels using various fiber lengths (25–75 mm) and preform thicknesses (2 mm–4 mm) along with variations in preforming compaction station time (10–60 s) and air temperature variables (180–240°C). Results so far have helped to establish initial thickness limits for processing at 3 mm without additional heat-stabilization modification to the materials. ORNL and ACC have each separately discussed with Vetrotex adding improved heat stabilization capability to the Twintex line. ORNL and Vetrotex have tentatively planned specific evaluation trials, but these trials have been on hold pending resolution of the sale of this business unit.

Material properties of the ORNL panels processed by EPFL are competitive with similar materials and, in some cases, significantly improved. Overall economics for this process were shown by EPFL analysis to approach targets as chopping speeds improved, leading to additional near-term focus on demonstrating the technical and economic feasibility of higher-speed chopping processes.

To potentially improve preforming throughput, ACC purchased a prototype chopper unit from Wolfangel. This chopper was designed to process up to 5 tows of fiber at a maximum peripheral speed of ~892 meters (m)/minute (min), which for

the 1,870 tex Twintex tows amounts to ~8.3 kilograms (kg)/min of throughput. For comparison, the P4 chopper is designed to process 2 tows at up to 625 m/min, which for 1,870 tex tows translates to ~2.3 kg/min. We were able to run 2 tows through each tube of the P4 chopper, which would effectively double the throughput, but this was difficult to sustain and certainly could not be exceeded with the current configuration. Economic goals were to be able to achieve 12 to 15 kg/min, which would require similar doubling of at least some of the tows through each position of the Wolfangel chopper, speeding up the peripheral speed, or combinations of both. The Wolfangel chopper, shown in Figure 3, allows chopping at two distinct fiber lengths, determined by blade spacing in either the inside or outside half of the cutter wheel, which is then controlled by manually switching the positioning of the cutter roller with respect to the fiber stream passed through the cutter. The P4 chopper allows selection of an infinitely variable fiber length within a relatively wide range, but use of more than two lengths within a single production operation has been very rare.

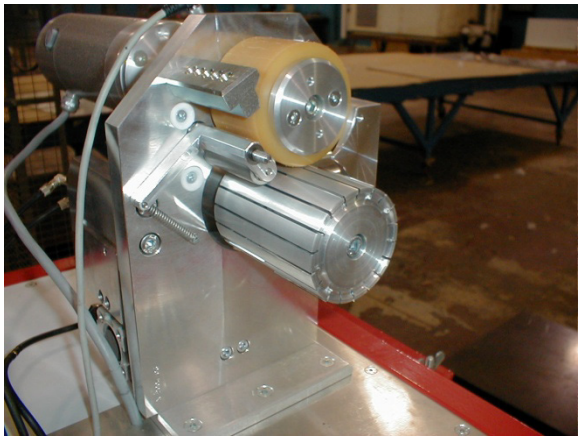

Figure 3. Wolfangel chopper showing cutter wheel extended. Cutting takes place on inner portion of the wheel in contact with the rubber roller.

Working with the ACC Processing Working Group, trials were conducted to check out the chopper using the supplied manual chopper controls and to capture representative chopper-control signals from the P4 machine to approximate simulation of the fabrication of a preform suitable for fabrication of a liftgate similar in shape to that shown in Figure 4.

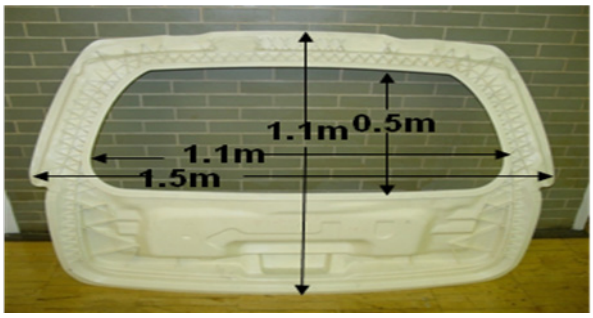

Figure 4. Approximate liftgate dimensions used in simulation program.

In typical processing, the chopper starts and stops very abruptly in tight coordination with the robot movement as the robot traverses across each pass and then indexes though multiple passes in uniformly spraying up the part profile. Obviously, the economics of the process are improved as speed of the preforming process is increased up to the repeatability and capabilities of the preforming system. A program was written in LabView to capture signals from the robot that could then be used to control the chopper for evaluation independent of operation of the entire preforming system. A separate LabView program was written to provide the necessary control signals to the chopper using the data previously captured, as shown in Figure 5. Also, hardware and program capability was provided to automatically switch fiber length during processing.

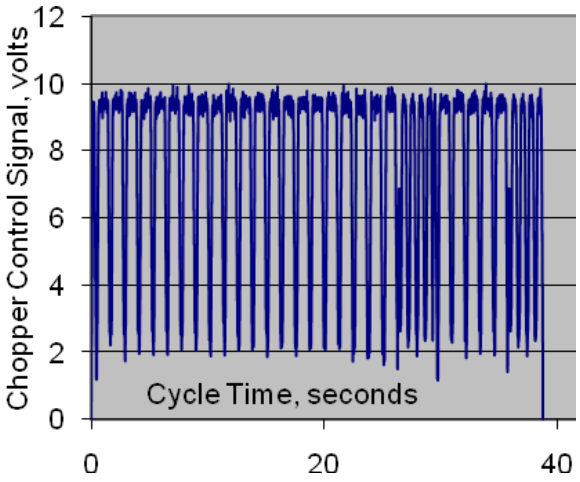

Figure 5. Chopper control signals in simulation program.

A larger set of trials was conducted at ORNL with ACC support to evaluate the Wolfangel chopper in liftgate fabrication simulations. During these trials, a number of enhancements were made to processing conditions and fiber handling as shown in Figure 6. It was determined that the chopper could easily handle up to 3 tows at close to the upper speed limit (892 m/min) to deliver about 5.0 kg/min but that the chopper did not have adequate torque to handle more tows due to the pressure required to fully sever the tows. However, it appeared that achieving both higher speeds and higher torque with a larger motor would be feasible with relatively minor modifications.

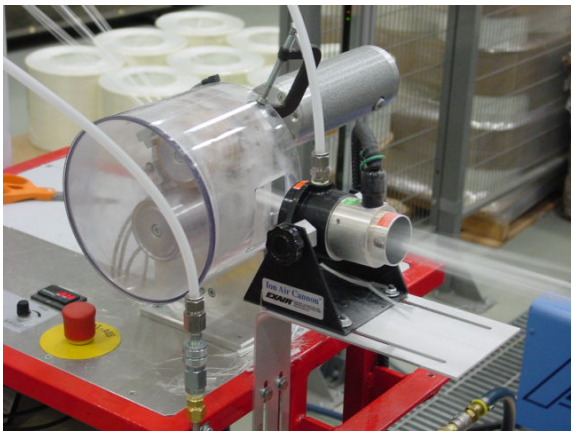

Figure 6. Photo showing ORNL-ACC trials which demonstrates improved fiber-processing techniques.

The existing Servowatt motor was rated at 0.75 Nm (Newton meter) maximum torque and 4,000 revolutions per min (rpm). An Allen Bradley MPL-B430 motor and drive system was located that rated at 20 Nm maximum torque and 5,000 rpm. With this motor operating at its speed rating, it should be able to achieve 12 kg/min using about 6 tows with a maximum output of more than 18 kg/min using 9 tows. The system was reconfigured with the new motor while using as much of the existing chopper hardware as possible, although a number of components had to be modified to use this higher-powered motor system.

The upgraded system, shown in Figure 7, has been characterized in extensive trials. It has been shown capable of achieving more than 18 kg/min instantaneous output when using 9 tows. Very

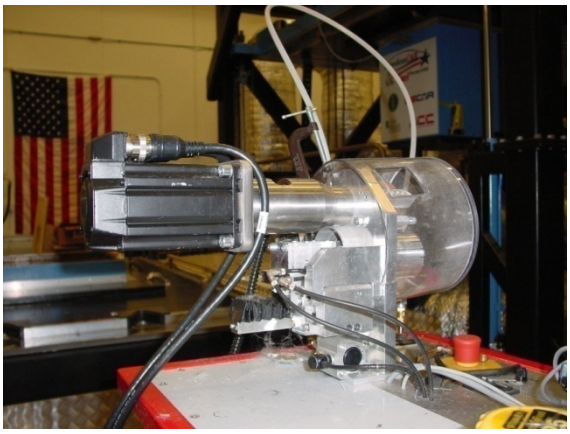

Figure 7. Chopper retrofitted with more powerful motor and adapters.

good severing was achieved at these conditions when using 150 pounds per square inch air pressure on the cutter/rubber roller interface for the 1-inch cut length, while the 3-inch length at these conditions was largely, but not completely, cut. (Typically, when not completely severed, the glass is more fully cut than the polypropylene.) This trend toward better cutting at the shorter length was essentially replicated for all conditions at which any difference was noted. As expected, improved severing was achieved at higher air pressures for essentially all speeds regardless of the number of tows being processed. Also expected was the finding that cutting quality decreased with the number of tows. However, we unexpectedly found that cutting quality actually improved with increased speed regardless of the number of tows being cut or interface pressure. Plans for FY 2009 are to further characterize the durability of this chopper. If the results continue to be as promising as those thus far, ORNL will make necessary hardware modifications and controls upgrades to mount the high-speed chopper to the robot to demonstrate the economic and technical feasibility for making preforms representative of those required to fabricate the liftgate shown in Figure 4.

As another part of the current focus on thermoplastics, ORNL has been working with Polycomp (inventor of the DRIFT process for making thermoplastic prepreg) and Fiberform (a key licensee) to evaluate the possibility of chopping the DRIFT product form in the ORNL preforming machine as well as providing one route

to evaluating the DRIFT material, in general. In the most recent work, a basic processing envelope, including both preforming and molding, adequate for fabricating evaluation panels was established and demonstration panels fabricated. Plans are to repeat the process to fabricate panels for testing. However, similar to problems with getting air flow into the preform for the compaction of the hybrid materials, the most recent ribbonized DRIFT form was very difficult to preconsolidate. We may get some improvement by reducing the compaction pressure as with the hybrid panels, but in this case, we feel that this could possibly be addressed by returning to the more oval-shaped form that was difficult to chop in the P4 chopper and instead use the upgraded Wolfangel chopper. With data from these experiments, plans are to focus efforts on developing more optimal processing techniques, taking into account material forms and chopper configurations that might be economically feasible for implementation. Discussions between ORNL and Polycomp are continuing concerning putting a prototype DRIFT line at the end of a low-cost CF pilot line to demonstrate and evaluate the technical and economic potential for various automotive applications of the DRIFT process.

Fiber-Severing Technology

ORNL is continuing to study mechanical chopping for various materials forms and techniques and also plans to continue evaluation of the potential for laser severing for rapid fiber cutting. In addition to evaluating the output capabilities of the Wolfangel chopper previously mentioned, we are also evaluating modifications to the chopper equipment including cutting wheels and blades for both units. As part of the extensive cutting experiments already completed involving a large amount of Twintex material, blades coated with thin layers of zirconium implanted with the C3 MIST were used alongside the standard stainless-steel blades supplied by Wolfangel. (MIST is a low-cost process that recently won an R&D 100 award.) Examination of the surface of the blades at the conclusion of these tests indicated that those blades coated with the MIST process showed fewer signs of wear, as shown in Figure 8. Conversely, use of MIST-coated carbon steel blades in the P4 chopper did not have immediately positive results. We had been experiencing

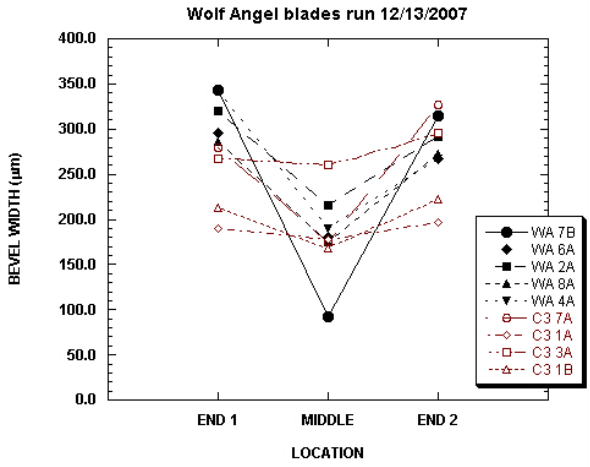

Figure 8. Comparison of wear on C3-coated and noncoated Wolfangel blades. Wear is indicated by difference of readings from the ends to the middle.

chopper jams and eventual blade breakage with the standard blades when cutting the hybrid materials in the P4 machine, largely due to binding of the polypropylene. When the standard blades were replaced with coated blades, the blades bent very quickly. It was apparent that although the MIST process is considered to be a relatively low-temperature process, it was indeed changing the steel properties. Additional data from upcoming tests using the Wolfangel chopper to cut a large amount of material under nearly identical conditions should afford a good opportunity to more fully evaluate these and several other blade options and other system components.

We will continue to work with C3 to better exploit the gains achieved with the Wolfangel blades and to better understand and use the information gained from failure of the P4 blades.

We have limited experience with the tungsten carbide blades in the original P4 chopper. Our initial experience was that binding of the polypropylene fractured these brittle blades; however, with changes in techniques and cutting of other materials, we may be better able to take advantage of the potentially higher wear capabilities of this blade material.

We are pursuing other sources for commercial blades and efficient, economical coatings. One of these is the low-temperature carburization process developed by Swagelok, which we found is not

directly applicable to blades manufactured from the carbon and stainless steels we have on hand. Nevertheless, we believe we will be able to find some blades made from the preferred alloys that will fit in our cutters.

Based on test data and other input, recommendations will be developed for enhancing the durability of cutter assemblies. This may include changing to more durable materials, changing the surface finish, changing design of the cutters or holders, and applying coatings or surface treatments to existing or alternative materials. With a better understanding of chopping mechanics and more experience with varying blade designs, blade materials, and cutting mechanisms, we will be able to better address a variety of cutting issues associated specifically with CFs as well as with other materials and material blends including somewhat unique products such as the DRIFT materials.

Due to significant differences in the physical properties of various reinforcement fibers as well as their available product forms, chopping technology that has been successful for glass-fiber systems has demonstrated less satisfactory results for the CF products that are currently available. It is expected that similar results will occur for reinforced thermoplastics and hybrid glass-carbon products. Accordingly, consideration has been devoted to identifying alternative severing technologies. Literature and patent searches were undertaken previously to assess promising technologies for benchtop investigation. Possibilities identified include mechanical-based, laser-based, CO_2 pellet, liquid nitrogen, water-jet, and ultrasonic. Based on the information available in the literature and consideration of project-team experience in related activities, laser-based choppers appear to offer the most promise for development and eventual deployment.

Although laser severing was demonstrated earlier in this project with Nd:YAG (i.e., neodymium-doped yttrium-aluminum-garnet) laser pulses, this took more energy than originally estimated. Even with modification to the delivery optics, we have not yet been able to demonstrate a pathway to a practical, cost-effective laser and optics system for this application in our experimental and limited modeling efforts to date. Although we still believe that this approach is likely technically feasible and intend to continue monitoring development of lower-cost laser systems and alternative means for optical delivery, we have halted active work in this area in the near term. We intend to revisit this technology and others that may have applicability at a later point.

Modeling of Preforming Processes

A process model has been established to analyze the effect of process variables on preform characteristics that affect further processing and performance of molded parts. The computer program can simulate deposition of long fibers and accounts for various processing conditions in automated manufacturing of fibrous preforms for automotive composites. The model accounts for different fiber types (e.g., glass, carbon, polymer) of different geometries and process deposition conditions (e.g., vacuum pull, fiber orientation and clustering, substrate traversal paths). The program uses a graphical user interface that allows the user to avoid mathematical details of the modeling process and concentrate on the physical aspects.

Recent improvements to the model include implementation of additional computational models that are relevant to the transport properties of the fiber preforms and therefore directly relevant to molding applications. A new method has been implemented for determining particle caging volumes. The topology of the fiber and void spaces can be related to physical measurements of tortuosity, porosity and characteristic lengths (viscous and thermal). The current model goes well beyond percolation-type and simple regular capillary geometry models. The transition between spanning connectivity, spanning cluster size, and fiber-particle-network caging capacity can also be used in preform permeability characterization. Realistic fiber deformation is a key provision along with strict enforcement of spatial rules (e.g., fibers are not penetrating as is the case in several commercial products). The basic consolidation model has been implemented and will be further developed based on particular processing conditions.

Near-term plans include correlating the capability to simulate fiber layups made of multiple fiber types deposited concurrently with experimental work in progress. We will compare predictions of the performance of the in situ blending with what is achieved and make comparisons with the theoretical predictions for offline commingling for different deposition scenarios. Longer-term plans include expanding the models and using these tools along with experiments for evaluation of manufacturing feasibility of the above preforming processes through consolidation and/or molding.

Summary and Conclusions

The Next-Generation Programmable Preforming Process project is continuing to build on past development and application of directed-fiber preforming processes, namely, those of the baseline P4, to extend the process to new material systems. Developments are expected to facilitate the use of lower-cost CF-reinforced thermoplastics and glass-carbon hybrid materials as effectively as with the current state-of-the-art glass-fiber technology. Using these materials is expected to lead to further reductions in vehicle weight in a more cost-competitive scenario than is currently possible.

A research-focused preforming system installed in the polymer composites laboratories at ORNL is currently being used to build preforms for evaluation. The system uses both glass fiber commingled with thermoplastic fiber and glass fiber preimpregnated with thermoplastic resin (DRIFT) as the composite matrix. EPFL and ACC evaluations of a large number of ORNL-fabricated preforms from off-the-shelf and the commingled Twintex product have been both technically and economically encouraging, especially if the projected speed increases can be achieved with the modified Wolfangel chopper. These modifications have been completed and the chopper characterized to establish capabilities and optimal operating parameters. Plans are to complete durability testing of this chopper in FY 2009 and, assuming results continue to be as promising as those thus far, to make necessary modifications and mount the high-speed chopper to the robot to demonstrate the economic and technical feasibility for making preforms representative of those required to fabricate a generic liftgate type structure.

During the first half of FY 2008, preforming and molding experiments were conducted to establish the necessary equipment setup requirements and process parameters to evaluate the potential for on-the-fly commingling of CF and glass fiber with polypropylene fibers to achieve hybrid blends. We were able to establish fiber intermixing, chopping, and preconsolidation techniques adequate for initial molding trials, which is encouraging for further development of this process. We investigated various techniques for charge heating and transfer of the charge to the press and demonstrated that we can mold panels fairly well using a relatively primitive setup before finalizing a design for better temperature control and faster transfer to the mold. Work to improve these techniques will be continued in FY 2009.

Severing investigations have been conducted in two areas: mechanical chopping and laser severing. The mechanical-chopping investigations included blade materials and coatings and various cutter configurations. Preliminary results indicate that low-cost C3 MIST coatings may improve blade life for specific applications, and this work is continuing. Since we have not yet been able to demonstrate a pathway to a practical, cost-effective, laser and optics system for this application, we intend to continue monitoring development of lower-cost laser systems and alternative means for optical delivery but have halted active work in this area in the near term with plans to revisit this technology and others that may have applicability at a later point.

Modeling of the fiber-deposition process continues through the development of an in-house code. It has unique characteristics compared to existing models reported in the literature and can simulate deposition of long fibers of various types and geometries and accounts for various processing conditions in automated manufacturing of fibrous preforms for automotive composites. Work is underway to evaluate the recently implemented capability to simulate layups made with multiple fiber types and to compare differences in manufacturing techniques.

Collectively, the technologies under development in this project will advance low-cost processing on two fronts. First, they will provide the opportunity to use additional materials in the net-shape preforming process, which is expected to lead to additional weight reduction and/or better performance. Second, they will provide the requisite tools to evaluate the effects of process parameters on the utility and performance of preforms and molded parts.

D. Low-Cost Carbon-Fiber Composites for Lightweight Vehicle Parts

Principal Investigator: Mark A. Janney
Materials Innovation Technologies LLC
320 Rutledge Road, Fletcher, NC 28732
(828) 651-9646; fax 828-651-9648; e-mail: mjanney@emergingmit.com

Technology Area Development Manager: Joseph A. Carpenter
(202) 586-1022; fax: (202) 586-6109; e-mail: joseph.carpenter@ee.doe.gov

---

Contractor: Materials Innovation Technologies LLC
Contract No.: DE-FG02-05ER84327[Small Business Innovation Research (SBIR) and Small Business Technology Transfer Program]

Objectives

- Develop at pilot scale the Three Dimensional Engineered Preform (3-DEP) process, a slurry-based, low-cost, high-volume production process for making net-shape, carbon-fiber preforms for use in polymer composite automobile parts.
- Optimize 3-DEP tooling development and evaluate how it influences fiber placement in the preform.
- Optimize carbon-fiber slurry development and determine how it affects preform properties.
- Develop process capabilities to include material handling, preform molding, preform drying, and reducing preform variability.
- Demonstrate the utility of 3-DEP preforms to make an in-production, thermoset composite, automotive component using production tooling (Corvette wheelhouse support).
- Build a process cost model for composites made using 3-DEP preforms.
- Write training and quality manuals.

Approach

- Investigate effects of processing parameters on properties of flat plate parts and Corvette wheelhouse support parts produced in the 3-DEP machine.
- Demonstrate ability to control part weight during a 3-DEP production run.
- Demonstrate ability to control within-part areal weight distribution (i.e., fiber areal density).
- Collaborate with a current Tier 1 automotive supplier to demonstrate the applicability of 3-DEP preforms in an existing production process.

Accomplishments

- Conducted a mock Part Qualification Test Protocol at Molded Fiber Glass (MFG) per the standard approach that MFG would use to qualify any new process or product for General Motors (GM).
- The Corvette wheelhouse supports made by the 3-DEP process passed the Part Qualification Test Protocol which demonstrated that the 3-DEP process can be used to make automotive-quality parts.
- Preforms were manufactured at two basis weights, which yielded molded parts at 20 and 23 % fiber volume fraction.
- Fabricated a total of 355 preforms (105 wheelhouse supports and 250 flat plaques) for the qualification test.

- Part-to-part coefficients of variation (COVs) for the preforms were between 2 and 4%; these COVs were lower than what MFG usually experiences.

Future Direction

- Develop preforming technology to achieve higher fiber loading (>50 vol %) in molded composites.
- Develop preforms having higher resin permeability to make infusion easier.
- Combine 3-DEP preforms with continuous fiber face sheets to make true structural composites.
- Identify opportunities within the automotive, industrial, and aerospace communities to commercialize the 3-DEP technology.
- Expand our forming capabilities to other fiber-reinforced composites including fiberglass, aramid, natural fibers, and hybrids of these.

Introduction

This work is being conducted under an SBIR Phase II project. The goal of the project is to develop at pilot scale a potentially low-cost, high-volume production process for making net-shape, carbon-fiber composites for use in polymer composite automobile parts. The main technical focus of the project is making components and optimizing their manufacture using the 3-DEP fiber forming process.

The overall objective of the Department of Energy (DOE) SBIR Phase II project is to complete the development of the technology started in the Phase I SBIR project by focusing on a complex-shaped component that will be commercially viable. The part chosen for the Phase II project is the front wheelhouse lower support for the Corvette (Figure 1).

Figure 1. Corvette wheelhouse lower support demonstration part molded at MFG using a carbon fiber preform made by the 3-DEP process.

This part is currently manufactured by our partner in the project, the MFG companies of Ashtabula, Ohio.

The specific technical objectives of our Phase II project are as follows.

1. Develop at pilot scale the 3-DEP process, a slurry-based, low-cost, high-volume production process for making net-shape, carbon-fiber preforms for use in polymer composite automobile parts.
2. Optimize 3-DEP tooling development and how it influences fiber placement in the preform.
3. Optimize carbon-fiber slurry development and how it affects preform properties.
4. Develop process capabilities to include material handling, preform molding, preform drying, and reducing preform variability.
5. Demonstrate the utility of 3-DEP preforms to make a thermoset composite, in-production automotive component using production tooling (Corvette wheelhouse support).
6. Build a process cost model for composites made using 3-DEP preforms.
7. Write training and quality manuals for the 3-DEP process.

Results and Discussion

Based on the excellent preforming and compression molding results we obtained in the first year of the project, we decided to conduct a full-scale mock qualification run for the Corvette

wheelhouse support part. The qualification runs were conducted using the same set of criteria that MFG would use for any new part or new process being considered for production for the Corvette. The qualification runs were conducted between March and July 2008. Preforms were made by Materials Innovation Technologies (MIT) LLC in March and April; molded flat plaques and Corvette wheelhouse support parts were made at MFG in April and May; testing was conducted at MFG and at Ashland, Inc. from April through July.

Preform Fabrication

Preforms were fabricated in six lots and at two different fiber loadings, which produced two different fiber volume fractions in the molded polyester parts (20 vol % and 23 vol %). A "lot" comprised a totally independent set of fabrication conditions. For each lot, the following procedure was used at MIT-LLC:

1. The 3-DEP machine was completely drained of water and carbon fiber.
2. The equipment was given a "super" cleaning to ensure that there was no carryover of fiber from one lot to the next.
3. The system was charged with fresh water (heated to 70°F), fresh carbon fiber, and fresh binder fiber.
4. This operation was conducted six times (six lots) for each fiber loading level.

Tables 1 and 2 summarize the preform runs that were conducted during this qualification run. For each volume fraction, Lot #1 comprised 50 wheelhouse support parts and a group of 23 or 60 flat preforms. For Lots #2 through #6 at each volume fraction, at least 15 flat preforms were run. The part-to-part COVs were between 2 and 3% for the 20 vol % preforms, and between 2.5 and 4.5% for the 23 vol % preforms. COVs in this range are considered excellent according to our contacts at MFG and GM. Figure 2 shows the probability distribution of part weights for Lot 1 runs for both 20 vol % and 23 vol % fiber loadings. The normal distribution of part weights demonstrates that the preforming process was in statistical control.

Table 1. MFG wheelhouse and flat preforms at 20 vol % carbon

Lot	Part Type	Number	Mean Wt	COV
			(g)	(%)
Lot 1	Wheelhouse	50	110	2.59
Lot 1	flat	23	117	2.10
Lot 2	flat	22	114	2.14
Lot 3	flat	16	117	2.99
Lot 4	flat	16	115	2.88
Lot 5	flat	16	114	2.92
Lot 6	flat	15	115	2.13

Mean - 23 vol % flats (6 runs)	115 g
Std Dev - flats - all 6 runs	3.18 g
COV - flats - all 6 runs	2.77 %

Table 2. MFG wheelhouse and flat preforms at 23 vol % carbon

Lot	Part Type	Number	Mean Wt	COV (%)
			(g)	
Lot 1	Wheelhouse	55	127	4.17
Lot 1	flat	60	137	3.20
Lot 3	flat	15	131	3.32
Lot 4	flat	20	127	4.28
Lot 5	flat	17	127	4.03
Lot 6	flat	15	131	3.25
Lot 7	flat	15	127	2.79

Mean - 23 vol % flats (6 runs)	132	g
Std Dev - flats - all 6 runs	6.38	g
COV - flats - all 6 runs	4.83	%

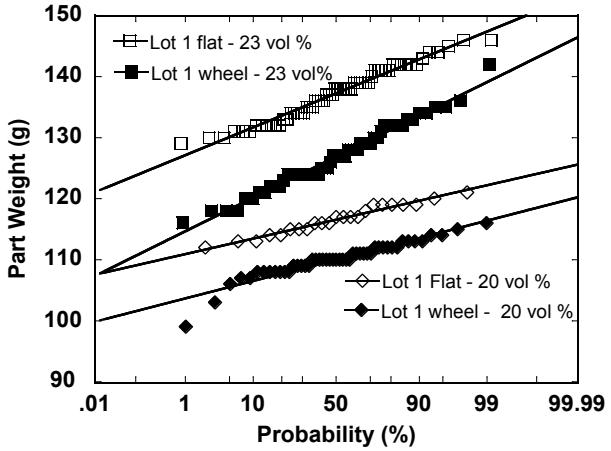

Figure 2. Probability plot of dry part weight for Lot 1 (20 vol %) and Lot 1 (23 vol %) parts showing that the part weights were normally distributed throughout the qualification runs.

Molding and Testing Activities

Flat coupon test specimens are required for acquiring basic material physical properties. In order to compare measured properties to existing material specifications, several tests on several lots were run to account for standard deviation adjustment to test average values. These test plans closely resemble a Qualification Run such as General Motors would likely require in the course of releasing a new material specification.

Flat plaque molding and Materials Testing was conducted at MFG Research. Adhesive testing was conducted at Ashland Inc., Analytical Services & Technology Division (http://ashlandanalytical.com).

MFG Research fabricated the 12 in. × 12 in. × 2.5 mm plaques by compression molding them in a hydraulic press with 500 tons capacity. The plaque tool is constructed of steel and has controlled heat in both halves. The edges of the plaque are produced by a telescoping shear feature in the mold which produces consistent molding pressure and a finished edge.

The test plan was designed to mimic a new material qualification submission plan such as General Motors would require prior to release of a new process into their Materials Specification System. An example of a GM Material Specification is GMP.UP. 011 (see Table 3). It is widely used in production at MFG in parts compression molded with directed fiber glass preforms and an unsaturated polyester resin filled with calcium carbonate and glass microspheres. The current production Corvette wheelhouse support falls under this GM Material Specification.

The GM procedure requires a minimum of six lots of test material. The test data are averaged, the standard deviation (STD DEV) calculated, and a final minimum specification is calculated by subtracting (STD DEV) × 3 from the mean value. This testing strategy enables us to make a direct comparison to approved materials than are presently in production at MFG.

Another feature of the GM Materials Specification is paragraph "1.1 Bondability." MFG offered that the question of bondability is always raised and would be important to the GM Materials Engineer in the consideration of new material specifications. To address this issue, sufficient preforms were supplied to MFG to construct plaques that were submitted to Ashland. Ashland screened the plaques with several surface preparation techniques as well as lap-shear strength testing and issued reports to MFG.

Table 3, Comparison of 3-DEP Properties to Other Molding Compounds, summarizes the physical test data gathered from 12 in. × 12 in. × 2.5 mm plaques molded and tested at MFG Research Company. In general, the mechanical properties of the parts molded from 3-DEP preforms compare favorably with the requirements of GMP.UP. 011.

Table 3. Comparison of 3-DEP material properties with GM molding compound specs

Material Description	Carbon Fiber 3-DEP Preform	GMP.UP.011 Directed fiber preform - lite
Fiber type	carbon	glass
Fiber length	25mm	25 mm
Fiber mass fraction %		40-48
Fiber volume fraction %	20%	
Resin type	polyester	polyester
Filler type	none	glass
		microsphere
Tensile Strength D-638	87.5 MPa min	85 MPa min
(Mean - 3σ)		
Tensile Modulus D-638	11012 MPa min	10100 MPa min
(Mean - 3σ)		
Flexural Strength D-790	176 MPa min	207 MPa min
(Mean - 3σ)		
Secant Modulus D-790		
(Mean - 3σ)		
At 22C Average	8727 MPa min	9200 MPa min
At 70C Average	6340 MPa min	6900 MPa min
Un-notched Izod D-4812	75 J/m min	10 J/m min
(Mean - 3σ)		
Specific Gravity D-792	1.32 max	1.50 max
(Mean + 3σ)		
Water Absorption D-570	0.90% max	0.95% max
(Mean + 3σ)		
Dynatup Impact D-3763		
Energy to Max Load	1.9 J	NA
Total Energy	6.6 J	NA

Molded Three-Dimensional Parts

The molded Corvette Parts were built into bonded assemblies in the same form that MFG supplies parts to the General Motors assembly plant at Bowling Green, Kentucky. That assembly consists of the front wheelhouse outer, front wheelhouse inner and the front wheelhouse lower reinforcement. Those assemblies were evaluated by collecting dimensional information and by performing destructive bond evaluations at Ashland.

General Comments from MFG regarding the qualification runs

- The properties the preforms were satisfactory for the type of molded parts that MFG produces.
- The consistency of the preforms was good; the part-to-part COVs were lower than what MFG usually experiences.
- The carbon preforms were more difficult to impregnate with polyester resin than are the customary air-laid fiberglass roving preforms. Molding trials on the 23 vol % flat plaques were successful in the flat tool press in their laboratory. However, in molding tests for the wheelhouse support part (run in the production tools at MFG's Premier Molding Company) the molding engineers and operators encountered difficulty in getting complete resin coverage with the 23 vol % preforms.
- Molding tests were rerun with the 20 vol % preforms; those preforms performed much better – the resin flowed through the preform satisfactorily.
- The bonded assemblies (comprising the wheelhouse inner, wheelhouse outer, and wheelhouse lower support) measured within production tolerances. The carbon 3-DEP based parts appeared the same as the production fiberglass parts.
- The bonded assemblies performed the same as production in the bond destruct evaluations. Fiber tear was observed at the bond sites.
- The adhesive screening report from Ashland Inc., Analytical Services & Technology Division indicates that the carbon parts perform as well as their current production parts. Three different surface preparation techniques were evaluated and all three produced satisfactory bonding.

Summary Comments Regarding the Qualification Runs

Engaging MFG to perform the physical testing of the 3-DEP carbon preforms had several advantages. MFG has more preform manufacturing and molding activity than any molder in the world. They have been developing air-directed, glass-fiber preforming for 50+ years. They have evaluated using that process to make a carbon-fiber preform and can appreciate the challenge of performing with very lightweight fibers. As an automotive and commercial truck supplier they have an interest in supplying new materials when their customers request them. Their willingness to provide access to a production molding tool and comments from their engineers gave this project more depth than had we just contracted with a prototype shop.

Summary and Conclusions

We have demonstrated that the 3-DEP process can be used effectively to make chopped fiber preforms in carbon fiber. Those preforms have been molded into final parts that would be acceptable to the automotive industry. Our demonstration part, the Corvette front lower wheelhouse support, was run through a mock **Part Qualification Test Protocol** at MFG per the standard approach that they would use to qualify any new process/product for GM. The protocol simulated the testing that would be required for a new production part including adhesively bonding the part into a test assembly. A total of 355 preforms (105 wheelhouse support preforms and 250 flat plaque preforms) were fabricated for the qualification test. The part-to-parts COVs for these preforms The Corvette wheelhouse support made by the 3-DEP process passed the **Part Qualification Test Protocol** which indicates that the 3-DEP process can be used to make automotive-quality parts.

The variability of the preforms made by the 3-DEP process is significantly lower than that

obtained for preforms made by competing processes such as air-laid, directed-fiber preforming. This is true for both within-part variation and part-to-part variation. The COV for both of these measures is consistently below 5% of the mean.

MIT LLC is moving forward with the commercialization of this technology with both government and industrial partners. We have won SBIR contracts/grants with the Department of Defense for manufacturing helicopter spare parts (Phase II) and with the National Science Foundation to investigate natural fiber-reinforced composites (Phase I). We were awarded a Phase II Supplemental contract with DOE for this project. We have process/product development contracts in place with Boeing, Plasan Carbon Composites, and Toho Tenax Americas. The Automotive Composites Consortium—Materials is conducting a third-party cost model evaluation of the 3-DEP process.

Presentations/Publications/Patents

1. Mark A. Janney, "Making Composites Using the Three Dimensional Engineered Preform (3-DEP) Process," presented at the AATCC Medical, Nonwovens, and Technical Textiles Symposium, Raleigh, NC October 6–7, 2008.
2. Mark A. Janney, "Manufacturing Composites Using the Three Dimensional Engineered Preform (3-DEP) Process," presented at the NDIA 9th Annual Science & Engineering Technology Conference DoD/Tech Exposition, Charleston, SC, 15–17 April 2008.
3. Mark A. Janney, "Interlayer Hybrid Composites of Chopped and Woven Carbon Fiber," presented at the SAMPE Fall Technical Conference, Memphis, September 8–11, 2008.

E. High Volume Processing of Composites (ACC115*)

Principal Investigator: Daniel Houston
Ford Motor Company, Manufacturing & Processes Department
2101 Village Road, Dearborn, MI 48121
(313)323-2879; fax 313)390-0514; e-mail: dhousto2@ford.com

Technology Area Development Manager: Joseph A. Carpenter
(202) 586-1022; fax: (202) 586-1600; e-mail: joseph.carpenter@ee.doe.gov

Field Project Officer: Aaron D. Yocum
(304) 285-4852; fax: (304) 285-4403; e-mail: aaron.yocum@netl.doe.gov

Contractor: U.S. Automotive Materials Partnership
Contract No.: DE-FC-59OR22545 through the DOE National Energy Technology Laboratory

Objective

- Develop and demonstrate high-volume manufacturing (molding) processes to produce lightweight composite automotive components.
- Expand the scope of the Automotive Composites Consortium (ACC) composite projects into the thermoplastic area.

Approach

- Work with a Tier One automotive composites supplier to investigate and develop an improved carbon-fiber sheet molding compound (SMC) material amenable to cost-effective high volume applications.
- Continue exploration of the root causes of bond-line read-through (BLRT) through application of developed quantification tool to enable use of reduced thickness panels.

Accomplishments

- Provided process support for Focal Project 4, the Composite Underbody and Composite Seat.
- Upgrade an existing SMC compounder at Tier One supplier, Continental Structural Plastics (CSP). Developed carbon-fiber chopping apparatus and successfully chopped carbon-fiber roving.
- Continued work on BLRT by the molding, bonding, and analysis of assemblies to develop understanding of the impact of various factors on BLRT severity.

Future Direction

- High volume processing of lightweight structural thermoplastic composites.
- Carbon-fiber SMC materials for structural automotive applications:
- Continue working with fiber and resin suppliers through the Tier One supplier (CSP) to develop a superior material with improved manufacturability within cost and supply constraints.
  - — Demonstrate material on potential applications.

*Denotes Project 115 of the Automotive Composites Consortium (ACC), one of the formal consortia of the United States Council for Automotive Research (USCAR) set up by Chrysler, Ford, and General Motors to conduct joint, precompetitive research and development.

- Initiate development of a modeling tool for predicting BLRT in the component design phase using experimental data obtained through this project to validate the model.
- Provide process support to Focal Project 4, Composite Underbody/Seat (ACC 007).

Introduction

The purpose of this project is to develop the high volume composite molding technologies germane to automotive production. The direction of ACC115 is to collaborate with suppliers to develop low cost – high volume molding processes that enable production of minimal weight components using materials and processes compatible with the material property and processing requirements of the automotive industry.

Two processing investigations are under way.

1. BLRT continued with studies of plaques molded with specific variations to assess the impact of various factors on the severity of the resultant surface distortions.
2. Develop high performance, cost-effective carbon-fiber SMC materials and associated processing techniques in conjunction with a Tier-1 supplier.

Bond-Line Read-Through

Phase 1

The focus of the fiscal year (FY) 2008 work in Phase 1 was evaluation and refinement of the procedure for converting raw curvature data into a quantitative measurement. The quantitative measurement needs to correlate to the visual perception of the severity of BLRT defects. The algorithm for converting the characteristics of a defect into a numerical value was established in FY 2007. The focus in FY 2008 was to identify the filters that would distinguish the regions on a panel that would be considered to be visible surface distortions from those that are not visible or that are due to defects other than BLRT. A large number of filtering schemes were evaluated and an initial combination of smoothing and thresholding filters was selected. The resulting severity scores and "score maps" (i.e., visual representations of the areas on a panel that were identified as visible distortions) for the reference panels were found to correlate well with visual assessments.

Unfortunately, application of the filtering procedure to assemblies constructed in Phase 2 of this work showed that the filters selected were not robust to high levels of orange peel in paint. When a high level of orange peel was present on an assembly, the score maps contained high levels of noise and the severity scores no longer adequately represented the severity of BLRT on the assembly. A number of other filtering combinations were evaluated, but filtering combinations that removed the orange peel also removed too much of the BLRT signature so that the severity scores obtained from those filtering combinations no longer reflected the apparent visual severity of the BLRT distortion. As a result, the team had to revert to the original algorithm and accept that the poor quality paint will impede the system's ability to acquire meaningful data.

The team also initiated gage repeatability and reproducibility (Gage R&R) evaluations in FY 2008. Since the ONDULO system that the ACC purchased for this project is a transportable system designed to be used on a wide variety of parts, very little of the system is fixed. As a result, the Gage R&R for the system was found to be unable to meet the expected level of repeatability and reproducibility. As an interim solution, the team is now repeating the measurements three times on every part and averaging the measurements. In FY 2009 the team intends to complete a Gage R&R using our parts, filtering procedure, and algorithm using a more production representative system. If that Gage R&R shows substantially better results than our system, the team will likely upgrade the existing system to improve its repeatability and reproducibility.

Phase 2

The objective of Phase 2 of this project is to conclusively determine which material and processing factors are the root causes of BLRT through the completion of multiple designed experiments. The measurement tool developed in Phase 1 of the project provides the objective data to quantify the change in BLRT severity in the

manufactured assemblies. The team made three trips to Meridian Automotive Systems' Shelbyville, IN plant in FY 2008 to complete designed experiments. The first trip consisted of a single experiment while multiple smaller experiments were completed during the second and third trips.

The first experiment was a screening experiment designed to determine whether any of the factors included in the experiment affect BLRT severity. The factors and factor levels included in this experiment are summarized in Table 1.

Table 1. Factors and Factor Levels Included in the First Screening Experiment

Factor	Low Level	High Level
Adhesive Modulus	364 MPa (Urethane)	3296 MPa (Epoxy)
Variation in Bond-line Thickness	None	3mm
Adhesive Application Pattern	Continuous	Drops
Warp in the Inner Panel	None	Warped
Outer Panel Substrate Stiffness	2.5mm SMC	0.7mm 210BH Steel
Bonding Temperature	RT	300°F
Degree of Cure of the Outer Panel	Undercured SMC	Fully Cured SMC
Bond Nest Configuration	Skeletal Nest	Full Nest

In Table 1, a "skeletal nest" refers to a bonding fixture in which only the bond lines are supported and heated whereas a "full nest" refers to a bonding fixture in which the entire panel is both supported and heated. These two types of fixtures are illustrated in Figures 1 and 2.

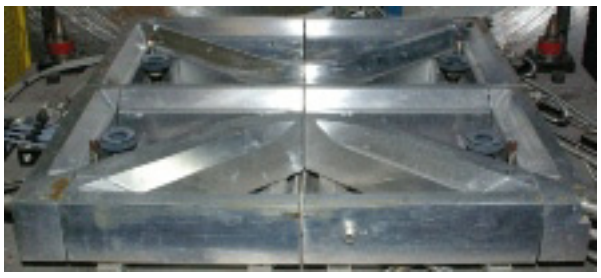

Figure 1: The bonding fixture in the "skeletal nest" configuration.

Figure 2: The bonding fixture in the "full nest" configuration.

The factor found to have the strongest effect on BLRT severity in the first experiment was the temperature at which the adhesive was cured in the bond cell. The type of material used for the outer panel was also found to have a strong effect. While the outer panel material was characterized by material type in this experiment, the team has since concluded that the bending stiffness of the outer panel, in which both the material stiffness and thickness of the panel are factors, has a greater effect on BLRT severity than the material stiffness itself. Finally, the bond nest configuration was not found to have an effect on BLRT severity. The team feels this result, however, is potentially misleading. The percentage of this assembly that is supported and heated in the skeletal configuration is substantially higher than what would typically be seen in a production application. Consequently, further investigation into the effect of the fixture design is planned. The effect of the other factors appeared to have been confounded by uncontrolled squeeze-out. Squeeze-out occurs when the adhesive bead intrudes into the radius of the bond flange and does not maintain a consistent, defined thickness.

The team chose to build a production representative bond fixture and bond press and to partner with Meridian Automotive Systems so that assemblies could be manufactured using a process as representative of production conditions as possible in order to reduce part-to-part variation. In the first screening experiment, only one assembly was made at each factor level combination, except for one combination. Four assemblies were manufactured for that combination, using what were assumed to be identical manufacturing conditions. Unfortunately,

there was a large difference in the BLRT severity within this set of assemblies. As a result, the team has manufactured three replicate assemblies at each condition in all subsequent experiments.

The results from the first experiment were used to determine the content and format of the majority of the following experiments. The primary experiment completed during the second trip to Meridian-Shelbyville attempted to determine the specific relationship between the temperature at which the adhesive was cured and BLRT severity. This experiment was a two- factor, full-factorial experiment. The factors and factor levels for this experiment are summarized in Table 2. The time required for the adhesive to reach handling strength varies with both adhesive and cure temperature. The time the assemblies were cured in the fixture for each combination of adhesive and cure temperature are summarized in Table 3.

Table 2. Factors and factor levels for the effect of cure temperature experiment

Factor	Factor Levels
Type of Adhesive	Urethane, Epoxy
Adhesive Cure Temperature	RT, 120°F,[a] 240°F, 270°F, 300°F

[a]Assemblies were not made at 120°F using the epoxy adhesive. Since the adhesive required three hours to cure at this temperature, there was not sufficient time allotted in the experiment to manufacture these assemblies.

Table 3. Cure time and temperature used in the effect of cure temperature experiment

Cure Temperature	Cure Time	
	Urethane	Epoxy
RT	2 hours	Overnight
120°F	25 min	3 hrs (est)[1]
240°F	120 s	300 s
270°F	105 s	180 s
300°F	90 s	120 s

Unfortunately, assembly-to-assembly repeatability in this experiment was insufficient to generate good data. The adhesive was dispensed at a volume that was intended to produce a 15 millimeter (mm) wide, 1-mm tall bead on all flanges, regardless of flange width. Since one bond flange is only 12 mm wide, this bead size was expected to always produce read-through on that flange. Unfortunately, either the adhesive volume and/or the bead location on the flange varied sufficiently to result in a high level of panel-to-panel variation and no statistically significant effect of cure conditions could be detected.

In addition to the primary experiment completed during the second trip to Meridian-Shelbyville, the team also built six assemblies with twice the normal amount of urethane adhesive. In one set of three replicates, the bond gap was left at 1 mm. The bond gap was increased to 3 mm for the other set of three replicates. All of these assemblies were bonded at 300°F for 90 seconds(s). The BLRT severity on these assemblies was then compared to the BLRT severity on the urethane assemblies bonded at 300°F for the primary experiment completed during that trip. The filtered curvature maps for one panel of each type are shown in Figure 3.

The images in Figure 3 suggest that BLRT severity is more strongly related to squeeze-out than to the volume of adhesive dispensed. This finding will be important when developing CAE models for predicting BLRT severity.

The third trip to Meridian-Shelbyville included two smaller experiments. The first experiment completed during that trip investigated the relationship between the amount of the bond flange that was covered with adhesive and BLRT severity. In addition, two different outer panel thicknesses (2.5 mm and 3.0 mm) were used to manufacture assemblies made with epoxy adhesive. While the fact that increasing outer panel thickness reduces BLRT severity is well established, building these assemblies provided data for validating CAE modeling results later in Phase 3 of this project. Assemblies with the thicker outer panel were made only with one adhesive to reduce the number of assemblies that had to be manufactured and analyzed. The factors and factor levels for this experiment are summarized in Table 4. Flange coverage was controlled by the amount of adhesive dispensed. Figure 4 illustrates the urethane adhesive dispensing patterns developed for each intended

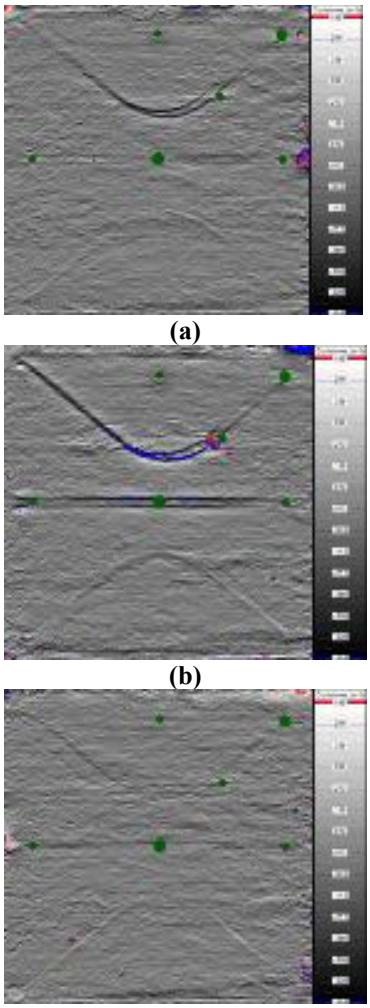

(a)

(b)

(c)

Figure 3. Curvature maps for raw assemblies bonded with differing amounts of urethane and differing bond gaps: (a) Standard adhesive volume and 1-mm gap, (b) 2X adhesive volume and 1-mm gap, (c) 2X adhesive volume and 3-mm gap.

Table 4. Factors and factor levels for the effect of cure temperature experiment

Factor	Factor Levels
Type of Adhesive	Urethane, Epoxy
Flange Coverage Level	25–50% 75–100% Assured Squeeze-out
Outer Panel Thickness	2.5 mm, 3 mm[a]

[a]3-mm outer panels were used only to manufacture assemblies bonded with epoxy adhesive.

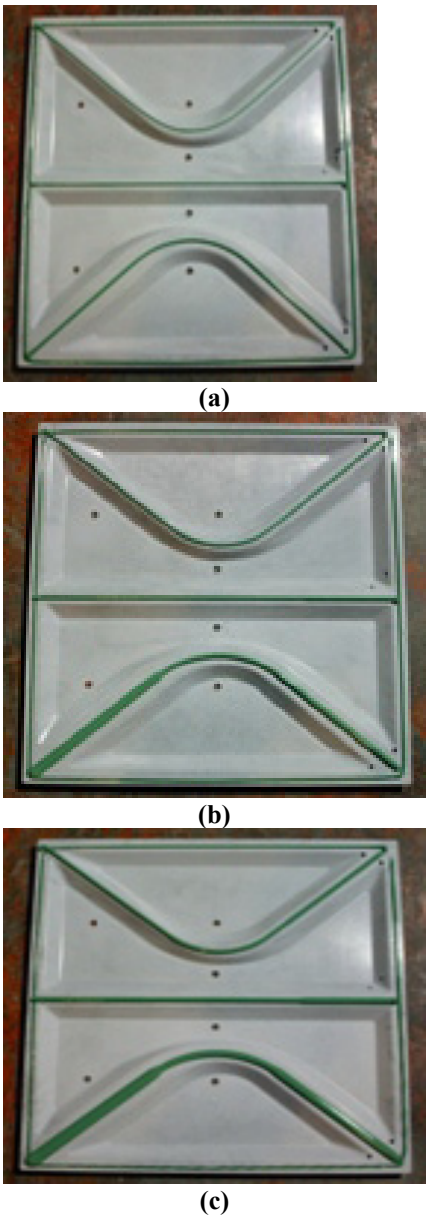

(a)

(b)

(c)

Figure 4. Adhesive dispensing patterns in the flange coverage experiment: (a) bead pattern for 25–50% flange coverage, (b) bead pattern for 75-100% flange coverage, (c) bead pattern for assured squeeze-out.

flange coverage. The dispensing patterns for the epoxy adhesive are similar.

The relationship between flange coverage and BLRT severity was evident even in the as-bonded (i.e., "raw") assemblies. The relationship is illustrated by the filtered curvature maps shown in

Figures 5 and 6. These figures show one assembly made with 2.5mm outer panels, each flange coverage level, and each adhesive. The maps for assemblies made with urethane adhesive are shown in Figure 5. The maps for the assemblies made with epoxy are shown in Figure 6.

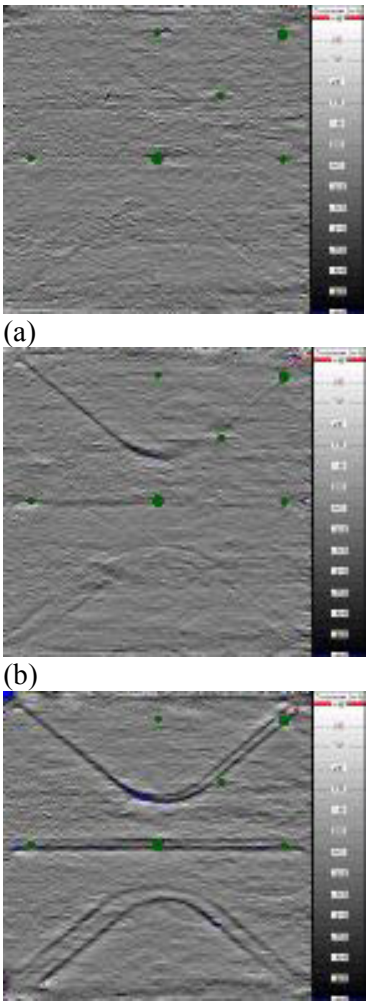

(a)

(b)

(c)

Figure 5. Curvature maps for raw assemblies bonded with urethane and differing levels of flange coverage. The percent of the flange surface covered by adhesive: (a) 25–50%, (b) 75–100%, and (c) assured squeeze-out.

These figures clearly show the strong relationship between the amount of the flange that is covered by adhesive and BLRT severity. While these assemblies have not been sectioned to

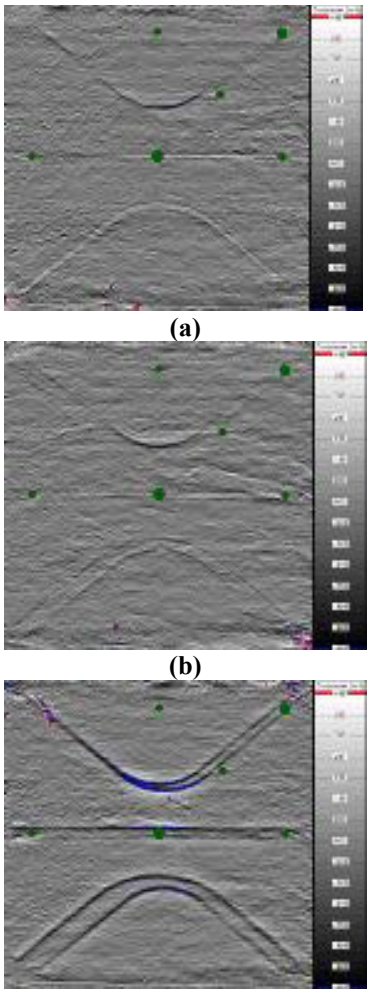

(a)

(b)

(c)

Figure 6. Curvature maps for raw assemblies bonded with epoxy and differing levels of flange coverage. The percent of the flange surface covered by adhesive: (a) 25–50%, (b) 75–100%, and (c) assured squeeze-out.

conclusively verify this, Figures 4(c) and 5(c) imply that the BLRT is particularly severe when the adhesive enters the radius of the flange. Combining the inferences from the assemblies made in the second trip that varied both the amount of adhesive dispensed and the bond gap with inferences that can be drawn from these assemblies, it appears that the BLRT visible in these assemblies' results from the presence of adhesive in the flange radius rather than the volume of adhesive dispensed. In addition, while the type of adhesive appears to have an effect on

BLRT severity, BLRT severity appears to be much more sensitive to the presence of adhesive in the radius of the bond flange than to the type of adhesive.

All of the inferences from the third experiment must be drawn from the data collected on the raw (i.e., as-bonded) assemblies. This is because the paint application process used to apply paint to these assemblies resulted in a very high level of orange peel in the paint. Consequently, the BLRT severity data from these assemblies was confounded by the variation in curvature caused by orange peel. The curvature due to orange peel could not be filtered out of the data without also filtering out too much of the curvature caused by BLRT. As a result, no meaningful data could be captured from these panels after painting.

The second experiment completed during the third trip to Meridian-Shelbyville was a screening experiment designed to investigate the relationship between the degree of softening of the outer panel during the painting process, the degree of cure of the adhesive, and the paint oven temperature. The factors and factor levels for this experiment are summarized in Table 5.

Table 5. Factors and factor levels for the substrate softening vs. paint temperature experiment

Factor	Factor Levels
Substrate Softening during Painting	SMC, GTX973[a]
Adhesive Degree of Cure	Uncured Partially Cured Fully Cured
Paint Oven Temperature	Simulated E-coat (365°F for 30 min) Low Bake (250°F for 25 min)

[a]GTX973 is an e-coat capable thermoplastic available from SABIC Innovative Plastics. This material is designed for electrostatic, on-line painting in automotive body shops.

GTX973 panels were molded at Husky in Novi, MI using the ACC injection molding tool. That tool is the same size as the compression molding tool. Unfortunately, the injection molding machine used to mold these panels did not have sufficient clamp tonnage to completely pack out the tool with this material and very few good quality panels were manufactured. In addition, the assemblies built by bonding a GTX973 outer panel to an SMC inner panel warped significantly. The high warpage made these assemblies unusable. Consequently, this experiment did not provide the team with the desired data.

Two additional trips to Meridian-Shelbyville in FY 2009 are planned at this time. The fourth trip will complete a screening experiment to investigate many of the factors evaluated in during the first experiment, but this time using mastic (a.k.a. anti-flutter) rather than adhesive. The primary experiment during the fifth trip will determine whether the density of the SMC inner and outer panels impacts BLRT severity. That experiment will also vary the inner panel thickness to determine how that factor affects BLRT severity.

Carbon-Fiber SMC

The objectives of this program are to develop high performance, cost-effective, carbon-fiber SMC materials and associated processing techniques for high-volume automotive components. The technical emphasis is to optimize properties, improve consistency of the properties, and to optimize the manufacturability of the compound. The project assumptions are that the material could be used for all current structural and Class-A SMC applications; that the current SMC compounding, molding processes, and equipment can be utilized; and that the thickness of the new materials will be in the range of 1.0 to 3.0 mm. In addition to the technical issues and constraints, business challenges have been addressed by working with CSP to leverage their production knowledge of what it takes to develop a marketable system. Zoltek (a low-cost carbon-fiber manufacturer) has agreed to work with CSP supplying appropriate carbon fibers and developmental sizing systems suitable for automotive resin systems.

The CSP SMC compounder was upgraded to provide carbon-fiber compounding capability. Early carbon-fiber chopping issues were resolved

and the fiber chopping system now performs flawlessly.

Initial compounding trials have consistently shown marginal wet-out of the 50K carbon fiber bundles. Future compounding trials will develop methods to open up the carbon-fiber bundles and resin system changes. Additionally, compounding with much smaller carbon-fiber bundles will be done, leveraging work done on an earlier P4 process. Similar fiber bundle wet-out improvements are expected, which should result in significantly improved material properties.

Conclusions

ACC115 explores different approaches to the high-volume processing of composites. Two programs are in progress, each with the objective of researching ways to save weight in automobiles, at the volumes appropriate to the industry. BLRT continued with studies of plaques molded with specific variations the impact of various factors on the severity of the resultant surface distortions. Carbon fiber SMC research is progressing well against constraints of cost and supply. Acquisition of new equipment specifically owned by ACC will speed research by eliminating time needed to move tools between suppliers, and will also provide the benefit of reducing variation in the test results.

F. Natural Fiber Composite Retting, Preform, Manufacture, and Molding

Principal Investigator: James Holbery
Pacific Northwest National Laboratory
P.O. Box 999, Richland, WA 99354
(509) 375-3686; fax: (509) 375-2379; e-mail: james.holbery@pnl.gov

Principal Investigator: Dan Howe
Pacific Northwest National Laboratory
P.O. Box 999, Richland, WA 99354
(509) 376-2923; e-mail: daniel.howe@pnl.gov

Principal Investigator: Kevin Simmons
Pacific Northwest National Laboratory
P.O. Box 999, Richland, WA 99354
(509) 375-3651; e-mail: kevin.simmons@pnl.gov

Principal Investigator: Leo Fifield
Pacific Northwest National Laboratory
P.O. Box 999, Richland, WA 99354
(509) 375-6424; e-mail: leonard.fifield@pnl.gov

Technology Area Development Manager: Joseph A. Carpenter
(202) 586-1022; fax: (202) 586-1600; e-mail: joseph.carpenter@ee.doe.gov

Field Technical Monitor: Mark T. Smith
(509) 375-4478; fax: (509) 375-4448; e-mail: mark.smith@pnl.gov

---

Contractor: Pacific Northwest National Laboratory (PNNL)
Contract No.: Prime Contract No. DE-AC06-76RLO 1830

Objective

- To develop, build, and demonstrate an economical, lab-scale, automated fiber retting process and apparatus suitable to bast-based fibers, including hemp, kenaf, and flax.
- To develop and demonstrate a thermoset polymer preform compression molding process and produce panels to develop a mechanical and thermal natural fiber polymer composite database.

Approach

- Explore existing and new fiber preparation approaches, including decortication techniques, high-speed fiber separation, steam explosion, chemical treatment, and modified extrusion methods.
- Develop the fundamental understanding of bast fiber structure that will provide direction for fiber separation.
- Conduct several lab-scale process trials of fiber preparation-retting processes enabling the development of the most appropriate process and instrumentation.
- Develop and construct a non-aqueous natural fiber preforming process capable of integrating surface modification and hybrid fiber and preform geometries.

- Explore alternative material forms, including sheet-molding compounds from natural fiber and hybrid reinforcements.
- Conduct full mechanical, thermal, and environmental characterization of manufactured panels.

Accomplishments

- Completed fiber analysis lab apparatus, developed fiber analysis procedure, and conducted fiber analysis on major natural fiber varieties.
- Procured several pieces of hardware assembled into the mechanical fiber preparation line, including fiber cutting apparatus, extruder modification, decorticator, and Wiler Mill.
- Completed supercritical fluid delignification study.
- Conducted fundamental research on ionic liquid delignification of natural fibers.
- Explored several natural fiber non-aqueous preform manufacture strategies and are currently exploring two further with mock-up, with construction of a prototype line in fiscal year (FY) 2009.
- Completed panel tool (approved by the Automotive Composites Consortium [ACC] and built by PNNL) and have produced sheet molding compound (SMC) panels from the tool.
- Established relationships with U.S. kenaf farm, Kengro Inc.; planted, harvested, and delivered 2 tons of kenaf.
- Developed relationships with resin suppliers (including AOC, Reichold, and Ashland Chemical) and processing companies (including Material Innovation Technology, TimTek, Inc., and Canadian hemp supplier, Stemergy).

Future Direction

- Integrate fiber decortication, separation, and preparation-retting techniques into a lab-scale fiber preparation unit.
- Deliver process and lab-scale unit to our customer in FY 2009.
- Determine the most economical approach to prepare fibers for surface modification.
- Explore non-aqueous natural fiber preforming processes capable of scaling to industrial volumes.
- Determine the most appropriate method to integrate fiber surface modification technology into the preform manufacture process.
- Interface with resin suppliers concerning SMC formulations for producing panels.
- Develop natural fiber SMC and hybrid-fiber architectures; produce panels and characterize in mechanical, thermal, and environmental.

Introduction

The objective of this project is to develop critical capability in the area of natural fiber retting, preform manufacture, and composite manufacture to enable the large-scale insertion of natural fiber reinforcement into the automotive industry. The benefits of natural fiber reinforced composites are well known, including lightweight, energy savings, cost reduction, carbon capture, recycling, and the environmental benefits from using renewable resources. However, several technical milestones must be met before the full confidence of engineering, manufacturing, and commercial sectors will embrace natural fiber reinforcement as a viable replacement for glass fiber. In this effort, three critical barriers restricting natural fiber usage in automotive manufacture are addressed: (1) develop an inexpensive, rapid, environmentally friendly mechanical process to remove natural fibers from plant stalks; (2) develop a rapid cost-effective method to create natural fiber preforms suitable for infusion of a thermoset polymer matrix; and (3) develop a natural fiber polymer composite molding process adaptable to hybrid

fiber composites and ester, soy, and urethane resin.

Retting is a fiber preparation process that traditionally has involved separating fibers via moistening or soaking fibers in water and partially rotting the fiber binders. This process consists of up to four methods: dew retting, water retting, warm water retting combined with heat, and chemical retting involving alkali solutions. Preparation should ideally prepare a fiber to be surface modified to promote bonding and adhesion and provide both dimensional stability and thermo-plasticity. Surface modification of natural fibers can be employed to optimize properties of the fiber-matrix interface and integrated within the fiber preform manufacturing process to produce a preform that may be stored for long periods of time before composite manufacture without a loss of properties (or more importantly excessive moisture uptake) with compromised composite interfacial properties.

Fiber Preparation

PNNL received 1,000 lbs of contractually grown kenaf fiber from Kengro, Inc. (Charleston, MS) in the beginning of FY 2008. In addition, research concentrated on the following fibers: (1) fresh water retted kenaf (Bangladesh), (2) un-retted from Kafus, Inc. (Raymondville, TX), (3) industrial hemp from Stemergy (Ontario, Canada), and (4) chemically modified kenaf from Professor Brian Baldwin (Agriculture Department, Mississippi State University).

PNNL personnel researched and developed the following processes and apparatus in an effort to develop a novel, mechanical-based fiber preparation process.

Decortication

Decortication (removal of kenaf core) using parallel rollers on a simple screw apparatus [see Figure 1(a)] appears to be a robust means of removing bast core; the method was originally developed at Georgia Pacific but was sold to TimTek to use in making wood panel board. The process unit consists of two offset screws turning at the same rate with a conveyor belt between the screw units that moves material. The unit has the

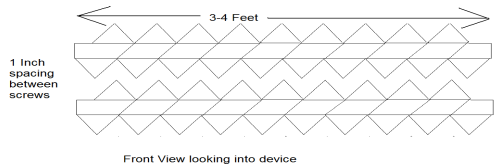

(a)

(b)

Figure 1. Decortication: (a) artist's rendering of apparatus and (b) decorticated kenaf fiber strands.

ability to vary the process speed up to >160 feet per minute of green material. Fibers are "dehusked" but need to be pulled off core by hand; PNNL has developed a design that eliminates this task.

The final decorticated fibers appear as fiber bundle "strands" as depicted in Figure 1(b).

Subsequently, PNNL procured a lab-scale roll laminator and has adapted it to perform the decortication process. The roll laminator and modification design are depicted in Figures 2 and 3. The decorticator rollers have been machined, and the unit is near operation.

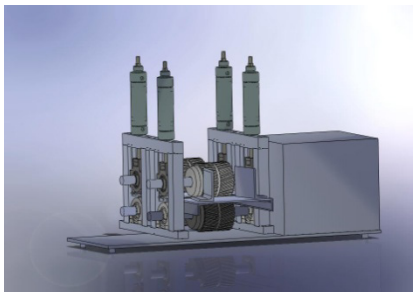

Figure 2. Solid model of decorticator.

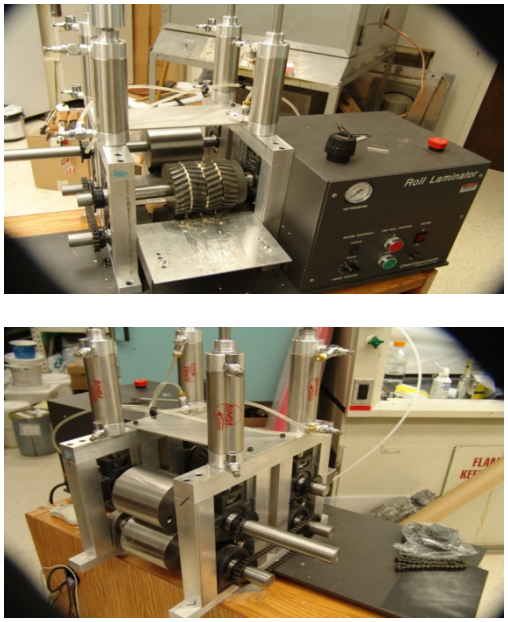

Figure 3. Front and rear views of the PNNL decorticator near completion.

To determine the pressure needed to decorticate the fibers, a set of experiments was designed and run to determine the compressive strength of the kenaf stalks as a function of the position along the stalk and its diameter (Figure 4). Moisture uptake experiments were also performed in order to evaluate maximum uptake of the whole stalk material and the effect moisture absorption has on the compressive strength of the material. This information is necessary to set the decorticator pressure applied to the material. It has been found that the kenaf stalk strength decreases as a logarithmic function the further from the butt end of the stalk the sample is cut, corresponding to decreasing lignin contents along the length of the stalk.

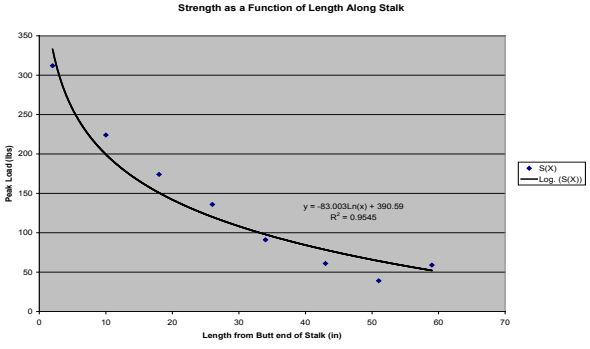

Figure 4. Fiber strength as a function of position along the fiber stalk.

The diameter of the stalk also plays a role in the force required to separate the core from the fiber sections. Up to a diameter of 0.7 in., the force required is near constant at ~115 lbs (Figure 5). At that point, however, the failure load begins to vary linearly.

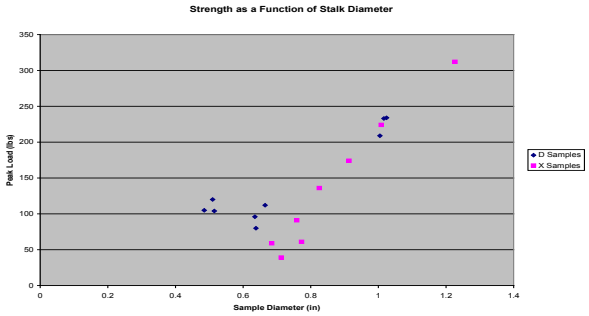

Figure 5. Strength as a function of stalk diameter.

Finally, it was demonstrated that whole stalk kenaf is capable of absorbing a large amount of water (up to 250% the weight of the sample; Figure 6). As water is absorbed, the strength of the material decreases; Figure 7 indicates the strength drops off due to soaking with an asymptote obtained at ~24 hours of soak time.

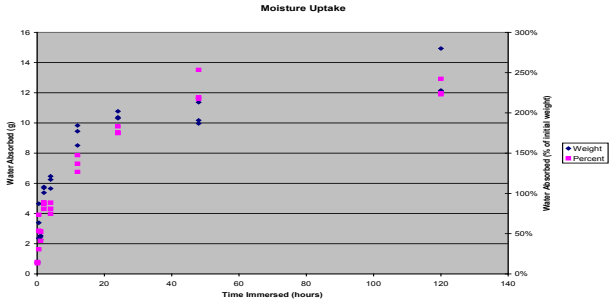

Figure 6. Moisture uptake in grams (g) (left y-axis) and % of original weight (right y-axis) with time.

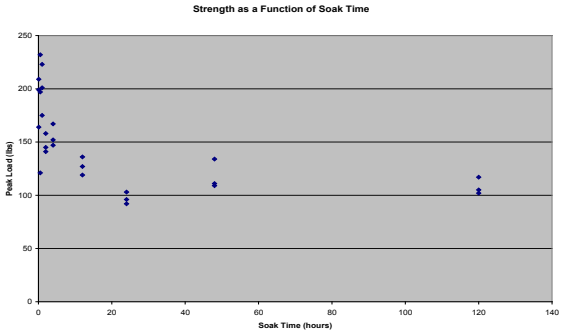

Figure 7. Strength of the stalk/core as a function of soak time.

Fiber Cut/Chop to Length

A pelletizer, which will be used to chop the fibers to the required length, was purchased from a used equipment vendor. Electrical work, including new switches and a face plate, was necessary to meet safety codes. The work was accomplished on July 31, 2008, and the unit has been tested. Fiber tests are planned in the immediate future, but preliminary tests show that the machine works well and produces material uniformly 1/8-2 in long (Figure 8).

Figure 8. Pelletizer used to chop fiber into specified lengths.

Ionic Liquid Delignification

A chemical process wherein diaza(1,3) bicyclo-undecane (DBU), sulfur dioxide gas, hexanol, and water are used to remove chemically the lignin present in lignocellulosic material has been tested and is shown to be effective. A salt that is liquid at room temperature, DBU is mixed with hexanol and then sparged at 0°C with sulfur dioxide (SO_2) gas (Figure 9). This liquid is then pumped under a vacuum to remove any non-chemically bound sulfur dioxide groups and added to a fiber or wood sample and water. It is stirred and heated to 90°C in a reaction chamber. The lignin is dissolved by a process where the sulfur groups chemically bound to the DBU form sulfurous acid, which hydrolyzes the lignin. These sulfurous acid groups then recombine with the water to reform the ionic liquid. The mixture is cooled down, and the pulp is washed with water, which removes all reactants from the delignified pulp (Table 1). Acetone washes may also be employed to remove residual hexanol. Due to low vapor pressure of the ionic liquid separation and consequent reuse of the reactants, creation of a completely closed loop system is possible. As a proof of concept, this method was used on the Pulp and Paper Research Institute of Canada (PAPRICAN) reference soft wood pulp.

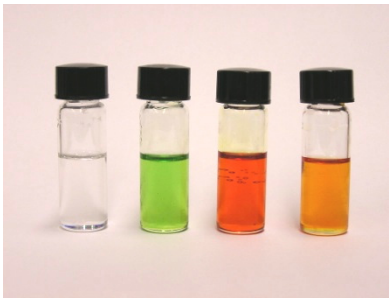

Figure 9. DBU+1-hexanol with (from left to right): CO_2, COS, CS_2 and SO_2.

Table 1. Ionic liquid delignification. Numbers are reported as percentages on an oven-dry basis. Lignin is quantified according to TAPPI–T222.

Type	Start Lignin	End Lignin	Delignification
PAPRICAN Pulp/ CS_2 IL	4.16%	1.52%	63.50%
	4.16%	2.76%	33.55%
	4.16%	2.83%	32.05%
PAPRICAN Pulp/ SO_2 IL	4.16%	1.52%	63.55%
	4.16%	1.40%	66.43%
	4.16%	3.23%	22.40%

Ethanolysis of Kenaf Lignin

Supercritical fluids, solvents controlled at temperatures and pressures above their critical point, can have liquid-like densities and solvation characteristics while exhibiting vapor-like diffusivities. Thus, reactants and solvents in the supercritical phase may effectively access a wide range of the micro and macro pores in a porous material to deposit chemical functionality or to extract material. In addition, the tuneability of supercritical solvent characteristics by temperature or pressure adjustment can enable ease of separation of dissolved species from reactant solutions. These promising functions of supercritical fluids have the potential to extract components (such as lignin from biomass) selectively to simplify clean up of lignin processing solutions and facilitate recycling of reaction solvents.

Motivated by the potential of supercritical fluids as processing solvents and the observation of selective lignin removal from woody biomass using supercritical alcohols by Shiro Saka's group at Kyoto University, ethanol as a supercritical reactant/solvent for lignin removal from kenaf fibers is being pursued.

Batch-type reactions of 1.5 in. long decorticated kenaf bast fibers with pure ethyl alcohol (ethanol) were carried out using a Parr-heated, high-pressure reaction system (Figure 10). Two grams of cut fiber and 50 mm of ethanol were added to the Hastelloy-C reaction vessel before it was sealed and inserted into a heating mantle. A thermocouple is connected to the vessel, where the temperature is maintained to a programmed set point using an attached controller. The reaction mixture was held at various temperatures from 20–300°C for two hours from the point at which the heated vessel reached 95% of the desired reaction temperature. After the set reaction time, the heated vessel was removed from the heating mantle and allowed to cool to 50°C. After cooling, the reaction solution was recovered from the fibers by filtering through a glass pre-filter and retained. The recovered fiber was rinsed with fresh ethanol and set aside to air dry. Recovered reaction solutions were analyzed to determine components being removed from the kenaf fibers at various reaction temperatures. Mass of recovered fiber was recorded to determine mass loss due to the reactions. Larger batch reactions of 12 g of fiber in 50 ml ethanol were carried out with two reaction temperatures to produce samples of adequate mass for the soxhlet-based total fiber analysis.

Figure 10. Parr high-pressure reaction system (left) and 1.5-in. decorticated kenaf fibers.

In Figures 11–12, the effect of treatment of the kenaf fibers in ethanol is visibly apparent. The fiber reacted with ethanol at 300°C was completely degraded into a dark powder.

Lignin is unique among the majority constituents of kenaf fiber (lignin, hemicellulose, and cellulose) in that its monomers contain aromatic functional groups. This feature provides a unique

Figure 11. Darkening of the fibers due to treatment.

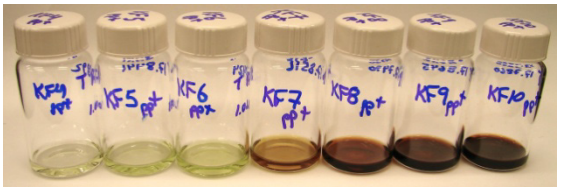

Figure 12. The portions of the recovered reaction solvents indicate a darkening of the solution beginning at 150°C increasing above 200°C.

signature for lignin that enables its spectroscopic detection and quantification in component mixtures. In the spectrophotmetric traces of recovered reaction solutions (Table 2), the characteristic lignin absorbtion at 280 nm is seen to increase with increasing reaction temperature. This trend continues up to 200°C, temperatures above which the lignin degrades during reaction. At 300°C, the characteristic lignin peak is no longer visible in the ultra-violet to visible spectrum.

Table 2. Change in initial fiber mass with reaction temperature.

20°C	50°C	100°C	150°C	200°C	250°C	300°C
0.6%	1.6%	4.2%	12.4%	29.4%	51.2%	82.0%

Some proton nuclear magnetic resonance (NMR) spectra of reaction solutions from selected process temperatures are portrayed. The axis displays 0–9 ppm chemical shift, with chloroform NMR solvent peak visible at 7.2 ppm. Note the absence of aromatic content from 6-7 ppm corresponding to extracted lignin in the lower temperature reactions. Increasing levels of lignin, hemicellulose, and cellulose decomposition products are visible above 200°C (Figures 13–14).

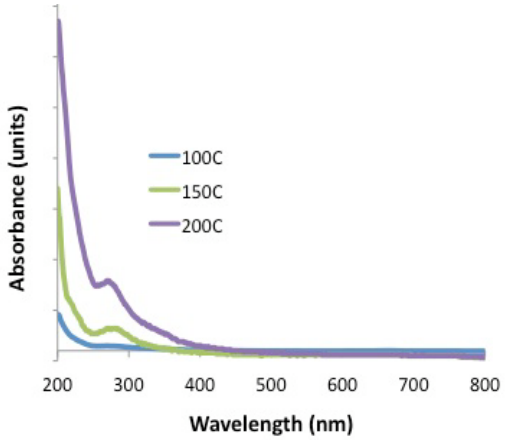

Figure 13. An increase in lignin absorption at 280 nm with increasing temperature.

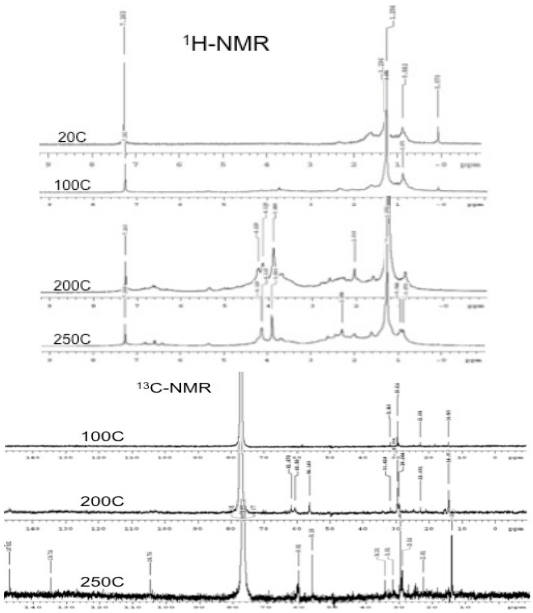

Figure 14. Carbon 13 NMR spectra of reaction solutions displayed with axis 0–150 ppm chemical shift.

High performance liquid chromatography (HPLC) was used to identify some of the components in the kenaf/ethanol reaction solution in addition to lignin. A few major observed species are displayed in Figure 15. Compounds identified in the effluent trace as glucose and fructose are the largest fractions observed at lower reaction temperatures. As glucose in alpha-cellulose is strongly bound, it is not expected that this observed sugar comes from that fraction of kenaf structure. Xylitol and arabanose (not shown) are detected in solutions reacted above 150°C. These

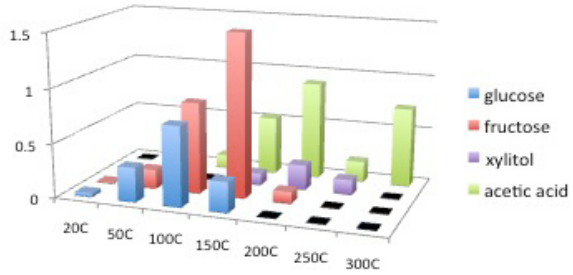

Figure 15. Kenaf/ethanol species from the effluent trace as a function of temperature.

compounds are indicative of hemicellulose breakdown. The small molecule degradation products are observed (not shown) in solutions reacted above 200°C and constitute in entirety of the mixture at 300°C.

If mass loss with temperature of reaction is plotted with lignin observed in the recovered and xylitol content in the reaction solution (Figure 16), information may be obtained regarding temperatures at which reaction under conditions used results in lignin (and hemicellulose) removal with minimum destruction of cellulose.

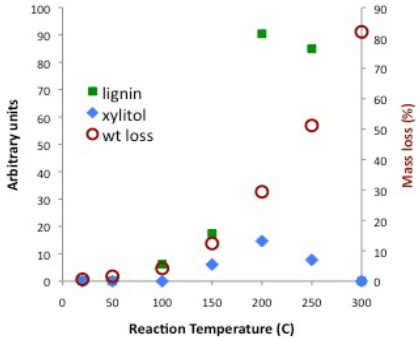

Figure 16. Mass loss at differenct reaction temps.

It is apparent from the characterization techniques used that the kenaf fiber undergoes signficant structural degradation at temperatures above 150–200°C under the reaction conditions used. Significant lignin removal is observed at reaction temperatures exceeding 100°C. Therefore, larger batches (>10g) of fiber were processed at 100 and 150°C for total fiber analysis to determine the effect on lignin, cellulose, and other fiber contents using the soxhlet method. The reaction time used in these experiments (2 hours) is long relative to 30 minute reaction time used by the Saka group.

At 270°C, that group observed the cellulose content in their beechwood sample a decrease of <10%, while lignin in their sample decreased to <20% of its original value. A 30% total mass loss was observed (Yamazaki M and S *J Wood Sci* 2006 [52]:527-532). At 350°C, they observed almost total loss of their beech wood after 30 minutes. No mention is made by those authors that their work is performed anaerobically. In addition to ethanol, there is air present at the sealing of the reaction vessel and adventitious moisture present on the fiber. It is perhaps a combination of oxidants included in the system and longer reaction times that lead to degradation of the samples at lower temperatures.

The supercritical temperature of ethanol is ~240°C. Therefore, ethanol in reaction systems is subcritical at temperatures below which significant structural degradation of the fibers is observed. If the presence of a supercritical fluid is desired in the current work at temperatures below those that give fiber degradation (<200°C), then one option is to use a cosolvent mixture of ethanol and carbon dioxide instead of ethanol alone. The supercritical temperature of carbon dioxide is less than 40°C, and ethanol is commonly added to supercritical carbon dioxide to improve its solvating characteristics for polar compounds (and the two are significantly soluble in one another). Combinations of the two would be expected to have intermediate supercritical temperature relative to the pure fluids. In the case of delignification of kenaf fiber, carbon dioxide may provide the attractive pore penetration, while the ethanol provides the reactant for ligning depolymerization and enable solubility of the lignin fragments in the reaction solution.

Additional options to achieve a supercritical reaction solvent without fiber destruction in the current system include shorter reaction times (<30 min) at high temperature (~250°C). In a continuous process, the residence time in the hot part of the reactor may be controlled short enough to prevent thermal degradation, though it is difficult in a batch pot reactor process. Another option may be to try to perform the reaction in a more anaerobic environment by flushing the fiber and ethanol with nitrogen before heating. It would be expensive and impractical to remove completely all the water from the fiber before the reaction for high volume processing of fibers.

Use of ethanol at an elevated temperature may remain an effective way to remove lignin from kenaf fiber while leaving cellulose chains intact. Reaction temperature between 100–200°C may be optimum for achieving this goal. Small amounts of additives can make these reactions more effective for lignin and other desirable components for removal. These additives may increase the effectiveness of ethanol alone in achieving the goal of a simple method for cellulose fiber preparation from kenaf bast fiber.

High-Energy Delignification

Numerous forms of high-energy delignification have been examined, and the two most promising methods seem to be ultrasonics and tunable microwaves. Ultrasound possesses the ability to form both OH* and H* radicals, which are the main components of the various chemical delignification systems. In addition, the mechanical stresses imparted during cavitation can possibly serve to pull depolymerized lignin away from the bulk material, negating any rinsing steps. Any OH or H radicals not utilized in the reactions will recombine almost instantly into water, negating the use of expensive and capital intensive recycling and cleaning processes. PNNL has recently designed an ultrasonic system capable of processing volume elements, as opposed to the industry standard ultrasonic horns that operate only at the fluid/horn surface area interface. Meanwhile, microwaves allow a specific frequency of energy to be focused on a sample. Since maximum power transfer occurs when energy input equals the resonance frequency of specific bonds, tuning the microwaves to the frequency of the β-O-4 ether linkages holding lignin together is possible.

Extruder Delignification

The use of an extruder to mimic steam explosion processes has been examined, but the currently available nozzles are incorrect geometry. A device has been designed (Figure 17) that will attach to the current extruder that consists of a collection chamber and a Venturi nozzle to screw together and allow for introduction of high pressure steam

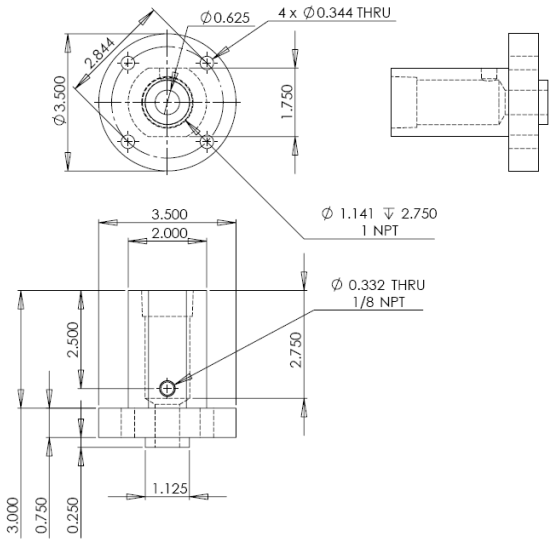

Figure 17. Newly designed device allowing for high pressure steam introduction.

once the fiber slurry has left the extruder. The Venturi nozzle will allow for a pulsing effect without the need for release valves. PNNL is currently exploring this process, which will continue into FY 2009 (Figure 18).

Figure 18. Current extruder apparatus with adapted tip. This work continues into FY 2009; results will be reported upon determination of the process viability.

Bast Fiber Structural Characterization

The structure of several bast fibers has been explored to determine the composition. This is important because process changes affect fiber structure and the separation of fiber from core fiber-fiber interaction, enabling fiber separation for follow-on steps (i.e., preform manufacture). To analyze these fibers, PNNL constructed a fiber structural analysis laboratory that will enable the structural analysis of *any* natural fiber. This consists of a six soxhlet extractor columns combined with a Rotovap to remove solvent. PNNL designed and built the table, had the glassware produced and assembled, and purchased columns for HPLC analysis of the organics. This is a beneficial addition to PNNL capabilities; coordinated tests are being conducted with the University of Idaho to verify process set-up and calibration (Figure 19).

Figure 19. PNNL fiber analysis lab apparatus.

Additionally, in support of this effort PNNL procured a used Wiley mill and adapted it to be used to produce small fiber fragments suitable for analysis (Figure 20). With a 7.5 in. cutting chamber, this 2 hp mill is used for grinding fiber samples to the specified size before analysis. The unit was successfully modified to meet safety regulations. Dust created when samples are ground was also a cause for concern. In order to minimize this hazard, a containment box was designed and built with a snorkel hood attached to a filter to provide negative pressure during operation to minimize the possibility of inhaling fiber dust. The polycarbonate enclosure will serve as both a blast shield in case of catastrophic failure of the unit and a fire containment device in the unlikely event of ground fiber ignition.

The characterization of kenaf acquired from KenGro in Mississippi has been completed. Previous experiments with KenGro material mechanically decorticated showed mass balances of ~65%. However, manual decortication of kenaf from the same planting gave much better balances. KenGro material that had been dew retted and mechanically separated also showed a mass balance above 90%. Average characterization results of several fiber test batches are given in Table 3.

Figure 20. Wiley mill with polycarbonate containment enclosure.

Table 3. Chemical characterization of natural fibers and reference pulp. All numbers reported as percentages of total mass on an oven-dry basis.

Fiber	Ash	Extractives	Klason Lignin	Acid Soluble Lignin	Cellulose	Hemicellulose
Hemp	2.42	0.59	8.12	N/A	71.43	8.43
Bangladesh	1.24	0	12.39	N/A	63.11	19.96
Mechanically separated dew retted Kengro kenaf	1.39	0.15	7.75	5.19	63.65	21.01
Hand separated non-retted Kengro kenaf	4.11	1.39	12.10	5.19	45.98	18.63
Texas Kenaf	4.35	0.27	8.36	N/A	57.28	25.35
PAPRICAN (standard)	0.5	0.26	4.16	0	83.04	9.99

Preform Processing

The goal of this task is to develop a preforming process to produce natural fiber reinforced preforms of a variety of geometries without an aqueous solution. This task is underway and will continue throughout FY 2009. At this time, two concepts are being explored, though others are under consideration.

The first process that has been conceptualized and mocked-up involves infrared heaters that set the kenaf to a sheet form via a micro-scale thermoset resin particulate which is subsequently stamped into the desired shape.

The first set of kenaf fiber preforms were produced and are shown in Figure 21.

Figure 21. Preform hat section and curved pieces.

Another approach under consideration is one that will utilize a fluidized bed to produce a series of layers of natural fiber on a conveyer, transported to the preform stamp station with the fibers bound by a surface modifier. This concept is still under development and will be further refined in FY 2009.

Composite Manufacture and Characterization

The compression molding tool was built and is fully operational (Figure 22). Trial panels produced from SMCs that have been made on this tool from glass and kenaf fibers are shown in Figure 23. In the near future, sandwiched kenaf and glass sheets will be molded. These will be characterized by measuring moisture uptake and mechanical properties, comparing straight glass and kenaf SMC.

Figure 22. PNNL SMC plaque tool (in press), producing kenaf-reinforced panel.

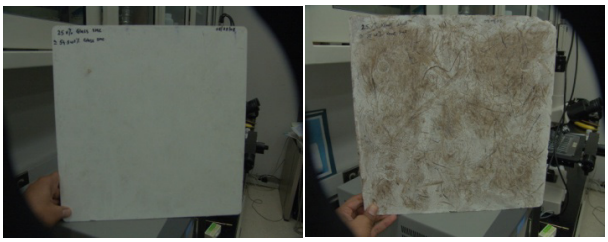

Figure 23. On the left, a 25 vol % SMC of glass fibers; on the right is a 25 vol % SMC panel of kenaf fibers.

As fibers are produced from the processes developed, full characterization will take place using PNNL personnel and outside vendors, as necessary. The focus will be on mechanical, thermal and environmental properties.

Conclusions

Begun on July 1, 2007, this effort has focused on the fiber preparation-mechanical retting process for industrial scale. A prototype line is near completion. The fiber preform line has been conceptualized and a mock-up has been assembled. A tool has been completed to produce SMC panels, and good progress has been made toward the fiber preparation steps necessary to produce quality repeatable natural fiber reinforced composite panels. Thus far, the focus has been on kenaf fiber; in FY 2009, hemp fiber will be incorporated into the testing and analysis. Fiber structural analysis capability is fully operational, and this will aid in process development. Fibers this year were grown by contract at the USDA WSU Prosser Irrigated Agriculture Research and Extension Center.

G. Natural Fiber Composites for Structural Component Design

Principal Investigator: Sheldon Q. Shi
Assistant Professor
Forest Products Department
Mississippi State University
Franklin Center, Rm. 222
100 Blackjack Road, Starkville, MS 39759
(662) 325-3110; fax: (662) 325-8126; e-mail: sshi@cfr.msstate.edu

Co-Principal Investigator: Jilei Zhang
Associate Professor
Forest Products Department
Mississippi State University
Franklin Center, Rm. 113
100 Blackjack Road, Starkville, MS 39759
(662) 325-9413; fax: (662) 325-8126; e-mail: jzhang@cfr.msstate.edu

Co-Principal Investigator: Yibin Anna Xue
Assistant Professor
Mechanical and Aerospace Engineering,
Utah State University
4130 Old Main Hill, Logan, UT 84322
(435) 797-2867; http://www.mae.usu.edu/personnel/faculty.php

Co-Principal Investigator: L. Catherine Brinson
Department of Materials Science and Engineering
Northwestern University
2220 Campus Drive, Evanston, IL 60208-3108
(847) 491-3537; fax: (847) 491-7820; e-mail: cbrinson@northwestern.edu

Technology Development Manager: Joseph Carpenter
(202) 586-1022; fax: (202) 586-6109; e-mail: joseph.carpenter@ee.doe.gov

---

Contractor: Mississippi State University
Contract No.: 4000054701

Objective

- Obtain material data on biomaterials (e.g., kenaf) by investigating microstructural characteristics, establishing fabrication methods (i.e., retting and formatting), and quantifying mechanical properties for use in automotive structural design.

Approach

- For automotive exterior applications, natural fiber-reinforced polymer-based composites are investigated in the following primary steps: (1) develop natural fiber retting technology and recommend solutions aiming at cost reductions of fiber retting processes, (2) use nanotechnology to enhance composite mechanical properties by improving the interfacial bond strength, (3) evaluate natural fiber composite processing techniques, and (4) develop micromechanical models for natural fiber composites.

Accomplishments

- Fiber retting/treatment—Developed a rapid chemical retting process with the aim of increasing the retting speed and reducing the cost; the inorganic nanoparticle impregnation process was optimized for the kenaf bast fiber obtained from the chemical retting process.
- Composite fabrication—Developed an innovative laminated sheet molding compound (LSMC) process with the aim of having a large natural fiber loading capacity and comparable properties to the commercial sheet molding compound (SMC) products with synthetic fibers.
- Fiber testing—Quantified the heat and time effects on the tensile properties of the kenaf bast fiber bundles.
- Micromechanical simulations—Applied a Drucker-Prager model to evaluate the effect of fiber waving and kinking on fiber properties; a three-dimensional Mori Tanaka model was applied for kenaf-epoxy composites with random fiber orientations and dispersed carbon nanotubes.

Future Direction

- Evaluate more environmentally friendly fiber retting options such as thermomechanical processes, bio-retting processes, and innovative fiber formatting methods.
- Continue to develop cost-effective bio-composite sheet molding process methods using different fiber/fiber bundle forms from different retting processes (such as chemically retted, mechanically retted methods).
- Conduct physical and mechanical tests on the fabricated composites, including bending, water absorption, impact resistance, etc.
- Obtain strength properties of single fibers and fiber bundles of kenaf bast fibers for composite modeling.
- Continue the effort of dispersing nanophase additives into the composites for property enhancement.
- Continue updating the present micromechanical models to better account for the physical factors, such as water absorption capacities and the spiraling angle of the fibers.

Chapter One: Chemical Retting, Inorganic Nanoparticle Impregnation, and Composite Fabrication

Sangyeob Lee, Sheldon Q. Shi, Jinshu Shi, H. Michael Barnes, and Mark F. Horstemeyer

Introduction

Kenaf bast fiber consists of cellulose, hemicellulose, lignin, and pectin, whose contents are 44–57%, 21%, 15–19%, and 2%, respectively [1]. However, the cellulose component of kenaf fibers contributes to the reinforcement in polymer-matrix composites [2, 3, 4, 5, 6, 7, 8, 9]. In general, lignin and pectin components hold the cellulose fibrils together so that fiber bundles are formed. To obtain fibers with high cellulose content, a chemical retting process can be used [10, 11, 12, 13, 14]. The removal of lignin and hemicellulose generates micropores in cell walls [15]. Inorganic nanoparticles can fill up the micropores and minimize the air in composites. The inorganic nanoparticles can also act as a modifier for the interfacial compatibility between natural fibers and polymer matrixes [16, 17]. The impregnation process is also an environmentally friendly and cost-effective process as it uses two ionic salts [18, 19].

The objectives of this study were: (1) to refine the rapid pressurized chemical process for the kenaf bast fiber retting, (2) to obtain an optimum inorganic nanoparticle impregnation condition for the kenaf bast fiber, and (3) to investigate a processing technique for the natural fiber—polymer composite fabrication.

Experimental

The flow charts of experimental steps are depicted below for retting, impregnation, and lamination processes (Figures 1–3).

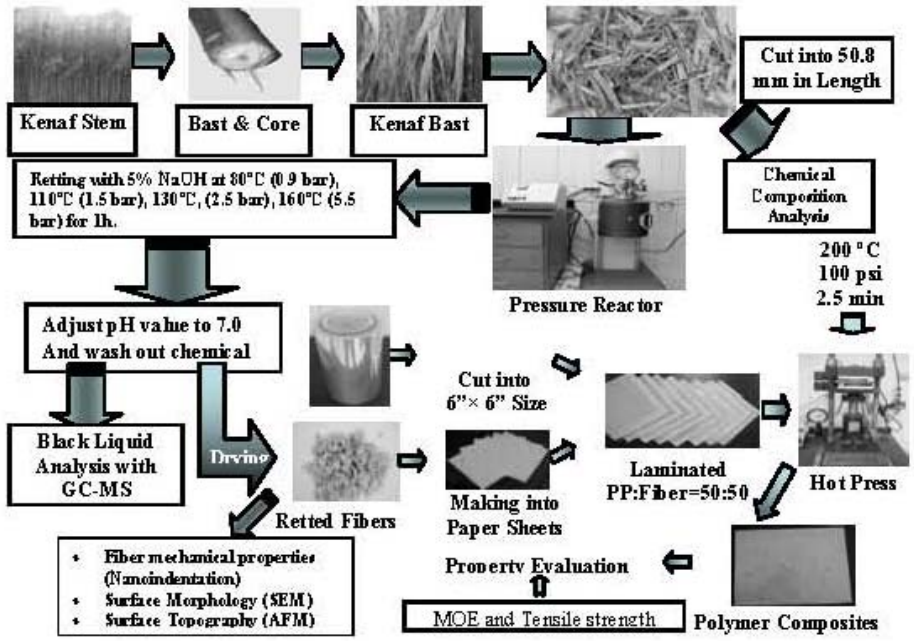

Figure 1. Chemical retting and characterization.

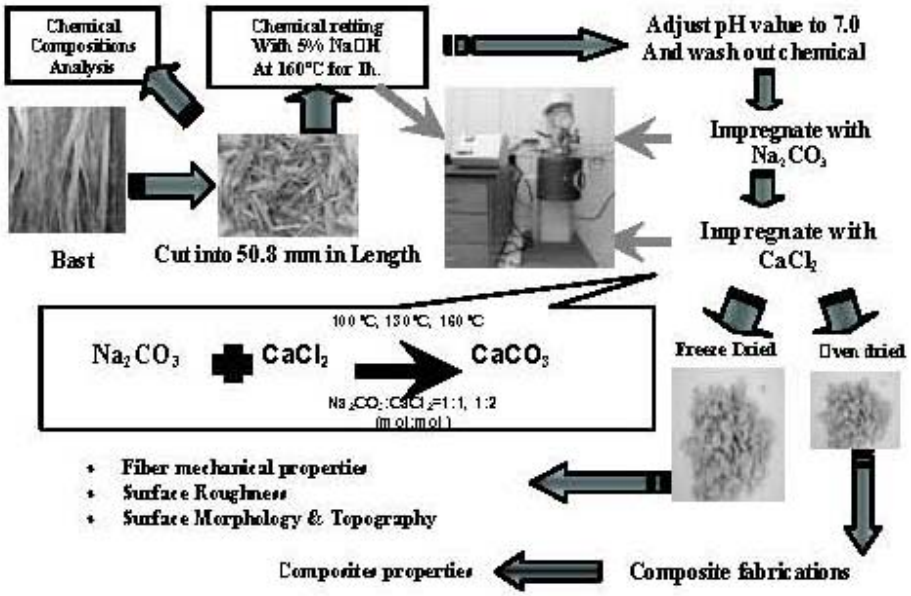

Figure 2. Inorganic nanoparticle impregnation and characterization.

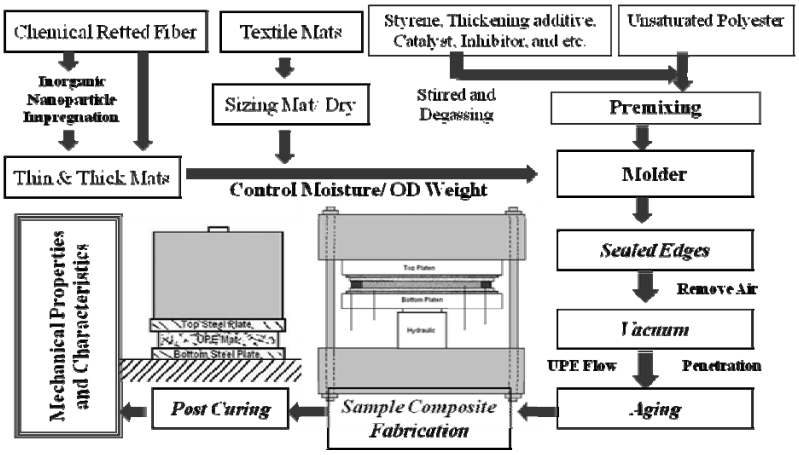

Figure 3. Lamination process for natural fiber-polyester composites.

Table 1 shows the chemical compositions, solvent extractives, and water solubility of the kenaf bast fibers. Figure 4 shows the fiber yields from retting at four different conditions. As shown in Figure 4, the fibers retted at 160ºC (0.55 MPa) gained 44.6% fiber yield, which was about equivalent to the α-cellulose content (45.95%) of kenaf bast fiber.

Table 1. Chemical compositions of kenaf bast fiber

Components	Content (%)
Moisture content	7.40
Ash	5.07
Klason Lignin	19.10
Holocellulose	75.83
α-cellulose	45.95
Extractives	
Hydrogen peroxide extractives	8.57
Methylenechloride extractives	0.99
Ethanol extractives	4.61
Hot water solubility	9.76
Cold water solubility	7.21

Py-GC/MS Analysis of the Black Liquid

Figure 5 shows the mass spectra (MS) from pyrolysis-gas chromatography/MS (Py-GC/MS) analysis on black liquid. The main peaks with a relative molar area greater than 1% were identified from the Py-GC/MS. The different levels of residue among the products suggested that the extraction of hemicellulose and lignin compounds was improved at higher retting temperatures and pressures. As shown in Figure 5, the majority of

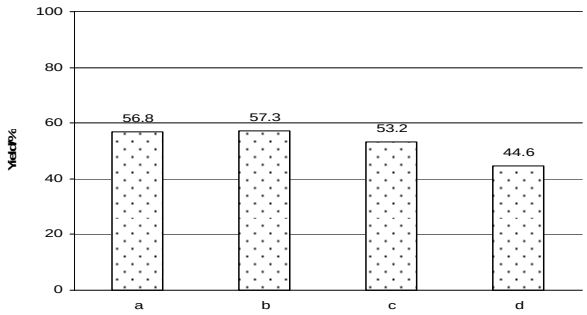

Figure 4. Fiber yield strength from the retting processes. a = 80ºC (0.09 MPa), b = 110ºC (0.15 MPa), c = 130ºC, (0.25 MPa), and d = 160ºC (0.55 MPa).

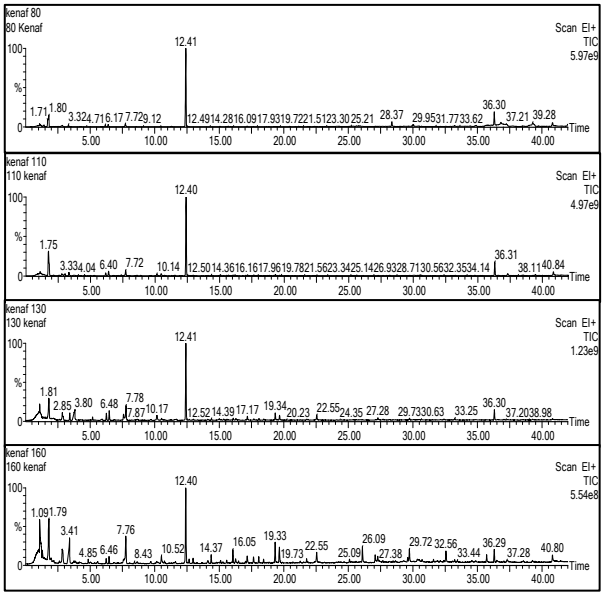

Figure 5. Retting rejects analysis using Py-GC/MS and identification of main peaks with relative molar area ≥1%.

the chemical compounds in the black liquid from chemical retting were lignin based.

Figure 6 shows the loading percentage of $CaCO_3$ in kenaf fibers. It indicates that the fibers impregnated at 130°C, with a molar ratio of 1:1 (Na_2CO_3 to $CaCl_2$), gave the highest $CaCO_3$ loading. However, a little increase of $CaCO_3$ nanoparticles in kenaf fibers could result in significant changes in fiber surface characteristics because of the large specific surface area of $CaCO_3$ nanoparticles. A small number of $CaCO_3$ nanoparticles can generate a large surface area, which may have a significant effect on composite properties.

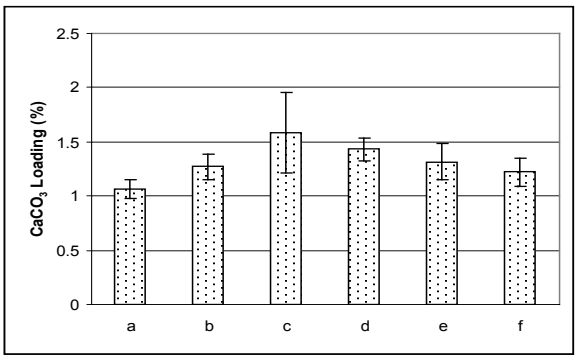

Figure 6. Percentage of $CaCO_3$ loading in the cell wall structure of weak chemical retted kenaf fiber. (a) = 100°C (0.15 MPa) at 1 : 1 ionic salt ratio, (b) = 100°C (0.15 MPa) at 1 : 2, (c) = 130°C (0.30 MPa) at 1 : 1, (d) = 130°C (0.30 MPa) at 1 : 2, (e) = 160°C (0.70 MPa) at 1 : 1, and (f) = 160°C (0.70 MPa) at 1 : 2.

Surface Characteristics

Figure 7 shows the microstructures of the retted and impregnated kenaf fibers examined with a scanning electron microscope. For the fibers generated at a retting temperature of 160°C, the micropores appeared in the fiber cell wall. As the retting temperature and pressure increased, more lignin and hemicelluloses were pyrolyzed and extracted from the fiber cell wall. More nanoparticles were shown on the fiber surface impregnated with the 1:2 molar ratio compared to that with the 1:1 ratio. Some particles generated at 160°C grew to a diameter of 100 to 500 nm (Figure 7[g] and [j]). The nanoparticles were found at the inner micropore structure in the kenaf fiber cell wall.

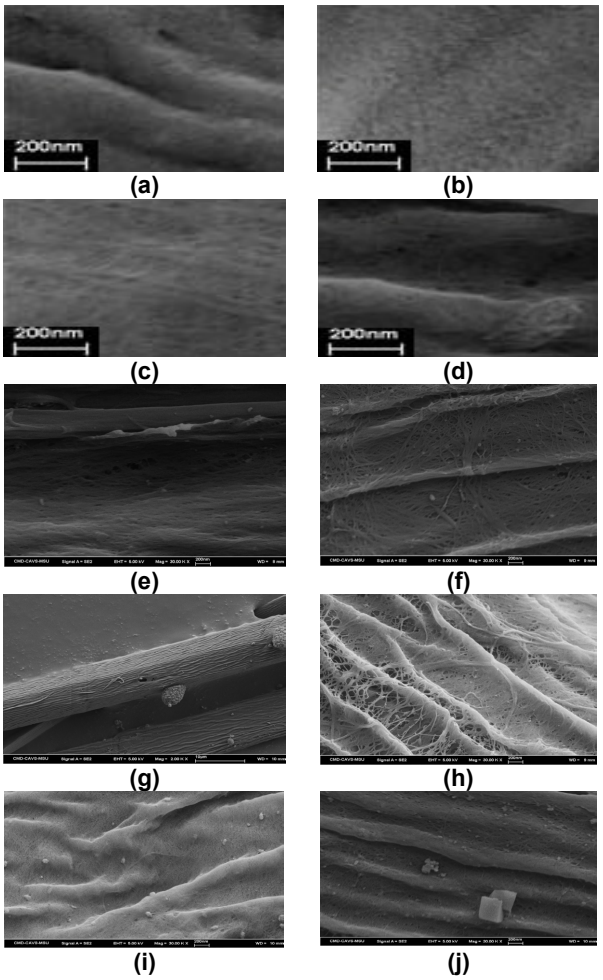

Figure 7. Surface morphology of kenaf fibers alkaline retted and impregnated with $CaCO_3$. (a) = 80ºC, 0.09MPa; (b) = 110ºC, 0.15MPa; (c) = 130ºC, 0.25MPa; (d) = 160ºC, 0.55MPa; (e) = 100°C (0.15 MPa) at 1 : 1 ionic salt ratio; (f) = 130°C (0.30 MPa) at 1 : 1; (g) = 160°C (0.70 MPa) at 1 : 1; (h) = 100°C (0.15 MPa) at 1 : 2; (i) = 130°C (0.30 MPa) at 1 : 2; and (j) = 160°C (0.70 MPa) at 1 : 2.

The porous structure at the inner cell wall held the inorganic nanoparticle crystals in position (Figure 8). Smaller nanoparticles (50 to 100 nm) were also formed on the surface of bigger inorganic particles. Root mean square (RMS) surface roughness of kenaf fibers retted with an alkaline solution and impregnated by the inorganic nanoparticles is shown in Table 2. The higher the retting temperatures, the lower the fiber surface roughness. The surface roughness of impregnated fibers increased due to the $CaCO_3$ particles deposited on the fiber surface.

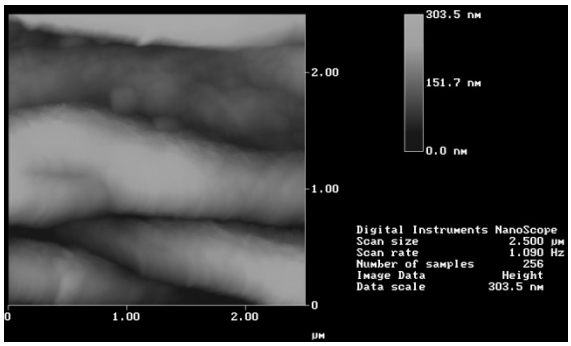

(a)

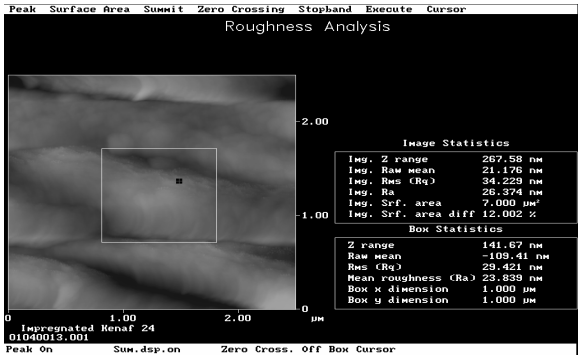

(b)

Figure 8. Surface roughness analysis of nanoparticle impregnated kenaf fibers (160°C, Na_2CO_3 : $CaCl_2$ = 1 : 1) using atomic force microscopy. (a) = 2.5 µm scan size and (b) = roughness analysis.

Table 2. RMS surface roughness of kenaf fibers retted with an alkaline solution and impregnated using two ionic salts.

Temp.	Pressure	Na_2CO_3 : $CaCl_2$ (mol : mol)	Scanning Size	
			2.5 µm	1 µm
80ºC	Retting fibers (5%NaOH)	N/A	73.2	32.6
110ºC		N/A	71.1	22.3
130ºC		N/A	43.7	25.4
160ºC		N/A	31.3	11.2
100°C	0.15 MPa	1:1	39.5	21.9
		1:2	29.8	20.4
130°C	0.30 MPa	1:1	40.2	19.0
		1:2	48.8	30.5
160°C	0.70 MPa	1:1	24.9	20.8
		1:2	40.1	23.1

Nanoindentation on Fiber Surfaces

Figure 9 shows the surface hardness and modulus of retted kenaf fibers and inorganic nanoparticle impregnated kenaf fibers tested using the Hysitron NanoIndenter instrument. The reduced modulus and surface hardness of kenaf fibers retted at

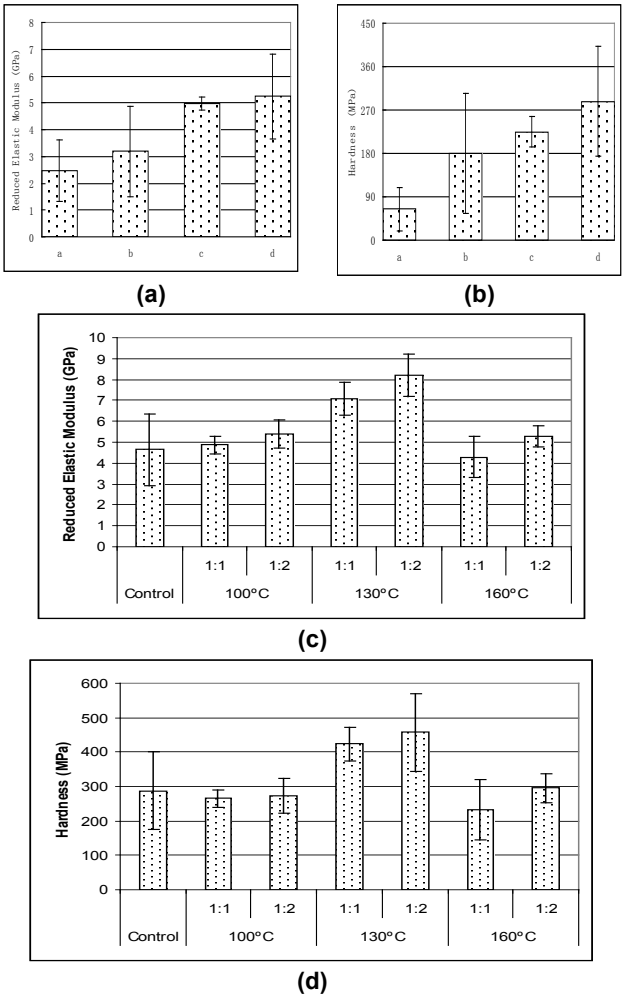

Figure 9. Surface hardness and elastic modulus of retted and nanoparticle impregnated kenaf fibers. The y-axes indicate (a) and (c) are elastic modulus and (b) and (d) are hardness; a = 80ºC, 0.09 MPa; b = 110ºC, 0.15 MPa; c = 130ºC, 0.25 MPa; and d = 160ºC, 0.55 MPa.

160ºC were more than two times higher than those retted at 80ºC. This may be due to a higher cellulose content obtained at the retting temperature of 160°C. Kenaf fibers impregnated with $CaCO_3$ at 130°C, with the two molar ratios of Na_2CO_3 to $CaCl_2$, yielded a 53–77% reduction in bending modulus and a 47–59% increase in hardness. From the surface image shown in Figure 7, lesser and smaller $CaCO_3$ nanoparticles were observed for the fibers impregnated at 100°C than those impregnated at 130°C, which reduced the elastic modulus.

Mechanical Properties of Composites

Figure 10 shows the bending modulus and tensile strength of the composites fabricated with retted and inorganic nanoparticle impregnated kenaf fibers. The tensile strength and bending modulus of composites were increased as the retting temperature and pressure increased. The composites reinforced with the kenaf fiber retted at 160ºC, 5.5 bar, resulted in a 33% increase in tensile strength and 16.7% in modulus of elasticity (MOE).

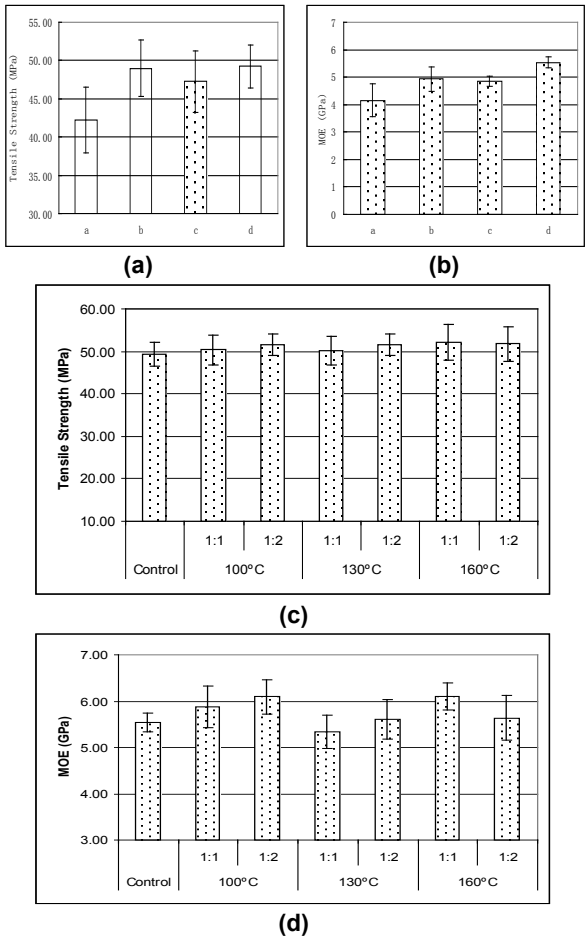

Figure 10. Mechanical properties of retted and impregnated kenaf fibers reinforced polypropylene composites. The y-axes indicate a and c are tensile strength and b and d are MOE ; a = 80ºC, 0.09 MPa; b = 110ºC, 0.15 MPa; c = 130ºC, 0.25 MPa; and d = 160ºC, 0.55 MPa.

The fibers with the highest surface hardness and modulus would not necessarily result in the highest elastic modulus [Figure 10(d)] for the composites because the contribution to the composite properties is not only from the fiber strength, but also from other factors such as fiber-polymer interfacial compatibility, microfibril angle, etc. The inorganic nanoparticle impregnation treatment gave about 10% improvement on the MOE property (Figure 10 [d] for the treatment conditions of 100°C with Na_2CO_3 : $CaCl_2$ = 1 : 2 [mol : mol] and 160°C with Na_2CO_3 : $CaCl_2$ = 1 : 1 [mol : mol]). Inorganic nanoparticle impregnation may improve the interfacial compatibility between the fiber and matrix and thus improve the bending performance of the composites. However, the impregnation treatment does not show a significant improvement on the tensile strength of the composites (Figure 10 [c]). The contribution to the tensile strength of the composites from some enhancements at the fiber-polymer interface may not be too significant compared with other factors such as fiber orientation and fiber network in the polymer.

Preliminary tests were conducted on the composites fabricated from the developed LSMC process using the unsaturated polyester resin matrix and a series of natural fiber loading (15–60%). The initial bending modulus for the composites was obtained as over 8 GPa, which is very close to the commercial SMC composites with 25% synthetic fiber glass, 8.5–14.0 GPa for SMC R25 (European Alliance for SMC 2001).

Conclusions

Alkaline retting at high temperature and high pressure generated micropores in fiber cell walls. The surface roughness of retted fibers decreased as the retting temperature and pressure increased. The removal of lignin and hemicellulose resulted in an improvement of fiber surface hardness and modulus. The polypropylene composites reinforced with the kenaf bast fibers retted at 160°C showed the highest MOE and tensile strength among the retting conditions investigated. Among the impregnation conditions used in this study, the highest nanoparticle loading in the fiber cell wall was obtained at 130°C. The $CaCO_3$ loading increases the surface hardness and elastic modulus. Improvement on the MOE of composites was observed at a 1.32% nanoparticle loading. The composites reinforced with the kenaf bast fiber

impregnated with $CaCO_3$ at 100°C (Na_2CO_3 : $CaCl_2$ = 1 : 2) and 160°C (Na_2CO_3 : $CaCl_2$ = 1 : 1) show about 10% improvement on MOE. The developed LSMC process may be suitable for natural fiber composite fabrication.

Presentations/Publications/Patents

1. S. Q. Shi, S. Lee, and J. Shi, "Lamination Process for Chemical Retted Kenaf Fiber/Thermoplastic Polymer Composites," 23rd Annual American Society for Composites Tech. Conf., September 9–11, 2008, Memphis, Tennessee.
2. S. Lee et al., "Inorganic Nanoparticle Impregnated Kenaf Fibers as Reinforcement for Polypropylene Matrix Composites in the Automobile Application," Intern. Cong. Nano-Bio Clean Tech 2008, October 27–30, 2008, San Francisco, California.
3. B. G. Lee et al., "Influence of surface morphology of the kraft pulp fibers on the growth of the transcrystalline layer of polypropylene," *J. Appl. Polym. Sci.* (2008) In Press.
4. S. Lee et al., "Nanoparticle Impregnated Kenaf Fibers for the Reinforcement for Polymer Matrix Composites, 4th Intern. Conf. Adv. Engin. Wood Hybrid Composites, **Bar Harbor, Maine, July 6–10, 2008.**
5. S. Lee, S. Q. Shi, and J. Shi, "High Pressure Chemical Retting for Kenaf Bast Fiber, Forest Products Society, 62nd Intern. Conv., St. Louis, Missouri, June 22–24, 2008.
6. J. Shi et al., Inorganic Nano-Particle Impregnation for Kenaf Bast Fiber, Forest Products Society, 62nd Intern. Conv., St. Louis, Missouri. June 22–24, 2008.
7. S. Q. Shi and S. Lee, 2008, "Laminated sheet molding compounding (LSMC) process from accelerated weak chemically retted natural fibers" (patent disclosure).

Acknowledgments

The authors would like to express special thanks to Dr. El Barbary Hassan and Dr. Philip H. Steele for their support on Py-GC/MS scanning.

References

1. L. Mwaikambo, *African J. Sci. Tech.,* Sci. Eng. Ser., **7**(2), pp. 120–133 (2006).
2. B. Aleksandra, et al., *J. Mater. Sci.* **42**, pp. 6501–6509 (2007).
3. T. Bullions et al., *Composites Sci. Tech.* **66**, pp. 102–114 (2006).
4. R. Anand et al., 6th Intern. Conf. Wood fiber and plastic composites (2001).
5. C. Clemons, and A. R. Sanadi, *J. Reinforced Plasti. Composites,* **26**(15), pp. 1587–1602 (2007).
6. J. Park, et al., *Composite Interf.,* **13**(2–3), pp. 105–129 2006).
7. T. Nishino et al., *Composites Sci. Tech.,* **63**, pp. 1281–1286 (2003).
8. S. Shibata, Y. Cao, and I. Fukumoto, *Polymer Testing,* **25**, pp. 142–148 (2006)
9. S. Aziz et al., *Composites Sci. Tech.,* 65, pp. 525–535 (2005).
10. K. H. Song and S. K. Obendorf, *Textile Res. J.,* **76**(10), pp. 751–756 (2006).
11. S. Keshk, W. Suwinarti, and K. Sameshima, *Carbohyd. Polym.,* **65**, pp. 202–206 (2006).
12. H. Lee, et al., *J. Korean Soc. Clothing Textiles,* **27**(9/10), pp. 1144–1152 (2003).
13. G. Ramaswamy, C. Ruff, and C. Boyd, *Texile Res. J.,* **64**(5), pp. 305–308 (1994).
14. J. Wang and G. Ramaswamy, *AATCC Review,* **06**, pp. 22–26 (2005).
15. A. P. Deshpande, M. B. Rao, and C. L. Rao, *J. Appl. Polym. Sci.,* **76**, pp. 93–92 (2000).
16. S. Lee, Ph.D. Dissertation, Louisiana State Univ., Baton Rouge, Louisiana, 2006.
17. S. Y. Lee et al., in T.F. Shupe (Ed.) (Forest Products Society, Madison, Wisconsin, 2006).

18. G. G. Allan, Y. C. Ko, and P. Ritzenthaler, *Tappi J.,* **74**(3), p. 205 (1991).

19. J. Kuusipalo, et al., *Tappi J.,* **4**(8), pp. 17–21 (2005).

Chapter Two: Temperature-Time Effects on Tensile Properties of Kenaf Bast Fiber Bundles

Yicheng Du, Jilei Zhang, and Yibin (Anna) Xue

Introduction

Typical processing temperatures for injection molding and compression molding for automotive part fabrication are 170ºC and 180ºC, respectively, with 1 hour duration, and the severe service conditions in automotive front-end structural application can be mimicked by conditioning the parts at 130ºC for 24 hours [1–2]. In addition to the process requirements, there are different testing procedures among automotive manufacturers for evaluating material strength performance under long-hour, high-temperature situations (Figure 11). This study was carried out to investigate temperature and time duration effects on the tensile properties of bacteria-retted kenaf bast fiber bundles (KBFBs) subjected to temperatures up to 190ºC, with different durations up to 9 hours.

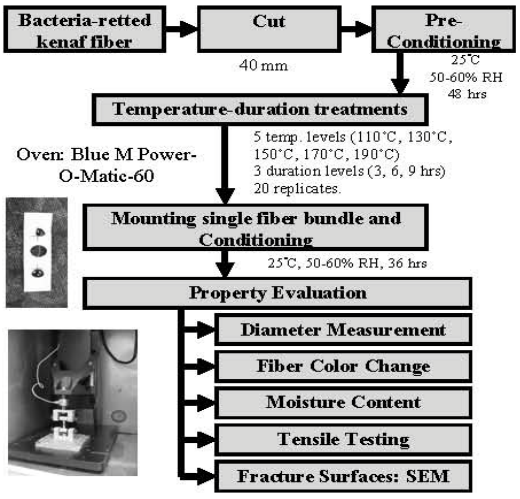

Figure 11. Experimental flow.

Experimental Procedure—Results and Discussion

Failure locations and modes

Under tensile loading, KBFBs had three main locations of failure: fiber breakage at the grips, fiber breakage in the middle of the specimen, and fiber explosion fracture (Figure 12). Table 3 summarizes the levels of KBFB failure for each of the three failure locations. The specimens of each combination had different average equilibrium moisture contents (MC), and in general, MC decreased as heat-treated temperature increased.

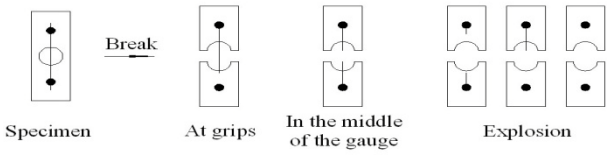

Figure 12. Failure modes of kenaf fiber bundles under tensile load.

Table 3. Failure locations and total number of kenaf fiber bundles tested in tension for each temperature-duration combination and moisture content (MC) of specimens after testing.

Temp. (°C)	Duration (hours)	Failure mode			Total	MC (%)
		Middle	Grip	Explosion		
	3	5	8	3	16	10.3
110	6	2	4	13	19	12.6
	9	6	10	3	19	10.3
	3	6	10	3	19	10.6
130	6	2	7	11	20	12.5
	9	8	4	7	19	9.9
	3	11	5	4	20	10.7
150	6	5	8	6	19	10.4
	9	2	10	7	19	9.2
	3	4	7	7	18	9.7
170	6	4	9	3	16	9.4
	9	1	6	3	10	9.5
	3	3	6	0	9	8.1
190	6	2	2	0	4	8.4
	9	2	2	0	4	8.8

Splintering mode was observed in specimens heated at 1,100°C, the combined splintering and brash modes were found in specimens heated at 150°C and 170°C, and brash mode occurred in specimens heated at 190°C (Figure 13). The failure modes were related to fiber color changes (from light blond to golden brown, then to brown). Changes indicated thermal degradation in chemical components (cellulose, hemicellulose, and lignin) of KBFBs.

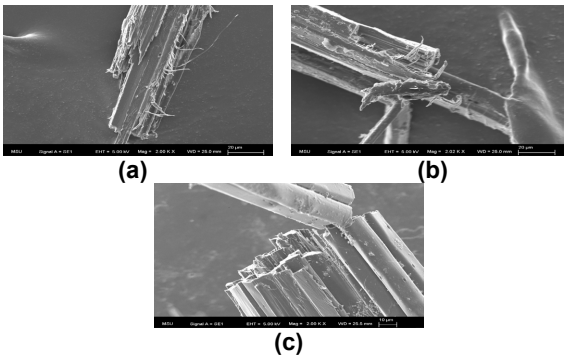

Figure 13. Scanning electron microscope micrographs of tensile fracture surfaces of KBFB specimens: (a) splintering tension, (b) combined splintering and brash tension, and (c) brash tension.

Data Analysis

Table 4 summarizes the mean values of the tensile modulus, tensile strength, and failure strain of tested specimens. A two-factor unbalanced analysis of variance general linear model procedure was performed for individual data, adjusted for the MC effect, to analyze the main effects and interaction factors on the mean values of the tensile modulus, tensile strength, and failure strain, respectively. The least square means a multiple comparison procedure was performed to determine the mean differences of the treatment combinations.

Table 4. Means of mechanical properties of tested kenaf fiber bundles for each combination of temperature and time. (COV=Coefficient of variance, N= Number of measurements)

		Tensile Modulus			Tensile Strength			Failure Strain		
Temp.	Duration	Mean	COV	N.	Mean	COV	N.	Mean.	COV	N.
°C	Hour	GPa	%		MPa	%			%	
110	3	12.0	22	16	136.5	40	8	1.17	23	8
	6	15.3	23	19	214.0	34	15	1.39	34	15
	9	13.0	19	19	176.6	26	9	1.33	11	9
130	3	13.8	21	19	162.6	34	9	1.13	22	9
	6	14.2	18	20	173.2	29	13	1.20	20	13
	9	14.3	16	19	166.7	30	15	1.24	28	15
150	3	14.4	22	20	140.1	33	15	1.05	28	15
	6	13.4	14	19	152.7	26	11	1.13	14	11
	9	13.7	18	19	146.3	28	9	1.02	14	9
170	3	15.0	25	18	147.8	36	11	0.92	31	11
	6	15.3	17	16	133.1	33	7	0.83	20	7
	9	14.3	22	10	91.3	50	4	0.57	38	4
190	3	9.2	47	9	49.7	39	3	0.72	23	2
	6	8.0	42	4	72.8	16	2	0.81	38	2
	9	6.8	59	4	41.4	42	2	0.47		1

Temperature effects

When the temperature increased from 110°C to 170°C, no significant change was observed in the KBFB tensile modulus. However, significant drops in tensile modulus occurred when the temperature increased from 170°C to 190°C. The average drops in tensile modulus were about 39%, 47%, and 55% for duration times of 3, 6, and 9 hours.

For the 6- and 9-hour tests, the tensile strength declined as the temperature increased and different declining rates were observed as the temperature increased (Figure 14). For the 6-hour test, the tensile strength declined at an average rate of 1.19 MPa per degree Celsius from 110 to 170°C. The average declining rate reached 3.07 MPa per degree Celsius from 170°C to 190°C, with 44% drop in tensile strength. Tensile strength had a significant drop of 51% from 150°C to 190°C. The significant drop in tensile strength can be explained by the severe degradation of the three major components of the KBFBs, cellulose, hemicellulose, and lignin, especially cellulose at the high temperature, plus long duration. The temperature had a significant effect on the tensile failure strain of KBFBs (Figure 15). It was noticed that a significant decline in strain started at about 150°C. The strain continued to drop significantly from 150°C to 170°C, but no further decline was observed at 190°C.

Duration Effects

There were no significant changes in tensile modulus, strength, and failure strain for temperatures ranging from 130°C to 190°C for a 3- to 9-hour duration (Table 5). A significant effect of duration on tensile modulus and strength was observed at 110°C for 3–6 hours of thermal exposure. The tensile modulus had a significant 28% increase, followed by a significant 16% drop as the duration increased from 6 to 9 hours. In the case of temperature at 190°C, the tensile modulus decreased as the time increased, although the decrease was not significant.

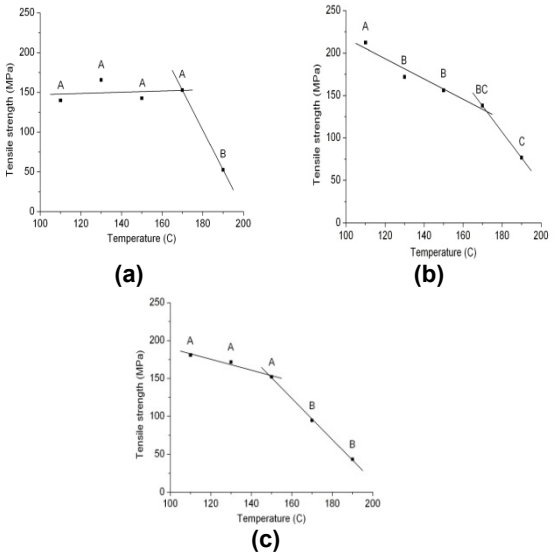

Figure 14. Mean comparisons for temperature effects on tensile strength for each duration of (a) 3, (b) 6, and (c) 9 hrs (values with the same capital letter are not statistically different at 0.10 confidence interval).

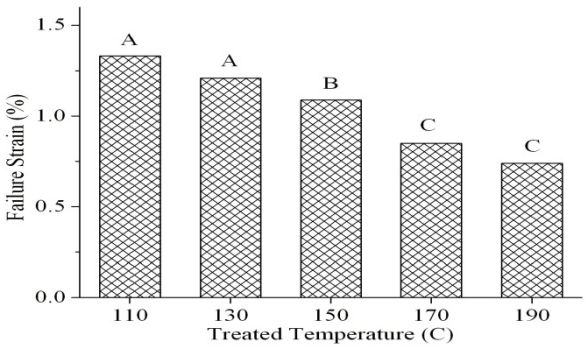

Figure 15. Effect of temperature on the ultimate strain of the kenaf fiber bundles (values with the same capital letter are not statistically different at the 10 percent significance level).

Table 5. Duration on tensile modulus and strength for each level of temperature.

Temperature	Duration (Hour)					
°C	3		6		9	
Tensile modulus (GPa)						
110	12.0	B	15.3	A	12.9	B
130	13.8	A	14.3	A	14.2	A
150	14.4	A	13.4	A	13.7	A
170	15.0	A	15.2	A	14.2	A
190	9.2	A	8.0	A	6.7	A
Tensile strength (MPa)						
110	139.9	B	212.3	A	181.0	A
130	165.7	A	172.0	A	171.7	A
150	142.6	A	156.1	A	152.2	A
170	152.7	A	138.0	AB	94.5	B
190	52.5	A	76.7	A	43.2	A

Values with the same capital letter are not statistically different at $\alpha = 0.10$.

Conclusions

A significant decrease in tensile modulus started when temperature increased from 170°C to 190°C, and the decreases in tensile moduli were 39%, 47%, and 55% for durations of 3, 6, and 9 hours, respectively. The tensile failure strain was significantly affected by temperature, but not by time duration. A significant decline in KBFB failure strain started at 150°C. The exposure duration seemed to have no significant effect on the tensile strength and modulus at temperatures of 130°C and above. The different stiffness behavior of the KBFBs can be explained by the degradation process of its major component, cellulose.

Presentations/Publications/Patents

1. Du, Y., J. Zhang, and Y. Xue. 2008. "Temperature-duration effects on tensile properties of kenaf bast fiber bundles," Forest Prod. J., 58(9) pp. 59–65.
2. Zhang, J. Y. Du, Y. Xue, and S. Q. Shi. 2008. "Temperature-duration effects on tensile properties of kenaf fiber bundle," Forest Products Society 62th Intern. Conv., Hyatt Regency Union Station, St Louis, Missouri, June 22–24, 2008.

References

1. Holbery J, Houston D. JOM 2006:80–6.
2. Sellers Jr T, Reichert Nancy A, Mississippi State University; 1999.
3. Bhuta M, Hall HL, Ziimmernman JM, Burcham TN, Columbus EP, Fuller MJ. In: Sellers Jr Terry, Reichert Nancy A, Eds. Mississippi State University; 1999. p. 401–20.
4. Roger RM, Sanadi A, Jacobson R, Caulfield D. In: Sellers Jr Terry, Reichert Nancy A, editors. Mississippi State University; 1999. p. 381–92.
5. Mohanty AK, Misra M, Dizal LT, Boca Raton, FL–CRC Press; 2005.
6. Mori T, Tanaka K. Acta Metall 1973;21:571–4.
7. Han JS et al. In: Sellers Jr Terry, Reichert Nancy A, Eds. Mississippi State University; 1999. p. 149–67.

8. Xue Y, Du Y, Elder S, Shame D, Horstemeyer M, Zhang J. In: Proc. 9th Intern. Conf. on wood and biofiber plastic composites, May 21–23, Madison WI; 2007.
9. Suzuki K, Kimpara I, Saito H, Funami K. J Soc Mater Sci Jpn 2005;54(8):887–94.
10. Standard test method for tensile strength and Young's modulus of fibers. ASTM C 1557-03. ASTM, West Conshohocken, PA; 2003.
11. Benveniste Y. Mech Mater 1987;6:147–57.
12. SAS Version 9.1.3, SAS Institute Inc., 100 SAS Campus Dr., Cary, NC.
13. Kollmann Franz FP, Cote Jr Wilfred A. New York: Springer; 1968.
14. Kocurek MJ et al. The pulp and paper manufacture series, vol. 3; 1987.
15. Mura T. Martinus Nijhoff, Hague. Netherlands; 1982.
16. Cox HL. J Appl Phys 1952;3:72–9.
17. Tucker III CL, Liang E. Compos Sci Technol. 1999; 59:655–71.

Chapter Three: Natural Fiber Composite Modeling

Section A: Kenaf-Epoxy Composite with Carbon Nanotubes

L.C. Brinson, S. Narayanan, and A. Schoch

Introduction

Composite materials can be analyzed at different length scales due to the different failure mechanisms. A micromechanical scale analysis helps to give us insightful knowledge of the local states of deformation and stress of the composite constituents (matrix and reinforcing fiber) and their interaction. This inspired us to follow micromechanical modeling approaches for the kenaf-epoxy composite and try to compare our results with the experimental results of its elastic moduli obtained by Xue et al. [1]. In the beginning phase of this project we were successful in modeling the kenaf-epoxy composite using the Mori-Tanaka model for the unidirectionally aligned composites and randomly oriented composites [2]. In the second phase of the project we were interested in investigating the enhancements in mechanical properties of the kenaf-epoxy composite when carbon nanotubes were randomly dispersed in it. The modeling for this was done by suitably extending the Mori-Tanaka model. The details of these two works and the ongoing and future works are presented in this report.

Modeling of Kenaf-Epoxy Composites

As mentioned previously, a three-dimensional Mori-Tanaka model (Figure 16) was used for modeling the kenaf-epoxy composite. The values of the mechanical properties required by the model were adopted from the available literature [1]. Justifiable assumptions were made for the mechanical properties whose values were not found in the literature.

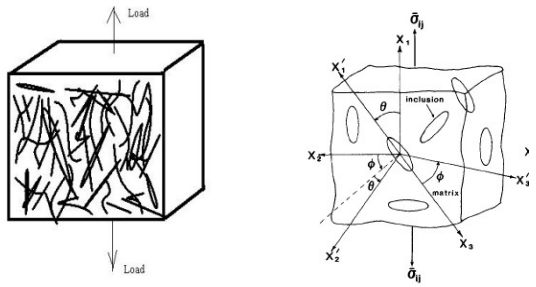

Figure 16. Comparing the schematic representations of the actual kenaf-epoxy composite sample and the 3D Mori-Tanaka model for randomly oriented fibers.

The moduli of elasticity were computed using the model, and their variation with fiber volume fraction was studied for a representative range of fiber aspect ratios (FARs) ranging from 100 to 1,000, as shown in Figure 17. The Young's modulus values obtained were very much comparable with the experimental values of 9.53 GPa (Yarn) and 4.76 GPa (Sliver), obtained by Xue et al [1]. It could be observed that there was no appreciable difference in the Young's modulus and the shear modulus for various aspect ratios of the fiber, due both to the small difference between Kenaf modulus and matrix modulus, as well as the single order of magnitude appropriate for the range of aspect ratios.

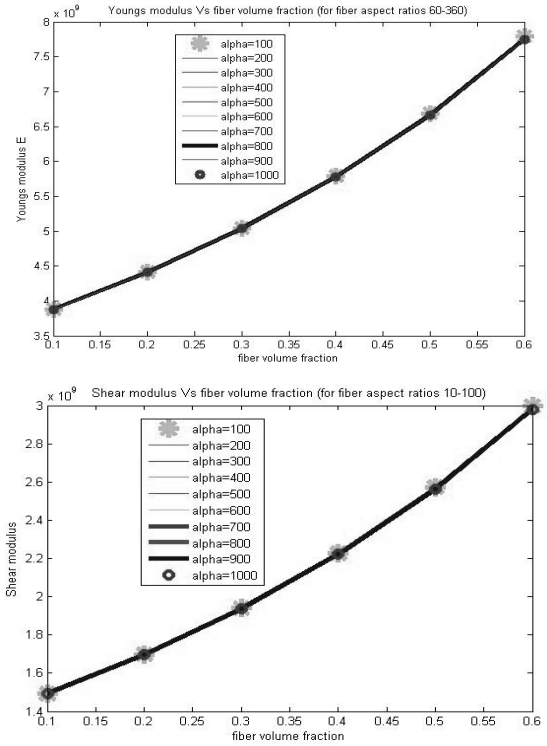

Figure 17. Young's modulus and shear modulus vs fiber volume fraction for various aspect ratios.

Modeling of Kenaf-Epoxy Composite With Carbon Nanotubes Dispersed

A small quantity (2%) of carbon nanotubes is embedded in the kenaf-epoxy composite. Note that both the Kenaf fibers and the nanotubes are embedded randomly in the matrix. The conventional Mori-Tanaka model is suitably extended to model the present case. The aspect ratio is chosen to be 100 for kenaf fibers and 1,000 for the nanotubes. The variation of Young's modulus with fiber volume fraction was studied for this case and compared to the earlier case, without nanotubes (Figure 18). For a fiber volume fraction of 0.6, the Young's modulus calculated was observed to be 21.94% greater than the case when nanotubes were not dispersed. This clearly indicates the possible advantages of introducing carbon nanotubes into the composite matrix in terms of enhanced modulus, strength, and other nonmechanical properties like thermal conductivity, electrical percolation, etc.

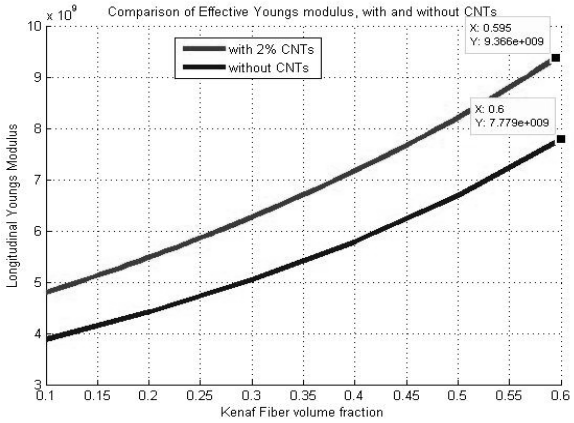

Figure 18. Effective Young's modulus of the kenaf-epoxy composite, with and without dispersed carbon nanotubes .

Presentations/Publications/Patents

1. K. Wakabayashi et al., "Polymer-Graphite Nanocomposites: Effective Dispersion and Major Property Enhancement via Solid-State Shear Pulverization," Macromolecules, 41(6) pp. 1905–1908 (2008).
2. L. M. Hamming et al., "Mimicking mussel adhesion to improve interfacial properties in composites," *Composite Science and Technology,* 2008 (in press).

References

1. Y. Xue et al., "Statistical tensile properties of kenaf fibers and composites," 9th Intern. Conf. Wood Biofiber Plastic Composites, May 21–23, 2007, Madison Wisconsin.
2. G. P. Tandon and G. J. Weng, "Average stress in matrix and effective moduli of randomly oriented composites," *Composites Sci. Tech.,* **27**, pp. 111–132 (1986).
3. G. P. Tandon and G. J. Weng, "The effect of aspect ratio of inclusions on the elastic properties of unidirectionally aligned composites," *Polym. Composites,* **5**(4) (October 1984).

Section B: Effects of Fiber Waving and Kinking On the Composite Performance

Yibin Anna Xue (MAE, USU), Scott Fletcher, Kunpeng Wang

Introduction

Linear and nonlinear elastic behaviors of wood fiber-plastic composites with discontinuous straight fibers arranged in regular and staggered arrays were obtained at various wood fiber volume fractions [1]. In this report a series of micromechanical simulations was conducted to predict the elastic and nonlinear elastic behaviors of wood-fiber-reinforced plastic composites (WPCs), considering the effects of fiber waving and kinking forms on the stress-strain relations, with the wood fiber volume fraction at 50%, a popular target volume fraction for automobile applications. The fiber kinks were presented as localized kinks in the middle of the fiber, uniform waving forms, and nonuniform waving forms. Figure 19 shows the unit cells contained fibers as (a) straight, (b) in a wave form, and (c) in a kinking form.

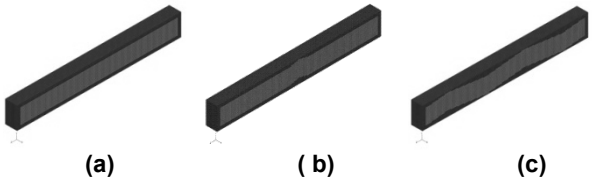

Figure 19. The unit cells of wood-fiber-reinforced polypropylene composites at the wood fiber volume fraction of 50%: (a) straight fiber, (b) uniform waving fiber, and (c) with local kink in the middle.

Composite Stress-Strain Relations

Figure 20 shows the stress-strain relations for WPCs with the wood FAR ranging from 5 to 100. For the particular WPC studied, when the fiber aspect ratio is 100, the stress-strain relation is very close to the case of that of continuous fibers when the total deformation is less than 4%.

Effects of Waving and Kinked Fibers

Numerical simulation of waving and kinked fibers demonstrates that the stress-strain relations of the composites are not sensitive to the forms of the wood fibers, as shown in Figure 21. Figure 22

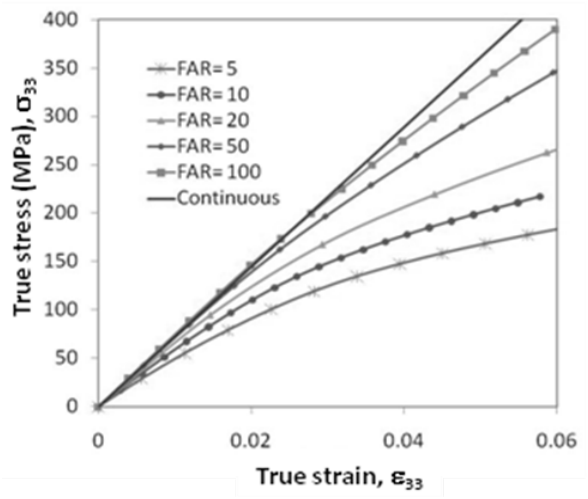

Figure 20. The true stress-strain relations for wood-fiber-reinforced polypropylene composites as a function of FARs.

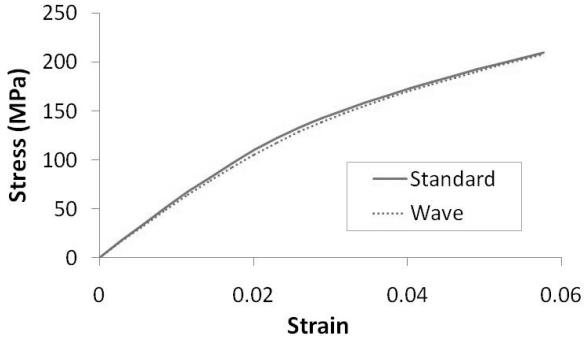

Figure 21. The true stress-strain relations for wood-fiber-reinforced polypropylene composites of uniformly distributed straight (standard) and waving fibers (wave).

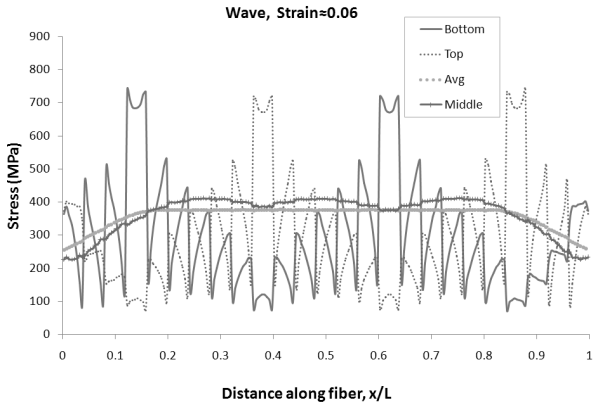

Figure 22. The distribution of stress along the length of fiber in the middle plane at the middle, top, and bottom of the fiber, in addition to the stress averaged over the cross-sectional area for waving fibers.

shows the normal stress distributions in the middle plane of the fiber at the top, center, and bottom of the fiber in composites with uniformly waved fibers. The stresses at the middle of the fiber in straight and waving fiber forms are similar. The most significant effect of the fiber forms relies on the local stresses in the fiber, especially the stresses on the top and bottom surface of the wood fiber. Figure 22 shows the stresses in the fiber at the peak of the waving fiber are more than twice the average of the stresses in the fiber at the corresponding points. The earlier surface failure of the wood fiber might induce fracture-type of stress intensity and cause earlier failure of the wood fiber.

Conclusions

1. For straight fibers, the high fiber aspect ratio enhances both the elastic modulus and nonlinear hardening of the composites. However, high fiber aspect ratio (greater than 50) may also induce high stresses in fiber, especially under loading greater than 4%, when the maximum stresses in fiber are greater than the tensile strength of the wood fiber.
2. For waving and kinked wood fibers (with the fiber aspect ratio of 10), the constitutive relation is not affected significantly by the fiber form. However, the local stress concentration on the surface of the wood fiber at the peak of wave and kink is more than double compared to the average stresses in the fiber, which may cause earlier failure of fibers.

Presentations/Publications/Patents

1. Y. Xue, S. A. Fletcher, and K. Wang, "Micromechanical simulations on waving and kinked natural fiber-reinforced plastic composites," Proceedings of IMECE2008, 67462, 2008 ASME International Mechanical Engineering Congress and Exposition, Boston, Massachusetts, October 31–November 6, 2008.
2. Y. Xue and K. Wang, "Micromechanical Simulations on Hydro-Mechanical Properties of Bio-Fiber Composites," MRS 2008 Spring Meeting Proceeding, 1097-GG-4-20, San Francisco, California, March 24–28, 2008.
3. Y. Xue and K. Wang, "Micromechanical Simulations on Hydro-Mechanical Properties of Bio-Fiber Composites," MRS 2008 Spring Meeting (poster).
4. Y. Xue, S. A. Fletcher, and K. Wang, "Micromechanical simulations on waving and kinked natural fiber-reinforced plastic composites," 2008 ASME International Mechanical Engineering Congress and Exposition (podium).
5. Z. Q. Zhang, D. Ward, and Y. Xue, "Molecular dynamics simulation on interfacial behavior of carbon nanotube and polyethylene," Micro/Nano Technology Society Function—2008 ASME International Mechanical Engineering Congress and Exposition (poster).

References

1. Y. Xue and K. Wang, K., "Micromechanical Simulations on Hydro-Mechanical Properties of Bio-Fiber Composites," MRS 2008 Spring Meeting Proceeding, 1097-GG-4-20, San Francisco, California, March 24–28, 2008.

H. Evaluation of Composite Natural Fiber/Resin Compatibility

Principal Investigator: Leonard S. Fifield
Pacific Northwest National Laboratory
P.O. Box 999, Richland, WA 99354
(509) 375-6424; fax: (509) 375-2186; e-mail: leonard.fifield@pnl.gov

Technical Contributor: Cheng Huang
Pacific Northwest National Laboratory
P.O. Box 999, Richland, WA 99354
(509) 375-6424; fax: (509) 375-2186; e-mail: cheng.huang@pnl.gov

Technical Contributor: Kevin L. Simmons
Pacific Northwest National Laboratory
P.O. Box 999, Richland, WA 99354
(509) 375-6424; fax: (509) 375-2186; e-mail: kevin.simmons@pnl.gov

Technology Area Development Manager: Joseph A. Carpenter
(202) 586-1022; fax: (202) 586-1600; e-mail: joseph.carpenter@ee.doe.gov

Field Technical Manager: Mark T. Smith
(509) 375-4478; fax: (509) 375-4448; e-mail: mark.smith@pnl.gov

---

Contractor: Pacific Northwest National Laboratory (PNNL)
Contract No.: Prime Contract No. DE-AC06-76RLO 1830

Objective

- To develop surface modification strategies applicable for industrial applications of woven and nonwoven natural fiber molding compound reinforcements.
- To manufacture thermoset polymer composite coupons for mechanical, thermal, extent-of-cure and environmental characterization.
- To develop material characterization data of composite material forms at the micro- and macroscopic scales with particular emphasis on fiber swelling, polymer-fiber interfacial adhesion and the effects of environmental exposure on composite mechanical properties.

Approach

- Develop a fundamental understanding of the natural fiber architecture to inform and tailor fiber surface modification strategies.
- Explore inexpensive and effective moisture barrier approaches for natural fibers including papermaking wet-end chemistry sizing agents and bio-based surface modifiers.
- Conduct lab trial iterations combined with screening tests to define the modification approaches best suited to natural fibers.
- Produce panels from modified natural fiber reinforcements to determine mechanical and moisture uptake characteristics relative to panels produced using unmodified natural fiber and glass fiber.
- Combine PNNL knowledge on sheet molding compound (SMC) materials with PNNL expertise in surface chemistry to develop new natural fiber materials capable of impeding moisture ingress as a function of time while providing advantageous specific mechanical properties.

Accomplishments

- Developed four unique surface modification strategies to combat moisture absorption in fibers and improve fiber-resin compatibility in natural fiber polymer composites.
- Performed initial experiments using two sizing agents from the papermaking industry to modify bast-type natural fibers from domestic and international fiber suppliers.
- Investigated the effect of surface treatments on the microscopic structure of fibers using scanning electron microscope (SEM) imaging.
- Used diffuse reflectance infrared spectral imaging on powdered samples of modified fibers to evaluate the effect of sizing type and reaction conditions on sizing efficiency.

Future Direction

- Complete evaluation trials of proposed natural fiber surface treatments.
- Develop new fiber surface modification strategies.
- Characterize moisture uptake and wettability of modified fibers to identify moisture resistance and polymer compatibility.
- Fabricate composite test samples from down-selected surface treatments to investigate strength of fiber/polymer interface.
- Produce SMC panels from modified natural fibers for mechanical and environmental characterization.
- Integrate developed surface treatments with fiber forms produced by the independently developed lab-scale fiber preparation unit.

Introduction

This project investigates the compatibility of natural fiber reinforcements with polymer systems that are of interest and applicable to automotive structural and semi-structural composite components. The project will evaluate and characterize composite strength, failure modes and time-dependent properties of select candidate natural fiber reinforced material systems. Novel fiber surface treatments and material processing variables will be designed and evaluated in an effort to optimize the compatibility and durability of the natural fiber composites. The project will focus on a limited number of natural fiber and polymer systems that meet requirements for automotive applications, including fiber cost and availability, strength and stiffness of fibers, and high-volume processing compatibility.

Plant-based natural fibers constitute a category of renewable biomass categorized as lignocellulosic; the major components of the fibers are cellulose, hemicellulose and lignin. Lignocellulosic fibers have appealing potential for use in polymer composite reinforcement and include bast, leaf and seed fibers, fruit fibers, wood fibers, grasses and reeds. A paramount challenge for the use of lignocellulosics as engineering materials is their inherent tendency to absorb moisture. The polar character of the fiber surface, which makes them hygroscopic, also limits utility of the fibers as reinforcement in common non-polar polyolefin thermoplastic matrices. Both physical and chemical methods have been used in attempts to control the interface of natural fibers and polymer resins to improve the performance of their composites. High moisture absorption, however, remains a barrier to widespread use of these materials. Moisture ingress causes fiber swelling, which leads to composite dimensional instability and a decrease in both fiber and composite mechanical properties.

The mechanical properties of fiber reinforced composites depend on the properties of individual components, including the fibers and the resin, and on the interfacial compatibility of the components. Plant fibers have a cellular composition that provides

mechanical support for the organism. The rigid cell well is made up of crystalline cellulose microfibrils glued together with amorphous lignin macromolecules. Bast fibers such those from flax, jute, kenaf and hemp are ~45-75wt% cellulose and ~5-25wt% lignin. Hydroxyl groups, acetyl groups and ether groups on the fiber molecules give the fiber is polar nature and inherent incompatibility with non-polar polymers such as polypropylene.

The moisture content inherent in lignocellulosic fibers is an important consideration in a chemical strategy to make the fibers compatible with a polymer resin. A large amount of energy is required to fully dry the fibers, but residual moisture can interfere with the coupling process by hydrolyzing reactants before they can add to the fiber. There remains significant opportunity for new methods to control fiber surface chemistry and minimize energy input required for fiber treatment.

An additional important consideration for fiber treatment methods is the temperature stability of natural fibers. Unless placed in an inert atmosphere, lignocellulosic fibers are generally limited to 150°C for longer processing durations and 200°C for brief exposures in order to prevent degradation of the fiber structure. Longer exposure can lead to discoloration of the fibers, volatilization of fiber components, and can have an adverse effect on fiber mechanical properties. The widespread use of lignocellulosic fibers in composite materials will require the development of scalable, low temperature fiber surface treatment methods.

Approach

Surface Modification Methodology

At the start of this project in July 2008, a thorough analysis of current modification strategies was conducted. Among the techniques that were considered include the following:

Mercerization

Mercerization is a process developed in the 19th century for improving the properties of cotton fiber for use in textiles. It involves treatment of fibers in a caustic solution containing sodium hydroxide. The concentration of solution, temperature, and process duration determines the extent of reaction. The treatment serves to swell the fiber bundles, lower the overall crystallinity of cellulose in the fibers and decrease hydrogen bonding in the fibril network structure. Though it can improve interfacial strength between the fiber and a polymer matrix, the mercerization process can lead to an increase in the tendency of fibers to absorb moisture.

Hydroxyl Group Blocking

Common reactions aimed to reduce the affinity of natural fiber to moisture involve blocking hydroxyl groups on the cellulose chains through the formation of esters. The yield of these reactions generally tracks with the dryness of the fiber.

$$\text{Fiber-OH} + \text{HOOC-R} \rightarrow \text{Fiber-OO-R}$$

Silane Coupling Agents

Organosilanes are the major coupling agents used for glass fiber reinforced polymers. Alkoxysilanes used for this purpose contain three alkoxy groups on a silicon atom that also contains a functional group for interfacing with the polymer. The alkoxy groups on the silane are hydrolyzed by residual moisture then displaced by the hydroxyl group's resident on the glass or natural fiber surface to form a silyl ether bond. After reaction the surface is less hydrophilic and more compatible with the polymer matrix.

$$\text{Fiber-OH} + (RO)_3\text{-Si-R}^2 \rightarrow \text{Fiber-O-Si}(OR)_2\text{-R}^2$$

Treatment with Isocyanates

Isocyanates, another common class of coupling agents, have N=C=O functional groups that can react directly with hydroxyl groups on the fiber surface.

$$\text{Fiber-OH} + \text{O=C=N-R} \rightarrow \text{Fiber-OO-CH-N-R}$$

Graft Copolymerization

An effective method of surface chemical modification of natural fibers is graft copolymerization. Redox initiation has been successfully implemented to graft

vinyl monomers onto natural fibers for composite application. Among the redox initiating systems, $CuSO_4$ - $NaIO_4$(Cu^{2+}-IO_4^-) is particularly interesting because no acid is used during the graft polymerization reaction; utilizing acid in a graft reaction degrades natural fiber properties. Optimized vinyl grafted natural fibers that consist of an orderly arrangement of grafted moieties act as compatible reinforcing fibers with several resin systems in obtaining better fiber-matrix adhesion.

The development of surface modifiers is critical to the success of this project. From the PNNL analysis of current technology, potential surface modifiers range from small molecules for blocking moisture to long-chain coupling agents that promote polymer matrix adhesion. An effective developed process with maximize reaction with bound –OH to minimize the lignocellulose moisture content prior to composite processing. This could potentially include a process deploying super critical CO_2.

All approaches seek to protect the entire surface with the goals of gaining moisture resistance, increasing fungal resistance, reducing processing temperatures and reducing of drying costs, simultaneously increasing physical and mechanical properties through improved fiber/resin compatibility and fiber/matrix bonding.

Surface Modification Plan

In this effort, innovative surface modification techniques outlined in the following paragraphs will be explored due to their potential for inexpensive, robust and effective application:

- Low molecular weight molecules currently used as paper sizings modified for structural composite applications.
- Bio-based, soy-derived modification strategies.

Sizing Chemistry and Paper Sizing Analogy

In this approach, we apply "papermaking wet-end chemistry" to natural fiber surface modification design. Paper sizes are designed to control moisture penetration into paper through modification of wood pulp fibers. The paper sizing mechanism can analogously be applied to control moisture of natural fibers for polymeric composite reinforcement. Commercial paper sizes are relatively inexpensive and available in quantities of tons per day. An example of one common sizing, alkylketene dimer (AKD), is depicted in Figure 1.

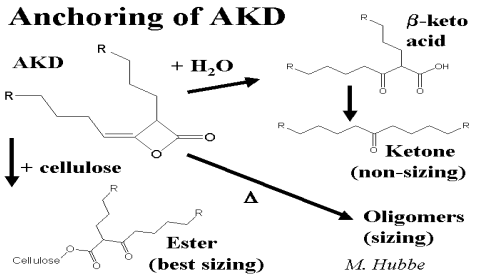

Figure 1. AKD paper sizing (www4.ncsu.edu/~hubbe/AKD.htm).

Bio-inspired Coupling Agents

Many plant biopolymers such as soy flour protein are being developed as sizes for natural fibers. Working with Professor Kaichang Li at Oregon State University's Department of Wood Science and Engineering, PNNL is investigating bio-based surface modifiers for natural fibers. Professor Li is exploring bio-inspired cure agents based on soy protein and other bio-molecules. Professor Li has issued patents for bio-derived adhesives. It is anticipated that new technology developed will utilize wet chemistry methods.

It is believed that these strategies will lead to a novel approach that will remain within the stringent process and economic parameters of the auto industry. Fibers that will be used as a baseline are hemp (Stemergy) and kenaf (Kengro).

Outlined below are two test methodologies that will be undertaken, one for screening different modification approaches and the other for more in-depth testing on those candidates that appear via screen testing to be viable natural fiber surface modification strategies.

A. Screening Tests
   1. Fourier Transform Infrared (FTIR)—Surface Chemistry
   2. Contact Angle (Packed Cell Method)—Surface Energy
   3. Zeta Potential—Surface Charging
   4. Moisture Uptake Tests

B. Advanced Testing
   1. Produce Panels—24 Hour Boil Test
   2. Produce Panels—Tensile Test
   3. SEM—Microscopic Structure

Experimental Testing and Analysis

Experimental characterization of the material surfaces will be undertaken utilizing several analytical techniques to determine the raw and surface treated natural fiber properties.

FTIR

Infrared spectra will be generated of the raw and surface-treated natural fibers to determine the surface-deposited chemistry and functionalization.

Moisture Absorption

Treated and untreated fiber samples will be characterized for moisture absorption, as will polymer composites produced from the fibers.

Panel samples first dried by heating will be weighed (W_1) and then soaked in a bath of deionized water at room temperature for a prescribed time (W_2). Water absorption, WA(%), will be determined by the following:

$$\mathrm{WA}(\%) = \left(\frac{W_2 - W_1}{W_1} \right) \bullet 100$$

.

Thickness swelling (TS) will be calculated on the fibers as follows:

$$TS(\%) = \frac{(t_c - t_o)}{t_o} \bullet 100$$

,

where t_c is the sample thickness after immersion and t_o is the thickness prior.

Scanning Electron Microscopy

SEM analysis will be conducted to reveal the effect of modification on the fiber surface structure (Figure 2). This will be particularly important for analysis of composite fracture surfaces to determine failure modes in composites produced and tested using the treated fibers.

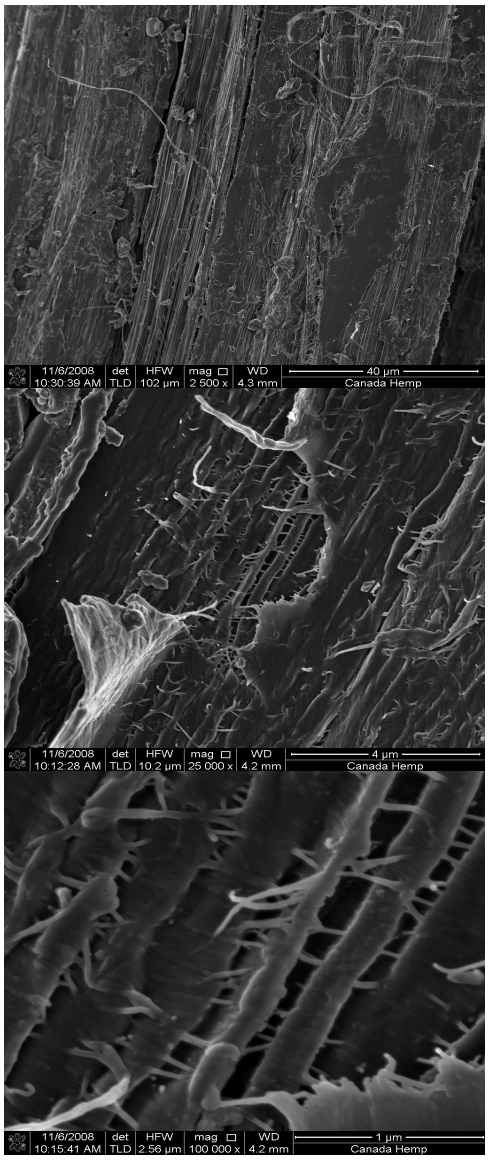

Figure 2. SEM images of Stemergy hemp with 40 µm, 4 µm and 1 µm scale bars.

Zeta Potential (ζ-Potential)

Due to the known hydrophilic character of cellulose-based materials, suitable methods that allow characterization of the wet state of these materials are

typically applied to study their surface properties. For this reason, the Zeta Potential (ζ-Potential) measurements have been established to characterize the potential difference in an otherwise uniform medium between a point some distance from the surface and a point on the plane of shear. The plane of slip between the electrochemical double layer and the medium involved (in this case, water) may be interpreted in terms of charge density. Thus, changes in surface composition and in the water uptake behavior due to fiber separation and subsequent surface treatment may be quantified by measuring the ζ-Potential. Additionally, it will be useful to quantify trends in the ζ-Potential as a function of pH and subsequent fiber swelling.

Sample Trials

SEM characterization of surface modification effects on natural fibers is ongoing. Below are SEM images of surface morphology of Kengro kenaf natural fibers without surface modification (Figure 3), obtained from FIB (Focused-Ion-Beam)-SEM, which exhibits clear fibrous textile microstructures, including microfibrils and lignin globules.

At this time, PNNL is conducting a series of experiments to determine the effect of paper sizing on surface chemistry. Kenaf and hemp samples have been modified with two sizes; in the future, size concentration, exposure time, temperature and fiber platform preparation will be explored.

Diffuse Reflectance Infrared Fourier Transform Spectroscopy (DRIFTS) for the identification of chemical modification of the natural fiber surface was applied (Figure 6). DRIFTS is an efficient, quasi-accurate (especially under Kubelka-Munk conversion) and convenient method for natural fiber surface modification analysis. Although the peak intensity ratios can be reliable for semi-quantitative determinations of functional groups, this technique will mostly be relied upon for qualitative evaluation of relative changes in surface chemistry.

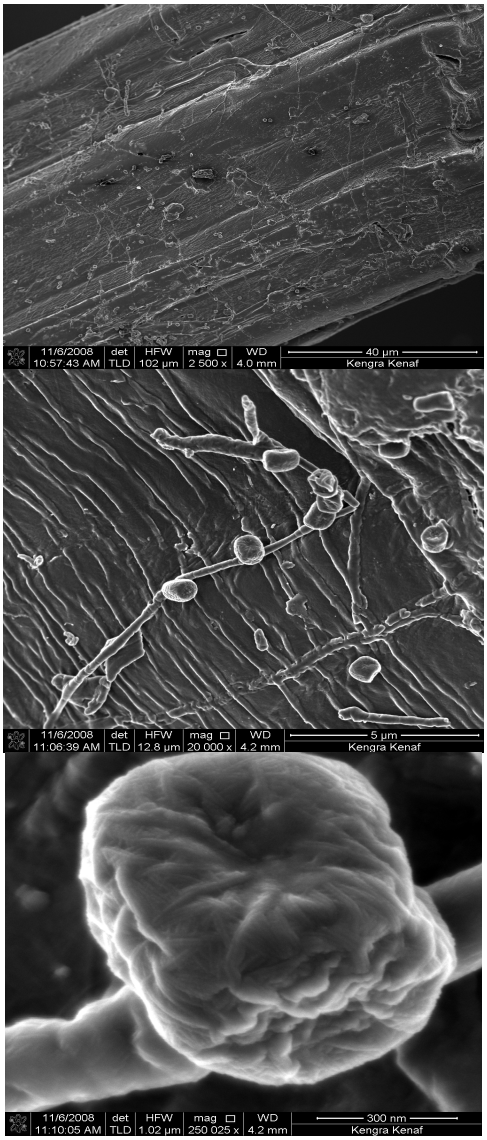

Figure 3. Kengro kenaf imaged with 40 µm, 5µm, and 300 nm scale bars.

With work newly begun mid-year, the next fiscal year will require a dedicated effort to move judiciously through the strategies outlined in this report to proceed with the most appropriate methods.

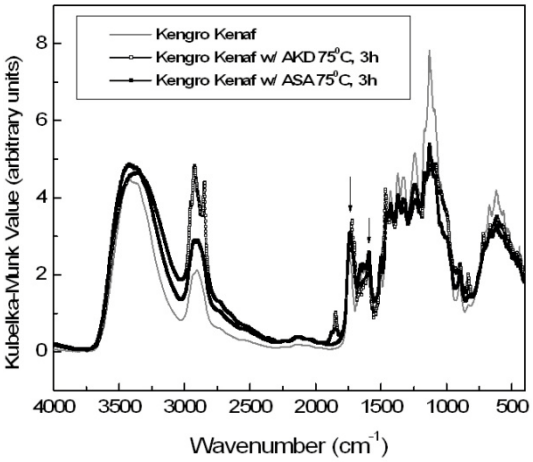

Figure 4. FTIR peaks of kenaf (Kengro, Charleston, MS), indicating change in fiber surface bonding sites with treatment.

Conclusions

Commenced in July 2008, this program had an initial focus on developing fiber surface modification strategies that will scale to the auto industry. At this time, PNNL has investigated several concepts and will be finalizing the experimental plan in the next quarter.

I. Composite Crash Energy Management (ACC100*)

Principal Investigator: Khaled W. Shahwan, Ph.D.
Chrysler LLC
Chrysler Technology Center—Scientific Labs.
800 Chrysler Drive (CIMS: 483-05-10)
Auburn Hills, Michigan 48326
(248) 576-5609; e-mail: kws8@chrysler.com

Technology Area Development Manager: Joseph A. Carpenter
(202) 586-1022; fax: (202) 586-1600; e-mail: joseph.carpenter@ee.doe.gov

Field Project Officer: Aaron D. Yocum
(304) 285-4852; fax: (304) 285-4403; e-mail: aaron.yocum@netl.doe.gov

Contractor: U.S. Automotive Materials Partnership (Cooperative Agreement) for the Automotive Composites Consortium Energy Management Working Group
Contract No.: DE-FC26-02OR22910 through the DOE National Energy Technology Laboratory

Objective

- Develop, verify, and validate efficient, robust, and physics-based modeling and analysis tools for predicting damage initiation, progression, energy absorption, and overall crush behavior of composite components in lightweight vehicle structures using micromechanical, phenomeno-logical, or hybrid computational approaches.
- Develop design, testing, modeling, and analysis guidelines for advanced lightweight automotive composites for safety and crashworthiness applications in vehicle development.

Approach

- Conduct extensive experimental tests to characterize the quasi-static and dynamic properties of selected structural composite materials and micro-architectures, including damage modes and progression mechanisms.
- Develop advanced models based on phenomenological and micro-mechanical approaches to predict the material and structural response during the full regimes of behavior including ascending branch, peak strength, post-peak and softening, and plateau characteristics of the stress-strain and force-displacement of coupons as well as structures.
- Verify and validate the computational tools by predicting quasi-static and dynamic behavior of experimental tests at the coupon and structural levels. Further validate by predicting structural crash performance of lightweight automotive composites.

Accomplishments

Carbon composites, especially braided textiles which exhibit mass density of about 1400 kg/m^3 (~ 80% lighter than common structural steels), have been characterized as viable materials for automotive structural applications. Their low densities as well as other characteristics such as equivalent structural stiffness, strength, and energy absorption, are well suited to meet many of the contemporary lightweighting challenges. The following specific accomplishments are aimed towards achieving that:

*Denotes Project 100 of the Automotive Composites Consortium (ACC), one of the formal consortia of the United States Council for Automotive Research set up by Chrysler, Ford, and General Motors to conduct joint, precompetitive research and development (see www.uscar.org).

- Demonstrated via extensive testing and modeling that post-peak softening in quasi-brittle textiles cannot be considered a constitutive property especially in homogenization techniques (as is commonly done), and the coupled local material-structural behavior plays a major role in characterizing such softening and overall response envelope.
- Demonstrated via extensive testing and modeling that the employment of models which contain mostly physically-defined and measurable quantities (non-phenomenological) is possible and achievable in order to predict the post-peak and softening behavior of such materials. Using such required fundamental understanding of the underlying physics and mechanics, and the full reliance on purely abstract mathematical concepts to quantify damage, is not sufficient.
- Identified the dominant mechanisms responsible for influencing the strength, post-peak softening response, and plateau (residual) strength in braided textiles. Extensive experimental and computational tests have been used to qualitatively characterize them.
- Revealed that modeling damage initiation and progression in braided textile composites necessitates the objective utilization of the concept of representative unit cell (RUC) as well as the inclusion of some measures for local/global imperfections. Because of the nature of damage, the minimum number of RUCs needed to accurately predict the damage zone and its progressions may not be known a priori and does depend on a host of factors.
- Exposed the dependence between compressive and bending strain fields and damage. Due to the multi-axial nature of damage, damage initiation and progression depends on the nature of the local stress field as well as remote applied loads.
- Experimental tests and computational analyses revealed that local in situ properties in textile composites can differ appreciably from their presumed virgin (bulk) values. Test-validated models (using optical techniques and nano-indentation) have quantified the dependence of the final elastic properties on cure time, cure temperature level, and distribution.
- Developed test-validated modeling (preliminary) techniques to study size effects in braided (quasi-brittle) composites. Recently, completed tests have confirmed and quantified size effects on the strength in such composites which is of importance for using finite-element modeling (FEM) techniques as well as designing sample sizes for laboratory tests.
- Completed a phase of study aimed at using multiscale modeling and analyses techniques to model and predict the damage initiation and progression during the quasi-static and dynamic crush of braided carbon tubes. A multiscale design system (MDS) was also developed to model the micromechanics including interface degradation and debonding, and couple the analysis procedure with a commercial software package.
- Completed and validated an automated FEM procedure for modeling random distribution of carbon fibers within a given spatial volume using a commercial software package to statistically investigate the influence of the RUC size on the elastic properties of the homogenized material.

Future Direction

- Develop a modeling database encompassing all models, associated material modules, coupled material-structural data, and special finite elements. This modeling database will serve as a central point for all predictive analyses and modeling developments for understanding and quantifying the strength and crashworthiness of lightweight automotive composites.
- Expand the current multiscale design system (MDS) to complete its functionality by including additional rate sensitivity effects, delamination, RUC optimization (with some adaptive capability), and size effects in order to enhance its proven predictive abilities.
- Investigate ways to minimize (or even mitigate) size effects in such quasi-brittle textile composites. Having characterized and quantified such important and inherent size effects within braided carbon textiles further investigations would provide important insights on how to minimize such effects at the early

material/architecture design/selection stages so that predictive tools, computational modeling and laboratory testing can be further simplified and streamlined.

- Material properties' changes with service/environmental factors (e.g., fatigue, high-frequency high-amplitude pulses/vibrations, moisture, and large thermal fluctuations, etc.) and their influence on energy absorption, mechanical response, and crash performance during a component's life-cycle. This could be focused on characterizing the in situ properties of in-service structural components and studying which factors influence (and to what degree) mechanical response and energy absorption capacity of lightweight carbon textile composites for automotive applications.
- Develop a demonstration project in which all completed accomplishments will be utilized to show the viability of carbon fiber-reinforced composites as a primary structural material in an actual automotive subassembly (e.g., front end), as well as the validity of the modeling and predictive tools developed thus far.

Introduction

The purpose of the Crash Energy Management Program is to develop and demonstrate the technologies required to apply production feasible structural composites in automotive crash and energy management applications. Projects within the program are intended to understand the mechanisms of polymer composite crash, develop analytical tools for use in design, and build a knowledge base for the application of lightweight polymer composites. The projects relate to materials, molding, and assembly process and design configurations that are useful in realistic applications. Design analysis methods will be developed that can be used at several different steps in the design process. These steps require different levels of precision and speed of use and the appropriate tools are expected to include both micro-mechanical and phenomenological approaches.

Multiscale Modeling for Crash Prediction with Interface Debonding

The previously developed multiscale composite crash prediction software system has been enhanced with the development of an interface model consistent with new experimental data. In addition, in situ inelastic phase properties of matrix and tows have been recalibrated to the coupon test data from the transverse tension, longitudinal tension, and longitudinal compression—all conducted on the 45° braided composite architecture.

The reduced-order multiscale model with interface debonding has been verified against an analytical solution on a model problem. Finally, the reduced order multiscale model with interface debonding has been validated against quasi-static tube crush experiments on various braid architectures (45°, 30°, and 60°) and different cross-sectional shapes of tubes (circular and square).

A close investigation of the experimental work performed at South Dakota School of Mines & Technology (see Figures 1 and 2) shows little or no interphase. The nanoindentation tests confirm this observation as well. Therefore, in the reduced-order multiscale model, the interface (rather than interphase) was modeled using a traction-separation law. In the traction separation law adopted, the value of fracture toughness in modes I, II, and III measured in quasi-static tests was used. The interface strength values were assumed to be identical to those of the matrix strength in the corresponding direction. These values were taken from the prior tests conducted elsewhere.

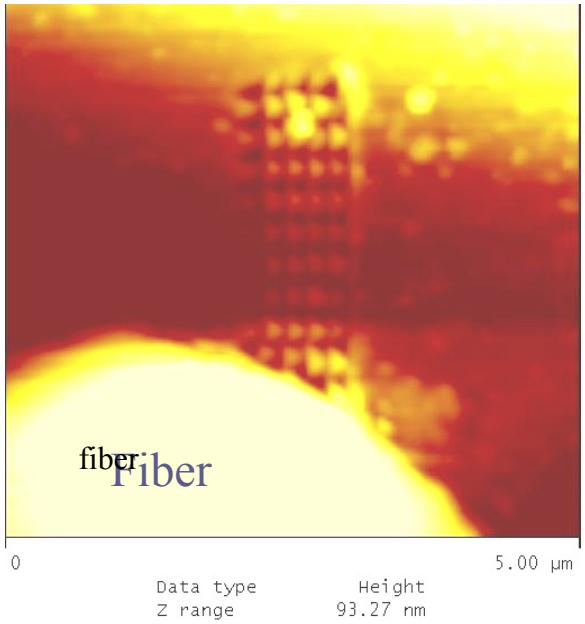

Figure 1. Fiber-matrix interface.

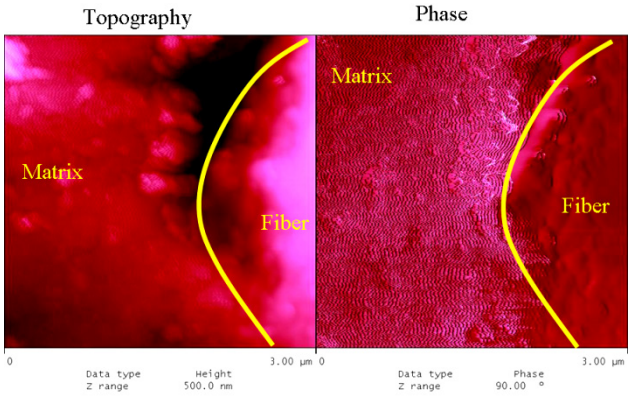

Figure 2. Close-up of an Atomic Force.

The theoretical aspects of the reduced-order multiscale model have been presented in past reports. It is instructive to comment on the computational complexity of the reduced-order multiscale model with interface debonding. The reduced-order multiscale model with interface debonding consists of 46 state variables, which include: six eigenstrain components times four phase partitions = 24, three components of eigenseparations times three interface partitions = 9, one phase damage state variable for each phase partition = 4 and three interface damage state variable for each of the three interface partitions = 9.

Microscopy (AFM) Phase Image of a Fiber-Matrix Interface

We now discuss the comparison of the simulation results on the ¼ tube model to the experimental results. We consider two layers of braided composite, an initiator plug with a specific fillet radius and loading rate of 0.5 in/min. Figure 3 compares the test data to the simulation results of the reduced-order multiscale model with and without interface debonding for 45° braid architecture.

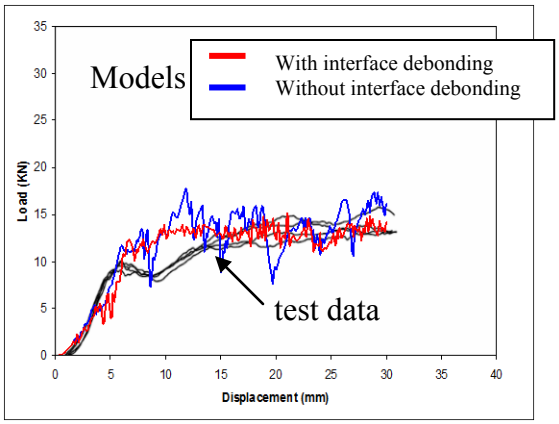

Figure 3. Predictions vs test for 45° carbon braided quarter tube.

It should be noted, however, that calibrated braid and matrix properties are different in the two simulations, i.e., in each case they have been calibrated to fit the test data in the transverse tension, longitudinal tension and longitudinal compression of the 45° braided composite architecture. Nevertheless, it can be observed that a notable improvement is obtained when the interface damage is considered in the model.

Figure 4 shows the comparison of the simulation and test data for the 60° braid architecture. In this case, the agreement between the experiment and simulation results is less remarkable and the improvement obtained due to modeling of interface damage is less pronounced, if any.

We suspect that the main reason for this less dramatic improvement is due to the fact that phase properties were calibrated based on the coupon tests of 45° braid architecture. This hypothesis can

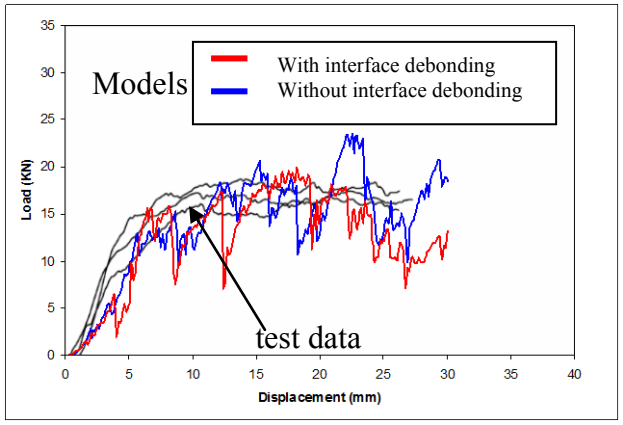

Figure 4. Predictions vs test for 60° braided quarter tube crush.

be easily verified if coupon tests on 30- and 60° architectures were available. Possible other reasons that will be investigated in the future are: consideration of a three-scale analysis (so far, the braid was assumed to have isotropic damage) and consideration of full-scale tube models.

Size Effects in Textile Composites

This project is focused on developing a qualitative and quantitative understanding of the important topic of meso- to macro-size effects in automotive structures made of quasi-brittle textile composite materials. Such an understanding plays a role in the accurate modeling and characterization of structural crashworthiness and energy absorption in components made of lightweight quasi-brittle materials (such as textile composites). Obtaining an understanding and useful insights of size effects, along with verifiable experimental evidence and clarification of the implications of the size effects for finite element (computational) modeling of structures made of two-dimensional triaxially braided composites (2DTBC), is the major goal of the project.

It is important at this point to clarify what is meant by "size" and what are the "effects." "Size" refers to the size of specimen/structural dimensions relative to the size of the damage zone and/or micro-structure. "Effects" refer to those effects on damage characteristics, nominal strength, and post-peak regime in materials exhibiting such strength–size dependence.

This project is motivated by the following fundamental question: What is the relationship between the measurements of energy released and dissipated (i.e., fracture properties and material nonlinearities) carried out in the laboratory at the coupon level of a 2DTBC, and their manifestations at the structural level in a real crash setting of a structure made of the same 2DTBC i.e., do the measured overall material/ structural properties change when different size specimens are tested? It is important to note that the primary interest in this topic (relating specimen size effects on measured material properties) does not stem from the well-known statistical distribution of micro-flaws in a material based on Weibull theory, but rather from an energetic consideration driven by the relatively recent findings that quasi-brittle materials exhibit size effects because their fracture process-zone is not negligible (in size) compared with the overall structural dimensions.
The work is focused on designing, manufacturing, testing and modeling different-size structural plaques using one matrix/resin system and three carbon fiber-braid architectures (+/-30°, +/-45°, and +/-60°). Various sizes of plaques were made encompassing a certain numbers of RUC as determined by the project's plan. Each plaque made was multi-layer (up to 8 layers), each having axial tows as well as braider tows exhibiting one the above angles. The main objective is to provide the sponsors with insights and guidelines on how best to model and test such materials in order to accurately model their true behavior under static and dynamic loads. It is worth noting that such an effort has not received significant attention in the past especially for this type of materials, architecture and manufacturing process.

Thus far, several tasks have been accomplished. Tests have been carried out on small samples and a larger one representing multiple RUCs. Based on the preliminary experimental data and observations, such braided carbon-fiber textiles exhibit strong and rapidly evolving size effects. i.e., the emergence of size effects, as one tests and compares one RUC vs multiple RUCs, is apparent and changes rapidly as larger-size plaques are tested.

The principal investigators (PIs) have proposed and developed a simplified way to model large

number of RUCs (e.g., 9, 14, 25… etc.) using "rugged" instead of "smooth" boundary condition per RUC (Figure 5). This resulted in a significant reduction in the number of finite elements (FE) needed to model each RUC. While it has been typical to have 5,000 FE or even 30,000 FE per RUC to achieve certain level of validity and accuracy, the current approach employs only 30 FE (approx.) and achieves similar results when compared to other models as well as laboratory experiments. This is a remarkable improvement and could be very useful once large, full-component or full-systems are modeled using FEM/finite-elelent analysis (FEA). Figure 5 also shows a modeled plaque with a total of 25 RUCs using the above technique.

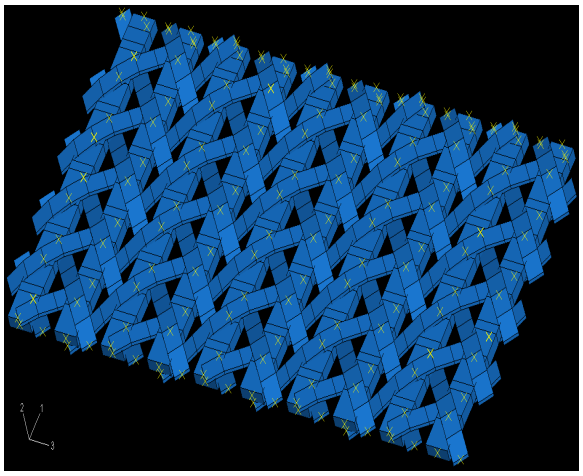

Figure 5. A full plaque modeled using multiple RUCs. There are 25 RUCs. Each RUC is made up of three-dimensional (3D) elements and irregular (rugged) boundary/edges. Only axial and braider tows are shown for clarity.

Figures 6 and 7 show the strong size effects that are present in such quasi-brittle textiles. This implies that strength characteristics depend not only on the material properties but also on the size of the specimen being tested and/or modeled. Ongoing work is focusing on developing an enhanced version of the popular Microplane Models used for modeling and analyzing damage and fracture in various types of materials (Figure 8).

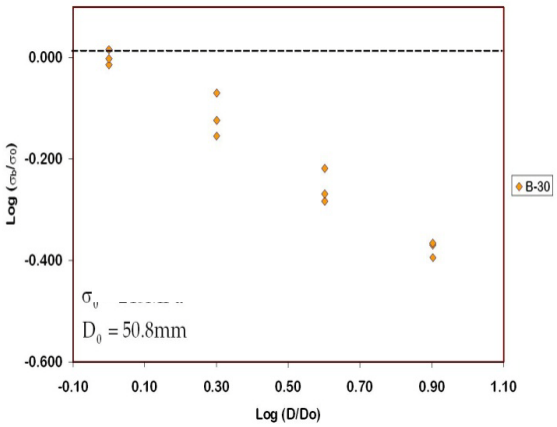

Figure 6. Experimental tests showing the change of the log of normalized strength (σ_N/σ_o) vs change in specimen size (shown as log D/D_o). The above results are for 30° braided-carbon fiber specimen.

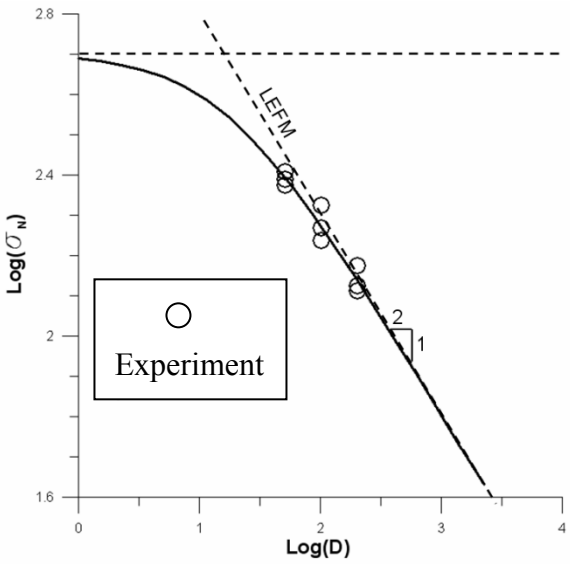

Figure 7. Experimental tests and fitted numerical predictions (solid line) showing the change of the log of normalized strength (σ_N) vs change in specimen size (shown as log D) for 30° braided carbon-fiber specimen.

Modeling of the Manufacturing Process Induced Effects (MPIE) on the Matrix Properties of Textile Composites

During the manufacturing process of textile reinforced composites (TRCs) the material properties of the polymer resin (matrix) change remarkably over the curing cycle. Resin's liquid-to-solid transition is accompanied by volume change. Coupled with mismatches in thermal

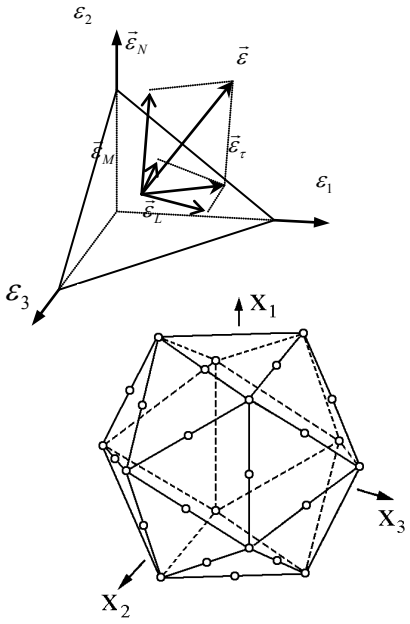

Figure 8. Microplanes modeling technique in which the stress-strain relationships at a material point are mapped onto a sphere with infinite tangent surfaces, and then simplified by selecting a finite number of surfaces.

coefficients between fibers and resin, and applied mechanical stresses, will result in inhomogeneous curing of TRCs structural specimen with built-in local residual stresses and pre-existing micro-cracks. Such local field-variations within the cured material can result in significant differences between virgin material properties and the actual in situ material properties.

The actual response of a structural component made of TRCs can be accurately predicted using only in situ material properties NOT the virgin properties which are typically the presumed input values into an analysis code. Such a practice can introduce inaccuracies which are typically attributed to other sources. It is the primary objective of this project to develop qualitative and quantitative methodologies (and modeling tools) to better understand and predict the in situ properties within a fully cured structural component made of TRCs.

Figure 9 shows the difference in response of one RUC model of a tri-axially-braided carbon-

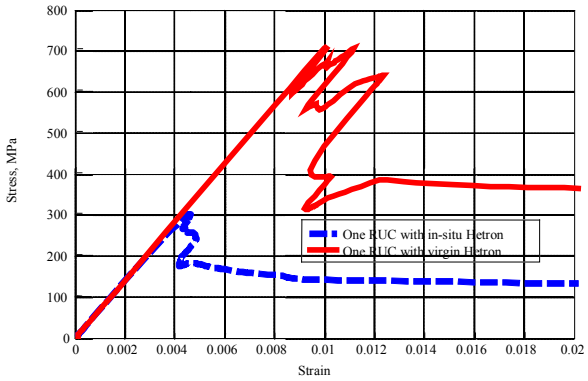

Figure 9. The effect of using virgin matrix properties vs their in situ counterparts on the response of an RUC using finite-element method. The RUC represents a triaxially braided carbon-composite material specimen.

composite material specimen. The figure demonstrates the effects of using virgin matrix properties vs their in situ counterparts on the response of an RUC using a nonlinear finite-element method. Figure 10 shows one of the major sources for such a difference in response which is mostly attributed to differences between (presumed/virgin) and in situ properties.

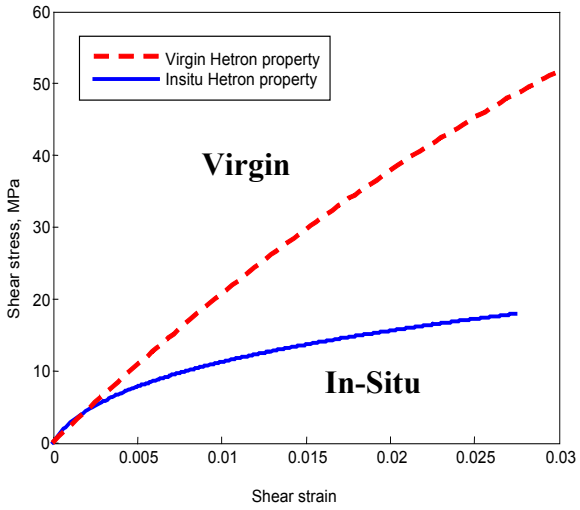

Figure 10. Shear stress vs shear strain of virgin matrix (dashed) as tested in the lab. However, the in situ matrix shear strength and stiffness properties (as shown in the solid blue stress vs strain curve) differ significantly for this specific case. Note that the in situ properties are back-calculated using test data and elasto-plastic theories.

TRC materials are quasi-brittle systems whose energy-dissipation characteristics are dominated

by micro-cracks which are controlled by local geometry and in situ properties. A need exists to develop a robust computational predictive tool which uses as input only stress-relaxation, evolution of extent-of-cure, and thermal conductivity properties measured/calculated from simple mechanical tests without resorting to back-calculations using full nonlinear finite element analysis (FEA) simulations.

Currently, the in situ properties are typically back-calculated using several laboratory tests as well as elasto-plastic analytical theories (in conjunction with computer models). Although this process has been verified and validated, and is based on well established theories from mechanics of materials, it is not efficient especially during the preliminary design process.

This project involves three major aspects: a) spatial material characterization of cured matrix in resin-rich locations, adjacent to fibers within a tow, as well as in between fibers and tows; b) temporal and thermal evolution of constitutive properties (using state-of-the-art optical techniques) as functions of time, extent-of-cure, as well as imposed thermal conditions at the boundaries; and c) development and validation of predictive tools which model the manufacturing and curing processes including mechanical and thermal stresses, visco-elasticity, and visco-plasticity.

More specifically, resin-filled cylinders will be subjected to temperature variations based on manufacturer curing profile. Time and radial variation of temperature, extent of cure, strains and stresses will be measured and calculated.

The cured resin will be removed and subjected to additional mechanical tests. The above detailed procedure will be repeated but with a fiber tow (simulating TRCs) placed concentrically in the cylinder prior to curing and repeated tests. A complete set of experimental results using nano-indentation [Figure 11(a)], Brillouin light scattering (BLS) and Raman light scattering (RLS) [Figure 11(b)], including refined resin properties during curing, and a FE code capable of simulating the MPIE (no flow simulation) are deliverables. The effects of process cure parameters and their effects on matrix cracking modeled through the thermomechanical FE code is a deliverable.

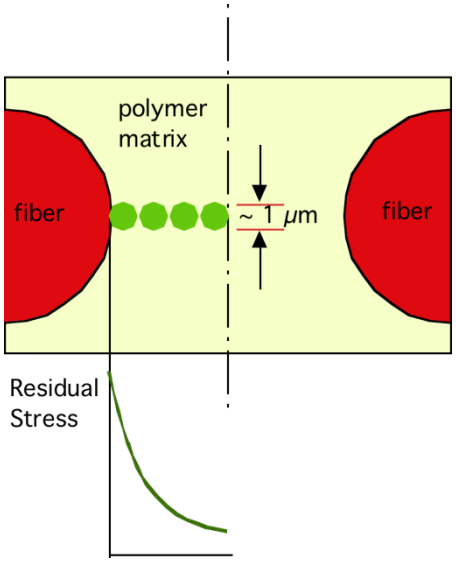

Figure 11(a). Schematic showing examples of locations (four green circles) where nano-indentation may be used to extract values for the modulus distribution near and away from the fiber as well as within resin-rich regions.

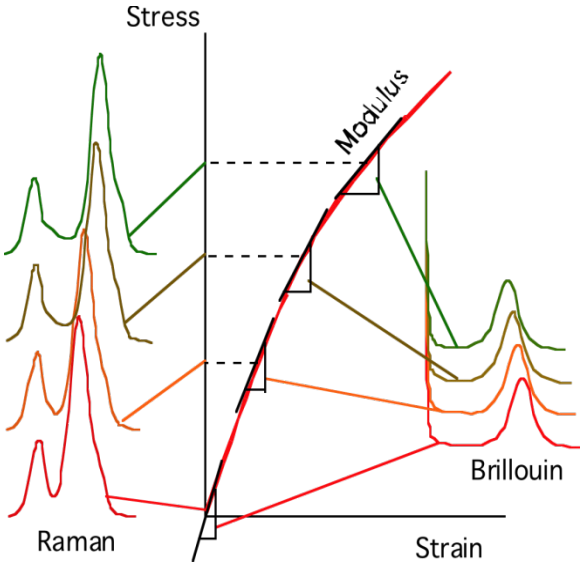

Figure 11(b). Schematic showing the basic idea of using BLS and RLS to estimate the mechanical properties via optical methods.

Figure 12 shows the preliminary results from laboratory tests designed to measure elastic modulus of an Epon resin sample while it is curing (plotted vs time) at different imposed boundary

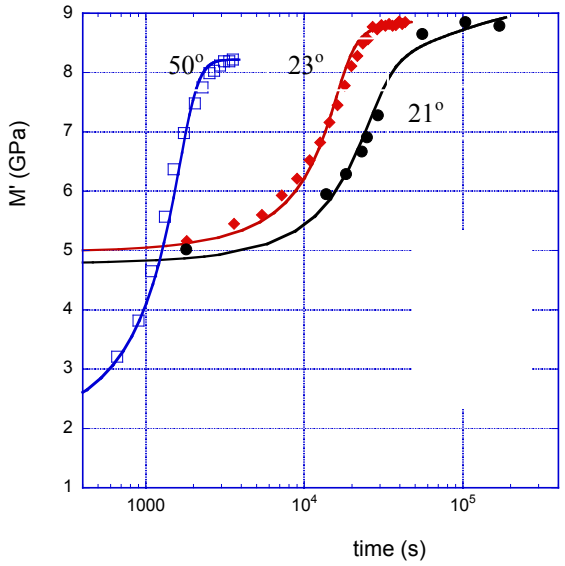

Figure 12. Preliminary laboratory test measurements of elastic modulus (M') vs curing time at different boundary temperatures (21° , 23° & 50° C) for Epon resin. AT higher temperature the resin sample cured faster however it attained a lower final elastic modulus. The tests used optical techniques to measure M'.

temperatures. The tests used optical techniques to measure the modulus.

One of the main outcomes of the project is the development of a predictive tool which can be incorporated into any existing composite material-damage model. Such a tool will eliminate the need for carrying out parallel (and additional) tests as well as extensive nonlinear FEA (as currently is the practice) in order to "back-out" the actual in situ material properties which influence the structural response and local damage characteristics.

Another important contribution of the project is to expose the main factors contributing to such in situ properties and their evolution during the manufacturing and curing process. For example, using nano-indentation it was found that not only matrix properties vary with time (while curing) and with location (i.e., how close to a fiber/tow) but also that because of the very nature of chemical curing, the apparent fiber properties within a tow differ depending on the type of resin (Figures 13 and 14). Here, the somewhat expected preliminary results highlight the importance of

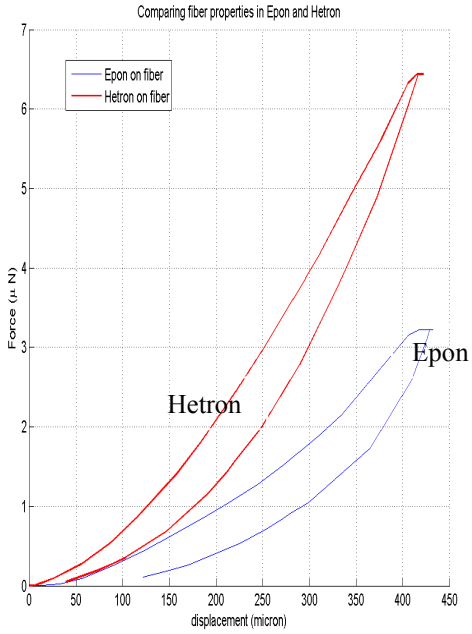

Figure 13. Preliminary laboratory test measurements show the results of using nano-indentation to measure the transverse force-displacement response of two carbon fibers each embedded in a different (cured) resin.

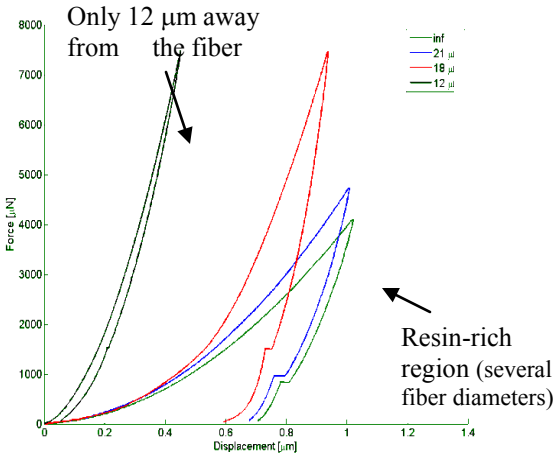

Figure 14. Preliminary laboratory test measurements show the results of using nano-indentation to measure the force-displacement response of the cured matrix as a function of the distance away from the edge of a single carbon fiber embedded in the cured matrix.

understanding the time history, the manufacturing process, and spatial variation of material properties within a cured structural component.

Crashworthiness Assessment of Tubular RaFCs Structures Based on Micro and Interfacial Mechanics

An integrated experimental-computational research program is carried out with the aim of creating a novel Hierarchical, Micro-Experimental and Computational Characterization (HiMECC) algorithm for Random fiber composites (RaFCs). This will be realized through the following four deliverables:

1. Develop computational tools for RaFCs micro-scale material characterization and damage modeling (Figure 15),
2. Conduct experimental work to determine required material parameters and validate numerical analysis tools,
3. Determine key mechanisms responsible for macro-scale damage, and
4. Determine key mechanisms responsible for interfacial damage.

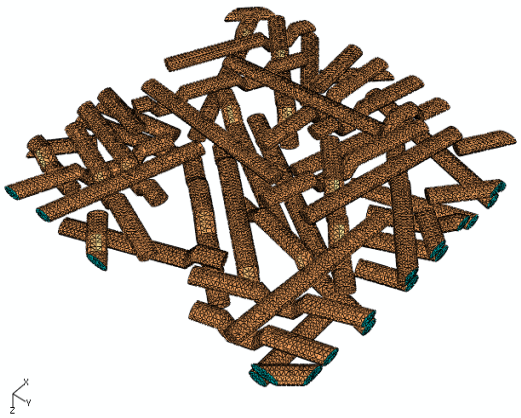

Figure 15. A finite element model of a network of random fibers.

The following milestones have been reached thus far:

1. Completion of an automated FEM analysis procedure using a commercial software package, to statistically investigate the influence of the representative volume element (RVE) size on the elastic properties of the homogeneous material.
2. Validation of the FEM results through comparison with analytical and semi-analytical approaches. In particular we compared our results with several validation algorithms and models.
3. Scanning Electron Microscopy (SEM) and optical characterization of Glass and Carbon/Urethane specimens.
4. Modeling of a fiber bundle with elliptical fiber bundle cross-section to accurately represent composite materials. We determined the shape of the cross sectional area of the fiber bundles with the aid of optical microscopy and SEM experiments. For the modeling part of the project, a dodecagon inscribed in the ellipse that covers 95.5% of the ellipse area. The 3D fiber bundle was formed by sweeping the ellipse into the 3D space. Moreover, we performed spline modeling, with 3D bundle intersection checks carried out by employing convex optimization algorithms.
5. RVE generation with curved and straight fiber bundles. We were able to generate RVEs (that correspond to real material parameters) with the following characteristics: (1) use of both straight and curved, (2) non-circular fibers, no intersection between fibers, and (3) volume fractions in the 35.1–36.7 % range.
6. We performed tensile experiments to fracture point on the following material systems:
   (1) E-Glass - vf 38%, and
   (2) Carbon/urethane–vf 35%, where vf denotes volume fraction.
7. Performed single fiber debonding simulations. It is well established that the interfacial strength of fiber and matrix affect the performance of fiber composites. We modeled the fiber debonding using cohesive elements. Simulations were run for single fiber composite (SFC) with perfect interface (Figure 16) and SFC with finite interfacial strength (Figure 17).

Each fiber is modeled with hundreds of finite element as well as cohesive elements near the interface. This is used to model the response of a fiber with infinite interfacial strength as well as finite one.

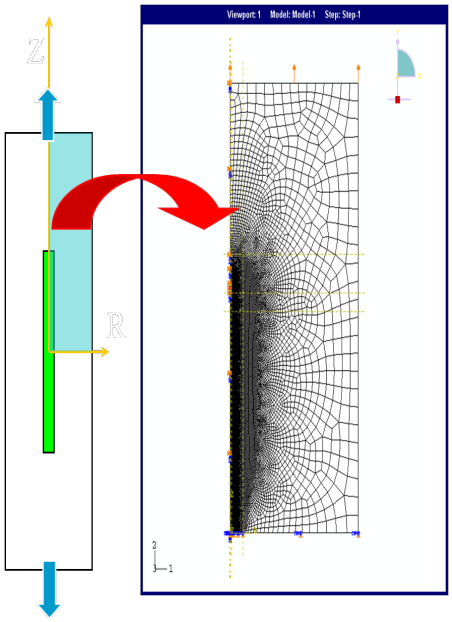

Figure 16. A finite element model of a single fiber, surrounding matrix, and interface.

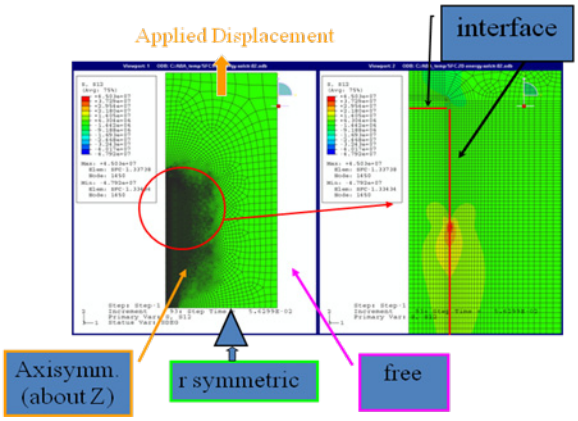

Figure 17. This figure provides an expanded view detailing the regions of interest, as well as the onset of damage initiation at the single-fiber-matrix interface (with finite bonding strength). The figure also shows the finite element modeling and analysis user-interface.

Publications/Presentations

1. Z. Bazant, F. Caner, and C. Hoover (2008), *Mesomechanical Multiscale Elastic-Fracturing Model for Braided Polymer Composites*, **49th AIAA/ASME/ASCE/ AHS/ASC Structures, Structural Dynamics & Materials Conference**, AIAA paper 2008-1932, April 7–10, Schaumburg, IL, p. 6.
2. K. W. Shahwan (2008), *Thinking Out of the Metallic Box—ACC Activities and Challenges*, 2008 Plastic and Composite Intensive Vehicle (PCIV) Safety Workshop, US-DOT/RITA Volpe Center, Cambridge, MA, August 4, p. 27. (http://www.volpe.dot.gov/safety/pciv/pcivagenda.html)
3. S. Song, A. Waas, K. Shahwan, O. Faruque, and X. Xiao (2009), *Effects of Matrix Microcracking on the Response of 2D Braided Textile Composites subjected to Compression Loads*, **J. of Composite Materials**, paper in print.
4. S. Song, A. M Waas, K. W. Shahwan, O. Faruque, and X. Xiao (2009), *Compression Response, Strength and Post-Peak Response of an Axial Fiber Reinforced Tow*, **International Journal of Mechanical Sciences**, paper in print.
5. S. Song, A. M Waas, K. W. Shahwan, O. Faruque, and X. Xiao (2008), *Compression Response of 2D Braided Textile Composites: Single Cell and Multiple Cell Micromechanics Based Strength Predictions*, **J. of Composite Materials**, Vol. 42, No. 23, pp. 2461–2482.
6. B. Shan, A. A. Pelegri, and Y. Pan (2008), *Interfacial Crack Kinking Subjected to Contact Effects*, **J. of Mechanics of Materials and Structure**s, 3(4):591–605.
7. A. A. Pelegri, L. Iorga, and Y. Pan (2008), *Analysis of 3D Random Chopped Fiber Reinforced Composites Using FEM and Random Sequential Adsorption*, **NSF CMMI Engineering Research & Innovation Conf.**, Knoxville, Tennessee, January 1–10.

J. Engineering Property Prediction Tools for Tailored Polymer Composite Structures

Principal Investigator: Ba Nghiep Nguyen
Pacific Northwest National Laboratory
P.O. Box 999, Richland, WA 99354
(509) 375-3634; fax: (509) 375-6736; e-mail: ba.nguyen@pnl.gov

Principal Investigator: Vlastimil Kunc
Oak Ridge National Laboratory
P.O. Box 2009, Oak Ridge, TN 37831
(865) 574- 8010; fax: (865) 574-0740; e-mail: kuncv@ornl.gov

Technology Area Development Manager: Joseph A. Carpenter
(202) 586-1022; fax: (202) 586-1600; e-mail: joseph.carpenter@ee.doe.gov

Field Technical Manager: Mark T. Smith
(509) 375-4478; fax: (509) 375-4448; e-mail: mark.smith@pnl.gov

---

Contractor: Pacific Northwest National Laboratory(PNNL), Oak Ridge National Laboratory (ORNL)
Contract Nos.: DE-AC06-76RL01830, DE-AC05-00OR22725

Objective

- Enable the optimum design of lightweight automotive structural components using long-fiber reinforced injection-molded thermoplastic composites.

Approach

Phase I: Technical feasibility assessment (9/1/05 to 3/31/06)

- Perform a technical assessment of current process models and computational methods for short-fiber polymer injection-molded composites in order to determine their accuracy, limitations and potential applications to long fiber thermoplastics (LFTs).
- Identify the research directions needed to develop process and constitutive models for LFTs.
- Understand and examine the LFT emerging microstructure, characterization techniques and material processing.
- Characterize fiber orientation in LFT samples.
- Examine the molding behaviors of glass and carbon fibers.

Phase II: Research and development (4/1/06 to 9/31/09)

- Develop an integrated approach that links process to structural modeling allowing the optimum design of LFT composite structures. This work includes:
  - — Develop process models for LFTs that allow simulations of LFT structures in order to predict flow-induced fiber orientation and other microstructural features.
  - — Develop and implement LFT constitutive models for structural finite-element analyses that make use of the composite microstructure predicted by process modeling. These constitutive models will predict the composite thermoelastic properties and its nonlinear behaviors due to damage, fatigue, creep and impact.
  - — Develop characterization methods for LFT materials.
  - — Injection-mold larger samples and complex geometries.

— Conduct experimental testing to determine the model parameters and validate the process and constitutive models.

Accomplishments

- Injection-molding of long-glass-fiber/polyamide 6,6 (PA6,6) plaques was planned with DuPont, Inc. and RTP Co., which then injection-molded these plaques for the project.
- A new fiber orientation model termed as the anisotropic rotary diffusion-reduced strain closure (ARD-RSC) developed for LFTs was implemented into the ORIENT and Molflow codes.
- ORIENT and Moldflow simulations of the injection-molding of glass/polypropylene (PP) and glass/PA6,6 samples were carried out using the ARD-RSC model.
- A mapping technique was developed to map fiber orientation results from a Moldflow analysis to an ABAQUS finite-element mesh for subsequent structural analyses.
- The elastic-plastic and strength prediction model for LFTs developed last year and implemented in ABAQUS was used to analyze the stress-strain responses of long-glass-fiber/PP specimens.
- An article on microstructural modeling and elastic property prediction for LFTs has been published in the *Journal of Composite Materials*. Another article on the prediction of the elastic-plastic response of LFTs has been accepted for publication in this journal.
- A creep model for LFTs was developed and implemented in ABAQUS, which has been validated against the experimental creep responses of glass/PP specimens.
- A theoretical framework for fiber breakage during injection molding was established.
- A damage model for LFTs was developed and implemented in ABAQUS, which has been validated against the experimental stress-strain responses of long-glass-fiber/PP specimens.
- An integrated approach linking Moldflow's process modeling to an ABAQUS structural analysis was demonstrated in the damage analysis of a holed glass/PP plaque subjected to tensile loading.
- Novel technique for through-thickness fiber length distribution measurement was developed.
- Fiber length distribution was found to vary through the thickness of LFTs.
- Creep properties of LFTs and polypropylene have been characterized.
- Miniature samples for detection of damage on microscopic level have been designed and analyzed.
- Digital image correlation technique was adapted to measure strain in X-ray mechanical tests.
- Injection-molded glass/PA6,6 plaques were X-rayed and analyzed.
- Fiber length distribution and fiber orientation were measured for glass/PA6,6 specimens.
- Quasi-static tests were performed on glass/PA6, 6 samples at -40, 25 and 80°C for 34.3 and 50% fiber weight fractions for 2.8 and 5.85 mm thick samples in flow and cross-flow directions.
- Fracture surfaces were examined using optical and scanning electron microscopy.
- Quasi-static, creep and fatigue tests on PA6, 6 were performed to provide input data for property prediction models.

Future Direction

- Complete the development of a fiber length attrition model.
- Integrate the ARD-RSC fiber orientation model into the fiber length attrition model, implement the integrated model into Moldflow and apply Moldflow to simulate more complex LFT parts.
- Develop a fatigue model and an impact damage model for LFTs.

- Characterize fiber architecture of new materials.
- Characterize creep, fatigue and impact behavior of LFTs.
- Acquire and analyze unique data on damage and plasticity in LFTs.

Introduction

Last year, a new fiber orientation model for long-fiber reinforced injection molded thermoplastic composites (LFTs) termed the anisotropic rotary diffusion-reduced strain closure (ARD-RSC) model was developed allowing fiber orientation in LFT samples to be predicted correctly [1]. This model was implemented in the ORIENT and Moldflow processing codes and was then used in the injection-molding simulation of LFT samples. Fiber orientation predictions using the ARD-RSC model reasonably agreed with the experimental results. Predicted fiber orientations were also used in the elastic-plastic computation of the stress-strain responses of glass/PP specimens loaded to failure. These results were reported in an article accepted for publication in the *Journal of Composite Materials* [2]. This article extends the modeling methodology developed in our previous article [3] to predict elastic-plastic LFT behavior.

Next, progressive damage due to monotonic loading was modeled as both damage and plasticity control the composite stress-strain response. An elastic-plastic damage model based on continuum damage mechanics was developed that accounts for matrix damage coupled with plasticity and fiber/matrix debonding [4]. The response of the composite was obtained using an incremental Eshelby-Mori-Tanaka approach (EMTA) similar to that developed in [2].

Creep modeling of LFTs was also performed that uses an incremental EMTA accounting for elastic fibers embedded in a nonlinear viscoelastic matrix [5]. The viscoelastic behavior of the matrix is described using Schapery's model [6].

A procedure was developed to map Moldflow fiber orientation results into an ABAQUS mesh accurately [7]. This work has enabled an ABAQUS analysis to be performed using orientation results predicted from a Moldflow analysis. Additionally, a theoretical framework for fiber length attrition model for injection-molding of LFTs was developed [8]. This highly challenging work started with the analysis of the forces due to fiber-fiber contacts that cause fiber breakage. A fiber breakage rate model was sought and will be used to predict fiber length distribution.

Experiments were performed on several material systems for model input and validation. Two molding trials were performed with glass/PA6, 6 materials. RTP Co. molded 15.2 × 15.2 cm plaques of 3 and 6.35 mm thicknesses. DuPont molded 30.5 × 30.5 cm plaques of 2.8 and 5.85 mm thickness with four fiber weight fractions. Initial fiber length measurements revealed significant fiber length attrition in the smaller plaques; therefore, subsequent measurements were performed on the larger samples.

Fiber architecture was analyzed by performing fiber orientation measurements, fiber length measurements and analysis of X-ray images of molded plaques. Quasi-static tests were performed at –40, 25 and 80°C for 34.3 and 50% fiber weight fractions for two thicknesses. Quasi-static tests for neat PA6, 6 samples were performed at identical temperatures along with creep tests to provide input data for model validation. Additional experiments were carried out to characterize creep behavior of glass/polypropylene (PP) material as well as the PP matrix. A novel method for fiber length measurement through the thickness was developed. Initial measurements confirmed prior qualitative observation of variation in fiber length distribution as a function of thickness [9].

Analysis of miniature specimens was carried out so that damage could be isolated from creep on a microscopic level. It was found that optical strain measurement was necessary at the specimen gage length to interpret material response [10]; therefore, a novel measurement technique was developed.

Approach

Modeling Fiber Orientation

The Folgar-Tucker model [11] has become the standard model for implementation in mold-filling simulation software. However, the reduced strain closure (RSC) model [12] has shown to give more accurate results for short-fiber thermoplastics. During fiscal year 2007, Phelps and Tucker [1] developed the ARD-RSC model for short-/long-fiber thermoplastics. This model was able to predict more accurately all the components of fiber orientation in long-glass-fiber/PP samples. More recently, the ARD-RSC model has been further validated against the experimental orientation data obtained for glass/PA6, 6 samples injection-molded by DuPont. Figures 1 and 2 present the through-thickness fiber orientation distributions predicted by the RSC and ARD-RSC models for a glass/PA6, 6 composite having 40% fiber weight fraction. The z-coordinates normalized by the specimen thickness h are used in Figures 1 and 2. The predictions agree well with the measured fiber orientation also shown in the same figures.

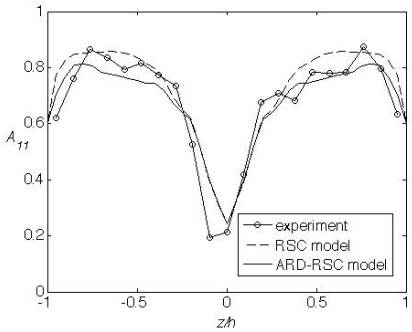

Figure 1. Predicted and measured fiber orientation tensor component A_{11} for a glass/PA6, 6 composite.

Modeling Fiber Length Attrition

Paramount to developing a model for fiber breakage rate is an understanding of the loads placed on fibers. Good models exist for the hydrodynamic loading of fibers in suspension [13], sliding forces arising from fiber-fiber contacts [14] and fiber-fiber contact statistics [15]. At this time, there are no good models for other loading modes such as normal fiber-fiber contact forces that give rise not only to bending (a suspected fiber failure mode) but also fiber networking. Finally, features in the injection molds such as sharp bends in the runner system or contractions at the gate cause high-stress regions in the flow of the melt and can trap fibers. Both a fiber breakage rate model that incorporates hydrodynamic fiber loading and a conservation equation for total fiber length have been developed. These two models give an evolution equation for the fiber length distribution. If experimental fiber length data suggest the necessity, other breakage rate models incorporating different modes of fiber loading and feature based breakage models may be developed later.

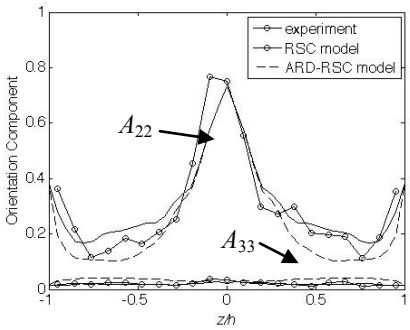

Figure 2. Predicted and measured fiber orientation tensor components A_{22} and A_{33} for a glass/PA6, 6 composite.

An Elastic-Plastic Damage Model

An elastic-plastic damage model for LFTs was developed that accounts for both plasticity and damage of the matrix material as well as fiber/matrix bonding [4]. Three stages of damage are considered. First, the initiation stage involves both matrix damage and fiber/matrix debonding that can occur simultaneously. Second, the development stage involves the evolution of both mechanisms up to the point of failure due to excessive matrix cracking and fiber/matrix debonding leading to fiber pull-out and rupture (final stage). The final stage corresponds to rupture of the composite.

In the first and second damage stages, the elastic-plastic and damage behavior of the thermoplastic matrix is described by the modified Ramberg-Osgood relation, which expresses equivalent stress in terms of the matrix-effective using the principle

of strain equivalence [16]. Further, using the three-dimensional damage model in deformation [17], a damage evolution law for the matrix material associated with the *J*-2 deformation theory of plasticity, is obtained. Fiber/matrix debonding is accounted for using the modified Mori-Tanaka model by Qu [18]. While Qu assumed slightly weakened interfaces with constant and low values of the interface compliance, progressive debonding is considered from an eventual perfect interface to a complete debonding state where total frictional fiber/matrix sliding can occur. In addition, a linear relation-ship between the matrix damage variable and damage parameter controlling fiber/matrix interfaces is assumed.

The next step is to compute the current tangent modulus of the matrix material that is affected by both plasticity and damage, and then to use it in incremental EMTA [2, 4] to compute the composite stress increment due to an overall strain increment. Damage can evolve to a critical state characterized by the critical values of the damage variables. Rupture of the composite is predicted to occur when the damage variables attain their critical values. This final stage of damage is modeled by a vanishing element technique that reduces the stress and stiffness of the composite to zero at the locations where rupture occurs.

This elastic-plastic damage model implemented in ABAQUS was used to compute the stress-strain response of LFT specimens up to failure. Figures 3 and 4 shows the flow- and cross-flow direction stress-strain responses of specimens removed from injection-molded glass/PP center-gated disks. The predicted curves using the predicted fiber orientation by the ARD-RSC model reasonably agree with the solutions based on measured fiber orientation and with the experimental results.

An Integrated Approach Linking Process to Structural Modeling

The incremental EMTA has been implemented in ABAQUS by means of user subroutines for structural analysis, an integrated process called EMTA-ABAQUS. In addition, a mapping technique was developed to map fiber orientation results from a Moldflow analysis into an

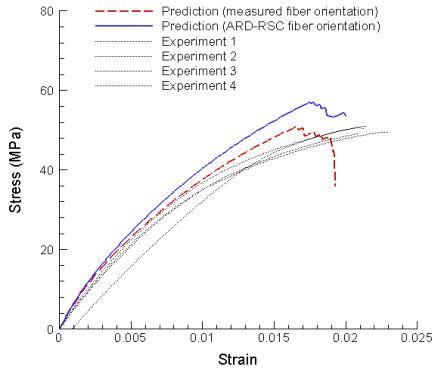

Figure 3. Predicted and experimental flow-direction stress-strain responses of specimens removed from glass/PP center-gated disks.

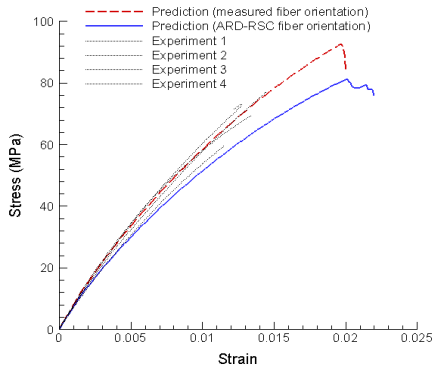

Figure 4. Predicted and experimental cross-flow-direction stress-strain responses of specimens removed from glass/PP center-gated disks.

ABAQUS mesh for subsequent structural analyses [7]. Figure 5 illustrates the position of an open-hole specimen removed from a glass/PP International Standards Organization (ISO)-plaque for an ABAQUS analysis. Figure 6 shows the contour of the orientation tensor component A_{11} for a shell layer that was mapped into the ABAQUS finite element mesh created for analyzing the open-hole specimen.

The ARD-RSC model was used in Moldflow for prediction of the fiber orientation distribution. Next, the elastic-plastic damage model implemented in ABAQUS was used to analyze this holed plaque subjected to tensile loading along its longitudinal direction. Figure 7 shows the contour of the matrix damage variable *D* in this plaque when the applied displacement has attained 0.58 mm. The critical value of this damage

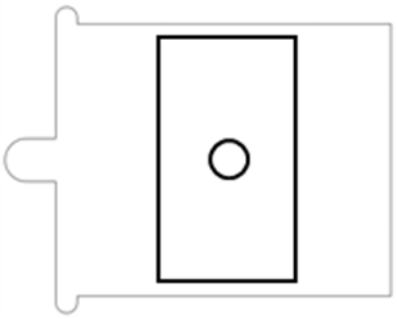

Figure 5. Position of the open-hole specimen removed from a glass/PP ISO-plaque for an ABAQUS analysis.

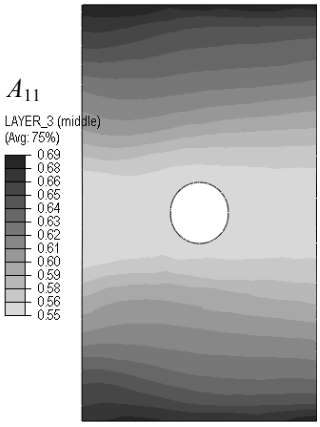

Figure 6. Mapping technique used to obtain the distribution of A_{11} in a shell layer of the open-hole specimen.

1.

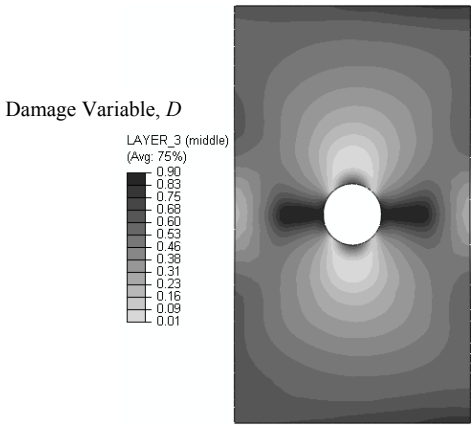

Figure 7. Contour of the matrix damage variable in a shell layer for the applied displacement of 0.58 mm.

variable is 0.9. Damage is predicted to occur from the hole and to expand perpendicularly to the loading direction. Figure 8 shows the crack propagations in the same layer that were captured by a vanishing element technique.

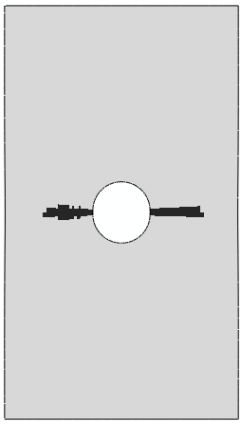

Figure 8. Prediction of crack propagations (black areas) in a shell layer for the applied displacement of 0.58 mm.

A Creep Model for LFTs

A creep model for LFTs was developed [5] that considers elastic fibers embedded in a nonlinear viscoelastic matrix obeying Schapery's model [6]. The computational procedure is as follows: the composite is first loaded to an overall stress level. The EMTA and fiber orientation averaging technique are then applied to compute the composite stiffness and resulting stress in the matrix. For a given time increment, the viscoelastic matrix experiences a creep strain increment and an increase in creep compliance according to Schapery's model. The stiffness of the composite is then updated at the end of the increment by EMTA using the current properties of the matrix. While the overall applied stress level is maintained constant, the composite experiences a creep strain increment during this time increment. The creep deformation process continues for the next time increment and the composite creep response for the whole period is then determined. The incremental EMTA for creep of LFTs was implemented in ABAQUS via user subroutines. It has been validated using the creep data obtained for glass/PP specimens.

Figure 9 presents the creep responses predicted for the specimens removed along the flow direction of a glass/PP center-gated disk. The computation

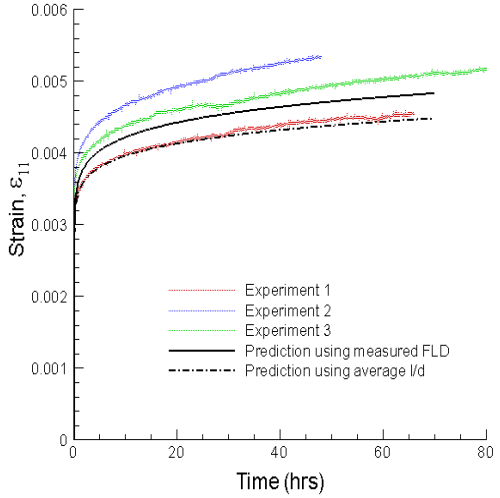

Figure 9. Flow direction glass/PP specimens' creep responses to the applied stress of 15 MPa.

used the experimental fiber length and orientation distributions. To study the effect of fiber length distribution (FLD) on creep response, computation was also performed using the average fiber aspect ratio *l/d* (*l/d*=125 for this composite). The applied stress level used in the experimental tests and computation was 15 MPa. Figure 9 also presents the experimental creep curves obtained for these specimens. Good agreements are found between the prediction using the FLD and experimental results. The solution using the average fiber aspect ratio under-predicts the creep strains. The scatter of the experimental creep results reflects the variation in the LFT microstructure that is strongly governed by fiber length and orientation distributions.

Microstructural Characterization of Glass/PA6, 6 Plaques

X-rays of 30.5 × 30.5 cm glass/PA6, 6 plaques of 2.8 and 5.85 mm thicknesses molded by DuPont were performed. Segmented X-ray image of the molded plaque in Figure 10 shows a significant size of border regions where filaments did not appear to be distributed uniformly and fiber orientation appeared to differ significantly from that of the center of the plaque. Thicker plaques exhibited higher degree of radial flow compared to thinner plaques.

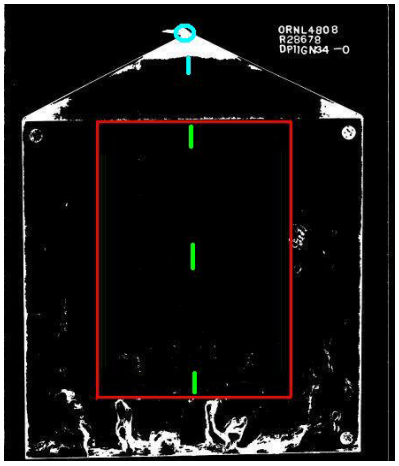

Figure 10. Segmented X-ray digital image of glass/PA6.6 plaque with border regions and sampling locations marked.

Results of fiber length measurements presented in Figure 11 show a notable percentage of fibers less than 1 mm in length regardless of plaque thickness or fiber content. The fraction of short fibers in glass/PA6, 6 samples was significantly higher compared to glass/PP samples.

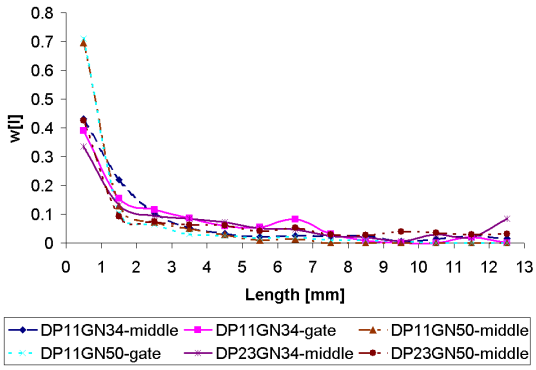

Figure 11. Fiber length distribution for glass/PA6, 6 samples.

Fiber orientation measurements were performed using the Leeds method [19]. Typical fiber results as a function of thickness were given in Figures 1 and 2. Distinct core and shell regions could be readily identified by visual observation.

Mechanical Properties of Glass/PA6, 6 Plaques

Mechanical tests were performed on both thin and thick plaques with 34.3 and 50% fiber weight fractions. The 34.3% glass/PA6,6 and previously

examined 40% glass/PP samples have the same fiber volume fraction; therefore, the validity of models developed to date could be checked with different matrix materials before examining materials with higher fiber volume fractions.

Quasi static tests at -40, 25 and 80°C have revealed the expected material behavior with stiffness and ultimate stress increasing with decreasing temperature. Five replicates for each material/thickness/temperature combination were tested in the flow and cross-flow directions in the dry state. Samples were dried in a vacuum at 50°C with periodic weight loss checks. Once their weight had been stabilized, the samples were kept in a vacuum at room temperature. Additionally, a few samples were tested under as-machined condition to check the effect of moisture presence in the material on its mechanical properties. Figure 12 shows typical stress-strain curves of the glass/PA6, 6 samples with flow-direction samples having higher stiffness and strength compared to cross-flow samples.

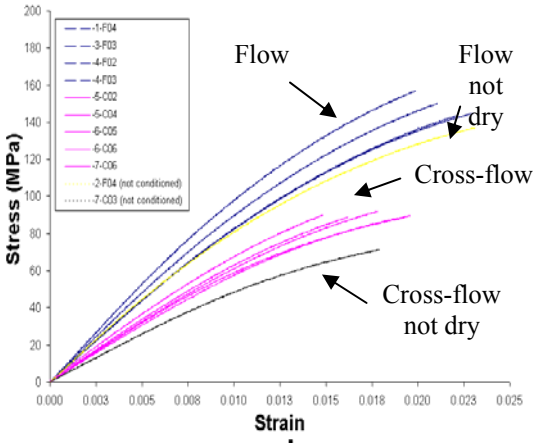

Figure 12. Stress strain curves for 2.8 mm thick glass/PA6, 6 specimens with 34% fiber weight fraction tested at 25°C (F-flow, C-cross-flow).

This behavior is opposite to that observed in glass/PP samples and reflects the difference in relative sizes of shell and core layers resulting from differing fiber length distributions. Plasticization of the matrix material due to moisture is also apparent from the material response. Figure 13 shows the fracture surface of a failed sample with distinct shell and core regions. Fracture surfaces were perpendicular to the direction of loading with some samples exhibiting considerable post-failure fiber bridging.

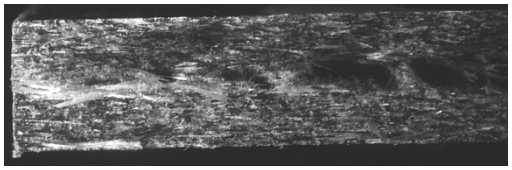

Figure 13. Fracture surface of 2.8 mm thick glass/PA6, 6 specimens with 34% fiber weight fraction tested at 25°C showing distinct shell and core region.

Fiber surfaces on the fracture faces were also examined with scanning electron microscopy to determine the nature of fiber-matrix adhesion. Figure 14 shows a typical fiber extending from the fracture face with matrix residuum on the fiber surface. These observations confirmed that the mechanical properties were not diminished due to poor fiber matrix adhesion.

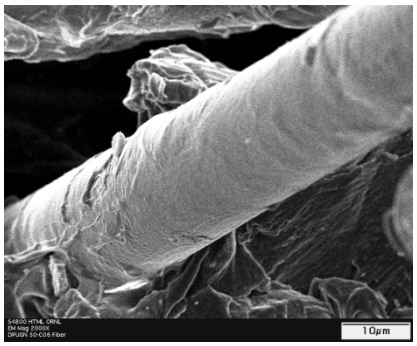

Figure 14. Scanning electron microscope image of a fiber extending from a fracture surface of glass/ PA6, 6 material.

In addition to tests on fiber-filled material, mechanical tests were also performed on neat PA6, 6 samples to provide input data for the property prediction models. Quasi-static tests on PA6,6 specimens at -40, 25 and 80°C showed expected increase in strength and stiffness with decreasing temperature, with dry samples attaining greater modulus, strength and lower strain at failure compared to samples containing moisture. Failures were brittle at -40°C and localized necking was observed at room temperature, while extensive material stretching in the gage length was observed at 80°C. Some specimens did not fail at 80°C before reaching the displacement limit of available equipment.

Creep tests on PA6, 6 plaques were performed at room temperature in the dry and as-machined states. The creep response of PA6, 6 was strongly dependent on conditioning.

Through Thickness Fiber Length Measurement

Previous measurements and models of FLD assumed no variation in the distribution as a function of thickness. This assumption appeared reasonable; however, it was observed that this assumption may not reflect reality. A method allowing measurement of the FLD at various locations through the thickness of a sample [9] relies on the expansion of the LFT fiber network during burn-off, which increases the sample thickness. The profile of expansion is characterized by measuring the relative displacement of thin wire pieces located through the thickness of a test sample. The location of wires before and after burn-off can be obtained by taking an X-ray and analyzing resulting image. Figure 15 shows the profile of expansion, which appears to be linear with the thickness of the fiber mat being three times that of the original sample thickness. Once the expansion profile is known, one can choose a desired location in the thickness of the original sample and extract fibers for measurement from the corresponding location in the expanded fiber mat. A well defined region of approximately spherical shape can be extracted by depositing a small drop of epoxy through a hypodermic needle in the fiber mat and curing the epoxy.

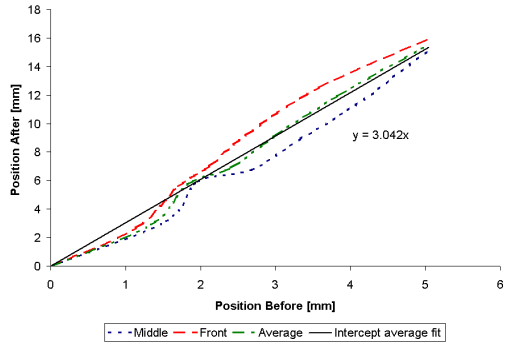

Figure 15. Linear expansion profile in burned-off samples.

Figure 16 shows the FLD measured in a 3 mm-thick long-glass-fiber/PP injection molded disk. Three locations were considered: skin - surface of the sample, 25% of the sample thickness, and core - middle of the sample. It is apparent from the experimental data that the core of the sample retains significantly longer fibers compared to the regions closer to the specimen surface. While the variation of FLD through the thickness should not influence in-plane property prediction, models with an accurate FLD distribution through the thickness should provide better property prediction for out-of-plane loading. These results should also be instrumental in the development and validation of predictive fiber length attrition model.

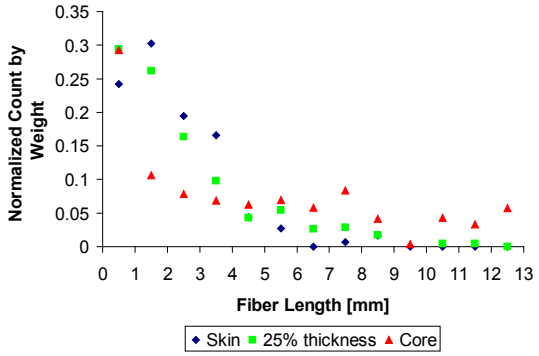

Figure 16. Fiber length distribution measurements through the thickness of three millimeter long glass/polypropylene disk sample.

Creep Testing of Glass/PP

Creep tests have been performed on a set of glass/PP samples to support the development of the creep model discussed above. Center of dogbone samples coincided with the location of previous fiber orientation and fiber length distribution measurements. A load level of 30% of the average ultimate tensile strength was selected so that the effects of plasticity would be negligible and only visco-elastic effects would be considered. The load level was 21 MPa for specimens with the longitudinal axis aligned in the cross-flow direction and 15 MPa for specimens with the longitudinal axis in the flow direction.

All samples were tested at room temperature, and the given load was ramped to the final value and held for one day. Samples were subsequently unloaded in ramp and held at zero load to observe

recovery. Three replicates of each specimen orientation and mold fill speed were obtained. The property prediction models use fiber and matrix material properties as input. While creep in the fibers can be neglected, it is essential to obtain the visco-elastic properties of the matrix in order to predict viscoelastic response of the composite material. Stress levels in the polypropylene matrix were estimated for the 30% load level. It was determined that adequate load levels of 1, 5, 7 and 10 MPa are adequate for determining the coefficients of Schapery's model for the neat PP [6], and tests were performed in the same manner as for composite samples.

Miniature LFT Specimens – Design and Analysis

The objective of upcoming experiments in this unit is to separate the effects of matrix plasticity and material damage such as micro-cracking and fiber-matrix interface slippage on the stress strain response of the composite material.

Due to inherent physical limitations, samples in these experiments must be very small. A shoulder loaded double-dogbone specimen with 1 x 1 mm cross-section has been designed. Two phenomena have been investigated using finite- element analysis. First, the effect of mismatch in shoulder radius between the sample and the grip due to imprecision in manufacturing of these miniature samples from fiber-reinforced thermoplastic was considered. It was concluded that the stress profile within the sample and its load-displacement response vary significantly as a function of the shoulder radius mismatch [10]. It is therefore imperative to measure deformation of the material in the gage length optically, because displacement measured at the sample shoulder will not provide useful information. Second, relaxation of the sample during pauses for imaging has been studied because the load loss during imaging has been significant in preliminary tests. It was determined that load loss of the sample is influenced by the shoulder radius mismatch; therefore, correlation between load shedding of the sample and material relaxation will not provide useful results. Since optical measurement of gage length deformation along with load data has to be considered in order to describe material response, a digital image correlation technique has been adapted to provide localized strain measurement in the sample gage length. Fiber crossings X-rayed at appropriate angle have been shown to provide an appropriate pattern for digital image correlation. This technique allows not only average strain measurement of the gage length but also provides information about the strain variation within the gage length.

Conclusions

Process and constitutive models as well as computational tools have been developed and integrated to predict the flow-induced fiber orientation successfully and the resulting linear and nonlinear responses of LFTs. The relevant nonlinear behaviors of LFTs that were studied are elastic-plastic, progressive damage and creep behaviors. An elastic-plastic damage model and a creep model for LFTs were developed and implemented in ABAQUS. Accounting for both plasticity and damage has enabled better predictions of the LFT stress-strain responses up to failure. The creep response of LFTs was modeled, and our analysis has shown important

effects of fiber length and orientation on the creep response. Fiber architecture was characterized via X-ray imaging, optical fiber orientation measurement and fiber length distribution measurement. The quasi-static response of LFTs was measured at three temperatures and the creep response was obtained at room temperature. Properties of the neat polymer were measured to provide input for property prediction models. Experimental characterization was coordinated with model development and validation to improve specific areas of predictive capabilities of process as well as property prediction models. Novel experimental techniques were developed for fiber length measurement as a function of thickness and for local strain measurement during a tensile test with X-ray imaging of LFTs. These techniques provide unique insight into the architecture and response of LFTs.

An integrated approach linking process modeling to structural analysis with support of microstructural characterization has been developed and improved in an ongoing effort to

enhance predictive capabilities for lightweight automotive structures using LFTs.

Presentations/Publications/Patents

1. See Reference 1.
2. See Reference 3.
3. See Reference 2.
4. See Reference 4.
5. See Reference 7.
6. See Reference 5.
7. Nguyen B. N. et al. 2008. "An Elastic-Plastic and Strength Prediction Model for Injection-Molded Long-Fiber Thermoplastics." Proceedings of the 23rd Technical Conference of the ASC, Memphis, TN.
8. Phelps J. H. and C. L. Tucker III. 2008. "An Anisotropic Rotary Diffusion Model for Fiber Orientation in Short- and Long-Fiber Thermoplastic Composites." American Regional Meeting of the Polymer Processing Society, Charleston, SC.

References

1. J. H. Phelps and C. L. Tucker III (2008). "An Anisotropic Rotary Diffusion Model for Fiber Orientation in Short- and Long-Fiber Thermoplastics," *J. Non-Newt. Fluid Mech.*, in press.
2. B. N. Nguyen, V. Kunc, J. H. Phelps, C. L. Tucker III, and S. K. Bapanapalli (2008). "Prediction of the Elastic-Plastic Stress-Strain Response for Injection-Molded Long-Fiber Thermoplastics," *J. Compos. Mater.*, in press.
3. B. N. Nguyen et al. (2008). "Fiber Length and Orientation in Injection-Molded Long-Fiber Thermoplastics – Part I: Modeling of Microstructure and Elastic Properties," *J. Compos. Mater.*, **42**:1003–1029.
4. B. N. Nguyen and V. Kunc (2008). "An Elastic-Plastic Damage Model for Long-Fiber Thermoplastics," *Int. J. Damage Mech.*, submitted.
5. B. N. Nguyen et al. (2008). "Creep Modeling for Injection-Molded Long-Fiber Thermoplastics," Proceedings of the ASME IMECE 2008, Boston, MA, paper # IMECE2008-66335.
6. R. A. Schapery (1969). "On the Characterization of Nonlinear Viscoelastic Materials," *Polym. Engn. Sci.*, **9**(4): 295–310.
7. B. N. Nguyen et al. (2008). "An Integrated Approach Linking Process to Structural Modeling with Microstructural Characterization for Injection-Molded Long-Fiber Thermoplastics," Proceedings of SAMPE 2008, Memphis, TN.
8. J. H. Phelps and C.L. Tucker III (2008). "Processing-Microstructure Modeling for Long-Fiber Thermoplastics," Internal Report submitted to PNNL.
9. V. Kunc et al. (2008). "Techniques and Results for Fiber Length Distribution Determination as a Function of thickness in Long fiber reinforced injection molded thermoplastics," Proceedings of 8th-Annual SPE Automotive Composites Conference & Exhibition, Troy, MI.
10. V. Kunc et al.(2008). "Design of Fiber Reinforced Polymer Specimens for Examination with Micro-tomography under Tensile Loading," Proceedings of SAMPE 2008, Memphis, TN.
11. F. Folgar and C. L. Tucker III (1984). "Orientation Behavior of Fibers in Concentrated Suspensions," *J. Reinf. Plast. Comp.*, **3**: 98–119.
12. J. Wang et al. (2008). "An Objective Model for Slowing Orientation Kinetics in Concentrated Fiber Suspensions: Theory and Rheological Evidence," *J. Rheol.*, **52**:1179–1200. See also: U.S. Patent 7,266,469 (2007).
13. S. M. Dinh and R. C. Armstrong (1984). "A Rheological Equation of State for Semi-Concentrated Fiber Suspensions," *J. Rheol.*, **28**(3): 207–227.
14. M. Djalili-Moghaddam, and S. Toll (2005). "A Model for Short-Range Interactions in Fiber Suspensions," *J. Non-Newt. Fluid Mech.*, **132**: 73–83.

15. S. Toll (1998). “Packing Mechanics of Fiber Reinforcements,” *Polym. Engn. Sci.*, **38**: 1337–1350.

16. J. Lemaitre (2002). “Introduction to Continuum Damage Mechanics,” in: *Continuum Damage Mechanics of Materials and Structures*, Allix, O. and Hild, F., eds., pp. 235–258, Elsevier Science Ltd, Oxford, United Kingdom.

17. J. Lemaitre and J. L. Chaboche (1985). “Mécanique des Matériaux Solides,” Dunod, Paris, France.

18. J. Qu (1993). “The Effect of Slightly Weakened Interfaces on the Overall Elastic Properties of Composite Materials,” *Mech. Mater*., **14**:269–281.

19. A. R. Clarke et al. (1990). "A Multitransputer Image Analyzer for 3D Fibre Orientation Studies in Composites," *Trans. Roy. Microsc. Soc.*, **1**: 305.

K. Predictive Modeling of the Structure and Properties of Polymer-Matrix Composites: NSF/DOE Grant Projects

DOE Technology Area Development Manager: Joseph A. Carpenter
(202) 586-1022; fax: (202) 586-1600; e-mail: joseph.carpenter@ee.doe.gov

National Science Foundation (NSF) Grant Monitor: Joycelyn S. Harrison
(703) 292-7088; e-mail: j-harris@nsf.gov

Objective

- The objective of the six projects in this program, jointly funded by NSF and DOE and administered by NSF as grants, is to perform fundamental development of modeling, simulation and processing of polymer composite materials. These projects support the DOE-funded "Engineering Property Prediction Tools for Tailored Polymer Composite Structures" project being conducted jointly by Oak Ridge National Laboratory (ORNL) and Pacific Northwest National Laboratory (PNNL) (see report 8.J). The NSF/DOE-funded projects are intended to investigate alternate modeling and processing approaches that can contribute to more fundamental understanding of the mathematical and physical behavior of fiber-reinforced polymer composites. The following sections provide a high-level summary of one grant's objectives and work progress during 2008. Full reports on four others are found in reports 8.L–8.O.

Comparative Determinations of Orientation in Injection-Molded Thermotropic Liquid-Crystalline Copolyester (TLCP) Plaques

Principal Investigator: Robert A. Bubeck
Michigan Molecular Institute (MMI)
1910 West St. Andrews Road
Midland, MI 48640
(989) 832-5555; fax: 989-832-5636;
e-mail:Bubeck@mmi.org

Co-Principal Investigator: Wesley R. Burghardt
Northwestern University
Robert McCormick School of Engineering and Applied Science
Dept. of Chemical Engineering
2145 Sheridan Road, Evanston, IL 60208-3120
(847)-467-1401;
e-mail: w-burghardt@northwestern.edu

NSF Award No. DMI-0521771

Objective

Thermotropic liquid crystalline polymers (TLCPs) offer considerable promise as high strength, lightweight engineering materials. Understanding, manipulation and control over the evolution of molecular orientation during injection molding is a necessary prerequisite towards optimized fabrication of TLCP net-shaped parts. Based upon knowledge gained in this and previous work, we shall implement new modeling strategies to predict orientation development, coordinated with cutting-edge synchrotron techniques to characterize the resulting orientation state.

Approach

1. The development and application of *in situ* capabilities to perform x-ray scattering measurements of molecular orientation *in real time* within the injection molding cycle.
2. Exploitation of novel spectroscopy techniques (Near Edge X-ray Absorption Fine Structure (NEXAFS) and Attenuated Total Reflectance Fourier Transform Infrared (ATR-FTIR)) that offer new capabilities for unprecedented three-dimensional (3-D) characterization of the molecular orientation distribution within the surface layer of moldings.
3. Formulation of new modeling strategies to predict orientation development employing so-called 'polydomain' description of orientation which facilitates direct connection to experimental measurements of orientation.

Research and Education Activities

The influences of molding parameters and mold thickness on the anisotropy, skin-core morphology, and mechanical properties of injection-molded commercial TLCPs are being studied. Key observations and milestones for the year 2008 include the following commentary.

A comprehensive NEXAFS characterization was performed on a selected 76 mm x 51 mm narrow-gated injection-molded plaque surface using the new 6-axis manipulator in the experimental chamber of the soft X-ray materials characterization beam line, U7A, at the National Synchrotron Light Source (NSLS) at Brookhaven National Labs. The narrow-gated plaques are of great interest because of their flow complexity. The samples were fabricated of commercially-available VECTRA A950 TLCP. Our graduate student on the project (Mr. Fang) gained further expertise in NEXAFS under the direction of Dr. Bubeck and wrote the driver routine that controlled the position and angles of the manipulator and sample programmatically while collecting an extensive set of NEXAFS spectra. Both the maximum orientation and its direction on the plaque surface were mapped for nine positions. This was the first time that so large a sample (38 mm × 51 mm) had been investigated using the manipulator in the U7A sample chamber.

A Herrick Seagull Variable Angle Reflectance ATR-FTIR dichroism accessory was used to determine maximum surface orientations and their directions corresponding to the positions interrogated using NEXAFS at the NSLS. An undergraduate student (Ms. Burgard), who is in cooperative employment at MMI and biology major at Saginaw Valley State University assisted us in performing the ATR-FTIR measurements. The agreement between the NEXAFS and ATR-FTIR mapping of surface orientation was excellent for magnitude and very good for directional maxima. This effort represents the first time that two surface spectroscopy techniques have been used in conjunction to determine the surface orientation of an injection-molded part.

Simulations of injection molding have been and continue to be performed by Mr. Fang under the direction of Professor Burghardt at Northwestern University using process parameters provided via the injection molding efforts undertaken at MMI to prepare plaques for mechanical, 2-dimensional wide angle X-ray scattering (2-D WAXS), and surface spectroscopy characterizations. The surface techniques and 2D-WAXS have been used to map orientation in the “skin” and “core”, respectively. The simulation strategy drawing upon Folgar-Tucker concepts within the Moldflow modeling platform has yielded results that mimic the experimental orientation mapping of the plaques.

Findings

Extensive mapping of the surface orientation of a complex injection-molded part (narrow-gated plaque) has been done for the first time. Two surface spectroscopy methods were utilized (NEXAFS and ATR-FTIR) with very good agreement between the two techniques. Computer simulations for our two plaque configurations predict the “skin” orientation fields, as well as those obtained via 2D-WAXS for the “core” very well.

Future Direction and Project Completion

- Complete any remaining required ATR-FTIR measurements.
- Perform “short shot” injection molding experiments to verify some predictions for mold filling derived from our simulations.
- Coauthor with Northwestern University colleagues and submit an extensive paper that will tie together the orientation mapping with the molding simulations.

Acknowledgments

The collaborative efforts with S. Burgard, L. Thomas, and K. Robertson (MMI) are invaluable. Thanks are extended to J. Quintana and the staff of the DND-CAT of the Advanced Photon Source, Argonne National Labs and to D. Fischer and the staff of beam line U7A of the National Synchrotron Light Source, Brookhaven National Labs. The gift of 55 lbs. of VECTRA A950 to our effort by Ticona is greatly appreciated.

Journal Publications

1. J. Fang, W. R. Burghardt, and R. A. Bubeck; "Polydomain Model Predictions of Molecular Orientation in Isothermal Channel Flows of Thermotropic Liquid Crystalline Polymers"; *Poly. Eng. Sci.*, 2259 (2008).
2. S. Rendon, J. Fang, W. R. Burghardt, and R. A. Bubeck; "An Apparatus for In-situ X-ray Scatting Measurements during Polymer Injection Molding"; Submitted to *Review of Scientific Instruments*, December, 2008.

Simulation of Compression-Resin Transfer-Molding Process for Manufacturing Net-Shape Structures

Principal Investigator: Suresh G. Advani
Department of Mechanical Engineering
University of Delaware
Newark, DE 19716
(302) 831-8975; fax: (302)-831-8525;
e-mail: advani@me.udel.edu

NSF Award ID: 0521789

All liquid composite molding (LCM) processes require one to place a fibrous preform inside the mold. The mold is sealed and a liquid resin is injected to saturate the preform. The fibers in the preform and the preform itself are usually stationary but in some variations they may undergo small (and slow) deformation during the injection process. Next, the resin is allowed to cure and the part is removed. Two commonly used techniques in this process are resin-transfer molding (RTM) and vacuum-assisted resin-transfer molding (VARTM).

The subject of this work, compression resin-transfer molding (CRTM) differs from the other LCM processes by injecting the resin before the mold is fully closed and preform compacted. The gap between preform and mold surface serves for uniform resin distribution over the part surface. Following mold closure and preform compaction then distributes the resin through the preform thickness.

This process offers the potential to manufacture moderately-sized structures in a few minutes while preserving the advantages of RTM, net-shape manufacturing of complex curvatures with Class A surface finish.

In all LCM variations, the flow of the resin through the preform is important. If particular sections of the preform remain dry after the injection is complete, the resulting void will seriously compromise the part properties. The cost of trial-and-error part design created a need for the simulation of the filling process using science-based process model. For conventional RTM processes, many reliable computer simulation tools have been established and validated with experiments. However, for the other LCM variations the modeling tools are scarce and RTM tools are usually adapted, though the results are sometimes not quite satisfactory.

The resin flow in CRTM process is more complex than in any other LCM variation. It exhibits three distinct stages. All of the phases can be modeled as flow through porous media under different boundary and initial conditions. The three stages are

1. Resin injection into the narrow gap between the mold platen and the fiber preform in the mold.
2. Closing of the gap while squeezing the resin into preform without direct contact between movable tool part and the preform.
3. Compaction of the preform by the mold platen along with continuing resin impregnation.

Research and Education Activities

No full report or summary submitted. A full report is expected in the annual progress report for fiscal year 2009.

L. Hierarchical, Structure-Oriented Stochastic Approach to Model Liquid Molding Processes

Principal Investigator: Thanasis D. Papathanasiou
Department of Chemical Engineering
University of South Carolina
Columbia, SC 29208
(803) 777-7219; fax: (803) 777-6245; e-mail: papathan@engr.sc.edu

Department of Energy Technology Area Development Manager: Joseph A. Carpenter
(202) 586-1022; fax: (202) 586-1600; e-mail: joseph.carpenter@ee.doe.gov

National Science Foundation Monitor: Joycelyn S. Harrison
(703) 292-7088; fax: (703) 292-9056; email: j-harris@nsf.gov

Contractor: University of South Carolina Research Foundation
Contract No.: (NSF) DMI-0522221 (jointly funded by National Science Foundation (NSF) and the Department of Energy (DOE)

Objective

- Our overall objective has been to develop models for the hydraulic permeability of fibrous media, taking explicit account of the underlying microstructure and its variability. A specific task for the preceding period was to investigate the effect of fiber clustering on the hydraulic permeability (K) of unidirectional random fiber arrays—this is covered in the first section of this report and the references identified therein. In addition, we computationally studied Stoke's flow at the interface between a fluid and a fiber bed. This was a collaborative study initiated by Prof. Pillai at the University of Wisconsin-Milwaukee and is covered in the second section. We also used the parallel boundary element method (BEM) to simulate solute transport across membranes filled with high aspect ratio platelets in order to elucidate the effect of microstructure on the anticipated barrier improvement factors (third section). Finally, experimental measurements of fluid velocities in the interstitial spaces within fiber arrays were carried out at Lulea University of Technology in Sweden (Prof. Lundstrom) using micro particle image velocimetry (PIV) in the fourth section.

Approach

- Our approach is computational. A large number of simulations have been carried out, using a parallel implementation of the BEM, in microstructures consisting of ~100s of fiber cross sections placed within a containing unit-cell by a Monte Carlo (MC) procedure. This allows a direct and unambiguous correlation between (K) and the microstructure of the fiber arrays.

Accomplishments

- The extent of fiber clustering is quantified using a new scalar metric, based on Ripley's K-function [1].
- The extent of fiber clustering is linked to the dimensionless temperature of the fiber assembly, as defined in the context of the Number-Volume-Temperature (NVT) Monte-Carlo process.
- Stokes flow simulations across such systems were carried out and the results, in terms of the principal permeabilities, were correlated with the above-mentioned microstructural metric.
- Analytical models for the transition of flow from an open channel into a fibrous medium have been evaluated by comparing their predictions to the results of first principles computation using the BEM.

- Analytical models for the effective transport coefficient of composite membranes have been evaluated by comparing their predictions to the results of first principles computation using the BEM.
- Obtained velocity profiles within fibrous media using the method of micro Particle Image Velocimetry.

Future Direction

- Not applicable since the project completed in September 2008.

Flow Through Clustered Systems [2]

This work has been published in [2] and relies on developments reported in our earlier work [3–5] to which interested readers are referred. Most previous studies of the permeability of fibrous media are based on periodic or random fiber arrays. There are relatively fewer studies that discuss the influence of the other commonly observed microstructural feature (i.e., fiber clustering, on the microscopic permeability). In fact, fiber clustering manifests in several ways. It is either naturally formed or purposely introduced. An example of the latter case can be found in a typical composite preform, where individual fiber strands are first bundled into tows and then the fiber tows are used to form a two dimensional or three dimensional woven mat. Direct numerical modeling studies of structured dual-scale fibrous medium, in which the arrangement of the fiber tows as well as the arrangement of fibers inside the fiber tow are periodic are limited. In this study we are concerned with the dependence of permeability on the microstructure that exhibits a random clustering feature. By the term "random clustering," we mean that the fiber cluster size distribution, the fiber cluster spatial distribution, and the fiber arrangement in a fiber cluster are not organized. Such clustering patterns may be induced by electrostatic forces or adhesive molecular forces, or by external forces that perturb an originally organized pattern. At this instance we are not interested in the physical mechanisms that underline the formation of such random clustering. Instead, we assume that a generic clustering model is suitable for us to establish the correlation between the permeability and a microstructural parameter that captures the key feature of clustering. For this purpose, we use the Monte Carlo method with the Lennard-Jones potential to generate different clustered fiber distributions, and determine the permeability of these distributions by solving the entire flow field using the boundary element method (BEM). Our numerical results show that the permeability can be statistically correlated with several microstructural parameters.

Continuing from studies reported earlier, we consider the introduction of a clustering or aggregation mechanism for placing fibers. It is assumed that clustering of fibers can arise due to the presence of a short-range attractive force among fibers. Such clustered fiber distributions can be generated by the Metropolis Monte-Carlo method, a process during which the minimization of the system potential energy is being sought. In this process, fibers are moved from their initial location; the change in the system potential energy is calculated for each attempted move; any downhill move in energy will be accepted and any uphill move in energy will be accepted with a probability of $\exp(-\Delta E / k_B T)$ (T is temperature, ΔE is the energy change and k_B is the Boltzmann factor). To carry out this Monte-Carlo process, an explicit form of pair potential that describes the repulsive and attractive forces between a pair of particles must be provided in order to compute the system potential energy. For simplicity, we assume the hard-disk potential at distances $r \le r_\sigma$, accounting for the fact that fibers are not penetrable, and at $r > r_\sigma$ we take the Lennard-Jones potential to include the attractive force. This is given as

$$v(r) = \begin{cases} \infty & r \le r_\sigma \\ 4\varepsilon\left[\left(\frac{r_\sigma}{r}\right)^{12} - \left(\frac{r_\sigma}{r}\right)^{6}\right] & r_\sigma < r < r_c \\ 0 & r > r_c \end{cases}, \quad (1)$$

where v is the pair potential, ε is the depth of the potential well, r_σ is the finite distance at which the potential becomes positive and r_c is the cutoff

distance after which the tail part of the potential is neglected. The fiber distributions thus generated are affected by T, ε and r_σ. In this study, we fixed ε (=1) and r_σ (=1.05D_f, where D_f is the fiber diameter), thus the resulting fiber distributions are dictated by T, as can be observed visually in Figure 1. In general, the extent of fiber clustering is inversely related to T.

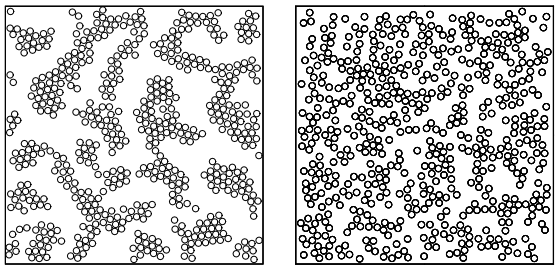

Figure 1. Sample distribution generated by the Metropolis MC method. The number of fibers in the assembly is N_f=576, the porosity ϕ=0.7, the minimum allowable inter-fiber distance is δ_{min}=0.05D_f and T^*=0.25 (left) and T*=1.0 (right). The extent of fiber aggregation decreases as the dimensionless temperature ($T^*=k_BT/\varepsilon$) is increased.

In principle, the Ripley's K function [1] is capable of discriminating between different fiber distributions. However, for quantification purposes, it is desirable to reduce $K(r)$ to some appropriate scalar value. In this direction we suggest the use of a microstructural parameter (χ), indicative of the deviation of a given pattern from complete randomness.

This is based on the averaging of the ratios between the $K(r)$ of a given microstructure and πr^2, the K(r) of a Poisson distribution. The definition is

$$\chi = \frac{1}{b-a}\int_a^b \frac{K(r)}{\pi r^2}\,dr \approx \frac{1}{m}\sum_{i=1}^{m}\frac{K(r_i)}{\pi r_i^2} \quad , \qquad (2)$$

where [a, b] is the length scale range of interest. Usually, a is the fiber diameter, and b has to be larger than the largest fiber cluster size. In this study, we chose b to be one fourth of the computational domain. For fiber distributions generated by the Metropolis Monte Carlo method at different T^* values, the χ measures were obtained and the results are plotted versus T^*, as shown in Figure 2. An inverse relation between T^* and χ is indicated for $0.25 \le T \le 1.0$. Outside this range, χ measure does not seem to vary much with T^*.

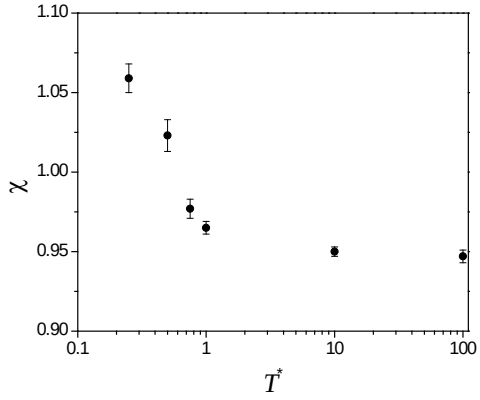

Figure 2. Plot of χ versus T^* for fiber distributions generated by the Metropolis method. At each T^*, ten distributions are generated. The microstructural parameter χ is evaluated for each distribution and the averages along with the ±σ error bars (based on the absolute values) are shown.

The Stokes equations are used to model saturated, slow viscous flow in the inter-fiber space, for the problems defined on the two-dimensional geometries shown in Figure 1. The governing equations are

$$\nabla \cdot \mathbf{u} = 0 \qquad \text{on } \Omega \qquad \mu\nabla^2\mathbf{u} = \nabla p \qquad \text{on } \Omega \ , \quad (3)$$

in two dimensions, where **u**, p, μ and Ω denote the velocity vector, pressure, viscosity and the flow domain, respectively. The boundary element method is used to convert Eq. (3) into boundary integral equations that involve boundary fluid velocities and tractions only. These are solved as presented in [3–5]. In this study, isoparametric quadratic boundary elements were used to discretize the governing equations. Typically, 36 nodes were used to discretize a fiber boundary. The resulting linear system of equations from the BEM is dense and asymmetric.

When hundreds of fibers (or $\ge 2 \times 10^4$ unknowns) are involved in a simulation, the solution task becomes computationally prohibitive on a single workstation. To overcome this difficulty, a parallel boundary element code that can use distributed-memory computing resources was developed. The

code was written in Fortran 90 and built on top of MPI, BLACS and ScaLAPACK libraries. The BEM solution yields the fluid velocities on the representative volume element (RVE) boundaries, from which the average velocity $\overline{u}$ can be obtained. The transverse permeability of the corresponding system can be computed by returning to Darcy's law, which gives $K = \overline{u}\mu L / \Delta p$, where (L) is the length of the RVE in the direction of the imposed pressure drop (ΔP), while (μ) is the fluid viscosity. One example velocity profile is shown in Figure 3.

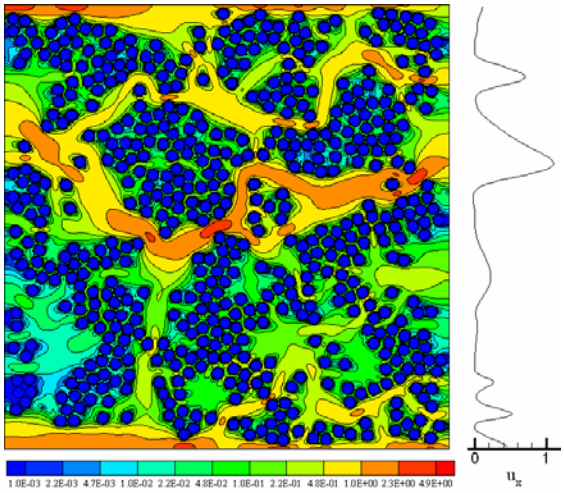

Figure 3. Plot of fluid speed contours and the resulting boundary velocity profile (u_x) from which the effective permeability is calculated, for a simulation containing 576 fibers at ϕ=0.7.

A correlation between the scalar metric (χ) and permeability has been obtained by carrying out a large number of simulations in geometries which exhibit various degrees of clustering. The results are summarized in Figure 4.

Flow at the Interface Between a Clear Fluid and a Fiber Bed [6]

Problems involving fluid flow through a channel bound by porous surfaces are often encountered while modeling flow in liquid composite molding (LCM) processes. To conduct flow simulations inside a fiber preform unit-cell, proper boundary conditions need to be applied at the interface between the clear-fluid region and the fibrous porous medium. Our intention is to study computationally Stokes flow at such an interface and compare the results with the predictions of existing models derived under certain assumptions concerning the boundary conditions at the clear-fluid/porous medium interface.

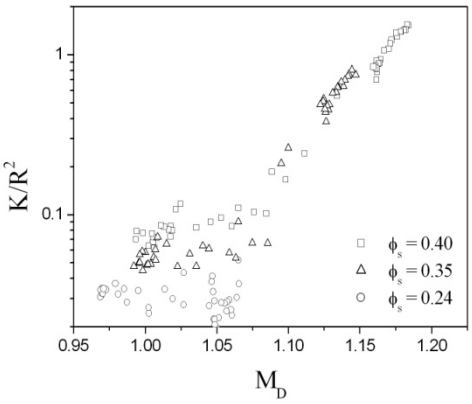

Figure 4. Correlation of the dimensionless permeability K_p/R_f^2, where R_f is the fiber radius, with the scalar metric (M_D=χ) defined by Eq. (2), for fiber distributions showing various degrees of clustering. Moving to lower χ, as indicated by the arrow, results in less clustered microstructures.

With this objective in mind, we place a 2-D porous medium, made of a square arrays of cylinders of radii 10μm each, adjacent to a clear-fluid region in form of a channel (Figure 5). The depth H of clear fluid region is 720μm. The porosity ε of the porous medium region varies from 0.5 to 0.9 by changing the inter-cylinder space e. The boundary element method (BEM) is employed to solve the point-wise Stokes equation in such a domain.

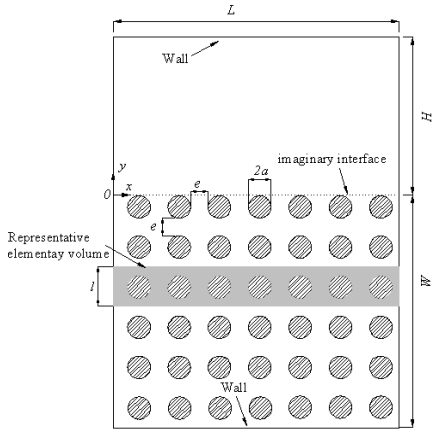

Figure 5. Simplified sketch of the model used in the point-wise simulation of Stokes equation using the BEM.

The Stokes and Brinkman equations are respectively used to model the steady-state creeping flow in the channel and porous medium shown in Figure 6.

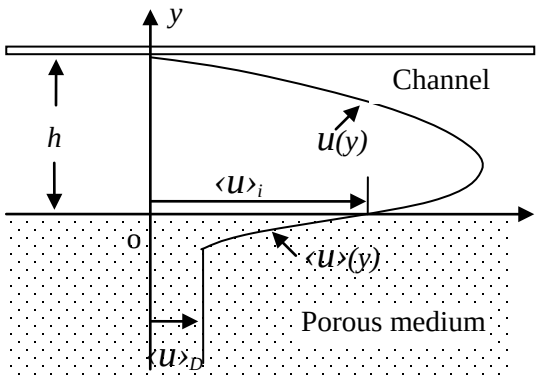

Figure 6. The geometrical model used in modeling a hybrid clear-fluid/porous-medium system.

If the velocity and stress are assumed to be continuous at the interface between the clear-fluid (channel) and porous-medium domains for the pressure-driven creeping flow, we can obtain the solution in terms of the velocity profiles in the clear-fluid and porous-medium domains as

$$u(y)=\langle u\rangle_i\left(1+\sqrt{\frac{\mu'}{\mu}}\frac{y}{\sqrt{K}}\right)+\frac{K}{2\mu}\frac{dp}{dx}\left(2\sqrt{\frac{\mu'}{\mu}}\frac{y}{\sqrt{K}}+\frac{y^2}{K}\right) \quad (4)$$

for $0\le y\le h$ and

$$\langle u\rangle(y)=\langle u\rangle_i+\left(\langle u\rangle_D-\langle u\rangle_i\right)\left[1-\exp\left(\sqrt{\frac{\mu}{\mu'}}\frac{y}{\sqrt{K}}\right)\right] \quad (5)$$

for $-\infty\le y\le 0$,

where velocity at the interface ‹*u*›$_i$ is given by

$$\langle u\rangle_i=\frac{-\frac{K}{2\mu}\frac{d\langle p\rangle^f}{dx}\left(2\sqrt{\frac{\mu'}{\mu}}\frac{h}{\sqrt{K}}+\frac{h^2}{K}\right)}{1+\sqrt{\frac{\mu'}{\mu}}\frac{h}{\sqrt{K}}} \quad . \quad (6)$$

If a boundary-layer thickness δ_c can be defined as the width of the region inside the porous medium near the interface where $\langle u\rangle\ge 1.01\langle u\rangle_D$, then

$$\delta_c=\sqrt{K}\sqrt{\frac{\mu'}{\mu}}\ln\frac{50\left(\frac{h^2}{K}-2\right)}{1+\sqrt{\frac{\mu'}{\mu}}\frac{h}{\sqrt{K}}} \quad (7)$$

is obtained from $\langle u\rangle\big|_{y=-\delta}=1.01\langle u\rangle_D$.

We can find that the boundary-layer thickness is quite small and is of order $K^{0.5}$. When Darcy's law with the slip boundary condition is used, instead of the Brinkman equation with the stress-continuity condition, the velocity profile in the clear-fluid region is identical to Eq. (4), as long as the slip coefficient (α) is $\alpha=(\mu'/\mu)^{0.5}$. The difference between the two models is that there is no boundary layer inside the porous medium when using the Darcy's law, while a boundary-layer regime exists inside the porous medium when the Brinkman equation is used. Therefore, we can correlate the result from Brinkman equation with the stress-continuity condition to the solution from Darcy's law with the slip-velocity boundary condition.

Ochoa-Tapia and Whitaker [7] proposed that the governing equation for flow inside porous medium near the clear-fluid porous-medium interface is

$$-\nabla\langle p\rangle^f+\frac{\mu}{\varepsilon}\nabla^2\langle\mathbf{u}\rangle-\frac{\mu}{K}\langle\mathbf{u}\rangle=0 \quad , \quad (8)$$

where ε is the porosity of porous medium. Equation (8) (hereafter referred to as the *modified Brinkman equation*) is identical to the Brinkman equation (hereafter referred to as the *original Brinkman equation*) as long as $\mu'=\mu/\varepsilon$. Ochoa-Tapia and Whitaker found that the average velocity is continuous at the interface while the stress may not be. Using the rigorous volume averaging method, they derived a complex mathematical expression to describe a jump in the stress at the clear-fluid porous-medium interface. For 1-D parallel flow, the complex stress-jump interfacial condition reduces to

$$\frac{1}{\varepsilon}\frac{d\langle u\rangle}{dy}\bigg|_{y=0^-}-\frac{du}{dy}\bigg|_{y=0^+}=\frac{\beta}{\sqrt{K}}\langle u\rangle \text{ at } y=0 \quad , \quad (9)$$

where β is a dimensionless coefficient on the order of one. Using the stress-jump boundary condition (9), solution to the Stokes and modified Brinkman equations can be expressed by the following:

$$u(y)=\langle u\rangle_i\left[1+\left(\frac{1}{\sqrt{\varepsilon}}-\beta\right)\frac{y}{\sqrt{K}}\right]+\frac{K}{2\mu}\frac{dp}{dx}\left(\frac{2}{\sqrt{\varepsilon}}\frac{y}{\sqrt{K}}+\frac{y^2}{K}\right) \quad (10)$$

for $0 \le y \le h$

and

$$\langle u\rangle(y)=\langle u\rangle_i+\left(\langle u\rangle_D-\langle u\rangle_i\right)\left[1-\exp\left(\sqrt{\varepsilon}\frac{y}{\sqrt{K}}\right)\right] \quad (11)$$

for $-\infty \le y \le 0$,

where velocity at the interface ‹*u*›$_i$ is given by

$$\langle u\rangle_i=\frac{-\frac{K}{2\mu}\frac{d\langle p\rangle^f}{dx}\left(\frac{2}{\sqrt{\varepsilon}}\frac{h}{\sqrt{K}}+\frac{h^2}{K}\right)}{1+\frac{h}{\sqrt{K}}\left(\frac{1}{\sqrt{\varepsilon}}-\beta\right)} \quad . \quad (12)$$

Using the condition $\langle u\rangle\big|_{y=-\delta_j}=1.01\langle u\rangle_D$, the thickness of boundary-layer in the porous-medium flow can be defined as

$$\delta_j=\sqrt{\frac{K}{\varepsilon}}\ln\frac{50\left(\frac{h^2}{K}+\frac{2h\beta}{\sqrt{K}}-2\right)}{1+\frac{h}{\sqrt{K}}\left(\frac{1}{\sqrt{\varepsilon}}-\beta\right)} \quad . \quad (13)$$

It is important to emphasize that the above solutions to the Brinkman equations are in terms of volume averaged quantities [i.e., the solutions are not on a point-wise scale but on the macro (RVE) scale]. More details on these analytical results for the stress-continuity and stress-jump conditions can be obtained in [6] and references therein.

The effective viscosity μ' must be determined in order to compare the Brinkman solution to the average velocity based on the point-wise solution. Similarly, the adjustable coefficient β in the stress jump condition needs to be determined as well. The parameter μ' is decided by adjusting μ' to match the total flow rate in the channel calculated from Eqs. (4)–(6) with that from the BEM solution; this is conceptually equivalent to the experimental procedure used to calculate the slip coefficient by comparing an experimental velocity profile to the one predicted by theory. The coefficient β in the stress jump condition is determined by the same approach as well. If Darcy's law with the slip-velocity boundary condition is used for the porous medium instead of the Brinkman model with the stress continuity condition, the slip coefficient α is related to μ' by $\alpha=(\mu'/\mu)^{0.5}$. Values of μ'/μ, β and of the resulting slip coefficient α have been determined in this manner [6]. Figure 7 shows streamlines for the pressure-driven channel flow over square arrays of circular cylinders; only flow details near the top two rows of cylinders are shown. The streamlines above the top row of cylinders are smooth, and the streamline spacing indicates a slight perturbation in the channel flow due to the presence of cylinders below. However below the center-line of the top row of cylinders, the streamlines appear very wavy, indicating a rapidly diminishing x-direction velocity (as spacing increases downward) and a significant transverse velocity around the cylinders. In the second row of cylinders, the effect of the channel flow is almost negligible and the streamline pattern resembles that of the pressure-driven flow through an infinite square array of circular cylinders. In the low porosity (ε=0.5) case, the outermost recirculation eddies resembles those in the inner row of cylinders, which indicates that the flow field decays very rapidly with a reduction in the porosity.

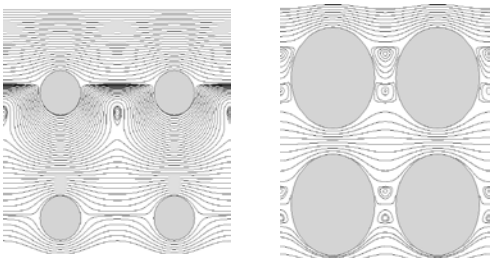

Figure 7. Streamlines for flow over an array of aligned fibers (left) ε=0.90, (right) ε=0.50.

It has frequently been assumed, in the context of the stress continuity condition, that the effective viscosity μ' is equal to the fluid viscosity μ. To

estimate the accuracy of this simplifying approach, we compare its solution with the volume averaged results obtained through the BEM. Figure 8 shows the comparison of the volume averaged velocity (essential detail on how this is calculated is omitted here for the sake of brevity; for more details see [6]) based on the point-wise BEM solution with the solution of the original Brinkman equation using the stress continuity condition with a suitable μ' or with $\mu'=\mu$, and with the solution of the modified Brinkman equation using the stress-jump condition.

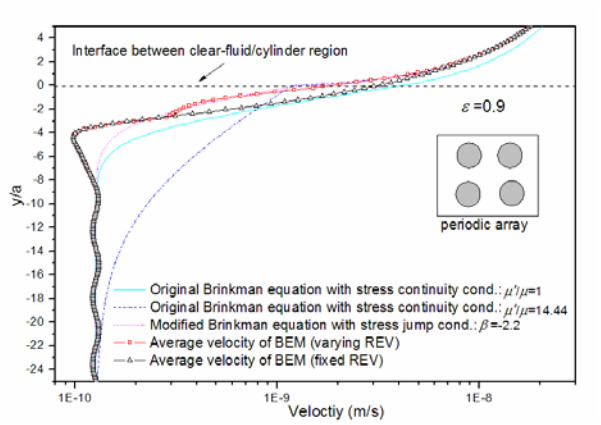

Figure 8. Comparison of average velocity based on the point-wise BEM solution with the Brinkman models using different interfacial conditions.

Overall, we have found that when the porosity (ε) is large, solution of the modified Brinkman equation using the stress-jump condition agrees well with the average-velocity profiles based on the point-wise BEM solutions, especially the varying RVE result. The slip velocity, the penetration depth of the boundary layer, and the velocity profile are well predicted through the use of the stress-jump condition. With a decrease in the porosity, the modified Brinkman equation with the stress-jump condition progressively fails to predict the volume averaged velocity near the interface; however it still predicts the penetration depth and slip velocity accurately. Our results also show that the original Brinkman equation with the stress-continuity equation cannot accurately predict the velocity profiles at the interfacial region for the full range of ε.

Transport Across Flake-Filled Membranes [8,9]

Flake-filled polymer membranes belong to an emerging class of composites that show promise as barrier materials in many industrial applications. Though the barrier property enhancement in flake-filled membranes is well known, its dependence on microstructural factors such as flake spatial distribution, size dispersion, and orientation is not well understood. In this study we carried out a micromechanics-based, direct numerical study to predict the Barrier Improvement Factors (BIF) of flake-filled membranes. Numerical calculations are conducted in two-dimensions for composite membranes containing aligned, impermeable flakes, using the fast multipole-accelerated boundary element method. The models that predict the barrier properties of flake-filled membranes are reviewed and evaluated by comparison with the boundary element calculations. Models evaluated in this study are two-dimensional, where flakes are aligned parallel to the membrane surface and diffusion is in the direction perpendicular to the membrane surface. The barrier improvement in the direction of diffusion is attributed to two phenomena: the increase in the diffusion path tortuosity and the reduction in the area available for diffusion. Therefore, the BIF can be approximated by

$$\frac{D_0}{D_f} = \left(\frac{A_0}{A_f}\right)\left(\frac{L'}{L}\right), \qquad (14)$$

where

A_0	=	area available for diffusion in a pure membrane,
A_f	=	area available for diffusion in a flake-filled membrane,
L	=	membrane thickness,
L'		distance a solute must travel to cross a flake-filled membrane.

The path tortuosity factor is defined by L'/L. For a membrane containing uniformly spaced monodisperse rectangular flakes, Nielsen's model for the BIF is written as

$$\frac{D_0}{D_f} = \frac{1+\frac{\alpha}{2}\phi}{1-\phi} \quad , \qquad (15)$$

where D_0 and D_f are the diffusion coefficients of the virgin and the reinforced (filled) resin, respectively and

α	=	flake aspect ratio = *l/t,*
l	=	flake length,
t	=	flake thickness.

Using a conformal mapping method, Aris [10] developed an analytical expression for the BIF in a two-dimensional periodic array of obstacles. This is

$$\frac{D_0}{D_f} = 1+\frac{\alpha^2\phi^2}{4(1-\phi)}+\frac{\alpha\phi}{2\lambda}+\frac{2}{\pi}\frac{\alpha\phi}{1-\phi}\ln\left[\frac{\pi\alpha^2\phi}{4\lambda(1-\phi)}\right] , \qquad (16)$$

where λ=2s/t and (s) is the half-gap between two flakes.

For the same geometry, a slightly different model due to Wakeham and Mason [11] is

$$\frac{D_0}{D_f} = 1+\frac{\alpha^2\phi^2}{4(1-\phi)}+\frac{\alpha\phi}{2\lambda}+2(1-\phi)\ln\left(\frac{1-\phi}{2\lambda\phi}\right) . \qquad (17)$$

The difference between Eq. (16) and Eq. (17) lies in the fourth term on the right hand side. In Eq. (16), the fourth term is dependent on α, while in Eq. (17) it is not.

Cussler et al. [12] extended Aris' result [10] by considering the limit of a membrane having many layers of flakes, which leads to the following:

$$\frac{D_0}{D_f} = 1+\frac{\alpha^2\phi^2}{4(1-\phi)}+\frac{\alpha\phi}{2\lambda} \quad . \qquad (18)$$

The second term on the right hand side of Eq. (18) becomes the leading term when $1/\lambda << \alpha\phi$. Equation (18) was also extended by the same authors to the case where flakes of uniform size are randomly placed. The relevant expression is

$$\frac{D_0}{D_f} = 1+\frac{\alpha^2\phi^2}{\beta(1-\phi)} \quad , \qquad (19)$$

where β is a geometric factor.

Recently, Lape et al. [13] developed models for the membranes containing randomly placed, monodisperse or polydisperse flakes, using an approach similar to Nielsen. For monodisperse flakes, the expression for BIF is

$$\frac{D_0}{D_f} = \frac{\left(1+\frac{1}{3}\alpha\phi\right)^2}{1-\phi} \quad . \qquad (20)$$

Implicit in the derivation of Eq. (20) is that the diffusion path around a flake is formed by straight lines. The BIF for polydisperse flakes was derived in a similar way. The expression for the BIF for flakes having a discrete size distribution is written as

$$\frac{D_0}{D_f} = \frac{1}{1-\phi_{tot}}\left(1+\frac{\phi_{tot}}{3}\frac{\sum_i m_i l_i^2}{t\sum_i m_i l_i}\right)^2 , \qquad (21)$$

and the expression for flakes having a continuous size distribution is

$$\frac{D_0}{D_f} = \frac{1}{1-\phi_{tot}}\left(1+\frac{\phi_{tot}}{3}\frac{\int_0^\infty l^2 g(l)dl}{t\bar{l}}\right)^2 . \qquad (22)$$

In Eq. (21), the subscript *i* is used to indicate different size classes; m_i and l_i are the number and the size of flakes in the *i*-th size class, respectively; ϕ_{tot} is the total flake volume fraction. In Eq. (22), $g(l)$ is the probability distribution function of sizes and $\bar{l}$ is defined as $\bar{l} = \int_0^\infty g(l)ldl$. The flakes thickness (t) is assumed constant. It is not difficult to find that Eqs. (21) and (22) can be obtained by replacing α in Eq. (20) with a properly defined size-average, that is

$\bar{\alpha} = \sum_i m_i l_i^2 \Big/ t\sum_i m_i l_i$ and

$\bar{\alpha} = \int_0^\infty l^2 g(l)dl \Big/ t\int_0^\infty g(l)ldl$, respectively.

According to the above, the diffusivity of a membrane filled with monodisperse flakes is higher than that filled with polydisperse flakes. Hence, the barrier improvement caused by

polydisperse flakes is predicted to be superior to monodisperse flakes with the same average size. Experimental data on a 50-50% mixture of flakes indicates that this is qualitatively correct. However, extensive quantitative comparisons are still lacking.

The models reviewed above are based on intuitive assumptions rather than first principles. Their applicability in predicting the BIFs of real systems is therefore open to question. It is natural for us to ask which model is the most appropriate and how its use can be justified. In general, it is very difficult to obtain accurate experimental data for aligned flake-filled membranes. The reason is that preparing perfectly aligned flakes has not been proven possible. Hence any comparison between the BIF of experimental specimens and models predictions is always subject to (frequently unreported) experimental details. Comparing model predictions to results of direct simulation is free from this limitation.

Figure (9) shows typical models used in the numerical work: a random array of monodisperse flakes and a random array of polydisperse flakes. They are more realistic as random spatial distribution and size distribution of flakes are considered. However, because the microstructure is nonuniform, a Representative Volume Element (RVE) should be chosen such that a sufficient number of flakes are included in the analysis. This not only increases the model size but also creates new problems in selecting RVEs. In common practice, one can either choose a periodic RVE or choose a nonperiodic RVE. In a periodic RVE, fractioned flakes are allowed to reside at the RVE boundaries, and both geometry and boundary conditions are periodic. In a nonperiodic RVE, flakes are completely confined within a simulation box, and boundary conditions are of common types. A periodic RVE has several advantages in modeling, but is not applicable here due to the limitations of the numerical method we use. Thus, nonperiodic RVEs are chosen in this study. In a nonperiodic RVE, places near the RVE boundaries are free of flakes. In these places, local diffusion fluxes are high because there are no obstacles. It is of concern that BIF will be systematically underestimated if the fluxes in these easy diffusion areas are counted. To reduce the influence from boundaries, a composite RVE is used, as illustrated in Figure 9(a), where the dashed lines divide the model into three regions. The middle region is a square of side length L, inside which the spatial distribution of flakes is random and periodic in the x direction. The flakes are separated by at least a distance of t from each other, and they are also apart from the horizontal boundaries by at least a distance of t.

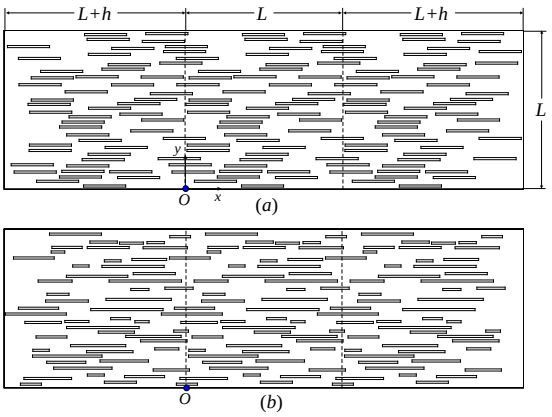

Figure 9. Computational models of random arrays of aligned flakes, (a) monodisperse flakes; (b) polydisperse flakes. The area of analysis is in the middle, separated from the rest by dashed lines.

Such random placement of nonoverlapping flakes at small volume fractions can be achieved without difficulty by using the random sequential addition algorithm. The flakes in the left and right regions are replicated from those in the middle by a translation of $-L$ and L, respectively. The x-dimensions of the left and right regions are increased by h so that the flakes are completely confined in the simulation box. The concentration field in the entire RVE will be solved, but the area of analysis is defined on the middle region, over which volume-average quantities are obtained and used to estimate effective properties. In this way, there is no artificially introduced easy diffusion path in the area of analysis except those naturally formed by randomly placed flakes. It is expected that the boundary influence will decay rapidly as it propagates inside, so its influence on the area of analysis should be insignificant provided that the sub-domain size is sufficiently large.

In general, the numerically predicted BIFs are higher than those predicted by theory (detailed

results are given in [8,9]. The deviations are more pronounced in the concentrated regime. To help explain this, Figure 10 shows a contour map of a concentration field in a nondilute geometry. Tortuous iso-concentration contour lines can be seen in Figure 10. As one would expect, if there were no flakes, the iso-concentration lines would be parallel to the *x*-axis and the diffusion paths, which are perpendicular to these iso-concentration lines, would be straight and vertical. In the presence of flakes, the iso-concentration lines are curved and so are the diffusion paths.

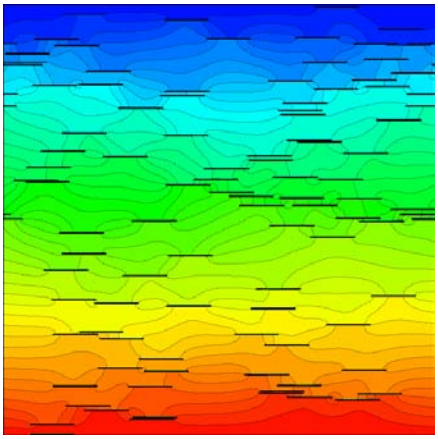

Figure 10. Contour map of concentration field in randomly placed monodisperse flakes,ϕ=0.01, α=100, N_f=100. The color scale is linearly distributed from 0 (blue) to 100 (red).

Because the flakes are impermeable, iso-concentration lines that end up on flake surfaces are normal to each flake surface. Therefore, in the vicinity of a flake, the diffusion path is parallel to the flake surface. This is commonly assumed by the analytical models to be the only contribution to the increase in the path tortuosity. According to these models, the concentration filed at a distance away from a flake is not perturbed; hence, the diffusion paths in these areas are still straight as if they were not influenced by nearby flakes. Such a simplification is only valid for dilute dispersions of flakes. It is evident in Figure 10 that in places where the local flake concentrations are high, the iso-concentration lines between nearby flakes are tilted with various angles to the *x*-axis rather than being straightly horizontal. This is an indicator of flake-flake interaction. As a result, the actual diffusion paths are more tortuous in these places than assumed by the models. Such a nondilute effect can only be rigorously modeled by a numerical approach. Additional comparisons between theoretical models and computational results have been published in [8,9].

Experimental Measurement of Interstitial Fuid Velocities in Fiber Arrays Using Micro-Particle Image Velocimetry (μ-PIV) [14]
Experiments were conducted on the flow cell of Figure 11. The porous region of the channel consists of borosilicate glass fiber rods which can be arranged in different formations, perpendicular to the bulk flow direction – from left to right in Figure 11. The rod radius is R=150 μm.

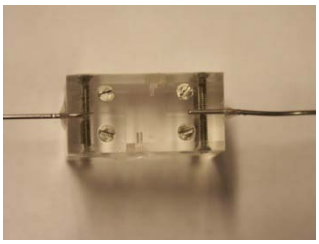

Figure 11. Flow cell, showing the inlet/outlet pipes.

The first investigation was made on a rectangular fiber array with relatively high porosity. The second investigation was made on a much denser hexagonally arranged fiber array with a fiber volume density of about 40 % (Figure 12).

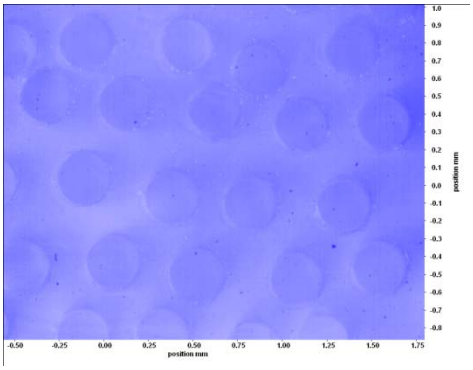

Figure 12. Image of a section of the fiber array obtained using 10x magnification. The bulk flow is in the direction perpendicular to the fiber axes.

In μ-PIV the flow is seeded with fluorescent particles and illuminated by a light source before it is imaged through a microscope into a CCD

camera. A schematic of the PIV setup is shown in Figure13.

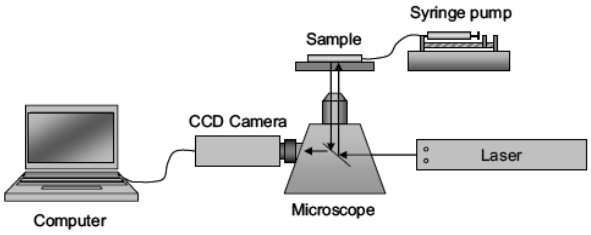

Figure 13. µPIV experimental setup.

A pulsed laser (Litron Lasers) emitting light with a wavelength of 532 nm was used as a light source in the experiments. The choice of fluid for the experiments was paraffin oil since it has a refraction index that is close to the refraction index of both, the glass walls of the channel and the fibers. The fluorescent particles used were 10.2 ± 0.17µm Rhodamine B particles from Microparticles GmbH. In order to get good results a homogenous distribution of particles in the fluid is needed. In order to get a constant velocity of the flow into the channel, a KDS Model 100 Series syringe pump was used with the volume flow rate set to 20 ml/h. A good signal-to-noise ratio was achieved by having as few particles as possible while still making it possible to obtain robust measurements.

The flow in the channel is three dimensional while the µ-PIV set-up used gives only the two planar components of the velocity field. It was therefore desired to measure the velocity field where the out-of-plane component of the flow had as little influence as possible, in other words in the centre of the channel. Since the permeability is much lower in the fiber bundle, the flow there is significantly slower. This implies that cross-correlation of the movement of the particle inside and outside of the porous domain at the same time is difficult. Either the flow is captured well around the fiber bundle and the fluid inside the bundle appears stationary, or the velocity field inside the bundle can be accurately described but the velocities obtained in the fast-moving fluid around the bundle are nonphysical. A typical velocity field obtained in the interstitial space is shown in Figure 14.

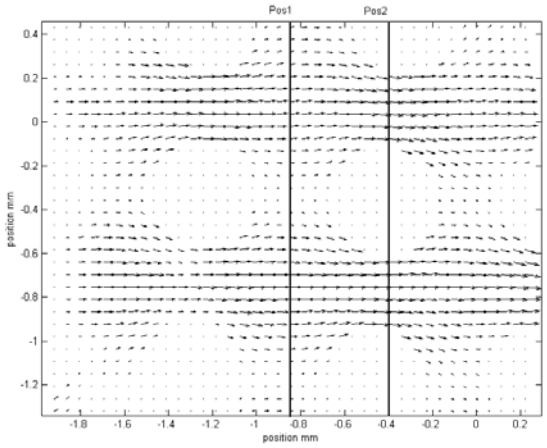

Figure 14. Velocity field in rectangular fiber array.

There is very limited movement between the rows of fiber and a converging-diverging flow can be observed. The periodic character of the flow in the interstitial spaces can also be visualised in Figure 15.

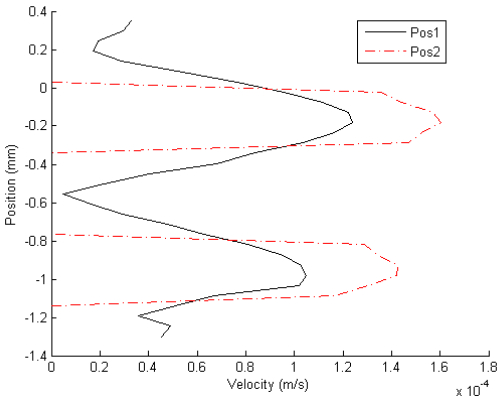

Figure 15. Velocity profiles for min and max cross-section area (reference figure 14 for positions 1 and 2).

References

1. B. Ripley, *Spatial Statistics*. Wiley: New York (1981).
2. X.-M. Chen, M. D. Woodward, and T. D. Papathanasiou, “Fiber clustering: Its quantification and influence on the permeability of unidirectional fibrous media,” Proceedings SAMPE-2007, Baltimore, MD, USA, June 2007.

3. X. Chen and T. D. Papathanasiou, "Micro-scale modeling of axial flow through unidirectional disordered fiber arrays," *Composites Science and Technology*, 67, 1286–1293, 2007.
4. X. Chen and T. D. Papathanasiou, "The transverse permeability of disordered fiber arrays: A statistical correlation in terms of the mean nearest interfiber spacing," Transport in Porous Media," 71, 233–251, 2008.
5. X. Chen and T. D. Papathanasiou, "On the variability of the Kozeny constant for saturated flow across unidirectional, disordered fiber arrays," *Composites Part A: Manufacturing and Applied Science*, 37(6), 836–846, 2006.
6. Hua Tan, Xiao-Min Chen, Krishna M. Pillai, and T. D. Papathanasiou, "Evaluation of boundary conditions at the clear-fluid and porous medium interface using BEM," Proceedings to FPCM-9, 9th International Conference on Flow Processes in Composite Materials, Montreal, Canada, July 2008.
7. J. A. Ochoa-Tapia and S. Whitaker, *Int. J. Heat and Mass Transfer*, 38, 2635, 1995.
8. X. Chen and T. D. Papathanasiou, "Permeability of flake-filled membranes: review and Numerical Evaluation," Proceedings ANTEC-2007, Cincinnati, OH, USA, May 2007.
9. X. Chen and T. D. Papathanasiou, "Barrier properties of flake-filled membranes: Review and numerical evaluation," *Journal of Plastic Film and Sheeting*, 23(4), 319–346, 2007.
10. R. Aris, On a problem in hindered diffusion, *Arch. Rat. Mech. Anal.*, 95:83–91, 1986.
11. W. A. Wakeham and E. A. Mason, Diffusion through multiperforate laminae. *Ind. Eng. Chem. Fundam.*, 18(4): 301–06, 1979.
12. E. L. Cussler, S.E. Hughes, and W. J. Ward, Aris R. Barrier Membranes. *J. of Membrane Science*, 38:161–74, 1988.
13. N. K. Lape, E. E. Nuxoll, and E. L. Cussler, Polydisperse flakes in barrier films, 236:29–37, 2004.
14. A. G. Andersson, L. G. Westerberg, T. D. Papathanasiou, and T. S. Lundström, "Fluid flow through porous media with dual-scale porosity," Proceedings 19th International Symposium on Transport Phenomena, Reykjavik, Iceland, 17–20 August 2008.

M. Simulating Injection Molding of Thermoplastics Reinforced with Short and Long Fibers

Principal Investigator: Donald G. Baird
Virginia Polytechnic Institute and State University
Department of Chemical Engineering
Blacksburg, VA 24061
(540) 231-5998, fax: (540) 231-2732, email: dbaird@vt.edu

Co-Principal Investigator: Peter Wapperom
Virginia Polytechnic Institute and State University
Department of Mathematics
Blacksburg, VA 24061
(540) 231-7252, email: pwappero@vt.edu

Participants
Aaron P. R. Eberle, PhD. student, email: eberle@vt.edu
Gregorio M. Velez, PhD. student, email: gvelez@vt.edu
Kevin C. Ortman, PhD. student, email: kco3@vt.edu

Contractor: Virginia Polytechnic Institute and State University
National Science Foundation (NSF) Contract No. DMI-052918, jointly funded by NSF and DOE

Objective

- Improve the accuracy of the simulation of short (rigid) and long (flexible) fiber orientation in thermoplastics during injection molding by using a modified constitutive relation that incorporates non-affine motion and flexibility in combination with state-of-the-art numerical techniques.
- Establish a method (independent of the injection molding process) for determining a unique set of material parameters which is based on the transient shear rheological behavior of the composite fluid.
- Evaluate the accuracy of the simulation technique by comparing numerical predictions of glass fiber orientation to that first found in rheometrical flows and then in injection molded parts produced using basic mold geometries (end and center-gated parts).

Approach

- Determine an approach to conduct quantitative and reproducible rheological experiments on glass fiber-filled polymeric fluids.
- Conduct transient shear rheological studies on glass fiber-filled polypropylene (PP) and polybutylene terephthalate (PBT) systems in which fibers of various lengths (length: 0.2–11 mm, diameter: 12.5 microns) are used to assess the effects of both fiber length and the viscoelastic nature of the matrix on the transient rheology.
- Experimentally characterize the relationship between the rheological behavior and the associated fiber microstructure.
- Identify the limitations of current approaches to predict the evolution of fiber orientation by comparing model predictions to experimental observations.
- Use modified theory to address these limitations.
- Define and evaluate specific rheological tests to determine the material parameters in the constitutive equation which are unique and give consistent results when used in numerical simulations.

- Develop a finite element method simulation program capable of predicting fiber orientation during the mold filling stage of thermoplastic composite fluids containing short and long glass-fibers in an injection molding process.
- Modify the simulation to include the extensional flow kinematics of the advancing front region which may be critical to predicting fiber orientation at the mold wall.
- Assess the performance of the simulation by comparing predicted fiber orientation against values determined experimentally from injection molded samples.

Accomplishments

- Rheological Characterization Technique (short fibers): Developed a novel rheological technique that addresses problems associated with the nonhomogeneous shear field found in parallel-plate rotational rheometers and boundary interactions in cone-and-plate rheometers.
- Rheological Characterization Technique (long fibers): A fully functional sliding plate rheometer incorporating a shear stress transducer has been designed and fabricated primarily for the purpose of performing unbiased and reproducible steady shear rheological experiments on long glass fiber-filled polymeric fluids that are otherwise impossible to perform on rotational rheometers. Moreover, the device has been calibrated, and its behavior has been verified using two reference materials, a viscosity standard and a commercial low density polyethylene (LDPE). In addition to rheological studies, the rheometer will also be used in tracking the transient evolution of long fiber orientation upon startup and cessation of shear flow.
- Rheology: Rheological characterization of the short glass fiber composites was performed, including intermittent stress growth/relaxation tests to elucidate the stress contribution of the fiber, matrix, and flow field on the transient evolution of fiber orientation. A novel approach using donut shaped samples in a cone-and-plate rheometer was developed for tracking transient shear behavior of short-fiber composites.
- Model (short fibers): A constitutive relation has been developed that incorporates stress contributions from the fiber and the viscoelastic suspending medium and includes the ideas of non-affine motion. Model predictions show good agreement compared to rheological experiments and preliminary results for the experimentally determined fiber orientation.
- Fiber Orientation Measurements: We have determined an approach to characterizing the three-dimensional (3D) fiber orientation within composite parts using confocal laser microscopy. Additionally, an improved method that uses optical microscopy was also developed, and was shown to provide a more economical means for acquiring orientation measurements. This latter method is, therefore, expected to be the chosen method for future acquisition. With these techniques, we have initiated the characterization of fiber orientation in both rheometrical flows and complex flow geometries.
- Model (long fibers): Various approaches to modeling flexible fibers have been investigated. These approaches include modifying current theory for rigid fibers to include a “flexibility parameter,” exploring constitutive equations resulting from bead-rod theory, track individual fibers using Hinch’s infinitely flexible fiber theory, and extending Hinch’s equations for concentrated polymer solutions through the concept of mobility. The choice of approach is still not determined but will be the emphasis of future research.
- Simulations (short): Developed a Galerkin/discontinuous Galerkin finite element simulation package to simulate the filling stage of injection molding. The features of this simulation package are: the use of multiple constitutive equations, the comparison with the Hele-Shaw approximation for an end-gated plaque and a center-gated disk, and a combined front tracking/ ALE technique for advancing front simulations.
- Simulations (long): Constructed a bead-rod orientation model for long fibers within the finite element simulation package. This model was used to gain preliminary results for long fiber orientation in injection molded center gated disks. Additionally, a program capable of utilizing an extension of Hinch’s equation for concentrated polymer melts, through the use of a mobility tensor, was also written.
- Injection molding: A complete set of short and long glass fiber reinforced parts were molded, from which variables affecting fiber orientation and polymeric behavior (i.e., Newtonian-like/viscoelastic matrices, geometry, part thickness, and fiber length) are being studied.

Future Direction

- Compare model predictions of short glass fiber theory including non-affine motion to that of experimental results.
- Complete the analysis of orientation in center-gated disks and end-gated plaques using the alternate nonambiguous protocol for fiber orientation measurement in short glass fiber composites.
- Incorporate frontal flow in the simulation and compare to previous predictions using just Hele-Shaw approximation.
- Simulate fiber orientation in the runner of an injection mold cavity in order to establish the initial fiber orientation at the entrance to the cavity.
- Focus our attention on characterizing the transient rheological behavior of long glass fiber suspensions using the sliding plate rheometer.
- Use the sliding plate rheometer to gain an understanding of long fiber orientation development in simple shear experiments.
- Use the sliding plate rheometer to gain an understanding of fiber mobility in concentrated fiber suspensions and to assess the performance of Hinch's equation and its extensions.
- Assess the performance of the bead-rod model for various (long) fiber lengths by comparing model predictions to fiber orientation obtained in injection molded parts.

Introduction

The overall goal of our research is to be able to accurately predict the orientation of short and long fibers suspended in polymer melts generated during injection molding using a finite element analysis. To accomplish this goal we first have to establish a constitutive relation capable of predicting both the stress response to deformation of a composite fluid and the associated microstructure. As discussed, our approach to accomplish this goal begins with comparing model predictions to the rheological behavior and experimentally determined microstructure in the startup of simple shear flow experiments. Furthermore, unique material parameters for a specific composite fluid are established by fitting to these rheological measurements. Once established, the constitutive equation, using the unique model parameters, is then implemented into a finite element code for complex flow simulations typically found in injection molding, i.e., center-gated and end-gated flow.

We will highlight our advancements in the following order. First, we will discuss a unique method to accurately quantify the transient rheological behavior of short glass fiber-filled composite fluids and update the reader on the development of the sliding plate rheometer. After this we will describe, in general, the transient rheological behavior of these fluids characterized using this technique. Then we will discuss the improvements/modifications made to the constitutive theory by incorporating the idea of non-affine motion and a parameter to control fiber flexibility. In addition, we will discuss current theories used for the dynamic simulation of long/flexible fibers. We then compare our experimental results and model predictions for short glass fiber suspensions and describe our approach at determining unique material parameters by fitting to the transient shear stress in start-up of flow. Following, we will describe our approach to characterizing the evolving microstructure of short glass fibers in simple flows and compare these results to model predictions. Finally we will outline our progress in the finite element simulation of a center-gated mold and describe our findings, i.e., the effect of initial conditions and non-affine motion.

Experimental Procedure

Rheological Characterization (Short Fiber Composite Fluids)

A key part of our research is to be able to *quantitatively* characterize the transient rheological behavior of glass fiber composite

fluids to assess our modeling approach and determine unique material parameters. Historically, researchers have used the parallel plate or disk geometry in rotational rheometers to characterize the transient rheological behavior of short glass fiber-filled fluids to minimize boundary-fiber interaction. To reduce the degree of boundary interaction, it has been suggested that the rheometer gap be at least three times the length of the longest dimension of the suspension particle. Experimental results using parallel plate geometry with various rheometer gaps confirmed that for the 30 wt% PBT there is a negligible effect on the sample rheological response when the gap is greater than twice the number average fiber length. The problem with this geometry (parallel plate) is the tangential velocity and, hence, shear rate varies with radial position from the center of the plates to the outside. Our experimental results have shown that this inhomogenous shear field causes unrealistic transient behavior and, therefore, cannot be used as a quantitative tool. As a result, we believe only a rheometer that imposes a homogeneous shear field should be used to quantitatively characterize suspensions of glass fibers.

The gap within the 50 mm cone and plate fixture varies linearly from 2.51 mm at the outer edge to 0.05 mm at the center. To remove the inevitable fiber-boundary interaction near the center, sample disks were pre-formed and a 25.4 mm diameter hole was drilled through the center creating a donut shaped sample. A schematic of the "donut" sample can be seen in Figure 1.

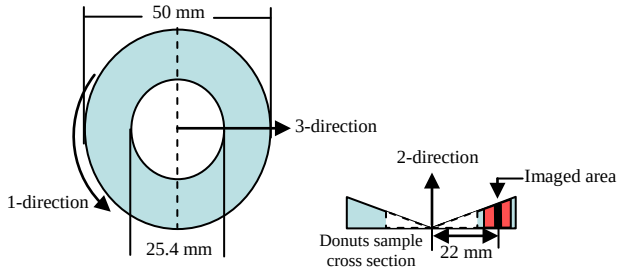

Figure 1. 50 mm cone and plate "donut sample" dimensions. The illustration defines the 1, 2, and 3 directions which are the direction of flow, velocity gradient, and radial directions, respectively. In the cross-sectional profile the black area is the area at which the confocal laser images were taken.

These samples combined with the cone and plate geometry ensure a homogeneous shear field and a gap that was always greater than two times the number average fiber length.

Sliding Plate Rheometer (Characterization of Long Fiber Composite Fluids)

After numerous attempts at characterizing suspensions containing long glass fibers using various techniques at our disposal, we concluded that the conventional melt rotational rheometers were inadequate. This was because of various difficulties posed by these rheometers, e.g., curvilinear streamlines and insufficient rheometer gap size. As a result, we initiated the design and fabrication of a sliding plate rheometer incorporating a wall shear stress transducer [shown in Figure 2(a–e)] with the primary purpose of being able to perform unbiased and reproducible steady shear rheological experiments on long glass fiber-filled polymeric fluids that are otherwise impossible to perform on rotational rheometers. After completion the device was calibrated and its behavior was verified. A viscosity standard and a commercial polymer Equistar PETROTHENE NA 952, a LDPE with no processing aids or antiblock agents, were used as reference materials in verification.

Localized shear stress measurement and a homogenous shear field with rectilinear streamlines are two key improvements the sliding plate rheometer offers over rotational rheometers. While localized stress measurement eliminates the problems arising due to edge effect, the homogenous shear field insures removal of unrealistic transient behavior. Moreover, theoretically it has no restriction on the gap size. Though the main purpose of sliding plate rheometer is to perform rheological measurements on long glass fiber composites but in future it will also be used in tracking the transient evolution of long fiber orientation upon startup and cessation of shear flow.

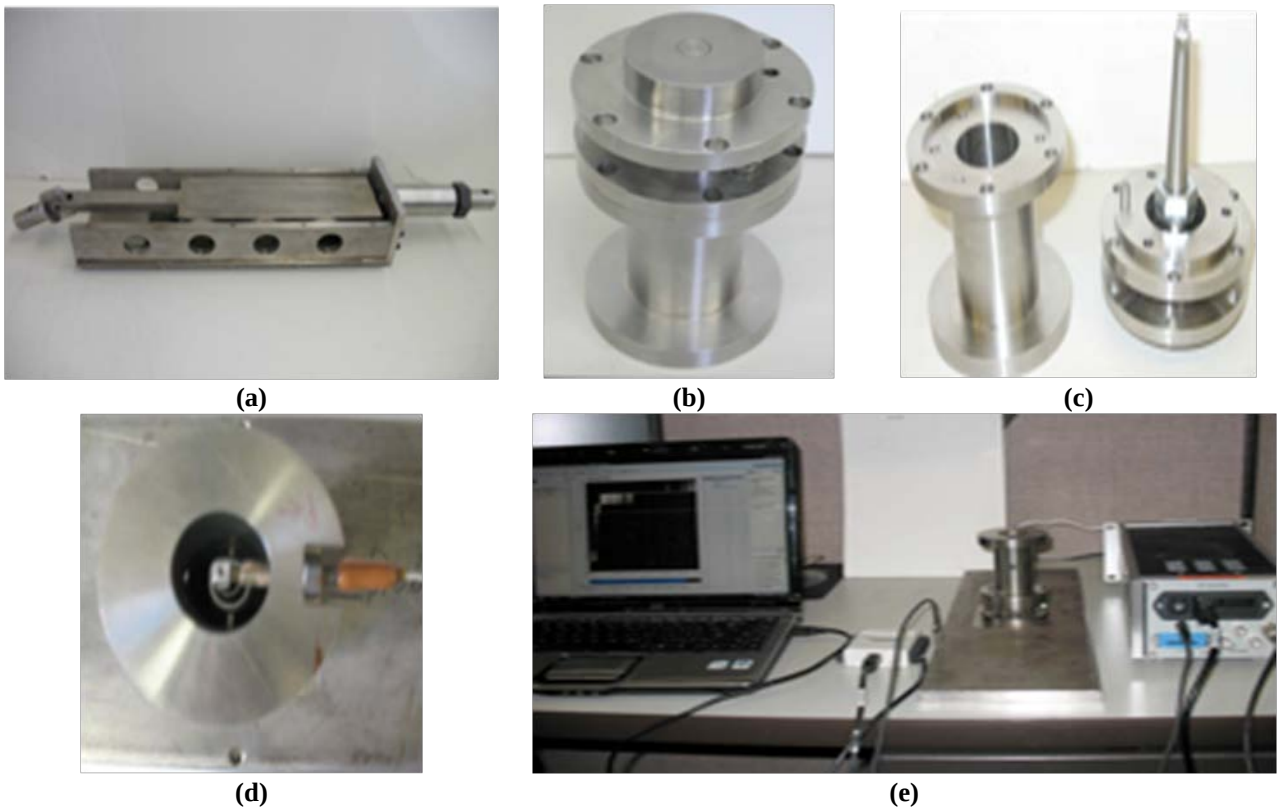

Figure 2. Sliding plate rheometer. (a) Sliding plate, (b) wall shear stress transducer, (c) disassembled shear stress transducer showing rigid beam, (d) shear stress transducer with capacitance probe, (e) complete assembly with all electrical components.

Rheological Behavior

Subsequently, we outlined the pertinent shear rheological behavior exhibited by the short glass fiber composite fluids as it will aid in the discussion on model development. When an undeformed sample is subjected to a start-up of flow experiment, the sample exhibits a relatively large stress overshoot in both the shear stress and the first normal stress difference. This behavior can be seen in Figure 3 (a) and (b) (τ^+ and N_1^+ vs. time, respectively) for the 30 wt% PBT. The relatively large overshoot is believed to be a result of the fibers rotating as a result of the flow field to align in the flow direction. Once the fibers reach a steady-state, the stresses reach a steady-state**.** An interesting observation is that when the flow is removed and then reapplied, after some period of time, the stresses return to their previous value. From this behavior we believe that during stress relaxation the fibers maintain their orientation so that when the flow is turned back on the stresses immediately grow to their previous value. Hence, the transient rheological behavior is coupled with the fiber orientation and being able to model the evolution of orientation is imperative to correctly predicting the rheological behavior and fiber orientation in complex flow simulations.

Theory: Model Development (Short Fibers)

Evolution of Fiber Orientation

The most common approach to represent the orientation state of a fiber is by defining a unit vector, **u**, parallel to the fiber backbone. In the case of an ideal suspension which consists of a large number of fibers that are identical in size and shape and whose concentration is spatially uniform the average orientation state of the fibers can be described with an orientation distribution function, $\psi(\mathbf{u},t)$. However, using the distribution function is numerically cumbersome. Another way to describe the average orientation state of the suspensions is with the second order orientation

tensor, **A**, and it is defined as the second moment of the orientation distribution function[1]:

$$\mathbf{A}(t) = A_{ij}(t) = \int \mathbf{uu}\,\psi(\mathbf{u},t)\,d\mathbf{u} \quad , \qquad (1)$$

where A_{ij} denotes the components of the second order orientation tensor. The trace of **A** is always equal to 1 and for a completely random orientation **A** = 1/3 **I**, where **I** is the identity tensor. In the limit where all the fibers are perfectly aligned in the 1-direction the only nonzero component is A_{11} = 1. In flow problems, in addition to the **A**, the fourth order orientation tensor ($\mathbf{A_4}$) is commonly used. For a more complete description of orientation tensors and their use in representing fiber suspension the reader is referred to Advani and Tucker [1].

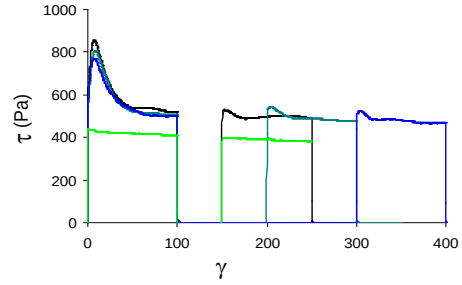

(a)

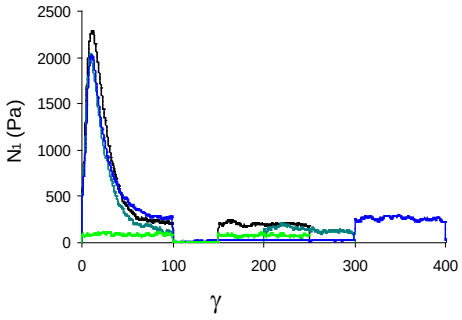

(b)

Figure 3. Stress vs strain for intermittent stress growth/relaxation tests performed on the 30 wt % short glass fiber filled PBT. (a) Shear stress, (b) first normal stress difference. The light green line is the suspending medium. All tests were performed using cone and plate geometry combined.

For suspensions containing rigid fibers the most common approach to modeling the evolution of fiber orientation is the Folgar-Tucker (F-T) model [2]. This model uses the generalized Jeffery equation [3] and adds an isotropic rotary diffusivity term, to represents the inter-particle interactions. For simple flows the Folgar-Tucker model can be written in terms of **A** as follows:

$$\frac{D\mathbf{A}}{Dt} = \left(\mathbf{A}\cdot\mathbf{W} - \mathbf{W}\cdot\mathbf{A}\right) + \lambda\left(\mathbf{D}\cdot\mathbf{A} + \mathbf{A}\cdot\mathbf{D} - \mathbf{D}:\mathbf{A}_4\right) + 2C_1\left|\mathbf{D}\right|\left(\boldsymbol{\delta} - 3\mathbf{A}\right) \quad , \qquad (2)$$

where $\mathbf{W} = [(\nabla v) - (\nabla v)^t]/2$, $\mathbf{D} = [(\nabla v) + (\nabla v)^t]/2$, ∇v is the velocity gradient, λ is a constant defining the ellipticity of the particle and C_1 is a constant named the interaction coefficient which is related to the magnitude of the inter-particle interactions. The first two terms in Eq. (2) correspond to the generalized Jeffery equation. For fibers it is common to assume the particle's aspect ratio approaches infinity and to use $\lambda = 1$.

As discussed later (Results and Discussion), the predictions using the generalized Jeffery equation will be compared to our experimental results. From this comparison our research shows that the generalized Jeffery equation overpredicts the rate of fiber reorientation. As a result, we are unable to predict the transient rheological behavior of these composite fluids. It is our hypothesis that this is a direct result of the fibers moving non-affinely with the suspending medium. To account for this behavior we add a term to the generalized Jeffery equation part in Eq. (2) referred to as the non-affine motion parameter, α. The resulting equation has the form

$$\frac{D\mathbf{A}}{Dt} = \alpha\left[\mathbf{A}\cdot\mathbf{W} - \mathbf{W}\cdot\mathbf{A} + \mathbf{D}\cdot\mathbf{A} + \mathbf{A}\cdot\mathbf{D} - \mathbf{D}:\mathbf{A}_4\right] \quad . \qquad (3)$$

The non-affine motion parameter effectively retards the rate of fiber reorientation predicted by the generalized Jeffery equation. Its values range between 0–1 and is thought to be function of fiber concentration, aspect ratio and the velocity gradient. Additionally, the non-affine parameter was used in the F-T model. Comparison between experimental data and model predictions for Jeffery and F-T model with and without the non-affine parameter can be found in the results and discussion section of this report.

Stress Contribution

With knowledge of the fiber orientation and deformation gradient the stresses can then be calculated from the following equation[4]:

$$\sigma = -P\boldsymbol{I} + 2\eta_s \boldsymbol{D} + 2\eta_s N_p \boldsymbol{D} : \boldsymbol{A}_4 \quad , \qquad (4)$$

where P is the isotropic pressure, η_s is the suspending medium viscosity, and N_p is a dimensionless parameter that describes the magnitude of the total hydrodynamic drag in the system. The terms on the right hand side of the equals sign are the contributions from the isotropic pressure, suspending medium, and hydrodynamic drag of the fluid on the fiber, respectively. The suspending medium viscosity, η_s, in Eq. (4) can be taken to be a constant for a Newtonian fluid, a generalized Newtonian fluid in which the viscosity depends on shear rate only and represented with an empiricism such as the Carreau-Yasuda model or predicted using a viscoelastic constitutive equation for fluids that exhibit both viscous and elastic responses. There are various theories for calculating N_p for dilute and semi-dilute systems (i.e., Dinh-Armstrong [4] and Shaqfeh-Fredrickson [5]), but none for concentrated systems. For our model predictions we fit N_p to the peak of the shear stress overshoot. This will be discussed in detail in the results and discussion section.

Theory: Model Development (Long Fibers)

It is of primary interest to try and extend the existing simulation approach for short glass fiber systems to long glass fiber systems. This has proven to be a difficult task, but we have come up with a possible approach by incorporating what we term a *flexibility parameter*, β, into the generalized Jeffery equation as follows:

$$\frac{D\boldsymbol{A}}{Dt} = \alpha\left[\boldsymbol{A}\cdot\boldsymbol{W} - \boldsymbol{W}\cdot\boldsymbol{A} + \boldsymbol{D}\cdot\boldsymbol{A} + \boldsymbol{A}\cdot\boldsymbol{D} - \beta\boldsymbol{D}:\boldsymbol{A}_4\right] \quad . \qquad (5)$$

In the generalized Jeffery equation the term $\boldsymbol{D}:\boldsymbol{A}_4$ is the term associated with stretch along the backbone of the fiber. If we take that same theory but treat the unit vector not as a unit vector along the backbone of the particle, as in Figure 4(a), but as a unit vector describing the end-to-end distance and average orientation state of the system, then we can control the amount of fiber flexibility by multiplying the term $\boldsymbol{D}:\boldsymbol{A}_4$ by some constant, β.

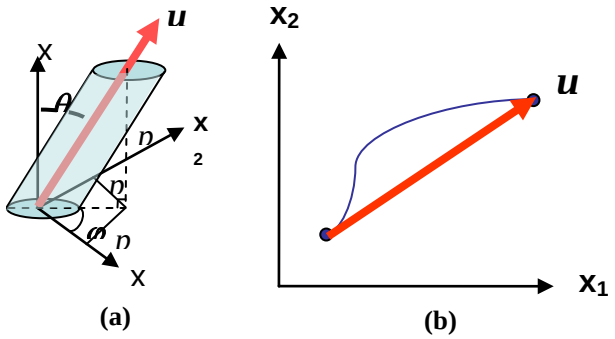

Figure 4. Unit vector **u**: (a) along the backbone of a rigid fiber, (b) an end-to-end vector representing the average position of a bent fiber.

The addition of this parameter β, has an interesting effect on the transient fiber orientation in start-up of flow. This can be seen in Figure 5 which is the A_{12}-component of the tensor **A** vs. strain. The magnitude of the shear stress is directly proportional to the magnitude of the A_{12}-component. From this figure one can see that an increase in β results in a decrease in the A_{12} component. Unfortunately, we currently do not have any rheological behavior of a long glass fiber system to compare to at this point (It is the emphasis of the continued research effort).

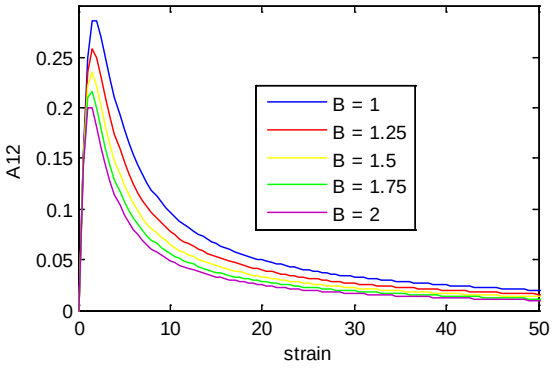

Figure 5. A_{12} component vs. strain for various β values in start-up of flow simulation.

Another approach to modeling long/flexible fiber systems is by simulating the dynamic behavior of individual fibers. This can be done in various ways but the most "straight forward" approach is to

begin with the theoretical work of Hinch [6] for an infinitely flexible fiber. In this theoretical development, the tension forces within the thread, *T*, are set equal to the viscous forces acting on the thread. As a result, two equations are formed, one describing *T* at discretized points along the thread, Eq. (6), and one defining the time rate of change of the nodal points as a function of *T*, Eq. (7).

$$\frac{\partial^2 T}{\partial s^2} - \frac{1}{2}\left(\frac{\partial^2 \vec{x}}{\partial s^2}\right) T = -\frac{\partial \vec{x}}{\partial s} \bullet \underline{\underline{D}} \bullet \frac{\partial \vec{x}}{\partial s} \quad . \tag{6}$$

$$\frac{\partial \vec{x}}{\partial t} = \underline{\underline{\nabla v}} \bullet \vec{x} + \frac{\partial T}{\partial s}\frac{\partial \vec{x}}{\partial s} + \frac{1}{2} T \frac{\partial^2 \vec{x}}{\partial s^2} \quad . \tag{7}$$

In Eqs. (6) and (7), *s* is the arc length, and ***x*** is the position vector. Given an initial fiber orientation, one can solve Eqs. (6) and (7) for the time rate of change of the fiber configuration. Model predictions for simple shear flow can be seen in Figure 6. Strain 0 relates to the initial fiber orientation and strains 1–4 show the evolution of orientation with a localized center of mass. This model predicts that, in simple flow, the fiber straightens and aligns itself with the flow direction.

In addition to Hinch's equation, Goddard and Huang [7] extended the work for a perfectly flexible fiber by encompassing the concept of mobility into the evolution equation. The Goddard and Huang model is described by

$$\frac{\partial \vec{x}}{\partial t} - K_L \frac{\partial T}{\partial s}\frac{\partial \vec{x}}{\partial s} = T \underline{\underline{K}}_T \bullet \frac{\partial^2 \vec{x}}{\partial s^2} + \vec{v}(\vec{x}, t) \tag{8}$$

and

$$-\frac{\partial \vec{x}}{\partial s} \bullet \frac{\partial \vec{v}(\vec{x},t)}{\partial s} = \frac{\partial}{\partial s}\left(K_L \frac{\partial T}{\partial s}\right) - \left(\frac{\partial^2 \vec{x}}{\partial s^2}\right) \bullet \left(K_L \underline{\underline{\delta}} + \underline{\underline{K}}_T\right) \bullet \left(\frac{\partial^2 \vec{x}}{\partial s^2}\right) T \quad , \tag{9}$$

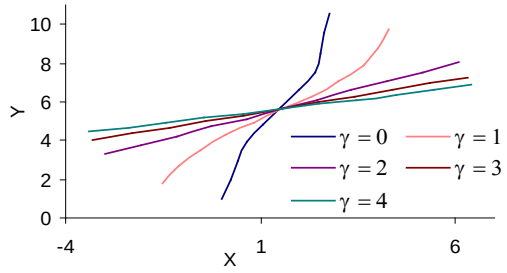

Figure 6. Model predictions for the Hinch infinitely flexible fiber in simple shear flow. Strain 0 relates to the initial orientation and strains 1–4 show the evolution of orientation with a common center of mass.

where the mobility tensor components K_L , K_n , and $\underline{\underline{K}}_T$ are denoted by the lateral mobility, the normal mobility, and the transverse mobility tensor, respectively. Again, T is the tension. This model suggests that in concentrated fiber suspensions there exists a preferred direction for the motion of a single fiber. The mobility tensor provides insight into the kinematic restrictions of a fiber caused by the presence of its neighbors. This restricted motion affects the orientation development of the fibers. Therefore, our future work will be to assess this model by studying the mobility tensor in simple shear flow, with the use of the sliding plate rheometer.

Lastly, a relatively recent model was published for semi-flexible fibers in dilute solutions by Strautins and Latz [8]. The authors construct a continuum model that provides a first approximation to flexibility. This is accomplished by modeling a fiber as two rods connected by a pivot allowing bead (Figure 7).

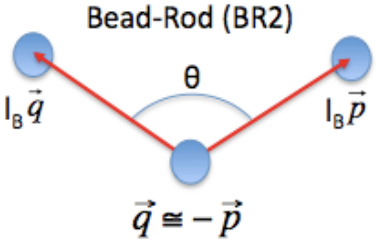

Figure 7. Fiber model, with segment length l_B, allowing semi-flexibility. The segment orientations are denoted by unit vectors $\vec{p}$ and $\vec{q}$, and are separated by an angle θ with some given bending rigidity.

The model considers the flexible fiber to consist of two rigid segments with length l_B that are allowed to slightly pivot about the connecting bead with some restorative bending rigidity, *k*. Both $\vec{p}$ and $\vec{q}$ are unit vectors that represent the orientation of the corresponding fiber segments with respect to the center bead. The tensor $\underline{\underline{\kappa}}$ is the velocity gradient. The model equations are developed and are given as

$$\frac{D\underline{\underline{A}}}{Dt} = \underline{\underline{A}}\cdot\underline{\underline{\kappa}}^T + \underline{\underline{\kappa}}\cdot\underline{\underline{A}} - [(\underline{\underline{\kappa}}+\underline{\underline{\kappa}}^T):\underline{\underline{A}}]\underline{\underline{A}} + \frac{l_B}{2}[\vec{C}\vec{\mu}+\vec{\mu}\vec{C}-2(\vec{\mu}\cdot\vec{C})\underline{\underline{A}}] - 2k[\underline{\underline{B}}-\underline{\underline{A}}\,tr(\underline{\underline{B}})] \quad , \qquad (10)$$

$$\frac{D\underline{\underline{B}}}{Dt} = \underline{\underline{B}}\cdot\underline{\underline{\kappa}}^T + \underline{\underline{\kappa}}\cdot\underline{\underline{B}} - [(\underline{\underline{\kappa}}+\underline{\underline{\kappa}}^T):\underline{\underline{A}}]\underline{\underline{B}} + \frac{l_B}{2}[\vec{C}\vec{\mu}+\vec{\mu}\vec{C}-2(\vec{\mu}\cdot\vec{C})\underline{\underline{B}}] - 2k[\underline{\underline{A}}-\underline{\underline{B}}\,tr(\underline{\underline{B}})] \quad , \qquad (11)$$

$$\frac{D\vec{C}}{Dt} = \underline{\underline{\kappa}}\cdot\vec{C} - (\underline{\underline{A}}:\underline{\underline{\kappa}})\vec{C} + \frac{l_B}{2}[\vec{\mu}-\vec{C}(\vec{\mu}\cdot\vec{C})] - k\vec{C}[1-(tr(\underline{\underline{B}})] \quad , \qquad (12)$$

and

$$\vec{\mu} = \sum_{i=1}^{3}\left(\sum_{j=1}^{3}\sum_{k=1}^{3}\frac{\partial^2 v_i}{\partial x_j \partial x_k}A_{jk}\right)\vec{e}_i \quad , \qquad (13)$$

where the two orientation tensors represent the second moment of the distribution function of the unit vectors, $\vec{p}$ and $\vec{q}$, in the following manner:

$$\underline{\underline{A}} = \int \vec{p}\,\vec{p}\;\psi(\vec{p},\vec{q})\,d\vec{p}\,d\vec{q} \quad , \qquad (14)$$

$$\underline{\underline{B}} = \int \vec{p}\,\vec{q}\;\psi(\vec{p},\vec{q})\,d\vec{p}\,d\vec{q} \quad . \qquad (15)$$

As a direct consequence to the bending rigidity, encompassed within the model parameter *k*, the expectancy of a segment orientation (with respect to the orientation distribution function) may be nonzero in general and is accounted for in Eq. (12) by the following definition:

$$\vec{C} = \int \vec{p}\;\psi(\vec{p},\vec{q})\,d\vec{p}\,d\vec{q} \quad . \qquad (16)$$

Lastly, Eq. (13) contributes second order derivatives of the velocity field that originate from a Taylor series approximation applied to the bead kinematics. In simple shear flow, for example, all components are *0*. This vector, in Eq. (13), is formed by the unit dyads $\vec{e}_i$.

Our future work will center on determining how well this model describes long fiber orientation. Currently, the bead-rod model is being explored for the case of a center gated disk, for which preliminary results have been obtained. It is also within our interest to understand what length scales this model best describes. It is believed that these efforts will greatly enhance our understanding of long fiber evolution.

Experimental Results vs. Model Predictions

Subsequently, we compared model predictions of startup of flow to that of experimental results obtained using the 30 wt% short glass fiber-filled PBT. First, we consider predictions using the generalized Jeffery equation, Eq. (2), in combination with Eq. (4) defining the stress contribution. Figure 8(a) depicts the model predictions for both the shear stress and first normal stress difference vs. strain in which the material parameters C_1 (from Bay and Tucker [9]) and N_p (from Dinh-Armstrong [4]) are calculated directly from current theory. These predictions are plotted in combination with the experimental rheological behavior. First, the model does predict an overshoot in both the shear and first normal stress difference. However, the model is incapable of predicting the magnitude or the width of either overshoot. It is our hypothesis that being able to predict this transient overshoot behavior is the key to then being able to predict the fiber orientation in the complex flow simulations.

To improve on the model predictions, we incorporated the non-affine motion term, Eq. (3), and fit the material parameters instead of calculate them based on theory. N_p we fit to the peak of the shear stress overshoot and α we fit to the width of the shear stress overshoot. Model predictions using this approach compared to the experimental results can be seen in Figure 8(b). Now we come much closer to predicting the transient behavior of both the shear and first normal stress difference.

(a)

(b)

Figure 8. Experimental results compared to model predictions for the transient stresses in start-up of flow at a shear rate of $1s^{-1}$. (a) Model predictions using current theory to calculate C_1 and N_p. (b) Model predictions incorporating non-affine motion and parameters fit to transient shear overshoot.

Measurement of Fiber Orientation

To characterize the evolving fiber orientation under dynamic conditions, donut samples composed of PBT-30 were deformed using the RMS-800 with the cone and plate geometry at a shear rate of 1 s^{-1} for a specified amount of time at 260°C in a nitrogen environment. Directly after the applied deformation, the sample temperature was lowered below the suspension melt temperature. The samples were then bisected at the center of the sample creating a plane perpendicular to the flow direction, encapsulated in epoxy and sanded/polished to a final abrasive particle size of 0.3 μm Al_2O_3 following standardized techniques. Images of the polished surface were taken using a Zeiss LSM510 confocal laser scanning microscope fitted with a 40× water immersion objective lens and a laser excitation wavelength of 543 nm. The confocal laser is able to focus on the sample surface and penetrate the sample to a depth of 10 μm. This allows us to construct a 3-D image of the fiber orientation. For each sample, ten sequential images were taken from the bottom of the donut sample to the top at a position of 22 mm from the center. An illustration depicting the position at which the pictures were taken can be seen in Figure 1. The cross-section of each fiber appears as a circle or an ellipse. To process the image, the circumference of each ellipse was traced by hand in Power Point to improve the contrast between the fibers and the matrix. A simple computer program was written combined with image analysis software in MATLAB that measured the position of the center of mass, the major and minor axis and θ angle of each ellipse. For each sample, the total number of ellipses analyzed varied from 321 for strain = 4 to roughly 456 for strain = 200.

Figure 9(a) shows experimental results (points) and model predictions using the generalized Jeffery equation (Jeff_A_{ii}) for the diagonal components of the tensor **A**. From this figure it is easy to see that the generalized Jeffery equation overpredicts the rate of fiber reorientation. We believe this is a result of direct fiber contact. Figure 9(b) depicts the experimentally determined A_{11}-component with various model predictions using the generalized Jeffery combined with the calculated F-T constant, Jeff+F-T(calc.)_A_{11}, and the generalized Jeffery combined with slip parameter fit to the transient rheology and the F-T constant fit to the steady state orientation value, Jeff(w/slip)+F-T(fit)_A_{11}. With the addition of the non-affine motion parameter and by fitting C_1 to the steady state orientation, we come much closer to predicting the dynamic behavior of the fiber.

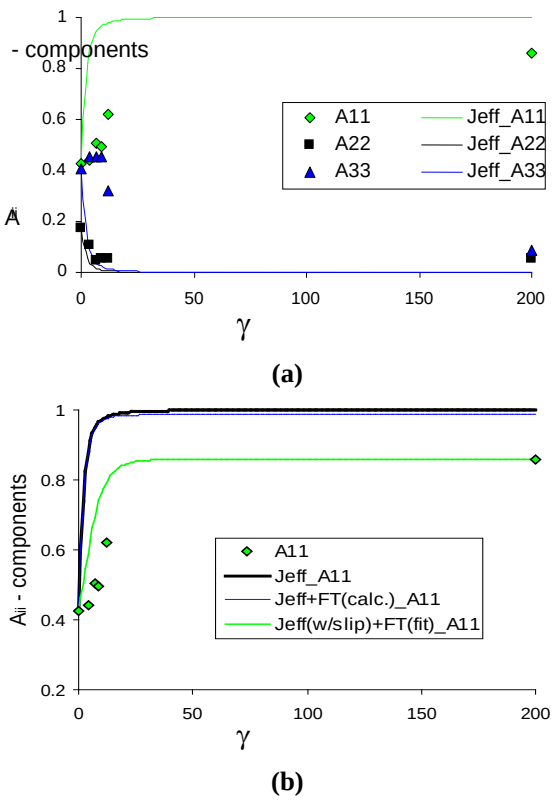

Figure 9. Experimental results from confocal laser microscopy compared to model predictions for start-up of flow vs. strain at a shear rate of 1 s^{-1}.
(a) Experimental results (points) and model predictions using the generalized Jeffery equation (Jeff_A_{ii}) for the diagonal components of the tensor **A**. (b) Experimental results of the A_{11}-component (points), model predictions with the generalized Jeffery equation plus theoretically calculated F-T constant [Jeff+F-T(calc.)-A_{11}], model predictions with the generalized Jeffery equation plus the fit non-affine motion term α F-T constant fit to the steady state orientation [Jeff(w/slip)+F-T(fit)-A_{11}].

Injection Molded Samples/Fiber Orientation Analysis

The experimental program dealing with the injection molding of parts was finished last year. It consisted of a study including four factors (i.e., matrix material, geometry, fiber length, and part thickness of cavity, in 12 combinations). The fiber concentration was chosen to be a constant parameter and selected to be in the concentration range of 30 wt%, typically found in commercially used composites. Figure 10 depicts the factors and combinations involved in the experimental program. The parts were molded to obtain short shots of 75% of the dimension of the full part. A center-gated disk of 1.3 mm in thickness, PBT matrix and fibers 500 μm have been analyzed. For this part, the short shot size (R) was determined as the difference of the outer minus inner radius. The evaluation of the orientation was performed using the method of ellipses with images taken from confocal laser microscopy following several publications of Clarke's group [10]. Figure 12 depicts the experimental profile of orientation component A_{11} along the height of the cavity (z-dir) in the gate 0R, 0.4R, and 0.9R. An asymmetric orientation profile can be seen at the gate region, which corroborates predictions indicated in the literature but never validated e.g., VerWeyst and Tucker [11] and Chung and Kwon [12]. This experimental result is important for assessing our simulations because the orientation needs to be prescribed at the gate. In the literature, the gate orientation has typically been assumed constant (random or averaged), especially for a center-gated disk. Figure 11 shows that the fibers aligned in the flow direction close to the walls, far away from the gate. However, A_{11} profiles are still asymmetric.

The confocal laser microscopy (CLM) technique used to determine the experimental orientation has similar ambiguity problems that are inherent to reflection microscopy techniques for the complex flow experiments. The penetration of the laser beam is limited to 5 μm due to the opacity of the matrix. The differences in the ellipses between images at the surface and at 5 μm below the surface are only perceptible for fibers with a large zenith angle. Therefore, there is an ambiguity for fibers almost perpendicular to the surface plane. A weakness in the CLM technique is the inability to detect fibers parallel to the surface plane inspected. This problem is evident in the regions close to the wall when the r,z-plane is analyzed. Figure 11 shows this limitation for the positions 0.0R and 0.4R. An alternative method is under development using the recommendations of Bay and Tucker consisting of images taken from two mutually perpendicular planes. A medical grade X-ray computed tomography was used to determine the orientation of fibers below the polished plane, but the resolution of the instrument was not good enough to obtain clear images of the fibers.

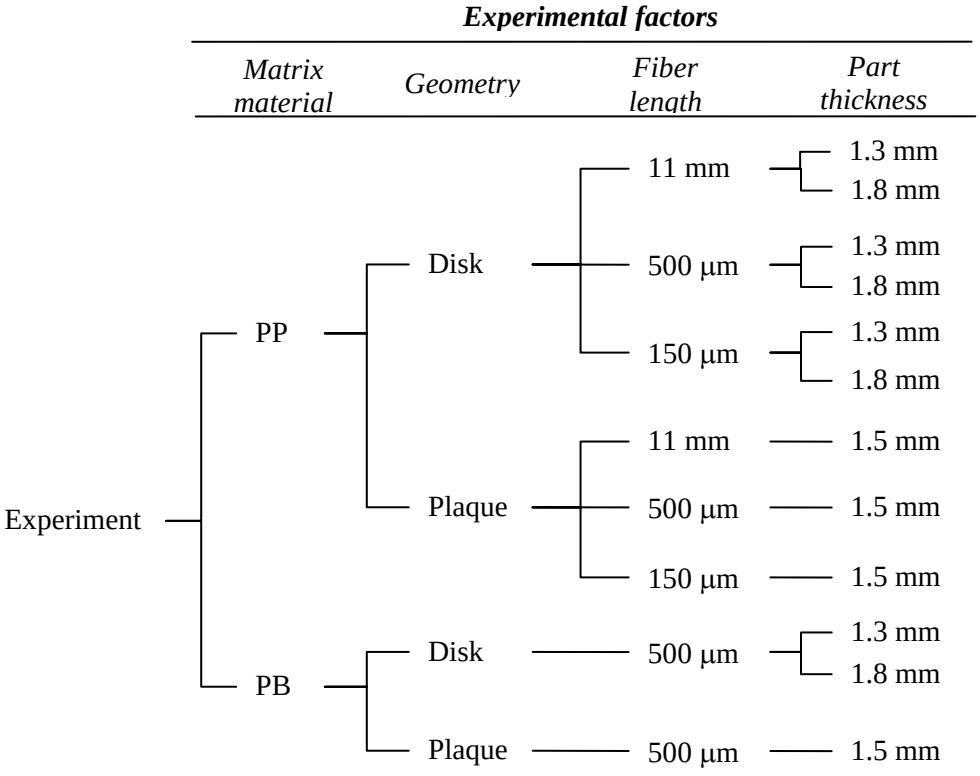

Figure 10. Experimental design.

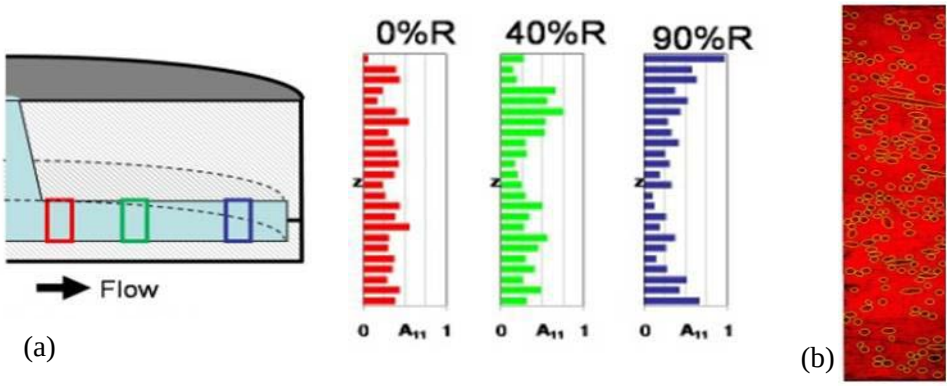

Figure 11. (a) Distribution of orientation component A_{11} along the gapwise direction in a center gated disk at 0%R, 40%R, and 90%R. (b) The typical images obtained by using confocal laser microscopy for the 30 wt% glass fiber-filled PBT.

A method for orientation and image analysis script has been developed to compute unambiguous values of the orientation tensor. This method consists of plasma etching of a polished plane with the purpose of excavating the surface surrounding the fibers. With this process, the fiber borders become exposed, allowing the fiber's unambiguous orientation to be detected and measured with the use of microscopy and digital imaging. The contribution of Vlastimil Kunc form Oak Ridge National Laboratory in the development of the modified method and the image-analysis tool should be noted.

Simulation

Short Glass Fibers

The generalized Jeffery equation containing the non-affine motion parameter, Eq. (5), and the Folgar-Tucker term, last term in Eq. (2), was implemented in the simulation package. In addition various closure approximations have been implemented which include the quadratic, hybrid, linear and Invariant Based Optimal Fitting (IBOF).

Decoupled Simulations Using Delayed Generalized Jeffery Model

Figure 12(a) shows the measured orientation at the top half of the gate (-x- symbol) and 0.9R (-•- symbol) for PBT filled with short glass fiber and the prediction at 0.9R using only Jeffery's model with measured orientation values at the gate (continuous line). The prediction using measured gate orientation shows several peaks and valleys that can be related to the layered structure formed at the gate which evolves locally as the flow progresses. The predicted profile at 0.9R can reproduce, at least qualitatively and in some regions quantitatively, the experimental profile. This is in sharp contrast with predictions using a random orientation at the gate (dashed line) or a prescribed constant orientation at the gate (not shown) which fail to show the layered structure.

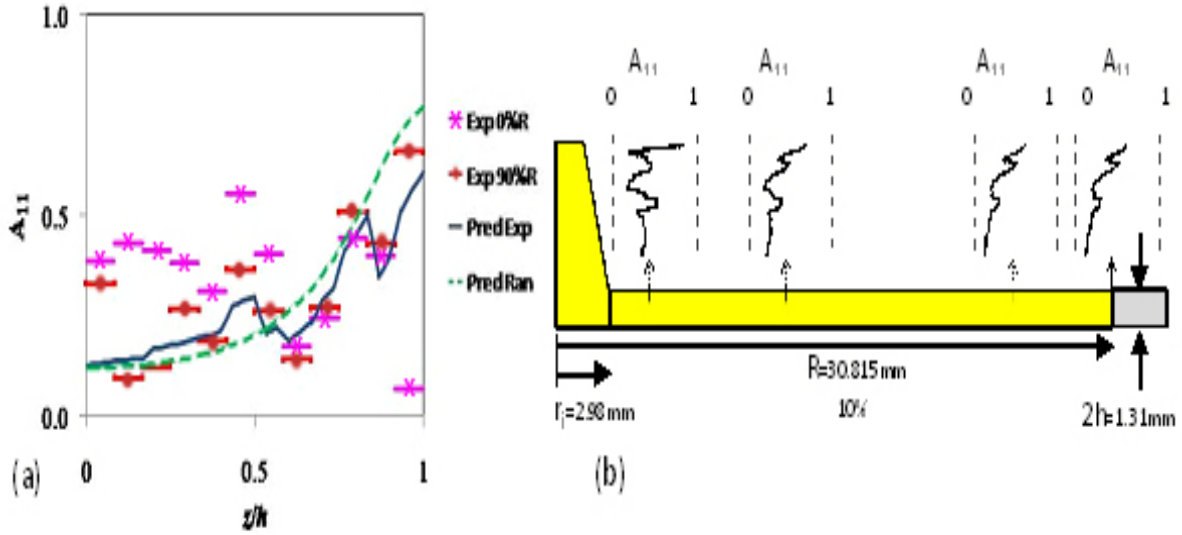

Figure 12. (a) Experimental values of A_{11} at the gate and close to the end of the mold (90% of radial flow length) with the predicted values of A_{11} orientation component close to the end of fill using random or measured orientation at the gate. (b) Evolution of orientation in a 75% short shot showing a layered structure expressed through the predicted A_{11} profiles at several locations in the top half of the disk.

These two gate orientations are always used in injection molding simulations and result in similar orientation profiles. All simulations fail to predict the measured orientation for the segment next to the axis of symmetry, the reason for this needs further investigation. Results for the orientation component A_{11} using piecewise gate orientation suggest a fading effect of the initial multilayered structure forming at least a shell-transition-core layer structure at long radial distances from the gate, as illustrated in Figure 12(b). A similar effect has been observed for the other dominant orientation component, A_{33}. The inter-particle interactions through the Folgar-Tucker term (C_I=0.001) were considered in the model to try to improve the predictions obtained with the Jeffery model. However, the predictions using the additional terms with experimental piecewise initial orientation produced only slight changes in the predicted orientation, almost overlapping the predictions obtained using the Jeffery's model. Increasing the value of C_I to values in the range of 0.016 to 0.003, commonly found in the literature (e.g., Larson [13] and Folgar and Tucker [2]), also did not significantly change the orientation predictions.

Decoupled Simulations Using the Delayed Folgar-Tucker Model

Figures 13(a) and (b) show decoupled simulation results for the radial locations of 40% and 90% (R-r_i), respectively, focused on the upper half cavity at a dimensionless simulation time of 290. These predictions (lines) overestimate the A_{rr} orientation components while they underestimate the $A_{\theta\theta}$ and A_{rz} orientation components, when compared to experimental results (symbols). The smooth predicted profile could not reproduce a series of peaks and valleys observed in the experimental profile of orientation. These features in the orientation profile can be related to the layered structure formed at the gate, which evolves locally as the flow progresses as indicated in the previous paragraph. However, when the experimental orientation profile is compared with simulation results at a dimensionless simulation time of 2.90 (1% of the simulation time), the values and features of orientation are successfully reproduced. This implies that the decoupled simulation using the delayed Folgar-Tucker model is evolving faster than the experimental evolution of orientation.

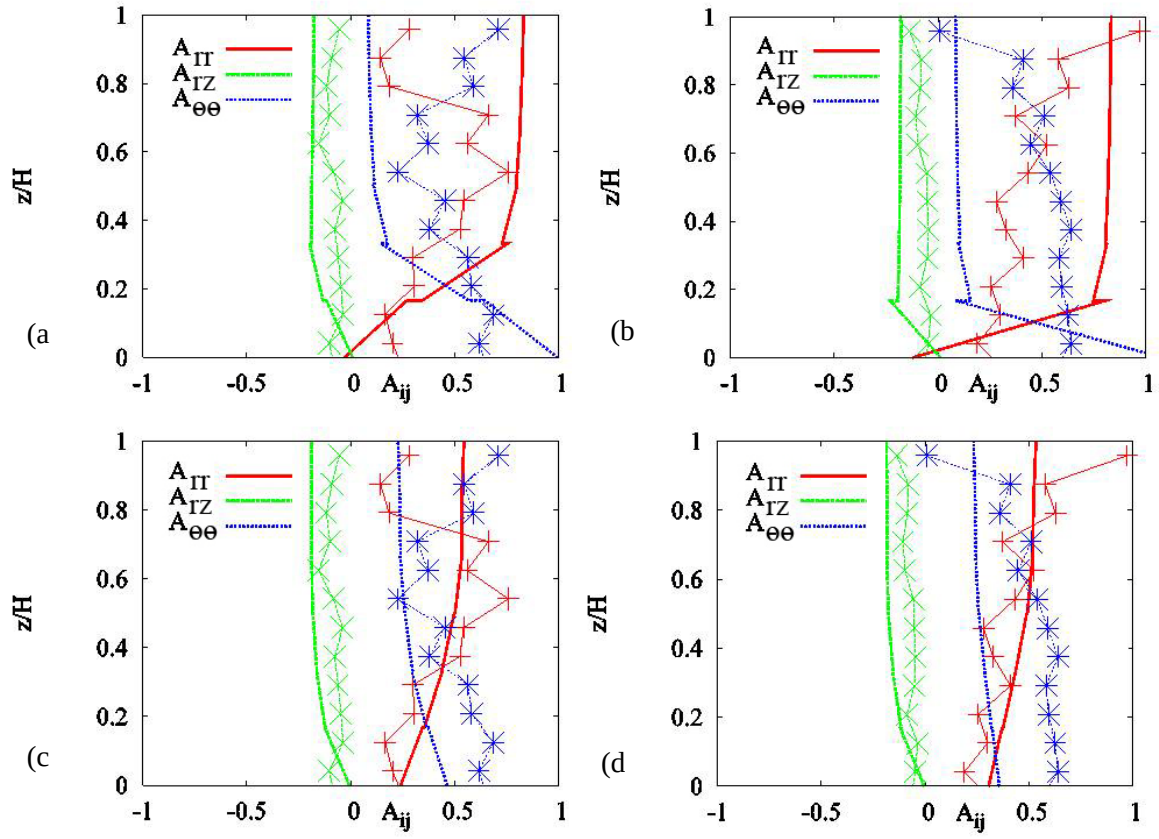

Figure 13. Experimental and predicted orientations from decoupled simulation at (a) 40% (R-r_i), and (b) 90% (R-r_i) and coupled simulation at (c) 40% (R-r_i) and (d) 90% (R-r_i). These simulations were run at a dimensionless time of 290. The lines denote the predictions, while the symbols are used to indicate the experimental results.

Coupled Simulations Using Delayed Folgar-Tucker Model

The results of the coupled simulation show improvement in the prediction of the orientation profile. Figure 13 depicts the upper half of the orientation profile at a dimensionless time of 290 for (c) 40% (R-r_i), and (d) 90% (R-r_i). The results are sensitive to the use of the delayed Folgar-Tucker model because the retardation of evolution considerably improves the prediction of A_{rr}, but the profile of the predicted orientation is smooth.

In general the $A_{\theta\theta}$ is under estimated, but not as severely as in the decoupled approach. An interesting observation in coupled simulations is that the difference between experimental and predicted $A_{\theta\theta}$ is greater at 90% (R-r_i) than at 40% (R-r_i). This can be an effect of using the Hele-Shaw approximation, because this simplification ignores the existence of the flow front. It is well known that the front is a region dominated by extensional flow that is the driving mechanism for $A_{\theta\theta}$. Therefore, these coupled results suggest the need for full simulations, which are especially important in small geometries where the evolution of orientation never reaches the stable structure of orientation.

Long Glass Fibers

The generalized Jeffery equation containing the flexibility parameter, Eq. (5), was implemented in the simulation package. The flexibility parameter accounts for the flexibility of the fibers in a simplified manner. The idea was to evaluate the flexibility as a shrinkage occurring in the end-to-end vector of long glass fibers. To evaluate the model, simulations for short glass fiber PBT composites were performed. Long glass fiber 3-D orientation determination was attempted using a micro X-Ray tomography instrument at Virginia Tech, but the resolution of the instrument was not enough to obtain reliable orientation results. Figure 14 illustrates the experimental and predicted orientation profile for the A_{11} components at 0.4R (a) and 0.9R (b) when the flexibility of the fibers is considered. The continuous line indicates the predictions for the Jeffery's model (β=1) while the dashed line the predictions for Jeffery's model with flexibility parameter β=0.80. The results indicate that the model does not change significantly in the core region with the addition of the β parameter but causes a slight increase in the predictions for A_{11} close to the wall. In order to predict the orientation in a more robust way, the approach of the approach of the bead-rod model in a flow-driven system recently introduced by Strautins and Latz[8] was written into the simulation package.

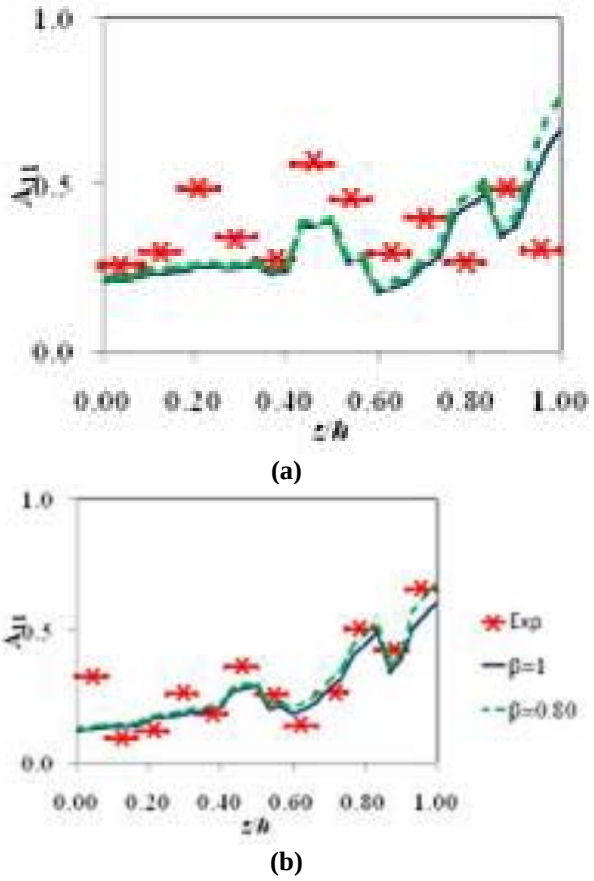

Figure 14. Predicted and experimental values of A_{11} at 0.40R (a) and 90R% (b) of a center-gated disk for the Jeffery model with β=1 and β=0.80 for the 30 wt% glass fiber-filled PBT.

In an effort to obtain preliminary results, the bead-rod model was used to simulate the case of a center-gated disk with random initial orientation at the gate. The simulation was performed with a velocity field obtained from parallel disk flow. The simulation results for the fiber orientation were then compared to experimentally determined orientations analyzed at 40% of the short shot length. Similar to the simulations conducted by the model's author (Strautins and Latz [8]), the parameter k is presently set equal to a dimensionless value of *0.5*. An analysis of this parameter's value will be conducted in the future to ensure its legitimacy. Additionally, the segment length l_B was given a dimensionless value that approximately corresponds to 0.5 mm; however, long fiber attrition data is currently being obtained for model length accuracy. The numerical results and experimental data are depicted in Figure 15. For comparison, a simulation using the Folgar-

Tucker model (with CI = 0.01) is also presented in this figure.

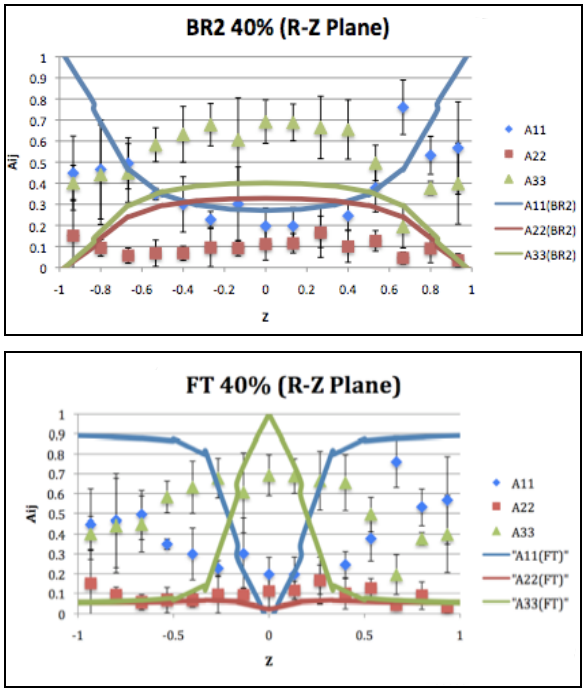

Figure 15. (top) Bead-Rod (BR2) and (bottom) Folgar-Tucker (F-T) simulation and experimentally measured results, for the trace components of the orientation tensor, versus the dimensionless mold thickness at 40% of the center gated disk length. The components are given by "r = 1," "z = 2," "θ = 3."

Preliminary results for the bead-rod simulation predict a much broader orientation distribution compared to what was obtained using the Folgar-Tucker model, which appears to more correctly describe the qualitative shape of the experimentally measured orientations. Additionally, an improvement in the A_{11} component is noticeable, but the A_{33} component is still underpredicted. More experimentation, however, is still in need before a complete opinion of this model's validity can be made. Future experiments will focus on fiber length and model parameter effects. Model predictions will then be compared to experiments for validation.

Conclusions

Short Glass Fiber Suspensions

We have determined a constitutive equation capable of predicting the transient rheological behavior of short glass fiber-filled polymeric fluids. In addition we have developed a method to determine unique material parameters that are independent of shear rate. In general, we have developed a scheme which allows us to obtain the fundamental parameters from simple shear flow and then incorporate these into the simulation package. This is an improvement over the existing approach which using injection molding data (which is what one is trying to simulate). We have also developed a coupled approach in which the velocity field and orientation are calculated simultaneously. The simulations indicate that the orientation measured at the gate is crucial in obtaining the correct orientation pattern inside the cavity. (It has been assumed to be random to date.)

Long Glass Fiber Suspensions

We have designed and fabricated a sliding plate rheometer primarily for the purpose of performing unbiased and reproducible rheological experiments on long glass fiber-filled polymeric fluids that are otherwise impossible to perform on rotational rheometers. In addition, we have developed a simple approach to incorporate fiber flexibility into existing simulation structures for short glass fiber suspensions by incorporating a flexibility parameter β. Also, the bead-rod model presented within this research was shown to produce broad orientation distributions, a characteristic that preliminary results show to be consistent with long fiber flexibility. The bead-rod model is currently being assessed to see if it can correctly explain the dynamics of long fibers in complex flow. Lastly, an extension of Hinch's equation was written for tracking single fibers in concentrated polymer solutions. The use of this model in cooperation with parallel plate experiments will be used to gain further knowledge of long fiber dynamics through the use of mobility. The thrust of the future efforts will be on predicting orientation and configuration of long fibers during molding (compression and injection molding).

Publications as a Result of this Work

1. G. M. Velez, K. Ortman, A. P. R. Eberle, P. Wapperom, and D. G. Baird, "Simulation of Orientation in Injection Molding of a Highly Concentrated, Short Glass Fiber

Thermoplastic Composites," *SPE ANTEC Technical Paper*, accepted on Jan 2009.
2. K. Ortman, P. Wapperom, and D. G. Baird, "Long Glass Fiber Orientation in Thermoplastic Composites Using a Model that Accounts for the Flexibility of the Fibers," *SPE ANTEC Technical Paper*, accepted on Jan 2009.
3. P. R. Eberle, D. G. Baird, P. Wapperom, and G. M. Velez-Garcia, "Obtaining Reliable Transient Rheological Data on Concentrated Short Fiber Suspensions Using a Rotational Rheometer," J. Rheol., Accepted.
4. P. R. Eberle, G. M. Velez-Garcia, D. G. Baird, and P. Wapperom, "Fiber Orientation Kinetics of a Concentrated Short Glass Fiber Suspension in Startup of Simple Shear Flow," J. Non-Newt. Fl. Mech., submitted.
5. P. R. Eberle, D. G. Baird, P. Wapperom, and G. M. Velez-Garcia, "Using Transient Rheology to Determine Material Parameters in Fiber Suspension Theory," J. Rheol., accepted.
6. G. M. Velez, K. Ortman, A. P. R. Eberle, P. Wapperom, and D. G. Baird, "2-D Simulations of Orientation in Highly Concentrated Short Glass Fiber Thermoplastic Composites Made by Injection Molding," *Proceedings of the PPS Americas Regional Meeting*, Charleston, South Carolina, 26–29 October 2008.
7. K. Ortman, D. G. Baird, and P. Wapperom, "Long Glass Fiber Orientation in Thermoplastic Composites Using a Model that Accounts for Flexibility of the Fibers," *Proceedings of the PPS Americas Regional Meeting*, Charleston, South Carolina, 26–29 October 2008.
8. A. P. R. Eberle, G. M. Velez, P. Wapperom, and D. G. Baird, "Fiber Orientation Kinetics of a Concentrated Short Glass Fiber Suspension in Start Up of Shear Flow," *Proceedings of the PPS Americas Regional Meeting*, Charleston, South Carolina, 26–29 October 2008.
9. G. M. Velez, K. Ortman, A. P. R. Eberle, P. Wapperom, and D.G. Baird, "Simulation of Orientation in Injection Molding of High Aspect Ratio Particle Thermoplastic Composites," *Proceedings of the XVth International Congress of Rheology*, Monterey, California, 3–8 August 2008.
10. A. P. R. Eberle, G. M. Velez, D. G. Baird, and P. Wapperom, "The Dynamic Behavior of a Concentrated Non-Brownian Glass Fiber Suspension in Simple Shear Flow," *Proceedings of the XVth International Congress of Rheology*, Monterey, California, 3–8 August 2008.
11. A. P. R. Eberle, D. G. Baird, and P. Wapperom, "The rheology of non-Newtonian fluids containing glass fibers: A review of experimental literature," Ind. Eng. Chem. Res., 47:9, 2849–2872 (2008).
12. A. P. R. Eberle, G. M. Velez, D. G. Baird, and P. Wapperom, "The Dynamic Behavior of a Concentrated Polymeric Suspension Containing Non-Brownian Glass Fibers in Simple Shear Flow," *SPE ANTEC Technical Paper*, **2008**, 868–872.

Presentations Directly Related to this Work (underline denotes presenting author)

1. G. M. Velez, K. Ortman, A. P. R. Eberle, P. Wapperom, and D. G. Baird, "Frontal Flow Effects in 2D Simulations of Orientation in High Aspect ratio Particles Composites Made by Injection Molding," *AIChe Annual Meeting*, Philadelphia, PA, USA, November 2008.
2. K. Ortman, G. M. Velez, A. P. R. Eberle, D. G. Baird, and P. Wapperom, "Long Glass Fiber Orientation in Thermoplastic Composites Using a Model that Accounts for the Flexibility of Fibers," *AIChe Annual Meeting*, Philadelphia, PA, USA, November 2008.
3. A. P. R. Eberle, G. M. Velez, D. G. Baird, and P. Wapperom, "Shear Rheology and Microstructure of a Concentrated Short Glass Fiber-Filled Polybutylene Terephtalate (PBT)," *AIChe Annual Meeting*, Philadelphia, PA, USA, November 2008.
4. G. M. Velez, A. P. R. Eberle, K. Ortman, P. Wapperom, and D. G. Baird, "2-D Simulations of orientation in Highly Concentrated Short Glass Fiber Thermoplastic Composites Made by Injection Molding," *PPS Regional Meeting*, Charleston, SC, USA, October 2008.
5. K. Ortman, G. M. Velez, A. P. R. Eberle, P. Wapperom, and D. G. Baird, "Long Glass

Fiber Orientation in Thermoplastic Composites Using a Model that Accounts for Flexibility of the Fibers," *PPS Regional Meeting*, Charleston, SC, USA, October 2008.
6. A. P. R. Eberle, D. G. Baird, P. Wapperom, and G. M. Velez, "Fiber Orientation Kinetics of a Concentrated Short Glass Fiber Suspension in Start Up of Shear Flow," *PPS Regional Meeting*, Charleston, SC, USA, October 2008.
7. G. M. Velez, A. P. R. Eberle, K. Ortman, P. Wapperom, and D. G. Baird, "Simulation of Orientation in Injection Molding of High Aspect Ratio Particle Thermoplastic Composites," *XVth International Congress of Rheology*, Monterey, CA, August 2008.
8. A. P. R. Eberle, G. M. Velez, D. G. Baird, and P. Wapperom, "The Dynamic Behavior of a Concentrated Non-Brownian Glass Fiber Suspension in Simple Shear Flow," *XVth International Congress of Rheology*, Monterey, CA, August 2008.
9. D. G. Baird, "Rheology and Simulation of Flows of Polymeric Fluids Containing Rigid and Flexible Fibers," University of Naples, June 13, 2008.
10. A. P. R. Eberle, G. M. Velez, D. G. Baird, and P. Wapperom, "The Dynamic Behavior of Concentrated Polymeric Suspension Containing Non-Brownian Glass Fibers," *SPE ANTEC Annual Technical Conference*, Milwaukee, WI, USA, May 2008.
11. A. P. R. Eberle, G. M. Velez, D. G. Baird, and P. Wapperom, "The Dynamic Behavior of Concentrated Non-Brownian Glass Fiber Suspensions," *Invited lecture: Virginia Tech*, Blacksburg, VA, March 2008.
12. A. P. R. Eberle, G. M. Velez, D. G. Baird, and P. Wapperom, "The Dynamic Behavior of Non-Brownian Glass Fiber Suspensions," *Invited lecture: University of Delaware*, Newark, DE, January 2008.

References

1. S. G. Advani and C. L. Tucker, "The use of tensors to describe and predict fiber orientation in short fiber composites," J Rheol **31** (8), 751–784 (1987).
2. F.P. Folgar and C. L. Tucker, "Orientation behavior of fibers in concentrated suspensions," J Reinf Plast Comp **3**, 98–119 (1984).
3. G. B. Jeffery, "The motion of ellipsoidal particles immersed in a viscous fluid," Proc. R. Soc. A **102**, 161–179 (1922).
4. S. M. Dinh and R. C. Armstrong, "A rheological equation of state for semi-concentrated fiber suspensions," Journal of Rheology **28** (3), 207–227 (1984).
5. E.S.G. Shaqfeh and G. H. Fredrickson, "The hydrodynamic stress in a suspension of rods," Phys Fluids A-Fluid **2** (1), 7–24 (1990).
6. E. J. Hinch, "The distortion of a flexible inextensible thread in a shearing flow," *J Fluid Mech* **74**, 317–333 (1976).
7. J. D. Goddard and Y. H. Hung, "On the motion of flexible threads in a Stoke's shear field," J Non-Newton Fluid Mech **13**, 47–62 (1983).
8. U. Strautins and A. Latz, "Flow-driven orientation dynamics of semi-flexible fiber systems," *Rheol Acta* **46**, 1057–1064 (2007).
9. R. S. Bay and C. L. Tucker, "Stereological measurement and error estimates for three-dimensional fiber orientation," Polym Eng Sci **32** (4), 240–253 (1992).
10. C. Eberhardt and A. Clarke, "Fibre-orientation measurements in short-glass-fibre composites. Part I: automated, high-angular-resolution measurement by confocal microscopy," Composites Science and Technology **61**, 1389–1400 (2001); A.R. Clarke, Eberhardt, C.N., *Microscopy techniques for materials science* (CRC Press Boca Raton, FL, 2002).
11. B. E. VerWeyst and C. L. Tucker, "Fiber suspensions in complex geometries flow/orientation coupling," Can J Chem Eng **80**, 1093–1106 (2002).
12. D. H. Chung and T. H. Kwon, "Numerical studies of fiber suspensions in an axisymmetric radial diverging flow: the effects of modeling and numerical assumptions," J. Non-Newtonian Fluid Mech. **107**, 67–96 (2002).
13. R. G. Larson, *The structure and rheology of complex fluids*. (Oxford University Press, New York, 1999).

N. Incorporating Higher-Order Tensors in the Computation of Polymer Composite Mechanical Properties

Principal Investigator: Douglas E. Smith
University of Missouri
E2411 Lafferre Hall/MAE Dept., Columbia, MO 65211
(573) 884-6552; fax: (573) 884-5090; e-mail: smithdoug@missouri.edu

Technology Area Development Manager: Joseph A. Carpenter
(202) 586-1022; fax: (202) 586-1600; e-mail: joseph.carpenter@ee.doe.gov

Participants: David A. Jack, Elijah C. Caselman and Joseph Middleton, University of Missouri

---

Contractor: University of Missouri
Contract No.: NSF Grant DMI-0522694

Objective

- Develop a predictive capability that incorporates higher-order orientation tensors to evaluate mechanical properties of short- and long-fiber reinforced polymer composites.

Approach

- Develop a model for predicting mechanical properties from higher-order orientation tensors derived from flow simulations or measurements that are not limited by the material symmetry requirements imposed by current models.
- Develop an automated three-dimensional (3D) voxel-based finite element modeling technique that may be used to predict the effective mechanical properties of short- and long-fiber suspensions.
- Integrate Micro-CT derived fiber reconstructions (obtained from industry or DOE) to illustrate the applicability of the proposed approach on production hardware.
- Perform a statistical assessment of mechanical property calculations to address sampling issues associated with using the proposed averaging techniques.
- Demonstrate the proposed methodology on an industrially-relevant polymer composite product where flow simulation software is to be provided by Moldflow Corporation.

Accomplishments

- Derived an analytical relationship between elastic mechanical properties and fiber orientation tensors for statistically independent short fibers, including both the property's mean and variance.
- Evaluated mechanical properties using existing property models from simple melt flow simulations that employ 4^{th} and 6^{th} order tensor closures.
- Developed a Monte Carlo method for computing mean and variance of elastic properties of short fiber composites from fiber orientation distribution functions.
- Evaluated mechanical properties of short fiber composites via Monte Carlo sampling procedures, validating analytical approach developed as part of this project.
- Developed a 3D voxel-based finite element model using a Representative Volume Element (RVE) and related periodic boundary conditions for predicting elastic material properties of short and long fiber polymer composites.

- Computed elastic properties for continuous, short aligned, and short random fiber composites and compared results with existing analytical models using the 3D voxel-based finite element modeling approach.
- Computed elastic properties for a long random fiber composite sample using the 3D voxel-based finite element modeling approach where fiber locations were determined from Micro-CT scans provided by Oak Ridge National Laboratory.

Future Direction

- Continue verification work for the 3D voxel-based finite element procedure for fiber reinforced polymer composites.
- Integrate 3D voxel-based finite element approach with loaded CT testing to better understand the local and global structural behavior of long fiber composites.
- Apply 3D voxel-based finite element approach to predict the structural response of actual products made of long fiber composite materials.
- Continue to develop an automated procedure for defining three-dimensional finite element models of a representative cell that may be used with analytically derived fiber orientation distribution functions, or fiber orientation states obtained from Micro-CT measurements.
- Develop computational approach to evaluate 3D long fiber locations and orientations from polymer flow simulations.
- Develop fracture analysis capability for 3D voxel-based finite element procedure.

Introduction

The purpose of this project is to develop a predictive capability that incorporates higher-order orientation tensors to evaluate mechanical properties of short- and long-fiber reinforced polymer composites. To realize this goal, the project will develop a computational methodology to predict elastic mechanical properties from orientation tensors of second- and fourth-order which are computed during melt flow simulations. The micromechanics of both short- and long-fiber suspension will be simulated with a three-dimensional (3D) voxel-based finite element modeling approach, so that the mechanical properties of randomly oriented fiber samples can be computed. Simulated fiber orientation states, as well as those obtained from Micro-CT scans will serve as input. Finally, fiber orientation states from industrially-relevant products will be evaluated with the new methodology to assess its applicability with complex geometries.

This report provides a brief description of the three year project, a predictive method for mean and variance of elastic properties using higher-order tensors, Monte Carlo Validation, and results from our 3D voxel-based finite element approach applied to continuous, short- and long-fiber composites.

Project Deliverables

The primary deliverable of this research is a relationship between higher-order (i.e., fourth-order) orientation tensors, fiber orientation distribution functions, and/or long fiber geometry and the elastic mechanical properties of the composite structure. An assessment of the variability of mechanical properties among fiber orientation states will be provided, along with a computational procedure for evaluating the same properties for a specific orientation state. This document serves as a final report generated to communicate the functional form of the mechanical properties and the relevant model parameters for the specific examples studied.

Background

Orientation tensors are used extensively to represent the stochastic nature of polymer composite fiber suspensions in a form that is suitable for large-scale melt flow simulations. Orientation tensor research over the past two decades has advanced the state-of-the-art related to polymer composites; however, the use of

tensors today is still basically the same as it was when these methods were first developed nearly twenty years ago. In addition, the application of orientation tensors to long-fiber composites is nearly non-existent.

The continued advancement of our basic understanding of short- and long-fiber reinforced polymer composites is critical in numerous industries including consumer products and automotive which rely heavily on the low cost, design flexibility, and superior performance offered by these materials. A major focus of the National Science Foundation/US Department of Energy/American Plastics Council sponsored workshop [1] co-organized by the PI in June, 2004 was the need for the US automotive industry to incorporate more fiber reinforced polymer composites in the design of future vehicles to reduce the weight, emissions, and fuel consumption.

For example, a specific goal of the 2010 FreedomCAR is to reduce the weight of an automotive structure by 50% for the same cost and durability as seen in today's products. The key to meeting these objectives is a comprehensive predictive engineering approach that is capable of accurately simulating critical attributes associated with the design of both the product and its manufacturing process. In this approach, a critical link that connects the computation of materials processing attributes with the prediction of a composite product's performance is the evaluation of structural mechanical properties from melt flow predictions.

Given the dramatic increases in affordable computing over the past decade and the anticipated demands on our predictive capabilities for composite materials over the next decade, it is now time to reconsider assumptions that compose today's fiber orientation models. For example, limiting fiber orientation predictions to solving for only the second-order orientation tensor components in an effort to reduce computational effort may not be necessary.

Evaluating Elastic Properties from Orientation Tensors

One task of this research is to develop a formulation for computing short- and long-fiber composite elastic properties from orientation tensors. Here we consider the expected value of the elasticity tensor $\langle C_{ijkl} \rangle$ defined in terms of the orientation distribution function $\psi(\mathbf{p})$ as

$$\langle C_{ijkl} \rangle = \int_S Q_{pi}(\mathbf{p}) Q_{qj}(\mathbf{p}) Q_{rk}(\mathbf{p}) Q_{sl}(\mathbf{p}) \overline{C}_{pqrs} \psi(\mathbf{p}) d\mathbf{p}$$

where **p** is a unit vector in the fiber direction as shown in Figure 1. In this calculation, $\overline{C}_{pqrs}$ is the

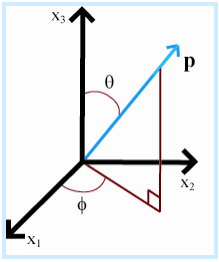

Figure 1. Coordinate system defining fiber direction with the unit vector p(θ,ϕ).

underlying unidirectional compliance tensor for a single fiber (computed using the Mori-Tanaka, Halpin-Tsai, or similar inclusion model) and $Q_{ij}(\mathbf{p})$ is a rotation tensor that rotates the unidirectional components into a selected coordinate system. Elasticity tensor components may be computed in this manner for various orientation distribution functions. However, when $\psi(\mathbf{p})$ is written in terms of the Fourier basis functions such as those given in Advani and Tucker [2], it can be shown that $\langle C_{ijkl} \rangle$ reduces to the well-known result

$$\begin{aligned} \langle C_{ijkl} \rangle = {} & B_1(a_{ijkl}) + B_2(a_{ij}\delta_{kl} + a_{kl}\delta_{ij}) \\ & + B_3(a_{ik}\delta_{jl} + a_{il}\delta_{jk} + a_{jl}\delta_{ik} + a_{jk}\delta_{il}) \\ & + B_4(\delta_{ij}\delta_{kl}) + B_5(\delta_{ik}\delta_{jl} + \delta_{il}\delta_{jk}) \end{aligned}$$

where a_{ij} and a_{ijkl} are the 2nd and 4th order fiber orientation tensors, δ_{ij} is the identity tensor, and the constants B_1–B_5 are computed from $\overline{C}_{pqrs}$.

This derivation shows that when the elastic properties are computed as the volume-averaged result of unidirectional fibers weighted by the orientation distribution function, the highest-order orientation tensor that contributes is the fourth. In this case, sixth- and higher-ordered orientation tensors do not define to the composite's elasticity tensor. What is important to note about this result is that the equations above implicitly assume that the fibers composing aij and aijkl do not interact when stresses are imposed on the fiber-matrix structure. While the effect of fiber interaction has received much attention in melt flow analyses, little effort has been devoted to understanding its role on elastic response of these composites. The elastic response of a high volume-fraction short-fiber composite, as well as long-fiber composites, is expected to be influenced by structural fiber-fiber interaction.

The variance σ^2_{ijkl} of the elastic properties may be computed in a similar manner by taking the second moment of the rotated unidirectional compliance tensor about the mean given as

$$\sigma^2_{ijkl} = \oint_{S^2} \left(Q_{qi}(\mathbf{p}) Q_{rj}(\mathbf{p}) Q_{sk}(\mathbf{p}) Q_{tl}(\mathbf{p}) \overline{C}_{qrst} - \left\langle C_{ijkl} \right\rangle \right)^2 \psi(\mathbf{p}) d\mathbf{S}$$

For relatively simple $\psi(\mathbf{p})$, an analytical result for variance may be obtained by integrating the above equation. This has been performed here for several fiber orientation distribution functions $\psi(\mathbf{p})$. These results are beyond the scope of this report but may be found elsewhere [3]. It is important to note here that while the mean value of the elasticity tensor $\left\langle C_{ijkl} \right\rangle$ contains orientation tensors through 4th order, the variance σ^2_{ijkl} is a function of orientation tensors through 8th order. Therefore, to use the result described here, analytical or approximate values of the 2nd, 4th, 6th, and 8th order orientation tensors are required.

Monte Carlo Simulation

A Monte Carlo simulation method was developed to validate analytical results for the mean and variance obtained above for the elastic properties of a short fiber composite. The Monte Carlo calculations included an Accept-Reject algorithm to obtain a set of fiber orientation angles for any given orientation distribution that is described by an orientation distribution function or set of orientation tensors. The mean and variance of the compliance matrix are computed in these Monte Carlo simulations using a discrete form of the continuous equations given above for $\left\langle C_{ijkl} \right\rangle$ and σ^2_{ijkl}.

Several example Monte Carlo calculations were performed that validate the analytical forms described above. Here we consider the fiber orientation distribution function

$$\psi(\theta, \phi) = c \sin^{2n}\theta \cos^{2n}\phi$$

where θ and ϕ describe fiber angles shown in Figure 1. Figure 2 illustrates the form of this distribution function (with n = 4, and c = 9/4π) which is highly aligned in the x1 direction. Figure 2 also shows a representative volume of fibers with a volume fraction of 10% that has generated for the Monte Carlo simulations. Computed results for C1111 are shown in Figure 3 for 108 Monte Carlo simulations where matrix and fiber properties are taken from Tucker and Lang [4] and the volume fraction is 10%. As shown in the figure, this component of the compliance tensor varies between a predictable lower and upper bound with a nearly linear probability distribution.

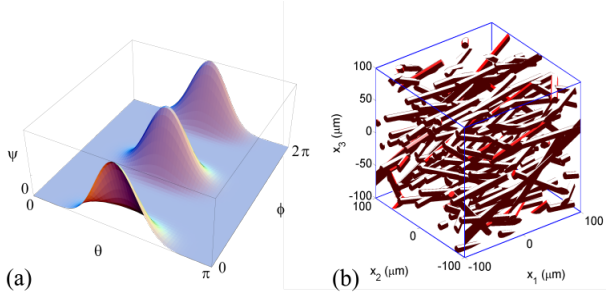

Figure 2. Fiber orientation distribution function used in example calculations (a) and a representative sample set of fibers (b).

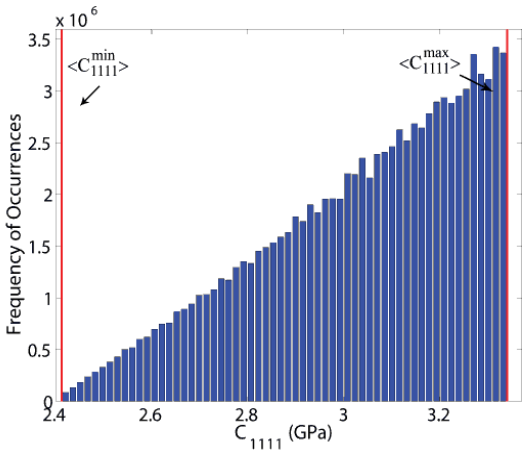

Figure 3. Histogram from Monte Carlo calculations for C_{1111} using 10^8 fiber occurrences.

Of more practical use is the predicted distribution and related statistical properties for multiple sets of fibers since we are typically interested in the elastic properties of a material point which can vary from part to part. To this end, we apply the Central Limit Theorem to compute the statistical nature of multiple sets of fibers such as that shown in Figure 2(b). Figure 4 shows the results of 10^6 sets of fibers where each set contains 101 fibers. As predicted by the Central Limit Theorem, the results become normally distributed. Also shown is the analytically evaluated normal distribution function obtained by applying the Central Limit Theorem to the analytical mean and variance equations given above. The figure clearly shows that the analytical form that we have derived for the statistical properties of fiber suspensions is verified through our Monte Carlo simulations.

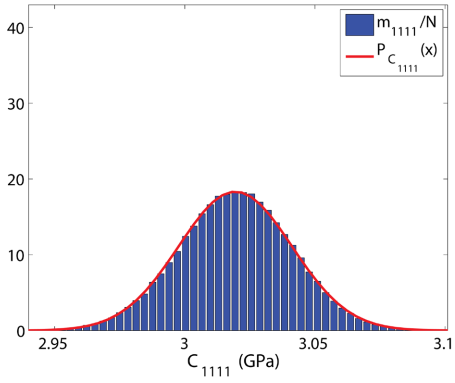

Figure 4. Histogram and normal probability distribution function for C_{1111} using 10^6 fiber sets of 101 fibers each.

Monte Carlo simulations have also been performed to predict the statistical behavior of the compliance tensor for composites that result from center-gated disk flow. Results are computed from the expression given above for the mean and standard deviation (Pc_{1111}) in addition to those obtained via Monte Carlo simulation (m_{1111}/N for 10^6 sets of N=203 fibers) for C_{1111} appear in Figure 5.

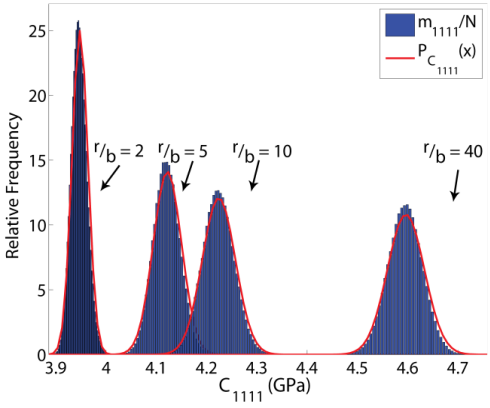

Figure 5. Center-gated disk elastic properties at various distances from gate (r = radius, b = disk thickness).

Three-dimensional Finite Element Analysis for Evaluating Mechanical Properties

All of the calculations described above are restricted to short fiber composites, and explicitly assume that the stress state around each fiber is not influenced by its neighbors. To address these shortfalls, a voxel-based 3D finite element modeling technique was developed that can be used to gain a better understanding of the effect of fiber-fiber interaction in the elastic solid. Our approach is to use a voxel-based finite element model to define a Representative Volume Element (RVE) within the composite structure. Properties of each point within the model are based on fiber distributions obtained analytically, or through experimentally derived procedures, making it possible to include short- and long-fiber composites in the analysis.

To reduce the number of degrees-of-freedom in these 3D finite element simulations, a custom element computed from

$$K^e = \int_{V_e} \hat{B}^T C \hat{B} J dV$$

which is evaluated numerically in the usual manner. Material properties at each sampling (or Gauss) point within the elements are defined based on their position within the composite structure. This allows for a more refined spatial definition without increasing the number of degrees of freedom in the system matrices. In the above, $\hat{B}$ is based on unique elemental shape functions that have been created to increase the complexity of the displacement field in each element. Using our modified shape functions, elements which contain both matrix and fiber are not over-constrained by the more traditional bi-linear response.

This modeling approach was implemented in the general purpose finite element program ABAQUS with a user defined element. RVEs [see e.g., Figure 2(b)] are defined by a uniform grid of 3D elements where the elastic properties of each Gauss point are defined by its spatial location in relationship to the position of the fibers. The number of Gauss points is increased within each element to provide the required spatial refinement. In addition, periodic boundary conditions are implemented so that both axial and shear loads may be accurately applied to the RVE. A fitting procedure has also been developed to compute the compliance tensor and elastic properties from multiple RVE runs where constraints are imposed to enforce a desired material symmetry.

Figure 6(a) shows a finite element model of a continuous boron (E = 379.3 GPa, ν = 0.1, volume fraction = 0.47) fiber embedded in an aluminum (E = 68.3 GPa, ν = 0.3) matrix that has been used to validate our calculation procedure. The dimensions and properties for this model are taken from Xia et al. [5], who provide analytical, numerical, and experimental results for comparison. Figure 6b shows a voxel-based finite element model of the same geometry where contours are provided to indicate the fiber's location. Note that this plot simply shows element by element values, and thus does not provide insight into the spatial refinement within each element that is included with our multiple-Gauss point approach. Both of these models were loaded in tension and shear to generate the response data required for our elastic property curve fitting procedure.

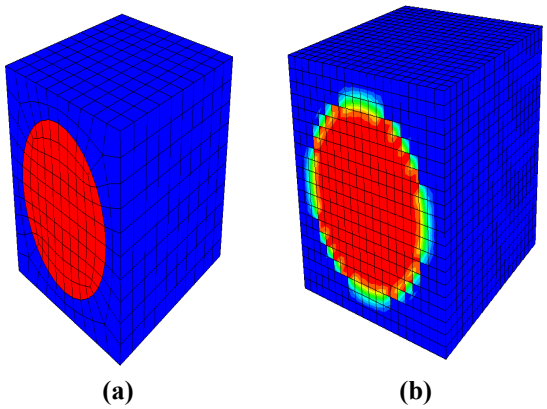

Figure 6. (a) Two material RVE finite element model as defined by Xia et al., and (b) contours illustrating elements that contain fiber, matrix, or both.

Table 1 compares engineering elastic constants obtained from the models in Figure 6 with values provided by Xia et al. It can be seen that our two-material model [Figure 6(a)] provides results that are nearly identical to Xia's results (as expected) which compare well with experimental data as reported in their paper. Table 1 also shows that results obtained with our 3D voxel-based FE [see Figure 6(b)] model agree quite well with the two material models. These latter results are computed with 10 elements in each of the x, y, and z directions where the elements have 6 Gauss points in each direction.

Table 1. Elastic properties computed from two material and voxel-based finite element models (Moduli in GPa).

Elastic Constants	Xia et al.	Two mat model Figure 6(a)	Voxel-based model Figure 6(b)
E_{11}	214	214.4	216.1
E_{22}	143	143.7	147
E_{33}	143	143.7	147
G_{12}	54.2	53.9	56.4
G_{23}	45.7	45.4	45.6
G_{13}	54.2	53.9	56.4
ν_{12}	0.195	0.195	0.194
ν_{23}	0.253	0.253	0.244
ν_{13}	0.195	0.195	0.194

Aligned Short Fiber Models

The voxel-based multi-Gauss point FEA method described above was also applied to aligned short fiber models. The composite structure evaluated in Tucker and Liang[4] is studied here to validate our computational procedure. Fibers in both a regular and staggered array have been modeled with a fiber volume fraction and aspect ratio of 0.2 and 8, respectively. Elastic properties of the fiber and polymer matrix appear in Table 2.

Table 2. Aligned short fiber polymer composite model elastic properties.

Material	*E* (GPa)	ν
fiber	30	0.2
matrix	1	0.38

Figure 7 shows a conventional finite element model (i.e., one with element boundaries that separate fiber and matrix) of a regular array short fiber composite. The uniform mesh model of the same composite (not shown) is a rectangular solid FE model of the same size with cubic finite elements with similar edge lengths as the model in Figure 7.

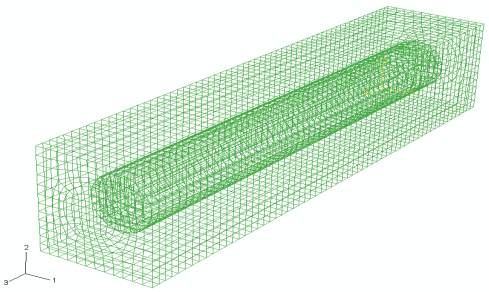

Figure 7. Conventional FE model of regular array aligned short fiber composite.

Figure 8 illustrates stresses in the conventional and uniform mesh FE models under axial loading along the fiber axis. The boundary of the fiber is clearly seen in the conventional model, while elements along the fiber's boundary in the uniform mesh model have average values between those in the fiber and matrix. The shear stress along the length of the fiber is shown in Figure 9 for the same two models. The shape of the boundary in both deformed models illustrate that the periodic boundary conditions are correct.

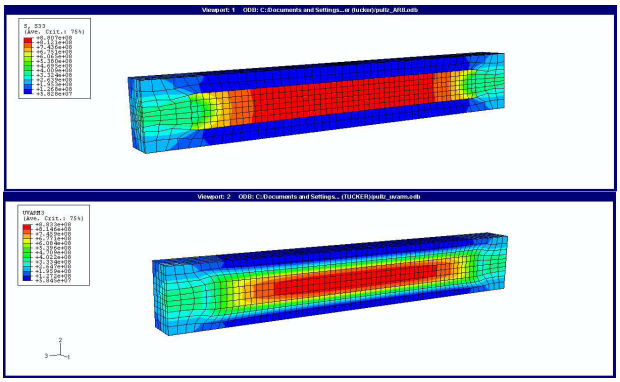

Figure 8. Axial stresses for the regular array aligned short fiber models under tension along the fiber's axis. Top: conventional model. Bottom: uniform mesh model.

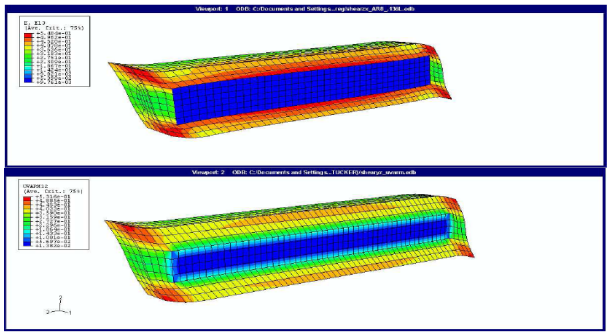

Figure 9. Shear strains for the regular array aligned short fiber models under shear along the fiber's axis. Top: conventional model. Bottom: uniform mesh model.

Table 3 summarizes calculated effective elastic properties for the aligned short fiber composite models studied here. Our results are compared with those given in Tucker and Liang[4] and the classical theory of Tandon-Weng. Results are in good agreement with minor deviations for some values. Note that the uniform mesh results were computed with 8 Gauss points in each of the three coordinate directions.

Random Fiber Orientations

The multi-Gauss point FE method described above was applied to random short fiber composites where individual fibers having a diameter of 10 microns and an aspect of 10 were generated in 200×200×200 micron cube following the analytical fiber orientation distribution function given above with $n = 4$ and $c = 9/4\pi$ and shown in Figure 2. Volume fractions considered ranged

Table 3. Effective elastic properties for aligned short fiber composite.

Elastic constant	Tucker-Liang[4]	Tandon-Weng	Conv. mesh	Uniform mesh
E_{11}/E_m	4.2	3.37	3.97	4.06
E_{22}/E_m	1.55	1.51	1.62	1.67
G_{12}/E_m	na	0.54	0.53	0.54
G_{23}/E_m	na	0.51	0.49	0.48
ν_{12}	0.335	0.362	0.338	0.338
ν_{23}	0.48	0.49	0.487	0.471

from 2% to 30% and a Monte Carlo simulation method was used to define the orientation vector **p** for each fiber in the cube. All results are compared with analytical results using both the Halpin-Tsai and Tandon-Weng procedures.

All calculations are based on 10 cubes of fibers where each cube includes fibers from the same distribution function and volume fraction. A convergence analysis was performed using a volume fraction of 0.1 with 8,000–64,000 elements and 6–10 Gauss points in each of the three coordinate directions. It was found that over this broad range of model parameters, elastic constants varied by less than 1.5%. All results reported below include 27,000 elements with 6 Gauss points in each direction.

Figure 10 shows average values of E_{11} and E_{22} for random short fiber composite samples over a range of volume fractions. Results agree well with similar results computed with the Halpin-Tsai and Tandon-Weng equations at low volume fractions. Stiffer results are computed using our FEA approach as the volume fraction increases. Fiber interactions in the structural model are expected to have increased the stiffness prediction in the uniform mesh FEA model when compared to the analytical methods which treat fibers as statistically independent. Poisson's ratios (not shown) tend to have larger deviations between our numerical results and those computed using the classical analytical procedures. Overall, the 3D voxel-based, multi-Gauss point approach provides elastic constants over a range of volume fraction that are potentially more accurate than those provided by prior methods.

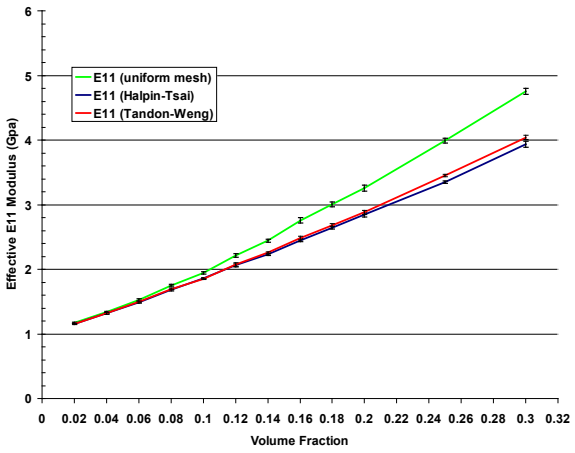

(a)

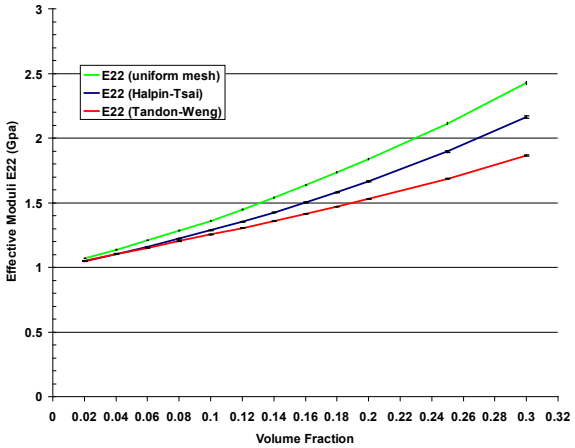

(b)

Figure 10. Elastic properties of a short fiber composite sample as a function of volume fraction: (a) E_{11} and (b) E_{22}

Long Fiber Composite Analyses

A long fiber composite material was evaluated using the uniform mesh, multi-Gauss point method described above. The long fiber geometry was evaluated from micro CT images obtained from Vlastimil Kunc at Oak Ridge National Laboratory. One thousand, two hundred slices of data were analyzed for the approximately 2×2×1.63 mm long fiber sample. A rendering of a sub region of the 3D sample appears in Figure 11. Raw data are shown here, however, calculations described below were performed after several image processing steps that filtered and smoothed the voxel values to better serve the needs of the present study.

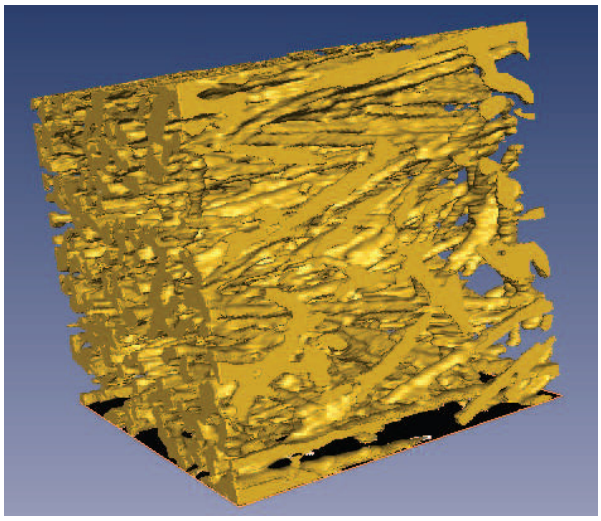

Figure 11. 3D rendering of sub region of long fiber composite model generated from micro CT slice data.

Data from the long fiber composite sample were split into 27 sub regions in a 3D grid of 3×3×3 along each edge of the original rectangular solid of material as shown in Figure 12. Then, FE models of each sub region were defined and analyzed to predict the elastic mechanical properties for the composite. Each sub region model contained 36×34×29 elements for a total of 35,496 elements. The spatial location of the mirco-CT data of each sub region was collocated with the finite element model for each analysis. Then, each Gauss point in all of the elements of the FE model were mapped onto the micro-CT data to determine if it is positioned within a fiber or the matrix. The appropriate material properties were then applied. Each sub region model was treated as a repeating volumetric unit with the appropriate periodic boundary conditions to accommodate axial and shear loading. Elastic properties were evaluated through the fitting procedure developed as part of this research project.

Figure 13 shows the computed results for E_{11} throughout the long fiber composite sample. Each bar chart shows nine values in each of the 3 model layers in the z-direction of Figure 12. The fiber and matrix material properties in the actual sample where not available, so the values in Table 2 where used in the current calculations. It is apparent from Figure 13 that there is a more compliant core in the sample that extends throughout the sample in the z-direction. Other

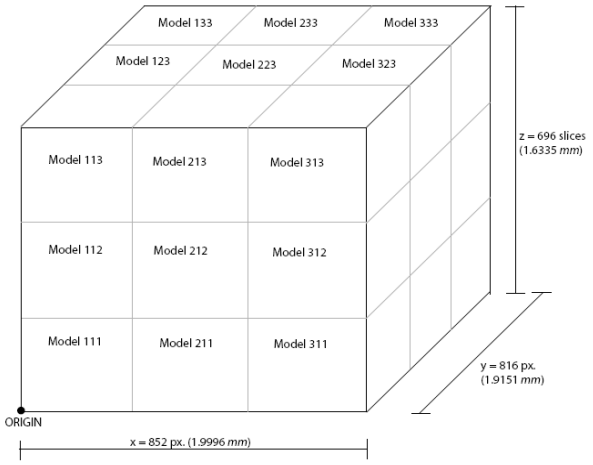

Figure 12. 3×3×3 array of sub regions used in the long fiber composite elastic property evaluations.

properties such as E_{22} (not shown) are also reduced through the core. Our calculation of volume fraction is also lower throughout the center of the sample, providing a possible cause for the reduced material properties.

The mean and standard deviation for all of elastic properties were computed based on the 27 values of each that were evaluated with the multi-Gauss point FE model as described above. Table 4 summarizes these results using elements with 6 Gauss points in each direction.

Conclusions

This research project focuses on the prediction of elastic mechanical properties from higher-order fiber orientation tensors, fiber orientation distribution functions, and/or micro CT data of actual composite samples. As part of this work, the expression for computing elastic properties form fiber orientation tensors is verified and shown to ignore fiber-fiber interaction. In addition, the role of higher-order tensors on mechanical property prediction when using this approach is explored. A 3D voxel-based finite element modeling procedure has been developed which has been found to be in good agreement with more conventional FE approaches for continuous fiber and aligned short fiber composites.

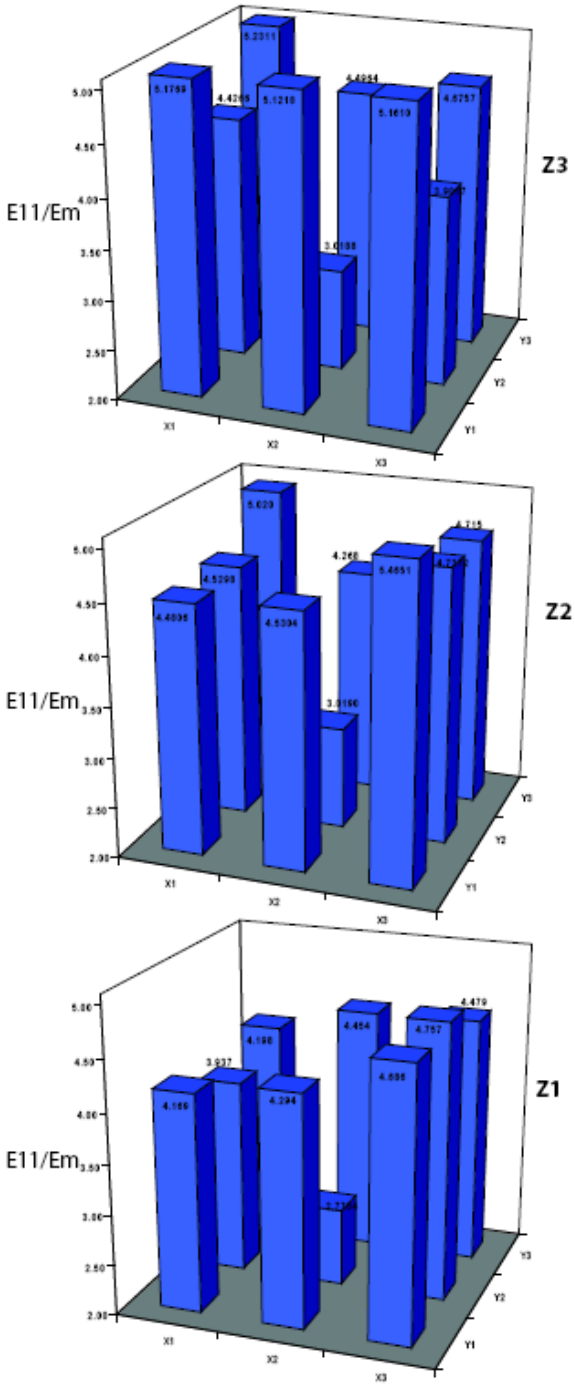

Figure 13. Computed results for E_{11} for each of the 27 sub regions in the long fiber composite sample.

Future Work

The work completed here provides tools and insight for future research in the understanding of short and long random fiber composites. A partial list follows:

Table 4: Computed elastic properties for a long fiber composite sample from 27 sub regions distributed as shown in Figure 12 (mean and standard deviation in GPa),

Material property	Mean	Standard deviation
vol. frac.	0.435	0.046
E_{11}/E_m	4.43	0.665
E_{22}/E_m	8.05	1.107
E_{33}/E_m	4.09	0.746
ν_{12}	0.09	0.008
ν_{21}	0.17	0.016
ν_{13}	0.20	0.027
ν_{31}	0.19	0.021
ν_{23}	0.19	0.019
ν_{32}	0.09	0.010
G_{12}/E_m	1.93	0.240
G_{23}/E_m	1.92	0.293
G_{31}/E_m	1.41	0.212

1. Perform additional detailed verification studies on long fiber composite samples.
2. Integration of the developed 3D voxel-based FE method with stress-strain testing of short and long fiber composites.
3. Application of FE approach developed here to actual long fiber composite products produced via molding processes.
4. Further integration of elastic property prediction method with polymer manufacturing process simulation.
5. Develop image processing methods to better extract long fiber geometry data from micro CT scans.
6. Development of a material fracture model within the 3D long fiber composites model.
7. Include elastic-plastic behavior to better represent the polymer matrix under load.
8. Further development of a packing algorithm for random short fibers at increasing volume fractions.
9. Addition of a flexible fiber model into the packing algorithm.
10. Include non-isotropic fiber constitutive models into the 3D voxel-based FE method.

11. Use 3D voxel-based FE results to develop a long fiber composite constitutive model.

References

1. http://web.missouri.edu/~smithdoug/nsf/index.htm.
2. S. Advani and C. L. Tucker, *J. of Rheology*, vol. 31, no. 8, pp. 751–784, 1987.
3. D. A. Jack and D. E. Smith, *J. of Composite Materials*, vol. 42, no. 3, pp. 277–308, 2008.
4. C. L. Tucker and E. Liang, *Comp. Science and Technology*, vol. 59, pp.655–671, 1999.
5. Z. Xia, Y. Zhang, and F. Ellyin, *Solids and Structures*, vol. 40, pp. 1907–1921, 2003.

Presentations/Publications/Patents

1. D. A. Jack and D. E. Smith, "Elastic properties of short-fiber polymer composites, derivation and demonstration of analytical forms for expectation and variance from orientation tensors," *J. of Composite Materials*, **42**:3, pp. 277–308, 2008.
2. J. E. Middleton, *Elastic property prediction of long fiber composites using a uniform mesh finite element method*, MS Thesis, University of Missouri, August, 2008.
3. E. C. Caselman and D. E. Smith, "A Multi-Gauss point finite element approach for the predicting elastic properties of short fiber composites," The Annual Meeting of the Polymer Processing Society, PPS-24, Salerno (Italy), 15–19 June 2008.
4. D. E. Smith and D. A. Jack, "Computing elastic material properties of short fiber composites via Monte-Carlo simulation," Poster presentation at the *2008 NSF Engineering Research and Innovation Conference*, Knoxville, Tennessee, January, 2008.
5. E. Caselman, *Elastic property prediction of short fiber composites using a uniform mesh finite element method*, MS Thesis, University of Missouri—Columbia, December, 2007.
6. D. A. Jack and D. E. Smith, "Mechanical Properties from the INV6 Closure for Short-Fiber Suspensions," SPE ANTEC 2006, Charlotte, North Carolina, May 7–11, 2006.
7. D. A. Jack, *Advanced analysis of short-fiber polymer composite material behavior with higher-order orientation tensor closure methods*. PhD thesis, University of Missouri—Columbia, December 2006.
8. D. E. Smith, M. T. Grimshaw, and D. A. Jack, "Incorporating higher order tensors in the computation of polymer composite mechanical properties," Poster presentation at the *2006 NSF Design, Service and Manufacturing Grantees and Research Conference*, St. Louis, Missouri, July 24–27, 2006.
9. D. A. Jack and D. E. Smith, "A statistical method to obtain material properties from the orientation distribution function for short-fiber polymer composites," IMECE2005-81263, Proceedings of ASME IMECE'05, Orlando, Florida, Nov. 5–11, 2005.
10. D. E. Smith and E. Caselman, "A 3D multi-Gauss point finite element method for computing elastic properties of composite materials," in preparation.
11. D. E. Smith, J. Middelton, V. Kunc, and B. N. Nguyen, "Computing elastic properties of random long fiber composite materials," in preparation.

O. Linking Process-Induced Properties to Thermoplastic-Matrix Woven-Fabric Composites Performance

Principal Investigator: James A. Sherwood
Department of Mechanical Engineering
University of Massachusetts Lowell
One University Avenue
Lowell, MA 01854
(978) 934-3313; fax: (978) 934-3048; e-mail: James_Sherwood@uml.edu

Co-Principal Investigators: Julie Chen, Larissa Gorbatikh
Department of Mechanical Engineering
University of Massachusetts Lowell
Lowell, MA 01854
(978) 934-2992; fax : (978) 934-3048; e-mail: Julie_Chen@uml.edu

Technology Area Development Manager: Joseph A. Carpenter
(202) 586-1022; fax: (202) 586-1600; e-mail: joseph.carpenter@ee.doe.gov

---

Contractor: University of Massachusetts Lowell
National Science Foundation Contract No. DMI-0522923, jointly funded by NSF and DOE

Objectives

- Provide a direct link among part geometry, material selection, process conditions, process-induced local properties, and part performance, allowing for informed feedback to the design process.
- Model the in-service performance of thermoplastic-matrix woven-fabric-reinforced structural composites – e.g., damage tolerance, crashworthiness, vibration.
- Attain a fundamental understanding of two governing physical phenomena – interlayer (fabric-fabric) friction.
- Validate and demonstrate the capabilities of the integrated structure-process-performance design tool to identify critical process and material parameters for one particular performance condition – vibration.
- Apply the proposed methodology to the thermostamping of woven-fabric composites to show how quality lightweight composite parts can be made at a rate and cost that is competitive with the currently used manufacturing process for stamping metal parts.

Approach

- Utilize an integrated analytical, experimental, and numerical effort to attain a fundamental understanding of two governing physical phenomena—interlayer (fabric-fabric) friction and interconnected through-thickness and in-plane compaction.
- Extend a combined inter-tow friction model, developed in a previous NSF-funded research program (DMII-0331267), based on the equilibrium equations of the unit cell of a balanced plain-weave glass/polypropylene woven fabric to account for fiber compaction.
- Design and build a friction-testing apparatus that is capable of examining tool/fabric and fabric/fabric friction for controlled load, speed and temperature conditions.
- Implement the methodology in commercially available finite element programs to simulate the composite forming process and have the result of the simulation of the manufacturing process be a finite

- element model of the formed composite part for use in structural analysis—thereby linking the manufacturing process to the resulting part performance.

Accomplishments

- Developed an analytical model that accounts for fiber compaction and can predict the shear behavior for woven fabrics and demonstrated the capabilities of the analytical shear model.
- Designed, built and implemented a self-contained friction testing apparatus that can replicate the tool/fabric and fabric/fabric interaction that occurs during the thermostamping process. The apparatus can be run under either load control or displacement control to characterize the static and dynamic friction coefficients as a function of speed, pressure and temperature.
- Confirmed that the friction behavior during the thermostamping for a Twintex® woven fabric, which is made from yarns of commingled fiberglass and polypropylene fibers, can be related to the Hersey number using Stribeck theory. When the polypropylene fibers melt and infuse the fiberglass fibers, the friction can be classified as hydrodynamic. The friction coefficient increases with increasing speed and decreases with increasing pressure for a given temperature. Such dependencies have been implemented in ABAQUS/Standard, ABAQUS/Explicit, and LS-DYNA (explicit version) through user-defined friction subroutines for finite element modeling of the thermostamping process.
- Characterized the mechanical behavior of three different Twintex® woven fabrics using experimental data from a series of shear frame and uniaxial tests.
- Developed constitutive models to describe the nonlinear shear behavior of woven fabrics and the nonlinear tensile behavior of crimped yarns in a woven fabric for large deformations. These constitutive models have been implemented in ABAQUS/Standard, ABAQUS/Explicit, and LS-DYNA (explicit version) through user-defined material subroutines for finite element modeling of the thermostamping process.
- Demonstrated a design tool to link part geometry, material behavior, and process conditions to the resulting process-induced local properties and overall structural performance from the thermostamping of woven-fabric composites for a simple hemisphere geometry and for a complex tub geometry.

Future Work and Direction

- Conduct parametric studies of the thermostamping process using the Hersey number friction model and different binder forces in the finite element simulations to enhance the understanding of the effect of the in-plane tension on the wrinkling and tearing of the fabric.
- Investigate the effect of fiber orientation on the friction coefficient to conclude the importance of yarn orientation and the state-of-shear on the friction behavior.
- Perform modal testing of a stamped part using a three-dimensional laser vibrometer and compare the experimentally found mode shapes and frequencies with finite element modal analysis results using the final shapes and fiber orientations predicted by the forming simulation. These comparisons will show the ability of the design tool to provide useful data for subsequent structural analyses.
- Extend the design tool to model the composite forming processes for composite wind turbine blades.

Introduction

Modeling of the in-service performance of thermoplastic-matrix woven-fabric-reinforced structural composites (e.g., damage tolerance, crashworthiness, vibration) is currently inadequate for parts of any geometric complexity because of the inability of existing performance models to capture the true deformed material properties. As a result, lightweight composite materials are utilized inefficiently or not at all; alternatively, extensive experimental trial and error or design of experiments must be conducted to develop a satisfactory product. The key to addressing this barrier is to provide a direct link among part geometry, material selection, process conditions, process-induced local properties, and part

performance, allowing informed feedback to the design process.

Fiber-reinforced thermoplastic composites have a variety of applications including structural components in the automotive, aerospace, marine, infrastructure and recreation industries. The main advantage of these composites over metals is their high specific strength. They also have other beneficial properties including low thermal expansion and good corrosion resistance when compared to metals. Woven fabrics offer many other advantages when compared to metals in terms of deformation capabilities, including dimensional stability, good conformability, and deep-draw shapability. Compared to nonwoven-fabric composites, the woven-fabric composites provide more balanced properties, higher impact resistance, easier handling and lower fabrication cost, particularly for parts with complex shapes. The objective of this research was to utilize an integrated analytical, experimental, and numerical effort to attain a fundamental understanding of two governing physical phenomena—interlayer (fabric-fabric) friction and interconnected through-thickness and in-plane compaction. The former is important in multiple-layer and multiple-step forming, both needed for industrial processes. The latter is a critical factor affecting the final part thickness, void content, fiber orientation, and fiber distribution—all are important for structural stiffness and damage tolerance. To validate and demonstrate the capabilities of the integrated structure-process-performance design tool, the model will be used to identify critical process and material parameters for one particular performance condition—vibration.

A combined inter-tow friction model, developed in a previous NSF-funded research program (DMII-0331267), based on the equilibrium equations of the unit cell of a balanced plain-weave glass/polypropylene woven fabric is extended to account for fiber compaction. To accomplish this extension of the model, fiber-compaction experiments were completed and the results are reported.

The design and use of a 3rd-generation friction-testing apparatus is presented. Previous research efforts used a constant-displacement control device to load the undeformed fabrics during the friction testing. While the information learned in these tests was valuable in developing a fundamental understanding of the tool-fabric behavior, the 3rd-generation friction-testing apparatus is a load-control device and yields a very complete fundamental understanding of the friction mechanisms by being able to study inter-layer friction between fabrics and tool/fabric friction on undeformed and deformed fabrics and to capture the static and dynamic friction behaviors of a woven-fabric system. Results are reported for two material systems—one has a thermoplastic matrix and the other has a thermoset matrix.

The methodology is implemented in the commercially available finite-element programs ABAQUS and LS-DYNA. The elements for the fabric models are inherent to these finite-element programs, so no special coding of elements is required. The material and friction behaviors are incorporated in the finite-element modeling by user-defined subroutines with simple input cards for specifying material and friction properties. Thus, the design tool is packaged in a form that should make the transition to industry relatively seamless and easily used by composite design engineers in industry.

The Thermostamping Manufacturing Process

Thermostamping is a manufacturing process that can produce quality composite parts with processing costs and time margins that are comparable to the fabrication of the currently stamped metal parts. The thermostamping process deforms a flat sheet of machine-woven continuous fibers (glass and/or carbon) commingled with thermoplastic fibers into a particular geometry using a pair of dies.

The thermostamping process (Figure 1) starts with the alignment of a sheet of fabric in a rigid steel frame. Multiple layers of fabric are stamped into one part to achieve the desired part thickness and mechanical properties. For a thermoplastic-matrix woven fabric, the frame and fabric are placed in an oven and are soaked until the fabric reaches a desired temperature for the thermoplastic

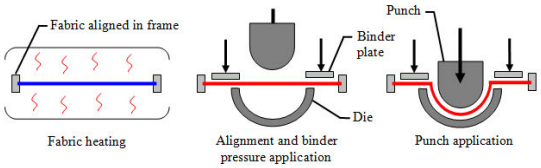

Figure 1. Schematic example of the thermo-stamping process.

polypropylene fibers, which are commingled with fiberglass fibers, to melt. The melting of the thermoplastic fibers infuses the fiberglass fibers with the resin. The frame is then aligned with a punch and die, and pressure is applied around the circumference of the punch area by binder plates. The application of force by the binder plate provides the in-plane forces that are necessary to reduce wrinkling of the fabric as the woven material is drawn into the die by the punch. The finished piece assumes the geometry of the die and punch and hardens into a firm part after the thermoplastic has cooled.

For the thermoset material, the woven fabric is compounded with a pliable thermoset resin. The frame holding the woven fabric is stamped into shape using the punch and die and then held at elevated temperature to harden the thermoset resin matrix.

A hemisphere formed from a commingled glass-polypropylene fabric using this thermostamping process is shown in Figure 2. The primary mode of deformation for the fabric is rotation (shearing) of the yarns, also known as ‘trellis deformation’.

Figure 2. Formed hemisphere using the thermo-stamping process.

The processing parameters associated with the thermostamping operation can have a significant effect on part quality. Figure 3 shows the resulting part quality in a section under the binder plate from the stamping process of a commingled glass-polypropylene woven-fabric as studied by Wilks [1]. The resulting part quality is shown for cases of different pressure-and-temperature combinations. For this test, the pressure applied by the binder plate was controlled by springs and the binder plate was either unheated or heated during the process. With the binder plate unheated, fiber separation and tow breakage occurred sooner than when the binder plate was heated as pressure was increased [Figure 3(d–f)]. The presence of fiber wrinkling was reduced as pressure increased [Figure 3(e)]. Thus, it can be observed that part quality is a function of temperature and applied force, and in turn friction between the fabric and the tool.

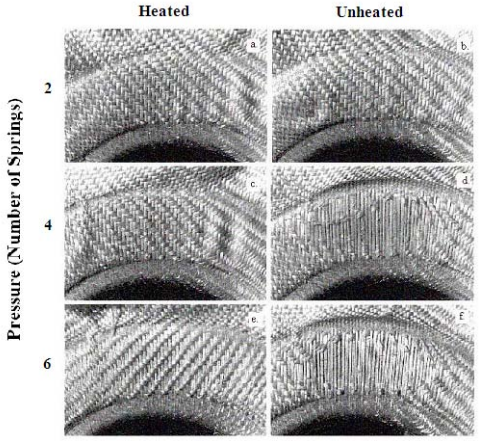

Figure 3. Effect of temperature and pressure on part quality during the thermostamping process [1].

The mechanical behavior of the woven fabric during the forming process is dominated by the evolution of the in-plane shear stiffness as the yarns rotate and the uncrimping of the yarns due to in-plane tensile forces. By using a series of simple tests to characterize the mechanical behavior of a woven fabric, material parameters can be found. As an alternative to experimental characterization, there has been some limited success to develop purely analytical models of woven fabrics to estimate the mechanical behavior of a woven fabric. These analytically and/or experimentally

determined material properties can be used in a finite-element program to simulate the manufacturing process of a composite structure.

The inextensible characteristic of the yarns (fiberglass and/or carbon) requires draw-in and shearing of the fabric to occur for the material to conform to the tool geometry in forming the part. During fabric draw-in, the fabric slides under the metal binder plate and over the surfaces of the punch and die. For multilayer parts, there is possibly going to be some sliding between adjacent layers of fabric. Considering the interactions that take place between the fabric and tool and between adjacent layers of fabric during the manufacturing process and the effect of the process parameters (e.g., pressure, temperature and rate, on part quality), it is clear that characterizing the friction between the tool and the fabric and the friction between adjacent layers of fabric is critical to modeling the manufacturing process accurately.

Analytical Modeling of the Shear Behavior of Woven-Fabric Composites

Trellis shear, as shown in Figure 4, is the main deformation mode during the stamping process of woven-fabric composites [2]. Thus, the formability of woven-fabric composites is primarily a function of the shear properties of the woven fabric. Therefore, analytical models to obtain the shear properties of woven-fabric composites would be very useful to characterize the mechanical behavior of an existing fabric without doing time-consuming experiments or for characterizing a yet to be made fabric for which experimentation is not an option.

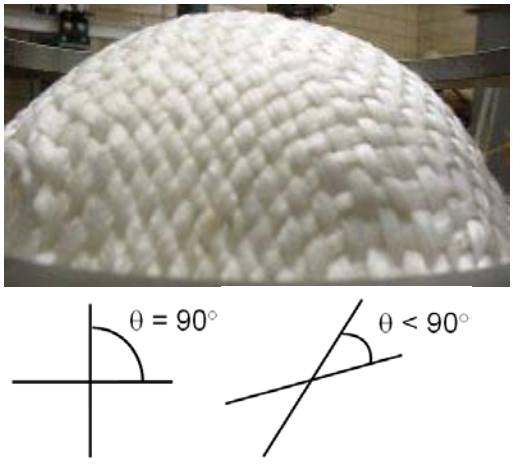

Figure 4. Trellis deformation of a stamped hemisphere.

An analytical unit-cell model, which includes (1) the key shear-deformation-resistant mechanisms, (2) the friction between the warp and weft yarns at every crossover, and (3) the lateral compaction between adjacent yarns, was developed by Liu et al. [3,4] to predict the shear properties of woven fabrics for the thermostamping process. In the model, some yarn parameters such as the yarn-to-yarn coefficient of friction μ, the fiber contact frequency ratio β, and the ideal maximum fiber volume fraction V_a, were chosen to develop an empirical model to fit the experimental data. Validation of those parameters is necessary to complete the unit-cell model.

The maximum yarn-fiber volume fraction V_a is an ideal limit to which fibers in a yarn can be compacted. As the yarn-fiber volume fraction approaches this maximum value, the stiffness in the transverse direction increases dramatically to approach the stiffness of the solid fiber material. According to the packing theory of uniform sizes of fibers, square packing corresponds to V_a of $\pi/4$ (or 0.785), and hexagonal packing results in a value of $\sqrt{3}\pi/6$ (or 0.907). Because the diameters of the polypropylene and glass fibers are different in the commingled polypropylene/glass yarn, the square packing theory is modified for the commingled fibers, and the obtained V_a equals 0.813 [5].

The compaction was studied using plane-strain compression tests, where 50-mm-long fiber bundles were placed in a channel fixture as shown in Figure 5. A compressive force was applied perpendicular to the axial direction of the fibers (*Z* direction) using an Instron machine at a rate of 0.042 meters (m)/second (sec). Load and extension data were logged so that stress and strain in the *Z* direction could be calculated. Because the transverse compliance can also be calculated in the fiber bundle model as a function of β, regression of the experimental data will give the mean value of β. In Figure 6, the predicted and

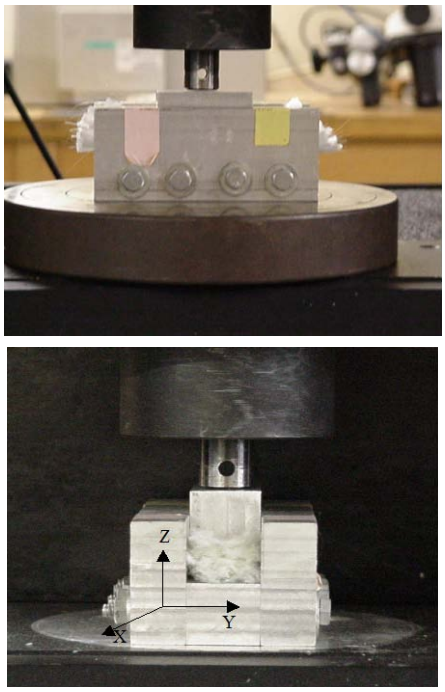

Figure 5. Plane-strain compression test fixture [5].

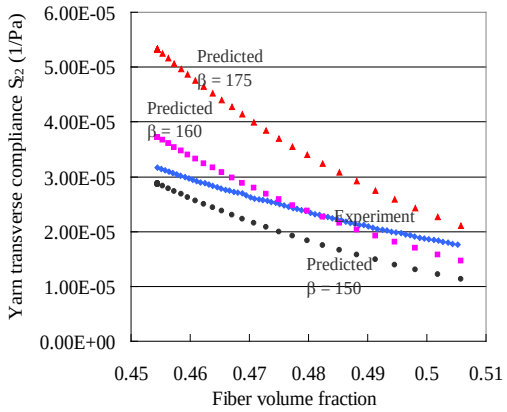

Figure 6. Comparison of the values of S_{22} obtained from the plane-strain compression tests and the fiber bundle modeling [6].

experimental values of the yarn transverse compliance S_{22} are compared for various values of β. The experimental results were obtained from the plane-strain compression tests for five layers of yarns as described in [6]. From Figure 6, it can be seen that the values of β are in the range from 150 to 175 for the commingled polypropylene and glass yarns explored in this research.

To investigate the sensitivity of the model to the yarn input parameters such as the maximum fiber volume fraction V_a, the fiber contact ratio β and the yarn-to-yarn coefficient of friction μ, a parametric study was conducted. To separate the individual contributions from friction and lateral compaction, intermediate models were studied separately (i.e., the lateral compaction resistant moment was set to be zero to study the coefficient of friction), while in the study of β and V_a, the friction resistant moment was set to be zero in the equilibrium equation.

Figure 7 shows the results of the simulation of β varying from 150 to 175. In the figure, it can be seen that as the value of β decreases, the shear load increases. The loads increase because at relatively low values of β, the yarn stiffness in the

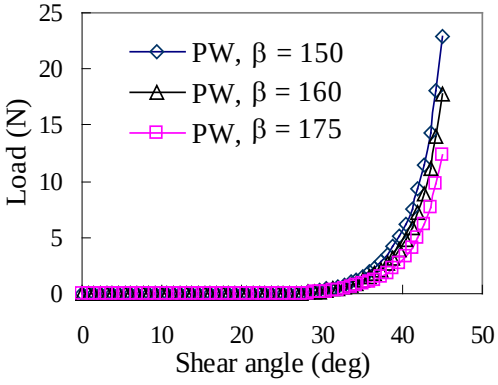

Figure 7. Simulation of the fiber contact frequency ratio.

transverse direction increases due to increased fiber bending. As shown in Figure 8, decreasing the value of V_a has a similar effect because, with relatively low values of V_a, yarn stiffness in the transverse direction increases due to decreased space for compaction.

Thus, with the main parameters all validated, the developed analytical model can be used to predict the shear properties of woven-fabric composites and reduce or eliminate the need for curve fitting of fabric-level experimental data.

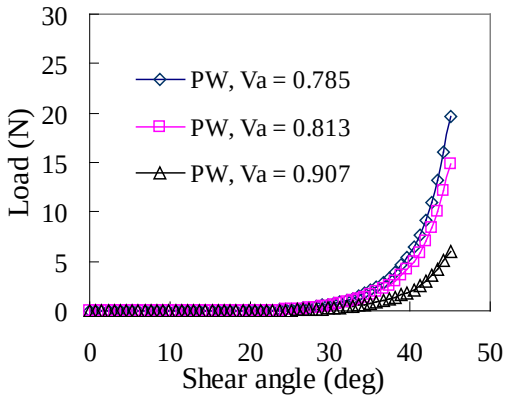

Figure 8. Simulation of the maximum fiber volume fraction.

Friction Behavior for Woven Fabrics

Past research led to advances in a user-defined friction subroutine for use in finite-element applications. The notations PW, TWI and TWII refer to the plain-weave; the thin-twill-weave and the thick-twill-weave fabrics, respectively. The Stribeck curve (Figure 9 [7]) and the Hersey number, *H*, (Eq. 1) were used to find the friction coefficient for the ranges of velocities and normal forces studied.

$$H = \frac{\eta \cdot U}{N} \qquad (1)$$

where η is the viscosity, U is the fabric velocity and N is the normal force.

The results of parametric studies conducted by Gorczyca [8,9] showed that the velocity of the fabric, tool temperature, and applied normal force had the greatest effects on the friction coefficient. From these results, she developed a model that related the friction coefficient μ to the Hersey number,

$$\mu = (6.1191 \cdot H + 0.2718) - \mu_{\upsilon} \qquad (2)$$

where μ_{υ} is a scaling term included for the effects of the tool temperature. Because the method of normal force application used in her research was displacement controlled, her results were limited to measuring only the static coefficient of friction [8,10,11].

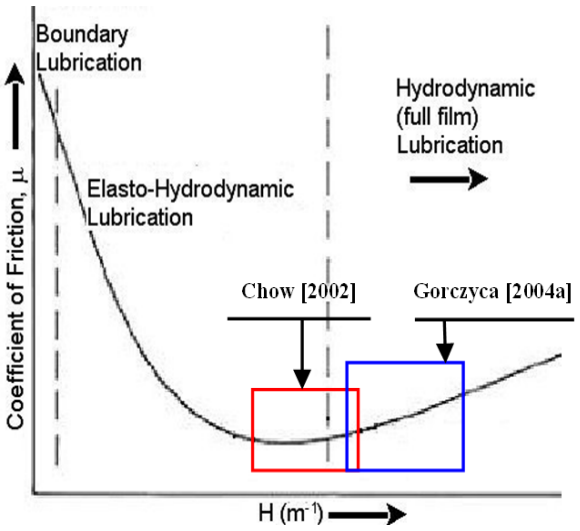

Figure 9. The Stribeck Curve and areas of interest pertaining to current research. Adapted from [7].

It was found that during a typical friction test the normal force applied to the fabric surface decreased, as shown in Figure 10 where the initial applied load was approximately 1500 N and dropped by ~400 N over the duration of the test. The mechanisms behind this decrease in normal force are fabric nesting and tow compaction. The fabric tows adjust their position as the adjacent layers of fabric nest, tow undulation decreases and fibers compact due to the combination of heat and pressure. Any one or more of these mechanisms causes a slight change in the displacement necessary to maintain the targeted normal force.

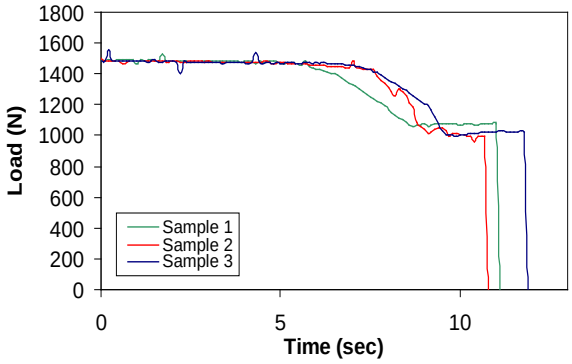

Figure 10. Normal force decrease over time for displacement controlled test of commingled glass-polypropylene plain-weave fabric.

Due to the drop in normal force, only the static coefficient of friction, which is the value obtained

at the first instant of fabric movement, could be reliably quantified by Gorczyca using the 2nd-generation displacement-control friction test apparatus. Being able to capture the dynamic coefficient of friction would give a friction model that accurately represents the frictional behavior over the entire duration of the thermostamping process where the friction is both static and dynamic.

To gain the ability to determine the dynamic coefficient of friction, a load-controlled application mechanism was designed and built as one component of the current research [12]. The force-controlled mechanism consists of a pneumatic air-spring actuator and a closed-loop control algorithm to continuously monitor and regulate the magnitude of force applied to the fabric throughout the duration of the friction test. The temperature of the tool and the pullout speed can be prescribed over a range of values that are observed to be present in the thermostamping process.

For the stamping of a hemisphere with a plain-weave fabric (as shown in Figures 1 and 2), the tows are initially oriented ~90° with respect to one another, and this angle decreases as the fabric conforms to the dual-curvature surface of the hemisphere as shown in Figure 4. The significance of the effect of tow orientation on the friction response is currently being investigated.

Test Fixture

The 3rd-generation friction-testing apparatus is a stand-alone test machine. The limiting factor for the previous test apparatus was its dependence on the Instron testing machine. By integrating all fabric movement into one test apparatus, the travel time from the oven to the press can be reduced from ~20 seconds to be less than 3 seconds, thereby reducing the influence of any cooling effects as the fabric is transferred from the oven to the press. Figure 11 shows a schematic of the overall 3rd-generation friction-testing system, and Figure 12 is a photograph of the press portion of the system.

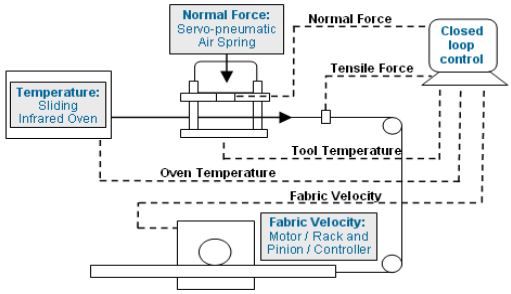

Figure 11. Schematic representation of the 3rd-generation friction test apparatus.

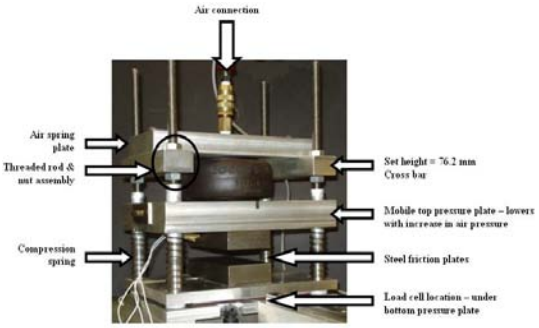

Figure 12. The friction press.

Experiments

The load-control friction test apparatus [13] was used to capture the static and dynamic coefficients of friction. The objective of the friction-test apparatus is to accurately simulate the combinations of pressure, temperature and speed observed in the actual thermostamping process.

In a friction test, the fabric is clamped in a holder [Figure 13(a)], heated in an infrared oven and subsequently shuttled to the press (similar to what is shown in Figure 1 for the thermostamping process), which features two heated platens. A direct current (DC) motor drives a rack and pinion to pull the sample through the press. The transfer from the oven to the press is done manually, and the fabric sample typically sits pressurized between the platens for about one second before the motor begins to pull. Experiments have shown that this one-second time is sufficient to keep the thermoplastic melted.

For the fabric/fabric friction characterization, one fabric layer is placed between two “outside” layers of fabric. The two outer layers are clamped

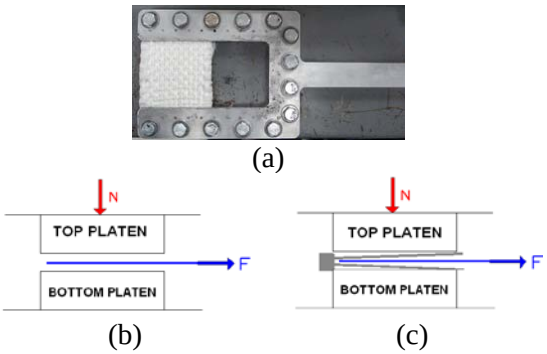

Figure 13. Fabric holder and schematics of the friction test setups for tool/fabric and fabric/fabric interfaces.

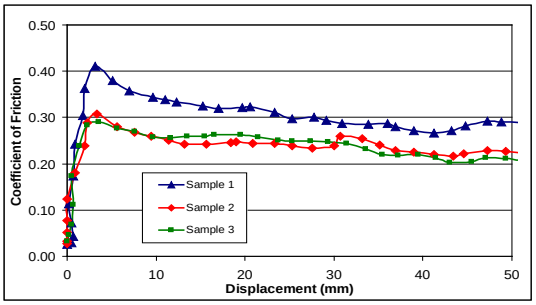

Figure 14. Coefficient of friction as a function of pullout length for three tests at a pressure of 110 kPa, pullout velocity of 16.7 mm/s, and tool temperature of 85°C.

together on one end, and the inner layer is pulled between these two outer layers. The fully compressed platens prohibit the clamp which holds the two outer layers from moving. The fabric holder which is used to pull the fabric through the press is shown in Figure 13(a) and schematics of the friction test setup for the fabric/tool and fabric/fabric conditions are shown in Figures 13(b) and (c), respectively.

The effective coefficient of friction is calculated by

$$\mu_{eff} = \frac{F}{2N} \qquad (3)$$

where the normal force, *N*, is multiplied by a factor of two to account for the two contacting surfaces on either side of the fabric sample.

The test conditions were also based on simulating a range of thermostamping process conditions. Experiments were performed on a Twintex® balanced plain-weave fabric. All samples were cut to be 51 × 76 mm^2, and tests were performed in triplicate to account for any variation among fabric samples.

The coefficient of friction was plotted against the pullout displacement. These curves can result in an initial peak, followed by a drop and then a relatively flat response for the Twintex® woven fabric used in this research. The peak and "flat" portions of the curves correspond to the static and dynamic coefficients of friction, respectively. The magnitude of the peak is a function of the pulling speed and pressure. Figure 14 shows typical coefficients of friction vs. displacement curves for three tests at a pressure of 110 kPa, pullout velocity of 16.7 mm/s, and tool temperature of 85°C.

A constant fabric area remains between the platens for approximately 50 mm of displacement. A drop in the fabric temperature after the fabric is in contact with the platens explains why small variations in the pullout force in the displacement range associated with the dynamic coefficient of friction are observed.

Friction Test Results

Figure 15 shows the static and dynamic coefficients of friction at the fabric/tool interface for the Twintex® balanced plain-weave fabric as a function of pullout velocity [14]. All tests were run with the baseline pressure of 387 kPa and a tool temperature of 85°C. The baseline values were determined from the typical processing conditions for the Twintex® fabric being considered in this research. In Stribeck theory, an increase in velocity causes an increase in the Hersey number. Similarly, an increasing velocity causes viscosity to increase, which also increases the Hersey number. In the hydrodynamic range of the Stribeck curve, an increasing Hersey number corresponds to an increasing coefficient of friction. Figure 15 implies that the friction response is in the hydrodynamic behavior region of the Stribeck curve (Figure 9) because the coefficient of friction increases with increasing velocity and likewise increasing Hersey number.

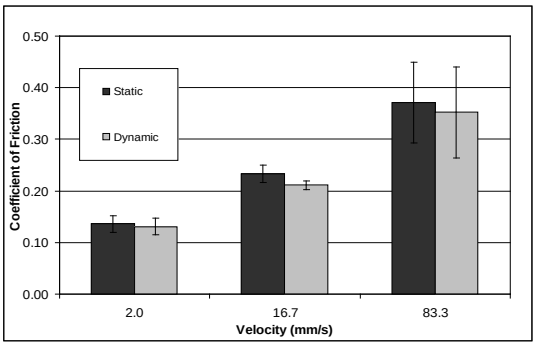

Figure 15. Experimental results (fabric/tool) at different pullout velocities with the baseline pressure of 387 kPa and the baseline tool temperature 85°C [14].

Quantifying the variation of the friction coefficient as a function of velocity is important because during the forming process, the fabric does not necessarily move at a constant velocity along the tooling. In addition, as the fabric conforms to the shape of the die, the tows of the fabric are sheared and reoriented, affecting the rate at which the fabric slides over the surfaces that it is contacting.

Figure 16 shows the variation of the static and dynamic coefficients of friction with changes in normal force (or pressure). The pullout speed was the baseline value of 16.7 mm/s. In Eq. (1), it can be seen that normal force is inversely related to the Hersey number. Therefore, the decrease in the friction coefficient with an increase in normal load shown in Figure 16 also implies the friction behavior to be in the hydrodynamic-friction region of the Stribeck curve (Figure 9).

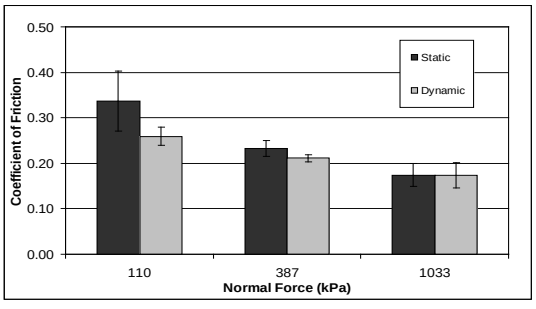

Figure 16. Experimental results (fabric/tool) at different normal loads with the baseline pullout velocity of 16.7 mm/s and the baseline tool temperature of 85°C [14].

Figure 17 shows the static and dynamic coefficients of friction for the balanced plain-weave fabric at the fabric/fabric interface as a function of pullout velocity. Similar to the fabric/tool interface, the coefficient of friction was observed to increase with increasing velocity at the fabric/fabric interface.

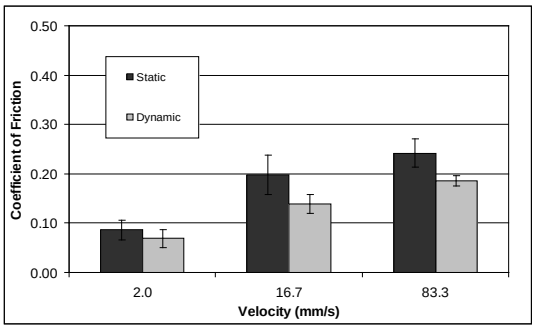

Figure 17. Experimental results (fabric/fabric) at different pullout velocities with the baseline pressure of 387 kPa and the baseline tool temperature of 85°C [14].

Figure 18 displays the effect of normal force on the friction coefficient at the fabric/fabric interface. The decrease in the coefficient of friction with increasing normal force follows the same trend as the results from the fabric/tool interface. Similar trends for the coefficients of friction as a function of normal force and velocity were observed at both the fabric/tool and fabric/fabric interfaces, where only the magnitude of the friction coefficients differed. These trends support that the Stribeck curve can explain the observed friction behaviors.

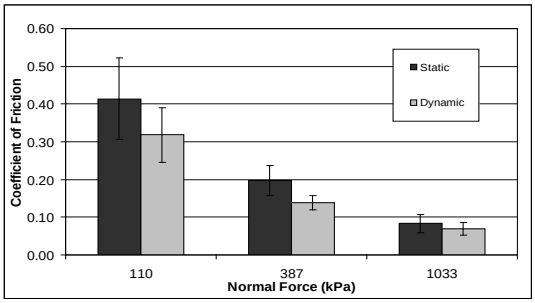

Figure 18. Experimental results (fabric/fabric) at different normal loads with the baseline pullout velocity of 16.7 mm/s [14].

Due to significant differences in friction coefficients under different processing conditions,

any finite-element simulation of the manufacturing process must be able to capture the coefficient of friction as a function of pressure, velocity and temperature. Such dependencies have been implemented in ABAQUS/Standard [**Error! Bookmark not defined.**] ABAQUS/Explicit, and LS-DYNA (explicit version) [15,16] through user-defined friction subroutines for finite-element modeling of the thermostamping process. The effect of fiber orientation on the friction coefficient is currently under further investigation to conclude the importance of yarn orientation on the friction behavior. If orientation is found to be important, then a yarn-orientation parameter will be incorporated in the user-defined friction subroutine.

Characterization of the Mechanical Behavior of the Woven Fabrics Using Experimental Methods

Experimental data were used to derive the material parameters for the constitutive models used in the simulation of the mechanical behavior of the fabrics studied in the forming simulations of the current research. For the forming of composite parts using woven fabrics, these material parameters were needed to describe the nonlinear tensile behavior of the yarns and the nonlinear shear behavior of the fabric.

A yarn behaves differently when incorporated within a crimped fabric than alone because of the undulations of the yarns and the influence of the perpendicular yarns in the fabric. A biaxial tensile test allows the stretching of the fabric in the two yarn directions at the same time, and hence, the determination of the tensile properties of the fabric due to a variety of in-plane-force combinations. In a first approximation, models generally do not account for the effect of the tension in the lateral direction, and that is why the simpler uniaxial testing of single yarns was chosen for the material characterization in this research.

The nonlinear tensile behavior of the fabric due to the decrimping is essential to perform reliable simulations [17]. If the crimp ratio (difference between the length of the yarn and the length of the fabric) is known, then the decrimping part of the stress-strain curve can be extrapolated from the experimental data.

The in-plane shear properties were obtained by a shear-frame test. In the speed range attainable with a conventional tensile machine, the fabric load-deformation response in the shear-frame test was not found to be rate dependent [3].

Experimental Results of the Mechanical Behavior

Three Twintex® woven fabrics composed of commingled polypropylene and glass fibers designed for thermostamping were tested [18]. The fabric characteristics can be found in [19].

Uniaxial tensile testing was performed on an Instron 4464 machine with a 2-kN load cell. Pneumatic cord and yarn grips were used, and the gauge length was set to approximately 1 m to minimize the effect of the deformation in the grips. The displacement rate was 5 mm/s. The stiffness of the yarns was determined from the slope of the load/true-strain curves. In addition, measurements of the crimp ratio were performed. The results, presented in Table 1, were used to assess the tensile behavior of the yarn within the fabric via an extrapolation of the decrimping (Figure 19).

Table 1. Yarn tensile stiffness [18]

Pattern	Tensile stiffness (kN)	Crimp ratio (%)
PW	24.6 ± 0.7	2.0
TWI (warp/weft)	25.1 ± 0.6/ 50.3 ± 0.4	4.4/0.8
TWII (warp/weft)	56.0 ± 0.6	3.0/0.0

Shear-frame tests were performed on the Instron 4464 machine. The geometry chosen for the specimen is shown in Figure 20. Note that to avoid the shearing contribution of the arms, the cross yarns were removed from this part of the sample. The length of the frame L_F was 216 mm, and the length of the fabric L_f was 120 mm.

The specimen was sheared at the rate of 2 mm/s. A mechanical conditioning of five pre-test shearing runs was applied. The mechanical conditioning

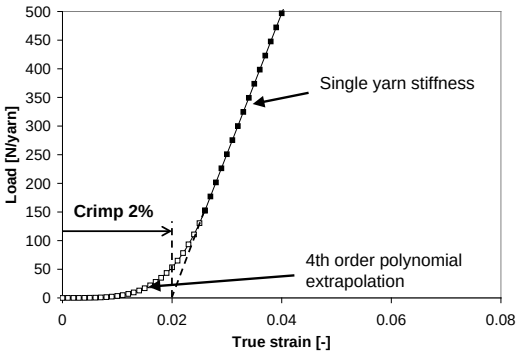

Figure 19. Extrapolation of the fabric tensile behavior from the single yarn stiffness and the crimp ratio for the plain-weave fabric.

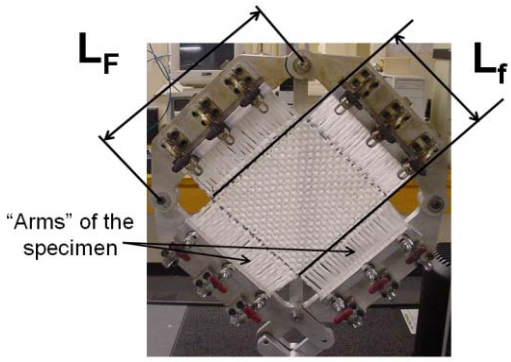

Figure 20. Geometry of the shear frame. Free yarns have been removed in the "arms" of the specimen.

ensured a uniform distribution of the yarns across the sample. The normalized shear force F_{sh} and the shear angle γ were determined from the crosshead displacement δ and the total load on the frame F by the following equations [19]:

$$\gamma = \frac{\pi}{2} - 2.\arccos\left(\frac{\delta}{2.L_F} + \frac{\sqrt{2}}{2}\right) \quad (4)$$

$$F_{sh} = \frac{L_F}{{L_f}^2} \frac{F}{2\cos\left(\pi/4 - \gamma/2\right)} \quad (5)$$

Tests were performed at room temperature and at 175°C, which is the recommended processing temperature for forming of these fabrics. The results are presented in Figures 21 and 22.

The TWI fabric has a very tight weave and exhibits logically higher shear stiffness than the two other Twintex® fabrics. It is worth noting that

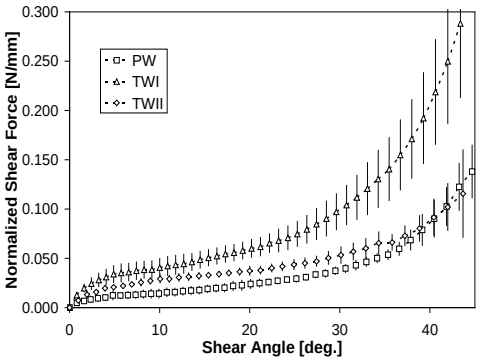

Figure 21. In-plane shear behavior at room temperature [18].

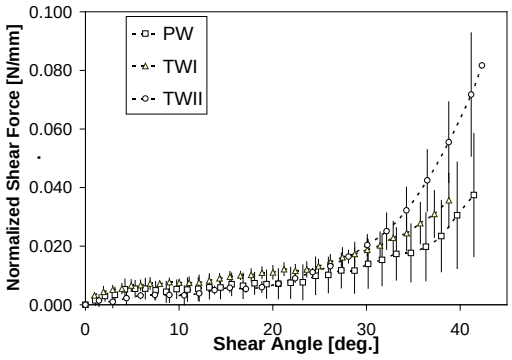

Figure 22. In-plane shear behavior at 175°C [18].

the repeatability (represented by the error bars) is good up to the locking angle (~30° for TWI, ~40° for PW and TWII). At least five tests were used to obtain a reliable average.

Finite-Element Modeling [20,21]

Several modeling approaches have been developed to account for the evolution of the orthotropic directions during high shearing, and these approaches include the continuous approach, the semi-discrete finite element approach and the mesoscopic approach [22]. The first two approaches, while giving good results and being efficient in terms of computing time are generally somewhat complex and sometimes very challenging to implement into commercially available finite element packages. In this research, a discrete mesoscopic approach, based on built-in elements and user-defined material and friction subroutines in commercially-available finite element codes was used. The explicit codes used are ABAQUS and LS-DYNA, and the material

parameters were derived from conventional tensile and shear-frame experimental data as previously discussed in this report.

The method was also implemented into ABAQUS/Standard (implicit solver) [23]. However, problems with convergence in ABAQUS/Standard due to the contact of the fabric with binders other than binder plates that covered all of the fabric could not be overcome. The elements needed for the methodology are not currently available in LS-DYNA's implicit solver, so using the LS-DYNA implicit solver for the process simulation was not an option for this research.

Model Description

The unit cell of the mesoscopic model used in this research for a plain-weave fabric consists of four one-dimensional (1-D) elements and one two-dimensional (2-D) element as shown in Figure 23 for a plain-weave fabric. The 1-D elements carry the tensile loads through the fabric and are able to rotate freely as the fabric is sheared. This rotation of the 1-D elements is a simple and automatic way of accounting for the local changes in orientation of the principal load directions through the fabric. The 2-D element is included in the model to capture the in-plane shear stiffness of the fabric and has no tensile stiffness. The respective material models for the 1-D and 2-D elements were implemented in the finite- element codes by user-defined subroutines. These material models capture the nonlinear load-displacement behavior of the fabric for in-plane tensile and shearing deformations. Unit cells can likewise be defined by a combination of 1-D and 2-D elements for other weave patterns, such as satin and twill weaves [20,23].

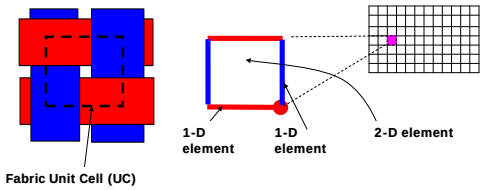

Figure 23. Representative unit cell of the hybrid mesoscopic modeling of a plain-weave fabric [23].

Constitutive Equation for 1-D Elements

The explicit finite-element codes ABAQUS and LS-DYNA allow for customized stress-strain relationships at each time step via a user-defined material subroutine [24]:

$$\Delta\sigma_{ij}^{t+1} = C_{ijkl}.\Delta\varepsilon_{kl}^{t+1/2} \quad (6)$$

where $\Delta\sigma_{ij}^{t+1}$ is the stress increment at time step $t+1$, C_{ijkl} is the constitutive matrix defined by the user-supplied material parameters at time step t, and $\Delta\varepsilon_{kl}^{t+1/2}$ is the midpoint strain increment from the solver. For 1-D elements, Eq. (6) becomes:

$$\Delta\sigma_{11}^{t+1} = C_{11}(\varepsilon_{11}).\Delta\varepsilon_{11}^{t+1/2} \quad (7)$$

where C_{11} is the tangent tensile modulus and is a function of ε_{11}. This tangent modulus is easily deduced from experimental tensile stress-true strain data of the fabric.

Constitutive Equation for 2-D Elements

The incorporation of the in-plane shear behavior in a shell/membrane element for finite-strain analysis is more challenging than the tensile behavior of the 1-D elements. Two reference frames as depicted in Figure 24 have to be considered as the

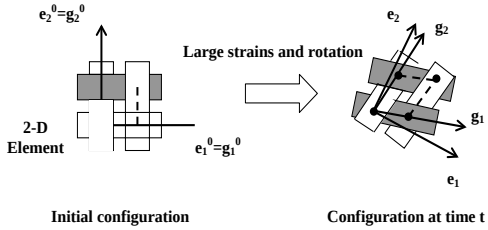

Figure 24. Schematic representation of the reference frames used.

fabric shears from its initial orthogonal configuration to a nonorthogonal configuration. The $\boldsymbol{e_i}$ unit vectors define the local orthogonal reference frame that rotates with the material, and the $\boldsymbol{g_i}$ basis vectors form a nonorthogonal frame that follows the fiber directions:

$$\vec{g}_i = \underline{\underline{F}}.\vec{g}_i^{\,0} = \underline{\underline{F}}.\vec{e}_i^{\,0} \quad (8)$$

where $\underline{\underline{F}}$ is the deformation gradient tensor known at each increment in the deformation process.

The in-plane shear-stress/shear-strain behavior of the woven fabric is captured by:

$$\Delta\tilde{\sigma}_{12}^{t+1} = \tilde{C}_{33}(\gamma_{12}).\Delta\gamma_{12}^{t+1/2} \quad \text{with } \Delta\gamma_{12}^{t+1/2} = 2.\Delta\varepsilon_{12}^{t+1/2} \tag{9}$$

where $\Delta\tilde{\sigma}_{12}^{t+1}$ is the shear-stress increment expressed in $\boldsymbol{g_i}$ and $\tilde{C}_{33}(\gamma_{12})$ is the tangent shear modulus that can be determined from experimental data or by using the analytical method described earlier in this paper. This constitutive equation uses the tensorial shear-strain increment $\Delta\varepsilon_{12}^{t+1/2}$ expressed in the $\boldsymbol{e_i}$ reference frame as it is given by the finite element solver to the user-defined material subroutine. However, the obtained stress increment is expressed in terms of the $\boldsymbol{g_i}$ basis and needs to be returned to the finite-element solver in the $\boldsymbol{e_i}$ basis at the end of the user-defined subroutine. The rotation matrix relating the two reference frames can be obtained from a geometric analysis [25]. The 1-D elements carry the stresses in the $\boldsymbol{g_1}$ and $\boldsymbol{g_2}$ directions, and consequently $\Delta\tilde{\sigma}_{11} = \Delta\tilde{\sigma}_{22} = 0$ in the $\boldsymbol{g_i}$ reference frame within the 2-D element. Therefore, the stress increments are returned to the finite-element solver in the $\boldsymbol{e_i}$ basis using:

$$\begin{aligned}\Delta\sigma_{11} &= 2.\cos\alpha\cos(\alpha+\theta).\Delta\tilde{\sigma}_{12}\\ \Delta\sigma_{22} &= 2.\sin\alpha\sin(\alpha+\theta).\Delta\tilde{\sigma}_{12}\\ \Delta\sigma_{12} &= \sin(2\alpha+\theta).\Delta\tilde{\sigma}_{12}\end{aligned} \tag{10}$$

where the $\Delta\sigma_{ij}$ are the stress increments in the $\boldsymbol{e_i}$ reference frame and the $\Delta\tilde{\sigma}_{ij}$ are the stresses in the $\boldsymbol{g_i}$ reference frame. The angle between $\boldsymbol{e_1}$ and $\boldsymbol{g_1}$ is α, and the angle between $\boldsymbol{g_1}$ and $\boldsymbol{g_2}$ is θ.
To be consistent with finite-element codes that use the logarithmic strains for the summation of the strains increments, the logarithmic definition of strains should be used to determine $\tilde{C}_{33}(\gamma_{12})$ from the experimental data or analytical shear-frame model of the fabric. The true or "logarithmic" shear angle γ^L can be obtained from the logarithmic strains in the principal stretch directions ε_I^L and ε_{II}^L by a 45° Mohr's circle transformation. In the case of a shear frame test, a geometrical analysis leads to the expression of γ^L as a function of the geometric shear angle γ:

$$\gamma^L = \varepsilon_I^L - \varepsilon_{II}^L = -\ln(\tan(\pi/4 - \gamma/2)) \tag{11}$$

The shear stress $\tilde{\sigma}_{12}$ is equal to the normalized shear force F_{sh} [18] divided by the thickness of the fabric. Finally, $\tilde{C}_{33}(\gamma^L)$ is obtained from a derivation of $\tilde{\sigma}_{12}$ versus γ^L of the experimental shear frame test data or using the analytical shear-frame model.

Implementation via the User-Defined Material Subroutines

The method has been implemented via user-defined material subroutines in the explicit finite element codes ABAQUS and LS-DYNA. For ABAQUS, B31 beam elements and S4R shell elements were used, and for LS-DYNA seatbelt elements and Hughs-Liu reduced integration shells (Shell 6) were used. Truss elements can also be used in either ABAQUS or LS-DYNA for modeling of the yarns. However, for large and complex deformations, the convergence of the analysis was found to be difficult to achieve when using truss elements. The LS-DYNA seatbelt element is very efficient in terms of computational time and has the added benefit of having zero compressive stiffness. The modeling of the shear contribution to the material stiffness could potentially be captured using either shell or membrane elements with careful attention being given to the accuracy of the element response at high shear strains.

To demonstrate the capabilities of the methodology to simulate the manufacturing process for Twintex® woven fabrics, plain-weave experimental data at room and elevated temperatures were used to conclude the material parameters for the user-defined material subroutines used in the finite element simulations. The shear stress versus γ^L curve was first developed from normalized experimental data:

- shear stress was assessed from normalized shear force F_{sh} assuming a fabric thickness of 0.5 mm, and
- γ^L was obtained from the geometrical shear angle γ using Eq. (11).

The tangent shear modulus $\tilde{C}_{33}(\gamma^L)$ was then obtained by fitting a 4th-order polynomial to the shear stress vs. γ^L experimental data.

Similarly the tangent tensile modulus was obtained from the tensile load vs. true strain experimental data. The "effective" section of the yarn A_{yarn}, with the assumption of no voids among the fibers was used. It was determined from the known data using the following equation [23]:

$$A_{yarn} = \frac{\rho_{yarn}}{VF_{glass} \cdot \rho_{glass} + (1 - VF_{glass}) \cdot \rho_{PP}} \qquad (12)$$

where VF_{glass} is the glass volume fraction, ρ_{yarn} is the yarn linear density, and ρ_{glass} and ρ_{PP} are the glass and polypropylene densities, respectively. The resulting A_{yarn} is for the fabric being considered in the study. A square beam section was chosen for ABAQUS beams. However, other cross-section geometries (e.g., circle or oval) can be implemented should they be deemed more representative of the fabric. Because of the specific formulation of LS-DYNA seatbelt elements, only the section area could be defined and no cross-section type could be described.

Validation

To validate the modeling approach, a shear frame test and a bias extension test were simulated at room temperature, and the results were compared to experimental data. A finite element model of the shear-frame test used at UMass Lowell was built, including the "arms" of the specimens [18]. The procedure used for completing the shear-frame testing required the removal of the free yarns in the arms of the specimens, so only 1-D elements were used in the model in the area of the arms [Figure 25(a)]. A bias-extension test was also simulated. The characteristic shear-strain field of this test [26] was obtained as shown in Figure 25.

Figures 26 and 27 show a comparison among finite-element results from ABAQUS and LS-DYNA and experimental data to previous experimental work at UMass-Lowell (Shear frame data [18]) and to experimental data from Peng and Cao (Bias extension data [25]) for the Twintex® woven-fabric thermoplastic composite. Very good correlation was obtained between the ABAQUS and LS-DYNA results for both test conditions. The error bars in Figure 26 denote one standard deviation. The simulations correlate well with the experimental data for the shear frame test, which validates the approach used, in particular the way the in-plane shear behavior is implemented.

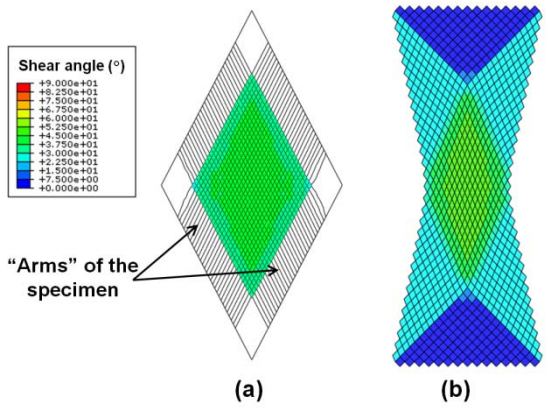

Figure 25. Shear angle contour of (a) the shear frame and (b) the bias extension models (ABAQUS).

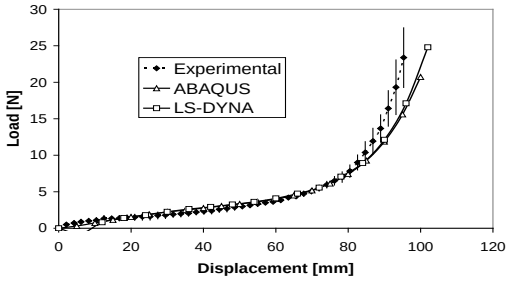

Figure 26. Comparison of the load-displacement curves for the experimental and finite-element simulations of the shear-frame test.

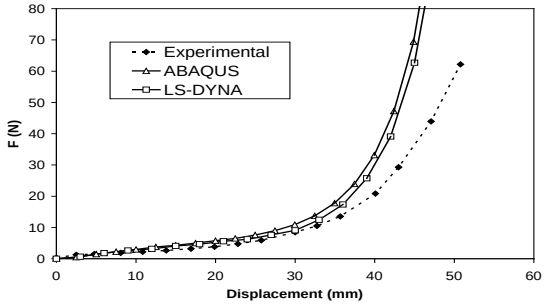

Figure 27. Comparison of the load-displacement curves for the experimental and finite-element simulations of the bias-extension test.

Concerning the bias-extension test, experimental and simulation curves tend to diverge after 35 mm of displacement. This divergence could be a consequence of yarn sliding during the experiment [27], that is not considered in the simulation. This fact has been recently confirmed by experimental data obtained with a Digital Correlation Image technique used to track the shear deformation during the bias-extension test [21]. However, this sliding occurs at very large shear angles that may not be practical in the manufacture of quality parts using this composite forming process.

Thermostamping Modeling

The stamping of a hemisphere was simulated to demonstrate the capability of the approach for compound curvatures. A binder was used to induce in-plane tensile forces within the fabric to eliminate wrinkling. The two finite-element codes give very similar results in terms of shear angle contours (Figure 28). Although an actual thermo-stamped part is not shown here, these finite-element results agree with what is observed in an actual part. For these simulations, the coefficient of friction was 0.3. Future work will use the varying friction coefficient as determined by the 3rd-generation friction testing apparatus.

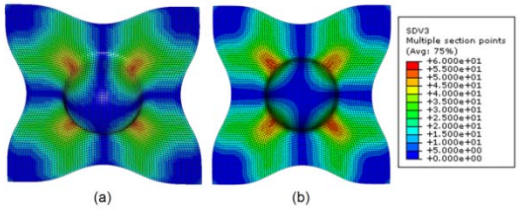

Figure 28. Shear angle contour comparison between (a) LS-DYNA and (b) ABAQUS simulations.

The proposed simulation methodology was also applied to the forming of a composite tub for the automotive industry [28]. The fabric used for these simulations was a plain-weave fabric compounded with a thermoset resin which is pliable at room temperature. This fabric was characterized experimentally using tensile, shear-frame and friction tests. The friction was determined by the 3rd-generation friction testing apparatus to be essentially zero due to the lubrication effect resulting from the compounding material. The woven-fabric material properties were incorporated in the finite element model to simulate the forming process. The resulting parts are shown in Figure 29.

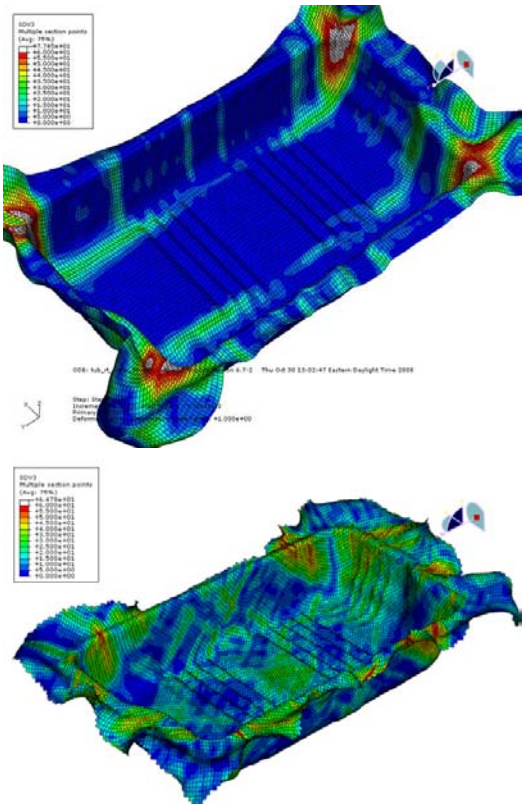

Figure 29. Forming simulation of the Tub for a 0°/90° ply orientation (left) and a ±45° (right). Shear angle contour (blue to red = 0° to 60°, white above 60°).

For the tub shown in Figure 29, the top contour plot shows the resulting shear-strain distribution across the part for a 0°/90° ply orientation, and the bottom is for a ±45° ply orientation. The shear contours range from 0° to 60° as the color contours span from blue to red, respectively. Any shear angles above 60° are shown in white. Note how the 0°/90° ply is blue over a majority of the part. As a result, there is very high shearing in the corners to allow the fabric to assume the shape of the tub. This high shearing of greater than 60° is associated with localized wrinkling. By rotating the fabric 45° as shown in the bottom contour plot, the shearing can be distributed across the part and thereby avoid locally high shearing which can result in wrinkling.

Future Work

Parametric studies of the thermostamping process using the Hersey number friction model and different binder forces will be done to achieve a better understanding of the effect of the in-plane tension on the wrinkling and tearing of the fabric. These studies will demonstrate the usefulness of the model to determine the most appropriate binder force to avoid wrinkling and tearing.

The effect of fiber orientation on the friction coefficient is currently under further investigation to conclude the importance of yarn orientation on the friction behavior. In addition, the importance of the state-of-shear is being investigated.

The modal testing of a stamped part will be performed using a three-dimensional laser vibrometer. Then, comparisons with finite element modal analyses using the final shapes and fiber orientations predicted by the forming simulations will be conducted. This final exercise will show the ability of the approach to provide useful data for subsequent structural analysis in addition to the information on the drapability.

A proposal has been submitted to DOE to use the design tool to simulate the composite forming process of wind turbine blades. The proposed research will investigate the root cause of wrinkling in large composite wind turbine blades which can lead to discarding the part completely or seriously comprising the maximum load capatity of the blade and useful life.

Conclusions

Yarn and fiber parameters were investigated and their ability to model the compaction behavior of commingled fibers has been demonstrated by their influence on the resulting shear load-deformation curve. A 3rd-generation friction-test apparatus using load-control to apply the normal force to the surface of the fabric has been designed, built and validated allowing for the static and dynamic coefficients of friction to be quantified for tool-fabric and fabric-fabric friction. A set of experiments has been developed to quantify the mechanical behavior of woven fabrics for the forming process. A set of constitutive models has been implemented in the ABAQUS and LS-DYNA explicit finite element codes. The ability of the numerical design tool to simulate the forming of composite parts for woven fabric composites has been demonstrated. The design tool is now being used to validate its ability to link the manufacturing process to the structural response of the formed part. This validation will be done by comparing experimental and finite element results for structural stiffness and vibration response of a relatively complex part.

Publications

1. L. Gamache, J. A. Sherwood, J. Chen, and J. Cao. Characterization of the Fabric/Tool and Fabric/Fabric Friction during the Thermostamping Process. Proceedings of the 10th International ESAFORM Conference on Material Forming. Zaragoza, Spain, 2007.
2. L. Gamache. The Design and Implementation of a Friction Test Apparatus Based on the Thermostamping Process of Woven-Fabric Composites, MS Thesis, Department of Mechanical Engineering. Lowell, MA: University of Massachusetts Lowell, 2007.
3. J. Cao, R. Akkerman, P. Boisse, J. Chen, H. S. Cheng, E. F. DeGraaf, J. Gorczyca, P. Harrison, G. Hivet, J. Launay, W. Lee, L. Liu, S. Lomov, A. Long, E. Deluycker, F. Morestin, J. Padvoiskis, X. Q. Peng, J. Sherwood, T. Stoilova, X. M. Tao, I. Verpoest, A. Willems, J. Wiggers, T. X. Yu, and B. Zhu. Characterization of mechanical behavior of woven fabrics: experimental methods and benchmark results. Composites: Part A, 39:1037–1053, 2008.
4. K. A. Fetfatsidis, J. A. Sherwood, J. Chen, and D. Jauffres. Characterization of the fabric/tool and fabric/fabric friction during the thermostamping process. Proceedings of the 12th International Conference. Twente, Nederlands, 2009.
5. D. Jauffres, C. D. Morris, J. Sherwood, and J. Chen. Simulation of the thermostamping of woven composites: determination of the tensile and in-plane shearing behaviors. Proceedings of the 12th International ESAFORM Conference. Twente, Nederlands, 2009.

6. D. Jauffres, C. D. Morris, J. Kremer, J. Sherwood, and J. Chen. Simulation of the thermostamping of woven composites: mesoscopic modeling using FEA explicit codes. Proceedings of the 12th International ESAFORM Conference. Twente, Nederlands, 2009.
7. D. Jauffres, C. D. Morris, J. Sherwood, and J. Chen. Discrete mesoscopic modeling for woven fabric reinforcement forming simulation. International Journal of Material Forming: (in preparation), 2009.
8. D. Jauffres, J. A. Sherwood, J. Chen, C. D. Morris, and J. Kremer. Mesosocopic finite element modeling of woven reinforcements applied to sheet molding compound forming simulation. Proceedings of the 17th International Conference on Composite Materials. Edinburgh, UK, 2009.
9. K. A. Fetfatsidis. Characterization of the Tool/Fabric and Fabric/Fabric Friction for Woven Fabrics: Static and Dynamic, MS Thesis, Department of Mechanical Engineering. Lowell, MA: University of Massachusetts Lowell, 2009.
10. C. D. Morris. Simulation of the Thermostamping Process for Woven Fabric Composites using LS-DYNA, MS Thesis, Department of Mechanical Engineering. Lowell, MA: University of Massachusetts Lowell, 2009.

Acknowledgements

The authors thank the NSF Division of Design, Manufacture, and Industrial Innovation (DMI #0522923), U.S. Department of Energy, and Ford Motor Company (Dr. Patrick Blanchard) for their support of this research. The letter of support from General Motors for the grant proposal is also appreciated. The contributions of Dr. Lu Liu, UMass-Lowell graduate and post doc, MSME students: Lisa Gamache, Corey Morris, Konstantine Fetfatsidis, and James Kremer, and undergraduate students David Winchester and Ezekial Radik are appreciated. The expertise of post doc Dr. David Jauffrès is especially appreciated in the completion of the overall project.

References

1. C. E. Wilks. Characterization of the tool/ply interface during forming. PhD Thesis, School of Mechanical, Materials, Manufacturing and Management. Nottingham, UK: University of Nottingham, 1999.
2. A. E. Long, C. D. Rudd, M. Blagdon, and P. Smith. Characterizing the processing and performance of aligned reinforcements during preform manufacture. Composites: Part A, 27:247–253, 1996.
3. L. Liu, J. Chen, J. Gorczyca, and J. Sherwood. Modeling of friction and shear in thermostamping of composites - Part II. Journal of Composite Materials, 38:1931–1947, 2004.
4. L. Liu, J. Chen, X. Li, and J. Sherwood. Two-dimensional macro-mechanics shear models of woven fabrics. Composites: Part A, 36:105–114, 2005.
5. L. Liu, J. Chen, and J. Sherwood. Analytical model of shear of 4-harness satin weave fabrics. American Institute of Physics Proceedings 712, 8th NUMIFORM Technical Conference, June 13–17. Columbus, OH, 2004.
6. A. Bulusu. Modeling of Architecture and Deformation of Dry Woven Fabrics during Shear. MS Thesis, Department of Mechanical Engineering. Lowell, MA: University of Massachusetts Lowell, 2001.
7. I. M. Hutchings. Tribology: Friction and Wear of Engineering Materials. Ann Arbor, MI: CRC Press, 2002.
8. J. Gorczyca. A Study of the Frictional Behavior of a Plain-Weave Fabric during the Thermostamping Process. DEng Dissertation, Department of Mechanical Engineering. Lowell, MA: University of Massachusetts Lowell, 2004.
9. J. Gorczyca-Cole, J. A. Sherwood, and J. Chen. A friction model for thermostamping commingled glass–polypropylene woven fabrics. Composites: Part A, 38:393–406, 2007.
10. J. Gorczyca, J. Sherwood, L. Liu, and J. Chen. Modeling of friction and shear in

Thermostamping process - Part I. Journal of Composite Materials, 38:1911–1929, 2004.

11. S. Chow. Frictional Interaction between Blank Holder and Fabric in Stamping of Woven Thermoplastic Composites. MS Thesis, Department of Mechanical Engineering. Lowell, MA: University of Massachusetts Lowell, 2002.
12. L. Gamache. The Design and Implementation of a Friction Test Apparatus Based on the Thermostamping Process of Woven-Fabric Composites, MS Thesis, Department of Mechanical Engineering. Lowell, MA: University of Massachusetts Lowell, 2007.
13. L. Gamache. J. A. Sherwood. J. Chen, and J. Cao. Characterization of the Fabric/Tool and Fabric/Fabric Friction during the Thermostamping Process. Proceedings of the 10th International ESAFORM Conference on Material Forming. Zaragoza, Spain, 2007.
14. K. A. Fetfatsidis, J. A. Sherwood, J. Chen, and D. Jauffres. Characterization of the fabric/tool and fabric/fabric friction during the thermostamping process. Proceedings of the 12th International Conference on Material Forming. Twente, Nederlands, 2009.
15. K. A. Fetfatsidis. Characterization of the Tool/Fabric and Fabric/Fabric Friction for Woven Fabrics: Static and Dynamic, MS Thesis, Department of Mechanical Engineering. Lowell, MA: University of Massachusetts Lowell, 2009.
16. C. D. Morris. Simulation of the Thermostamping Process for Woven Fabric Composites using LS-DYNA, MS Thesis, Department of Mechanical Engineering. Lowell, MA: University of Massachusetts Lowell, 2009.
17. A. Willems, S. Lomov, D. Vandepitte, and I. Verpoest. Double dome forming of woven textile composites. Proceedings of the 9th International ESAFORM Conference on Material Forming. Glasgow, UK, 2006.
18. D. Jauffres, C. D. Morris, J. Sherwood, and J. Chen. Simulation of the thermostamping of woven composites: determination of the tensile and in-plane shearing behaviors. Proceedings of the 12th International ESAFORM Conference on Material Forming. Twente, Nederlands, 2009.
19. J. Cao, R. Akkerman, B. Boisse, J. Chen, H. S. Cheng, E. F. DeGraaf, J. Gorczyca, P. Harrison, G. Hivet, J. Launay, W. Lee, L. Liu, S. Lomov, A. Long, E. Deluycker, F. Morestin, J. Padvoiskis, X. Q. Peng, J. Sherwood, T. Stoilova, X. M. Tao, I. Verpoest, A. Willems, J. Wiggers, T. X. Yu, and B. Zhu. Characterization of mechanical behavior of woven fabrics: experimental methods and benchmark results. Composites: Part A, 39:1037–1053, 2008.
20. D. Jauffres, C. D. Morris, J. Kremer, J. Sherwood, and J. Chen. Simulation of the thermostamping of woven composites: mesoscopic modeling using FEA explicit codes. Proceedings of the 12th International ESAFORM Conference on Material Forming. Twente, Nederlands, 2009.
21. D. Jauffres, C. D. Morris, J. Sherwood, and J. Chen. Discrete mesoscopic modeling for woven fabric reinforcement forming simulation. International Journal of Material Forming: (in preparation), 2009.
22. P. Boisse, N. Hamila, F. Helenon, B. Hagege, and J. Cao. Different approaches for woven composite reinforcement forming simulation. International Journal of Material Forming, 1:21–29, 2008.
23. X. Li. Material characterization of woven-fabric composites and finite element analysis of the thermostamping process. DEng Dissertation, Department of Mechanical Engineering. Lowell, MA: University of Massachusetts Lowell, 2005.
24. K. J. Bathe. Finite Element Procedures. Englewood Cliffs: New Jersey: Prentice Hall, 1996.
25. X. Q. Peng and J. Cao. A continuum mechanics-based non-orthogonal constitutive model for woven composite fabrics. Composites: Part A, 36:859–874, 2005.
26. S. Lomov, P. Boisse, E. Deluycker, F. Morestin, K. Vanclooster, D. Vandepitte, I. Verpoest, and A. Willems. Full-field strain

measurements in textile deformability studies. Composites: Part A, 39:1232-1244, 2008.

27. P. Harrison, M. J. Clifford, and A. Long. Shear characterization of viscous woven textile composites: a comparison between picture frame and bias extension experiments. Composites Science and Technology, 64:1453–1465, 2004.

28. D. Jauffres, J. A. Sherwood, J. Chen, C. Morris, and J. Kremer. Mesosocopic finite element modeling of woven reinforcements applied to sheet molding compound forming simulation. Proceedings of the 17th International Conference on Composite Materials. Edinburgh, UK, 2009.

P. Structural Nanocomposite Design

Principal Investigator: Thomas E. Lacy
Associate Professor, Aerospace Engineering
Mississippi State University
316c Walker Bldg., P.O. Box A
Mississippi State, MS 39762
(662) 325-2754; fax: (662) 325-7730; e-mail: Lacy@AE.MsState.edu

Co-Principal Investigator: Chuck Pittman
Lecturer, Chemistry
Mississippi State University,
Hand Land, Rm 3337
Mississippi State, MS 39762
(662) 325-7616; e-mail: cpittman@chemistry.msstate.edu

Co-Principal Investigator: Hossein Toghiani
Associate Professor, Chemical Engineering
Mississippi State University,
Swalm Engineering Bldg.
Mississippi State, MS 39762
(662) 325-8607; e-mail: hossein@che.msstate.edu

Co-Principal Investigator: Yuanxin Zhou
Assistant Professor, Tuskegee Center for Advanced Materials (T-CAM), Department of Mechanical Engineering
Tuskegee University
Tuskegee AL 36088
(334) 724-4222; fax: (334) 727-8801; e-mail: yzhou@tuskegee.edu

Co-Principal Investigator: Shaik Jeelani
Director, Tuskegee Center for Advanced Materials (T-CAM)
Vice President, Research and Sponsored Programs
Tuskegee University
Tuskegee, AL 36088
(334) 727-8970; fax: (334) 724-4224; e-mail: jeelanis@tuskegee.edu

Technology Area Development Manager: Joseph A. Carpenter
(202) 586-1022; fax: (202) 586-1600; e-mail: joseph.carpenter@ee.doe.gov

Field Project Officer: Aaron D. Yocum
(304) 285-4852; fax: (304) 285-4403; e-mail: aaron.yocum@netl.doe.gov

---

Contractor: Mississippi State University (MSST)
Contract No.: 4000054701

Objective

- Design low-cost nanoreinforced composite systems for automotive structural applications.
- Approach

- A multiscale design methodology is being employed to investigate the effects of nanoreinforcements on the mechanical properties of fiber-reinforced composites for automotive structural applications. Critical issues being addressed include: selection of key combinations of fibers (glass, carbon, natural, *etc.*), matrix materials (thermoset, thermoplastic), and relatively cost-effective nanoreinforcements (vapor grown carbon nanofibers, nanoclay particles, *etc.*); fabrication of fine-scale and coupon-scale material samples for static and dynamic testing; and development of a multiscale materials modeling strategy for assessing high-performance nanocomposites that accounts for the influence of material processing parameters on mechanical properties of the material under static and dynamic loads. This effort involves completion of five primary objectives.
- Determine appropriate composite fiber-matrix systems and identify and prioritize candidate nanoreinforcements for evaluation.
- Investigate the effects of different mixtures of nanoreinforced fibers/polymer matrices from a manufacturing and cost perspective.
- Quantify nanoreinforced structure-property relations experimentally.
- Study material failure modes and energy absorption characteristics under different loading conditions
- Development of a multiscale materials model based upon micromechanics models and experiments for nanocomposites.

Accomplishments

- Selected readily available low-cost thermoset resins (vinyl ester, polyester) as the primary matrix materials in this investigation; other polymer resins (*e.g.*, epoxy, polypropylene) may be considered as part of supplemental investigations associated with this work (Year 1).
- Selected Applied Science, Inc. PR-24 vapor grown carbon nanofibers (VGCNFs) as the primary nanoreinforcement for use in this examination (Year 1).
- Selected E-glass unidirectional and woven fabric plies as the primary traditional continuous fiber reinforcement phase in this investigation because of their widespread use in automotive applications (Year 1).
- Fabricated nanophased resin test specimens comprised of thermoset (vinyl ester, polyester) resins and varying weight fractions of VGCNFs using a combination of mechanical mixing, sonication and high shear mixing and dispersing agent (Year 1, 2).
- Evaluated the dispersion of nanoreinforcements within polymer resins using scanning electron microscopy (SEM) and transmission electron microscopy (TEM) (Year 1, 2).
- Evaluated VGCNF surface functionalization and use of dispersants in order to enhance nanofiber dispersion in and interaction with the thermoset matrices, as well as to minimize VGCNF agglomeration (Year 1, 2).
- Fabricated continuous fiber E-glass laminates and sandwich composites with nanophased thermoset using vacuum-assisted resin transfer molding (VARTM) (Year 1).
- Performed three-point bend experiments for two-phase (nanoreinforced) resin test specimens comprised of polyester reinforcement with varying weight fractions of CNFs (0.0%, 0.5%, 1.0%, 1.5%, 2.0%, 3.0%) (Year 1).
- Established a student exchange between MSST and T-CAM, where two MSST minority undergraduate students fabricated CNF/ polyester three-point bend test specimens and compression test specimens using T-CAM experimental facilities (Year 1).
- Used SEM to assess damage morphology and failure mechanisms for nanophased resins (Year 1).
- Performed dynamic mechanical analysis (DMA), thermo-gravimetric analysis (TGA), standard coupon and split Hopkinson bar testing to assess the thermal/ mechanical properties of nanophased polymer resins (Year 1, 2).
- Initiated development of a multiscale-materials modeling strategy that employs a combination of micromechanics models, three-dimensional (3D) finite elements (ABAQUS, GENOA), and validation experiments for nanocomposites (Year 1, 2).

- Established a partnership with AlphaStar, Inc. for the modeling of nanocomposites using the finite-element code, GENOA (Year 1, 2).
- Submitted and published two refereed journal articles and two conference papers (Year 1, 2).

Future Direction

- Continue ongoing dynamic mechanical analysis (DMA), thermo-gravimetric analysis (TGA), and standard coupon and split Hopkinson bar testing of VGCNF/ vinyl ester resins to assess the thermal and mechanical properties of nanophased polymer resins.
- Conduct structure-property tests for three-phase composite systems (nanophased resin, E-glass plies) in order to assess the mechanical behavior and failure of the structural nanocomposites.
- Determine weight fractions of nanoreinforcements that lead to optimal nanophased resin and structural nanocomposite properties.
- Determine material failure modes and energy absorption characteristics for structural nanocomposites subjected to static and dynamic loading conditions. Perform flexure, tension, fatigue, fracture, and dynamic tests of structural nanocomposites.
- Validate micromechanical model for determining effective properties of nanophased resins using structure-property data.
- Incorporate effective nanophased resin properties from micromechanical models into 3D finite- element models of three-phase composites. Validate numerical models using structure-property data.

Introduction

A multiscale design methodology is being employed to investigate the effects of nanoreinforcements on the mechanical properties of fiber-reinforced composites for automotive structural applications. Critical issues being addressed include: selection of key combinations of fibers (glass, carbon, natural, etc.), matrix materials (thermoset, thermoplastic) and relatively cost-effective nanoreinforcements (vapor grown carbon nanofibers, nanoclay particles, etc.); fabrication of fine scale and coupon scale material samples for static and dynamic testing; and development of a multiscale materials modeling strategy for assessing high-performance nanocomposites that accounts for the influence of material processing parameters on mechanical properties of the material under static and dynamic loads. A literature review of recent experimental and modeling activities related to nanoreinforced composites, particularly those involving glass fibers coupled with thermoset resins (e.g., vinyl ester, polyester, as well as epoxy) was performed (cf., Odegard, et al., 2001; Ghoniem, et al, 2003; Thostenson, et al., 2004; Buryachenko, et al., 2005; Gates, et al., 2005; Odegard, et al., 2005; Valavala and Odegard, 2005; Hussein, et al., 2006*;* Liu and Brinson, 2006*;* Fischer, et al., 2007). Such material systems are of particular interest to the Automobile Composites Consortium (ACC). A dialogue has been initiated with the ACC in order to solicit guidance and feedback on relevant aspects of the research, including identification of additional industry partners to participate in cost-share relationships with MSST, T-CAM and the DOE. A summary of year two accomplishments is included in the following discussion.

Determination of Composite Fiber-matrix Systems and Nanoreinforcements

Because of their widespread use and relatively low cost, two commercially available thermoset resins (U.S. Composites, Inc. polyester and Ashland Co. vinyl ester) were selected as the primary matrix materials in this investigation; other polymer resins (e.g., epoxy and polypropylene) are being considered as part of supplemental investigations associated with this work (cf., Zhou, et al., 2007; Ingram, et al., 2008). Applied Science, Inc. PR-24 vapor grown carbon nanofibers (VGCNFs) (typical diameters, 60–200 nm; typical lengths, 20–100 μm) were selected as the primary nanoreinforcement for use in this examination.

VGCNFs are relatively inexpensive and possess excellent mechanical properties. Because of prevalent use in automotive applications, E-glass unidirectional and woven fabric plies are being used as the primary traditional continuous fiber reinforcement phase in this investigation.

Investigation of the Effects of Different Mixtures of Nanoreinforced Fibers/ Polymer Matrices on Manufacturing Vinyl Ester Nanocomposite Formulation

In year two, nanophased resin test specimens comprised of a thermoset vinylester (VE) resin and varying weight fractions of VGCNFs were fabricated at MSST using a combination of mechanical mixing, sonication, high shear mixing, addition of dispersing agents, and cure. Vinyl esters possess superior mechanical properties compared to unsaturated polyesters. Derakane 441–400 (Ashland Co.), with a relatively low styrene content (33%), was selected as the candidate matrix. In order to assess the effect of nanoreinforcement surface-modification on mechanical properties of the nanocomposite, two different grades of VGCNFs were used: (1) PR-24-XT-LHT (Applied Sciences, Inc.), which is a pristine (unmodified) VGCNF similar to the one used previously with unsaturated polyesters (year one), and (2) PR-24-XT-LHT-OX (Applied Sciences, Inc.), which is a surface-oxidized VGCNF with mainly carboxylic-type functional groups on the nanofiber surface. Nanoreinforcement functionalization is an established methodology for the enhancement of dispersion and load transfer capabilities of the resin-embedded nanoreinforcements.

In order to investigate the effect of nanocomposite formulation, mixing/processing, and curing conditions on the mechanical properties of the VGCNF/ VE nanocomposites, a factorial design of experiments approach is being employed. The goal of this work is to establish nanocomposite formulation and processing conditions resulting in optimal mechanical properties. A total of 48 different combinations of processing and configuration parameters were considered in this study. The individual factors (independent variables) considered in this study include:

1. Nanofiber "loading" level (0.25, 0.50, 0.75, and 1.00 phr). Here, "phr" stands for "parts per hundred resin," which is a standard basis for formulations common in the resin industry. Essentially, 1.0 phr suggests that a mixture contains one part of a given constituent (by weight) for every 100 parts of resin (by weight). VGCNF loading levels in excess of 1.00 phr were not considered in this examination due excessive viscosity of the resin/ nanoreinforcement mixture. Relatively low viscosity nanophased resins are desirable because of potential use in future vacuum-assisted resin transfer molding (VARTM) or other resin infusion process.
2. Nanofiber type (pristine and oxidized). The effect of different nanofiber surface chemistries on the dispersion characteristics and overall mechanical properties are being investigated. The oxidized nanofibers (PR-24-XT-LHT-OX) were used as received. Additional VGCNF surface functionalization is planned for year three.
3. Use of chemical dispersing agents (i.e., dispersants or surfactants) to facilitate nanofiber dispersion within the resin. A preliminary study was conducted using several readily available inexpensive dispersing agents (BYK-9076, BYK-9077, BYK-996, and Disperbyk-191 from BYK Chemie Co.). Based upon this study, BYK-9076 was selected as the most effective surfactant for use in the experimental design. The effect of a dispersing agent on nanofiber dispersion quality and ultimate mechanical properties of the nanocomposite is being investigated.
4. Mixing method (ultrasonication, high-shear mixing, and coupled high-shear mixing/ ultrasonication). One of the key steps in the fabrication of polymer nanocomposites is the incorporation of nanoreinforcements into the matrix by means of a suitable mixing method. The efficiency of the mixing method in dispersing and distributing nanofibers in the matrix plays a crucial role in achieving optimal nanocomposite properties. VGCNFs tend to agglomerate, due to high van der Waals interactions. Ideally, such agglomerates and VGCNF clusters must be separated into individual nanofibers during mixing. This can be achieved, though not completely, by

different means: ultrasonication, shearing action of special blades, etc. In this study, a novel high shear mixer is used alongside the more traditional ultrasonicator used in year one.

The VGCNF/VE nanocomposite formulations considered in this study are shown in Table 1. Due to rigorous mixing of nanofibers into the resin, excessive void formation is a concern. Hence, a surfactant (BYK-A515) and antifoam (degassing) agent (BYK-A555) were used as an integral part of each formulation to aid degassing of the mixture. A promoter, cobalt naphthenate 6% (North American Composites Co.), was used in each formulation to facilitate the resin curing reaction. One phr of methyl ethyl ketone peroxide (MEKP) was used as the curing agent (hardener); this amount provides a gelling time of 30–50 minutes, which is necessary for degassing of the mixture and pouring it in the mold.

Table 1. Formulation of nanocomposites

Ingredient	Weight (g)
Derakane 441–400 (vinyl ester resin)	100
Cobalt naphthenate 6%	0.20
BYK-A 515	0.20
BYK-A 555	0.20
BYK-9076[a]	1:1 ratio with VGCNF
VGCNF[b]	0.25/0.50/0.75/1.00
MEKP	1.00

[a]BYK-9076 was not used in all configurations
[b]Pristine and oxidized nanofibers were used in different configurations

Vinyl Ester Nanocomposite Specimen Preparation

VGCNF/VE test specimens were fabricated for use in dynamic mechanical analysis (DMA), four-point bending, and tension and split Hopkinson bar experiments. The following procedure was used in specimen preparation:

1. Individual ingredients were weighed and added to a 240 ml cup in the following order: resin, promoter, air release agents, dispersing agent (if used), and VGCNFs. Prior to the addition of nanofibers, the initial mixture was blended by hand to ensure that the promoter, air release agents, and the dispersing agent were uniformly distributed within the resin.
2. The liquid resin mixture was then processed in one of several ways depending on the configuration: (a) five minutes in a mechanical stirrer at 1500 revolutions per minute (rpm), followed by one hour sonication at an amplitude of 20% in continuous mode (no pulse). The cup was mounted on a special vortex mixer that shakes the cup for a uniform power input and was kept cool by a high-speed fan; (b) 15 min. in a Silverson high-shear mixer. The cup was immersed in an ice bath during mixing to avoid overheating of the liquid resin; and (c) 15 min. of high-shear mixing followed by one hour of sonication in the same manner as described above.
3. The hardener was then added to the mixture and mixed by hand for five minutes.
4. The mixture was degassed for 5–15 min. using a vacuum pump until all the air bubbles were removed. The degassing time varied for each configuration due to of differences in the viscosity of each mixture. Care was to taken to avoid removing an excessive amount of styrene during degassing.
5. The resin was gently poured into specimen molds and cured in an oven at elevated temperatures (five hours at 60°C and two hours at 120°C). It should be noted that the presence of a dispersing agent had a minor effect on the curing reaction (i.e., the exposed surface of these specimens in the mold appeared somewhat "tacky"). This issue will be addressed in year three.

The dispersion of nanoreinforcements within the cured resin for each configuration is being evaluated using a combination of scanning electron microscopy (SEM) and transmission electron microscopy (TEM); this assessment will continue into year three of the project.
As mentioned in an earlier report, vacuum assisted resin transfer molding (VARTM) has been established as a viable technique to fabricate continuous fiber E-glass laminates with

nanophased thermoset resins involving a variety of different nanoreinforcements (cf., Chisholm, et al., 2005; Chowdhury, et al., 2006, Zhou, et al., 2006). VARTM may be used to produce high quality composite parts and is an attractive alternative to autoclave processing. One key concern, however, is that a gradient in the distribution of VGCNFs may result due to filtering by continuous fiber plies in the vicinity of the infusion ports used in the VARTM process. The issue will be investigated in year three; continuous fiber composites with VGCNF/ VE resins fabricated using the VARTM technique will be destructively sectioned and examined using TEM and/or SEM imaging to assess the degree of VGCNF filtration.

Experimental Structure-Property relations for Nanoreinforced Materials

Dynamic Mechanical Analysis (DMA) of VGCNF/VE Nanocomposites

Dynamic mechanical analysis (DMA) and thermo-gravimetric analysis (TGA) testing of VGCNF/VE nanocomposites are currently being performed to assess the thermal properties of nanophased thermoset resins. The nanocomposite storage modulus (measure of material stiffness), loss modulus (measure of material toughness and energy dissipation capability), and tan delta (measure of damping) were selected as mechanical responses for the comparison between different material and fabrication conditions. The tests were conducted in a DMA Q800 instrument in single cantilever mode at a fixed frequency of 10 Hz and with a heating rate of 5˚C/min. The temperature scan was from room temperature to 160˚C.

At the time of this report, a total of 17 VGCNF/VE samples that were prepared using ultrasonication alone as the primary mixing technique had been tested. These specimens include: 1) one neat VE specimen (0 phr VGCNF); 2) four specimens were prepared using 0.25, 0.50, 0.75, and 1.0 phr of pristine (unoxidized) VGCNFs, respectively; 3) four specimens were prepared using 0.25, 0.50, 0.75, and 1.0 phr of pristine (unoxidized) VGCNFs and BYK-9076 dispersant, respectively; 4) four specimens were prepared using 0.25, 0.50, 0.75, and 1.0 phr of oxidized VGCNFs, respectively; and 5) four specimens were prepared using 0.25, 0.50, 0.75, and 1.0 phr of oxidized VGCNFs and BYK-9076 dispersant, respectively. The testing of other specimens prepared using high-shear mixing and coupled ultrasonication/ high-shear mixing is ongoing.

Figure 1 contains a plot of the measured storage modulus as a function of temperature for neat VE resin and pristine VGCNF/VE nanocomposites (no dispersing agent). As can be seen from the figure, the storage modulus (and nanocomposite stiffness) increased significantly as the weight fraction of pristine VGCNFs increased from 0 to 0.5 phr. At room temperature, the storage modulus for a nanocomposite specimen with 0.50 phr VGCNF was roughly 22% higher than the neat resin. As the weight fraction of nanofibers is further increased (0.75 and 1.0 phr), however, the improvement in storage modulus *decreased* to roughly 12% over the neat resin. The apparent degradation in storage modulus that occurs once the weight fraction of VGCNFs exceeds some optimal value is likely due to relatively poor nanofiber dispersion. For example, Figures 2 and 3 show typical SEM images of highly clustered VGCNFs in the VE resins for specimens containing 0.50 and 0.75 phr nanofibers, respectively. These regions act as potential stress raisers within the matrix, while providing relatively little in the way of stiffness increase. These results suggest that inclusion of relatively small amounts of nanoreinforcements can have a noticeable effect on nanocomposite material properties, provided that the nanofibers can be dispersed properly.

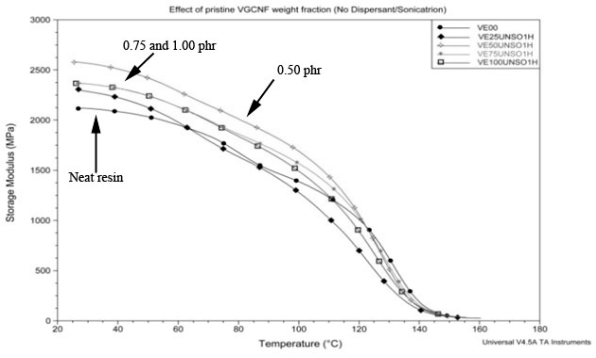

Figure 1. Effect of pristine VGCNF weight fraction on storage modulus (no dispersing agent).

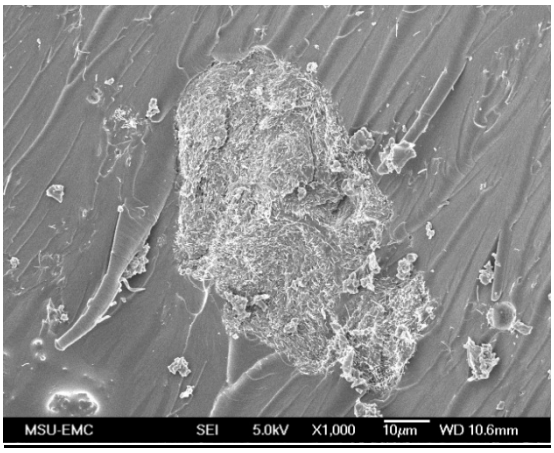

Figure 2. SEM image of a cluster of carbon nanofibers in the VE matrix (0.50 phr pristine VGCNF/ no dispersing agent/ ultrasonication).

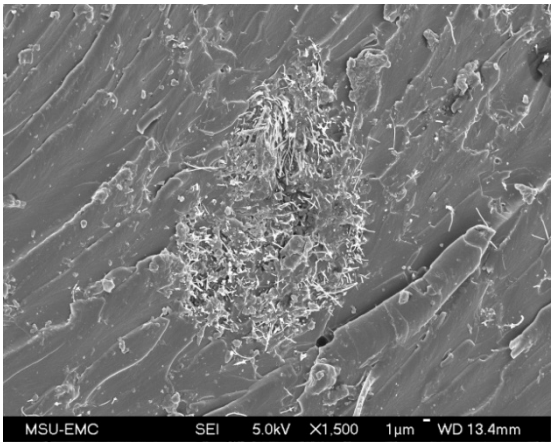

Figure 3. SEM image of a cluster of carbon nanofibers in the VE matrix (0.75 phr pristine VGCNF/no dispersing agent/ ultrasonication).

Figure 4 contains a plot of the measured storage modulus as a function of temperature for neat VE resin and pristine VGCNF/ VE nanocomposites where a dispersing agent was employed to facilitate nanofiber dispersion (the ratio of dispersing agent to VGCNF was 1:1 for each configuration). Similar to the results presented in Figure 1, the storage modulus increased with increasing weight fraction of VGCNFs. At room temperature, the storage modulus for nanocomposite specimens with 0.25, 0.50, and 0.75 phr VGCNFs were each roughly 17% higher than the neat resin. In contrast to the preceding results, however, the greatest improvement in storage modulus (~25%) occurred for 1.0 phr weight fraction of nanofibers.

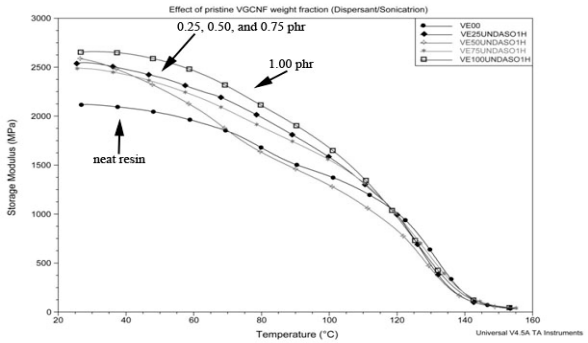

Figure 4. Effect of pristine VGCNF weight fraction on storage modulus in the presence of the dispersing agent.

Figure 5 contains a plot of the measured storage modulus for 1.0 phr VGCNF/VE resin specimens fabricated with and without a dispersing agent. Included in the figure is the measured storage modulus for the neat resin. As can be seen from the figure, the use of small amounts of dispersant can improve the mechanical properties of the nanocomposite through improved dispersion of nanofibers. One concern, however, is that the dispersing agent may have a negative effect on the properties of the neat resin. This issue will be addressed in year three.

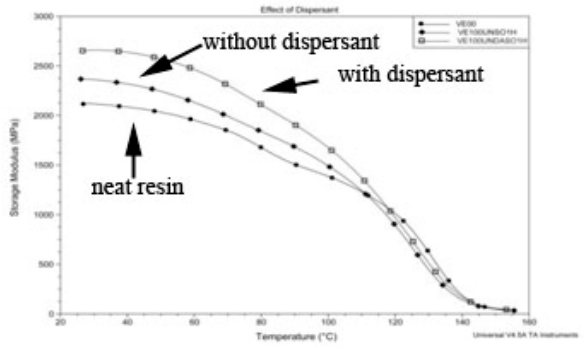

Figure 5. Effect of dispersing agent on storage modulus (1.0 phr pristine VGCNF).

Figure 6 contains a plot of the measured loss modulus as a function of temperature for neat VE resin and pristine VGCNF/VE nanocomposites (no dispersing agent). As can be seen from the figure, the loss modulus for the neat resin generally increased with increasing temperature up until the temperature approached the glass transition temperature (~140˚C). In addition, a characteristic "hump" or local maxima in loss modulus can be observed at around 80˚C. This suggests that the

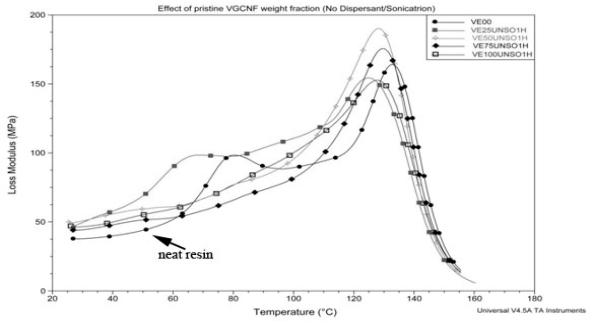

Figure 6. Effect of pristine VGCNF weight fraction on loss modulus (no dispersing agent).

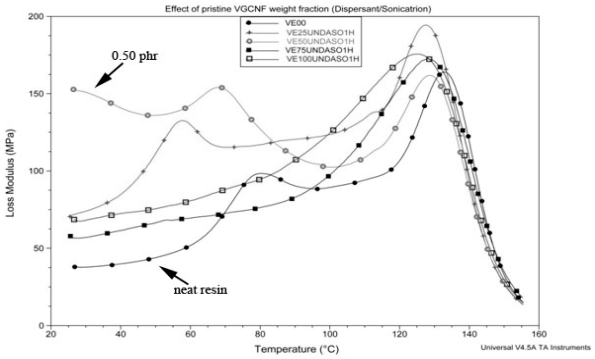

Figure 7. Effect of pristine VGCNF weight fraction on loss modulus in the presence of dispersing agent.

neat resin is better able to dissipate energy in the vicinity of this temperature. In the absence of a dispersing agent, the inclusion of VGCNFs only has a modest effect on the loss modulus. For the 0.25 phr VGCNF nanocomposite, the loss modulus was slightly larger than that of the neat resin with a local maxima occurring at around 60˚C. As the nanofiber weight fraction is increased, however, the difference in loss moduli of the nanocomposite specimens and the neat resin was minimal. Moreover, at higher weight fractions of nanofibers, no local maxima were observed at lower temperatures. While the nanocomposite loss moduli (energy dissipating capability) at moderate temperatures were slightly larger than that of the neat resin, the relative improvement was small in comparison to the improvement in storage modulus (stiffness).

When a dispersing agent is used in the nanocomposite processing, however, the relative improvement in loss modulus is more pronounced. Figure 7 contains a plot of the measured loss modulus as a function of temperature for neat VE resin and pristine VGCNF/VE nanocomposites fabricated using a dispersing agent. At moderate temperatures, the nanocomposite loss moduli were all somewhat larger than that of the neat resin. In addition, the 0.5 phr specimen demonstrated an appreciable increase in loss modulus and consistent with the neat resin, retained a local maximum value in the vicinity of 60˚C. These results suggest that the nanophased resins are better able to dissipate energy (and have greater stiffness) than the neat resin. As mentioned previously, one concern is that the bulk properties of the resin are affected by the presence of the dispersant. In order to investigate whether the improvement in loss modulus was due to better dispersion of nanofibers or due to a change in properties of the modified resin (VE plus dispersant), additional DMA tests are planned for year three involving the modified resin with no nanoreinforcements.

Figures 8 and 9 show SEM images of two typical regions within a 1.00 phr pristine VGCNF specimen prepared using a dispersing agent. While VGCNF clusters are not completely eliminated (cf., Figure 9), the distribution of individual nanofibers is somewhat more uniform throughout the matrix. This is an indication of relatively better dispersion of nanofibers in the presence of the dispersing agent.

Figures 10 and 11 show the effect of different nanofiber weight fractions on a material's tan delta behavior (ratio between loss and storage modulus) for specimens prepared with and without a disperant, respectively. As can be seen in the

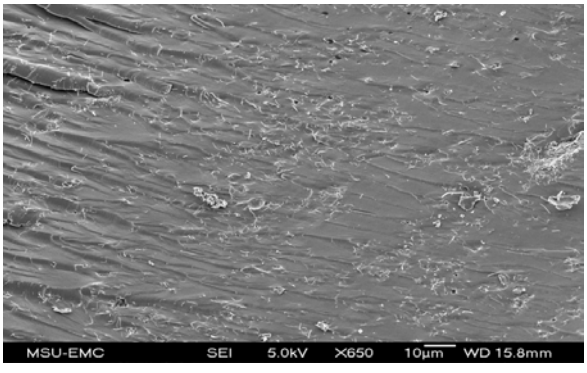

Figure 8. SEM image nanocomposite region with well-dispersed nanofibers (1.00 phr pristine VGCNF/ dispersing agent/ ultrasonication).

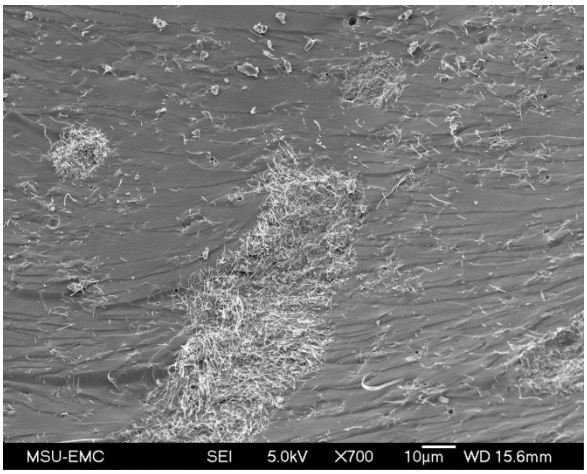

Figure 9. SEM image of a nanofiber cluster surrounded by well-dispersed nanofibers (1.00 phr pristine VGCNF/dispersing agent/ultrasonication).

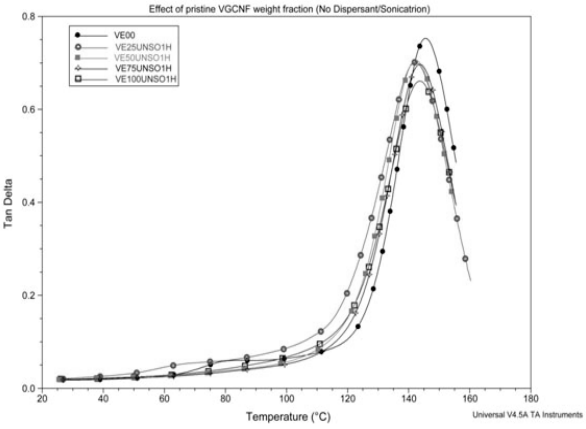

Figure 10. Effect of pristine VGCNF weight fraction on tan delta in the absence of dispersing agent.

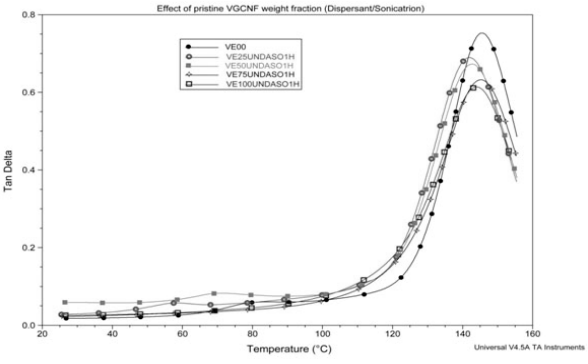

Figure 11. Effect of pristine VGCNF weight fraction on tan delta in the presence of dispersing agent.

figures, the location of the peak tan delta values (an indication of material's glass transition temperature) is not changed appreciably. This suggests that the glass transition temperature and damping behavior of the nanocomposites are almost independent of the nanofiber weight fraction and degree of nanofiber dispersion.

A similar set of DMA experiments were performed using specimens fabricated with oxidized VGCNFs. In general, such specimens would be expected to possess superior mechanical properties due to enhanced interaction with the thermoset resin in comparison to those obtained from specimens using unoxidized (pristine) nanofibers. Oxidized VGCNFs, however, tend to absorb moisture and clump together. As a consequence, oxidized nanofibers were somewhat difficult to disperse in the VE resin using ultrasonication alone. Ongoing efforts suggest that oxidized VGCNFs can be well dispersed in VE using a combination of high shear mixing and sonication. This work will continue in year three.

For comparison purposes, however, DMA tests were performed on oxidized VGCNF/VE specimens fabricated using ultrasonication alone. Figure 12 contains a plot of the measured storage modulus as a function of temperature for neat VE resin and *oxidized* VGCNF/VE nanocomposites (no dispersing agent). In contrast to the results obtained for pristine (unoxidized) fibers, at room temperature the storage moduli for 0.25 and 1.00 phr nanocomposites were slightly lower than that of the neat resin (i.e., no improvement in stiffness). At room temperature, the storage modulus for a nanocomposite specimen with 0.75 phr VGCNF was roughly 13% larger than that of the neat resin (recall that 0.50 phr of unoxidized VGCNFs yielded a 22% improvement in storage modulus; cf., Figure 1) . These results are likely a consequence of poor dispersion of oxidized VGCNFs within the matrix. SEM imaging of these specimens will be used in year three to assess nanofiber dispersion. Of course, the efficient breakup of nanofiber clumps is crucial for achieving optimal material property enhancement.

Surprisingly, the use of a dispersing agent in the fabrication of oxidized VGCNF/VE specimens had very little effect on the measured storage modulus (cf., Figure 13); here the ratio of dispersing agent to VGCNF was 1:2 for each

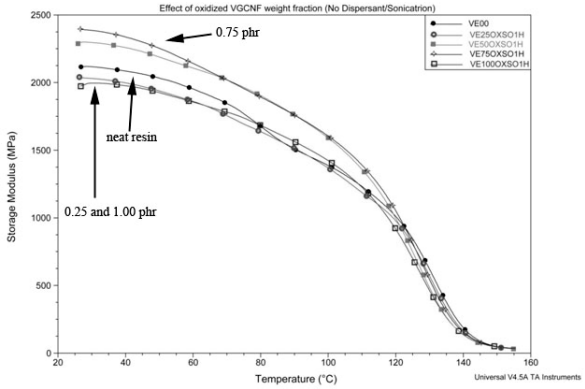

Figure 12. Effect of oxidized VGCNF weight fraction on storage modulus (no dispersing agent).

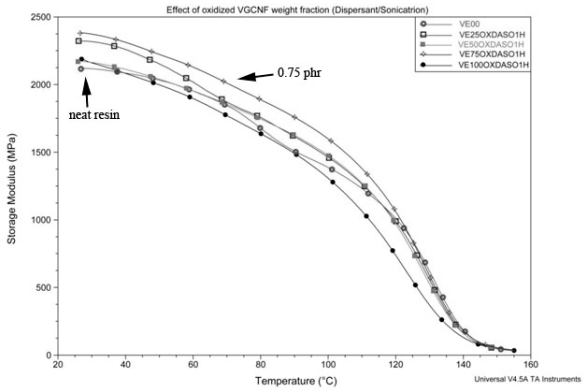

Figure 13. Effect of oxidized VGCNF weight fraction on storage modulus in the presence of dispersing agent.

configuration. As can be seen from the figure, the greatest improvement in storage modulus (~12%) occurred for 0.75 phr VGCNF. As an aside, an investigation aimed at determining the optimal weight fraction of dispersing agent will be performed in year three.

Unexpectedly, the property enhancement associated with the use of oxidized VGCNFs was not as pronounced as for unoxidized (pristine) VGCNFs. For example, Figure 14 compares the measured storage moduli for nanocomposite specimens prepared using pristine and oxidized nanofibers with no dispersant. Note that specimen containing 0.50 phr pristine VGCNFs resulted in the greatest improvement in storage modulus. These results underscore the coupled influence of nanofiber surface functionalization and dispersion on mechanical properties. Future work will focus on obtaining optimal dispersion of oxidized

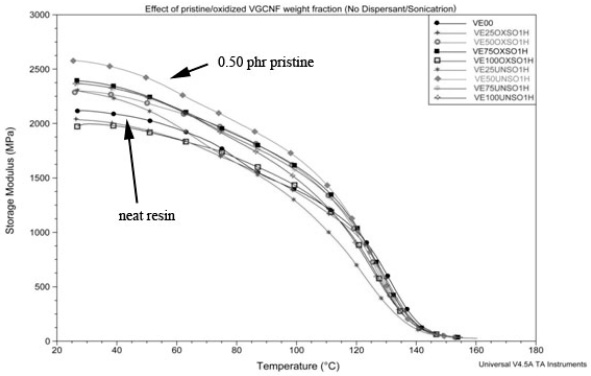

Figure 14. Effect of oxidized and pristine VGCNF weight fraction on storage modulus (no dispersing agent).

VGCNFs using coupled high-shear mixing and sonication, as well as characterization of nanofiber dispersion using a combination of SEM and TEM.

Figures 15 and 16 show the effect of oxidized nanofiber weight fraction on nanocomposite loss modulus for specimens fabricated with and

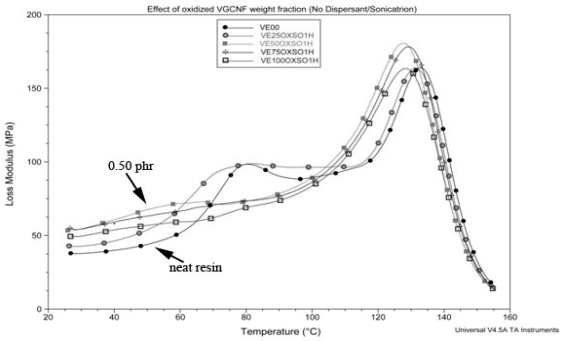

Figure 15. Effect of oxidized VGCNF weight fraction on loss modulus (no dispersing agent).

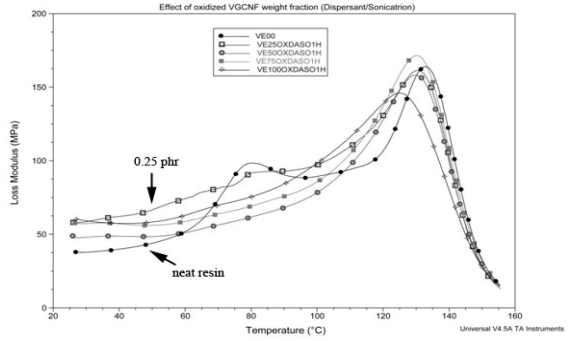

Figure 16. Effect of oxidized VGCNF weight fraction on loss modulus in the presence of dispersing agent.

without a dispersing agent, respectively. In both cases, the change in the loss modulus is relatively small for all nanofiber weight fractions. Similar to the case with pristine nanofibers, the measured tan delta behavior for oxidized nanofibers is not changed appreciably for different nanofiber weight fractions (cf., Figures 17 and 18).

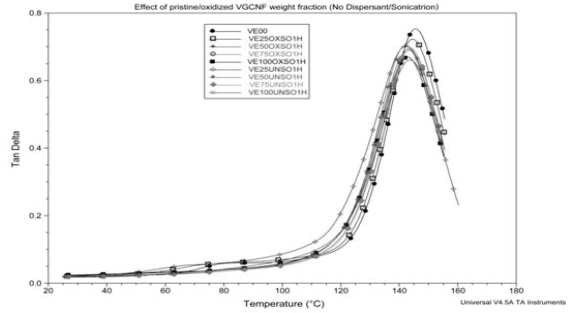

Figure 17. Effect of pristine/oxidized VGCNF weight fraction on tan delta (no dispersing agent).

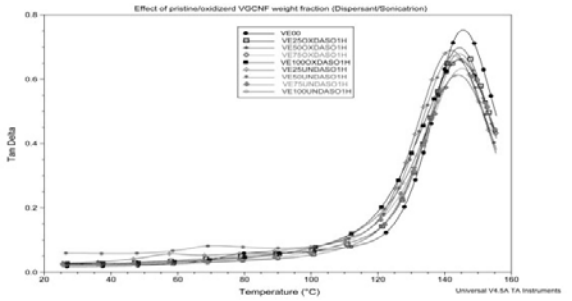

Figure 18. Effect of pristine/oxidized VGCNF weight fraction on tan delta in the presence of dispersing agent.

Recall that the preliminary results presented here are for specimen prepared using ultrasonication alone. Ongoing work suggests that significant additional enhancements in nanocomposite properties are possible using a combination of high-shear mixing and ultrasonication, coupled with the use of a dispersing agent. This work will be completed in year three.

Assessment of Nanocomposite Material Failure Modes and Energy Absorption Characteristics under Different Loading Conditions

Once optimal levels of VGCNFs have been determined for the candidate thermoset and thermoplastic resins, the static and dynamic failure behavior of test specimens comprised of three-phase composites will be investigated using a number of standard tests, with an emphasis on energy absorption/ crash applications. The goal of this work is to establish relationships between composite processing, constituent morphology, properties, and macroscale performance. The effects of nanoreinforcements on macroscale physical properties (stiffness, toughness, energy absorption, etc.) will be examined using a combination of three-point bend tests (American Society for Testing and Materials (ASTM) D790), tensile tests (ASTM D3039), fatigue tests, crush tests, fracture tests, Hopkinson bar tests and other experiments involving specimen geometries and lay-ups of interest to the ACC. A combination visual inspection, light microscopy, TEM and SEM will be used to assess damage development and failure of structural nanocomposite specimens. The motivation for this work is to fabricate cost-effective nanoreinforced composite materials suitable for automobile primary structural applications. The majority of these activities will be performed in year three of this project.

Structure-property tests are being developed for three-phase composite systems (nanophased resin, E-glass plies) in order to assess the mechanical behavior and failure of the structural nanocomposites. These activities will continue into year three of the project.

High Strain Rate Behavior of Nanofiber Reinforced Resins

In order to understand the dynamic response of the two-phase (nanofiber reinforced) VE resin system, split Hopkinson bar (SHB) compression tests were performed at strain rates ranging from 600/s–1800/s. The strain-rate dependent stress-strain response of neat VE resin was measured and compared to that of VE reinforced with 0.5 and 1.0 phr unoxidized VGCNFs. The ratio of dispersing agent to nanofibers was 1:2. The nanofibers were dispersed using a high-shear mixer for 15 minutes and an ultrasonication mixer for one hour. The specimens then cured at 60°C for six hours, followed by a two-hour post cure at 120°C. In year three, a comprehensive test matrix will be executed to investigate the effect of nanofiber functionalization and weight fraction,

mixing technique (sonication, high-shear mixing, coupled sonication/ high-shear mixing), dispersant and strain rate on the stress-strain response of VGCNF/ VE nanocomposites.

The nanofiber dispersion within the samples was assessed via TEM. For example, Figure 19(a) shows a typical dispersion of VGCNFs in a VE resin at 6,700X and 8,000X magnification respectively. It is clear from the figures that while the nanofibers appear to be well wetted by the VE resin with little nanofiber entanglement, the distribution is still not uniform.

The SHB tests were performed with the neat VE resin, as well as 0.5 phr and 1.0 phr VGCNF reinforced VE at three different strain rates: 600/s, 1200/s, and 1800/s. Moreover, in order to investigate the effect of dispersant on the stress-strain response of the neat resin, an additional set of specimens were prepared using neat VE plus 1.00 phr dispersant (i.e., no VGCNFs). Five tests were performed for each material configuration at each strain rate and the resulting stress-strain responses were averaged at increments of constant strain. For example, Figure 20 shows the typical dynamic stress-strain response for three neat VE SHB specimens loaded at 600/s; included in the figure is the nominal response with error bars. All of the SHB tests exhibited similar repeatability. Hence, the SHB results shown in this report only include the average response for each series of tests and the error bars are omitted for the sake of clarity and ease of viewing.

Figures 21(a–c) show the average compressive stress-strain response for each of the four material configurations at target strain rates 600/s, 1200/s, and 1800/s, respectively. Not surprisingly, the measured results were highly strain-rate dependent. One key result, however, was the presence of a small amount of dispersant (1.00 phr) significantly affecting the properties of the neat resin. For example, Figure 21(a) shows the compressive stress strain response for all four material configurations subjected to a strain rate of 600/s. As can be seen from the figure, the apparent yield stress and plateau stress for VE specimens prepared with a dispersing agent were significantly lower than those of the neat resin. This confirms that dispersants, while facilitating

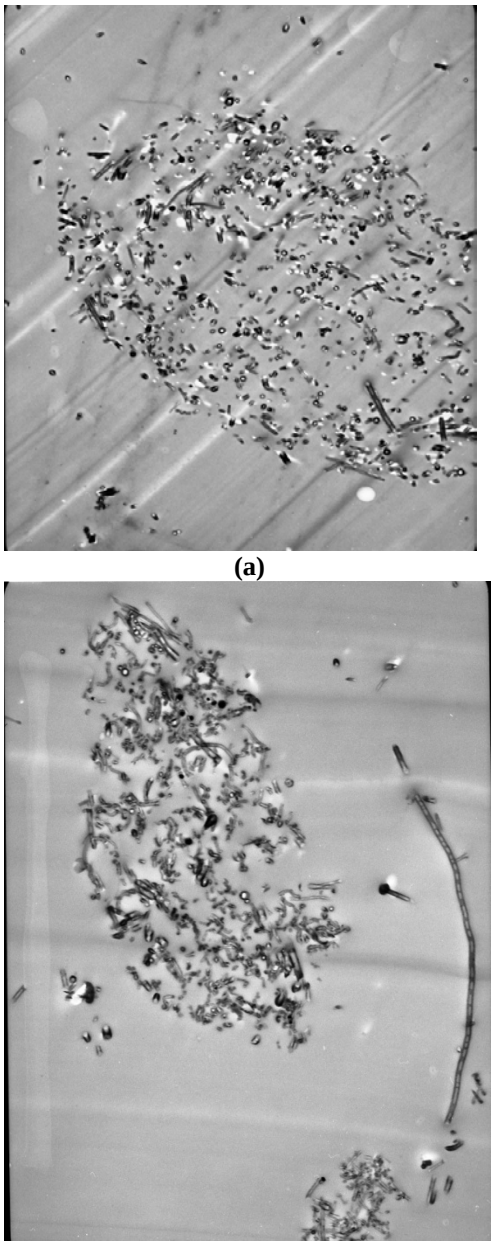

(a)

(b)

Figure 19. (a) TEM images of VGCNF dispersion for 0.5 phr VGCNF in VE resin at 6,700X magnification. (b) TEM images of VGCNF dispersion for) 1.0 phr VGCNF in VE resin at 8,000X magnification.

the distribution of nanofibers, alter the bulk properties of the VE resin. Since the SHB nanocomposite specimens discussed here were all prepared using a dispersant, then the nanocomposite stress-strain responses should compare to those of the VE resin plus dispersing agent. At a strain rate of 600/s, the measured

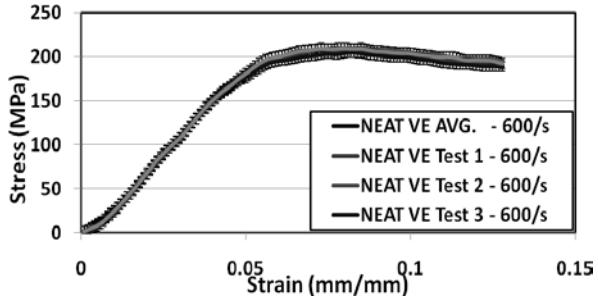

Figure 20. Stress-strain response of neat VE resin at a strain rate of 600/s.

apparent yield and plateau stresses increased with the increasing weight fraction of VGCNF. This suggests that at the given strain rate, the 1.00 phr VGCNF/VE nanocomposite demonstrated the highest yield strength and energy absorption capability relative to the resin modified with dispersant. At a target strain rate of 1200/s, the 1.00 phr VGCNF specimens also produced apparent yield and plateau stresses in excess of those of the resin [cf., Figure 21(b)]. Interestingly, at this strain rate the initial stress-strain response for the 0.50 phr specimen was similar to that of the modified resin, whereas the plateau stress was somewhat below that of the modified resin. In addition, the apparent yield and plateau stresses for the neat resin (no dispersant) were significantly larger than those of the nanocomposite specimens. This underscores the importance of investigating the effect of all constituents over a wide range of loading conditions. In contrast to the previous results obtained of lower strain rates, at 1800/s the 0.50 phr specimens yielded both the highest apparent yield and plateau stresses [cf., Figure 21(c)]. The 1.00 phr specimens produced somewhat lower values, followed by two VE specimens. Note that at 1800/s, the effect of dispersant on the stress-strain response was much less than at lower strain rates. The underlying physical mechanisms behind these phenomena are not obvious. Clearly, the presence of dispersing agent and varying amounts of VGCNFs activate, or inhibit, microstructural rearrangements as a function of strain rate. Temperature effects and/or thermal softening may also play a key role; the specimens tested at 1800/s were noticeably hot to the touch.

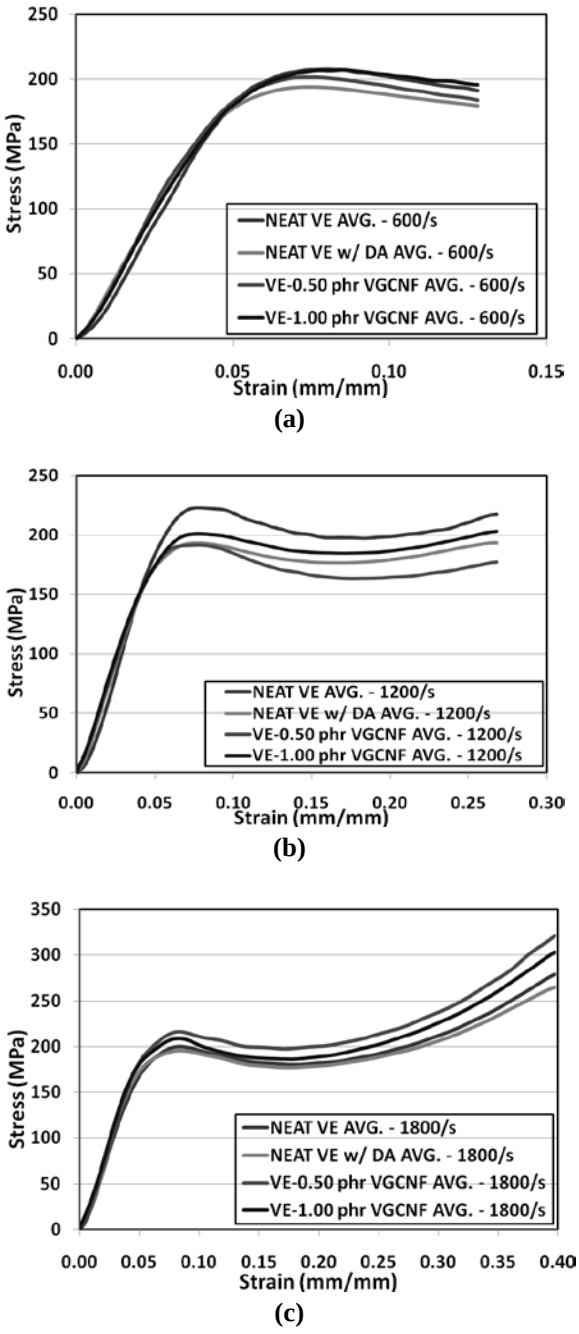

Figure 21 Average stress-strain response for neat VE resin, neat VE resin with dispersing agent, 0.5 phr VGCNF reinforced VE, and 1.0 phr VGCNF reinforced VE at strain rates of (a) 600/s, (b) 1200/s, and (c) 1800/s

As an aside, a series of preliminary tests were conducted at intermediate strain rates between the final target strain rates. A transition in apparent failure mechanism was observed as the strain rate

was increased. Tests conducted at strain rates between 500–650/s typically exhibited ductile deformation, but specimens tested at strain rates in the range 700–950/s typically failed, due to brittle fracture [cf., Figure 22(a)]. However, at strain rates in the range of 1000–1800/s, specimens tended to exhibit more ductile failure [cf., Figure 22(b)]. Again, this may be due the internal temperature rise in the specimens during the higher strain rate tests.

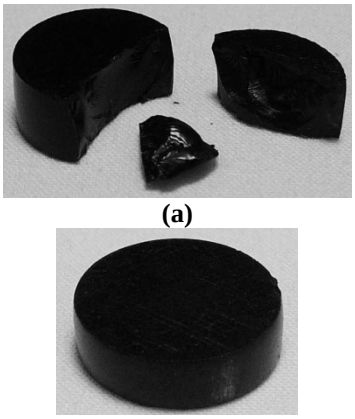

(a)

(b)

Figure 22. Alternating failure mechanisms for tests at (a) lower intermediate strain rates ~800/s and (b) higher strain rates between 1000–1800/s.

Once ongoing DMA tests are completed that will identify the optimal combination of fabrication and processing parameters (i.e., dispersing agent, unoxidized/ oxidized fibers, high shear mixing, ultrasonication, and nanofiber weight fraction), an additional series of quasi-static tests (tension compression, flexure, etc.) and SHB tests will be performed.

Development of Multiscale Materials Model Based upon Micromechanics and Experiments for Nanocomposites

Materials property data obtained from structure-property tests are being used in the development and validation of representative volume element (RVE) based micromechanical models of the two-phase (nanoreinforced) resins. The multiscale modeling methodology developed in this work involves both nanoscale and mesoscale homogenizations. The former is required to establish effective properties of the nanoreinforced matrix (here the characteristic size of a typical nanoreinforcement may be several orders of magnitude smaller than a typical glass fiber diameter). One key issue is the establishment of an empirically validated material model (and appropriate homogenization technique) for predicting effective properties of the two-phase matrix; a variety of methods (molecular dynamics, finite elements, *etc.*) are currently being considered.

Three-dimensional finite-element (FE) models of two-phase resin systems are being developed to establish effective properties of the nanoreinforced matrix. Effective nanophase resin properties obtained from FE simulations are being compared to those obtained using analytic micromechanics solutions (e.g., Mori-Tanaka method and similar effective medium idealizations; cf., Mura, 1991; Nemat-Nasser and Hori, 1993). Effective property data from these simulations, as well as from bulk structure property tests performed by T-CAM, will be employed in a RVE-based FE model of the fiber system/enhanced resin subjected to both load control and displacement control boundary conditions. Standard homogenization techniques (cf., Mura, 1991; Nemat-Nasser and Hori, 1993) will be employed to determine the effective properties of the three-phase composite systems (i.e., nanophased polymer matrix, traditional continuous fiber system architectures), with an initial focus on E-glass plain-weave woven fabric laminates. Modeling and simulation activities will continue into the third year of the project.

Conclusions

The goal of this investigation is to exploit expertise in polymer chemistry, composite materials processing and computational solid mechanics to design, synthesize, test and analyze cost-effective multiscale engineered nanocomposites for automobile primary structural applications. One key challenge is to establish empirically validated, multiscale methodologies, based on the morphologies and geometries of real heterogeneous materials, to obtain structure-property relationships over a wide range of length scales.

A crucial aspect of the work is that structure-property relations will be experimentally validated using a combination of fine-scale and macroscale tests. This study should facilitate the development of engineered multiscale materials designed by providing insight into relationships between nanomaterial fabrication/processing, chemical and physical characteristics and interaction and evolution of structure across disparate spatial scales that leads to improved macroscale performance.

Presentations/Publications/Patents

1. J. Ingram, Y. Zhou, S. Jeelani, T. Lacy, and M. F. Horstemeyer, 2008, "Effect of Strain Rate on Tensile Behavior of Polypropylene and Carbon Nanofiber Filled Polypropylene," *Materials Science & Engineering A*, 489 (1), 99–106.
2. Y. Zhou, S. R. Akanda, S. Jeelani, and T. E. Lacy, 2007, "Nonlinear Constitutive Equation for Vapor-Grown Carbon Nanofiber-Reinforced SC-15 Epoxy at Different Strain Rate," *Materials Science & Engineering A*, 465 (1), 238–246.
3. Y. Zhou, M. Shaik, S. Jeelani, T. Lacy, and M. Horstemeyer, "Experimental Study on Thermal and Mechanical Properties of Clay Modified Carbon Fiber Reinforced Epoxy," in the *Proceedings of the ASC 23rd Annual Technical Conference*, Memphis, TN, September 9–11, 2008.
4. Y. Zhou, S. Jeelani, and T. Lacy, "Strain Rate Dependent Behavior of Carbon Nanofiber Filled Polypropylene," in the *Proceedings of the 49th AIAA/ ASME/ ASCE/ AHS/ ASC Structures, Structural Dynamics, and Materials Conference*, Schaumburg, IL, April 7–10, 2008.

References

1. V. A. Buryachenko, A. Roy, K. Lafdi, K. L. Anderson, and S. Chellapilla, 2005, "Multi-scale mechanics of nanocomposites including interface: Experimental and numerical investigation," *Composites Science and Technology*, **65**, 2435–2465.
2. N. Chisholm, H. Mahfuz, V. K. Rangari, A. Ashfaq, and S. Jeelani, 2005, "Fabrication and mechanical characterization of carbon/SiC-epoxy nanocomposites," *Composite Structures*, **67**, 115–124.
3. F. H. Chowdhury, M. V. Hosur, and S. Jeelani, 2006, "Studies on the flexural and thermomechanical properties of woven carbon/nanoclay-epoxy laminates," *Materials Science and Engineering A*, **421**, 298–306.
4. F. T. Fisher, R. D. Bradshaw, and L. C. Brinson, "Fiber waviness in nanotube-reinforced polymer composites: I. Modulus predictions using effective nanotube properties," submitted to *Composites Science and Technology*, 2007.
5. T. S. Gates, G. M. Odegard, S. J. V. Frankland, and T. C. Clancy, 2005, " Computational materials: Multi-scale modeling and simulation of nanostructured materials, *Composites Science and Technology*, **65**, 2416–2434.
6. N. M. Ghoniem, E. P. Busso, N. Kioussis, and H. Huang, 2003, "Multiscale modeling of nanomechanics and micromechanics: an overview," *Philosophical Magazine*, 83 (31–34), 3475–3528.
7. A. Hussain, M. Hojjati, M. Okamoto, and R. E. Gorga, 2006, "Review Article: Polymer-Matrix Nanocomposites, Processing, Manufacturing, and Application: An Overview," *Journal of Composite Materials*, 40(17), 1511–1575.
8. J. Ingram, Y. Zhou, S. Jeelani, T. Lacy, and M. F. Horstemeyer, 2008, "Effect of Strain Rate on Tensile Behavior of Polypropylene and Carbon Nanofiber Filled Polypropylene," *Materials Science & Engineering A*, 489 (1), 99–106.
9. H. Liu and L. C. Brinson, 2006, "A hybrid numerical-analytical method for modeling the viscoelastic properties of polymer nanocomposites," *Journal of Applied Mechanics*, **73,** 758–768.
10. T. Mura, 1991, *Micromechanics of Defects in Solids, Second Edition*, M. Nijhoff Publ., The Hague.

11. S. Nemat-Nasser and M. Hori, 1993, *Micromechanics: Overall Properties of Heterogeneous Materials*, North-Holland, Amsterdam.

12. G. M. Odegard, T. S. Gates, L. M. Nicholson, and K. E. Wise, 2001, "Equivalent-Continuum Modeling of Nano-Structured Materials," NASA/TM 210863, 1–30.

13. G. M. Odegard, T. C. Clancy, and T. S. Gates, 2005, "Modeling of the mechanical properties of nanoparticle/polymer composites," *Polymer*, 46, 553–562.

14. E. T. Thostenson, C. Li, and T.-W. Chou, 2004, "Nanocomposites in context," *Composites Science and Technology*, 65, 491–516.

15. P. K. Valavala and G. M. Odegard, 2005, "Modeling techniques for determination of mechanical of polymer nanocomposites," *Review Advance Material Science*, **9**, 34–44.

16. Y. Zhou, F. Pervin, V. Rangari, and S. Jeelani, 2006, "Fabrication and evaluation of carbon nano fiber filled carbon/epoxy composite," *Materials Science and Engineering A*, **426**, 221–228.

17. Y. Zhou, S. R. Akanda, S. Jeelani, and T. E. Lacy, "Nonlinear Constitutive Equation for Vapor-Grown Carbon Nanofiber-Reinforced SC-15 Epoxy at Different Strain Rate," accepted for publication in *Materials Science & Engineering A*, 2007.

9. JOINING

A. Forming Limits of Weld Metal in Aluminum Alloys and Advanced High-Strength Steels

Principal Investigator: Richard W. Davies
Pacific Northwest National Laboratory
P.O. Box 999, Richland, WA 99352-0999
(509) 375-6474; fax: (509) 375-5994; e-mail: rich.davies@pnl.gov

Technology Area Development Manager: Joseph A. Carpenter
(202) 586-1022; fax: (202) 586-1600; e-mail: joseph.carpenter@ee.doe.gov

Field Technical Manager: Mark T. Smith
(509) 375-4478; fax: (509) 375-4448; e-mail: mark.smith@pnl.gov

Participants: Elizabeth V. Stephens and Glenn J. Grant
Pacific Northwest National Laboratory, General Motors, Chrysler, Ford, U.S. Steel

---

Contractor: Pacific Northwest National Laboratory
Contract No.: DE-AC06-76RL01830

Objective

- Develop, validate, and disseminate a combined experimental and numerical method to describe statistically and quantify systematically the forming limits of welded aluminum alloys and high-strength steels.

Approach

- Develop a standard tool for weld process development that will systematically quantify failure probabilities during forming.
- Provide accurate, standardized methods of experimentally characterizing weld metal formability using unique but simple test methods available on the shop floor.
- Provide predictive models for more accurate forming simulations of tailor-welded blanks (TWBs) and hydroforming operations. Predict parts-per-thousand failure rates during production from finite element analysis.
- Characterize static/fatigue properties and forming behavior of several weld populations and correlate with statistical-based tool.

Accomplishments

- Established an industrially relevant procedure to determine the forming limit diagram (FLD) of welded DP600 steel alloys.
- Developed a more general procedure that can be applied to welded thin sheets.
- Completed the combined forming limit prediction for DP600, AA5182-6111 and AA5182 welded alloys.
- Quantified the combined FLD using the statistical approach for each welded alloy population.

- Conducted program review meeting in February 2008 to Industrial Team Advisory Committee.
- Participated in Plasticity 2008 and presented project-related work.

Future Direction

- With original equipment manufacturer (OEM) participation, validate the experimental and numerical methodology and general procedure generated with any existing TWB applications in a production environment.
- Complete all final work and submit journal articles detailing work and findings.
- Conduct final project presentation summarizing results with Industrial Team Advisory Committee.

Introduction

This work is a collaborative effort among DOE, Pacific Northwest National Laboratory (PNNL), the U.S. Automotive Materials Partnership (USAMP) team of the U.S. Council for Automotive Research, U.S. Steel, Olympic Controls, and Alcoa. This project will develop, validate, and disseminate combined experimental and numerical methods that systematically quantify the forming limits of weld materials in aluminum alloys and high-strength steels through a combination of experimental and deformation modeling analysis. This work will enable high-volume, robust deployment of TWBs and seam- and tailor-welded tubes in emerging materials. Figure 1 is a schematic of the project.

The deformation of weld materials and their limits of formability are important aspects to both TWB and hydroforming technologies. The conventional low-carbon steels used in automotive applications are easily fusion-welded using conventional technologies and suffer no appreciable strength degradation near the weld. Aluminum alloys are more difficult to weld than low-carbon steels due to high conductivity and reflectivity as well as low-molten viscosity. Aluminum also has a high propensity for porosity to form during fusion welding as well as hot cracking and heat-affected zone (HAZ) related issues in heat-treatable aluminum alloys. Many of the high-strength steel alloys that are finding increased application in the automotive industry suffer from degradation of strength in the HAZ.

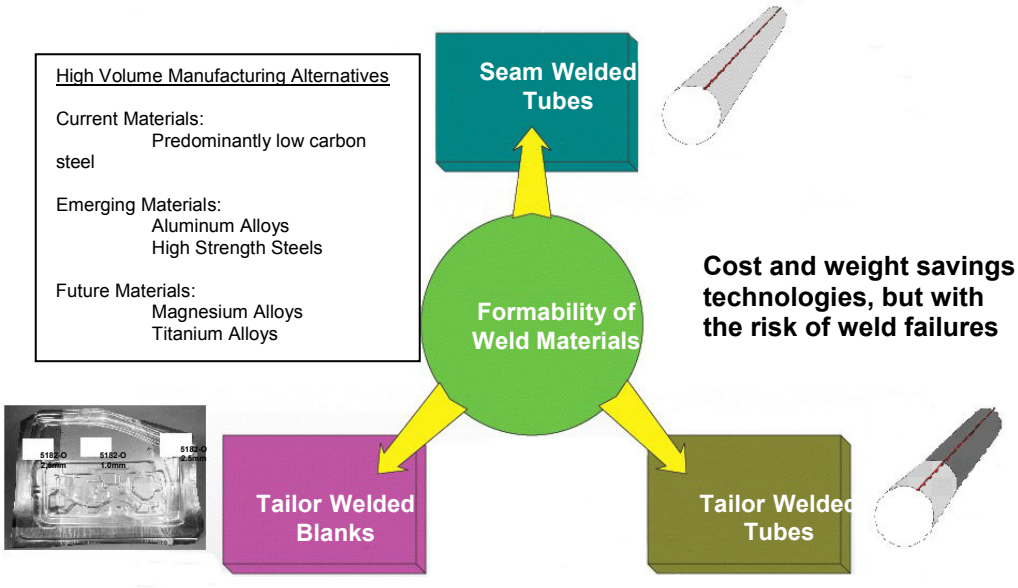

Figure 1. A schematic of the formability of weld materials project.

Further, nearly all fusion welds suffer from irregular geometries and elevated levels of surface roughness compared to the parent materials, which also influence formability and component performance.

This project focuses on developing a generalized numerical method to predict material-forming limits in weld materials and verifying deformation and forming limit predictions. The approach will rely on developing standardized test methods for weld material populations to establish a statistical description of material imperfection and mechanical properties in their weld region and developing statistically based forming limit diagrams (FLD) or continuum damage models that predict material failure in the weld region.

This project includes numerical model development, validation, and supporting experiments. A number of candidate weld methods were examined in combination with selected aluminum alloys and high-strength steels. The project materials will include 5000 and 6000 series aluminum and relevant high-strength steel alloys, including high-strength, low alloy; transformation-induced plasticity; and dual phase steels. The selection of sheet materials and welding methods will be coordinated with the participating OEMs and will be representative of high-volume commercially viable materials and processing technologies.

The deliverables will include a standard procedure for weld material evaluation coupled with a numerical approach for establishing weld region forming limits. The results will also allow the evaluation and development of candidate weld processes and the interaction between materials and weld parameters. The overall objective is to develop test methods and experimental results to enable the widespread deployment of weight- optimized TWB and tube hydroforming and to avoid weld failures during production. Figure 2 is a schematic of the typical manufacturing process development.

During this fiscal year, much emphasis was spent on developing an industrially relevant procedure to determine the FLD of welded aluminum and high-strength steel alloys. A procedure was first applied to DP600 welded alloys and then generally modified, so the procedure may be applied to aluminum-welded alloys or any thin sheet-welded alloy to determine the forming limit. The following describes results to date and the development of the industrially relevant procedure.

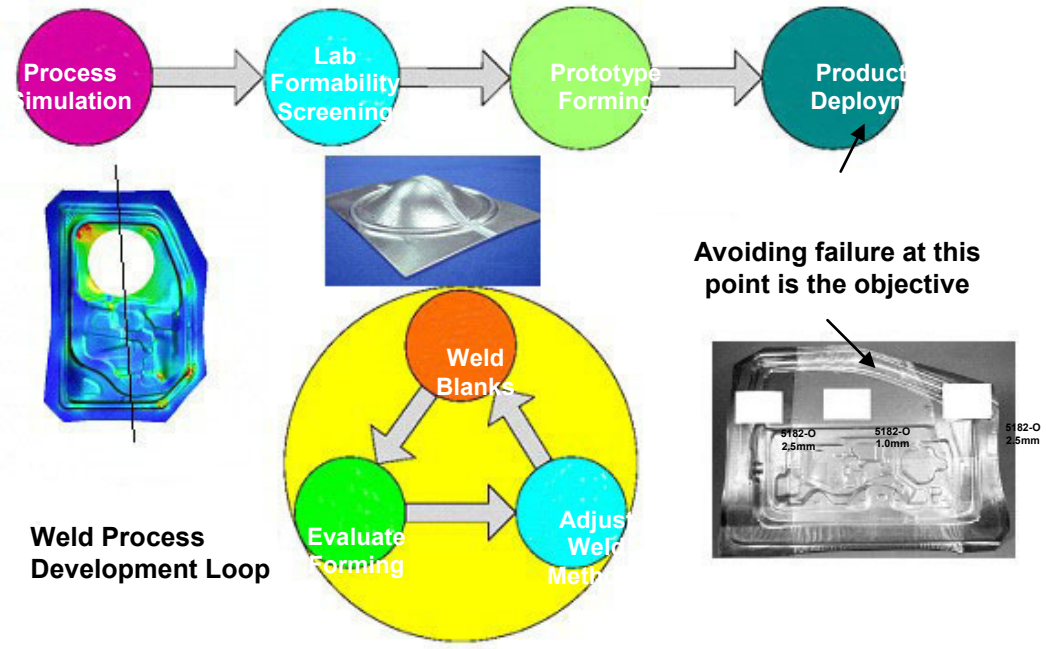

Figure 2. A schematic of the typical manufacturing process development.

M-K Method to Predict Formability

FLDs for the DP600 and 5182 welded to 6111 TWBs were generated using a Marciniak-Kuczynski (M-K) method approach that can track development of plastic strains in the monolithic sheet and weld materials under applied external loading. The model also tracks the evolution of imperfections and predicts the localization and failure of specimens. Theoretical FLDs are generated based on uniaxial tensile results and statistical probability. The level of imperfection that must exist in the specimens in order to describe the formability for each of the 30 longitudinal specimens is determined. A Weibull probability distribution is then applied to describe the longitudinal specimen imperfections, and the predicted FLD for the TWBs is generated.

Previously, the 5182-6111 full dome biaxial test experiments were compared to the theoretical FLD generated. Discrepancies of the model and biaxial experiments were observed, so all test results were combined in an FLD where the strain longitudinal to the weld and the strain transverse to the weld was plotted. The FLD of the parent sheet material (from literature) was also plotted. Results showed that there was a region in the FLD where the weld will always fail and a region where the sheet will fail. In between is a "gray area" where either the weld or HAZ of the thin sheet 6111 material will dictate the failure.

Additional limited dome height tests were completed to investigate how the FLDs would be suppressed in these "gray areas." Nine full dome width specimen tests and fifteen 4-in. width specimen tests were completed. Three different failure modes were observed among the full width specimens, and all 4-in. width specimens failed in the weld transverse to the weld. Modifications to the forming limit prediction were completed. The M-K model was extended to include weld thickness difference and two orientations of imperfection in the weld (schematic shown in Figure 3).

Work continued on the development of the FLD for the 5182-5182 TWB populations. Figure 4 shows the combined experimental results and compares these results to the monolithic 5182-O sheet FLD. These results indicate that our approach becomes more difficult to validate as the weld FLD becomes nearly identical to the thin sheet FLD.

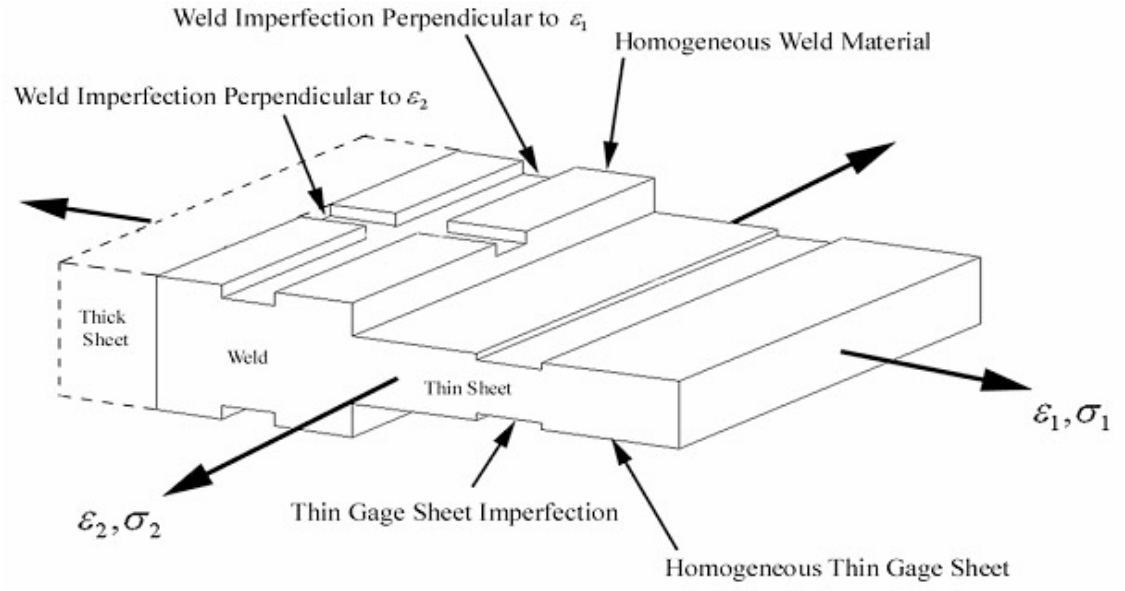

Figure 3. Schematic illustration of the M-K model extended to include weld thickness differences and two orientations of imperfection in the weld where ε_1 and ε_2 represent the major and minor strain, respectively, and σ_1 and σ_2 represent the associated stress for the major and minor strain, respectively.

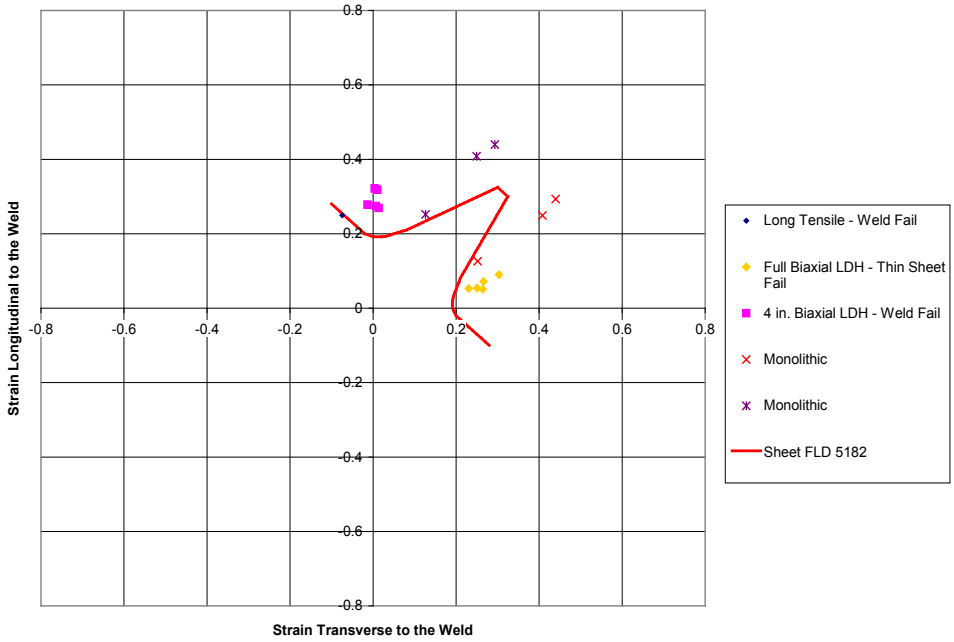

Figure 4. 5182-5182 friction stir welded materials combined test results and compared it to the FLD for 5182 monolithic sheet.

General Procedure in Determining the FLD of Welded Alloys

Currently, there is no industrial standard that describes the formability of TWBs that include the effects of the weld region. One of the goals of this project is to develop a procedure for industry to use by characterizing the variability of these materials and treating it probabilistically so we may have a better understanding of the operating envelope of these TWB materials. The general procedure was first applied to DP600 welded alloys. Figure 5 depicts the DP600 TWB FLD generated from the 10-step process described below. In-depth details of the industrially relevant procedure developed and the assumptions required will be published in future work.

1. Establish the thin (or the weaker) sheet FLD and draw a three-quadrant FLD where longitudinal strain is the ordinate (y-axis) and the transverse strain is the abscissa (x-axis).
2. Conduct approximately 30 longitudinal tensile tests and measure the "safe" level of strain in the thin sheet adjacent to the weld for each specimen.
3. Calculate the statistical distribution for the level of imperfection for the longitudinal specimens.
4. Conduct approximately 30 transverse tensile tests and measure the "safe" level of strain in the thin sheet adjacent to the weld for each specimen and *verify that no weld related failures occurred.*

   Note: In previously reported work, experimental results showed that in the transverse weld condition, there was no fracture in the weld or in the heat affected zone of the DP600 welded specimens. Localization occurred in the thin sheet, and fracture was determined by the properties of the 1 mm parent sheet material.
5. Assume the acceptable failure rate for a given metal forming application (recommendation is 1 part per 1000).
6. Calculate the imperfection level for the longitudinal population that corresponds to the acceptable failure rate.
7. Calculate the "safe" level of strain along the longitudinal tensile direction that corresponds to the acceptable failure rate (Locate Point 1).

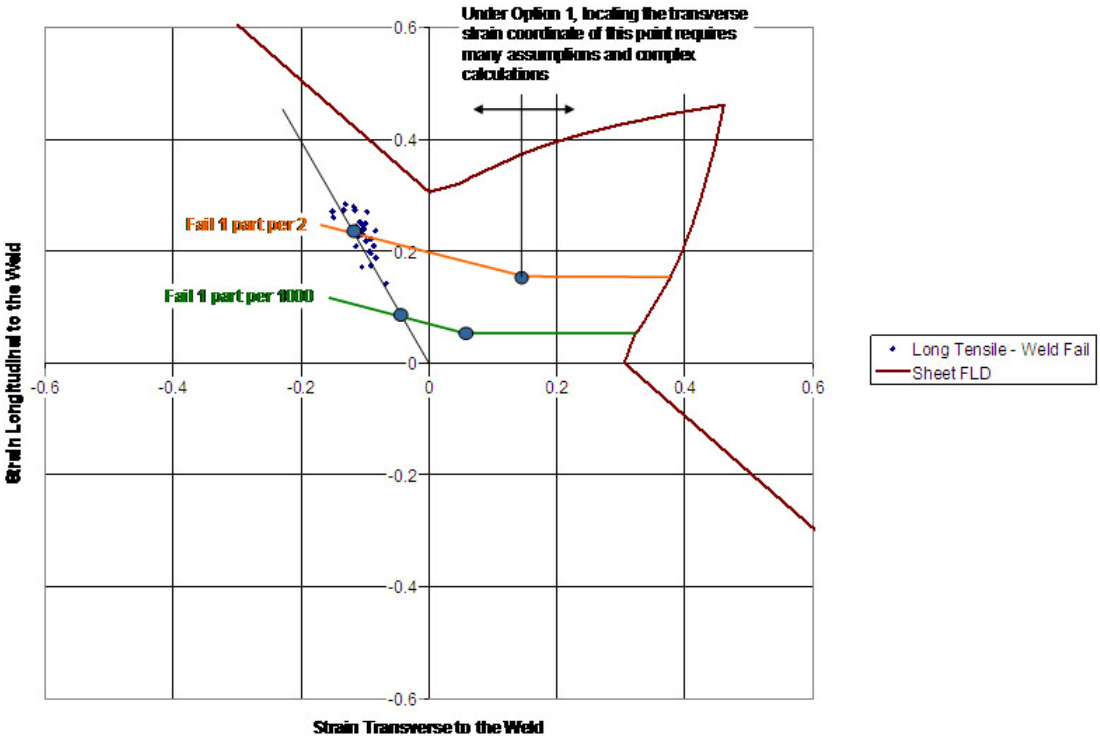

Figure 5. DP600 TWB FLD developed utilizing the industrially relevant procedure.

8. Calculate the strain path direction developing in the thin sheet when the weld is being loaded in plane strain longitudinal to the weld and place a point on the FLD that corresponds to the "safe" longitudinal plane strain and the transverse strain in the thin sheet (Locate Point 3).
9. Connect Points 1 and 3 via a line.
10. Draw a horizontal line from Point 3 horizontal to the transverse strain axis to the right of Point 3.

Further validation of the industrially relevant procedure is anticipated through plant trial validation. Five random blanks over several weeks will be gathered where the strain level achieved during forming would be determined. We will apply the PNNL procedure to predict the failure rate of a real production process.

We will track the failure rate in the plant and compare the predicted and actual failure rates.

Conclusions

From this investigation, the following conclusions were derived:

- Forming of welds has the potential to simultaneously reduce the cost AND weight of lightweight automotive structures.
- Emerging materials (aluminum and HSS) are generally more challenging to join and form.
- We developed methods/standards for describing the forming limits that include the effects of the weld region, which predicts forming failure rates at quantitative levels of deformation.

Further work will include preparing final validation and publications of the project work.

Presentations/Publications/Patents

1. "Forming Limits of Weld Material in Aluminum Alloys and High-Strength Steels." 2008. Presented to Industrial Team Advisory Committee, Southfield, MI. February 21.
2. "Formability and Strength of Dissimilar Aluminum Welds in Thin Sheets During Biaxial Stretching." 2008. Presented at Plasticity 2008, Kona, HI. January 7.
3. "Forming Limits of Weld Material in Aluminum Alloys and High-Strength Steels." 2007. Presented at U.S. Automotive Materials Partnership AMD Offsite Annual Review Meeting, Southfield, MI. October 25.

B. Impact Modeling and Characterization of Spot Welds

Principal Investigator: Zhili Feng
Oak Ridge National Laboratory
P.O. Box 2008, Oak Ridge, TN 37831-6095
(865) 576-3797; fax: (865) 574-4928; e-mail: fengz@ornl.gov

Co-Principal Investigator: Srdjan Simunovic
Oak Ridge National Laboratory
P.O. Box 2008, Oak Ridge, TN 37831-6164
(865) 241-3863; fax: (865) 574-7463; e-mail: simunovics@ornl.gov

Technology Area Development Manager: Joseph A. Carpenter
(202) 586-1022; fax: (202) 586-1600; e-mail: joseph.carpenter@ee.doe.gov

Field Technical Monitor: C. David Warren
(865) 574-9693; fax: (865) 574-6098; e-mail: warrencd@ornl.gov

---

Contractor: Oak Ridge National Laboratory
Contract No.: DE-AC05-00OR22725

Objective

- Develop a new, robust spot weld element (SWE) model that can accurately simulate the various deformation and fracture modes of advanced high-strength steel (AHSS) spot welds as a function of impact, welding conditions, and materials while maintaining computational efficiency and ease of use.
- Develop the implementation procedure to incorporate the SWE model in crash simulation finite-element analysis (FEA) codes used by automotive crash modelers.
- Generate a companion experimental database on the performance of AHSS spot welds under various loading conditions and deformation rates to support and validate the modeling approach.

Approach

- Develop a new SWE model and associated constitutive models.
- Perform modeling and characterization of weld microstructure and related properties.
- Integrate the SWE model and weld process and microstructure model.
- Perform weld deformation and failure behavior testing under different dynamic-loading conditions.

Accomplishments

- Developed the initial version of the SWE model.
  - — Capable of handling weld geometry and weld property gradient.
  - — Capable of predicting different fracture modes and fracture load limits experimentally observed in impact tests.
- Developed the initial version of an integrated electrical-thermal-mechanical-metallurgical resistance spot weld model.
  - — Capable of predicting weld geometry, microstructure, and microhardness distributions.
  - — Includes user-friendly input interface for welding parameters, sheet thickness, and steel chemistry.

- Collected baseline spot weld impact test data on dual phase (DP) 780 and draw-quality, semi-killed (DQSK) steels.
  - — Characterized effects of impact speeds and loading modes.
  - — Created web-based database for user-friendly interactive data analysis and retrieval.

Future Direction

- Further expand and validate the SWE model to cover a wide range of AHSS grades and spot weld configurations to demonstrate the applicability of the SWE model for the current generation of AHSSs.
- Extend the SWE model to the weld bond for AHSSs.
- Extend the SWE model to other materials and joining processes.
  - — Joining of steels to other materials [such as aluminum (Al) alloys, magnesium alloys, polymer composites] for multi-material body structure.
  - — Friction-bit joining, friction-stir joining, laser welding.
- Continue failure criteria evaluation and development.
  - — Incorporate the effect of heat-affected zone (HAZ) softening in ultra-high-strength steels and Al alloys.
  - — Develop failure criteria for other processes, including adhesive bonding.
- Further refine SWE formulation for robustness.

Introduction

A primary factor that drives increased use of AHSSs in auto-body structures is their ability to drastically improve crash performance while reducing the weight. Resistance spot welding (RSW) is by far the most common joining process used in automotive manufacturing. Typically, there are thousands of spot welds in a vehicle. Because the separation of spot welds can affect the crash response of a welded structural component, the static and dynamic behavior of spot welds has been one of the critically important considerations in vehicle design and manufacturing.

RSW of AHSSs presents unique technical challenges for automotive structural applications. Due to their high carbon and alloying element contents, AHSSs are considerably more sensitive to the thermal cycle of welding than the conventional steels used in auto-body structures. The higher grade AHSSs (e.g., DP 800/1000, TRIP steels, and boron steels) are more difficult to weld and more susceptible to forming brittle microstructures and solidification-induced defects in the weld region. In addition, HAZ softening can occur. Therefore, resistance spot welds of AHSSs can exhibit very different structural performance characteristics than welds of conventional steels. For example, AHSS spot welds can fail under different failure modes (button pullout, interfacial, or mixed). In addition, impact experiments on joints and structural components (top-hat and double-hat sections) have shown that resistance spot welds have different responses under static and dynamic loads. The spot-welded structural performance among different AHSSs can be drastically different and highly dependent on the grades and types of AHSS. Furthermore, there can be considerable variations in microstructure and properties in the weld region for a given type and grade of AHSS made by different steel suppliers due to differences in steel chemistry and the processing routes used.

In recent years, computer-aided engineering-(CAE-) based simulation of dynamic (impact) behavior of auto-body structures during crash tests has become an indispensable tool that enables rapid and cost-effective design and engineering of crash-resistant auto-body structures. This program aims to develop a new spot weld model, supported by experimental data, which can be implemented in crash-simulation FEA codes used by automotive crash modelers. The essential feature of this new model will be its ability to handle various deformation and fracture modes, the effects of microstructural and strength changes in AHSS spot welds, and the deformation rates and loading modes encountered in vehicle crash. A three-pronged approach has been adopted in the development of the new spot weld model:

- development of a robust new SWE model with the complexity to incorporate weld geometry and microstructure effects and the associated constitutive models for use in CAE simulation;
- development of an integrated electrical-thermal-mechanical-metallurgical spot weld process model to generate the weld geometry, microstructure, and residual-stress results needed by the SWE model; and
- development of a companion weld characterization and impact test database for development and validation of the new spot weld model.

In recognition of the complexity and scope of efforts required to develop and mature this new model for the wide variety of AHSSs currently used in auto-body structures, this project has been divided into two phases. Phase I is an 18-month concept-feasibility effort aimed at developing the initial version of the SWE model and generating the companion testing data for an initial set of steels, weld configurations, and impact testing conditions. Phase II will be a comprehensive technical-feasibility research and development process that will cover a wider range of materials, thickness ranges, and weld configurations and microstructures to refine, improve, mature, validate, and demonstrate the SWE model for eventual implementation in CAE by industry users.

The progress made in Phase I of the project is summarized in the fiscal year (FY) 2007 progress report and this report. Phase I is jointly sponsored by the DOE Lightweighting Materials area and the Auto/Steel Partnership (A/SP) Strain Rate Characterization Program (see report 5.F).

Materials, Welding, and Testing

Details on steel selection, welding, weld microstructure characterization, and impact testing of the spot welds are given in the FY 2007 progress report.

Two steels, dual-phase AHSS DP 780 steel (1.15 mm thick) and DQSK mild steel (1.0 mm thick), were selected for the initial development in Phase I. For each steel, the welding schedule was varied to produce three different weld nugget sizes acceptable to the industry specification for studying the effects of weld size on the fracture behavior of spot welds in impact testing.

Microstructural analyses were performed to characterize the microstructure and microhardness gradients and the weld defects (if any) in the weld and HAZ of the spot welds. The microstructure and microhardness results were used to validate the weld process model for RSW.

Both dynamic and static tests of the spot welds, in lap-shear, cross-tension, and mixed torsion/tension loading configurations, were performed at four loading velocities: quasi-static, 2.6 m/s (5.8 mph); 3.6 m/s (8.1 mph); and 5.8 m/s (12.5 mph). A drop-tower impact test machine was used for the impact tests.

The fracture modes and peak loads to failure of all spot welds were recorded during the test. The impact testing results are retrievable online by A/SP members. Dependency of fracture mode and peak load on weld size, loading mode, and loading rate were observed. These data were used to validate the SWE modeling approach.

Weld Microstructure and Property Modeling and Characterization

An integrated electrical-thermal-mechanical-metallurgical welding process model for electric RSW is used in this project. It is based on earlier work [1] with further refinement of the microstructural model for AHSS.

The RSW process model predicts the weld size, microstructure, and residual stresses in a spot weld based on the following user inputs.

- Steel chemistries and base metal microstructure.
- Surface coating.
- Sheet stackups.
- Welding conditions (current and electrode force).
- Electrode geometry.

A key feature of this integrated weld process model is that it predicts the microstructure

evolution based on calculations of the thermodynamics and kinetics of steel phase-transformation processes. There is no need to experimentally measure the continuous cooling transformation curves for a given steel, an impossible task for all possible thermal cycles experienced in different locations of the weld and HAZ of a spot weld.

The integrated weld process model was applied to the two steels and different welding conditions used in Phase I. The simulation results compared well with measurement results of the weld microstructure and microhardness distributions in the spot welds. Figures 1 through 4 show examples of the weld process modeling results and compares the results with the experimental hardness measurement results.

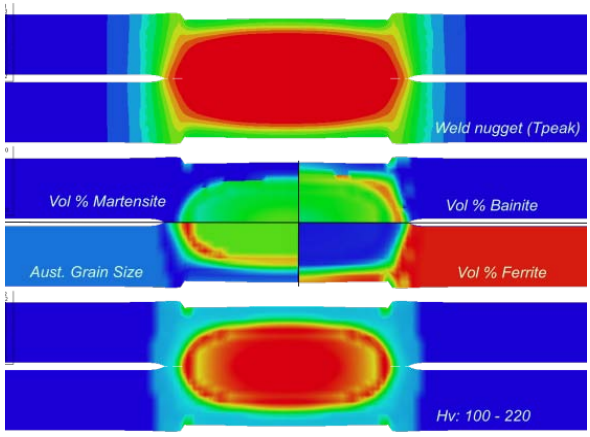

Figure 1. Predicted weld nugget as represented by: the peak temperature (top), volume fractions of different phases (middle), and microhardness distribution (bottom) in a DQSK spot weld.

The predicted microhardness results were then converted to the yield strength [1] and used in the SWE formulation.

Development of Spot Weld Element

Spot welds in finite-element method impact simulations are usually modeled with two submodels: (1) a kinematics model of the joint and (2) the associated constitutive model describing the material-related response of the joint. Currently, the kinematics of the joint is primarily modeled as point-to-point connection by means of

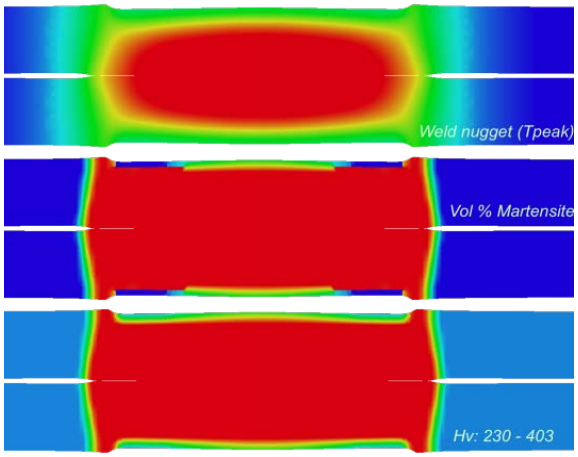

Figure 2. Predicted weld nugget profile as represented by: the peak temperature distribution (top), volume fractions of different phases (middle), and microhardness distribution (bottom) in a DP 780 spot weld.

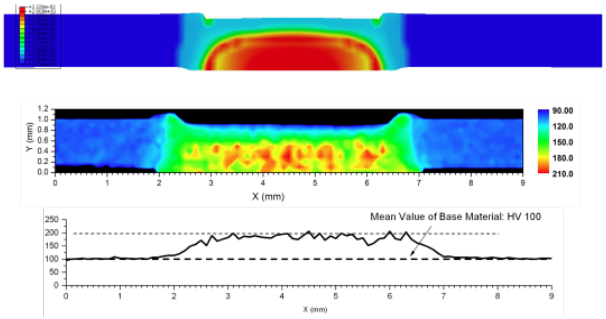

Figure 3. Comparison of microhardness distribution in a DQSK spot weld: (top) prediction, (middle) microhardness measurement, and (bottom) line plot along the middle plane of the steel sheet.

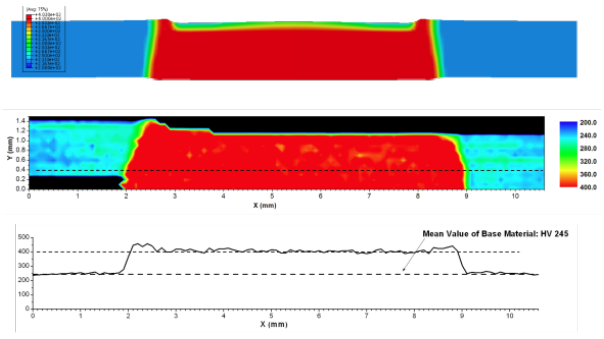

Figure 4. Comparison of microhardness distribution in a DP 780 spot weld: (top) prediction, (middle) microhardness measurement, and (bottom) line plot along the middle plane of the steel sheet.

flexible or rigid (i.e., constrained) line finite elements.

The line connection is restricting the constitutive spot weld models to force-based laws. This in turn requires new experiments for model parameters with new RSW configurations. One of the principal problems with beam-based kinematics models in AHSS spot welds is that the stress and strain distributions in the weld area are not accurately represented. For RSW in conventional steel structures, the dominant failure mode is the button pullout, and the inadequate calculation of the shear stress may not be a major concern in impact simulation of vehicles. However, for AHSS RSW, accurate determination of the shear stress may be critical because of the reported interfacial failure or mixed interfacial plus pullout failure mode. In addition, the multiple failure modes and the changes in failure modes under different loading conditions require development of more versatile failure criteria based on the fracture and damage mechanics principles than the resultant force-based ones. From the structural stiffness perspective, the bar and beam models typically yield acceptable accuracy under tension, out-of-plane torsion, and bending loads. For in-plane torsion and shear, the stiffness values are highly inaccurate. The brittle fracture associated with the interfacial failure of the spot weld is more likely during impact, where plastic deformation of the base material may be constrained by large elastic stress fields. Compared to a gradual increase in hardness in the HAZ in mild steel resistance spot welds, the AHSSs exhibit a sharp hardness change that adds to brittleness and notch sensitivity of the joint.

The objective of this research was to develop an RSW model that would be able to predict the stress distribution in the weld zone and would be computationally feasible for crash simulations. The recent RSW models based on solid elements inserted between shell elements of the sheet material have shown much better accuracy than the line-based elements. We have extended that approach to the model configurations illustrated in Figure 5. The schemes depict through-thickness direction of the spot weld.

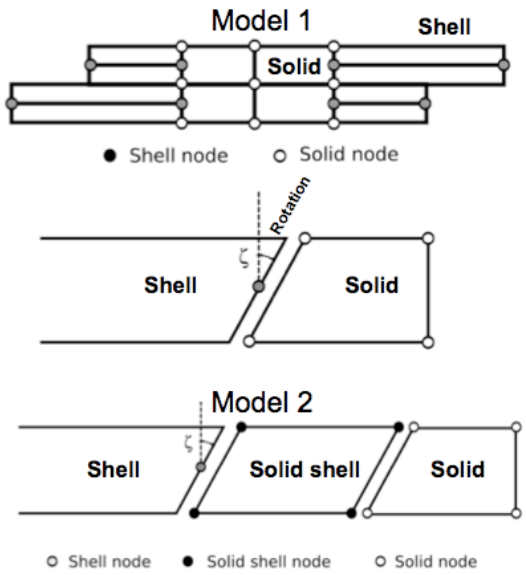

Figure 5. Configuration of the spot weld model in the through-thickness direction. Model 1 has shell elements in the HAZ and the plate; whereas Model 2 used an eight-node solid shell for the HAZ. The middle figure shows the coupling between the four-node shell and solid.

The models have compatible connections between the plate (shell) and the nugget (solid) regions. The principal difficulty is the element meshing of the region, but with the current computational design tools such connections should be easily managed.

Additional simplification of the connection comes from the fact that the inner region of the spot weld is relatively stress-free compared to its periphery. Accordingly, the inner region of the weld can be replaced by computationally inexpensive rigid elements or, equivalently, kinematic constraints. The constraints computationally stabilize the solid elements in the deformable region of the spot weld and provide additional mass that can be used for computational speedup of the region using mass time-scaling.

Possible failure regions in the new spot weld connection are shown in Figure 6. The stress-strain values in those regions can be used to evaluate various fracture criteria that would initiate failure of the spot weld. In the current research, a simple failure criterion based on equivalent strain to failure was used. The material properties in the weld region were based on the

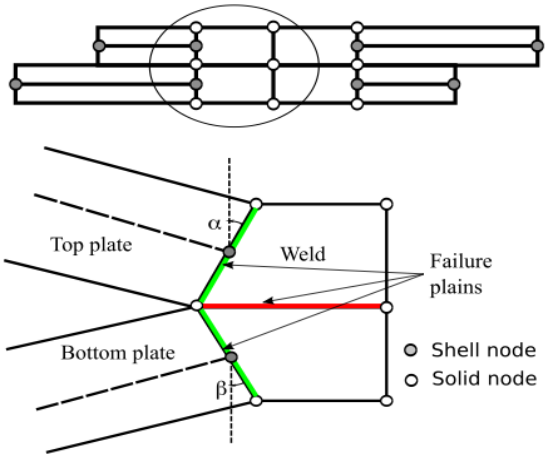

Figure 6. Failure zones in the spot weld model.

hardness measurements and simulations. Base material properties were scaled with the simulated/measured hardness coefficient, and equivalent strain-to-failure was reduced accordingly. This constitutes a very simplistic model that will need to be replaced by more accurate criteria in the future.

Figure 7 shows the simulation of the lap-shear test with small spot weld diameter. The failure of the spot weld in simulation and experiments was along the interface between the two connected sheets.

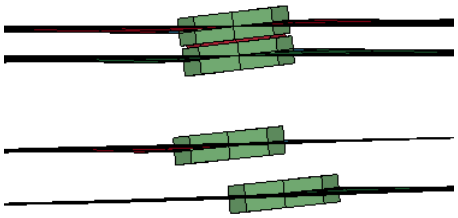

Figure 7. Lap-shear test simulation for small spot weld diameter.

The resulting force comparison is very close given the experimental scatter and the simplicity of the failure model (Figure 8). Figure 9 shows the simulation of the lap-shear test for large spot weld diameter. The resulting force comparison is again reasonably close to the resulting force and stiffness of the assembly (Figure 10).

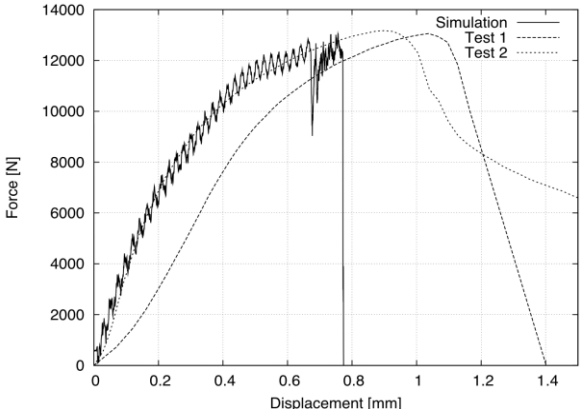

Figure 8. Comparison of the resulting force for experiments and simulations for small spot weld diameter.

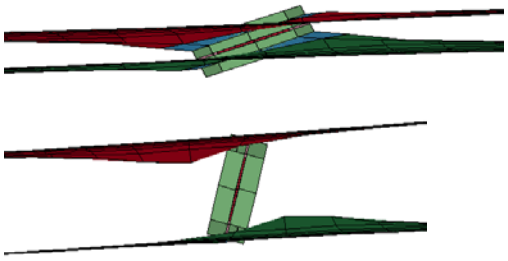

Figure 9. Lap-shear test simulation for large spot weld diameter.

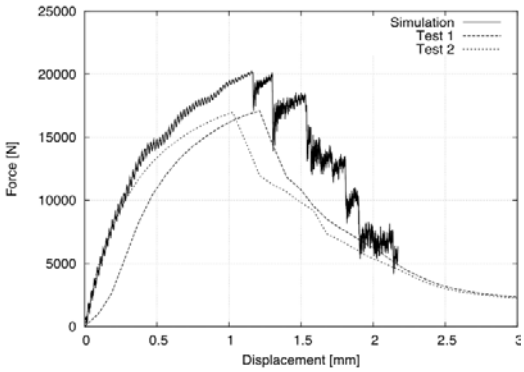

Figure 10. Comparison of the resulting force for experiments and simulations for large spot weld diameter.

The model accurately recovers geometry effect without the need for separate experiments for the new spot weld configuration. This is because the failure condition, even though very simple, is based on material properties instead of the extrinsic properties of the overall joint. The model was also compared with other spot weld configuration experiments conducted during the

project and has shown good agreement for the relatively simple failure criteria used. New experiments are planned for creating the complex states of stress in spot welds that can be used for further model refinement and development of the failure criteria for the spot welds.

Reference

1. Z. Feng et al., "Modeling of Resistance Spot Welds—Process and Performance," *Welding in the World,* **45**(11/12), pp. 18–25 (2001).

C. Friction Stir Spot Welding of Advanced High-Strength Steel

Principal Investigator: Michael L. Santella
Oak Ridge National Laboratory
P.O. Box 2008, Oak Ridge, TN 37831-6096
(865) 574-4805; fax: 865-574-4928; e-mail: santellaml@ornl.gov

Principal Investigator: Glenn J. Grant
Pacific Northwest National Laboratory
902 Battelle Boulevard, P.O. Box 999, Richland, WA 99352
(509) 375-6890; fax: (509) 376-6034; e-mail: Glenn.Grant@pnl.gov

Principal Investigator: Yuri Hovanski
Pacific Northwest National Laboratory
902 Battelle Boulevard, P.O. Box 999, Richland, WA 99352
(509) 375-3940; fax: (509) 376-6034; e-mail: Yuri.Hovanski@pnl.gov

Technology Area Development Manager: Joseph A. Carpenter
(202) 586-1022; fax: (202) 586-1600; e-mail: joseph.carpenter@ee.doe.gov

Field Technical Co-Monitor: C. David Warren
(865) 574-9693; fax: (865) 574-6098; e-mail: warrencd@ornl.gov

Field Technical Co-Monitor: Mark Smith
(509) 375-4478; fax: (509)375-4448; e-mail: mark.smith@pnl.gov

---

Contractors: Oak Ridge National Laboratory (ORNL) and Pacific Northwest National Laboratory (PNNL)
Contract No.: DE-AC05-00OR22725 & DE-AC06-76RLO1830

Objective

- Develop friction stir spot welding (FSSW) as a superior method to join advanced high-strength steels (AHSSs).
  - Phase 1 activities addressed the critical questions of whether there are tool materials available that have potential for reasonable life and whether friction stir spot welds (FSSWs) made in AHSSs are feasible and can demonstrate similar or better mechanical performance than welds made by conventional processes like resistance spot welding (RSW).
  - Phase 2 activities seek to increase joint strength through a more systematic investigation into weld process parameters and tool design. This will be accomplished primarily by using new tools and refined operating parameters, the selection of which will be guided by analysis of process output data, microstructure analysis, and strength testing.

Approach

- The project is a collaboration between ORNL and PNNL, and includes an advisory committee with representatives from Chrysler, Ford, General Motors (GM), two automotive steel suppliers, and a friction stir welding tool supplier.
- Produce lap-shear specimens and perform lap-shear tests to correlate tensile shear strength with processing parameters and microstructures.

Accomplishments

- Made hundreds (~500) of FSSWs on uncoated dual phase (DP) 780, galvannealed DP 780 (DP 780GA), and uncoated hot-stamp boron steel (HSBS) using a wide range of welding conditions.
- Compiled data on the effects of weld time, tool rotation speed [revolutions per minute (rpm)], and tool shape on appearance, bonding, fracture, microstructures, properties, and process loads.
- Performed mechanical tests on Phase 1 DP 780 and HSBS lap-shear coupons. While overall strengths for certain weld parameters were in the range of acceptable values defined by the American Welding Society (AWS) specification for RSW of steel, the specific strength under nearly every condition exceeded the minimum stress condition.
- Performed mechanical testing of FSSWs joined using Phase 2 tools, which showed dramatic increases in lap-shear strength when compared to the results from welds produced with Phase 1 tools.
- Determined that for weld times of 4 seconds (s), the maximum lap-shear tensile strengths measured are 17 kN for DP 780, 22 kN for galvannealed DP 780, and 16 kN for HSBS. All of these values exceeded the minimum specified in the AWS specification for RSW.
- Determined that lap-shear strengths tend to increase with removal of mill, which indicated that surface condition of the sheets has an important influence on mechanical properties and bonding.
- Determined that for otherwise identical welding conditions, increasing tool rotation speed from 800 to 1,600 rpm increased strength values for spot welds made with DP 780 and DP 780GA. Using a two-step schedule rather than a one-step schedule had a similar effect. Metallographic examinations indicated this is at least partly related to increased size of bonded area.
- Made and evaluated stir tools of six different tool materials. These materials are tungsten 25% rhenium alloy, polycrystalline cubic boron nitride (PCBN), silicon nitride (Si_3N_4), titanium diboride (TiB_2), tungsten carbide-cobalt, and a cermet made of complex carbides bonded by a refractory metal alloy.
- Determined PCBN has the most promise as a stir tool material. Wear rates in PCBN tools are very low, although the overall durability, availability, and cost may prove prohibitive for widespread commercial applicability.
- Confirmed that tool shape can have a significant influence on lap-shear strength.

Future Direction

- Evaluate performance of friction spot welds in the cross-tension test.
- Evaluate the response of DP 780 with a broader range of zinc coatings (hot-dipped and electrogalvanized, in particular), similar to what will be encountered in the manufacturing environment. Modified Al-Si coatings will also be evaluated for HSBS.
- Continue to evaluate tool materials, including reformulated PCBN and Si_3N_4.
- Continue detailed microstructure characterization including fracture behavior.
- Continue study of the relation of strength to sheet surface condition.
- Initiate fatigue testing of joints.
- Develop nondestructive evaluation (NDE) strategies.

Introduction

The technology for implementing FSSW of aluminum in automotive manufacturing environments exists. C-gun-type FSSW heads have been developed and adapted to robotic systems that are now commercially available for FSSW of aluminum alloys. This project addresses the questions of whether the FSSW process is viable for joining AHSSs and whether FSSW has advantages over conventional processes like RSW.

Preliminary work on FSSW of AHSSs suggested that several features of the process (fine-grained microstructure in the nuggets of AHSSs, potentially higher-strength joints and higher energy absorption in crash, low energy consumption and environmental emission during manufacturing) may give FSSW cost and energy saving advantages over RSW. In addition, the process may be viable for high-strength, lightweighting alloys that are difficult to join using conventional techniques (DP 1000, martensitic steels such as HSBSs, etc.).

Important questions remain about effective, economical application of FSSW to AHSSs. Critical questions being addressed in this study include the following.

- Are tool materials available that have potential for reasonable life?
- Are joint strengths of FSSWs comparable to or better than those of welds produced with conventional processes?
- Are manufacturing conditions appropriate (cycle time, tool wear, process robustness and sensitivity to production variation)?
- Do FSSW-produced joints have any advantage for NDE or for real-time process control over RSW?
- Are total life-cycle costs appropriate?
- Can the process be modeled and predictive tools be developed to aid designers?

If the effectiveness of FSSW for joining AHSSs is established, this could accelerate the insertion of these high-strength lightweighting alloys into automotive body construction to help meet FreedomCAR goals.

Approach

The primary goal of this project is to characterize the responses of AHSSs to FSSW to establish whether FSSW is an acceptable method for joining AHSSs and can be incorporated in current manufacturing processes. The project is organized into two phases. Phase 1 activities addressed the critical questions of whether there are tool materials available that have potential for reasonable life and whether FSSWs made in AHSSs could develop strengths comparable to those in welds made by conventional processes like RSW. Phase 2 focuses on the factors crucial to industrial implementation of FSSW; therefore, the second phase of the project concentrates on evaluation of several specific targets including cycle time, tool durability, process robustness, and repeatability.

The Phase 1 results and the initial work under Phase 2 highlight two important challenges: the development of robust tool materials and the development of the weld parameters needed to achieve consistently high joint strengths. Both sets of issues, those related to tooling and those related to joint strength, appear to be interrelated.

Currently, PCBN is the most durable, effective material from which to make stir tools for welding AHSSs; however, PCBN is relatively expensive, difficult to machine into the needed shapes, and not widely available for purchase. These characteristics significantly complicate modifying tool designs, but such modification is a critical element in maximizing joint strengths. In addition, the intrinsic durability of PCBN has not been well characterized. Thus, there is considerable interest in identifying and evaluating alternatives to PCBN, particularly any that would reduce tool costs and improve durability.

A second set of challenges identified in prior work relates to developing consistently high joint strengths. Joint strengths are being obtained that compare favorably with minimum values specified in industry standards for spot welds such as AWS D8.1M [1]. However, the consistency of obtaining these strength levels must be improved. In addition, welding times must be minimized. These conditions can be met by increasing the bonded area of FSSWs.

In addition to addressing the issues discussed above, in Phase 2 we intend to evaluate joint microstructures and mechanical properties, assess the potential for in-process NDE, and establish the framework of a design database for spot friction-welded structures. The project is a 50-50 collaboration between ORNL and PNNL, and it includes an advisory committee with representatives from Chrysler, Ford, GM,

ArcelorMittal Steel Corp., and Gestamp U.S. HardTech, Inc.

Materials and Experimental Details

Until recently, most of this work was done using two uncoated AHSSs: DP 780 and an HSBS sourced from a Swedish supplier, the parent of U.S. HardTech. The DP 780 is 1.5 mm thick sheet; the thickness of the HSBS is 1.4 mm. More recently, a lot of galvannealed DP 780 (U.S. Steel) was included in the activities. The nominal thickness of this sheet was also 1.5 mm. [The suffix GA is added to specifically identify galvannealed steel (e.g., DP 780GA) and results obtained with it.]

The FSSW performed during Phase 1 as well as during the initial portion of Phase 2 was done almost exclusively with PCBN tools. However, several lower-cost alternatives are being evaluated for FSSW tool materials during the Phase 2 program, including Si_3N_4, TiB_2, and a new tungsten-based cermet alloy.

All spot welds are made in displacement-control mode by varying the parameters of tool plunge depth and tool plunging rate. In addition to these control parameters, a number of other process variables are typically recorded for each weld, including weld time, spindle torque, normal force, and temperature on the back side of the two-sheet "stackups." This additional information is archived for future use and analysis.
Joint strength is evaluated by tension testing lap joints to determine their shear-tension strengths. Strengths are correlated with processing parameters and microstructures. Microhardness mapping is also being used to assess the characteristics and properties of the joints.

Results and Discussion

Results from the lap-shear testing are presented in Tables 1–4. Tabulated data include the tool rotation speed, the number of programmed steps, the maximum measured load on the tool during welding, the maximum measured temperature, the actual values from lap-shear testing, and the average lap-shear strength value. The maximum tool load was determined by a load cell integrated into the spindle of the MTS ISTIR machine. Temperatures were measured with a thermocouple embedded in the supporting anvil that contacted the bottom of the two-sheet stackups. The thermocouple was located on about the centerline of the stir tools.

Several trends are apparent in the data. For the uncoated DP 780, there was a clear tendency for both lap-shear strength and maximum temperature to increase when using a two-step rather than a one-step weld procedure. This occurred at both 800 and 1,600 rpm. Also, increasing tool rotation speed with a given weld procedure tended to increase both lap-shear strength and maximum temperature. These trends were consistent for both stir tool shapes. The zinc coating did not have a detrimental effect on lap-shear strength, and in three of the four combinations, spot welds made with the DP 780GA had higher strengths than their uncoated counterparts. For identical welds, measured temperatures were lower for DP 780GA. This could be due either to the ceramic coating used on the backing anvil for the welds or to the effect of zinc reducing the initial friction coefficient between stir tools and sheet.

Table 1. Lap-shear test results for DP 780 steel welded with BN77 tool.

Rpm	No. of steps	Max. tool load (kN)	Max. temp. (°C)	Actual lap-shear strength values (kN)	Avg. lap-shear strength (kN)
800	1	32.5	410	4.8, 4.4, 4.0	4.4
800	2	33.0	537	7.5, 8.3, 8.4	8.0
800GA	2	40.8	493	10.8, 10.8, 11.8, 11.6	11.3
1,600	1	23.7	510	9.5, 9.7, 9.7, 9.4	9.6
1,600	2	31.3	641	10.4, 12.4, 11.5, 10.6	11.2
1,600GA	2	32.7	591	11.2, 11.5, 11.5, 10.7	11.2

Table 2. Lap-shear test results for DP 780 steel welded with BN46 tool.

Rpm	No. of steps	Max. tool load (kN)	Max. temp. (°C)	Actual lap-shear strength values (kN)	Avg. lap-shear strength (kN)
800	1	29.8	452	7.9, 8.2, 9.1	8.4
800	2	38.2	645	13.6, 14.7, 15.7	14.7
800GA	2	49.1	534	14.7, 16.4, 15.9, 14.1	15.3
1,600	1	34.3	606	10.3, 9.8, 11.0	10.4
1,600	2	31.8	712	17.4, 13.4, 16.0	15.6
1,600GA	2	32.1	683	22.6, 18.1, 17.0, 14.3	18.0

Table 3. Lap-shear test results for HSBS welded with BN77 tool.

Rpm	No. of steps	Max. tool load (kN)	Max. temp. (°C)	Actual lap-shear strength values (kN)	Avg. lap-shear strength (kN)
800	1	31.7	408	10.1, 10.0, 10.6	10.2
800	2	41.1	539	10.7, 12.1, 11.6	11.4
1,600	1	24.5	545	10.8, 11.0, 11.6	11.1
1,600	2	32.7	646	11.4, 11.4, 10.0	10.9

Table 4. Lap-shear test results for HSBS welded with BN46 tool.

Rpm	No. of steps	Max. tool load (kN)	Max. temp. (°C)	Actual lap-shear strength values (kN)	Avg. lap-shear strength (kN)
800	1	32.8	471	10.0, 8.0	9.0
800	2	44.2	633	12.0, 12.6	12.3
1,600	1	35.1	593	8.9, 10.5	9.7
1,600	2	30.8	717	15.0, 16.1	15.5

An initial reduction in friction properties may be more likely since maximum loads also tended to be higher for the DP 780GA. In all cases except spot welds of HSBS with the BN77 stir tool, maximum loads were experienced early in the plunges regardless of tool design.

The effect of rotation speed on temperature is expected because heat is generated in friction stir welding by two mechanisms. One is through friction at the interfaces of the tool surfaces and the workpiece material; the second is through viscous dissipation of metal flow in the vicinity of the tool [2–5]. A simplified view [6] indicates that temperature rise, ΔT, at a fixed location and set of conditions during friction stir welding can be expressed as

$$\Delta T \propto \frac{\mu P \omega}{K} \quad ,$$

where μ is a friction coefficient, P is a pressure related to tool force, ω is tool rotation speed, and K is a constant. Increasing tool rotation speed has a direct effect on increasing temperature in the stir weld zone.

Using a two-step welding procedure at fixed rotation speed produced higher lap-shear strengths than a one-step schedule basically because a larger stir tool-sheet surface area was engaged for a longer period of time. This was determined by first associating the projected area of the BN77 and the BN46 tools with distance from their tips. A coordinate measurement machine was used to

determine the variations of tool radius with axial distance for both stir tools. These values were then used to calculate the variations of total projected area with axial distance, as shown in Figure 1. The relationship between axial distance from the tool tip and total projected area was then used to convert the tool load-time responses during welding into pressure-time data. An example of the differences between the one-step and the two-step welding procedures is shown in Figure 2

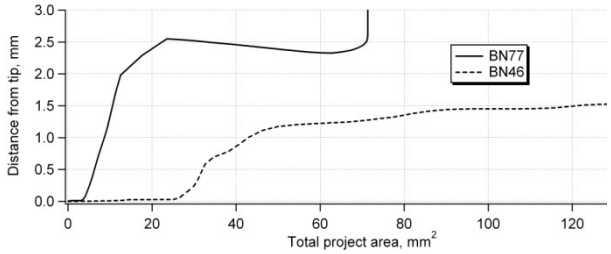

Figure 1. Variation of total projected area with axial distance from stir tool tips.

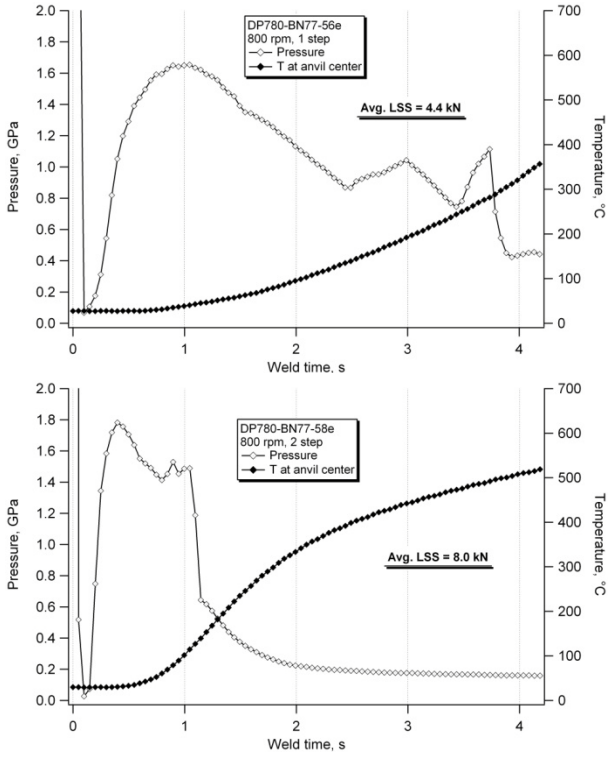

Figure 2. Variations of pressure and temperature for spot welds of uncoated DP 780 made at 800 rpm with either a one-step (top) or a two-step (bottom) welding procedure.

for spot welds made at 800 rpm with the BN77 tool on uncoated DP 780. Both the pressure and temperature are plotted with weld time in Figure 2.

The one-step approach involves a peak pressure early in the process near 1 s weld time, but the temperature at the pressure peak is relatively low. In addition, projected area at the pressure peak is also relatively small. The BN77 stir tool did not fully engage the sheet metal until this weld was about 80% complete. In the two-step approach, the stir tool became fully engaged with the sheet metal in about 1 s. From that point until the 4 s weld time was reached, the spinning tool continued to heat the weld zone and to maintain it under a relatively steady pressure. FSSWs appear to be characterized by regions of intense stirring near the stir tool-sheet metal interfaces, and this observation is consistent with metal flow analysis in the process [7]. However, interface bonding extends beyond distances where intense stirring occurs. This implies that diffusional processes (i.e., diffusion bonding) help to create the bonded interfaces of FSSWs.

Both pressure and temperature are important to diffusion bonding processes [8]. Thus, the higher strength of the two-step welds must be the result of having high projected area engaged with the sheet for relatively longer times at higher temperatures.

The overall characteristics of the pressure-time and temperature-time signatures of welds made with the BN46 stir tool were similar to those made with the BN77 tool. However, the peak pressures reached with the BN46 tool were lower by about 40%. Likewise, the temperature profiles were similar in shape, but those for the BN46 tool were higher by 50–100°C throughout the welding. This would be caused by the greater area of engagement of the BN46 tool with the sheet at any point during the welding. The characteristics of the pressure-time and temperature-time signatures were not substantially influenced by the presence of zinc on the DP 780GA. Analysis of the machine output data from welds of the HSBS are incomplete at the present time.

Unlike the behavior of DP 780 and of the HSBS welded with the BN46 stir tool, the lap-shear strengths of all welds made in HSBS with the BN77 stir tool (Table 3) were relatively insensitive to changing weld conditions. At the moment, it can only be suggested that this is related to the pin length on the BN77 tool. In friction spot welding of aluminum alloys, for example, it has been found that, for a set pin length, spot-welding condition, and metal thickness, lap-shear strength will increase with plunge depth up to a certain point. As plunge depth increases further, lap-shear strength values will reach a plateau and eventually start decreasing due to excessive thinning of the top sheet. It is clear that the BN77 pin length and HSBS thickness put this combination in a region of welding parameter space near a lap-shear strength plateau. This behavior appears analogous to that of aluminum alloys.

The ranges of lap-shear values presented in Tables 1–4 can be placed in perspective by comparing them to values required for resistance spot welds on the same steels. AWS D8.1M [1] was used to calculate minimum required shear strengths for both steels. The minimum values were calculated using tensile strengths of 790 MPa for DP 780 and 1,500 MPa for the HSBS. The results for required lap-shear strengths are 10.3 kN for DP 780 and 12.0 kN for the HSBS. The tabulated data show that the minimum values can be met for FSSW of either uncoated or galvannealed DP 780 using a two-step schedule and either the BN77- or the BN46-type stir tool. The minimum value can also be met for the HSBS using the two-step process and the BN46 stir tool.

Conclusions

Lap-shear testing showed that for otherwise identical welding conditions, increasing tool rotation speed from 800 to 1,600 rpm increased strength values for spot welds made with DP 780 and DP 780GA. Using a two-step schedule rather than a one-step schedule had a similar effect. Spot welds made with either tool and a two-step schedule had lap-shear strengths that exceeded the required minimum value of 10.3 kN for resistance spot welds.

Lap-shear testing showed that spot welds made in the HSBS with the BN77 stir tool were relatively insensitive to tool rotation speed and weld schedule strategy. It was suggested this was related to the ratio of pin tool length to sheet thickness, but no conclusive evidence was provided to support the claim. The lap-shear strengths of this group of spot welds were all in the range of 10–11 kN, slightly below the minimum value of 12 kN required of resistance spot welds

Similar to DP 780, increasing tool rotation speeds from 800 to 1,600 rpm or using a two-step rather than a one-step weld schedule increased the lap-shear strength of spot welds made with the BN46 stir tool on the HSBS. The minimum shear strength required for resistance spot welds of 12 kN was exceeded for the HSBS using the two-step process and the BN46 stir tool.

Presentations/Publications/Patents

1. Y. Hovanski, M. L. Santella, and G. J. Grant, "Friction Stir Spot Welding of Hot-Stamped Boron Steel," *Scripta Materialia,* **57**, pp. 873–876 (2007).
2. Y. Hovanski, M. L. Santella, and G J. Grant, *Friction stir spot welding of advanced high strength steels*, presentation at MS&T, September 2007.
3. G. J. Grant, Y. Hovanski, and M. L. Santella, "Friction Stir Spot Welding of Advanced High Strength Steels for Automotive Applications," in A. M. da Silva, J. F. dos Santos, and G. Amancio (eds.) *International Symposium on Friction-based Spot Welding Processes,* (International Institute of Welding, GKSS Forschungszentrum, Geesthacht, Germany, 2007), pp. 107–148.
4. Michael Santella et al., "Friction Stir Spot Welding of DP 780 and Hot-Stamp Boron Steels," *Proceedings of Sheet Metal Welding Conference XIII* (American Welding Society, 2008).
5. Michael Santella et al., *Friction Stir Spot Welding of DP 780 and Hot-Stamp Boron Steels*, presented at Sheet Metal Welding

Conference XIII, Livonia, Michigan, May 16, 2008.

6. Y. Hovanski, M. L. Santella, and G. J. Grant, *Friction Stir Spot Welding of Advanced High Strength Steels,* presentation at MS&T, September 2008.

References

1. AWS D8 Committee on Automotive Welding, *Specification for Automotive Weld Quality—Resistance Spot Welding of Steel,* AWS D8.1M:2007 (AWS, Miami, 2007).
2. H. Schmidt, J. Hattel, and J. Wert, "Modelling of the Contact Condition at the Tool/Matrix Interface in Friction Stir Welding," in H. Cerjak, H. K. D. H. Bhadeshia, and E. Kozeschnik (eds.), *Mathematical Modelling of Weld Phenomena 7,* (Verlag Technischen Universität Graz, 2005), pp. 925–941.
3. Ø. Frigaard, Ø. Grong, and O. T. Midling, *Met. Trans. A*, **32A**, pp. 1189–1200 (2001).
4. P. Reynolds et al., in S. A. David et al. (ed.), *6th International Trends in Welding Research Conference Proceedings,* (ASM International, 2003), pp. 297–301.
5. G. Buffa et al., *Mat. Sci. Eng. A*, **419**, pp. 389–396 (2006).
6. J. E. Gould and Z. Feng, *J. Mat. Proc. Mfg.*, **7**, pp. 185–194 (1998).
7. R. Nandan et al., "Three-dimensional heat and material flow during friction stir welding of mild steel," *Acta Mat.*, **55**, pp. 883–895 (2007).
8. N. F. Kazakov (ed.), *Diffusion Bonding of Materials,* Pergamon Press, Oxford, U.K. 1985.

D. Friction Stir and Ultrasonic Solid State Joining Magnesium to Steel

Principal Investigator: Glenn J. Grant
Pacific Northwest National Laboratory
902 Battelle Blvd., P.O. Box 999, Richland, WA 99352
(509) 375-6890 ; fax: (509) 376-6034; e-mail: glenn.grant@pnl.gov

Principal Investigator: Yuri Hovanski
Pacific Northwest National Laboratory
902 Battelle Blvd., P.O. Box 999, Richland, WA 99352
(509) 375-3940; fax: (509) 376-6034; e-mail: yuri.hovanski@pnl.gov

Principal Investigator: Michael L. Santella
Oak Ridge National Laboratory
P.O. Box 2008, Oak Ridge, TN 37831-6096
(865) 574-4805; fax: (865) 574-4928; e-mail: santellaml@ornl.gov

Technology Area Development Manager: Joseph A. Carpenter
(202) 586-1022; fax: (202) 586-1600; e-mail: joseph.carpenter@ee.doe.gov

Field Technical Co-Monitors: C. David Warren, Mark Smith
(865) 574-9693; fax: (865) 574-6098; e-mail: warrencd@ornl.gov
(509) 375-4478; fax: (509) 375-4448; e-mail: mark.smith@pnl.gov

---

Contractors: Oak Ridge National Laboratory (ORNL) & Pacific Northwest National Laboratory (PNNL)
Contract Nos.: DE-AC05-00OR22725 & DE-AC06-76RLO1830, respectively

---

Objective

- Establish the applied technical understanding necessary to produce robust joints between magnesium alloys and steel using solid state joining (friction stir welding [FSW] and ultrasonics).
- Develop the fundamental relationships influencing bond formation in metallurgical, mechanical and chemical forms created during FSW and ultrasonic welding (USW) solid state processes. Ascertain their responses to changing alloys, product forms and surface conditions as they affect creation of structural joints between magnesium and steel.
- Determine the effect of FSW and ultrasonic joining on corrosion protection coatings and characterize the corrosion performance of joined assemblies.

Approach

- Systematically evaluate the application of friction stir and ultrasonic processes to welding of magnesium to steel. Develop an improved understanding of the interaction of each unique energy source with appropriate alloy/product form combinations.
- Investigate the fundamental aspects of bond formation (metallurgical and/or mechanical) during the solid state process and investigate the response to changing alloys, product forms (wrought, castings) and surface conditions (coatings).
- The materials being joined (magnesium and steel) form a strong galvanic couple. Strategies to prevent corrosion in the joint, including potentially unbroken interlayers or transition materials, complete encapsulation,

coatings or hermetic adhesives that are welded through during the joining process will be employed to mitigate the potential for galvanic coupling.

Accomplishments

- A steering committee was established that includes representatives from the automotive original equipment manufacturers (OEMs) Ford, GM, and Chrysler. This committee will meet by conference call once a month so that project progress and direction can be reviewed.
- Initial project kickoff meeting was held with the OEM steering committee members in the third quarter 2008 to identify issues related to joint geometry, fit-up, processing, etc. for dissimilar material welding. An agreement was reached on applicable alloy forms and gauges.
- Performed literature review in relevant topic areas to provide starting points for process development.
- Developed introductory experimental design parameters for magnesium to steel joints using both friction stir and ultrasonic welding techniques.
- Procured initial materials in several of the applicable alloy forms and gauges to begin testing. Coordinated with the Magnesium Front End Research and Development group to obtain materials in support of dissimilar joining goals.
- Initiated systematic evaluation of applicable joining parameters on several combinations of magnesium and steel in lap configurations.

Future Direction

- Complete preliminary testing of FSW and USW in Mg-steel joints using variations of uncoated and coated steels with AZ31B and AM60 magnesium alloys.
- Perform investigation into bond formation and performance as a function of joining parameters.
- Develop an improved understanding of the interaction of the energy source with appropriate alloy/product form combinations in FSW. Factors affecting joint strength will include tool design, process speed and feed and pin design and location relative to interface.
- Determine the effect of sonotrode tip wear in Mg-steel joints and investigate a limited number of alternative tip materials or process strategies to mitigate wear.

Introduction

Decreasing automobile weight can directly contribute to reducing fuel consumption. Increasing the use of lightweight materials and implementing manufacturing technologies that enable the use of lightweight materials are the two primary paths toward weight reduction. In some situations, lightweight materials can be directly substituted for higher density materials, but there are barriers to direct substitution. In a modern multi-material vehicle, lightweight materials such as aluminum and magnesium alloys can be a challenge to attach to underlying substructure, which is usually composed of steel. Even in aluminum- and magnesium-intensive designs where entire substructures may be constructed of lightweight metals, there remains a need to join the substructure with other parts of the body-in-white such as the predominantly steel passenger safety cage. Joining methodologies available in the cost environment relevant to automotive manufacturing include resistance spot welding, adhesives, linear fusion welding, hemming, clinching, bolting and riveting. However, because of the highly dissimilar natures of the materials, magnesium/steel joints are extremely problematic. Magnesium-to-steel joints cannot be simply fusion welded due to the extreme differences in their melt temperatures, and joining methods that require a large amount of plastic strain in the magnesium component suffer from magnesium's poor ductility at room temperature.

As alternative joining methodologies, friction stir welding (FSW), friction stir spot welding (FSSW), and ultrasonic welding (USW) may be able to overcome traditional barriers to join and construct hybrid magnesium/steel components. These solid state joining methods provide unique joining capabilities that, if realized, may potentially produce faster and more economical alternatives to current technologies (bolting/riveting). However, FSW and USW for dissimilar magnesium/steel combination are significantly underdeveloped for broad deployment.

The purpose of this project is to develop an applied understanding of the following:

- localized metal forming and potential metallurgical bonding that develops during FSW, FSSW, and USW
- the influence of process parameters on joint strength and performance
- the interaction of both joining processes with existing corrosion protection methods and their corrosion performance.

Approach

While the potential for utilizing solid state joining processes such as FSW and USW to overcome the traditional difficulties associated with joining magnesium to steel is emerging, many challenges remain. Insufficient understanding of the proper processing conditions required to achieve robust joints has hampered any comprehensive evaluation of performance (strength, fatigue, durability, crash performance). Minimal existing research has yet to evaluate feasible joint geometries, and no emphasis on employing the benefits of solid state technologies in mitigating the galvanic corrosion in magnesium/steel joints has been evaluated.

This project is designed to overcome many of these technical barriers by performing three primary tasks. Task 1 will focus on systematically evaluating the application of friction stir and ultrasonic processes to the welding of magnesium to steel in a lap configuration. The work includes developing an improved understanding of the interaction of each unique energy source with appropriate alloy/product form combinations and is intended to provide a baseline conceptual feasibility for the remaining work.

If Task 1 is completed successfully, Task 2 will concentrate on investigating the fundamental aspects of bond formation (metallurgical and/or mechanical) during the solid state process. This phase of the project will also include an investigation into the response to material variation due to changing alloys, product forms (wrought, castings) and surface conditions (coatings). This task will allow for further investigation of favorable methodologies outlined during the concept feasibility phase with the potential of further increasing joint strength.

Task 3 will focus on investigating strategies to prevent corrosion in the joint. This will include evaluating the effects of potentially unbroken interlayers or transition materials as well as coatings or hermetic adhesives that are welded through during the joining process. These tasks and associated deliverables are intended to enable a broader application of solid state joining technologies while further facilitating the joining of magnesium to steel.

Materials and Experimental Details

As the solid state joining technologies evaluated herein are completely different, unique hardware is being used for the development of each joining process.

Friction Stir Welding

Friction stir technologies will be developed primarily using a high-stiffness precision friction stir welding machine located at PNNL (Figure 1). This machine is capable of maintaining tool runout at less than 0.0004 inch (in.) and can apply vertical process loads in excess of 30 kilo-pounds per square inch (Kip). With the capability of producing welds of 96 in. long and an operating envelope that can accommodate part configurations larger than 48 in. high, this machine provides flexibility in evaluating the various product forms applicable to Mg/steel structures.

Figure 1. Precision FSW machine located at PNNL.

Friction stir joints between magnesium and steel are produced in a lap configuration with the magnesium located on the tool side of the joint. FSW tools are plunged through the thickness of the magnesium to the interface of the two materials and are subsequently translated at depth for a predetermined length. Various techniques have been designed to promote the joining characteristics of the interface, including tools that beneficially disturb the steel surface creating clinch points or rough surfaces for the locally plasticized magnesium to adhere.

Ultrasonic Welding

Research and development in ultrasonic solid state capabilities will take place primarily at ORNL. The research scale ultrasonic test frame shown in Figure 2 is capable of applying up to 2500 Watts (W) at 20 kilo-Hertz (kHz).

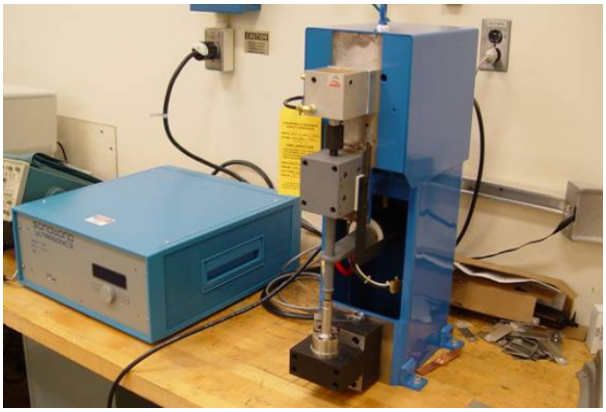

Figure 2. USW machine located at ORNL.

Results

Preliminary ultrasonic welds were made with a Sonobond CLF2500 using a pedestal welding station. The rated conditions at the welding tip on this equipment are 20 kHz frequency with 25 micrometers (μm) amplitude. A variety of on-hand materials are being used for ultrasonic welding trials, while reference materials are being acquired. The magnesium alloys used for the initial welds were 1.6 mm thick AZ31-H24 sheet and 2 mm thick AM60B die castings. Coupons of both alloys were welded to those of 1 mm thick hot-dip galvanized mild steel (MSHDG) to provide specimens for metallographic examination. Optical micrographs of these spot welds are shown in Figures 3 and 4. For this combination of metals, there were no indications of defects or chemical reactions that might compromise weld integrity.

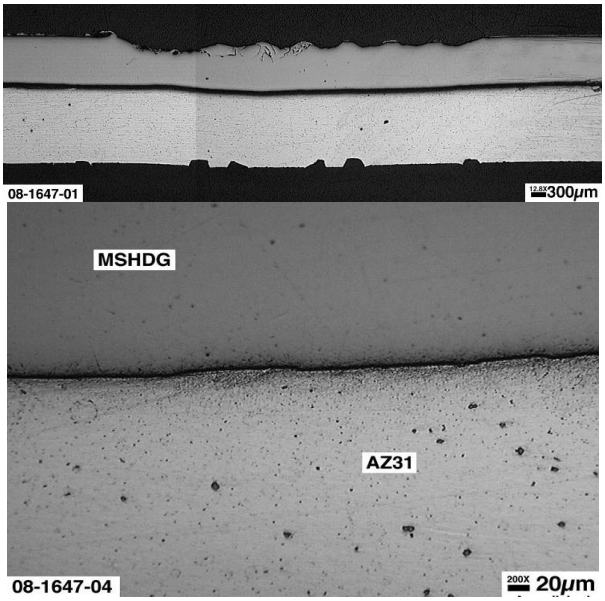

Figure 3. The top micrograph shows the overall view of hot-dip galvanized mild steel ultrasonically spot welded to AZ31; the dark line at the interface is a polishing artifact. The bottom provides detail at the welded interface between the mild steel (MSHDG) and AZ31.

Coupons of AZ31 nominally 25 mm wide x 100 mm long were also welded to mild steel coupons of the same size to produce specimens for lap-shear testing. A 25 mm overlap was used for making lap-welded coupons with spot welds centered in the overlap regions. The lap-welded

specimens were shear tested using a crosshead velocity of 10 mm/min. The specimens were not shimmed in the grips, and no guides were used to constrain specimen rotations during testing. Eleven AZ31-mild steel specimens were tested to arrive at an average lap-shear strength of 2.68 ± 0.41 kiloNewtons (kN).

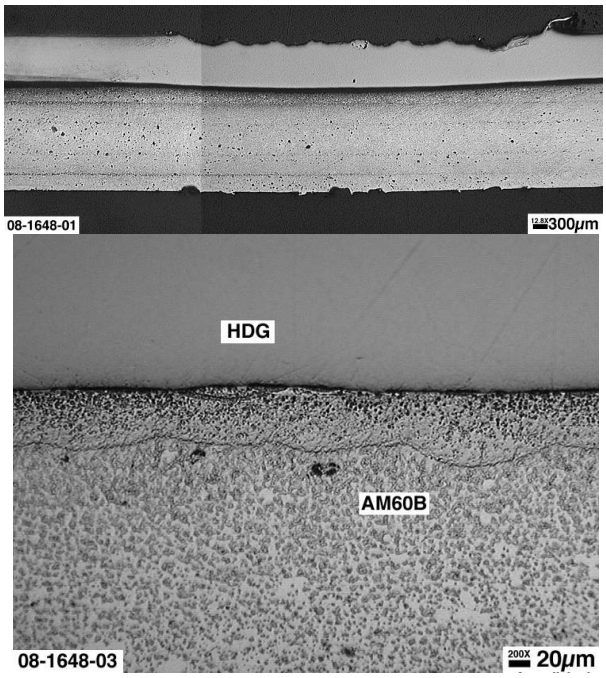

Figure 4. The top micrograph shows the overall view of hot-dip galvanized mild steel ultrasonically spot welded to AM60B; the dark line at interface is a polishing artifact. The bottom provides detail at the welded interface between the mild steel (MSHDG) and AM60B.

Conclusions

The project was initiated in the latter half of 2008, and a kickoff meeting with the principals from PNNL, ORNL, and members from the OEM steering committee took place in the third quarter of 2008. With this late start in 2008, much of the intended initial project scope is still in progress. As one of the initial project goals was to concentrate on alloys and forms corresponding to those used in the Magnesium Front End Research and Development program, some delay was also experienced in attaining corresponding materials.

The project is poised to make rapid progress in the first quarter of 2009 as magnesium materials become available. The initial work on ultrasonic bonding has already shown joint strength above the project's targeted values for Phase 1 of the program, so reaching the later project goals and milestones is considered feasible.

E. Friction Bit Joining—An Innovation in Dissimilar Metal Joining

Principal Investigator: Zhili Feng
Oak Ridge National Laboratory
P.O. Box 2008, Oak Ridge, TN 37831-6095
(865) 576-3797; fax: (865) 574-4928; e-mail: fengz@ornl.gov

Principal Investigator: Michael P. Miles
Brigham Young University
265 CTB, Provo, UT 84602
(801) 422-1858; fax: (801) 422-0490; e-mail: mmiles@byu.edu

Technology Area Development Manager: Joseph A. Carpenter
(202) 586-1022; fax: (202) 586-1600; e-mail: joseph.carpenter@ee.doe.gov

Field Technical Monitor: C. David Warren
(865) 574-9693; fax: (865) 574-6098; e-mail: warrencd@ornl.gov

---

Contractor: Oak Ridge National Laboratory (ORNL)
Contract No.: DE-AC05-00OR22725

Objective

- Develop the technical basis for and demonstrate the viability of a newly invented solid-state joining process—friction bit joining (FBJ)—for joining dissimilar metals such as aluminum (Al) or magnesium (Mg) alloys and advanced high-strength steels (AHSSs) for use in auto body structures to achieve a balance in cost savings, lightweighting, structural durability, and impact performance.

Approach

- Perform Design of Experiment (DoE) for key process variables that influence the joint strength.
- Characterize bonding interface for better understanding of the basic bonding mechanisms between dissimilar metals.
- Develop process window for different material and gauge combinations.

Accomplishments

- Demonstrated the feasibility of FBJ of dissimilar metals (Mg to steel and Al to steel).
- Achieved metallurgical bonding and relatively low process load.
- Demonstrated initial joint strength exceeded the Phase I target and that of self-piercing rivets.
- Achieved reasonably fast process time (less than 3 s) with good properties.

Future Direction

- Continue DoE evaluation of key process variables that influence joint strength.
- Continue bonding interface characterization and bonding mechanisms investigation.
- Determine feasibility of combining FBJ with adhesive bonding for weld bonding.
- Determine feasibility of FBJ corrosion control and prevention through process innovation and coating.

- Develop mechanized joining-bit feeding system for high-speed, high-volume production.
- Conduct an industry implementation business case analysis for the process.
- Explore and develop a technology-transfer and commercialization partnership.

Introduction

The automotive industry and the U.S. government are aggressively pursuing increased use of lightweight materials such as Mg alloys and Al alloys in auto-body structures for improved vehicle fuel efficiency. Next generation vehicles will require optimum use of a variety of engineering materials, ranging from AHSSs to lightweight materials such as Al and Mg alloys, composites, and other materials, to achieve a balance in cost, lightweighting, durability, and crashworthiness. Use of vastly different lightweight material combinations in body structures presents a number of technical challenges in automotive body-in-white assembly. One of them is joining dissimilar materials to form integrated structural components to meet design and performance requirements [1,2].

Dissimilar metal joining—joining of vastly different materials such as Mg and steel, Mg and Al, and Al and steel—is generally considered to be out of the "comfort zone" of the existing joining and attachment technologies used in high-volume mass production. Conventional fusion welding processes, including gas metal arc welding, laser welding, and resistance spot welding (RSW), are not suitable for welding dissimilar materials because of the metallurgical incompatibility of these materials during melting and solidification. Self-piercing riveting (SPR) is difficult to apply to AHSSs due to the inadequate strength of rivet materials and the equipment limitations. Application of SPR for Mg alloys is also problematic because of their low ductility. Mechanical fastening and adhesive bonding have cost and performance penalties.

This project aims at developing a new solid-state joining process particularly suitable for dissimilar metals. This newly invented process, FBJ, combines the process advantages and overcomes the fundamental shortcomings of the solid-state friction stud welding process and the mechanical SPR process. A proof-of-concept study has produced surprisingly good results in joining dissimilar materials.

A two-phase, gated programmatic approach has been adopted for this project. This report covers the progress in the first 3 months of a 12-month, Phase I, Concept Feasibility research project that started in June 2008.

Phase I research and development (R&D) focused on further evaluating and identifying the critical factors/variables governing the FBJ process, the process characteristics, and the metallurgical bonding mechanisms between dissimilar metals. More comprehensive R&D will be performed in Phase II (Technical Feasibility) of the project, leading to eventual field demonstration of the FBJ technology. Phase II will also include identifying potential commercial partners and eventual partnership with technology-transfer and commercialization candidates.

The Department of Energy's FreedomCAR and Vehicle Technologies Lightweighting Materials thrust and the National Science Foundation's Materials Processing and Manufacturing Technology Program cosponsored the Phase I effort, which is being carried out jointly by ORNL and Brigham Young University.

Process Principle of FBJ

FBJ creates a metallurgically bonded spot joint in two or more sheets of the same metal or dissimilar metals by a combination of the cutting and friction bonding action of a high-strength consumable joining bit. The essence of the FBJ process is illustrated in Figure 1. FBJ comprises two essential phases. It starts with an initial cutting phase where the top layer (or layers) is penetrated by the rotating joining bit under applied axial load. The process then transitions to the frictional-joining phase in which the rotating bit and surrounding sheet materials are frictionally heated to a high temperature to facilitate material flow and bonding. In a manner similar to friction stud

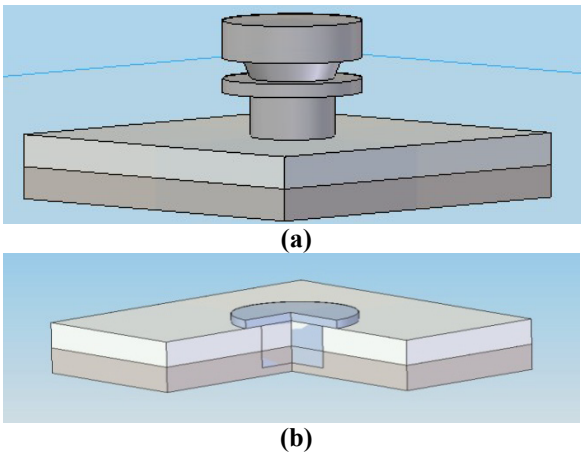

Figure 1. Schematic representation of FBJ process. The operation begins with cutting through the top layer of material, shown in (a). The rotational speed of the bit is then increased to generate frictional heating and material flow to join the sheets. At the end, the top part of the bit held by the machine is self-separated from the bottom, bonded to the workpiece, leaving a relatively smooth joint, as seen in (b).

welding, at the end of the operation a metallurgical bond is formed between the joining bit and the different sheet materials as a result of diffusion across the interface of different metals under high temperature and high pressure. The joining bit is consumable—it is left in the workpiece and forms an integral part of the weld.

FBJ incorporates a unique self-break-off feature by means of special machine spindle design and simple joining bit geometry design. The part of the joining bit bonded to the workpiece is automatically sheared off from that in the machine holder at the end of the operation, leaving a relatively smooth joint surface above the bit flange, as shown in Figure 1. The unique self-break-off feature makes it possible to automate the process in a high-speed production environment and eliminate the need for the after-welding cutting operation. FBJ is fast: the total process time in the concept feasibility study ranged from 2 to 5 seconds.

A prototype machine, shown in Figure 2, was designed and built for FBJ during Phase I. The C-frame support configuration is very similar to that commonly used in robotic RSW machines on body assembly lines. As shown in the figure, the C-frame in this first prototype machine is quite

Figure 2. Prototype FBJ machine with a C-frame.

bulky. However, the surprisingly low axial loads obtained in the welding trials (ranging from 8 kN to 12 kN) indicate that the size of the C-frame can be greatly reduced in future production systems.

Progress in FY 2008

Experiments were carried out on two material combinations: 1.4-mm-thick uncoated dual phase (DP) 980 steel welded to 1.8-mm-thick Al alloy 5754 (AA 5754) and 1.4-mm-thick uncoated DP 980 welded to 1.8-mm-thick Mg alloy AZ91. Figure 3 shows an example of FBJ spot welds made between AA 5754 and DP 980. The weld cross-section and bonding interfaces are shown in Figure 4 and Figure 5,

Figure 3. Appearance of FBJ between DP 980 and AA 5754.

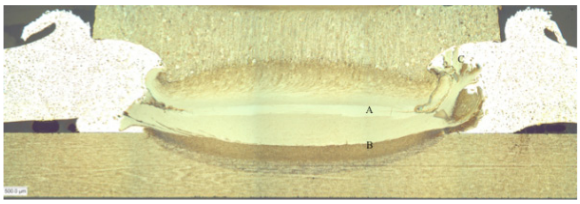

Figure 4. Cross section of FBJ composed of AA 5754 (top sheet), DP 980 (bottom sheet), and 4140 steel joining bit (center).

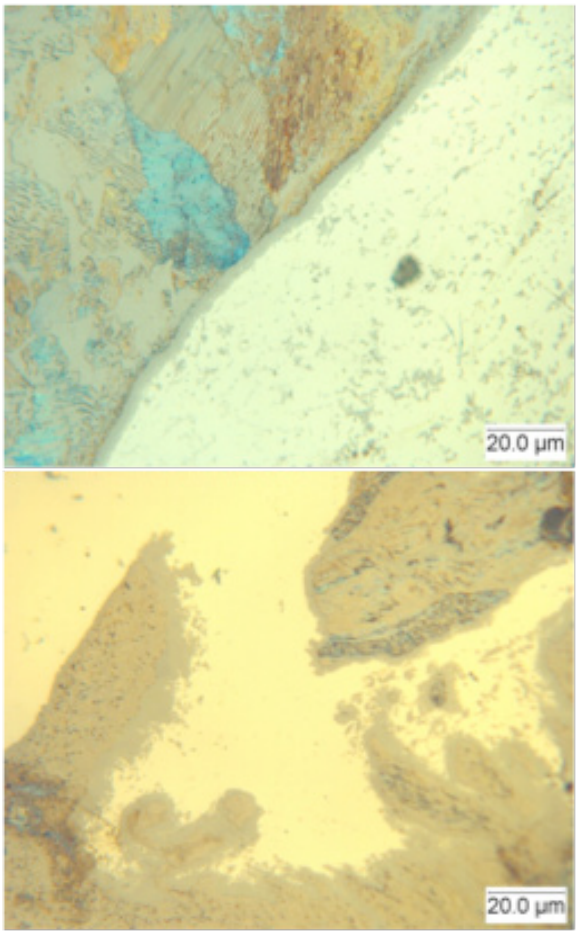

Figure 5. Bonding interface between AA 5754 and DP 980. Metallurgical bonding is evident.

respectively. Clearly, metallurgical bonding has been achieved between DP 980 steel and AA 5754. Metallurgical bonding was also achieved between DP 980 steel and Mg alloy AZ91.

A series of experiments was carried out to determine the effects of different process variables on lap-shear failure load. Table 1 shows the parameter variables that had the most influence on the lap-shear tensile strength for the DP 980-AA 5754 material combination. The shading indicates the process conditions that resulted in the best lap-shear strength—reaching an average of 6.5 kN from three replicate specimens.

Table 1. Joining parameters with the greatest influence on lap-shear failure loads

Bit length (mm)	Joining plunge rate (mm/min)	Depth of plunge (mm)
4.4	36	2.8
6	66	3.3

In the feasibility welding trials conducted so far with Mg alloy, the lap-shear strength for Mg alloy AZ91-DP 980 steel dissimilar welds ranged from 3.0 to 4.8 kN.

The joint strengths of dissimilar FBJ welds are very encouraging. Both Mg-steel and Al-steel FBJ welds far exceed the 1 kN feasibility target strength for Mg-steel and Al-steel joining set forth by the U.S. Automotive Materials Partnership (USAMP).

Sun et al. [3] reported SPR experiments performed on combinations of high-strength, low-alloy (HSLA) 350 steel and AA 5754. Their results were used to benchmark the FBJ results obtained so far in this study. Although the steels used in the two studies were different (DP 980 vs HSLA 350), the weaker material (AA 5754) was the same in both studies and provided the basis for comparison. To effectively compare FBJ and SPR, the bond areas must be known because bond area affects the strength of the joint. The bond area for the FBJ joints was determined by optical measurement of the fracture surface across two diameters of the weld, 90° apart. For SPR, the effective bond area was estimated by considering the rivet geometry, material thickness, and failure mode (rivet-head pullout or a rivet-tail pullout) [3]. SPR results for a joint composed of 1.6-mm HSLA 350 and 2.0-mm AA 5754-O can be found in reference [3]. These material thicknesses are slightly greater than the joints presented in this paper, but as stated before, the weaker materials are the same alloy of similar gauge, so joint

strengths were compared using bond areas. The bond area for the FBJ joints was 28 mm^2 and for the SPR joints 47 mm^2. Lap-shear failure loads were 6.3–6.5 kN for FBJ and about 5.2 kN for SPR. Based on these results, the FBJ joint supports a much greater load per unit bond area than the SPR joint by a factor of 2.

Figure 6 shows the failure mode of FBJ in lap-shear tensile tests. For both steel-Al and steel-Mg joints, it was possible to demonstrate a weld-button-pullout failure mode in which the steel joining bit remained joined to the steel sheet and the Al or Mg sheet was separated from the joining bit. This failure mode is typically associated with high failure strength.

Figure 6. Weld button pullout failure mode observed in FBJ of AA 5754 to DP 980.

Future Direction

The focus of R&D activities in FY 2009 will be on completing the following tasks.

- **DoE Evaluation of Process Conditions**. DoE studies will be conducted to further identify the key process variables influencing the strength of FBJ joints.
- **Microstructure Characterization of the Bonding Interface.** Different microstructural and compositional analysis techniques will be used to study and understand the bonding interface to elucidate the bonding mechanisms between the dissimilar metals.
- **Feasibility of Combining FBJ with Adhesive Bonding.** Initial trials will be on steels to Al alloys.
- **Feasibility of Corrosion Prevention of FBJ.** Various coatings as well as process innovations will be explored for corrosion prevention and control.

Presentations/Publications/Patents

1. M. Miles et al., "Friction Bit Joining of Dissimilar Material Combinations of High Strength Steel DP 980 and Al Alloy AA 5754," *SEA 2009 World Congress*, Detroit, Michigan, Paper No 09M-0232.
2. M. Miles and Z. Feng, "Spot Joining of Dissimilar Combinations of Steel and Light Metals Using a New Consumable Bit Technology," (Invited) *Joining Dissimilar Metals Conference II*, American Welding Society, March 3–4, 2009, Orlando, Florida.

Acknowledgements

We would like to acknowledge the contributions of the following individuals and organizations.

Industry Advisory Committee:
- Chrysler: W. Marttila
- Ford: W. Charron, E. Hetrick
- GM: J. Quinn, J. Fickes, D. Hutchinson

USAMP Metals Joining Team
USAMP Multiple Materials Vehicle Team
Auto/Steel Partnership Joining Technologies Team
USAMP Manufacturing Team

References

1. J. F. Quinn, "Joining Challenges in the Automotive Industry," ORNL Materials Joining Advisory Committee Meeting, November 2, 2007, Oak Ridge National Laboratory, Oak Ridge, Tennessee.
2. *HYBRIDMAT 2: Strategies in the Joining of Hybrid Materials in Automotive Structures—a Mission to France and Germany, May 2004.* Global Watch Mission Report (UK Department of Trade and Industry Global Watch Service, September 2004).
3. X. Sun and M. A. Khaleel, "Strength estimation of self-piercing rivets using lower bound limit load analysis," *Science and Technology of Welding and Joining*, **10**(5), pp. 624–625 (2005).

F. Weld Element and Joining Process Technology Development

Principal Investigator: Douglas J. Bammann
Professor, Mechanical Engineering
Mississippi State University
210 Carpenter Bldg.
Mississippi State, MS 39762
(662) 325-3260; e-mail: djb215@me.msstate.edu

Co-Principal Investigator: Sergio Felicelli
Associate Professor, Mechanical Engineering
Mississippi State University
210 Carpenter Bldg.
Mississippi State, MS 39762
(662) 325-1201; e-mail: felicelli@me.msstate.e

Postdoctoral Associate: Liang Wang
Center for Advanced Vehicular Systems, CAVS 2182-B
Mississippi State University
Mississippi State, MS 39762-5405
(662) 325-9235; e-mail: liangw@cavs.msstate.edu

Co-Principal Investigator: Ted Belyteschko
Walter P. Murphy Professor and McCormick Professor
Departments of Civil and Mechanical Engineering
Northwestern University
2145 Sheridan Road
Evanston, Illinois 60208-3111
(847) 491-7270; fax: (847) 491-3915; e-mail: tedbelytschko@northwestern.edu

Co-Principal Investigator: Wing Kam Liu
Walter P. Murphy Professor
Director of the NSF Summer Institute on Nano Mechanics, and Materials
Department of Mechanical Engineering
Northwestern University
2145 Sheridan Road
Evanston, Illinois 60208-3111
(847) 491-7094; fax: (847) 491-3915; e-mail: w-liu@northwestern.edu

---

Contractor: Mississippi State University (MSST)
Contract No.: 4000054701

Objective

- Develop the next generation of weld element and joining process technology (i.e., spot welding) and assess the applicability of new technology for impact simulations and process optimization using lightweight alloys.

Approach

- Currently, weld element performance and failure are based on a simple beam model in which the weld is modeled as a single element between two welded sheets, and failure is postulated to occur when the tension or a moment exceed a certain specified threshold. This type of model does not reflect the thermomechanical details

of the welding process and consequently is unable to address variations in strength due to differences in weld process parameters and the metallurgy of the materials being joined.

- To develop the next generation of weld analysis technology in which details of the welding process and the metallurgy of the parent material are reflected in the behavior of the weld element, the physics of the resistance welding process must be modeled in detail. The nature of the solidification process within the weld will be studied. The computed thermal history induced during the welding process will be used to predict microstructural evolution within the weld and adjacent material, thereby allowing prediction of the large mechanical property gradients associated with the weld. The evolution of damage in the weld under subsequent high strain rate loading will be studied with strain rate dependent constitutive models.
- The development of the resistance spot welding process has remained largely empirical because the process is extremely complex due to friction-induced deformation and heat generation. We plan to assess the feasibility of developing a weld element technology and a three-dimensional (3D) process model which will enable better design of the spot welding process.

Accomplishments

- Developed thermoelectrical and thermomechanical models with ABAQUS to predict temperature distribution and residual stress during the spot welding process.
- Developed a two-phase Bammann-Chiesa-Johnson (BCJ) model, and implemented the UMAT for this model in ABAQUS.
- Developed a multiscale fracture model to apply the multiresolution continuum theory to formation and propagation of adiabatic submicro-, micro-, and macro-shear bands resulting from microstructure damage, growth, and coalescence, which eventually form submicro-, micro-, and macro-cracks in steel alloys.

Future Direction

- Compare the results from ABAQUS with Sysweld results.
- Perform an experimental study for spot welding, including investigating the effects of process parameters on the nugget size and residual stress. The experimental data will be used to validate the thermoelectrical and thermomechanical models.
- Use Gleeble simulator to simulate the welding process and obtain the material constants for BCJ model for low carbon steel AISI 1018.
- Integrate the thermoelectrical and thermomechanical models with UMAT (two phase BCJ model) to predict the stress-strain curve with different process parameters (current, pressure, and weld time).

Introduction

Resistance spot welding is a common joining process used in automotive manufacturing, with thousands of spot welds in a single vehicle. To realistically simulate the behavior of a vehicle under crash conditions, the mechanical behavior of spot welds under dynamic loading must be incorporated [1–2]. Currently, spot welds are simulated using general shell elements for each sheet of a spot-welded joint and a single bar element for each spot weld, which connects the two sheets of a joint at two nodal joints [3–4]. This approximation is very rough and causes an unreliable evaluation of the stiffness around the spot weld [5].

Other techniques [6] make use of a 3D nugget connected to the shell elements. But in this case a good approximation of the stresses is achieved only through a considerable refinement of the mesh next to the spot. As a result, this modeling procedure is not very practical when several spot welds are present. Knowledge of the stress field surrounding spot welds requires an accurate modeling of the entire structure. Salvini et al. [5] proposed a new finite element (FE) assembly to account for the structural behavior of the region surrounding a spot weld. The assembled elements, connected by a link, form the spot weld connection between two metal sheets. Zhang and

Taylor [7] proposed a so-called umbrella model to account for the radial stresses around a spot weld for stiffness analysis and fatigue prediction for different types of spot-welded structures. A recent review on the subject of different FE models of spot welds for various types of analysis has been published by Palmonella et al. [8].

A next generation spot weld element is needed in which details of the welding process and the metallurgy of the parent material are reflected. In this report, an FE model was developed to predict the process-property relations in the resistance spot welding, which will be implemented in the spot weld element formulation.

Mathematical Model with ABAQUS

Advantages of ABAQUS

To obtain more accurate predictions of the final mechanical properties of spot welds than those produced using SYSWELD, a similar FE model was developed using a commercial FE analysis package, ABAQUS. Using ABAQUS to simulate spot welding process has several key advantages.

- Allows for use of user-defined internal state variable (ISV) models to calculate residual stress and material phase distributions.
- Includes mechanical aspects of spot welding process (applied electrode force) through coupled thermomechanical analysis package—affects residual stresses and contact resistances.
- Allows for use of kinetically based calculations for phase transformation.

The BCJ ISV model is used to model the residual stress resulting from the mechanical loading of the workpieces and the thermal expansion due to heating and accounts for differences in mechanical response among phases present in material. The BCJ model includes the interface stresses, transformation induced plasticity that occur in multiphase materials, improving the accuracy of residual stress calculations. This model also predicts the change in phase volume fraction throughout the welding process using a physically based kinetic phase transformation model, a more accurate method than the empirically based approach adopted by SYSWELD. More accurate predictions of the residual stresses and phase distributions lead to more accurate predictions of mechanical properties for spot welds.

Model Structure

To model the complex coupling of thermal, electrical, mechanical, and metallurgical processes occurring in the spot welding process, the integration scheme shown in Figure 1 was developed to pass output data between the coupled thermomechanical and thermoelectrical packages already available in ABAQUS.

The steps laid out in Figure 1 represent all thermal, electrical, and mechanical aspects of the actual spot welding process, where the initial mechanical loading transmitted through the electrodes is represented by a purely mechanical analysis. The deformation resulting from this step is then passed into a thermal-electrical analysis, representing electrical loading of the weld assembly, where a current load is applied via the electrodes. The resulting temperature field generated by the heating is passed into a coupled thermal-mechanical analysis to capture the temperature-dependency of the deformation, after which the newly deformed geometry is passed back to the thermal-electrical analysis. The thermal-electrical and thermal-mechanical analyses proceed to update one another at small time steps ($\theta \sim 10^{-6}$ sec) until some specified total time is achieved. At this point the geometry and temperature field are exported to a final coupled thermal-mechanical analysis to calculate final values of temperature and geometry, as well as residual stress and phase distribution via the BCJ model. The final state of the spot weld is then made available through analysis of the final stress state of the weld, temperature distribution, phase distribution, and nugget size.

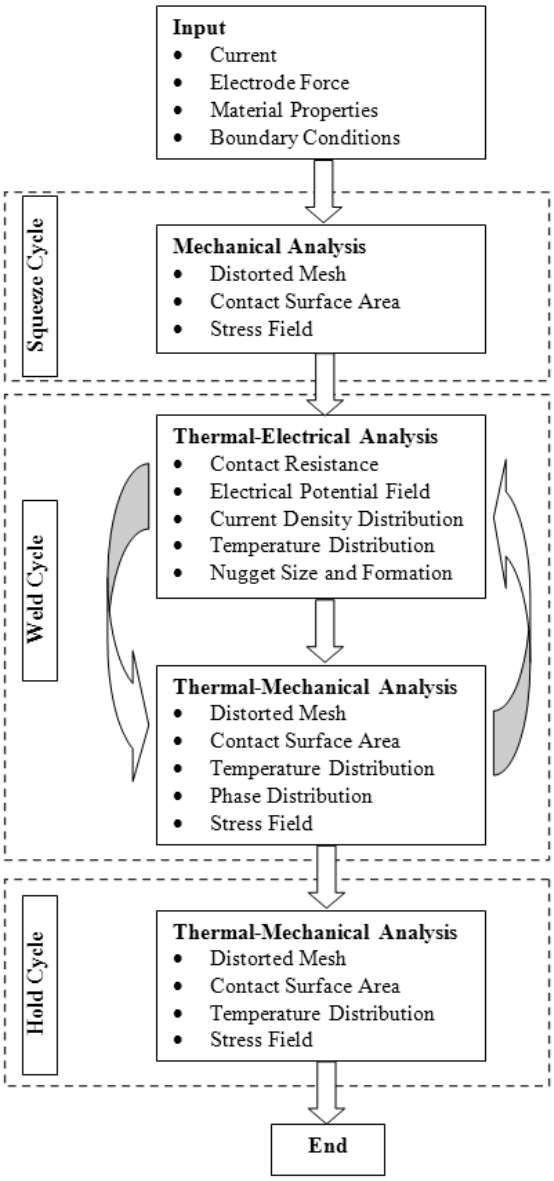

Figure 1. Integration scheme for ABAQUS spot welding procedure.

The nugget size and phase distribution may be validated experimentally through metallographic techniques and microindentation on test specimens made under different loading conditions. The accuracy of the final stress state in the weld may be tested by comparing simulated and experimental stress vs strain response for cases of tensile loading.

Temperature and Strain Rate Dependent Test Using Gleeble Thermomechanical Simulator

The goal of this test is to obtain material constants for a constitutive model (BCJ model developed by Doug Bammann) for steel alloys that contains phases such as martensite and austenite phases for AISI 1018 low carbon steel material. This BCJ model will be able to predict stress-strain relationships of steel alloys under high temperature processing conditions where phases are evolved with temperature and deformation.

Test Matrix

At least two strain rates (S1, S2) and two temperature settings (T1, T2) are required for tension, compression, and reverse loading tests for each phase. The tested coupon samples will be heated through a thermal cycle such that phases will be in solution and a single phase will be precipitated with control thermal cycles. Once the coupon sample is close to 100% of a particular phase, testing will be conducted to collect stress-strain–strain rate responses. The constitutive BCJ model will then be correlated with those responses measured from a Gleeble machine.

Multiscale Fracture Simulator

This work was performed by Wing Kam Liu, Rong Tian and Ted Belytschko (Northwestern University) and Leveraged by the Dynamic Microstructure Design Consortium (ONR Contract: N00014-05-C-0241), under a program titled Microstructure-Property Relations, Multiresolution continuum simulation and its Applications to damage, adiabatic shear band, and fracture failure.

In the past 12 months, the numerical simulation work focused on application of the multiresolution continuum theory to formation and propagation of adiabatic submicro-, micro- and macro-shear bands resulting from microstructure damage, growth, and coalescence, which eventually form submicro-, micro- and macro-cracks in a steel alloy. The multiresolution continuum theory has been extended to three dimensions, and a 3D parallel multiresolution code has been developed. Further improvement is needed.

In multiscale materials, permanent deformation is accompanied by energy dissipation at several distinct scales. This materials system also

undergoes inhomogeneous deformation at more than one length scale during damage initiation, growth, and final failure. Furthermore, during the extreme high strain rates, large strains, high temperatures, and high pressures dynamic loading of the microstructured materials system, thermal diffusion also affects the scale of the resulting nested adiabatic shear band (ASB) multiscale fracture.

This research seeks to develop a probabilistic microstructural continuum theory (PMCT) for the nested multiresolution ASB assisted fracture. The goal is to achieve fundamental understanding of the strength, toughness, damage initiation and progression, and multiscale failure of microstructural material systems under extreme loading conditions. In addition, the proposed PMCT can also be used in innovative materials design and fabrication of materials and structures that absorb energy, deflect penetrators, and/or laterally disperse momentum.

As shown in Figure 2, the proposed theory begins with a prototype material sample. We use advanced experimental and imaging techniques to create the digital data sets for material microstructure. The microstructure evolution can be mapped at multiple scales. A rigorous mechanical-science framework for multiscale modeling is being developed to predict macroscale properties accurately based on microstructure descriptions without resorting to empiricism. This framework is constructed based on a statistical inference theory where validation and model uncertainty quantification are done by combining both high fidelity stochastic simulations and limited physical experimental data.

For the first time, we have developed a multiresolution 3D simulation of the fracture process zone model with the aid of advanced experimental techniques that rapidly reconstruct the 3D microstructures and computational science as shown in Figure 3. Figure 3 depicts the macroscale and microscale experiments providing the crack opening displacement (COD) versus the applied load and the microsctructures within the multiscale fracture process zone. Using high performance computing, a 3D microstructure simulation reveals the microstructure evolutions

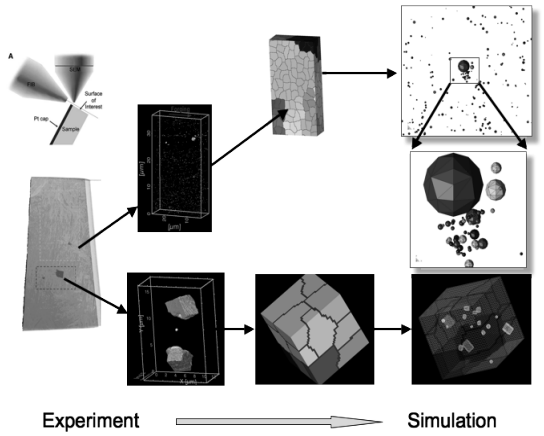

Figure 2. Focused ion beam/scanning electron microscopy experiments and imaging data to multiresolution analysis.

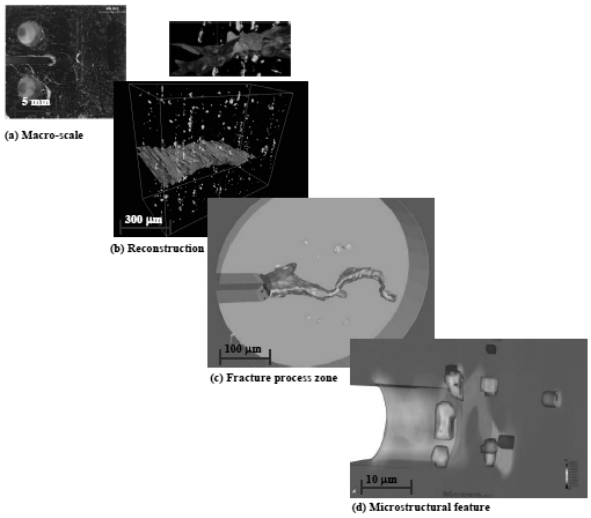

Figure 3. Three-dimensional microstructure reconstructions and simulations of fracture process zone. (a) and (b) show the crack tip specimen and microstructure reconstruction providing the microstructures within the fracture process zone and COD versus the applied load, respectively. Using high performance computing, a 3D microstructure simulation [(c), (d)] reveals clearly the microstructural features and interplay during the development of the fracture process zone and provides a deeper understanding of the effects of microstructures on materials properties.

and the effects of microstructures on materials properties. The combination of the 3D microstructure data sets and the 3D large-scale simulations provides a unique opportunity in developing a comprehensive understanding of

microstructure-property relationships to systematically design materials and structures with specific desired properties.

While materials science and experimental observation can heavily influence the model, it is ultimately mathematical theory that will unify these ideas. We envision that the science based mathematical foundation starts with linking spatial scales for continuous resolution of a microstructure. We aim to zoom into a microstructure in the same way that modern satellite technology allows us to zoom into images anywhere, anytime, and with any resolution. Hence, the separation of data by scales is done through the use of computer imaging and materials science knowledge. The quantification of nanostructured and microstructured data sets is performed through the use of statistical, complexity, and decision making theories, whereas the scale linking is done via testing and characterization of the data set samples.

To establish the validity of our models for these very heterogeneous microstructure evolutions subject to extreme environments, we are making comparisons with data on known materials subjected to mechanical, thermal, and chemical diffusion environments. We then use multiscale physics to design better multifunctional materials and use the above refined multiresolution data sets to develop a technique to extract the missing information that would otherwise remain hidden in the results of the carefully designed experiments. A good start is to link the missing science with existing single scale models by introducing microstructure fluxes, identifying microstructure transition events, and linking scales by introducing microstructure couple fluxes. In this context, models of random media can be efficiently used to derive an estimation of the macroscopic behavior of a physical system from the knowledge of the microscopic behaviors of its constituents.

Conclusions

Thermoelectrical and thermomechanical models were implemented in ABAQUS. The BCJ two-phase model was developed and implemented into ABAQUS as UMAT. The Gleeble simulator will be used to obtain the BCJ model constants. Spot welding experiments will be performed to validate the thermoelectrical and thermomechanical models.

Presentations/Publications/Patents

None.

References

1. S. D. Sheppard and M. Strange, “Fatigue Life Estimation in Resistance Spot Welds: Initiation and Early Growth Phase,” *Fatigue & Fracture Engineering Materials & Structures*, **15**(6), pp. 531–549 (1992).
2. X. Deng, W. Chen, and G. Shi, “Three-dimensional Finite Element Analysis of the Mechanical Behavior of Spot Welds,” *Finite Elements in Analysis and Design*, **35**, pp. 17–39 (2000).
3. S. Xu and X. Deng, “An Evaluation of Simplified Finite Element Models for Spot-welded Joints,” *Finite Elements in Analysis and Design*, **40**, pp. 1175–1194 (2004).
4. W. Chen and X. Deng, “Performance of Shell Elements in Modeling Spot-welded Joints,” *Finite Elements in Analysis and Design*, **35**, pp. 41–57 (2000).
5. P. Salvini, F. Vivio, and V. Vullo, “A Spot Weld Finite Element for Structural Modeling,” *International Journal of Fatigue*, **22**, pp. 645–656 (2000).
6. D. Radaj, “Local Fatigue Strength Characteristic Values for Spot Welded Joints,” *Engineering Fracture Mechanics*, **37**(1), pp. 245–250 (1990).
7. Y. Zhang and D. Taylor, “Optimization of Spot-welded Structures,” *Finite Elements in Analysis and Design*, **37**, pp. 1013–1022 (2001).
8. M. Palmonella et al., “Finite Element Models of Spot Welds in Structural Dynamics: Review and Updating,” *Computers and Structures*, **83**, pp. 648–661 (2005).

10. NONDESTRUCTIVE EVALUATION

A. Nondestructive Inspection of Adhesive Metal-Metal Bonds (NDE601*)

Principal Investigators: David G. Moore
Sandia National Laboratories
P.O. Box 5800, MS 0863
Albuquerque, NM 87185
(505) 844-7095; e-mail: dgmoore@sandia.gov

Dennis Roach
Sandia National Laboratories
P.O. Box 5800, MS 0615
Albuquerque, NM 87185
(505) 844-6078; e-mail dproach@sandia.gov

Ciji L. Nelson
Sandia National Laboratories
P.O. Box 5800, MS 0615
Albuquerque, NM 87185
(505) 843-8722; e-mail: cijnels@sandia.gov

Cameron J. Dasch
General Motors Research & Development
30500 Mound Road, Warren, MI 48090
(586) 986-0588; fax: (586) 986-3091; e-mail: cameron.j.dasch@gm.com

Technology Area Development Manager: Joseph A. Carpenter
(202) 586-1022; fax: (202) 586-1600; e-mail: joseph.carpenter@ee.doe.gov

Field Project Officer: Aaron D. Yocum
(304) 285-4852; fax: (304) 285-4403; e-mail: aaron.yocum@netl.doe.gov

---

Contractor: U.S. Automotive Materials Partnership (USAMP)
Contract No.: DE-FC26-02OR22910

Objective

- Identify and develop one or more nondestructive inspection (NDI) methods for adhesive bond evaluation to be used in an automotive manufacturing environment that would foster increased confidence and use in adhesive joining. The wider use of adhesive joining could result in reduced vehicle weight, increased body stiffness, and improved crashworthiness. Adhesives are also seen as a critical enabler for the joining of dissimilar materials in order to avoid corrosion from dissimilar metals.
  - To accomplish this goal, the various attributes that determine the bond strength must be identified along with an NDI method to measure that property. The success of this approach will be quantitative correlations of NDI to measured bond strengths.

* Denotes Project 601 of the Nondestructive Evaluation (NDE) Working Group of the United States Automotive Materials Partnership, one of the formal consortia of the United States Council for Automotive Research set up by Chrysler, Ford, and General Motors to conduct joint, precompetitive research and development (see www.uscar.org).

— The target methods must be able to perform the inspection on the plant floor in at least an off-line audit time window and be able to inspect most of the adhesive bonds on current production vehicles.

Approach

- There are five major attributes that contribute to the strength of an adhesive bond on a metal flange: the width of the adhesive area, the adhesive thickness, the location of the bead relative to the edges of the flange, the state of cure, and the quality of the adhesion. The general approach is to develop inspection techniques that can be used on the manufacturing floor which allow all the required adhesive characteristics to be measured nondestructively.
- The chosen methods must be single-side inspections that can follow a flange, navigate large changes in geometry, have spatial resolution near 1millimeter (mm) and have an overall inspection speed of at least 1 meter per minute (m/min).
- To accomplish this, there is a two step validation process: first, successfully inspect the flat adhesively bonded specimens, representative of automobile flanges. This includes comparison to measurements of the bond strength. Second, deploy the inspection method on production car bodies.
- The flat specimens vary in adhesive, adherent type and thickness, stackup (2–3 layers), cure state, and surface contaminants. These conditions bound the processing parameters for the adhesive assembly process. A through-transmission ultrasonic inspection is performed to characterize the flat specimens and is considered a "gold standard" reference inspection method. Selected samples are also peel tested to measure bond strengths.
- Multiple automotive bodies-in-white (BIW) containing many adhesive joints were produced by the Original Equipment Manufacturers (OEMs) to determine whether complex geometries significantly impede the inspection and to develop body-inspection strategies.

FY 2008 Accomplishments

- The team completed the evaluation of the first generation array and probe holder on three BIW structures. The BIW evaluations involved constructing inspection plans, inspecting over 100 beads with a wide variety of geometries and probe orientations, and generating evaluation reports. Over 80% of the adhesive structure could be imaged at a speed of over 1 m/min with this feasibility system. These images elucidate large scale features such as adhesive spread and the fill-factor of the flange. The 1 mm resolution also allows small features such as surface springback, air entrainment, bead dribbles, and weld expulsion damage to be imaged.
- The project team designed, built, and evaluated a second generation ultrasonic array and probe holder that is intended as a production prototype. This device is simpler and smaller than the first generation and should be able to inspect 95% of the BIW while imaging 85% of the area under the probe. The system works with a commercially available closed-loop water circulation system and should have a significantly reduced system cost
- A new signal processing effort was initiated to reliably extract the adhesive thickness from the ultrasonic array echo data. This analysis can rapidly compensate for probe to surface distance variations.
- The ability of ultrasonic inspection to accurately predict the bond strength was tested. On flat coupons, nondestructive measurements of the bond area and the bond thickness can predict the strength to within 10% over 90% of the adhesive bead. The primary shortcoming is that the scaling law presently underpredicts the bond strength at the beginning of the adhesive bead. This is the area where the peel crack is initiated.
- Reproducible procedures for constructing weak (kissing) bond samples using a wide variety of contaminates and controlled cures were established. Multiple sets (nine) of samples were produced with reduced shear strength. The strength ranges are from 10% to 100%. Two types of containments were added throughout the bond strength range. Over 150 strengths tests were completed to characterize the weak bonds. NDI evaluations using ultrasonic and other NDI methods are underway. The resulting images could be correlated to the subsequent strength measurements. Some initial promising results have been obtained from several methods but additional study is necessary before any conclusions can be made. This will be the focus of the activities in the last year of the project.

Future Direction

- In the final year of the project, the second generation ultrasonic array system will be deployed on BIW samples at Sandia National Laboratories and one U.S. Council for Automotive Research (USCAR) facility. This development effort is geared to improve inspectability and reliability, reduce overall system cost, and to reach a production-ready system. This will include a written procedure for probe deployment on automotive flanges,
- Ultrasonic signal analysis to determine reliably the bead thickness and quality of all adhesive/adherent interfaces will be pursued as funding allows.
- The final year will also complete the study of inspection methods to detect weak bonds. The technologies selected primarily include advanced ultrasonic technologies.
- Funding for fiscal year (FY) 2009 is an issue. The continuing resolution within the federal government will only allow quarterly step funding. Deliverables and timing have been modified to accommodate the budget.

Introduction

Adhesive bonding is an important joining tool for modern automotive structures. Structural adhesives can greatly increase the strength as well as stiffness of joints and can significantly improve the crash performance of vehicles. Structural adhesives also allow more efficient structures to be designed that may be difficult to weld. Structural adhesives will play an increasingly important role in the joining of dissimilar materials such as aluminum (Al) to steel or magnesium (Mg) to other metals: the adhesive acts both as a galvanic barrier and as a stress spreader on materials that are more brittle.

The NDE601 project is directed at filling a major technical gap for adhesives: how to determine whether an adhesive bond on a vehicle will perform as designed without actually destroying the bond, that is, how to nondestructively inspect the adhesive and assure that the bond has its designed strength. This year we completed verification of the wedge peel method as a new, high spatial resolution method that can quantify the variation of bond strength along long bond lines and with the presence of contaminants. In this period it was shown that ultrasonic measurements can accurately predict wedge peel strengths.

The major goal of the previous phase of this project was to select and develop an NDE method to inspect automotive flange joints when the adhesion was good. After evaluating several alternatives, ultrasonic pulse/echo inspection with a manually scanned linear array was targeted as a near term solution. A unique phased array probe system with a closed-loop circulation system was built by the team and successfully passed testing on over 150 flat coupons. Over 100 m of adhesive bonding were imaged.

This year the evaluation of this first generation ultrasonic array system was completed. In this round, the entire adhesive bonds on three production car bodies were subjected to inspection. This allowed issues of inspection plan organization, report generation, accessibility, ultrasonic coupling, operator skill, and operator ergonomics to be evaluated. The system performed quite well delivering high resolution images of the adhesive area, perhaps the most important element of needed inspection.

Based on the performance of the Gen 1 probe, a second ultrasonic probe system was designed specifically for automotive adhesive bond inspections. This is targeted as a production-intent system. This custom array and probe were built, assembled, and tested and shown to significantly improve accessibility and reduce system cost.

Extensive work was also completed on bonds that have intimate contacts but are weak: so called kissing bonds. Several new contaminates, in addition to grease, were shown to reproducibly reduce bond strength. It was shown that grease reduces both shear and tensile strength with the same sensitivity dependence and that grease contamination can be detected with ultrasonic pulse/echo inspection. A large suite of coupons

with reduced bond strengths were built for a round robin test of advanced inspection methods.

Mechanical Strength Characterization of Automotive Adhesive Joints

Ultimately, the selected NDI methods need to predict the failure loads of adhesively bonded joints. This project has both evaluated load measurement methods and tested bonds with varying bond width, thickness, and contamination. From this earlier work, a wedge-peel destructive test was selected as the method of choice. This method can handle wide variations in bond strength over short distances and can handle spot welds that are used along with adhesives (weld bonding).

The wedge-peel method uses an instrumented load frame to pull a standard wedge (ISO11343) through the adhesive bond as seen in Figure 1. The load vs. displacement curve can be compared with either an NDE image obtained before peeling such as ultrasonic through transmission or with the actual peel surface (see Figures 2 and 3 for examples). The ultrasonic through transmission has been our gold standard since it tests all the interfaces and the time-of-flight gives the location bond thickness.

Figure 1. Wedge peel fixture at USCAR

Simple adhesive strength laws based on bond width and thickness are adequate for predicting the wedge peel strength if the bond strength varies over multicentimeter length scales. Figure 2 shows a prediction of bond strength for a sample with

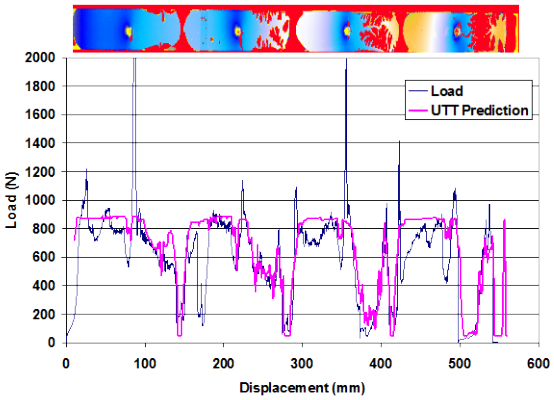

Figure 2. Adhesive wedge-peel strength compared with scaling law prediction based on UT-TT measurement of bond width and thickness (see image insert below).

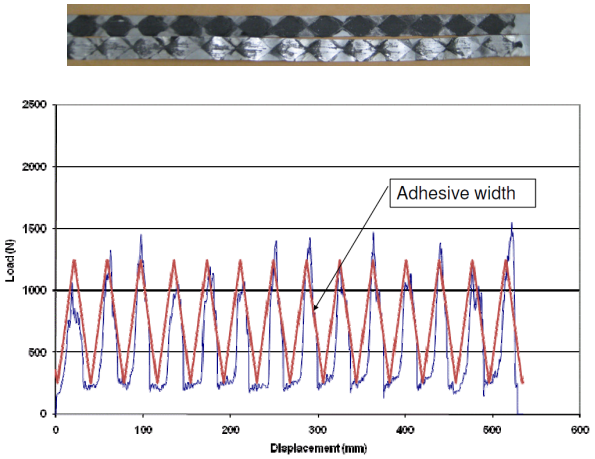

Figure 3. Adhesive wedge-peel strength for the diamond shaped bond pattern shown in the image insert. This demonstrates the effect of varying crack length when the failure load varies rapidly.

severe springback and large adhesive thickness variations.

The predicted strength is typically within 10% of measured over 90% of the bead length. The major errors occur at the spot welds and at the leading edge of the bond where the crack is initiated.

To test the limits of simple strength laws, additional samples with more rapid strength variation were made such as the diamond shaped adhesive bond in Figure 3. This shows more significant departures from the simple scaling law predictions. This is understood to arise from the crack length which varies throughout the test. This

moves the crack tip back and forth relative to the displacement location. These conditions will require a dynamical prediction of strength rather than a scaling law.

In previous work, it was shown that the bond shear strength of these automotive adhesives could be systematically reduced by a precisely applied grease layer. Oil- and grease-tolerance is a feature of automotive-grade adhesives that are required/designed to work directly on surfaces that are coated with mill oil. This year, the wedge-peel strengths of similar greasy bonds were measured. It was found that both the wedge peel strength (mostly Type 1 failure) and shear strength (mostly Type 2 failure) had the same relative dependence on the amount of grease contamination.

Ultrasonic Pulse/echo Technologies

After extensive testing in the first year of the project, ultrasonic pulse/echo using linear ultrasonic arrays was selected as the target inspection technology when there is good bonding. Linear array probes are comprised of many small piezoelectric elements, each of which are individually wired and can be controlled independently. A focused, ultrasonic beam is generated and electronically scanned along the array axis transverse to the bead and manually scanned along the bead. At each location, a short ultrasonic pulse is launched through the outer adherent and the train of echoes from the various adhesive-adherent interfaces is detected; variations of interface reflectivity and echo delay times are used to determine the joint condition.

While ultrasonic pulse/echo technologies have been available for many decades, only recently have they become portable and practical tools. Besides the earlier cost and complexity, the primary barriers for using this on the automotive plant floor have been the complex joint geometries and the thinness of the sheets (0.7 to 3 mm) that dictate high frequency transducers and cause difficulty in analyzing the ultrasonic echoes.

This year saw major milestones reached on the path towards implementing linear ultrasonic arrays as a production inspection technology. The evaluation of the Gen 1 ultrasonic phased array probe on three production car bodies was successfully completed. A second generation scanner, designed specifically for automotive flange inspections, was built and tested. Limited progress on signal processing was made. In addition, four different pulse/echo inspections have been applied to weak (kissing) bonds samples.

Deployment of the Gen 1 Linear Array Probe on Production Bodies

The four goals of the BIW assessment were: (1) create inspection plans for each BIW, i.e., record deployment information for each adhesive bead such as metal stackup, location, bead length, and probe orientation, (2) develop a manual scanning procedure that optimizes the beam coupling to the surface and maximizes the inspection area, (3) construct a matrix of features and rate the system performance, and (4) document the bead images along with images of the BIW.

Currently the system is configured in a C-scan mode using simple time gating in order to inspect the first adherent/adhesive interface. This provides a rapid, high resolution scan of the adhesive bead position and area. The system can scan at up to 1 meter per minute with 1mm resolution. This is more than enough to inspect 100 meters of adhesive in an off-line, two hour inspection window.

These inspections included two premium sedan BIW bodies with extensive adhesive bonding (20–30 m per vehicle) and a truck floor subsystem with embedded discrepancies. Over one hundred individual bead areas were imaged over the three bodies. Two examples are shown in Figure 4. This figure shows the rear passenger floor pan of a car along with the blue/white C-scan images of adhesive wet-out area. The variation of the bond width along the flange is readily seen, including the spread around each spot weld. Closer examination of the images show features such as surface springback, air entrainment, bead dribbles, and weld expulsion damage.

Figure 4. Floor section of the A-body showing the phased array scans positioned next to the imaged area.

Several flange configurations are present on the OEM BIWs including hem flanges. The specimens include mild steel bonded to Al and mild steel with several production adhesives. All adhesives are in an uncured state. The three bodies gave a good inventory of different flange designs currently in production and different flange orientations. Vertical flanges presented no special difficulties.

An inspection procedure was also developed that explains the operation and maintenance of the equipment.

Gen 2 Linear Array Ultrasonic Scanner

Based on the Gen 1 experience, a second linear array system (Gen 2) was designed and built. Figures 5 through 9 show the Gen 2 prototype probe and the water delivery system. This system is less than half as wide as the Gen 1 while having comparable inspection width and the same 1 mm resolution.

The linear array can be seen at the middle of the probe holder in Figure 5. This shows how the probe holder width has shrunk to the probe length; the blind area between the array and the probe holder envelope is dramatically reduced. The new probe is half as tall and 30% shorter than the Gen 1 probe. Figure 6 shows the probe being scanned along a flat coupon that is similar to an automotive flange that is weld bonded.

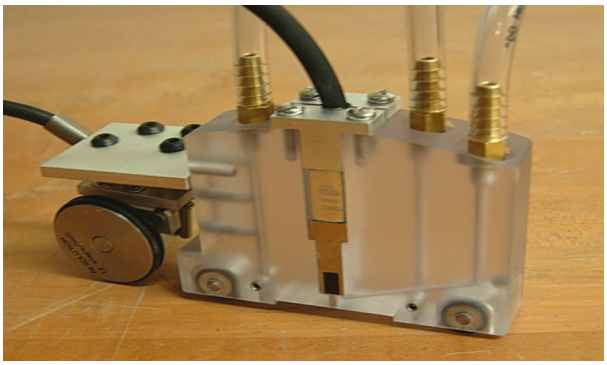

Figure 5. High frequency linear array embedded in a custom probe holder (Gen 2).

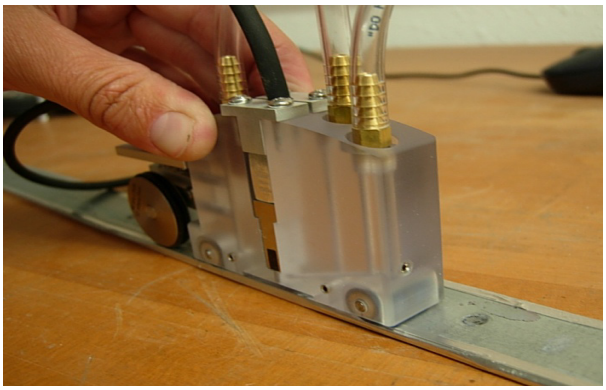

Figure 6. Linear array probe holder and encoder on a wide weld-bonded coupon.

This configuration of the probe uses a wheel encoder to measure the location of the probe along the bead. The encoder is spring mounted to more accurately follow the flange curvature. The encoder can also be raised so that the probe can be placed in narrow U-channels. In another configuration, the wheel encoder is removed and a string encoder is used.

The miniaturization of the probe (technical advance) will also allow flanges with smaller radii of curvature to be inspected. Figures 7 and 8 show BIW flanges being inspected.

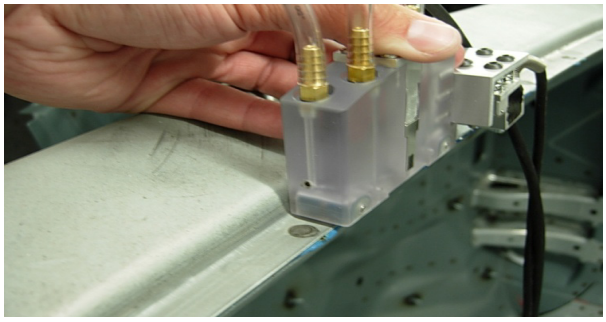

Figure 7. Linear array probe holder and encoder on BIW flange. Note: the probe now rests on a curved flange.

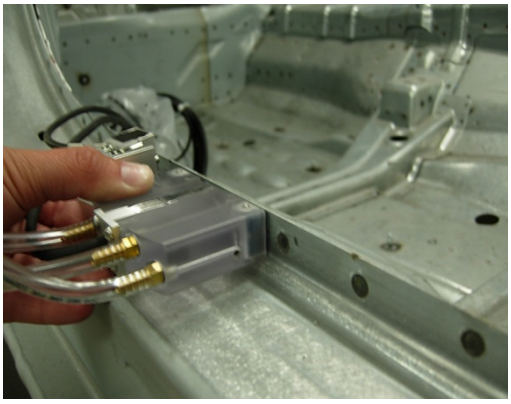

Figure 8. Linear array probe holder and encoder on BIW flange (side position).

The holder uses a closed-loop water circulation system to maintain a water column between the array and the flange surface. One angled inlet port supplies the water to the array while the two vertical ports vacuum excess water from the part (Figure 5 far right port is the water supply). The redesigned water column system is much simpler and allows a commercially available, closed loop water system to now be used (see Figure 9). It includes a filtered water supply, return pump, simple valve, and water aspirator. This water delivery system is in a self contained shipping case.

Figure 9. The closed-looped circulation system is commercially available.

The Gen 2 system performance was validated on flat test specimens. Again the system is configured in a C-scan mode using simple time gating to inspect the first adherence-adhesive interface. This system can scan at up to 5 meters per minute with 1 mm resolution. Ultrasonic images comparing performance from the Generation 1 and 2 probes are shown in Figure 10. The test sample selected was 1.5 mm aluminum weld bonded to 1.5 mm aluminum. The contrast, signal to noise, and sensitivity uniformity of the two array systems are comparable. The phased array resolution is comparable to an ultrasonic inspection using an immersion tank, i.e., about 1 mm.

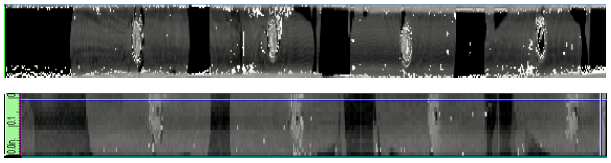

Figure 10. Ultrasonic image comparison between Generation 1 (top image) and Generation 2 (bottom image).

The next step will be to exercise the Gen 2 system on the large BIW samples especially on areas that were not inspectable by the Gen 1 system.

Preliminary Pulse/echo Signal Analysis

The short burst of high frequency sound waves travels through the material with some loss of energy and is reflected at any interface. The reflected echo signal is captured and analyzed to determine the presence and location of reflected interfaces. Variations in reflectivity or scattering can be used as the basis of flaw detection. Transit times of the echoes can be used to assess bond-line thickness.

Dr. Steve Neal, University of Missouri—Columbia, was placed under contract with Sandia National Laboratories. Dr. Neal has extensive knowledge in ultrasonic signal analysis and post processing techniques. His work in the area of correlation coefficients for ultrasonic detection has potential as a post processing technique for adhesive thickness measurements. This method was able to compensate for variations in the water column height over the sample scan in approximately 1 sec at PC analysis speeds.

Simulations of the echo train were used to evaluate different analysis strategies. These echo simulations were accurate for up to six reflections in the top sheet even for thin adherents (0.8 mm thick) with closely spaced echoes. However, Dr. Neal concluded that the reduced amplitude echoes from the adhesive-second sheet interface are too small to be extracted on stackups with sub-millimeter sheets and typical adhesive thicknesses with the current arrays and array controller. Dr. Neal's report is stored in the USCAR project archives.

Work on determining the limits of analysis on stackups with thicker sheets will be pursued depending on project funding.

Weak (Kissing) Bond Samples

A procedure to make weak bond samples reproducibly was developed at USCAR. This procedure has been transferred to Sandia National Laboratories for further development. This stage of work is devoted to testing the performance of advanced NDI methods that are reported to be sensitive to weak bonds, and to quantifying their ability to correlate with the reduced bond strength. This includes looking for small-scale variations in the bonded interface. The data analysis will look at subtle changes in the response and signal trends in order to link differences to bond quality parameters.

The adhesive manufacturing matrix of test coupons included three structural adhesives identified by the USCAR representatives. The test coupons were designed to be larger than the USCAR production flanges. The increased area is necessary to properly assess all advanced NDI methods. Six similar coupons were fabricated for each variable identified by USCAR. Three of these samples were pulled to assure the sample set bond strength and three will be used for NDI inspection assessments. Figure 11 displays the test coupon drawing and material specifications.

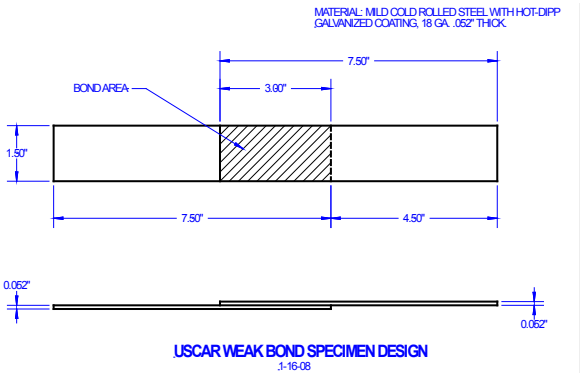

Figure 11. Test coupon for weak bond assessment. The contaminate is added to the bond line adhesive before curing takes place.

Conclusions

Steady progress was made on the project objectives during the second full year of funding. The first generation linear ultrasonic array tool for off-line inspections was successfully tested on production vehicles. While this ultrasonic array system is currently only able to inspect the wet-out on the outer skin, the system performance appears to be adequate to allow the adhesive mapping. The second generation version of this ultrasonic array scanner is now being built and is the final prototype development. It improves the performance on narrow flanges and on curved surfaces. The high resolution wedge-peel test has been established as a bond strength standard. Simple scaling laws allow NDI measurements of bond width and thickness to predict the bond

strength over a wide range of conditions. Finally, promising results were obtained from the USCAR transferred technology to Sandia National Laboratories to produce weak-bond samples.

Acknowledgements

This project team consisted of members from the automobile industries, federal research laboratories, and universities. The team members were: Ciji Nelson, Kirk Rackow, Steve Neil, Kim Lazarz, Dan Ondrus, Dave Biernat, Jessica Schroeder, John Fickes, Ray Bis, Mike Golden, Dave White, Rajat Agarwal, Bill Brown, Kent Wen and Marvin Klein. We also would like to thank IOS and Olympus NDT for their input and Mittal Steel and Novellis for supplying metal blanks.

References

1. *NDE601-FY2006 Annual Progress Report for DOE ALM*, Joseph DiMambro and Dennis P. Roach, Sandia National Laboratories and Cameron J. Dasch, General Motors Research & Development, December 15, 2006.
2. *Engineering Report on NDI of Adhesively Bonded Mild Steel Flat Coupons for USCAR/USAMP Project NDE 601—NDI of Adhesive Metal Bonds*, Cameron Dasch, Joe DiMambro, John Fickes, Jessica Schroeder, Jim Lazarz, Dan Ondrus, Dave Biernat, Raj Agarwal, Ray Bis, and Andy Terry, February 15, 2008.
3. *Draft Engineering Report on NDI of Adhesively Bonded Flat, Aluminum Coupons for USCAR /USAMP Project NDE 601—NDI of Adhesive Metal Bonds*, Cameron Dasch, Joe DiMambro, Ciji Nelson, John Fickes, Jessica Schroeder, Kim Lazarz, Dan Ondrus, Dave Biernat, Raj Agarwal, Ray Bis, Andy Terry, and Dave Sigler, August 14, 2008.
4. *NDE601-FY2007 Annual Progress Report for DOE ALM*, David G. Moore and Joseph DiMambro, Sandia National Laboratories; and Cameron J. Dasch, General Motors Research & Development, December 12, 2007.
5. *NDE601-FY2008 Mid-year Progress Report for DOE ALM*, David G. Moore and Ciji L. Nelson, Sandia National Laboratories; and Cameron J. Dasch, General Motors Research & Development, May 15, 2008.
6. *Final Report Phase 1: Developing Ultrasonic Signal Analysis Tools for Metal/Metal Adhesive Bonded Joints*, Steven Neal, September 15, 2008.

Presentation/Publications/Patents

1. Disclosure of Technical Advance Dated February 20, 2007, "*Probe Deployment Device for Optimal Ultrasonic Wave Transmission and Area Scan Inspections*," Joseph DiMambro, Dennis Roach, Kirk Rackow, and Ciji Nelson, Sandia National Laboratories, and Cameron Dasch, General Motor Corporation.
2. *Correlating Adhesive Bond Strength with Non-Destructive Test Methods*, K. Lazarz, C. Dasch, and R. Agarwal, presented at the Annual Meeting of the Adhesion Society, Austin TX, February 2008.
3. *Nondestructive Inspection of Adhesive Bonds in Automotive Metal/Metal Joints (NDE 601)*, C. J. Dasch, USAMP Off-site Review, October 29, 2008.
4. *Using Quantitative Ultrasonic NDE to Accurately Predict Adhesive Bond Strengths*, Cameron Dasch, Kim Lazarz, and Rajat Agarwal, Quantitative Nondestructive Evaluation Conference, Chicago, IL, July 2008.

B. Laser Ultrasonic Inspection of Adhesive Bonds Used in Automotive Body Assembly

Principal Investigator: Marvin Klein
Intelligent Optical Systems
2520 West 237th Street
Torrance, CA 90505
(424) 263-6361; fax: (310) 530-7417; e-mail: mklein@intopsys.com

Technology Area Development Manager: Joseph A. Carpenter
(202) 586-1022; fax: (202) 586-1600; e-mail: joseph.carpenter@ee.doe.gov

---

Contractor: Intelligent Optical Systems
Contract No.: DE-FG02-06ER84545

Objective

- Adhesive bonding is widely used in automotive production, especially for body assembly. It is critical to be able to measure the strength of adhesive bonds during manufacture in a nondestructive, effective and rapid manner. There are no current means for inspecting these bonds in real time. The specific inspection requirement is to: (1) map the adhesive spread, (2) measure the thickness over the full area, and (3) measure the bond strength. All inspections must be performed from one side and must be able to function on contoured surfaces with ~1 mm resolution. The ideal tool must be able to perform the above measurements simultaneously (i.e., in one pass across the bond). In this project we have applied the technique of laser ultrasonics to the adhesive-inspection requirements described above. The specific goals of this project are to determine the best inspection configuration and signal-processing approach, followed by the development and demonstration of a prototype inspection system.

Approach

- The technology which we will apply to this inspection requirement is laser ultrasonics, in which a pulsed laser beam is directed to the surface to generate ultrasonic waves in the sample, and a continuous-wave laser receiver is used to detect the waves after they interrogate the required sub-surface feature and return to the surface. Laser-based ultrasonic inspection has a number of benefits over transducer-based ultrasonic inspection, including: (1) lack of physical contact with the workpiece; (2) high spatial resolution obtained using focused laser beams; (3) high scan rate associated with rapid beam scanning; and (4) high bandwidth, thereby improving the measurement accuracy.
- This project is closely coordinated with Sandia National Laboratories' phased-array project, "Nondestructive Inspection of Adhesive Metal/Metal Bonds," funded by the Department of Energy (DOE). The United States Council for Automotive Research (USCAR) Nondestructive Evaluation (NDE) Working Group acts as an advisory group. The fore mentioned project has produced a large number of adhesive-bonded specimens. The flat specimens vary in adhesive, adherent type and thickness, stackup (2–3 layers), cure state, and surface contaminants. These conditions bound the processing parameters for the adhesive assembly process. These specimens have been used to optimize the beam configuration and signal-processing techniques. The remaining portion of our project is devoted to the development and demonstration of a prototype scanning inspection system that can be scaled to a measurement speed of 1 meter/minute.

Accomplishments

- In 2008, we completed months 4–15 of a 24-month Small Business Innovation Research (SBIR) Phase II project that started in 2007. During the course of this effort, we tested a number of steel and aluminum specimens prepared for the Sandia project, thus improving our ability to determine the configuration of both

laser beams (separation, size, shape, energy) that provides the best signal-to-noise. We have identified an algorithm for processing the raw signals to provide accurate mapping of the adhesive spread. Finally, we have engineered a measurement head that is based on the required beam configuration and that is intended to be integrated into a robot-based prototype inspection system.

Future Directions

- In 2009 we will complete the software and hardware development required for assembly and testing of the prototype inspection system. This system will be demonstrated for interested parties.

Introduction

Adhesive bonding is widely used in automotive production, especially for body assembly. The most common use is the lap joining of two or three sheet-metal panels. Adhesive bonding adds strength, and thus allows the use of lighter components at equal performance. Adhesive bonding allows the joining of dissimilar materials such as aluminum (Al) and steel. Modern adhesives (especially epoxy resins) have excellent fatigue and thermal shock resistance, and less critical design tolerances because of their gap-filling capabilities. Their service range extends from space environments to high temperatures. It is critical to be able to measure the strength of these bonds during manufacture in a nondestructive, effective, and rapid manner.

The most important manufacturing issues that can influence the strength of an adhesive bond are the maintenance of the proper fit-up and proper surface preparation. While adhesive bonds are tolerant of some range of gap between the panels, if the gap is too large, the adhesive will not cover the required area, and the intrinsic strength of the adhesive itself is reduced. If surface contamination (e.g., oil, grease, surface oxides, corrosion, and water infiltration) is present, the bond adhesion will be reduced. In the limit of very low adhesion, weak bonds may have intimate contact, but little or no bond strength ("kissing").

The corresponding requirements for nondestructive evaluation of adhesive bonds fall into three areas: (1) mapping of the adhesive coverage, (2) measurement of adhesive thickness, and (3) measurement of the adhesion of each metal/adhesive bond.

All inspections must be performed from one side and must be able to function on contoured surfaces. The ideal tool must be able to perform the above measurements simul-taneously (i.e., in one pass across the bond).

At the current time, nondestructive inspection is not performed during the bonding process. The only quality control techniques now implemented are careful process control, machine-vision inspection of the adhesive bead before joining, and selective destructive evaluation. A nondestructive technique for in-line measurement of adhesive integrity would reduce scrap and warranty costs, and thus allow wider use of adhesive joining.

Laser ultrasonics offer an attractive approach for nondestructive evaluation over a broad range of applications. The full complement of ultrasonic waves (longitudinal, shear, Lamb, and Rayleigh) can be produced with known directionality. The pulses are high in bandwidth, thereby providing the high depth resolution required for thin sheets and bonds. The spot sizes on the part can be much less than 1 mm in diameter, thereby providing high spatial resolution.

The objective of this project is to develop a real-time system for inspection of adhesive panels during auto body assembly (see Figure1). This system will incorporate a fiber-delivered robotic measurement head containing a scanning mirror that will be able to scan narrow sections of adhesive very rapidly.

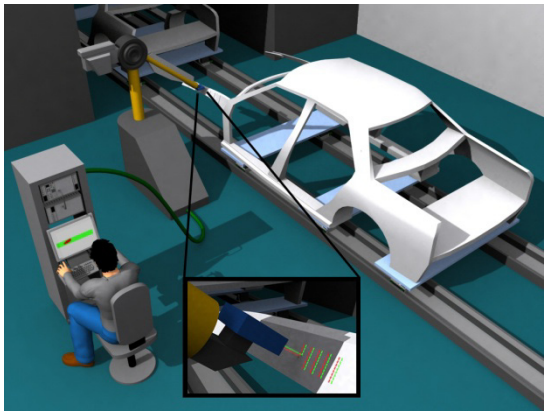

Figure 1. Depiction of robot-driven inspection system performing a two-dimensional scan of an adhesive-bonded auto body panel.

Samples Provided

General Motors and the project carried out at Sandia National Laboratory were kind enough to provide a number of samples for testing in 2007. The samples consisted of a two sheet stackup with three adhesive joints distributed along the length of the samples, each joint having a spot weld near the center. A number of plate thicknesses and adhesives were included among the samples. In 2007, we were able to obtain clear scans of these samples in the through transmission configuration that provided mapping and thickness measurement with good accuracy.

In 2008, we continued to use these samples for the continued development of the pulse echo configuration, and for software development. We also received samples with varying bond strength from Sandia that were prepared for their project. There were 10 samples with bond strength that varied from 11% to 88%. The goal in this case was to develop a measurement technique and algorithm that could measure the bond strength.

Samples Scans

A typical map or C-scans of a portion of Sample A3 obtained in through-transmission is shown in Figure 2. This amplitude map clearly captures the adhesive spatial coverage with sharp edge definition, limited only by the 1 mm step size.

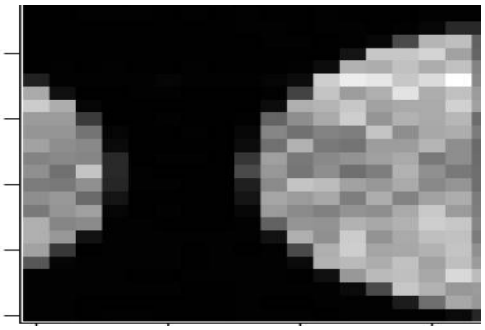

Figure 2. Through transmission zoom image of a portion of Sample A3. Step size = 1 mm.

All subsequent measurements were performed with both beams on the same side (pitch-catch configuration) and spaced 1–2 mm apart. In this configuration, multiple echoes are expected from both the A and B interfaces (with A being the adhesive interface closest to the measurement head, and B being the adhesive interface furthest away from the measurement head). The value of the reflectivity at these interfaces is dependent on the impedance values of each material. Specifically, the reflectivity of a steel/adhesive interface (~0.9 in amplitude) is smaller than that of a steel/air interface (very close to 1.0). This difference is not large, but it is sufficient to yield a measurable difference in the amplitude of the reflected waves from the A-interface.

In pulse-echo we obtained C-scans by windowing on a late-arriving echo in order to take advantage of multiple reflections from the A interface and thus amplify the expected amplitude difference. A typical pulse echo C-scan of a portion of sample A3 is shown in Figure 3.

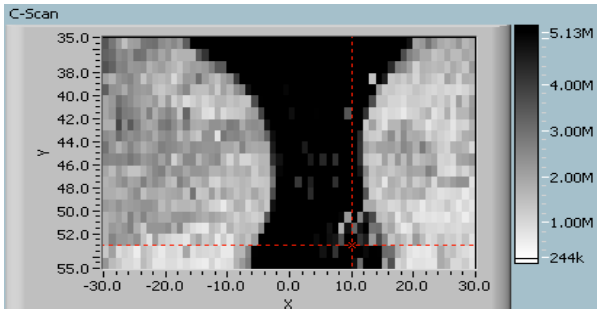

Figure 3. Pulse echo zoom image of a portion of Sample A3. Step size = 1 mm.

We have also obtained data on aluminum Sample K26. Typical A-, B- and C-scans are shown in Figures 4 to 6. In the A-scan, the back wall echoes in a region without adhesive are strong. The cursors shown in this figure identify the time gate used for the C-scan of Figure 6.

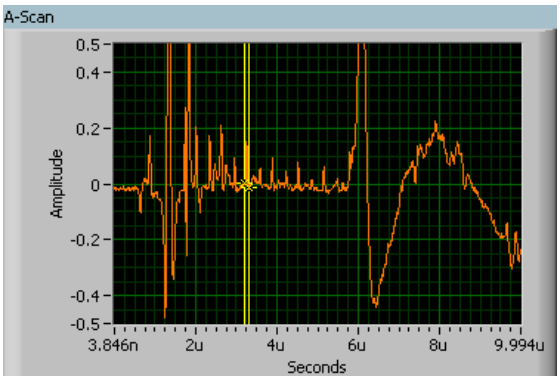

Figure 4. Typical A-scan on Sample K26.

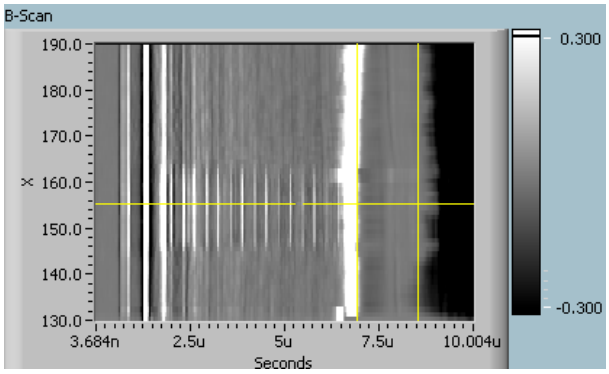

Figure 5. Typical B-scan on Sample K26.

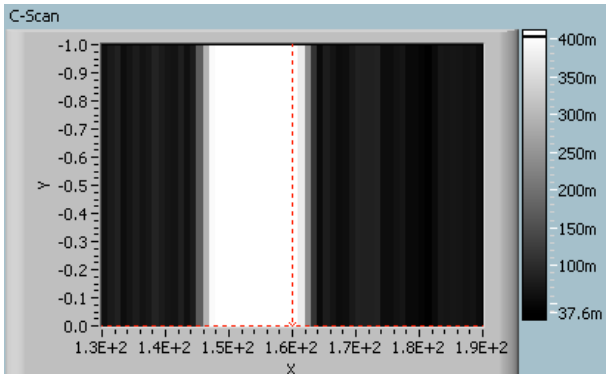

Figure 6. Typical 1D C-scan on Sample K26, based on the amplitude in the window defined in Figure 4.

The B-scan shows the dramatic difference in signals between the adhesive at low values and high values of X, and the gap near X = 150–160. It is clear that the aluminum and adhesive are nearly impedance matched, so the A-interface echoes are very weak. The C-scan of Figure 6 was taken in only one direction, and is based on the amplitude of the signal in the cursor-defined window shown in Figure 4. Note the large contrast that results from the strong differences in the signals shown in the B-scan of Figure 5.

Signal Processing Development

We have made good progress in mapping the adhesive spread. In order to map the adhesive thickness, it is important to clearly identify and measure the echoes from within the adhesive. We are developing an approach that involves enhancing of the B-scan features using line-finding techniques applied to the images.

The line-finding approach is illustrated in Figure 7. The raw B-scan image is processed by a MATLAB based algorithm that identifies lines and tracks them.

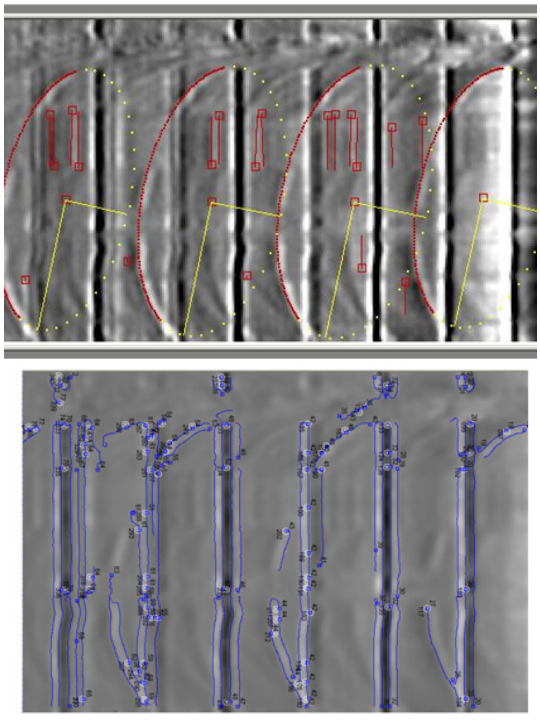

Figure 7. Line-finding technique applied to two adhesive B-scans taken on the same sample.

The straight lines represent echoes in the top sheet and the curved lines represent echoes in the adhesive. Both are easily identified. Once the echoes are identified, a separate algorithm can find arrival time of the adhesive echoes in order to determine the adhesive thickness.

Measurement Head Development

As a result of the testing we performed, we have redesigned and simplified the measurement head. In the prior design, the generation beam consisted of five separate beams derived from a single pulsed laser and delivered through a fiber bundle. Our testing determined that the beam separation and delivery system was subject to optical damage. In the new design, an off-the-shelf pulsed laser with a fiber pigtail is being used, with a single 1 mm core fiber delivering the generation beam to the measurement head. The detection and signal beams are now routed from a single optical module that is self-aligning. The new head is much simpler and less prone to optical damage than the previous one.

Conclusions

In 2008, good progress was made on the overall project objectives.

We have successfully applied laser ultrasonics to the requirement for evaluating adhesive bonds used in auto body assembly. Techniques have been developed to map the adhesive spread and measure the thickness. The signal processing efforts have indicated a pathway for processing the raw data in real time. We have designed prototype scanning hardware that will be robot-mounted for automated measurements. Continued work in 2009 will be required to refine the signal processing and complete the development of a prototype.

Presentations/Publications/Patents

1. Marvin Klein and Homayoon Ansari, “Laser Ultrasonic Inspection of Adhesives Used in Auto Body Manufacture,” *First International Conference on Laser Ultrasonics,* Montreal, Canada, July 16–18, 2008.
2. Marvin Klein and Homayoon Ansari, “Laser Ultrasonic Inspection of Adhesives Used in Auto Body Manufacture,” *ASNT Topical Conference on Automotive Industry Advancements with NDT,* Greenville, SC, May 11–12, 2009.

C. Online Nondestructive Weld Quality Monitor and Control with Infrared Thermography

Principal Investigator: Zhili Feng
Oak Ridge National Laboratory
P.O. Box 2008, Oak Ridge, TN 37831-6095
(865) 576-3797; fax: (865) 574-4928; e-mail: fengz@ornl.gov

Principal Investigator: Hsin Wang
Oak Ridge National Laboratory
P.O. Box 2008, Oak Ridge, TN 37831-6064
(865) 576-5074; fax: (865) 574-3940; e-mail: wangh2@ornl.gov

Technology Area Development Manager: Joseph A. Carpenter
(202) 586-1022; fax: (202) 586-1600; e-mail: joseph.carpenter@ee.doe.gov

Field Technical Monitor: C. David Warren
(865) 574-9693; fax: (865) 574-6098; e-mail: warrencd@ornl.gov

---

Contractor: Oak Ridge National Laboratory (ORNL)
Contract No.: DE-AC05-00OR22725

Objective

- Develop an infrared- (IR-) thermography-based weld-quality detection technology capable of reliable and cost-effective online nondestructive monitoring and feedback control of welding assembly operations in high volume auto production environment.
    - — Phase I: Demonstrate the technical merit and potential of the IR-based weld-quality monitoring technology for resistance spot welds (RSWs).
    - — Phase II: Conduct a field demonstration of a prototype system for real-time welding operation monitoring and online weld-quality evaluation, including technology transfer and dissemination for future commercialization.

Approach

- Produce welds with different levels of quality and geometry attributes.
- Catalog and quantify weld-quality attributes by means of destructive characterization.
- Develop quantitative correlation between various weld-quality attributes and their characteristic IR thermal signature through combined welding heat-flow simulation and laboratory IR experiments.
- Develop field-deployable IR measurement techniques for cost-effective detection of the characteristic thermal-signature patterns during welding operations (real-time) and/or in online postmortem inspections.
- Develop efficient IR data analysis algorithms for thermal-signature recognition.
- Integrate the field-deployable IR measurement system and the data analysis algorithm to develop a prototype IR weld-quality monitor and control expert system for field demonstration.

Accomplishments

- Identified and ranked weld-quality attributes in RSWs for IR-based inspection through industry survey.
- Produced and characterized an initial set of controlled RSWs with various types and levels of quality attributes.
- Completed a comparative study on various heating and cooling approaches for IR-thermography measurement for postmortem online inspection.
- Performed initial computer simulation of heat-flow pattern in RSWs with varying weld-quality attributes to identify most effective experiment set-up for IR measurement.

Future Direction

- Phase I:
  - — Complete the evaluation and "down-select" the heating/cooling method for postmortem IR thermography.
  - — Complete feasibility evaluation of real-time IR thermography.
  - — Complete computational simulation and establish the theoretical basis for IR-inspection sensitivity.
- Phase II:
  - — Determine the sensitivity of IR signals obtained in real time to the weld-quality and production environment.
  - — Develop the IR thermal-signature recognition algorithms of the expert system for postmortem inspection.
  - — Expand to wide range of weld and materials combinations.

Introduction

Welding is an essential technology used in auto-body structure assembly. Variations in welding conditions, materials, part dimensions, and other production conditions inevitably occur in the high-volume and highly complex auto-body assembling process, resulting in variations of weld quality and "out-of-tolerance" situations which impair the quality and performance of the vehicles. Despite extensive research and development (R&D) efforts over the years, nondestructive weld-quality inspection remains a critical need in the auto industry, largely due to the unique technological and economical constraints of the auto production environment—any weld-quality inspection technique must be fast, cost-effective, low in false rejection rate, and nonintrusive (i.e., not interfere with the highly automated welding fabrication process).

The goal of this project is the development of a prototype, field-deployable, online weld-quality monitoring system based on state-of-the-art IR thermography. IR thermography detects surface temperature changes due to geometric discontinuity or inhomogeneity. A distinct advantage of IR thermography as a nondestructive evaluation (NDE) tool is its nonintrusive and noncontact nature, making it especially attractive in high-volume production environments. IR for weld-quality inspection in the auto-assembly environment has been explored in the past, mostly postmortem. The development so far has been unsuitable for implementation in the mass-production environment of the auto industry.

Working with industrial partners, we recently demonstrated several novel concepts and approaches that would overcome some of the key technical barriers inhibiting the use of IR thermography as an effective weld NDE tool in auto assembly lines. A unique advantage of the ORNL approach is the potential for real-time weld-quality detection as the weld is being produced. This would offer the opportunity of real-time welding process feedback for in-process adjustment and control.

This project builds upon our recent work, and consists of a two-phase, gated R&D effort to further advance the IR-thermography-based weld-quality monitoring and control technology to a stage that can be deployed in high-volume auto production environments. The first phase is a 12-month Concept Feasibility study. Started in

May 2008, Phase I focuses on further improving ORNL's IR thermography approach, establishing the scientific basis, and demonstrating the ability to detect various types of defects (lack of bonding, cold weld, porosity) and determining the critical weld-quality attributes (weld size and indentation) in RSWs produced under the welding practices used by the industry.

At the end of first phase (Gate 1), decisions will be made with respect to the technical merit, the effectiveness, and the potentials of the IR-based weld-quality monitoring and control methodology. If warranted, more comprehensive R&D will be performed in the second phase (Technical Feasibility) study, leading toward eventual field demonstration of the technology. The second phase will also include identifying and partnering with potential technology transfer and commercialization entities.

The R&D in Phase I has been primarily carried out at ORNL, with support from the industry collaborators. An industry technical advisory committee has been formed for this project, consisting of representatives from Chrysler, Ford, General Motors, and ArcelorMittal.

Based on the recommendations of the industry advisory committee, Phase I includes exploratory studies on both real-time and postmortem IR thermography to determine the feasibility of the two different approaches for weld-quality inspection. The real-time approach detects the weld quality as a weld is being made by detecting the changes in temperature patterns during welding, whereas the postmortem approach applies an external heat source after a weld is made such that the inspection is performed as a separate step after welding. Both approaches can be implemented for online inspection. According to the industry advisory committee, the two different approaches address different application needs.

From May to September 2008, Phase I focused on the following tasks:

- producing the initial set of controlled RSWs with various types and levels of weld-quality and defect attributes,
- comparatively studying various heating and cooling approaches for IR-thermography measurement, and
- producing the initial computer simulations of heat-flow patterns during IR-thermography measurement.

RSW Samples for IR Thermography

An initial set of RSW samples has been produced for use in the postmortem IR-thermography study. This set of samples was designed to cover the range of weld defects and quality attributes that are commonly encountered by the industry and are known to influence the structural performance of the spot welds in auto-body structures. These attributes are listed below, in the order of decreasing importance according to the industry advisory committee:

- weld with no or minimal fusion,
- cold or stuck weld,
- weld nugget size,
- weld expulsion/indentation,
- weld porosity, and
- weld cracks.

To ensure consistency in producing different levels of weld defects and quality attributes, all welds were made at the welding laboratory of ArcelorMittal's R&D center, according to the specifications of the project. ArcelorMittal, a primary steel supplier to the automotive industry, has extensive experience in welding procedure development and qualification for applications of advanced high-strength steels in automotive body structures.

All welds were made on hot-dipped galvanized DP 590 steel of 1.85 mm nominal thickness, in the common two-stack configuration. For each welding condition, a total of six replicate welds were made. Two of the six replicates were sectioned destructively to determine the weld nugget size and type and degree of weld defects. The other four welds of the same set were used in IR-thermography measurements. In addition, extensive IR measurements were also conducted on one of the sectioned welds before it was sectioned.

Representative weld cross sections are provided in Figure 1 through Figure 5.

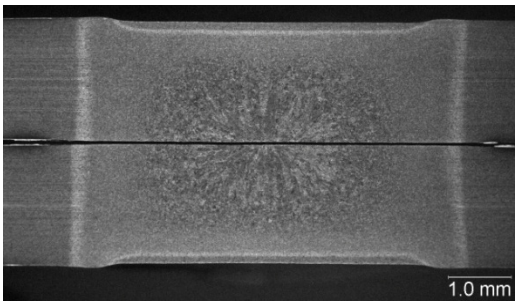

Figure 1. Cross-sectional view of a stuck weld with very small fused weld nugget.

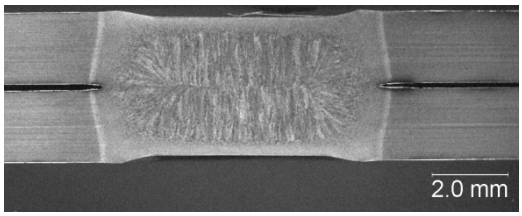

Figure 2. Cross-sectional view of a weld with acceptable weld nugget size and no defect.

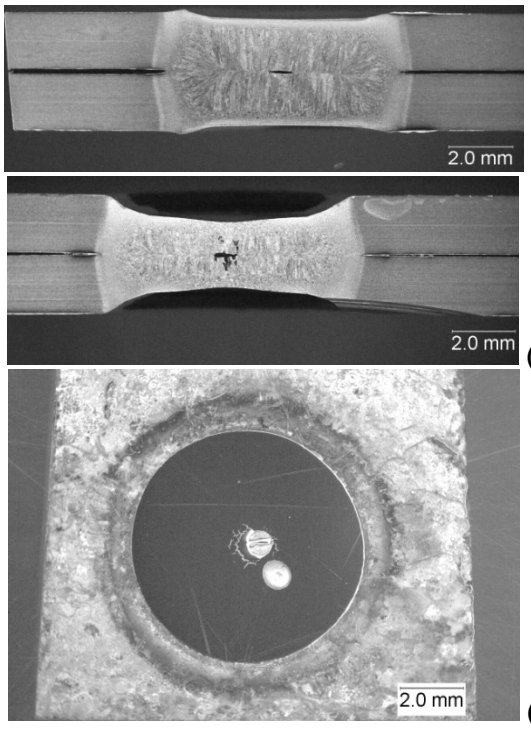

Figure 3. Welds with solidification shrinkage voids as revealed in cross-sectional view, (a) and (b), and by machining off one of the steel sheets (c).

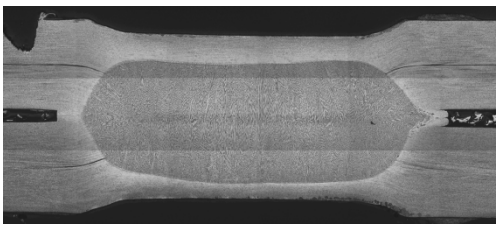

Figure 4. Cross-sectional view of a weld with expulsion.

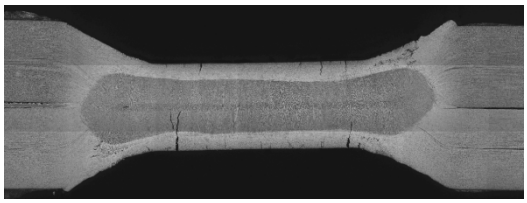

Figure 5. Cross-sectional view of a weld with expulsion, cracking, and surface indentation.

Table 1 summarizes the welds made for different weld defects and quality attributes. Each set of welds is characterized by its weld nugget size, surface indentation, and type and/or extent of defects. The weld nugget represents the fused region of the weld, and its diameter was determined under optical microscope from both the cross-section samples and the samples with one of the sheet steels carefully removed by machining and polishing to the faying surface of the weld.

Table 1. Weld samples with different weld-quality attributes for postmortem IR measurement.

Condition	Weld IDs	Weld Nugget (mm)	Void Dia (mm)	Indent (mm)	Est. Brassing	Cracking
Stuck Weld	34-39	0	None	0.06	None	None
Undersized weld	53-58	4.15	None	0.17	None	None
Minimum weld	65-70	5.8	None	0.21	None	None
Maximum weld	99-104	6.3	None	0.24	None	None
Void A	93-98	6.2	0.7	0.32	None	None
Void B	87-92	6.3	1.4	0.27	None	None
Indent/ crack	117-122	7.4	None	0.62	None	None
Indent/ crack	124-129	6.6	None	1.84	None	None
Indent/ crack	131-136	6.6	None	1.04	Light	Yes
Indent/ crack	138-143	7.9	None	1.72	heavy	Yes

Evaluation of Heating/Cooling Methods for Postmortem Inspection

In postmortem IR inspection, an external heating source is applied to induce transient temperature changes in the weld and its surrounding area. For the same effect, a cooling source can also be used. An IR-thermography camera is strategically placed near the weld to detect the characteristic temperature changes and relate the changes of weld quality. The measurement principle is illustrated in Figure 6. The type of the external heating or cooling sources and the way they are applied will influence the heat flow in the weld and thereby the sensitivity and accuracy of weld defect and quality attribute detection.

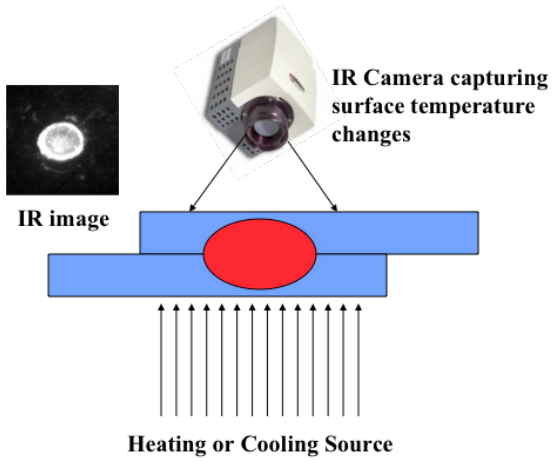

Figure 6. IR weld-quality inspection principle (postmortem approach).

In this task, different heating and cooling methods were evaluated for their suitability for postmortem IR inspection. The method of choice should be capable of generating a noticeable temperature change (10 to 20°C) and subject to easy and quick manipulation of the duration of heating or cooling (from subsecond to several seconds). Factors related to suitability in the auto-body assembly environment such as cost, reliability, and automation must also be considered in selecting the heating/cooling method.

Several methods were evaluated in this task. They included two heating methods (a xenon flash lamp and a hot-air gun) and three cooling methods (ice cubes, a cold-air gun, and a commercial gas duster).

Xenon Flash Lamp. The flash lamp had adjustable controls for the heating duration and power, resulting in relatively consistent tests among samples. With a high power and duration of around 8 milliseconds (ms), the flash was treated as a pulse function.

Ice Cubes. Ice cubes had unique advantages over most of the other methods. Because ice is always at a constant 0°C when melting, the temperature at the contact point can always be assumed to be consistent. Also, since the ice melts on contact, the liquid layer creates a very conductive area through which heat can be transferred, resulting in the surface temperature condition of 0°C during the test. However, the presence of liquid water during the test and the physical contact between the cooling media (ice tube) with the workpiece are two major drawbacks of this technique.

Cold-Air Gun. A Vortex Tube, which is a device that causes compressed air to separate into hot and cold regions, was used to generate the cold air. Hot air is expelled through a radiator, while cold air is blown out a nozzle. The air from the nozzle was approximately 8°C but could be varied slightly by varying the pressure of the compressed air used.

Hot-Air Gun. An industrial strength hot-air gun, similar to a personal hair dryer only capable of much higher temperatures, was used to generate the hot air. The heat gun did not allow for precise temperature control; however, it was capable of producing the largest temperature difference of all the methods tested, around 200°C.

Gas Duster. The final cooling method tested was a gas duster (Figure 7). Most commercial gas dusters are filled with a volatile liquid such as difloroethane, which has a boiling point of −25°C. When turned upside down, the canister nozzle releases the chemical in liquid form, which quickly evaporates at room temperature. This method exhibited the advantage of greatest controllable temperature difference created, allowing for relatively large distinctions between spot welds.

It is a common practice in IR thermography to treat the measurement surface with chemicals or

Figure 7. Commercial gas duster. When used upright, gas is expelled through the nozzle to clean dust from keyboards and electronics. When turned upside down, liquid difloroethane is expelled.

paints to provide better contrast or clarity for the IR images. Because such treatments or coatings of spot-weld surfaces are prohibited on automotive production lines due to the cost and production rate concerns, surface treatments were purposely avoided in our experiment. Instead, the IR images were digitally enhanced during image analysis.

Temperature change was measured using an IR camera with a capturing rate at either 60 Hz or 20 Hz, depending on the length of time and method used. Using the series of images and computer software, the change in IR image signal intensity measured over time was plotted and compared for welds with different quality attributes. Examples of the characteristic heating/cooling curves obtained by different heating/cooling methods are given in Figure 8 and Figure 9. In these figures, the IR signal intensity was normalized with respect to the baseline IR intensity before applying the external heating/cooling source to the weld region. The normalization made it possible to differentiate the thermal-signature patterns associated with different levels of weld defects and quality.

Figure 8 compares the surface temperature changes (as represented by the intensity of IR measurement) of different welds using the gas duster as the cooling medium. It is evident that

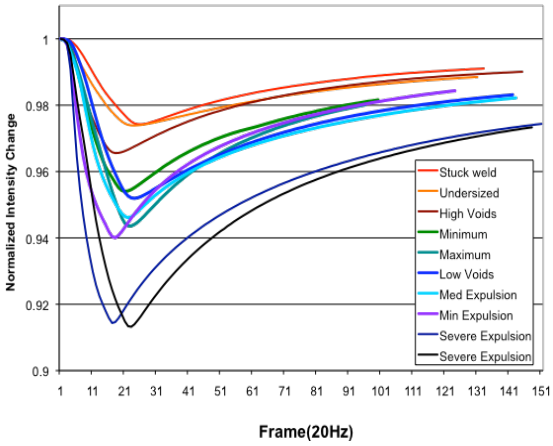

Figure 8. Intensity curves of controlled welds with different weld-quality attributes generated using the gas duster cooling method.

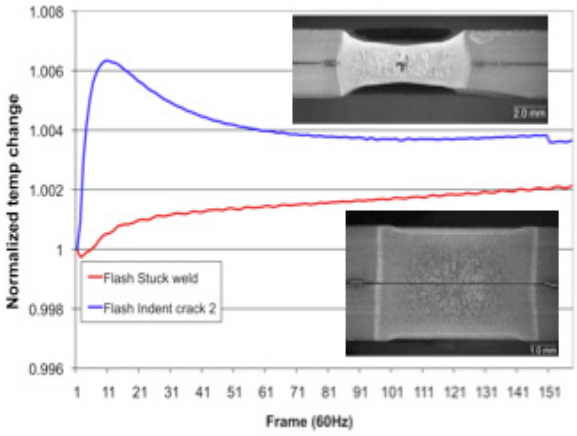

Figure 9. Intensity curves of a stuck weld and a cracked weld with heavy indentation as measured with xenon flash lamp heating method.

welds with different defects and geometry attributes have distinguishable temperature transient profiles. More encouragingly, the transient temperature curves can be roughly grouped into three distinct groups corresponding to the weld quality: (1) the welds with the acceptable quality are in the middle pack of the curves; (2) the welds with unacceptable quality attributes such as stuck welds, undersized weld (weld diameter less than the minimum specification by the industry), and high volume of voids or porosities are shown in the upper pack of the curves; and (3) the welds with severe expulsion and cracking are distinctively in the lower pack of the curves.

Figure 9 shows the normalized intensity curves measured by means of the xenon flash lamp heating method for two different types of defects: stuck weld vs weld with severe surface indentation due to expulsion. The thermal responses are clearly different for the two different cases.

In addition, the IR measurement results appeared to be highly consistent. This is illustrated in Figure 10 using the ice cube cooling method. Two different types of welds with known quality problems, stuck weld or weld with severe surface indentations, were tested. For each weld condition, five replicate welds were used. It is evident from these results that the IR thermography technique is highly repeatable and consistent.

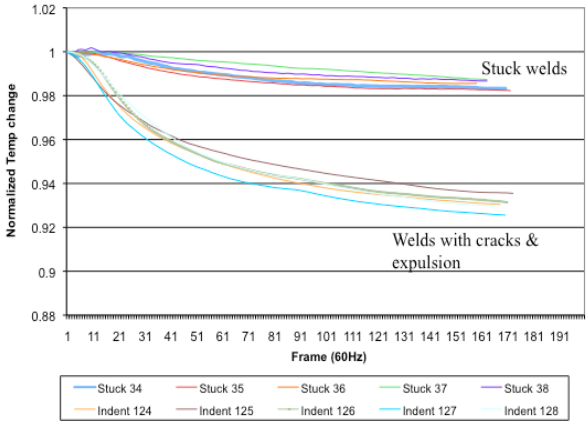

Figure 10. IR measurement on replicate welds using the ice cube cooling method.

The above findings clearly suggested the feasibility of IR thermography for weld-quality inspection.

Computational Simulation

Initial computer simulations of the heat flow by postmortem external heating were carried out as part of the Phase I work.

The purposes of the simulations were (1) to establish the analytical basis for quantitative correlation of various weld attributes with the heat-flow and temperature patterns caused by the external heating/cooling source, and (2) to provide information on the optimal heating/cooling arrangement and IR thermal-image data collection and analysis to maximize the resolution and sensitivity of defect detection and to minimize the inspection time necessary for eventual assembly-line implementation.

The finite-element heat-flow simulation matrix included a series of weld nugget sizes, surface-indention depths, sheet thicknesses, voids, and cracks to represent the weld-quality attributes. It also included various heating patterns, heating times, and heating-intensity levels.

Figure 11 shows the simulation results for three representative cases: a cold weld with minimal fusion bonding (Case1), a normal weld (Case 2), and a weld with excessive indentation and expulsion (Case 3). The simulation clearly shows that there are intrinsic thermal signatures (heating

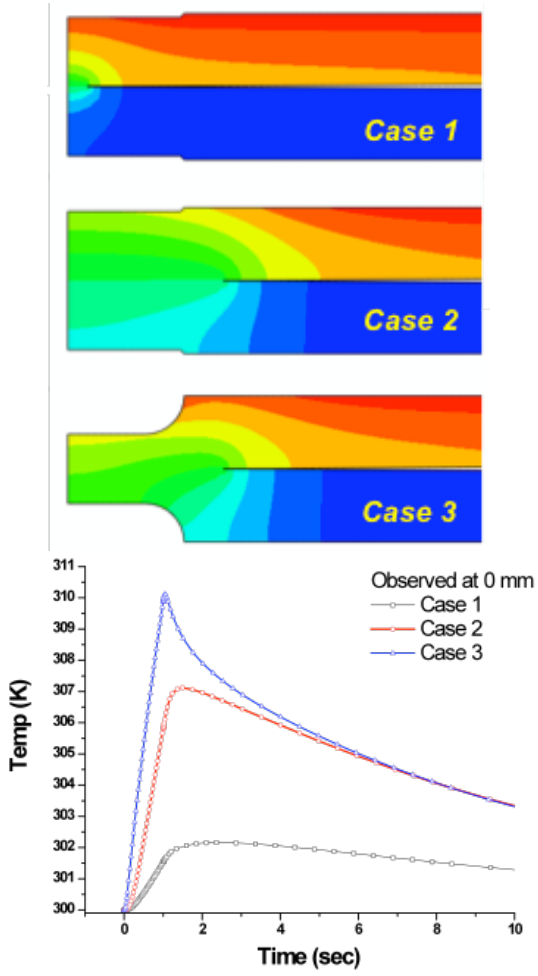

Figure 11. Thermal signatures of three representative welds of different quality obtained from heat-flow simulation.

rate, cooling rate, peak temperature, etc.) associated with welds of different qualities. These characteristic thermal signatures are the scientific basis for IR-based weld-quality detection technology. The computational simulation results are being analyzed and used to develop the IR thermal-signal-recognition expert system for weld-quality detection.

It is interesting to compare the temperature variation with time in Figure 11 and Figure 8. The observed grouping of cooling curves by weld quality in Figure 8 is clearly supported by the simulation of the intrinsic heat-flow characteristics of welds with different qualities in Figure 11.

Conclusions

The initial study conducted in fiscal year 2008 suggested the potential of IR thermography as a spot-weld quality-inspection technique. Welds having different quality attributes exhibited distinctive temperature transients that were readily measurable by IR thermography. Finite-element heat-flow simulation revealed that the observed distinctive temperature transients were indeed related to the differences in weld qualities.

Presentations/Publications/Patents

1. W. Woo et al., “Application of Infrared Imaging for Quality Inspection in Resistance Spot Welds,” SPIE Defense, Security and Sensing Conference, Orlando, Florida, April 13–17, 2009.

D. Enhanced Resonance Inspection for Light Metal Castings (NDE701*)

Principal Investigator: Xin Sun
Pacific Northwest National Laboratory
P.O. Box 999, Richland, WA 99352
(509) 372-6489; fax: (509) 372-6099; e-mail: xin.sun@pnl.gov

Principal Investigator: Martin H. Jones
Nondestructive Evaluation Laboratory, Ford Motor Company
(313) 805-9184; fax: (734) 458-0495; e-mail: mjone147@ford.com

Technology Area Development Manager: Joseph A. Carpenter
(202) 586-1022; fax: (202) 586-1600; e-mail: joseph.carpenter@ee.doe.gov

Field Technical Monitor: Mark T. Smith
(509) 375-4478; fax: (509) 375-4448; e-mail: mark.smith@pnl.gov

---

Contractor: United Sates Automotive Materials Partnership (USAMP) and Pacific Northwest National Laboratory (PNNL)
Contract No.: DE-FC26-02OR22910 and DE-AC06-76RL01830, respectively

---

Objective

- To ensure the structural integrity of light metal castings by satisfying the need for rapid, reliable nondestructive evaluation (NDE).
- To assess the capability of modeling approaches to predict accurately the vibrational mode and variability of frequencies.
- To evaluate quantitatively the sensitivity of resonance inspection (RI) to anomalies of various types and sizes in various locations.

Approach

- Manufacturing acceptance of RI is limited by its empirical methodology; therefore, augment current empirical methodology with predictive tools. Initially use a "simple" part and compare experimental and finite-element analysis (FEA) predictions of resonance frequencies and shapes.
- Develop a set of tools to enable predictive capability:
  - — Make current setup/training time shorter by using computer modeling to simulate response of actual parts and flaws.
  - — Identify response to critical flaws thereby allowing "fault" to be specified and subsequently fixed (process feedback).
- Model to translate materials properties and geometry into predicted frequencies:
  - — Use computer-aided design (CAD) model or preferably three-dimensional (3D) scanning to provide exact as-is geometry to FEA model.
  - — Generate FEA 3D mesh directly from scanned data.

*Denotes Project 701 of the Nondestructive Evaluation Working Group of the United States Automotive Materials Partnership, one of the formal consortia of the United States Council for Automotive Research set up by Chrysler, Ford, and General Motors to conduct joint, precompetitive research and development (see www.uscar.org).

- Methods to identify mode shapes for each frequency:
  - The ability to identify exact modal shapes is critical in determining what frequency changes correspond to which features in the part.
  - Will need to perform for all modes in practical sampling range of approximately 1–80 kiloHertz (kHz).
- Sensitivity matrix for critical anomalies:
  - From FEA only, predict the response sensitivity to a specified feature (flaw) anywhere in the part.
- Validate by comparing predicted and measured frequencies and mode shapes:
  - Have multiple vendors collect data over full frequency range and compare these experimental results with FEA predictions.
- Complete approach by performing same steps for a more "complicated" real-world part.

Accomplishments

- Connecting rod testing completed:
  - Automatic identification of modes based on comparison of calculation and laser vibrometer measurements.
  - Dimensional check of CAD model using computed tomography (CT)—discrepancies found.
  - Accurate prediction of mode frequencies.
- Calculations based on both CAD model and CT data:
  - Extensive numerical testing of efficient variational method to predict resonance shifts for porosity and slits (oxide film model).
- Real-world part (automotive knuckle casting) testing and modeling completed:
  - In-plant selection of parts.
  - Resonance measurements of the parts by Quasar, The Modal Shop (in-plant), and Polytec.
  - Precision material property measurements (1 part in 10,000).
  - 3D dimensional measurements (1 part in 1000) by computed tomography.
  - Finite-element natural frequency extraction of knuckle and mesh sensitivity study.
  - Modal analysis and steady state dynamic analysis for knuckle casting.
  - Correlation of predicted mode shapes between measured resonance peaks.

Future Direction

- Work on frequency shift prediction for connecting rod and knuckle parts.
- Prediction of flaw size and location based on RI spectral data to be tested.

Introduction

The ability to use RI for testing and flaw identification has been long desired. The RI technique is quick and sensitive, making it an ideal choice in production environments. This project set out to determine if it is feasible to make RI more usable in everyday testing. There are several ways this might be accomplished: decrease the required size of the training set, choose the frequencies to watch more intelligently, predict the sensitivity of the test to a specific feature, and the like. Because of the complexity of the resonance structure in even simple parts, computer modeling of the RI process has been deemed intractable in many instances.

This project has shown that modeling the resonant behavior of simple parts is not only possible but also quite accurate. Simulated and experimental results from three commercial vendors (The Modal Shop [TMS], Magnaflux Quasar, and Polytec) were compared. It was shown that the use of laser vibrometry resolves ambiguities as to the actual mode shape present at a particular frequency.

During this project, there has been great progress in casting real-world parts, experimental testing,

and cooperation with and between commercial partners. Progress has been made in automating mode identification and in predicting accurate mode frequencies. Additionally, errors were identified in the CAD model of the connecting rod part through the use of CT inspection, and 3D computer-aided engineering (CAE) meshes of the part directly from the CT scan data were generated.

Frequency calculations have been performed with CAD and CT data. A computationally efficient variational method to predict resonance shifts for porosity slits (oxide film model) and slots (more crack-like model) have been implemented, and the results are encouraging.

The project demonstrated that finite element and variational principle-based computational methods can be used to model and predict accurately the natural frequencies and vibrational mode shapes of a real-world part. A more realistic part with complex surface features yields better correlations between predictions and measurements because of shorter wave length (i.e., higher frequency) needed to trigger any possible mode switches between the predicted and measured frequency spectra.

Approach

Automatic Identification of Modes Based on Comparison of Calculation and Laser Vibrometer Measurements

The project identified the need to provide the exact resonance mode occurring at any given frequency, which is necessary to compare experimental and CAE results. A commercial partner specializing in laser vibrometry, Polytec, measured the actual motion of the parts as they were being acoustically excited. A practical problem was quickly obvious: many of the resonance modes are similar in frequency and shape.

PNNL went through the early results and correlated the measured mode shapes from Polytec data with the finite element-predicted modes by carefully looking at each mode by hand (eye) and making the assignment. Aside from being tedious, this process is difficult to do under the best of conditions. A method of performing comparison by evaluating a surface integral over the part was proposed and implemented by PNNL as a computer program. The results were examined by several skilled individuals and found to be accurate. Figure 1 gives a comparison of the hand performance with the computed correlation.

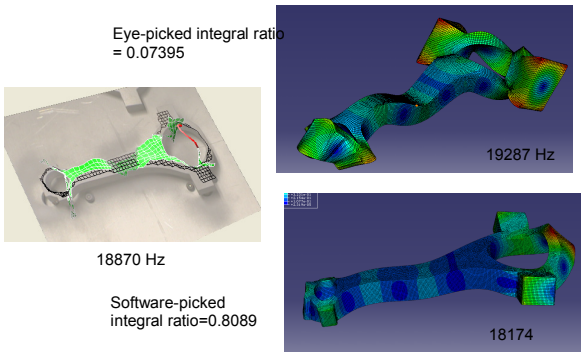

Figure 1. Mode shape comparison.

Because this technique relies on an analysis of the actual/predicted physical movement of the part, it is impervious to computational errors. In fact, it correctly identifies the mode shapes even in the presence of errant model data and predicted frequencies, as discussed in the next section. This has become the final arbiter in the identification of experimental and calculated mode shapes.

Dimensional Check of CAD Model Using Computed Tomography (CT)

The connecting rod was originally designed in CAD as a 3D solid part, and necessary drawings were also generated from the CAD system. Early predictions of the resonant frequencies based on the CAD model were not as accurate as hoped (Figure 2). When the CT-based model of the data became available, it was discovered that it was showing a thickness of 18.00 millimeters (mm), whereas the actual part measured 19.75 mm. It was also found that the diameter of the holes in both ends were undersized in the CAD model by ~1.0 mm each.

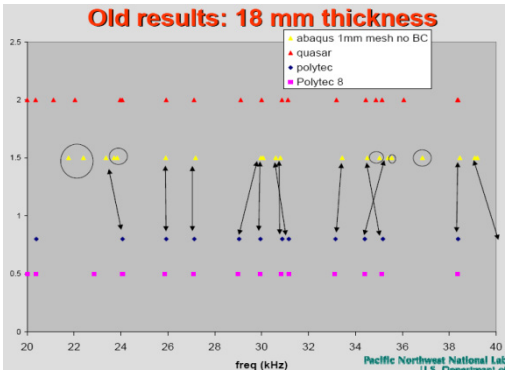

Figure 2. Comparison between predictions and various measurements based on original CAD dimensions. Note: shifts in frequency (angle of arrows) and switches (crossing arrows) became available.

Upon investigation, it was found that the parts were cut from material plate already on hand in the machine shop, hence the change in thickness. Water-jet cutting of the shapes also allowed the diameter to grow slightly with the depth of the cut: the "top" of the holes is slightly smaller in diameter than the "bottom." Predictions made with models containing the correct thickness based on the CT data yielded more accurate results and made correlation and analysis more satisfying all around (Figures 3–5).

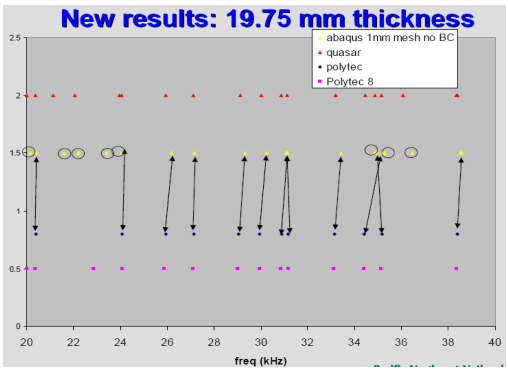

Figure 3. Comparison between predictions and various measurements 20-40 kHz based on as-built dimensions.

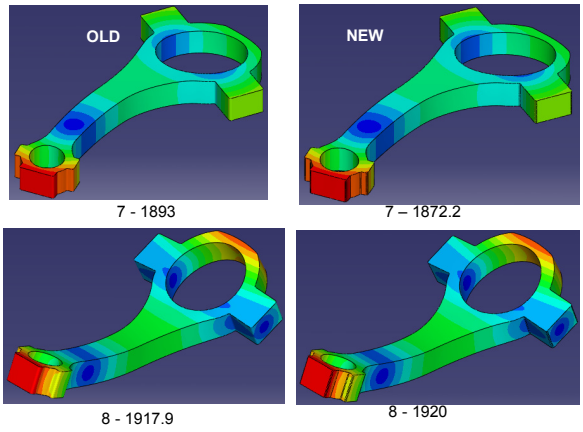

Figure 4. Comparison of old and new model sizes on resonant modes: low frequencies.

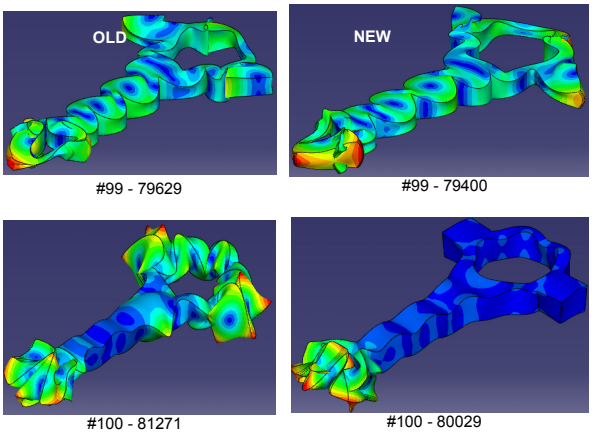

Figure 5. Comparison of old and new model sizes on resonant modes: high frequencies.

Accurate Prediction of Mode Frequencies

Calculations based on both CAD model and CT data have been carried out and analyzed. The CAD model has been corrected for the observed errors and the results predicted from CAD- and CT-based data are essentially the same. Figure 6 shows the full spectrum of predicted, experimental RI and laser vibrometry (Polytec) measured data. The predicted frequencies are quite close and within the expected error due to geometry, material properties and measurement error.

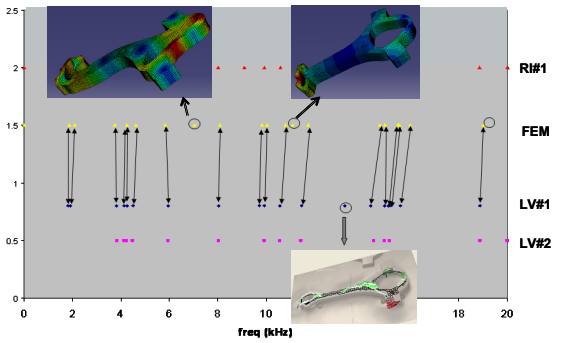

(a) 0–20 kHz

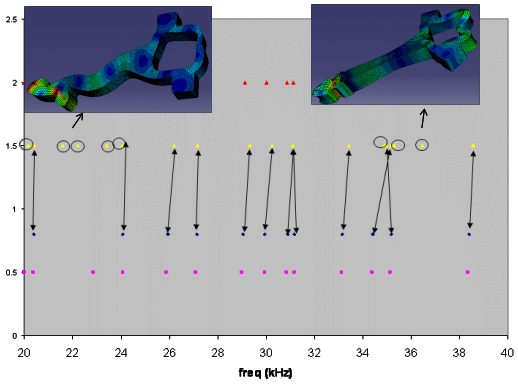

(b) 20–40 kHz

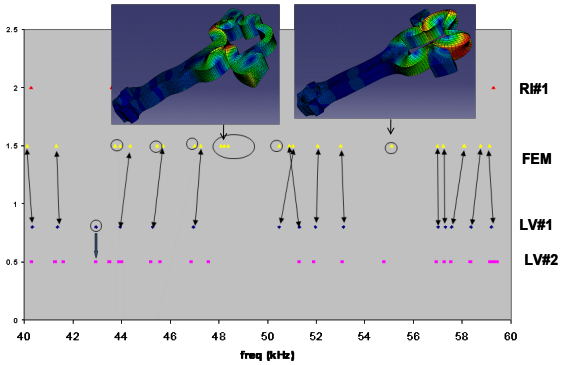

(c) 40–60 kHz

Figure 6(a)–(c). Comparison of predicted and measured frequencies.

Implementation of Computationally-efficient Variational Method to Predict Resonance Shifts for Porosity and Slits (Oxide Film Model)

The effect of different types of flaws (features) on the resonant frequencies has been tested extensively. There are examples of porosity (missing material in a small internal region) slits, where surfaces are free to move but with no gap when at rest (Figure 7) and slots where a small straight line of mass has been removed as a way to simulate a small crack's behavior (Figure 8).

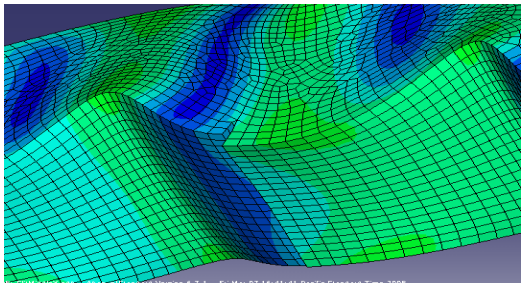

Figure 7. A slit in motion due to RI excitation. Note the surfaces are free to move but have no gap when at rest.

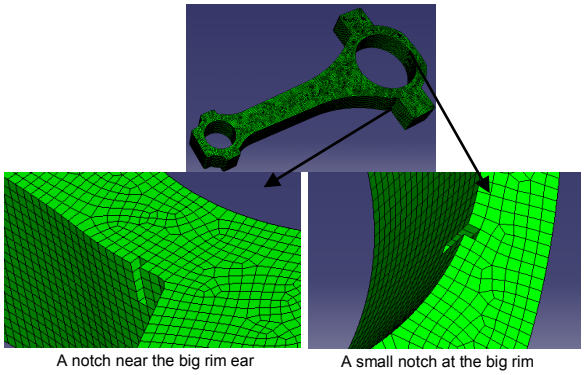

Figure 8. An example of a slot.

When analyzed, these features suggest that for small features, the frequency shifts obey superposition laws (i.e., the effects of each feature can be evaluated independently and summed with all other shift forces at the end; Figure 9).

► Goal: detectability of multiple defects
► Can linear superposition be used to predict frequency shift when there is more than one defect in the part?

- A notch in a part produces a frequency shift Δf_1 for every mode
- Second notch produces a frequency shift Δf_2 for every mode
- If both notches are small, so Δf_1 and Δf_2 are both small, will the frequency shift be $\Delta f_1 + \Delta f_2$ with both notches?

► Result from Abaqus simulation validates this assumption

$$\Delta f_{1+2} \approx \Delta f_1 + \Delta f_2$$

Figure 9. Rational for frequency shift linear superposition.

Linear superposition makes computing the frequency shift from a given feature easier to calculate and allows computation of the sensitivity to an RI test to any feature. The sensitivity calculation continues to be the subject of

refinement but is good and usable at this time (Figure 10).

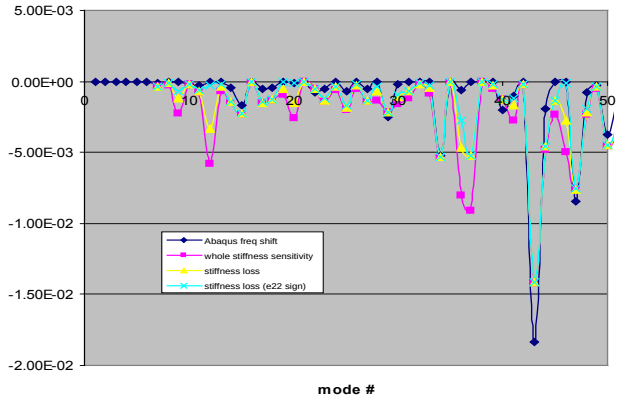

Figure 10. ABAQUS prediction vs stiffness sensitivity.

Real-world Part with Complex Surface Features—Knuckle Casting

With the selection of an automotive knuckle casting (Figure 11) as the target part, an event was held at the casting supplier's facility. A population of 150 parts was selected based on X-ray and dye penetrant inspection. Quasar and TMS tested all 150 parts in the plant and recorded the full spectrum resonance measurements of each.

Figure 11. An automotive knuckle chosen for testing.

Figure 12 shows the detailed spectra comparison between Quasar and TMS in the frequency range of 30–40 kHz. Overall good agreement has been achieved, with several frequency peaks called out by Quasar but not by TMS, possibly due to the low energy input delivered at high frequency levels by the hammer impact used by TMS.

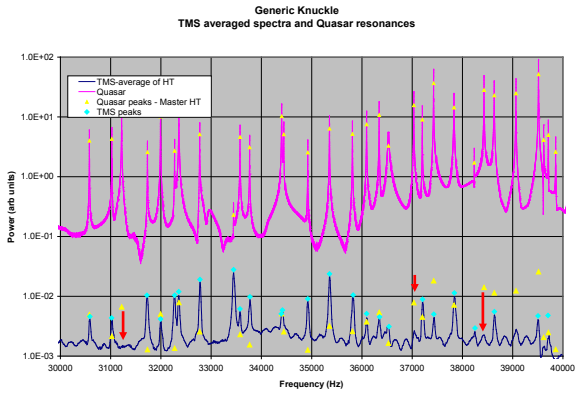

Figure 12. Frequency spectra measured for the knuckle by Quasar and TMS with extracted peaks.

The actual part geometry obtained from the CT scan was used to generate the finite element model (FEM) using Shrinkwrap of Hypermesh (Figure 13). The finest mesh that can be generated using Hypermesh Shrinkwrap is 0.8 mm, below which the finer details of the surface finish of the knuckle require extensive surface repair prior to meshing. The material properties for the finite element analysis are obtained using resonance spectroscopy with small cuboids machined from the knuckle at various locations. The isotropic material model fits the measurement data with high accuracy: density = 2.6711g/cm^3, Poisson's ratio = 0.3358, Young's modulus = 73.8989GPa.

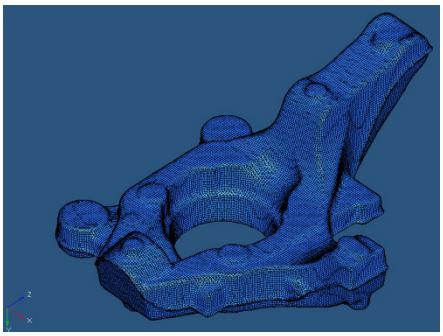

Figure 13. Typical finite element mesh used for the knuckle with 1.75 mm mesh size.

Mesh size convergence study was carried out from 2 to 1.2 mm. The finite-element-predicted frequencies for the knuckle presented in Figure 14 are 99.65% of the frequency values calculated with 1.2 mm mesh, based on the mesh size convergence study.

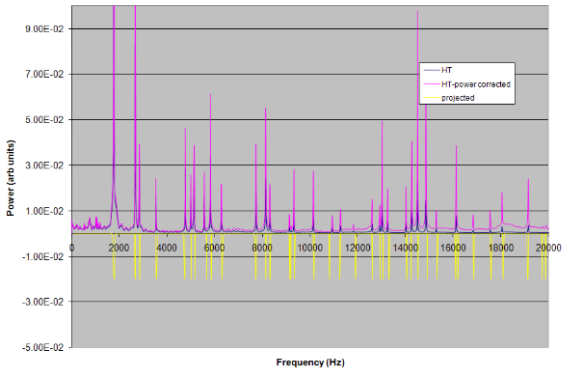

(a) 0-20kHz

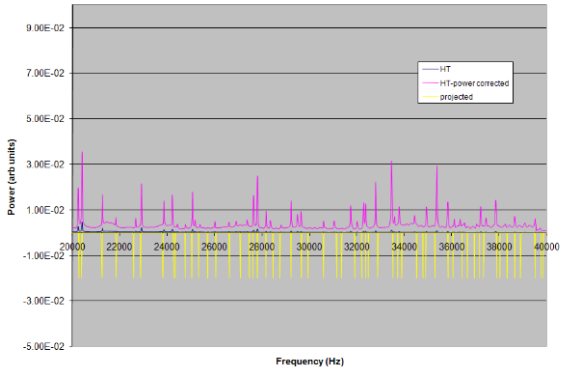

(b) 20-40kHz

Figure 14(a)–(b). Comparison of predicted and measured resonance spectra for the knuckle.

Steady state dynamic analyses were also performed for the knuckle to calculate the relative magnitude of each resonant frequency. This is done by exciting the knuckle at the driver point similar to that used in the Quasar experiment around each resonant frequency. The reaction forces at the two receiver points are averaged to represent the magnitude of the forced vibration at that specific frequency. Figure 15 shows the predicted vibration magnitude at each frequency level in comparison with the experimental measurements.

Discussion

The quantitative prediction and analysis of the resonance properties of two very different parts have now been completed. The first was the connecting rod shape, which is relatively small (0.3 kg) and symmetric. The second is a typical automotive knuckle casting, which is fairly large (3 kilograms [kg]) and entirely asymmetric. These

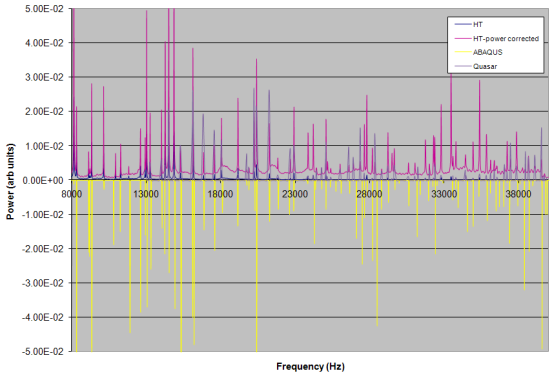

Figure 15. Comparison of steady state dynamics prediction and experimental measurements.

two cases have helped to develop a systematic procedure that puts resonance inspection on a new quantitative basis.

The relatively good resonant frequency comparison between the predicted and measured spectra for connecting rod and knuckle (as shown in Figures 6–14) indicates that experimentally measured resonances can be uniquely identified and matched to a finite element predicted mode shape.

Steady state dynamics analyses can also be used to obtain the relative response magnitude for each frequency. The discrepancies observed between the predictions and measurements are within the range allowed by the material property variations.

Two cases of mode switching are predicted around 35 kHz and 51 kHz for the connecting rod based on the FEM results. The predicted frequency gaps between the switched modes are much smaller than the measured frequency gaps, making mode switch easy to occur for a part that is slightly different from the FEM model in terms of both geometry and actual material input.

Better correlations between predictions and measurement have been achieved for the geometrically complex knuckle. For a symmetrical part such as the connecting rod, a slight deviation from the case simulated in the FEM (either in material properties or in part geometry) will lead to possible mode switch, frequency shifts and splitting of some degenerate modes due to original part symmetry. Conversely, the knuckle has more

complex surface features and no part symmetry; therefore, it will not have potentially degenerated modes to be split easily by material and geometry variation. It should be noted that the finite element predicted frequency and mode shapes also provide a basis for predicting frequency shift sensitivity of the model part to casting defects such as voids and oxide inclusions.

Conclusions

Overall, the experimental and modeling results generated to date in this study demonstrated that the modeling tools can be used to enhance the RI techniques and put RI on a quantitative basis. The overall success of the concept feasibility phase warrants the team to propose a follow-on technical feasibility study on computationally enhanced RI.

Presentations/Publications/Patents

1. C. Dasch, X. Sun, C. Lai, J. Saxton, G. Stultz, G. Palombo, C. Grupke, G. Harmon, L. Ouimet, D. Simon, and M. Jones. 2008. "Towards Quantitative Resonance Inspection: Resonance Mode Identification and Modeling." *Review of Progress in Quantitative E NDE*.
2. "NDE 701: Enhanced Resonance Inspection for Light Metal Castings." 2007. *AMD Offsite*, Southfield, MI. September 27.
3. "NDE 701: Enhanced Resonance Inspection for Light Metal Castings." 2008. *AMD Offsite*, Southfield, MI. October 29.

E. Global Quality Assessment of Joining Technology for Automotive Body-in-White

Principal Investigator: Xin Sun
Pacific Northwest National Laboratory
P.O. Box 999, Richland, WA 99352
(509) 372-6489; fax: (509) 372-6099; e-mail: xin.sun@pnl.gov

Technology Area Development Manager: Joseph A. Carpenter
(202) 586-1022; fax: (202) 586-1600; e-mail: joseph.carpenter@ee.doe.gov

Field Technical Monitor: Mark T. Smith
(509) 375-4478; fax: (509) 375-4448; e-mail: mark.smith@pnl.gov

---

Contractor: Pacific Northwest National Laboratory
Contract No.: DE-AC06-76RL01830

Objective

- Evaluate quantitatively the effects of missing bondline or missing welds on the global resonance signature of an automotive body-in-white (BIW).
- Assess the feasibility of a new inspection technique that will provide a global quality factor of the joining technology used for an automotive BIW.

Approach

- Evaluate the sensitivity of resonance spectroscopy to detect defects such as a partial weld or an improperly cured adhesive in a simple structure.
- Determine target values for sensitivity, reference surrogates of defects, functional requirements to be acceptable in a manufacturing environment and compatible with either inline or offline quality assurance (QA) and cost targets to ensure an inspection is economically affordable to the manufacturer.
- Determine techniques of exciting vibrational modes and other methods of stimulus that will intentionally stress a predetermined region to increase sensitivity to a selected site.
- Investigate novel means to reduce implementation cost.
- Determine advantages, technology gaps and implementation issues, investigate cost-effective means for implementation at automotive assembly plants and define paths for future development.

Accomplishments

- Fabricated spot welded samples with simple strip-like geometry: perfect and imperfect.
- Fabricated adhesively bonded samples with simple strip-like geometry: perfect and imperfect.
- Performed resonance spectroscopy measurement on both the welded and adhesively bonded samples with the Quasar system; performed resonance spectroscopy measurement on the spot-welded samples with The Modal Shop system.
- Performed preliminary finite element simulations on the natural frequencies and mode shapes for the spot-welded samples.

Future Direction

- Experimentally measure the frequency-dependent modulus for the structural adhesive used in order to perform finite element frequency extraction for the bonded samples.
- Quantify the effects of part geometric tolerance on the measured resonance spectroscopy for parts with simple geometry.
- Fabricate welded and bonded hat sections for resonance inspection (RI).
- Perform RI testing with different excitation techniques provided by different vendors.
- RI signal sensitivity study on perfect and imperfect parts.
- Perform finite element natural frequency extraction and mode shape analysis.
- Determine advantages, technology gaps, and implementation issues.

Introduction

While the domestic automotive industry continues to introduce new lightweight materials and associated joining technologies to the body-in-white (BIW), the need emerges for a global QA tool that is nondestructive and able to evaluate quickly the joining technology for an entire automotive BIW. Current practices employ statistical testing with destructive measurements that are labor intensive, ergonomically unfriendly, costly and time delayed. Further, continuous joints such as adhesive bonds or laser welds can be difficult to inspect destructively, and joints in high-strength steel can be too strong to be pried apart.

Facing these challenges, we propose to examine the concept feasibility of using a global joint quality evaluation and assurance approach by quantifying the contributions of the joint integrity (discrete as well as continuous) to the overall structural stiffness of the BIW through vibration mode and natural frequency analyses. The proposed method is computationally intensive in that it examines the BIW natural frequency and vibration modes using structural finite element analyses. Different means of structural excitation and effects of different boundary conditions will be established by detailed finite element structural/modal analyses on the BIW models provided by the original equipment manufacturers (OEMs).

Partnering with automotive manufacturers is critical to assure the techniques of straining the BIW and performing three-dimensional (3D) imaging is conducive to a manufacturing environment and existing online production practices. Various experimental measurements including resonant spectroscopy (RS) and whole body strain measurements by techniques such as shearography (shearing speckle interferometry) will be used as experimental model validations.

The proposed techniques are capable of whole body imaging where either static or dynamic stress is applied and displacement on the order of nanometers is quantified. Comparing analyses results, the 3D displacement measurements will show a characteristic pattern when joining methods have been properly used and permit an objective means of evaluating quality.

The objective of the project is to assess the feasibility of a global inspection technique for the various joining technologies used for an automotive BIW.

Fabrication of Bonded and Welded Parts with Simple Geometry

Some 1.5 mm dual phase (DP) 980 steel sheets are used to fabricate the bonded and welded parts with simple geometry. A strip-like simple geometry is selected as the first sample geometry of this project. Two joining technologies most commonly used in an automotive BIW are used: resistance spot welding and bonding with structural adhesive. Figure 1 shows the top and bottom view of the spot welded samples with the conditions of the welds specified. The two perfect samples are

Figure 1. Illustration of the spot welded specimens.

welded with the specified weld diameter of 6 mm. The actual weld size has been verified through metallurgical cross sectioning. Samples with sub-sized welds are labeled as poor weld and three other specimens are made with missing welds at specified locations. It should be mentioned that these welded specimens are fabricated with a regular alternating current (ac) welder under handheld condition. No sample holder or weld positioning fixture was used in the coupon fabrication process. This process will introduce some manufacturing-induced sample geometry variations in terms of weld alignment, sample edge offset and the like.

Figure 2 shows the schematic of the adhesively bonded samples with the bonding conditions illustrated. The structural adhesive Dow Betamate*73305GB is used in the bonding process. Three perfectly bonded samples are made

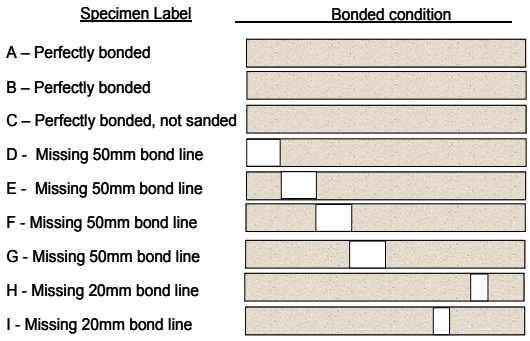

Figure 2. Illustration of the bonded samples.

and cured under vacuum condition; the rest are made with intentionally missed bond lines of 50 and 25 mm at various locations.

Resonance Spectroscopy Measurements with Quasar System

Figure 3 shows the boundary conditions used in the RI tests with the Quasar system: one point contact with Transmitter and two points contact with Receivers 1 and 2. Figure 4 shows the measured resonance signatures of the two good welded samples in the low frequency range of 0–1000 Hertz (Hz). Some similarities can be found from the resonance signatures for the two good parts, which are indicated by the blue boxes in Figure 4. The width of the blue box indicates the frequency shifts from among the two good specimens.

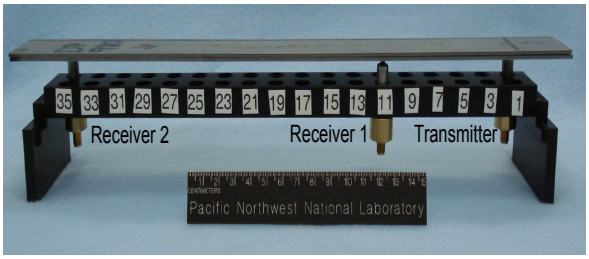

Figure 3. Experimental setup with the Quasar system.

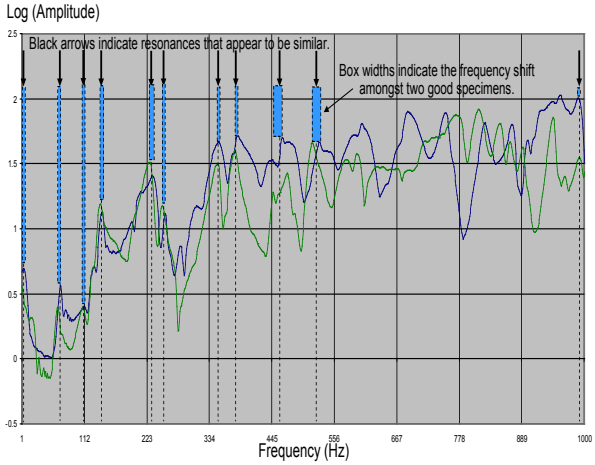

Figure 4. Measured resonance signatures of the two good welded samples: 0–1000 Hz.

Figure 5 shows the measured low frequency resonance signatures of one bad part compared with those of two good parts. Red arrows indicate the peaks for the bad part that do not match the

peaks for the two good parts. Various degrees and patterns of spectra mismatches are also obtained for the rest of the discrepant parts compared with the two good parts, similar to those shown in Figure 5.

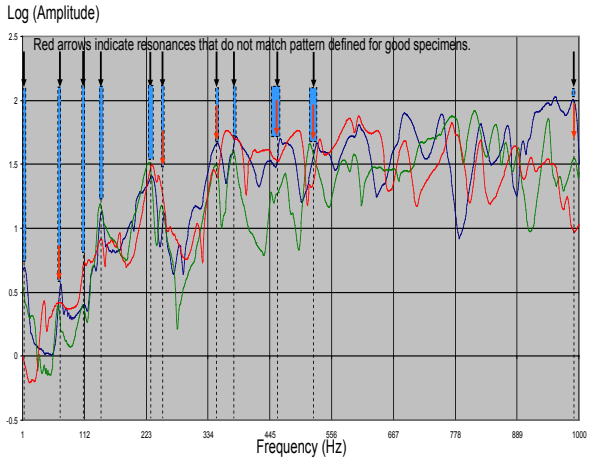

Figure 5. Comparison of resonance signatures among one bad part and two good parts.

Figure 6 shows the spectra comparison between one good part and three discrepant parts in the higher frequency range of 20–30 kilo Hz (kHz). Similar to the results in lower frequency range, noticeable frequency shifts are observed for higher frequency ranges. These results indicate that for the spot-welded samples with simple strip-like geometry, the resonance spectra show many peaks with distinguishable magnitudes. There are also detectable differences between the measured spectra for the good and discrepant parts for both

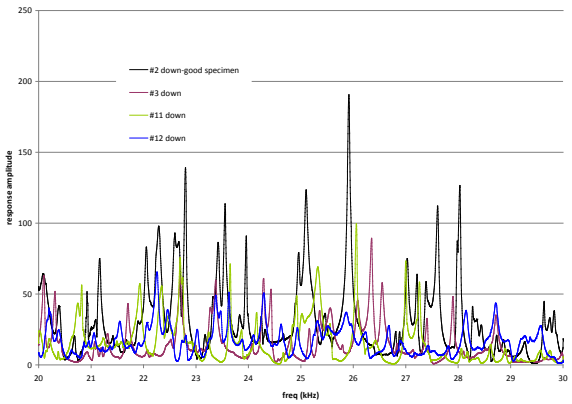

Figure 6. Comparison of resonance spectra among good and bad welded parts.

lower and higher frequencies. These results show the potential applicability in identifying missing welds and undersized welds using RI signatures/patterns.

In contrast to welded samples, the RI spectra for bonded strip-like samples do not show as much promise as those demonstrated for spot-welded samples in this preliminary stage of our work. First, RI patterns for the two perfectly bonded specimens show limited resemblance in both resonance frequencies and peak values (Figure 7). Possible reasons for the dissimilarity may be lack of consistency in line thickness between two perfectly bonded samples. Also, resonance spectra seem controlled by a global structural level resonance, with maximum peaks for most samples occurring at 17–18 kHz. Response magnitudes for all samples are in the low frequency range of 35–50 kHz due to the attenuating effect of structural adhesive. These features make it difficult for the RI technique to identify improperly bonded samples for the strip-like coupon geometry. Possible improvements to the sample design are needed.

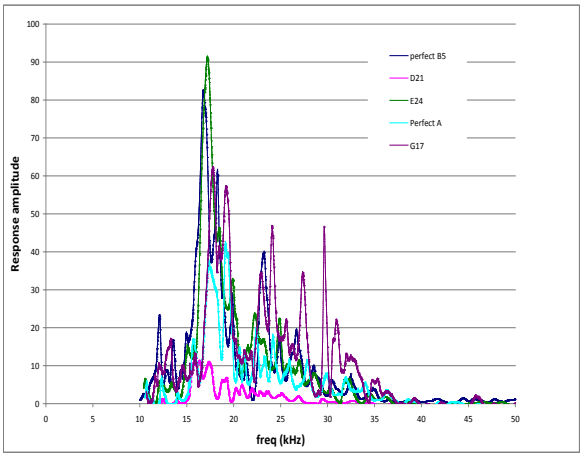

Figure 7. Comparison of resonance spectra amongst good and bad bonded parts.

Conclusions

This project received its initial funding in July 2008 and is still in initial research stages. Our next steps in this project include:

1. Fabricate small-scale hat sections using resistance spot welding and adhesive bonding on perfect and imperfect parts.
2. Obtain resonance spectra with two different RI methods (i.e., Quasar and The Modal Shop) and compare resonance spectra between perfectly and imperfectly welded/bonded parts.
3. Perform finite element natural frequency extraction and mode shape analysis on hat sections with experimentally determined frequency dependent modulus for adhesive.
4. Correlate the measured spectra with the predicted spectra for the hat sections.
5. Determine concept feasibility, technology gaps, and implementation issues for global quality assessment of joining technology for automotive BIW.

11. RECYCLING

A. Recycling Assessments and Planning

Principal Investigator: Bassam Jody
Argonne National Laboratory
9700 S. Cass Ave., Argonne, IL 60439
(630) 252-4206; fax: (630) 252-1342; e-mail: bjody@anl.gov

Technology Area Development Manager: Joseph A. Carpenter
(202) 586-1022; fax: (202) 586-1600; e-mail: joseph.carpenter@ee.doe.gov

Participants:
This project is conducted as part of the cooperative research and development agreement among Argonne National Laboratory (ANL); United States Council for Automotive Research's Vehicle Recycling Partnership, LLC; and the American Chemistry Council Plastics Division

CRADA Partner Principal Investigators:
Claudia Duranceau, VRP, Ford Motor Co., (313) 390-0504; e-mail: cdurance@ford.com
John Haubert, VRP, Chrysler LLC., (248) 576-7458; e-mail: jah59@chrysler.com
Jacquiline Quinn, VRP, General Motors Corp., (586) 575-7078; e-mail: jacquiline.quinn@gm.com
James Kolb, ACC-PD, (248) 244-8920; e-mail: james_kolb@americanchemistry.com

---

Contractor: ANL
Contract No.: DE-AC02-06CH11357

Objectives

- Eliminate any real or perceived recycling barriers that might preclude the use of advanced automotive materials.
- Enable the optimum recycling of all automotive materials, current and future, thereby obviating the need for legislative recycling mandates.
- Assess the critical needs for cost-effective recycling of automotive materials and components.
- Establish research priorities to enable cost-effective recycling of advanced automotive materials and components.
- Communicate a collaborative industry/government approach to issues related to the recycling of automotive materials.
- Coordinate research with other agencies and stakeholders in the United States, Europe, and Asia.

Approach

- Consult with automotive manufacturers and recycling industries, USCAR and its affiliates, national laboratories, universities, and other relevant organizations to assess critical recycling needs/barriers.
- Develop a recycling research plan that will serve as a "working document" to guide the U.S. Department of Energy (DOE) in establishing priority goals, with an initial emphasis on lightweighting body and chassis materials.
- Establish an outreach/communication function to enable cooperation amongst, and leveraging of resources with, all stakeholders and the international community.

- Assist DOE in establishing advanced recycling research and development (R&D) initiatives and provide technical oversight to ensure that priority objectives/goals are accomplished.

Accomplishments During This Reporting Period (10/1/07–9/30/08)

- Conducted progress review meetings with CRADA team members.
- The Engineering Project Oversight Committee (EPOC) of the VRP also held meetings twice a month and an ANL representative attended as necessary to discuss CRADA issues.
- Made presentation to the VRP management committee which holds monthly meetings and to the Environmental Technology Leadership Council of USCAR to update them on the CRADA accomplishments.
- Presented progress at the 2008 Office of Vehicle Technologies Annual Merit Review meeting (Feb 27, 2008).
- Held meetings with the FreedomCAR Materials Technical Team.
- Conducted a workshop (September 24–25, 2008) to develop a roadmap for recycling lightweighting metals (aluminum, magnesium and titanium) and to identify R&D needs for recycling these metals.
- Updated the CRADA website: http://www.es.anl.gov/Energy_systems/CRADA_Team_Link/Index.html.
- Continued gap analysis with CRADA team.
- Reached agreement with a shredder to build a 20-ton-per-hour validation plant to confirm process yields, process economics, and to confirm qualities of the recovered polymers.
- Modified the Annual Operating Plan in order to assist the shredder who is building a 20-ton-hr validation plant based on the ANL recycling technology.
- Prepared the statement of work for a new 5-year extension of the CRADA.
- Identified new lightweighting materials being considered for vehicles of the future.
- Prepared and/or presented technical papers on recycling automotive materials. One of the papers was published in the November 2007 issue of the *Journal of Metals* and has been selected to receive the 2009 Technology Award of the Extraction and Processing Division of The Minerals, Metals & Materials Society (TMS).
- Continued liaison with the Institute of Scrap Recycling Industries (ISRI), the Automotive Recycling Association (ARA) and visited the facilities of two automotive dismantlers and a shredder.
- Reviewed Small Business Innovation Research proposals for DOE.

Prior Accomplishments

FY 2007

- Conducted bimonthly progress reviews with CRADA Team.
- Identified new automotive lightweighting materials that are being considered for vehicles of the future.
- Continued gap analysis with CRADA team.
- Prepared several papers outlining the industry/government collaboration at national and international conferences.
- The CRADA team received the (SPE), Environmental Division, Global Plastics Environmental Conference (GPEC) “Enabling Technologies in Processes & Procedures,” 2007 Award. The award is in recognition of the work of the CRADA team in the development of enabling processes and procedures to facilitate the recovery and recycling of automotive plastics from end-of-life vehicles.
- Continued liaison with ISRI, ARA, and individual shredders.
- The ACC-PD Operating Committee visited the ANL pilot plant.

FY 2006

- Conducted quarterly progress reviews with CRADA team.
- Conducted annual project review and gap analysis with CRADA team.
- Developed CRADA team presentation brochure (was prepared by Energetics) and one-pager.
- Launched United States (U.S.) End-of-Life Vehicles (ELVs) CRADA Team Website. It includes an overview of the CRADA team activities, downloadable CRADA team brochures, a bibliography of recycle literature, and presentations and annual reports of the team.
- Presented papers outlining the industry/government collaboration at international conferences.
- The CRADA team held a media event for America Recycles Day. Press releases and related news stories are accessible through the CRADA Team website.
- Continued liaison ISRI and ARA and held several meetings with the CRADA partners and representatives of ISRI and ARA.

FY 2005

- Conducted quarterly progress reviews with CRADA team.
- Conducted annual project review and gap analysis with CRADA team.
- Conducted one-day, peer-review progress review. It was attended by experts in the field, in addition to the CRADA partners.
- Conducted one-day roadmap workshop to update the 2001 Roadmap for Recycling ELVs of the Future.
- Continued liaison with the ISRI and held several meetings with the CRADA partners and representatives of ISRI.

FY 2004

- Conducted quarterly progress reviews with CRADA team.
- Conducted annual project review and gap analysis with CRADA team.
- Held a CRADA announcement event at ANL on December 2, 2004 — the event was attended by representatives of the press, industry, and government.
- Established liaison with ISRI and held several meetings with the CRADA partners and representatives of ISRI.

FY 2003

- Developed 5-year project plan.
- Negotiated a CRADA with the VRP and the American Plastics Council (APC. Now the ACC-PD) and ANL as partners; effort under the CRADA was initiated in August 2003.

Future Direction

- Pursue extension of the present CRADA for 5 more years.
- Continue development and management of the R&D plan with the CRADA partners.
- Continue ongoing efforts toward the milestones and objectives of the CRADA.
- Conduct scheduled progress reviews and continue gap analysis with the CRADA partners.
- Maintain and update the U.S. ELVs CRADA team website.
- Continue outreach efforts to broaden the basis for cooperation among stakeholders.

- Continue ongoing project efforts to assist DOE in preparation of planning documents, priority recycling R&D needs, proposal reviews, and related tasks.

Introduction

The objective of this project is to establish priorities and develop cost-effective recycling technologies and strategies in support of DOE's Energy Efficiency and Renewable Energy (EERE) Vehicle Technologies long-term objectives and goals. The major goals of this research are to (1) enable the optimum recycling of all automotive materials, (2) ensure that advanced automotive materials that improve the life-cycle energy use of vehicles are not precluded from use as a result of a perception that those materials are not recyclable, and (3) enable market-driven vehicle recycling.

Today, cars that reach the end of their useful service life in the United States are profitably processed for materials and parts recovery by an existing recycling infrastructure. That infrastructure includes automotive dismantlers, automotive remanufacturers, and scrap processors (shredders). The dismantlers recover useable parts for repair and reuse. The dismantlers also recover some of the automotive fluids including the refrigerants and the engine oil. The refrigerants can be purified and reused. Facilities for recycling engine oil also exist. The oil can be used as an energy source or it could be refined and used to make new engine oil. Remanufacturers remanufacture a full range of components, including starters, alternators, transmissions, and engines, to replace defective parts. The scrap processors recover ferrous and nonferrous metals from the remaining auto "hulk."

The recyclability of the plastics and elastomers of the ELVs is limited at present by the lack of (1) commercially-proven technologies to identify and cost-effectively separate materials and components and (2) profitable post-use markets. The presence of polychlorinated biphenyls (PCBs) on the plastics severely limits their end use. During the next 20 years, both the number and complexity of ELVs are expected to increase, posing significant challenges to the existing recycling infrastructure. The automobile of the future will use significantly greater amounts of lightweighting materials (e.g., ultra-high strength steels, aluminum (Al), magnesium (Mg), titanium (Ti), plastics, and composites) and more sophisticated/ complex components such as fuel cell stacks, hydrogen storage systems and electronic controls.

Roadmap Recommendations

A workshop to update the original roadmap, published in 2001, was held on September 14, 2005, at ANL. Representatives from DOE, key stakeholders, universities and other experts attended the meeting. The workshop evaluated the original Roadmap and its recommendations. The following were identified as some of the factors that can affect the recyclability of future shredder residue:

- Vehicles containing new materials of construction for lightweighting (composites, Al alloys, Mg and Ti);
- Catalysts for better environmental control; and
- Vehicles powered by fuel cells, electric batteries, hydrogen, and hybrids.

The key recommendations from the original roadmap, which was developed with input from key stakeholders to guide DOE's recycle research, were:

- Come together as a unified recycling community to cost share in the development of required new technology.
- Incorporate reuse, remanufacturing, and recycling into the design phase for vehicles whenever possible.
- Recycle as early in the recycling stream as possible, while relying on the market to optimize the value and amount recycled at each step.
- Maintain a flexible recycling process that can adapt to diverse model lines fabricated with different techniques and materials from various suppliers.
- Develop automated ways to recover bulk materials.

- Emphasize R&D on post-shred material identification, sorting, and product recovery.
- Focus R&D efforts on materials not recycled today by sorters (e.g., post-shred plastics, glass, rubber, fluids, and textiles).
- Develop uses for recovered materials (whether in the same or different applications) and testing specifications.
- Encourage investment in the infrastructure needed to achieve the recyclability goal. Build on the existing infrastructure.
- Develop a means to prevent the entry of PCBs and other hazardous materials into the recycling stream and promote acceptable limits in shredder residues.
- Consider the recycling requirements of new technologies entering fleets as early as possible.

A one-and-a-half day seminar was conducted on September 24 and 25, 2008 to develop a roadmap and identify R&D needs for recycling lightweighting metals (Al, Mg, and Ti). A roadmap report with recommendations will be issued during the next reporting period.

The Five-Year Research and Development Plan

On the basis of the 2001 roadmap and continuing discussions with key stakeholders, a 5-year research plan was prepared. The plan includes three focus areas, as discussed below.

Area 1. Baseline Technology Assessment and Infrastructure Analysis

The focus of the work under this activity is to develop the tools and document the information necessary to make effective decisions relative to technology needs to facilitate sustainable future vehicle recycling and to make effective decisions regarding the allocation of R&D resources.

Area 2. Materials Recovery Technology Development and Demonstration

Research to be conducted in this area will initially focus on addressing technology needs for post-shred materials recovery, including mechanical recycling and conversion to fuels and chemicals. Projects that enhance pre-shred recovery—including disassembly for materials recovery and direct reuse and remanufacturing of components—will also be considered. In the long term, such components as fuel cells, advanced batteries, and onboard hydrogen reformers are more likely to enter the recycle stream through pre-shred recovery for remanufacturing, repair, and materials recovery. Research will be undertaken to determine the technology needs to ensure the recyclability of these advanced automotive components.

Area 3. Recovered Materials Performance and Market Evaluation

Understanding and enhancing recovered materials performance is an essential ingredient to a successful recycling program. This is especially true in automotive systems when the materials and components that are recovered have been in use for an average of from 10–15 years. Area 3 includes projects to quantify the relative performance of recovered materials vis-à-vis new or virgin materials; research on compatibilization of recovered polymers to improve performance properties; development of technologies to upgrade the recovered materials, such as separation of fibers from polymeric substrates; and development of applications for other recovered materials, such as rubber and glass.

CRADA Projects

A CRADA among ANL, the VRP, and the ACC-PD has been structured to provide a core team of expertise and the resources to enable the optimum recycling of all automotive materials.

The CRADA team's R&D agenda focuses on the following key objectives:

- Develop and demonstrate sustainable technologies and processes for ELV recycling.
- Demonstrate the feasibility of resource recovery from shredder residue, including materials recovery for reuse in automotive and other applications, chemical conversion of residue to fuels and chemicals, and energy recovery.

- Develop viable strategies for the control and minimization or the elimination of substances of concern.
- Benchmark recycling technology and provide data to stakeholders.
- Stimulate markets for reprocessed materials to support economic collection, processing, and transportation.
- Transfer technology to commercial practice.

This project (Recycling Assessments and Planning) provides for the overall management of the CRADA team activities and for communication and advocacy with other organizations. The other major projects that have been initiated under the CRADA include the following:

- Baseline Assessment of Recycling Systems and Technology.
- Post-Shred Materials Recovery Technology Development and Demonstration.
- Development of Technology for Removal of PCBs and Other Substances of Concern from Shredder Residue.
- Compatibilization/Compounding Evaluation of Recovered Polymers.

The objectives and progress on these projects are discussed in their respective sections of this report. Effort under the CRADA was initiated in the fourth quarter of FY 2003.

Outreach Efforts

While the CRADA team provides a core of expertise, cooperation with other organizations is a key to achieving the overall program objectives. In the United States, a market-driven recycling infrastructure is in place. The CRADA team is actively pursuing cooperation with the organizations and companies that are a part of that infrastructure. Cooperation with other stakeholders is also essential.

We were contacted by a U. S. shredder who was willing to validate ANL's process for recycling materials from shredder residue by building a validation plant at one of his yards. During this reporting period, we reached agreement with the shredder to build a 20-ton-per-hour validation plant to confirm process yields, process economics, and to confirm qualities of the recovered polymers. In order to support the shredder's effort, we prepared a modified operating plan and the modified plan was approved.

The CRADA team members also held their regular review meetings to review progress and identify technology gaps. Members from ANL and the VRP attended two Materials Technical Team meetings and discussed the validation plant plans. We also attended the 2008 Office of Vehicle Technologies Annual Merit Review meeting in Bethesda, Maryland, in February of 2008 and presented our progress to the review panel.

The CRADA team received the SPE Environmental Division's GPEC, "Enabling Technologies in Processes & Procedures," 2007 Award. The award was in recognition of the work of the CRADA team in the development of enabling processes and procedures to facilitate the recovery and recycling of automotive plastics from ELVs. The team also prepared and/or presented a number of papers on recycling automotive materials. One of the papers was published in the November 2007 issue of the *Journal of Metals* and has been selected to receive the 2009 Technology Award of the Extraction and Processing Division of TMS.

Many shredders, polymer recyclers, and the ACC-PD's operating committee visited ANL's automotive recycling pilot plant and discussed plastics recycling activities. Representatives of ANL, VRP, and ACC-PD also held discussions with ARA and visited two dismantlers and a shredder and discussed present recycling activities and the industry's needs for expanding these activities.

The VRP established a Communications/ Outreach project to create more visibility and awareness among the public, industry, and legislative audiences regarding the work the VRP performs. This outreach occurred via participation at conferences, seminars, and auto shows and featured trade show booths, brochures, videos, mouse pads, and tote bags. It is believed that communicating with the public, industry, and

legislative audiences will bring in new collaborators, project partners, and even more leveraged funding. The project is preparing a video reflecting the recycling infrastructure in the United States. The video provides a quick way to explain the vehicle recycling infrastructure and the role VRP initiatives and projects play in the infrastructure. The VRP initiated another project the objective of which is to provide guidance to optimize design of future vehicles by focusing on improved recyclability, resource optimization, and reduction of the amount of shredder residue by recovering reusable materials.

A website was launched in March of 2006 to provide for better communication and networking with stakeholders and other research teams: http://www.es.anl.gov/Energy_systems/CRADA_Team_Link/Index.html. The website provides an update of the CRADA progress and provides access to relevant information and publications including a bibliography of mechanical, thermo-chemical conversion, and energy recovery technologies for recycling automotive materials. During this reporting period, the website was updated with more information including access to additional information sources.

The CRADA team held a media event at ANL for *America Recycles Day*. It was attended by a number of media organizations. Articles featuring the work done by the CRADA team were written by the media members who attended. CRADA team members were interviewed by several radio stations after the media event.

Several presentations and publications were made to further communicate with interested parties including a paper "Market Driven Technology Development for Sustainable End-of-Life Vehicle Recycling: A Perspective from the United States," presented by Edward Daniels at the 6th International Automobile Recycling Congress, Amsterdam, Netherlands, March 15-17, 2006. A joint DOE, USCAR, and APC paper on "Market Driven Recycling in North America" was presented as the keynote paper at the 2004 International Car Recycle Congress in Washington, D.C.

Several meetings with representatives of ISRI, the ARA and shredder operators were held to brief them on the CRADA objectives and projects and to elicit their participation.

To further communicate the U.S. approach to ELV recycling, a one-page CRADA summary and a CRADA brochure have been prepared and it is available at the CRADA website.

As previously mentioned, a review of the projects and ongoing efforts of the CRADA team was held on September 13, 2005 and a workshop was also held on September 14, 2005, to review and update the ELV Roadmap. Another review of the projects and ongoing efforts of the CRADA team was held on February 27, 2008. We also conducted a workshop on September 24 and 25, 2008 to develop a roadmap for recycling lightweighting metals (Al, Mg, and Ti).

Publications

1. Automotive Recycling in the United States: Energy Conservation and Environmental Benefits, J. A. Pomykala Jr., B. J. Jody, J. S. Spangenberger, and E. J. Daniels, The Journal of Metals, Vol. 59, No. 11, Nov. 2007, pp. 41–45.
2. *The R&D of the FreedomCAR Materials Program*, J A. Carpenter Jr., E. J. Daniels, P. S. Sklad, C. D. Warren, and M. T. Smith, Proc. Of the International Auto Body Congress, Novi, MI, September 19, 2006.
3. *Market Driven Technology Development for Sustainable End-of-Life Vehicle Recycling: A Perspective from the United States*, E. J. Daniels, B. J. Jody, J. A. Pomykala Jr., and J. S. Spangenberger, presented at the 6th International Automobile Recycling Congress, Amsterdam, Netherlands, March 15–17, 2006.
4. *Industry and Government Collaboration to Facilitate Sustainable End-of-Life Vehicle Recycling*, E. J. Daniels, 2005 ASME International Mechanical Engineering Congress & Exposition, BRTD-4: Sustainability Applications in Product Design and Manufacture, Orlando, Florida, November 5–11, 2005

5. *Market Driven Automotive Recycling in North America*, C. Duranceau, presented at the Institute of Scrap Recycling Industries Shredder Meeting, Dallas, TX (Oct. 30, 2004).
6. *Sustainable End-of-Life Vehicle Recycling: R&D Collaboration between Industry and the U.S. DOE*, E. J. Daniels, J. A. Carpenter Jr., C. Duranceau, M. Fisher, C. Wheeler, and G. Winslow, JOM, The Mineral, Metals & Materials Society, vol 56, no 8, pp. 28–32 (Aug. 2004).
7. *Market Driven Automotive Recycling in North America*, C. Duranceau, USCAR, J. Carpenter, U.S. DOE, M. Fisher, American Plastics Council, keynote at the 2004 International Car Recycling Workshop, May 19, 2004, Washington D.C.
8. *Automotive Materials Recycling: A Status Report of U.S. DOE and Industry Collaboration*, E. J. Daniels, Ecomaterials and Ecoprocesses, Proc. of the International Symposium on Ecomaterials and Ecoprocesses, August 24–27, 2003, Vancouver, BC, Canada, pp. 389–402.
9. *Effects of Transportation on the Ecosystem*, J. A. Carpenter Jr., Ecomaterials and Ecoprocesses, Proc. of the International Symposium on Ecomaterials and Ecoprocesses, August 24–27, 2003, Vancouver, BC, Canada, pp. 13–22.
10. *Automotive Technology: Looking Forward*, R. Sullivan, D. Hamilton, and J. A. Carpenter, Jr., Ecomaterials and Ecoprocesses, Proc. of the International Symposium on Ecomaterials and Ecoprocesses, August 24–27, 2003, Vancouver, BC, Canada, pp. 49–67.
11. *A Roadmap for Recycling End-of-Life Vehicles of the Future*, prepared by Energetics for the U.S. Department of Energy, Office of Advanced Automotive Technologies (May 2001).

B. Baseline Assessment of Recycling Systems and Technology

Principal Investigator: Bassam Jody
Argonne National Laboratory
9700 S. Cass Ave., Argonne, IL 60439
(630) 252-4206; fax: (630) 252-1342; e-mail: bjody@anl.gov

Participants:
This project is conducted as part of the cooperative research and development agreement among Argonne National Laboratory; United States Council for Automotive Research's Vehicle Recycling Partnership, LLC; and the American Chemistry Council Plastics Division.

CRADA Partner Principal Investigators:
Claudia Duranceau, VRP, Ford Motor Co., (313) 390-0504; e-mail: cdurance@ford.com
John Haubert, VRP, Chrysler LLC., (248) 576-7458; e-mail: jah59@chrysler.com
Jacquiline Quinn, VRP, General Motors Corp., (586) 575-7078; e-mail: jacquiline.quinn@gm.com
James Kolb, ACC-PD, (248) 244-8920; e-mail: james_kolb@americanchemistry.com

Technology Area Development Manager: Joseph A. Carpenter
(202) 586-1022; fax: (202) 586-1600; e-mail: joseph.carpenter@ee.doe.gov

---

Contractor: Argonne National Laboratory (ANL)
Contract No.: DE-AC02-06CH11357

Objective

- Establish the baseline or state-of-the-art for automotive materials recovery/recycling technology.

Approach

- Review the state-of-the-art of worldwide automotive materials recovery/recycling technologies.
- Develop technology profiles of emerging automotive materials recycling technologies.
- Review international, federal, and state regulatory information regarding vehicle recyclability, substances of concern, and recycle laws and mandates.
- Conduct life-cycle studies to quantify the environmental burdens associated with various end-of-life recycling technologies.
- Conduct reference case end-of-life recyclability studies.

Accomplishments During This Reporting Period (10/1/07–9/30/08)

- Work on this project was deferred in the later part of fiscal year (FY) 2008 in favor of supporting the shredder who is building the 20 ton/hr validation plant. Accomplishments are:
  - — Updated the data base of recycle technologies.
  - — Compiled data for updating the document reviewing technologies for recycling shredder residue.
  - — Complete the life cycle analysis model for the automotive recycling infrastructure

Prior Accomplishments

FY 2007

- Updated the data base of recycle technologies.
- Initiated the life cycle study of current shredding operations.
- Prepared and published the document reviewing technologies and the state-of-the-art for recycling shredder residue.

FY 2006

- Completed compilation of recycle bibliography, structured as a pull-down PDF file, posted on US End-of-Life (ELV) CRADA Team website http://www.es.anl.gov/Energy_systems/CRADA_Team_Link/Index.html
- Completed Changing World Technologies (CWT) life-cycle case study.
- Completed life-cycle study of ANL process technology.
- Completed second draft of state-of-the-art assessment in recycling of vehicles and automotive materials.

FY 2005

- Conducted a literature search that identified mechanical, thermo-chemical conversion, and energy recovery technologies and completed first draft of state-of-the-art assessment.
- Completed Salyp life-cycle case study, initiated CWT life-cycle case study.

FY 2004

- Compiled and structured recycle bibliography.
- Characterized North American recycle infrastructure.
- Conducted a review of U.S. regulatory issues.
- Initiated life-cycle studies of end-of-life recycle technologies (Salyp case study).
- Completed reference recyclability calculations for reference cases and three lightweight alternatives: lightweight steel, composite materials, and aluminum (Al).

Future Direction

- The focus of this task in future years will be on:
  - — Updating the data base of recycle technologies.
  - — Updating the document reviewing technologies and the state-of-the-art for recycling automotive materials with emphasis on lightweighting metals [Al, magnesium (Mg), and titanium (Ti)].
  - — Conduct life-cycle and sustainability studies of lightweighting automotive materials.

Introduction

The objectives of this project are to (1) benchmark the automotive materials recycling industry and (2) compile information in an accessible format regarding the status of existing and emerging recycling technology and research.

The focus of the work under this activity is (1) to develop the tools and document the information necessary to make effective decisions relative to technology needs to facilitate sustainable future vehicle recycling and (2) to make effective decisions regarding allocation of research and development (R&D) resources.

The state-of-the-art of worldwide automotive materials recovery/recycling technologies and associated resource recovery infrastructures has

been reviewed to identify technology gaps and needs and to identify differences in automotive recycling strategies among the North America, Europe, and Asia. Technologies that are included in this review include, but are not limited to, post-shred materials-recovery technologies, pre-shred materials-recovery technologies, materials-identification technologies, automated-dismantling technologies, technologies for the recycling of specific components of vehicles (such as bumpers), and thermochemical conversion technologies.

Life-cycle analyses of alternative recycle technologies have also been conducted to identify differences between technologies, such as mechanical recycling vis-à-vis thermochemical recycling, relative to energy and environmental benefits.

Regulations at the international, federal, and state levels are examined to identify the impact that proposed and existing regulations may have regarding recycling of automotive materials.

Reference-case recyclability calculations are made to quantify the expected recyclability of alternative vehicle designs.

Infrastructure

The North American recycling infrastructure has been characterized and a representative Figure was shown in previous annual reports.

Technology Profiles

The recent literature has been reviewed, and summaries and profiles of available and emerging recycle technologies have been compiled into a draft working document and will be updated annually as new information becomes available.

- A bibliography of abstracts of papers that discuss automotive recycling issues has been compiled (Table 1). The bibliography is organized in fifteen sections.

The bibliography was compiled from an extensive literature search, which included reviewing the following sources:

1. Society of Automotive Engineers (International) World Congresses from 1997 to 2007
2. Environmental Sustainability Conference and Exhibition, 2001
3. Society of Plastics Engineers:
   - (International) Automobile Recycling Congress (ARC) from 1998 to 2000
   - Global Plastics Environmental Conference (GPEC) from 2002–2007
4. Other conference proceedings:
   - International Automobile Recycling Congress from 2001 to 2006
   - The Minerals, Metals, and Materials Society (TMS) Fourth International Symposium of Recycling of Metals and Engineered Materials, 2000.
   - Ecomaterials and Ecoprocesses, The Conference of Metallurgists, COM 2003

Table 1. Citations included in the recycling bibliography.

Bibliography Section	Number of Citations
Recycling infrastructure	20
Design for recycling	5
Legal and regulatory issues	23
Life-cycle analysis	12
Research programs	11
Substances of concern	5
Disassembly technologies and case studies	12
Reuse of automotive parts and subassemblies	1
Remanufacturing	0
Mechanical separation technology	20
Thermochemical conversion technology	14
Energy recovery technology	11
Advanced materials recycle technology	9
Other technology	40
Case studies of materials recycled for auto applications	23
Total citations	206

The bibliography has been posted on the US ELV CRADA Team website: http://www.es.anl.gov/Energy_systems/CRADA_Team_Link/Index.html

More references will be added to the bibliography as they become available.

Recycling Technologies: State-of-the-Art

The final document has been published and has been posted on the U.S. ELV CRADA Team website: http://www.es.anl.gov/Energy_systems/CRADA_Team_Link/Index.html. Because post-shred residue contains residue from shredded white goods and other obsolete items (in addition to vehicles), these were also discussed in the document.

Regulatory Situation

The European Union has issued End-of-Life Vehicle Recycle Directives. The enforcement of these directives is, however, the responsibility of each member state. Although the United States has not developed a federal policy or mandate, regulations at the federal and state level can impact the technology needs for recycling automotive materials. For example, U.S. Environmental Protection Agency (EPA) regulations regarding polychlorinated biphenyl (PCB) limits the concentration of PCBs on recycled materials to below the detectable limit (i.e., 2 ppm). State regulations regarding other substances of concern such as mercury and polybrominated diphenyl ethers (PBDEs) can impede materials recycling. Nickel, lithium, and cobalt, which will be used in electric batteries for hybrid and plug-in vehicles, could also impact materials recycling and will have to be recycled themselves to prevent sharp increases in their prices.

Life-Cycle Studies

The objective is to use life-cycle analysis to assess the environmental impacts of various separation and alternative end-of-life recycling technologies. This information will then be used to create a flexible, computerized life-cycle inventory model, which is process-specific and yet can be modified to include additional recycling technologies and various material inputs. Life-cycle involves assessing all of the upstream burdens associated with the production of the materials and energies used in the process, including the transport of all materials to the facility.

PE Europe GmbH, a company that is experienced in conducting life-cycle assessments and in model development using its own GaBi (Ganzheitliche Bilanzerung) software, was contracted to perform these analyses. Four analyses have been completed for: (1) Salyp NV's mechanical separation process, (2) CWT's thermal conversion process, (3) ANL's mechanical and froth-flotation process, and (4) automotive recycling infrastructure analysis.

The CRADA team is planning to conduct a study where late-model vehicles will be shredded in a new shredder that is being built at this time. Older vehicles will then be shredded followed by shredding a normal mix of materials. This study is expected to take place on October 4th, 2008 and data analysis will be completed in February, 2009. Data generated from this study will be used to update the life-cycle study of current automotive recycling operations.

PE Europe has developed a flexible end-of-life model which was used to compare the two different approaches to recycling shredder residue. The model allows the user to run simulations on shredder-residue separation within different boundary conditions. The following boundary conditions can be modified: (1) shredder-residue composition, (2) location of the facility, (3) type and distance of transportation, (4) market values for the separated fractions, (5) new potential applications for separated fractions, and (6) utilization ratio of the facility.

Salyp's separation process combined equipment developed by ANL and several others to create a facility that separates shredder residue into discrete fractions of metals, foam, mixed plastics, and fiber-rich and fines streams. On the other hand, the CWT process converts organic materials into hydrocarbon fuels and other potential products.

Data were collected for each analysis, including all energy, water, and material inputs, plus data on emissions to air and water, wastes, and products produced. The four sets of data were entered into

the GaBi software to create a flexible model of the process.

In the case of the Salyp separation process, three different scenarios for handling the various materials recovered from shredder residue were determined. These scenarios included using specific material fractions as fuel for cement kilns (energy recovery), as well as using mixed plastics to replace such products as wood pallets and polypropylene (PP) pellets (material substitution). The various scenarios were assessed by using a variety of impact categories, including primary energy demand and CO_2 emissions. In the case of primary energy demand, all scenarios showed a net credit in total energy use. For the three scenarios studied, substituting recovered polypropylene/polyethylene (PP/PE) in a new PP application had the greatest benefit. However, if the mixed plastic stream were used to replace wood (e.g., decking material, park benches, wood pallets, etc.), the benefits to primary energy demand were less than if the recovered materials were simply used for energy recovery. In terms of CO_2 emissions, the PP application again showed the greatest benefit. Substituting PP for wood applications was next with a lower benefit, while the energy-recovery scenario showed an increase in CO_2 emissions.

In the case of the CWT process, two basic scenarios were assessed. They involved using the light hydrocarbon oil generated by the process for fuel oil used in power plants to generate electricity and substituting light hydrocarbon oil for diesel oil (both with and without an added hot-oil processing step). While the oil product generated is more refined than an actual crude oil, it would require additional steps before it could be considered a true diesel oil. Therefore, reality is probably located somewhere between scenarios 1 and 2. In this study, the impact on primary energy demand resulted in a benefit in all cases. The benefits in the diesel-substitution case were slightly greater than in the fuel oil case. In the case of CO_2 emissions, all scenarios again showed an overall benefit. However, the diesel- substitution case had a greater benefit than the fuel-oil substitution case.

Life-cycle analysis of the ANL process considered both the mechanical separation of the shredder residue to produce a polymer concentrate and recover residual metals, followed by froth flotation to separate plastics from the polymer concentrate for recycling as plastics (material substitution). The analysis concluded both the mechanical and the froth-flotation processes resulted in environmental benefits, Figure 1. The environmental benefits of the ANL process were also compared with those of the Salyp (Table 2) and CWT processes (Table 3). The environmental benefits are higher for the ANL process compared to the Salyp process except for the acidification potential and higher for the ANL process compared to the CWT process except for the impact category EP and NO_x emissions. Energy-wise the ANL process was the most advantageous. Interestingly, the analyses concluded that the best results can be obtained by combining both (ANL and CWT) processes, where organic fractions separated by ANL which do not meet the requirements for material substitution (such as mixed plastics and rubber by-products) are processed by CWT for fuel production.

A life-cycle analysis model for the automotive recycling infrastructure was also completed. This model will facilitate the analysis of various automotive recycling technologies and compare their performance.

Recyclability Studies

Recyclability studies were conducted to examine the effect of using automotive lightweighting material on recyclability. A Toyota Prius hybrid was selected as a reference case. This vehicle is a second-generation hybrid with a gas/electric powertrain. Evaluating the recyclability of this vehicle and its new technology will be a step in identifying changes that will impact end-of-life recycling of vehicles of the future.

In collaboration with Johnson Controls, Inc. (JCI), the VRP dismantled the vehicle according to VRP procedures to single material components and entered data for each part into a database. A material list that identified the breakdown of materials into separate classifications (such as ferrous and nonferrous metals, as well as composite materials and plastics) was prepared.

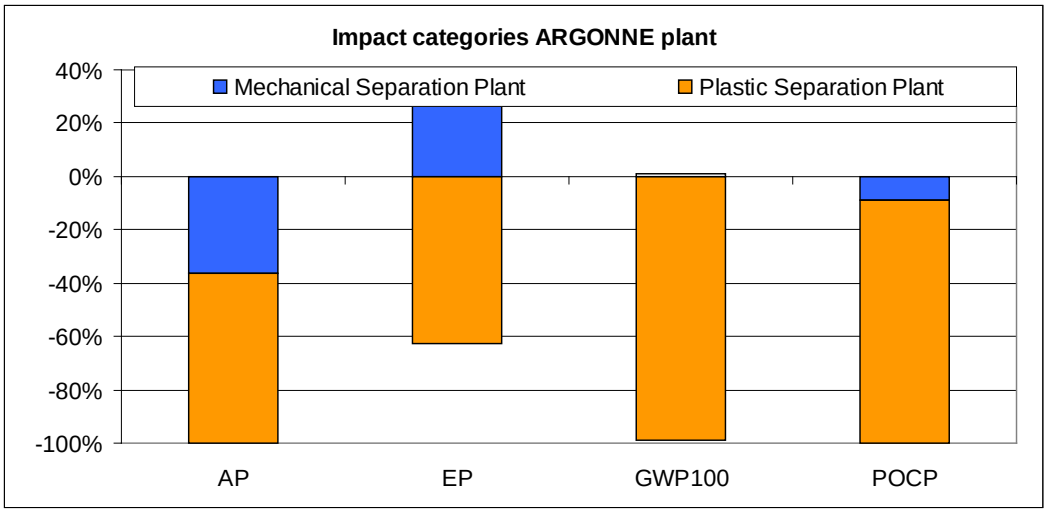

Figure 1. Impact Categories of the ANL Plant. (AP is acidification potential, EP is eutrophication (depletion of oxygen in water) potential, GWP is global-warning potential and POCP is photochemical ozone creation potential). [Y axis indicates increase (+) or decrease (-) in the impact of the different categories].

Table 2. Comparison of the ANL and Salyp processes—Relative Environmental Impact. [A negative value indicates a reduction in the pollution category (an environmental benefit) while a positive value indicates an increase in the pollution category.]

	ANL process (mechanical and Froth Flotation)	**Salyp process**
AP [lb SO2-Equivalent.]	–0.0060	–0.0165
EP [lb Phosphate-Equivalent.]	–0.00011	0.00148
GWP100 [lb CO2-Equivalent.]	–1.354	0.861
POCP [lb Ethene-Equivalent.]	–0.0026	0.0126

Table 3. Comparison of the ANL Froth-Flotation and CWT processes—Relative Environmental Impact. Both processes require mechanical separation of the inorganic fraction. [A negative value indicates a reduction in the pollution category (an environmental benefit) while a positive value indicates an increase in the pollution category.]

	ANL process (Froth Flotation[a])	**CWT process**
AP [lb SO2-Equiv.]	-0.01103	-0.00662
EP [lb Phosphate-Equiv.]	-0.00055	-0.00079
GWP100 [lb CO2-Equiv.]	-4.167	-0.309
POCP [lb Ethene-Equiv.]	-0.0088	-0.0044

[a]Comparison is done here only with the froth-flotation process because both ANL's froth-flotation process and CWT's process require mechanical separation of the inorganic materials.

The materials breakdown is summarized in Table 4. In comparison, the materials composition of a production Ford Taurus is summarized in Table 5.

Table 4. 2004 Toyota Prius materials breakdown.

Materials	Mass (lb)	%
Ferrous metals	1713	60.6
Nonferrous metals	507	17.9
Plastics	341	12.1
Elastomers	87	3.1
Inorganic material	77	2.7
Other	62	2.2
Organic materials	42	1.5
Vehicle mass (less fluids)	2829	100.0

Table 5. 2004 Ford Taurus materials breakdown.

Materials	Mass (lb)	%
Ferrous metals	2223	70.4
Plastics	340	10.8
Nonferrous metals	312	9.9
Elastomers	152	4.8
Inorganic material	90	2.9
Other	38	1.2
Organic materials	4	0.1
Vehicle mass (less fluids)	3159	100.0

Three different recyclability calculations were made (Table 6). The Federal Trade Commission (FTC) recyclability number is the percentage by weight of the material that is currently being recycled; it includes metals, fluids less fuel, and batteries. The European guidelines include FTC materials plus fuel at 90% of a full tank, plastics that could be recycled, and up to 10% by weight energy recovery. Note that Europe requires 95% recyclability for new vehicles. The feasibility-to-recycle number includes the FTC materials plus plastics that can be recycled. Changes to the current infrastructure would be required to increase recycling beyond the current FTC percentage.

To establish an indication of the impact of lightweight materials on the reference case recyclability calculations, the 2004 Toyota Prius is compared with a proposed Al-intensive lightweight vehicle and a proposed composite lightweight vehicle, both of which are also based on the 2004 Prius. The production 2004 Toyota Prius hybrid vehicle body was steel with an Al hood and decklid. The suspension was of steel except for an Al steering knuckle on the front suspension. This vehicle was used as the base for this study.

Table 6. Reference case recyclability: 2004 Toyota Prius.

Calculation Method	Recyclability %
Federal Trade Commission	80.86
European	97.61
Feasibility of recycling	85.58
Ref. 2000 Ford Taurus	80.50

The Al alternative is for a 2004 Toyota Prius with an Al body and a Mg engine cradle and a rear axle substituted for the production parts. In addition, seat frames, body brackets, and the instrument panel cross-car beam have been changed from steel to Al. As a result, the weight has been reduced by approximately 630 lb or 21%. Because the weight reduction is entirely in the currently recycled portion of the vehicle, the recyclability is adversely affected and is reduced from 80.86% to 76.10%. No changes were made to the currently non-recycled portion of the vehicle. Al replaced steel at 50% by weight of the original steel.

The composite alternative is for a 2004 Toyota Prius that consists of (1) a carbon-fiber body with 40% carbon fiber and 60% thermoset polyurethane/urea resin by volume, 49.72% carbon, and 50.28% thermoset polyurethane/urea resin by weight and (2) a Mg engine cradle and rear axle substituted for the production parts. In addition, seat frames, body brackets, and the instrument panel cross-car beam have been changed from steel to composite. As a result, the weight has been reduced by approximately 711 lb, or 24%. Because the weight reduction is entirely in the currently recycled portion of the vehicle, the recyclability is adversely affected and is reduced from 80.86% to 57.20% if none of the composite is recycled or 74% if all of the composite material is recycled. No changes were made to the currently non-recycled portion of the vehicle. The

composite material replaced steel at 40 wt% of the original steel.

There are reductions in all three recyclability calculations for lightweighted vehicles, even though the rest of the vehicle is not changed (Table 7). Where the Al and composite material is being recycled, the same amount of material would be disposed of in landfills in each of the three scenarios. The only difference is that the recycled portion of the lightweighted vehicles would be lighter. Although the recyclability would be less, there would be no difference in the amount of material disposed of in landfills, and the lighter vehicles would use less fuel during their life. As can be seen, lightweighting presents challenges in the European market. Note that these calculations do not take into account the downsizing of related components that would accompany any lightweight vehicle, such as powertrains, brakes, and tires. Because the downsized components are high in metallic content, downsizing will further reduce recyclability and make it difficult to meet the European 95% requirement.

Table 7. 2004 Toyota Prius recyclability, reference case vs aluminum and composite body materials.

Calculation Method	As Produced (%)	Aluminum Body (%)	Composite Body (%)
FTC	80.9	76.1	74.0[a]
European	97.6	96.0	94.5[a]
Recycling feasibility	88.3	85.6	83.9[a]

[a]If the composite material were not recycled, then the numbers would be FTC, 57.2%; European, 78.2%; and feasibility of recycling, 67.1%. Recycling of the composite material would require significant changes in the current recycling infrastructure. In addition, a market for the recycled carbon fibers would need to be developed. Current technology for recycling carbon fibers results in a 20% loss in fiber properties and would limit their reuse to short fiber applications.

In conjunction with this study, additional evaluations are planned by using these data as a starting point for assessing the recyclability of cars of the future. The impact of vehicle lightweighting and material selection on recyclability will be evaluated. In addition, the impact of powertrain changes in future vehicles (including hybrid and fuel cell alternatives) on recyclability will be determined in comparison to powertrains in current vehicles. An assessment of various alternatives on recycling and the effect on the current recycling infrastructure will be produced. No downsizing of other components was included in this study. Future studies will reflect the downsizing of powertrains, brakes, tires, and other components in recyclability calculations. Items requiring further study resulting from these assessments will support future projects to determine the feasibility of various alternative vehicle configurations and choices of materials.

These results demonstrate the need for technology to recycle lightweighting automotive materials if recycling mandates are to be met and to ensure that lightweighting materials are not excluded because of the inability to recycle them.

It is interesting to point out that even if the lightweighting metals that replace steel and iron are recycled at the same rate as the present rate of recycling steel and iron, the overall recyclability rate of the obsolete vehicle will decrease because the relative weight of the metals in the vehicle will decrease. Therefore, in order to maintain high vehicle recycling rates it is important that non-metallic materials that are presently not recycled, such as polymers, be recycled.

Publications

1. *A Life Cycle Look at Making Oil From End-of-Life Vehicles*, C. S. Wheeler, N. L. Simon, M. Binder, G. R. Winslow, and C. M. Duranceau, SAE 2006 World Congress, Detroit, Michigan, 2006. SAE-2006-01-0374.
2. *Modular Life Cycle Model—Basis for Analyzing the Environmental Performance of Different Vehicle End-of-Life Options*, M. Binder, N. L. Simon, C. M. Duranceau, C. S. Wheeler, and G. R. Winslow, Proc. of the 5th International Automobile Recycling Congress, Amsterdam (Mar. 9–11, 2005).

3. *Modular Life Cycle Model of Vehicle End-of-Life Phase—Basis for Analysis of Environmental Performance*, C. S. Wheeler, N. L. Simon, C. M. Duranceau, G. R. Winslow, and M. Binder, SAE Paper 2005-01-0847.

4. *United States National Life Cycle Inventory Database Project, A Status Report*, J. L. Sullivan, C. S. Wheeler, and N. L. Simon, SAE Paper 2005-01-0852.

C. Development of Technology for Removal of PCBs and Other Substances of Concern from Shredder Residue

Principal Investigator: Bassam J. Jody
Argonne National Laboratory
9700 S. Cass Ave., Argonne, IL 60439
(630) 252-4206; fax: (630) 252-1342; e-mail: bjody@anl.gov

Participants:
This project is conducted as part of the cooperative research and development agreement among Argonne National Laboratory, United States Council for Automotive Research's Vehicle Recycling Partnership, LLC, and the American Chemistry Council Plastics Division.

CRADA Partner Principal Investigators:
Claudia Duranceau, VRP, Ford Motor Co., (313) 390-0504; e-mail: cdurance@ford.com
John Haubert, VRP, Chrysler LLC., (248) 576-7458; e-mail: jah59@chrysler.com
Jacquiline Quinn, VRP, General Motors Corp., (586) 575-7078; e-mail: jacquiline.quinn@gm.com
James Kolb, ACC-PD, (248) 244-8920; e-mail: james_kolb@americanchemistry.com
Steve Niemic, The Polyurethane Recycle and Recovery Council (PURCC), (734) 479-4927; email: sfniemiec@wowway.com

Technology Area Development Manager: Joseph A. Carpenter
(202) 586-1022; fax: (202) 586-1600; e-mail: joseph.carpenter@ee.doe.gov

---

Contractor: Argonne National Laboratory (ANL)
Contract No.: DE-AC02-06CH11357

Objective

- Develop viable strategies and technology for the control and minimization or elimination of polychlorinated biphenyls (PCBs) and other substances of concern (SOCs) from recycled automotive materials.

Approach

- Identify efficient and environmentally-acceptable process solutions for removal of contaminants, including PCBs, from materials recovered from shredder residue.
- Define variances in analytical procedures/test results for PCB analysis.

Accomplishments During This Reporting Period (10/1/07–9/30/08)

- Tests were conducted on ANL's two-stage process using a 5 lb reactor.
- Conducted swipe tests on auto parts made with polyolefins recovered from shredder residue.
- ECO_2 conducted tests using their proprietary process.
- Midland Compounding/Energy Anew conducted vacuum de-volatilization tests in a twin-screw extruder to explore removal of PCBs.
- Tests were conducted on a proprietary process developed by an independent organization.

Prior Accomplishments

FY 2007

- Additional bench-scale testing of ANL's two-stage cleaning process was conducted. The testing consistently produced plastics from the polypropylene (PP)/polyethylene (PE) product with <2 parts-per-million (ppm) PCBs.
- Tested new methods to clean the plastics and remove the PCBs including:
  - Conducted preliminary testing of a proprietary process developed by an independent organization.
  - A catalytic process tested at ANL.
  - Cleaning using a bio-degradable solvent.
- Developed a design for an apparatus to test ANL's two-stage process at a larger scale (15–25 lb/h). Quotes for the major system components were obtained.
- Hosted and participated in forums and seminars on SOCs including perfluorooctanoic acid (PFOA)/ perfluorooctanesulfonates (PFOS), brominated fire retardants, and emerging lead- and mercury-free technologies.

FY 2006

- ANL developed a two-stage cleaning process which, in bench-scale tests, consistently produced plastics from the PP/PE product with <2 ppm PCBs.
- Completed tests in the commercial solvent washing equipment using proprietary, solvent-based solutions and in CO_2.
- Cooperated with the Bromine Science and Environmental Forum (BSEF) in preparing the BSEF brochure entitled "Deca-BDE Flame Retardant."

FY 2005

- Completed the study to explain discrepancies in PCBs analytical results.
- Initiated testing of commercial solvent washing processes for cleaning plastics.
- Conducted a study to understand the interactions between PCBs and plastics.
- Identified and initiated testing of alternative methods for PCB removal.

FY 2004

- Completed the solvent/detergent screening study for removing PCBs and heavy metals from plastics.
- Completed aqueous cleaning tests in commercially-available equipment.
- Initiated a study to explain discrepancies in PCBs analytical results.

Future Direction

- Determine the scalability and economics of ANL's two-stage process.
- Develop a conceptual design and perform cost analysis of the ANL process.
- Incorporate the process into the overall process design for recovering materials from shredder residue.
- Continue testing at ECO_2 using their proprietary process.

- ANL's two-stage process has successfully produced recovered plastics, at least PP/PE materials, with less than 2 ppm PCBs in multiple tests. Operational problems including sticking of the plastics to the walls of the reactor have been encountered in the larger-scale tests. Granulation of the desorbed plastics is also required. Further evaluation is necessary to investigate the scalability of the process and to establish its final flow diagram and economics.

Introduction

The objective of this project is to develop techniques and/or technology to identify, quantify, and/or cost-effectively remove PCBs and other SOCs from recycled automotive materials.

SOCs can impact the recyclability of automotive materials in a number of ways. Certainly, their presence in either recycled materials and/or materials source streams impact the overall costs of recovering recyclable materials. In some cases, their presence at parts-per-million levels, such as in the case of PCBs, can prevent the reuse of the recovered materials.

The strategy that is required for control of the SOCs may vary regionally. For example, requirements are different in Europe, North America, and Asia for various SOCs. Strategies for controlling SOCs can also depend on the technology used for recycling the automotive material and the materials end use.

The presence of SOCs in vehicles and/or in other durable goods that are presently recycled with end-of-life vehicles (ELVs) is likely to continue to impact the materials-recycle stream for the foreseeable future. Consequently, the control of certain SOCs will require technologies that will effectively remove the SOCs from recovered materials consistent with current regulatory requirements and consistent with the market requirement for the recovered material.

Other materials that have been used in automobiles could also become SOCs in the near future. Examples include some of the brominated fire retardants.

The focus of the work in this project is on the development of technology for the removal of PCBs from potentially recyclable materials recovered from shredder residue. PCBs, at ppm levels, are routinely found in shredder residue. The source of the PCBs is not completely understood, but historically it has been associated with liquid PCB-containing capacitors, ballasts, and transformers that inadvertently escape the inspection and control process at the shredders. Unless PCBs are removed from the recovered materials, with the exception of metals, introducing the recovered materials into commerce will not be possible.

The criteria for the selection of a cleaning method must include (1) impact of the cleaning process on the properties and marketability of the polymers, (2) nature and cost of disposal of the waste generated by the process, and (3) overall cost of the cleaning process.

Development and Testing of a Two-Stage Process at ANL

The work done so far on cleaning of polymers recovered from shredder residue suggests that different washing methods and solutions appear to be able to reduce the PCBs concentration down to about 5–10 ppm in a reasonably short time. Further reduction in the concentration of PCBs requires more extensive and prolonged washing in fresh solution. In addition to added cost, prolonged washing, particularly in organic solvents, is further complicated by the absorption of the solvent by the plastics which may alter the properties and the value of the plastics.

This behavior of PCBs suggests that the PCBs on the plastics are removed by more than one mechanism. Some of the PCBs are in the oils and dirt that are on the plastics and some are adsorbed on the plastics and do not desorb easily during washing. This hypothesis was tested in the lab. Washing tests were conducted using several washing solutions and solvents including a non-flammable solvent to wash the plastics under conditions that minimized the absorption of the

solvent by the plastics. This reduced the concentrations of PCBs from about 30 ppm to about 5–10 ppm under a range of operating conditions. The washed plastics were then processed in an environment that induces desorption (high temperature with or without reduced pressure). The PCBs concentration was consistently reduced from 5–10 ppm to below 2 ppm. Tests were also conducted where unwashed samples were exposed to the same environment that induces desorption. The PCBs concentration could not be reduced below 2 ppm under the same operating conditions.

A two-stage process, based on this concept, has been developed and tested first at the bench scale at ANL and then in a 5 lb reactor that processed 5 lb of plastics per test. It has repeatedly reduced the PCBs concentration in PP/PE samples to less than 2 ppm. For example, at sufficient residence times and temperature conditions that do not cause the plastics to oxidize, the concentration of PCBs on the recovered polyolefins was reduced from about 32 ppm to as low as 0.58 ppm. A preliminary design for an apparatus to test this process at a larger scale (15–25 lb/h) was developed. Commercially-available equipment that could be adopted with modification to this process was identified. Quotes for some of the system components have been obtained. The design was changed after discussions with ANL's safety committee. It was then decided to run larger batch tests (5 lb per test). The apparatus, Figure 1, was designed and built and five tests were conducted. After completing the running of the first test, it was discovered that some of the polymers dissolved/ melted and, when the solvent was removed and the reactor cooled, the polymers stuck to the reactor walls. Samples of the processed polymers were sent for PCBs analysis and for properties analysis. It appears that this occurred due to localized heating in parts of the reactor.

This problem was resolved by modifying the experimental procedure including having better control of the heating system as well as better circulation of the solvent through the plastics. Four more tests were conducted without any of the material sticking to the reactor wall. The washed-and-rinsed samples were then transferred to a plastics drying oven at an elevated temperature to

Figure 1. Experimental apparatus for testing the ANL two-stage process.

desorb the residual PCBs from the plastics. Samples of the plastics after washing and rinsing as well as after desorption were sent for analysis. Samples were also sent for evaluating the mechanical properties of the cleaned plastics in order to determine if the cleaning process caused any degradation of the properties of the plastics. Results are pending.

Swipe tests were conducted on two auto parts made with recycled PP/PE recovered from shredder residue using acetone. The objective was to see if PCBs can leach from such parts. The procedure for the swipe tests involved first marking the area on which the test is to be performed and determining its surface area. The surface area was 1 ¾ in. × 2 ¾ in. on one object and 2 in. × 3 in. on the other object. The surface areas were then cleaned with soap and water and allowed to air-dry completely. A hexane wipe cloth was then removed from one of the jars that was provided and was used to generously wipe the denoted surface area. The hexane wipe cloth was then placed back in a jar and the jar was closed. The hexane wipe cloths were then sent for analysis. Analysis of the acetone-containing swipe cloth showed no detectable PCBs on the wipe cloths.

Testing of a New Proprietary Process

An independent organization tested a proprietary process that they developed for cleaning the plastics. Testing of the process was conducted and processed samples were analyzed. The results

were unsatisfactory and no further testing is planned.

Testing of a Catalyzed Ozonation/Ultra Violet (O_3/UV) Process

Preliminary testing of a catalyzed O3/UV process was conducted to determine if the PCBs can be selectively degraded. The initial results were not encouraging.

Testing of a Biodegradable Solvent Process

Tests using a biodegradable solvent were conducted to determine if this solvent can remove the PCBs. It was successful in reducing the concentration to about 10 ppm but further reduction to below 2 ppm did not appear likely. Testing using this solvent was discontinued because its effectiveness degrades when water is present.

Testing of a Devolatilization Process in a Vacuum Extruder

Midland Compounding/Energy Anew conducted a series of vacuum devolatilization tests on polyolefin samples recovered from shredder residue using a 30-mm twin-screw vacuum extruder. An experimental design was developed to test the impact of three variables on the PCBs removal process: screw speed (high, 300 revolutions per minute (rpm) and low, 100 rpm), feed rate (high, 20 lb/h and low, 10 lb/h), and temperature (high, 325°C and low, 250°C). A mid-point at 200 rpm, 15 lb/h, and 287°C with and without vacuum was also tested. The apparatus is shown in Figure 2. The results are summarized in Table 1. The results indicate that devolatilization alone was not sufficient to remove PCBs from the polyolefin blend. The IZOD property of the treated polymers did not change.

Additional tests were conducted at Midland Compounding where high-pressure water or water/glycol/NaOH were injected to help de-chlorinate and steam strip the polymer after the samples were first homogenized by extrusion and post-blending. The extruder was sectioned into three zones: high-pressure liquid injection, atmospheric vent, and then a vacuum vent. The samples were then run through the extruder under different conditions. Samples were sent for analysis and for property evaluation. The results are pending.

Figure 2. Extruder with die and vacuum knockout pot used in the devolatilization testing.

Table 1. PCBs and Impact Test Results from Vacuum Devolatilization Testing

Sample No.	Temp. °C	Screw RPM	Feed Rate lb/h	PCB 1242 ppm
1	325	300	20	18.2
2	325	300	10	13.6
3	325	100	20	16.9
4	325	100	10	16.2
5	287	200	15	12.4
6[a]	287	200	15	12.6
7	250	300	20	17.9
8	250	300	10	19.7
9	250	100	20	17.7
10	250	100	10	15.4
11[b]	287	200	15	21.4
12[c]	-	-	-	22.2

[a]No vacuum.
[b]Water at feed.
[c]Raw feed.

Testing at ECO_2 Plastics

A contract was also awarded to ECO_2 to conduct tests using their proprietary process. Phases 1–3 of testing have been completed and further testing is planned.

Evaluation and Testing of Solvent-Based Washing Systems

Three companies with equipment and/or proprietary washing solvents and solutions that could potentially be used for non-aqueous removal of PCBs from plastics were identified by Troy Polymers, Inc. (TPI):

- Environmental Technology Unlimited (Wilmington, North Carolina);
- Cool Clean Technologies, Inc. (Burnsville, Minnesota); and
- itec Environmental Group, Inc. (Oakdale, California).

Each company was supplied with a sample of plastics with the determined concentration of PCBs of 11 ppm. Samples were washed at the three companies, and the washed samples were evaluated for PCB levels.

Environmental Technology Unlimited performed six treatments of shredder-residue plastics, and five out of the six washed samples reduced the PCBs concentration to below 2 ppm. Unfortunately, the company does not have equipment to conduct large-scale testing of the process using plastics. Cool Clean Technologies technology used CO_2 only. The washing failed to remove the PCBs. itec Environmental Group (name changed to ECO_2) reduced PCB levels in the plastics from 11 ppm to 2.8 ppm via solvent washing; no CO_2 treatment, which normally follows the basic process, was used. Further testing was conducted by itec. The plastics were washed using itec's proprietary solvent and then with liquid CO_2. Two samples received by ANL were analyzed and both showed residual PCBs concentration on the order of 5 ppm. Another series of trials was conducted at different process conditions. The residual PCBs were still higher than 2 ppm.

Evaluation and Testing of Commercially-Available Aqueous-Based Washing Systems

Before testing the solvent-based systems, large-scale cleaning/washing tests were conducted using plastics from shredder residue using aqueous solutions and a surfactant. The objective was to identify the limitations of the various types of existing washing equipment. Testing was done using an ALMCO rotary-drum washer equipped with a dryer and SeKoN centrifuge equipment. The tests were carried out on about 100 lb of plastic chips each. The particles were between 0.2 and 0.5 in. in size. Under a CRADA contract, GraPar Corporation built for TPI and tested a specially-designed machine that has a design capacity of about 300 lb/h of plastics. TPI conducted further testing on this machine in its facilities.

In each of these tests, the washed material was "visually" clean. However, PCBs analyses were highly variable and indicated that, in some cases, the PCBs concentration had increased after washing. As a result, it was determined that the PCBs analysis procedures should be reexamined, as is discussed in the next section. The results suggest that existing aqueous-based equipment, as is, is not likely to reduce the concentration of PCBs to acceptable levels.

Evaluation of the Variability of PCB Sampling and Analytical Procedures

Experiments were performed to explain the variability in the results and to develop a consistent procedure for the determination of the concentration of PCBs.

The variability may be due to a number of factors including sample size, plastics particle size, PCBs-extraction procedure, analytical procedures, and/or interference from other compounds. A one-day seminar was held and attended by analytical experts from the United States and overseas to develop recommendations for improved sampling and analysis techniques specific to plastics chips.

To investigate the possible interference of phthalates in the PCBs analysis, a sample of plastics chips derived from shredder residue was thoroughly mixed and then divided into four parts. The first part was analyzed by using gas chromatography and an electron-capture detector (GC-ECD) and by using gas chromatography/mass spectroscopy (GC/MS). The other three parts were spiked with different quantities of phthalates, as shown in Table 2, and the spiked samples were

Table 2. Effect of phthalates on PCBs analysis

Weight-Percent of Phthalates added	PCBs Concentration (ppm) by GC-ECD	PCBs Concentrations (ppm) by GC/MS
0	4.6+/-0.3	7.9+/-1.0
0.5	4.7+/-0.3	7.4+/-0.2
1.0	5.1+/-0.6	7.0+/-0.4
2.5	4.8+/-0.3	7.4+/-0.3

analyzed by using the same two methods. The results show no interference of the phthalates in the PCBs analysis. Interestingly, the GC/MS results were always higher than the GC-ECD results.

To investigate the effects of plastics particle size on extraction efficiency of PCBs, a series of laboratory experiments were conducted at TPI on 300-g samples of plastics with two different particle sizes (one made of chips about 0.2 in. in size and the other was granulated to about 0.04 to 0.08 in. in size). Typically in PCBs analyses, extractions are done on a few grams of material, even though the dirt, oil, and the PCBs are not evenly distributed on the shredder residue plastics.

Samples of the plastics before and after washing were analyzed directly by three different laboratories by using standard PCBs analytical procedures. Extracts from nine sonications of 300-g samples were also analyzed for PCBs by three laboratories. The results show that:

1. The results from the three labs are fairly consistent for each set of samples.
2. Direct analysis of the samples from the three labs showed that the concentration of PCBs in the granulated plastics was about 5 ppm, and for the un-granulated, it was 10 ppm. Obviously, the granulated samples have larger surface area per unit mass than the other samples. Therefore, more efficient extraction of PCBs from the plastics would be expected in the case of the granulated chips. Because this was not the case, the results indicate that the particle size does not affect the PCB results. After extraction, the samples all had less than 2 ppm of PCBs, except for one sample that showed 2.8 ppm.
3. Calculation of the concentration of PCBs in the original samples based on the determined PCBs in the hexane extracts (prepared via nine sonications of 300-g samples) showed that the concentrations of PCBs in the granulated samples were comparable with those of the un-granulated samples.
4. These results further indicate that the PCBs are predominantly on the surface and not absorbed in the plastics, otherwise the granulated samples would have shown higher concentrations.

Two of the labs identified Aroclor 1242 as the only PCB present. The third found Aroclors 1232 and 1254 as the only two present. TPI also conducted an analysis of various plastics samples by using GC-ECD and GC/MS methods. The results are compared in Table 3. Results from the two methods are in reasonable agreement, even though the GC-MS method showed higher values.

Evaluation of Soxhlet Method for PCBs Extraction

Successful commercialization of technology for recovering polymers from shredder residue depends on a reliable and inexpensive technique to analyze samples for PCBs in the field. The U.S. Environmental Protection Agency (EPA) and European protocols for PCBs analysis were reviewed and experiments were conducted to understand the requirements for on-site analysis. A Soxhlet-based method appears to be appropriate for testing because of its simplicity and because it is among the methods specified in both the U.S. EPA protocols and in the European protocols (Table 4). Limited experiments to define the operating conditions for the Soxhlet method were conducted. The results are discussed below.

Selection of a Solvent

Two solvents were tested: hexane and toluene. Three 120-g samples were extracted with hexane for 8 h, and another three 120-g samples were extracted with hexane for 24 h. Similarly, three 120-g samples were extracted with toluene for 8 h, and another three 120-g samples were extracted with toluene for 24 h. All extractions were carried

Table 3. PCBs analysis using GC-ECD and GC/MS [extraction using hexane at 2,000 pounds per square inch absolute and 100°C]

Sample Type	PCB Concentration, Using GC-ECD (ppm)	PCB Concentration, Using GC-MS (ppm)
Ungranulated Chips	7.55	9.67
Ungranulated Chips	3.70	5.07
Ungranulated Chips	1.50	3.3
Ungranulated Chips	1.35	2.66
Granulated Chips	7.56	9.37
Granulated Chips	0.93	1.82
Granulated Chips	0.82	2.11
Hexane Solution	9.93	9.50
Hexane Solution	8.3	11.13
Hexane Solution	1.41	1.72
Hexane Solution	0.78	0.92
Hexane Solution	0.53	0.65

Table 4. Protocols for PCBs analysis

Parameter	European Protocols	U.S. EPA's Protocols	Recommended Protocols
Particle size (mm)	0.5	Not specified	1
Sample size for extraction (g)	3	30	30
Extraction equipment	Soxhlet	Sonication Soxhlet Pressurized fluid	Soxhlet
Extraction time	Not specified	Not specified	>/= 4 h Siphoning cycles at 8–10-min intervals
Solvent	Toluene	Hexane 50/50 Hexane/acetone 50/50 Methylene chloride/acetone	Hexane
Analytical method	MS	GC-ECD MS	MS
Quantification method	6 congeners multiplied by 5	Aroclors	Aroclors

out while maintaining the siphoning time at 8–10-min intervals. This procedure resulted in 24 samples of extracts and 12 samples of extracted plastics that were analyzed. The results indicated that hexane is a better solvent than toluene.

Determination of Extraction Time

Three additional 120-g samples were extracted with hexane for 4 h each. This procedure resulted in six samples of extracts and three samples of extracted plastics that were analyzed. The results indicate that a Soxhlet extraction time of 4 h is adequate because it reduced the PCBs concentration in the extracted plastics to below the detectable limits in two of the three samples and reduced it in the third to 1 ppm, even though these samples apparently had more PCBs initially as evidenced by the higher level of PCBs in the solvent.

Determination of Adequate Sample Size

In addition to the six 120-g samples extracted for 24 h discussed above, six 60-g samples and six 30-g samples were processed and sampled in the same manner as before (24-h extraction time and same siphoning intervals) by using hexane. The results indicate that a 30-g sample size appears to be adequate.

Comparison of the U.S. EPA and the European Quantification Methods

Four of the extracts from the 120-g samples that were extracted with hexane for 24 h and two of the 120-g samples that were extracted with hexane for 8 h were also quantified by using the European method. The results were essentially identical within analytical errors (Table 5).

Table 5. Comparison of the U.S. EPA and the European quantification methods

Extract Time (h)	PCBs (ppm)	
	EPA method	European method
24	10.8	9.8
24	9.8	10.9
24	8.0	10.7
24	11.2	11.5
8	11.7	12.3
8	10.8	10.8

These results lead to the following conclusions.

1. A conventional Soxhlet extractor using hexane is effective for PCBs extraction from plastics.
2. A total extraction time of 4 hours with siphoning intervals of 8–10 min is adequate for complete extraction of the PCBs.
3. The EPA and the European quantification methodologies yield close results.

Other Accomplishments

Because of potential concern over other SOCs, the VRP hosted and participated in forums and seminars on several related topics including PFOA/PFOS, brominated fire retardants, nickel, and emerging lead- and mercury-free technologies.

Publications

1. *Overview of Washing Systems for Commercial Cleaning of Plastics Separated from Automotive Shredder Residue*, I. Sendijarevic, V. Sendijarevic, G. R. Winslow, C. M. Duranceau, N. L. Simon, S. F. Niemiec, and C. S. Wheeler, SAE Paper No. 2005-01-0851.
2. *Screening Study to Evaluate Shredder Residue Materials*, V. Sendijarevec, N. Simon, C. Duranceau, G. Winslow, R. Williams, C. Wheeler, S. Niemiec, and D. Schomer, SAE Paper No. 2004-01-0468.

D. Post-Shred Materials Recovery Technology Development

Principal Investigator: Bassam Jody
Argonne National Laboratory
9700 S. Cass Ave., Argonne, IL 60439
(630) 252-4206; fax: (630) 252-1342; e-mail: bjody@anl.gov

Participants:
This project is conducted as part of the cooperative research and development agreement among Argonne National Laboratory; United States Council for Automotive Research's Vehicle Recycling Partnership, LLC; and the American Chemistry Council Plastics Division.

CRADA Partner Principal Investigators:
Claudia Duranceau, VRP, Ford Motor Co., (313) 390-0504; e-mail: cdurance@ford.com
John Haubert, VRP, Chrysler LLC., (248) 576-7458; e-mail: jah59@chrysler.com
Jacquiline Quinn, VRP, General Motors Corp., (586) 575-7078; e-mail: jacquiline.quinn@gm.com
James Kolb, ACC-PD, (248) 244-8920; e-mail: james_kolb@americanchemistry.com

Changing World Technologies is cost-sharing on the evaluation of its thermal depolymerization process. The Polyurethanes Recycle and Recovery Council is also participating and cost-sharing on the evaluation of the Troy Polymers, Inc. process for converting polyurethane foam to polyols.

Technology Area Development Manager: Joseph A. Carpenter
(202) 586-1022; fax: (202) 586-1600; e-mail: joseph.carpenter@ee.doe.gov

---

Contractor: Argonne National Laboratory (ANL)
Contract No.: DE-AC02-06CH11357

Objective

- Develop technology for the cost-effective recovery of materials from post-shred residues.

Approach

- Characterize shredder residue from a number of sources to determine composition variability.
- Conduct bench-scale and large-scale process/technology tests to benchmark technology.
- Build and operate a pilot plant for the separation of shredder residue to recover materials for market evaluation and to provide "control" samples for testing of alternative technologies.
- Conduct cost and performance analysis of alternative technologies to establish the business case for the technologies and to identify technology gaps.

Accomplishments During This Reporting Period (10/1/07–9/30/08)

Validation Plant Activities

- Agreement has been reached with a shredder to build a 20-ton-per-hour validation plant to confirm process yields, process economics, and to confirm qualities of the recovered polymers

Controlled Auto-Shredding Project

- An agreement has been reached with a company that recently completed building a new shredding facility to separately shred into four categories of vehicles. The four categories are: (1) late model domestic—2002–2007 model-year vehicles from Chrysler, Ford and General Motors, (2) late-model transplants—2002–2007 model-year vehicles from foreign companies which are manufactured in the United States, (3) pre-2000 normal end-of-life vehicles (ELVs) which are typical of what is shredded currently, and (4) imported federalized vehicles that are not designed for U.S. end users, but retrofitted to qualify for sale in the U.S. The resulting shredder residues will be processed to determine if differences in the residues exist. Changes in the levels of substances of concern (SOCs) such as polychlorinated biphenyls (PCBs) will be evaluated. Preparation for the test including sourcing of the vehicles to be shredded, arrangement for conducting PCB testing of the shredded material and arrangements for the shipping of the shredder residue to ANL and to Energy Anew has been completed. Shredding of the vehicles which was originally scheduled to take place in July, 2008 took place October 4–5, 2008.

Mechanical Separation of Shredder Residue

- Completed processing of the last 20,000 pounds of shredder residue, out of a 30,000 pound batch, received from the shredder who is building a plant to validate the ANL technology.

Shredding of Auto Parts Containing Nano Materials

- USCAR, ANL, and the National Institute for Occupational Health and Safety (NIOSH) developed an experimental design. A “Request for Proposals” was prepared and released by USCAR for a third party to conduct analysis of nano particles in the dust generated during the shredding of the auto parts. Professor Peter C. Raynor, from the University of Minnesota, School of Public Health, was selected to do the analysis. Contract negotiations between USCAR and the university are underway.

Froth-Flotation Separation of the Plastics

- ANL designed, built, and tested modifications to the flotation process which reduced waste water production by over 50% by minimizing the need for salts and dewatering techniques.

Recycling of Hybrid-Vehicle Batteries

- OnTo Technology, sponsored by the VRP, conducted tests on recycling two battery chemistries—nickel-metal hydride (NiMH) and lithium ion—using small batteries. The process starts by discharging and dismantling of the battery followed by CO_2 extraction of the electrolyte. The battery is then shredded at room temperature and the metals are separated. The remaining material is then pulverized and the plastics are separated from the pulverized material. The powder containing the Li is then recovered. Copper and cobalt are then recovered from the residual material by an electrowinning process. Early results show great promise. Recovered materials have been analyzed and tested in new batteries with good results. The method has the potential to cost-effectively remove more materials of value including the lithium and electrolyte fractions than current technologies. OnTo is continuing their research to look at additional battery chemistries.

Energy Anew Process for Recycling Shredder Residue Fines

- Energy Anew has constructed a mobile cyclonic system to process shredder fines with a throughput capability of approximately 3 tons per hour.

Changing World Technologies (CWT) Thermal Conversion Process

- CWT completed the large-scale test using actual shredder residue material. The results confirmed the results of the earlier small-scale tests.

Prior Accomplishments

FY 2007

- ANL was approached by two shredders who expressed interest in building a large-scale validation plant based on the ANL technology for recovering materials from shredder residue.

Mechanical Separation of Shredder Residue

- Completed testing of 10,000 pounds of shredder residue out of a 30,000 pound batch from the shredder who is building the plant to validate the ANL technology.
- Completed engineering designs of the basic mechanical separation system including equipment specifications, equipment cost, operating requirements, and utility requirements.
- Conducted cost analysis of the process including sensitivity of the cost of producing the polymer concentrate to yield, value of by-products (ferrous, nonferrous metals) and cost of utilities.
- Completed the recovery of plastics and metals from fines (< 0.25 inch).

Froth-Flotation Separation of the Plastics

- Designed, built, and tested a 5,000 lb/h plastics-separation sink/float module.
- Defined process conditions for upgrading the polycarbonate (PC)—acrylonitrile-butadiene-styrene (ABS)/PC alloy concentrate to 90–95%.
- Completed engineering designs of the basic froth-flotation process to include equipment specifications, equipment cost, operating requirements, and utility requirements.
- Proved the technical feasibility of upgrading the filled ABS from 70% to greater than 90% and of the unfilled ABS and polystyrene (PS) from the ABS/PS concentrate to greater than 90% and 85%, respectively

CWT's Thermochemical Process for Producing Hydrocarbon Liquids

- Evaluation of the CWT technology was continued. Preparation for the 2,000-lb test was started.

Emerging Technologies for the Rapid Identification and Sorting of Plastics

- Conducted performance testing and cost analysis of color sorters and near infra-red (NIR) systems for plastics, wood and rubber separation.

MBA's Plastics Separation Test

- Tests were completed and the report was submitted.

Energy Anew Process for Recycling Fines

- Energy Anew completed a study to recover metals and polymers from fines (<7/8 in. in size).

On-To Technologies

- The VRP awarded a contract to OnTo Technology of Bend, Oregon to develop technology to recycle batteries used in hybrid and electric vehicles. Initial testing results were promising.

FY 2006

Mechanical Separation of Shredder Residue

- Ran one 10-ton production campaign (fractions supplied to commercial equipment vendors for performance verification).

- Initiated engineering design for full-scale bulk separation system.
- Obtained budgetary quotes from vendors for major equipment.
- Confirmed performance of commercial equipment with field trials by vendors/ANL of the as-is shredder residue and of the fractions generated at ANL.
- Conducted preliminary investigation of costs and performance of commercial color sorters, electrostatic separators, and infra-red (IR) sorters for removal of wood and rubber
- Developed a dry process for separating rubber from plastics.

Froth-Flotation Process for Recovering Plastics

- Ran first campaign of the middling plastics fraction.
- Recovered a 60% unfilled ABS/PS and a 50% filled ABS concentrates from the middling plastics.
- Upgraded the filled ABS concentrate from 50% to 70% and defined process conditions to further upgrade this fraction to 90%.
- Defined process conditions for separating and recovering unfilled ABS and PS from the unfilled ABS/PS concentrate, to greater than 90% and 85%, respectively.
- Defined process conditions for recovering an 85% PC-ABS/PC alloy from the middling plastics.
- Other Accomplishments
- Completed testing of Troy Polymers Inc.'s (TPI's) process for conversion of urethane foam to polyol initiators. Over 1,200 lb of foam were used, and produced over 100 gal of polyol initiators.
- Conducted pilot-scale testing of CWT's process for converting shredder residue to fuels. Pre-processed shredder residue from another shredder was evaluated and shipped to CWT for further testing.
- Completed a large-scale plastics separation test at MBA Polymers Inc. using a plastic concentrate produced by Salyp's mechanical separation system.
- Completed testing of the VW-SiCon plastics separation process.

FY 2005

Mechanical Separation of Shredder Residue

- Ran four 15-ton production campaigns and conducted material balance on all runs.
- Modified bulk separation operation resulting in an increase in polymer yield in concentrate from 40% to over 90%.
- Conducted trials on gravity tables, mineral jigs, and a kinetic density separator in the U.S. and Europe primarily for removal of wood and rubber.

Froth-Flotation Process for Recovering Plastics

- Conducted bench-scale research on settling velocities and density distributions of actual shredder residue polymers including the wood and rubber.
- Ran a production campaign of the base process with polymer concentrate to yield three polymer fractions: the polyolefin fraction, middling plastic fraction, and "heavies" plastic fraction.
- Developed a wet process for removal of wood and rubber from the recovered polyolefin fraction.
- Recovered 5,000 lb of polyethylene (PE)/polypropylene (PP) essentially free of wood and rubber.

Other Accomplishments

- Conducted bench-scale tests and in a five-gallon reactor of TPI's, of a glycolysis process for conversion of urethane foam to polyol initiators.
- Conducted bench and pilot-scale testing of CWT's thermal depolymerization process for converting shredder residue to fuels.
- Developed an Excel-based process cost model that incorporates two primary modules for the recovery of automotive plastics. The first module includes the unit operations required for recovering a plastics concentrate from shredder residues and the second module includes the unit operations required to recover selected plastics from the mixed plastics concentrates.

FY 2004

Mechanical Separation of Shredder Residue

- Completed construction, shakedown, and start-up of the bulk separation facility.
- Ran six 5-ton trial campaigns in the 4th quarter.

Froth-Flotation Process for Recovering Plastics

- Completed construction and shakedown of the pilot plant with electronics plastics.
- Ran a shakedown campaign with shredder-residue polymer concentrate.

Other Accomplishments

- Completed large-scale tests of Salyp's "thermoplastics sorting" technology by using residue from two European locations and one U.S. location as feed materials.

FY 2003

- Initiated construction of bulk separation facility.
- Initiated construction of froth flotation pilot-plant.

Future Direction

Validation Plant

- Support the shredder in the design, construction, and operation of the validation plant.
- Analyze data from the validation plant.
- Evaluate the quality of recovered materials.
- Determine the economics of the process based on the full-scale validation-plant operation.

Mechanical Separation of Shredder Residue

- Process shredder residue generated by controlled shredding of selected items (autos only).
- Shred automotive nano composites to determine potential release of nano particles.
- Investigate necessary process modifications, if any, for recovering new lightweighting materials and their impact on recycling of other materials.

Froth-Flotation Process for Recovering Plastics

- Conduct process improvement studies to increase value and reduce cost.

Other Future Plans

- Evaluate new, novel processes for recycling shredder residue including its conversion to fuels and chemicals.
- Develop and evaluate processes for recycling automotive lightweighting materials including lightweighting metals (aluminum, magnesium, and titanium).

Introduction

The objective of this project is to develop technology for the cost-effective recovery of materials from post-shred residues. Research will provide data essential to establishing a business case for sustainable recycling of automotive materials from post-shred residue. Technologies specific to the recovery of materials from post-shred material streams are being evaluated and demonstrated to determine their commercial viability. The performance (e.g., yield, purity, efficiency, and cost) of emerging technologies will be determined to enable the development of an integrated process for recovering materials from shredder residue.

Research has been completed on the Salyp, MBA, TPI, VW-SiCon, CWT, Energy Anew, and ANL mechanical separation processes. Process improvement research is ongoing on the ANL flotation process. Work is also continuing with OnTo on battery recycling.

Validation Plant

Two shredders have expressed interest in building a plant on their sites to validate the results obtained in ANL's pilot plant. Agreement has been reached with a shredder to build a 20 ton/h validation plant to confirm process yields, process economics, and to confirm qualities of the recovered polymers. Before the agreement was signed, 15 tons of shredder residues from three of the plants of this shredder were processed in our pilot-plant to determine if a business case exists. The material was first separated in the mechanical-separation plant to recover the polymer concentrate and then the polymer concentrate was processed in the flotation plant. Discussions followed to explore licensing opportunities and an agreement has been reached. Process flow diagrams have been finalized. The building for housing the flotation part of the process and the critical parts of the mechanical process has been undergoing renovation and utilities have been brought to it. Specification of the equipment for the mechanical-separation system is complete and some of the equipment for the mechanical system and for material handling has been ordered. Placement of purchase orders for the equipment is underway and is expected to be completed by mid-November 2008. Specifications of the equipment for the flotation system are essentially complete. Placement of purchase orders for the equipment is expected to be completed by mid-December 2008. Specifications of the equipment for the polyolefins upgrade system are complete. Placement of purchase orders for the equipment is expected to be completed by end of January 2009.

Characterization of Shredder Residue

Over 130 tons of shredder residues from eight facilities were processed in ANL's mechanical-separation plant. Table 1 shows the average composition of the different fractions produced. Large variations in the concentration of fines, metals, rubber and wood and less variation in the composition of the plastics fraction were observed.

The weight percent (wt %) of the polymer concentrate recovered from eight runs totaling 80,000 lb of shredder residue from a given source conducted over a 6-month period was reasonably consistent (41%, 26%, 36%, 39%, 45%, 37%, 43%, and 45%; average 40%). The composition of the different polymer concentrates was also similar.

Table 1. Streams produced by mechanical separation of an average shredder residue

	Shredder Residue	Oversized Heavies	Oversized Foam rich	Fines[a]	Ferrous Rich	Nonferrous Rich	Lights	Polymer Concentrate
Weight (lb)	40,000	2,148	756	17,640	656	1,468	1,968	10,044
PP	1,075	0	0	0	17	33	129	897
PP (filled)	403	0	0	0	0	0	9	393
ABS	763	0	0	0	5	9	13	737
PE	941	0	0	0	9	18	85	830
High Impact Polystyrene (HIPS)	261	0	0	0	4	8	15	234
Nylon	379	0	0	0	4	9	19	347
Polyvinyl Chloride (PVC)	512	0	0	0	0	0	0	511
Polyoxyphenylene (PPO)	139	0	0	0	0	0	4	135
PC-ABS	151	0	0	0	0	0	1	150
PC	212	0	0	0	0	0	12	200
Other Plastics	597	0	0	0	1	0	17	579
Rubber	4,505	20	0	0	6	172	61	4,246
Polyurethane (PU)	273	3	0	0	1	23	9	237
Wood	239	0	0	0	0	0	0	239
Metals	2,911	1,117	0	0	590	954	0	249
Foam, Fiber and others	21,320	1,008	756	17,640[a]	19	241	1,597	59
Moisture	5,320	0	0	0	0	0	0	0
Total	40,000	2,148	756	17,640	656	1,468	1,968	10,044

[a]Fines are material smaller than 0.25 inch in size and also contain some polymers and metals.

ANL Pilot-Plant

The plant consists of a dry mechanical-separation facility and a wet density/froth-flotation facility. The pilot-plant is used to:

1. Recover materials from shredder residue,
2. Conduct process improvement studies,
3. Generate design and scale-up data,
4. Produce samples for evaluation,
5. Define the effectiveness of alternative separation technologies and systems, and
6. Serve as a user/demonstration facility.

Mechanical-Separation Pilot-Plant

The mechanical-separation facility processes raw shredder residue to yield a polymer concentrate, ferrous and nonferrous concentrates, a fines fraction, and other fractions. The plant achieved over 90% recovery of the plastics targeted for recovery as a polymer concentrate and over 95% recovery of the metals in the shredder residue.

The polymer concentrate included high and varying amounts of wood and rubber. Wood was about 1–4 wt %.

Separation of Wood and Rubber

Trials using commercial air aspirators, air classifiers, gravity tables, and mineral jigs to remove wood and/or rubber from the polymer concentrate did not yield satisfactory results. Trials using wet methods removed almost 100% of the wood and over 90% of the rubber with a nominal loss (~5%) of the plastics.

A modular dry process for separating rubber from plastics has been tested at rates of up to 200 lb/h of polymer concentrate. The process separated over

75% of the rubber and produced a rubber fraction containing less than 10% of nonrubber material.

Froth-Flotation Pilot-Plant

This facility includes six continuous stages for the separation of targeted plastics. A shakedown of the facility was conducted using 4,000 lb of post-consumer electronics and appliance mixed plastics and by using a mixture of colored plastics. Over 30,000 lb of polymer concentrate from shredder residue has been processed in this facility. The recovered fractions are described in the following sections.

Recovered PP/PE Fraction

More than 5,000 lb of an unfilled PP/PE fraction that is over 95% PP/PE have been consistently produced. It contains less than 0.2% wood and less than 4% rubber. However, when the material was palletized, most of the rubber in this fraction was compatible with the PP/PE. The recovered PP/PE has properties similar to those of some commercially-available PP materials. The unfilled PP/PE product is about 5%–6% of the starting shredder-residue weight. Table 2 summarizes the recoverable plastics from 10,000 lb of typical shredder residue.

Table 2. Composition of an average polymer concentrate and recovered polymer fractions

	Polymer Concentrate	PP/PE Product	ABS Product	ABS/PC Product	Rubber Product	HIPS/ABS Concentrate	Mixed Plastics	Mixed Stream[a]
Weight (lb)	10,044	1,736	141	108	689	856	1,203	5,311
PP	897	827	0	0	0	0	63	7
PP (filled)	393	0	0	0	11	43	194	146
ABS	737	0	105	2	0	365	176	88
PE	830	787	0	0	10	12	21	0
HIPS	234	0	2	0	0	186	25	21
Nylon	347	0	5	0	0	5	42	296
PVC	511	0	0	0	3	0	123	385
PPO	135	0	13	1	0	62	21	37
PC-ABS	150	0	0	6	0	0	0	143
PC	200	0	0	85	1	0	19	94
Other Plastics	579	0	9	2	2	12	8	547
Rubber	4,246	90	2	9	628	104	263	3,149
PU	237	21	4	2	18	0	96	96
Wood	239	0	1	0	17	66	146	8
Metals	249	0	0	0	0	0	0	249
Foam, Fiber	59	10	0	0	0	1	5	42
Total	10,044	1,736	141	108	689	856	1,203	5,311

[a]Rubber and metals are to be recovered from these streams.

Filled ABS Fraction

ABS that has a specific gravity between 1.07 and 1.1 was isolated by the basic froth-flotation process as an ABS concentrate, Table 2. It contains 50% ABS, 20% rubber, 10% rigid urethane rubber, and 20% of other materials. Removing wood and rubber increased the ABS concentration to 70% and reduced the rubber and urethane to 3% and 2%, respectively. When this material was blended with virgin ABS at 10% and 25% recovered material, the properties of the blends were slightly different from the properties of the virgin ABS. Laboratory tests have established process conditions to increase the ABS concentration to over 90%.

Unfilled ABS and PS

A fraction of ABS, PS, and PPO that has a specific gravity between 1.0 and 1.07 (43% ABS, 22% PS, 7% PPO and 28% other materials including rubber and some wood) was produced by the basic process. Lab tests separated this fraction and produced

fractions with over 90% ABS and over 85% PS/PPO.

PC-ABS/PC Alloy

Laboratory tests produced a PC-ABS/PC fraction having a combined concentration of over 85%. Work is ongoing to isolate a large sample of ABS/PC-PC fraction for further evaluation.

PVC

Recovery of the above fractions leaves behind a fraction made of high specific-gravity materials. Rubber constitutes over 50% of the total and metals about 5%. Separating rubber, metals, glass, and rocks from this stream leaves a fraction containing over 50% PVC. It is also rich in filled nylons.

Rubber

Recovered rubber fraction was upgraded by the ANL dry rubber separation process to over 90% rubber. The other 10% were mostly plastics.

In summary, the process has recovered the unfilled polyolefins, and isolated the filled ABS, unfilled ABS/PS, PC-ABS/PC, and PVC into more manageable fractions.

The basic wet process has also produced a styrenics fraction containing over 75% by weight "targeted plastics," primarily ABS, PS, PPO, and filled PP. MBA polymers established that this fraction can be separated to produce recyclable products.

A 5,000 lb/h flotation module has been built and tested using over 10,000 lb of mixed polymers. Modifications to the tank and to the operating procedures resulted in over 90% reduction in the amount of chemicals used and in the amount of waste water generated.

Development of a Process Flow Sheet

A general process conceptual design for a 20 ton/h mechanical-separation plant has been developed. The flow sheets for the validation plant have been finalized. The process steps for the general conceptual design include (1) a device to separate large metals and rocks, (2) a screen to separate large pieces of fabrics, foam and tire rubber, (3) a shredder, (4) a screen or a trommel to separate "fines," (5) a magnet and eddy current to separate metals, (6) a granulator, and (7) an air classifier to remove "lights" from the granulated material. Tests using shredder residue were conducted to evaluate the performance and cost of various equipment used in the design.ANL conducted analysis of the sensitivity of the cost of producing the polymer concentrate to yield per ton of shredder residue, value of the by-products (ferrous, nonferrous, etc.), cost of utilities, number of operating shifts, cost-of-capital, etc. The cost can be as low as $0.02 per pound of polymer concentrate for a plant operating three shifts per day and the polymer concentrate is about 45% of shredder residue to over $0.075 per pound for a plant operating one shift and the polymer concentrate is only 15%. The value of the recovered metals has a significant impact on the overall cost. The value of the metals depends on their concentration in shredder residue and on the composition of the metal fraction produced. Evaluation of Color and Infrared Sorters ANL conducted performance testing and cost analysis of color sorter and IR sorters. The following systems were tested: (1) Satake (chip monochromatic and IR), (2) Key (chip full color and laser), (3) MSS (full color and IR), (4) S+S Separation and Sorting (full color and IR), (5) NRT (chip full spectrum and IR), and (6) PROTEC (chip full spectrum). Based on the results of these tests, it appears that at this time these systems cannot recover marketable polymer products from shredder residue nor can they separate wood and rubber from the recovered polymer fractions. ANL's process for the separation of wood and rubber from plastics appears to be the most economical for separating the wood and the rubber from the plastics. The primary reason is the high loss of the targeted plastics by the optical sorters.

Recycling of Fines

ANL conducted tests to recover polymers and metals from the <0.25-in. fines. The polymer concentrate recovered from the material in the 2–6 mm range was between 30 and 50 wt % of the weight of the fines fraction. It contained up to 50% by weight rubber and about 20 wt % plastics. A sample of this concentrate was processed in the wet-separation system to produce a polyolefin concentrate, a styrenics concentrate, and a mixed plastic and rubber concentrate and recover the

residual metals as a metal concentrate. About 20% of the plastics had specific gravity < 1.

The ferrous material, including oxides, in the fines has been reduced significantly compared to years ago. Shredders are using more-efficient metal-separation equipment and less rust forms on later-model vehicles.

Processing of Polymer Concentrate at MBA

Salyp built a mechanical-separation plant that started with ANL's original mechanical-separation system and added an optical sorter and a plastics-washing system. Salyp's starting shredder residue contained less rubber and wood than the U.S. residue. MBA processed about 40,000 lb of Salyp's polymer concentrate and recovered five materials: polyolefin "A" and "B," filled PP, ABS, and HIPS. The total yield was estimated to be 48.5% of the plastics-rich fraction. This yield is 88% of the amounts of these plastics in the feed material. The products were extruded, molded, and tested. The properties were reported to be "encouraging" and it is expected that most of the products could be used in some durable-good applications.

CWT

CWT processed a shredder-residue stream after separating the < 1/16-in. fines (~36% by weight). About 700 lb of the remaining material were processed along with 80 lb of tires and 1,700 lb of used motor oil. The products were hydrocarbon oil (84%), a fuel-gas (10%), and a solid-carbon product (6%). Distillation of the oil generated gasoline (12%), diesel (32%), and heavy-hydrocarbon oils (15%), and 3% as gas.

PCBs in the input shredder residue was 21.8 parts per million (ppm) and in the products were bellow the detection limit. This indicated that the PCBs degrade during the process. The char contained several metals. The heavy oil from the dissolver contained about 3,200 ppm of total chlorine but no chlorine was found in the light distillates and only 14 ppm was found in the heavier distillate and 11 ppm in the distillate bottoms. Bromine was found in the heavy oil from the dissolver (~135 ppm) and in the char (87 ppm). None was found in the output liquid products.

The analysis also indicates that sulfur compounds degraded in the process. A test using about 1,000 lb of a pre-processed organic fraction derived from about 2,000 lb of shredder residue has been completed. The results confirmed the ability of the CWT process to produce a 18,000 BTU/lb diesel oil, a 12,000 BTU/lb solid carbon, and a 5,000 Btu/lb fuel gas with the largest fraction being methane.

CWT also completed a large scale (2,000 lb) test using actual shredder-residue material. The results confirmed the results of the earlier small-scale tests.

Energy Anew Recycling of Fines

Energy Anew conducted tests on 300-lb samples of fines (< 1 in.). Shredder residue was screened using a 7/8-in. screen and the material that passed the screen was processed to yield organic- and inorganic-rich fractions. Energy Anew constructed a mobile cyclonic system to process shredder fines with a throughput capability of about 3 ton/h. The system successfully sorts the fine fraction into a nonferrous metal concentrate, polyolefin concentrate, styrenic plastic concentrate and an organic fluff fraction. The process can be used in combination with coarse size-reduction systems to produce enriched-plastic products from a wide variety of raw materials including automotive shredder residue and shredded appliance, electronic and packaging scrap. Nonferrous concentrates of greater than 75% metal content have been demonstrated with use of additional down-stream grinding and sorting. Economic analysis of the process shows that recovery of plastic concentrates, metals and sand from windshield glass may be viable.

TPI Glycolysis Process

The process converted foam from shredder residue to polyol initiators at yields of 88% and 72%, for clean and dirty foam, respectively. Activated carbon reduced the concentration of PCBs in the products to < 2 ppm. Over 100 gal. of polyol initiator were produced from about 1,200 lb of foam.

Twenty gallons of the polyol initiator were propoxylated and were tested for making rigid foams. They required less or no catalyst and had better flame resistance than the foams made with

virgin polyols. Initial economic analysis indicated that the process is potentially economical.

OnTo Technology

OnTo Technology, under contract from USCAR, conducted research on recycling two kinds of advanced battery chemistries—NiMH and lithium ion—to determine the technical feasibility of recycling these types of automotive batteries. The process starts by discharging and dismantling of the battery followed by CO_2 extraction of the electrolyte. The battery is then shredded at room temperature.

Ferrous and nonferrous metals are then separated by magnets and eddy currents, respectively. The remaining material is then pulverized and the plastics are separated from the pulverized material. The powder containing the Li is then recovered. Copper and cobalt are then recovered from the residual material by an electrowinning process. Early results show promise.

Recovered materials have been analyzed and tested in new batteries with good results. The method has the potential to cost-effectively remove more materials of value including the lithium and electrolyte fractions than current technologies. OnTo is continuing their research to look at additional battery chemistries.

Co-Combustion of Plastics-Rich Material with Biomass

The ACC-PD co-funded a study with Plastics Europe to study the synergies of co-combustion of plastics-rich fuels and biomass. The study concluded that the benefits include fast drying and ignition of the biomass, higher furnace temperature and improved combustion efficiency. The study noted that chlorine and metallic aluminum contents in the fuel mixture should be compatible with the boiler type.

Publications

1. *Recovery and Recycling of Polymers from Shredder Residue*, B. J. Jody, J. A. Pomykala Jr., J. S. Spangenberger, and E. J. Daniels, The Journal of Solid Waste Technology and Management, Vol. 23, No. 4, Nov 2006, pp. 228–236.
2. *Technologies for Recycling Shredder Residue,* B. J. Jody and E. J. Daniels, SAE Paper No. 2007-01-0526, 2007 SAE World Congress, Detroit, Michigan, April, 2007.
3. *Mass Balance and Composition Analysis of Shredder Residue*, J. A. Pomykala Jr., B. J. Jody, J. S. Spangenberger, and E. J. Daniels, SAE Paper No. 2007-01-0527, 2007 SAE World Congress, Detroit, Michigan, April, 2007.
4. *Metal Recovery from Shredder Residue Fines, T.* Allen, SAE Paper No. 2007-01-0528, 2007 SAE World Congress, Detroit, Michigan, April, 2007.
5. *Thermoplastic Separation and Recovery from Various Mixed Scrap by the ANL Developed Froth Flotation Technology, J. A.* Pomykala Jr., B. J. Jody, and E. J. Daniels, Proc. Of the 13th Annual Global Plastics Environmental Conference (GPEC), Orlando, Florida, March 6–7, 2007.
6. *A Mechanical Separation Process to Recover Metals and Polymers from Shredder Residue,* J. A. Pomykala Jr., B. J. Jody, E. J. Daniels, J. Yang, and J. S. Spangenberger, TMS 2007 Annual Meeting & Exhibition, Orlando, Florida, Feb. 25–Mar. 1.
7. *Scale Up Study on Converting and Recycling Shredder Residue Into a Fuel Oil*, G. R. Winslow, B. S. Appel, T. N. Adams, N. L. Simon, C. M. Duranceau, and C. S. Wheeler, SAE 2006 World Congress, Detroit, Michigan, 2006. SAE-2006-01-1580.
8. *Scale Up Study on Converting and Recycling Shredder Residue Into a Fuel Oil*, G. R. Winslow, B. S. Appel, T.N. Adams, N. L. Simon, C. M. Duranceau, and C. S. Wheeler, paper # SAE-2006-01-1580.
9. *Recycling of Polyurethane Foams Recovered From Shredder Residue Via Glycolysis Process Into Polyurethanes,* V. Sendijarevic, I. Sendijarevic, K. Mayne, G. R. Winslow, C. M. Duranceau, N. L. Simon, and C. S. Wheeler, paper # SAE-2006-01-1579.

10. *Chemical Recycling of Mixed Polyurethane Foam Recovered from Shredder Residue into Polyurethane Polyols, V.* Sendijarevic, I. Sendijarevic, G. R. Winslow, C. M. Duranceau, N. I. Simon, and C. S. Wheeler, SAE paper # 2005-01-0850.

11. *Recycling Shredder Residue Containing Plastics and Foam Using a Thermal Conversion Process*, G. R. Winslow, B. S. Appel, T. Adams, N. I. Simon, C. M. Duranceau, C. S. Wheeler, and Sendijarevic, V., SAE Paper #2005-01-0848.

12. *Advanced Separation of Plastics from Shredder Residue*, G. R. Winslow, N. I. Simon, C. M. Duranceau, R. Williams, C. S. Wheeler, M. Fisher, A. Kistenmacher, and I. VanHerpe, SAE Paper No. 2004-01-0469.

13. *Recycling Automotive Shredder Residue and Plastics Using the CWT Thermal Process*, G. R. Winslow and T. Adams, Proc. of the 10th Annual Global Plastics Environmental Conference (GPEC), Detroit, MI, February 18, 2004.

14. *Screening Study to Evaluate Shredder Residue Materials*, G. R. Winslow, C. S. Wheeler, R. L. Williams, C. M. Duranceau, N. L. Simon, and D. R. Schomer, SAE paper # 2004-01-0468.

15. *Processes for Recycling the Non-Metallic Portion of Obsolete Automobiles*, B. J. Jody, E. J. Daniels, and J. A. Pomykala Jr., U.S. Environment-2003 On-Line Conference, July 14–25, 2003.

16. *Cost Effective Recovery of Thermoplastics From Mixed Scrap*, B. J. Jody, J. A. Pomykala Jr. and E. J. Daniels, Materials Technology, Volume 18 Number 1, March 2003, pp. 18–24.

17. *Separation and Recovery of Thermo-plastics From Mixed-Scrap Plastics*, J. A. Pomykala Jr., B. J. Jody, E. J. Daniels, and J. Greminger, Proc. of the 9th Annual Global Plastics Environmental Conference (GPEC), Detroit, MI, February 26–27, 2003, pp. 7–16.

E. Development of High Speed Multispectral Imaging for Sorting Automotive Plastics

Principal Investigator: Edward J. Sommer, Jr.
National Recovery Technologies, Inc.
566 Mainstream Drive, Nashville, TN 372289
(615) 734-6400; fax: (615) 734-6410; e-mail: ejsommer@nrtsorters.com

Technology Area Development Manager: Joseph A. Carpenter
(202) 586-1022; fax: (202) 586-1600; e-mail: joseph.carpenter@ee.doe.gov

Contractor: National Recovery Technologies, Inc. (NRT)
Contract No.: DE-FG02-06ER84559 Small Business Innovation Research (SBIR) and Small Business Technology Transfer Program

Objective

- Develop a cost-effective technology for the identification of end-of-life automotive plastics and their sortation according to polymer type.

Approach

- Design a primary optical system for imaging the infrared (IR) characteristics of automotive polymers.
- Design a high-speed, IR filtering system which integrates with the optical system and provides the mechanism for isolating a polymer signature.
- Design a secondary optical system which transfers the filter response to a multi-sensor detection array.
- Develop software for high-speed control of the filtering system and detection array utilizing a real-time operating system (RTOS).
- Develop software to identify the unique signatures of various polymers and subsequently segregate these pieces into desired groupings.
- Develop software for system-level configuration and control.
- Integrate and test sortation system.

Accomplishments During this Reporting Period (10/01/2007–09/30/2008)

Commercialization Activity

- NRT has realized a Ph III sale of an advanced real-time computing module based upon the Phase II technology under development.
- Development of the computing module is underway according to specifications received from the Ph III client.
- Delivery of the advanced computing module to the Phase III client is expected in spring 2009.

Primary Optical System

- Determined specifications for an IR lighting system—an innovative approach is being investigated that can optimize resolution and enhance sensitivity of the detection system.

- Mechanical design of a high-luminance IR lighting system is in process as an adjunct to the innovative approach discussed above.
- Began design of the primary optical system using an optical design software package.

IR Filtering System

- Have selected a high-speed, reconfigurable IR filters that meets design parameters.
- Have constructed an optical model of a reconfigurable IR filter for the purpose of simulation and testing.
- Using a Phase I prototype reconfigurable IR filter for testing and evaluation.

Secondary Optical System

- Design underway of the secondary optical system using an optical design software package.
- Design underway of mechanical components to integrate the primary optical, IR filtering, and secondary optical systems and IR detection array.

Detection Array and Data Acquisition Hardware

- Determined specifications for a multi-sensor infrared detection array.
- Determined specifications for detector acquisition hardware.
- Acquired a high-speed, Camera Link-based camera which incorporates the desired detection array.
- Acquired a Camera Link-based frame grabber which enables communication with and data acquisition from the IR detection array.
- Tests underway using QNX real-time system data acquisition rates and camera control with camera parameter setup through a Windows-based system.

Real-Time-Operating-System Software for Filter and Detector Control

- Evaluated various aspects of several RTOSs and selected QNX for this project.
- Ordered, received, and activated QNX developments tools – these are essential for programming and interacting with QNX.
- Ordered, received, and put into service a single-board computer (SBC), chassis and other ancillary hardware for hosting QNX and our proprietary software.
- Performed configuration design of RTOS and subsystems.
- Software development is underway of the RTOS and subsystems, including that needed for the Phase III advanced computing module.

Identification and Sortation Software

- Investigating potential algorithms for identifying polymers.

System Configuration and Control Software

- Have performed detailed examination of QNX to understand the interactions among its internal components.
- Development underway of communications between proprietary software components.
- Primary hardware and software structures defined—driver developments underway.

Investigate Complications from Coated Polymers

- Obtained samples of painted polymers from Argonne National Laboratory.
- Sent samples to a laboratory for analysis using a laser-induced breakdown spectroscopy (LIBS) technology which automatically penetrates surface coatings to expose underlying material.
- Testing performed on the samples using a double pulse laser and LIBS analyses to analyze underlying polymer materials. Test report received from laboratory performing tests and results analyzed.

Prior Accomplishments

Determined Desirable Polymers Present in Automobile Shredder Residue

- Met with personnel from the Transportation Technology R&D Center at Argonne National Laboratory, toured the Vehicle Recycling Partnership Plant, and learned about various plastics derived from automobile shredder residue.
- Received and preliminarily evaluated shredder residue plastics samples from Argonne.

Constructed a Bench-Scale Unit to Determine and Demonstrate Feasibility

- Determined preliminary technical requirements for an optical module for integration with a sensing module.
- Determined technical feasibility of developing a primary beam-shaping module which collects, collimates, and condenses broadband radiation for transmission to a sensing module.
- Determined the technical requirements for an analog amplification circuit that converts the detector response into an appropriate voltage signal.
- Designed and constructed a bench-scale unit comprising rudimentary features of the proposed detection system.
- Demonstrated technical feasibility for development of the new sensing technology.

Future Direction

- Effort in fiscal year (FY) 2009 will continue to focus on this SBIR Phase II project. A summary of Phase II plans for this period is provided below.

Design, Fabricate, and Test Commercial Computing Module

- Design and testing to be performed under this program.
- Component costs and manufacture costs to be provided by NRT external to this program.

Design of Primary Optical System

- Finish design of the primary optical system.
- Fabricate mechanical components.
- Assemble optical and mechanical components and test.

Design of IR Filtering System

- Determine optimal physical configuration of the reconfigurable filter through simulations with optical model.
- Order a reconfigurable filter with the desired configuration.
- Verify proper operation of the filtering system.

Design of Secondary Optical System

- Finish design of the secondary optical system.
- Finish design of mechanical components to integrate the primary optical, IR filtering, and secondary optical systems and IR camera.
- Assemble integrated systems.
- Verify intended performance of the integrated systems.

Develop Real-Time-Operating-System Software for Filter and Detector Control

- Finish development of filter and detector control.
- Test controlling software.

Develop Identification and Sortation Software

- Develop various algorithms for identification.
- Test algorithms for speed, efficiency, and accuracy with simulated data.
- Test algorithms with acquired data.
- Develop controlling software for grouping materials.

Develop System Configuration and Control Software

- Finish interface protocols for communication between proprietary software components.
- Implement system control and configuration modules.
- Test system control and configuration software.

Test Integrated Sortation System

- Assemble components into a small but commercial-scale prototype sorting system.
- Evaluate overall performance of the assembled system.
- Evaluate sortation performance of the system by sorting shredder residue.

Introduction

The objective of this project is to develop a cost-effective technology for the identification of end-of-life automotive plastics and their sortation according to polymer type. This technology will be capable of simultaneously acquiring polymer spectra from multiple spatial locations, yet operate at high speeds when compared to current state-of-the-art detection systems.

The prospective sortation system may be considered as composed of three sub-systems: an optical filtering unit, a real-time processing unit and a control unit. Specifications, simulations, and mechanical designs for the optical filtering unit have begun. Development of the real-time components has progressed significantly, where many of the subtasks (e.g., acquiring hardware and toolsets) are completed. Likewise, significant progress toward implementing the control unit has been made due to investigating the underlying operating system, charting an implementation strategy, and testing several concepts with software applications.

Technological developments in this pro-gram have enabled the commercial sale to an NRT customer of a computing module based upon the systems being developed under this SBIR program. The unit that has been ordered by our customer will incorporate certain aspects of the RTOS developments described more fully in this report.

Optical and Filtering Unit

The initial processing segment of the intended sortation system is composed of a complex optical and filtering unit which images the IR characteristics of automotive polymers. It is intended that this unit continuously image the spectral signature of pieces which are larger than 0.25" and lie within a 24" processing width. An inherently low-intensity polymer signature coupled with short acquisition times (required for high-speed and high-volume sorting) requires complex and efficient imaging optics. The tight optical constraints of a high-speed, reconfigurable IR filter further complicate the optical design.

The manufacturer of a reconfigurable IR filter is assisting in the development of an optically valid model of a filter for use in simulations. Incorporating this model into an optical design software package enables evaluation of several possible configurations before a prototype is constructed. It is estimated that 40% of the effort for developing this unit has been completed.

Real-Time Components

The real-time components may be considered as the hardware and software necessary to effect the high-speed sortation. The hardware components consist of a single-board computer (SBC) with a multi-core processor, high-speed line-scan camera, frame-grabber, and digital input/output (I/O) controller. The software components consist of an RTOS, hardware drivers, polymer identification algorithms, and material removal routines.

An early step in planning for this project was to produce a compilation which functionally described the various components of the intended system and chart their interactions. Once completed, the specifications for individual components were further refined so that hardware selection could occur. As a result, much of the hardware has been ordered and received.

The foundation for all of our real-time software components is QNX. This commercially available RTOS seems to be the best solution for the project and some extended period of effort has been directed towards familiarization with and the understanding of its intricacies. We have acquired the development tools for QNX, installed the operating system on the SBC, explored the various aspects of the system, and are now in the process of constructing code specific to our project.

User Interface and Control Software

The control unit may be considered both as a system supervisor and as a means for personnel to adjust sortation parameters. In its supervisory role, the control unit provides a mechanism for programmatically controlling external hardware (e.g., conveyors, lights, alarms) as well as invoking the sortation process. The control unit also provides a set of applications, collectively termed a "user interface" (UI), which allow an operator to readily manipulate sortation parameters.

The response latency criterion for the control unit software is considerably less stringent than for that of the sortation software. This relaxed requirement permits us to implement the software on a non-RTOS, such as Windows XP. Isolating the non-real-time control from the real-time sorting process provides two advantages. First, the sorting process is more stable since any critical failures in the non-real-time software has a much lower probability of corrupting the real-time processes. Second, since the UI applications may execute on a computer with a network connection to the sorting module the sorting system may be controlled from any remote location or simultaneously monitored from various locations.

Defining the base structures for UI applications and protocols for control software is a significant task. We are well into this endeavor and reached the point of implementing and testing several of these concepts in Windows XP.

Conclusion

The research on this Phase II project is generally progressing as intended. No outstanding difficulties have been encountered.

Publications

1. *Phase I Final Report, Development of High Speed Multispectral Imaging for Sorting Automotive Plastics*, U.S. Department of

Energy SBIR Program, Contract DE-FG02-06ER84559, National Recovery Technologies, Inc., Nashville, TN, March 2007.

2. *SBIR Phase I: Development of High Speed Multispectral Imaging for Sorting Automotive Plastics*, U.S. Department of Energy SBIR Program, Contract DE-FG02-06ER84559, National Recovery Technologies, Inc., Nashville, TN, March 2008.

12. MATERIALS CROSSCUTTING RESEARCH AND DEVELOPMENT

A. Technical Cost Modeling

Principal Investigator: Sujit Das
Oak Ridge National Laboratory
National Transportation Research Center
2360 Cherahala Boulevard
Knoxville, TN 37932-6472
(865) 946-1222; fax: (865) 946-1314; e-mail: dass@ornl.gov

Technology Area Development Manager: Joseph A. Carpenter
(202) 586-1022; fax: (202) 586-1600; e-mail: joseph.carpenter@ee.doe.gov

Field Technical Monitor: C. David Warren
(865) 574-9693; fax: (865) 574-6098; e-mail: warrencd@ornl.gov

---

Contractor: Oak Ridge National Laboratory (ORNL)
Contract No.: DE-AC05-00OR22725

Objectives

- Address the economic viability of new and existing lightweight materials technologies.
- Develop technical cost models to estimate the cost of lightweight materials technologies.

Approach

- Address the economic viability of lightweight materials technologies supported by Lightweighting Materials (LM) technology area development.
- Use cost modeling to estimate specific technology improvements and major cost drivers that are detrimental to the economic viability of these new technologies.
- Derive cost estimates based on a fair representation of the technical and economic parameters of each process step.
- Provide technical cost models and/or evaluations of the "realism" of cost projections of lightweight materials projects under consideration for LM technology area development funding.
- Examine technical cost models of lightweight materials technologies that include (but are not limited to) aluminum (Al) sheet; carbon-fiber (CF) precursor and precursor processing methods; fiber-reinforced polymer-matrix composites (FRPMCs); and methods of producing primary Al, magnesium (Mg), and titanium and Mg alloys with adequate high-temperature properties for powertrain applications.

Accomplishments

- Completed an analysis of the cost-effectiveness of a 25% body and chassis weight reduction LM goal for 2008.
- Completed life-cycle inventory (LCI) data collection for the life-cycle analysis (LCA) of CF-reinforced polymer-matrix composites and initiated the LCA.
- Completed LCI data collection for several Mg manufacturing technologies and completed the first-cut LCA.

- Updated an earlier paper on primary Mg production costs for automotive applications for publication in *Journal of Metals*.

Future Direction

- Perform the joint Ontario-DOE LCA study on natural-fiber-reinforced bioresin-matrix composites for automotive applications.
- Complete the cost-effectiveness assessment of a fiscal year (FY) 2009 40% body and chassis weight reduction goal in light-duty vehicles.
- Continue project-level cost modeling to identify specific technology improvements and major cost drivers that are detrimental to the economic viability of these technologies.

Cost-Effectiveness of a 25% Body and Chassis Weight Reduction Goal in Light-Duty Vehicles

The LM component of the Department of Energy (DOE) Vehicle Technologies Program has a 50% weight reduction goal for passenger vehicle body and chassis systems with safety, performance, and recyclability comparable to 2002 vehicles. To achieve this long-term weight reduction goal, LM has set annual intermediate weight reduction goals, starting with 10% in FY 2007 and finally achieving 50% by FY 2010. The focus of the current work is on the 25% body and chassis weight reduction goal of FY 2008, with emphasis on assessment of the cost-effectiveness of this goal.

Cost-effectiveness of the LM 2008 body and chassis weight reduction goal of 25% in light-duty vehicles was assessed based on the use of lightweight material options for various body and chassis components under two plausible mid-size vehicle scenarios, each scenario focusing on a specific lightweight material option, either Al or glass-FRPMCs. The lightweight material substitution options considered here focused on body systems, but to achieve the desired overall weight reduction goal, additional chassis components were also selected for substitution for the glass-FRPMC scenario. The analysis also considered the effect of primary weight savings of 25% on other vehicle components that can be resized while maintaining the same level of vehicle performance with the reduced vehicle weight. These weight savings are known as secondary weight savings. Estimated secondary weight savings varied between the two scenarios because of the difference in total number and type of components considered for primary weight savings. Due to consideration of secondary weight savings, total body and chassis weight savings is estimated to be in the range of 27–32%, whereas final vehicle weight savings is estimated to be 16–19%. The cost-effectiveness of the 25% body and chassis weight reduction goal is estimated in terms of both vehicle retail price and life-cycle cost using the detailed 35+ component-level automotive-system cost model developed by ORNL and Ibis Associates, Inc. Cost data of components considered for lightweight material substitution are collected from the recently completed major studies, thereby reflecting the latest technology developments and material prices.

Because of the consideration of powertrain resizing and secondary body and chassis mass savings, both lightweight material vehicle options are cost-effective in meeting the LM 25% body and chassis weight reduction goal from the life-cycle cost perspective, as shown in Figure 1. Use of lightweighting materials such as Al and glass-FRPMC would be sufficient to achieve the goal, but cost-effectiveness needs to be considered beyond just the component-to-component material substitution and vehicle retail price bases.

Consideration of secondary weight savings and vehicle life-cycle cost perspectives are important when considering the economic viability of lightweighting vehicles. Among the two lightweight material options considered, glass-FRPMC appears to be more cost-effective because the cost of using Al as a structural material is still high, even with the latest technology

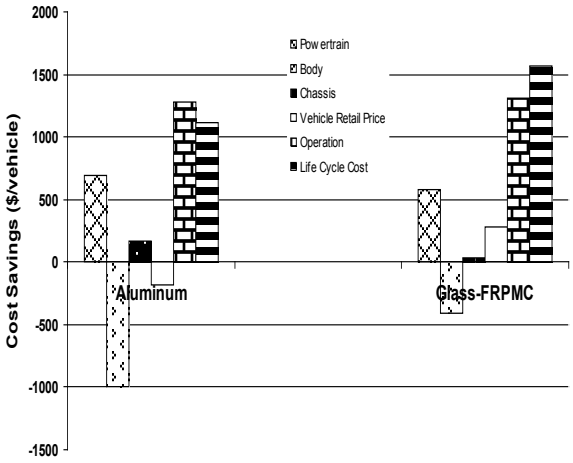

Figure 1. Estimated cost savings of two 25% body and chassis weight reduction vehicle scenarios.

developments and material pricing. In the Al scenario, the vehicle retail price would be about $180 higher; a reduction in Al sheet price to a value of less than $3.00/lb would improve its competiveness at the vehicle retail price level.

Because of consideration of secondary weight savings, the cost penalty due to lightweighting vehicles has been found to be more favorable than previously reported in the literature. As a result of the cost penalty for use of body lightweighting technologies, estimated to be in the range of $400–$1,000/vehicle under the two scenarios when not accounting for secondary weight savings, it is likely that a significantly higher fuel price would be necessary for the cost-effectiveness without secondary weight savings to be achieved on a life-cycle cost perspective, at least for the high-end body structure cost-penalty case.

Life-Cycle Analysis of Mg Front-End Research and Development

This is a Canada-China-U.S. collaborative research and development project which was kicked-off during the second quarter of FY 2007 as one of the 10 enabling technology development tasks to analyze the energy consumption and greenhouse gases effect of Mg production (i.e., CO_2 emissions in primary Mg production via the electrolytic process and traditional and improved Pidgeon processes) and SF_6/SO_2 and other emissions in Mg casting, wrought-alloy processing, and recycling. A total LCA including vehicle use and the end-of-life stages was considered to capture the benefits of lightweighting automobiles such as fuel-economy improvements and associated emission reductions. The functional unit for this study is the service of front-end auto parts (equivalent to 82.2-kilogram [kg] front-end parts made of carbon steel), used in a 1,595 kg, North American (NA)-built, large, luxury, rear-wheel-drive, 4-door 2007 GM-Cadillac CST sedan, driven for 200,000 kilometers (km) in North America, including the end-of-life phase. The baseline steel functional unit includes 79 parts, 90% of stamped hot-dip galvanized coil and 10% of finished cold-rolled coil. The Mg front end for the analysis has a weight of 45.2 kg with only 27 parts (due to consolidation) and a 45% weight reduction compared to conventional stamped steel. Die casting, stamping, and extrusion technologies are used for part manufacturing in weight ratios of 67%, 9%, and 24%, respectively. The corresponding alloys for these technologies are AM60B, AZ31, and AM30, respectively. Part manufacturing, vehicle use, and end-of-life are three major life-cycle stages considered in the analysis. Part manufacturing is based on primary metal production using the LCI data collected directly from existing NA manufacturing facilities. However, Chinese primary Mg production data are used, reflecting recent Mg market trends. Energy-use and emission estimates during the use phase of the life cycle are made separately at the levels of well-to-pump and pump-to-wheel. The consequential allocation approach is considered for end-of-life recycling, providing incentives for recycling at the end of product life, and thereby supports resource conservation. SimaPro, an LCA software package developed by PRé Consultants in the Netherlands and designed for analyzing the environmental potential impact of products and services, was used to perform this life-cycle assessment.

Life-cycle energy estimates, shown in Figure 2, indicate that the Mg front end has about 16.5% lower energy than the conventional stamped steel front end. Estimates for part production and recycling in this figure are based on several pre- and post-processing steps, respectively, considered in the analysis. As one would expect, Mg-part production is more than five times more energy intensive than steel-part production, but

substantial energy savings at the vehicle-use and recycling stages cause its overall life-cycle energy to be lower (about 46 gigajoules [GJ]/part versus 56 GJ/part for conventional stamped steel). The use phase dominates the life-cycle energy use, with Mg energy use estimated to be 42% lower than steel after 200,000 km vehicle life-time distance. Mg's higher energy requirements at the part-production stage have been recovered at the vehicle use stage; thus the difference in life-cycle energy is roughly equal to the savings obtained at the vehicle-recycling stage. The negative primary energy at the recycling stage, illustrated in Figure 2, is the net environmental benefit after considering the energy required to recycle Mg and the energy benefits of recycling.

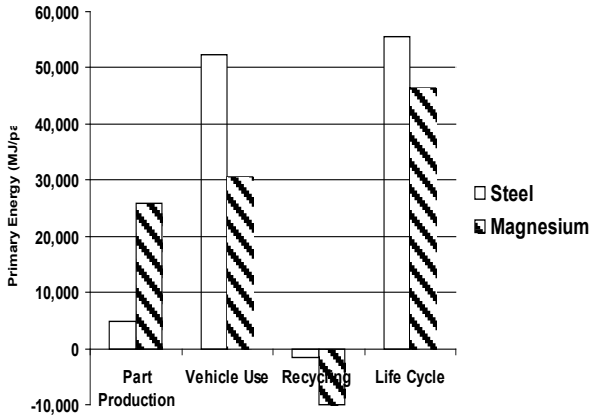

Figure 2. Life-cycle primary energy estimates of an automotive front end.

Life-cycle greenhouse gas (GHG) emissions indicate a trend similar to energy: 3.8 tons (t) CO_2 for the Mg automotive front end compared to 4.5 t CO_2 for baseline steel design. It is likely that a substantial reduction in GHG emissions could be achieved if Mg parts were based on more energy efficient and environmentally friendly primary production or enhanced recycling technologies. Other major pollutant emissions considered in the analysis follow similar trends to GHGs, with the exception of emissions of methane, nitrogen oxides, sulfur oxides, and particulates increasing over the vehicle life cycle. Higher emissions of these pollutants mainly occur at the part-manufacturing step, since most of these criteria pollutants are not as highly regulated at the part-manufacturing stage as at the vehicle-use stage. It is estimated that Mg front-end substitution would achieve life-cycle equivalence in terms of both primary energy and GHG emissions within the life cycle. Primary energy equivalence would be achieved around 116,000 km compared to 148,000 km for GHG emissions.

Life-Cycle Analysis of Carbon-Fiber-Reinforced Polymer-Matrix Composites

An LCA of carbon-FRPMCs has been initiated to compare the potential energy and environmental impacts of alternative carbon-fiber precursor materials and production technologies for manufacturing a representative automotive part, in this case the floor pan of an NA-built, 4-door, large, luxury, rear-wheel-drive vehicle. Although the focus is on the carbon-fiber production step using alternative precursor materials, other life-cycle stages such as part production, vehicle use, and part recycling/disposal are also considered. Conventional polyacrylonitrile and a renewable resource material such as lignin are the two carbon fiber precursor materials considered for the analysis. Lignin is currently isolated from the chemical pulping of wood for paper production, but the byproduct generated during the cellulosic ethanol production provides an alternative, inexpensive resource which has been considered in this analysis. Sheet molding compound and programmable powdered preforming process (P4; see report 8.C) followed by compression molding in each case are the two part manufacturing technologies considered for the floor pan. End-of-life recycling of carbon-FRPMCs will be by the thermal treatment method developed by Argonne National Laboratory. Vinyl ester and polyester are the resin matrix materials considered for P4 and sheet molding compound technologies, respectively. For comparison purpose, hot-dipped mild steel has been considered as the baseline.

LCI data collection for various technologies considered at various life-cycle stages has been completed. Most data collection is by contacting directly the industry personnel involved in the development of such a technology, particularly in the case of lignin-based carbon-fiber production technology. Data collection for conventional carbon-fiber production technology was based on the data available from a commercial production facility. Commercial LCA software such as

SimaPro, containing some of the LCI databases for commercially available processing technologies, will be used for the comparative LCA of alternative carbon-FRPMC floor-pan production technologies. The LCA under investigation would not only provide the positive (lightweighting vehicles for reduced energy and emissions) and negative (energy use and emission during part production) aspects of carbon-FRPMC use in light-duty vehicles but also recommendations for improved environmental impacts when using this material. Sensitivity analysis would be a key element of this assessment, providing information on the robustness of energy and environmental performance of the competing processing technologies.

Conclusions

The specific goal of LM is to develop cost-effective material and manufacturing technologies by 2010 that, if implemented in high volume, could reduce the weight of vehicle body and chassis systems by 50% with safety, performance, and recyclability comparable to 2002 vehicles. The intermediate body and chassis weight reduction goal of 25% in 2008 can be met through either the use of Al or glass-FRPMCs in major body and chassis components. With the consideration of secondary weight savings, a higher body and chassis weight reduction (26–32%) than the 25% weight reduction goal was achieved under two lightweight material scenarios. Powertrain resizing and secondary weight savings can provide cost-effectiveness both at the retail price and life-cycle cost levels for glass-FRPMC vehicles, but in the case of Al vehicles, a vehicle retail price premium of $180/vehicle would be necessary. Consideration of powertrain resizing, secondary weight savings, and life-cycle cost perspectives are therefore important to maximizing the fuel economy gains from a lightweight structure and to eventual successful market penetration of lightweight vehicles in the future.

Life-cycle results here indicate that Mg can have life-cycle advantages over steel, even with the dominance of the energy-intensive and less environmentally friendly primary Mg processes in use today. It is likely that Mg will become increasingly favorable from energy and emissions perspectives with the ongoing improvements being undertaken by Chinese suppliers. It is important that future LCAs capture these ongoing primary metal and part manufacturing technology improvements, including the various end-of-life recycling options, as some of these will become economically viable with increased Mg demand for automotive applications. By analyzing several scenarios, realistic answers to a wide range of major issues such as sustainable material management, product stewardship, energy efficiency, GHG reduction, and the impact of alloy-making and component-production technologies can be obtained from a holistic life-cycle perspective.

Carbon-FRPMCs offer significant potential for reducing vehicle weight while maintaining strength and stiffness. These composites are up to 30% lighter than Al and 50% lighter than steel and can reduce the overall weight of a vehicle up to 10%. Carbon-fiber production is one of the most energy-intensive production steps in the manufacturing of carbon-FRPMCs; its CO_2 emissions are estimated to be 15 times more than conventional steel on a weight basis. Low-cost and renewable precursor materials such as lignin offer significant energy- and emission-reduction potential in the manufacturing of these materials. A life-cycle assessment of this material has been started to compare the potential energy and environmental impacts of manufacturing a representative automotive part, the floor pan, with a focus on comparison of conventional and lignin-based precursor materials technologies for carbon-fiber production. LCA would determine not only the positive (lightweighting vehicles for reduced energy and emissions) and negative (energy use and emissions during part production) aspects of this type of material use in light-duty vehicles, but also recommendations for improved environmental impacts of using this material.

The updated paper on primary Mg production costs for automotive applications indicates that potential for Mg use in automotive applications has been affected during the last 2 years because the prices of competing lightweight materials are trending upward to a lesser extent even with the

availability of lower-price Chinese Mg (recent Chinese Mg is priced commensurate with its production cost). Mg will continue to suffer as long as the supply situation does not improve even with the strong demand pressure on other lightweight materials. It is estimated that the Chinese magnesium production cost is around $1.11/lb, but higher raw-material, energy, and labor costs; reduced tax incentives for exports of raw materials; a booming Chinese economy; currency revaluation; and environmental compliance costs may further increase the cost of Chinese-produced Mg even with the continuation of ongoing improvements in its Pidgeon process. A tight supply situation will prevail worldwide with only new plants being built in China in addition to an increase in Chinese domestic consumption and more exports of its final products at the expense of reduced primary Mg. The lack of available financing for the huge capital investment would be the major barrier to expanding existing electrolytic plant capacity or adding new electrolytic capacity in the West, although Mg production costs appear to be economically viable with recent high market prices. New or expanded Western Mg supplies will only occur with continuation of higher prices and assurance of strong market demand in the future (see, for example, Alcoa's consideration of restarting its Addy, Washington, Mg plant). It is unlikely that some of the yet-to-be commercialized technologies considered here will come online, although they do hold significant promise to be competitive with the low-cost Chinese Pidgeon process.

Presentations/Publications/Patents

1. S. Das, "Primary Magnesium Production Cost for Automotive Applications," *Journal of Metals*, **60**(11), pp. 51–57 (2008).

B. Intermediate-Rate Crush Response of Crash-Energy Management Structures

Principal Investigator: J. Michael Starbuck
Oak Ridge National Laboratory
P.O. Box 2009, Oak Ridge, TN 37831-8048
(865) 576-3633; fax: (865) 574-8257; e-mail: starbuckjm@ornl.gov

Technology Area Development Manager: Joseph A. Carpenter
(202) 586-1022; fax: (202) 586-1600; e-mail: joseph.carpenter@ee.doe.gov

Field Project Monitor: C. David Warren
(865) 574-9693; fax: (865) 574-6098; e-mail: warrencd@ornl.gov

---

Contractor: Oak Ridge National Laboratory (ORNL)
Contract No.: DE-AC05-00OR22725

Objective

- Develop unique characterization facilities for controlled progressive-crush experiments, at intermediate rates, of automotive materials (polymer composites, high-strength steels, and aluminum) and structures.
- Study the deformation and failure mechanisms of automotive materials subjected to crush forces as a function of impact velocity.
- Obtain specific-energy-absorption and strain data and correlate with deformation and failure mechanisms to describe the unknown transitional effects from quasi-static to high loading rates for polymer composites.
- Characterize the strain rate effects for metallic materials and components.
- Provide access to the unique test capabilities that are developed to university, industry, and government users for collaborative research.

Approach

- Develop a unique high-force [500 kiloNewton (kN)], high-velocity [8 meters (m)/second], servohydraulic machine to conduct progressive-crush experiments on structural components at intermediate rates.
- Develop a low-force (40 kN), high-velocity (18 m/s), servohydraulic machine for conducting tensile strain rate characterization tests.
- Use high-speed imaging to observe and document deformation and damage mechanisms during the crush event.
- Conduct strain measurements at discrete locations and explore full-field measurement of strains and curvatures.
- Coordinate polymer composite investigations with the Automotive Composites Consortium (ACC) Energy Management Working Group (see the ACC report *Crash Energy Management*).
- Coordinate steel investigations with the Auto/Steel Partnership (A/SP; see the A/SP-ORNL report *Strain Rate Characterization*).

Accomplishments

- Continued diagnostic testing on high-velocity (18 m/s) test machine to better understand inertial effects in the test data.

- Explored electrical-resistance strain gages, extensometers, and optical methods for measuring local and average strains.
- Completed three-point bend tests on the Test Machine for Automotive Crashworthiness (TMAC) second user project with L&L Products.
- Completed tests on high strain rate tensile coupons for the General Motors- (GM-) ACC user project.
- Completed octagonal-tube tests in support of the A/SP Strain Rate Characterization project.
- Completed base-metal tests on dog-bone specimens in support of the A/SP Strain Rate Characterization project.

Future Direction

- Explore techniques for full-field measurement of strains and curvatures.
- Develop real-time data analysis interface.
- Complete a second user project with U. S. Army Corps of Engineers.

Introduction

Progressive crush is an important mechanism by which the kinetic energy of a traveling automobile is dissipated in a collision to protect the safety of occupants. Unfortunately, the mechanisms governing the progressive-crush response of some emerging automotive materials are not well understood. Additionally, many of these materials are known to exhibit responses that are sensitive to rate of loading.

Understanding the influence of impact velocity on the crush response of materials and structures is critically important for crashworthiness modeling inasmuch as collisions occur at a range of velocities. Additionally, from a structural standpoint, the deformation (or strain) rate is generally not unique from either a spatial or temporal standpoint. Consequently, it is important to quantify the behavior of materials at various strain rates.

TMAC

Typically, standard test machines are used for experiments at quasi-static rates, whereas drop towers or impact sleds are the convention for dynamic rates. These two approaches bound a regime within which data for experiments at constant impact velocity are not available by conventional experimental practice. This regime is referred to as the "intermediate strain rate" regime in this report and is defined by impact velocities ranging from 1 m/s to 5 m/s. Investigation of rate effects within this regime requires experimental equipment that can supply a large force with constant velocity within these rates.

Using a drop tower or sled at intermediate strain rates, although technically possible, is problematic due to the prohibitively large mass required to maintain constant velocity during the crush. Consequently, ORNL and ACC collaborated to define specifications for a unique experimental apparatus that mitigates the shortcomings of existing equipment. MTS Systems Corporation designed and built the servohydraulic test machine, TMAC. TMAC is uniquely suited for controlled progressive-crush tests at constant velocity in the intermediate-velocity range (i.e., less than 5 m/s) because of the large energy available at those rates and the sophisticated simulation and control software that permits velocity uniformity to within 10%.

The TMAC experimental facility is used to understand the crush behavior between static and dynamic (8 m/s) conditions. TMAC was originally installed at the National Transportation Research Center (NTRC), Knoxville, Tennessee, as shown in Figure 1. Since then TMAC has been relocated to ORNL.

Figure 1. Installation of TMAC in the NTRC Composite's Laboratory.

Status

Since the last reporting period, activities have focused on completing user projects, developing and promoting new user projects, improving data acquisition, and expanding test capability for higher-rate coupon tests.

Interactions with industry and academia for potential new user projects have taken place with Rutgers, Massachusetts Institute of Technology, SAE High Strain Rate Plastics Consortium, GM, Ford, Imperial College (London, England), Washington University, University of Utah, and L&L Products. Also, discussions continued with the University of South Carolina and Correlated Solutions on developing a full-field, dynamic strain measurement system using digital image-correlation techniques.

In addition to promoting user programs, continued support was provided to the development of a crashworthiness chapter for the military's composite design guide, CMH-17 (formerly MIL-HDBK-17), and the start of a technical division on the Dynamic Response of Materials within the Society for Experimental Mechanics.

Project Support Activities

Tube tests were completed on TMAC in support of the A/SP Strain Rate Characterization project (see report 5.F) These tubes had an octagonal shape with spot welds down the edges of the tube. A base plate having a flange with holes drilled for bolting to existing TMAC fixtures was welded to one end of the tube. The progressive-crush end of the tube was machined at an angle for the triggering mechanism. Three different material systems were tested at three different velocities. In addition to the tube tests, coupon-level strain rate characterization tests were completed on seven different high-strength base metals.

User Programs

A follow-on user project was completed for L&L Products. L&L Products manufactures reinforced composite-steel box-beam structural components that are integrated into key locations in vehicles to improve vehicle crashworthiness. TMAC can conduct tests at rates higher than normally available from other test methods and can supply the needed structure performance data necessary for evaluating L&L's box beams. To help L&L Products define their test plan, 14 exploratory bend-crush tests were conducted in fiscal year (FY) 2007 to explore the suitability of their custom, three-point-bend test fixture and verify the suitability of the test for collecting the desired high strain rate data. Figure 2 shows the test setup, and Figure 3 shows some of the failed specimens.

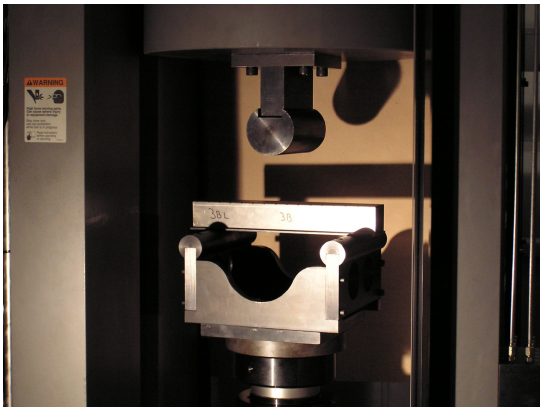

Figure 2. Three-point-bend test setup on TMAC.

Figure 3. Failed L&L Products specimens.

All tests were successful, but minor modifications were needed for the L&L Products test fixture to harden the supports and loading nose. The complete test matrix consisted of more than 100 specimens at various rates up to 8 m/sec. Different specimens were tested to evaluate the role that different beam insert materials had on energy absorption. This was the first non-axial crush testing to be preformed on TMAC and was successful in demonstrating its use for studying side impact crash effects. A follow-on proposal for conducting high strain rate lap-shear tests on coupons is being developed. The prototype specimen is shown in Figure 4.

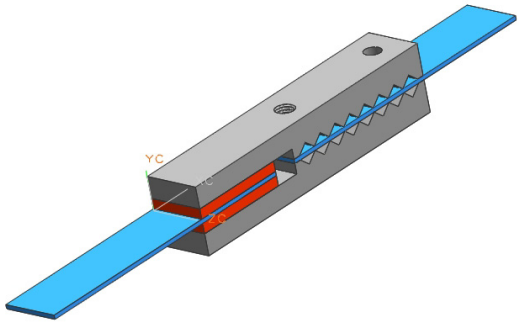

Figure 4. High strain rate lap-shear specimen for L&L Products.

The object of the GM-ACC User Project is to conduct high strain rate coupon tests on carbon-fiber braided material. This same material has been used extensively in other ACC projects for tube-crush studies. The data to be generated from these tests are in support of a rate-sensitive material model developed by Stanford University for predicting the crush behavior of carbon-fiber tubes. These tests were conducted on the high strain rate coupon test machine described in the next section. The coupons used for these tests were machined from unidirectional braided plaques. The test plan consisted of 25°, 45°, and 65° off-axis coupons tested at five different nominal strain rates (0.01, 0.1, 1.0, 10.0, and 100.0/s). The preliminary tests were completed to determine load- and strain-measuring requirements and any corresponding data acquisition modifications. It was determined that updates to the data-acquisition hardware were needed to increase scan rates and that strain gages were the preferred method for measuring strain. The hardware was updated and all specimens were returned to GM to instrument with strain gages. The specimens were returned to ORNL, and all of the planned tests were completed. A typical test setup is shown in Figure 5, and typical failed specimens are shown in Figure 6. The test data were then provided to ACC for analysis.

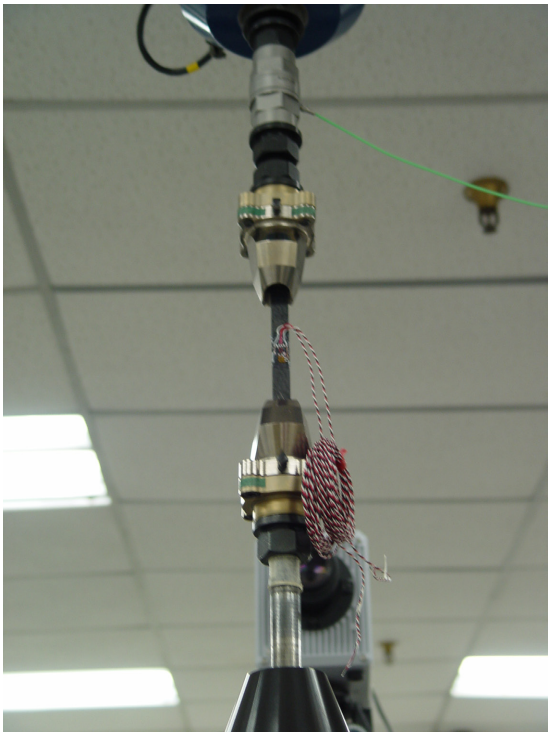

Figure 5. Typical coupon test setup on high strain rate tension machine.

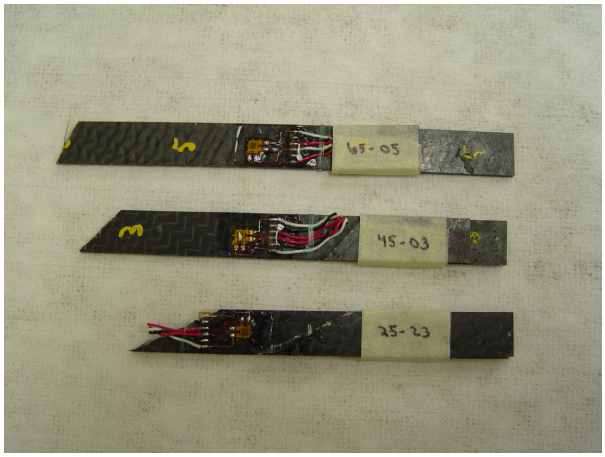

Figure 6. Typical failed off-axis tension specimens.

High Strain Rate Coupon Test Machine

To complement the TMAC capability, a high strain rate coupon test machine was designed, fabricated by MTS, and installed at ORNL (Figure 7). Where TMAC provides the capability for a large-force (500 kN static), structural-level test, this machine was designed to conduct low-force (40 kN static), coupon-sized tests under primarily tensile loads. A typical coupon would be a dog-bone strip where the gage section is 15 mm wide with a thickness of 3 mm. This type of test is ideal for generating rate-sensitive stress-strain curves in development of basic material constitutive laws. The machine has a maximum crosshead speed of 18 m/s with a 400 mm total stroke capacity. The actually working stroke is reduced to 175 mm when installing a slack adapter to allow for the actuator to get up to constant speed before loading the specimen. These specifications were accomplished by a using a 400-gallon-per-minute servovalve and 50-gallon accumulators (see Figure 8). Another feature of the test machine is the use of low mass grips designed to reduce ringing in the system thereby minimizing inertial effects in the load signal. The grips were based on a Colorado School of Mines design and are shown in Figure 9.

Figure 7. High strain rate (18 m/s) coupon test machine.

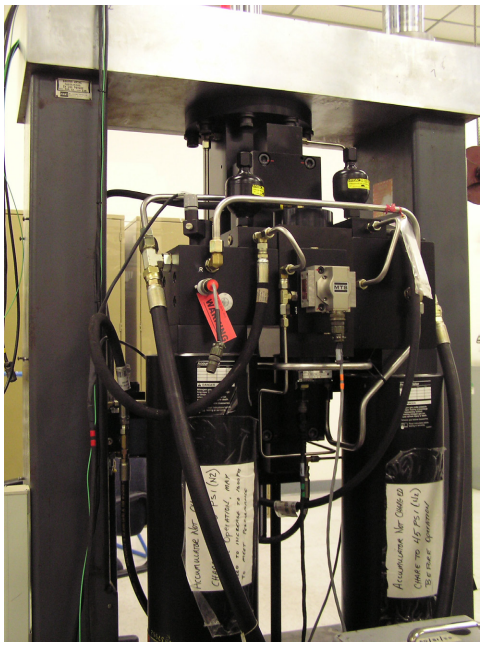

Figure 8. Accumulators and servovalve for high strain rate test machine.

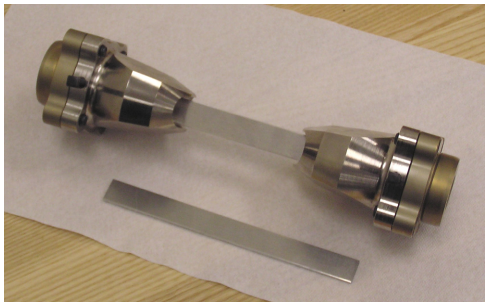

Figure 9. Low-mass grip used in high strain rate test machine.

Conclusions

TMAC provides a unique capability to measure the specific energy absorption on crush tubes and other specimen geometries as a function of (constant) impact velocity within a range from quasi-static to 8 m/s. To complement this capability, a new machine was installed for conducting coupon-level tests up to 18 m/s.

User interest in this equipment remains very high with follow-on projects and new projects being in the draft stage. TMAC was also instrumental in meeting project objectives for the A/SP. In all of these tests, high-speed video was recorded to document the failure mechanisms using a state-of-the-art complementary metal-oxide semiconductor camera that was procured for the TMAC installation.

Presentations/Publications/Patents

None

C. Mission Eggcellence—K–12 Outreach Program

Principal Investigator: Mark F. Horstemeyer
Chair in Solid Mechanics & Professor, Mechanical Engineering
Center for Advanced Vehicular Systems
Mississippi State University
206 Carpenter Bldg., P.O. Box ME
Mississippi State, MS 39762
(662) 325-7308; fax: (662) 325-7223; e-mail: mfhorst@me.msstate.edu

Co-Principal Investigator: Rosemary Cuicchi
Center for Advanced Vehicular Systems
Mississippi State University
200 Research Blvd.
Mississippi State, MS 39762
Office: (662) 325-8518; e-mail: *rcuicchi@cavs.msstate.edu*

Co-Principal Investigator: Shaik Jeelani
Director, Center for Advanced Materials
Vice President, Research and Sponsored Programs
Tuskegee University
101 Chappie James Center
Tuskegee, AL 36088
Office: (334) 727-8970; fax: (334) 724-4224; e-mail: jeelanis@tuskegee.edu

Technology Area Development Manager: Joseph A. Carpenter
(202) 586-1022; fax: (202) 586-1600; e-mail: joseph.carpenter@ee.doe.gov

Field Project Officer: Aaron D. Yocum
(304) 285-4852; fax: (304) 285-4403; e-mail: aaron.yocum@netl.doe.gov

---

Contractor: Mississippi State University (MSST)
Contract No.: 4000054701

Objective

The project is designed to develop a commitment from Center for Advanced Vehicular Systems (CAVS) and MSST to the children of the state of Mississippi through curriculum instruction and competitions dealing with the design of a vehicle bumper and/or seatbelt for passenger safety. These instruction and student competitions will create an awareness of the importance of design in safety implications, and the real-world applications of mathematics, science, and engineering problem-solving skills. Mission Eggcellence will also create awareness among the Mississippi school-age population of future job opportunities in the state of Mississippi, as well as college majors associated with these jobs.

Approach

- Create a grade appropriate curriculum, with experiments associated with the physics of car crashes for grades K–2. (Objective 1)
- Create a grade appropriate curriculum, with experiments associated with the physics of car crashes for grades 3–5. (Objective 2)

- Develop a Teacher Workshop for grades K–2 teachers for training in the use of grade appropriate curriculum in the regular classroom. Equipment necessary to conduct the experiments and compete in the competitions would be given to each teacher participant. (Objective 3)
- Develop a Teacher Workshop for grades 3–5 teachers for training in the use of grade appropriate curriculum in the regular classroom. Equipment necessary to conduct the experiments and compete in the competitions would be given to each teacher participant. (Objective 4)
- Design a competition for grades K–2, incorporating bumper design for passenger safety. (Objective 5)
- Design a competition for grades K–2, incorporating car design for passenger safety. (Objective 6)
- Design a competition for grades 3–5, incorporating bumper design for passenger safety. (Objective 7)
- Design a competition for grades 3–5, incorporating car design for passenger safety. (Objective 8)
- Create a grade appropriate curriculum, with experiments associated with the physics of car crashes for grades 6–8. (Objective 9)
- Create a grade appropriate curriculum, with experiments associated with the physics of car crashes for grades 9–12. (Objective 10)
- Develop a Teacher Workshop for grades 6–8 teachers for training in the use of grade appropriate curriculum in the regular classroom. Equipment necessary to conduct the experiments and compete in the competitions will be given to each teacher participant. (Objective 11)
- Develop a Teacher Workshop for grades 9–12 teachers for training in the use of grade appropriate curriculum in the regular classroom. Equipment necessary to conduct the experiments and compete in the competitions will be given to each teacher participant. (Objective 12)
- Design a competition for grades 6–8, incorporating bumper design for passenger safety. (Objective 13)
- Design a competition for grades 6–8, incorporating car design for passenger safety. (Objective 14)
- Design a competition for grades 9–12, incorporating bumper design for passenger safety. (Objective 15)
- Design a competition for grades 9–12, incorporating car design for passenger safety. (Objective 16)
- Expand the Mission Eggcellence Program throughout the state of Mississippi by continuing the teacher workshops and student competitions. (Objective 17)

Accomplishments

- Completed curriculum for grades K–2. (Objective 1)
- Completed curriculum for grades 3–5. (Objective 2)
- Completed Teacher Workshop for teachers of grades K–2. (Objective 3)
- Completed Teacher Workshop for teachers of grades 3–5. (Objective 4)
- Completed Bumper Design Competition for grades K–2. (Objective 5)
- Completed Car Design Competition for grades K–2. (Objective 6)
- Completed Bumper Design Competition for grades 3–5. (Objective 7)
- Completed Car Design Competition for grades 3–5. (Objective 8)
- Completed curriculum for grades 6–8. (Objective 9)
- Completed curriculum for grades 9–12. (Objective 10)
- Completed Teacher Workshop for teachers of grades 6–8. (Objective 11)
- Completed Teacher Workshop for teachers of grades 9–12. (Objective 12)

- Completed Bumper Design Competition for grades 6–8. (Objective 13)
- Completed Car Design Competition for grades 6–8. (Objective 14)
- Completed Bumper Design Competition for grades 9–12. (Objective 15)
- Completed Car Design Competition for grades 9–12. (Objective 16)

Future Direction

The major emphasis for the Mission Eggcellence Program is to expand the range of this program in the state of Mississippi through the teacher workshops (Objective 17). The teacher workshops will provide an avenue for K–12 teacher training in the use of the curriculum in their classrooms. The equipment will be provided to teachers who participate in the teacher workshops. This will give more students the opportunity to learn the physics associated with car crash safety and to incorporate the physics into the design of the car bumper and the car chassis. The student competitions, which are grade appropriate, are held for students of any teacher who has previously attended the teacher workshops. Teachers can enter a team of one to three students in the Mission Eggcellence (bumper) Competition and a team of one to three students in the Automotive (car design) Competition for each of the grade sections (K–2, 3–5, 6–8, and 9–12).

Introduction

MSST CAVS is teaming with the local school districts and the Mississippi Children's Museum (MCM) to develop a sophisticated science and technology curriculum, using teachers and workshops in the museum to inspire young minds to explore the worlds of math, science, and engineering. We will create powerful interactive learning/teaching kits for K–12 students with a program based upon materials design, which will be supported by ASM International, entitled Mission Eggcellence.

Mission Eggcellence provides students with a hands-on introduction into vehicular crashworthiness through applying basic concepts of physics (students are provided with simple definitions from physics such as Mass, Velocity, Momentum, and Energy and how they are used during crash), explanations of what actually happens during a crash (using the physics terms and defining what is necessary to enable passengers to survive a crash), and examples of safety devices (explanations and examples of some devices such as Bumpers, Seatbelts, Airbags, and Safety Cages used in cars and trucks, with simulations to demonstrate how they work). Other explanations provided will include manufacturer goals (creating a vehicle that is lightweight for the lowest price possible, creating a vehicle that demonstrates good fuel efficiency and creating a vehicle that is aesthetically pleasing in appearance) versus consumer goals (a vehicle that is strong enough to protect passengers from impact, a vehicle that is light enough to provide economical fuel consumption, a vehicle that has a pleasing appearance, a vehicle that has a memory of its shape and can be repaired faster, less expensive, and easier) and the difficulties involved in balancing these requirements.

Vehicles, materials, eggs, workbooks/worksheets, and instruction will be provided to the students, with which they must design a safety barrier for each team's vehicle that will prevent the egg from breaking upon impact during an impact competition. The vehicles are released upon a ramp, which is elevated to a higher degree of angle (from 15 to 70 degrees) at each step of the impact competition and the vehicles in which the eggs do not break can win. The winners are determined by the lightweight designs. Competitions are expected to be statewide. Undergraduates and graduate students will play a large role in communicating the principles and overseeing the activities. They will also be used to help monitor the tournaments and mentor some of the K–12 students.

Each curriculum consists of eight grade-appropriate experiments for the physics concepts of velocity, acceleration, Newton's Third Law, momentum, impulse, elastic and inelastic collisions. These experiments will include a bumper design and car design. In the bumper design competitions for grades K–2, 3–5, 6–8, and

9–12, the bumper is tested by rolling a wooden car, with the bumper attached, down a ramp using a raw egg as the passenger. The winner is the car that can make it down the steepest incline with the egg intact. The tie breaker is the car with the lightest mass. In the grades K–2 and 3–5 car design competitions, a car is designed using K'nex pieces from a kit. In the grades 6–8 and 9–12 car design competitions, students will use a car designed from balsa wood. The winner is the car that can make it down the steepest incline with the egg intact. The tie breaker is the car with the lightest mass.

Academic/Research Excellence Basis

An overarching theme of multidisciplinary design integration motivates our research, as well as our multilevel educational activities in K–PhD and continuing education. Our educational approach is structured to overcome the knowledge compartmentalization and overspecialization of traditional technical education that stand as barriers to the implementation and dissemination of science-based engineering. Core university collaboration seeks to empower a broad range of students through a fusion of exciting new science-based tools, with design habits of mind, team creativity, and effective multidisciplinary communication. Our Mission Eggcellence design project work will be enhanced by the emerging technology of a distributed Web-based collaborative environment. We have a clear education accountability structure administered by the CAVS chair professor, Mark Horstemeyer. In addition, MSST CAVS has a strong extension/ outreach center in which quick implementation of research is plausible.

Children's Museum **Student Crash Competition**

Project Objectives and Expected Outcomes/Impacts

In alignment with the objectives and expected outcomes of this task, which is to empower and inspire all our state's children regardless of their social, educational, or economic background and to discover their potential through tapping their curiosity and creativity, through hands-on and engaging exhibits and programs, we will create a dynamic and competitive program that will do the following.

- Provide children the opportunity to perform hands-on experiments; to learn the value of mathematics, physics, and engineering and how their uses in the experiments correlate with "real world" engineering problems; and to create for themselves the experience of mastering tasks they would normally perceive to be difficult, which will increase their self-esteem, demonstrated by increased performance levels in school.
- Address the needs of Mississippi children, especially in the areas of math, science, and engineering.
- Reach children in schools and communities throughout the state through our Outreach Program.
- Complement the mathematics, physics, and science programs being taught in school. Correlated to the math and science standards in the state of Mississippi.
- Promote a desire to learn more about the world in which the children live and how it works.

We need a creative K–Ph.D. program that anticipates the current and future high-tech jobs revolving around the automotive industry in our state. Children need to be excited by math, science, and engineering and the MCM can enkindle that passion. If we can help children develop a passion for learning, they are going to want to understand how things work and how to make things work better. For Mississippi to advance in the science and technology fields, children must become excited about learning, and this is the fundamental mission of a children's museum.

Mission Eggcellence, among other materials design projects, can provide a science/engineering experience that will inspire children to want to return time and time again. Each time that they return, they will learn things about their world that inspire them to want to return and learn more. The imaginative and experimental Mission Eggcellence is relevant to the students' classwork and can be correlated with "real world" safety, reliability, and crashworthiness issues that are faced today within the automotive industries.

Contributions to the Long-Term and Sustainable Engagement of the Team/Unit

MSST is developing an "Automotive Experience" strategic program that includes K–12, undergraduate work, and graduate level work. A new course and certificate are being developed in real time for this endeavor. For MSST to have an excellent Ph.D. pool, we need to have aligned in the pipeline K–12 students. We are viewing these grant funds as start-up funds only, but the program will continue long into the future.

From the Southern Regional Center for Lightweight Innovative Design (SRCLID) Statement of Program Objectives, the transfer of knowledge obtained from leading-edge research to K–12 educational programs is a core requirement: CAVS is required to develop an educational program to integrate lightweighting design concepts with crashworthiness into student curricula. A K–Ph.D. program will be developed that communicates the important issues of crashworthiness and safety. Crash kits will be developed for appropriate educational levels, and state and regional tournaments will be fostered to further interest in the technology and resultant designs.

Specific subtasks include the following.

- **Task 1**—Develop crash kits for K–2, 3–6, 6–8, and 9–12.
- **Task 2**—Develop tournaments with crash kits for Mississippi-wide contests.
- **Task 3**—Assist in the development of modules for MCM.

CAVS will design materials kits and crash kits with their associated documentation (student and instructor) and provide engineering specialists as keynote speakers, trainers, and lecturers. Rosemary Cuicchi (retired teacher—32 years experience) and Dr. Paul Cuicchi (Starkville High Physics teacher and MS Teacher of the Year 2002) are involved in developing the program. ASM will also be involved in helping develop the program. Nissan North America (Canton, Mississippi) and Vista Engineering, Inc. have both donated in-kind contributions to the SRCLID program with specific interest in the educational development aspects of the program.

The MCM administrators and staff will be involved in designing and setting up the exhibits within the museum, as well as establishing agendas for exhibit changes. Dr. Mark Horstemeyer is helping design the regions within the children's museum to help explain the math, science, and engineering aspects.

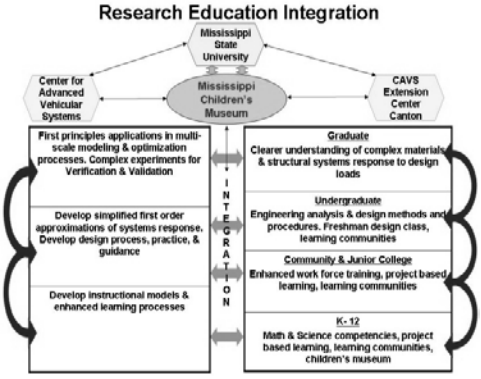

The graphic above represents the CAVS research resource vision, through which data, research materials, materials design methodologies, and basic science aspects will be made available to students through this task, sponsored by DOE and the MCM.

Evaluation/Assessment

The program will be evaluated internally, by MSST staff, and externally, by partnering organizations, committee members, and visitor surveys. Internal evaluation will take place at monthly meetings, where staff members take the opportunity to debrief with the entire group, provide feedback, and troubleshoot issues.

External evaluations will be completed through a MCM partner survey. During the evaluation of the program, staff will review the types of programs/activities offered to ensure that they accurately represent the culture and decide if an organization's participation in the program helped to provide access to the MCM for members of the community. In addition, staff will track the following:

- number of individuals who participated in the special events, workshops, and programming;
- number of communities served (examples are Latino, Native American, African-American, Asian, and Caucasian);
- number of community-based organizations with which we partner;
- number of opportunities created for cross-cultural programming; and
- number of events we will offer at the museum during the year's Passport programs.

Making a Difference within the Community and the University

University metrics will demonstrate the effectiveness of the program by showing increases in students coming to MSST and other colleges and universities, in the fields of math, science, and engineering. Within the community, we expect to see a higher rate of students becoming involved in math, science, and engineering, and in the long run, expect to see more high-tech companies moving into the state as a result of this program. If we increase the rates of students in math, science, and engineering, indicating a more highly educated future work force, the number of incoming high-tech companies will increase.

Interpreting the Accompanying Logic Model

(refer to p. 12-19)

Situation—The situation, as it applies to this project, is that children in Mississippi do not have access to innovative open-ended educational hands-on programs in which they can be exposed to viable applications of math, science, and engineering. Because the Mississippi public educational system is not considered to be strongly effective in graduating students who are strong in math, science, and engineering, few high-tech companies consider Mississippi to be an economically viable target for relocation or expansion of businesses.

Priorities and Intended Outcomes—The priorities of this project are thoroughly integrated within the mission and vision of CAVS, especially as defined by the DOE-SRCLID Statement of Program Objectives (SOPO). Specifically, the transfer of knowledge obtained from leading-edge research to K–12 educational programs via developing an educational program to integrate lightweighting design concepts with crashworthiness into student curricula, will be accomplished by developing crash kits for appropriate educational levels and by fostering state and regional tournaments to further interest in the technology and resultant designs. The intended outcome will be an increased number of students at all educational levels who will have a deeper understanding of math, science, and engineering and an appreciation of these fields of study in real-world applications.

Inputs—CAVS (MSST), the CAVS Extension (Canton), and the community will integrate into a synergistic teaming effort to provide staff, volunteers, time, money, basic research, materials, equipment, technology, and partners to ensure the success of this program

Outputs—What Will We Do? Personnel from the core facilities mentioned above will conduct workshops and meetings, will deliver services, will develop products, curriculum and provide resources, will provide training, will provide counseling, will assess the program and its effectiveness, will work with the partnering organizations, and will work with media to ensure proper dissemination of information to the public.

Outputs—Who Will We Reach? We will reach participants (children, parents, and teachers) and provide satisfaction feedback.

Outcomes—Short-Term Impacts. We anticipate an increased interest by students in math, science, and engineering as demonstrated by improved learning, awareness, knowledge, attitudes, skills, opinions and motivations, as a result of student participation in the workshops, et cetera.

Outcomes—Medium-Term Impacts. We anticipate seeing an increase in museum student participation (Actions), an increase in classroom participation (Practice), an increase in understanding and application of lessons-learned by students in their respective schools (Decision-making), an increase in awareness of potential impacts upon society of vehicle lightweighting and crashworthiness (Social Action), and an increase in students interested in math, science, and engineering.

Outcomes—Long-Term Impacts. We anticipate students graduating from their respective schools and entering colleges and universities to pursue degrees in math, science, and engineering, who will have a stronger working knowledge and understanding of math, science, and engineering as they relate to societal/behavioral, economic, civic, and environmental impacts, as well as seeing an increase in the number of high-tech companies moving to Mississippi, as a result of having a more informed and more highly educated student labor base from which future employees can be selected.

Evaluation. The effectiveness of this program will be determined by follow-up investigations, over time, to collect data, analyze and interpret the data, and report on the increase in students who enroll in institutions of higher learning in the fields of math, science, and engineering.

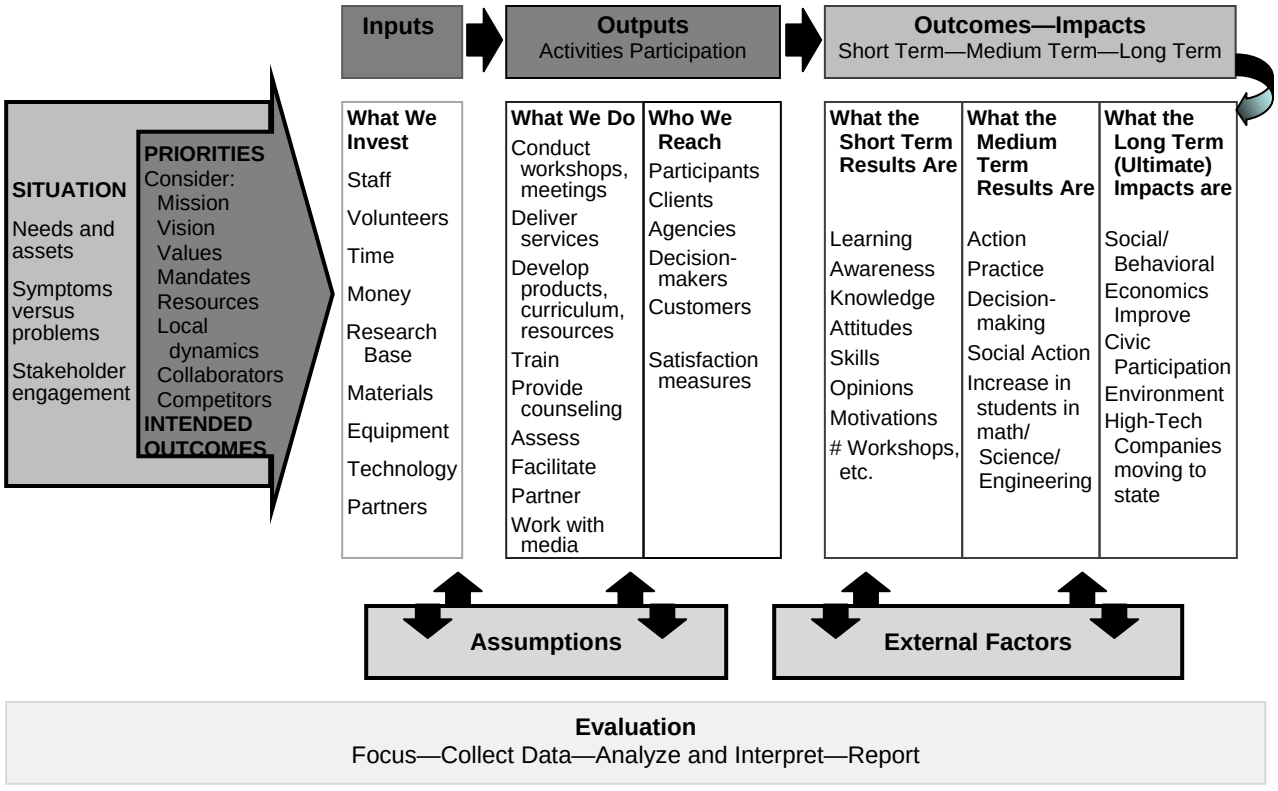

Materials Design Logic Model

Conclusions

The Mission Eggcellence Program has been developed for grades K–2, 3–5, 6–8, and 9–12. The Teacher Workshops for these grades were very successful. Ninety-five teachers have been trained in the Teacher Workshops. Two-hundred forty students have competed in the student competitions. Eighty percent of the teachers who attended the workshop had students compete in both the bumper design and car design competitions. Feedback was excellent.

Acknowledgement

The authors would like to acknowledge funding from the Center for Advanced Vehicular Systems at Mississippi State University and the Department of Energy. We also acknowledge valuable curriculum guidance and ramp construction received from Dr. Paul Cuicchi.

APPENDIX A. ACRONYMS AND ABBREVIATIONS

°C	degrees centigrade (Celsius)
°F	degrees Fahrenheit
µm	micrometer(s)/micron(s)
µs	microsecond(s)
1D, 1-D	one-dimensional
2D	two-dimensional
2DTBC	two-dimensional triaxially-braided composite
2T	two-thickness
3D, 3-D	three-dimensional
3DAP	three-dimensional atom probe
3-DEP	Three Dimensional Engineered Preform
3T	three-thickness
A/SP	Auto/Steel Partnership
ABS	acrylonitrile-butadiene-styrene
ac	alternating current
ACC	Automotive Composites Consortium
ACC-PD	American Chemistry Council, Plastics Division
ACCU	ACC Underbody
ADI	austempered ductile cast iron
AEL/ALE	Arbitrary Eulerian Lagrangian/Arbitrary Lagrangian Eulerian
AFM	atomic-force microscope/microscopy
AFM1	single-layer antiferromagnetic
AFMD	double-layer antiferromagnetic
AFR	amplified frequency ratio
AFS	American Foundry Society
AGT	Atmospheric Glow Technologies
AHSS	advanced high-strength steel
AISI	American Iron and Steel Institute
AJAX	Asynchronous JavaScript and XML
Al	aluminum
AKDQ	aluminum-killed draw quality
ALMR	arbitrary local mesh replacement
AMD	Automotive Metals Division (of USAMP)
ANL	Argonne National Laboratory
ANOVA	analysis of variance
ANSI	American National Standard Institute
AP	acidification potential
APC	American Plastics Council
API	application program interface
APS	Advanced Photon Source
ARA	Automotive Recycling Association
ARC	(International) Automobile Recycling Congress
ARD	anisotropic rotary diffusion
ARL	Army Research Laboratory
A/SP	Auto/Steel Partnership
ASB	adiabatic shear band
ASTM	American Society for Testing and Materials

at	atomic
ATR-FTIR	attenuated total reflectance Fourier transform infrared (spectroscopy)
AWS	American Welding Society
B	boron
bcc	body-centered cubic
BCJ	Bammann-Chiesa-Johnson
BDE	brominated diphenyl ethers
BE	blended element/elemental
BEM	boundary element method
BET	Brunauer-Emmett-Teller
BFI	body-frame-integral
BH	bake hardenable
BIF	barrier improvement factor
BIW	body-in-white
BL	black liquor
BLRT	bond-line read-through
BLS	Brillouin light scattering
BME	ballistic mass efficiency
BOF	body-on-frame
BPEL	Business Process Execution Language
BR2	Bead-Rod
BS	British Standard
BSEF	Bromine Science and Environmental Forum
C	carbon
C	compression
CA	cooperative agreement
CAD	computer-aided design/drafting
CAE	computer-aided engineering
CAFE	corporate average fuel economy
CANMET	Canada Centre for Mineral & Energy Technology
CAVS	Center for Advanced Vehicular Systems
CB	cylinder block
cc	cubic centimeter
CC	continuous cast/casting
CCT	continuous cooling transformation
CD	compact disc
CDC	channel die compression
CDF	cumulative distribution function
CF	carbon fiber
CFM	continuous-filament mats
CG	conjugate gradient
CLM	confocal laser microscopy
CLTE	coefficient of linear thermal expansion
cm	centimeter
CNC	computerized numerical control
CNF	carbon nanofiber
CO_2	carbon dioxide
COD	crack opening displacement
COE	coefficient of expansion

COF	coefficient of friction
COM	Conference of Metallurgists
COV	coefficient of variance/variation
CP	commercial purity/complex phase
CPMT	Center for Powder Metallurgy Technology
CPU	central processing unit
cr	cold rolling
Cr	chromium
CRADA	Cooperative Research and Development Agreement
CSM	Composite Spray Molding/Colorado School of Mines
CSP	Continental Structural Plastics
CT	computed tomography/cross-tension
C/T	compression/tension
CTE	coefficient of thermal expansion
Cu	copper
CVDM	Center for Virtual Design and Manufacturing
CWL	cell-wall loading
CWT	Changing World Technologies
DACE	design and analysis of computer experiments
DAIS	direct-access interface system
DAS	data-acquisition system
DAW	drawn-arc welding
DBF	draw bend formability
DBMS	Database Management System
DBS	draw-bend springback
DBU	diaza(1,3)bicycloundecane
dc	direct current
DC	direct chill/die cast
DFL	dry-film lubricant
DFT	density functional theory/discrete Fourier transform
DIC	digital imaging correlation
DICTRA	Diffusion Controlled TRAnsformations
DLFT	direct long-fiber thermoplastic
DMA	dynamic mechanical analysis/analyzer
DOE	U.S. Department of Energy
DoE	design of experiment
DoF	degree(s) of freedom
DoD	Department of Defense
DP	dual phase (steel)
DRV	dynamic recovery
DRX	dynamic recrystallization
DQ	drawing quality
DQSK	drawing-quality special-killed/draw-quality, semi-killed (steel)
DR	dimension reduction
DS	driver seat
DSA	dynamic strain aging
DRIFT	Direct Reinforced/Reinforcement Fabrication Technology
DRIFTS	diffuse reflectance infrared Fourier transform spectroscopy
DRX	dynamic recrystallization
DSA	dynamic strain aging

DSC	differential scanning calorimeter/calorimetry
DTA	differential thermal (thermogravimetric) analysis/analyzer
DTS	Deep Thermal Shock Test
DTUL	deflection temperature under load
DWT	die wear test
E	Young's modulus (of elasticity)
EAM	embedded-atom method
EB, E-beam	electron beam
EBSD	electron backscatter diffraction
ECAE	equal channel angular extrusion
ECAP	equal channel angular extrusion
ECD	electron capture detector
EDS	energy dispersive X-ray spectra
EDX	energy-dispersive X-ray
EEM	Element Exchange Method
EERE	Energy Efficiency and Renewable Energy
EG	electro-galvanized
EGLD	extended generalized lambda distribution
EH&S	environmental, health, and safety
EHF	electrohydraulic forming
EIFS	equivalent initial flaw size
EIS	electrochemical impedance spectroscopy
ELV	end-of-life vehicle
EMF	electromagnetic forming
EMT	Eshelby-Mori-Tanaka
EMTA	Eshelby-Mori-Tanaka approach
EP	eutrophication potential
EPA	Environmental Protection Agency
EPFL	Ecole Polytechnique Fédérale de Lausanne (Swiss Federal Institute of Technology)
EPOC	Engineering Project Oversight Committee
EPR	endpoint reference
ERW	electric resistance welding
ESB	enterprise service bus
ESR	electron spin resonance
eV	electron volt(s)
EVO	engineering virtual organization
EWI	Edison Welding Institute
FAME	Flexible Advanced Metamodeling Estimator
FAR	fiber aspect ratio
F_b	normalized back force
fcc	face-centered cubic
FCVT	FreedomCAR Vehicle Technologies
Fe	iron
FE	finite element
FEA	finite-element analysis
FEC	front-engine cover
FEFRAC	finite-element fracture
FEG-SEM	field-emission gun scanning electron microscope (microscopy)

FEM	finite-element modeling
FESEM	field-emission scanning electron microscope (microscopy)
FFNN	feed-forward neural network
FFI	full-frontal impact
FGPC	Future Generation Passenger Compartment
FHWA	Federal Highway Administration
FLAPW	full-potential linearized augmented plane wave
FLC	forming limit curves
FLCA	front-left control arm
FLD	fiber length distribution/forming-limit diagram
FM	ferromagnetic
FMEAM	force-matching embedded-atom method
FMVSS	Federal Motor Vehicle Safety Standard
FOD	fiber-orientation distribution
FORM	first order reliability method
FOTS	first-order Taylor series
FP	Focal Project (ACC)
FRP	fiber-reinforced plastic
FRPMC	fiber-reinforced polymer-matrix composite
FS	failure sampling
FSP	fiber saturation point
FSW	friction-stir welded/welding
FSSW	friction-stir spot weld/welding
FTC	Federal Trade Commission
FTIR	Fourier transform infrared
FVF	fiber volume fraction
FWHM	full-width at half maximum
FY	fiscal year
g	gram(s)
GA	genetic algorithm/galvannealed (steel)
gal.	gallon(s)
GaBi	Ganzheitliche Bilanzerung software
GBD	generalized beta distribution
GC	gas chromatography
GC-ECD	gas chromatography–electron-capture detector
GC-MS	gas chromatograph(y)-mass spectrometer(ry)
Gen	Generation (as in Generation I, II, or III AHSSs)
GE	General Electric
GDIS	Great Designs in Steel
GGA	generalized gradient approximation
GHG	greenhouse gas
GJ	gigajoule(s)
GLD	generalized lambda distribution
GM	General Motors Corporation
GMAB	gas metal arc brazing
GMAS	Group Membership Authorization Service
GMAW	gas metal arc welding
GMSE	generalized mean square error
GMT	governing metal thickness
GND	geometrically necessary dislocation

GOS	grain orientation spread
GP	Guinier-Preston/Gaussian process
GPEC	Global Plastics Environmental Conference
gpm	gallon(s) per minute
GRAM	grid resource allocation management
gridFTP	grid file transfer protocol
GT4	Global Toolkit 4
GUI	graphical user interface
GWP	global-warning potential
h, hr	hour
H	hydrogen
HAZ	heat-affected zone
HBA	hydroxybenzoic acid
HCF	high-cycle fatigue
HCl	hydrochloric acid
hcp	hexagonal close-packed
HDG	heavy duty galvanized/hot-dip galvannealed (galvanized)
HDH	hydride-dehydride
HDPE	high-density polyethylene
HDPE	high-density polyethylene
HEC	high elongation core
HEEDS	Hierarchical Evolutionary Engineering Design System
Hz	hertz
HEXRD	high-energy X-ray diffraction
HFVFSI	High Fiber Volume Fraction Sequential Inclusion
HIMAC	high-integrity magnesium automotive castings
HiMECC	Hierarchical, Micro-Experimental and Computational Characterization
HIPing	hot isostatic pressing
HIPS	high-impact polystyrene
HMPP	high-modulus polypropylene
HNA	hydroxynaphthoic acid.
HPDC	high-pressure die casting
HPLC	high-performance liquid chromatography
hr	hot rolling
HS	high-spin
HSB	hot-stamped boron
HSBS	hot-stamped boron steel
HSLA	high-strength, low-alloy
HSS	high-strength steel
HTML	High-Temperature Materials Laboratory
HTTP	hypertext transfer protocol
H/V	Holloman/Voce
HWL	hardwood lignin
IA	indentation area
IABC	International Automotive Body Congress
IAFR	integrated amplified-frequency ratio
ICME	Integrated Computational Materials Engineering
ICP/MS	induction-coupled plasma/mass spectroscopy
ID	indentation depth/inner diameter

IDDRG	International Deep Drawing Research Group
IF	interstitial-free
IIHS	Insurance Institute for Highway Safety
IISI	International Iron & Steel Institute
IMR	Institute for Metal Research
in	inch(es)
I/O	input/output
IP	integration points/intellectual property
IPT	in-plane transverse
IQ+T	isothermal quench and tempering
IR	infrared
IS	importance sampling
ISO	International Standards Organization
ISRI	Institute of Scrap Recycling Industries
ISV	internal state variable
IT	information technologies
ITC	independent technical consultant
ITP	International Titanium Powder
J2EE	Java 2 Platform, Enterprise Edition
JBI	Java Business Integration
JCI	Johnson Controls, Inc.
JD	Job Descriptor
JMS	Java Message Service/Job Metadata Service/job monitoring service
jpm	jobs per minute
JSDL	Job Submission Description Language
JSS	job status service/Job Submission Service
K	hydraulic permeability
kA	kiloampere(s)
KBFB	kenaf-bast-fiber bundle
Kg, kg	kilogram(s)
kHz	kilohertz
Kip, kip	kilopound(s) (1 kilopound = 1,000 pounds)
kJ	kilojoule(s)
km	kilometer(s)
kN	kiloNewton(s) (force unit)
KR	Kriging
Ksi	kips per square inch
lb(s).	pound(s)
LBNL	Lawrence Berkeley National Laboratory
LC	long crack
LCA	life-cycle analysis
LCF	low-cycle fatigue
LCCF	low-cost carbon fiber/Low Cost Carbon Fiber (initiative)
LCI	life-cycle inventory
LCM	liquid composite molding
LDA	local-density approximation
LDH	limited dome height
LDPE	low-density polyethylene

LEAP	local-electrode atom probe
LFI	long fiber injection
LFI-PUR	Long Fiber Injection - Polyurethane
LFT	long fiber thermoplastic
LHS	Latin Hypercube Sampling
LIBS	laser-induced breakdown spectroscopy
LM	Lightweighting Materials
LPPM	low-pressure permanent mold
LPS	liquid phase sintering
LRDV	large rear-drive vehicle
LS	lap-shear/low-spin
LSF	laser shock forming
LSEM	large-strain extrusion machining
LSF	laser shock forming
LSMC	laminated sheet molding compound
LSTC	Livermore Software Technology Corporation
LTC	large thin casting
LU	laser ultrasonics
LW	laser-welded
LWFS	Lightweight Front Structure
m	meter(s)
M	million (used with dollar sign and numeral)
M&P	material and process
MA	methyl acetate
MAG	microwave-assisted gasification
MAP	microwave-assisted plasma
MBC	main bearing cap
MC	Monte Carlo/moisture content
MCS	Monte-Carlo simulation
MD	molecular dynamics
MDS	Multi-scale Design System
MEAM	modified embedded-atom method
MEARS	Mass Efficient Architecture for Roof Strength
MEKP	methyl ethyl ketone peroxide
MENA	Magnesium Elektron of North America
meV	millielectron volt(s)
MFE	magnesium front end
MFEDD	Magnesium Front End Design and Development (AMD603—USAMP project)
MFERD	Magnesium Front End Research and Development (AMD604—USAMP project)
MFG	molded fiberglass
MFR	melt flow rate
Mg	magnesium
MHz	megahertz
MI	melt index
MIG	metal inert gas
MIT	Massachusetts Institute of Technology
min	minute(s)
MIST	Metal Infusion Surface Treatment

M-K	Marciniak-Kuczynski
ml	milliliter(s)
mm	millimeter(s)
MMI	Michigan Molecular Institute
MMV	multi-material(s) vehicle
MOE	modulus of elasticity
MOO	multi-objective optimization
MOR	modulus of rupture
Mn	manganese
MnS	manganese sulfide (sulphide)
Mo	molybdenum
MPa	megapascal(s)
MPCC	Magnesium Powertrain Cast Components
MPIE	Manufacturing Process Induced Effects
MPIF	Metal Powder Industries Federation
MPP	most probable point of failure
MPS	material and process system
MPT	multipurpose Test Ware
MR&TD	Magnesium Research and Technology Development
MRI	Magnesium Research Institute
ms	millisecond(s)
MS	mass spectroscopy/mass spectra/characterized length scale of interaction with Microstructural Features/martensitic steel/Master of Science
MSC	microstructurally small crack
MSF	multistage fatigue
MSST	Mississippi State University
MS&T	Materials Science and Technology
MTL	Materials Technology Laboratory
MTT	Materials Technical Team (FreedomCAR)
MWS	minimum weld size
MWV	MeadWestvaco Corporation
N	Newton
N/D or N.D.	not detected
NA	numerical aperture/North America(n)
NADCA	North American Die Casting Association
NASA	National Aeronautics and Space Administration
NC	numerical control/neighborhood compliance
NCAP	New Car Assessment Program
NCC	National Composite Center
ND	normal direction
NDE	nondestructive evaluation
NDI	nondestructive inspection
NDT	nondestructive testing
NEXAFS	near-edge X-ray absorption fine structure (spectroscopy)
NFC	natural-fiber composite
NHTSA	National Highway Transportation Safety Administration
Ni	nickel
NiMH	nickel-metal hydride
NIOSH	National Institute for Occupational Health and Safety
NIST	National Institute for Standards and Technology

NIT	nanoindentation test
NIR	near infrared
nm	nanometer(s)
Nm	Newton meter(s) (measure of force/torque)
NM	nonmagnetic
NMR	nuclear magnetic resonance
NOx	nitrogen oxides
NPC	natural-fiber polymer (polyolefin) composite
NPSS	nano-precipitate-strengthened steel
NRT	National Recovery Technologies, Inc.
NSF	National Science Foundation
NTRC	National Transportation Research Center
NUCAPT	Northwestern University Center for Atom Probe Tomography
NVH	noise, vibration, and harshness
NVT	number-volume-temperature
NWU	Northwestern University
O	oxygen
OD	outside diameter
ODB	oven-dry-basis/Offset Deformable Barrier
OEM	original equipment manufacturer
OFAT	one-factor-at-a-time
OFHC	oxygen-free high-conductivity
OFI	offset frontal impact
OGSA	Open Grid Services Architecture
OGSA-DAI	Open Grid Services Architecture Data Access and Integration
OM	optical microscope/microscopy; optimum microstructure
ORNL	Oak Ridge National Laboratory
OSU	Ohio State University
P	phosphorous
P4	programmable powdered preform process
PA	phased-array/prealloyed
PAH	polycyclic aromatic hydrocarbon
PAN	polyacrylonitrile
PAPRICAN	Pulp and Paper Research Institute of Canada
PAW	projector augmented wave
PBDE	polybrominated diphenyl ether
PBS	portable batch system
PBT	polybutylene terephthalate
PC	polycarbonate
PCB	polychlorinated biphenyl
PCBN	polycrystalline cubic boron nitride
PDF	probability distribution function/probability density function
PE	polyethylene
PET	polyethylene terepthalate
PFOA	perfluorooctanoic acid
PFOS	perfluorooctanesulfonates
phr	parts per hundred resin
PI	principal investigator
PIM	powder injection molding/powder impression molding

PIV	particle image velocimetry
PLC	Portevin-Le Châtelier (effect)
PM	permanent mold; powder metal/metallurgy
PMC	polymer-matrix composite
P/M	powder metal/powder metallurgy
PMCT	probabilistic microstructural continuum theory
PNGV	Partnership for a New Generation of Vehicles
PNNL	Pacific Northwest National Laboratory
POCP	photochemical ozone creation potential
PP	polypropylene
PP/PE	polypropylene/polyethylene
PPF	pulse pressure forming
PPM, ppm	part(s) per million
PPO	polyphenylene oxide
PR	polynomial regression
ps	picosecond(s)
PS	polystyrene
PSC	Project Steering Committee (MFERD)/physically small crack
psi	pounds (force) per square inch
PSIA	pounds per square inch absolute
PSN	particle stabilized nucleation
PSO	particle swarm optimization
PSP	processing-structure-property
PTC	Project Technical Committee (MFERD)/project technical coordinator
PTFE	polytetrafluoroethylene
PU	polyurethane
PURCC	Polyurethanes Recycle and Recovery Council
PVC	polyvinyl chloride
PW	plain weave
Py-GC/MS	pyrolysis-gas chromatography/mass spectra
Q&P	quenching and partitioning
Q-P-T	quenching, partitioning, and tempering
QA	quality assurance
QRM	quarterly review meeting
QT	quench temperature
R	stress ratio/bend radius
R&D	research and development
R&R	repeatability and reproducibility
RA	relative accuracy
RaFC	random-fiber composite
RBDO	reliability-based design optimization
RBF	radial basis function
RD	rolling direction
RFQ	request for quote/quotation)
RH	relative humidity
RI	resonance inspection
RLS	Raman light scattering
RMS	root mean square
RMSE	root mean square error

ROS	reactive oxidative species
RPM, rpm	revolutions/rotations per minute
RS	response surface
RSA	Random Sequential Adsorption
RSC	rear-seal carrier/reduced strain closure
RSL	RAISE specification language
RSM	response service methodology/response surface methodology
RSW	resistance spot weld/welding
RT	room temperature
RTOS	real-time operating system
RUC	representative unit cell
RVE	representative volume element
RWD	rear-wheel drive
s, sec	second(s)
S	sulfur
SAE	Society of Automotive Engineers
SAML	Security Assertion Markup Language
SBC	single-board computer
SBIR	Small Business Innovation Research
sc	simple cubic
SCC	stress-corrosion cracking
SCMD	Structural Cast Magnesium Development
SD	standard deviation
SDAS	secondary dendrite-arm spacing
SE	strain energy
SEA	specific energy absorption
Seagull	a trademark of Herrick Scientific Products, Inc.
SEL	solvent extracted lignin
SEM	scanning electron microscope/microscopy
SES	Society of Engineering Science
SF_6	sulfur hexafluoride
SFC	single fiber composite
SG	specific gravity
Sh	rolled sheet per plate
SHB	split Hopkinson bar
SHPB	split-Hopkinson pressure bar
Si	silicon
Si_3N_4	silicon nitride
SIMP	solid isotropic material with penalization
SIMS	secondary ion mass spectrometry
SIR	seat with integrated restraint
SLC	Sub-Liquidus Casting
SLI	starting, lighting, ignition
SLS	super lap shear
SMC	sheet molding compound
Sn	tin
SO_2	sulfur dioxide
SOA	service-oriented architecture
SOAP	simple object access protocol
SOC	substance of concern

SOP	structural oil pan/standard operating procedure
SOPO	Statement of Program Objectives
SORM	second order reliability method
SORPAS	Simulation and Optimization of Resistance, Projection, and Spot Welding Processes
SOW	statement of work
SP	single phase
SPARC	Strategic Planning and Review Committee
SPBK	support bracket
SPD	severe plastic deformation
SPE	Society of Plastics Engineers
SPF	superplastic forming
SPR	self-piercing rivet/riveting
SQL	structured query language
SRB	Storage Resource Broker
SRCLID	Southern Regional Center for Lightweight Innovative Design
SRIM	structural reaction injection molding
STD	standard seat (without integrated restraint, cf "SIR" above)
STL	sound transmission loss
STTR	Small Business Technology Transfer
SUV	sport-utility vehicle
SVDC	super vacuum die casting
SVE	statistical volume element
SVR	support vector regression
SWE	spot weld element
SWL	softwood lignin
SWSG	Structural Weld Sub-Group
t	ton/thickness
T	temperature/ton(s)
T	tension
T^3	time-temperature-tension
TA	transmission area
TAPPI	(previously "the Technical Association of the Pulp and Paper Industry, now just "TAPPI")
TBF	TRIP aided bainitic ferrite
T/C	tension/compression
T-CAM	Tuskegee Center for Advanced Materials
TC	transcrystalline region
TD	transverse to rolling direction/transverse direction
TE	thermoelectric
TEM	transmission electron microscope/microscopy
T_g	glass transition temperature
TGA	thermogravimetric analysis/analyzer
ThD	thermal drilling
Ti	titanium
TiB_2	titanium diboride
$TiCl_4$	titanium tetrachloride
TIG	tungsten inert gas
TLCP	thermotropic liquid-crystal polymer
TMAC	Test Machine for Automotive Crashworthiness

TMCP	thermomechanically controlled processing
TMP	thermomechanical pump/thermomechanical processing
TMS	The Minerals, Metals & Materials Society
TPI	Troy Polymers, Inc.
TPO	thermoplastic olefins
TRC	textile reinforced composites
TRC-NCMS	Technologies Research Corporation of the National Center for Manufacturing Sciences
TRIP	transformation-induced plasticity
TRS	transverse rupture strength
TS	tensile strength/thick swelling
TT	through thickness
TTT	time-temperature-transformation
TTU	through-transmission ultrasonics
TWB	tailor-welded blank
TWI	thin-twill-weave/thermal-wave imaging
TWII	thick-twill-weave
TWIP	twinning-induced plasticity
TWT	tailor-welded tube
TYE	tensile, yield, and elongation
U.S.	United States
UAB	University of Alabama-Birmingham
UCF	University of Central Florida
UD	unidirectional
UDRDF	uncertainty analysis using dimension reduction and distribution fitting
UDRI	University of Dayton Research Institute
UFG	ultrafine grain
UHMW	ultra-high molecular weight
UHSS	ultra high-strength steel
UI	user interface
UK	United Kingdom
ULC	ultra-large casting
UMF	uncertainty magnification factor
UPC	uncertainty percentage contribution
UPE	Unsaturated Polyester
URI	uniform resource identifier
URL	uniform resource locator
USAMP	United States Automotive Materials Partnership
USCAR	United States Council for Automotive Research
USPTO	United States Patent Office
USW	ultrasonic welding
UT	University of Tennessee
UT-PE	ultrasonic testing using pulse/echo
UTS	ultimate tensile strength
UT-TT	ultrasonic testing using through-transmission
UV	ultraviolet
UV-Vis	ultraviolet-visible
UVA	University of Virginia

V	volt(s)
VA	vinyl acetate
V&V	verification and validation
VARTM	vacuum-assisted resin-transfer molding
VPB	viscous pressure bulge
VE	vinylester
VGCNF	vapor grown carbon nanofiber
VOMS	Virtual Organization Membership Service
VPA	volume per annum
VRP	Vehicle Recycling Partnership
VT	Vehicle Technologies
VTP	Vehicle Technologies Program
VW	Volkswagen
W	watt(s)
WA	water absorption
W/L	ratio of specimen width to length
WPC	wood-fiber-reinforced polymer composite
WRC	woodfiber-reinforced composites
WSDL	Web Service Definition/ Description Language
wt	weight
wt %	weight percent
WY	Weyerhaeuser Company
X-EDS	X-ray-electron diffraction spectroscope/spectroscopy/spectrometer
XML	eXtensible Markup Language
XPS	X-ray photoelectron spectroscopy/spectrometer/spectrometry
XRD	X-ray diffraction
XRS	X-ray photoelectron spectroscopy
YAG	yttrium-aluminum-garnet
YE	year-end
YS	yield strength
Zn	zinc
Zr	zirconium

This document highlights work sponsored by agencies of the U.S. Government. Neither the U.S. Government nor any agency thereof, nor any of their employees, makes any warranty, express or implied, or assumes any legal liability or responsibility for the accuracy, completeness, or usefulness of any information, apparatus, product, or process disclosed, or represents that its use would not infringe privately owned rights. Reference herein to any specific commercial product, process, or service by trade name, trademark, manufacturer, or otherwise does not necessarily constitute or imply its endorsement, recommendation, or favoring by the U.S. Government or any agency thereof. The views and opinions of authors expressed herein do not necessarily state or reflect those of the U.S. Government or any agency thereof.

Printed on
recycled
paper

DOE/CM-3026

A Strong Energy Portfolio for a Strong America

Energy efficiency and clean, renewable energy will mean a stronger economy, a cleaner environment, and greater energy independence for America. Working with a wide array of state, community, industry, and university partners, the U.S. Department of Energy's Office of Energy Efficiency and Renewable Energy invests in a diverse portfolio of energy technologies.

For more information contact:
EERE Information Center
1-877-EERE-INF (1-877-337-3463)
www.eere.energy.gov